AM3P 2025

Advances in Materials and Pavement Performance Prediction

Advances in Materials and Pavement Performance Prediction IV

Editors

Lukas Eberhardsteiner
Bernhard Hofko
Ronald Blab

TU WIEN · Bau & Umwelt _transport

CRC/TRR 339 · Digital Twin Road

Advances in Materials and Pavement Performance Prediction IV

Editors

Lukas Eberhardsteiner
Institute of Transportation, TU Wien, Austria

Bernhard Hofko
Institute of Transportation, TU Wien, Austria

Ronald Blab
Institute of Transportation, TU Wien, Austria

AM3P 2025
4ᵗʰ International Conference on Advances in Materials and Pavement Performance Prediction
7-9 May 2025, Vienna, Austria

ORGANISATION

CHAIRS

Ronald Blab, TU Wien, Austria

Lukas Eberhardsteiner, TU Wien, Austria

Bernhard Hofko, TU Wien, Austria

Michael Kaliske, TU Dresden, Germany

STANDING INTERNATIONAL ADVISORY COMMITTEE

CHAIRS

Amit Bhasin, The University of Texas at Austin, USA

Eyad Masad, Texas A&M University, Qatar

Tom Scarpas, TU Delft, The Netherlands & KU, Abu Dhabi

MEMBERS

Kumar Anupam, TU Delft, The Nederlands
Panos Apostolidis, University of Texas at Austin, USA
Amit Bhasin, University of Texas at Austin, USA
Bjorn Birgisson, University of Georgia, USA
Ronald Blab, TU Wien, Austria
Andrew Braham, University of Arkansas, USA
Silvia Caro, Los Andes University, Colombia
Bora Cetin, Michigan State University, USA
Karim Chatti, Michigan State University, USA
Matthew Corrigan, Federal Highway Admin., USA
Eshan Dave, University of New Hampshire, USA
Lukas Eberhardsteiner, TU Wien, Austria
Michael Greenfield, University of Rhode Island, USA
Elie Hajj, University of Nevada, USA
Hamzeh Haghshenas, Univ. of Nebraska-Lincoln, USA
Theuns Henning, The University of Auckland, NZL
Jaime Hernandez, Marquette University, USA
Bernhard Hofko, TU Wien, Austria
Baoshan Huang, University of Tennessee, USA
Tatsuya Ishikawa, Hokkaido University, Japan
Behnam Jahangiri, Genex Systems/TFHRC, USA
Denis Jelagin, KTH Royal Inst. of Technology, Sweden
Michael Kaliske, TU Dresden, Germany
Lev Khazanovich, University of Pittsburgh, USA

Yong-Rak Kim, Texas A&M University, USA
Murali Krishnan, Indian Inst. of Technology Madras, India
Emin Kutay, Michigan State University, USA
Nizar Lainef, Michigan State University, USA
Zhen Leng, The Hong Kong Polytechnic University, China
Pengfei Liu, RWTH Aachen University, Germany
Rajib Mallick, The University of Texas at El Paso, USA
David Mensching, Federal Highway Administration, USA
Mahdi Nasimifar, McLean, USA
Soheil Nazarian, The University of Texas at El Paso, USA
Jose Norambuena-Contreras, Swansea University, UK
Markus Oeser, BASt, Germany
Anand Puppala, Texas A&M University, USA
Nadarajah Sivaneswaran, Federal Highway Admin., USA
Wynand Steyn, University of Pretoria, South Africa
Jamilla Teixeira, University of Nebraska-Lincoln, USA
Erol Tutumluer, Univ. of Illinois at Urbana-Champaign, USA
Shane Underwood, North Carolina State University, USA
Katerina Varveri, TU Delft, The Nederlands
Kamilla Vasconcelos, University of Sao Paulo, Brazil
Hao Wang, State University of New Jersey, USA
Claudia Zapata, Arizona State University, USA
Xingyi Zhu, Tongji University, China

SCIENTIFIC COMMITTEE

S. Farhad Abdollahi, Genex Systems, Turner-Fairbank Highway Research Center, United States
Quentin Félix Adam, RWTH Aachen, Germany
Yaw Okyere Adu-Gyamfi, University of Missouri - Columbia, United States
Taha Ahmed
Mohammad Al-Assi
Amir Alavi, University of Pittsburgh, United States
Stefan Alber, Universität Stuttgart, Germany
Erik Alpizar-Reyes, Universidad del Bío-Bío, Chile
Osama Altarawneh, HVJ Associates, United States
Allex Alvarez, Universidad Industrial de Santander, Colombia
Garcia Hernandez Alvaro, RWTH Aachen, ISAC, Germany
Adrian Andriescu
Kumar Anupam, TU Delft, Netherlands
Panos Apostolidis, The University of Texas at Austin, United States
Edith Arambula-Mercado, Texas A&M Transportation Institute, United States
Akash Bajaj, University of Illinois, United States
Jose Tadeu Balbo, University of Sao Paolo, Brazil
Gabriel Bazi, pulsuus, llc, United States
Birgit Beckmann, TU Dresden, Germany
Atanu Behera, Indian Institute of Science Bangalore, India
Mahsa Beizaei
Amit Bhasin, The University of Texas at Austin, United States
Bjorn Birgisson, University of Georgia, United States
Ronald Blab, TU Wien, Austria
Anita Blasl, Technische Univerität Dresden, Germany
Stefan Böhm, TU Darmstadt, Germany
Paul Gustav Bolz, TU Dresden, Germany
Jan-Hinrik Borchers, Federal Highway and Transport Research Institute (BASt), Germany
Andrew Braham, University of Arkansas, United States
Lelio Brito, UFRGS, Brazil
James Bryce, West Virginia University, United States
Johannes Büchner, TU Braunschweig, Germany
Francesco Canestrari, Università Politecnica delle Marche, Italy
Augusto Cannone Falchetto, University of Padova, Italy
Gustavo Canon Falla, TU Dresden, Germany
Fabrizio Cardone, Università Politecnica delle marche, Italy
Silvia Caro, Universidad de los Andes (Colombia), Colombia
Veronica TF Castelo Branco, Federal University of Ceara, Brazil
Daniel Castillo, Michigan State University, Finland
Cassie Castorena, North Carolina State University, United States
Bora Cetin, Michigan State University, United States
Halil Ceylan
Karim Chatti, Michigan State University, United States
Ruiqi Chen
Xianhua Chen, Southeast University, China
Huailei Cheng, Tongji University, China
Ahmad Chihadeh, TU Dresden, Germany
Rami Chkaiban
Venkaiah Chowdary, National Institute of Technology Warangal, India
Erdem Coleri, Oregon State University, United States
Jose L Concha, Universidad del Bio-Bio, Chile
Matthew Corrigan, Federal Highway Administration, United States
Eshan Dave, University of New Hampshire, United States
Katie DeCarlo, Heritage Research Group, United States
Yared Dinegdae, vti, Sweden
Bhanoj Dokku, Cube Highways, India
Qiao Dong, Southeast University, China

Charles Ambrose Donnelly, Texas A&M University, United States
Lukas Eberhardsteiner, TU Wien, Austria
Mohamed ElGawady
Nicole Elias, California State Polytechnic Pomona, United States
Michael Elwardany, Florida State University, United States
Alexis Enriquez-Leon, Federal University of Rio de Janeiro, Brazil
Yulou Fan, Southeast University; The Hong Kong Polytechnic University, China
Adalberto Leandro Faxina, University of Sao Paulo, Brazil
Gilda Ferrotti, Università Politecnica delle Marche, Italy
Chaoliang Fu, RWTH AACHEN UNIVERSITY, Germany
Tien Fang Fwa, National University of Singapore, Singapore
Nishant Garg
Arpan Ghosh
Pratanu Ghosh
Pawel Gierasimiuk, Bialystok University of Technology, Poland
Franziska Gober, TU Wien, Austria
Arunkumar Goli, Rowan University, United States
Amir Golroo, University of Oulu, Finland
Michael Greenfield, University of Rhode Island, United States
Saqib Gulzar, Colorado State University Pueblo, United States
Meng Guo, Beijing University of Technology, China
Lu Guoyang, City University of Hong Kong, Hong Kong
Aakash Gupta, CSIR-Central Road Research Institute, India
Ankit Gupta, IIT (BHU) Varanasi, India
Jhony Habbouche, Asphalt Institute, United States
Syed Haider, Michigan State University, United States
Elie Hajj, University of Nevada, Reno, United States
Ramez Hajj, University of Illinois Urbana-Champaign, United States
Andrew Hanz, MTE Services, United States
Reem Hassan
Theuns Henning, The University of Auckland, New Zealand
Jaime Hernandez, Marquette University, United States
David Hernando, University of Antwerp, Belgium
Bernhard Hofko, TU Wien, Austria
Baoshan Huang, University of Tennessee, United States
Soohyok Im, TxDOT, United States
Tatsuya Ishikawa, Hokkaido University, Japan
Bernard Izevbekhai, Minnesota Department of Transportation, United States
Behnam Jahangiri, Turner Fairbank Highway Research Center (TFHRC), United States
Sean Jamieson, University of the Sunshine Coast, Australia
Angeli Jayme, Arizona State University, United States
Denis Jelagin, KTH Royal Institute of Technology, Sweden
Li Jenny, TxDOT, United States
Jiwang Jiang, Southeast University, China
Xi Jiang, The Hong Kong Polytechnic University, Hong Kong
Lakshmi Kakumanu, Hamad Bin Khalifa Univeristy, Qatar
Michael Kaliske, TU Dresden, Germany
Pravat Karki, TxDOT, United States
Mohamed Kastouri, RWTH Aachen, Germany
Derya Kaya Ozdemir, University of Warwick, United Kingdom
Farzan Kazemi
Kathryn Kennebeck, University of Pittsburgh, United States
Sadaf Khalighi, Tu Delft, Netherlands
Lev Khazanovich, University of Pittsburgh, United States
Yong-Rak Kim, Texas A&M University, United States
Dan King
Jayantha Kodikara
Satyavati Komaragiri, Indian Institute of Science, India
Santosh Reddy Kommidi, Texas A&M University, United States

Murali Krishnan, Indian Institute of Technology Madras, India
Kazuo Kuchiishi, Virginia Transportation Research Council, United States
Yogesh Kumbargeri, Western Research Institute, Austria
Muhammed Emin Kutay, Michigan State University, United States
Nizar Lajnef, Michigan State University, United States
Abinaya Lakshmi Narayanan, Indian Institute of technology Madras, India
Aaron Leavitt, FHWA, United States
Hyung Lee, Applied Research Associates, Inc., United States
Sabine Leischner, TU Dresden, Germany
Zhen Leng, The Hong Kong Polytechnic University, Hong Kong
Eyal Levenberg, Technical University of Denmark, Denmark
Danning Li, The Hong Kong Polytechnic University, Hong Kong
Hui Li, Tongji University, China
Jue Li, Chongqing Jiaotong University, China
Xuyang Li, Pennsylvania State University, United States
Yi Li, Delft University of Technology, Netherlands
Peng Lin, Rijkswaterstaat, Netherlands
Zengyao Lin, Institute of Highway Engineering, RWTH Aachen University, Germany
Jia Liu, Verkehrswegebau, TU Darmstadt, Germany
Pengfei Liu, RWTH Aachen University, Germany
Zhen Liu, Penn State University, United States
Davide Lo Presti, University of Palermo, Italy
Qing Lu, University of South Florida, United States
Yongjie Lu, China
Joacim Lundberg, Lund University, Sweden
Lili Ma, Delft University of Technology, Netherlands
Tao Ma
Rohit Maheshwari, DIT University, India
James W. Maina, University of Pretoria, South Africa
Rajib Mallick, The University of Texas at El Paso, United States
Athira Mangalath Shine, TU Dresden, Germany
Evangelos Manthos, Aristotle Univeristy of Thessaloniki, Greece
Eyad Masad, Hamad Bin Khalifa University, Qatar
Dave Mensching, Federal Highway Administration, United States
Miomir Miljković, University of Niš, Serbia
Johannes Mirwald, TU Wien, Austria
Deb Mishra, Oklahoma State University, United States
Kiran Mohanraj, The Transtec Group, United States
Juliana Montanez, Texas A&M University, United States
Raquel Moraes, NCAT, United States
Ali Morovatdar, ARA, United States
Hamad Bin Muslim, National Institute of Transportation, Pakistan
Atish Nadkarni, Engineering & Software Consultants, LLC., United States
Mahdi Nasimifar, Engineering & Software Eng, United States
Julia Neumann, Germany
Dujardin Niels Skov
M R Nivitha, PSG College of Technology, India
Jose Norambuena-Contreras, Swansea University, United Kingdom
Mohammad Notani
Markus Oeser, Federal Highway and Transport Research Institute, Germany
Egemen Okte
Eman Omairey, Teesside University, United Kingdom
Ghim Ping Ong, National University of Singapore, Singapore
Jian Ouyang
Hasan Ozer
A Padmarekha
Harsh Patel
Troy Pauli, HF Sinclair Parco Refining LLT, United States
Xinghai Peng, RWTH Aachen University, Germany

Martin Peyer, TU Wien, Austria
Georgios Pipintakos, University Antwerp & FWO, Belgium
Johannes Pistrol, TU Wien, Austria
Christina Plati
Maria Pomoni, National Technical University of Athens, Greece
Lily Poulikakos, Empa, Switzerland
Philipp Preinstorfer, TU Wien, Austria
Anand Puppala, Texas A & M University, United States
Vishnu R, India
Arbin Raj, Indian Institute of Technology Madras, India
Punyaslok Rath, University of Missouri, United States
Shisong Ren, University of Antwerp, Belgium
Marcos Rocha
Iran Gomes da Rocha Segundo, University of Minho, Portugal
Mrinali Rochlani, Indian Institute of Technology Madras, India
Jeffery Roessler
Silvio Roth, TU Wien, Austria
Neethu Roy, Mar Baselios College of Engineering and Technology (Autonomous), India
Eduardo J. Rueda, Pontificia Universidad Católica de Chile, Chile
Ignacio Nilo Ruiz-Riancho, RWTH Aachen, Germany
Nikhil Saboo, IIT Roorkee, India
Francisco Thiago Sacramento Aragão, Federal University of Rio de Janeiro, Brazil
Lucio Salles de Salles, Rochester Institute of Technology, United States
Catherine Sanchana, Indian Institute of Technology Madras, India
Diana Sanchez, AtkinsRealis, United Kingdom
IJS Sandeep, Indian Institute of Technology Madras, India
Joao Santos, University of Twente, Netherlands
Donia Savio
Paul Schoenauer, TU Wien: Technische Universitat Wien, Austria
Kairen Shen, Rutgers, United States
Shihui Shen
Xianming Shi
Xijun Shi, Texas State University, United States
Aditya Singh
Avishreshth Singh, Delft University of Technology, The Netherlands, Netherlands
Dharamveer Singh, India
Nadarajah Sivaneswaran, USDOT/Federal Highway Administration, United States
Rami Skaff, Applied Research Associates, United States
Mason Ridge Smetana, University of Pittsburgh, United States
Mark Snyder, Pavement Engineering and Research Consultants (PERC), LLC, United States
Mena Souliman, The University of Texas at Tyler, United States
Anand Sreeram, University of Nottingham, United Kingdom
Wynand Steyn, University of Pretoria, South Africa
Mayank Sukhija, Oregon State University, United States
Daquan Sun, China
Ehsan Tabasi
Jamilla Teixeira, University of Nebraska, United States
Senthil Thyagarajan
Amarjeet Tiwari, University of Arkansas, United States
Mahsa Tofighian
Kairat Tuleubekov
Erol Tutumluer, University of Illinois Urbana-Champaign, United States
Shane Underwood, NCSU, United States
Poornachandra Vaddy, Michigan State University, United States
Julie Vandenbossche, University of Pittsburgh, USA
Aikaterini Varveri, Delft University of Technology, Netherlands
Kamilla Vasconcelos, University of São Paulo, Brazil
Angelica Viana-Sepulveda, Universidad de los Andes, Colombia
William Villamil, University of Illinois at Urbana-Champaign, United States

Dawei Wang, Harbin Institute of Technology, China
Di Wang, University of Ottawa, Canada
Hainian Wang, Changan University, China
Hao Wang, Rutgers University, United States
Linbing Wang, University of Georgia, United States
Yuhong Wang
Christiane Weise, TU Dresden, Germany
Yong Wen
Stefan Werkovits, TU Wien, Austria
Greg White, University of the Sunshine Coast, Australia
Christopher Willams
Van den bergh Wim, University of Antwerp, Belgium
Michael P. Wistuba, Technische Universität Braunschweig, Germany
Ines Wollny, TU Dresden, Germany
Ben Worel, Minnesota Department of Transportation, United States
Feipeng Xiao, Tongji University, China
Lu Xiaohu, Nynas, Sweden
Liu Xueyan, TU Delft, Netherlands
Tianhao Yan, FHWA's Turner-Fairbank Highway Research Center, United States
Bin Yang, The Hong Kong Polytechnic University, Hong Kong
Jun Yang, Southeast University, China
Xu Yang, China
Linyi Yao
Farzad Yazdipanah, University of Nebraska-Lincoln, United States
Binbin Yin, Hong Kong, China
Fan Yin, National Center for Asphalt Technology, United States
Taesun You, TxDOT, United States
Zhanping You, Michigan Technological University, United States
Bin Yu
Miao Yu, Chongqing Jiaotong University, China
Shuai Yu, Penn State Altoona, United States
Zhao Yunpeng
Eyoab Zegeye
Waleed Zeiada
Alexander Zeißler, Dresden University of Technology, Germany
You Zhan
Cheng Zhang, Purdue University, United States
Hancheng Zhang, China
Jiake Zhang, China
Tianjie Zhang, Rutgers University, United States
Jitong Zhao, Institute of Construction Materials, Dresden University of Technology, Germany, Germany
Qingwen Zhou
Jiqing Zhu, Swedish National Road and Transport Research Institute (VTI), Sweden
Xingyi Zhu, Tongji University, China

CO-ORGANIZERS:

TU Wien
Institute of Transportation
https://www.tuwien.at/en/cee/transport/road

CRC/TRR 339
Digital Twin Road
https://www.sfbtrr339.de/en/

SPONSORS:

STRABAG SE
https://newsroom.strabag.com/en

GESTRATA
https://gestrata.at/

Österreichische Forschungsgesellschaft
Straße – Schiene - Verkehr
https://www.fsv.at/cms/start.aspx?LN=EN

VÖZ
Vereinigung der Österreichischen Zementindustrie
https://www.zement.at/

City of Vienna
https://www.wien.gv.at/english/

FQP
Forum Qualitätspflaster
https://fqp.at/forum-qualitatspflaster

INTERNATIONAL SUPPORTERS:

EUPAVE
European Concrete Paving Association
https://www.eupave.eu/

EAPA
European Asphalt Pavement Association
https://eapa.org//

TRB
Transport Research Board
https://www.nationalacademies.org/trb/transportation-research-board

APSE
Academy of Pavement Science and Engineering
https://apse.wildapricot.org/

CONTENTS

CONTENT OVERVIEW:

KEYNOTE ABSTRACTS

1.1 ADVANCES IN PAVEMENT ANALYSIS AND DESIGN METHODOLOGIES

1.2 ADVANCES IN THE MODELLING OF PAVEMENT CONSTRUCTIONS

1.3 MODELING, PERFORMANCE PREDICTION AND DESIGN OF RIGID PAVEMENTS

2.1 MODELING AND EXPERIMENTAL EVALUATION OF MOISTURE DAMAGE IN ASPHALT MIXTURES

2.2 MATERIALS TESTING AND MODELING: CALIBRATION, VERIFICATION AND VALIDATION

3.1 CHEMO-MECHANICAL AND OTHER TOOLS FOR PERFORMANCE EVALUATION OF ASPHALT BINDERS

3.2 SELF-HEALING/REJUVENATION METHODOLOGIES FOR EXISTING PAVEMENT STRUCTURES

4.1 PAVEMENT SURFACE CHARACTERISTICS FOR SAFETY

4.2 MODELING AND MONITORING TECHNIQUES FOR VEHICLE-PAVEMENT INTERACTION

5.1 SUSTAINABLE AND RESILIENT PAVEMENTS AND MATERIALS

5.2 ENVIRONMENTAL IMPACT & ECONOMIC LIFE CYCLE PERFORMANCE OF PAVEMENTS

7.2 AI AND MACHINE LEARNING TECHNOLOGIES IN PAVEMENT ENGINEERING AND PERFORMANCE PREDICTION

KEYNOTE ABSTRACTS

Leveraging Molecular Dynamics to Validate Mechanisms of Bond Strength and Moisture Resistance in Asphalt Composites

Dallas Little
Texas A&M University, USA

ABSTRACT: The composite that provides the major structural component of trillions of dollars of pavement infrastructure throughout the world is a complex blend of components. These include at a minimum the asphalt binder or bitumen and each mineral aggregate comprising both a larger, structural component and a smaller mineral filler component. The APSE distinguished lecture will describe how atomistic modeling provides a deeper understanding of how mineral fillers interact with the asphalt binder to form a robust, tough, and resilient mastic. Specifically, atomistic modeling validates experimental results that define how specific mineral fillers such as hydrated lime bond with specific asphalt moieties to form a stronger mastic with the ability to increase fracture toughness, aid damage recovery or healing and resist moisture damage. The atomistic modeling paints a picture of asphalt mastic comprising mineral filler ranging from only a few microns to as large as one hundred microns surrounded by a region of asphalt moieties bonded to the mineral inclusions. The moieties that interact with the calcium hydroxide filler, for example, introduce a "halo effect" surrounding the filler. This "halo region" can absorb and dissipate crack energy toughening the mastic and even control crack tip size to a level consistent with microcrack healing. The adsorption of specific moieties allows other moieties to migrate toward the interface with larger mineral aggregate inclusion and form a more tenacious and durable bond, more resistant to debonding in the presence of moisture. Atomistic modeling supports decades of key research by experts at Western Research Institute, at Texas A&M and in France. The lecture also describes how free energies of dissociation are used to characterize the nature, strength, and durability of bonds. The atomistic modeling results correlate with thermodynamic calculations derived from experimental constants and are consistent with infrared spectrometric data.

Digital Twin of the Road – Recent Advances, Potentials and Challenges

Michael Kaliske
TU Dresden, Germany

ABSTRACT: The road infrastructure, which serves as a crucial foundation of our modern society, is currently facing various challenges, including increasing traffic and loads, damage and necessary maintenance, as well as the need to conserve energy and resources. Additional challenges are expected in the future due to mobility changes, autonomous driving, and climate change. To address these challenges, there is a strong demand for more sustainable and long-lasting roads, coupled with an optimized design and operational approach. On the other hand, the potential of digitalization has so far been rarely utilized in the design and operation of road systems. To tackle these issues, the interdisciplinary research center (SFB/TRR 339) hosted at TU Dresden and RWTH Aachen is currently focused on the development of a digital twin of the road. The presentation covers the recent research on the required sub-models and components, such as physical models for tire-road interaction, data generation and collection from various sensors, the development of a geographic information system, and first approaches for linking available sensor data with corresponding models.

Chemomechanics and Data-driven Modelling to Understand and Predict Paving Material Behaviour

Katerina Varveri
TU Delft, The Netherlands

ABSTRACT: Advances in pavement engineering rely more and more on our ability to understand and predict the behaviour of complex material systems, including recycled, modified, and bio-based binders. At the same time, large volumes of experimental and field data are being generated and yet remain underutilised in the design and optimisation of infrastructure materials.
This keynote speech highlights the importance of integrating chemomechanical understanding with data-driven modelling to improve the accuracy and reliability of performance predictions. By combining physical insights with statistical learning and uncertainty quantification, we can develop models that capture both performance trends and the underlying mechanisms of material behaviour. By bringing data and fundamental understanding together, we can go beyond characterisation, using this synergy to learn from materials more effectively and engineer systems that are more durable, circular, and resilient.

1.1

ADVANCES IN PAVEMENT ANALYSIS AND DESIGN METHODOLOGIES

Effects of Heavy Vehicle Lateral Distribution on Pavement Service Life

A. Blasl*[1], T. Roggendorf*[3], W. Uhlig*[2], T. Kathmann*[3], Alexander Zeißler*[1]

*[1] *Institute for Pavement and Urban engineering, Technical University of Dresden, Dresden, Germany*

*[2] *Uhlig & Wehling GmbH Ingenieurgesellschaft, Mittweida, Germany*

*[3] *DTV-Verkehrsconsult GmbH, Aachen, Germany*

ABSTRACT: This paper presents selected results of an interdisciplinary research project (Uhlig et al. 2023) on the measurement and evaluation of the lateral distribution of heavy vehicles in dependence of lane width and rut depth, and the subsequent implementation of the analysed results in asphalt pavement design procedures to determine service life and failure rates according to the German design procedures. The following explanations focus on the influence of lane width and rut depth on the lateral distribution of heavy vehicles, the adaptation of known design procedures and finally the quantification of the effect of considering the lateral distribution on the calculated service life.

1 INTRODUCTION

Known design methods assume a guided traffic flow. However, when traffic is distributed across the lanes, the load and consequently the resulting stress in the pavement structure is also distributed.

For design purposes, generally only heavy goods vehicles are relevant.

In general, it is assumed that the lateral distribution of vehicles depends primarily on the carriageway width and any potential ruts.

To develop standardized lateral distributions for design methods, it is therefore necessary to first investigate whether there is a correlation between road characteristics and the qualitative behavior of lateral distributions.

2 MEASURING SYSTEM

To determine meaningful lateral distributions, it is essential to accurately measure the position of the wheels of relevant vehicles. For this purpose, a suitable measurement system was developed, which can be installed outside the carriageway without influencing the drivers.

With the developed system, continuous measurements were taken over a one-week period at each investigated section. Using this measurement system and the developed evaluation methodology, wheel positions within the lane cross-section can be determined with a resolution of 5 cm.

3 TEST SECTIONS

The test sections were only selected on straight sections of road (no curves, no built-up areas). In total, 13 sections were evaluated, consisting of 11 asphalt and 2 concrete pavements. The sections were chosen to include different classes of lane widths and rut depths, each in accordance with the German regulations (Figure 1, Table 1). Concrete pavements generally have no ruts and are typically used for wider, more heavily trafficked roads.
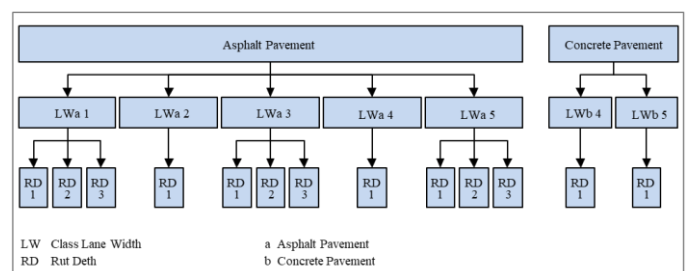
Figure 1. Test sections depending on lane width and rut depth.

Table 1. Classes of lane width and rut depth.

Class	Lane Width [m]	Class	Rut depth [mm]
LW 1	< 2,50	RD 1	0 - 1,2
LW 2	≥ 2,50; < 2,75	RD 2	8,5 - 11,5
LW 3	≥ 2,75; < 3,25	RD 3	> 17
LW 4	≥ 3,25; < 3,75		
LW 5	≥ 3,75		

4 LATERAL DISTRIBUTIONS

In general, the lateral distributions were recorded separately for both front wheels and differentiated according to single and dual tyres.

In the next step, double-tyred wheels were assumed to be single-tyred wheels before a distribution for both front wheels was determined for each of the 13 test sections.
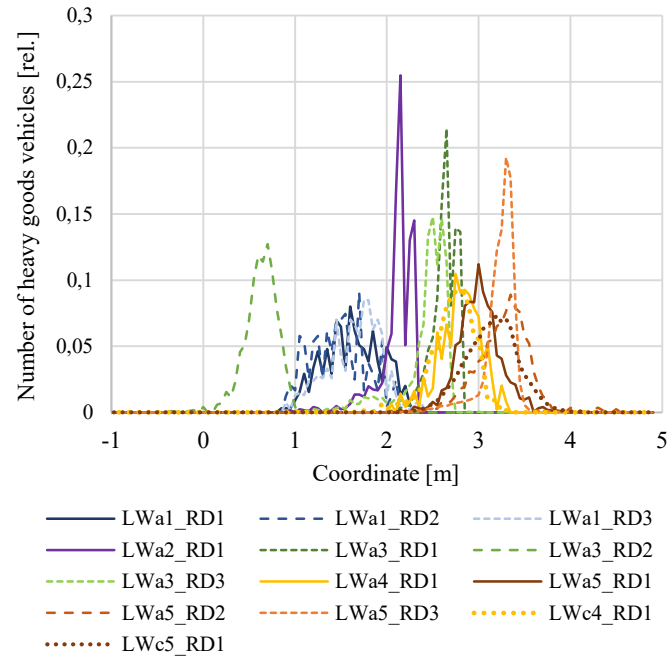
Figure 2. Lateral distributions of heavy vehicles in cross-section; representation of relative values.
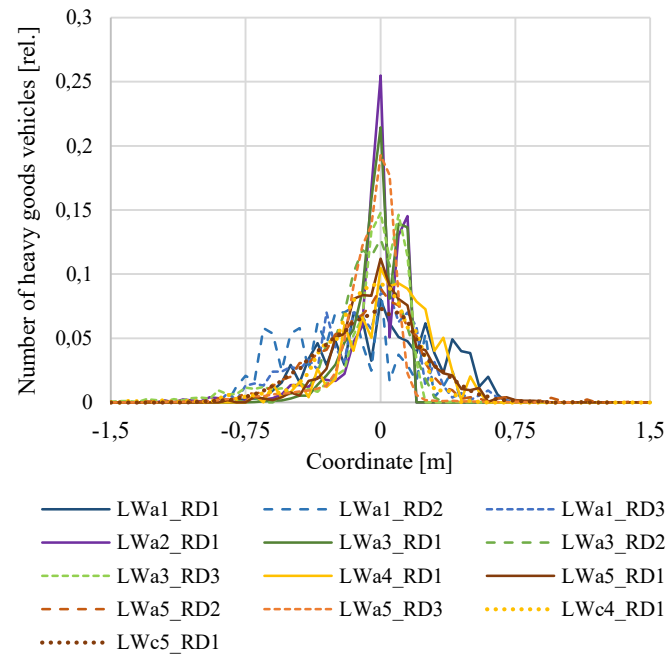
Figure 3. Normalised lateral distributions of heavy vehicles in cross-section; representation of relative values.

Roads of different widths generally represent different road categories. Consequently, the individual test sections differ significantly in terms of the number of heavy goods vehicles counted. Thus, for better

comparison, normalized distributions are presented in Figure 2. Therefore, the sum of the frequencies under each graph is equal to one. The same color class represents the same carriageway width, while the same line type corresponds to the same rut depth.

As the individual sections have different widths, the distributions are located differently in the cross-section (x-coordinate). Consequently, in Figure 3, all distributions have been shifted so that their respective maximums are aligned at zero. This allows for better comparability.
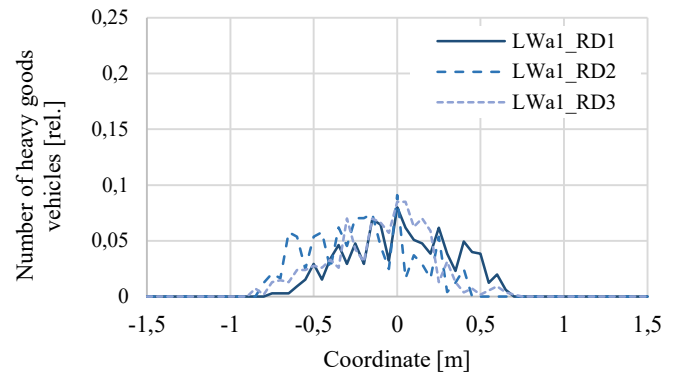
Figure 4. Normalised lateral distributions of heavy vehicles in cross-section; representation for the smallest lane width.
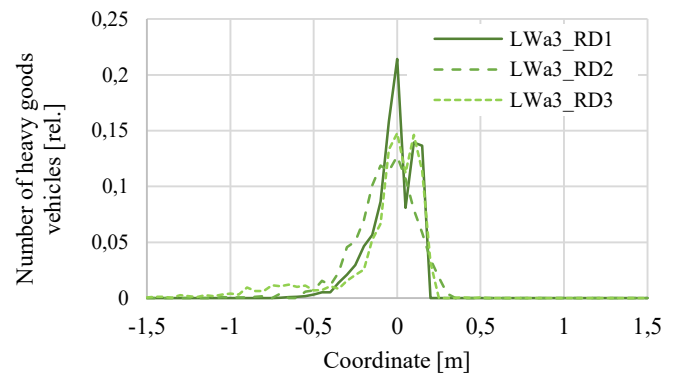
Figure 5. Normalised lateral distributions of heavy vehicles in cross-section; representation for the mean lane width.
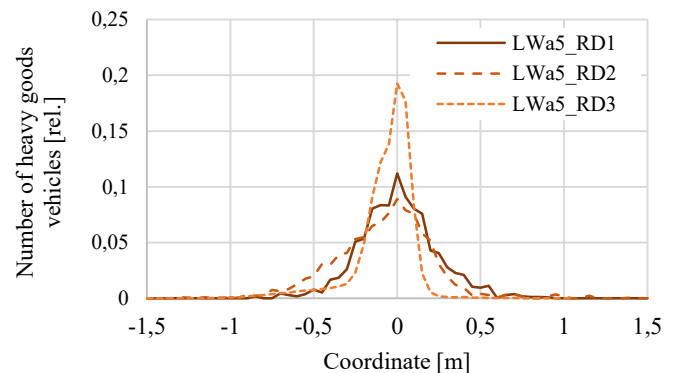
Figure 6. Normalised lateral distributions of heavy vehicles in cross-section; representation for the largest lane width.

A more detailed assessment of the graphs regarding the influence of lane width and rut depth is provided in Figure 4 to Figure 6. Before the experimental plan was established, it was assumed that an increase in lane width would lead to a broader lateral distribution of vehicles, and that an increase in rut depth

would result in a narrower lateral distribution. However, both assumptions could not be confirmed.

Surprisingly, the lanes with the smallest width show the widest distribution (Figure 4). This is due to the lack of road center markings on this type of road. An influence of the rut depth could not be determined at all.

5 DESIGN PROCEDURE IN DEPENDENCE OF LATERAL DISTRIBUTION

One of the most common forms of damage to asphalt pavements is cracking due to fatigue, occurring both from below and from above (Blasl, A. et al. 2021). To perform the fatigue proof in accordance with the German regulations for any asphalt layers, the maximum tensile strain is decisive, independent of the layer type.

In asphalt base layers, the maximum tensile strain occurs at the bottom of the base layer, directly beneath the load axis, i. e. under the wheel. In asphalt wearing courses, however, a maximum occurs on both sides of the wheel, which is also found just below the surface.
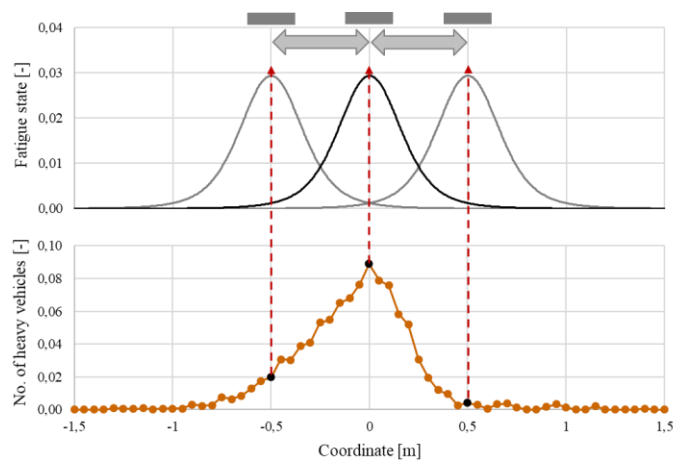
Figure 7. Fatigue status at the bottom of the asphalt base layer for different load positions.

Valid design regulations for road pavements always consider the worst-case scenario. In other words, it is assumed that all vehicles in one lane use the same track (= same position in the cross section of a lane) and do not drive in different tracks. When vehicles use different tracks in the cross-section, the relevant design-related stresses shift accordingly. Regardless of the position of a vehicle, for example, the same stress always occurs at the bottom of the asphalt base layer under the wheel. Therefore, for each load position or stress point, the same fatigue status is also determined.

In Figure 7 und Figure 8, the fatigue status at the bottom of the asphalt base layer and in the asphalt wearing course, at the height of maximum strain, is shown for various load positions. Starting from the centre of a load application area, the strains decrease

towards the outside. In the region of the asphalt wearing course, a particularly rapid (steep) decline can be observed.

Additionally, it can be seen that when considering different load positions in the cross-section, the individual strains or fatigue statuses overlap (= crossing of the graphs). As a result, one observation point is stressed by several load positions. However, the individual stresses must be weighted differently, according to the frequencies of the lateral distribution of heavy traffic at that point, as shown in Figure 7.

The weighted fatigue statues for a given observation point are then summed. The result is the fatigue status in the cross-section of the pavement, at any given height, which can then be converted into a service life (Figure 9).
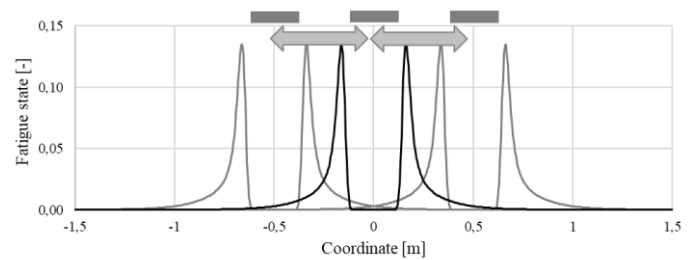
Figure 8. Fatigue status in the asphalt wearing course at the height of maximum tensile strain for different load positions.
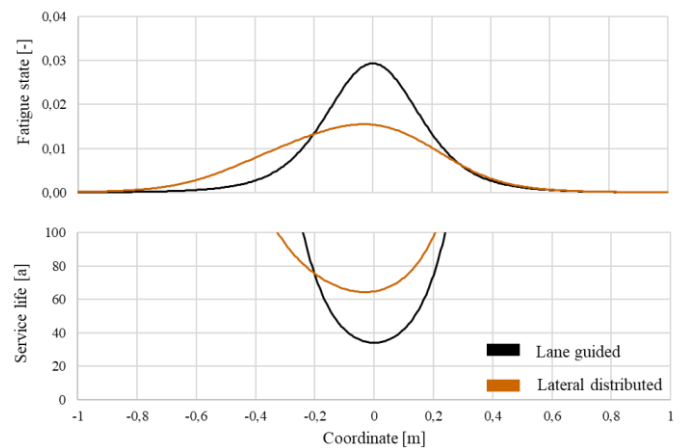
Figure 9. Fatigue status and predicted service life at the bottom of the asphalt base layer due to lateral distribution (using lateral distribution in Figure 7, orange) and under the assumption of lane-guided traffic (black).

Finally, it should be noted that discontinuous lines occur, when evaluating the calculated service lives for the asphalt wearing courses. These result from the strong changes in the strains next to the load application area (Figure 8), combined with the measurement intervals of 5 cm.

6 PAVEMENT SERVICE LIFE IN DEPENDENCE OF LATERAL DISTRIBUTION

The overall objective was to incorporate universally applicable lateral distributions into design procedures

and to quantitatively assess the effect of these distributions. For this purpose, two clearly different cross-distributions were initially identified (Figure 10).
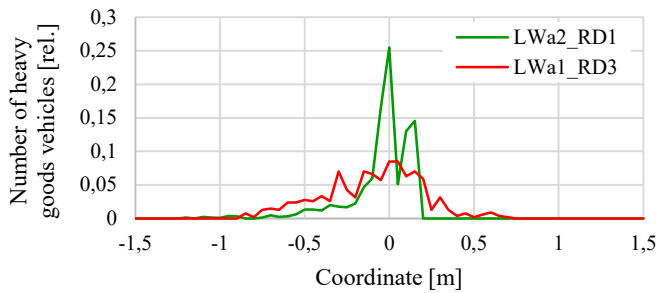
Figure 10. Selected normalised and shifted lateral distributions of heavy vehicles in cross-section.

To model universal lateral distributions using established mathematical distribution functions, various approaches were explored. The Normal distribution and the Laplace distribution proved to be the most suitable. Figure 11 illustrates the fit of both distribution approaches to the lateral distributions shown in Figure 10.
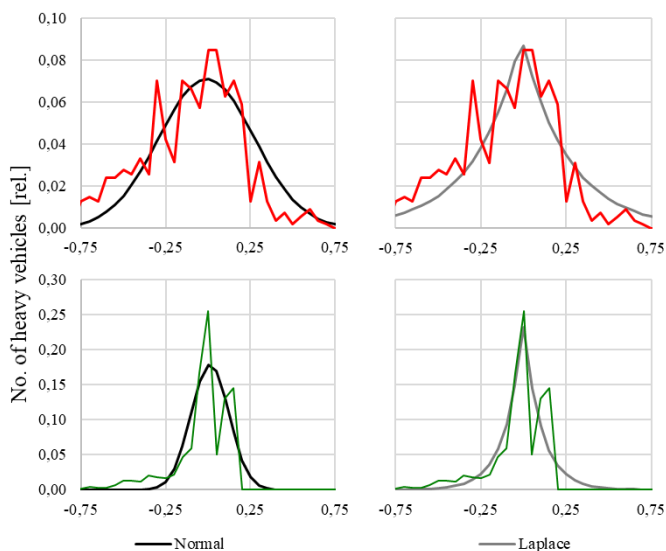
Figure 11. Normal and Laplace distributions of lateral distributions in Figure 10.

The narrower a distribution is, i. e. the truer vehicles drive in a lane cross-section, the better a measured lateral distribution can be modelled using a Laplace distribution. In this case, a Laplace distribution shows a better fit than a normal distribution. Broader lateral distributions, on the other hand, can usually be modelled very well using normal distributions. For the cases studied, if a normal distribution is suitable, a Laplace distribution can also be selected.

Using the normal and Laplace distributions shown in Figure 11, this means the standardized lateral distributions, design life calculations were conducted. The resulting fatigue status and remaining service life at the bottom of the asphalt base layer and in the wearing course (at the height of the maximum strain) were calculated. Figure 12 summarizes the results of the

calculated service lives in the cross-section of a lane (grey and black). The results obtained when track-guided traffic is assumed are also shown for comparison (red and green).

The influence of the type of distribution function used, Normal or Laplace, is largely negligible.
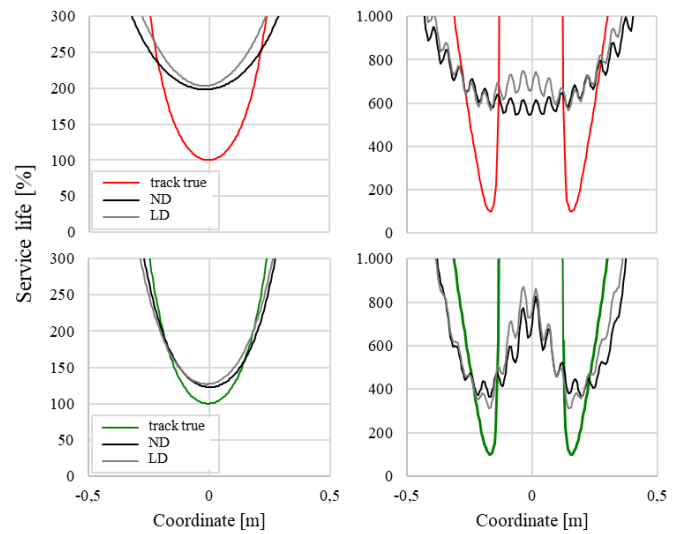
Figure 12. Remaining service life under consideration of the Normal and Laplace distributions in Figure 11.

However, taking the calculated universal lateral distributions into account the calculated service lives are increased by 25% to 100%. This effect should be taken into account when calibrating safety factors and other parameters within design procedures.

7 ACKNOWLEDGEMENT

8 REFERENCES

Uhlig, W. et al. 2023. FE 04.0337/2021/ORB - Einfluss der Pendelbewegung der Fahrzeuge des Schwerverkehrs auf die Beanspruchung und Nutzungsdauer von Straßenbefestigungen, final report of research project, FGSV, Germany, 2023.

Blasl, A. et al. 2021. Case study: Crack propagation in situ vs. service life prediction, International Symposium on Frontiers of Road and Airport Engineering iFRAE, Delft, Neverlands, 2021.

Development of a Correction Method for the Current Pavement ME Methodology in Equivalent Loading Frequency Calculation

P. Chen, K. Chatti & B. Cetin
Department of Civil and Environmental Engineering, Michigan State university, East Lansing, MI, USA

ABSTRACT: The AASHTOWare Pavement ME Design uses linear-elastic analysis to simulate the strain responses under axle loadings, and it relies on equivalent loading frequencies to determine the representative elastic modulus of the asphalt concrete (AC) layer. The Pavement ME employs a highly simplified approach for calculating equivalent loading frequency, which often leads to an overestimation of these frequencies, particularly near the AC surface. This paper presents a simple correction method for the current Pavement ME method in loading frequency calculations based on two novel frequency calculation methods. The correction procedure is straightforward, computationally efficient, and readily implementable within the Pavement ME design software. The corrected loading frequencies are validated by calculating critical strains using these frequencies in three representative pavement structures under Michigan's climate conditions. The results indicate that the corrected loading frequency significantly enhanced the accuracy of vertical strain predictions, particularly at the shallow depth of the AC layer.

1 INTRODUCTION

The primary advantage of mechanistic-empirical design procedures over the 1993 AASHTO Guide is its ability to allow pavement engineers to fundamentally analyze a variety of materials, loading conditions, and corresponding responses, rather than solely relying on observed pavement performance and ride quality. However, the accuracy of the Pavement ME method in estimating loading frequencies has been scrutinized in several studies (Al-Qadi et al., 2008a, 2008b; Losa & Di Natale, 2012; Ulloa et al., 2013), largely due to its dependence on overly-simplified and inaccurate assumptions.

To examine the loading time calculated by the Pavement ME method, Al-Qadi et al. (2008a) simulated vertical stress pulses with a 3-D finite element model by the Abaqus software, incorporating the viscoelastic properties of the AC material measured from the laboratory. This method defines the boundary of the loading duration by locating the instances at which the slope of the vertical stress pulse shifts from negative to positive. Then the loading frequency is calculated as the reciprocal of the loading time ($f=1/t$). Their research concluded that, relative to the proposed method, the Pavenent ME method overestimates loading frequency by up to 300% near the surface of the pavement layer, with both methods' frequency estimates gradually

converging as depth increases. Hu et al. (2010) simulated the vertical stress pulse based on the layered elastic theory and found that the loading duration is not only a function of the vehicle speed and depth of interest, but also a function of the moduli ratio between the layer of interest and the directly underlying layer. Al-Qadi (2008b) performed FFT (Fast Fourier Transform) for vertical stress pulses measured from the field testing and took the frequency values that corresponded to the centroid of area formed by the FFT amplitude curve as the dominant frequency of the pulses. These frequencies were then compared with those calculated by the Pavement ME method ($f=1/t$) and the angular frequency "$f=1/(2\pi t)$". Results showed that the Pavement ME method exhibits errors from 40% to 140% depending on vehicle speed and pavement depth. Losa & Di Natale (2012) developed a method to calculate equivalent loading frequencies for three directions (longitudinal, transverse, and vertical) using an iteration procedure without determining the loading time. The equivalent frequency is iteratively adjusted and employed to back-calculate the elastic modulus until the critical strains determined by this back-calculated elastic modulus converge with those obtained from dynamic viscoelastic analysis. The study by Losa & Di Natale (2012) suggests that the Pavement ME method generally overestimates loading frequencies, whereas Al-Qadi's approach tends to underestimate them. Chen et al. (2024)

comprehensively evaluated the accuracy of the Pavement ME method by comparing the Pavement ME method with two novel methods in terms of frequency and critical strains predicted by loading frequencies. The findings suggest that the Pavement ME significantly overestimates loading frequencies, consequently leading to an underestimation of vertical strain near the AC surface. However, it provides a reasonably accurate prediction of horizontal tensile strain at the bottom of the AC layer.

This paper presents a correction method that addresses limitations in the Pavement ME approach for calculating equivalent loading frequencies. The proposed method is straightforward in its application and can be readily integrated into the Pavement ME design software.

2 LIMITATIONS OF THE ORIGINAL PAVEMENT ME METHOD

The original Pavement ME method transfers the AC layer into an equivalent layer with a different thickness (effective thickness) as a function of the ratio between the AC and subgrade moduli based on the revised Odemark's method. Then it assumes the vertical stress pulse propagates linearly at 45 degrees within the transformed AC layer. Finally, the frequency is calculated as the reciprocal of the loading time, which is equal to the pulse width divided by the vehicle speed (ARA 2001).

Three main flaws have been identified in the Pavement ME method (Hu et al., 2010; Chen et al. 2024). Firstly, the frequency-time relationship of "$f=1/(2t)$" should be used, instead of "$f=1/t$". Secondly, the vertical stress distribution slope is influenced by the ratio between the moduli of the AC layer and the layer immediately beneath it, typically the base layer, instead of the subgrade layer. In addition, the actual layer moduli should be used instead of generic values. Thirdly, the Pavement ME method always underestimates the pulse width near the surface of the AC layer.

3 CORRECTION PROCEDURE

The correction procedure addresses the three limitations of the original Pavement ME method through a two-stage approach, incorporating two novel methodologies proposed by Chen et al. (2024): the centroid of PSD (Power Spectral Density) and the Equivalent Frequency, respectively. The centroid of PSD method takes the weighted center under the PSD (equals the square of the Fourier amplitude) curve as the dominant frequency of the loading pulse. The Equivalent Frequency is determined by iteratively adjusting the frequency value until the responses obtained from linear-elastic analysis using these

loading frequencies align with those produced by viscoelastic analysis.

Twelve hypothetical cases with a combination of different vehicle speeds, AC thickness, stiffness, and temperature (Al-Qadi et al. 2008a, Chen et al. 2024) are utilized to calculate the pulse width by the centroid of PSD method and the Equivalent Frequency method. Examples of vertical stress pulse widths obtained by different methods at mid-temperature (25°C) for both thin and thick pavement are shown in Figure 1.
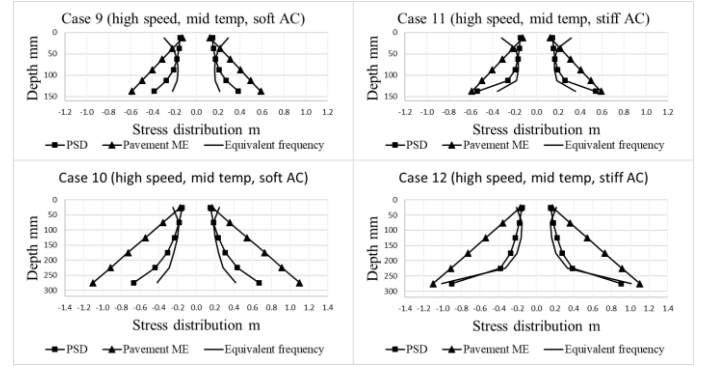
Figure 1. Pulse width by Pavement ME, PSD method, and Equivalent Frequency.

3.1 Stage I: Correction for Vertical Stress Distribution Slope

The centroid of PSD method generally agrees well with the Equivalent Frequency except for near the AC surface. In stage one, the centroid of PSD method is used to derive the vertical stress pulse distribution slope along the depth as a function of the ratio between the moduli of the AC layer and the base layer. The centroid of PSD method does not calculate the pulse duration explicitly. Therefore, its pulse duration must be indirectly estimated using the time-frequency relation of "$f=1/(2t)$" (Chen et al. 2024). As can be seen in Figure 1, the vertical stress distribution slope obtained by the centroid of the PSD method does not follow a linear trend. Instead, the profile exhibits a concave shape that can be characterized by two distinct slopes for the upper 75% and the lower 25% of the AC layer thickness, as illustrated in Figure 2 (Chen 2024).
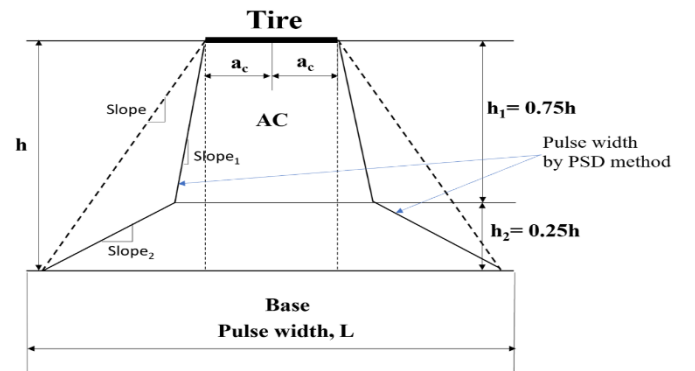
Figure 2. Simplified vertical stress distribution slope by the centroid of PSD method.

The average modulus of the AC layer, as calculated by Equation 1, ensures that when the modulus of each AC sub-layer is substituted with a uniform average value, the overall vertical strain remains unchanged.

$$E_{AC} = \left(\frac{1}{h_{AC}} \sum_1^n h_i \times \frac{1}{E_i}\right)^{-1} \quad (1)$$

where: E_{AC} is the average elastic modulus of the AC layer; h_{AC} is the thickness of the AC layer; h_i is the thickness of each sublayer; n is the number of sublayers; E_i is the modulus of each sublayer, which is a function of temperature and loading frequency calculated by the Pavement ME method.

According to Odemark's method, the gradient of the vertical stress distribution within the AC layer is linearly dependent on $(E_{AC}/E_{Base})^{1/3}$, where E_{Base} is the modulus of the base layer. The slope derived from the centroid of PSD method (dashed lines in Fig. 2) is calculated and plotted against $(E_{AC}/E_{Base})^{1/3}$ for the twelve cases as shown in Figure 3. The trend line in Figure 3 demonstrates the linear relationship between the slope and $(E_{AC}/E_{Base})^{1/3}$.

The base modulus across the twelve cases remains consistent at 207 MPa. To extend the relationship depicted in Figure 3 to other base moduli, twenty-four additional hypothetical cases, designated as cases 13 through 36, were developed. These cases feature AC moduli ranging from 345 MPa to 6,895 MPa and base moduli ranging from 69 MPa to 689 MPa. The analysis results for cases 13 through 36 are presented in Figure 4, with the linear trend line coefficient closely aligning with that observed in Figure 3, suggesting that the modulus of the base layer exerts minimal influence on the slope of the vertical stress distribution. Consequently, the slope can be determined using Equation 2.

$$Slope = \left(\sqrt[3]{\frac{E_{AC}}{E_{base}}}\right)^{-1} \quad (2)$$
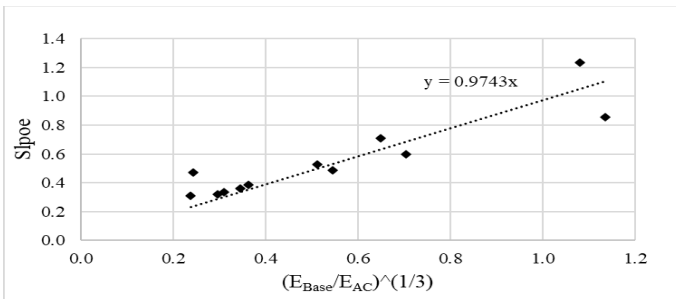
Figure 3. Vertical stress pulse distribution slope versus the ratio between AC and base moduli (Cases 1 to 12).

As previously noted, the stress pulse distribution slope by the centroid of PSD method comprises two distinct segments for the upper 75% and the lower 25% of the layer thickness. An analysis similar to that illustrated in Figures 3 and 4 is conducted to determine the ratio (denoted as R_{75}) between the actual pulse width at a depth corresponding to 75% of the AC thickness and the pulse width defined by the slope calculated by Equation 2 for cases 1 to 36. The results indicate that R_{75} roughly equals 1.35 times the quantity of $(E_{Base}/E_{AC})^{1/3}$.

Once R_{75} is obtained, the stress pulse distribution slopes and the corresponding pulse widths can be easily calculated by Equations 3 to 6:

$$Slope_1 = \frac{Slope}{R_{75}} = 0.741 \quad (3)$$

$$Slope_2 = \frac{0.25}{1/Slope - 0.75/Slope_1} \quad (4)$$

$$L_1 = 2 \times \left(\frac{h}{Slope_1} + a_c\right) \quad (5)$$

$$L_2 = 2 \times \left(\frac{h - 0.75h_{AC}}{Slope_2} + \frac{0.75h_{AC}}{Slope_1} + a_c\right) \quad (6)$$

where $Slope$ is the uniform stress pulse distribution slope obtained from Equation 2; $Slope_1$, L_1 and $Slope_2$, L_2 are stress pulse distribution slopes and the corresponding pulse widths within the upper 75% and lower 25% of the AC layer thickness, respectively; h is the depth of interest; h_{ac} is the thickness of the AC layer; a_c is the radius of the tire footprint.
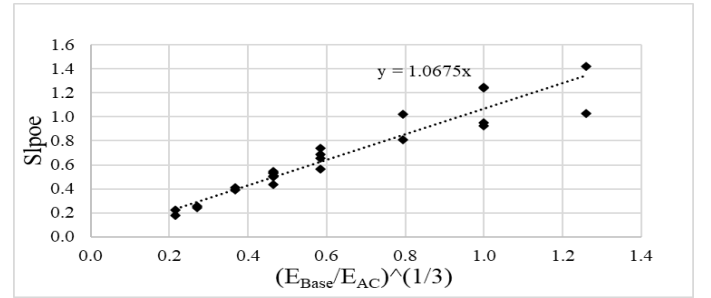
Figure 4. Vertical stress pulse distribution slope versus the ratio between AC and base moduli (Cases 13 to 36).

3.2 Stage II: Correction for the stress pulse near the surface of the AC layer

As can be seen from Figure 1, the pulse width determined using the centroid of the PSD method is considerably shorter than that obtained through the Equivalent Frequency method at the AC surface. However, this discrepancy diminishes progressively with increasing depth, and the pulse widths determined by these two methods tend to converge at a depth of approximately 65 mm regardless of pavement structures (Chen 2024). The pulse widths derived from Stage I must be refined by applying correction factors specifically for the upper 65 mm of the AC layer as defined in Equation 7.

$$CF = (L_e - L_1)/(2 \times a_c) \quad (7)$$

where CF is the correction factor; a_c is the radius of the tire-pavement contact footprint; L_e is the pulse width determined by the Equivalent Frequency. The correction factor reaches its maximum value at the AC surface and decreases linearly until it reaches zero at a depth of 65 mm. The correction factor is also affected by the modulus of the AC layer, though it exhibits significantly less sensitivity compared to the pulse distribution slope. A similar analysis to that

depicted in Figure 2, as conducted by Chen (2024), indicates that the correction factor at the surface is proportional to the logarithm of the AC modulus. The correction factor, within the top 65 mm of the AC layer can be calculated by Equations 8 and 9:

$$CF_{max} = 0.62 \times \log(145 \times E_{AC}) \quad (8)$$

$$CF = \frac{-CF_{max}}{2.5} h + CF_{max} \quad (9)$$

where CF_{max} is the correction factor at the surface of the AC layer; E_{AC} is the average AC modulus in MPa.

By applying the correction factor, the pulse width and loading frequency for the corrected Pavement ME method can be determined using Equations 10 and 11, respectively:

$$L_{corrected} = L_i + CF \times 2a_c \quad (10)$$

$$f_{corrected} = \frac{1}{2 \times L_{correct}/V} \quad (11)$$

where $L_{corrected}$ is the pulse width of the corrected Pavement ME frequency method; L_i (i = 1, 2) is the pulse width calculated by Equations 5 or 6; and V is the vehicle speed.

4 VERIFICATION OF THE CORRECTED PAVEMENT ME LOADING FREQUENCY

The corrected Pavement ME loading frequency calculated by Equation 11 is verified by comparing critical strains predicted by linear elastic analysis using these frequencies with those obtained from dynamic viscoelastic analysis. The simulation scenarios involve three hypothetical pavement structures located in the climatic conditions of East Lansing, Traverse City, and Detroit, Michigan, subjected to a 16-ton tandem-axle load traversing at a velocity of 96 km/h. Two temperature quintiles from July were selected for analysis, as July represents the hottest month of the year, thereby reflecting the most critical conditions for pavement responses.

As shown in Figure 5, the corrected loading frequency substantially improved the prediction of vertical strain at the shallow depth of the AC layer, closely aligning with viscoelastic analysis results within Quintile 5 (highest temperature) across all three pavement structures. The effect of the corrected loading frequency on improving vertical strain prediction is less evident in Quintile 1, which is of lower criticality for pavement responses, as it represents the lowest temperature in July. In summary, the correction procedure markedly enhances the accuracy of the Pavement ME method in predicting vertical strains near the AC surface.
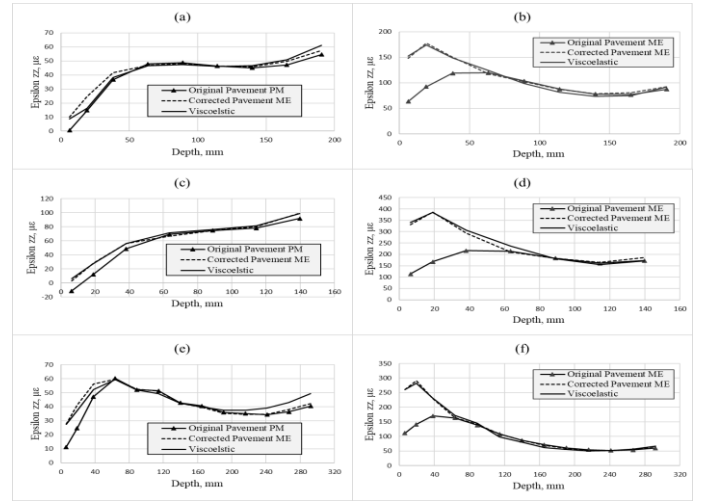
Figure 5. Vertical strains predicted by different methods (a) Quintile 1 of July for East Lansing climate; (b) Qquintile 5 of July for East Lansing climate; (c) Quintile 1 of July for Traverse City climate; (d) Quintile 5 of July for Traverse City climate; (e) Quintile 1 of July for Detroit climate; (f) Quintile 5 of July for Detroit climate.

5 REFERENCES

Al-Qadi, I. L., Elseifi, M. A., Yoo, P. J., Dessouky, S. H., Gibson, N., Harman, T., D'Angelo, J., & Petros, K. (2008b). Accuracy of current complex modulus selection procedure from vehicular load pulse: NCHRP Project 1-37A mechanistic-empirical pavement design guide. Transportation research record, 2087(1), 81-90.

Al-Qadi, I. L., Xie, W., & Elseifi, M. A. (2008a). Frequency determination from vehicular loading time pulse to predict appropriate complex modulus in MEPDG. Asphalt Paving Technology-Proceedings, 77, 739.

ARA, Inc., ERES Division. (2001). Appendix CC-3 of the Guide for Mechanistic-Empirical Design of New and Rehabilitated Pavement Structures. NCHRP 1-37A. https://onlinepubs.trb.org/onlinepubs/archive/mepdg/2appendices_CC.pdf

Chen, P. (2024). Impact of Equivalent Axle Loading Frequencies on Critical Strains and Distress Predictions in Asphalt Concrete Pavements (Doctoral dissertation, Michigan State University).

Chen, P., Chatti, K., & Cetin, B. (2024). Evaluation of the Accuracy of Pavement ME Methodology in Calculating Equivalent Loading Frequency and Its Effect on Strain Response Predictions in Flexible Pavements. Journal of Transportation Engineering, Part B: Pavements, 150(1), 04023042.

Hu, X., Zhou, F., Hu, S., & Walubita, L. F. (2010). Proposed loading waveforms and loading time equations for mechanistic-empirical pavement design and analysis. Journal of Transportation Engineering, 136(6), 518-527.

Losa, M. & Di Natale, A. (2012). Evaluation of representative loading frequency for linear elastic analysis of asphalt pavements. Transportation research record, 2305(1), 150-161.

Ulloa, A., Hajj, E. Y., Siddharthan, R. V., & Sebaaly, P. E. (2013). Equivalent loading frequencies for dynamic analysis of asphalt pavements. Journal of Materials in Civil Engineering, 25(9), 1162-1170.

Impact of Pavement Solar Collector Systems on Asphalt Temperature and Service Life

H. Cuyx, T. Ghalandari & D. Hernando
Sustainable Pavements and Asphalt Research (SuPAR), University of Antwerp, Belgium

ABSTRACT: This paper investigates the impact of pavement solar collectors (PSCs) on the service life of flexible pavements. While previous studies have focused on heat extraction and mitigating the urban heat island effect, little research has been conducted on the mechanical response of a flexible pavement considering the presence of a PCS and the resulting temperature change. This study focuses on two key parameters: pipe depth and pipe length, which are assessed in terms of service life. The findings show that pipe length has a more pronounced influence on service life than pipe depth. Shorter pipe lengths increase temperature reduction during the warm season and improve service life. This study concludes that PSCs can extend the service life of flexible pavements by reducing extreme surface temperatures.

1 INTRODUCTION

1.1 Background

The service life of flexible pavements is influenced by a large number of factors, including traffic loading and pavement temperatures. In recent studies, pavement solar collectors (PSCs) have been used to reduce the temperature variations that asphalt pavements are subjected to. A PSC consists of a pipe network embedded in the pavement through which a fluid at a certain temperature is pumped. During the warm months, cool water runs through the pipes to simultaneously extract heat from the pavement and cool down the asphalt. In winter, warm water heats up the surface, aiding in removing snow and ice. In doing so, extremely high or low surface temperatures can be reduced as well as temperature variations between day and night. These repetitive thermal cycles cause temperature-induced stresses and may result in thermal fatigue cracking (Bayat et al., 2012). Additionally, high temperatures in the pavement are unwanted as they contribute to the urban heat island effect (UHI) and increase the risk of permanent deformation (Abu El-Maaty, 2017, Mallick et al., 2009). This paper focusses on the benefit of reducing pavement temperature in the warm season.

1.2 Pavement solar collector

A PSC involves a pipe network that is embedded in a flexible pavement in a serpentine pattern. Figure 1 depicts an overview of a PSC prototype.
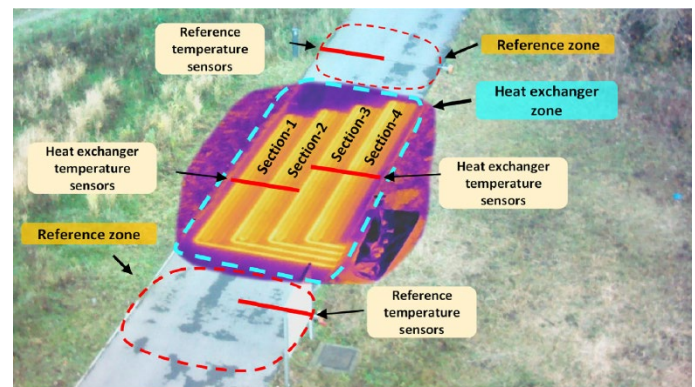
Figure 1. Schematic view of PSC prototype on Campus Groenenborger, University of Antwerp, Belgium (taken from (Ghalandari et al., 2023))

The performance of the system depends on several boundary parameters. The most influential are pipe depth, pipe length, pipe spacing, pipe diameter, the inlet temperature of the fluid, and the flow rate (Saleh et al., 2020). This paper investigates pipe length and depth. Pipes placed closer to the surface result in a more significant reduction in surface temperature, while pipes placed deeper have a smaller impact on surface temperature, but create a downward shift in the temperature profile. The pipe length influences both the efficiency of the system and the temperature reduction. With a shorter pipe length,

both the cost and input energy per square meter are higher; however, the temperature reduction is larger than in the case of longer pipe lengths.

2 OBJECTIVE AND SCOPE

The main objective of this research is to investigate how the performance of a pavement solar collector affects the service life of an asphalt pavement in terms of load-induced fatigue cracking. Specifically, the pipe length and depth are examined. The pavement structure that is used for the calculations is presented in Figure 2. This is a thin structure that is implemented for lightly loaded roads, like bicycle paths or local roads.
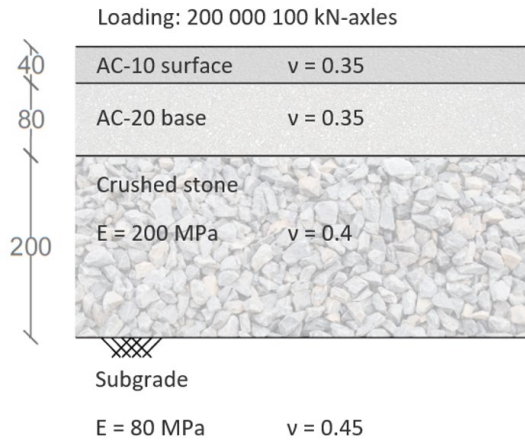
Figure 2. Pavement structure and material properties

3 PSC SETUP AND THERMAL MODELING

Finite element (FE) models were used to predict pavement temperatures for the different PSC scenarios (Ghalandari et al., 2023). The geometry of the pavement in the models is presented in Figure 3. The pavement consists of six connected sections. Each section has a surface area of 7.65 m² (1.80 m x 4.25 m) and contains 50 m of embedded pipes. With six adjacent sections, the total surface area of the pavement is 45.9 m² (4.25 m x 10.80 m) and the total pipe length is 300 m. This study investigates pipe lengths of 50 m, 150 m and 300 m. In addition to the PSC model, a reference structure without a PSC is modeled.
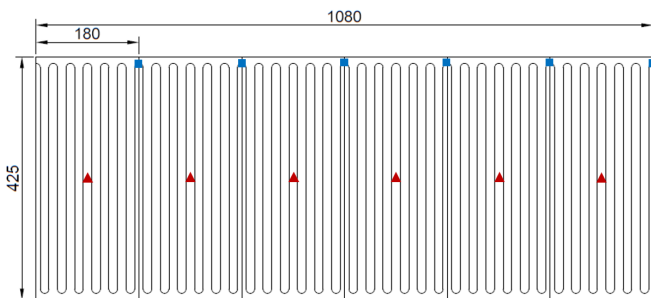
Figure 3. Plan view of pavement solar collector

4 SERVICE LIFE ASSESSMENT

The calculation of service life consists of several steps. The first step is to analyze the temperature data resulting from the FE models and create groupings. A time resolution analysis was performed, where the findings indicated that temperature data can be grouped in 3-hour intervals without negatively affecting the accuracy of the results. Secondly, pavement temperatures are used to calculate the stiffness of the asphalt mixtures. To determine this, the master curves of the surface and base layer are needed. The following master curve equation (Eq. 1) is used (AASHTO, 2013) based on the parameters listed in Table 1.

$$\log|E^*| = \delta + \frac{\alpha}{1+exp[\beta+\gamma[\log f+a_1(T_r-T)+a_2(T_r-T)^2]]} \quad (1)$$

where E^* = dynamic modulus [MPa]; f = frequency (10 Hz for this analysis); T_r = reduced temperature (15°C in this case); T = asphalt temperature [°C]; α, β, γ, δ = shape factors of sigmoidal function; a_1, a_2 = fitting parameters of time-temperature shift function.

Table 1. Master curve parameters

Factor	AC-10 surf	AC-20 base
α	5.2546	4.3894
β	-2.0299	-2.5447
γ	-0.3342	-0.3938
δ	-0.7036	0.2448
a_1	0.1524	0.1465
a_2	0.0014	0.0014

Consequently, the Layered Elastic Theory Stress-Strain calculator embedded in the Rubicon software is implemented to calculate stress, strain, and deflection in the pavement (Rubicon, 2024). Here, a multi-layered linear elastic analysis of the pavement structure shown in Figure 2 is performed. The service life is calculated in terms of load-induced fatigue cracking. For this calculation, the horizontal tensile strain at the bottom of the asphalt base is needed. The damage ratio is based on Miner's rule and is defined as the ratio of the number of 100-kN axles applied on the pavement to the number of cycles that the pavement can withstand for fatigue cracking ($N_{f,f}$) before failure (Eq. 2).

$$N_{f,f} = 7\left(\frac{0.0016}{-\varepsilon_t}\right)^{4.76} \quad (2)$$

where $N_{f,f}$ = number of cycles the pavement can withstand before failure due to fatigue cracking and ε_t = horizontal tensile strain measured at the bottom of the asphalt base.

Based on this, the damage ratio (DR) is calculated following Equation 3.

$$DR = \frac{Number\ of\ applied\ 100\ kN-axles}{N_{f,f}} \quad (3)$$

Equation 4 is used to calculate service life (SL) from damage ratio.

$$SL = \frac{20\ years}{DR} \tag{4}$$

In order to compare the scenarios with a PCS to the reference section, this paper will not evaluate the damage ratio or service life. Instead, a Service Life Factor (SLF) will be calculated according to Equation 5.

$$SLF_x = \frac{SL_x}{SL_{No\ PSC}} \tag{5}$$

where SLF_x = service life factor of PSC scenario x; SL_x = service life of PSC scenario x [years] and $SL_{No\ PSC}$ = service life of pavement without PSC [years].

To clarify, if the SLF of a specific scenario is 2, the service life of that section is twice as long as that of the reference section. The SLF of the reference section is always 1, and therefore not included in the results below.

5 RESULTS

The results in Figure 4 indicate that the SLF ranges from 1.53 to 2.37 for all considered scenarios. This means that the implementation of a PSC can extend the service life by at least 50% and in the best case, even more than double it.

An increase in pipe length results in a lower service life factor. This is due to the fact that longer pipe lengths cause a smaller change in the average pavement temperature.

With an increase in pipe depth, the service life first increases slightly, and then decreases again. The highest service life is found at a pipe depth of 6 and 8 cm, although the difference between the results at 4, 6 and 8 cm is very minor. SLF is the lowest at a pipe depth of 10 cm. This can be explained by the fact that the temperature in the pavement is reduced less for this pipe depth with pipes installed closer to the surface.
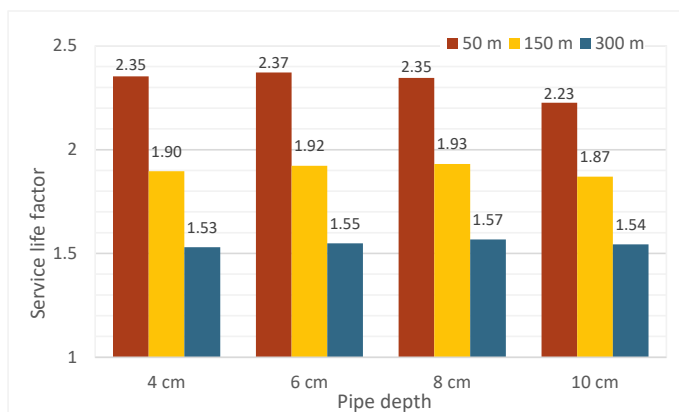
Figure 4. Results service life factor for multiple pipe depths and lengths

The mean temperature profile over the depth of the pavement of all measurements in the months May through August is presented in Figure 5. This figure clearly shows the temperature reduction resulting from the application of a PSC. It also shows how a pipe depth of 10 cm has the smallest temperature reduction over most of the thickness. A higher pavement temperature brings a lower stiffness, a larger deformation and thus, a higher damage accumulation.
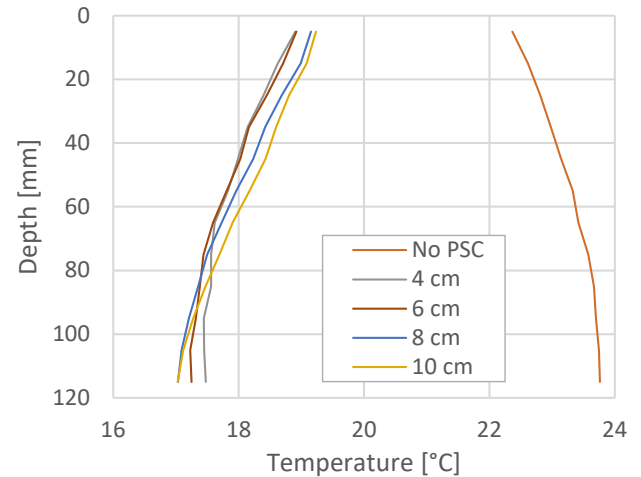
Figure 5. Mean temperature profile for the months May through August for a pipe length of 50 m

6 CONCLUSIONS

This study demonstrates that Pavement Solar Collectors (PSCs) are an effective method for extending the service life of flexible pavements by reducing pavement temperatures during the warm season. By examining varying pipe lengths and depths, the results highlight that pipe length has a more pronounced influence on the results than pipe depth. Shorter pipe lengths realize greater reductions in surface temperature and lead to improved service life. It is important to note that shorter pipe lengths also have a higher operational cost of the system. A cost-benefit analysis could therefore provide more insight into the optimal configuration.

The impact of pipe depth is less obvious. The optimal pipe depth is found to be 6-8 cm. Deeper installations have a smaller temperature reduction and therefore, result in a smaller improvement in service life.

Overall, the implementation of a PSC can extend the service life of an asphalt pavement by a factor of more than 2 in the cases with the shortest pipe length. Even in the worst configurations presented in this paper, the service life is still improved by 50%.

Global slippage or global failure of the section due to the presence of the pipe network is out of the scope of the study. Measures have been proposed for reducing the chance of global slippage by, for example, installing the pipes on a grid that stiffens the in-

terface. Further analysis of additional distresses, like rutting in the asphalt mixtures, along with the use of more sophisticated material models are recommended in future work.

7 REFERENCES

AASHTO 2013. AASHTO R62 Standard Practice for Developing Dynamic Modulus Master Curves for Asphalt Mixtures. American Association of the State Highway and Transportation Officials Washington DC.

ABU EL-MAATY, A. 2017. Temperature Change Implications for Flexible Pavement Performance and Life. *International Journal of Transportation Engineering and Technology,* 3**,** 1.

BAYAT, A., KNIGHT, M. A. & SOLEYMANI, H. R. 2012. Field monitoring and comparison of thermal- and load-induced strains in asphalt pavement. *International Journal of Pavement Engineering,* 13**,** 508-514.

GHALANDARI, T., KIA, A., TABORDA, D. M. G., VAN DEN BERGH, W. & VUYE, C. 2023. Thermal performance optimisation of Pavement Solar Collectors using response surface methodology. *Renewable Energy,* 210**,** 656-670.

MALLICK, R. B., CHEN, B.-L. & BHOWMICK, S. 2009. Harvesting energy from asphalt pavements and reducing the heat island effect. *International Journal of Sustainable Engineering,* 2**,** 214-228.

RUBICON. 2024. *LET Stress-Strain Calculator* [Online]. Available: https://secure.rubicontoolbox.com/Pages%20 for%20Tools/Design%20Tools/LETStressStr ainCalc.aspx [Accessed 2023].

SALEH, N. F., ZALGHOUT, A. A., SARI AD DIN, S. A., CHEHAB, G. R. & SAAD, G. A. 2020. Design, construction, and evaluation of energy-harvesting asphalt pavement systems. *Road Materials and Pavement Design,* 21**,** 1647-1674.

Gap Analysis and Roadmap for Improvement of Asphalt Pavements in Kuwait

Haya Almutairi, Nayef Al-Othman, Salah Zoorob, Suad Al-Bahar
Kuwait Institute for Scientific Research

Eyad Masad
Hamad Bin Khalifa University

John D'Angelo
D'Angelo Consulting, LLC

ABSTRACT: This paper documents the findings of a study conducted by the Kuwait Institute for Scientific Research (KISR) to identify primary factors contributing to low ride quality, performance, and durability of asphalt pavements in Kuwait. The study was motivated by the initiation of major rehabilitation and reconstruction projects that aim to rectify major distresses in asphalt pavements. The study conducted detailed gap analysis of factors that have potential to adversely affect the performance of asphalt pavements in Kuwait. Consequently, the study outlined the main elements of a roadmap that aims to improve specifications, material selection, mixture design, mixture testing, mixture production, construction operations, evaluation, preservation and rehabilitation techniques.

1 INTRODUCTION

There have been several studies and reports in recent years documenting problems with severe raveling in Kuwait. This problem was compounded following heavy rainy seasons (Ahmed et al. 2021). Almutairi and Alfadhli (2023) attributed such distresses to a combination of factors, including lack of quality control during construction, poor mixture design in terms of low bitumen (or asphalt binder) content and high air voids, unregulated axle loading, and rain intensities higher than the typical rates recorded in previous years. A review of several investigation reports by government committees highlighted poor quality control and using a thin open graded asphalt wearing course mix type known as Plant Mix Seal (PMS), described in section 409 of Kuwait Specifications (Ministry of Public Works Administration 2012). The PMS mixture composition is shown in Table 1. This mix has a higher bitumen content than other mixture designs in Kuwait and the region. It is also specified to have a minimum air void of 15%, which is very high for hot climate regions that do not typically have high rain intensities. Some of the technical committees the Ministry of Public Works formed indicated existing mixtures did not incorporate antistrip additives, weakening the resistance to moisture damage in heaving rain seasons. The committees also highlighted inadequate quality control processes at the asphalt plants and during construction.

Additionally, Kuwait Institute for Scientific Research conducted a study to evaluate prevalent asphalt pavement maintenance practices (Al-Owmi et al., 2024). This study identified several gaps, such as the lack of a comprehensive local maintenance and rehabilitation guide, inadequate machinery calibration, and limited personnel certification programs. The outcomes of this study highlighted the need to adopt international standards to enhance local maintenance practices and pavement management systems to improve quality and durability in Kuwait's pavements.

Table 1: Composition of Plant Mix Seal, extract from Kuwait General Specifications 2012 (Ministry of Public Works Administration 2012).

Sieve Size	Percent passing by weight	Maximum Allowable Tolerances from the Job Mix Formula
1/2 inch	100	0
3/8 inch	95 - 100	± 5
No. 4	30 - 50	± 7
No. 8	5 - 15	± 3
No. 200	3 – 6 Gradation may include hydrated lime	± 2
Asphalt Cement (% by weight of aggregate)	5.5 to 7.5	± 0.4
Antistripping Additive (% by weight of bitumen)	1.5 Maximum	-

2 OBJECTIVES

The primary objectives of this preliminary study were to:
- Conduct a gap analysis of the various technical factors that may have contributed to Kuwait's poor performance of asphalt pavements.
- Review current specifications used in Kuwait and recommend improvements to various aspects of material selection, testing, quality

control/acceptance, construction specifications, and rehabilitation practices.

- Outline the main elements of a roadmap to improve asphalt pavement design, construction operations, and performance.

3 GAP ANALYSIS OF MATERIAL SPECIFICATIONS

Following the significant problems of raveling in Kuwait in winter 2018, the Ministry of Public Works adopted Qatar Construction Specifications (QCS), issued in 2014. This decision was motivated by the fact that specifications in Qatar have been subjected to major reviews and updates. However, this study concluded that the QCS requires an update given the experiences and developments in the past decade. The main issues that require updates are:

- The Marshall design specifications in QCS have restrictive gradation bands and relatively low binder contents. The aggregate gradation bands should be wider (less restrictive than the current bands) to facilitate more flexibility in achieving a balanced mix design. Consequently, more significant benefits from the properties of polymer-modified binders (PMBs) in terms of resistance to rutting can be expected while simultaneously achieving better resistance to fatigue cracking and thermal aging).
- QCS 2014 specifies polymer-modified binders (PMB) with grades of PG76S-10, PG76H-10, PG 76V-10, and PG 76E-10 based on AASHTO M332. This temperature grade is suitable for Kuwait's climatic conditions. Recently, MPW-Kuwait specified using PG 76H-10 for highways and other heavily trafficked roads (Ministry of Public Works 2307-2019). This recommendation is a major improvement since existing pavements in Kuwait were constructed primarily using unmodified asphalt binders (Pen 60/70, equivalent to PG 64-10).
- QCS has Quality Control (QC) specifications for relative density and in-place air voids. Relative density relates the density of the field core to the density of laboratory-compacted specimens of mixtures taken from the field. The specimens are compacted using the design number of blows in the Marshal method or the design number of gyrations in the Superpave method. Including both criteria (relative density and in-place air voids) could lead to conflicting results. Also, using relative density can lead to high air voids in the pavement that will negatively affect performance. It is therefore recommended that only percent air voids be used instead of relative density.
- The specifications of the Superpave mix design criteria require 125 gyrations for compaction

under high traffic conditions (> 30 million ESLAs), which has generally led to dry mixes with low bitumen content. Lowering the gyration levels for high traffic is recommended to design more durable mixes.

- The QCS specifications do not include tests to achieve a balanced mix design between cracking and rutting resistance. It is recommended that mixture tests and associated specifications be included. This will lead to a more balanced mixture design. Figure 1 includes initial recommendations based on experiences gained in the performance of roads in regions in the United States with hot climatic conditions in the United States. Adopting such characterization tests will promote a more balanced mixture design that achieves improved resistance to both cracking and rutting. These specification limits will need to be updated based on tests conducted on mixtures in Kuwait.
- Current specifications do not sufficiently cover the design of recycled asphalt pavements. In addition, the specifications must include guidelines and procedures for evaluating the performance of asphalt mixtures that include recycled materials.
- It is recommended that the Superpave mix design criteria be adopted as the preferred methodology, which would increase bitumen content relative to current Marshall mixes. The increase in bitumen content combined with the use of PG 76-10 grade PMB and a strong aggregate structure will contribute to achieving a balanced mix design as part of the Superpave mix design framework.
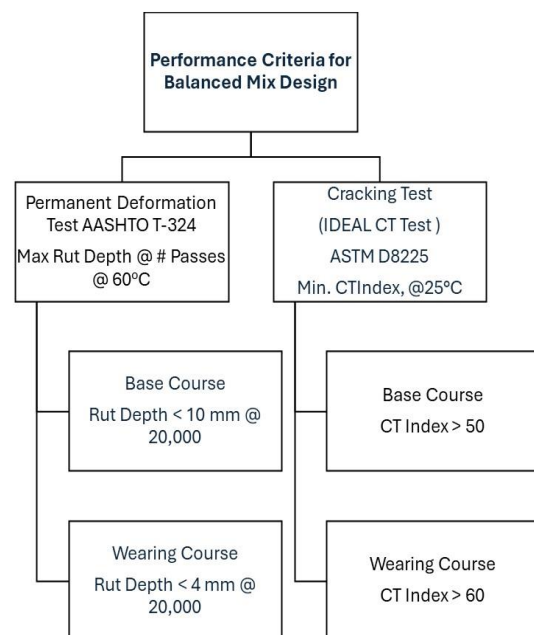
Figure 1. Preliminary recommendations for performance tests and criteria.

4 RECYCLED ASPHALT PAVEMENTS

Incorporating RAP into the hot mix production process is cost-effective and environmentally friendly. Specifically, RAP saves money in areas where high-quality aggregates are scarce or importing virgin aggregate is more expensive. Using RAP in rehabilitation and new pavement construction can also reduce the demand for landfills.

The study developed guidelines for RAP stockpiling, management, and plant processing to maximize its use. Multiple techniques exist to introduce RAP into the hot mix batch facility. The optimum process will vary depending on the condition of the RAP, the percentage to be added, and the plant layout. Minor variations to plant operations can achieve a 30% RAP mix addition; however, it will require some changes in the plant configuration. Even higher percentages can be achieved with significant changes to the plant.

Given the low bitumen content in the current Kuwaiti Marshall mixtures, it is recommended that the RAP content in the current mixes does not exceed 20% by weight. RAP used in small quantities only requires minor modifications to the asphalt mix design and moderate adjustments to production processes while providing economic and environmental benefits. Including more than 20% RAP in batch plants would require some modifications to control the RAP temperature and mixing of RAP and virgin aggregates. It is recommended that the Superpave mixture design process be used to accommodate a higher RAP content. With time and experience, the RAP percentages can be increased to enhance economic and environmental benefits.

5 QUALITY ASSURANCE SYSTEM

The Quality Assurance (QA) system in the current QCS does not include clear and specific designation of responsibilities for quality control (QC), acceptance (A), and Independent Assurance (IA) operations. AASHTO R10 and AASHTO R42 guidelines are recommended for developing a QA/QC system and assigning responsibilities. Quality acceptance (A) must be included in the specifications. These tests would be at less frequency than the QC program. The recommended lot size per layer for the base course is a minimum of 2000 tons and a maximum of 4000 tons, with one test per 500 tons. The lot size for the wearing course is a minimum of 1000 tons and a maximum of 2000 tons, with one test per 250 tons.

The recommended specifications include specific material tests and tolerances. Adopting a statistical approach for analyzing Quality Control and Quality Acceptance data is also recommended. Such an approach will encourage the implementation of measures to reduce variation, which can also help output to remain within the specification limits. The concept of percent within limits (PWL) is highly suitable for data analysis and relating the results to pay factors for each lot.

6 ASPHALT PAVEMENT EVALUATION

Kuwait employs a process for evaluating asphalt pavement conditions based on ASTM D6433, which evaluates the Pavement Condition Index (PCI). The PCI is determined using visual surveys, which is similar to the distress identification manual by the long-term pavement performance program (Miller and Bellinger 2014). Automated surveying systems that incorporate cameras and lasers for pavement evaluation are needed.

It is not sufficient to assess only visual surface conditions to decide on the extent and severity of distress and damage in various layers and then subsequently select the proper optimum rehabilitation method. Lack of structural evaluation raises the risk of placing overlays on damaged layers, which is not a suitable strategy as damage will develop rapidly due to the existing damaged underlayers.

The study developed guidelines for using a combination of nondestructive evaluation methods (Dynamic Cone Penetrometer (DCP), Falling Weight Deflectometer (FWD), Ground-Penetrating Radar (GPR), roughness profilometers, and skid resistance and destructive methods (trenching and coring) should be used to assess the conditions of asphalt pavement layers.

7 ASPHALT PAVEMENT PRESERVATION TREATMENTS AND REHABILITATION

The study additionally developed guidelines for preservation treatments and rehabilitation of asphalt pavements. As defined by Hall et al. (2001), "pavement rehabilitation is defined as a structural or functional enhancement of a pavement that produces a substantial extension in service life by substantially improving pavement condition and ride quality. Pavement maintenance activities, on the other hand, are those treatments that preserve pavement condition, safety, and ride quality, and therefore aid a pavement in achieving its design life." The term pavement preservation is used in the literature to refer to preventive maintenance and some forms of minor rehabilitation and corrective maintenance (Peshkin et al. 2011).

Hall et al. (2001) categorize rehabilitation treatments to the "4 Rs"– restoration, resurfacing, recycling, or reconstruction. Some Certain types of treatments may be carried out as part of a restoration or resurfacing effort. The guidelines developed in

this study include the classification of various activities under maintenance and the 4Rs of rehabilitation, as shown in Table 2. Also included are guidelines for the various preservation and rehabilitation strategies depending on the type and severity of distress, as shown in Table 3.

Table 2. Classification of Different Pavement Treatments Under Preventive Maintenance and Rehabilitation.

Pavement Activity	Preventive Maintenance	Rehabilitation			
		Restoration	Resurfacing	Recycling	Reconstruction
Structural Overlays				X	X
Functional) Overlays			X	X	
Thin Overlays			X		
Crack Sealing	X	X			
Fog Seal	X	X			
Slurry Seal	X	X			
Chip Seal	X	X			
Microsurfacing			X		

Table 3. Guidelines for Using Surface Treatments Based on Distress Type and Severity Level.

	Crack Sealing			Fog Seal			Slurry Seal			Chip Seal			Microsurfacing		
	Minor	Mod	Major	Minor	Mod	Major	Minor	Mod	Major	Minor	Mod	Major	Minor	Mod	Major
Fatigue Cracking	M			M			M			M			M		
Linear & Block Cracking	E	M		M			E	M		E	M		E	M	
"Stable" Rutting													E	M	
Raveling				M			E	M		E	E	M	E	E	M
Flushing/Bleeding										E			E	M	
Roughness													E	M	
Friction Loss							E	E	E	E	E	E	E	E	E
Moisture Damage	E			E			E			E			E		
Typical Traffic Volume	All			Low			Low			Low to Moderate			Moderate to High		
Expected Performance (Treatment Life) (yr)*	2-5			1-2			2.0-3.50			2-5 (single course) 3.5-7.0 (double course)			2-4 (single course) 3-5 (double course)		
Expected Performance (Pavement Life Extension) (yr)*	2-5			1-2			4-5			5-6 (single course) 8-10 (double course)			3-5 ((single course) 4-6 (double course)		

E: Efficient, M: Marginal

*Except for fog seal, data is according to SHRP2 Report S2-R26-RR1 (Peshkin et al. 2011). High traffic volume is defined as greater than 5,000 vpd for rural roads and greater than 10,000 vpd for urban roads.

8 CONCLUSIONS

This paper documents the primary outcomes of a strategic initiative to develop a comprehensive roadmap for asphalt pavement improvements in the State of Kuwait. The focus is creating practical, long-term solutions to improve construction quality, rehabilitation, and maintenance practices. The development of this roadmap began with identifying gaps in the current system, including technical, operational, and procedural shortcomings. Subsequently, the team developed a roadmap with specific deliverables and action items.

- Gap analysis with action items for improvements.
- Improved specifications for asphalt materials and construction methods.
- Guidelines for asphalt pavement evaluation, rehabilitation, and maintenance operations.
- Processing, stockpiling, and managing Recycled Asphalt Pavements (RAP) and a customized design procedure for asphalt mixes containing RAP.
- Establishment of training and certification programs for engineers and technicians.
- Integration of advanced technologies for real-time quality control and pavement assessment.

9 REFERENCES

Ahmed, T., Hajj, E., Warrag, A., and Piratheepan, M. (2021). "Evaluation of in-service raveled asphalt pavements in Kuwait,". *Advanced in Materials and Pavement Performance Prediction II,* Kumar, et al. (eds), Taylor and Francis Group, London, ISBN 978-0-367-46169-0, 127-130.

Almutairi, N., and Alfadhli, M. (2023). "Causes of Failure of Asphalt Pavements in Hot Countries (Kuwait)," *International Journal of Engineering Research and Applications*, 13(9), 262-265.

Al-Owmi, F., Al-Othman, N., Almutairi, H., and Al-Bahar, S. (2023). "Evaluation of asphalt pavement Maintenance Practices in Kuwait." Presented at CEES Conference, AL-Khobar, Saudi Arabia.

Hall, K. T., Correa, C. E., Carpenter, S. Elliott, R. (2001). Rehabilitation Strategies for Highway Pavements, NCHRP Web Document 35 (Project C1-38), National Cooperative Highway Research Program, Transportation Research Board, National Research Council.

Miller, J.S., and Bellinger, W. Y. (2014). *Distress Identification Manual for the Long-Term Pavement Performance Program (Fifth Revised Edition)*, Federal Highway Administration, US Department of Transportation.

Ministry of Public Works Administration (2012). General Specification for Kuwait Roads and Highways, Ministry of Public Works, State of Kuwait

Peshkin, D., Smith, K. L., Wolters, A., Krstulovich, J., Moulthrop, J., and Alvarado, C. (2011). *Preservation Approaches for High-Traffic-Volume Roadways,* SHRP 2 Report S2-R26-RR-1, Washington D.C.

Developing a catalogue for cold recycled pavement designs for Germany

M. Kalantari
Federal Highway Research Institute (BASt)

A.H. Greyling, C. Whitehead & A.J. Robertson
Loudon International

ABSTRACT: An overview of a conservative approach integrating Bitumen Stabilised Materials (BSM) into established German design practices. The structural equivalence of these designs to the existing RStO 2012 standard is confirmed using the Mechanistic-Empirical design method. Bitumen stabilised material characteristics, Mechanistic-Empirical design steps, assumed inputs and the first results for the German catalogue are discussed. The increasing interest in BSM in Germany and the demonstrated financial and environmental benefits in several projects worldwide suggest BSM as a suitable base layer alternative.

1 INTRODUCTION

The standards for pavement structures for urban and rural roads in Germany are set out in the *Guidelines for the standardisation of pavement structures of traffic areas (RStO 2012)*. These designs are based on research findings, calculations to estimate the performance of various pavement structures, and construction experience. For pavements with an asphalt surface course, the RStO 2012 offers a variety of base and subbase alternatives, such as asphalt base, cement stabilised base, crushed stone and gravel layers.

Currently, RStO 2012 does not include Bitumen-Stabilised Materials (BSM), which has not yet been implemented on a large scale in the German market. In response to the increasing interest in BSM in Germany and its globally demonstrated financial and environmental benefits, BSM base layers are being investigated as a cold recycling alternative.

2 WHAT IS BITUMEN STABILISED MATERIAL

BSMs are non-continuously bound materials composed of either 100% reclaimed asphalt pavement (RAP) material, graded crushed stone (GCS) or a blend of both, and treated with foamed bitumen or bitumen emulsion. The material is treated with a maximum of 1% active filler (hydrated lime or cement) and 1.8% - 2.2% bitumen to produce a material that performs similarly to a granular material in a pavement structure. BSM is a cost-effective approach to pavement rehabilitation while reducing energy consumption and, as a result, CO_2 emissions.

The failure mechanism of the BSM layer is permanent deformation, which only requires resurfacing to ensure the road's appropriate serviceability.

2.1 *The behaviour of BSM*

BSM behaves similarly to unbound granular materials but with considerably better cohesion and reduced moisture sensitivity. In contrast to hot-mix asphalt, bitumen is distributed among the finer particles in a BSM, leaving the larger particles uncoated. The bitumen-rich mortar created between the coarse particles improves cohesion but has little influence on the internal friction angle.

The dispersed bitumen's visco-elastic properties provide BSM with its flexural strength and stiffness. The BSM maintains the granular properties of the parent material since the coarser aggregate remain uncoated and the individual bitumen particles are not connected. Therefore, since the stiffness is stress dependent, BSM is not susceptible to fatigue cracking (Sabita, 2020).

2.2 *The benefits of BSM*

There are several advantages to recycling with BSM, such as an environmentally friendly approach, early trafficking following compaction that reduces traffic interruptions, and a significant decrease in heavy construction site's traffic (Sabita, 2020).

2.3 Foamed bitumen

When water is injected into hot bitumen, a spontaneous foaming reaction occurs, resulting in foamed bitumen. The injected water quickly vaporises when it encounters hot bitumen, producing a large number of tiny bubbles that momentarily change the bitumen's physical characteristics. This foaming process occurs in an expansion chamber, where bitumen and water are injected under high pressure. The foam generated is inherently unstable and typically collapses within one minute.

During the mixing process, the bitumen bubbles burst, creating small bitumen splinters that disperse throughout the aggregate mix. These splinters adhere to the fine particles, forming a mastic. During compaction, the bitumen particles within the mastic are physically pressed against the larger aggregate particles, forming localized, non-continuous bonds (Wirtgen, 2012).

2.4 Permanent deformation of BSM

The material experiences both plastic strain and elastic strain during a load cycle (Theyse, 2007). Repeated loading causes unbound granular materials and BSM to deform due to the accumulation of residual plastic strain that remains after each load cycle.

3 MECHANISTIC-EMPIRICAL DESIGN STEPS

3.1 BSM design approach

The design process for pavements incorporating BSM is essentially the same as for all other pavement structures. Firstly, the structural capacity (traffic load class) is determined, and construction material availability is established. The existing pavement structure and environmental implications are both considered when rehabilitating carriageways. To classify the various materials, including the material that will be bitumen stabilised, site investigations and laboratory testing are conducted.

Further investigation and testing are necessary for rehabilitation projects that consider in-situ recycling of the existing pavement. The material's shear properties and BSM classification must be determined by treating it with suitable active filler and bitumen stabilising agent.

In order to determine a cost-effective mix and ensure reliable performance, a BSM mix design is performed. This process consists of material sampling and characterisation, followed by mixing, compaction, curing, and testing to determine the optimum active filler and bitumen application rate (Sabita, 2022). Table 1 provides the minimal requirements for Indirect Tensile Strength (ITS) tests.

3.2 Design for permanent deformation in BSM

Traditional European and North American design philosophies solely evaluate the base layers and surfacing, ensuring the subgrade has sufficient cover to prevent deformation under load and protect the pavement layers from frost damage.

When unbound granular materials or BSM are applied as base or subbase layers in a pavement structure, it is imperative to determine the long-term permanent deformation of the layer as greater shear stresses on the pavement layers higher up in the structure result in significant plastic strain. The stress conditions within the layer are consequently examined while modelling a pavement with a BSM base layer.

The principal stresses in the BSM, along with the predetermined material properties, are used to calculate the ratio of applied stresses to the maximum failure stress. The calculated deviator stress ratio, combined with the material's density and moisture resistance properties, helps to estimate the number of allowable load repetitions that the layer can withstand before reaching the terminal level of permanent deformation. The calculation of load repetitions to failure is performed using a Mechanistic-Empirical design approach, which relies on established material properties and data from extensive long-term pavement studies (Sabita, 2020).

4 DESIGN INPUTS FOR THE GERMAN COLD RECYCLED PAVEMENT CATALOGUE

The proposed pavement structures incorporating BSM were designed to be equal to the standard structures in RStO 2012. Therefore, the asphalt base course was replaced with a BSM base layer that provides the required structural capacity. The pavement structures were analysed in Rubicon Toolbox® using Linear Elastic Theory. The input parameters of each layer as well as the results of the analysis were based on the South African Mechanistic Pavement Design Method (SAPDM) transfer functions.

BSMs are designed utilising the material's shear properties, the focus is on the angle of friction and cohesion of the material. Table 1 below indicates the minimum specification limits for BSM and implemented in the Rubicon Toolbox® analysis.

Table 1. Minimum specification limits for BSM

| Class | RAP (%) | ITS | | Triaxial | | |
		ITS$_{DRY}$ (kPa)	ITS$_{WET}$ (kPa)	Cohesion (kPa)	Friction Angle (°)	Retained Cohesion (%)
BSM	< 50	225	125	250	40	75
	80-100	225	125	265	38	75

4.1 Design traffic load

The load class for carriageways is usually determined by the design traffic load, as set out in Table 2 below. The design axle load is the 10-ton single axle, which is the German design standard, used in the analysis (RStO, 2012).

While still providing adequate structural capacity, the pavement designs are intended to optimise the pavement structure for each load class.

Table 2. Relevant design traffic and assigned load class (RStO, 2012)

Equivalent 10-t-standard axles (million ESALs)	Load class
Above 32	Bk 100
From 10 to 32	Bk 32
From 3.2 to 10	Bk 10
From 1.8 to 3.2	Bk 3.2
From 1.0 to 1.8	Bk 1.8
From 0.3 to 1.0	Bk 1.0
to 0.3	Bk 0.3

4.2 Material-specific properties

4.2.1 Asphalt

All pavement structures for all load classes have a 4 cm thick asphalt surface course. For the binder course a thickness of 6 cm and for the asphalt base course a minimum thickness of 8 cm was considered. For all asphalt types a resilient modulus of 5000 MPa was considered. In Rubicon Toolbox®, the binder course and asphalt surface were represented as a single layer. Poisson's ratio of 0.35 was considered for all asphalt types.

In Rubicon Toolbox®, the bitumen content of the asphalt was set as 10% by volume and modelled using the Shell Asphalt Fatigue transfer function. However, as an additional requirement, the fatigue criteria on the asphalt layer will be controlled with the German analytical method.

4.2.2 BSM

The BSM parameters for cohesion (C), angle of friction (φ) and retained cohesion were used as indicated in Table 3 below. Poisson's ratio of 0.3 was used for the BSM layer.

Table 3. BSM input criteria

Description	Parameter
Relative density	86%
Allowed deformation	5% of thickness
Retained cohesion	75%
Cohesion	250 kPa
Angle of friction	40°

The maximum resilient modulus for a BSM is normally considered as 1000 MPa, contingent on the support conditions. In the model, a design resilient modulus of 900 MPa was applied when only one BSM layer was used. For configurations with two BSM layers, the resilient modulus values of 700 MPa and 900 MPa were applied.

The BSM layer must have a minimum thickness of 10 cm. If the BSM thickness exceeds 20 cm, it will be constructed in two layers.

4.3 Anti-frost layer

The anti-frost layer has different thicknesses according to the frost penetration depth of each region. During this analysis, a 30 cm thickness with a plate-load based stiffness (E_{V2}) of 120 MPa was considered for all pavement structures (except for Bk 0.3, for which 100 MPa was selected).

The resilient modulus of the anti-frost layer was kept at a constant of 200 MPa, over the subgrade with a resilient modulus of 45 MPa to reach the desired E_{V2} value of 120 MPa below the base layer.

Poisson's ratio of 0.5 was considered, however, 0.49 was used in the Rubicon Toolbox® analyses as 0.5 is not permitted as an input parameter.

After many design revisions, the cohesion of 30 kPa and friction angle of 40.5° were selected to model the anti-frost layer's material.

5 FIRST RESULTS

The first catalogue design focused on alternative asphalt base designs on top of the anti-frost layer. As mentioned above, load classes Bk 1.0 to Bk 100 were based on a plate-load stiffness of E_{V2} = 120 MPa under the BSM, while load class Bk 0.3 was based on E_{V2} = 100 MPa. In practical cases, it can happen that the bearing capacity under the recycling horizon is less than 120 MPa; therefore, the next step will be to perform the designs with other E_{V2} values too.

The design alternatives incorporating BSM are listed in the tables below for each load class.

Table 4. BSM catalogue, E_{V2} = 120 MPa, Bk 100 & Bk 32

Load class (million ESALs)	Bk 100 (> 32)		Bk 32 (10-32)	
	RStO 12	BSM	RStO 12	BSM
Asphalt surface	12 cm	10 cm	12 cm	10 cm
Asphalt base	22 cm	8 cm	18 cm	8 cm
BSM	-	20 cm	-	15 cm
Anti-frost	30 cm	30 cm	30 cm	30 cm

Table 5. BSM catalogue, E_{V2} = 120 MPa, Bk 10 & Bk 3.2

Load class (million ESALs)	Bk 10 (3.2-10)		Bk 3.2 (1.8-3.2)	
	RStO 12	BSM	RStO 12	BSM
Asphalt surface	12 cm	10 cm	10 cm	10 cm
Asphalt base	14 cm	-	12 cm	-
BSM	-	20 cm	-	15 cm
Anti-frost	30 cm	30 cm	30 cm	30 cm

Table 6. BSM catalogue, E_{V2} = 120 MPa, Bk 1.8 & Bk 1.0

Load class (million ESALs)	Bk 1.8 (1.0-1.8)		Bk 1.0 (0.3-1.0)	
	RStO 12	BSM	RStO 12	BSM
Asphalt surface	4 cm	4 cm	4 cm	4 cm
Asphalt base	16 cm	-	14 cm	-
BSM	-	25 cm	-	20 cm
Anti-frost	30 cm	30 cm	30 cm	30 cm

Table 7. BSM catalogue, E_{V2} = 100 MPa, Bk 0.3

Load class (million ESALs)	Bk 0.3 (<0.3)	
	RStO 12	BSM
Asphalt surface	4 cm	4 cm
Asphalt base	10 cm	-
BSM	-	20 cm
Anti-frost	30 cm	30 cm

6 CONCLUSION

Integrating BSM as a cold recycling alternative is advantageous due to the financial and environmental benefits demonstrated in several projects across the world and caters for the growing interest in BSM in Germany. One of the main requirements for implementing this material in German pavements is to establish an accepted pavement design method. This paper aimed to present the first results of a plan to address this requirement.

The pavement structures presented in this study offer a conservative approach as the first step of a plan to integrate BSM into well-established design procedures in Germany. The Mechanistic-Empirical design method was used to verify that these proposed designs are structurally equivalent to the RStO 2012 loading classes. The next steps are to check other criteria like the fatigue in the lower asphalt layer based on the German analytical pavement design method and to extend the designs to cater for other bearing capacity levels under the BSM layer.

7 REFERENCES, SYMBOLS AND UNITS

– Forschungsgesellschaft für Straßen- und Verkehrswesen e.V., (German Road and Transportation Research Association), (Edition, No. 30/2012) 2012. *Guidelines for the standardisation of pavement structures of traffic areas*. Cologne.
– Sabita (4th ed.) 2020. Technical Guideline: Bitumen Stabilised Materials Guideline for the Design and Construction of Bitumen Emulsion and Foamed Bitumen Stabilised Materials. *Technical Guideline TG 2*. Pretoria: Sabita.
– Theyse, H. L. 2007. *A mechanistic-empirical design model for unbound granular pavement layers.*
– Wirtgen Group. (1st ed.) 2012. *Cold Recycling Wirtgen Cold Recycling Technology*. Windhagen: Wirtgen.

Influence of braking conditions on the stress-strain response of bituminous pavements

Safeena Nazeer & Priti Maheshwari
Indian Institute of Technology Roorkee, Uttarakhand, India

J Murali Krishnan
Indian Institute of Technology Madras, Chennai, India

ABSTRACT: Load transfer from tire to the pavement is influenced by complex driving maneuvers, pavement roughness, and the magnitude of the applied loads. To simulate these conditions, it is necessary to model the tire-pavement interaction under moving loads using realistic loading conditions. In the present numerical study, a computational model is developed to incorporate both vertical and horizontal time-varying truck loads during braking maneuver. The influence of braking conditions and slip on horizontal strain is studied at two critical locations for both an unladen and overloaded truck. The front axle position is identified as the critical location for maximum horizontal tensile strains at the bottom of the bituminous layers in both cases. However, maximum horizontal strains are higher for the overloaded truck compared to the unladen truck at all studied locations.

1 INTRODUCTION

Current pavement design methodologies incorporate static axle load data for design and damage estimation for bituminous pavements (AASHTO, 2008; IRC:37-2018, 2018). However, it is established that when a truck traverses the pavement, it experiences various types of motion, viz. yawing, pitching, and rolling (Mamlouk, 1997; Rajamani, 2011). In free-rolling conditions, the loads transferred from the tire to the pavement can be assumed to be purely vertical and equal to the static loads on the axles. However, this assumption may not hold well during the non-free rolling conditions. Horizontal forces are substantial during acceleration, braking, and cornering. Past research has revealed that horizontal surface forces contribute to a complex stress state at the tire-pavement interface (Wang and Al-Qadi, 2009; Gideon and Krishnan, 2012). Apart from this, during acceleration, the load shifts from the front axle to the rear, while braking transfers the load from the rear axle to the front, increasing the overall vertical load on the front axle. The extent of this load redistribution is influenced by the roughness of the road, the speed of the vehicle, the intensity of the load, and the braking intensity (Collop and Cebon, 1995; Pais et al., 2013; Kubo et al., 2016; Rys et al.,2016; Said and Al-Qadi, 2023; Savio et al., 2023). These observations have been well documented in the past literature. However, studies related to the quantification of these factors in terms of the stress-strain response of the pavement structure are overlooked. This paper primarily focuses on braking conditions and presents a related computational model.

2 SIMULATION OF VERTICAL AND HORIZONTAL TRACTION DURING BRAKING

2.1 Data Collection

The realistic data corresponding to gross vehicle weight (GVW), road profile, truck velocity, and load transfer during braking condition was taken from Savio et al. (2023). In this investigation, an axle load survey was carried out on a national highway (NH-21) in India. Two representative gross vehicle weight for trucks were identified: 85.82 kN for the unladen truck, and 217.5 kN for the overloaded truck. A rough road profile corresponding to the international roughness index (IRI) value of 8.62 m/km was considered according to the International Organization for Standardization (ISO:8608,2016). This road profile was generated in MATLAB using the sinusoidal approximation method, in which the road profile is expressed in terms of the power spectral density

(PSD) of vertical displacement (Tyan et al., 2009). The load transfer data corresponding to a 4 × 2 full truck model with a tire specification of 315/80R22.5, during the braking maneuver, was computed using the hardware-in-loop (HiL) setup integrated with the vehicle dynamic software, TruckMaker. The HiL setup used a rapid prototype hardware that communicates between the TruckMaker and the braking system. A complete braking effort of 100% was considered and designated as 'panic braking'. In the virtual vehicle module of the software, the truck loading data served as an input, while the IPGROAD model utilized the generated road profile in the virtual pavement module. Detailed information regarding the generation of forces can be found in Savio et al. (2023).

Following the above discussion, two critical cases are considered in the present study: an overloaded truck and an unladen truck, both braking with 100% intensity from an initial velocity of 80 kmph on a road with roughness index of 8.62 m/km. In addition, one case of overloaded truck moving with a constant velocity on the same road profile is taken for comparison purposes.

F_z = Total vertical load during braking maneuver ; S_z = Total vertical load during static condition ; F_A = Front axle ; R_A = Rear axle
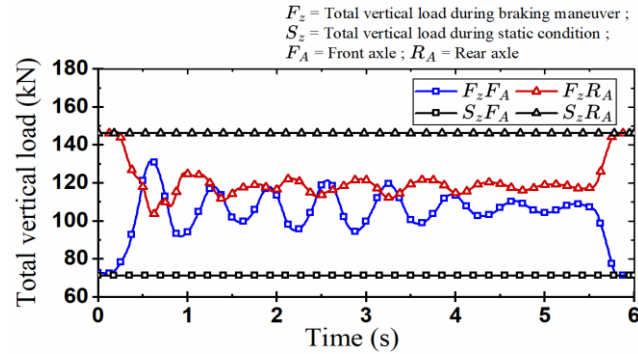
Figure 1a. Total vertical load for overloaded truck

F_y = Total horizontal load during braking maneuver
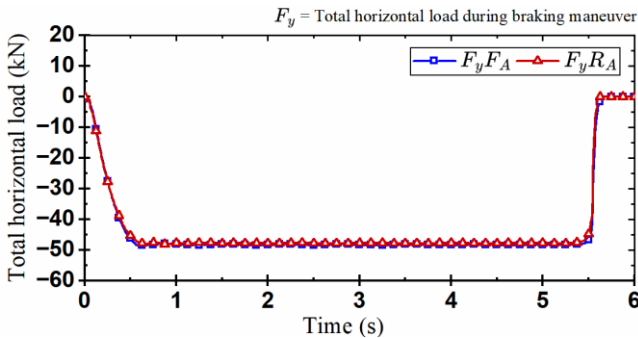
Figure 1b. Total horizontal load for overloaded truck

2.2 Data processing and interpretation

The data collected corresponding to the overloaded and unladen truck are shown in Figure 1 and 2 respectively. The shifting of vertical load from rear to front during braking is evident from Figure 1a and 2a. Equal amount of total horizontal force is being developed at the front and the rear axle tires in case of overloaded truck whereas the total horizontal

force developed is carried by the front axle tires in case of the unladen truck as shown in Figure 1b and 2b respectively.
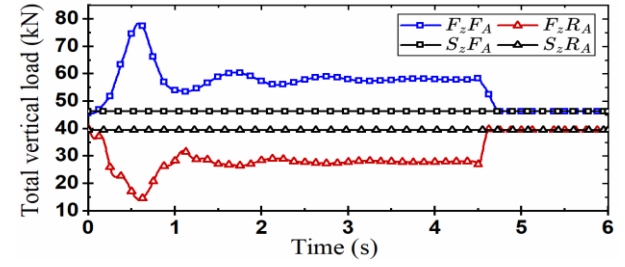
Figure 2a Total vertical load for unladen truck
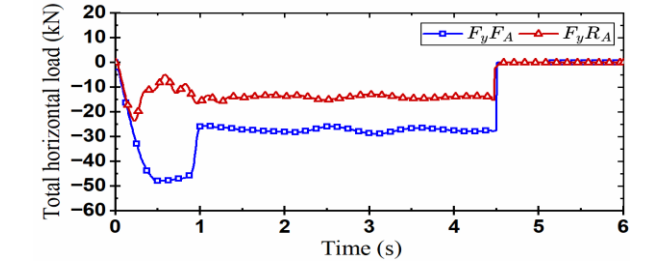
Figure 2b Total horizontal load for unladen truck

3 PAVEMENT MODEL

In the present study, the overall stress-strain response of a five-layered bituminous pavement structure is numerically investigated using PLAXIS 3D v2024 (Brinkgreve and Vermeer, 1998). A typical pavement cross section is taken from IRC:37-2018 for a pavement structure having subgrade CBR value of 5% and design traffic capacity of 50 msa (IRC:37-2018, 2018). The top two layers are the bituminous concrete (BC) and dense bitumen macadam (DBM), followed by the granular base (GB) course, granular sub-base (GSB) course and bottom is the subgrade layer. A layered linearized elastic analysis is carried out with thickness and material properties of each layer as shown in Figure 3a.

All the pavement layers are modeled using a full model with 10-noded tetrahedral volume elements. The interfaces are assumed to be in complete bonded condition with continuity of stress, strain and displacements across and along the interfaces. The truck tires are idealized as line loads of width equal to the tire width (= 315 mm) with the axle dimensions as shown in the Figure 3b. Both the static and dynamic loading is taken as load per unit width of the line load (kN/m). The vertical and horizontal line load is represented by 'q_z' and 'q_y' respectively. Dynamic multipliers in both the vertical and horizontal directions are introduced to incorporate the time varying loading during braking maneuver. Movement function is assigned to each line load corresponding to the variation of velocity with time.
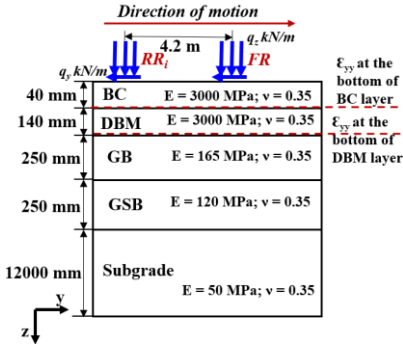
Figure 3a. Cross section of pavement structure with truck load

FL = Front wheel (Left); FR = Front wheel (Right)
RR_i = inner rear wheel (Right); RR_o = outer rear wheel (Right)
RL_i = inner rear wheel (Left); RL_o = outer rear wheel (Left)
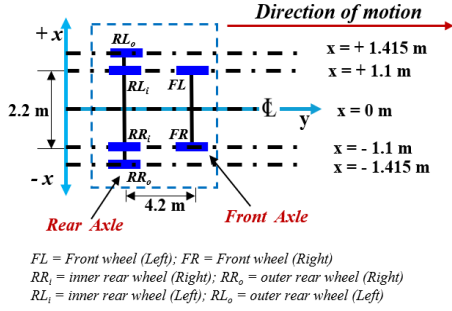
Figure 3b. Top view of pavement structure (not to scale)

The top and the bottom horizontal boundaries are kept free and fixed respectively. The right and left boundaries are also fixed for any lateral deformations. Along with the standard boundary conditions, special absorbent boundary conditions are employed at the vertical boundaries, to absorb the increments of stresses caused by the dynamic loading, thereby preventing spurious wave reflections that do not occur in reality. Dimensional and Mesh sensitivity analysis was carried out to fix the model dimensions, optimal mesh density and optimum time step for the analysis. Consequently, number of elements and nodes were fixed to 297882 and 439520 respectively. The optimal time step for the analysis was found to be equal to 0.005 sec that coincides with the time interval for the braking data. The final computational model with meshing is shown in figure 4.

4 RESULTS AND DISCUSSION

4.1 *Influence of braking condition*

A case of an overloaded truck braking with an initial velocity of 80 kmph on a road with IRI value of 8.62 m/km is simulated and the horizontal strains ($\mathcal{E}_{yy}$) are computed along the direction of motion for the front and inner rear right wheel, at the BC and DBM bottom for time 't' and comparison is made with the free rolling case for the same spatial position as shown in Figure 5. It is evident from Figure 6a that there is a development of horizontal tensile strain ($\mathcal{E}_{yy}$) at the BC bottom at the front right wheel

in case of panic braking due to the introduction of horizontal loading. In addition, there is a substantial increase in the magnitude of horizontal compressive strain at the front right wheel position by about 216% as compared to free-rolling condition. This can be attributed to the shifting of the vertical load from rear to front during braking maneuver. Likewise, the peak horizontal tensile strain is observed at the DBM bottom beneath the front wheel for the braking condition as shown in Figure 6b.
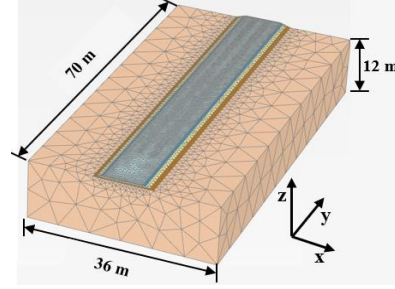
Figure 4. Computational Model for present study
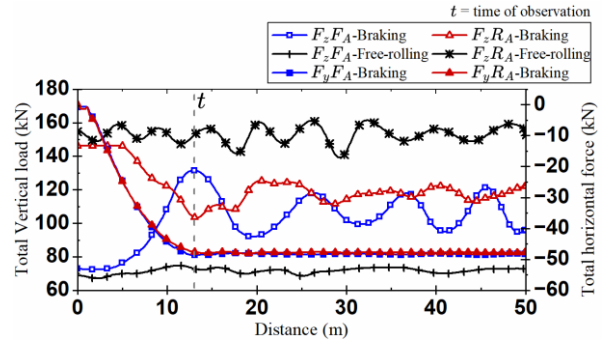
Figure 5. Total loads on overloaded truck (v = 80 kmph)

4.2 *Influence of slip*

A case of an overloaded truck braking with an initial velocity of 80 kmph is simulated and the horizontal strains ($\mathcal{E}_{yy}$) are computed along the direction of motion of the front and inner rear right wheel, at the BC and DBM bottom for the time when the shift from rear to front axle is maximum (t=0.595 s). Comparison is made with the unladen truck case with the same braking conditions and has reached the same spatial position at t=0.585 s. It is clear from Figure 7a and 7b that the horizontal strain at the rear right wheel of the unladen truck is negligible as compared to the overloaded truck at both the BC and DBM bottom. This is due to the fact that the horizontal force developed at the rear axle is negligible in case of the unladen truck. Moreover, the horizontal tensile developed at the BC bottom under the front wheel is same in both the truck cases. This is due to the identical horizontal load carried by the front axles in both scenarios. In addition, maximum horizontal tensile strain can be observed at the DBM bottom beneath the front wheel for the overloaded truck case.
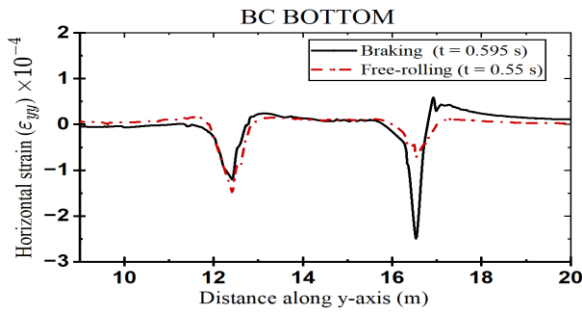
Figure 6a. ε_{yy} for overloaded truck
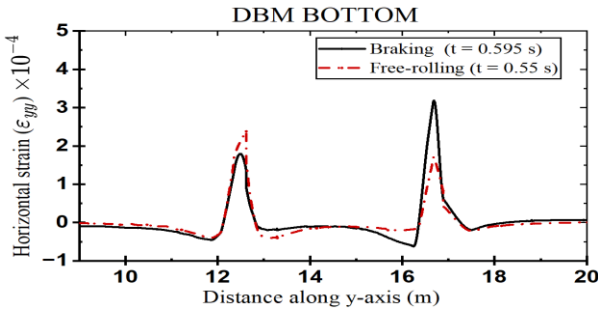
Figure 6b. ε_{yy} for overloaded truck
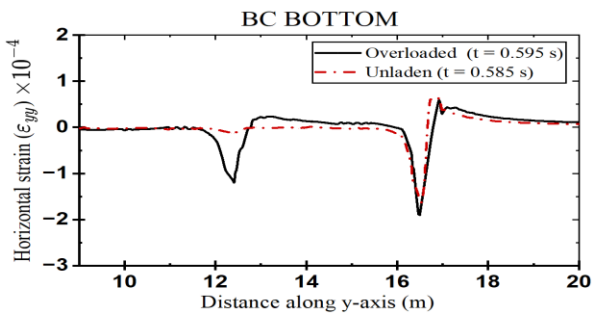
Figure 7a. ε_{yy} along the direction of motion
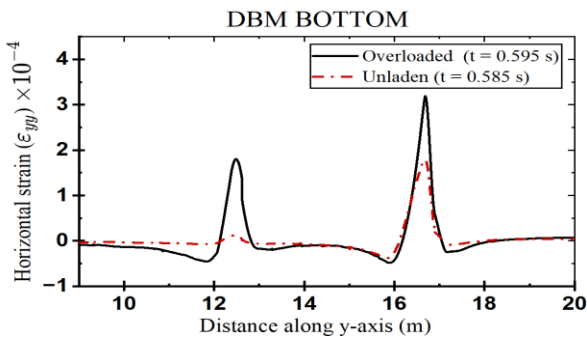
Figure 7b. ε_{yy} along the direction of motion

5 SUMMARY AND CONCLUSIONS

A numerical study was carried out for an overloaded and unladen truck subjected to realistic braking conditions. A total of three simulations were carried out: Overloaded truck with panic braking, unladen truck with panic braking and overloaded truck with free-rolling condition on the same rough road profile with IRI value 8.62 m/km. The effect of braking and slip on horizontal tensile strain at the BC & DBM bottom was analyzed by comparing rolling versus braking and overloaded truck versus unladen truck case respectively. Significant horizontal

tensile strain develops at the BC bottom beneath the front axle during braking, compared to rolling, for both trucks analyzed. The front axle is the critical location for horizontal tensile strain development under both braking and slip conditions, regardless of the truck's loading intensity. However, horizontal strains are higher for the overloaded truck than for the unladen truck at all studied locations.

6 REFERENCES

AASHTO (2008), Pavement Design Guide *A manual of Practice*, Interim Edition.

Brinkgreve, R. and Vermeer, P. (1998), 'Plaxis version 7.2 manual, finite element code for soil and rock analyses', *AA Balkema/Rotterdam/Brookfield, Rotterdam*, The Netherlands.

Collop, A. and Cebon, D. (1995), 'A model of whole-life flexible pavement performance', *Proceedings of the Institution of Mechanical Engineers, Part C: Journal of Mechanical Engineering Science* 209(6), 389–407.

Gideon, C. and Krishnan, J. M. (2012), Influence of horizontal traction on top-down cracking in asphalt pavements, in *'7th RILEM International conference on cracking in pavements: Mechanisms, modeling, testing, detection and prevention case histories'*, Springer, pp. 1069–1079.

IRC:37-2018 (2018), 'Guidelines for the design of flexible pavements', *Indian Roads Congress*.

ISO:8608,2016 (2016), 'Mechanical vibration-road surface profiles-reporting of measured data.', *International Organization for Standardization*.

Kubo, P., Paiva, C., Larocca, A. and Dawson, J. (2016), 'Quantification of the vertical load applied to the pavement during braking maneuver of a commercial vehicle', *Journal of Transportation Engineering* 142(4), 06016001.

Mamlouk, M. S. (1997), 'General outlook of pavement and vehicle dynamics', *Journal of transportation engineering* 123(6), 515–517.

Pais, J. C., Amorim, S. I. and Minhoto, M. J. (2013), 'Impact of traffic overload on road pavement performance', *Journal of transportation Engineering* 139(9), 873–879.

Rajamani, R. (2011), *Vehicle dynamics and control*, Springer Science & Business Media.

Rys, D., Judycki, J. and Jaskula, P. (2016), 'Analysis of effect of overloaded vehicles on fatigue life of flexible pavements based on weigh in motion (WIM) data', *International Journal of Pavement Engineering* 17(8), 716–726.

Said, I. M. and Al-Qadi, I. (2023), 'Incorporation of pavement dynamic loading in mechanistic–empirical design frameworks', *Transportation Research Record* 2677(12), 14–28.

Savio, D., Challa, A., Subramanian, S. C. and Murali Krishnan, J. (2023), 'Influence of road profiles and truck braking on the dynamic load transfer to the pavement', *International Journal of Pavement Engineering* 24(2), 2090559.

Tyan, F., Hong, Y., Tu, S. and Jeng, W. (2009), 'Generation of random road profiles', Journal of Advanced Engineering 2(4), 1373–8.

Wang, H. and Al-Qadi, I. L. (2009), 'Combined effect of moving wheel loading and three-dimensional contact stresses on perpetual pavement responses', *Transportation research record* 2095(1), 53–61.

Ageing effects on interfacial bonding properties in asphalt pavements

Ali Rahman

School of Civil engineering, Faculty of Engineering and Physical Sciences, University of Leeds, Leeds, UK.

Rabea Al-Jarazi & Chaoyang Li

School of Civil Engineering, Southwest Jiaotong University, Chengdu, China.

ABSTRACT: This study investigated the effects of temperature and aging on the interfacial bonding performance of asphalt pavements using two tack coat materials: cationic modified emulsified bitumen (BCR) and SBR emulsified asphalt. Double-layered specimens were subjected to shear testing at 30°C and 40°C for both aged and unaged conditions. The interface shear modulus (ISM) and peak energy (E_{peak}) were evaluated to assess interface stiffness and energy absorption. Results indicated that both temperature and aging significantly reduced interlayer shear performance. Aged specimens exhibited approximately 50% lower ISM and E_{peak}, reflecting weakened bonding due to oxidation and stiffening. While BCR tack coat demonstrated better stability at elevated temperatures, SBR outperformed in energy absorption but showed higher temperature sensitivity. These findings emphasize the need for careful material selection to ensure long-term pavement durability under varying temperature and aging conditions.

1 INTRODUCTION

1.1 *Background*

The performance and longevity of asphalt pavements heavily rely on adequate bonding between the consecutive layers that form their multi-layered structure. Each layer serves a distinct role, with the interlayers acting as critical transition zones for load and stress transfer throughout the system (Canestrari et al., 2013). Notably, the interface between the surface course and underlying layer is susceptible to extreme temperatures and stresses, potentially leading to distresses like slippage, delamination, and top-down cracking if bonding is insufficient (Rahman et al., 2017). Consequently, ensuring robust bonding conditions, especially at upper layer interface, is crucial to prevent bond failure and associated distresses that can undermine the structural integrity of the asphalt pavement system. For this reason, numerous studies were conducted to better understand the bonding mechanism and improve interlayer bonding performance in asphalt pavements (Al-Jarazi et al., 2024, Tozzo et al., 2014, Diakhate et al., 2006, Raab et al., 2012). Despite these efforts, the exact causes of poor bonding are not fully known. There are a number of factors at play, including the type and compaction of base materials , characteristics of the bitumen and tack coat materials , weather conditions during construction, surface contamination, water penetration between layers, and so on (White, 2017). Therefore, it is of great significance to ascertain the effects of various factors affecting interface bonding. Aging is a critical factor influencing asphalt pavement performance, impacting not only bituminous materials but also the interfacial bonding between layers (Raab et al., 2015). As asphalt ages, it undergoes oxidation and volatilization, leading to increased stiffness and brittleness, which can weaken the bonding essential for structural integrity and load distribution of the pavement structure. Despite its significance, the study of aging effects on interfacial bonding has not been fully explored.

1.2 *Objective*

The present investigation aims to evaluate the aging effects on the interface bonding strength of asphalt pavements. To this end, two types of tack coat materials and testing temperatures were considered. Microstructure analysis was conducted using scanning electron microscopy (SEM) to assess the impact of aging on the bonding strength.

2 EXPERIMENTAL PROGRAM

2.1 *Materials and methods*

Double-layered asphalt specimens, comprising SMA-13 as top layer and AC-20 as bottom layer were manufactured using AH-70 (60/80 penetration grade) base asphalt binder. The interlayer bonding strength was assessed through a newly developed inclined
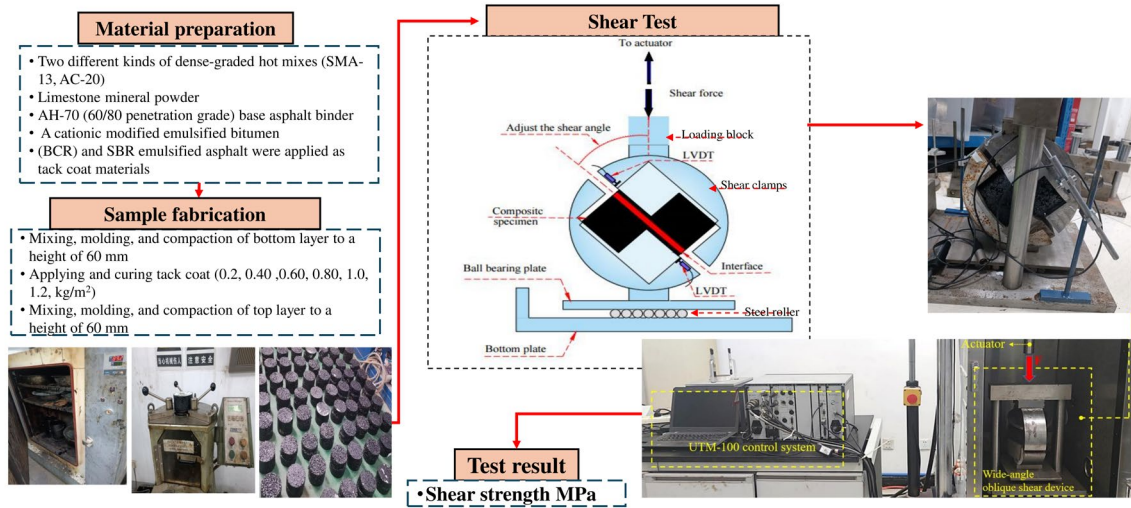
Figure 1. Experimental plan and procedure for measurement of the interlayer shear strength.

shear device, which measures the shear strength at the interface between the layers. A cationic modified emulsified bitumen (BCR) and styrene butadiene rubber (SBR) emulsified asphalt were applied as tack coat materials at varying application rates. All material properties met the technical requirements specified by the Chinese specification JTG F40-2004. In the first phase of this study, residual tack coat application rates ranging from 0.20 to 1.20 kg/m² were selected to explore the effects of tack coat dosage on the measured shear strength. The tests were conducted at the temperature of 25°C and a shear angle of 35 degrees. Subsequently, the optimal value of the tack coat rate was identified for both tack coat materials.

In the second phase, a group of specimens, denoted as aged specimens, were selected and conditioned to long-term aging condition while the second group was unaged as control specimens. To simulate aging condition, the specimens were stored in an oven for five days at 85°C. After the aging period, the oven was switched off, and the specimens were left to cool to room temperature. Subsequently, both groups were subjected to shear testing at a designated testing temperature. In addition, the microstructural assessment of aged specimens was conducted by SEM. The experimental plan and procedure for determining the interlayer shear stress (ISS) are displayed in Figure 1.

2.2 *Measures of interface shear performance*

To measure monotonic behavior of interlayer bonding properties, three measures were utilized in this study.

(a) Interface shear strength (ISS_{max}). The ISS_{max} is the peak value of shear stress in the shear stress vs. shear displacement curve. It represents the point at which the interface can no longer sustain increasing shear forces, leading to slippage or debonding.

(b) Interface shear modulus (ISM). The ratio of interface shear strength to the corresponding displacement or the gradient of the stress/strain plot is commonly referred to as the interface shear stiffness or shear stiffness modulus. It quantifies the stiffness of the interface at the point where the peak shear strength is achieved, reflecting the shear resistance relative to the displacement at failure.

(c) Peak energy (E_{peak}). The peak energy is explained as the specific energy utilized to cause failure at the specimen interface and is computed as the area under stress-displacement curve until the peak value ISS_{max}.

The schematic presentation of three concepts is demonstrated using a typical shear stress–displacement plot of aged and unaged specimens in Figure 2.
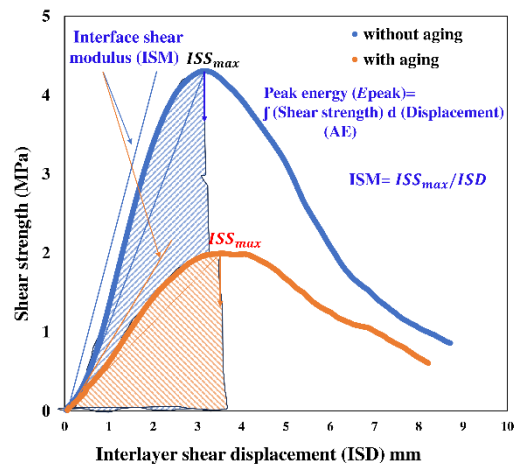
Figure 2. Shear stress vs. displacement curve of aged and unaged specimens and key measurement parameters.

3 RESULTS AND DISCUSSION

3.1 *Text and indenting*

Figure 3.a shows the effects of tack coat rates on interface bond shear strength for SBR and BCR tack coats. For SBR, shear strength peaked at 0.80 kg/m²
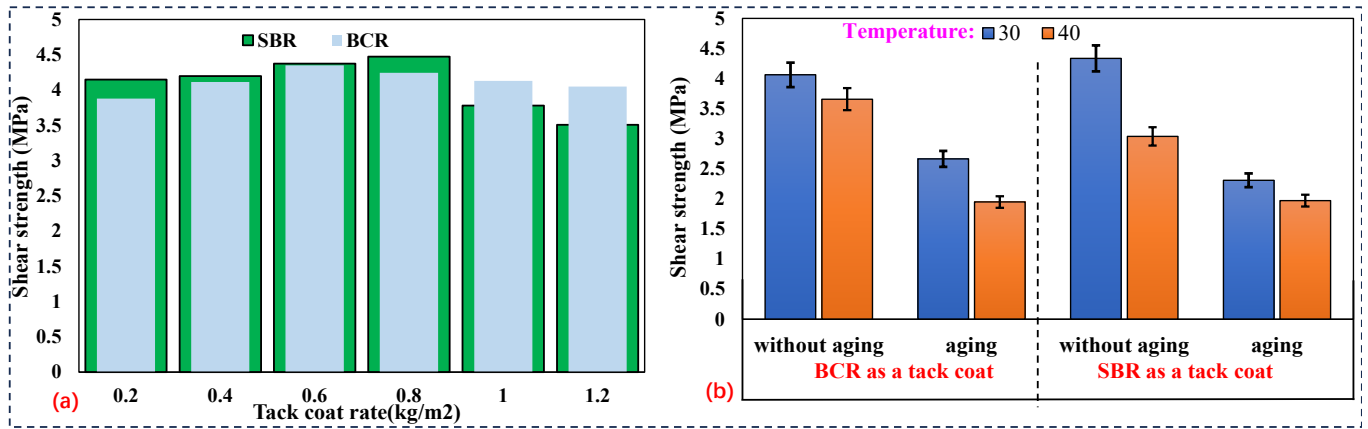
Figure 3. Effects of tack coat dosage and aging on interface bond shear strength.

while shear strength reached its maximum value at 0.6 kg/m² for BCR. No matter what tack coat material being applied, the shear strength declined with further tack coat dosage. Adequate tack coat application is crucial for optimal bonding, but excessive dosages adversely impact shear strength.

Figure 3.b illustrates the effect of aging on the interface bond shear strength for BCR and SBR tack coats at 30°C and 40°C. A significant reduction in shear strength due to aging was observed for both materials. While aging caused a 34% reduction at 30°C and 47% at 40°C for BCR tack coat, it resulted in a decline of 47% at 30°C and 35% at 40°C for SBR material. This decrease in shear strength can be attributed to aging and oxidation processes, making the tack coats stiffer and more brittle, compromising interlayer bonding. The extent of reduction varied between tack coats and temperatures. These findings highlight the importance of considering aging effects on long-term tack coat performance and selecting materials that maintain adequate bonding properties over the pavement's service life, especially at elevated temperatures.

The results of the interface shear performance for two tack coat materials under varying temperatures and aging conditions are presented in Table 1. The analysis focuses on two critical performance parameters: the (ISM) and the E_{peak}.

Table 1. Margin settings for A4 size paper and letter size paper.

Temperature (°C)	Unaged		Aged	
	30	40	30	40
ISM$_{BCR\ tack\ coat}$ (MPa/mm)	0.98	1.22	0.54	0.51
ISM$_{SBR\ tack\ coat}$ (MPa/mm)	1.35	0.61	0.48	0.47
$E_{peak,\ BCR\ tack\ coat}$ (N/mm)	21.01	18.14	11.99	9.49
$E_{peak,\ SBR\ tack\ coat}$ (N/mm)	20.23	16.18	12.21	10.40

The ISM shows a notable decrease as the temperature increased from 30°C to 40°C for both unaged and aged specimens. For unaged specimens, the ISM of BCR increased slightly from 0.98 MPa/mm to 1.22 MPa/mm, whereas the SBR tack coat decreased significantly from 1.35 MPa/mm to 0.61 MPa/mm, suggesting a greater sensitivity of SBR to elevated temperatures. Under aging conditions, the ISM values are considerably lower for both materials, with reductions of approximately 50%, reflecting the deterioration of interface stiffness due to long-term exposure to aging.

The peak energy, representing the energy absorbed at the interface before failure, follows a similar trend. For unaged specimens, peak energy decreased with increasing temperature, dropping from 21.01 N/mm to 18.14 N/mm for BCR and from 20.23 N/mm to 16.18 N/mm for SBR. The aged specimens exhibit significantly lower peak energy values, highlighting the negative impact of aging on the interface's capacity to absorb shear deformation. Although both tack coats experience reduced performance with aging and temperature, SBR consistently shows slightly higher peak energy values compared to BCR, indicating better deformation capacity and energy absorption, albeit with greater sensitivity to temperature.

3.2 Microstructural assessment and aging

The SEM analysis (Fig. 4) of aged specimens revealed significant microstructural degradation, including the presence of micro and thermal cracks. This deterioration can be attributed to the stiffening and embrittlement of the asphalt binder due to aging, leading to a higher potential for crack formation and compromised mechanical strengths. The observed cracks and degraded microstructure directly impair interface bonding characteristics by disrupting the continuity and adhesion between asphalt layers, resulting in reduced interfacial shear strength. The aging-induced stiffening and brittleness of the asphalt increases the susceptibility to fatigue and thermal cracking, contributing to the overall deterioration of mechanical performance over time. These findings
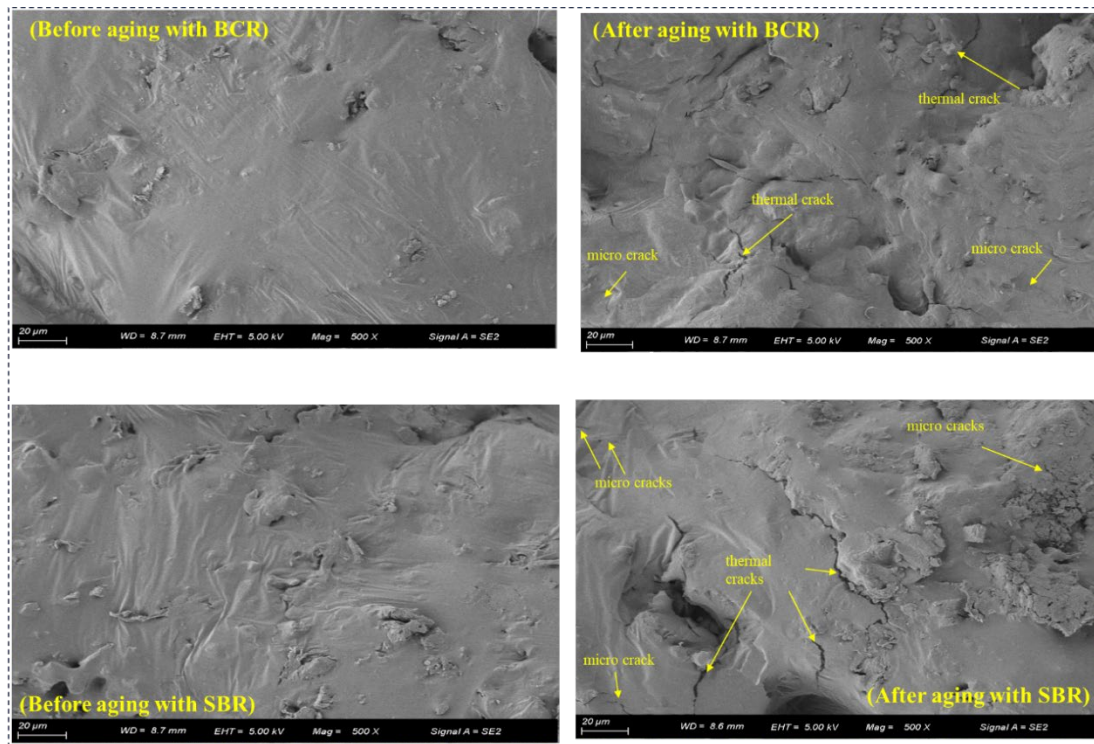
Figure 4. SEM micrographs of aged and unaged specimens.

underscore the importance of aging mitigation strategies and selecting materials that can maintain their integrity throughout the pavement service life.

4 CONCLUSIONS

This study evaluated the interfacial bonding performance of asphalt pavements under varying temperatures and aging conditions, focusing on two tack coat materials, BCR and SBR emulsified asphalts. The results highlight that both temperature and long-term aging have a significant negative impact on interlayer bonding performance. The ISM, which reflects interface stiffness, decreased with rising temperature and aging, with aged specimens showing reductions of approximately 50%. Notably, the SBR tack coat exhibited greater sensitivity to temperature compared to BCR, while BCR demonstrated more stable shear stiffness at elevated temperatures.

The peak energy representing the interface's ability to absorb deformation energy before failure, also declined with temperature and aging. Despite this, the SBR tack coat consistently exhibited higher peak energy values than BCR, indicating superior deformation capacity and energy absorption. These findings suggest that while SBR offers enhanced energy dissipation, its greater temperature sensitivity must be considered in practical applications.

In summary, the study underscores the importance of selecting tack coat materials based on their temperature stability and resistance to aging effects to optimize long-term interlayer bonding performance in asphalt pavements. The results provide valuable insights for improving pavement durability and inform material selection for varying service conditions.

5 REFERENCES

Al-Jarazi, R., Rahman, A., Ai, C., Al-Huda, Z. & Abdelhliem, B. L. E. 2024. Interface bonding strength between asphalt pavement layers under mixed shear-tensile mode: laboratory evaluation and modeling predictions. *Journal of Materials in Civil Engineering, 36*, 04023565.

Canestrari, F., Ferrotti, G., Lu, X., Millien, A., Partl, M. N., Petit, C., Phelipot-Mardelé, A., Piber, H. & Raab, C. 2013. Mechanical testing of interlayer bonding in asphalt pavements. *Advances in Interlaboratory Testing and Evaluation of Bituminous Materials.* Springer.

Diakhate, M., Phelipot, A., Millien, A. & Petit, C. 2006. Shear Fatigue Behaviour of Tack Coats in Pavements. *Road Materials and Pavement Design, 7*, 201-222.

Raab, C., El Halim, A. A. & Partl, M. N. 2012. Interlayer bond testing using a model material. *Construction and Building Materials, 26*, 190-199.

Raab, C., Grenfell, J., Abd El Halim, A. O. & Partl, M. N. 2015. The influence of age on interlayer shear properties. *International Journal of Pavement Engineering, 16*, 559-569.

Rahman, A., Ai, C., Xin, C., Gao, X. & Lu, Y. 2017. State-of-the-art review of interface bond testing devices for pavement layers: toward the standardization procedure. *Journal of Adhesion Science and Technology, 31*, 109-126.

Tozzo, C., Fiore, N. & D'andrea, A. 2014. Dynamic shear tests for the evaluation of the effect of the normal load on the interface fatigue resistance. *Construction and Building Materials, 61*, 200-205.

White, G. 2017. State of the art: interface shear resistance of asphalt surface layers. *International Journal of Pavement Engineering, 18*, 887-901.

Establishing the Rutting Threshold for Marshall Samples Using HWTT

Sadiya Shaikh[*]
Research Scholar, Department of Civil Engineering, IIT (BHU), Varanasi. India-221005, Email: sadiyashaikh.rs.civ21@iitbhu.ac.in ORCID Id: 0009-0006-5349-9652

Ankit Gupta
Associate Professor and MoRTH Chair Professor, Department of Civil Engineering, IIT (BHU), Varanasi. India-221005, Email: ankit.civ@iitbhu.ac.in ORCID Id: 0000-0003-1789-9502

[*] *Corresponding author*

ABSTRACT: The study proposes a threshold value for selecting rut-resistant Marshall-designed bituminous mixtures. The study also determines the association of 100 mm and 150 mm Hamburg Wheel Tracking Test (HWTT) samples. Samples of 100 mm and 150 mm diameter comprising different binder grades (VG-30, VG-40 and PMB-40) and compactive efforts (35, 75 and 110 blows) were tested using HWTT. The study emphasizes the stronger correlation ($R^2 \geq 0.85$) between 100mm and 150mm samples in HWTT results providing useful information to pavement engineers. The test result also shows that polymer-modified mixtures have better rutting resistance because of their increased viscosity while higher compactive efforts improve resistance by minimizing air voids. Overall, the study emphasizes the significance of performance testing and specification (rut depth=6.5mm for the Marshall mixtures) in pavement design for ensuring resilience and durability. These findings provide valuable guidance for engineers and researchers aiming to increase the performance of bituminous pavements through effective material selection and design strategies.

1 INTRODUCTION

Rutting in road pavements is a common distress that occurs due to various factors such as heavy traffic loads, high temperatures and the properties of the materials (aggregate and binder) used in the pavement (Zheng *et al.* 2015). It is characterized by the deformation/displacement of the pavement surface particularly in bituminous layers, leading to a significant reduction in the pavement's service life and posing risks to drivers (Nahi *et al.* 2016). Understanding and addressing rutting in road pavements is crucial for ensuring the longevity of transportation infrastructure (Haider and Harichandran 2009). Also, by implementing appropriate materials, design considerations, and maintenance strategies, it is possible to minimize rutting and enhance road pavements overall performance and durability.

As we are moving toward the balanced mix design (BMD) concept (Yin *et al.* 2021), there is a need to incorporate simple performance tests at the design stage and for quality assurance and checks during production. It is important to note that there are currently no specific performance tests designed for Marshall mixes with a 100 mm diameter despite their widespread use in many countries (Hwang *et al.* 2004, Chakroborty *et al.* 2010, Hesami *et al.* 2013).

Therefore, the motivation of this study lies in addressing the shortcomings of relying solely on volumetric properties, through the integration of a performance test in the current Marshall mix design method. Table 1 presents the HWTT Performance Specifications for different DOT's using different BMD approaches for 150 mm samples.

Since Marshall mixes are still used, we need to find the correlation of 100 mm diameter samples with the 150mm ones. To move forward in that direction, the main objectives of the present study are defined as follows:
• To establish the threshold specification for HWTT for 100mm Marshall samples.
• To determine the association of 100 mm and 150 mm Marshall samples by the HWT test.
• To evaluate the effect of binder grade and compaction levels on the rutting potential of bituminous mixtures.

2 RESEARCH METHODOLOGY

Twenty-seven specimens (1 Design Aggregate Gradation × 3 Binder Content × 3 Binder Grade × 3 Replicates) of bituminous concrete (BC-1) gradation having a Nominal maximum aggregate size (NMAS) of 19 mm were prepared. As a result, 3 OBC's were obtained for different combinations of mixtures. Further, using obtained OBC's, specimens were thereby made at three different levels of compactive efforts i.e., 35, 75 and 110 blows. This was done for replicating the primary and secondary compaction that occurs during the service life of the road. 35 blows represent

approximately 7 % air voids simulating initial compaction during construction and 110 blows represent approximately 2.5 % air voids simulating the effects of traffic-induced secondary compaction over time. Thereby HWTT was performed on 72 samples (100mm and 150 mm samples) to evaluate the rutting resistance.

3 MATERIAL SELECTION

3.1 *Aggregate and Binder*

Granite aggregates were used for the study. It was selected because of its higher strength and low absorptive characteristics which make it more durable and watertight. Mixtures were prepared using viscosity graded and polymer modified binders namely VG-30, VG-40 and PMB-40. These binders were selected based on their common use in road construction applications so that the results of this study could be extended to standard paving industry practices. The physical and mechanical properties of aggregate and binders have been evaluated as per the Bureau of Indian Standards and the Ministry of Road Transport and Highways (MoRT&H) specifications (MORT&H Guidelines 2013) .

Table 1. HWTT Performance Specifications for different DOT's using different approaches

Approach	DOT's	Mixture type	HWTT Performance Specifications
Approach A: Volumetric Design with Performance Verification	Illinois (Barry 2016)	Hot Mix Asphalt	The minimum number of wheel passes required to achieve **12.5 mm** rut depth, corresponding to various binder grades as indicated: PG58-xx (or lower)-5000 passes PG64-xx-7500 passes PG70-xx- 15000 passes PG76-xx (or higher)-20000 passes
	Texas (Alkhayat 2020)	Surface Mix	The minimum number passes to **12.5 mm** rut depth for the different virgin grade binders as: PG64-xx (or lower)-10000 passes PG70-xx- 15000 passes PG76-xx (or higher)-20000 passes
Approach B:Volumetric Design	Missouri (Yin *et al.* 2021)	Stone Matrix Asphalt	The minimum number of wheel passes required to achieve **12.5 mm** rut depth, corresponding to
with Performance Optimization			different binder grades as given under: PG58S-xx-5000 passes PG64S-22-7500 passes PG64H-22-15000passes PG64V-22- 20000passes
Approach C: Performance-Modified Volumetric Design	California (Yin 2018)	Surface Mix	The number of wheel passes to **12.5 mm** rut depth is greater than 20,000
Approach D: Performance Design	Tennessee (Yin *et al.* 2021)	All mixtures	≥ 10,000 passes to 12.5 mm rut depth for ADT < 10000; ≥ 15,000 passes to 12.5 mm rut depth for ADT & ≥ 20,000 passes to **12.5 mm** rut depth for Interstates and controlled access State Routes

4 EXPERIMENTAL INVESTIGATION

4.1 *Gradation*

Aggregate gradation is one of the most important properties which affect the final behavior of the mix (Kandhal and Mallick 1999). This study considered bituminous mixes prepared using bituminous concrete (BC-1) gradation. The choice of the gradation is consistent with the MoRT&H specifications. Figure 1 shows the design aggregate gradations i.e., mid-gradation for the bituminous mixes (BC-1) incorporated in the study. It is anticipated to have a similar trend even if the aggregate gradation changes. The primary reason for this expectation is that the underlying mechanisms governing rutting behavior such as the properties of the binder, the compaction effort, and the environmental conditions which would still apply across different gradations. While the absolute values of rut depth might vary with changes in aggregate gradation due to differences in particle size distribution, shape, and texture, our study's relative performance trends and correlations are likely to remain consistent. This is because the fundamental interactions between the binder and aggregate and the load distribution characteristics would still follow the same principles.

4.2 *Bituminous mix design*

This study employed Marshall mix design methodology following Indian standards to design the bituminous mixtures (IRC:111-2009 *Specifications for Dense Graded Bituminous Mixes,* 2009). The OBC was identified at 4% air voids in line with the MS-2 guidelines (*MS-2 7th Edition Asphalt Mix Design*

Methods 2009). Following this, the Marshall parameters were evaluated at the established OBC's. The resulting parameter values conform to the IRC:111-2009 specifications. To keep the manuscript concise, Marshall parameters have not been presented. Table 2 represents the different OBC's for various combinations of mixtures.

Table 2. OBC (%) of Mid Gradation for different Binder grades

Design Aggregate Gradation (DAG)	BC-1 (NMAS-19mm)		
	VG-30	VG-40	PMB-40
Mid Gradation	5.01	5.09	5.21

4.3 *Test Methods*

4.3.1 *Hamburg Wheel Tracking Test*
HWTT was performed at 60°C in a dry environment in accordance with AASHTO T324-2017. Four samples (for two sets) were evaluated. Marshall compacted specimens of diameters 100 mm and 150 mm were used for the testing. A load of 705 N was put on the compacted specimen by a steel wheel. Linear Variable Differential Transformers (LVDTs) were used to detect the rut depth. The termination criteria were 20,000 passes or 12.5 mm rut depth whichever happened first. Figure 2

5 RESULT AND DISCUSSION

HWTT methods assess the rut depth of the bituminous mixture wherein a higher value of permanent deformation/rut depth indicates lower rutting resistance and conversely. Figure 3 illustrates the rut depth values obtained for various combinations of bituminous mixes encompassing varied compactive efforts for different binder grades. It was seen that the 100 mm samples exhibited a lower rut depth than the 150 mm samples in the HWTT test because the strain rate for both size samples was significantly different (Brown and Bassett 1990). Further, Figure 4 shows the association between 100 mm and 150 mm Marshall samples. The relationship between HWTT results and sample dimensions can be described using the linear regression equation (1): $y = 1.9466x - 0.3634$

where y represents the predicted performance value in millimeters and x is the independent variable, likely related to HWTT parameters. The regression model has a strong correlation, as indicated by $R^2 = 0.98$. For 150 mm HWTT samples, the performance specification is set at 12.5 mm as outlined in Table 1. Using this model, the corresponding HWTT result for 100 mm Marshall samples can be calculated. Based on the regression and the established correlation, the predicted value for the 100 mm samples is approximately 6.5 mm. This calculation helps in establishing performance equivalence between samples of different sizes.

Further, the test result indicates that the polymer-modified mixes outperformed the mixtures prepared with viscosity graded binders (VG-30 and VG-40) for a particular DAG and compactive effort. This can be due to polymer modified binders increased viscosity (Habeeb *et al.* 2014). It was also found that for a given DAG and binder grade, the rut depth increases with decreasing compactive effort. Bituminous mixes with a higher percentage of air void have a higher rutting potential due to increased ductility and porosity (Barry 2016). Conversely, stiffness increases with increased compactive effort which improves the rutting resistance.

6 CONCLUSION

The study evaluates the resistance of the Marshall mixes against rutting using HWTT. This study examined Marshall compacted samples of 100 mm and 150 mm diameter comprising different binder grades (VG-30, VG-40 and PMB-40) and compactive efforts (35, 75 and 110 blows) for the HWTT. 100 mm samples correlate well ($R^2 \geq 0.98$) with 150 mm samples of HWTT. The regression analysis indicates that 100 mm Marshall samples can achieve performance equivalence with 150 mm samples with a predicted HWTT value of approximately 6.5 mm. This supports the feasibility of using smaller sample dimensions under the same test conditions. These findings provide valuable guidance for engineers and researchers aiming to increase the performance of bituminous pavements through effective material selection and design strategies.

Results also indicate that polymer-modified mixtures have improved rutting resistance due to their increased viscosity. Additionally, increased compactive efforts improve the rutting resistance. This was so because the bituminous mixes with a higher percentage of air void have a higher rutting potential due to increased ductility and porosity. Conversely, stiffness increases with increased compactive effort which improves the rutting resistance.

7 REFERENCES

Al-khayat, H., 2020. Balanced Mix Design for Asphalt Mixtures, (March).

Barry, M.K., 2016. An analysis of Impact Factors on the Illinois Flexibility Index Test (Master's thesis).

Brown, E.R. and Bassett, C.E., 1990. Effects of maximum aggregate size on rutting potential and other properties of asphalt-aggregate mixtures. *Transportation Research Record*, (1259), 107–119.

Chakroborty, P., Das, A., and Ghosh, P., 2010. Determining reliability of an asphalt mix design: case of marshall method. *Journal of Transportation Engineering*, 136 (1), 31–37.

Habeeb, H., Chandra, S., and Nashaat, Y., 2014. Estimation of moisture damage and permanent deformation in asphalt mixture from aggregate gradation. *KSCE Journal of Civil Engineering*, 18 (6), 1655–1663.

Haider, S.W. and Harichandran, R.S., 2009. Effect of axle load spectrum characteristics on flexible pavement performance. *Transportation Research Record*, (2095), 101–114.

Hesami, S., Roshani, H., Hamedi, G.H., and Azarhoosh, A., 2013. Evaluate the mechanism of the effect of hydrated lime on moisture damage of warm mix asphalt. *Construction and Building Materials*, 47, 935–941.

Hwang, S.-D., Yoon, A.-S., and Kim, B.-I., 2004. Improvement of Marshall Mix Design and Comparative Evaluation with Current Marshall Mix Design Method. *Journal of the Korean Society of Road Engineers*, 6.

Kandhal, P.S. and Mallick, R.B., 1999. Evaluation of Asphalt Pavement Analyzer for HMA Mix Design. *NCAT Report 99-04*, (99).

MORT&H Guidelines, 2013. Specifications for Road and Bridge Works for State Road Authorities, Fifth Revision, 448.

MS-2 7th Edition Asphalt Mix Design Methods, 2009. Asphalt Institute.

Nahi, M.H., Kamaruddin, I., and Napiah, M., 2016. Rutting Prediction in Asphalt Pavement Based on Viscoelastic Theory. *MATEC Web of Conferences*, 78.

Specifications for Dense Graded Bituminous Mixes, 2009.

Yin, F., 2018. Development of a Framework for Balanced Mix Design.

Yin, F., West, R., and Technology, A., 2021. *DESIGN*. NAPA IS-143 BMD Resource Guide.

Zheng, M., Han, L., Wang, F., Mi, H., Li, Y., and He, L., 2015. Comparison and analysis on heat reflective coating for asphalt pavement based on cooling effect and anti-skid performance. *Construction and Building Materials*, 93, 1197–1205.

8 FIGURES
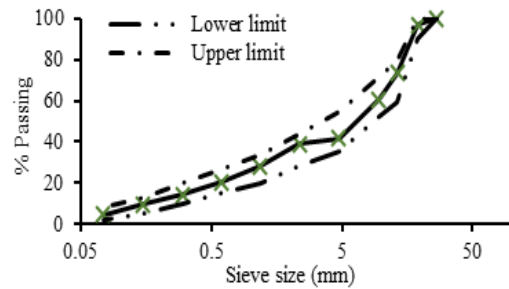
Figure 1. Design Aggregate Gradation (Mid Gradation) for the Bituminous Mix (BC-1)

a) 150mm samples   b) 100mm samples
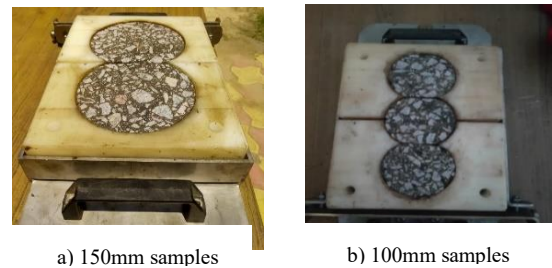
Figure 2. Specimens for performance tests
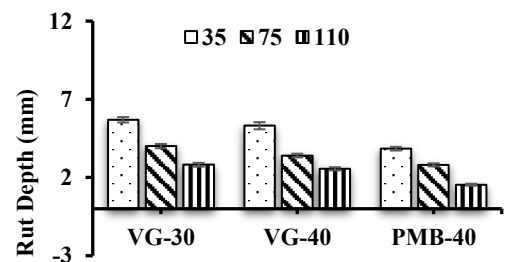
a) Rut depth of HWTT samples of 100 mm
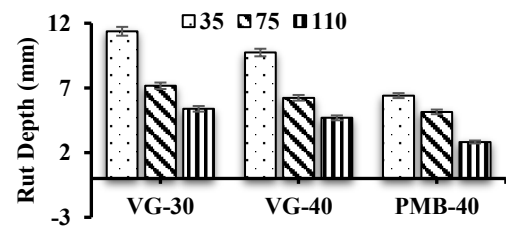
b) Rut depth of HWTT samples of 150 mm

Figure 3. Rut Depth values obtained for different bituminous mixtures
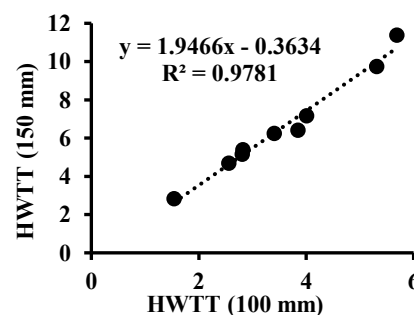
Figure 4. HWTT (100 mm) Vs HWTT (150 mm)

Developing a Statistically Based Correlation between ACN and ACR for Conversion of Runway PCN to PCR Under the New International Airport Pavement Strength Rating System

G. White
University of the Sunshine Coast, Sippy Downs, Queensland, Australia

S. Jamieson
University of the Sunshine Coast, Sippy Downs, Queensland, Australia

ABSTRACT: Since 1981, runway pavement strength has been controlled by an international rating system. The system is operationally simple, with an index of relative aircraft induced damage compared to an index of pavement strength, with aircraft operators requiring permission to operate when the aircraft damage index exceeds the pavement strength index. The original system was based on the simple mathematics available for pavement thickness determination at the time it was developed. However, pavement thickness determination now uses more sophisticated methods. For consistence between strength rating and design, a new runway strength rating system was introduced in 2024. For many regional airports, transitioning to the new system is a burden, with limited operational benefit, and a simple conversion is therefore desired. Based on comparison of old and new aircraft index values, a statistically reasonable correlation was developed. For runways with a clear and reliable existing strength rating, the correlation between old and new aircraft damage index can be used to estimate the new pavement strength rating from the old strength rating. Although this approach is likely to be reasonable for flexible runways with a known critical aircraft forming the basis of the old strength rating, it still remains preferable to calculate the actual aircraft damage index for the identified critical aircraft, and adopting that value as the basis of the new strength rating.

1 INTRODUCTION

Since 1981, runway pavements have been strength rated and protected against overloads by a strength rating system known as Aircraft Classification Number – Pavement Classification Number (ACN-PCN) (ICAO 1983). The system is simple in its operation, in that a unique aircraft ACN value is compared to the published PCN for that runway (AAA 2017) which can be set at the discretion of the airport owner, but in some countries a prescription process is required for determining a PCN value (FAA 2014a). In some instances, it has been noticed that these prescriptive processes return a PCN that was lower than the highest ACN of the aircraft in the design traffic loadings (Tipnis & Patil 2014). That means that the aircraft operator requires a Pavement Concession from the airport to operate, which is illogical for an aircraft that was part of the design traffic loadings. These anomalies resulted from differences between the simplified processes and mathematics used to calculate ACN values, and the more sophisticated mathematics used in modern airport pavement thickness determination methods, which include layered elastic and finite element methods (White 2024).

To overcome these anomalies of pavements not being rated for the design aircraft, a new system was developed, known as the Aircraft Classification Rating-Pavement Classification Rating (ACR-PCR) (ICAO 2022). The ACR-PCR system uses the same methods to calculate ACR values as is used by FAARFIELD (FAA 2023) and other contemporary pavement thickness methods. ACR-PCR was approved by the International Civil Aviation Organisation (ICAO) in 2020 and came into effect in 2024 (Brill & Garg 2023) although some countries have already announced deferral until 2025 or later.

Although aligning runway strength rating with pavement design methods provides many advantages (White 2024) it does require every airport to transition from a PCN to a PCR, which will be challenging and potentially costly for many regional airports (White 2022). Consequently, some researchers have attempted to develop correlations between PCN and PCR using the two prescriptive protocols, per ICAO (1983), FAA (2014a) and ICAO (2022).

Fundamentally, ACN-PCN, and ACR-PCR, are operational tools designed to allow an airport owner to be aware of, and to discretionary allow, the overloading of the runway pavements at their airport (AAA 2017). Despite the attempts to correlate PCN values to PCR values, the most appropriate PCR for

any runway is equal to the highest ACR of all the aircraft that are intended to operate regularly on that runway in an unrestricted manner, which is most reasonably based on the aircraft included in the traffic loadings when the pavement was designed or was most recently technically evaluated (White 2022). A PCR set equal to the highest of the intended aircraft ACR values will allow all the aircraft included in the design (or evaluation) traffic loadings to operate, as well as other less damaging aircraft, but more damaging aircraft operators will be required to obtain a Pavement Concession. It follows that a correlation between ACN and ACR, which can be used to transition from PCN to PCR, is a more useful tool for airport owners. Even for airports that have applied discretion and published a usage-based PCN value, transitioning to a PCR that still allows that using aircraft to operate, but not more damaging aircraft, remains a practical, efficient and reasonable outcome.

Although there is available software to convert individual aircraft ACN to ACR, such as PCASE (USACE 2023), many airports will not have the technical resources to properly employ these software programs. To that end, this research aimed to develop a statistical correlation between ACN and ACR values, for a range of aircraft, that can be used to assist airports in their transition from PCN to PCR. This is particularly important for the less sophisticated regional airports that often have a single clear critical aircraft, and limited resources for determining a PCN from first principles and using the prescriptive process published by ICAO (2022).

2 AIRCRAFT ACN TO ACR CORRELATION

White (2022) compared ACN and ACR values for a range of aircraft, subgrade conditions and pavement types. It was found that the ratio between ACN and ACR ranged from 7.7 to 12.0, with an average ratio of 9.5. It was also found that subgrade support had only little effect on the ratio between ACN and ACR, while the ratio was generally higher for rigid pavements than it was for flexible pavements.

For this study, the comparisons made by White (2022) were extended to include a total of 23 commercial aircraft, ranging in weight from the King Air 350 (6.8 tonnes) to the A380 (575 tonnes) (Appendix 1). The aircraft included dual, dual-tandem and dual-tridem (ICAO 2022) wheel configurations and an approximately uniform distribution of ACN values from 5 to 108, to avoid an unbalanced data set. The software ICAO-ACR (FAA 2020) was used to calculate ACR values, and after the aircraft weight and wheel configuration was manually checked or created (for missing aircraft) the software COMFAA (FAA 2014b) was used to calculate the equivalent ACN values for each aircraft. For each aircraft, the ACN and ACR were calculated for the

four subgrade categories and for both rigid and flexible pavement types, resulting in 92 pairs of ACN and ACR (Figure 1).

The ratio of ACN to ACR ranged from 7.7 to 12.6, with an average ratio of 9.8, which is similar to that reported by White (2022). The results were statistically analyzed and a linear regression was developed to allow the estimation of ACR from any ACN value. Initially all the factors were included in the regression and the most statistically non-significant term was removed iteratively, until only statistically significant terms remained (Equation 1).

$$ACR = ACN \times (8.833 + 0.355 \times W_4 + 0.841 \times W_6 + 1.382 \times Rigid) \quad (1)$$

Where: W_4 and W_6 denote dual-tandem and dual-tridem main wheel gears, respectively, and Rigid denotes an ACR for a rigid pavement. The value of each is 1 when true and 0 when not.

When Equation 1 was used to predict the ACR for each aircraft, pavement type and subgrade support category, the differences were just 0.7%, on average, and the linear regression R^2 value was 99.6%. The errors were normally distributed, evenly distributed around 0, and averaged less than 1 ACR unit, indicating a reasonable best-fit predictive model.
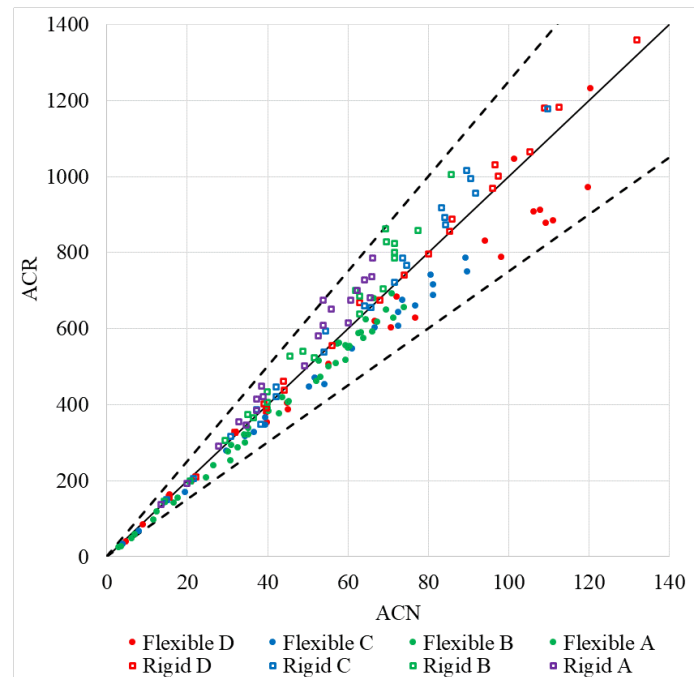
Figure 1. Comparison of ACR values to ACN values.

3 RUNWAY PCN TO PCR TRANSITION

For any airport that has a reliable and clear critical aircraft, for which the runway PCN is currently equal to that aircraft ACN, it is reasonable and efficient to determine the new runway PCR based on the ACR of the same critical aircraft. However, many regional airports will not be able to verify these conditions and will not be able to calculate the critical

aircraft ACR value. In such cases, Equation 1 provides a reasonable estimate of the critical aircraft ACR value, which can be used as the basis of the future PCR. For example, a reliably known PCN 20 (Dash 8-Q400 on flexible pavement with subgrade B) would be transitioned to PCN 172, which is approximately equal to the actual ACR of that aircraft, which is 170. It follows that the PCR of that runway can be estimated by the same equation, but with ACN replaced by PCN, and ACR replaced by PCR (Equation 2).

$$PCR = PCN \times (8.833 + 0.355 \times 4W_4 + 0.841 \times W_6 + 1.382 \times Rigid) \qquad (2)$$

The differences between actual ACR and predicted ACR, and therefore between PCR and estimated PCR, generally increased with the ACR of the aircraft, within a generally consistent percentage error band (Figure 2). That is, the larger aircraft were associated with larger absolute differences than the smaller aircraft. In practice, the regional airports that are likely to rely on this estimated ACR for an approximate PCR value, are limited to aircraft with dual main gear wheels, up to B737 or A320 size aircraft. These airports predominantly have flexible pavements (White et al. 2021). For these dual wheeled aircraft on flexible pavements, the differences between actual ACR and estimated ACR were up to 48 ACR units, with 60% of predicted ACR values within 10 of the actual ACR value (Figure 3).
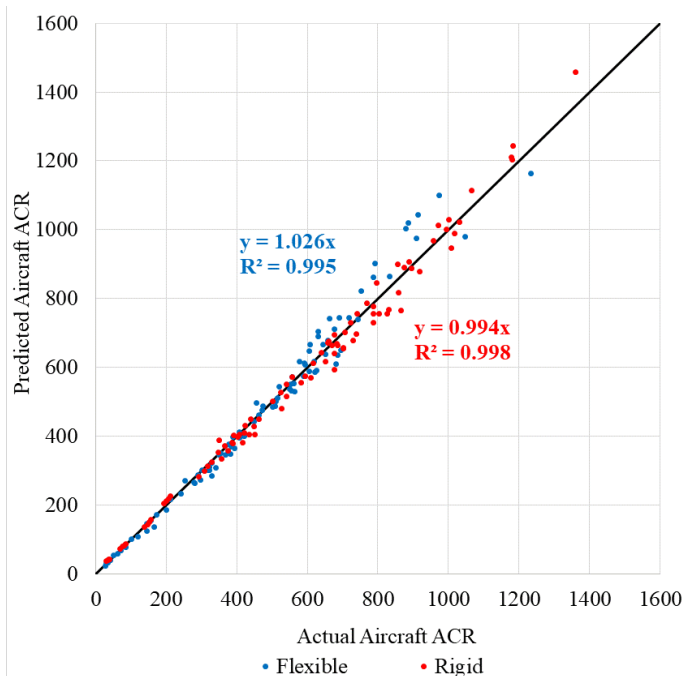
Figure 2. Comparison of actual ACR and predicted ACR.

That is, for regional airports with flexible runway pavements, using Equation 2 would mean that 60% of estimated runway PCR values would be within 10 of the critical aircraft ACN value. Given that ACR values are rounded to the nearest 10, for the purpos-

es of calculating runway PCR values (ICAO 2022), that is not unreasonable.

4 CAUTION AND LIMITATION

If not using a prescriptive method for first principles PCR determination, such as that published by ICAO (2022), it is clearly preferable to calculate an actual PCR value based on the critical aircraft that has the highest ACR value of all the regularly using or design traffic aircraft. Consequently, the use of Equation 2 should only be considered as an approximate basis for transitioning from PCN to PCR. It is much better to identify the actual critical aircraft for which the ACN value is the basis of the PCN, and to calculate the actual ACR value using available software for setting the PCR. This process also relies on the reliability of the current PCN value, and it is important that the critical aircraft, that is the basis of the current strength rating (PCN) be identified before it is adopted as the basis of the future strength rating (PCR).
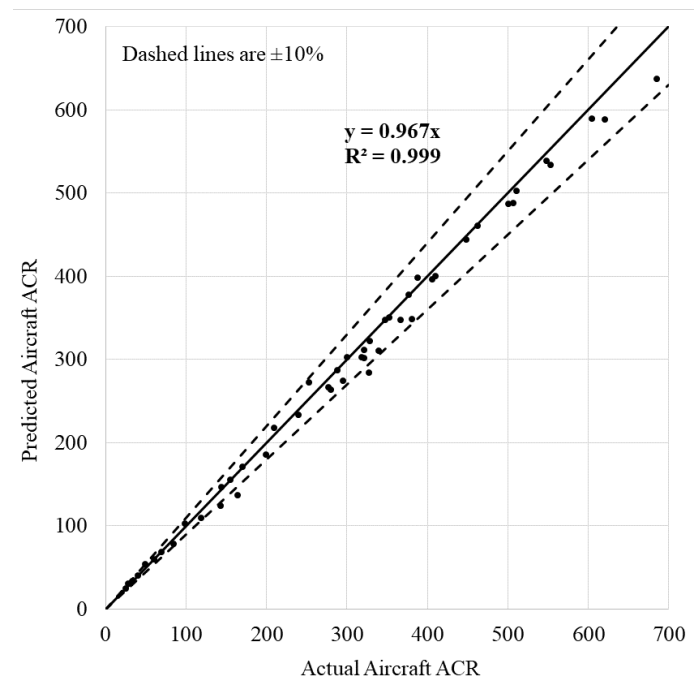
Figure 3. Comparison of dual wheeled aircraft flexible ACR and predicted ACR.

5 CONCLUSION

The transition from ACN-PCN to ACR-PCR is associated with many benefits. However, for many regional airports with limited resources, it is a burden that is unlikely to provide any practical benefit. To assist those airports with the transition, a reasonable correlation between ACN and ACR was developed and can be used to estimate PCR from an existing PCN. For the majority of regional airports with flexible pavements and only dual wheel aircraft, this will provide a PCN value within 10 units of the true val-

ue. However, this approach is not as sound as identifying the critical aircraft that forms the basis of the current PCN value, and using the actual calculated ACR of that aircraft as the basis of the future PCR.

REFERENCES

AAA, 2017. Airport Practice Note 12 - Airfield Pavement Essentials, Australian Airports Association, Canberra, Australian Capital Territory, Australia.

Brill, D.R. & Garg, N. 2023. Airport Pavement Design and Evaluation Workshop - Introduction to FAARFIELD2.0 and ICAO's ACR-PCR System, *International Airfield & Highway Pavements Conference*, 12-14 June, Austin, Texas, USA.

FAA, 2014a. *Standardized method of reporting Aircraft Pavement Strength – PCN*, Advisory Circular 150/5335-5C, Federal Aviation Administration, Washington, District of Columbia, USA, 14 August.

FAA, 2014b. *COMFAA 3.0*. Federal Aviation Administration, 14 August, <www.airporttech.tc.faa.gov/Products/Airport-Pavement-Software-Programs/Airport-Software-Detail/ArtMID/3708/ArticleID/10/COMFAA-30>, accessed 11 August 2024.

FAA, 2020. *ICAO-ACR 1.4*. Federal Aviation Administration, Washington, District of Columbia, USA, 16 March, <www.airporttech.tc.faa.gov/Products/Airport-Pavement-Papers-Publications/Airport-Pavement-Detail/ArtMID/3684/ArticleID/2838/ICAO-ACR-13>, accessed 13 August 2024.

FAA, 2023. *FAARFIELD 2.1.1*. Airport Design Software FAARFIELD 2.1.1, Federal Aviation Administration, Washington, District of Columbia, USA, 22 December, <www.airporttech.tc.faa.gov/Products/Airport-SafetyPapers-Publications/Airport-Safety-Detail/ArtMID/3682/Article ID/2841/FAARFIELD-20>, accessed 11 August 2024.

ICAO, 1983. *Aerodrome Design Manual: Part 3*, ICAO 9157. (2nd edn.), International Civil Aviation Organization, Montreal, Quebec, Canada, January.

ICAO, 2022. *Aerodrome Design Manual: Part 3*, ICAO 9157. (3rd edn.), International Civil Aviation Organization, Montreal, Quebec, Canada, January.

Tipnis, M. & Patil, M. 2014. Design program based PCN evaluation of aircraft pavements, *FAA World Wide Airport Technology Transfer*, Galloway, New Jersey, USA, 5-7 August.

USACE, 2023. *PCASE*: *Pavement-Transportation Computer Assisted Structural Engineering*, version 7.0.6, 27 September, <transportation.erdc.dren.mil/pcase/software.aspx>, accessed 23 August 2024.

White, G. 2022. Practical implications for the implementation of the new international airport pavement strength rating system, *11th international Conference on the Bearing Capacity of Roads, Railways and Airfields*, 28-30 June, Trondheim, Norway, vol. 1, pp. 210-225.

White, G. 2024. Critical Review and Potential Improvement of the new International Airport Pavement Strength Rating System, *Applied Sciences*, vol. 14, no. 8491, pp. 1-19.

White, G., Farelly, J. & Jamieson, S. 2021. Estimating the value and cost of Australian aircraft pavement assets, *International Airfield and Highway Pavement Conference*, a virtual event, American Society of Civil Engineers, 8-10 June.

Appendix 1 – Aircraft Included in ACN to ACR Correlation

Aircraft	Weight (tonnes)	Wheels in each main landing gear
Super King Air 350	6.8	2
SAAB 340B	13.2	2
Challenger CL 604	21.9	2
Dash 8-400	29.3	2
Fokker 100	45.8	2
B717-200	55.3	2
A220-100	60.8	2
A220-300	67.6	2
A319-100 opt	68.4	2
B737-800	79.2	2
A321-200 opt	93.9	2
A321XLR	101.0	2
B767-300	163.7	4
B787-8	228.4	4
A330-300 std	230.9	4
B777-200	248.1	4
B787-9	255.4	4
A350-900	272.9	4
A350-1000	308.9	6
B777-300ER	352.4	6
A340-600	369.2	4
B747-400	397.8	4
A380-800	575.0	6

Improving Index-Volumetrics Relationship Using Air Voids and Effective Binder Content

Dong Ho Yoo
Ph.D. Student
North Carolina State University

Youngsoo Richard Kim, Ph.D., P.E.
Jimmy D. Clark Distinguished University Professor
North Carolina State University

ABSTRACT: This study focuses on improving the index-volumetrics relationship (IVR) for asphalt mixture performance prediction by replacing the original parameters, in-place voids in mineral aggregate (VMA_{IP}) and in-place voids filled with asphalt (VFA_{IP}), with more intuitive ones, in-place air voids ($V_{a,IP}$) and effective binder content (AC_{Eff}). Using these new parameters, the IVR equation was redeveloped, resolving issues with S_{app} trends as a function of air void content and enhancing the prediction accuracy for plant-mixed lab-compacted samples. The proposed method provides a practical approach for predicting field construction performance using the 'four corners' method.

1 INTRODUCTION

1.1 Index-Volumetrics Relationships

The North Carolina State University (NCSU) research team conducted research to develop performance-related specifications (PRS) of asphalt pavements using the Asphalt Mixture Performance Tester (AMPT) and its associated test methods. However, the use of AMPT performance testing for quality assurance (QA) purposes poses practical challenges that are difficult to overcome. Therefore, the PRS framework preferably should employ conventional acceptance quality characteristics (AQCs) that are commonly used in QA processes for asphalt pavements. For that purpose, the research team developed index-volumetrics relationships (IVRs) to link conventional AQCs with AMPT performance test indexes (S_{app} for cracking and the Rutting Strain Index (RSI) for rutting) (Wang et al. 2019). The idea behind these relationships is to pre-calibrate the index property variations as a function of conventional AQCs and then to use the calibrated IVRs to predict the as-constructed performance index values using the conventional AQCs measured during production.

1.2 AMPT Performance Indexes

S_{app} and RSI are the AMPT performance index parameters for cracking and rutting, respectively. In this paper, improvement of the IVR for S_{app} is described. S_{app}, defined in Equation (1), accounts for the effects of a mixture's modulus and toughness on the mixture's fatigue resistance and is a measure of the amount of fatigue damage the mixture can toler-

ate under fatigue loading. Higher S_{app} values indicate better fatigue resistance.

$$S_{app} = 1000^{\frac{\alpha}{2}-1} \frac{a_{T(S_{app})}^{\frac{1}{\alpha+1}} \left(\frac{D^R}{C_{11}}\right)^{\frac{1}{C_{12}}}}{\left|E^*\right|_{LVE,S_{app}}^{\frac{\alpha}{4}}} \quad (1)$$

where α = damage evolution rate, $a_{T(S_{app})}$ = time-temperature shift factor at S_{app} temperature, $\left|E^*\right|_{LVE,S_{app}}$ = reference modulus for S_{app}, C_{11}, C_{12} = coefficients of damage characteristic curve model, and D^R = failure criterion.

1.3 Four Corners

The core idea of the IVR is that the performance of an asphalt mixture under various volumetric conditions can be predicted by testing the mixture at a few selected volumetric conditions. To simplify the volumetric characteristics of mixture samples in place, the research team developed straightforward equations for IVRs whereby in-place voids in mineral aggregate (VMA_{IP}) and in-place voids filled with asphalt (VFA_{IP}) are used to represent the volumetric properties of the in-place samples. The IVR equation for S_{app} is presented as Equation (2).

$$S_{app} = a \times VMA_{IP} + b \times VFA_{IP} + d \quad (2)$$

where VMA_{IP} = the in-place VMA, VFA_{IP} = the in-place VFA, and a, b, and d = the fitting coefficients for S_{app}.

Equations (3) and (4) are derived from the Superpave mix design but are rewritten here in terms of in-place density and binder content to calculate the VMA_{IP} and VFA_{IP}.

$$VMA_{IP} = 100 - \frac{\%G_{mm} \times G_{mm} \times P_s}{100 \times G_{sb}} \qquad (3)$$

where $\%G_{mm}$ = constructed compaction level, G_{mm} = theoretical maximum density of asphalt mixture, P_s = aggregate content, and G_{sb} = bulk specific gravity of the aggregate.

$$VFA_{IP} = 100 \times \frac{VMA_{IP} - V_{a,IP}}{VMA_{IP}} \qquad (4)$$

where $V_{a,IP}$ = the in-place air void content.

As an initial step in developing the IVR, the asphalt mixture should be tested at several distinct volumetric conditions in terms of VMA_{IP} and VFA_{IP}. A previous study by Wang et al. (2019) suggests that four volumetric conditions are sufficient to develop the IVR for a given mixture. These conditions are referred to as the 'four corners' because they represent the furthest points from each other within the quadrangular range of the volumetric conditions, as illustrated in Figure 1.
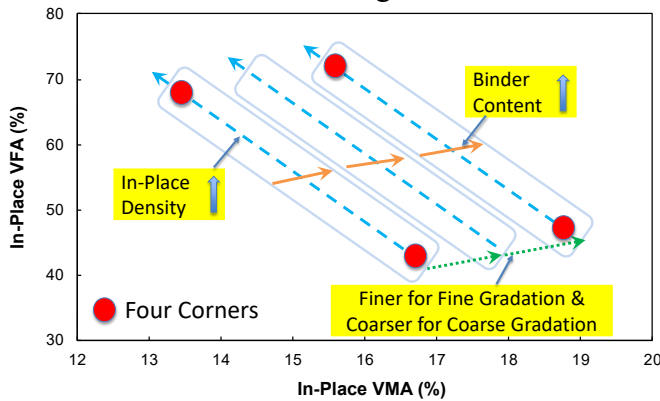
Figure 1. Four corners methodology: Changes in VMA_{IP} and VFA_{IP} based on mixture properties.

To achieve these four corners, two gradations, fine side and coarse side of the job mix formula gradation, are developed by modifying the proportions of the aggregate stockpiles to fully encompass the variation of the gradation in the field-constructed pavement. Additionally, the binder content is adjusted based on the design samples for each modified gradation. In these four corners, the binder content typically is adjusted to target design air voids of 3% and 5%, while the air void content of the test specimen is varied to target 3% and 7%.

These three parameters (gradation, binder content, and air void content) are then combined to create four new conditions designated as FF33, FF57, FC33, and FC57. In this naming convention, the first two letters represent the original gradation type and the modified gradation type relative to the original

(F is fine, C is coarse). The first digit indicates the percentage of the design air void content that corresponds to the total asphalt content in the mixture, and the second digit represents the percentage of the air void content of the test samples.

2 MATERIALS

This research team utilized eight different mixtures sampled from various locations: MN12.5, NC9.5B50RAP, NC9.5C, NC9.5D, NC19.0, MD12.5, FL12.5, and IN9.5. The letter at the beginning of each designation indicates the state where the mixtures are used, while the digits represent the nominal maximum aggregate size of the mixture. Each mixture features a distinct binder content and gradation. Figure 2 presents the gradations of all eight mixtures in a single plot. Most of the mixtures are fine-graded, except for MN12.5, MD12.5, and IN9.5.
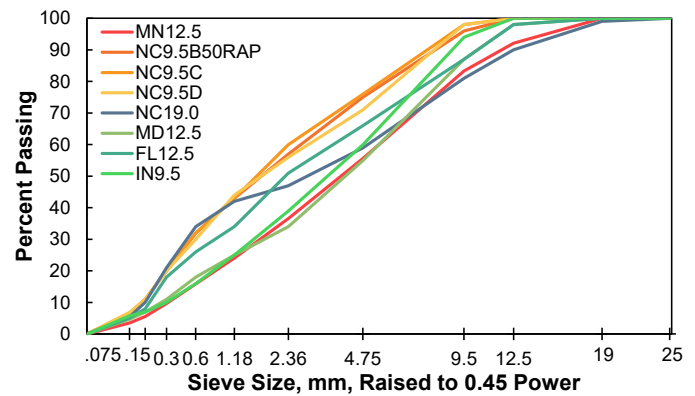
Figure 2. Gradations of eight mixtures used in study.

3 METHOD

3.1 Volumetric Domain for Four Corners

The four corners selected in all the mixtures except NC9.5C and IN9.5 were FF33, FF57, FC33, and FC57. Adjustments to the design air voids or test air voids were made to NC9.5C and IN9.5 in order to increase the sensitivity of the mixes to the binder content or air void content.

3.2 AMPT Testing and IVR Development

The dynamic modulus and cyclic fatigue tests were conducted in accordance with AASHTO TP132 and T 411, respectively. Asphalt mixtures tested include four corner samples (F33, F57, C33, and C57), additional lab-mixed lab-compacted (LMLC) samples (F44, C44, and the Superpave volumetric optimum, or SVO), and plant-mixed lab-compacted (PMLC) samples. The AMPT test results were input into FlexMAT^{TM} to determine the S_{app} value. The IVR function was developed using multilinear regression with the S_{app} values and volumetric properties of the four corner samples in Excel, utilizing the

'=LINEST' function. The remaining LMLC samples and PMLC samples then were used to verify the IVR function and evaluate its prediction performance.

4 RESULTS AND DISCUSSION

4.1 IVR Using VMA_{IP} and VFA_{IP}

Table 1 presents the calibration results for the eight different mixtures.

Table 1. Calibration Results for Eight Mixtures.

Mixture	a	b	d
MN12.5	0.940	3.700	-105.587
NC9.5B50RAP	2.006	0.470	-53.407
NC9.5C	2.207	0.488	-58.448
NC9.5D	2.401	0.599	-51.413
NC19.0	3.751	0.393	-69.698
MD12.5	-0.017	0.126	5.360
FL12.5	3.971	0.831	-103.531
IN9.5	4.115	0.628	-94.092

The IVR equations developed from the four-corner data were used to predict the S_{app} values of the remaining LMLC samples and PMLC samples. Figure 3 presents the prediction results.
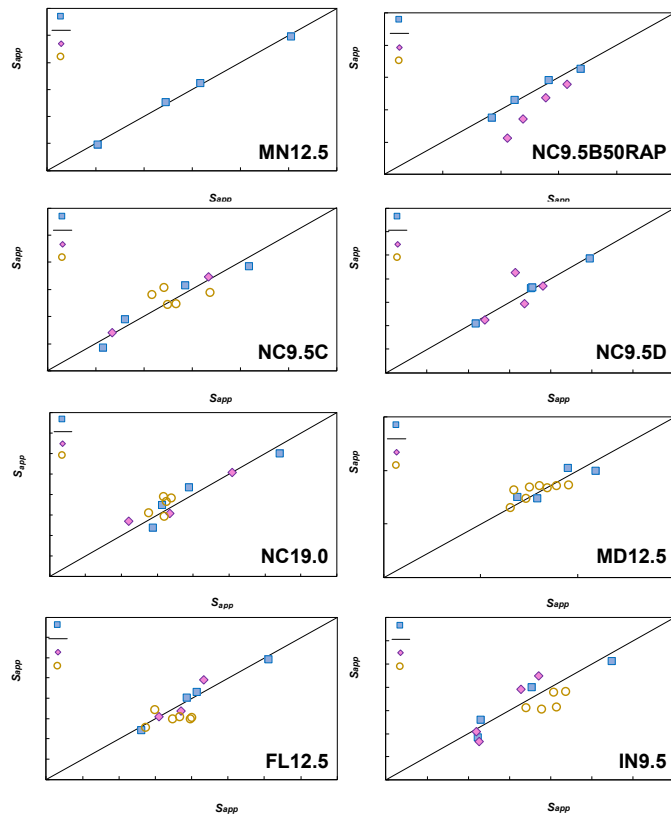
Figure 3. Comparison between measured and predicted S_{app} values using developed IVR equation for each mixture.

Although the verification results in Figure 3 seemed reasonable, seven out of eight samples exhibited an incorrect trend for S_{app} as a function of in-place air void content. Only the MD12.5 mixture displayed the correct trend. To overcome this issue, the research team proposes two new, more intuitive parameters for the S_{app} IVR: in-place air void content ($V_{a,IP}$) and effective binder content (AC$_{Eff}$).

4.2 IVR Using $V_{a,IP}$ and AC_{Eff}

The two new parameters, $V_{a,IP}$ and AC$_{Eff}$, are more intuitive variables compared to VMA$_{IP}$ and VFA$_{IP}$ because the effects of these two variables can be directly represented in IVR. An increase in $V_{a,IP}$ will decrease the cracking index value, while an increase in AC$_{Eff}$ will increase the cracking index value. One of the reasons to use VMA$_{IP}$ and VFA$_{IP}$ for the IVR was because the three primary factors affecting the asphalt mixture performance, i.e., aggregate gradation, binder content, and air void content, can be captured by the VMA$_{IP}$ and VFA$_{IP}$ parameters. In the new set of $V_{a,IP}$ and AC$_{Eff}$ parameters, the effect of aggregate is implicitly represented by G_{se} and G_{sb} that are used in calculating AC$_{Eff}$ as shown in Equation (5).

$$\mathrm{AC}_{\mathrm{Eff}} = P_b - G_b \times \left[(100 - P_b) \times \frac{G_{se} - G_{sb}}{G_{se} \times G_{sb}} \right] \quad (5)$$

where P_b = total asphalt content in mixture, G_b = specific gravity of binder (assume 1.03), G_{se} = effective specific gravity of the aggregate blend, and G_{sb} = bulk specific gravity of the aggregate blend.

Revised IVR equation, Equation (6), were developed for all the eight mixtures using $V_{a,IP}$ and AC$_{Eff}$ instead of VMA$_{IP}$ and VFA$_{IP}$. Table 2 presents the calibration coefficients for the revised IVRs.

$$S_{app} = a_n \times V_{a,IP} + b_n \times \mathrm{AC}_{\mathrm{Eff}} + d_n \quad (6)$$

where a_n, b_n, and d_n = the fitting coefficients for S_{app}.

Table 2. Calibration Coefficients for Eight Mixtures Using $V_{a,IP}$ and AC$_{Eff}$.

Mixture	a_n	b_n	d_n
MN12.5	-1.010	11.670	-31.400
NC9.5B50RAP	-0.258	6.537	-18.950
NC9.5C	-0.046	6.398	-19.640
NC9.5D	-0.530	6.978	-2.762
NC19.0	1.419	9.286	-35.457
MD12.5	-0.580	0.689	13.660
FL12.5	0.356	13.300	-47.900
IN9.5	0.955	11.010	-40.840

The advantage of the new parameters is that the signs of the coefficients directly correspond to the trend of S_{app} as a function of the variables. Specifically, the coefficient a_n represents the effect of air void content and should be negative whereas the coefficient b_n represents the effect of binder content and should be positive. Although the trend of S_{app} as a function of binder content aligns with expectations in all the mixtures, three out of eight mixtures (NC19.0, FL12.5, and IN9.5) still exhibited issues with the S_{app} trend with regard to air void content.

As mentioned earlier regarding the four corners concept, the four calibration points must exhibit a well-distributed pattern along the variables. For the three mixtures with the trend issues (NC19.0, FL12.5, and IN9.5), additional volumetric conditions

were tested to allow for the selection of four new corners to redevelop the IVR equation. Figure 4 illustrates the four corners that achieve the correct S_{app} trend as a function of air void content. Note that the four points are distributed reasonably well in both $V_{a,IP}$ and AC_{Eff} axes.
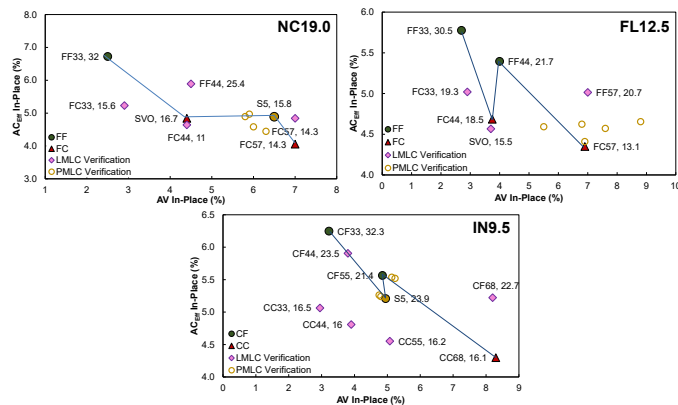
Figure 4. New selected four corners to obtain well-distributed calibration points for air void content and effective binder content.

New IVR equations were developed using the four new selected corners shown in Figure 4. Table 3 presents the coefficients of the IVR equations based on these new corners, which align with the expected direction of the S_{app} trend.

Table 3. Calibration Results Obtained Using New Selected Corners.

Mixture	a_n	b_n	d_n
NC19.0	-0.321	6.564	-12.316
FL12.5	-1.176	8.026	-14.488
IN9.5	-1.194	4.617	5.187

The prediction results of the IVR equation developed with the new parameters were compared against the measured S_{app} values in Figure 5. The prediction results for the IVR using $V_{a,IP}$ and AC_{Eff} in Figure 5 show minimal differences when compared to those using VMA_{IP} and VFA_{IP} in Figure 3. Percent errors averaged for all the eight mixtures for the calibration, LMLC prediction, and PMLC prediction using the new IVR are 5.0%, 17.9%, and 10.1% respectively, whereas percent errors using the original IVR are 5.9%, 11.1%, and 11.6%. However, considering the ultimate goal of the IVR, i.e., the accurate prediction of the mixture performance of field construction, the research team recommends the use of $V_{a,IP}$ and AC_{Eff} as the volumetric variables in the IVR equation.

5 CONCLUSION

Eight different asphalt mixtures were tested using the dynamic modulus and cyclic fatigue tests to determine the S_{app} values. VMA_{IP} and VFA_{IP} at four different volumetric conditions were used along with the S_{app} values to develop the IVR equation. Although the verification results using the LMLC samples at volumetric conditions different from the four corners and the PMLC samples at in-place air voids showed a reasonable agreement between the measured and predicted S_{app} values, the S_{app} values predicted from the IVR function showed an incorrect trend as a function of air void content for three out of eight mixtures.

To address the issues identified in the original IVR equation that uses VMA_{IP} and VFA_{IP}, the research team developed and utilized $V_{a,IP}$ and AC_{Eff} to redevelop the IVR equation. This approach successfully resolved the problems with the S_{app} trend as a function of air void content and, with the additional reconfiguration of the four corners, improved the PMLC mixture verification results. These findings suggest that $V_{a,IP}$ and AC_{Eff} should be used in developing the IVR equation.
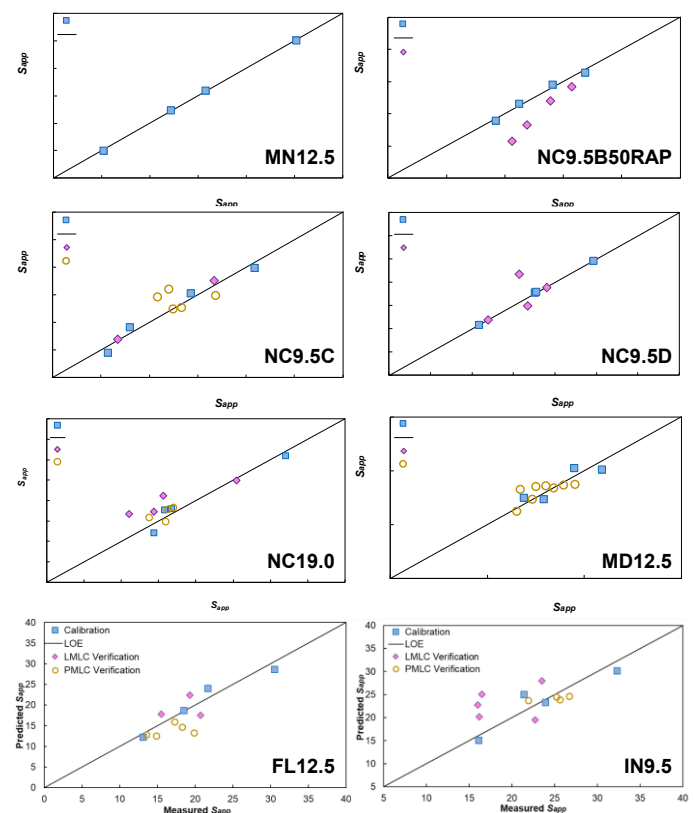
Figure 5. Comparisons of measured Sapp and predicted S_{app} using new parameters in IVR equation.

REFERENCE

Wang, Y.D., Ghanbari, A., Underwood, B. S. and Kim, Y. R., 2019. Development of a performance-volumetric relationship for asphalt mixtures. Transportation Research Record, 2673(6), 416-430.

1.2

ADVANCES IN THE MODELING OF PAVEMENT CONSTRUCTIONS

From gyratory data to field compacity – a numeric model

J. Crucho, A. Margaritis, T. Tanghe, B. Duerinckx, B. Beaumesnil, S. Vansteenkiste, A. Vanelstraete
Belgian Road Research Centre (BRRC), Brussels, Belgium

ABSTRACT: The compaction of an asphalt mixture is a dynamic process influenced by various factors, including mixture properties, cooling rate and timing of the roller passes. At times, the target compacity may not be reached or achieved inefficiently. Laboratory compaction tests, done at constant temperature and energy level, often fall short in predicting real field compaction. To bridge the gap between laboratory and field compaction, a numerical model designated as Field Compacity Model (FCM) is proposed. The FCM is based on gyratory data and integrates field specificities by accounting for the mixture's cooling curve, roller types, number of passes and their timing. The objective of the FCM is to identify potential risks of field compaction issues at an early stage in an accessible and efficient manner. Following an initial verification stage, the model was used to estimate field compacity in three practical case studies, where it showed good predictive performance.

1 INTRODUCTION

1.1 Background

Regardless of the new technologies implemented in paving works, such as intelligent compaction (IC) and paver-mounted thermal profiling (PMTP), there remains some uncertainty regarding the final density of the compacted asphalt layer.

In the field, compaction depends on several factors, with the most important being compaction temperature, compaction energy, and the mixture properties. During compaction, the asphalt mixture undergoes a cooling process driven by several environmental conditions, including air temperature, wind, solar radiation and precipitation (Bijleveld et al. 2016). Regarding heat loss, the thickness of the layer being paved and the temperature of the layer beneath also have an influence (MultiCool 2024). The compaction energy will be a function of the type of roller, its configuration and the number of passes given. In fact, more important than the total number of passes is the timing (i.e. temperature compaction window) at which they occur.

In terms of mixture properties, due to the selected materials and composition, some mixtures will have better compactability than others (Francken & Leonard 2002, Margaritis et al. 2023). Ideally, this behavior should be identified in the laboratory beforehand. To evaluate compaction in the laboratory, the gyratory compactor (EN 12697-31 and ASTM D6925) is one of the most commonly used methods. This test provides a dataset that shows the relation between compacity and the number of gyrations (energy). In short, compacity is equal to 100 minus the volume of air voids (in %). The European approach is that at certain energy levels (typically, 60, 100 or 120 gyr, depending on the mixture type), air voids are quantified and checked against the thresholds set in specifications.

In a simplified manner, laboratory compaction is approximately a continuous process (all compaction energy is applied at constant temperature and in a very short period), whereas field compaction is more of a discrete process (every roller pass happens at a different temperature with occasionally several minutes break between passes).

In brief, standard laboratory compaction ignores mixture cooling, roller differences and the effect of the underlaying road structure. Part of the uncertainty around field compacity can be explained by this missing link between laboratory and field compaction.

1.2 Motivation and objective

The main motivation of this work is to predict field compacity based on laboratory data in order to prevent and to explain field compaction failures more quantitatively.

The objective is to develop a numeric model that helps bridge the gap between laboratory and field compaction. The model should clearly identify the risk of compactability problems and demonstrate how different field compaction scenarios may help mitigate or exacerbate this risk.

2 GYRATORY COMPACTION AND THE SIGMOIDAL MODEL

To study the workability and compactability of asphalt mixtures, the analysis of compaction data – particularly the gyratory compactor – has gained widespread attention. An advantage of the gyrations-compacity curve is that it captures all the specific characteristics of the asphalt mixture (binder content, binder grade, aggregate geometry, grain size distribution, etc.). However, drawing conclusions from the raw data can be quite challenging. Therefore, the use of fitting models can be very helpful.

The sigmoidal model (Equation 1), proposed by Moutier (1996), fits the gyrations-compacity data in a log-linear scale using a sigmoid curve.

$$C = \frac{C_0 + C_\infty \times \beta_4 \times N_g^{\beta_3 \times (C_\infty - C_0)}}{1 + \beta_4 \times N_g^{\beta_3 \times (C_\infty - C_0)}} \qquad (1)$$

where N_g = number of gyrations; C = compacity at N_g; C_0 = lower asymptote; C_∞ = upper asymptote; β_3 and β_4 are shape parameters associated with the slope and inflection point of the curve.

This four parameters (further designated as sigmoidal parameters) – C_0, C_∞, β_3 and β_4 – drive the behavior of the curve and allow the determination of important characteristics, such as the position of the compaction inflection point (CIP) and the slope of the curve at the CIP.

Earlier work quantified the repeatability and reproducibility of the sigmoidal parameters and concluded that the sigmoidal model provides a good fitting, showing low root mean squared errors (Crucho et al. 2024).

However limited to the laboratory conditions, the analysis of the sigmoidal parameters can give clear indications regarding the workability and compactability of a specific asphalt mixture. Two interactive diagrams – C_0-C_{CIP} and β_4/β_3-β_3 – provide an easy-to-follow visual representation (Margaritis et al. 2023).

3 MODEL TO PREDICT FIELD COMPACITY

3.1 *Model*

The field compacity model (FCM) assumes the energy-compacity law as defined by the gyratory compaction test and is based on the sigmoidal fit. To account for different roller loads (vertical pressure) and mixture cooling (compaction temperature) several gyrator tests were performed (temperatures of 150, 135, 120, 105 and 90°C, and vertical pressures of 200 and 600 kPa) and respective sigmoidal parameters determined. The evolution of the sigmoidal parameters within the range of temperature and vertical pressure was established through linear regression. Finally, by interpolation, each sigmoidal parameter was determined for the desired temperature and vertical pressure. Thus, an infinite number of sigmoidal curves

can be generated, matching the temperatures and compaction pressures applied in the field.

To predict field compacity through the sigmoidal curve, the number of roller passes have to be converted into number of gyrations. To tackle the variety of rollers and compaction configurations, it is proposed the concept of equivalent number of loads (ENL). In static compaction, ENL is the number of axle passes over a certain point, and when vibration is applied, a factor of 1.43 is used to account for the dynamic effects. Following, ENL are converted into number of gyrations considering an axle type factor k, equal to eight for steel drums and four for pneumatic tire axles. The vertical pressure given by each axle was estimated through the manufacturer's technical specification.

The FCM predicts field compacity by analyzing the sequence of compaction actions applied to the pavement in a step-by-step manner. Initially, the effect of the paver ($n = 0$), which provides some degree of compaction, is assumed equivalent to four gyrations ($Ng_0 = 4$) at 150 kPa, with the corresponding compacity determined using Equation 2. Subsequently, for each roller pass (n), FCM predicts compacity using Equation 2 and Equation 3.

$$CP_n = \frac{C_{0n} + C_{\infty n} \times \beta_{4n} \times Ng_n^{\beta_{3n}(C_{\infty n} - C_{0n})}}{1 + \beta_{4n} \times Ng_n^{\beta_{3n}(C_{\infty n} - C_{0n})}} \qquad (2)$$

$$Ng_n = k_n \times ENL_n + 10^{\left(\frac{\log \frac{CP_{n-1} - C_{0n}}{\beta_{4n}(C_{\infty n} - CP_{n-1})}}{\beta_{3n}(C_{\infty n} - C_{0n})}\right)} \qquad (3)$$

where n = roller pass number; Ng_n = number of gyrations at n; CP_n = compacity at n; C_{0n}, $C_{\infty n}$, β_{3n} and β_{4n} are the sigmoidal parameters determined for the conditions (temperature and vertical pressure) of pass n; ENL_n = equivalent number of loads corresponding to pass n and k_n = axle type factor.

To practicaly demonstrate the FCM-approach, Figure 1 presents a simple example with three roller passes (at 135, 120 and 90°C).
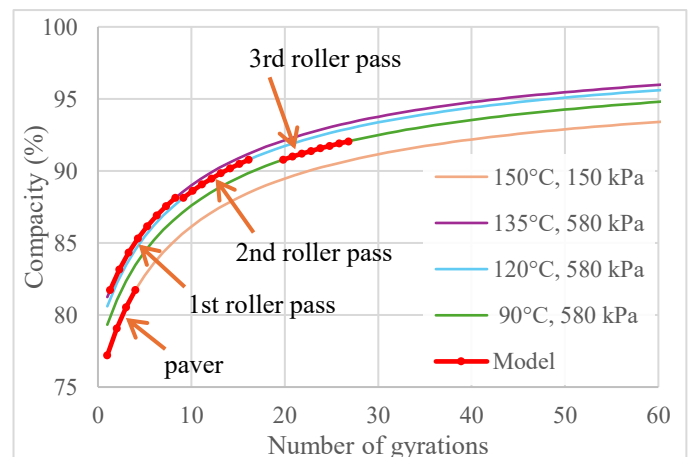
Figure 1. Example of gyrator curves obtained at different temperatures and compacity evolution according to the FCM.

3.2 Initial verification

The initial validation of the model was made through a job site monitored by the BRRC. During laying and compaction, data about the number of passes, mid-layer temperature and density of the mixture after each pass was collected. A 4 cm surface layer of conventional hot mix asphalt (AC 10) was paved. At this job site, the compaction started (at 135°C) with a pneumatic-tire roller (6 passes) and then with a three-wheeled steel drum roller (12 passes). The vertical pressures were 230 and 520 kPa for the axles of the pneumatic-tire roller and the three-wheeled steel drum roller, respectively. The final pass was at 70°C. In the laboratory, gyratory tests were conducted following the program indicated in § 3.1.

Figure 2 shows the FCM prediction and the respective field compacity. Field compacity was calculated based on field density measurements taken with a Troxler nuclear density gauge. The repeatability and reproducibility of the nuclear density gauge were determined to be 39 and 42 kg/m³, respectively (Duerinckx & Vanelstraete 2021), resulting in a variability of approximately ± 1.6% in compacity. In Figure 2 the grey dashed lines represent the measured value ± repeatability. The point where a temperature of 90°C was reached, is also indicated. Below 90°C (all points to the right of the red dashed line), the values of the sigmoidal parameters were obtained by extrapolation. On this jobsite, the density at ENL=0 (after the paver and before the 1st roller pass) was not measured. In general, FCM predicted well field compacity. A limitation of this approach is that the over-compaction effect is not considered. In the field, density can start to decrease if the compaction effort is too high or happens under too low temperatures. Caution should be taken when using FCM for such conditions.

4 CASE STUDIES

4.1 Mixture AC 14 surf

Following the approach described in § 3.2, BRRC monitored another job site (Francken & Leonard 2002) where the paved mixture was a 5 cm thick conventional AC 14. At this site, only the static three-wheeled roller was used (similar to the one used in the previous case). In total, 18 roller passes were applied. The first pass occurred at 130°C and the final pass at 56°C. With respect to the gyrator data, as information for this exact mixture was not available, a similar mixture from the BRRC database, and respective temperature sensitivity, was used. In this case, the vertical pressure sensitivity was assumed equal to the previous AC 10 mixture. Figure 3 presents the results of the model. Regardless of the considered simplifications, the overall prediction was acceptable.
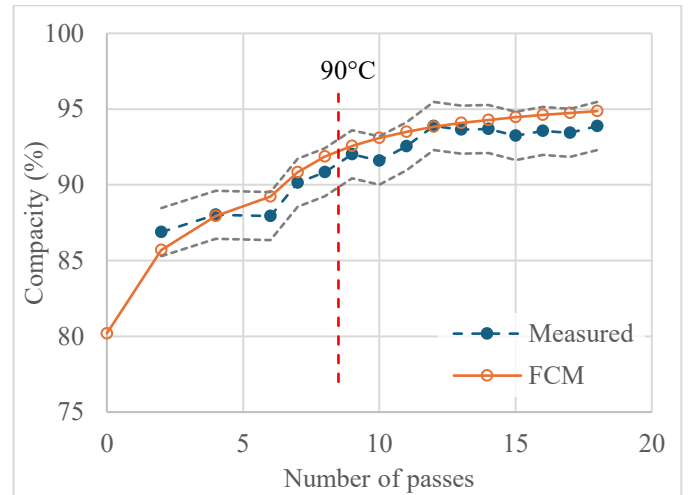
Figure 2. Measured compacity and prediction of the FCM for the case of an AC 10 surface layer.
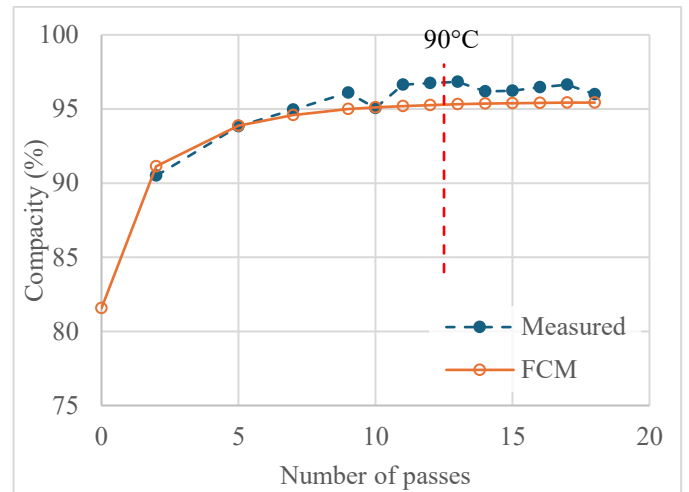
Figure 3. Measured compacity and prediction of the FCM for the case of an AC 14 surface layer.

4.2 Mixture AC 16 base

In the literature, Bijleveld et al. (2016) reported field compaction data for an 8 cm thick base layer (mixture AC 16) compacted by a 10 ton combined roller (pneumatic tire front axle and steel drum rear axle). However, no gyratory data were reported. To bypass the lack of data, a similar mixture was found in the BRRC database, and the respective gyrator data used here. Also, the temperature and vertical pressure sensitivity were assumed. The FCM prediction is presented in Figure 4.

4.3 Mixture AC 20 base

Another case study is an AC 20 base mixture that in the field (6 cm thick layer) presented problematic compaction. Some deviations during the production process led to a mixture with a low binder content and the respective gyratory specimens revealed 11.5% air voids (at N_g=60).

Regarding field compaction, only the type of rollers, production temperature, date and time of the day were known. In this case, MultiCool (2024) was used to generate the cooling curve. The number of passes was estimated based on our experience and the usual workflow of that contractor. The gyratory data was obtained, but only at a compaction temperature of 150°C. Thus, the temperature and vertical pressure sensitivity were assumed. Despite the lack of accurate field monitoring and all the necessary assumptions, the FCM predicted the insufficient final compacity well (Fig. 5). FCM predicted 85.9% of compacity where field cores showed an average of 85.3%.
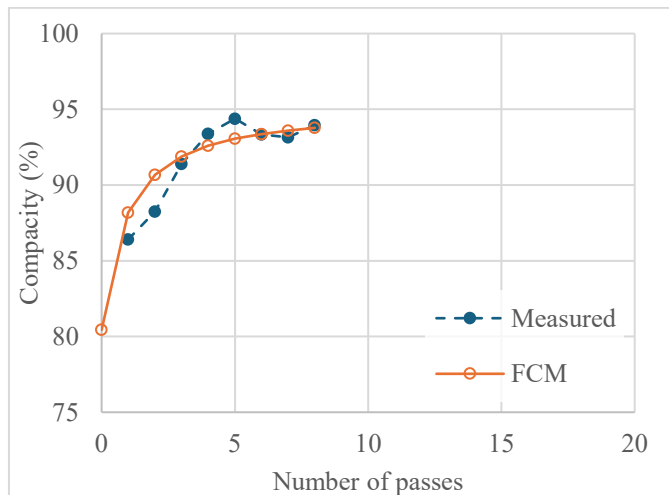
Figure 4. Measured compacity and prediction of the FCM for the case of an AC 16 base layer.
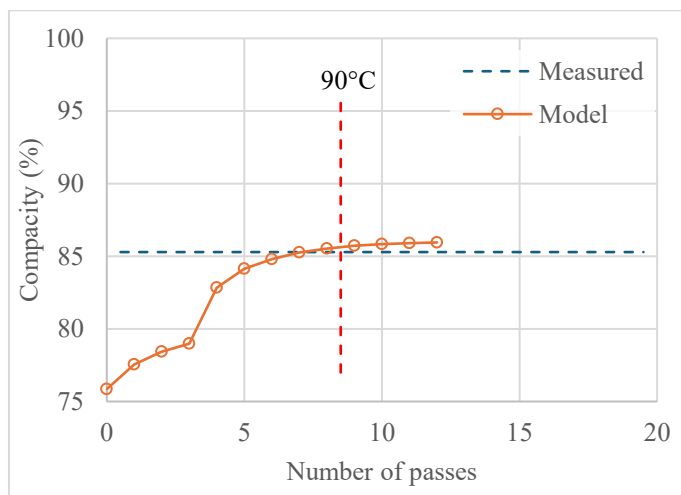
Figure 5. Final compacity and prediction of the FCM for the case of an AC 20 base layer.

5 CONCLUSIONS

The FCM was able to predict field compacity well for a variety of asphalt mixtures and field compaction conditions, including a mixture with known compaction problem. This highlights the ability of the model to pinpoint mixtures with potential problematic compaction, facilitating the study of new mixture compositions and/or additives (e.g. WMA production).

When gathering all gyratory data (compaction under different temperatures and vertical pressures) is not possible, the use of generic parameters can be considered. In the analyzed case studies this approach gave acceptable results.

By using mixture cooling models and rollers properties, the FCM enables the simulation of an infinite variety of field scenarios in a rapid manner.

Despite the positive conclusions reached thus far, the FCM should be further validated with additional cases of problematic compaction. Future research should also explore other mixture types, such as stone mastic asphalt and porous asphalt, and further investigate the effects of temperature and vertical pressure sensitivity depending on the mix type.

REFERENCES

Bijleveld, F.R., Miller, S.R., Bondt, A.H. & Dorée, A.G. 2016. Aligning laboratory and field compaction practices for asphalt – the influence of compaction temperature on mechanical properties. *International Journal of Pavement Engineering* 17(8): 727-740.

Crucho, J., Margaritis, A., Tanghe, T., Vansteenkiste, S. & Vanelstraete, A. 2024. Repeatability and Reproducibility of Analysis Methods for Asphalt Mixture Gyratory Compaction. In P. Pereira & J. Pais (eds), *Proceedings of the 10th International Conference on Maintenance and Rehabilitation of Pavements*: 178-187. Cham: Springer Nature Switzerland.

Duerinckx, B. & Vanelstraete, A. 2021. *Méthode de mesure pour l'utilisation du densimètre nucléaire lors de la détermination de la densité et du contrôle des revêtements bitumineux*. Brussels: Belgium Road Research Centre.

Francken, L. & Leonard, D. 2002. Use of Gyratory compaction for the design of asphalt mixes. In *9th International Conference on Asphalt Pavements (ISAP 2002), Copenhagen, 17-22 August 2002*.

Margaritis, A., Tanghe, T., Vansteenkiste, S., Visscher, J. & Vanelstraete, A. 2023. Impact of the mastic phase and compaction temperature on the sigmoidal gyratory compaction curve of asphalt mixtures. *Construction and building materials* 391: 131283

Moutier, F. 1996. Modelisation des resultats de la p.c.g. reflexions a propos du seuil ultime de compactage. In *Proceedings of the Eurasphalt & Eurobitume congress, Strasbourg, 7-10 May 1996*. Brussels: European Asphalt Pavement Association.

MultiCool. 2024. www.eng.auburn.edu/users/timmdav/MultiCool/FinalRelease/Main.html (accessed September 20th 2024)

Effects of a further developed test-based description of the layer bond between asphalt layers on the service life of the asphalt pavement

B. Gerowski, U. Reinhardt

Institute of Urban and Pavement Engineering, TUD Dresden University of Technology, Dresden, Saxony, Germany

ABSTRACT: The layer bond, which is among others represented by the shear stiffness between the asphalt layers, plays a decisive role in the service life of asphalt pavements. In order to be able to assess the individual asphalt layers with regard to the design and the predicted service life, it is necessary to include the layer bond realistically in the computational design. For this purpose, a new functional model approach was integrated into a finite element model and thus the influence of the layer bond on the service life of the asphalt pavement was analyzed.

1 INTRODUCTION

Due to the drastic increase in traffic expected in the coming years and the negative effects of global warming, asphalt pavements will be exposed to higher stresses. In order to investigate and assess the consequences of these influences, existing model descriptions must be adapted and further developed.

Usually asphalt pavements are divided into different layers for economic and technical reasons. As a rule, these are the asphalt surface course, asphalt binder course and asphalt base course. The individual layers should or must form a compact structure that functions as a unit. This is the only way to ensure a long service life and a high level of road safety. This task is performed by the layer bond, which represents the connection between the individual asphalt layers and is achieved through the interaction of friction, layer bonding and interlocking at the layer boundaries. An intact layer bond makes the road construction more resistant to cracks, deformation, wear and tear. This results in a longer service life and lower maintenance costs.

In order to evaluate this connection between the individual asphalt layers with regard to dimensioning and predicted service life, it is necessary to include the layer bond realistically in the mathematical forecast. In Germany, the dimensioning and prediction of the service life is based on the guideline "Richtlinien für die rechnerische Dimensionierung des Oberbaus von Verkehrsflächen mit Asphaltdeckschicht - RDO Asphalt 09" (FGSV 2009) using the multi-layer theory. The layer bond between the different asphalt layers is assumed to be "full layer bond", "reduced layer bond" or "no layer bond" here.

However, it has been shown that influencing factors must be taken into account for a comprehensive evaluation of the layer bond. Against this background, the Dresden Dynamic Shear Tester was developed at the TU Dresden, Institute of Urban and Pavement Engineering, which takes into account the temperature, the load frequency and the normal stress to describe decisive parameters of friction, layer bonding and interlocking. The result is a shear stiffness modulus.

Due to the model limitations of the multi-layer theory and the non-linear properties of the model for describing the results of the Dresden Dynamic Shear Tester, it was necessary to develop an extended or new calculation approach. This is the first time that a model describing the shear stiffness as a function of various parameters has been implemented in a finite element model. This allows the influence of the layer bond on the expected service life of asphalt pavements to be realistically analyzed and evaluated.

2 TEST DEVICE AND TEST PROCEDURE OF THE DRESDEN DYNAMIC SHEAR TEST

2.1 *Test device*

During the test, a cyclic shear load was applied in the vertical direction and an alternating static normal axial load in the horizontal direction. The specimen, fixed in steel adapters, was inserted into the device and fixed in two shear jaws so that a half of the specimen was in each of the shear jaws (see Figure 1). The distance between the jaws was 1.0 mm as defined by the steel adapters of the specimen. The steel adapters

were screwed into the jaws so that movement of the specimen in the device was virtually impossible.

The shearing load was applied to the lower layer of the specimen by a hydraulic cylinder of the servo-hydraulic testing machine via the vertically movable shearing jaw. The upper layer of the specimen was held by the fixed shear jaw. The normal axial pressure was applied to the back of the asphalt specimen by a pneumatic cylinder through a steel plate.
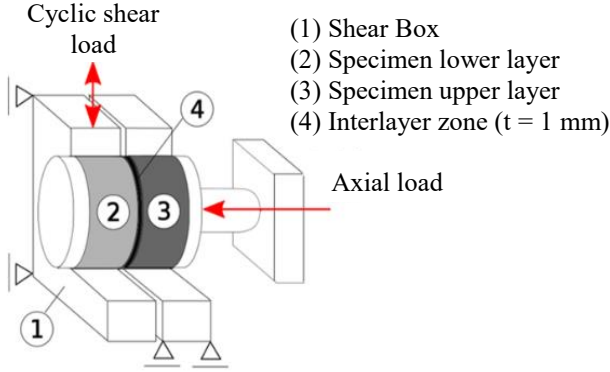
Figure 1. Mechanical model of the Dresden Dynamic Shear Testing device (Canon Falla et al. 2018).

2.2 *Test procedure*

The cyclic shear stiffness tests are carried out on the basis of an extensive test program with a wide range of influencing parameters. The test device developed in 2007 at the Chair of Pavement Engineering at TU Dresden, which maps the factors influencing the layer bond, namely temperature, normal stress, load frequency and shear displacement, has been further developed and optimized over time.
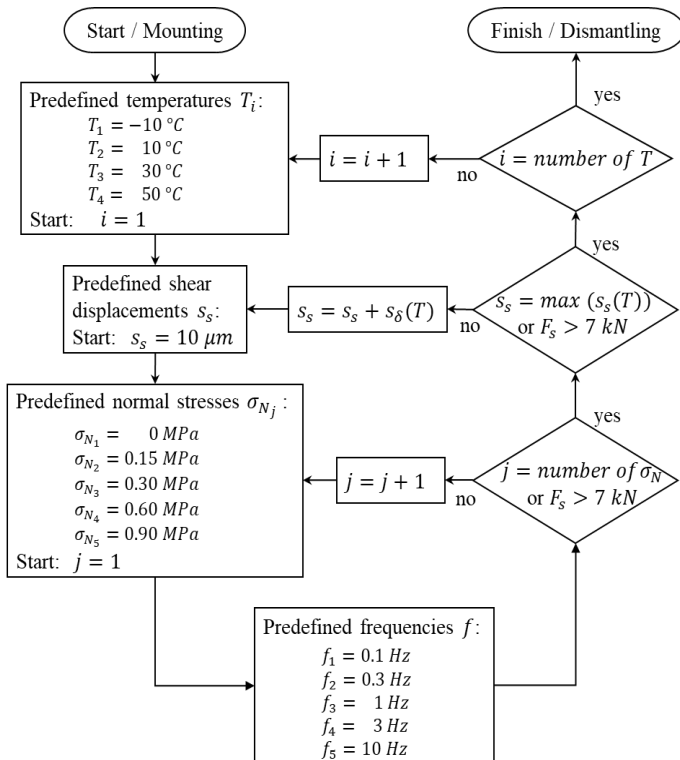
Figure 2. Test program of the Dresden Dynamic Shear Test.

Figure 2 shows the current test procedure, where each test specimen is subjected to a multi-stage test at combinations of four different test temperatures (-10 °C, 10 °C, 30 °C, 50 °C), five normal stresses (0 MPa, 0.15 MPa, 0.3 MPa, 0.6 MPa, 0.9 MPa), five test frequencies (0.1 Hz, 0.3 Hz, 1 Hz, 3 Hz and 10 Hz) and a temperature dependent set of maximal five shear displacements. If the needed testing force exceeds 7 kN, the test of this stage will be interrupted and the next combination will be tested. The shear displacements to be applied vary for the test temperatures from 10 µm to 50 µm at -10 °C and from 10 µm to 130 µm at 50 °C.

A test shall begin at: temperature -10 °C; normal stress 0 MPa; frequency 0.1 Hz and shear displacement 10 µm. Finally, the test ends at: temperature 50 °C; normal stress 0.9 MPa; frequency 10 Hz; shear displacement 130 µm.

3 MODELLING THE LAYER BOND

After changing the test procedure, the influence of the shear displacement on the shear stiffness has to be taken into account. Therefore, the aim was to develop a model function which includes this dependency in addition to the parameters temperature, frequency and normal stress. The derivation of this model approach has already been described in Gerowski et al. (2024) and in detail it will be part of Gerowski (unpubl.).

Equation 1 is composed of three summands, where each summand can be interpreted as one of the main influences on the layer bond: the quasi constant interlocking, the temperature and frequency dependent layer gluing and the normal stress dependent friction.

After evaluation of the measured test values the best fitting results were achieved by including the shear displacement in the friction part of the equation, which also represents the bituminous part of the layer bond.

$$G_S = G_{S_{min}} + \frac{G_{S_{max}} - G_{S_{min}}}{1 + e^{(a \cdot x^* + b \cdot s + c)}} + d \cdot \sigma_N \quad (1)$$

with

$$x^* = \frac{\varphi \cdot \left(\frac{1}{T+273.15} - \frac{1}{T_0+273.15}\right) + ln(f)}{ln(10)} \quad (2)$$

where G_S = shear stiffness; G_{Smin} = minimal shear stiffness; G_{Smax} = maximal shear stiffness; s = shear displacement; σ_N = normal stress; φ = material-specific parameter; T = current temperature; T_0 = reference temperature; f = load frequency; and a,b,c,d = stiffness parameters.

The quality of the fitting is shown in Figure 3 by comparing all measured and the corresponding regression values of an exemplary test. With this representation the quality of the fit can be seen and it is confirmed by the coefficient of determination R², which is almost 1 (0.9971) here.
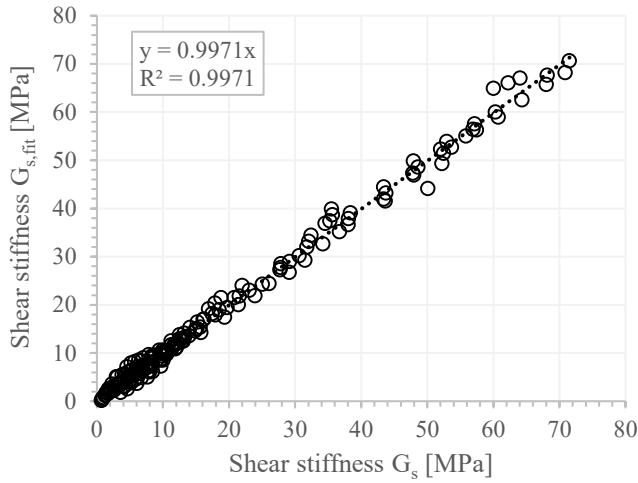
Figure 3. Correlation of measured (G_s) and calculated ($G_{s,fit}$) shear stiffness values.

Another possibility of presenting the quality of the agreement is the comparison of the measured test values and the fitted area function. Figure 4 shows the area function of the exemplary result for the normal stress of 0 MPa. For other normal stresses the shape of the area function is equal but, due to the normal stress dependent term of Equation 1, linearly shifted. Minor deviations between the measured and the calculated values could be due to measurement uncertainties or unmodeled influences, but appear negligible. Overall, it can be seen that this model provides a solid basis for predicting shear stiffness tested with the Dresden Dynamic Shear Test.
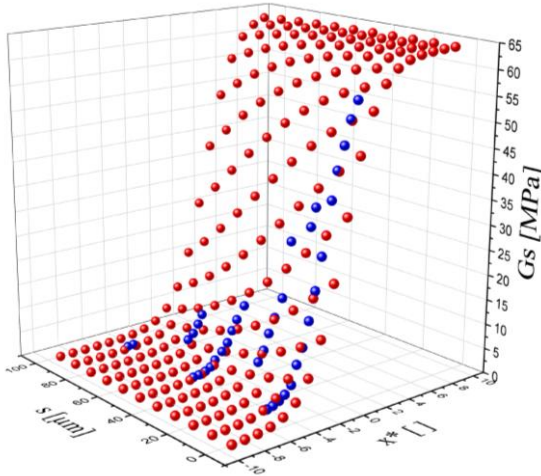
Figure 4. Area function of shear stiffness calculated with the fitted parameters of Equation 1 (red dots) and the measured values (blue dots) at the normal stress of 0 MPa.

The values of $x*$ of Equation 2 represent the temperature und frequency behavior of the layer bond. In the area function of Figure 4 high $x*$-values, i.e. at low temperatures or high load frequencies, mean high shear stiffnesses and low $x*$-values (high temperatures or low load frequencies) results in shear stiffnesses of nearly 0 MPa. At both extremas there are nearly no dependency of the shear displacement. In

between the thermal and frequency properties of the layer bond are in a state in which the shear displacement has a noticeable influence on the material behavior – due to for example a different amount of viscosity.

Based on these findings, the model approach was integrated into a finite element model that not only calculates the stresses and strains in the asphalt pavement, but also computes the expected service life of different asphalt layers, taking into account the parameters of temperature, normal stress, frequency and shear displacement.

4 SERVICE LIFE FORECAST FOR SELECTED LAYER BONDS

4.1 *Model assumptions*

An axially symmetrical finite element pavement model with a model radius of 2.5 m and three asphalt layers (4 cm, 8 cm, 22 cm), an unbound base course (51 cm) and a subgrade (200 cm) was constructed to analyse stresses and strains as a function of different interlayer bond conditions.

The stiffnesses of the asphalt layers were calculated as a function of temperature, while the stiffnesses of the unbound layers were assumed to be constant. To calculate the service life of a pavement structure in accordance to the German design guideline RDO Asphalt 09 (FGSV 2009), 143 strain conditions due to different temperature conditions and wheel loads as well as a high number of load changes were taken into account.

4.2 *Results*

The aim of this prognosis calculations is to investigate the influence of the layer bond on the service life of the asphalt pavement, in this case of the asphalt base course. Therefor the two layer bonds between the three asphalt layers were varied, all others are completely excluded as specified in the guideline.

The analyzed layer bonds were the same for both interlayers and they were the theoretical extremes of "full layer bond" and "no layer bond" as well as "high layer bond" and "low layer bond", which were selected from a large number of previously conducted tests. The theoretical layer bonds are not realistic, but they were selected for comparison with the results calculated in accordance with the guideline.

Figure 5 is a qualitative example and shows the asphalt condition for a single load case (surface temperature 47.5 °C, wheel load 11 t) as a cross-section through the construction with the load axis on the left-hand side. The four subfigures illustrate how the asphalt construction reacts due to a decreasing quality of the layer bonds using the example of the first principal strains. With every quality step of the decreasing

layer bonds the maximum of the tensile strains increases. The point of the maximum tensile strains in all four cases and under these exemplary circumstances is on the bottom of the asphalt surface layer next to the load area.
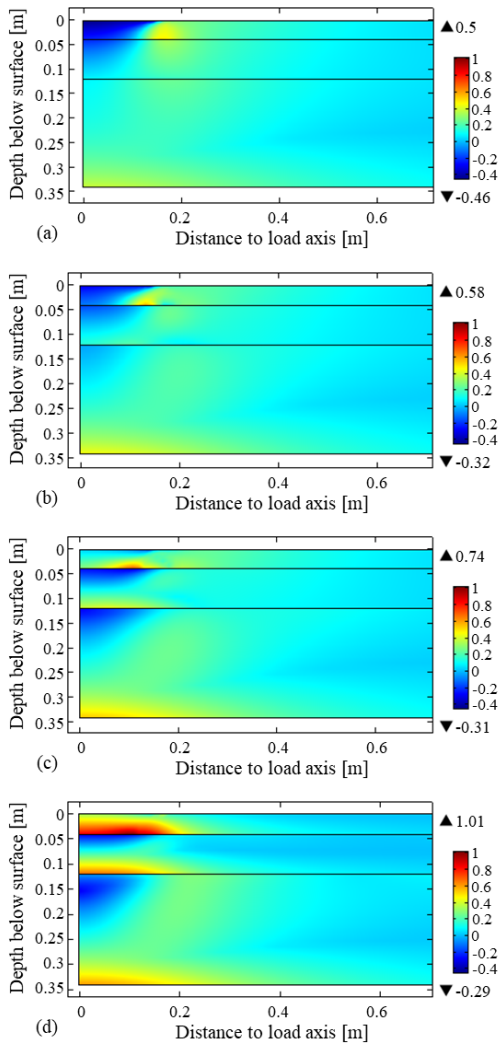
Figure 5. First principal strains [‰] of the layer bond combinations (a) "full layer bond", (b) "high layer bond", (c) "low layer bond" and (d) "no layer bond" for the temperature condition at 47.5 °C and the wheel load of 11 t.

For the calculation of the fatigue status of every asphalt layer the point of the maximum bending tensile stress is decisive. In order to illustrate the influence of the layer bonds, the service life of the different layer bond combinations were calculated for the asphalt base course. The progression of the fatigue statuses are shown in Figure 6 in relation to the "full layer bond"-variant and assuming a fatigue status of 100 % and a service life of 30 years. The difference between the two realistic layer bond variants are 7 years or +50 % related to the "low layer bond" variant.

It is clearly visible that the quality of the layer bond between the asphalt layers got a major impact of the service life of asphalt layers. That's why it is economically and ecologically necessary to test the layer bond respectively use realistic layer bond models for

dimensioning asphalt constructions and predicting the asphalt layer service life.
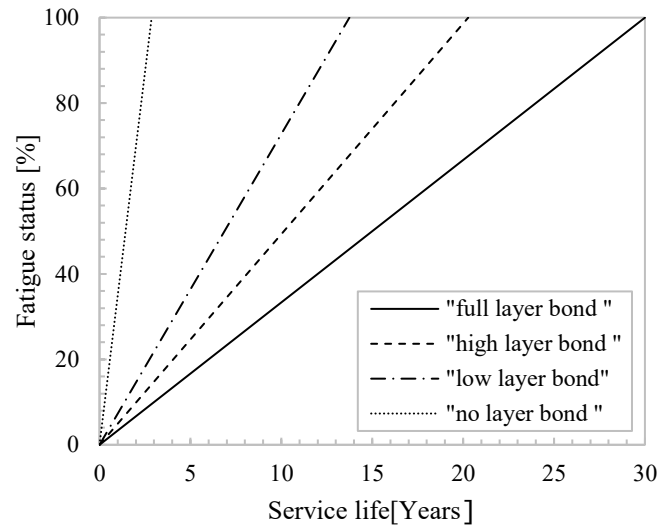
Figure 6. Fatigue status at the bottom of the asphalt base course for different layer bond conditions between the three asphalt layers.

5 CONCLUSIONS

The further developed layer bond model was integrated into a finite element model that takes into account the influences temperature, normal stress, frequency and shear displacement. This makes it possible to calculate the service life as a function of the realistic layer composition based on test results. Thanks to this new approach, the non-linear behavior of the layer bond and its influence on asphalt pavements can now be predicted more precisely.

6 REFERENCES

Canon Falla, G. A., Gerowski, B., Leischner, S., Wellner, F., Wang, D. & Oeser, M. 2018. Experimental determination of interlayer shear layer bond stiffness using the Dresden dynamic shear tester. In E. Masad, A. Bhasin, T. Scarpas, I. Menapace & A. Kumar (eds), *Advances in Materials and Pavement Prediction*: 323-326. London: CRC PRESS.

FGSV (German Road and Transportation Research Association). 2009. *Richtlinien für die rechnerische Dimensionierung des Oberbaus von Verkehrsflächen mit Asphaltdeckschicht - RDO Asphalt 09*. Cologne: FGSV Verlag.

Gerowski, B., Blasl, A., Reinhardt, U. & Zeissler, A. 2024. Development of a model for a realistic description of the interlayer layer bond between asphalt layers based on results of cyclic shear tests. In A. F. Nikolaides & E. Manthos (eds), *Bituminous Mixtures and Pavements VIII*: 862-869. London: CRC PRESS.

Gerowski, B. unpublished. *Entwicklung eines Modellansatzes zur realitätsnahen Beschreibung des Schichtenverbundes*. Draft version of dissertation. TUD Dresden University of Technology.

Comparison of Brazilian and Austrian Low-Traffic Pavement Design Methods

L.J.S. Santos, F.G.R.G. Silva & L.M. Gondim
Universidade Federal do Cariri, Juazeiro do Norte, Ceará, Brazil

P.M. Souza
Universidade Regional do Cariri, Juazeiro do Norte, Ceará, Brazil

L. Eberhardsteiner & S. Roth
TU Wien, Vienna, Austria

ABSTRACT: Comparison of pavement design methods is essential for developing a universal approach adaptable to different regions of the world. Brazil and Austria have adopted Mechanistic-Empirical (M-E) methods: MeDiNa and RVS 03.08.68, respectively, for pavement design. This study compares these methods for low-traffic roads using Brazilian data. The analysis highlights key differences: MeDiNa provides customized designs, while RVS 03.08.68 simplifies low-traffic pavement design through pre-dimensioned solutions. RVS resulted in a wider pavement structure than MeDiNa, for the condition evaluated. Rutting analysis shows that the Austrian method results in lower deformation (1.57 mm after 120 months) than MeDiNa's (2.27 mm after 120 months), as a consequence of the larger structure. A life-cycle assessment (LCA) is recommended to evaluate long-term economic and environmental impacts. This study contributes to the harmonization of international pavement design methodologies, aiming to promote more efficient and sustainable road infrastructure.

1 INTRODUCTION

In the last 20 years, several Mechanistic-Empirical (M-E) methods have been developed and implemented in different countries. For asphalt pavements, Brazil developed the New National Design Method (MeDiNa), whose implementation was initiated by the National Department of Transport Infrastructure (DNIT) (Franco & Motta, 2020). Also, in Austria a new M-E method has been developed, taking advantage of greater detail on the stiffness and fatigue properties of materials, as well as more information on traffic conditions (Eberhardsteiner & Blab, 2019).

This work represents a preliminary report resulting from the collaborative efforts between Austria and Brazil in the development of new pavement design methodologies. The study seeks to identify similarities and differences between the Brazilian MeDiNa method and the Austrian RVS 03.08.68 method, as well as how these methods can communicate with each other. Such comparisons play a crucial role in enabling the technical and scientific community to better understand the realities of different countries. This understanding paves the way for more comprehensive characterizations of traffic variables and material properties, fostering the continuous improvement of pavement design methods and their applicability to diverse environmental and operational conditions.

This can support the adaptation of methodologies to distinct regions, promote the harmonization of design practices, and encourage future collaborative developments in pavement engineering.

To this end, a comparison was made, primarily assessing low traffic conditions, weather, and material performance properties. Next, the interchangeability of the two methods was evaluated to adapt the Brazilian data for use in the Austrian method. Finally, a comparison of the final structures for low traffic resulting from both methods was conducted.

2 COMPARISON OF THE MEDINA AND RVS 03.08.68 METHODS

To perform design based on M-E principles, three stages are considered: input data, structural analysis and performance, and output data. The procedures required by MeDiNa and RVS 03.08.68 for each step are outlined below.

2.1 *Input data*

The input data stage involves traffic, weather, and material data. In MeDiNa, traffic data is converted into an equivalent standard axle using load spectra and axle configurations. Load factors, axle factors, and vehicle factors are calculated to estimate the destructive effects of axle loads. The RVS 03.08.68

method uses 11 vehicle classes, divided into groups, with parameters to determine total weight distribution and axle load distributions. Both methods require a design period, road lane configuration, and annual traffic growth rate.

Regarding weather data, MeDiNa does not yet account for temperature and humidity effects in structural analysis, while RVS 03.08.68 divides the year into six representative temperature periods, with further difference between day and night, considering the temperature dependence of asphalt properties and traffic distribution. This results in 12 temperature periods, enabling realistic distributions in the pavement structure across two different geographical conditions in Austria.

For materials, both methods rely on laboratory testing but differ in tests and calculations. MeDiNa includes tests for stabilized, granular, and subgrade materials, while RVS 03.08.68 classifies materials using a system based on particle size, shape, and resistance. Additionally, both MeDiNa and RVS 03.08.68 utilize performance-related approaches to determine the stiffness and fatigue behavior of bituminous materials.

2.2 Structural analysis and performance

An M-E method uses computational resources to assess pavement structural responses for calculating lifetime damage. In MeDiNa, failures due to rutting and fatigue are considered, as these are the most common in Brazilian pavements. Although rutting is not calculated for the asphalt layer in MeDiNa, the method considers the Flow Number as a requisite for the mix design, to help prevent asphalt mixtures prone to rutting. In RVS 03.08.68 fatigue failure of bituminous materials is considered as a factor resistant to traffic loads.

2.3 Output data

MeDiNa presents reports detailing the monthly progression of fatigue and rutting, a summary of permanent deformations, and deflection basins, which are obtained through the Falling Weight Deflectometer (FWD) and the Benkelman Beam. However, RVS 03.08.68 reports whether the design of the pavement was accepted or rejected according to the data provided.

3 PAVEMENT DESIGN METHODS

The data obtained for Brazilian traffic, weather, and materials are directly used in the design of the pavement with the MeDiNa method. However, to carry out pavement design using the RVS 03.08.68

method, it is necessary to establish equivalence between the two methods for these data. Below is a summary of the main steps of the procedure, as well as the data to be used in the Austrian design.

3.1 Traffic data

Brazilian traffic data for 2023 was obtained from the National Infrastructure Department (DNIT) website (DNIT, n.d.). The study focused on BR-020 highways in Ceará, Brazil.

The data allows for identifying vehicle axles but not the vehicles themselves, needing the selection of a vehicle class based on axle count. Unlike the Austrian method, the Brazilian design typically uses standard vehicle weights. This research applied current axle weights without considering tolerances permitted by Brazilian laws.

Various Brazilian vehicle axle configurations are outlined in standards from agencies like DNIT (DNIT, 2006) and National Traffic Council (CONTRAN) (Brazil, 2021). The Brazilian vehicle classes and their similar Austrian counterparts are presented in Table 1.

Table 1. Equivalent Vehicle Classes Adopted.

Brazilian axle number	Brazilian	Austrian
2	2C	FK2-1
3	2S1	FK3-3
4	2C2	FK4-3
5	2I3	FK4-7
6	3D3	FK4-7
7	3Q4	FK3-3 + FK4-3
8	3M5	FK3-3 + FK4-7
9	3T6	FK4-3 + FK2-1 + FK2-1

Equivalence was based on the total weight of the Austrian vehicle to identify the Brazilian vehicle with the closest axle weight. For four Brazilian configurations with 6 to 9 axles, no similar configurations were found in Austria. In these cases, vehicles with the closest total weight were selected, ignoring axle weight distribution and count.

Table 2 summarizes vehicle quantities and classes to use in the Austrian method, considering the low traffic data obtained in Brazil.

Table 2. Brazilian vehicle quantities and classes adapted for the Austrian method.

Austrian Vehicle Class	BR-020
FK2-1	5
FK3-3	4
FK4-3	1
FK4-7	3
AADTT	13

It is important to highlight that the Brazilian method calculates the average daily traffic volume by accounting for all vehicles, whereas the Austrian equivalent Annual Average of the overall Daily Truck Traffic (AADTT) considers only heavy good vehicles (HGV) with gross weight above 3,5 t. The AADTT found (13) confirms the low volume of traffic.

The Austrian method indicates that additional standards should be used for low-traffic roads, such as RVS 03.08.63 and RVS 03.03.81, which use pavements designed based on a standard axle (DESAL) (Equation 1). Table 3 presents the data used for DESAL determination for RVS, while Table 4 shows the traffic data for the MeDiNa method.

$$DESAL = ESAL_{day} \cdot R \cdot V \cdot S \cdot 365 \cdot n \cdot z \qquad (1)$$

Table 3. Traffic data for RVS 03.03.81

A_{AADTT} (Average equivalent factor of vehicle category)	1.6
R (Traffic direction)	1
V (Lanes per direction)	0,9
S (Distribution of wheel tracking in one lane)	1
n (Design life in years)	10
ESAL/day (Average daily load application)	20,8
z (Growth factor)	1.146388
DESAL	39,166

where, ESAL/day is obtained by multiplying A_{AADTT} with AADTT. Furthermore, MeDiNa uses the number N based on the USACE method, which is described in Equation 2.

$$N = 365 \cdot VMD \cdot FV \cdot S \cdot \frac{(1+p)^n - 1}{p} \qquad (2)$$

Table 4. Traffic data for MeDiNa

Vehicle factor (FV)	1
% Vehicles in the design lane (S)	100
% Traffic growth rate (n)	3
Period (Design life in years) (p)	10
Road Type	local road
N	$9.96 \cdot 10^5$

3.2 Weather data

This design focuses on Fortaleza, the capital of Ceará in northeastern Brazil. Using INMET (2024) data from 2004 to 2023, it highlights minimal temperature variation while providing maximum, minimum, and pavement subgrade temperatures.

To obtain the surface temperatures, presented in Table 5, the study conducted by the SHRP program (Asphalt Institute, 1994) was used, which allows for estimating the maximum pavement temperature (near the surface).

Table 5. Temperature variation profile of Fortaleza, Brazil, for application in the Austrian method.

PERIOD	Air Temperature	DEPTH (cm)							
		0	5	10	15	20	25	30	35
1	27.96	48.26	38.44	32.60	29.76	27.98	26.70	25.73	24.96
2	27.44	47.77	37.95	32.10	29.27	27.48	26.21	25.24	24.46
3	27.30	47.63	37.81	31.97	29.13	27.34	26.07	25.10	24.33
4	26.76	47.12	37.30	31.45	28.62	26.83	25.56	24.59	23.81
5	27.25	47.59	37.77	31.92	29.09	27.30	26.03	25.06	24.28
6	26.67	47.03	37.21	31.37	28.53	26.74	25.47	24.50	23.73
7	27.14	47.48	37.66	31.82	28.98	27.19	25.92	24.95	24.18
8	26.48	46.85	37.03	31.18	28.35	26.56	25.29	24.32	23.54
9	28.06	48.36	38.53	32.69	29.86	28.07	26.80	25.82	25.05
10	26.85	47.21	37.39	31.54	28.71	26.92	25.65	24.68	23.90
11	28.59	48.87	39.05	33.20	30.37	28.58	27.31	26.34	25.56
12	27.36	47.69	37.86	32.02	29.19	27.40	26.13	25.16	24.38

3.3 Materials data

Table 6 presents the material data to be used for low traffic pavements, for both methods.

Table 6. Characterization of Brazilian materials for applications in the RVS (Elastic Modulus) and MeDiNa (Resilient Modulus)

Materials	Layer	Period	Elastic Modulus	Resilient Modulus
			MN/m²	
Silty Soil	Subgrade	(Jan -Jun) (Jul-Dec)	105 205	189
Fine Sandy Soil	Base	Entire year	331	494
Double Surface Treatment	Surface	Entire year	Standard material	1000

It is worth noting that for low-traffic conditions in Brazil, a double surface treatment is used, and, according to RVS 03.08.68, no equivalent layer is specified.

4   DESIGNED PAVEMENT STRUCTURES

It was observed that the RVS 03.03.81 specifies a base layer with a thickness of 40 cm, complemented by an asphalt surfacing layer. In contrast, the MeDiNa method proposes a 15 cm thick base layer combined with a 2 cm double surface treatment as the surfacing. It is important to note that, according to the Austrian design model, the thickness of the surface treatment layer is not specified. This is why the layer is graphically represented in Figure 1 for MeDiNa only.

Figure 1. Structures of pavement designed
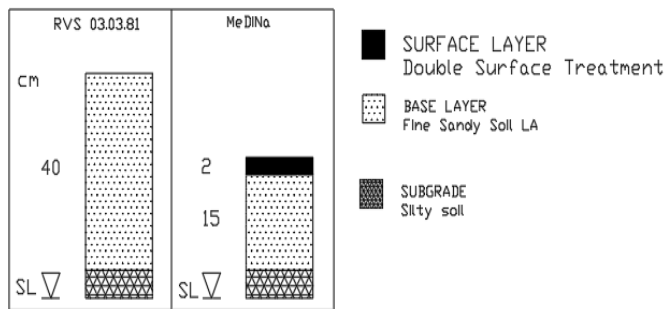
Moreover, the MeDiNa software was applied to the designed structures for the analysis of rutting. Table 7 presents the results obtained, highlighting the performance of the pavement layers under the expected traffic conditions. The rutting analysis was performed based on the structural configuration, providing insights into the deformation behavior of the materials used. As expected, RVS design resulted in lower rutting than MeDiNa, due to the wider thickness. Nevertheless, both results may be considered low, compared to the failure criteria for low volume road in MeDiNa (20 mm for local roads) (Franco & Motta, 2020).

Table 7. Rutting Analysis Results

Pavements designed	Period (Month)	Rutting (mm)
RVS 03.03.81	30	1.36
	60	1.46
	120	1.57
MeDiNa	30	2.27
	60	2.40
	120	2.53

Finally, fatigue analysis was not conducted for these pavement designs, as the low traffic volume requires the use of a double surface treatment as the wearing course, which is not prone to fatigue due to its small thickness. Consequently, the Medina software does not evaluate fatigue in surface treatment layers, whether in terms of cracked area or other fatigue-related parameters.

5 FINAL CONSIDERATIONS

The comparison between the Brazilian MeDiNa method and the Austrian RVS 03.08.68 method highlighted key differences in pavement design for low-traffic conditions: MeDiNa uses tailored solutions for all traffic levels, while the Austrian method simplifies low-traffic design with pavements designed based on a standard axle, reserving detailed analysis for higher traffic volumes; MeDiNa provides customized designs based on detailed analysis, whereas the Austrian method offers standardized, efficient solutions for low-traffic roads; the Austrian method results in a thicker base layer, which, although initially more costly, may be more durable and require less maintenance, as suggests the lower rutting observed. A life-cycle assessment (LCA) is recommended to evaluate long-term economic and environmental impacts, helping to identify the most sustainable and cost-effective approach.

These findings show the strengths of both methods: MeDiNa excels in adaptability and detailed analysis, while the Austrian method emphasizes simplicity and efficiency for low-traffic roads. The study is being expanded to include comparisons for medium and high-traffic volumes, aiming to offer more insights into the methods' effectiveness in different traffic scenarios. This will help guide better decision-making for pavement design across varying road usage levels.

Initiatives like this comparison of design methods are essential for the evolution of a universal pavement design method that could be generic for all locations while allowing the necessary adaptations for each specific situation.

REFERENCES

ASPHALT INSTITUTE. 1994. *Superpave mix design manual for new construction and overlays* (SHRP-A-407). Strategic Highway Research Program. National Research Council.

BRAZIL. 2021. National Traffic Council. Resolution no. 882. Establishes the weight and dimension limits for vehicles on land routes and other provisions. Official Gazette of the Union: section 1, Brasília, DF, Dec. 17, 2021. Accessed: Dec. 12, 2024.

DNIT .2024. *Pavement Coverage Research*. National Department of Transportation Infrastructure. Accessed: November 20, 2024. https://servicos.dnit.gov.br/dadospnct/PesquisaCobertura.

DNIT. 2006. *Traffic Studies Manual*. Rio de Janeiro: National Department of Transport Infrastructure.

Franco, F. A. C.; Motta, L. M. G. da. 2020. *Execução de estudos para a elaboração do método mecanístico-empírico de dimensionamento de pavimentos asfálticos. Manual de utilização MeDiNa.* Rio de Janeiro, Brazil

Instituto Nacional de Meteorologia (INMET). Climatological Data (2004–2023). Available at: https://portal.inmet.gov.br. Accessed: November 20, 2024

Eberhardsteiner, L.; Blab, R. 2019. Design of bituminous pavements – a performance-related approach. Road Materials and Pavement Design, 20:2, 244-258, DOI:10.1080/14680629.2017.1380689.

FSV. 2011. RVS 03.03.81. Ländliche Straßen und Güterwege, Wien. (in German)

FSV. 2016. RVS 03.08.63. Oberbaubemessung, Wien. (in German)

FSV. 2018. RVS 03.08.68. Dimensionierung von Asphaltstraßen, Wien. (in German)

Backcalculation of the roller-compacted concrete pavement structure with cement and special additives stabilized base layers

Audrius Vaitkus
Vilnius Gediminas Technical University, Vilnius, Lithuania

Rafal Mickevič
Vilnius Gediminas Technical University, Vilnius, Lithuania

Martynas Karbočius
Vilnius Gediminas Technical University, Vilnius, Lithuania

ABSTRACT: Slip-form concrete (JPCP) has demonstrated reliable performance over many years. An alternative to slip-form concrete is roller-compacted concrete (RCC), which contains a higher proportion of fine aggregates. This composition results in a non-slump mix that is compacted using rollers. RCC offers strength and performance equal to or exceeding that of conventional concrete. Its advantages make RCC particularly suitable for industrial areas and low-volume rural roads. In Lithuania, RCC pavement structures typically incorporate a base (CTB) and a subbase stabilized with cement and special additives (CTS). Typical cement content in CTB is 3-8 %, in CTS – 3-5 %. Modulus of the elasticity of the layer is one of the most important mechanical property in the mechanistic–empirical pavement design method. In light of that bearing capacity tests with falling weight deflectometer were performed on local road and deflections were used in evaluation of the CTB and CTS modulus of elasticity.

1 GENERAL INSTRUCTIONS

Roller-compacted concrete (RCC) is a dry concrete mix that can be placed using an asphalt paver and compacted with rollers (Vaitkus et al., 2022). Characterized as a no-slump concrete, RCC achieves high strength levels through compaction and aggregate interlock (Chhorn et al., 2018). While its consistency is comparable to that of conventional concrete, RCC differs in its mix proportions (Vaitkus et al., 2021; Rambabu et al., 2023).

To ensure optimal performance of RCC pavements, a strong foundation for the RCC top layer is crucial. In Lithuania, RCC pavement structures typically incorporate a base stabilized with cement and special additives. This stabilized base is designed to endure traffic loads and environmental stresses effectively. The primary goal of stabilization is to enhance the bound layer's performance by incorporating a relatively high cement content, often up to 10% (Yeo, 2011). Additionally, hydrothermal conditions have minimal impact on the bearing capacity of RCC pavement structures with stabilized subbase and base layers when built on a water-permeable subgrade (Vaitkus et al., 2022).

Design of the pavement structures are based on a mechanistic–empirical pavement design method. The procedure incorporates mechanistic components such as load, stresses, deflections and also mechanical properties of the pavement structure. The main pavement structure input data in the mechanistic–empirical pavement design method is thickness of the pavement structure layers and modulus of the elasticity E. Modulus of elasticity E is a property of the stiffness of materials that describes the formation of elastic deformation in a material under the action of axial stress. Modulus of the elasticity of a cement-stabilized pavement base is significantly affected by the cement content and the curing duration (Nusit et al., 2015). It can be obtained from several laboratory tests, such as triaxial and unconfined compression tests or in situ tests like standard penetration tests, pressure meters, plate-load tests and bearing capacity tests using falling weight deflectometers.

RCC pavements are more cost-effective than traditional concrete pavements and are easier and faster to construct on-site (Sengun et al., 2018; Chhorn et al., 2017). The RCC layer can be installed using a standard asphalt paver equipped with a high-density screed and compacted with rollers. Due to the straightforward installation process, which closely resembles asphalt layer placement, RCC can be laid more efficiently than conventional concrete which reflects in the reduced installation costs up to 30 % (Fardin et al., 2021; Mohammed et al., 2018).

2 EXPERIMENT

2.1 *Test location*

An experimental section of RCC pavement with a cement-stabilized base layer and subbase was constructed on local road No. 130 in Lithuania. he reconstruction of this road took place between June and August 2021. The length of the reconstructed local road No. 130 was 699 m, the width of the concrete pavement 10 m, the unbound shoulders – 1 m.

2.2 *Pavement structure*

The pavement structure of the local road No. 130 is represented in Fig. 1 and consists of:
- 16 cm of RCC layer;
- 40 cm cement and special additives stabilized base layer;
- 20 cm cement and special additives stabilized subbase layer;
- subgrade.
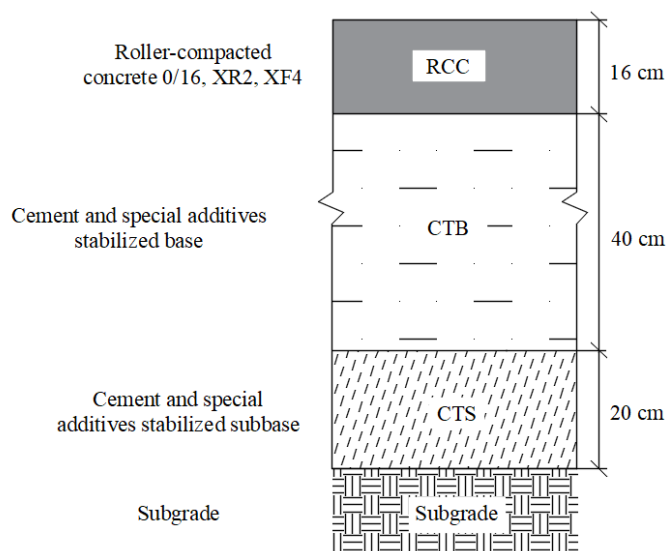
Figure 1. Pavement structure.

RCC mixture was produced in mobile concrete batching plant and consists of:
- 4/16 fraction crushed aggregates (48.8 %);
- 0/4 fraction fine aggregates (30.9 %);
- cement (14.7 %);
- water (5.5 %);
- concrete plasticizer (0.07 %).

Cement and special additives stabilized base consists of:
- 5 % portland cement;
- ion exchange enhancing chemical additive (0.2 l per m3 of soil);
- water;
- soil.

Requirements for cement and special additives stabilized subbase:

- compressive strength after 28 days not less than 1.5 MPa;
- the ratio of compressive strength of samples after refrigeration and thawing cycles to reference samples (after 28 days) is at least 0.6;
- compaction rate not less than 98%.

Cement and special additives stabilized subbase consists of:
- 3 % portland cement;
- ion exchange enhancing chemical additive (0.2 l per m3 of soil);
- water;
- soil.

Requirements for cement and special additives stabilized subbase:
- deformation modulus Ev2≥100 MPa;
- compressive strength after 28 days not less than 1.0 MPa;
- compaction rate not less than 98%.

2.3 *Field testing*

The bearing capacity of pavement structure was conducted using a falling weight deflectometer (FWD). The falling weight deflectometer (FWD) is non-destructive testing (NDT) device to evaluate the bearing capacity of the pavement, which is use widely all around the world. A FWD transfers a 50 kN and 200 kN load to the road pavement through a 300 mm diameter circular plate, which results in 707 MPa pressure. The generated haversine pulse lasts about 30 ms. Dynamic deflections on the road surface due to applied loads are captured by sensors (geophones), which are positioned at different distances from the center of the loading plate (0, 200, 300, 450, 600, 900, 1200, 1500 and 1800 mm).

Measurements of the bearing capacity of the pavement structure on the cement and special additives stabilized subbase (CTS) were carried out on June 10, 2021. Within the scope of the study, the bearing capacity was measured at 48 points using a falling weight deflectometer (FWD) (more information provided in Fig. 2).

Measurements of the bearing capacity of the pavement structure on the cement and special additives stabilized base (CTB) were carried out on June 23, 2021. Within the scope of the study, the bearing capacity was measured at 80 points using a falling weight deflectometer (FWD) (more information provided in Fig. 2).

Measurements of the bearing capacity of the pavement structure on the roller-compacted concrete (RCC) were carried out on July 6, 2021. Within the scope of the study, the bearing capacity was measured at 80 points using a falling weight deflectometer (FWD) (more information provided in Fig. 2).

Based on the bearing capacity study, the modulus of elasticity for both CTS and CTB layers was evaluated in two different ways:
- using the deflections from direct measurements on the CTS and CTB (after installation of each layer);
- using the deflections from measurements taken on RCC layer (28 days after installation of the wearing course RCC).

The modulus of elasticity of the CTS and CTB were determined with the automated ELMOD6 software, using the "Deflection Basin Fit" calculation algorithm. Moreover, the modulus E of CTB and CTS was evaluated from directed

Figure 2. Pavement bearing capacity measurements with FWD.

3 RESULTS AND DISCUSSION

3.1 CTS backcalculated E modulus

Taking into account the direct calculations of the E modulus of the CTS layer, it was determined that in the right lane of the examined section of the local road No. 130, the E modulus of the CTS layer varies from 140 MPa to 1013 MPa, the average is 347 MPa, the standard deviation is 233 MPa. In the left lane of the examined section of the local road No. 130, the E modulus of the CTS layer varies from 103 MPa to 816 MPa, the average is 288 MPa, the standard deviation is 139 MPa (more information provided in Fig. 3).

The calculated E modulus of the CTS layer after the installation of the RCC layer showed that in the right lane, the E modulus of the CTS layer varied from 188 MPa to 516 MPa, with an average of 323 MPa and a standard deviation of 52 MPa. In the left lane, the E modulus of the CTS layer varied from 273 MPa to 469 MPa, with an average of 339 MPa and a standard deviation of 49 MPa (more information provided in Fig. 3).
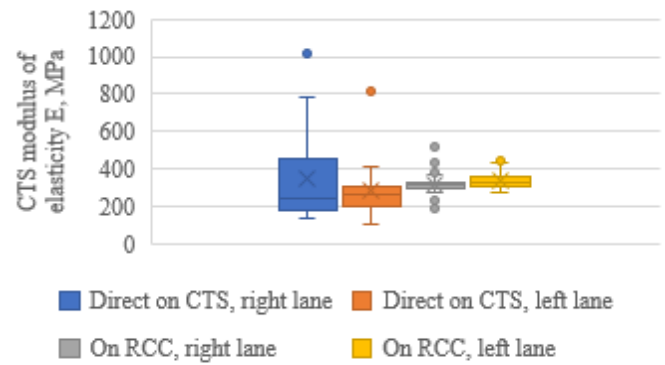
Figure 3. CTS backcalculated E modulus.

3.2 CTB backcalculated E modulus

Taking into account the direct calculations of the E modulus of the CTB layer, it was determined that in the right lane of the examined section of the local road No. 130, the E modulus of the CTB layer varies from 725 MPa to 7738 MPa, the average is 3232 MPa, the standard deviation is 2015 MPa. In the left lane of the examined section of the lo-cal road No. 130, the E modulus of the CTB layer varies from 687 MPa to 7581 MPa, the average is 2657 MPa, the standard deviation is 1599 MPa (more information provided in Fig. 4).

The calculated E modulus of the CTB layer after the installation of the RCC layer showed that in the right lane, the E modulus of the CTB layer varied from 542 MPa to 5581 MPa, with an average of 2385 MPa and a standard deviation of 1071 MPa. In the left lane, the E modulus of the CTB layer varied from 514 MPa to 5246 MPa, with an average of 2304 MPa and a standard deviation of 1082 MPa (more information provided in Fig. 4).
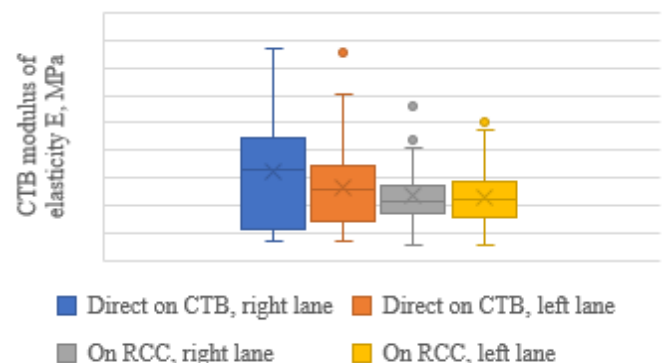
Figure 4. CTB backcalculated E modulus.

4 CONCLUSION

The analysis of FWD data on different pavement layers led to the following conclusions:

- a comparison of the E modulus measurements of the CTS and CTB layers taken directly with those conducted on the RCC layer revealed a more stable E modulus in the underlying layers, along with a smaller standard deviation (CTS right lane 52 MPa, left lane 49 MPa; CTB right lane 1071MPa, left lane 1082 MPa) after the installation of the RCC layer. The increased stability of the E modulus in the CTS and CTB layers may be attributed to the additional compaction of the entire pavement structure following after the installation of RCC layer;
- the analysis of the E modulus measurements for the CTS and CTB layers also showed slight variations between the left and right lanes, particularly during the direct measurements on CTS and CTB. The aforementioned differences could have been influenced by the inhomogeneity of the soils and the lack of uniformity in the technological installation of the layer (water and cement content, soil moisture, compaction etc.).

5 REFERENCES

Vaitkus A, Mickevič R. 2022. Performance of roller-compacted concrete pavement structure with stabilized soil base layers during spring thaw. *The 7th International Conference on Road and Rail Infrastructure.*

C. Chhorn, S.J. Hong, S.W. Lee. 2018. Relationship between compressive and tensile strengths of roller-compacted concrete. *Journal of Traffic and Transportation Engineering, 5 (3), pp. 215-223.*

Vaitkus A, Mickevič R., Šernas O. 2021. Roller compacted concrete – best practice of Lithuania. *The 30th International Baltic Road Conference, 2021.*

Rambabu, Dadi & Sharma, Shashi & Akbar, M. 2023. A review on suitability of roller-compacted concrete for constructing high traffic resisting pavements. *Innovative Infrastructure Solutions. 8. 20. 10.1007/s41062-022-00989-4.*

Yeo, Y. S. 2011. Characterisation and Classification of Cement Treated Crushed Rock Basecourse for Western Australian Roads. *Ph.D. thesis, Curtin University, Perth WA, Australia.*

Korakod Nusit, Peerapong Jitsangiam, Jayantha Kodikara, Ha H. Bui and Gordon Lai Ming Leung. 2015. Dynamic Modulus Measurements of Bound Cement-Treated Base Materials. *Geotechnical Testing Journal. DOI: 10.1520/GTJ20140233.*

Aydın Kici, Mesut Tiğdemir, Şengül Figen Kalyoncuoğlu. 2018. Parametric Study of The Parameters Affecting Concrete Pavement Thickness. *Journal of the Institute of Science and Technology.*

Chhorn, C., Hong, S. J., & Lee, S.-W. 2017. A study on performance of roller-compacted concrete for pavement. *Construction and Building Materials, 153, 535–543.*
https://doi.org/10.1016/j.conbuildmat.2017.07.135.

HE Fardin, A. Goulart dos Santos. 2021. Predicted responses of fatigue cracking and rutting on roller compacted concrete base composite pavements. *Constr. Build. Mater., 272, Article 121847.*

B.S. Mohammed, M. Adamu. 2018. Mechanical performance of roller compacted concrete pavement containing crumb rubber and nano silica. *Construction and Building Materials, 159, pp. 234-251.*

ACKNOWLEDGEMENTS

1.3

MODELING, PERFORMANCE PREDICTION AND DESIGN OF RIGID PAVEMENTS

Determining the effect of sub-base type and friction coefficient on load transfer values for rigid aircraft pavements

S. Jamieson
University of the Sunshine Coast, Sippy Downs, Queensland, Australia

G. White
University of the Sunshine Coast, Sippy Downs, Queensland, Australia

ABSTRACT: Rigid aircraft pavement load transfer can be affected by several factors, including loading regime, sub-layer support, joint type and climate. The effect of using a bound sub-base instead of an unbound sub-base on load transfer is not well understood, with previous literature reporting either an increase, decrease, or no significant effect on load transfer values. Additionally, when modelling load transfer, the friction coefficient between slab and sub-base has been modelled using a large range of values. This research aimed to isolate the effect of sub-base type, as well as quantifying the effect of slab to sub-base friction coefficient on load transfer values. Through finite element methods, it was determined that sub-base type has only a minor effect on typical load transfer values for dowelled and butt construction joints. Consequently, for these joint types, the selection of sub-base type is not critical to achieve effective load transfer. However, the effect on sinusoidal construction joints was significant. It was also determined that modifying the slab to sub-base friction value increased joint deflection and bending stress, however, had negligible impact on load transfer.

1 INTRODUCTION

Rigid aircraft pavements are typically comprised of unreinforced Portland cement concrete base slabs over an unbound or bound sub-base layer, constructed on the subgrade (AAA 2017). The concrete slabs are square or almost-square, typically ranging from 4 m to 8 m in length, (Jamieson and White 2023, FAA 2021). The slabs are separated by joints, which also provide load transfer to the adjacent slabs, resulting in reduced slab-edge stresses. Because edge stresses can be the critical stress for pavement thickness design (FAA 2021), effective load transfer reduces the required slab thickness.

It is generally assumed in airport pavement thickness design programs that joints provide 25% load transfer to adjacent slabs (FAA 2021). However, load transfer is variable, and is affected by many factors, including loading regime, sub-layer support, joint gap width and joint details (Byrum 2011b). Of interest to this research is the effect that sub-base characteristics have on load transfer values, specifically the sub-base type and the friction coefficient between slab and sub-base. This is because different researchers have determined that a bound sub-base can decrease load transfer (Hammons et al. 1995), increase load transfer (UK MOD 2011) or have no significant effect on load transfer, compared to an unbound base (Jamieson and White 2024b). Additionally, the friction coefficient between the slab and sub-base has been modelled using a large

range of values. However, the effect of friction on design load transfer is not well understood. Consequently, this research investigated these two factors by using a previously validated finite element (FE) model for a range of typical rigid pavement construction joints.

2 BACKGROUND

2.1 *Load transfer*

Load transfer is the ability for a joint in a concrete pavement to transfer load from one slab to the next when trafficked. Load transfer relies on joint stiffness, which contains three physical contributors: stiffness from dowels, stiffness from aggregate interlock, and apparent stiffness provided by elastic solid base effects (Byrum 2011b). Load transfer is generally characterized by load transfer efficiency, via deflection (LTE_δ) (Equation 1), or free-edge stress transferred (LT) (Equation 2). LTE_δ is the percentage of the unloaded slab deflection over the loaded slab deflection, and this can be relatively easily calculated from deflections measured in the field using a falling weight deflectometer (White 2018, Gkyrtis et al. 2021). In contrast, LT is the portion of stress that is transferred to an unloaded slab, relative to the loaded slab, when under a free-edge loading condition. That is, the condition when no adjacent slab is connected. Although LTE_δ is routinely measured for existing pavements, LT is commonly used for design

practices, has a range of 0% to 50%, and as discussed earlier, is assumed to be 25% in contemporary thickness design methods (Byrum 2011a, FAA 2021).

$$LTE_\delta = \frac{\delta_U}{\delta_L} \times 100 \qquad (1)$$

$$LT = 100 \times \frac{(\varepsilon_F - \varepsilon_L)}{\varepsilon_F} \qquad (2)$$

Where, LTE_δ = Load transfer efficiency by deflection (%); LT = Percent of free-edge stress transferred (%); δ_L = Deflection of loaded side of the joint (mm); δ_U = Deflection of unloaded side of the joint (mm); ε_L = Bending strain in the loaded slab edge at the joint; and ε_F = Bending strain in the free-edge loading condition for the loaded slab edge.

2.2 *Sub-layer effect on load transfer*

Sub-base and subgrade support provide apparent stiffness to the joint through elastic solid base effects, but in reality, this is not joint stiffness itself, as joint stiffness is generally defined by the interaction of the concrete slab elements only (Byrum 2011b).

However, bound and unbound sub-base types have been reported to affect joint behaviour differently, with a higher LTE_δ associated with bound sub-bases (Colley and Humphrey 1967). In fact, United Kingdom airport pavement design practice is to generally use a dry lean concrete sub-base without any dowels at the construction joints, because they have found that bound bases provide an adequate level of LT without requiring the addition of dowels (UK MOD 2011). In contrast, research by Hammons et al. (1995) showed that bound sub-bases reduce LT compared to unbound sub-bases, because unbound bases allow for more deflection, which allows for more dowel resistance, or aggregate interlock, to be engaged. A similar trend was observed for subgrade strength, with earlier FE modelling demonstrating an increase in LTE_δ for decreased subgrade strength (Brill and Guo 2000), and recent modelling demonstrating an increase in LT for decreased subgrade strength (Jamieson and White 2024b), with an approximate 1% increase of LT, for a 1% reduction in subgrade CBR value. However, the later modelling also demonstrated that the effect of sub-base type was insignificant for both LTE_δ and LT in dowelled construction joints, with wheel configuration, subgrade strength, dowel spacing and dowel looseness the only factors significantly effecting load transfer (Jamieson and White 2024b).

Because of the contradiction in earlier results of sub-base type on load transfer, further investigation into the effect of sub-base type on load transfer ability is required.

Furthermore, slabs resting on sub-bases will experience friction at the slab to sub-base interface, with aircraft pavements generally including a de-bonding layer to reduce friction, and therefore the risk of uncontrolled cracking during curing (AAA 2017). Past researchers have used Coulomb friction coefficients between 0.03 and 1.4 to represent the effect of debonding layers on the slab to sub-base interface (Holschemacher and Lober 2019), with the change in friction coefficient effecting the stress induced in the concrete during slab movement (Jeong et al. 2014). However, research by Hammons (1998) showed that friction coefficient had a less than 1% effect on the LTE_δ of a joint, from friction coefficients of 0.1 to 10. Because that research did not include the effect on LT, further research is required to determine if the effect is consistent for both LTE_δ and LT.

3 METHODS

The primary objective of this study was to determine and quantify the effect of sub-base type and slab to sub-base friction coefficient on load transfer values. This was achieved using an FE model developed by Jamieson and White (2024a), and validated against full scale physical testing (Jamieson and White 2024c). The model was built in the general-purpose FE program Abaqus 2023 (Dassault Systemes 2023), and assessed loading in two conditions, one with the slabs connected, and one in the free-edge condition as shown in Figure 1. This enabled accurate calculation of LTE_δ, and LT.

(a) (b)

Figure 1. FE model with (a) two slabs connected, and (b) free edge condition.

Four different construction joint types were investigated: round dowelled, diamond plate dowelled, butt and sinusoidal, as shown in Figure 2.

(a) (b) (c)
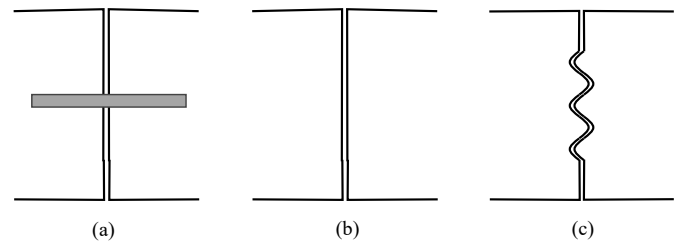
Figure 2. Side view of construction joints analysed, (a) round and diamond dowels, (b) butt, and (c) sinusoidal.

The joints were subject to 24.9 T wheel loads in either dual or tridem gear arrangement, in either

longitudinal or transverse alignment across the edge of joint. For each joint type, five different joint arrangements were modelled, with different loading regimes, gap widths, subgrade strengths, and where applicable, dowel details. For all FE model runs, the rigid pavement consisted of 350 mm thick concrete slabs, over a 152 mm thick sub-base, over the subgrade. For each load and joint configuration, the model was run using a bound sub-base, and then again using an unbound sub-base, to isolate the relative effect of sub-base type on load transfer values. Consequently, a total of 20 FE model runs with bound sub-bases and 20 model runs with unbound sub-bases. The bound sub-base was represented by a lean mix concrete with elastic modulus (E) = 5,000 MPa, and Poisson's ratio (μ) = 0.2. The unbound sub-base was represented by a fine crushed rock with an E = 517 MPa, and μ = 0.35. These mechanical properties were selected as they are used in the common aircraft pavement design program FAARFIELD (FAA 2021).

To determine the effect of slab to sub-base friction coefficient, a standard sinusoidal construction joint was analysed, with all parameters kept constant, except for slab to sub-base friction coefficient, which was adjusted for a Coulomb friction coefficient of 0.05, 0.7, 1 and 1.4, to represent typical values used for debonding layers in rigid pavement FE models.

4 RESULTS

4.1 *Change in sub-base type*

Figure 3 and Figure 4 show the change in LTE_δ and LT, respectively, when modifying the sub-base type from an unbound to a bound sub-base for the 20 construction joints investigated.
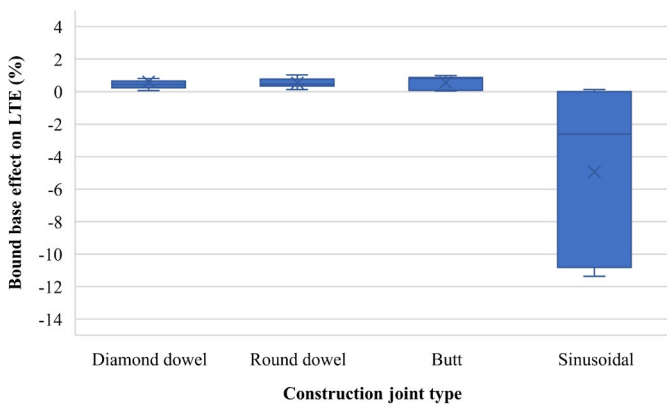
Figure 3. Change in LTE_δ from an unbound base to a bound base.

4.2 *Change in slab to sub-base friction coefficient*

Figure 5 demonstrates the change in maximum bending stress and deflection for a range of friction coefficients for a single sinusoidal joint. Figure 6 shows the effect of slab to sub-base friction coefficient on LTE_δ and LT for the same joint.
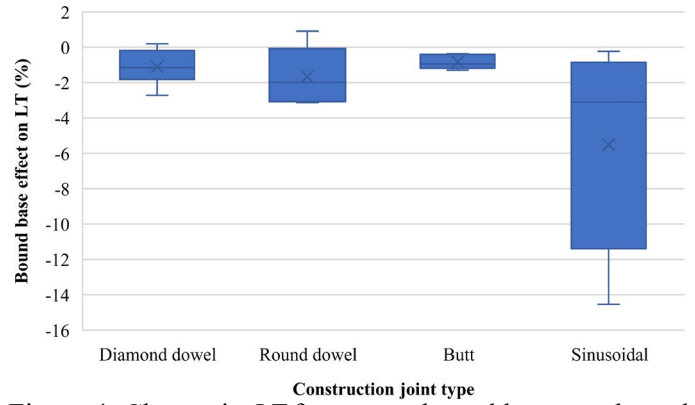
Figure 4. Change in LT from an unbound base to a bound base
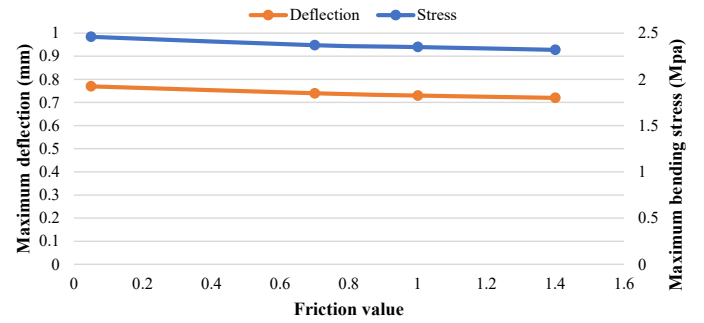
Figure 5. Sub-base to slab friction coefficient effect on maximum deflection and bending stress.
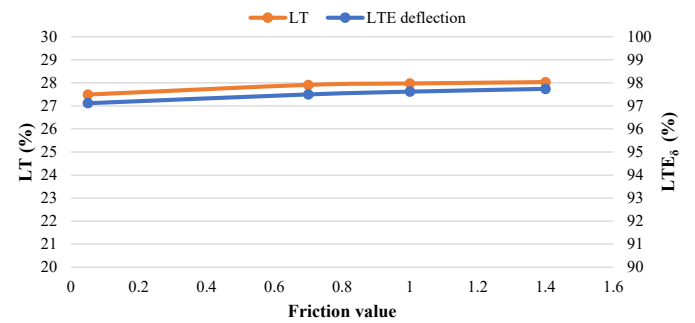
Figure 6. Sub-base to slab friction coefficient effect on LT and LTE_δ.

5 DISCUSSION

As shown in Figure 3, the change from an unbound to bound sub-base generally increased the LTE_δ of dowelled and butt joints. However, the increase was small, with a mean of 0.6%. Conversely, sinusoidal joints were significantly affected by the change in sub-base type, with a decrease of LTE_δ up to 11.4% for bound bases. Similarly, the change from an unbound to bound sub-base had little effect on LT for dowelled and butt joints, with a mean decrease of 1.2%. Whereas sinusoidal joints had a mean decrease of 5.5% LT when using a bound sub-base. There were two joints that demonstrated an increase in LT by 0.2% and 0.9%, but these were outliers, and likely reflected simplifications in the FE model.

Although it seems counter-intuitive for a stiffer sub-base to reduce LT, the lower stiffness materials allow for more slab deflection, thereby increasing the stress taken up by the dowels, or the frictional interface of the concrete. This was evidenced by

dowels having a mean 13 MPa increase in stress when slabs were resting on an unbound sub-base, compared to slabs with a bound sub-base. However, considering other recent research on dowelled construction joints that determined a reduction in subgrade CBR of 1% improves LT by approximately the same degree (Jamieson and White 2024b), the effect of sub-base type on LT magnitude for dowelled construction joints is of less importance.

The largest LT change was for two sinusoidal joints that were modelled with large gaps (3 mm) between slabs. These two joints exhibited a change of 14.5% and 8.3% LT. This indicates that unbound sub-bases provide significantly better load transfer for sinusoidal joints, especially during slab contraction periods when joint gap widths are increased. That is, the unbound sub-base increases the deflection across the gap width, enabling the loaded slab to better engage with the unloaded slab. However, further research is recommended to quantify the significance of sub-base type across multiple sinusoidal joint conditions, and how it compares with other joint factors, such as subgrade.

Regarding friction coefficient, Figure 6 shows that for an increase of slab to sub-base friction coefficient from 0.03 to 1.4, the maximum deflection and bending stress are decreased by 6.5% and 5.7%, respectively. However, because the effects of friction coefficient are equally applied to the unloaded slab, loaded slab, and free-edge condition slab, the effect on LTE_δ and LT are minor, with an increase of 0.6% and 0.5%, respectively. Consequently, the assignment of slab to sub-base friction coefficient has negligible impact on the load transfer values.

6 CONCLUSION

Based on 40 model runs of 20 different construction joints, it was concluded that sub-base type has minor impact on load transfer values for butt and doweled construction joints. Consequently, for these joint types, the selection of sub-base type is not critical to achieve effective load transfer. In contrast, the effect of sub-base type on sinusoidal joints was significant, with unbound sub-bases providing higher LTE_δ and LT. Further research is recommended to quantify the significance across a range of sinusoidal joints and loading conditions. It was also concluded that the magnitude of the slab to sub-base friction coefficient had negligible impact on load transfer values. Consequently, when modelling load transfer, other factors are of higher importance.

7 REFERENCES

AAA, 2017. *Airport Practice Note 12 - Airfield Pavement Essentials.* Australia: Australian Airports Association.

Brill, D. R. and Guo, E. H., 2000. Load Transfer in Rigid Airport Pavement Joints. *26th International Air Transportation Conference.* San Francisco, United States.

Byrum, C. R., 2011a. *Report IPRF-01-G-002-05-2 Joint Load Transfer in Concrete Airfield Pavements: Appendix B: Literature Review Summary.* Rosemont, United States: Innovative Pavement Research Foundation.

Byrum, C. R., 2011b. *Report IPRF-01-G-002-05-2 Joint Load Transfer in Concrete Airfield Pavements: Final Report.* Rosemont, United States: Innovative Pavement Research Foundation.

Colley, B. E. and Humphrey, H. A. 1967. Aggregate Interlock at Joints in Concrete Pavements. *Highway Research Record,* 189, 1-18.

Dassault Systemes, 2023. Abaqus CAE 2023.

FAA, 2021. AC 150/5320-6G - Airport Pavement Design and Evaluation. Washington D.C., United States: Federal Aviation Administration.

Gkyrtis, K*., et al.* 2021. Structural Performance Assessment of Airfield Concrete Pavements Based on Field and Laboratory Data. *Infrastructures,* 6.

Hammons, M. I., 1998. *Advanced Pavement Design: Finite Element Modeling for Rigid Pavement Joints. Report 2: Model Development.* Washington D.C., United States: U.S. Department of Transportation Federal Aviation Administration.

Hammons, M. I., Pittman, D. W. and Mathews, D. D., 1995. *DOT/FAA/AR-95-80 - Effectiveness of Load Transfer Devices.* Washington, D.C.: Federal Aviation Administration.

Holschemacher, K. and Lober, P., 2019. Experimental investigation on friction between foundation slabs and substructure. *13th International Conference Modern Building Materials, Structures and Techniques.* Vilnius, Lithuania.

Jamieson, S. and White, G., 2023. Review of Rigid Aircraft Pavement Joint Types, Effectiveness, Distress, Maintenance and Analysis. *International Airfield & Highway Pavment Conference.* Austin, Texas, USA.

Jamieson, S. and White, G., 2024a. Developing a thoeritical Model for Load Transfer of Common Joints in Rigid Airport Pavements. *13th International Conference on Concrete Pavements.* Minneapolis, USA.

Jamieson, S. and White, G. 2024b. Parametric analysis of a dowelled construction joint for rigid aircraft pavement load transfer using finite element methods. *International Journal of Pavement Engineering.* Article-in-review.

Jamieson, S. and White, G. 2024c. Validating a Finite Element Model for Rigid Aircraft Pavement Load Transfer against Full Scale Testing. *International Journal of Pavement Engineering.*

Jeong, J.-H*., et al.* 2014. Testing and modelling of friction characteristics between concrete slab and subbase layers. *Road Materials and Pavement Design,* 15(1), 114-130.

UK MOD, 2011. Design & Maintenanc Guide 27 - A Guide to Airfield Pavement Design and Evaluation. United Kingdom: Construction Support Team, Defence Estates, Ministry of Defence.

White, G., 2018. Use of Falling Weight Deflectometer for Airport Pavements. *5th GeoChina International Conference.* HangZhou, China.

Re-evaluating the relationship between load transfer characterisation values for rigid aircraft pavement construction joints

S. Jamieson
University of the Sunshine Coast, Sippy Downs, Queensland, Australia

G. White
University of the Sunshine Coast, Sippy Downs, Queensland, Australia

ABSTRACT:
Rigid aircraft pavement load transfer is typically characterised by load transfer efficiency via deflection (LTE_δ), or free-edge stress transferred (LT). LTE_δ is relatively easily calculated from falling weight deflectometer field measurements and is routinely assessed for existing slabs. In contrast, LT is commonly used as an input for thickness design. However, LT is difficult to measure in the field. Consequently, understanding the relationship between LTE_δ and LT can improve rigid aircraft pavement design and evaluation strategies. Although relationships exist for load transfer characterisation values, they are built on generalised assumptions for free-edge deflection and stress. This study re-evaluated the relationships between typical load transfer values for three different construction joint types using finite element methods. It was determined that the relationship between LT and LTE_δ is largely dependent on construction joint type. Furthermore, predictive models for different construction joints were developed to relate LTE_δ to LT. The findings from this research can be used to better relate load transfer field measurements, to thickness design assumptions, for rigid aircraft pavements.

1 INTRODUCTION

Rigid aircraft pavements are typically comprised of unreinforced Portland cement concrete base slabs over an unbound or bound sub-base layer, constructed on the subgrade (AAA 2017). The concrete slabs are square or almost-square, typically ranging from 4 m to 8 m in length, (Jamieson and White 2023, FAA 2021). The slabs are separated by joints, which also provide load transfer to the adjacent slabs, resulting in reduced slab-edge stresses. Because the edge stress is usually the critical stress for pavement thickness determination (FAA 2021), effective load transfer reduces the required slab thickness.

It is generally assumed in airport pavement thickness design programs that joints provide 25% load transfer to adjacent slabs (FAA 2021). However, load transfer is variable, and is affected by many factors, including loading regime, sub-layer support, joint gap width and joint details (Byrum 2011b). To predict load transfer, multiple relationships have been developed for typical load transfer values that can be measured through instrumented slabs or a falling weight deflectometer (FWD). However, these relationships require assumptions for loading condition (Guo 2003), and generally characterise load transfer through a stiffness value to simplify the complex interaction between dowels, aggregate interlock, and formed concrete faces (Byrum 2011b).

Recent research has challenged the assumptions for load transfer loading condition (Jamieson and White 2024b), and due to the advances in finite element (FE) models for load transfer analysis, the interaction between dowels and formed concrete faces can now be more accurately modelled, enabling the assessment of different types of commonly used joints.

The aim of this research was to re-evaluate the relationships between typical load transfer characterisation, and to determine if load transfer is consistent for a range of loading conditions and construction joint types. This was achieved through FE methods, using a previously validated load transfer model.

2 BACKGROUND

2.1 *Load transfer characterisation*

Load transfer is possible due to joint stiffness, which is provided by dowels, aggregate interlock and elastic solid base effects (Byrum 2011b). Load transfer is generally characterised by load transfer efficiency, via deflection (LTE_δ) (Equation 1) or stress (LTE_σ) (Equation 2), or free-edge stress transferred (LT) (Equation 2). LTE_δ can be relatively easily calculated from deflections measured in the field using a FWD (White 2018, Gkyrtis et al. 2021).

In contrast, LT is the portion of stress that is transferred to an unloaded slab, relative to the loaded slab, when under a free-edge loading condition. That is the condition when no adjacent slab is connected. Although LTE_δ is routinely measured for existing pavements, LT is commonly used for thickness design, is a fundamental first principle of aircraft pavement load transfer, has a range of 0% to 50%, and as discussed earlier, is assumed to be 25% in contemporary thickness design methods (Byrum 2011a, FAA 2021).

$$LTE_\delta = \frac{\delta_U}{\delta_L} \times 100 \quad (1)$$

$$LTE_\sigma = \frac{\sigma_U}{\sigma_L} \times 100 \quad (2)$$

$$LT = 100 \times \frac{(\varepsilon_F - \varepsilon_L)}{\varepsilon_F} \quad (3)$$

Where, LTE_δ = Load transfer efficiency by deflection (%); LTE_σ = Load transfer efficiency by stress (%); LT = Percent of free-edge stress transferred (%); δ_L = Deflection of loaded side of the joint (mm); δ_U = Deflection of unloaded side of the joint (mm); σ_L = Stress of loaded side of the joint (MPa); σ_U = Stress of unloaded side of the joint (MPa); ε_L = Bending strain in the loaded slab edge at the joint; and ε_F = Bending strain in the free-edge loading condition for the loaded slab edge.

Because LT is difficult to measure, due to requiring a loaded strain from a slab in the free-edge condition, past researchers have used the stress based LT_σ as an approximation (Ahmed et al. 2021, Guo 2003). LT_σ can be calculated without a free-edge slab by determining LTE_σ from strain gauges embedded in unloaded and loaded slabs, using Equation 4. This assumption holds true if approximations for free-edge deflection and free-edge stress are satisfied, as described in Equation 5 and Equation 6, respectively. However, these approximations also require a Winkler foundation, small aircraft loads, full contact between the slab and sub-base, and flat slabs (Byrum 2011b, Guo 2003). These conditions are not always met for aircraft pavements, requiring re-consideration of the relationship between LT_σ and LT.

$$LT_\sigma = 100 \times \frac{LTE_\sigma}{(1 + LTE_\sigma)} = 100 \times \frac{\sigma_U}{(\sigma_L + \sigma_U)} \quad (4)$$

$$\delta_L + \delta_U = \delta_F \quad (5)$$

$$\sigma_L + \sigma_U = \sigma_F \quad (6)$$

Where, LT_σ = LT stress-based approximation (%); δ_F = Deflection of loaded slab in free-edge condition (mm); σ_F = Stress of loaded slab in free-edge condition (MPa).

2.2 *Load transfer relationships*

Early work to determine relationships between load transfer values was performed by Mikhail S. Skarlatos in 1949, and revisited in the 1990s by Ioannides and Hammons (1996). Their work produced a general solution for edge load transfer, whereby maximum deflection and bending stress of an unloaded slab could be calculated. Also developed was a relationship between LTE_σ and LTE_δ. Recently, the relationship between LTE_δ and LT has become of high importance, because FWDs can easily measure LTE_δ, which can in turn be used to determine if a joint has failed (Gkyrtis et al. 2021), or is achieving the load transfer design assumption (LT). For example, the US Department of Defense pavement design program PCASE has an in-built relationship between LTE_δ and LT, that can be used to assess the structural capacity of an existing rigid aircraft pavement (Tingle 2023). Ensuring the relationship between LTE_δ and LT is accurate will significantly enhance rigid pavement design and evaluation strategies.

3 METHODS

The primary objective of this study was to determine the relationships between load transfer values for a range of loading conditions and construction joints. This was achieved using an FE model developed by Jamieson and White (2024a), and validated against full scale physical testing (Jamieson and White 2024c). The model was built in the general-purpose FE program Abaqus 2023 (Dassault Systemes 2023), and assessed loading in two conditions, one with the slabs connected, and one in the free-edge condition, as shown in Figure 1.
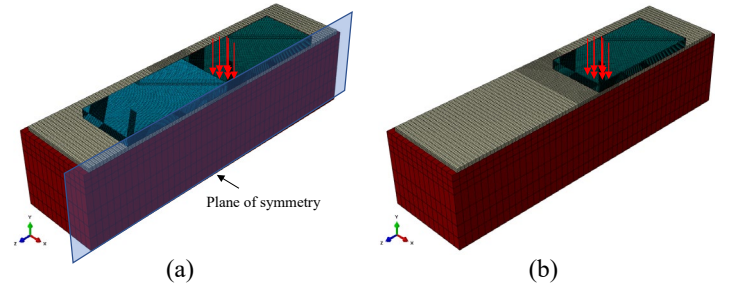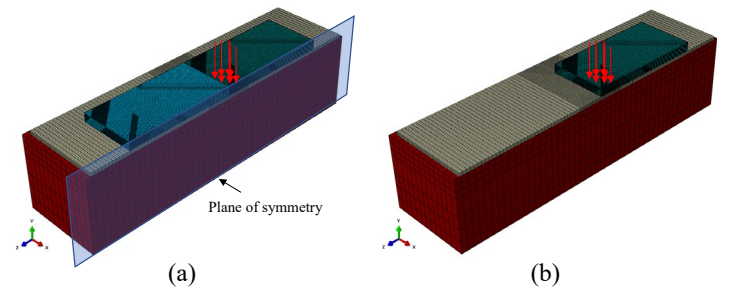

Figure 1. FE model with (a) two slabs connected, and (b) free edge condition.

Three different construction joint types were investigated: round dowelled, diamond-shaped plate (DSP) dowel, and sinusoidal, as shown in Figure 2. The joints were subject to 24.9 T wheel loads in either dual or tridem gear arrangement, in either longitudinal or transverse alignment across the edge of joint. Multiple joint arrangements were modelled, with different joint gap widths, subgrade strengths, sub-base types, dowel details, dowel looseness, and where applicable, sinusoidal shape. In total, 43 round dowelled joints, 24 DSP dowelled joints, and 32 sinusoidal joints were assessed. For all FE model

runs, the rigid pavement consisted of 350 mm thick concrete slabs, over a 152 mm thick sub-base, over the subgrade.
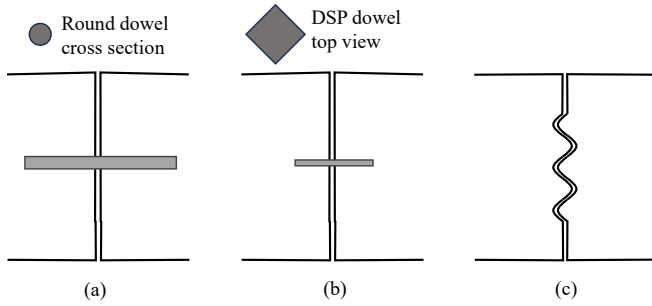
Figure 2. Side view of construction joints analysed, (a) round (b) DSP dowels, and (c) sinusoidal.

4 RESULTS

Figure 3 shows the relationship between LTE_δ and LT_σ for round dowelled and DSP dowelled construction joints. Figure 4 shows the relationship between LTE_δ and LT_σ for sinusoidal construction joints. For this graph, any zero LTE_δ results were omitted to avoid skewing the trendline. Also included in both figures is the relationship between LTE_δ and LT_σ used in the PCASE program.
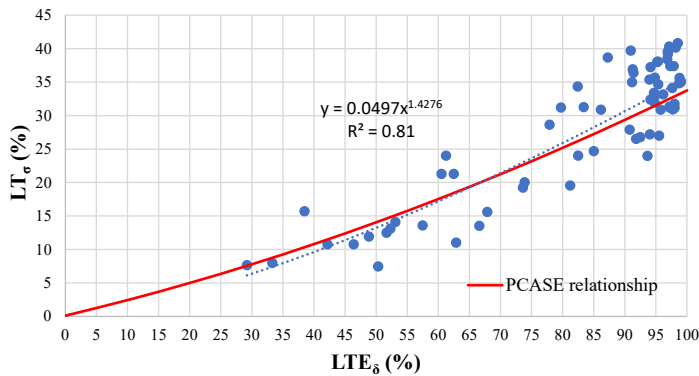
Figure 3. LTE_δ versus LT_σ for dowelled construction joints.
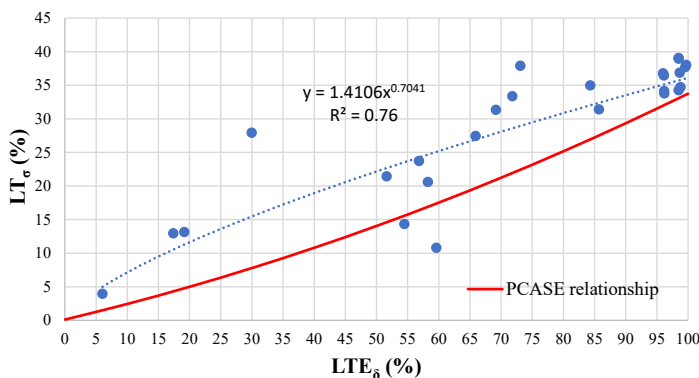
Figure 4. LTE_δ versus LT_σ for sinusoidal joints.

Figure 5 shows the relationship between LT_σ and LT for round dowelled and DSP dowelled construction joints. Figure 6 shows the relationship between LT_σ and LT for sinusoidal construction joints. Included in both figures is the line of equality for the condition that LT_σ equals LT.
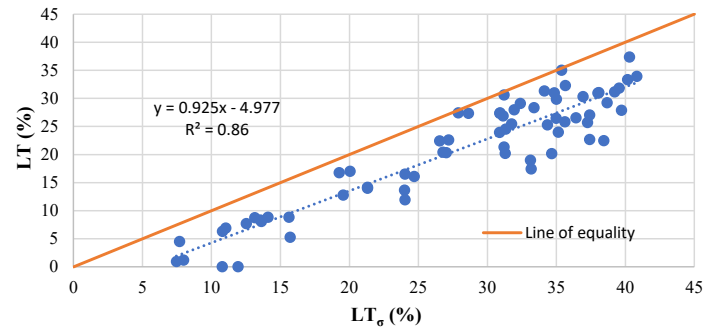
Figure 5. LT_σ vs LT for dowelled construction joints.
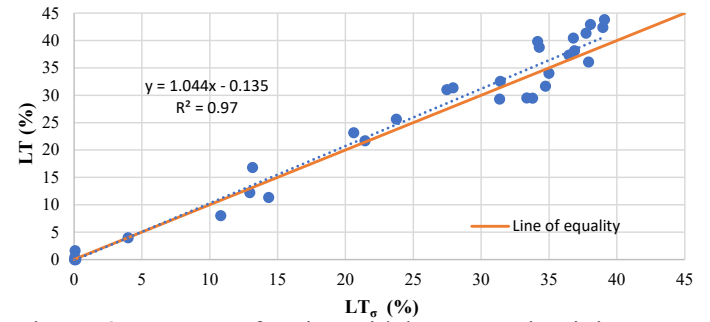
Figure 6. LT_σ vs LT for sinusoidal construction joints.

5 DISCUSSION

As demonstrated in Figure 3 and Figure 4, the relationship between LTE_δ and LT_σ is not consistent for all construction joints. Rather, joints with dowels have a strongly correlated relationship to existing literature, as evidenced by the closeness to the PCASE relationship. Sinusoidal joints, in contrast, respond differently to dowelled joints, when subject to aircraft loads. Evidenced by a lower R^2 value, LT_σ does not predict LTE_δ as well as it does for dowelled joints. That is because sinusoidal joint load transfer is affected by joint openings. When an opening is present, the loaded slab and unloaded slab act as two separate elements. This contrasts with dowelled joints that are always connected by the dowels, meaning that there is always some interaction between the loaded and unloaded slabs. When a sinusoidal joint with a joint opening is loaded, there will be a certain distance where the loaded slab deflects but does not engage with the unloaded slab. Because this un-engaged distance is related to load type, subgrade strength and sinusoidal shape, there will be a large range of LT_σ for a specific LTE_δ.

Similarly for LT_σ and LT is that the construction joint type affects the relationship between the two values. As demonstrated in Figure 5, there is a strong linear relationship between LT_σ and LT for dowelled construction joints. However, LT_σ is not equivalent to LT, rather, LT_σ over-predicts LT. For the dowelled construction joint model runs, the free-edge deflection and stress equations (Equation 5 and Equation 6) had an absolute mean error of 37.0% and 8.8%, respectively, indicating that the free-edge assumptions were not met. Consequently, LT_σ is not

a good predictor of first-principles LT for dowelled construction joints, without a transform equation. For sinusoidal construction joints, the LT_σ and LT were determined to be equivalent. This was due to the simpler interaction between the two slab elements when compared to the more complex interaction around dowels. Interestingly, the free-edge stress absolute mean error was 3.3%, whereas the deflection error was 18.6%. This demonstrates that free-edge stress is a better indicator of equivalence of LT_σ and LT than free-edge deflection.

Because the relationship between load transfer values were found to be dependent on the joint type, two predictive relationships between LTE_δ and LT were developed. These equations are based on data provided in Figure 3 to Figure 6, and should aid practitioners in converting serviceability checks of LTE_δ when using an FWD to the first-principles LT used in airport pavement thickness determination. Equation 7 provides the relationship between LT and LTE_δ for a dowelled construction joint. Equation 8 provides the relationship between LT and LTE_δ for a sinusoidal construction joint.

$$LT_{DCJ} = 0.046 \times LTE_\delta^{1.427} - 4.98 \quad (7)$$

$$LT_{SCJ} = 1.411 \times LTE_\delta^{0.704} \quad (8)$$

Where, LT_{DCJ} = LT of a dowelled construction joint (%); LT_{SCJ} = LT of a sinusoidal construction joint (%).

6 CONCLUSION

The relationship between LT and LTE_δ is important to develop rigid pavement design and evaluation strategies that are accurate, and well-defined. This study investigated the relationships between typical load transfer values using FE methods for three different construction joint types. Based on the analysis of the results from 99 model runs, it was concluded that the relationship between LT_σ, LT and LTE_δ is largely dependant on the construction joint type. Furthermore, predictive models for dowelled construction joints and sinusoidal construction joints were developed to relate LTE_δ to LT. Consequently, the findings from this research can be used to better relate FWD results to design assumptions used in aircraft pavement thickness determination.

7 REFERENCES

AAA, 2017. *Airport Practice Note 12 - Airfield Pavement Essentials.* Australia: Australian Airports Association.

Ahmed, M., *et al.*, 2021. Evaluation of Concrete Pavement Joint Performance at the FAA National Airport Pavement Test Facility. *12th International Conference on Concrete Pavements.* Virtual Conference.

Byrum, C. R., 2011a. *Report IPRF-01-G-002-05-2 Joint Load Transfer in Concrete Airfield Pavements: Appendix B: Literature Review Summary.* Rosemont, United States: Innovative Pavement Research Foundation.

Byrum, C. R., 2011b. *Report IPRF-01-G-002-05-2 Joint Load Transfer in Concrete Airfield Pavements: Final Report.* Rosemont, United States: Innovative Pavement Research Foundation.

Dassault Systemes, 2023. Abaqus CAE 2023.

FAA, 2021. AC 150/5320-6G - Airport Pavement Design and Evaluation. Washington D.C., United States: Federal Aviation Administration.

Gkyrtis, K., *et al.* 2021. Structural Performance Assessment of Airfield Concrete Pavements Based on Field and Laboratory Data. *Infrastructures,* 6.

Guo, E. H. 2003. Proof and Comments on Extensively Used Assumption in PCC Pavement Analysis and Evaluation. *Journal of Transportation Engineering,* 129(2), 219-220.

Ioannides, A. M. and Hammons, M. I. 1996. Westergaard-Type Solution fo Edge Load Transfer Problem. *Transportation Research Record,* 1525(1), 28-34.

Jamieson, S. and White, G., 2023. Review of Rigid Aircraft Pavement Joint Types, Effectiveness, Distress, Maintenance and Analysis. *International Airfield & Highway Pavment Conference.* Austin, Texas, USA.

Jamieson, S. and White, G., 2024a. Developing a thoeritical Model for Load Transfer of Common Joints in Rigid Airport Pavements. *13th International Conference on Concrete Pavements.* Minneapolis, USA.

Jamieson, S. and White, G. 2024b. Parametric analysis of a dowelled construction joint for rigid aircraft pavement load transfer using finite element methods. *International Journal of Pavement Engineering.* Article-in-review.

Jamieson, S. and White, G. 2024c. Validating a Finite Element Model for Rigid Aircraft Pavement Load Transfer against Full Scale Testing. *International Journal of Pavement Engineering.*

Tingle, J., 2023. Unpublished presentation - Performance of dowelled versus undowelled joints for relatively thin airfield pavements. Woolongong, Australia: Australian Society for Concrete Pavements (ASCP).

White, G., 2018. Use of Falling Weight Deflectometer for Airport Pavements. *5th GeoChina International Conference.* HangZhou, China.

The microlayer model: using numerical analyses to uncover the potential of a continuously carbon-reinforced concrete pavement

M. May, J. Platen, I. Wollny, M. Kaliske
Institute for Structural Analysis, TU Dresden

J. Zhao, M. Liebscher, V. Mechtcherine
Institute of Construction Materials, TU Dresden

V. Yordanov, L. Eckstein
Institute for Automotive Engineering, RWTH Aachen

B. Kupfernagel
Johne & Groß GmbH, 01936 Schwepnitz, Germany

ABSTRACT: Continuously reinforced concrete pavements (CRCPs) are non-standard in road construction but reduce maintenance needs by eliminating joints and controlling cracking through continuous longitudinal reinforcement. However, conventional steel reinforcements are prone to stress corrosion cracking in chloride-rich environments. This study explores the mechanical feasibility of replacing steel by mineral-impregnated carbon fiber reinforcement (MCF). Due to limited large-scale experimental data, Finite Element Method (FEM) simulations are utilized, employing the microlayer framework for efficient MCF modeling. Numerical comparisons are carried out between MCF-reinforced pavement and a standard German road design. The parameters of the material model are determined through four-point bending tests conducted on laboratory specimens. A tire stiffness test rig is used to simulate a more realistic tire-road interaction through accurate tire contact patch determination.

1 INTRODUCTION

There is a growing need for durable, low-maintenance pavement structures as the current traffic network is at its capacity limit. A promising concept to address these challenges is to build continuously reinforced concrete pavements (CRCP), which offer high resistance to dynamic loads, as the size and spacing of unavoidable cracks are controlled by continuous longitudinal reinforcement. The durability of CRCP is impressive, lasting between 30 and 60 years without major repairs (Schmidt et al. 2021). However, in Germany, almost all federal highways are built without reinforcement. As a result, longitudinal joints, which are maintenance-intensive, need to be added to the concrete surface after construction. Compared to traditional construction methods without reinforcement, the spacing of cracks in CRCP is smaller. This results in shorter slab lengths and reduced internal stresses, which in turn allow for a reduction in pavement thickness by 10 to 20% (Schmidt et al. 2021). However, further height reduction is limited due to the need of a protection of the classical steel reinforcement from corrosion.

To overcome the latter drawbacks, this study investigates the use of mineral-impregnated carbon fibers (MCF) in CRCP. MCF reinforcements represent an innovative alternative to steel and fiber-reinforced polymer reinforcements in construction by combining high-performance fibers with durable inorganic matrix materials. This approach provides a number of advantages, including significantly enhanced temperature resistance, cost-effectiveness, physical and chemical compatibility with cementitious substrates, multifunctionality and technological flexibility in production and application (Mechtcherine et al. 2020). Due to the increased tensile strength by a factor of 10, the required minimum cross-section of the reinforcement is reduced (Zhao et al. 2024a). In combination with small selectable concrete cover dimensions, this results in completely new structural reinforcement arrangements.

Until now, the reinforcement has been arranged in the centre or in the upper third of the pavement (Schmidt et al. 2021) in order to keep the crack width and spacing small. The reinforcement can, then, not become statically effective in the tensile stress areas of the bending load caused by tires. The aim of this work is to utilize multiple reinforcement levels to enable control of crack formation while also involving the reinforcement in load transfer, thereby allowing for a reduction in slab thickness.

The paper proposes utilizing numerical simulations to investigate the potential of carbon fiber-reinforced concrete pavements. While laboratory experiments are typically limited to small-scale specimens, large-scale tests are complex and costly. Thus, initial investigations will focus on numerical approaches. For realistic numerical simulations, it is necessary to account for the reinforcement-induced anisotropy and damage mechanisms such as crack formation. To determine the parameters of the material model for the MCF reinforced concrete, bending tests are carried

out on small-scale specimens. Due to the expected multi-axial three-dimensional stress states, a direction-dependent damage of the concrete is to be expected. Since the volume of the reinforcement is small compared to the component geometry, discrete modeling should be avoided. A material model that meets these requirements is the microlayer model (ML), which is introduced in the following section. The work concludes with a comparison of numerical simulations of conventional pavement designs and the innovative approach.

2 MATERIAL MODEL

2.1 Selection criteria and theory

The pavement structure loaded by a tire can be regarded as a bending situation. While the areas below the tire are under compressive stresses, tensile stresses occur at the transition to the weaker base course in the horizontal directions (Wollny et al. 2019). The initially isotropic stiffness characteristics of the concrete material become strongly anisotropic under the effect of plasticity, softening and damage depending on these direction-dependent stress states. To model these phenomena (inspired by the fact that the real mechanical behavior of concrete is determined by its microstructure), a representative volume element (RVE) is introduced in the numerical formulation (Platen et al. 2024). For a time-efficient simulation, the RVE is described using simplified geometric shapes (Storm & Kaliske 2018). The ML for concrete consists of an infinitely stiff, chamfered dodecahedron-shaped aggregate Ω^K on which 42 surface layers Ω^i are imprinted (Fig. 1).
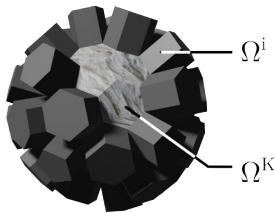
Figure 1. Geometry of the microstructure for the concrete matrix.

These layers contain the actual material definition. Thus, the temporal evolution of plasticity is different for each layer, which leads macroscopically to the desired anisotropic properties. A Neo-Hooke model combined with classical von Mises plasticity

$$\psi_{e,p}^i = \frac{\varkappa}{2}(\det[\boldsymbol{F}_e^i])^2 + \frac{\mu}{2}(\operatorname{tr}([\bar{\boldsymbol{F}}_e^i]^T \cdot \bar{\boldsymbol{F}}_e^i) - 3) + \frac{1}{2}H^\alpha \alpha^2 \quad (1)$$

is chosen in this work, of which few parameters can already be measured in the experiment or quickly determined by optimization. Equation 1 shows the underlying free Helmholtz energy for the material of a layer i and contains the elastic parameters for the shear modulus μ, bulk modulus κ and the plastic parameters H^α and α. The relationship between the strain measure $\boldsymbol{F}^i$ and the stress measure $\boldsymbol{P}^i$ on each layer according to

$$\boldsymbol{P}^i = \frac{\partial \psi^i}{\partial \boldsymbol{F}^i} \quad (2)$$

is obtained by differentiation. The scale transition from the micro to the macro level takes place by means of a thermodynamically consistent homogenization process (Storm & Kaliske 2019). Equation 3 shows the scale transition to the macro level M

$$\boldsymbol{P}^{\mathcal{M}} = \frac{1}{V}\left[\sum_{i=1}^{n} \int_{\Omega^i} \boldsymbol{P}^i \mathrm{d}V + \int_{\Omega^K} \boldsymbol{P}^K \mathrm{d}V\right] \quad (3)$$

for the stresses exemplarily. The damage and softening behavior are taken into account via an additional, non-local field η as the maximum of all layers η^i in the FEM, to avoid localization effects with numerical instabilities (Dimitrijevic et al. 2008). It is considered that tensile stresses are more damaging than compressive stresses. At each layer, the damage variable d^i is determined by the time evolution of η^i

$$d^i = 1 - \frac{\gamma_0}{\eta^i}\left[1 - \alpha + \alpha \exp[\beta(\gamma_0 - \eta^i)]\right] \quad (4)$$

and takes degradation and softening into account via the parameters α and β. As soon as the damage threshold γ_0 is exceeded, irreversible damage occurs.

The MCF reinforcement is taken into consideration by extending the Neo-Hooke material model

$$\psi_f = a(\bar{I}_4 - 1)^2 + b(\bar{I}_5 - 1)^2 \quad (5)$$

with an additional summand ψ_f. The stiffness of the reinforcement is given via the parameters a and b and the invariants I_4 and I_5 are functions of fiber direction vectors (Platen et al. 2024). This non-discrete embedding of the reinforcement into the structure avoids computationally intensive, fine-meshed discretization and a mesh dependency of the solution.

2.2 Production of reinforced bending specimens

Four-point bending tests have been performed on the specimens with a universal Zwick Z1200Y testing machine. The displacement is controlled at a rate of 1 mm/min at a testing span of 1200 mm until the fiber breakage (Fig. 2). The specimen geometry of 1420 × 120 × 40 mm³ is designed to embed five longitudinal yarns perpendicular to the loading direction. Details on the MCF manufacturing are available in (Zhao et al. 2024b). The MCF mesh structure is incorporated into a concrete matrix, which consists of cement, limestone, sand, fine gravels, rough gravel and fly ash, associated with a 28-day compressive strength of 50.6 MPa. The load $F_{m,z}$ is measured by the load sensor, while the mid-span deflection is measured by two linear variable differential transformers (Figs. 3b, c).
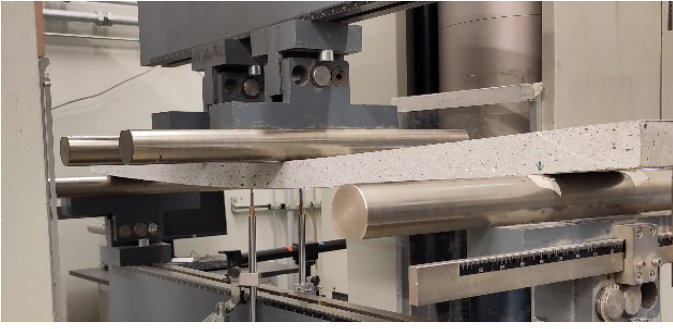
Figure 2. Four-point bending test.

Figure 3. (a) Stress distribution in the x-direction of the specimen at t = 60 s, as well as the time behavior of (b) the load stamp force and (c) mid-span deflection.

2.3 Parameter Identification

The bending test described in Section 2.2 is used to determine the parameters of the ML. The reinforcement is smeared over the entire length of the x- and y-direction. In z-direction, the smearing is only carried out over the width of the geometric diameter $d_{geo} = 3.75$ mm for a meaningful assessment of the static effect. The reduced stiffness E_{red} of a smeared surface section A is determined by the percentage of the statically MCF area $A_{eff} = 1.87$ mm² of the reinforcing bar within it. The tensile stiffness of the concrete can be neglected. The reduced stiffness in lateral direction is obtained by

$$E_{red} = \frac{A_{eff}}{A} E_{CF} = \frac{5 \text{ yarns} \cdot A_{eff}}{d_{geo} \cdot 120 \text{ mm}} E_{CF} \quad . \quad (6)$$

The elastic constants κ and μ, as well as the stiffness $E_{cf} = 225$ GPa of the carbon fibers, their position, and the degree of reinforcement, are derived from experimental data. Other parameters are optimized to minimize the error between simulation and experimental data for the mid-span deflection and the load-stamp force curves (Tab. 1, Fig. 3). As in the experiment, the simulation is carried out quasi-statically at 1 mm/min under displacement control. It can be seen that the simulated graphs are in good agreement with the experimental results. The stress distribution characteristics in longitudinal direction of the beam indicates that tensile stresses are primarily concentrated along the reinforcement fibers. The macroscopic damage evolution d at point M2 is also illustrated. Following the initially linear elastic behavior, tensile failure of the concrete occurs, causing d to increase. Once the tensile strength of the MCF is reached (d = 1), the structure fails.

Table 1. Material Parameters.

Measure	Bending Beam/ MCF Pavement	Concrete Pavement
$h_{ML,con}$	0.31 mm	1.0 mm
$r_{AGG,con}$	1.0 mm	1.0 mm
E_{con}	17000 MPa	17000 MPa
μ_{con}	0.21	0.20
k_r	10.4	10
γ_0	0.000075	0.00069
α	0.98	0.98
β	0.096	0.069
$h_{ML,CF}$	1.38 mm	1.0 mm
$r_{AGG,CF}$	1.0 mm	1.0 mm
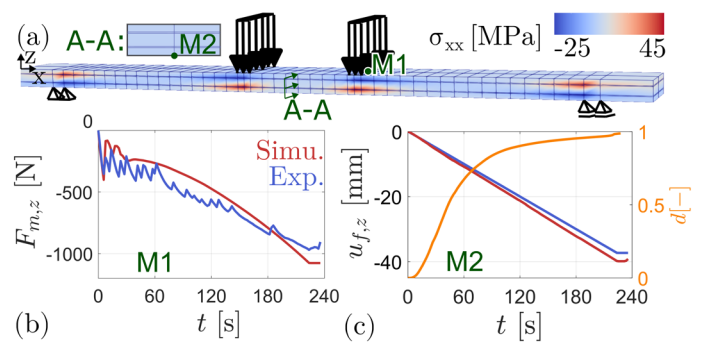
3 NUMERICAL SIMULATIONS

3.1 Tire footprints

For a more realistic representation of the pressure distribution from tire-pavement interaction, tire footprints are obtained using the tire stiffness test rig developed at the Institute for Automotive Engineering (ika), RWTH Aachen University. This rig (Fig. 4a) enables automated, precise quasi-stationary measurements of vertical, longitudinal, lateral, and torsional stiffness on non-rotating tires, adhering to VDA specifications [AK351]. It accommodates various surfaces and obstacles for stiffness evaluation. Equipped with three electric drive actuators and spindle drives, the rig ensures precise translational and rotational movements. A strain gauge-based wheel hub measures forces up to 40 kN and moments up to 5.1 kNm. In this study, tire footprints are measured using a truck tire pressure-mapping sensor (X3 IX500:256.256.16) from XSENSOR Technology Corporation, employing capacitive pressure imaging with a resolution of 1.6 mm and a pressure range of 69–2070 kPa (Fig. 4a). The sensor is placed on a flat surface mounted on the test rig's platform. The tire used (Fig. 4b), a Pirelli ST:01T (dimensions 385/55R22.5, load index 160, speed index K), is tested at 35.3 MPa under 10-bar inflation pressure. The resulting footprint is shown in Figure 4c.
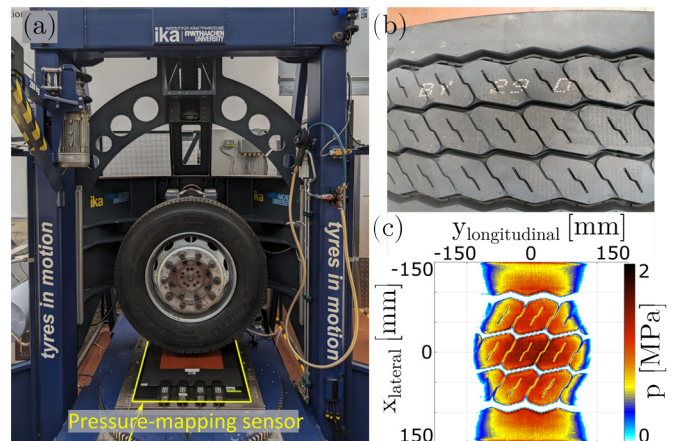
Figure 4. Measurement setup and results: (a) ika tire stiffness test rig, (b) tire specimen, (c) footprint under load of 35.3 kN.

3.2 Performance comparison with conventional concrete surface layers

To evaluate the static effectiveness of MCF reinforcement, a pavement structure with a 29 cm concrete layer, a 30 cm gravel base, and an anti-frost layer (RStO 12/24, BK 100) is numerically analysed. The model parameters are determined using uniaxial compression tests for C40/50 concrete (Tab. 1). Unbound layers are modelled as linear elastic based on the E_{v2} minimum value. The compressive stress field (Section 3.1) is distributed over a 19 x 18 nodal surface via bilinear interpolation. Figure 5 shows the road superstructure, meshing, and resulting footprint.
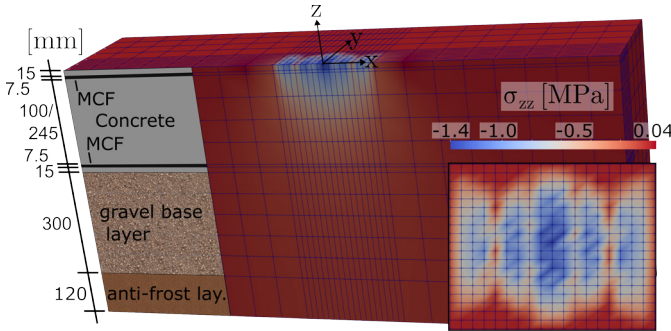
Figure 5. Pavement structure, mesh and interpolated footprint.

Following this, two mats of MCF reinforcement are placed at a distance of 15 mm from the surfaces while maintaining the superstructure geometry. The upper layer is needed for targeted crack widening control. Based on the displacements at the interface between concrete and the gravel base in Figure 6a, it is shown that the max. deflection of the reinforced road section (MCF) is approx. 50% lower with identical geometry. The stiffening effect of the reinforcement under load can therefore be confirmed. In a second step, the height of the concrete slab is reduced by 50%, while the surface spacing of the reinforcement is maintained. It can be seen that the max. vertical deflection (0.5 H) is only increased by a factor of 1.4 compared to the unreinforced variant (Con). For all the variants studied, no damage evolution is detectable (Fig. 6b).
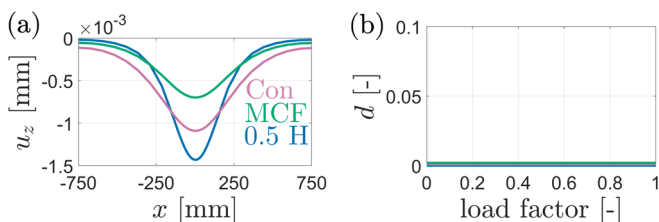
Figure 6. (a) Vertical displacement characteristics along x-direction at the concrete-gravel base interface and (b) damage evolution.

4 DISCUSSION

This work uses FEM to enable a fundamental evaluation of the contribution of carbon reinforcement to static load transfer of a concrete pavement structure. It is numerically demonstrated that halving the concrete layer thickness is feasible without damage evolution and with an acceptable mid-span deflection. It, thus, provides a basis and motivation for further numerical investigations and experiments on large-scale road structures, which in turn can be used for a more precise validation of the numerical material model. For a better assessment of the load on the road structure in the horizontal direction, dynamic effects of the rolling tire, such as acceleration and deceleration, should be included in the boundary conditions in future work.

ACKNOWLEDGEMENTS

REFERENCES

Dimitrijevic, B.J. & Hackl, K. 2008. A method for gradient enhancement of continuum damage models. *European Journal of Engineering Mechanics* 28: 43–52.

Schmidt, C., Bollin, M., Cramer, J., Chudoba, R. Freudenstein, S. Empelmann, M. & Hegger, J. 2021. Untersuchungen zur Rissbildung in durchgehend bewehrten Betonfahrbahnen. *Bauingenieur* 96: 358–375.

Platen, J., Storm, J., Bosbach, S., Claßen, M., & Kaliske, M. 2024. The microlayer model: A novel analytical homogenisation scheme for materials with rigid particles and deformable matrix - applied to simulate concrete. *Computers & Structures* 293: 107258.

Storm, J. & Kaliske, M. 2018. A consistent multi-scale derivation of a micro-plane model within the framework of RVE homogenisation. *Proceedings in Applied Mathematics and Mechanics* 18: e201800364.

Mechtcherine, V., Michel, A., Liebscher, M., Schneider, K. & Großmann, C. 2020. Mineral-impregnated carbon fiber composites as novel reinforcement for concrete construction: Material and automation perspectives. *Automation in Construction* 110: 103002.

Zhao, J., Ahmed, A.H., Liebscher, M., Karalis, G., Al Saif, R., Butler, M. & Mechtcherine, V. 2024. Temperature induced fast-setting of cement based mineral-impregnated carbon-fiber reinforcements for durable and lightweight construction with textile-reinforced concrete. *Cement and Concrete Composites* 154: 105766.

Zhao, J., Ahmed, A.H., Liebscher, M., Bartsch, A., Ivaniuk, E., Butler, M., Kohout, J., Hájková, P. & Mechtcherine, V. 2024. Thermomechanical behavior of textile-reinforced geopolymer concrete based on mineral-impregnated carbon-fibers (MCFs) composites. *Cement and Concrete Composites* 150: 105555.

Wollny, I., Hartung, F., Kaliske, M., Canon Falla, G. & Wellner, F. 2019. Numerical investigation of inelastic and temperature dependent layered asphalt pavements at loading by rolling tyres. *International Journal of Pavement Engineering* 22: 97–117.

Influence of Modelling Techniques for Undowelled Transverse Joints on the Technical Service Life of Whitetopping Overlays

M. Peyer, L. Eberhardsteiner
Institute of Transportation, TU Wien, Austria

ABSTRACT: This paper examines the impact of various interface modeling techniques for undowelled transverse joints on the technical service life of whitetopping overlays. Calibrated and validated multi-layer models of an existing whitetopping test track were modeled with four different modeling approaches, to simulate the interface behavior of the un-dowelled transverse joints. Finite-element-calculations using these multi-layer models were performed for determination of traffic load stresses which were further used as input parameters for the determination of the technical service life of the modeled whitetopping pavements. The resulting values for the technical service life were analyzed based on the influence of the different interface modeling approaches.

1 INTRODUCTION

Rehabilitating damaged hot mix asphalt (HMA) pavements by applying a new concrete overlay is a cost-effective rehabilitation strategy used in many countries. This approach, known as whitetopping, involves the installation of thin concrete slabs with closely spaced joints. The performance of whitetopping overlays depends on several different parameters, such as the residual load-bearing capacity of the existing pavement, the bonding properties in the asphalt-concrete interface or the dimensions of the whitetopping slabs (length, width, thickness). The condition of the transverse joints between adjacent concrete slabs also has an influence on the performance of whitetopping overlays. Transverse joints can be dowelled, as is usual for conventional concrete pavements or whitetopping overlays with a thickness of > 20.0 cm [1, 2]. However, in the case of thin concrete layers, which are common in low-ranking road networks, the installation of dowels is neglected due to low concrete coverage or for reasons of cost efficiency. In this case, the load transfer capacity between adjacent concrete slabs in the driving direction is way more dependent on the aggregate interlocking and friction effects in the interfaces of the transverse joints than for dowelled concrete slabs.

While the modeling of dowelled transverse joints using the finite-elements-method and their influence on stress and strain characteristics and the technical service life is well investigated [3-8], this is not sufficiently the case for thin whitetopping overlays with a layer thickness of around 10cm and undowelled transverse joints. The goal of this work is to investigate the influence of different modeling approaches for aggregate interlocking and friction within the joints, on the technical service life of undowelled thin whitetopping overlays. For this purpose, calibrated and validated 3D FE models of an existing and instrumented whitetopping test section were used to determine traffic load stresses due to axle loads for heavy-load vehicle collectives according to [9] and [10]. Combined with calculated curl stresses according to the adapted theory of Eisenmann [11, 12], the traffic load stresses were used as input parameters in a mechanistic-empirical design method for concrete pavements [10], which allowed the determination of the technical service life of whitetopping overlays under consideration of Smith's fatigue criterion.

2 WHITETOPPING TEST-SECTION

In December 2019, a test section for the whitetopping construction method was built on the L45, a low-ranked road in the federal state of Lower Austria. As part of this process, the existing hot-mix asphalt (HMA) layer was milled to a remaining thickness of 15 cm and replaced by new Portland cement concrete (PCC) slabs with a thickness of 10 cm and a length-to-width ratio of 3.0 m / 3.0 m = 1.0. Due to the low traffic volume at the existing road section and the small concrete slab dimensions of its whitetopping overlay, it was possible to realize transverse

joints without dowels. To examine the performance of undowelled transverse joints, the whitetopping overlay was instrumented with strain and temperature sensors near the transverse joints during its construction.

3 PAVEMENT MODEL

3.1 *Overall model structures and properties*

For the calculation of traffic load stresses calibrated and validated FE models of the whitetopping test, described in section 2, were used. This multi-layered pavement was modeled in the FE program Abaqus 2020 and consists of 10 cm thick concrete slabs with lengths and widths of 3.0x3.0 m on top of a 15 cm thick layer of hot mix asphalt (HMA). Below the HMA layer, there is a 50 cm thick unbound base layer and the subgrade, which was modeled with a sufficient thickness of 120 cm. To save computing time later, only half of the road cross-section was modeled using a corresponding symmetry plane and symmetry conditions (Figure 1).
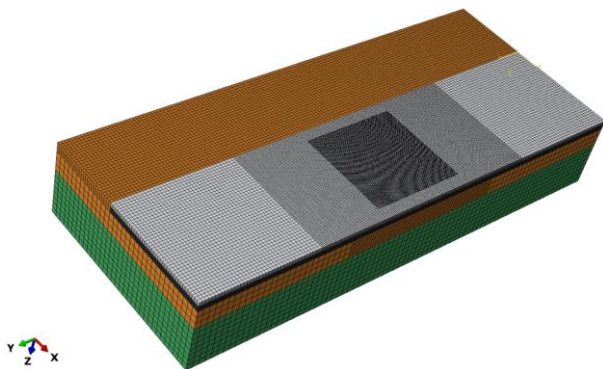
Figure 1. 3D multi-layer models used for FE-calculations (closer mesh in area of load impact)

The Young's modulus of the modeled concrete layer was assumed to be constant at 40,000 MPa, in accordance with the results of final laboratory tests during the construction of the whitetopping road section. Due to the temperature-dependent material behavior of asphalt and the seasonal varying stiffness of the unbound base layer and the subgrade, Young's moduli of these layers were also varied and assigned to four seasonal periods P1 to P4, assuming all material properties remained constant within each period. Due to this, Young's modulus for the HMA layer between a range of 5.315 MPa (pre-summer and summer) and 14.925 MPa (winter) was used for modeling. The stiffness values of the unbound base layer (1.115 to 2.045 MPa) and the subgrade (460 to 845 MPa) were also varied. All the varying values of Young's moduli were determined within model calibration and validation using field measurement data from strain and temperature sensors installed

in the existing test section as part of a previous project.

Since the existing asphalt pavement was prepared by suitable cleaning and roughening measures before the whitetopping surface layer was applied with a good bond between the existing asphalt layer and the new concrete layer, the FE models were also modeled with good bonding properties at the concrete-asphalt interface. For this purpose, the cohesive zone model approach was applied using temperature-dependent model parameters according to [13].

3.2 *Modeling of joints*

For the investigation of different modeling approaches of undowelled transverse joints on the technical service life of thin whitetopping overlays, four different approaches were modeled to describe bonding properties due to interlocking and friction within the transverse joint interface of adjacent panels, which are listed and explained below:

- Friction model with $\mu = 0.9$ and $\mu = 0.1$: The friction modeling approach models the interface using Coulomb friction, where the shear stress at the interface is limited by the normal contact pressure multiplied by the friction coefficient μ [14]. To also consider different joint conditions, FE calculations with a friction value of $\mu=0.9$ (good joint condition) and $\mu=0.1$ (bad joint condition) were done.
- Frictionless interface: In this modeling approach, no resistance to tangential motion exists, meaning the interface can slide freely without any shear stress transfer [14]. Although this approach may not be physically realistic for the characterization of transverse joints, it served as a lower-bound reference that simulates extremely bad joint conditions.
- Full bonding using rough interface modeling [14]: A rough interface assumes that no slip occurs at the contact surface (after the first contact), meaning the interface behaves as if it were fully bonded in the tangential direction. Although this approach may be more accurate for the modeling of dowelled transverse joints, it served as an upper-bound reference that simulates very good joint conditions.
- Springs elements used as node connectors: This approach models the interface as a set of spring elements that provide tangential resistance dependent on the modeled spring stiffness. Two different values for spring stiffness were used based on the lowest (for poor joint condition) and highest (for good joint condition) values according to [15].

In comparison to the transverse joints, the longitudinal joints of the whitetopping road section were sup-

ported by inserted steel tie bars (3 tie bars per slab) to prevent the concrete slabs from drifting apart in the direction of travel. In the modeling, however, none of the steel elements were simulated, but a simplified elastic foundation approach was modeled instead.

3.3 *Modeling traffic loads*

As no appropriate traffic data was available for the existing whitetopping test section, relevant traffic loads were determined by a mechanistic-empirical design method for concrete pavements [10]. This method defines eleven different heavy-goods-vehicle (HGV) categories (Figure 2), which represent the most common HGV configurations appearing on the Austrian road network. It also allows the calculation of total weight distributions for HGVs of each of these vehicle categories and their respective axle loads by using parameters from statistical analyses of traffic counting and weighing data obtained from the Austrian road network. All HGVs within the above-mentioned HGV categories can be split into two or more combinations of single-axle, double-axle, or triple-axle units. Hence, only the wheel load positions of these three unit-types were modeled in the multi-layer models.

The individual wheel loads were modeled by circular areas with a static uniform load at the central edge of the slabs using wheel load positions and the radius of the load areas according to [10].
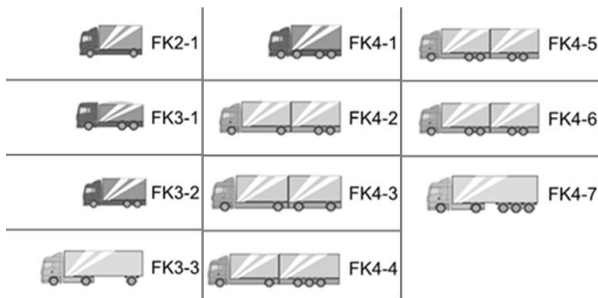
Figure 2. Overview of eleven HLV categories

4   DESIGN METHOD

For the determination of the technical service life of the modeled whitetopping pavements (N_{res}), the Austrian design guide for the mechanistic-empirical design for concrete pavements [10] was applied according to [9]. The most important input parameters for this method are the traffic load stresses the curl stresses, and the bending tensile strength of the concrete overlay.

The traffic-induced stresses were determined for the aforementioned seasonal periods P1 – P4, by finite-element calculations using the multi-layer pavement models explained in Section 2. Climatically induced stresses (curl stresses) were calculated

based on Eisenmann's theory revised by Houben [12] for six different seasonal temperature periods TP1 - TP6 according to [10] and [16]. A concrete bending tensile strength of $f_{ct} = 8.20$ MPa was used for the calculations. This value represents the results of laboratory tests with concrete samples during the construction of the whitetopping test track.

As part of this design method, the traffic load stresses for each variant of the considered axle load distributions of P1 – P4 were cumulated with the curl stresses of TP1 – TP6 according to the superposition principle (Minor's law). In the next step, Smith's fatigue criterion [11] was applied to estimate the technical service life. The resulting values of technical service life were further determined as the reciprocal values of the cumulative damages due to passages of HGVs from the different HGV categories.

5   RESULTS

The analysis of the deviations in technical service life resulting from different modeling approaches shows that the highest values (using rough modeling) are around +64.1 % higher than the lowest values (using frictionless modeling) of technical service life (Figure 3). This also shows a good correlation between the results due to the application of the frictionless modeling approach, which represents bad interlocking within the transverse joints (as a lower bound reference), and the rough full bonding approach, which represents very good joint conditions (as an upper bound reference).

In comparison to the frictionless approach for modeling poor joint conditions, the use of a friction model with a low friction coefficient of μ=0.10 results in a negligible deviation of the value of the technical service life. However, modeling good joint conditions by using a friction model approach with a high friction coefficient of μ = 0.90 results in a 35.6 % lower technical service life in comparison with the results due to a rough (full bonding) approach.

Modeling poor transverse joint conditions using springs with a low spring stiffness ($k_{s,low} = 7.2$ kN/mm) results in significantly higher values (+33.3 %) of the calculated technical service life than using a frictionless modeling approach. The use of springs with a high spring stiffness ($k_{s,high} = 3.0$ MN/mm) for modeling a good joint condition results in a 13.4 % lower value for the technical service life than using a rough approach. Comparing the results between spring modeling with low ($k_{s,low}$) and high spring stiffnesses ($k_{s,high}$) reveals only small differences in the determined values for the technical service life. The use of nearly 422 times higher spring stiffness results in a +6.5 % higher value for the technical service life.
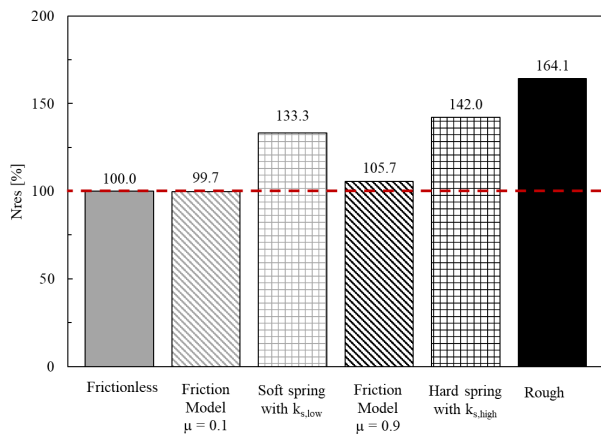
Figure 3. Calculated technical service life N_{res} of thin concrete overlays due to different modeling approaches of undowelled transverse joints.

6 CONCLUSION

For finite-element modeling of whitetopping pavements with undowelled transverse joints, these findings emphasize the need for carefully selecting joint modeling approaches to ensure realistic technical service life determinations.

Friction-based models tend to underestimate joint performance under good conditions, particularly when using high friction coefficients (e.g., $\mu = 0.90$). Therefore, relying solely on friction models for well-performing joints may lead to underestimating predictions of technical service life.

Spring-based models, on the other hand, tend to overestimate service life, especially when using low spring stiffness values. The relatively small difference in service life between low and high spring stiffness suggests that these models may not accurately capture joint behavior. To improve accuracy, spring stiffness values should be carefully calibrated against experimental or field data.

For practical applications, a combination of approaches may be necessary: friction models with calibrated μ-values for poor joint conditions and adjusted spring stiffness values for better-performing joints. By refining these parameters, finite-element models can provide more reliable predictions, supporting better pavement design and maintenance decisions.

7 REFERENCES

1. IS405, A.C.P.A., *Concrete pavements with undoweled joints for light traffic facilities.* Concrete information.
2. Rasmussen, R.O. and D.K. Rozycki, *Thin and Ultra-Thin Whitetopping: A Synthesis of Highway Practice*, in *NCHRP Synthesis 338.* 2005, Transportation Research Board: Washington, D.C.
3. Foltin, K., et al. *Assessment of load transfer across transverse joints.* in *Proceedings of the International Conference on Concrete Pavements.* 2016.
4. Li, Z. and J.M. Vandenbossche, *Redefining the failure mode for thin and ultrathin whitetopping with 1.8-× 1.8-m joint spacing.* Transportation research record, 2013. **2368**(1): p. 133-144.
5. Jamieson, S. and G. White, *Validating a finite element model for rigid aircraft pavement load transfer against full scale testing.* International Journal of Pavement Engineering, 2024. **25**(1): p. 2363943.
6. Nishizawa, T., T. Fukuda, and S. Matsuno. *A refined model of doweled joints for concrete pavement using FEM analysis.* in *Proceedings of the International Conference on Concrete Pavements.* 1989.
7. Sii, H.B., et al., *Evaluation of doweled joints in concrete pavements using three-dimensional finite element analysis*, in *Design, analysis, and asphalt material characterization for road and airfield pavements.* 2014. p. 115-129.
8. Schmitt, R., S. Owusu-Ababio, and J. Crovetti, *Performance Evaluation of Open Graded Base Course with Doweled and Non-Doweled Transverse Joints.* 2010.
9. Bayraktarova, K., et al., *Design life of rigid pavements under dynamic wheel loads.* Road Materials and Pavement Design, 2023. **24**(9): p. 2263-2279.
10. FSV, *RVS 03.08.69: Rechnersiche Dimensionierung von Betonstraßen.* 2020, Österreichische Forschungsgesellschaft Straße - Schiene - Verkehr: Wien.
11. Eisenmann, J. and G. Leykauf, *Concrete pavements - design and construction.* 2003: Wiley.
12. Houben, L.J.M. *Structural Design of Pavements.* CT 4860 Part IV Design of concrete Pavements [Report] 2009; 01.2009:[69-101].
13. Bayraktarova, K., et al., *Towards a better consideration of the interface bonding conditions in the design of bonded concrete overlays.* Materials and Structures, 2023. **56**(2): p. 30.
14. Simulia, D.S., *Abaqus FEA.* 2020, Dassault Systems: Providence, USA.
15. Maitra, S.R., K. Reddy, and L. Ramachandra, *Load transfer characteristics of aggregate interlocking in concrete pavement.* Journal of Transportation Engineering, 2010. **136**(3): p. 190-195.
16. Bayraktarova, K., L. Eberhardsteiner, and R. Blab, *Seasonal temperature distribution in rigid pavements*, in *Bearing Capacity of Roads, Railways and Airfields.* 2017, CRC Press. p. 2087-2093.

Design Recommendations for Short Continuously Reinforced Concrete Pavement

L.S. Salles
Rochester Institute of Technology

J.T. Balbo
University of Sao Paulo

L. Khazanovich
University of Pittsburgh

ABSTRACT: Four short (50 m) sections of continuously reinforced concrete pavement (CRCP) were constructed as a proposed solution for bus stops and terminals, critical areas of public infrastructure. Initial analysis revealed that these short CRCP sections exhibited distinct cracking behavior compared to traditional CRCP. To better understand their performance, a combination of ultrasonic testing and stress simulations was conducted. This paper presents key findings from stress simulations, which account for various pavement parameters as well as traffic and environmental loads. These simulations aim to develop rapid, reliable, and intuitive design recommendations for short CRCP applications. Additionally, a fatigue model was applied to assess the performance of the experimental sections. This approach successfully identified the causes of three failures, which were traced to thickness deficiencies detected by ultrasonic testing.

1 INTRODUCTION

The implementation of bus lanes in large urban areas provides significant traffic benefits, such as increasing average bus speeds, making public transportation more competitive with private vehicles. However, the constant need for rehabilitation and maintenance poses challenges for highly urbanized areas. Therefore, the pursuit of more durable pavement structures is critical for public transport infrastructure.

From a structural perspective, hot climates combined with the specific traffic characteristics of buses—channeled, slow, and heavy—make conventional asphalt less suitable for bus corridors, stops, and terminals. Conversely, poor construction practices in concrete pavements, particularly regarding joint placement, present difficulties in countries without a strong tradition of concrete pavement construction. For both asphalt and jointed plain concrete pavements (JPCP), the most common areas of distress in bus corridors are bus stops and terminals, where slower speeds, frequent braking, and acceleration occur, as well as stationary vehicles.

In response to these issues, this paper focuses on the design of short continuously reinforced concrete pavements (CRCP) as a potential solution for bus corridor stops and terminals. CRCP is a type of concrete pavement without contraction joints, allowing the slab to extend without length restrictions as long as concrete pouring continues. If the pouring is halted, a construction joint is introduced. While concrete is known for its susceptibility to cracking, CRCP differs from JPCP by using a high percentage of steel reinforcement placed above the slab's midheight. This reinforcement is intended to keep the inevitable cracks tightly closed, ensuring minimal

impact on users and maintaining excellent load transfer through aggregate interlock (Roesler et al. 2016). Studies suggest that CRCP's key advantages are its durability and reduced maintenance needs, making it a promising option for bus corridors (Tayabji et al. 1995; Gharaibeh et al. 1999; Won, 2011).

To gain a deeper understanding of CRCP's behavior in tropical climates, four short CRCP sections, each 50 meters long, were constructed in Sao Paulo (Brazil) in 2010. These short sections exhibited an unusual crack pattern, with fewer cracks than anticipated. This was likely due to the short length and lack of edge anchorage, which slowed the development of surface cracks. However, falling weight deflectometer (FWD) and dynamic load testing confirmed typical CRCP performance, such as high load transfer efficiency (LTE), low deflections (except at the longitudinal edges), and low stresses (Salles et al. 2015). Additionally, a complete structural assessment was carried out using ultrasonic nondestructive testing equipment (Salles et al. 2019a). Based on the detailed characterization of these sections, numerical simulations were conducted using the ISLAB finite element software for concrete pavements. A shift factor was determined by comparing field stresses obtained from dynamic load testing with theoretical stresses (Salles et al. 2019b). Using this model, critical environmental and vehicle loading scenarios were analyzed to identify optimal design parameters for short CRCP. This paper presents the resulting design recommendations.

1.1 Short CRCP

The experimental short CRCP sections were constructed between July and September 2010 during São Paulo's dry winter season. Designed to simulate a bus stop, each section was 50 meters long, much shorter than traditional CRCP, which can exceed 400 meters. The sections had no anchorage at the ends, allowing longitudinal slab movement. Daily unidirectional traffic included about 378 buses, 145 medium trucks, and 750 cars. The old asphalt pavement, heavily distressed by rutting and cracking, was completely removed. The CRCP sections were 5.5 meters wide with 240 mm thick slabs, designed based on traffic and international urban pavement experience. The concrete had a flexural strength of 4.5 MPa at 28 days, using granite aggregates and 350 kg/m³ cement content.

Transverse reinforcement used 20 mm diameter bars spaced 0.9 m apart, made from local CA-50 steel with a tensile strength of 500 MPa. Higher steel content increases cracking but provides tighter cracks (Verhoeven, 1992; Suh & McCullough, 1994; Kim et al. 1998.) The longitudinal reinforcement was positioned 110 mm from the surface, 10 mm above slab mid-height, ensuring crack control and preventing water-induced corrosion (Verhoeven, 1992; Gharaibeh et al. 1999). More detailed construction practices are documented elsewhere (Balbo et al, 2012).

Initial performance of the short CRCP sections was assessed through FWD and dynamic load testing in section 3, revealing performance consistent with well-functioning concrete pavements (Salles et al. 2015). An ultrasound evaluation revealed variations in slab thickness and reinforcement spacing, resulting in recalculated steel percentages (Table 1). The ultrasonic analysis accurately predicted the development of 10 surface cracks after testing (Salles et al. 2019a). Finite element modeling of the sections, informed by ultrasonic, FWD, and dynamic load testing data, showed that the field stresses aligned with theoretical models (shift factor near 1) only when assuming a 50-meter slab with no joints or cracks (Salles et al. 2019b). Due to construction deficiencies, longitudinal cracks at the edges of sections 1 and 4 indicated early signs of punchouts.

Table 1. Design and Post-construction features

Sec.	Design Data			Ultrasonic Data		
	h* (mm)	s** (mm)	Steel %	Avg. h (mm)	Avg. s (mm)	Actual Steel %
1	240	300	0.44	216.1	284.4	**0.52**
2	240	230	0.57	201.2	218.5	**0.71**
3	240	170	0.77	221.1	171.7	**0.82**
4	240	200	0.67	195.3	195.9	**0.83**

*h = slab thickness
**s = reinforcement steel spacing

2 STRESS SIMULATIONS

The short CRCP structure was simulated using the actual dimensions of 50 meters in length and 5.05 meters in width. The fixed and variable input parameters are outlined in Table 2. The variables included vehicle load (standard dual-wheeled single axle), temperature differential, concrete slab thickness, and modulus of rupture. Vehicle load and temperature differential were varied to account for the different loads and thermal stresses the slab may face. The modulus of rupture variation was based on the fatigue model used in the study, while slab thickness, a key design factor, was adjusted according to typical CRCP thicknesses found in the literature.

Table 2. Input parameters for short CRCP simulation

Variable	Vehicle Load (Q)	kN	60 -140
	Thermal Differential (ΔT)	°C	0 - 25
	Concrete Slab Thickness	mm	200 - 400
	Concrete Modulus of Rupture (MR)	MPa	3.5 – 6.0
Fixed	Concrete Density	kg/m³	2,400
	Coefficient of Thermal Expansion	°C^{-1}	8x10-6
	Modulus of Elasticity	MPa	30,000
	Poisson's Ratio	-	0.15
	Base Thickness	mm	60
	Asphalt Density	kg/m³	2,200
	Resilient Modulus	MPa	7,000
	Poisson's Ratio	-	0.35
	Modulus of Subgrade Reaction	MPa/m	100

For the fixed parameters, the simulation assumed the use of a standard concrete mix with aggregates having a low coefficient of thermal expansion (CTE) and proper curing procedures (Ryu et al. 2013; Ren et al. 2012). The asphalt base layer was modeled to have a high resilient modulus, simulating conditions where the base is not directly exposed to environmental temperature fluctuations. The subgrade reaction modulus was selected based on the stiffness of the concrete asphalt base, as previous studies have shown that asphalt bases enhance CRCP performance due to their non-erodible nature (Johnson & Surdahl, 2006).

2.1 Short CRCP simulation analysis

Numerical simulations were conducted using the inputs from Table 2 on ISLAB 2000. Each slab thickness was tested with all combinations of axle loads and thermal differentials. Figure 1a (80 kN axle load) shows that in a 200 mm slab, vehicle-only loading (ΔT=0) produces stresses comparable to those in a 400 mm slab subjected to both vehicle loading and a 10°C thermal differential. This highlights the significant impact of environmental loads on concrete slabs. Thicker slabs exhibit less stress variation than thinner slabs for the same thermal differential. For instance, the stress difference between

200 mm and 250 mm slabs is greater than between 350 mm and 400 mm slabs, indicating that increasing thickness beyond 400 mm is less effective in mitigating uniform thermal effects.

In Figure 1b, for a 250 mm slab, stress increases linearly with axle load, while thermal differential causes a constant stress increase, similar to Figure 1a. Notably, unlike traditional CRCP design, which focuses on top stresses, continuous short CRCP slabs experience principal stress at the slab bottom.

(a)

(b)
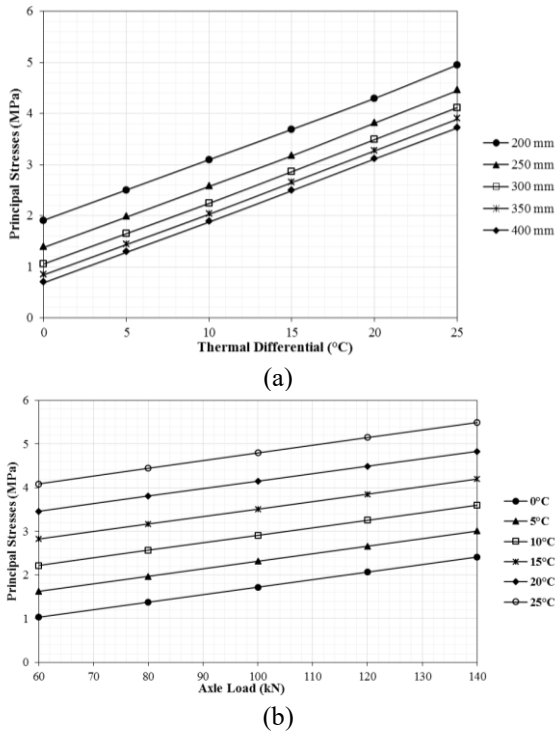
Figure 1. Short CRCP stresses due to (a) thermal differential variation for several slab thickness; (b) axle load and thermal differential variation

3 SHORT CRCP DISTRESS ANALYSIS

The experimental short CRCP exhibited three distresses (Figure 2): corner cracking at the start of Section 1, longitudinal cracking at the start of Section 4, and between cracks F3.7 and F3.11 in Section 3. These are referred to as distress 1, 4, and 3, respectively. Distress 1 was noticed in October 2012, while distresses 4 and 3 appeared in November 2016 and January 2017, respectively. Ultrasonic and coring data showed thickness deficiencies in areas affected by distresses 1 and 4, both averaging just under 200 mm. For distress 3, nearby measurements indicated a thickness variation between 163 and 267 mm. For simplicity, a uniform thickness of 200 mm was assumed in all distressed areas.

To investigate fatigue life consumption, traffic was analyzed. The average daily traffic (ADT) included 378 buses and 145 medium-sized trucks. Buses were assumed to have 60 kN front axles and 100 kN rear axles, while trucks had 80 kN rear axles. The number of axle load repetitions and fatigue consumption

were based on the Cervo and Balbo (2012) fatigue model as it is based on conventional Brazilian concrete and the Palmgren-Miner linear damage hypothesis. Additionally, since the short CRCP exhibits a stress configuration that differs from traditional CRCP design and is not related to crack spacing, the MPDGE method was deemed inapplicable. Results considering 200 mm slab thickness and a 10°C thermal differential are in Table 3. The 60 kN and 80 kN loads did not cause significant damage, but after two years, the 100 kN load reached 93% fatigue consumption. Over six years, fatigue consumption approached 300%.
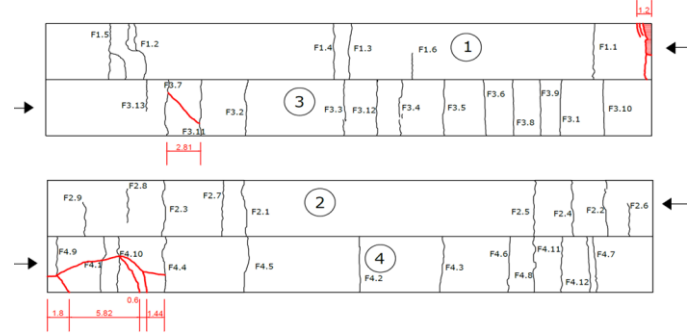
Figure 2. Cracking distresses visible at the short CRCP surface

Table 3. Fatigue consumption analysis

		Section/Distress	1	4	3
Axle Load (kN)	Principal Stress (MPa)	Number of Repetitions (N)	Fatigue Damage		
60	2.62	1.71E+10	0	0	0
80	3.09	8.09E+07	0	0	0
100	3.57	3.09E+05	0.93	2.75	2.83

Based on city standards for thermal differentials (Balbo & Severi, 2002), in Table 4, the 100 kN load combined with peak thermal differential (13 to 15 hours, spring) accounted for 43% fatigue life consumption for distress 1 and over 126% for distresses 3 and 4. No traffic was observed between 19 and 8 hours. These results align better with the observed failures. The distress in Section 1 was likely worsened by rutting in the adjacent interlocked pavement, causing higher axle loads. This underscores the importance of accurate traffic, axle load, and thermal differential data for pavement design and evaluation.

Table 4. Traffic distribution and respective thermal differentials

Time	ADT (%)	ΔT (°C)			
		Spring	Summer	Fall	Winter
8-9h	7	6.25	5.75	0	0
9-13h	14	6.25	5.75	4	5
13-15h	4	12.5	11.5	8	10
15-17h	13	6.25	5.75	4	5
17-18h	8	6.25	5.75	4	0
18-19h	8	0	5.75	0	0

4 SUMMARY AND RECOMMENDATIONS

To propose durable, low-maintenance pavement solutions for bus stops and terminals, field performance evaluations and simulations of experimental short continuously reinforced concrete pavement (CRCP) sections were analyzed, leading to several conclusions: the center edge is the critical location for short CRCP design and analysis; increasing thickness in thinner slabs (approximately 200 mm) is more effective in reducing thermal differential-related stresses than increasing thickness in thicker slabs (around 400 mm); positive thermal differentials create principal stress at the slab bottom, which differs from classic CRCP design that focuses on top stress.

The following guidelines and recommendation short CRCP design are proposed:

1. Short CRCP for bus stops and terminals should focus on a service life of over 25 years in areas with heavy vehicle traffic. Slabs should be at least 250 mm thick, considering vehicle and environmental loading. A 60 mm minimum hot-mix asphalt base is required for maintaining a high subgrade modulus and providing a non-erodible foundation.

2. The allowable number of load repetitions should align with the expected load repetitions (project N), using the Palmgren-Miner fatigue life consumption hypothesis. Accurate axle load and thermal differential data, including hourly variations, should be used in design.

3. The longitudinal steel percentage should range between 0.7% and 0.8% to ensure adequate crack width. Steel depth should be between 76 mm and 100 mm from the surface to protect against corrosion and ensure tight cracks.

4. Aggregates with low CTE should be used in the concrete mix design. Strict curing practices must be followed to prevent shrinkage, with curing compound applied at 2.5-5 m²/liter for seven days (Roesler et al. 2016).

5. Transition joints should be placed at the transverse edges of the 50 m short CRCP to prevent joint-related distresses. The FHWA CRCP manual suggests four transition options for CRCP to JPCP, with the doweled joint (option 3) preferred for simplicity (Roesler et al. 2016). For asphalt transitions, the manual recommends a sleeper slab connected by an I-beam to the asphalt pavement.

References

Balbo, J. T. & Severi, A. A. 2002. Thermal gradients in concrete pavements in tropical environment. Experimental appraisal. *Transportation Research Record*, v. 1809, p. 12 – 22.

Balbo, J. T., Massola, A. & Pereira, D. 2012. Structural aspects of the experimental CRCP in São Paulo. *Proceedings of the 10th International Conference on Concrete Pavements*, International Society for Concrete Pavements, Quebec.

Cervo, T. C. & Balbo, J. T. 2012. Calibration of a Shift-Factor for the Fatigue Prediction of High Strength Concrete Pavement in the Field. *International Journal of Pavement Research and Technology*, v. 5, p. 153-160.

Gharaibeh, N. G., Darter, M. I. & Heckel, L. B. 1999. Field performance of continuously reinforced concrete pavement in Illinois. *Transportation Research Record*, v. 1684, pp. 44 – 50.

Johnston, D. P. & Surdahl, R. W. 2006. Effects of base type modelling long-term pavement performance of continuously reinforced concrete sections. *Transportation Research Record*, v. 1979, pp. 93 – 101.

Kim, S. M., Won, M. & Mccullough, B. F. 1998. Numerical modeling of continuously reinforced concrete pavement subjected to environmental loads. *Transportation Research Record*, v. 1629, p. 76 – 88.

Kohler, E. & Roesler, J. 2006. Nondestructive testing for crack width and variability on continuously reinforced concrete pavements. *Transportation Research Record*, v. 1974, p. 89 – 96.

Ren, D., Houben, L. J. M. & Rens, L. 2012. Monitoring Early-age Cracking of Continuously Reinforced Concrete Pavements on the E17 at Ghent (Belgium). *Sustainable Construction Materials*, p. 30 – 41.

Roesler, J., Hiller, J. E. & Brand, A. S. 2016. Continuously Reinforced Concrete Pavement Manual. Guidelines for Design, Construction, Maintenance, and Rehabilitation. *FHWA-HIF-16-026*. Federal Highway Administration.

Ryu, S. W., Won, H., Choi, S. & Won, M. C. 2013. Continuously reinforced bonded concrete overlay of distressed jointed plain concrete pavements. *Construction and Building Materials*, v. 40, p. 1110 – 1117.

Salles, L. , Balbo, J. T. & Pereira, D. S. 2015. Non-destructive Performance Evaluation of Experimental Short Continuously Reinforced Concrete Pavement. *International Journal of Pavement Research and Technology*, v. 8, p. 221-232.

Salles, L., Khazanovich, L. & Balbo, J. T. 2019a. Non-Destructive Evaluation of Crack Initiation and Propagation in Continuously Reinforced Concrete Pavements. *Transportation Research Record*, Volume 2673, Issue 3.

Salles, L. S., Khazanovich, L. & Balbo, J. T. 2019b. Structural analysis of transverse cracks in short continuously reinforced concrete pavements, *International Journal of Pavement Engineering*, DOI: 10.1080/10298436.2019.1570194

Suh, Y. C. & Mccullough, B. F. 1994. Factors affecting crack width of continuously reinforced concrete pavement. *Transportation Research Record*, v. 1449, p. 134 – 140.

Tayabji, S., Stephanos, P. & Zollinger, D. G. 1995. Nationwide field investigation of continuously reinforced concrete pavements. *Transportation Research Record*, v. 1482, pp. 7 – 18.

Verhoeven, K. 1992. Cracking and corrosion in continuously reinforced concrete pavements. *Proceedings of the 5th International Conference on Concrete Pavement Design and Rehabilitation*, Purdue University, West Lafayette, Indiana.

Won, M. C. 2011. Continuously reinforced concrete pavement: identification of distress mechanisms and improvement of mechanistic-empirical design procedures. *Transportation Research Record*, v. 2226, p. 51 – 59.

Effect of water film thickness on skid resistance of Tined concrete pavement

Chann Seng, Ph.D. Candidate
Department of Civil Engineering, Gangneung-Wonju National University, Jeebeon-gil 7, Gangneung-si, Gangwon-do, 25457, South Korea, Tel: +82-10-7317-0506, E-mail: sengchann2356@gmail.com

Young Kyu Kim, Ph.D., Research Professor
Institute for Disaster Prevention, Gangneung-Wonju National University, Jeebeon-gil 7, Gangneung-si, Gangwon-do, 25457, South Korea, Tel: +82-10-5789-4446, E-mail: kingdom1980@nate.com

Seung Woo Lee, Ph.D., Professor (Corresponding Author)
Department of Civil Engineering, Gangneung-Wonju National University, Jeebeon-gil 7, Gangneung-si, Gangwon-do, 25457, South Korea, Tel: +82-10-4725-7415, Fax: +82-33-641-1391, E-mail: swl@gwnu.ac.kr

ABSTRACT: Wet pavement friction decreases with increased water film thickness (WFT), significantly raising the risk of vehicle crashes. The British Pendulum Test is used to measure wet pavement friction for design and management. The British Pendulum Number (BPN) in wet conditions varies with WFT. Following ASTM E303-93 standard procedures, WFT was simulated by spraying water on the pavement surface. However, the measurement of BPN did not include specific information about the thickness of the water film present during testing. To address these issues, WFTs and BPNs were measured using rainfall simulator across various intensities, drainage lengths, slopes, and textures. This study examines WFT's impact on BPN for wet friction and determines WFT for each BPN on various surfaces. This study shows significant BPN decreases with increasing WFT for non-tined and 25mm tined surfaces, while 16mm tined surfaces decrease slightly. These insights improve friction values, enhancing road safety, better design, and reducing crash risks.

1 INTRUDUCTION

Road safety has been a primary concern for drivers since the inception of roads designed for high-speed and long-distance travel. In addition to roadway geometric design, pavement skid resistance is a crucial element that directly impacts driving safety (Fwa, 2021). Moreover, road crash investigations and historical statistical data by researchers in different parts of the world have indicated that the number of wet-weather crashes increases as pavement skid resistance decrease (Ivan, et al., 2010; Merritt, et al., 2015). Based on statistical data, the possibility of accident occurrence on wet pavements is 10 times greater than on dry pavements (Ling, et al., 2023). Consequently, the reduction of wet pavement friction through the mechanism of water film thickness typically involves the creation of a thin layer of water between the tire and the road surface (Fwa, 2021). Water film thickness (WFT), illustrated in Figure. 1, was calculated to be the thickness of water film on the pavement during rainfall, measured from the top of the pavement surface (Ling, et al., 2023; Xie, et al., 2018). Water film on pavements creates uplift forces on vehicle tires, potentially causing a portion of the tires to lift off the pavement surface. This film acts as a lubricant layer, reducing the friction between the vehicle tire and the pavement (Pourhassan, et al., 2021). the decrease in friction reduces skid resistance and overall vehicle control in wet or rainy conditions (Fwa, 2021).

In contemporary highway engineering, particularly in the formulation of road safety-related models and analyses concerning pavement skid resistance, practitioners often resort to empirical correlations or predefined values for pavement skid resistance. However, it is important to note that wet pavement friction can vary depending on factors such as pavement surface texture, water film thickness, and vehicle speed (Fwa, 2021). Thus, this study is specifically concerned with investigating the influence of pavement surface texture and water film thickness on wet pavement friction for tined concrete pavement.

The British Pendulum Tester (BPT) has been the most common device used worldwide for laboratory skid resistance testing of pavement materials for more than 50 years (Guo, et al., 2021). The British pendulum number (BPN) is commonly employed to determine friction for geometry design, including design speed and stopping sign distance, as well as for pavement management systems (Leu & Henry, 1978; Xie, et al., 2018). This procedure is outlined in the ASTM E303-93 standard (ASTM, 1998) creates water film thickness by spraying water onto the pavement surface. However, this standard lacks specifications regarding the required amount of water and fails to provide specific information about the thickness of the water film during testing. Consequently, it cannot deliver precise data on water film thickness alongside the BPN. Furthermore, reliable estimation of friction for specific water film thicknesses, especially in the case of thicker water films, may not be achievable

through this method. To address these issues, in this study, water film thickness (WFT) and the British Pendulum Number (BPN) were measured by creating controlled rainfall using a rainfall simulator across various pavement surfaces, rainfall intensities, pavement slopes, and drainage path lengths. The aim is to establish the relationship between WFT and BPN for wet pavement friction across various pavement surfaces. Additionally, the study aims to determine water film thicknesses corresponding to the British Pendulum Numbers measured when employing the ASTM E303-93 standard. This study considers five pavement surface textures: a smooth surface, a transversely tined surface with 16mm spacing, a transversely tined surface with 25mm spacing, a longitudinally tined surface with 16mm spacing, and a longitudinally tined surface with 25mm spacing. Measurements were conducted for WFTs under dry conditions, wet conditions with water spraying, and using a rainfall simulator.
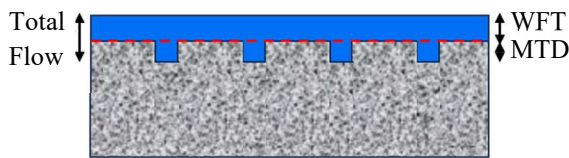
Note: MTD = Mean Texture Depth,
WFT = Water film Thickness

Figure 1. Definition of Water Film Thickness

2 MECHANISM OF THE WET PAVEMENT FRICTION GENERATION

Hydroplaning can occur when vehicles travel at high speeds on pavement surfaces with a relatively thin film of water. Hydroplaning is initiated when water pressure builds up at the pavement-tire interface, causing a separation between the vehicle tire and the pavement surface. This separation results in a near-zero level of friction, as depicted in Figure. 2 (NCHRP, 2009).

Figure 2. Hydroplaning

According to the Guide for Pavement Friction (NCHRP, 2009), the coefficient of friction of a vehicle tire sliding over a wet pavement surface decreases exponentially as WFT increases, and a very small amount of water can significantly reduce pavement friction. According to previous studies (Ling, et al., 2023; Xie, et al., 2018), WFT is considered to be highly correlated with local rainfall coefficients (including rainfall intensity and duration) and pavement

properties (including pavement geometry and texture). Therefore, this study considers factors such as rainfall coefficient, drainage path length, texture properties, and pavement geometric indices to produce various WFT values, and evaluate the influence of WFT on the BPN.

3 RESEARCH METHODOLOGY

3.1 Test section

For the purpose of accurate representation of actual rainfall, a simulator was designed with a capacity of 0 to 130 mm/h, using six pipelines with six sprinklers each (36 in total), as shown in Figure. 3. The required rainfall intensity was controlled through water pressure and sprinkler speed, and measured by collecting water over 15 minutes, then converting the volume to mm/hr.
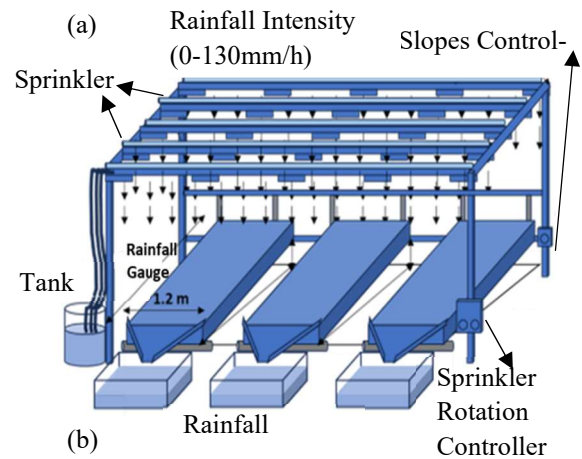
Figure 3. Rainfall Simulator (a) Experiment conditions (b) Actual Rainfall Simulator

3.2 Experiment Conditions

In this study, WFT and BPN were measured using artificial rainfall simulated with a rainfall simulator across various pavement surfaces as shown in Figure. 4. A total of 135 tests were conducted during this experimental study to investigate the effect of WFT on BPN for each slab. Each test was repeated at least four times to obtain reliable results. The slabs were exposed to varying rainfall intensities, measured at 30 mm/h, 80 mm/h, and 130 mm/h. For each of these

intensity levels, tests were conducted on the slabs at 2%, 5%, and 10% slopes, representing the slopes of road surfaces.
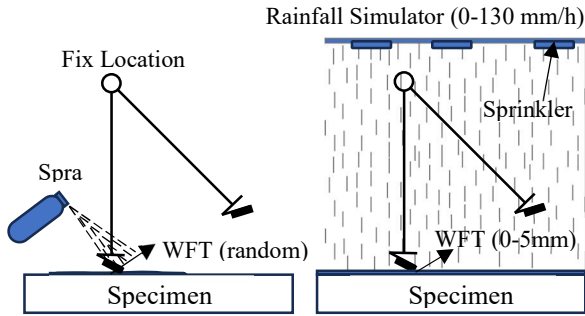
Figure 4. Experiment Conditions

3.3 *Measurement of the British pendulum numbers*

The BPT is globally accepted due to its versatility (Zaid et al., 2019). The resulting measurement is known as the British Pendulum Number (BPN). BPN was measured under three conditions: dry, wet with sprayed water, and wet using a rainfall simulator. Tests in both wet and dry states were performed in two directions, as shown in Figure. 5. For sprayed wet conditions, water was applied continuously per ASTM E303-93 standards (ASTM, 1998). For rainfall-simulated wet conditions, BPN and WFT were measured under various parameters like pavement slope, rainfall intensity, and drainage path length (Figure. 6). In this setup, BPN and WFT were taken at three points per drainage path length, totaling 45 points across 5 path lengths and three pavement surfaces. Each BPN reading was repeated at least four times. BPN values were recorded in two directions: longitudinally along the tined line and transversely, with spacings of 25 mm and 16 mm, respectively.
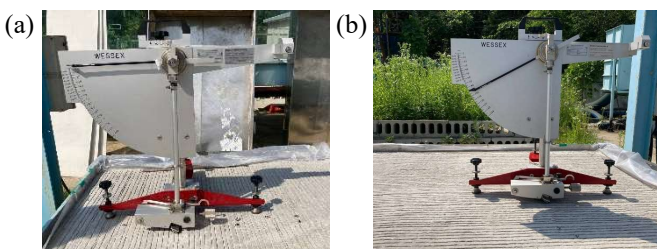
Figure 5. British Pendulum Number measurement of the dry and wet condition according to ASTM E303-93 (a) Transverse tined (b) Longitudinal tined
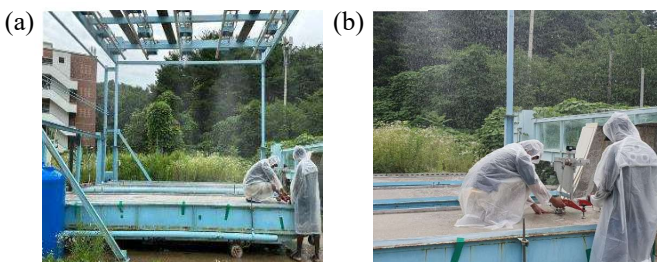
Figure 6. (a) Distant view of British Pendulum Number measurement in wet conditions, (b) Close-up view of British Pendulum Number measurement in wet conditions.

4 RESULTS AND DISCUSSION

4.1 *Determination of the water film thickness for the British pendulum test*

Table 1 shows a summary of the WFT corresponding to the average BPN under wet conditions achieved by spraying water according to ASTM 303-93 standards for each pavement surface. For the non-tined surface, the WFT of 1.2mm corresponds to a BPN of 62. Additionally, WFT of 0.3mm corresponding to BPN is 78 for longitudinal tined with 25mm spacing and 80 for longitudinal tined with 16mm spacing. Additionally, WFT of 0.6mm corresponds to BPN of 78 for longitudinal tined surfaces with 25mm spacing, and 80 for those with 16mm spacing. Test results for both dry and wet pavement friction were obtained according to ASTM E303-93 by simulating water film thickness through spraying

Table 1. Summary the results

Pavement Surface	BPN dry condition	BPN wet condition	WFT (mm)
Non-Tined (smooth surface)	83	62	1.2
Longitudinal Tined Surface with 25 mm spacing	83	78	0.2
Longitudinal Tined Surface with 16 mm spacing	85	80	0.3
Transverse Tined Surface with 25 mm spacing	87	78	0.6
Transverse Tined Surface with 16 mm spacing	84	80	0.6

4.2 *The Effect of Water Film Thickness on British Pendulum Numbers in Various Pavement Surfaces*

Figure. 7 illustrates that BPN significantly decreases as WFT increases. The figure shows a BPN reduction from 80 to 40 with an increase of WFT from 0 to 2.4mm, signifying a declining rate of approximately 14.6 BPN per millimeter increase in WFT. As earlier shown in Table 1, the spraying wet condition BPN measured according to ASTM E 303–93 on a non-tined surface is 62, corresponding to a WFT of 1.2mm. Thus, it can be inferred that spraying water on the non-tinning surface produces a WFT of 1.2mm, reducing the BPN from the dry condition value of 83 to a value of 62. Moreover, for the relationship between BPN and WFT, noting a decrease in BPN by 11.9 per mm increase in WFT for longitudinal tined with 16mm spacing and 13.1 per mm increase in WFT for longitudinal tined with 25mm spacing. Similarly, the BPN significantly decreases in BPN by 8.57 per mm increase in WFT for traverse tined with 16mm spacing and 8.31 per mm increase in WFT for traverse tined with 25mm spacing.

In comparison to the transversely tined surface, it was observed that non-tined and longitudinally tined surfaces exhibited a significant decrease in BPN as WFT increased, as illustrated in Figure. 6. The relationship between BPN and WFT for longitudinal tinning closely mirrors that of non-tined surfaces. This similarity can be attributed to the lower friction resistance observed in both non-tined and longitudinally tined pavements, in contrast to surfaces with transverse tinning. Moreover, both 25 mm longitudinal and transverse tined surfaces exhibited significantly greater decrease in BPN compared to 16mm spacing at same WFT. This can be attributed to the improved friction in the 16 mm spacing due to the higher number of tined lines.
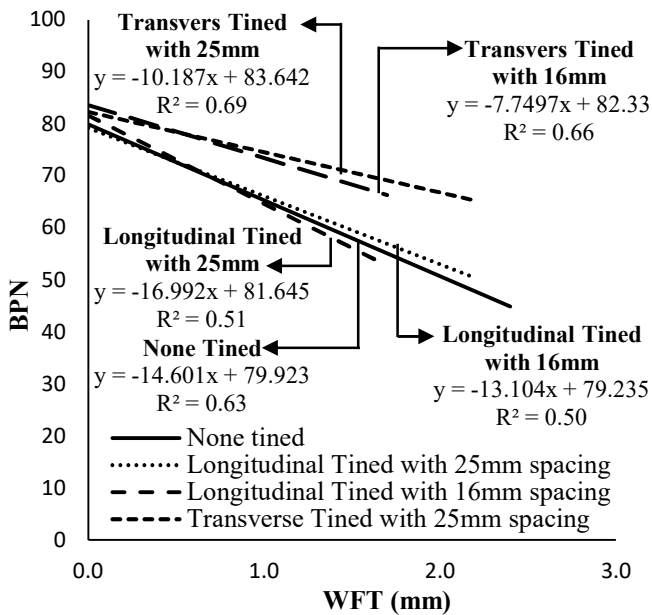
Figure 7. Relationship between water film thickness and British pendulum number

5 SUMMARY AND CONCLUSION

In conclusion, this study demonstrates the importance of considering water film thickness in pavement friction design. Ensuring that the British Pendulum Number provides a more reliable representation of wet pavement friction requires accounting for actual water film thickness, which is influenced by various factors such as pavement slope, rainfall intensity, drainage path length, and pavement surface texture. Based on the test results, it was determined that the non-tined surface had a WFT of 1.2mm, corresponding to a BPN of 62. The longitudinal tined surfaces with 25mm and 16mm spacing had WFTs of 0.3mm, corresponding to BPNs of 78 and 80 respectively, while the transverse tined surfaces with 25mm and 16mm spacing had WFTs of 0.6mm, corresponding to BPNs of 78 and 80. Furthermore, the relationship between BPN and WFT for longitudinal tinning closely mirrors that of non-tined surfaces, attributed to the lower friction resistance in both non-tined and

longitudinally tined pavements, in contrast to surfaces with transverse tinning.

6 DATA AVAILABILITY STATEMENT

All data, and models that support the findings of this study are available from the corresponding author upon reasonable request.

7 ACKNOWLEDGMENTS

8 REFERENCES

ASTM, 1998. ASTM E 303-93: Standard Test Method for Measuring Surface Frictional Properties Using the British Pendulum Tester, West Conshohocken, PA, USA: ASTM.

FHWA CPSCP GS 4-11., 2011. Texturing Concrete Pavement for Reduced Tire/Pavement Noise using Transverse Tining. Federal Highway Administration.

Fwa, T. F., 2021. Determination and prediction of pavement skid resistance–connecting. Journal of Road Engineering, Volume 1, pp. 43-62.

Guo, W., Chu, L. & Fwa, T. F., 2021. Mechanistic harmonization of British pendulum test measurements. Measurement, Volume 182, p. 109618.

Ivan, J.N., Ravishanker, N., Jackson, E., Guo, S. and Aronov, B., 2010. Incorporating Wet Pavement Friction into, s.l.: JHR 10-324.

Leu, M. C. & Henry, J. J., 1978. Prediction of skid resistance as a function of speed from pavement texture measurements. Transportation Research Record, 666(2), pp. 7-13.

Ling, J., Yang, F., Zhang, J., Li, P., Uddin, M.I. and Cao, T., 2023. Water-film depth assessment for pavements of roads and airport runways: A review. Construction and Building Materials, Volume 392, p. 132054.

Merritt, D. K., Lyon, C. & Persaud, B., 2015. Evaluation of pavement safety performance, United States: Federal Highway Administration.

NCHRP, 2009. Guide for Pavement Friction, Washington, DC: National Cooperative Highway Research Program.

Pourhassan, A., Gheni, A. A. & ElGawady, M. A., 2021. Water film depth prediction model for highly textured pavement surface drainage. Transportation Research Record, 2676(2), pp. 100-117.

Xie, X., Lu, G., Liu, P., Zhou, Y., Wang, D. and Oeser, M., 2018. Influence of temperature on polishing behaviour of asphalt road surfaces. Wear, Volume 402, pp. 49-56.

Zaid, N.B.M., Hainin, M.R., Idham, M.K., Warid, M.N.M. and Naqibah, S.N., 2019. Evaluation of skid resistance performance using British pendulum and grip tester.

Notched Beam Specimen Flexure through Modified Crack Propagation Finite Element Model

M. Smetana & L. Khazanovich
Department of Civil and Environmental Engineering, University of Pittsburgh, Pittsburgh, Pennsylvania, United States of America

S. Sen
Department of Civil Engineering, Indian Institute of Technology, Gandhinagar, Gujarat, India

ABSTRACT: Cohesive Zone Models (CZMs) are valuable tools in finite element modeling of crack propagation in concrete structures, including concrete pavements. A recent 2D crack element, developed by Sen & Khazanovich (2021), provides a simplified and computationally efficient approach for modeling crack behavior, including the simulation of concrete's flexural performance. While effective, the model does not currently account for notched beam geometries, which are essential for comparisons with experimental data. Additionally, the existing solution procedure involves matrix inversions for all elements, including those with unchanged stiffness, leading to computational inefficiencies. This paper extends the crack element model by incorporating notched beam geometry and introducing a modified solution procedure to reduce computational demands. Results show that increasing notch depth decreases tensile strength, while sensitivity to the kink-point ratio in the bilinear traction law remains limited. The proposed modifications significantly enhance computational performance and accuracy, laying the groundwork for future calibration and validation against experimental data.

1 INTRODUCTION

In rigid pavements, the tensile failure of concrete is intentionally utilized as a design mechanism due to the relatively large tensile stresses caused by heavy traffic loading conditions and thermal gradients. Since the tensile strength of concrete is difficult to measure directly, indirect methods such as the modulus of rupture have been adopted (Wittman, 2005).

The modulus of rupture (f_r), or flexural strength, is a measure of the maximum amount of stress that a material can withstand before breaking or failing under a bending load. Higher f_r values correspond to the materials' ability to have a greater resistance to cyclic loading (e.g., traffic loads or freeze-thaw cycles). While this property characterizes the apparent flexural strength of concrete, it is evident that it is also dependent on related fracture mechanisms such as the size effect or the overall fracture energy required to initiate crack propagation (Bažant and Li, 1995).

Due to the quasi-brittle nature of concrete, linear elastic fracture mechanics (LEFM) only provide a limited accuracy in numerical analyses. Quasi-brittle materials tend to exhibit a large, nonlinear, fracture process zone (FPZ) in front of the crack tip, which other models like Cohesive Zone Models (CZMs) seek to address (Hillerborg et al., 1976). Essentially, a CZM characterizes the relationship between traction and separation at the crack tip; Therefore, traction laws can be defined to represent these processes at crack interface.

Roesler et al. (2007) implemented a bilinear traction law for CZM analysis of concrete flexural tests. In their study, cohesive elements were placed at the boundary of a crack at the center of a beam model, closely resembling testing conditions. However, finite element models like this typically require extremely fine meshes near the crack. More recently, Sen & Khazanovich (2021) developed a simplistic 2D finite element model, referred to as the "self-contained" crack element, to reduce mesh complexity and improve computational efficiency.

This model has effectively simulated crack propagation in beams in both flexural and tension scenarios, showing relationships between f_r and CZM parameters. However, the model has not yet been adapted to include a notch in the beam geometry. The inclusion of a notch is particularly important for facilitating mode I (pure bending) fracture, ensuring that a crack propagates at midspan during three- or four-point bending laboratory tests (Yin et al., 2019).

This paper proposes a modified version of the self-contained crack element model. The inclusion of a notch enables future comparisons with experimental data. Additionally, the modified model reduces the number of matrix inversion operations, further enhancing computational speed. These changes aim to improve the model's accuracy and provide more refined estimates of values such as the modulus of rupture for use in rigid pavement design.

2 ELEMENT MODELING

The model consists of an intermediate self-contained crack element surrounded by Euler beam elements, as shown in Figure 1. Each connecting node allows for rotation and translation in the x and y direction. The two nodes connected to the boundary of the crack element undergo iterative displacements to simulate the loading conditions.

A beam in this analysis is comprised of a length (L) in the y direction, height (h) in the x direction, and a unit thickness (b) for simplified 2D modeling. The $L/3$ dimensions serve as an example of four-point bending conditions.
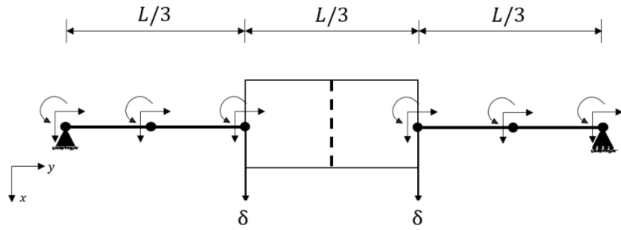
Figure 1. Self-contained crack element model

2.1 Crack element

The crack element is defined by a combination of cohesive Park–Paulino–Roesler (PPR) elements (Park et al., 2009) with pre-meshed bulk elements, as shown in Figure 2. There are N_x bulk elements in the x direction and $2N_y$ in the y direction. The multiplication by two in the y direction accounts for model symmetry about the center of the beam, only requiring user input for half of the number of elements. There must be an additional element along the length of the beam to include the zero-width cohesive elements, resulting in a total number of $N_x \times (2N_y + 1)$ elements.
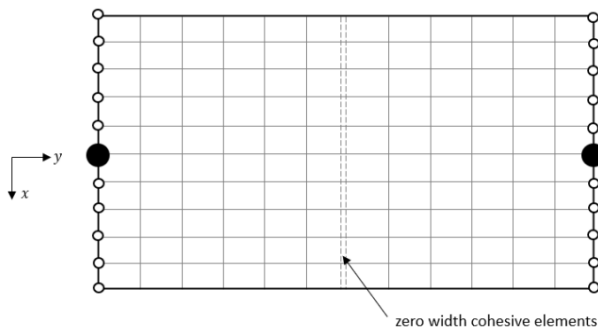
Figure 2. Bulk and zero-width cohesive elements within crack element

2.1.1 Bulk elements
The stiffness matrix of the bulk elements are based on bilinear, quadrilateral elements, described by Young's modulus (E), Poisson's ratio (ν), and two degrees of freedom (DOF) at each node for translations. Since this is a 2D finite element analysis, it is assumed that the thickness of the beam, b, is much smaller than the length and height; thus, a plane stress state is used for stiffness matrix evaluation.

2.1.2 Cohesive elements
A bilinear traction separation law (Figure 3) characterizes crack propagation in the cohesive elements. Other CZM models can be implemented in future analyses, if necessary. This bilinear law is a function of crack opening width (w), stress (σ), total fracture energy (ϕ), and kink-point ratio (ψ) – which relates to the transition between initial linear elastic behavior and subsequent softening behavior for materials under tension (Roesler et al., 2007). This ratio is critical for understanding how cracks initiate and propagate, as it helps define the tensile strength (f_t') and crack opening metrics of the material (Tompkins et al., 2015).
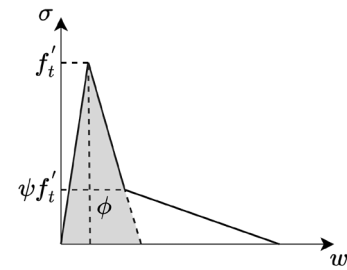
Figure 3. Bilinear softening curve adapted from Roesler et al. (2007)

2.2 Euler beam elements and connections

Each beam element is then characterized by their geometry and Young's Modulus (E). The development of a transverse crack creates an additional moment, coupling with axial displacements (Rice & Levy, 1972), leading to three DOFs (axial, transverse, and rotational) instead of the typical two in conventional beam elements (only axial and transverse). Individual stiffness matrices are evaluated as a combination of Euler-Bernoulli beam theory and rod theory (Zienkiewicz et al., 2000).

Part of the modeling process involves linking the crack element to the neighboring rod elements, which is further described in the original paper (Sen & Khazanovich, 2021).

2.3 Notched beam adaptation

To implement a notched beam into the model, a new user input for notch ratio (a/h) is required. In this case a is the depth of the notch and h is the height of the beam (Figure 4), as previously mentioned.

During the iterative solution procedure, the cohesive stress between nodes connecting the zero-width element to the bulk elements is set to zero. This allows the solver to treat these elements as already separated and to focus on the remaining, unsevered

elements for stress development. By fixing one support condition and allowing the other support to move freely in the y-direction, this resembles similar conditions to experimental testing.

This four point bending configuration ensures that the beam will be loaded in a purely bending fashion and eliminate the effect of any shear forces developing within the crack, which is commonly adjusted in the experimental post-processing of three point notched beam fracture tests.
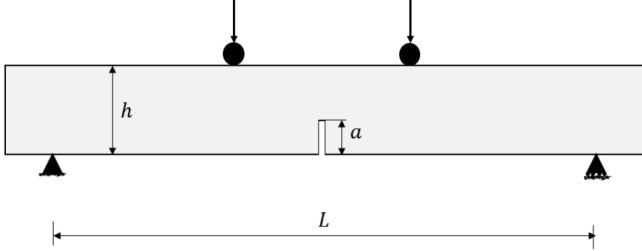
Figure 4. Typical notched beam four-point bending test configuration

3 MODFIED SOLUTION PROCEDURE

This self-contained crack element model significantly reduces the computational complexity required to run analyses – relative to other finite analyses that require a much finer mesh around the crack zone. An accurate analysis with the model proposed in this study requires approximately 10 elements in both the x and y direction of the crack element, which is the only part of the model that has any bulk elements.

Sen & Khazanovich (2021) proposed the following five-step procedure for modeling crack propagation:

Step 1: Evaluation of Element Properties: The stiffness matrix and force vector for beam elements and the crack element are computed, incorporating bulk and cohesive components. Displacements from the previous time increment are used for cohesive elements.

Step 2: Reduction of Crack Element: The stiffness matrix and force vector of the crack element are reduced to boundary nodes using static condensation. The algorithm involves partitioning the stiffness matrix of the crack element, K_{cr}, as well as the corresponding force and displacement vectors, f_{cr} and u_{cr} respectively, into boundary (subscript b) and interior (subscript i) DOFs to obtain the relationship:

$$\begin{bmatrix} K_{bb} & K_{bi} \\ K_{ib} & K_{ii} \end{bmatrix} \begin{pmatrix} u_b \\ u_i \end{pmatrix} = \begin{pmatrix} f_b \\ f_i \end{pmatrix} \tag{1}$$

Then, the condensed stiffness matrix and force vector corresponding to the boundary nodes, K_{bb}^* and f_b^*:

$$K_{bb}^* = k_{bb} - K_{bi}K_{ii}^{-1}K_{ib}; f_b^* = f_b - K_{bi}K_{ii}f_i \tag{2}$$

Step 3. Integration into Beam Model: The reduced crack element is connected to adjacent beam elements.

Step 4. Assembly and Solution: All element matrices and vectors are assembled, boundary conditions are applied, and the system is solved using an FE solver.

Step 5. Displacement Reconstruction: Node displacements (u_b and u_i) are reconstructed for use in the next iteration, completing the time-step loop.

This approach was adapted in this study, wherein Step 2 was significantly modified. The drawback of the procedure described above is the requirement to inverse the stiffness matrix K_{ii} at every time increment. However, the majority of the elements forming this portion of the structure are linear elastic, i.e. not changing from one time-step to another, while stiffnesses of only a small number of cohesive elements have to be adjusted. To address this limitation, the nodes of the crack element were partitioned into three groups: boundary (subscript b), cohesive (subscript c) and interior (subscript e), i.e. not belonging either to the boundary oi cohesive elements leading to the following relationship:

$$\begin{bmatrix} K_{bb} & K_{be} & K_{bc} \\ K_{eb} & K_{ee} & K_{ec} \\ K_{cb} & K_{ce} & K_{cc} \end{bmatrix} \begin{pmatrix} u_b \\ u_e \\ u_c \end{pmatrix} = \begin{pmatrix} f_b \\ f_e \\ f_c \end{pmatrix} \tag{3}$$

Then, the condensed stiffness matrix and force vector corresponding to the boundary nodes, K_{bb}^* and f_b^*:

$$K_{bb}^* = K_{bb} - K_{be}K_{ee}^{-1}K_{eb} - K_{be}K_{ee}^{-1}K_{ec}(K_{cc} - K_{ce}K_{ee}^{-1}K_{ec})^{-1}K_{ce}K_{ee}^{-1}K_{eb} \tag{4}$$

$$f_b^* = f_b + K_{be}K_{ee}^{-1}K_{ec}(K_{cc} - K_{ce}K_{ee}^{-1}K_{ec})^{-1}(f_c - K_{ce}K_{ee}^{-1}f_e) \tag{5}$$

The advantage of this approach is that only matrix K_{cc} changes from one time increment to another. All other matrixes should be computed only in the first time increment. Computation of the condensed stiffness matrix for other steps requires only inversion of the matrix $(K_{CC} - K_{CE}K_{EE}^{-1}K_{EC})$ and its multiplication to the pre-computed matrixes. This significantly improves computational efficiency of the process.

4 EFFECT OF NOTCH ON FLEXURAL STRENGTH

From a single crack element simulation, the flexural strength (f_r) is computed with the resulting peak load P, as defined in the following equation:

$$f_r = \frac{PL}{bh^2} \tag{6}$$

To investigate the effect of notch depth on flexural strength, a factorial analysis of the inputs described in Table 1 was conducted, resulting in over 3,000 cases.

A notch ratio of zero is not considered, as it corresponds to the original model solution. The notch ratio was incremented by 0.1, ranging from 0.1 to 0.5, where 0.5 represents a notch depth equal to half the beam height.

Material properties such as E, ϕ, and ψ, were selected within typical ranges for concrete. The beam geometry was fixed to a height of 150 mm and an overall span length of 450 mm to reflect standard laboratory flexural tests. For the 2D plane-stress finite element analysis, a unit width of 1 mm was used. A tensile strength (f_t') of 3.4 N/mm^2 was assumed and applied to produce nondimensional results.

Table 1. Ranges of variables for factorial

Variable	Desc.	Unit	Range
a/h	notch ratio	~	0.1-0.5
E	elastic modulus	N/mm^2	31,000-50,000
ϕ	total fracture energy	N/mm	0.100-0.250
ψ	kink-point ratio	~	0.200-0.500

Figure 5 presents the results of the factorial analysis for flexural strength versus Hillerborg's characteristic length (I_{ch}), used to characterize fracture based on the associated inputs and scaled to the input tensile strength (Hillerborg et al., 1976):

$$\frac{I_{ch}}{h} = \frac{\phi E}{h f_t'^2} \qquad (7)$$
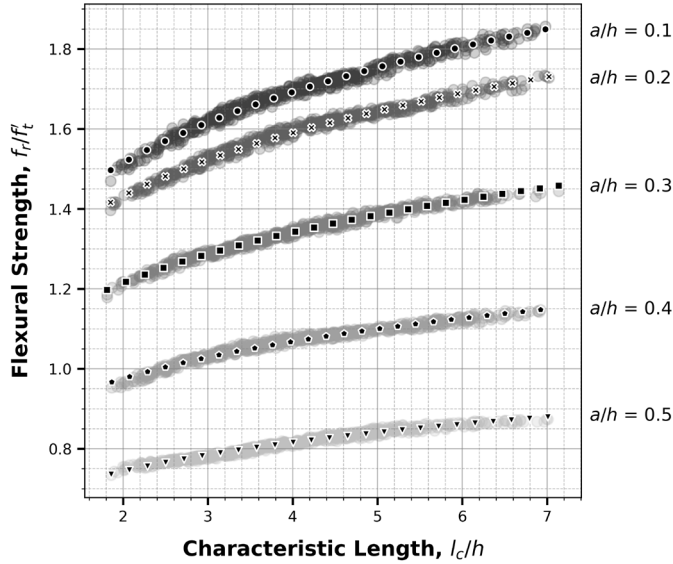
Figure 5. Nondimensional flexural strength versus characteristic length

This factorial reveals a minimum flexural strength of 2.50 N/mm^2 when the notch ratio is 0.5 with a characteristic length of 1.86 ($\phi = 0.102$ N/mm, $E = 31,000$ N/mm^2). A maximum flexural strength of 6.31 N/mm^2 is observed when the notch ratio is 0.1 with a characteristic length of 6.98 ($\phi = 0.248$ N/mm, $E = 48,800$ N/mm^2).

5 CONCLUSION

This paper presents an adaptation of the self-contained crack element developed by Sen & Khazanovich (2017), incorporating the notch ratio as a user input and modifying the solution procedure to enhance computational efficiency. The results demonstrate the expected influence of notch depth on the flexural strength. Furthermore, the analysis reveals that the model exhibits limited sensitivity to the kink-point ratio, ψ, suggesting that fracture in notched specimens is primarily governed by fracture energy in the bilinear CZM formulation and the four-point bending configuration.

The proposed approach enables rapid simulation, providing an opportunity to compare the results with experimental data from four-point bending tests for further calibration and validation of the model. However, the model still requires the total fracture energy (ϕ) as an input, necessitating nontrivial experimentational procedures involving precise monitoring of crack mouth opening displacement (CMOD). In the future, this demanding testing may be replaced by a simplified method to measure the flexural strength, provided a reliable correlation between fracture and other engineering properties is established.

6 REFERENCES

Bažant Z.P. & Li, Z. 1995. Modulus of Rupture: Size Effect due to Fracture Initiation in the Boundary Layer. *Journal of Structural Engineering* 121: 739-746.

Hillerborg, A., Modeer, M. & Peterson, P-E. 1976. Analysis of crack formation and crack growth in concrete by means of fracture mechanics and finite elements. *Cement and Concrete Research* 6: 773-782.

Park, K., Paulino, G. H., & Roesler, J. R. (2009). A unified potential-based cohesive model of mixed-mode fracture. *Journal of the Mechanics and Physics of Solids* 57(6): 891-908.

Rice J.R. & Levy, N. 1972. The part-through surface crack in an elastic plane. *Journal of Applied Mechanics* 39(1): 185-194

Roesler, J., Paulino, G. H., Park, K. & Gaedicke, C. 2007. Concrete fracture prediction using bilinear softening. *Cement & Concrete Composites* 29: 300-312.

Sen, S. & Khazanovich, L. 2021. A self-contained element for modeling crack propagation in beams. *Engineering Fracture Mechanics* 242: 107460.

Tompkins, D., Khazanovich, L. & Bolander, J.E. 2015. Lattice modeling of fracture in composite concrete pavements and overlays. *International Journal of Pavement Engineering* 16(1): 56-68.

Wittman, F.H. 2005. Modulus of Rupture, Tensile Strength, and Fracture Energy – An Application of Non-linear Fracture Mechanics. *Restoration of Buildings and Monuments* 11(3): 141-150.

Yin, Y., Qiao, Y. & Hu, S. 2019. Four-point bending tests for the fracture properties of concrete. *Engineering Fracture Mechanics* 211: 371-381.

Zienkiewicz, O., Taylor, R. L. & Taylor R. L. 2000. The finite element method: solid mechanics. *Butterworth-Heinemann*.

Influence of Embedment Length on the Bond Performance of mineral-impregnated Carbon Fiber Reinforcements in fine-grained Concrete

Jitong Zhao*,
Institute of Construction Materials, Technische Universität Dresden, 01062 Dresden, Germany

Borong Fan,
Institute of Construction Materials, Technische Universität Dresden, 01062 Dresden, Germany

Kai Zernsdorf*,
Department of Structural Engineering, Hochschule für Technik und Wirtschaft Dresden, 01069 Dresden, Germany

Marco Liebscher*,
Institute of Construction Materials, Technische Universität Dresden, 01062 Dresden, Germany

Viktor Mechtcherine
Institute of Construction Materials, Technische Universität Dresden, 01062 Dresden, Germany

ABSTRACT: Mineral-impregnated carbon fibers (MCFs) represent an innovative reinforcement system that integrates high-performance fibers with inorganic matrices, offering superior thermal resistance, enhanced bonding with cementitious substrates, improved cost efficiency, and remarkable versatility and multifunctionality for advanced structural applications. As a promising alternative to traditional steel and fiber-reinforced polymer (FRP) systems, MCFs address critical limitations in thermal performance and concrete's compatibility. A key factor influencing the engineering performance of reinforced concrete structures is the embedment length of the MCF reinforcement for reliable structural design. This study investigates the bond behavior of geopolymer (GP)-based MCF reinforcements in concrete numerically and experimentally, with a focus on the influence of embedment length. Experimental pullout tests revealed a bond stress–slip relationship (BSR) characterized by a linear elastic phase, exponential softening during debonding and stabilization at residual frictional stress levels. Longer embedment lengths improved energy absorption but resulted in reductions in maximum bond stress due to non-uniform stress distribution. Numerical simulations employing a spring element model accurately replicated experimental data, providing an efficient predictive tool for analyzing bond behavior. These findings establish a solid framework for optimizing the bond performance of MCFs and advancing their application in high-performance, resilient structural systems.

1 INTRODUCTION

Construction industry increasingly demands innovative materials and technologies to meet the challenges of durability, sustainability, and structural efficiency. Among the recent advancements, reinforced concrete structures utilizing internal carbon fiber (CF) reinforcements have emerged as a promising alternative to traditional building materials due to their superior mechanical properties and durability under various environmental conditions [1]. However, fiber-reinforced polymer (FRP) reinforcements faces critical limitations when exposed to elevated temperatures, especially during fire incidents. Polymer matrices that impregnate CFRP decomposes severely under heat, significantly reducing their load-bearing capacity and restricting their service temperature to 80 °C [2]. Additionally, weak chemical bonding between polymers and concrete further compromises the reliability of FRP systems [3].

To address these challenges, mineral-based impregnation materials, such as microcements and geopolymers (GPs), have been proposed as thermally resistant alternatives to polymer matrices. This approach has led to the development of mineral-impregnated carbon fibers (MCFs), which demonstrate remarkable thermal stability, retaining mechanical integrity up to 500 °C, and superior physical and chemical bonding with concrete matrices [4,5]. A more uniform crack distribution with narrower crack widths enhances the durability by minimizing the ingress of aggressive agents [6]. Furthermore, geometric flexibility of fresh MCFs enables their application in advanced robotic and additive manufacturing processes [7]. GPs, as impregnation material, combine properties typical of ceramics, polymers, and cements, allowing for rapid setting, high early strength, excellent thermal resistance and reduced carbon footprint. These materials are synthesized through an activated polycondensation reaction, often utilizing naturally occurring minerals such as metakaolin or industrial byproducts like fly ash [8].

A critical factor affecting the structural performance of MCF-reinforced systems is the embedment length of the reinforcement. Embedment length directly impacts pullout behavior, which is a key indicator of bond performance and force transfer efficiency. Optimizing embedment length ensures the full utilization of the tensile capacity of the reinforcement, preventing premature debonding or pullout [9]. The bond-slip relationship (BSR), a parameter that captures the interaction between reinforcement and concrete, governs the pullout behavior of MCFs. Unlike traditional reinforcements, MCFs exhibit unique bonding characteristics due to their improved compatibility with the cementitious substrate. Numerical and experimental investigation of their BSR provides valuable insights into the force transmission mechanism and helps establish performance-based criteria for the reliable design in construction.

This study is motivated by the need to address these gaps and investigate how varying embedment lengths affect the pullout behavior of GP-impregnated MCFs in concrete. Experimental and numerical analyses were conducted to evaluate bond-slip behavior and develop performance-based design criteria for MCF-reinforced systems. Numerical modeling using a spring element approach was applied to simulate the constitutive debonding process, and the results were validated against experimental data.

2 MATERIALS AND METHODS

Materials and experimental tests

MCFs were produced using commercial carbon yarn (SIGRAFIL® C T50–4.4/255-E100, SGL Group, Germany) with a metakaolin (MK)-based geopolymer (GP) impregnating suspension via a custom-designed pultrusion system at the Institute of Construction Materials, TU Dresden. A detailed manufacturing process can be found in [10]. GP concrete was composed of MK, a potassium silicate activator, fine and rough sands. The mix design and mixing procedure are described in [6]. Pull-out specimens consisted of a testing block (t × 80 × 80 mm³, t = 10–40 mm), a free length of 120 mm and an anchorage block (90 × 80 × 80 mm³). After 28 days of curing under controlled conditions, pullout tests were conducted using a servo-hydraulic machine, with displacements recorded at the pullout and pull-in sites.

Numerical Models

The numerical analysis employed a spring element model [11] to simulate MCF pullout behavior in GP concrete systems with varying embedment lengths. The accuracy and applicability of this model were validated by comparing its results with experimental data. The bond behavior of MCF reinforcement was characterized using the global BSR, which describes the average bond stress as a function of the slip. The bond stress was assumed to be uniformly distributed along the bond length.

The spring element model was developed based on the fib Model Code 2010, which uses an exponential representation in the ascending branch and a linear decline for the descending branch of the BSR. This formulation is well-suited for modeling the bond behavior of smooth reinforcement elements. Parameters for the spring element model were calibrated by approximating the global BSR derived from experimental observations. However, the assumption of uniform bond stress distribution is valid only for embedment lengths shorter than five times the reinforcement diameter. For longer embedment lengths, stress non-uniformity introduces significant differences between the relative displacements at the loaded and free ends of the reinforcement. To address this, a local BSR approach was implemented to capture the bond stress variation along the embedment length. This approach employed a differential equation with closed-form solutions previously established in the literature [9]. The geometric configuration for the simulations consisted of an MCF reinforcement embedded at one end within a concrete matrix block, as illustrated in **Figure 1**. The stiffness of the concrete block was assumed to be significantly higher than that of the yarn–concrete interface, ensuring its negligible influence.
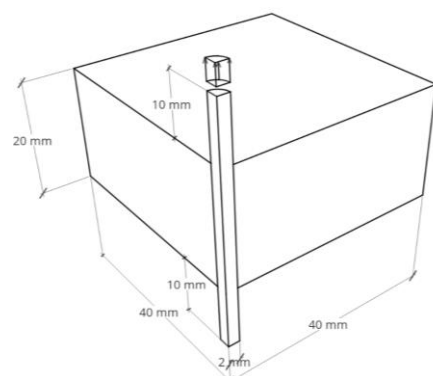
Figure 1: Geometric setup of the numerical model.

To ensure accurate simulation of the frictional pullout phase, a 10 mm length was maintained at both the pullout and load-free ends. To enhance computational efficiency, the simulations exploited symmetry by modeling only a quarter of the structure. A parametric investigation was also conducted to evaluate the mechanical response of yarn pullout behavior across various embedment lengths.

3 DISCUSSION

Figure 2 illustrates the representative bond shear stress–slip curves for MCFs at varying embedment lengths. In the initial phase of the BSR, the bond shear stress increases linearly with slip, indicating an elastic response. As the bond stress approaches its maximum value, marking the onset of debonding, the curve's slope progressively diminishes to zero. Beyond this peak, the BSR curve exhibits a sharp decline, reflecting a rapid loss of bond strength, before stabilizing at a near-constant residual stress level. This behavior signifies a transition in the primary bonding mechanism from adhesive bonding to frictional resistance as debonding progresses.
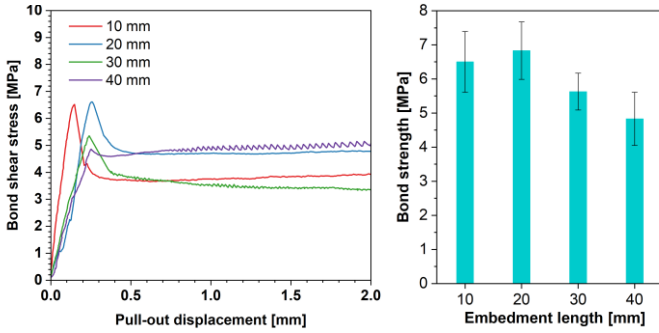
Figure 2: Experimental mean stress-slip curves for various bond lengths (left) and the development of bond strength to the reinforcement embedment length (right).

The analysis of the variation in bond strength as a function of reinforcement embedment length reveals a gradual reduction in maximum bond shear stress with increasing bond length, attributed to heightened non-uniformity in stress distribution along longer embedment lengths. This non-uniformity leads to a decrease in the average calculated bond stress. These findings emphasize the importance of optimizing embedment length to balance stress distribution and ensure effective force transfer.

Further numerical analysis using a nonlinear spring model reveal BSR curves at the debonding interfaces. Unlike the cohesive zone model (CZM), which requires detailed physical parameters, the nonlinear spring model directly establishes the local BSR, necessitating an analytical representation of bond behavior. To achieve a more precise depiction of the local BSR, the analytical model developed by Dai *et al.* [11] was applied. An additional exponential function was incorporated into the model to capture interactions between debonded surfaces during the frictional sliding phase. The implemented model demonstrated good agreement with experimental data, effectively replicating the experimental BSR

curves. The proposed model is mathematically defined by the following equation:

$$\tau(s) = 2G_f \cdot a \cdot \left(exp(-a \cdot s) - exp(-2a \cdot s) \right) + b \left(1 - exp(-c \cdot s) \right)$$

where τ represents the bond shear stress, s denotes the slipping distance between surfaces, and a, b, and c are parameters governing the exponential modification of the curve.

Figure 3 compares the mean bond stress–slip curves derived from experimental investigations with those obtained from numerical simulations using the proposed spring element model. Across all investigated embedment lengths, the numerical results showed strong agreement with experimental data, underscoring the high accuracy and predictive capabilities of the models. These results highlight the models' ability to reliably represent failure mechanisms in novel MCF systems.
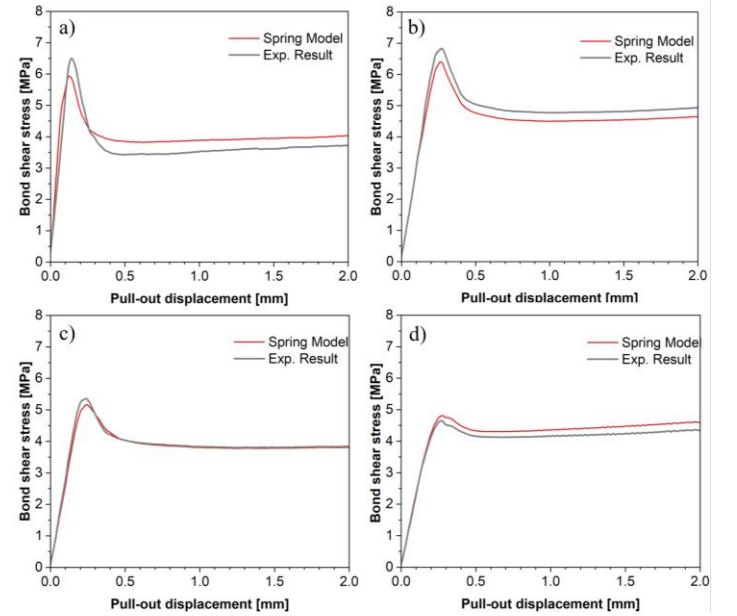
Figure 3: Numerical results of a) 10 mm, b) 20 mm, c) 30 mm and d) 40 mm embedment length for MCFs in comparison with experimental results.

4 CONCLUSIONS

This study investigated experimentally and numerically the bond behavior of GP-based MCF reinforcement in GP concrete systems with varying embedment lengths. A simple method to define the local BSR of MCF-concrete interfaces is proposed, which can be derived from only a few parameters of the pull-out force-slip curve data. The interfacial fracture energy crucially affects the interfacial load carrying capacity and the configuration of the BSR. The bond stress–slip behavior of MCF is characterized by an initial steep ascending stage and a subsequent exponential softening behavior due to the de-

lamination from the surrounding concrete matrix. Following the sudden drop of the peak stress, the BSR curves finally reach an almost stabilization at a constant stress level. With the considered embedment lengths, local bond models show better agreement with experimental results than global models.

Longer embedment length increases the energy absorption but reduces bond stress and modulus due to the nonlinear stress-strain behavior of the reinforcement. Numerical simulations based on both a local bond shear-slip law and a physical parameter-defined cohesive traction-separation law accurately replicated the experimental pullout tests, predicting position-dependent bond stress distribution. The developed numerical models simplify the analysis of bond behavior and provide a framework for optimizing material performance, paving the way for advanced structural applications of carbon concrete composites.

5 ACKNOWLEDGMENTS

6 REFERENCE

[1] Liu T, Liu X, Feng P. A comprehensive review on mechanical properties of pultruded FRP composites subjected to long-term environmental effects. Compos Part B Eng 2020;191:107958.

[2] Hamad JAR, Johari MAM, Haddad RH. Mechanical properties and bond characteristics of different fiber reinforced polymer rebars at elevated temperatures. Constr Build Mater 2017;142:521–35.

[3] Nadiv R, Peled A, Mechtcherine V, Hempel S, Schroefl C. Micro- and nanoparticle mineral coating for enhanced properties of carbon multifilament yarn cement-based composites. Compos Part B Eng 2017;111:179–89.

[4] Schneider K, Michel A, Liebscher M, Terreri L, Hempel S, Mechtcherine V. Mineral-impregnated carbon fibre reinforcement for high temperature resistance of thin-walled concrete structures. Cem Concr Compos 2019;97:68–77..

[5] Zhao J, Zhao D, Liebscher M, Yin B, Mohammadi M, Butler M, et al. Temperature-Dependent Pullout Behavior of Geopolymer Concrete Reinforced with Polymer- or Mineral-Impregnated Carbon Fiber Composites: An Experimental and Numerical Study. ACS Sustain Chem Eng 2023;11:8474–86.

[6] Zhao J, Ahmed AH, Liebscher M, Bartsch A, Ivaniuk E, Butler M, et al. Thermomechanical behavior of textile-reinforced geopolymer concrete based on mineral-impregnated carbon-fibers (MCFs) composites. Cem Concr Compos 2024:105555.

[7] Mechtcherine V, Michel A, Liebscher M, Schneider K, Großmann C. Mineral-impregnated carbon fiber composites as novel reinforcement for concrete construction: Material and automation perspectives. Autom Constr 2020;110:103002.

[8] Zhao J, Trindade ACC, Liebscher M, Silva F de A, Mechtcherine V. A review of the role of elevated temperatures on the mechanical properties of fiber-reinforced geopolymer (FRG) composites. Cem Concr Compos 2023;137:104885.

[9] Benmokrane B, Tighiouart B, Chaallal O. Bond strength and load distribution of composite GFRP reinforcing bars in concrete. ACI Mater J 1996;93:246–53.

[10] Zhao J, Liebscher M, Michel A, Junger D, Trindade ACC, de Andrade Silva F, et al. Development and testing of fast curing, mineral-impregnated carbon fiber (MCF) reinforcements based on metakaolin-made geopolymers. Cem Concr Compos 2021;116:103898.

[11] Zernsdorf K, Mechtcherine V, Curbach M, Bösche T. Numerical simulation of the bond behavior of mineral-impregnated carbon-fiber reinforcement. Struct Concr 2024;25:2447–64.

[12] Dai, J., Ueda, T., & Sato, Y. (2006). Unified Analytical Approaches for Determining Shear Bond Characteristics of FRP-Concrete Interfaces through Pullout Tests. Journal of Advanced Concrete Technology, 4(1), 133–145.

2.1

MODELING AND EXPERIMENTAL EVALUATION OF MOISTURE DAMAGE IN ASPHALT MIXTURES

Clustering mechanisms of calcium species in bituminous medium: an insight to physical effects of hydrated lime filler via molecular dynamics

Javier A. Grajales
Universidad Tecnológica de Panamá, Panama City, Panamá
Texas A&M University, College Station, Texas, United States of America

Dallas N. Little
Texas A&M University, College Station, Texas, United States of America

This research work addresses the behavior of a hydrated lime-filled bituminous medium rich in carboxylic acids, specifically dodecanoic acid, to investigate mechanisms underlying known beneficial effects of improvement in performance and durability. Classical molecular modeling is implemented as the theoretical basis. This includes the use of molecular dynamics simulations and mean squared displacement (MSD) dynamic analysis to characterize the molecular mobility of the bituminous moieties. Significant improvement mechanisms occur due to the presence of calcium ions from hydrated lime. These include the agglomeration and formation of large clusters of calcium carboxylate complexes as well as the overall reduction of the mobility of the bituminous system. The self-diffusion coefficient determined from the MSD dynamic analysis is presented as numerical evidence of these, which decreases by two orders of magnitude when comparing the unreacted carboxylic acid rich system to the reacted hydrated lime-filled system.

1 INTRODUCTION

1.1 *Hydrated lime and the problem of moisture in bituminous materials*

Moisture damage is one of the leading causes of degradation of bituminous composites worldwide. The more humid the region, the more oppressive the climate is causing the bituminous material, often pavements, to undergo a deleterious moisture flow cycle that in extreme cases visibly ends with the evaporation of the moisture upwards from the pavement course itself. Most bituminous pavements suffer from this issue due to a common disparity between the polarity of the bituminous phase with that of the surface of aggregates in the mixture (or fines if they have been used as fillers). In most cases, the bituminous surface of contact is very apolar whereas the surface of contact of the mineral aggregates is highly polar. Thus, a high mismatch between the latter one and the former exists. As a result, the polar mineral aggregate surface has a net preference for adsorption of water in-between the bitumen surface. This preference of the mineral aggregate for water adsorption finally ends up in reduction of adherence and detachment of the bitumen-mineral aggregate binding interface.

As a classical measure of remediation for the moisture problem in bituminous materials, hydrated lime has been used for a long time. Much is known about the positive effects (Little & Petersen 2005) that mixing hydrated lime with bituminous mixtures has on keeping the binding interface of bitumen and mineral strong and durable. For one or several rea-

sons, hydrated lime has the capability of inhibiting bituminous binding species that are prone to forming weak adherence with the mineral aggregate surface, and thus may easily undergo replacement by moisture. However, the causative mechanisms of this ability of hydrated lime have not yet been fully understood as to assert in a simple way why the inhibitory phenomenon occurs or in some cases the selective fashion in which it occurs. This is the motivation of this research work and its methods of molecular analysis, to define: a) how the mechanisms occur and b) understanding the selectivity and impact of their occurrence upon the type of species in the physical systems of study.

1.2 *Approaches to defining the active role of hydrated lime mechanisms in bitumen*

Throughout the years several approaches have been attempted to define the effects and possibly the mechanisms of action of hydrated lime in bituminous materials. Within experimental ones, rheological (Lesueur & Little 1999) and mechanical characterizations are abundant and as well are analytical chemistry techniques that combine concentration measurements and spectroscopy (Petersen & Plancher 1981, Lesueur et al. 2013). However, modeling approaches have seldom been used due to the length scale at which the interaction of hydrated lime occurs with the bitumen and the nature of the interaction. Recently, the nature of such interaction was modeled at the atomistic scale using both classical dynamics and quantum chemical models (Grajales et. al. 2020). They were able to prove two ma-

jor facts in defining the nature of the interactions of hydrated lime with bitumen: a) the improvement in adherence when hydrated lime is present in the system is not of a physical nature (via surface group interactions), and b) hydrated lime selectively reacts chemically with some bitumen moieties. Especially, those in which a hydrolysis of a carboxylic group and the formation of a calcium complex can develop. In this study, the authors seek to define further ripples caused physically to the hydrated lime-bitumen material matrix once the reactions have occurred and calcium complexes have formed via classical molecular dynamics of larger, "already reacted" systems.

2 MOLECULAR MODELING METHODOLOGY

2.1 *Computational overview*

The theoretical basis used for modeling computations at the molecular level is classical molecular mechanics. Calculations of geometry optimization and molecular dynamics are presented. Based on results from these simulations, post-processing calculations of mean square displacement dynamic analysis are conducted. In this way, it is possible to determine the dynamic behavior of selected molecular species quantifying their level of movement depending on the aggregation states they develop across the simulations time spans. All the preparatory cell building steps and simulations are conducted using the modeling suite 3DS Biovia Materials Studio (3DS MS). Specifically, the Forcite module is used, which allows conducting classical molecular mechanics simulations with customized force fields. The force field used for all simulations is the INTERFACE force field (Heinz et al. 2013). The INTERFACE force field is used because of its versatility to perform calculations with parametrization for both inorganic species such as those involving the alkaline earth calcium ion and hydrated lime as calcium hydroxide, $Ca(OH)_2$.

2.2 *Einstein's theory of quantification of the motion of molecules via the mean square displacement (MSD)*

It is common to observe the quantification of the motion of matter in the continuum via diffusion laws. This way of treating the motion of matter is correct and highly versatile to simulate and predict transport on most phenomena in nature. However, when trying to describe the uniquity of the motion of building units of matter, molecules and atoms, it falls short. This occurs because every molecule composed of atoms is a discrete entity and has its own geometry that is governed by intramolecular and intermolecular forces. Such uniquity becomes even more preeminent when the size of molecules is such that a point without volume or area does not represent their unique dynamic behavior as is the case of materials composed of macromolecules.

Bitumen is such a material, composed of molecules of various sizes and macromolecules such as the asphaltenes. Consequently, the diffusion of a non-reactive phase within asphalt as a dispersant is intricate. However, more intricate is the diffusion of a reactive phase. Especially, when the phase is small enough to migrate to regions or sites prone to react in asphaltene macromolecules. When this happens, the behavior of a single molecule is partitioned, and domains of different physical and chemical behavior are formed. Some domains respond with dynamics that are dictated by the ongoing reaction whereas some other domains remain in motion as they normally would, with perhaps some indirect effect of the reactive region. For this reason, for example, part of a molecule may be restrained moving slowly whereas the other part moves faster. This example is an exact depiction of the scenario when hydrated lime is added as a reactive filler in bitumen. Upon exposure to hydrated lime, some bitumens react chemically. For those with carboxylic heteroatomic sites the reaction is swift. Through hydrolysis, a hydrogen is stripped away of the -COOH carboxylic group and calcium forms a carboxylate complex product $-Ca(COO)_2$ and releasing two water molecules (Grajales et al. 2020). To simulate the diffusive effects of such complex scenario, a different theory is needed, and such theory is fulfilled with Einstein's doctoral dissertation work on Brownian movement (Einstein 1906).

According to Einstein's diffusion equation, the motion of a point-like discrete particle can be quantified as the average accumulated sum of its squared displacement over a time span of interest. Einstein applied this concept to the movement of molecules, where the point-like particle is each atom composing the molecule. Thus, he formulated the parameter now commonly denominated as the mean squared displacement (MSD) in angstrom squared units ($Å^2$), which defines the self-diffusion coefficient of a molecule or set of molecules (D) as the limit when a time differential tends to infinity of the averaged squared displacement, MSD, with respect to a delta time step (Equation 1).

$$D = \frac{1}{6} \lim_{\Delta t \to \infty} \frac{d\text{MSD}}{d\Delta t} \quad (1)$$

where D is the self-diffusion coefficient of a chemical species, Δt is the time step of motion recorded in a molecular dynamics simulation, and the 1/6 quotient corresponds to the degrees of freedom that can occur in atomic motion over a given three-dimensional space.

With this approach to diffusion, it is conspicuous that the various levels of motion of diverse portions of a single macromolecule or set of molecules can be accounted for depending on their state of restraint or

freedom of motion. Therefore, accounting for the uniquity of phenomena such as that when hydrated lime reacts with specific portions of bituminous moieties.

2.3 *Models of the bitumen-hydrated lime system constituent species*

The models chosen for this study represent the aliphatic phases present in bitumen. Specifically, n-docosane linear chains with a carboxylic end were modeled. The purpose of choosing these moieties is bifold: on one hand these are the most mobile moieties in bitumen if considering the bitumen as a mixture of phases such as it is conceived by the SARA fraction scheme (Saturates, Aromatics, Resins, Asphaltenes) so a pronounced change in their level of motion is expected, and secondly, these are the weakest portion of most bituminous phases so strengthening due to restraining and agglomeration would be more significative in these aliphatic chains (Figure 1).
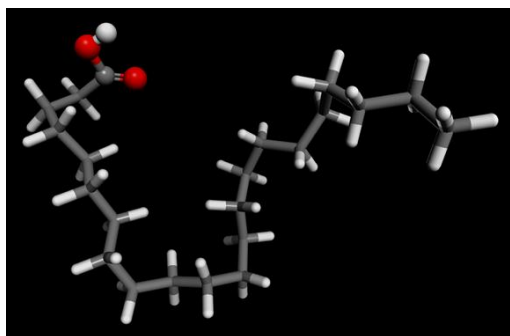
Figure 1. Docosane chain with carboxylic head (docosanoic acid) used as molecular model of the aliphatic phase in bitumen (oxygen atoms represented in red, hydrogen atoms in white and carbon atoms in grey).

With respect to the hydrated lime phase, already dissociated calcium ions were introduced to form a "reacted" complex (Figure 2). After every species was relaxed via geometry optimization, supercells were built using the Amorphous Cell module that is part of the 3DS MS suite system. The packed supercells were then relaxed via geometry optimization to lower the internal configuration energy as a preparative step.
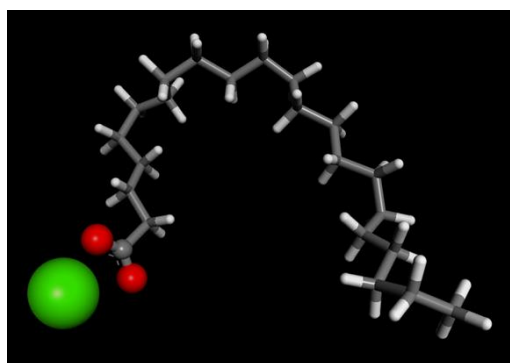
Figure 2. Docosane chain with calcium complexed head (calcium carboxylate complex) used as molecular model of the hydrated lime reacted aliphatic phase in bitumen (calcium ion represented in green, other atom colors same as Figure 1).

Finally, the relaxed supercell systems were used as input for the classical molecular dynamics simulation through which the agglomeration effects were monitored over the modeled dynamics trajectory length.

3 RESULTS

3.1 *Overview of molecular dynamics trajectories*

Molecular dynamics simulations were conducted on supercell systems built for the unreacted and reacted hydrated lime filled system. After relaxation of the supercells, a first trajectory was conducted using the NPT ensemble (constant number of molecules, constant pressure, constant temperature) for a time span of 25 ps. The system was set to stabilize to standard conditions (1 atm of pressure and 298.15 K temperature). The Berensden barostat was used to reach equilibrium without distorting the cell shape. A density of 0.9 g/cm^3 was obtained, which is representative of that of bitumen. Temperature was monitored with a Nose thermostat. After, NPT equilibration, NVT (constant number of molecules, constant volume, constant temperature) trajectories were set up to monitor the agglomeration states of the different systems (unreacted and calcium-reacted) for 50 ps. Figures 3 and 4 illustrate the final states of the unreacted and calcium-reacted bitumen systems. The figures do not show the carbon atom chains for comparison of the differences in agglomeration states caused when calcium complexes from hydrated lime filling form.

Figure 3. Unreacted docosanoic acid supercell system after NVT molecular dynamics simulation. Supercell illustrates carboxylic heads with a magenta highlight.

3.2 *Mean square displacement (MSD) analysis*

The MSD dynamic analysis methodology was conducted on both unreacted and calcium-reacted filled bitumen aliphatic systems. The 50 ps NVT MD trajectories were analyzed. The resulting MSD curves were plotted, and self-diffusion coefficients were calculated. A significant difference (of nearly two orders of magnitude) was found between the self-diffusion coefficients of the unreacted (D_{COOH} = 2.11×10^{-2} Å^2/ps) and calcium-reacted (D_{Ca} = 5.62×10^{-3} Å^2/ps) systems. Figure 5 illustrates the MSD curves obtained along with the fit for the self-diffusion coefficients.

"Looking inside"
(carbon chains hidden)

Large conglomerates of Ca^{2+} complexes behave as less mobile "hardened inclusions"
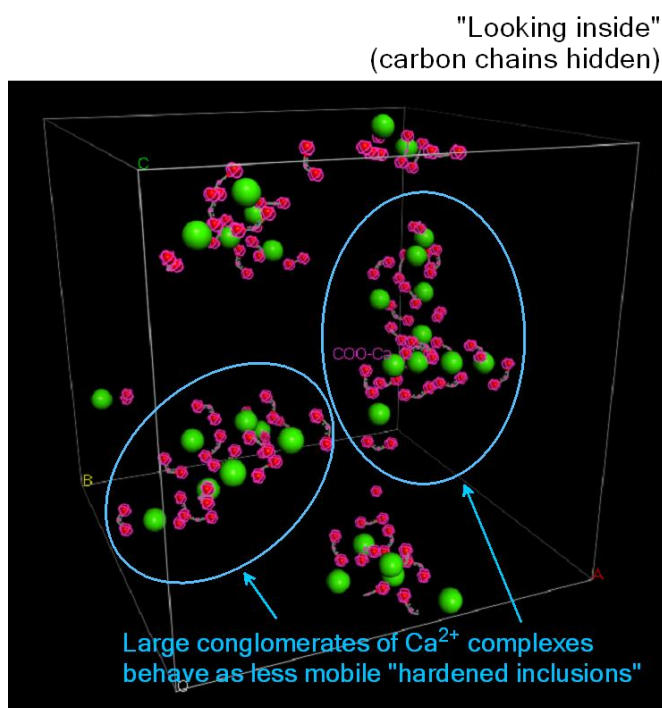
Figure 4. Reacted hydrated lime-filled supercell system after NVT molecular dynamics simulation. Agglomeration of calcium carboxylate complexes is visually significant compared to the docosanoic acid unreacted system (Figure 3). Calcium ions shown in green, and carboxylate ligands with a magenta highlight.
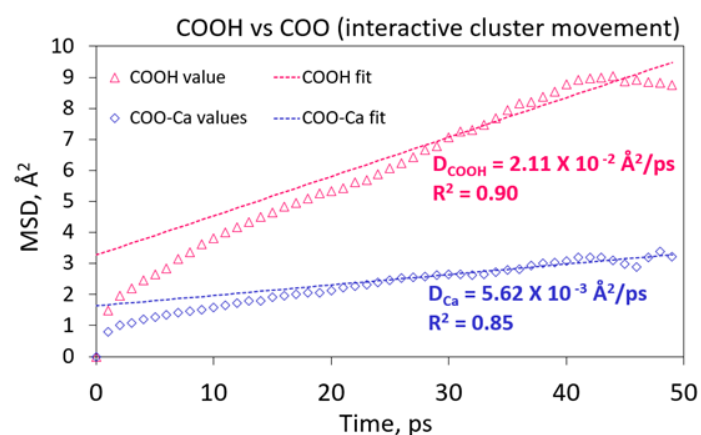
Figure 5. MSD curves for the unreacted docosanoic acid system and the reacted hydrated lime-filled system composed of calcium carboxylate complexes.

4 CONCLUSIONS

This research study proves that the addition of hydrated lime to the aliphatic phase of a carboxylic acid rich bitumen has a profound impact on the dynamics of the functional groups composing the bituminous matrix. More specifically, the results show that a larger physical effect occurs when calcium ions from hydrated lime populate the system after the reaction occurs because large clusters of calcium carboxylate complexes form in contrast with the unreacted docosanoic acid bituminous system, which shows to be significantly more dispersed and mobile. The nearly two-order of magnitude difference found in the self-diffusion coefficient of the systems is a numerical proof of a reduction in molecular mobility, which supports the experimental evidence in the literature of a stiffening or hardening effect due to the calcium inclusions formed upon the addition of hydrated lime.

5 REFERENCES

Einstein, A., 1906. A new determination of molecular dimensions. Annln., Phys., 19, pp.289-306.

Grajales, J.A., Perez, L.M., Schwab, A.P. and Little, D.N., 2021. Quantum chemical modeling of the effects of hydrated lime (calcium hydroxide) as a filler in bituminous materials. ACS omega, 6(4), pp.3130-3139.

Heinz, H., Lin, T.J., Kishore Mishra, R. and Emami, F.S., 2013. Thermodynamically consistent force fields for the assembly of inorganic, organic, and biological nanostructures: the INTERFACE force field. Langmuir, 29(6), pp.1754-1765.

Lesueur, D., Petit, J. and Ritter, H.J., 2013. The mechanisms of hydrated lime modification of asphalt mixtures: A state-of-the-art review. Road materials and pavement design, 14(1), pp.1-16.

Lesueur, D. and Little, D.N., 1999. Effect of hydrated lime on rheology, fracture, and aging of bitumen. Transportation Research Record, 1661(1), pp.93-105.

Little, D.N. and Petersen, J.C., 2005. Unique effects of hydrated lime filler on the performance-related properties of asphalt cements: Physical and chemical interactions revisited. Journal of Materials in Civil Engineering, 17(2), pp.207-218.

Petersen, J.C. and Plancher, H., 1981. Quantitative determination of carboxylic acids and their salts and anhydrides in asphalts by selective chemical reactions and differential infrared spectrometry. Analytical Chemistry, 53(6), pp.786-789.

Impact of water on asphalt mortars with aggregates of different chemical composition

L. Leon
Universidad de los Andes, Department of Civil and Environmental Engineering, Bogotá D.C., Colombia.

S. Caro
Universidad de los Andes, Department of Civil and Environmental Engineering, Bogotá D.C., Colombia.

X. Sanchez
University of New Brunswick, Department of Civil Engineering. Fredericton, NB, Canada.

ABSTRACT: This work examines the influence of aggregate mineralogy and water exposure on the rheological behaviour of asphalt mortars. Three different mortars, fabricated with a single asphalt binder and three types of aggregates (quartzite, granodiorite, and serpentinite) with the same gradation, were tested after immersion in water for 0, 10, 60, and 160 days. Results show that aggregate mineralogy significantly affects performance under moisture. Quartzite mortars hardened steadily due to binder oxidation and the inert nature of the aggregates. Granodiorite mortars initially stiffened but softened over time. Serpentinite mortars showed marked stiffness reductions after 60 days, indicating water-induced damage. In summary, aggregate mineralogy plays a critical role in the early and long-term moisture resistance of asphalt mortars.

1 INTRODUCTION

Moisture damage in asphalt mixtures is characterized by the progressive degradation of its mechanical properties due to the presence of water. This degradation phenomenon results from loss of adhesion at the asphalt-aggregate interface and a change in the cohesive properties of the asphalt binder (Kiggundu & Roberts, 1988). Addressing moisture damage is crucial to developing durable and sustainable pavements.

Despite extensive research, the mechanisms behind moisture damage are not fully understood. Several theories, including boundary layer, mechanical, electrostatic, chemical and thermodynamic theories, have been proposed to explain these mechanisms (Hefer &Little, 2005; Kiggundu & Roberts, 1988; Rice, 1959; Tarrer & Wagh, 1991; Bagampade et al., 2004). However, there is no comprehensive theory that fully explains the processes involved, so the causal mechanisms remain somewhat speculative (Bagampade et al., 2004).

There is consensus that the chemical composition and mineralogy of aggregates significantly influence the quality of adhesion between binder and aggregate under moisture conditions (Bagampadde et al., 2006; Cala & Caro, 2021; Hefer & Little, 2005; Rice, 1959). Studies have found strong correlations between silicon dioxide (SiO_2) content in the aggregates and the susceptibility to moisture damage, while ferric oxide (Fe_2O_3) and calcium oxide (CaO) promote more moisture-resistant adhesive bonds between aggregate and asphalt (Cala et al., 2019, 2021).

While significant progress has been made in understanding the moisture degradation of the adhesion between binder and aggregates, less attention has been paid to how moisture affects the cohesive properties of asphalt binders, mastics or mortars. Recognizing that pavement durability depends on both adhesion and cohesion conditions—and that moisture affects both equally (Hicks et al., 2003)—it becomes essential to explore both aspects simultaneously.

This study aims to improve understanding of moisture damage by examining the effect of water on the mechanical response of asphalt binders and mortars, focusing specifically on the role of aggregate mineralogy in mortar samples. This work complements previous efforts that have explored the change in the cohesive properties of mastics with different aggregates subjected to moisture conditions (Leon & Caro, 2023).

Mortar samples were prepared using a 60-70 (1/10 mm) penetration asphalt binder and fine aggregates with three different mineralogical compositions. The asphalt binder and mortar samples were subjected to four moisture conditioning processes: dry condition (environmental conditions) and immersion in water for 10, 60, and 160 days. The linear viscoelastic properties of the materials were quantified using dynamic shear rheometer (DSR) tests, and Fourier transform infrared spectroscopy (FTIR) was performed on the binder samples to track the chemical changes induced by water exposure.

By studying the changes caused by water in the properties of asphalt binder and mortar separately, it

becomes possible to distinctly analyse the effect of water on pure asphalt and the combined effect on the asphalt-aggregate system within the mortar. This approach provides a comprehensive understanding of moisture-induced degradation affecting both binder cohesion and binder-aggregate adhesion, addressing the lack of detailed information on how moisture affects these critical components.

2 MATERIALS AND METHODS

An asphalt binder with a penetration grade of 60–70 (mm/10) was selected along with three aggregates with different chemical compositions: serpentinite (SPT), quartzite (QTZ), and granodiorite (GRT).

The use of a single asphalt binder allows for the isolation of the effect of aggregate chemistry. The selected aggregates cover a different lithological spectrum, ranging from a mafic rock (SPT) to a felsic rock (QTZ), and including an intermediate rock (GRT). Aggregates had low porosity and similar specific gravities to ensure comparable physical properties for fair comparisons in the mortar designs. Specific gravity tests performed following the ASTM D854-10 resulted in values of 2.73, 2.75, and 2.74 for SPT, QTZ, and GRT, respectively. Additionally, X-ray fluorescence (XRF) testing was conducted in accordance with ISO 12677-2011 to determine the chemical compositions of the rocks. The results are presented in Table 1, showing the percentage by weight of the main oxides present in each aggregate.

Table 1. Chemical composition of the aggregates studied (% by weight total).

| Oxide | Aggregate | | |
	QTZ	GRT	SPT
	% Weight total		
SiO_2	98.18	65.75	40.21
Al_2O_3	1.09	15.26	7.81
Fe_2O_3	0.09	4.09	10.24
MgO	0.01	2.45	23.45
CaO	0.06	3.77	6.35
TiO_2	0.07	2.68	0.42
P_2O_5	0.01	0.14	0.04
SO_3	0.00	0.01	0.23
Volatiles lost after igniting	0.46	1.63	9.29
Other basic oxides	0.07	4.14	1.96

By selecting aggregates with distinct chemical and mineralogical properties but similar physical characteristics, the study aims to evaluate the influence of aggregate chemistry on the moisture-induced mechanical response in asphalt mortars.

2.1 *Design and fabrication of mortar samples*

A representative mortar of the fine fraction of a dense-graded hot dense asphalt mix with maximum nominal aggregate size of 19 mm was designed and prepared. The mortar includes the binder and the material passing through the #16 sieve (1.18 mm). The asphalt binder content of the mortars was 9.75% and they were fabricated at a target air void content of 10%.

The maximum theoretical specific gravity (G_{mm}) of each type of mortar, computed according to the AASHTO T 209–12 standard, was 2.38 for SPT, 2.41 for QTZ, and 2.43 for GRT.

Cylindrical specimens measuring 50 mm in height and 13 mm in diameter were fabricated individually using a metallic mould. The asphalt, aggregates, and steel mould were preheated and mixed at 160 °C. The material was then subjected to short-term aging for two hours to simulate the natural aging during the production and placement of asphalt mixtures.

The loose mortar was then poured into the preheated mould and compacted in a press at a pressure of 0.80 MPa for 45 minutes to achieve the desired density and void content, using the procedure proposed by Caro et al. (2011). This method was calibrated to ensure a final air void content between 9.7% and 10.3%. Finally, metal holders were placed at the ends of specimens to facilitate their installation in the rheometer.

2.2 *Moisture conditioning*

Binder and mortar samples were submerged in distilled water at room temperature, avoiding the incorporation of high temperatures or pressures since they could act as catalysts for more complex chemical reactions that would hinder the isolated effect of water in the materials. The selected conditioning times were 0, 10, 60 and 160 days.

2.3 *Fourier Transform Infrared Spectroscopy characterization of the asphalt binder*

To determine the changes in the chemical composition of the asphalt binder samples, FTIR testing using a Total Attenuated Reflectance Cell (FTIR-TARA) was performed at each conditioning period.

2.4 *Frequency and temperature sweep tests*

Four replicates were tested at each conditioning period (i.e. 0, 10, 60, and 160 days in water) to determine the linear viscoelastic properties of asphalt and mortars. The oscillatory tests consisted of frequency and temperature sweep procedures under a controlled percentage angular strain of 0.01 for the asphalt binder and 0.00075 for the mortar. These strain values were selected after verifying that the materials were in the linear viscoelastic range based on the results of oscillatory shear deformation sweep test.

The tests were performed in a temperature range between 25°C and 65°C with steps of 10°C and frequencies between 1 and 30Hz with steps of 1 Hz using an TA AR2000ex rheometer with 8 mm parallel

plate geometry for the asphalt and with a solid geometry for the mortar specimens.

3 RESULTS AND DISCUSSION

3.1 *Linear viscoelastic and chemical changes of the asphalt binder with water conditioning time*

The master curves of the average dynamic shear modulus ($|G^*|$) of the asphalt binder at a reference temperature of 25°C in the different water conditioning periods are presented in Figure 1.
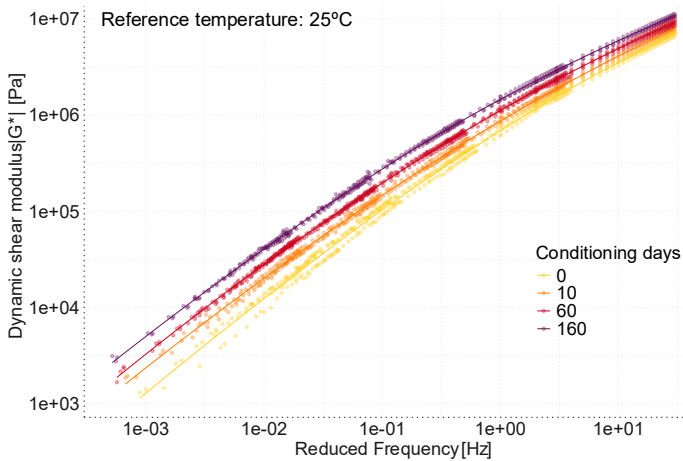
Figure 1. Master curves of $|G^*|$ of the asphalt binder at 25°C

The results show a significant increase in stiffness with increasing conditioning time. Specifically, compared to the unconditioned samples, the average modulus increased by 16.7% after 10 days, 39.8% after 60 days, and reached 69.1% after 160 days of water immersion. Statistical testing at a significance level of 0.05 to evaluate the effect of conditioning time on the dynamic modulus confirmed that these changes were significant, particularly for the conditioning periods of 60 and 160 days (p-value < 0.01 and p-vale < 0.001, respectively).

Chemical analysis using the FTIR-TARA results revealed significant changes in the functional groups of the asphalt binder after conditioning in water for 0, 10, 60, and 160 days, as observed in Figure 2.
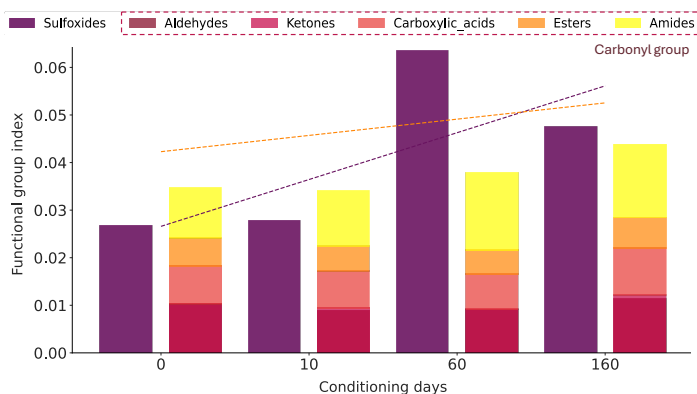
Figure 2. Functional group indices of the conditioned asphalt

Data show a progressive increase in the total carbonyls (aldehydes, ketones, carboxylic acids, and esters) and sulfoxides groups, with growth rates of 0.241% and 0.776% per day, respectively. Total carbonyls exhibited the highest correlation with the dynamic shear modulus (r=0.94), followed by amides (r=0.81) and sulfoxides (r=0.64), indicating that oxidation and the formation of polar compounds are the primary factors responsible for the observed hardening.

3.2 *Linear viscoelastic changes of the asphalt mortars*

Figure 3 illustrates the evolution of the mean modulus values ($|G^*|$) for the three mortars (QTZ, SPT, and GRT) subjected to water conditioning. The error bars represent the 95% confidence interval of the mean
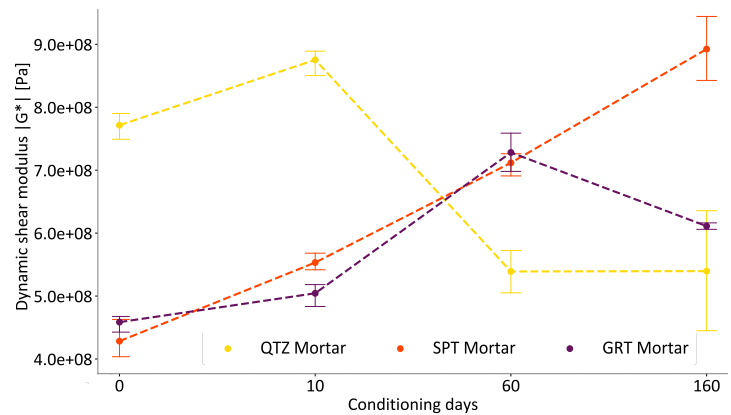
Figure 3. Variation of the dynamic shear modulus ($|G^*|$) as a function of conditioning time in QTZ, SPT and, GRT mortars

For the mortar with QTZ, $|G^*|$ increased consistently with water conditioning. After 10 days, there was an increase of 34.9%, followed by further increases of 22.7% and 26.4% at 60 and 160 days, respectively. This stiffening progress may be mainly due to the oxidative aging of the asphalt binder.

In the mortar with GRT, $|G^*|$ had an initial increase of 8.7% during the initial 10 days. The stiffening became more pronounced after 60 days, reaching an increase of 40.4% compared to the initial value. However, a reduction of 14.5% was reported between the 160 and the 60 days exposure period, although $|G^*|$ remained higher than in the dry state. This suggests that while short-term water exposure stiffened the GRT mortar due to asphalt oxidation, prolonged immersion could start degrading the adhesive properties between the binder and the aggregates.

In the case of the mortar with SPT, $|G^*|$ increased by 17.1% after 10 conditioning days. However, a significant reduction of 40.9% was observed at 60 days. At 160 days, there was a slight recovery of 2.2%, but the value remained below the unconditioned modulus. Similar to the GRT mortar, prolonged water

immersion negatively impacts the mechanical integrity of the material, likely due to adhesive degradation.

The effect of water conditioning was statistically significant (*p*-value<0.001) in all cases, indicating that immersion time substantially influences the mechanical properties of the mortars. Similarly, the aggregate type exhibited a highly significant effect (*p*-value<0.001), confirming that the mineralogical composition of the aggregate impacts the properties of the mortar. The significant interaction between conditioning time and aggregate type (*p*-value<0.001) suggests that the impact of water conditioning varies with the type of rock.

3.1. Additional considerations on QTZ mortars

It is noteworthy that the QTZ mortars, despite being associated with aggregates that typically show higher moisture susceptibility due to weaker asphalt-aggregate adhesion (Cala et al., 2021), did not display signs of adhesive damage within the studied conditioning periods. This result contrasts with expectations and previous findings on more basic and intermediate rock types.

Several factors may contribute to this apparent contradiction. For instance, differences in the filler particle size distribution (passing sieve # 200) were not fully controlled in this study and could have led to a denser internal structure in the QTZ mortars, slowing down water infiltration and delaying the onset of adhesion loss. Additionally, the high silica content in quartzite may foster stronger initial interactions with the increasingly polar asphalt species formed during oxidation, temporarily reinforcing the asphalt-aggregate bonds. While these hypotheses provide plausible explanations, further research—incorporating more controlled filler gradations, advanced pore structure characterizations, and detailed chemical analyses of the asphalt-aggregate interface—is needed to fully understand the interplay of microstructural and chemical factors delaying moisture-induced damage in QTZ mortars.

4 CONCLUSIONS AND RECOMMENDATIONS

This study evaluated the effect of water conditioning on the rheological properties of one control asphalt binder and asphalt mortars fabricated with three different aggregates. The materials were subjected to four moisture conditioning periods of 0, 10, 60 and 160 days of water immersion. The main findings of this study are:

The asphalt binder exhibited a continuous increase in |*G**| with conditioning time. FTIR results confirmed the progression of oxidation with an increase in the total carbonyl and sulfoxide groups.

Significant differences were observed on the impact of water conditioning on the viscoelastic properties of the mortars. Such differences were a function of the aggregate type and conditioning period. While the QTZ mortar showed a consistent increase in |*G**| with conditioning time, the other two mortars showed a reduction in stiffness after a specific conditioning – in the 60-160 days period for GRT and in the 10-60 days period for SPT–. This reduction in modulus is attributed to the initiation of moisture degradation of the aggregate-binder interfaces.

Since it has been proven that the felsic nature of QTZ produce highly moisture susceptible aggregate-binder adhesion binds, it is anticipated that when adhesion degradation initiates in the QTZ mortars, the rheological properties will drop at a faster rate than in in the other two mortars. Additional conditioning times would be required to confirm this hypothesis.

In conclusion, these findings highlight the critical role of both aggregate type and water conditioning in determining the mechanical response of asphalt materials. They also show the need for a better understanding of the coupling mechanical-climate effects on these materials to assess the durability of asphalt pavements.

5 REFERENCES

Bagampadde, U., Isacsson, U. & Kiggundu, B.M. 2004. Classical and contemporary aspects of stripping in bituminous mixes. Road Materials and Pavement Design 5(1): 7-33.

Bagampadde, U., Isacsson, U. & Kiggundu, B.M. 2006. Impact of bitumen and aggregate composition on stripping in bituminous mixtures. Materials and Structures 39(287): 303-315.

Cala, A. & Caro, S. 2021. Predictive quantitative model for assessing the asphalt-aggregate adhesion quality based on aggregate chemistry. Road Materials and Pavement Design.

Caro, S., Sánchez, D. & Caicedo, B. 2014. Methodology to characterise non-standard asphalt materials using DMA testing: application to natural asphalt mixtures. International Journal of Pavement Engineering 16(1): 1-10.

Hefer, A. & Little, D. 2005. Adhesion in bitumen-aggregate systems and quantification of the effects of water on the adhesive bond. Research Report ICAR-505-1.

Hicks et al. 2003. Moisture sensitivity of asphalt pavements: a national seminar. San Diego, California. Transportation Research Board - The National Academies Press: Washington, D.C.

ISO 2011. ISO 12677:2011: Chemical analysis of refractory products by X-ray fluorescence (XRF) — Fused cast-bead method. Geneva: ISO.

León, L. & Caro, S. 2023. Influence of water on the rheological properties of asphalt mastics fabricated with fillers having different mineralogical compositions. In Airfield and Highway Pavements 2023: 139-149.

Rice, J. 1959. Relationship of aggregate characteristics to the effect of water on bituminous paving mixtures. Transportation Research Record: Journal of the Transportation Research Board 59: 1-10.

Moisture susceptibility and fracture behaviour of fine asphalt mixtures with high RAP

D.B. Sánchez,
AtkinsRéalis, Birmingham, United Kingdom

S. Caro. L. Avendaño, M.C. Santos
Universidad de los Andes, Bogotá, Colombia

ABSTRACT: Rejuvenators are used to enhance the properties of hot asphalt mixtures with high Reclaimed Asphalt Pavement (RAP) content (>40%). While it is well recognized that these materials restore the mechanical performance of the RAP for another life-service period, the impact of climate-related factors in their mechanical performance and durability over time is still not fully understood. This study assesses the moisture susceptibility and fracture behaviour of various Fine Aggregate Matrix (FAM) materials containing 30% FAM-RAP and two palm oil rejuvenators (crude palm oil and soft stearin) by means of the Semi-Circular Bending (SCB) under dry and wet conditions. The results suggest that the palm oil rejuvenators at the selected doses preserved the structural integrity of the material after moisture conditioning in comparison to the FAM samples fabricated with virgin binder and with virgin+RAP binder.

1 INTRODUCTION

Rejuvenators are products obtained from different sources (i.e., petroleum based, vegetable oils and tall oils) used to revert the ageing effect of the asphalt binder present in Reclaimed Asphalt Pavement (RAP) materials. They are generally added in hot mix asphalt (HMA) containing high RAP content (i.e., over 40% by total weight) to control and prevent fatigue and cracking due to the presence of the oxidized RAP binder. Their use in high RAP content mixtures is associated with enhanced workability due to a reduced stiffness and with additional binder availability to satisfy mix volumetrics and better virgin aggregates coating (Epps Martin et. al, 2020).

In general, the literature shows that all types of rejuvenators can produce recycled mixtures with similar properties as their virgin counterpart at the initial service life of these materials as part of the pavement structure (e.g. Sánchez et al 2022, Rathore et al. 2021). However, there is still lack of information on how climate-related factors impact the mechanical performance and durability of the rejuvenated mixtures over time.

On the other hand, it is well recognized that the presence of moisture within asphalt mixtures leads to a reduction in their mechanical properties, triggering several failure mechanisms in flexible pavements such as ravelling, potholes and cracking (Elseifi et al, 2012). This phenomenon deteriorates the adhesive bonds between the aggregates-asphalt systems, and the cohesive bonds between the mortar contacts (Caro et al. 2008). Besides, water infiltration through the cracks may subsequently cause weakening of the base and/or subgrade. Rehabilitation of pavement damage caused by cracking and moisture damage is costly. Therefore, to avoid premature failure of asphalt mixtures, particularly when new materials are incorporated (i.e. rejuvenator and RAP material), it is necessary to understand their durability properties in the laboratory prior to installation in field.

This work explores the deterioration potential of moisture damage on the fracture behaviour of fine asphalt mixtures (FAM) or asphalt mortar (i.e., mix of asphalt binder and aggregates smaller than 1.18 mm) with high RAP content and two different vegetable-based rejuvenators. The study of FAM has become popular in the last two decades, as it is considered that several degradation mechanisms in asphalt mixtures initiate and propagate within this 'meso' phase (Montepara et al. 2011).

To accomplish this goal, semi-circular bending (SCB) tests were conducted for mortar specimens with and without water immersion. Several fracture parameters were obtained and two of them were selected and analysed to provide insights into the fracture performance and moisture susceptibility of the asphalt mixtures. It is noteworthy that although the SCB test has been widely used to study HMA materials, no work has been reported to date on their use to evaluate the performance of asphalt mortars with high-RAP content and rejuvenators.

2 MATERIALS

2.1 *Virgin binder and rejuvenation agents*

A virgin bitumen with a penetration of 62 dmm at 25ºC and a softening point of 48ºC was used as the base binder. This binder was also used to artificially produce the 'RAP binder' by subjecting it to the Rolling Thin Film Oven (RTFO) test (ASTM D2872), followed by the Pressure Aging Vessel (PAV) (ASTM D6521).

Two rejuvenation agents were selected for this study: (i) Crude palm oil and (ii) Soft stearin. The crude palm oil is the first product extracted from the fruit of the African oil palm. It has a semi-solid consistency at room conditions (Figure 1a), and it reaches a liquid consistency at 37ºC (Figure 1a). The soft stearin is a by-product of the crude palm oil obtained after various fractioning, thermodynamic and refinery processes. It also has a semi-solid consistency at room conditions (Figure 1b) and reaches a liquid consistency at 38ºC (Figure 1b).

At room Tº   At 37Cº   At room Tº   At 38Cº
   (a) Crude palm oil   (b) Soft stearin
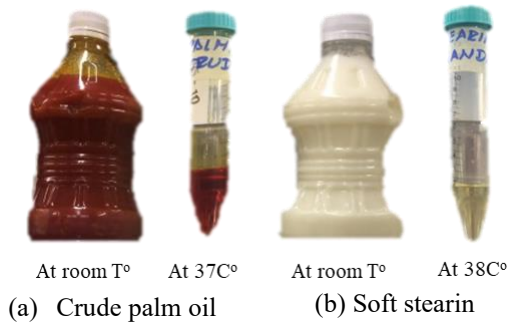
Figure 1. Rejuvenators at room conditions and at their melting point: (a) Crude palm oil, and (b) Soft stearin.

2.2 *FAM materials*

The FAM material corresponds to the asphalt matrix of a 0/25mm size dense graded base course containing 4.5% (by weight) of bitumen (Figure 2). They have approximately 9.7% of bitumen by total weight.

Four FAM mixtures were produced: i) a virgin FAM mixture (i.e., virgin binder), ii) a FAM mixture with 70% of virgin FAM and 30% of lab produced FAM-RAP, herein called base FAM, iii) a FAM mixture with 70% of virgin FAM and 30% of FAM-RAP and 3% of crude palm oil, and iv) FAM mixture with 70% of virgin FAM and 30% of FAM-RAP and 2.3% of the soft stearin.

The doses of each rejuvenator used in this study were those determined by Sánchez et al. (2023), which correspond to the amounts required to simultaneously restore the High temperature Superpave Performance Grade (PGH) of the virgin binder after verifying the Fatigue Low temperature Superpave Performance Grade (PGFL).

The FAM-RAP was produced in the laboratory by subjecting a loose mixture of virgin FAM material to the oven at 95ºC for 5-days. The percentages of virgin and 'RAP' FAM materials were determined in a previous study (Sánchez et al. 2023).
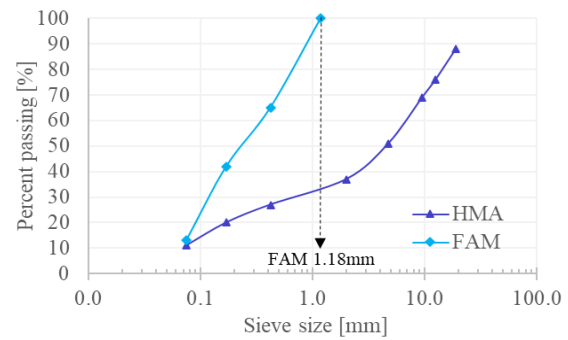
Figure 2. Gradation of the full mixture and the FAM.

3 EXPERIMENTAL SETUP AND SAMPLE PREPARATION

Cylindrical specimens of 80 mm in height and 150 mm in diameter were compacted for each FAM mixture using the Superpave gyratory compactor, at a target AV of 10±1%. Slices of 50 mm in height were cut from the middle of the cylinder, which were then cut symmetrically into two semi-circular specimens with a notch in its planar side of 15 mm height and 2 mm width.

A total of 6 cylindrical specimens were manufactured for each of the materials. Three specimens for each type of mixture were retained for testing under dry conditions and three specimens for each mixture were subjected to a moisture protocol. The moisture conditioning protocol consisted of submerging the cylindrical specimens to a water bath prior to the test for 24h at 60°C, and for one additional hour at 25°C. The dry specimens were conditioned in a temperature chamber for 24h at 25°C, based on the Tensile Strength Ratio test (AASHTO T283).

These specimens were used to conduct Semi-circular bending (SCB) testing. The test was conducted at a loading rate of 50 mm/min and a temperature of 25ºC. A load cell and a linear variable differential transducer (LVDT) were used to measure the applied load and displacement at the top centre of the sample (Figure 3). Different parameters are obtained from this curve, as observed in Figure 4. Among those, the following were selected for this study:

- Maximum force (P_{max}), which corresponds to the maximum force in the load-displacement curve, and provides information about the strength of the material.
- Cracking index (*CRI*), which is computed as the fracture energy divided by the peak load (Kaseer et al. 2018), and quantifies the energy required to crack the material relative to its strength.

The following sections present the results and corresponding analyses.
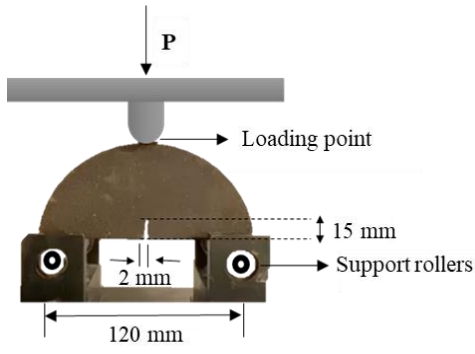
Figure 3. FAM materials *SCB test set up*.
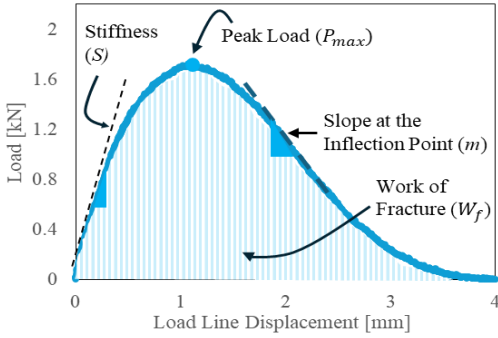
Figure 4. *Load Line Displacement (LLD) curve*.

4 RESULTS

This section presents the resulting SCB testing parameters for the FAM materials with rejuvenators.

4.1 *Fracture parameters*

Figure 5 presents the load versus displacement curves for all the replicates tested for the FAM mixtures under dry and wet conditions. A marked difference can be noted within the SCB test results for the FAM materials under both conditions. For instance, under dry conditions, Figure 5a shows that the curves for all FAM mixtures with RAP FAM appear to be similar with the base FAM material (i.e. without palm oil rejuvenators) presenting marginally the highest peak load, reflecting the high stiffness of the aged binder. After moisture conditioning (Figure 5b) the virgin FAM and the base FAM mixtures reach their maximum loads at lower values and higher displacements compared to their dry counterparts. Moreover, the curves for the FAM materials with palm oil rejuvenators reach marginally higher peak loads and higher displacements as compared to their dry counterparts.

4.1 *Maximum force (P_{max})*

Figure 6 shows the values of P_{max} for all FAM mixtures under dry and wet conditions. This figure also shows the percentage change in P_{max} in the dry condition compared to the wet condition. Under dry conditions, this figure shows that the base FAM material – without palm oil rejuvenators– exhibits the highest P_{max}, as expected, due to the presence of the aged

binder. After the FAM materials are subjected to moisture, the magnitude of P_{max} for the base and the virgin FAM decreased by 21 and 25%, respectively, suggesting that their internal structural integrity is severely affected by moisture. The FAM containing palm oil rejuvenators, on the contrary, exhibited a slight increase in the P_{max} (7% and 4% for the FAM with palm oil and soft stearin, respectively). These results suggest that the presence of rejuvenators enhance the preservation of the strength of the material due to moisture, in comparison to the virgin or control FAM.
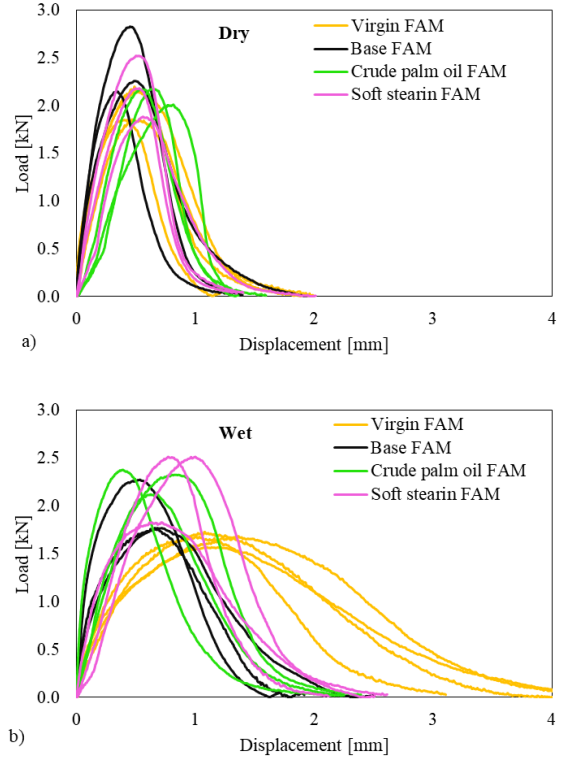
Figure 5. Load-displacement curves for FAM materials with rejuvenators a) under dry condition and b) after moisture conditioning.
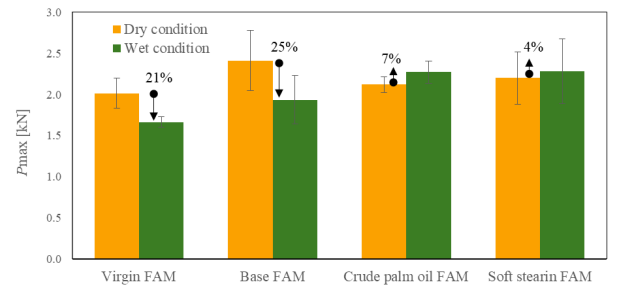
Figure 6. *P_{max} for FAM materials with rejuvenators*.

4.2 *Fracture index (CRI)*

Figure 7 shows the CRI index for the FAM materials under dry and wet conditions. This figure also shows the percentage change in this property in the dry condition compared to the wet condition. Recalling, a material with higher CRI values is considered more resistant to fracture. Figure 7 shows that under dry conditions, all the FAM materials exhibit marginally

the same CRI values. Since there are observed differences in the maximum load (P_{max}) among the FAM materials (Figure 6) in this condition, it seems that this fracture parameter is unsensitive to the differences in the resulting effective binder of the different FAM mixtures produced.

Nevertheless, the CRI values for all FAM mixtures increased by 30% to 65% in the wet condition with respect to the dry condition. This may be attributed to an increase in flexibility induced by moisture (i.e. reduction in stiffness), which results in an overall increase in the fracture resistance of the materials. However, this result needs to be critically assessed, because such increase in CRI is believed to be due to moisture degradation (i.e. strong impact in the maximum load and in the stiffness of the material, as observed in Figures 5 and 6), which could cause other type of durability issues. Among all FAM materials, the virgin FAM had the highest increased in CRI. When rejuvenators are incorporated, the FAM materials exhibit lower CRI values with respect to those of the virgin FAM and closer to those of the base FAM. These results suggest that even though the incorporation of the palm oil rejuvenation agents does not have an impact in the CRI under moisture conditions when compared to the base FAM, their internal damage induced by moisture is less severe than in the virgin FAM sample.
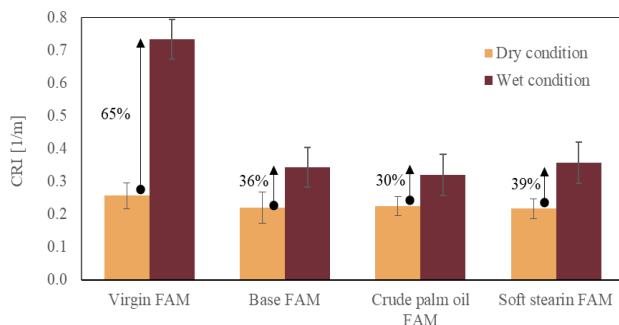
Figure 7. *CRI for FAM with rejuvenators*.

5 CONCLUSIONS

SCB tests were conducted on FAM samples rejuvenated with two different palm oil-based agents. A control virgin FAM (no RAP FAM material) and a base FAM (with RAP FAM with no rejuvenators) were tested for comparison. The following are the main conclusions obtained:

- Although differences in maximum force were observed among the FAM materials under dry condition, with the base FAM presenting the highest values, they had similar CRI values, suggesting that the latter parameter hinders the presence of RAP-FAM and rejuvenators.
- All FAM materials exhibited changes in P_{max} and an overall increase in CRI after moisture

conditioning, but this effect was more pronounced in the virgin FAM. This is attributed to the effect of water, which appears to enhance the material's flexibility, leading to a more prolonged failure. Such an increase in fracture properties under wet conditions, however, is believed to be caused by the degradation of the structural integrity of the material by moisture, which rises other durability concerns. In this sense, although the rejuvenators had smaller CRI values than the virgin mixture in wet state, they seem to preserve the structural integrity of the material to moisture effects.

These results highlight that an appropriate selection of a rejuvenator should consider not only the improvement of the mechanical and performance related properties in the initial stage of the pavement operation, but also its capability to maintain these positive effects under the effects of moisture.

6 REFERENCES

Caro, S., Masad, E., Bhasin, A., & Little, D.N (2008). Moisture susceptibility of asphalt mixtures, Part 1: mechanisms. International Journal of Pavement Engineering, 9, 81-98.

Elseifi, M. A., Mohammad, L. N., Ying, H., & Cooper, S. (2012). Modeling and evaluation of the cracking resistance of asphalt mixtures using the semi-circular bending test at intermediate temperatures. *Road Materials and Pavement Design*, 13(sup1), 124–139.

Epps Martin A., Kaseer, F.., Arámbula-Mercado, E., Bajaj, A., García Cucalon, L., et al. (2020) Evaluating the effects of recycling agents on asphalt mixtures with high RAS and RAP binder ratios. *NCHRP Report 927*, NAP, Washington, D.C.

Kaseer, F., Yin, F., Arámbula-Mercado, E., Epps Martin, A., Daniel, J. S., & Salari, S. (2018). Development of an index to evaluate the cracking potential of asphalt mixtures using the semi-circular bending test. *Construction and Building Materials*, 167, 286–298.

Montepara, A., Romeo, E., Isola, M., & Tebaldi, G. (2011). The role of fillers on cracking behavior of mastics and asphalt mixtures. *Journal of the Association of Asphalt Paving Technologists* (AAPT), 80, 161–192.

Sánchez, D., B. Saldarriaga, J. F., & Caro, S. (2022). Chemical and Thermodynamic Properties of Palm Oil-Based Materials and Their Impact on Recycled Binder Blends. *Construction and Building Materials, 348* (128490).

Sánchez, D. B., Caro, S., & Alvarez, A. E. (2023). Assessment of methods to select optimum doses of rejuvenators for asphalt mixtures with high RAP content. *International Journal of Pavement Engineering*, 24:1, 2161544.

Rathore, M., Haritonovs, V., Merijs Meri, R., & Zaumanis, M. (2021). Rheological and chemical evaluation of aging in 100% reclaimed asphalt mixtures containing rejuvenation agents. *Construction and Building Materials*, 318, 126026.

Impact of palm-oil rejuvenators on the adhesion durability of asphalt-aggregate systems

L. Vargas
Universidad de los Andes, Department of Civil and Environmental Engineering, Bogotá, Colombia

S. Caro
Universidad de los Andes, Department of Civil and Environmental Engineering, Bogotá, Colombia

D. B. Sánchez
AtkinsRéalis, Birmingham, United Kingdom

ABSTRACT: Moisture damage in asphalt mixtures impacts the durability of asphalt pavements, leading to increased transportation costs and reduced service life. While anti-stripping additives are commonly used to mitigate this phenomenon, ensuring durability remains a challenge, particularly in mixtures that include new components, such as reclaimed asphalt pavement (RAP). Although rejuvenators have been proposed to restore the performance properties of high-RAP-content mixtures, their impact on adhesion durability remains unexplored. This study assesses the effect of palm-oil rejuvenators on the adhesion durability of asphalt-aggregate systems. Aggregate-binder specimens fabricated with one type of aggregate and multiple binders (virgin asphalt, blends of asphalt and aged RAP-binder, and rejuvenated asphalts blends) were tested using a recently developed adhesion pull-off method under dry conditions and after 3 and 7 days of water conditioning. The results demonstrate that palm-oil rejuvenators effectively restore adhesion durability in asphalt-aggregate systems, highlighting their potential for enhancing not only the performance properties of the mixture, but also its durability.

1 INTRODUCTION

Moisture damage in asphalt mixtures is defined as the degradation of the material's mechanical properties due to changes in the cohesive properties of the asphalt binder or the loss of adhesion at the asphalt-aggregate interface, due to the presence of moisture in liquid, vapor or solid state (Caro et al., 2008). This phenomenon has a significant impact on the durability of asphalt pavements and represents a considerable financial problem. For instance, moisture-related deterioration in 2005 was associated with an increase in transportation costs exceeding $54 billion annually in the United States (Copeland, 2005).

According to the NCHRP Synthesis 595 (Shah et al. 2022), one-third of state departments of transportation (DOTs) require the use of anti-stripping additives in all asphalt mixtures, while another third mandate their use in mixtures that fail to meet minimum performance requirements. However, ensuring the durability of asphalt mixtures remains an increasingly complex challenge due to the incorporation of different additives and components, such as Reclaimed Asphalt Pavement (RAP) and rejuvenation agents.

The use of rejuvenators has been proposed as a solution to ensure the performance of mixtures with high RAP contents, as they make their rheological and performance properties to be comparable to those of mixtures manufactured with virgin asphalt (Gulzar et al., 2023). However, research efforts in this area have primarily focused on analysing mechanical, chemical and performance-related properties, while the durability of these mixtures with rejuvenators remains unexplored.

The objective of this study is to assess the impact of two palm oil-based rejuvenators (i.e., crude palm oil and soft stearin) on the adhesion durability of asphalt-aggregate adhesive systems in mixtures with high RAP content. Previous works have demonstrated the effectiveness of these agents to recover several mechanical and performance-related properties of these mixtures (Sánchez et al., 2022, 2023). Direct tensile tests using the adhesion pull-off method proposed by Cala et al. (2019, 2021) were used to attain the goals of this work. From these tests, the maximum load at failure (F_{max}), the adhesive failure area on the surface of the rock after the test ($A_\%$), and some moisture damage parameters for F_{max} (MDP$_{Fmax}$), and $A_\%$ (MDP$_{A\%}$) were computed, using combinations of one type of rock and virgin asphalt binder, a blend of virgin asphalt and 30% lab produced aged binder, and two rejuvenated binder blends.

2 MATERIALS

2.1 *Aggregate*

Adhesion quality has been observed to depend primarily on the type of aggregate and its chemical composition (Caro et al., 2008; Cala et al., 2019; Cala &

Caro, 2021). In order to control the chemical effects of the aggregate source on the results and efficiently isolate the influence of the asphalt binder blends, one type of aggregate was used. Specifically, a serpentinite rock obtained from the Cajamarca Complex (Tolima region, Colombia) was used due to its high resistance against moisture damage, as demonstrated by Cala et al. (2019, 2021).

2.2 Asphalt binders

A virgin asphalt binder, classified as a pen. 60-70 1/10 mm was chosen for this study due to its widespread use in the country. An artificial aged-RAP binder, herein named as 'aged binder', was produced by subjecting the virgin binder to the Rolling Thin-Film Oven (RTFO), followed by the Pressurized Aging Vessel (PAV) test according to ASTM D2872 and ASTM D6521, respectively. The virgin and aged asphalt were used to create a combination named 'Base blend', which consists of 30% aged binder and 70% virgin asphalt. This combination represents the effective asphalt expected to be present in new asphalt mixtures containing RAP contents between 40% and 70% by weight of the total mixture (Sánchez et al., 2023). Finally, to rejuvenate the Base blend, the optimum dosage of two palm oil-based rejuvenators was incorporated (i.e., rejuvenated blends), as explained in the following section.

2.3 Rejuvenators

Two palm oil-based agents were used: i) crude palm oil, and ii) soft stearin. Crude palm oil is the primary product obtained from the African oil palm. This material is subjected to refining processes, yielding multiple products, including the soft stearin. The asphalt rejuvenators were incorporated into the Base blend explained above according to the optimum doses obtained by Sánchez et al. (2021). Table 1 presents the composition of these combinations.

Table 1. Composition of asphalt combinations.

Material	Rejuvenator's dose*	Composition
Virgin binder (V)	-	100% pen. 60-70 (1/10 mm) binder
Base blend (B)	-	70% virgin binder + 30% aged binder
Base blend + Crude palm oil (Po)	3.0%	67% virgin binder + 30% aged binder + 3% crude palm oil
Base blend + Soft stearin (Ss)	3.0%	67% virgin binder + 30% aged binder + 3% soft stearin

* Percentage by weight of virgin binder

3 EXPERIMENTAL METHODS

The stages of the experimental work included: i) rock sample preparation, ii) aggregate-asphalt adhesive systems preparation, and iii) experimental testing.

3.1 Rock sample preparation

Rock samples were prepared following the methodology proposed by Cala et al. (2019). The process began with the extraction of 25 mm diameter cores from field-obtained rock specimens. These cores were cut into cylindrical samples at a height of 10 mm. Both faces of the cylindrical specimens were polished using a diamond cup with a particle size of 40 μm with a high-precision cutting and polishing machine (Struers Ref: Accutom-100), which ensured parallel faces with ±1 μm tolerance and equivalent surface roughness across replicates. This eliminated texture as a variable in the asphalt-aggregate interface. Finally, samples were subjected to an ultrasonic bath at 60 °C for 10 minutes to remove any residual material.

3.2 Aggregate-asphalt adhesive system preparation

The aggregate-asphalt adhesive systems were prepared according to Cala et al. (2019), using cylindrical rock samples, a metallic stub and the modified micrometer (Figure 1), as follows:
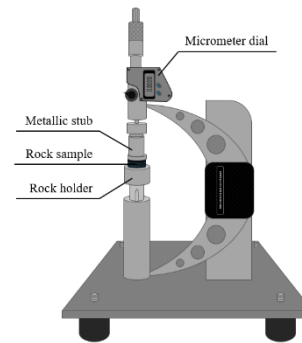
Figure 1. Modified micrometer for the adhesive system preparation.

1. The rock sample and the metallic stub were heated in an oven at 150 °C for at least 30 minutes to ensure complete water evaporation.
2. Simultaneously with step 1, 1.50 g of asphalt was placed in the oven for the last 15 minutes, ensuring all components reach 150 °C.
3. The metallic stub and the rock sample were placed in the micrometer and it was zeroed where the metallic stub touches the rock sample.
4. The asphalt binder was applied to the bottom of the metallic stub.
5. The metallic stub was lowered until the micrometer's dial reaches 20 μm.
6. The complete setup was left cooling down for 2 hours until the adhesive system reached 20 °C ± 2 °C and then dismounted (Figure 2a).

7. If the system required water conditioning, it was placed upside down in a container with type 1 water (i.e., ultrapure water that has been depleted of most contaminants) (Figure 2b).
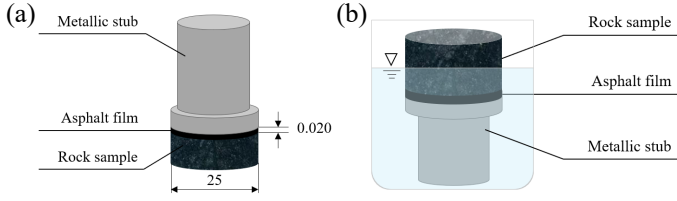
Figure 2. (a) AAS system (dimensions in mm), and (b) water conditioning of the AAS system.

3.3 *Experimental pull-off test*

The pull-off test consisted of applying tensile forces using a hydraulic press under a displacement condition of 10 mm/min (Cala et al. 2019, 2021). During the test, the rock was secured to a descending piston, while the metallic stub was attached to the load cell. Data were recorded using a load cell with a sampling interval of 0.166 s.

The results included Load [N] vs. Time [s] curves. Additionally, the adhesive failure area ($A_\%$) of the system was determined as the amount of adhesive loss or asphalt-aggregate debonding on the surface of the aggregate after the pull-off test (Figure 3(b)). These values were obtained after processing high-resolution images of the surface of the aggregate specimens (Figure 3(a)) using the ImageJ software (Abràmoff et al., 2004). When the failure was fully cohesive, the value of $A_\%$ was 0.0%. These experimental results were used to compute two moisture damage parameters, one for F_{max} (MDP$_{Fmax}$), and one for $A_\%$ (MDP$_{A\%}$). These parameters correspond to the area under the curve of the relative loss of F_{max} and the change in $A_\%$ as a function of the water conditioning time compared to the dry values (Cala et al., 2019). The higher the values, the higher the moisture susceptibility of the adhesive systems. Three replicates were tested per case.
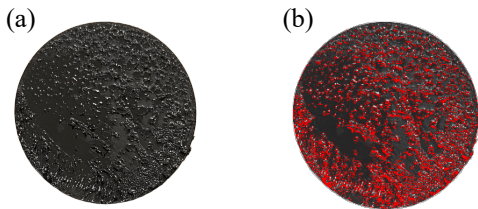
Figure 3. (a) Failure surface of an adhesive system after seven days of water conditioning, and (b) cohesive (red) and adhesive (black) failure areas.

4 RESULTS AND ANALYSIS

The samples were labelled based on i) rock lithology (e.g., SPT for serpentinite), ii) asphalt type (*V* for virgin asphalt, *B* for base binder blend, *Po* for the base binder blend+crude palm oil and, *Ss* for the base binder blend+soft stearin), iii) water conditioning time (0, 3, or 7 days), and iv) the replicate number.

Thus, sample SPT-Ss-3-1 is the first replicate of the serpentinite sample with a base blend binder with soft stearin conditioned for three days. If the label includes only one number (e.g., SPT-B-7), it is the average of all replicates for that rock and asphalt type at the specified conditioning time.

4.1 *Mechanical degradation*

Figure 4 shows the degradation of F_{max} for the adhesive systems as a function of the water conditioning time for all binders. The base binder blend samples exhibit the steepest reduction, indicating the highest moisture susceptibility. In contrast, the samples with virgin binder and rejuvenated binder blends show a more gradual reduction and comparable performance, suggesting better moisture resistance.

After seven days of moisture conditioning, the F_{max} values for the base binder blend experience significant degradation (78% reduction with respect to the dry condition). The rejuvenated blend samples remain close to those of the virgin samples, demonstrating that the palm oil-based rejuvenators effectively restored the adhesion durability of the AAS systems.
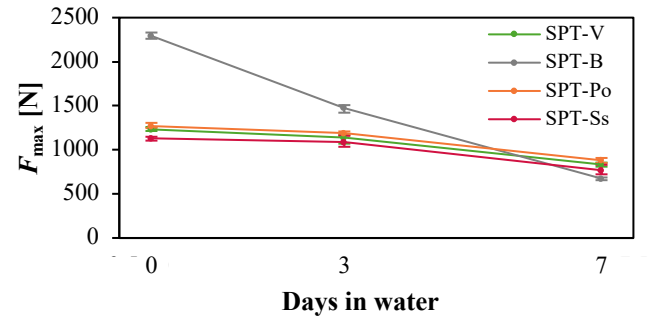
Figure 4. Change of F_{max} with water conditioning time.

4.2 *Adhesive failure area*

Moisture damage in asphalt-aggregate systems typically includes adhesive damage between the binder and the aggregate. The transition from cohesive to adhesive failure is a key indicator of the system's susceptibility to moisture. Figure 5 illustrates the evolution of $A_\%$ with water conditioning for AAS systems.
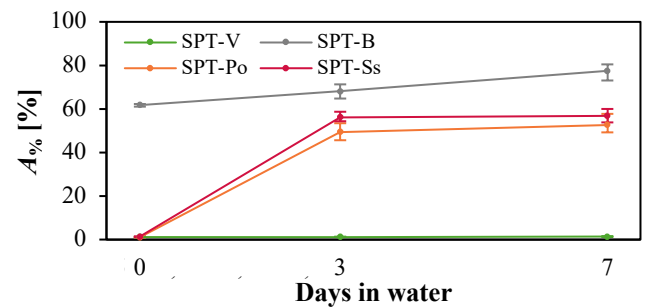
Figure 5. Evolution of the $A_\%$ with the water conditioning time.

Samples with the virgin binder demonstrate exceptional adhesion durability, maintaining $A_\%$ values equal to zero (i.e., cohesive failure) even after seven days of water conditioning. The base binder blend samples with no rejuvenators (i.e., virgin and aged-

binder blend in high-RAP content mixtures), exhibit the highest susceptibility to moisture damage, with an increase in $A_\%$ over time, reaching values of 80% after seven conditioning days. Meanwhile, the rejuvenated blend samples show intermediate adhesion performance, with an initial rise in $A_\%$ during the first three days, followed by a stabilization, indicating improved moisture resistance compared to the base blend samples. Overall, these results confirm the positive impact of the palm oil-based rejuvenators in recovering the adhesion durability of virgin + aged binder blend systems, mitigating the moisture-induced damage in mixtures with high-RAP content.

Figure 6 summarizes the adhesion quality and durability parameters of the asphalt-aggregate systems for each type of asphalt binder studied. Reduced adhesive performance is represented by an increased distance from the centre of the plot (i.e., a larger polygon area for each material in the durability diagram).
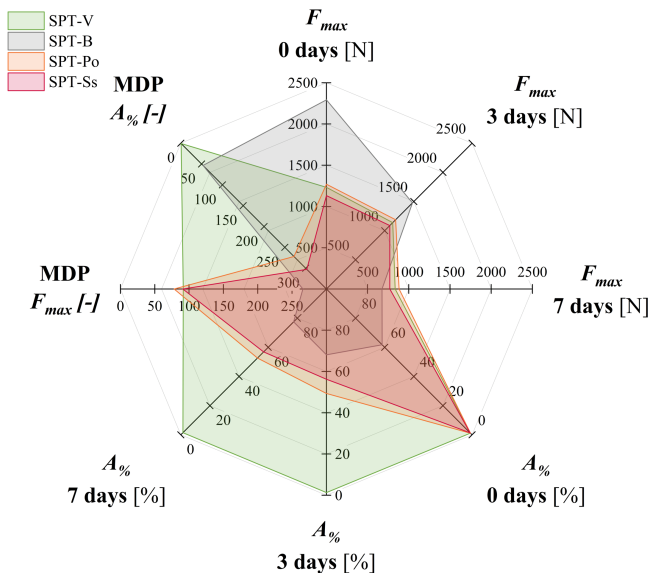
Figure 6. Durability diagram of AAS systems.

Data in Figure 6 show that the samples with virgin binder exhibited the highest results, indicating its superior adhesion performance. The samples with rejuvenated asphalt binder blends displayed intermediate results, showing an improvement compared to the samples with the base blend binder, which had the smallest area and, consequently, the highest susceptibility to moisture damage. These results highlight the effectiveness of the studied rejuvenators in improving the adhesive durability of the aggregate-binder systems.

5 CONCLUSIONS

The results from this study show that the adhesion quality of all aggregate-asphalt adhesive systems (i.e., serpentinite with a virgin binder, a base binder blend simulating the effective binder in a mixture with high-RAP content, and binder blends rejuvenated with crude palm oil and soft stearin) decreased with an increase in the water conditioning time, as expected.

However, the systems with rejuvenated asphalt blends had a better moisture resistance than those of the base binder blend (i.e., blend with no rejuvenators), with an adhesive performance comparable to the samples with virgin asphalt.

These results, along with previous studies that have shown the effectiveness of these palm oil-based rejuvenators in restoring the mechanical performance of RAP-blends, show their potential as effective rejuvenators.

This study was limited to one aggregate type. Therefore, additional tests with rock types of different mineralogic properties are recommended.

6 REFERENCES

Abràmoff, M. D., Magalhães, P. J., & Ram, S. J. (2004). Image processing with ImageJ. *Biophotonics International*, *11*(7), 36–42.

Cala, A., & Caro, S. (2021). Predictive quantitative model for assessing the asphalt-aggregate adhesion quality based on aggregate chemistry. *Road Materials and Pavement Design*, *23*(7), 1523–1543. https://doi.org/10.1080/14680629.2021.1900896

Cala, A., Caro, S., Lleras, M., & Rojas-Agramonte, Y. (2019). Impact of the chemical composition of aggregates on the adhesion quality and durability of asphalt-aggregate systems. *Construction and Building Materials*, *216*, 661–672. https://doi.org/10.1016/j.conbuildmat.2019.05.030

Caro, S., Masad, E., Bhasin, A., & Little, D. N. (2008). Moisture susceptibility of asphalt mixtures, Part 1: Mechanisms. *International Journal of Pavement Engineering*, *9*(2), 81–98. https://doi.org/10.1080/10298430701792128

Copeland, A. (2005). *Moisture in asphalt pavements in the United States: a financial perspective.*

Gulzar, S., Fried, A., Preciado, J., Castorena, C., Underwood, S., Habbouche, J., & Boz, I. (2023). Towards sustainable roads: A State-of-the-art review on the use of recycling agents in recycled asphalt mixtures. *Journal of Cleaner Production*, *406*(December 2022), 136994. https://doi.org/10.1016/j.jclepro.2023.136994

Sánchez, D. B., Caro, S., & Alvarez, A. E. (2021). Determining optimum doses of palm oil rejuvenators for recycled blends. In *Advances in Materials and Pavement Performance Prediction II*. https://doi.org/10.1201/9781003027362-79

Sánchez, D. B., Caro, S., & Alvarez, A. E. (2023). Assessment of methods to select optimum doses of rejuvenators for asphalt mixtures with high RAP content. *International Journal of Pavement Engineering*, *24*(1). https://doi.org/10.1080/10298436.2022.2161544

Sánchez, D. B., Saldarriaga, J. F., & Caro, S. (2022). Chemical and thermodynamic properties of palm oil-based materials and their impact on recycled binder blends. *Construction and Building Materials*, *348*(July 2022). https://doi.org/10.1016/j.conbuildmat.2022.128490

Shah, A., Olek, J., & McDaniel, R. (2022). NCHRP Synthesis 595. In *Practices for Assessing and Mitigating the Moisture Susceptibility of Asphalt Pavements*. https://doi.org/10.17226/26725

2.2

MATERIALS TESTING AND MODELING: CALIBRATION, VERIFICATION AND VALIDATION

Development of a simple RAP extraction and recovery method for smaller material quantities

Dheeraj Adwani
Department of Civil, Architectural and Environmental Engineering
The University of Texas at Austin, Texas, USA

Pravat Karki
Texas Department of Transportation (TxDOT), Austin, Texas, USA

Amit Bhasin
Department of Civil, Architectural and Environmental Engineering
The University of Texas at Austin, Texas, USA

ABSTRACT: As road networks expand globally and existing pavements are upgraded, the need for recycling in asphalt pavements continues to grow. However, the quality of RAP materials varies significantly, necessitating reliable assessment methods to determine their suitability for new pavements and ensure optimal performance. Rapid and efficient RAP quality assessment is especially critical in regions managing multiple RAP stockpiles, where informed decisions rely on accurate material evaluation. This study presents a novel microextraction procedure combined with a vacuum oven recovery method to extract small binder quantities for characterization. The vacuum oven recovery method was developed and refined through simulation trials using binder pellets, while various microextraction filtration techniques were evaluated with loose asphalt mixtures. The proposed procedure was validated through rheological characterization of binders and benchmarked against conventional extraction and recovery methods, demonstrating its efficacy and potential for widespread application.

1 INTRODUCTION

1.1 *Background and Motivation*

The incorporation of reclaimed asphalt pavement (RAP) in road construction has become nearly indispensable in today's world due to the need for recycling, sustainability, and cost considerations. However, the quality of RAP varies significantly, influenced by factors such as its source, location, age, and the original materials used in its composition. This variability results in a wide range of RAP binder quality across different stockpiles. For instance, the state of Texas alone exhibits substantial diversity in RAP characteristics, necessitating rapid and efficient methods for quality assessment to support informed decision-making.

Each RAP possesses unique properties, making proper evaluation critical for distinguishing between materials of differing quality. Among the key components of asphalt mixtures, the asphalt binder plays a crucial role in determining the long-term performance of the pavement. To assess RAP binder quality, the binder properties must be characterized, which requires its extraction from RAP materials. Conventional binder extraction and recovery methods typically involve the use of large quantities of organic solvents and specialized laboratory setups. Centrifuge-based methods are widely employed for binder extraction, where the RAP is soaked in an organic solvent to obtain a binder-solvent solution. For binder recovery, methods such as the Abson recovery technique and the use of a rotary evaporator (rotovap) are commonly utilized (McDaniel et al., 2000).

Although these conventional methods are well-established and widely used, they are inherently time-consuming, require large volumes of solvents, and have limited throughput. A single centrifuge and rotovap setup in a laboratory can process only one RAP binder sample at a time, making the evaluation process slow and inefficient, particularly for regions with numerous RAP stockpiles. Additionally, the proposed EPA ban on trichloroethylene (TCE) for laboratory use the urgent need for alternative methods that employ safer, less chlorinated solvents like toluene. As the asphalt industry faces the need to evaluate large volumes of RAP, faster, safer, and high-throughput methods are becoming essential.

Recent advancements in dynamic shear rheometer (DSR) technology have enabled the use of smaller diameter plates, such as 4 mm and 8 mm plates, for low temperature testing (Hajj et al., 2019, Filonzi et al., 2020). This allows comprehensive rheological characterization, including high, intermediate, and low temperature testing, to be performed exclusively on the DSR using minimal binder quantities. Consequently, RAP extraction and recovery methods that yield small binder quantities can be highly effective, provided they are fast, simple, and capable of high throughput.

1.2 Scope

This study focuses on the development of a microextraction and recovery method for RAP. To establish the vacuum oven recovery method using toluene as the solvent, initial trials were conducted with simulated binder pellets, without using RAP or asphalt mixtures. Through multiple iterations, key recovery parameters, such as temperature, duration, vacuum level, and other relevant conditions, were optimized. Subsequently, the refined procedure was applied to loose asphalt mixtures, simulating lab-produced RAP.

The rheological characteristics results for the recovered binders were compared with binders recovered through conventional extraction and recovery to validate the developed approach. The proposed method offers a simple, fast, and high throughput method to recover small binder quantities, making it highly suitable for RAP quality assessment.

2 METHOD DEVELOPMENT WITH BINDER PELLETS

2.1 Simulated binder-solvent solution

For method development, the researchers simulated the proposed approach using asphalt binders to establish extraction and recovery parameters. Instead of utilizing asphalt mixtures or RAP samples, asphalt binder pellets were dissolved in toluene inside a glass bottle. During the micro-recovery simulations, small 2 g binder pellets were dissolved in 20 ml solvent, as illustrated in Figure 1.

To ensure homogeneity, the binder-solvent solution was placed on a magnetic stirrer equipped with a chemical-resistant covered magnet inside the bottle. The solution was stirred at approximately 200 rpm for an extended duration, preferably overnight, to achieve complete dissolution.

Figure 1. Binder pellet dissolved in a solvent in a glass bottle stirred on a magnetic stirrer.

2.2 Vacuum oven recovery procedure

Binder recovery was conducted using a conventional vacuum oven. The binder solution was transferred to 4 oz steel cans, commonly used in asphalt laboratories for binder storage. Earlier trials employed glass dishes for this process, but to increase throughput, the glass dishes were replaced with disposable 4 oz steel cans (Filonzi et al. 2020). These cans containing the binder solutions were placed in the vacuum oven for recovery. The oven's initial temperature was adjusted based on the solvent, which in this study was toluene, a solvent with a relatively high boiling point. The temperature was gradually increased from 60°C to 165°C, with increments of 20–25°C every 30 minutes, making the entire recovery process approximately 5 hours long. Figure 2 illustrates a typical vacuum oven setup with samples undergoing the recovery procedure.

Figure 2. Vacuum oven used for recovery of binder from the binder-solvent solution.

A vacuum of 70 cm of Hg was applied in the oven using a chemical-resistant vacuum pump. This high vacuum level is critical for reducing the boiling point of the solvent, facilitating efficient removal of solvent vapors from the oven while minimizing binder aging at elevated temperatures. The amount of binder solution in the sample cans was carefully calibrated to ensure that the recovered binder quantity was sufficient for DSR measurements.

For these simulations, conventional high- and intermediate-temperature PG testing was performed, with complex modulus, phase angle, and stiffness parameters compared between the base binders and the recovered binders. Trials were conducted on four binders (designated B1, B2, B3, and B4), representing three different PG grades: two PG 64-22, one PG 70-22, and one PG 76-22. These binders were tested in both rolling thin film oven (RTFO) and pressure aging vessel (PAV) aged conditions.

2.3 DSR evaluation on recovered simulated binder

The DSR results for 25 mm plate testing of RTFO aged base and recovered binders are presented in Figure 3 (a). As shown, the $G^*/sin\delta$ values for the

base RTFO binders and binders recovered through vacuum oven recovery simulation were highly comparable, with negligible d2s% differences between the two measurements. These findings indicate that, from a rheological standpoint, toluene is an effective solvent for recovering the original binder using the vacuum oven micro-recovery process, with complete removal of the solvent during recovery. Similarly, Figure 3 (b) presents the $G^*.sin\delta$ values for base and recovered PAV aged binders. The results further confirm the effectiveness of the toluene-based recovery process, demonstrating the success of the simulation trials in preserving the rheological properties of the original binders, and no evidence of solvent in the recovered binder.

(a)

(b)
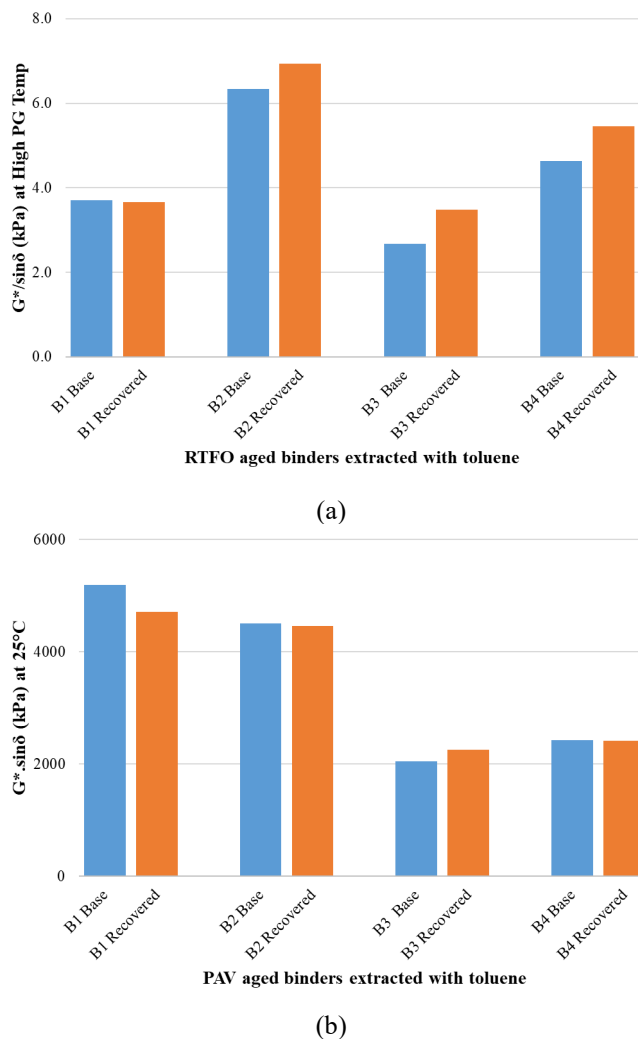
Figure 3. Stiffness parameters at high and intermediate temperatures for RTFO and PAV aged original and recovered binders.

3 MICROEXTRACTION AND RECOVERY TRIALS WITH LOOSE ASPHALT MIXTURES

The previously described recovery trials simulated the recovery of binder from binder-solvent solutions using the vacuum oven procedure. The preceding step obtaining the binder-solvent solution involves extracting binder from the RAP, or lab simulated RAP in this study in the form of loose asphalt mixture. This section focuses on the efforts to develop a fast and simple microextraction method to obtain the binder-solvent solution ready for recovery process.

3.1 Different filtration methods

The binder microextraction process begins by soaking asphalt mixture or RAP in a solvent for a sufficient duration to dissolve the binder into the solvent. Approximately 50 g of loose mixture was soaked in 50 mL of toluene within a glass bottle, same as the one illustrated in Figure 1. The solvent amount was adjusted based on the container dimensions to ensure the mixture was adequately submerged. A magnetic stirrer was used to agitate the mixture at around 200 rpm overnight, ensuring effective binder dissolution.

The next step involved filtering the binder-solvent solution to separate aggregates and fine materials. Previous research utilizing 1-micron syringe filters effectively removed fine particles but required a significant number of filters when processing mixtures with higher fine content (Filonzi et al. 2020).

Two plant-produced loose asphalt mixtures were used for these trials. The first was produced using a PG 64-22 binder, and the second with a PG 70-22 binder, both incorporating 20% RAP. Several filtration methods were explored, summarized as follows:

3.1.1 Method-1
This trial introduced a two-stage filtration process to improve efficiency over earlier methods. The first stage utilized generic coffee filters with a pore size of 10–20 microns to remove larger particles, as shown in Figure 4. Vacuum flask assistance was tested to expedite this step. In the second stage, the filtrate was passed through a 1-micron syringe filter with vacuum assistance (Figure 4). While this method slightly reduced the number of filters needed, the additional effort did not justify the limited savings in efficiency.

Figure 4. Trial with coffee filter as the first stage in the two-step filtration and vacuum manifold with syringe filters

3.1.2 Method-2
In this method, a single-stage filtration using 1-micron syringe filters was employed. To reduce the number of filters required, the binder-solvent solution was left undisturbed overnight after a few hours stirring, allowing fine particles to settle. This waiting period reduced the load on the filters without compromising the homogeneity of the solution.

3.1.3 *Method-3*

This method eliminated magnetic stirring, instead manually stirring the solvent-mixture solution for a few minutes after a few hours of soaking time. The bottle was then left undisturbed overnight or around 16 hours depending on the operator's schedule, allowing fines to be settled. After the settling period, the supernatant was manually drawn into a syringe through a 1-micron filter directly attached to the syringe as shown in Figure 5, significantly reducing the number of filters needed and simplifying the process. This approach efficiently recovered the binder with minimal time and filter usage.
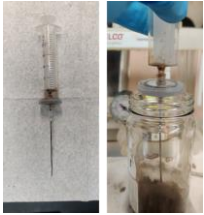
Figure 5. Manual method of drawing supernatant through a syringe filter from the undisturbed solution (without vacuum assistance and stirring)

The filtrates obtained through the methods discussed above were then subjected to the vacuum recovery procedure outlined earlier.

3.2 *DSR measurements on recovered binders*

The binders recovered from the filtrates were tested for DSR measurements and compared to binders recovered using conventional extraction and recovery with a centrifuge and rotovap. The recovered binders were tested for 25 mm high temperature and 8 mm intermediate temperature PG, and stiffness parameters $G*/sin\delta$ at 64°C and $G*.sin\delta$ at 25°C were compared. The results, shown in Figure 6, clearly demonstrate that all microextraction and recovery trials produced binders with stiffness values similar to those recovered by conventional methods. These findings confirm that the microextraction and recovery method is a suitable, efficient approach for recovering binder from RAP or asphalt mixtures in small quantities.
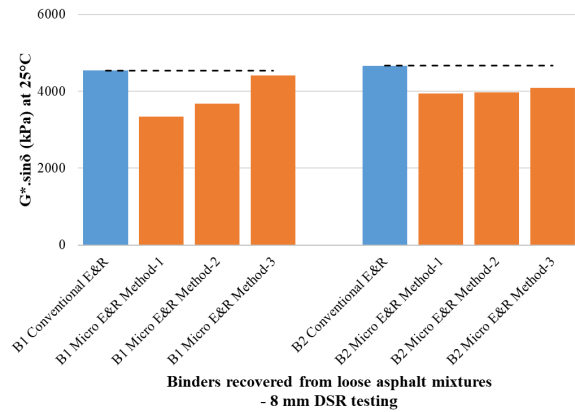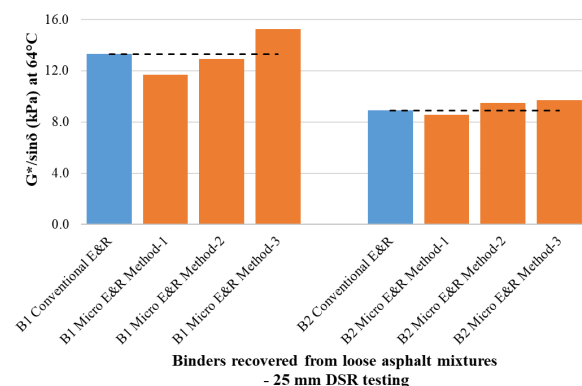
Figure 4. Summary of stiffness parameters for recovered binders from different extraction and recovery methods

4 CONCLUSIONS AND DISCUSSION

This study introduces a simple, rapid, and safer microextraction and recovery method for assessing RAP binder quality. The developed method uses just 50 g RAP and 50 ml of solvent in a glass bottle, syringes, filters, and a vacuum oven to extract and recover sufficient binder for DSR rheological testing.

The proposed method was validated through rheological characterization of the recovered binders and benchmarked against conventional extraction and recovery method. The proposed method provides a practical, efficient, and high-throughput solution for RAP quality assessment, and supports the asphalt industry in achieving sustainability goals.

5 ACKNOWLEDGEMENTS

6 DISCLAIMER

This study does not constitute a standard or specification or represent views of TxDOT.

7 REFERENCES

McDaniel, R.S. and Anderson, R.M., 2001. Recommended use of reclaimed asphalt pavement in the Superpave mix design method: technician's manual (No. Project D9-12 FY'97). Transportation Research Board.

Hajj, R., Filonzi, A., Rahman, S. and Bhasin, A., 2019. Considerations for using the 4 mm plate geometry in the dynamic shear rheometer for low temperature evaluation of asphalt binders. Transportation Research Record, 2673(11), pp.649-659.

Filonzi, A., Lee, S.K., Ferreira, W., Hajj, R. and Bhasin, A., 2020. A micro-extraction method for use with 4 mm plate geometry in the Dynamic Shear Rheometer to evaluate asphalt binder rheology. Construction and Building Materials, 252, p.119024.

Estimating the Dynamic Moduli and Viscosities of Bitumens via Oscillatory Strain-Controlled Molecular Simulations

Eli I. Assaf
Civil Engineering and Geosciences, Delft University of Technology, Delft, The Netherlands

Peng Lin
Ministry of Infrastructure and Water Management (Rijkswaterstaat), The Netherlands

Xueyan Liu
Civil Engineering and Geosciences, Delft University of Technology, Delft, The Netherlands

Sandra Erkens
Ministry of Infrastructure and Water Management (Rijkswaterstaat), The Netherlands

ABSTRACT: This study uses strain-controlled oscillatory deformations in all-atom Molecular Dynamics (MD) simulations to examine the viscoelastic properties of SARA fractions in bitumen. Frequency sweep tests revealed distinct moduli and viscosity ranges, aligning with experimental observations. Saturates were the softest and thinnest, while Asphaltenes were the stiffest and least thermally susceptible. MD simulations identified five viscoelastic regimes—Elastic, Glassy, Rubbery, Rubbery Flow, and Viscous—and highlighted accelerated dynamics, with faster relaxation times of simulations allowing exploration of equivalent Hertz-long oscillations in experimental tests. Ensuring that characteristic timescales in MD simulations correspond to comparable Deborah numbers is critical for accurately capturing stress-related phenomena—an insight that represents a previously unrecognized necessity in MD studies involving bitumens.
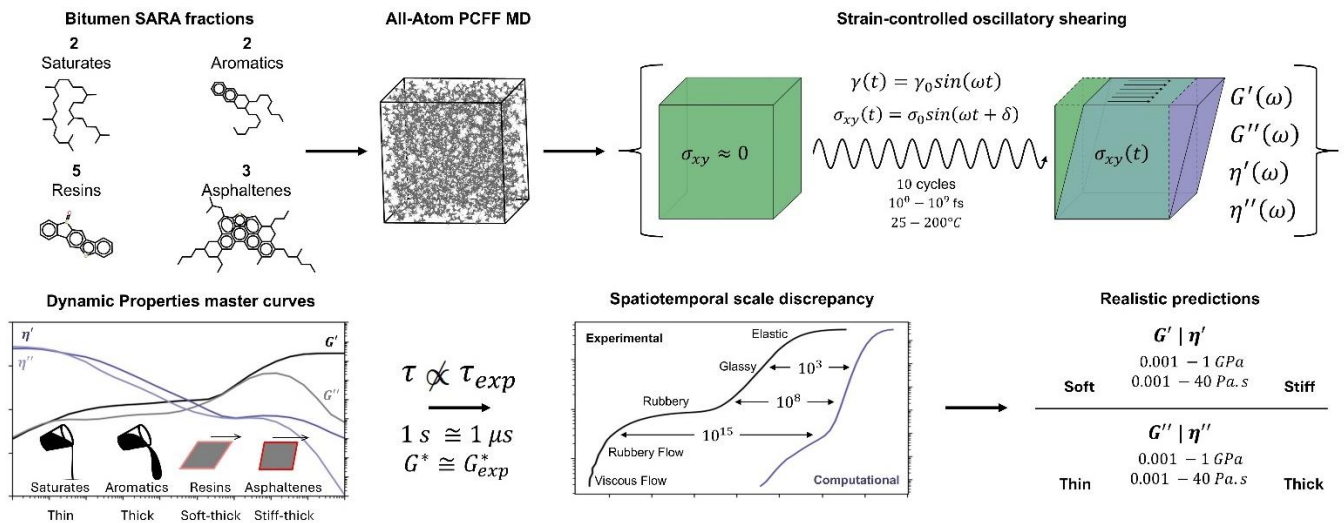
1. INTRODUCTION

Bitumen, a complex mixture of hydrocarbons, is a byproduct of petroleum distillation with significant industrial application[1]. Its molecular diversity—comprising oily, resinous, and asphaltenic fractions—imparts unique viscoelastic properties, essential for construction but challenging to characterize[2]. Experimental techniques like Dynamic Mechanical Analysis (DMA) subject bitumen to oscillatory shear strains to measure its mechanical response across strain rates and temperatures, yielding master curves of viscoelastic behaviour[3]. However, computational modelling of these properties is less common due to the complexities of stress definition in Molecular Dynamics (MD) simulations[4].

Stress in MD simulations, defined as potential energy per unit volume, is ambiguous due to the lack of a defined atomic volume and the inclusion of numerous interaction terms, such as van der Waals forces and bond strains, in force field equations[5]. These complexities, combined with the time-dependent nature of stress responses, lead to discrepancies in characteristic timescales between computational and experimental setups. Materials may exhibit fluid- or solid-like behaviour depending on the perturbation timescale relative to

their internal dynamics, complicating the comparison of MD and experimental DMA results[6].

Force field simplifications, necessary for simulating molecular interactions, inherently introduce faster material dynamics in MD, requiring careful interpretation of stress-related phenomena[7]. While methods like Green-Kubo provide insights into stress at equilibrium, they fail to capture the dynamic responses observed in DMA tests, particularly for highly viscoelastic materials[8]. Non-equilibrium methods, such as those by Müller-Plathe and Zhao introduce stress perturbations to study material responses but lack the precision to mimic experimental DMA setups, further contributing to difficulties when capturing rheological properties using conventionally accepted MD methods[9].

Research on bitumen remains predominantly application-driven, often overlooking molecular-level characterizations. Consequently, MD simulations for bitumen face challenges in achieving accuracy, with studies frequently reporting stress tensors in gigapascal ranges or viscosities far below experimental values. These errors arise from unaccounted differences in characteristic timescales between experimental and computational configurations[6].

This study addresses these challenges by employing strain-controlled oscillatory deformations in all-atom MD simulations to compute the dynamic properties of bituminous materials using DMA-like setups. By conducting frequency- and temperature-dependent sweep tests across hydrocarbon blends, this work integrates principles of Rheology and Civil Engineering into Computational Chemistry, proposing a standardized simulation framework. The study emphasizes the role of characteristic timescales in ensuring meaningful comparisons between simulation and experimental results, enhancing the design and analysis of viscoelastic materials using all-atom MD simulations.

2. METHODOLOGY

Twelve molecular systems representing bitumen's SARA fractions were modelled using Greenfield's bituminous molecules[9] (shown in Figure 1) and the Polymer Consistent Force Field (PCFF)[10], selected for its ability to simulate complex hydrocarbon interactions akin to those in bitumens.

These systems, comprising up to 30,000 atoms, were initialized using RDKit to generate low-energy configurations and prepared into their condensed form using LAMMPS through compression and annealing under NPT conditions. Residual stresses were minimized through 50 annealing cycles, ensuring equilibrium configurations suitable for stress tensor measurements and thus rheological analysis.
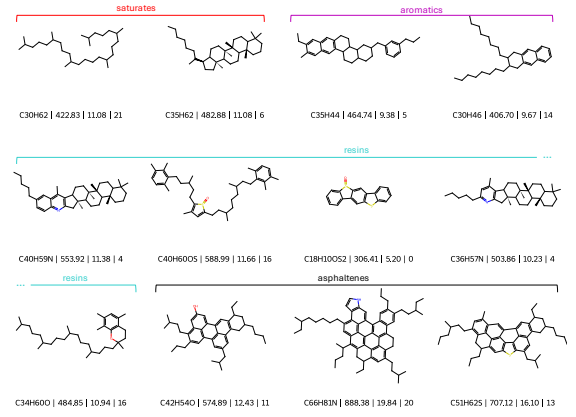
Figure 1. The chemical structures of molecules employed in this study are depicted herein, separated into Saturates (red), Aromatics (purple), Resins (cyan), and Asphaltenes (black).

Dynamic properties were computed in a methodology akin to that applied by Ebrahimi et Al.[11], applying strain-controlled oscillatory deformations in a triclinic simulation box (see Figure 2 for simulation geometry definitions). A sinusoidal strain ($\gamma(t)$) waveform was imposed to cyclically deform the xy-plane, defined in Equation 1 and depicted in Figure 2:

$$\gamma(t) = l_{xy}(t) = \gamma_0 sin(\omega t) \qquad \text{Equation 1}$$

Where γ_0 is the strain amplitude and ω the angular frequency. Stress tensors were calculated using the virial equation, especially on σ_{xy}, from Equation 2 as:

$$\sigma_{\alpha\beta} = \frac{1}{V}\left(\sum_i m_i v_{i\alpha} v_{i\beta} - \sum_{i<j} r_{ij\alpha} f_{ij\beta}\right) \qquad \text{Equation 2}$$

where $\sigma_{\alpha\beta}$ is stress, V is volume, m is mass, v is velocity, r is position, f is force between particles i and j in directions α and β. The shear stress response ($\sigma_{xy}(t)$), characterized by its amplitude (σ_0) and phase lag relative to the strain (δ), obtained from Equation 3 as:

$$\sigma_{xy}(t) = \sigma_0 sin(\omega t + \delta) \qquad \text{Equation 3}$$

enabled the computation of storage modulus (G'), loss modulus (G''), and complex modulus (G^*), computed using Equation 4 and Equation 5:

$$G'(\omega) = \frac{\omega}{N_c \pi \gamma_0^2} \sum_i \sigma(t)\gamma(t)dt \qquad \text{Equation 4}$$

,

$$G''(\omega) = \frac{1}{N_c \pi \gamma_0^2} \sum_i \sigma(t)\dot{\gamma}(t)dt \qquad \text{Equation 5}$$

Additionally, dynamic viscosities—storage (η'), loss (η''), and complex (η^*)—were derived to quantify viscoelastic behaviour under varying frequencies and temperatures.
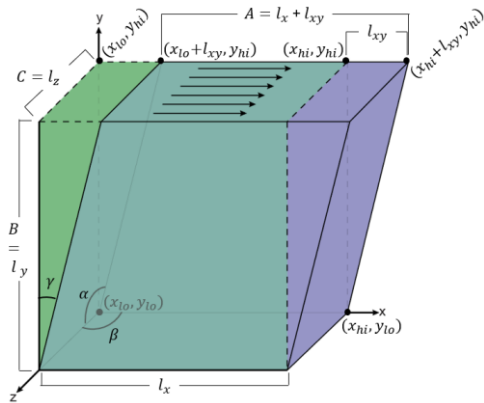
Figure 2. Illustration and expressions used by LAMMPS correlating the simulation box's vertices with the box's edge lengths and tilt/shear factors.

The selection of frequency values for use in simulations involving bituminous materials is not straightforward as the experimental frequency range commonly used to test bitumens in laboratory conditions (0.01 to 100 s^{-1}) would correspond to about 10^{13} to 10^{17} simulation steps in all-atom simulations. This time scale initially suggests that replicating real-life frequency timescales in molecular simulations is unfeasible due to the large number of simulation steps. However, molecular phenomena often stabilize at a faster rate than observable in experiments (as $\tau \ll \tau_{exp}$), as denoted by other MD-related studies[12]. This accelerated stabilization allows the simulations to reflect experimentally equivalent responses within computationally tractable durations (significantly fewer than 10^{13} steps) but introduces a discrepancy between the timescales of all-atom simulations dictated by the PCFF force field and real-world phenomena.

The characteristic times of the simulations, defined as the timescale over which an applied perturbation dissipates (denoted as τ), restoring the system to equilibrium, were determined through exploratory simulations[13]. These times were identified primarily at crossover points where $G' = G''$, typically observed near the transition between the Elastic and Glassy regions. Using these points as a reference, frequency sweep tests were designed to span a range of 30 frequencies, logarithmically distributed between 0.05 and 50 times τ. This approach ensured that the stress-related phenomena captured a comprehensive viscoelastic profile within the scope of the simulations, rather than being limited to exclusively elastic or viscous regimes[11].

Simulations were conducted across a range of temperatures, specifically 0°C, 25°C, 60°C, 135°C, 160°C, and 200°C, which are critical for investigating the rheological behaviour of bituminous materials. By combining results across different temperatures using Time-Temperature Superposition (TTS), master curves were generated to characterize the materials' behaviour across Elastic, Glassy, Rubbery, and Viscous regimes. This approach bridges experimental and computational timescales, addressing the spatiotemporal discrepancies inherent in MD simulations. The resulting framework establishes a robust methodology for evaluating viscoelastic properties of bituminous materials at the molecular level.

3. RESULTS

Dynamic properties, including storage modulus (G'), loss modulus (G''), and complex modulus (G^*), as well as their corresponding viscosities (η', η'', and η^*), revealed distinct viscoelastic behaviours across the SARA fractions. Saturates exhibited the lowest moduli and viscosities at 25°C (G'=3145 MPa, G''=1421 MPa, G^*=3643 MPa, η'=2.14 Pa·s, η''=0.97 Pa·s, η^*=2.48 Pa·s), reflecting a soft and predominantly elastic nature. Aromatics, with intermediate values (G'=4555 MPa, G''=3239 MPa, G^*=5792 MPa, η'=3.10 Pa·s, η''=2.21 Pa·s, η^*=3.95 Pa·s), demonstrated significant thermal susceptibility, transitioning to viscous responses at higher temperatures. Resins and Asphaltenes were the stiffest fractions, with G' and G^* exceeding 12,000 MPa at 25°C, and viscosities as high as 9 Pa·s. Even at 200°C, Asphaltenes maintained substantial stiffness (G'=1579 MPa, η^*=1.49 Pa·s), emphasizing their resistance to thermal stress. These values are summarized in Figure 3.

Frequency-dependent plots revealed distinct viscoelastic regions across all fractions. Asphaltenes and Resins dominated in stiffness, with broader Rubbery and Viscous Flow regimes, while Saturates and Aromatics displayed narrower viscoelastic ranges, transitioning to fully viscous responses at lower frequencies. Scaling of characteristic times was critical in capturing these transitions, ensuring observed mechanical moduli reflected equivalent deformation rates across simulation and experimental setups in the form of equivalent Deborah numbers – being 7 to 8 decades faster in simulations, displayed for each viscoelastic region in Table 1. Figure 3 (right) presents the Mastercurves of the simulations and for Polyisobutylene obtained experimentally[14]. These curves exhibit a characteristic "S" shape, indicating the major viscoelastic regions. However, the profiles derived from MD simulations are shifted by 7 to 8 decades to the right, highlighting that the simulations capture stress-related phenomena at significantly shorter or faster equivalent timescales.

Thermal susceptibility factors (χ) quantified the impact of temperature on viscoelastic properties. Saturates and Aromatics displayed the highest χ values, indicating significant softening under thermal stress. In contrast, Resins and Asphaltenes retained high stiffness and viscosities, even at elevated temperatures, underscoring their structural robustness.

The use of all-atom PCFF dynamics reveals a significant limitation: the standard deviation in stress tensor measurements (±20 MPa) exceeds the amplitude of the stress values induced by applied strain, rendering such measurements statistically unreliable or undetectable. Consequently, stress-related phenomena are challenging to capture using this approach, particularly in the low-frequency domain (e.g., the viscous regime). Stress values below 20 MPa would require alternative methodologies, such as different dynamic models or the application of the Time-Temperature Superposition (TTS) principle, which in this study enabled the detection of stress phenomena as low as 5 MPa.

Table 1. Frequency ranges for all 5 Characteristic regions for both experimental and MD samples of bitumen at 25°C.

Region	Experimental [s^{-1}]	Experimental [fs^{-1}]	MD [fs^{-1}]	Shift [fs^{-1}]
Elastic	$> 10^8$	$> 10^{-7}$	$> 10^{-2}$	10^5
Glassy	$10^8 - 10^4$	$10^{-7} - 10^{-11}$	$10^{-2} - 10^{-5}$	10^6
Rubbery	$10^4 - 10^{-3}$	$10^{-11} - 10^{-18}$	$10^{-5} - 10^{-8}$	10^8
Rubbery Flow	$10^{-3} - 10^{-4}$	$10^{-18} - 10^{-19}$	$10^{-8} - 10^{-10}$	$10^8 - 10^9$
Viscous Flow	$< 10^{-4}$	$< 10^{-19}$	$< 10^{-10}$	10^9
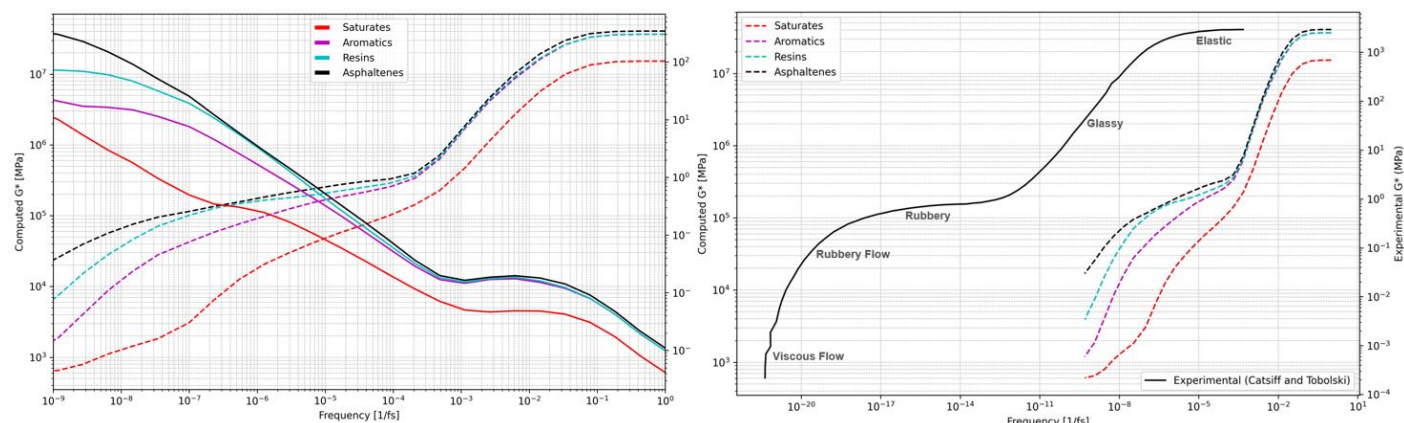
Figure 3. (Left) Mastercurves of G^* (solid) and η^* (dashed) for each SARA fraction. (Right) Mastercurves of G^* from (Left) in place with the experimentally obtained G^* values for Polyisobutylene by Catsiff and Tobolski[14].

4. CONCLUSION

This study demonstrates that strain-controlled oscillatory deformations in MD simulations effectively capture the dynamic properties of bitumen's SARA fractions if the characteristic times between observations are carefully aligned. By employing frequency sweep tests across a wide range, the simulations revealed moduli spanning 1000–20 MPa and viscosities ranging from 40 Pa·s to 0.001 Pa·s, providing insights into the viscoelastic behaviours of these molecular systems.

1. Oscillatory shear deformation in MD effectively characterizes bitumen's dynamic properties, complementing experimental approaches.

Frequency sweep tests revealed distinct moduli and viscosity ranges, aligning well with experimental observations.

2. Mechanical differences among SARA fractions were evident: Saturates were the softest and thinnest, while Asphaltenes were the stiffest and least thermally susceptible.

3. MD simulations highlighted faster relaxation times compared to experiments, allowing the study of Hertz-long oscillations within computationally accessible spatiotemporal scales.

4. Five distinct viscoelastic regimes—Elastic, Glassy, Rubbery, Rubbery Flow, and Viscous—were identified, showcasing transitions in mechanical responses.

Aligning the simulation's characteristic times with those of experimental setups to achieve a comparable Deborah number is essential for capturing realistic stress-related phenomena in MD simulations of bituminous materials.

5. REFERENCES

[1] D. Lesueur, The colloidal structure of bitumen: Consequences on the rheology and on the mechanisms of bitumen modification, Advances in colloid and interface science 145(1-2) (2009) 42-82.
[2] E. Behzadfar, S.G. Hatzikiriakos, Viscoelastic properties and constitutive modelling of bitumen, Fuel 108 (2013) 391-399.
[3] R.P. Chartoff, J.D. Menczel, S.H. Dillman, Dynamic mechanical analysis (DMA), Thermal analysis of polymers: fundamentals and applications (2009) 387-495.
[4] G.D. Airey, A.E. Hunter, Dynamic mechanical testing of bitumen: sample preparation methods, Proceedings of the Institution of Civil Engineers-Transport, Thomas Telford Ltd, 2003, pp. 85-92.
[5] D. Tsai, The virial theorem and stress calculation in molecular dynamics, The Journal of Chemical Physics 70(3) (1979) 1375-1382.
[6] L. Lin, M. Kedzeriski, Prediction of Lubricant Viscosity from Nonequilibrium Molecular Dynamics Simulation, (2021).
[7] R. Metzler, T.F. Nonnenmacher, Fractional relaxation processes and fractional rheological models for the description of a class of viscoelastic materials, International Journal of Plasticity 19(7) (2003) 941-959.
[8] A. Franck, T. Germany, Viscoelasticity and dynamic mechanical testing, TA Instruments, New Castle, DE, USA AN004 (1993).
[9] D.D. Li, M.L. Greenfield, Viscosity, relaxation time, and dynamics within a model asphalt of larger molecules, The Journal of Chemical Physics 140(3) (2014).
[10] H. Sun, S.J. Mumby, J.R. Maple, A.T. Hagler, An ab initio CFF93 all-atom force field for polycarbonates, Journal of the American Chemical society 116(7) (1994) 2978-2987.
[11] J.P. Ewen, H.A. Spikes, D. Dini, Contributions of Molecular Dynamics Simulations to Elastohydrodynamic Lubrication, Tribology Letters 69(1) (2021) 24.
[12] T. Dotson, Relaxation Behavior in Molecular Dynamics Simulations of Simple Polymers, Citeseer, 2008.
[13] A.Y. Kuksin, I. Morozov, G. Norman, V. Stegailov, I. Valuev, Standards for molecular dynamics modelling and simulation of relaxation, Molecular Simulation 31(14-15) (2005) 1005-1017.
[14] E. Catsiff, A. Tobolsky, Stress-relaxation of polyisobutylene in the transition region (1, 2), Journal of Colloid Science 10(4) (1955) 375-392.

RAPToRS – **R**apid **A**nalysis and **P**rocessing **To**ol for **R**andom Granular Structures

P.G. Bolz

Technische Universität Dresden, Department of Civil Engineering, Institute for Urban and Pavement Engineering, Georg-Schumann-Straße 7, 01187 Dresden, Saxony, Germany

ABSTRACT: The *RAPToRS* tool (Rapid Analysis and Processing Tool for Random Granular Structures) is a *Python*-based application designed for efficient generation, analysis, and processing of granular structures with specified grain parameters. It supports the serial calculation of mechanical properties for composite granular materials, such as concrete and asphalt, enabling applications such as AI-driven property prediction and statistical material analysis. *RAPToRS* leverages *Python's* parallelization capabilities for enhanced computational performance. In test calculations, it generated and analysed 100 random models in about 64 s per model on a single processor. Integrating with *OpenSeesPy's* extensive library of 73 material models, *RAPToRS* also facilitates advanced analyses of complex material behaviours of multiphase materials with varied properties.

1 PARTICLE SHAPE GENERATION

1.1 *Shape Generation Algorithms*

The generation of randomly shaped particles and the detection of overlapping are crucial for the numerical simulation of granular structures. Among others, the following algorithms and methods are used for the generation of irregularly shaped particles: R(θ) method (Wang et al. 1999), Voronoi grain-based method (Liu et al. 2018), (Mollon & Zhao 2012), (Emig et al. 2023), digital image-based method (Shan & Lai 2019), image-based clump library method (Zheng & Hryciw 2016), (Zheng & Hryciw 2017), Fourier-based method (Lianheng et al. 2017), (X. Wang et al. 2019), (Nie et al. 2019) and the Z-R shape function (Z. Wang et al. 2019). However, the majority of these algorithms are time-consuming and computationally complex to implement, meaning that a large number of calculations can only be realised to a limited extent.

1.2 *Shape Descriptors*

Numerous studies have attempted to quantitatively analyse the geometric properties of particles or grains. These morphological characteristics are typically described in three main dimensions: form (overall shape), roundness (angularity) and surface texture (roughness) (Lianheng et al. 2017), (Wang et al. 2005), (Blott & Pye 2008).

Form, considered the primary characteristic, refers to large-scale spatial irregularities in particle shape. Common shapes include circles, ellipses, rectangles, etc. To quantify a particle's basic shape, descriptors such as elongation index (EI), aspect ratio, and flatness index are used.

The EI is determined using the width W and length L of the smallest rectangular box containing the particle as follows (Mollon & Zhao 2012):

$$EI = W/L. \tag{1}$$

Roundness, a secondary characteristic, refers to variations in particle shape at the intermediate scale, capturing the average sharpness of the particle's corners. It is not influenced by the overall shape. Shape descriptors such as the angularity index, roundness index (RI) and others are used to quantify this feature. The degree of roundness is determined and calculated as follows (Janoo 1998):

$$RI = 4\pi A/P^2 \tag{2}$$

where A is the projected area, while P is the perimeter of the particle contour.

Surface texture, a tertiary characteristic, refers to small-scale surface features relative to the particle's overall size. The roughness index and regularity index are commonly used methods to quantify surface texture. The regularity index (RE) is calculated as (Mollon & Zhao 2012):

$$RE = \log\left(\frac{P}{P - P_{conv}}\right) \tag{3}$$

where P is the perimeter and P_{conv} is the convex perimeter of the particle.

1.3 *New Approach for Particle Shape Generation*

A new and simple approach was developed using the *Python* programming language. This approach uses the *polygenerator* package, made available by Radovan Bast in 2021, which is licensed under the MIT License and can be obtained via *GitHub* (Bast 2021a) or *pip* (Bast 2021b). The code of the package or the method for generating polygons will not be discussed in detail here, but the code is available on *GitHub*.

The package provides three functions for generating random polygons. The function *random_polygon()* creates random and chaotic polygons, whereas the function *random_star_shapd_polygon()* yields random star shaped polygons as the name suggests. In this paper, the function *random_convex_polygon()* was used for creating random convex polygons with a specific number of points as a function argument.

In order to ensure the reproducibility of polygons using this function, the random state was initially set by the *Python* function *random.seed()* before creating the polygon. Within a for-loop from 0 to 10209 for the initial random state, 98 polygons were created per random state with a nested for-loop from 3 to 100 number of points. A total of 1,000,580 different polygons were thus created, the shape descriptors and other parameters were determined and the parameter sets were saved in a text file. By re-importing the text file, polygons that satisfy certain conditions can be recreated rapidly and efficiently.

Figure 1 illustrates the relationship between the minimal polygon size, the number of points and the elongation index according to equation (1) and Figure 2 depicts the relationship between the polygon area, the number of points and the roundness index according to equation (2) for all 1,000,580 polygons. All polygons are created in a square box of 1 mm by 1 mm, hence the range for the minimal polygon size from almost 0 for very elongated polygons (EI ≈ 0) with a small number of points to 1 for polygons resembling almost perfect circles with a high number of points and a ratio of width to length of 1. Given that the roundness index for these polygons is equal to 1, the polygon area corresponds to the area of a circle with diameter 1 mm (0,785 mm²) as can be seen in Figure 2. Since the regularity index for convex polygons approaches infinity according to equation (3), this index is not considered further here.

2 MODEL GENERATION AND ANALYSIS

2.1 *Granular Structure Generation*

The initial step is to define the dimensions of the model in the x and y direction. Using *Python*, an algorithm was written that starts by taking a random subset with a specific number of grains (polygons) matching the user-defined criteria from the entirety of the aforementioned 1,000,580 polygons. The grains are then scaled in size and randomly arranged within the model boundaries. This process starts with the largest grains and the size of the grains is gradually reduced until all grains are placed within the model.

The algorithm checks for each grain if it overlaps with or is entirely within the boundaries of an already placed grain. If the former is the case, the grain is rotated up to 360° on the spot to check whether it fits into the current granular structure in a different orientation. If this also fails or the grain is inside another grain, a new position for the grain is randomly initiated and the algorithm starts anew.

This method enables the creation of random two-dimensional granular structures consisting of grains with a specific shape and size that can be created with high temporal and computational efficiency. Figure 3 depicts an exemplary random granular structure with dimensions 125 mm by 125 mm and 100 grains with EI between 0.45 and 0.55, a max. grain size of 16 mm and a min. grain size of 5 mm that was created using the described algorithm. The determination of the resulting particle size distribution is implemented in the algorithm, but is not considered further here.
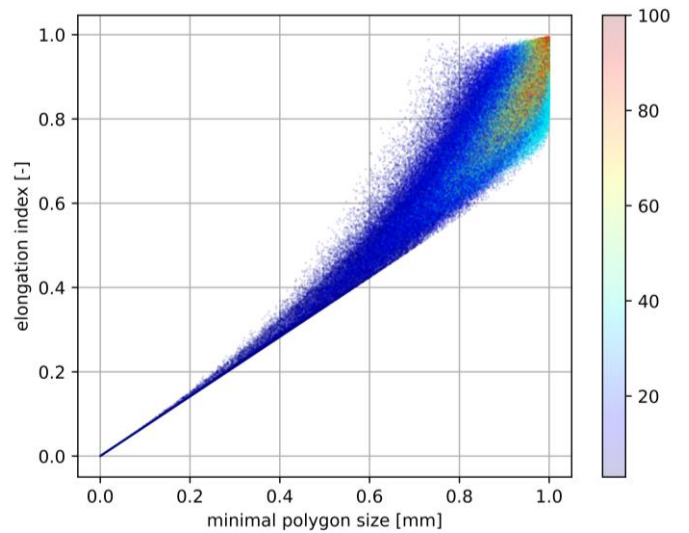
Figure 1. Minimal polygon size vs. elongation index for all 1,000,580 polygons with colour-coded number of points
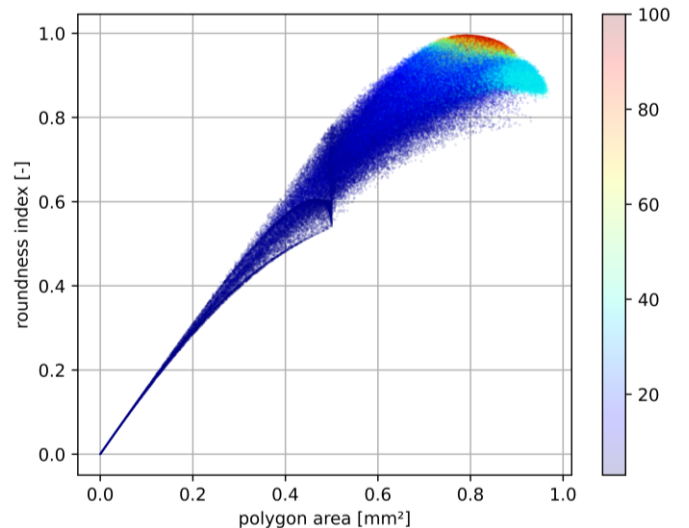
Figure 2. Polygon area vs. roundness index for all 1,000,580 polygons with colour-coded number of points
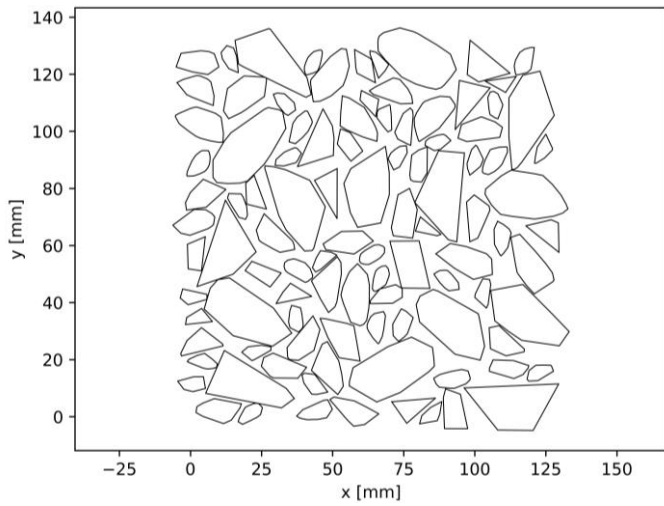
Figure 3: Random granular structure with dimensions 125 mm by 125 mm consisting of 100 grains with an elongation index between 0.45 and 0.55, a maximum grain size of 16 mm and a minimum grain size of 5 mm

2.2 Model Generation

The actual model for calculating the deformations and stresses of the granular structure is created using *OpenSeesPy*. This is a version of the *OpenSees* finite element software framework adapted for use in *Python*, which is maintained by the University of California at Berkeley. Further information on *OpenSees* and *OpenSeesPy* can be found in the respective documentation (OpenSees 2024), (OpenSeesPy 2024).

The granular structure model is generated by first choosing a resolution for the model and by then iterating over every centre point of the resulting discreet model and checking, whether the point lies within a grain (polygon) of the granular structure. If this is the case, the designated model parameters for the grains or aggregates are chosen. If otherwise the point lies within the mastic or cement stone, the respective model parameters are selected. A *FourNodeQuad element* which uses a bilinear isoparametric formulation is then created at the position of the centre point with model parameters accordingly using the four adjacent corner nodes. In order to accelerate this process, a KDTree is used for faster assignment of the elements to the respective material phases.

Thus, a plane stress / plane strain elastic model with thickness t = 1 mm is created for which boundary conditions can be defined. Figure 4 depicts the model created in this way for the exemplary granular structure mentioned in the last section.

Note that the grains are cut off at the specified edges of the model. Using this approach, a variety of different model geometries can be created. For example, a circular disc can be considered by checking whether the centre points of the model lie inside a circle with a defined radius. Thus, the indirect tensile test, which is widely used in pavement engineering can be modelled.
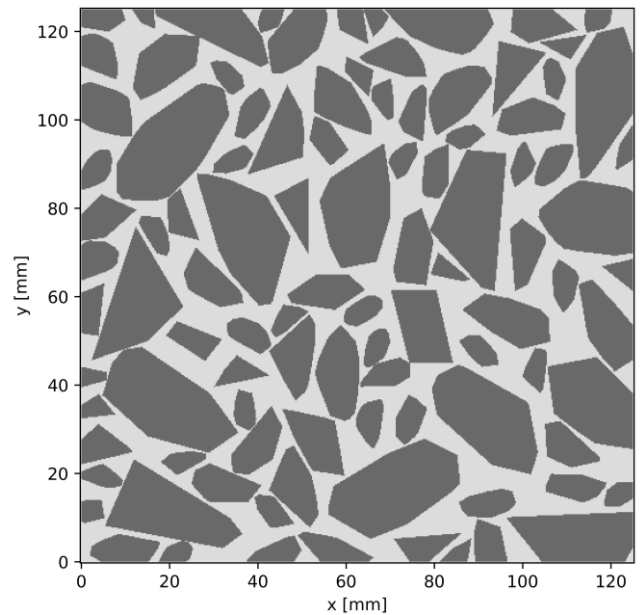
Figure 4. Generated granular model using *OpenSeesPy* with a resolution of 0.25 mm and thickness t = 1 mm; dark grey: aggregates / grains with E = 80,000 N/mm² and ν = 0.2; light grey: cement stone with E = 5000 N/mm² and ν = 0.3

2.3 Model Analysis and Processing

Continuing with the previously considered example, the following boundary conditions are applied to explain the model analysis using *OpenSeesPy*. The displacement of the nodes at y = 0 is fixed in x and y direction and the displacement of the nodes at y = 125 is fixed in x direction. Additionally, a multi-point constraint is defined between the nodes at y = 125, forcing a synchronised movement in y direction. A force of 1000 N is equally distributed over all nodes at y = 125. The model is subsequently analysed using the respective *Analysis Commands* provided by *OpenSeesPy* in *Python*. Figure 5 depicts the resulting von Mises stress in the exemplary model with the aforementioned boundary conditions.
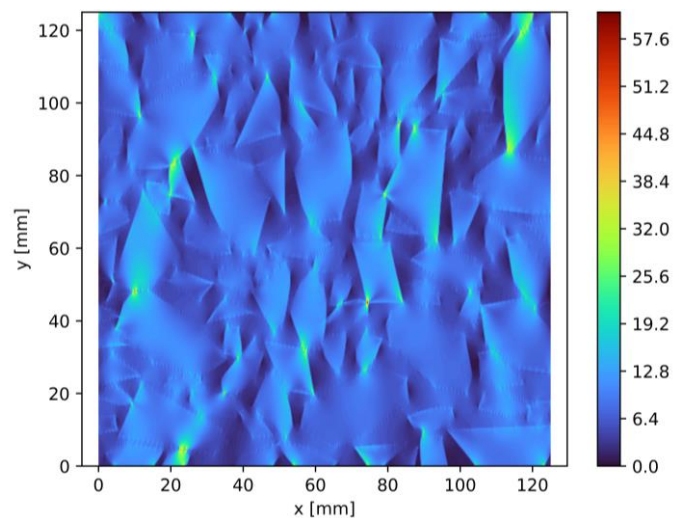
Figure 5. Von Mises stress of the granular model with defined boundary conditions plotted using *Opsvis*

As all results are available in *Python*, further analyses or processing of the results or the model in general can be carried out conveniently via efficient modules such as *NumPy* or *matplotlib*. For example, the visualisation presented in Figure 5 is the result of the *Opsvis* module (Opsvis 2024), which is based on *matplotlib* and was designed specifically for plotting models and results of *OpenSeesPy*.

3 CONCLUSION AND OUTLOOK

The algorithms described are summarised in the **R**apid **A**nalysis and **P**rocessing **To**ol for **R**andom Granular **S**tructures - *RAPToRS*. This tool allows for the time and computational effective generation, analysis and processing of random granular structures consisting of grains with specific parameters all within the *Python* programming language.

The *RAPToRS* tool enables the realisation of serial calculations of mechanical properties of all kinds of composite granular materials such as concrete or asphalt. This data can then be used e.g., for the learning of artificial intelligence metamodels for the prediction of said properties or for the statistical analysis of the properties of one specific material. As the tool is written entirely in *Python*, other useful modules and packages can be used, e.g. for the parallelisation of calculations.

A test calculation of 100 random models each measuring 125 mm by 125 mm with 80 grains (0.45 < EI < 0.55, 16 mm maximum and 5 mm minimum grain size) and a resolution of 0.5 mm using one processor (AMD Ryzen 7 PRO 4750U) took 64.17 s on average (standard deviation of 1.44 s). Computing 10,000 models with the same parameters using a moderately performant computer with 64 processors would therefore take around 167 min or 2.8 h.

The *OpenSeesPy* framework currently offers a total of 73 different material models for linear, non-linear, elastic, viscous, plastic and other complex material behaviour. This allows not only trivial calculations to be carried out, as demonstrated in this paper, but also complex relationships resulting from the granular material structure to be analysed. The presented approach for generating granular structures also allows the consideration of multiphase materials with an arbitrary amount of material phases.

It should be noted however, that the tool is not without limitations. On the one hand, only two-dimensional, plane stress / plane strain problems can be considered. Secondly, no contact conditions between the individual material components are currently taken into account. The aggregates are firmly embedded in the mastic. Further development of the tool may allow contacts to be taken into account in the future, e.g. by implementing interface elements. Finally, only convex polygons (particle shapes) are currently considered. However, concave polygons can also be generated using the *polygenerator* package, which will be implemented in the *RAPToRS* tool in the future.

REFERENCES

Wang, Z. M. et al. 1999. Mesoscopic study of concrete I: generation of random aggregate structure and finite element mesh. *Computers & structures, 70(5), 533-544.*

Liu, Q. et al. 2018. A Voronoi element based-numerical manifold method (VE-NMM) for investigating micro/macro-mechanical properties of intact rocks. *Engineering Fracture Mechanics*, *199*, 71-85.

Mollon, G. & Zhao, J. 2012. Fourier–Voronoi-based generation of realistic samples for discrete modelling of granular materials. *Granular matter 14*: 621-638.

Emig, J. et al. 2023. A stochastic neural network based approach for metamodelling of mechanical asphalt concrete properties. International Journal of Pavement Engineering 24.1: 2177650.

Shan, P. & Lai, X. 2019. Mesoscopic structure PFC~ 2D model of soil rock mixture based on digital image. *Journal of Visual Communication and Image Representation*, *58*, 407-415.

Zheng, J. & Hryciw, R. D. 2016. A corner preserving algorithm for realistic DEM soil particle generation. *Granular Matter*, *18*(4), 84.

Zheng, J. & Hryciw, R. D. 2017. An image based clump library for DEM simulations. *Granular Matter, 19(2), 26.*

Lianheng, Z. et al. 2017. Reconstruction of granular railway ballast based on inverse discrete Fourier transform method. *Granular Matter 19*: 1-17.

Wang, X. et al. 2019. Stochastic numerical model of stone-based materials with realistic stone-inclusion features. *Construction and Building Materials, 197, 830-848.*

Nie, Z. et al. 2019. Investigating the effects of Fourier-based particle shape on the shear behaviors of rockfill material via DEM. *Granular Matter*, *21*, 1-15.

Wang, Z. et al. 2019. A random angular bend algorithm for two-dimensional discrete modeling of granular materials. *Materials*, *12*(13), 2169.

Wang, L. et al. 2005. Unified method to quantify aggregate shape angularity and texture using Fourier analysis. *Journal of Materials in Civil Engineering 17.5*: 498-504.

Blott, S. J. & Pye, K. 2008. Particle shape: a review and new methods of characterization and classification. *Sedimentology 55.1*: 31-63.

Janoo, V. C. 1998. Quantification of shape, angularity, and surface texture of base course materials.

Bast, R (a). 2021. Polygenerator. URL: https://github.com/bast/polygenerator. Retrieved on November 5, 2024.

Bast, R (b). 2021. Polygenerator. URL: https://pypi.org/project/polygenerator/. Retrieved on November 5, 2024.

OpenSees. 2024. OpenSees Online Documentation. URL: https://opensees.berkeley.edu/index.php. Retrieved on November 5, 2024.

OpenSeesPy. 2024. OpenSeesPy Online Documentation. URL: https://openseespydoc.readthedocs.io/en/latest/. Retrieved on November 5, 2024.

Opsvis. 2024. Opsvis Online Documentation. URL: https://opsvis.readthedocs.io/en/latest/. Retrieved on November 5, 2024.

Generation of isothermal relaxation spectrum for bitumen

I. Catherine Sanchana
Research scholar, Department of Civil Engineering, Indian Institute of Technology Madras, Chennai, India

J. Murali Krishnan
Professor, Department of Civil Engineering, Indian Institute of Technology Madras, Chennai, India

ABSTRACT: The relaxation spectrum is a critical tool for characterising the viscoelastic properties of bitumen. This study investigates the challenges associated with generating an isothermal relaxation spectrum from frequency domain data spanning a short range of frequencies. Experiments were carried out on unmodified VG30 bitumen at 0 °C and 60 °C across a limited frequency range spanning 1.39 decades. This was extended using generalised linear viscoelastic models with an appropriate number of relaxation modes to derive continuous relaxation spectra. The range of the relaxation time is found to be more for 0 °C than for 60 °C and in both the cases, the corresponding frequency range to capture the dominant relaxation modes was found to be too high to be accessed by the testing equipment.

1 INTRODUCTION

A relaxation spectrum (discrete or continuous) offers a distribution of relaxation times (Findley et al. 1976, Ferry 1980) and provides a fundamental representation of the mechanical response of a material. Each relaxation time corresponds to a distinct mode of stress relaxation, with the spectrum quantifying the contribution of each mode to the overall viscoelastic behavior. The distribution of relaxation times can be either discrete or continuous, comprising infinitesimal contributions across an infinite range of relaxation times (Ferry 1980). Studies have highlighted several challenges in determining the discrete relaxation spectrum (DRS), including the non-uniqueness of values and the occurrence of negative spectra (Zhang et al. 2020). Though the continuous relaxation spectrum (CRS) also poses problems due to the inversion of integrals, it is preferred over the DRS as it is said to represent the fundamental nature of the relaxation process in many materials (Bhattacharjee et al. 2012).

For bituminous binders and mixtures, scant data exists related to computing the CRS and DRS. The relaxation spectrum can be obtained from experimental data carried out in the time domain (Nivitha et al. 2023), such as stress relaxation or in the frequency domain, such as frequency sweep experiments (Zhao et al. 2018). When the stress relaxation data is used, the time duration of testing influences the relaxation spectrum. In addition to this, the difficulties associated with generating an instantaneous deformation and tracking the rapid initial decay of stress exist in the case of stress relaxation experiments (Narayan et al. 2012, Yu et al. 2020, Xi et al. 2022). Hence, the frequency domain experiments are usually preferred over the time domain experiments, where the experiments are generally carried out over a range of frequencies in the small amplitude oscillatory shear mode. However, the range of frequencies that could be accessed by the equipment typically spans no more than three decades, owing to the limitations of the equipment (Yu et al. 2020). This short frequency range may be insufficient to fully capture the relaxation characteristics of bitumen.

To overcome this issue, most studies on the relaxation spectrum derived from frequency domain experiments utilise information from the master curve obtained through the time-temperature superposition principle (TTSP), which extends the experimental frequency range (Behera et al. 2024, Medam et al. 2024). However, due to the transitory response of bitumen in the temperature range of 20 to 60 °C (Padmarekha & Krishnan 2013, Nivitha et al. 2020), it is not always possible to construct a unique master curve in this temperature range, in addition to the practical difficulty of collecting data over a large range of decades of frequency. Considering this limitation, alternative methods have to be used to extend the frequency window in such instances, which might be using linear viscoelastic models.

This study focuses on the issues concerning the generation of the isothermal relaxation spectrum using frequency sweep experiments carried out over a short frequency range.

2 EXPERIMENTAL INVESTIGATION

The material used in this study is an unaged unmodified bitumen of Viscosity Grade VG30 as per Indian Standards, IS 73 (2018).

The material was subjected to frequency sweep experiments in the strain-controlled mode at temperatures of 0 and 60 °C in a parallel plate system in a Dynamic Shear Rheometer (DSR). The sample dimensions were 8 mm diameter and 2 mm height when tested at 0 °C and 25 mm diameter and 1 mm height when tested at 60 °C. The following frequencies were applied in a step-wise manner, starting with the highest frequency: 0.1, 0.3, 0.5, 0.7, 0.9, 1.3, 1.5, 1.7, 1.9, 2.1 and 2.5 Hz. Twenty cycles of data were collected for each frequency. The amplitude was kept constant across the frequencies and was chosen such that the material response is linear as per ASTM D7175(2023). This was ensured by carrying out an amplitude sweep experiment at the highest frequency of 2.5 Hz for each temperature. The test matrix is shown in Table 1.

Table 1. Test matrix.

Temperature (°C)	Strain amplitude (%)	Frequency (Hz)
0	0.27	0.1, 0.3, 0.5, 0.7, 0.9,
60	8.6	1.3, 1.5, 1.7, 1.9, 2.1, 2.5

3 ANALYSIS AND RESULTS

The storage and loss modulus values in terms of the CRS are given as,

$$G'(\omega) = \int_{-\infty}^{\infty} \frac{\omega^2 \tau^2}{1 + \omega^2 \tau^2} h(\tau) d\ln\tau \tag{1}$$

$$G''(\omega) = \int_{-\infty}^{\infty} \frac{\omega\tau}{1 + \omega^2 \tau^2} h(\tau) d\ln\tau. \tag{2}$$

Here, ω is the angular frequency, τ is the relaxation time and $h(\tau)$ is the relaxation spectrum. To construct the CRS, the regularisation method is used and this is achieved with the help of an open-source Python programmed code, pyReSpect (Takeh & Shanbhag 2013). Here, the CRS, $h(\tau) = e^{H(\tau)}$ is obtained by minimising the cost function using the Tikhonov regularisation. This yields the $H(\tau)$ curve, which is a trade-off between the smoothness of the curve and the overfitting of the curve. Following this, this program requires the values of frequency, storage modulus and loss modulus to generate the CRS.

The pyReSpect program yields the relaxation spectrum spanning the range given by $e^{\frac{B\pi}{2}}/\omega_{max} \leq \tau \leq e^{-\frac{B\pi}{2}}/\omega_{min}$ by allowing for the choice of B which takes the values of -1, 0 or 1. The value of $B = 0$ generates the relaxation time range where it is

restricted by the experimental frequency range, i.e., $1/\omega_{max} \leq \tau \leq 1/\omega_{min}$. When $B = 1$, the range of the relaxation time gets reduced by 1.36 decades, i.e., 0.68 decades on either side of the range. When the value of $B = -1$, the experimental frequency range is increased by 0.68 decades on either side of the maximum and minimum values of frequency, i.e., the entire frequency range increases by 1.36 decades. In this study, the experiment covers frequencies ranging from 0.1 to 2.5 Hz, which is only 1.39 decades of frequency. Even the choice of $B = -1$ may not be able to yield the necessary frequency window that is required to capture the relaxation characteristics of bitumen, as pointed out by Yu et al. (2020) and hence, the experimental frequency range is extended using a linear viscoelastic model.

3.1 *Choice of the linear viscoelastic model*

Since the material response is obtained at two different temperatures, the same model may not be able to capture the material response across both the test temperatures. In this context, a Generalised Maxwell (GM) model is proposed to capture the response of bitumen at the higher temperature of 60 °C and a Zener model is proposed to capture the response of bitumen at the lower temperature of 0 °C. The GM model consists of several Maxwell models connected in parallel with n relaxation modes and the linear viscoelastic parameters, storage and loss modulus as obtained from the model are given by,

$$G'(\omega) = \sum_{i=1}^{n} \frac{G_i \omega^2 \tau_i^2}{1 + \omega^2 \tau_i^2} \tag{3}$$

$$G''(\omega) = \sum_{i=1}^{n} \frac{G_i \omega \tau_i}{1 + \omega^2 \tau_i^2}. \tag{4}$$

Here, G_i and τ_i are the relaxation modulus and relaxation time corresponding to the ith relaxation mode. The Zener model is very similar to the GM model but with an additional spring parallel to the Maxwell elements and hence a modulus term G_0 gets added to the storage modulus in Equation (3). The loss modulus remains unchanged. For a given number of modes, the Zener model is found to show better predictions of the linear viscoelastic parameters across the frequencies for the data collected at 0 °C and this is represented as a decrease in the normalised root mean square error (NRMSE) values compared to the GM model as shown in Figure 1.
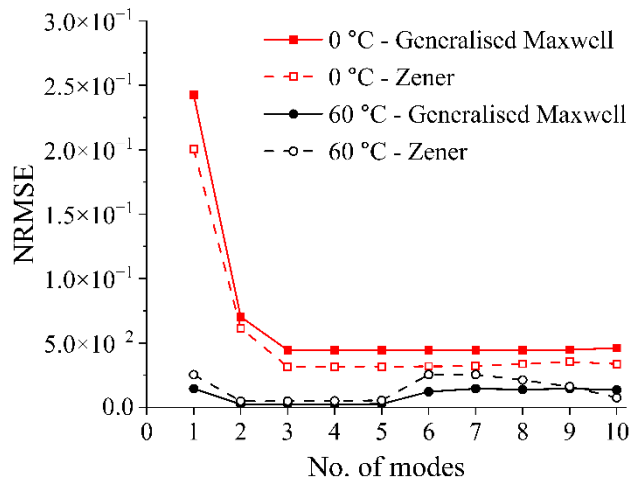
Figure 1. Variation of NRMSE against number of modes for different models.

3.2 *Choice of the number of modes*

It is observed that the NRMSE value decreases significantly with an increase in the number of modes up to a certain value of n and beyond this, there is no significant change or there is an increase in the NRMSE values (Fig. 1). The value of n beyond which there is no further significant decrease in the number of modes is identified as the number of modes for the respective models to predict the material response at the corresponding temperatures. In this context, the number of modes required to predict the material response at 0 and 60 °C are 3 and 2, respectively. The parameters (G_i) associated with the number of modes indicate the DRS of bitumen against the relaxation times (τ_i). An increase in the number of modes beyond the ones identified at the given test temperature was found to yield similar values of the relaxation times, thereby showing redundancy, meaning they do not provide additional insight into the relaxation characteristics of bitumen. Table 2 shows the relaxation moduli and times for different number of modes for 60 °C. It can be observed that beyond $n = 2$, some of the relaxation times are similar and the total distinct values of relaxation time for any number of modes are only 2.

Table 2. Model parameters for different modes for 60 °C

n	G_i (kPa)	τ_i (s)
2	328.33, 0.48	0.001, 0.080
3	131.8 148.20, 0.45	0.001, 0.001, 0.083
4	69.27, 112.99, 96.39, 0.44	0.001, 0.001, 0.001, 0.083

Having identified the suitable model and the number of modes, the frequency range is extended beyond the experimental frequency window and a representative plot is shown in Figure 2.

The CRS is generated using the storage and loss modulus values corresponding to the extended frequency range using the pyReSpect program. The CRS

determined for the material at 0 and 60 °C are shown in Figure 3. From the figure, it can be observed that the distribution of relaxation times is greater for 0 °C than for 60 °C.
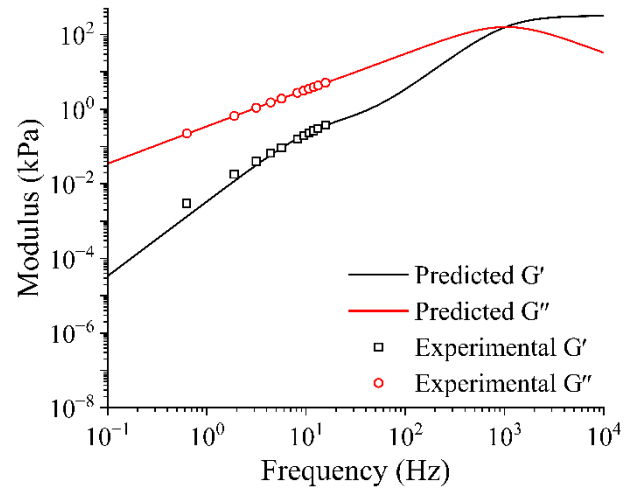
Figure 2. Predicted moduli for extended frequency window at 60 °C.

(a) 0 °C
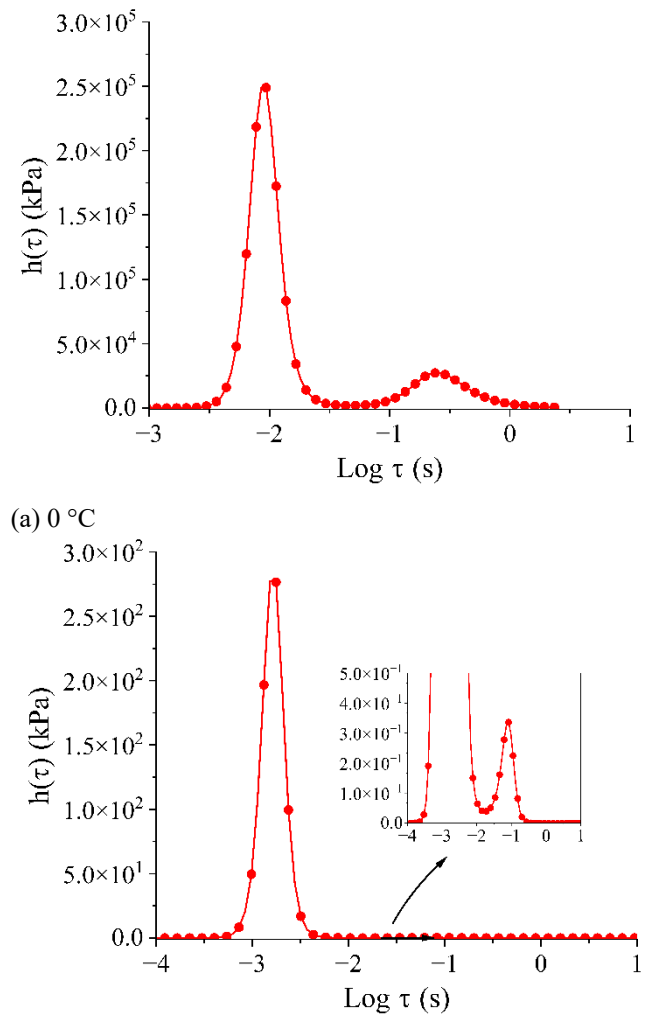
(b) 60 °C

Figure 3. Continuous relaxation spectrum.

The position and intensity of the peaks observed in all the cases were found to be almost similar to those obtained from the linear viscoelastic model (DRS). In

this context, ideally, the CRS at 0 °C should show three peaks, with the third peak occurring at higher relaxation times. However, it was observed that the model predictions were poor at lower frequencies and hence, were not included in the generation of the CRS for this temperature.

From Figure 3a, it can be observed that the relaxation time required to capture the dominant relaxation characteristics of bitumen spans approximately 3.5 decades at 0 °C, ranging from $\tau_{min} = 10^{-3}$ s to $\tau_{max} = 10^{0.5}$ s. The corresponding frequency range for this relaxation time is $\omega_{min} = 0.32$ rad/s to $\omega_{max} = 1000$ rad/s. Similarly, as shown in Figure 3b, at 60 °C, the frequency range spans approximately 1.5 decades (ignoring the second peak, which is insignificant), extending from $\omega_{min} = 100$ rad/s to $\omega_{max} = 3162$ rad/s. These high frequencies exceed the capabilities of the equipment due to its limitations. Therefore, extending the experimental frequency range is crucial to capture the relaxation characteristics of bitumen.

In this study, the DRS of bitumen is determined first to extend the frequency range required for generating the CRS. This approach contrasts with methodologies in some existing literature, where the CRS is determined first, and the DRS is subsequently derived to overcome the limitations of the DRS (Bae & Cho 2016). However, such methodologies can be applied only when the experimental frequency range can be extended using the TTSP. In cases where TTSP is not applicable, the DRS must be determined first, followed by the CRS.

4 CONCLUSION

The relaxation spectrum is a crucial parameter in understanding the viscoelastic behavior of materials, particularly bitumen. This study highlights the challenges in generating isothermal relaxation spectra when the frequency range is short. An unmodified VG30 bitumen is subjected to frequency sweep experiment at 0 and 60 °C at 11 frequencies spanning 1.39 decades. The experimental frequency range is extended by appropriate generalised linear viscoelastic models with a suitable number of modes and continuous relaxation spectra were obtained. It was observed that the frequencies required to capture the relaxation behavior of bitumen are much larger than that could be accessed by the equipment.

5 REFERENCES

ASTM D7175 2023. Standard test method for determining the rheological properties of asphalt binder using a dynamic shear rheometer. *ASTM International*, West Conshohocken, PA.

Bae, J. E., & Cho, K. S. 2016. A systematic approximation of discrete relaxation time spectrum from the continuous spectrum. *Journal of Non-Newtonian Fluid Mechanics*, 235: 64–75.

Behera, A., Thushara, V. T., & Krishnan, J. M. (2024). Linear viscoelastic response of emulsified-asphalt cold recycled mixtures. *Mechanics of Time-Dependent Materials*, 28(3): 1-25.

Bhattacharjee, S., Swamy, A. K., & Daniel, J. S. 2012. Continuous relaxation and retardation spectrum method for viscoelastic characterization of asphalt concrete. *Mechanics of Time-Dependent Materials*, 16(3): 287–305.

Ferry, J. D. 1980. *Viscoelastic Properties of Polymers*, 3rd ed. New York: Wiley.

Findley, W. N., Lai, J. S., & Onaran, K. 1976. *Creep and Relaxation of Nonlinear Viscoelastic Materials*. New York: Dover Publications.

IS 73 2018. Indian standard for paving bitumen. *Bureau of Indian Standards*, New Delhi.

Medam, T., Thushara, V. T., & Krishnan, J. M. 2024. Statistics-based design of experimental framework to formulate ternary RAP binder blends. *Journal of Materials in Civil Engineering*, 36(3): 04023638.

Narayan, S. P. A., Krishnan, J. M., Deshpande, A. P., & Rajagopal, K. R. 2012. Nonlinear viscoelastic response of asphalt binders: An experimental study of the relaxation of torque and normal force in torsion. *Mechanics Research Communications*, 43: 66–74.

Nivitha, M. R., Krishnan, J. M., & Rajagopal, K. R. 2020. Viscoelastic transitions exhibited by modified and unmodified bitumen. *International Journal of Pavement Engineering*, 21(6): 766–780.

Nivitha, M. R., Devika, R., Krishnan, J.M., & Roy, N. 2023. Influence of bitumen type and polymer dosage on the relaxation spectrum of styrene-butadiene-styrene (SBS)/styrene-butadiene (SB) modified bitumen. *Mechanics of Time-Dependent Materials*, 27(1): 79–98.

Padmarekha, A., & Krishnan, J. M. 2013. Viscoelastic transition of unaged and aged asphalt. *Journal of Materials in Civil Engineering*, 25(12): 1852–1863.

Takeh, A., & Shanbhag, S. 2013. A computer program to extract the continuous and discrete relaxation spectra from dynamic viscoelastic measurements. *Applied Rheology*, 23(2): 24628.

Xi, L., Luo, R., Ma, Q., Tu, C., & Shah, Y. I. 2022. An improved method to establish continuous relaxation spectrum of asphalt materials. *Construction and Building Materials*, 354: 129182.

Yu, D., Yu, X., & Gu, Y. 2020. Establishment of linkages between empirical and mechanical models for asphalt mixtures through relaxation spectra determination. *Construction and Building Materials*, 242: 118095.

Zhang, F., Wang, L., Li, C., & Xing, Y. 2020. The discrete and continuous retardation and relaxation spectrum method for viscoelastic characterization of warm mix crumb rubber-modified asphalt mixtures. *Materials*, 13(17): 3723.

Zhao, K., Wang, Y., Chen, L., & Li, F. 2018. Diluting or dissolving? The use of relaxation spectrum to assess rejuvenation effects in asphalt recycling. *Construction and Building Materials*, 188: 143–152.

Large-scale production validation of Warm Mix Asphalt containing Crumb Rubber for motorway porous wearing course

S. D'Angelo, F. Cardone, G. Ferrotti, F. Canestrari
Università Politecnica delle Marche, via Brecce Bianche 12, 60131 Ancona (Italy)

F. M. Colasanti
Autostrade per l'Italia, via A. Bergamini 50, 00159 Rome (Italy)

ABSTRACT: Warm Mix Asphalt (WMA) technology in combination with crumb rubber (CR) from end-of-life tires (ELTs) can lead to a sustainable low environmental impact solution, while enhancing mechanical and acoustic performance of asphalt pavements. As part of a broader project, including a preliminary laboratory investigation, this research aims at evaluating the technical feasibility of WMAs modified with CR by dry process for porous wearing courses. Large-scale production and field trial on motorway section were conducted to assess the performance of the selected mixtures according to the Technical Specifications for the Italian motorway network. The experimental investigation included volumetric and workability analyses, mechanical tests and surface characterization on both laboratory specimens and cores taken from the field trial. The results show that when the CR content is lower than a critical amount no specific precaution has to be undertaken at production plant and during lay-down activities in order to guarantee satisfying workability, mechanical and surface properties.

1 INTRODUCTION

Warm Mix Asphalt (WMA) Technology has gained increasing attention in recent years as a sustainable alternative to traditional hot mix asphalt (HMA) (Milad et al. 2022). WMA is produced at temperatures 20-40 °C lower than HMA, resulting in reduced fuel consumption and greenhouse gas emissions during production and paving operations (Ferrotti et al 2024). Additionally, the lower mixing temperatures of WMA can lead to improved working conditions and longer hauling distances.

To enhance pavement performance and address environmental concerns related to tire disposal, the incorporation of crumb rubber (CR) from end-of-life tires (ELTs) into asphalt mixtures has also been explored. Furthermore, CR can improve the acoustic performance of pavements by reducing traffic noise (Puccini et al. 2019).

Combining WMA technology with CR presents a promising approach to produce environmentally friendly and high-performance asphalt mixtures (Wang et al. 2018). The reduced production temperatures of WMA minimize the degradation of CR particles, potentially improving the overall performance of the modified asphalt (Yu et al. 2018). Several studies have investigated the laboratory performance of WMA-CR mixtures, demonstrating their potential in terms of mechanical properties, workability and surface characteristics (Ziari et al. 2018).

Additionally, the synergy between WMA and CR can further reduce the environmental impact by lowering emissions and enhancing the use of recycled materials (Picado-Santos et al. 2020). It has also been shown that this technology is promising when porous asphalt mixtures are considered. In fact, the rubber particles can improve durability and noise reduction properties of porous mixtures (Cetin 2013).

The purpose of this research, which is part of a wider project that started with a preliminary comprehensive laboratory characterization (D'Angelo et al. 2024), is to evaluate the technical feasibility of large-scale production of WMA-CR mixtures for Italian motorway network applications. The in-plant production of porous mixtures, the construction of a trial section and the performance assessment according to Italian motorway technical specifications were carried out.

2 EXPERIMENTAL RESEARCH

2.1 *Materials*

This research is focused on two rubberized semi-porous warm asphalt mixtures, previously optimized (D'Angelo et al. 2024) and produced with 6.5% polymer modified bitumen (PmB) and 1.5% or 2.0% CR from ELTs added by dry method (coded as M1.5_plant and M2.0_plant, respectively). The

PmB, classified as 45/80-70 and with a dynamic viscosity of 0.40 Pa·s at 160 °C, contains 4% SBS polymers. The CR, from truck tires, has a grain size of 300 to 600 μm.

The aggregate gradation of both WMAs included virgin basaltic aggregate which was proportioned to obtain a gap-graded structure ensuring an air voids content higher than 15% as well as a certain tire/road noise reduction. Additionally, 0.3% cellulose fibers (by aggregate weight) were added to prevent bitumen draindown, and 0.45% WMA chemical additive (by bitumen weight) was used for guaranteeing suitable mixing at a production temperature of 130 °C. Both WMA-CR mixtures were produced at a batch plant near the jobsite to avoid long hauling time.

2.2 Trial section

To evaluate the workability, the mechanical performance and the surface properties of the rubberized WMA mixtures, a trial section was built at the movement area of Calenzano tollbooth on the Italian A1 motorway. The test section (100-meter long and 10-meter-wide) consisted in laying the two warm semi-porous mixtures with CR at 120 °C, in contiguous lanes. The construction operations included milling the existing pavement to a depth of 4 cm, cleaning the milled surface and applying a tack coat.

During resurfacing activities, the loose asphalt mixtures were taken from trucks for laboratory analysis. Two weeks after paving, cores (100 mm and 225 mm diameter) and slabs (500×500 mm^2) were taken from both trial section lanes and subjected to innovative tests for the evaluation of surface properties.

2.3 Methods & experimental program

According to the Italian motorway technical specifications, the loose mixtures were used to produce 100 mm-diameter specimens through a gyratory compactor (50 revolutions) or a Marshall equipment (50 blows on each side), depending on the test to be performed. The compaction temperature was kept constantly at 120 °C for all compaction methods.

The workability of the mixtures at 85% of the theoretical maximum density was assessed by calculating the Compaction Energy Index (CEI) from the gyratory compactor data, (Mahmoud & Bahia 2004). Strength properties were evaluated on gyratory specimens through Indirect Tensile Strength (ITS) test at 25 °C (EN 12697-23), while raveling resistance was assessed on Marshall specimens through Cantabro Test at 25 °C (EN 12697-17). Mechanical characterization was performed on both dry-conditioned (at 25 °C for 72 hours in a climatic chamber) and wet-conditioned specimens (at 40 °C for 72 hours in a water bath, followed by 3 hours at 25 °C in a climatic chamber, as per EN 12697-12) to evaluate the water sensitivity of the mixtures through the Indirect Tensile Strength Ratio (ITSR).

Surface properties were studied on the extracted slabs through innovative testing equipment, the Darmstadt Scuffing Device (DSD) (De Visscher & Vanelstraete 2016) and the Wehner-Schulze (WS) machine Canestrari et al. 2024). The DSD, in accordance with CEN/TS 12697-50, simulates raveling caused by shear and normal stresses of a tire on an asphalt specimen. Tests were conducted at 40 °C on both dry (72 hours in a climatic chamber at 40 °C) and wet (72 hours in a water bath plus 3 hours in a climatic chamber at 40 °C) conditioned slabs, rectified at 260×260 mm^2. Raveling resistance was evaluated by calculating the Mass Loss per Area (MLpA) parameter after 30 double thrust cycles.

The WS machine is equipped with specific units to first simulate the polishing effects due to the traffic loading and then measure the corresponding friction offered by the specimen surface which was properly wetted. The output data allows the calculation of friction after polishing (μFAP) at various intervals of polishing passes on 225 mm-diameter cores (EN 12697-49), conditioned at 20 °C. The μFAP$_{60}$ of each core is determined as the friction value at 60 km/h, derived from the characteristic 6th order polynomial of the fitted curve.

The overall experimental program, carried out on the two rubberized semi-porous warm asphalt mixtures (M1.5_plant and M2.0_plant), is summarized in Table 1. Moreover, the testing results obtained in this trial section were compared with those of the preliminary laboratory characterization, detailed in D'Angelo et al. 2024 coded as M1.5_lab and M2.0_lab.

Table 1. Number of specimens tested.

Mixture	CEI	ITT*	Cantabro*	DSD*	WS
M1.5_plant	10	5+5	5+5	2+2	2
M2.0_plant	10	5+5	5+5	2+2	2

* Dry + wet conditioned specimens.

3 RESULTS AND DISCUSSION

3.1 Workability and mechanical performance

Figure 1 shows that the volumetric characteristics (air void AV content) and CEI values of the two plant-produced mixtures are very similar, with minimal deviation. Thus, the different percentages of CR do not affect the workability and the AV of the plant-produced mixtures, while meeting the technical specification limit (AV@50girations≥15%). Compared with the lab-produced mixtures, the plant-produced mixtures show a slightly penalized aptitude for compaction (higher CEI values), resulting in higher AV content.
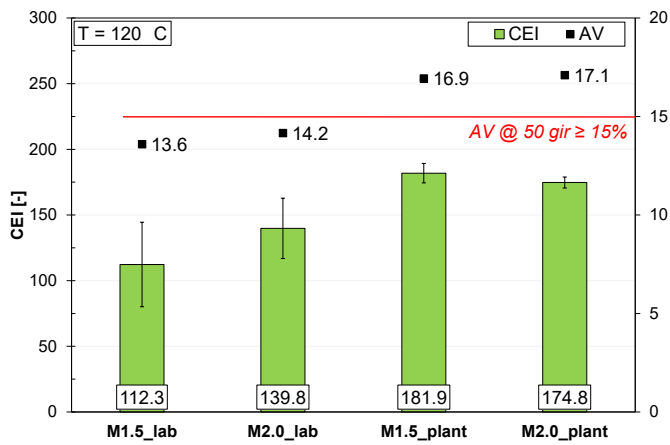
Figure 1. Workability (CEI) and volumetric characteristics (AV) of plant- and lab-produced mixtures, and Italian Motorway Technical Specification limit.

Figure 2 indicates that the increase in the CR content in both plant- and lab-produced mixtures results in lower average ITS values. The lower ITS of the plant-produced mixtures as compared with laboratory mixtures can probably be attributed to the higher AV content (Figure 1). This means that the CR effect, combined with the volumetric structure of the specimen, results in a penalized resistance of the plant-produced mixtures with respect to the technical specification requirements.
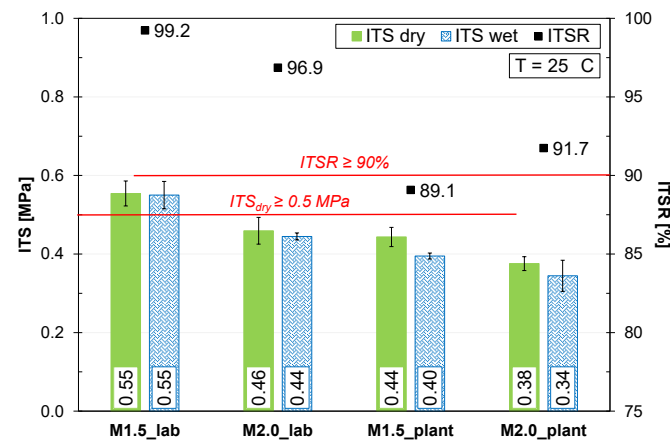
Figure 2. ITS and ITSR values of plant- and lab-produced mixtures, and Italian Motorway Technical Specification limit.

As regards the ITSR values, Figure 2 shows acceptable water susceptibility of plant-produced mixtures, which substantially meet the Technical Specification limit. The comparison between dry and wet conditions shows that plant mixtures have reduced water resistance compared to lab data, likely due to higher AV content (Figure 1) which promotes the water action.

Figure 3 shows Cantabro test results in terms of Particle Loss (PL), whose lower values result in higher raveling resistance.
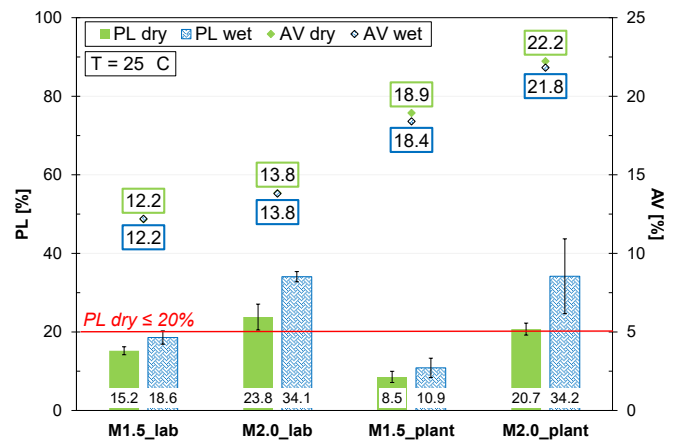
Figure 3. Raveling resistance in terms of PL and AV of plant- and lab-produced mixtures, and Italian Motorway Technical Specification limit.

Figure 3 indicates that for both plant- and lab-produced mixtures, the PL value increases with the AV and the CR content increase, in both dry and wet condition. Moreover, the plant-produced mixtures show better resistance to raveling than the lab ones and fully meet the Italian Motorway Technical Specification limit (PL dry ≤ 20%) especially for the M1.5_plant mixture.

3.2 Surface properties

The raveling resistance of the warm rubberized mixtures was also investigated with the DSD test and expressed as Mass Loss per Area (MLpA), whose lower values result in higher raveling resistance. Figure 4 shows that the higher the CR amount, the higher the MLpA value, consistently with Cantabro test results (Figure 3) in both dry and wet condition. Moreover, the mixtures with lower CR amount seem to be less sensitive to water effect with improved raveling resistance for wet with respect to dry condition. Similarly to other test findings, the higher average AV content characterizing the cores from the trial section as compared to the lab ones results in a lower raveling resistance of the plant-produced mixtures.

The WS tests on dry-conditioned cores allowed the pavement friction, expressed as μFAP_{60}, to be measured for the studied mixtures. Figure 5 shows the average μFAP_{60} at 20 °C versus the number of polishing cycles, for both plant mixtures and for a reference hot mix (HP_ref) without CR, currently used on Italian motorway network, reported for comparison purpose. The results indicate that both plant-produced mixtures provide comparable friction values throughout all polishing cycles, with no significant differences. This suggests that increasing the CR content from 1.5% to 2.0% does not negatively affect pavement friction.
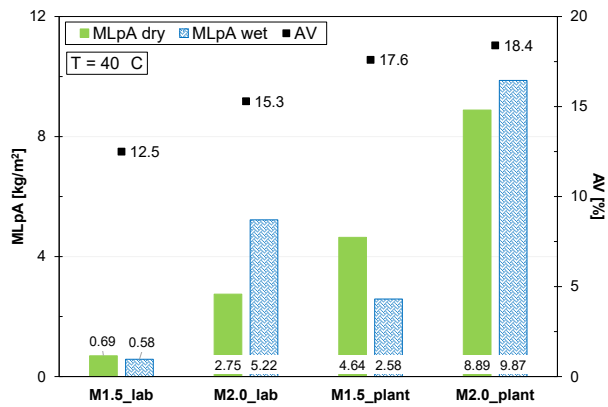
Figure 4. Raveling resistance in terms of MLpA and AV of plant- and lab-produced mixtures.
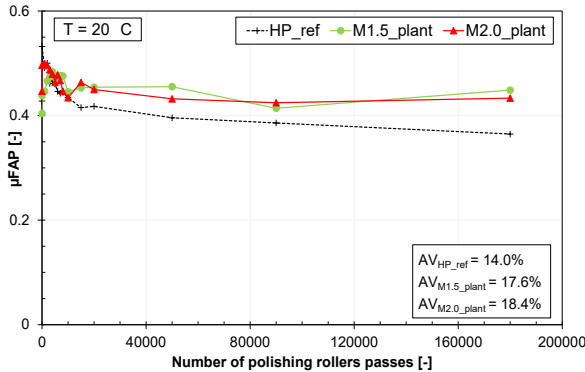
Figure 5. Friction in terms of μFAP of plant-produced mixtures and current hot mix without CR.

Furthermore, the results show that the warm rubberized mixtures (M1.5_plant and M2.0_plant) guarantee better μFAP values even after extensive polishing action than the HP_ref mixture, currently used on Italian motorways. These findings suggest that large-scale production and lay-down operation of asphalt porous mixture with CR and WMA technology do not compromise the friction level of semiporous wearing course of road pavement.

4 CONCLUSIONS

Based on the experimental results, the following conclusions can be drawn:
- large-scale production of rubberized warm semiporous asphalt mixtures is technically feasible without specific precaution in both plant and lay-down activities and it can guarantee satisfying workability and volumetric characteristics;
- however, failure to meet the Technical Specifications requirements in terms of ITS, suggests caution in the use of warm mixtures with crumb rubber on the Italian motorway network, especially for the 2% CR mixture which is strongly discouraged;
- differently, the warm mixture with 1.5% CR, showed encouraging ravelling performance, such that a comprehensive evaluation on its technical suitability in different real-world operating environments would validate its use for routine maintenance activities on the Italian motorway network.

REFERENCES

Cetin, A. (2013). Effects of crumb rubber size and concentration on performance of porous asphalt mixtures. *International Journal of Polymer Science*, *2013*(1), 789612.

D'Angelo, S., Cardone, F., Cuciniello, G., Virgili, A., & Canestrari, F. (2024, July). Laboratory Investigation of Warm Porous Asphalt Mixtures Containing Crumb Rubber for Motorway Wearing Course. In *International Conference on Maintenance and Rehabilitation of Pavements* (pp. 352-361). Cham: Springer Nature Switzerland.

De Visscher, J., & Vanelstraete, A. (2016). A new performance test for resistance to ravelling by traffic: laboratory and field experience in Belgium. In *8th RILEM International Symposium on Testing and Characterization of Sustainable and Innovative Bituminous Materials* (pp. 785-796). Springer Netherlands.

Ferrotti, G., Mancinelli, E., Passerini, G., & Canestrari, F. (2024). Comparison of energy and environmental performance between warm and hot mix asphalt concrete production: A case study. *Construction and Building Materials*, *418*, 135453.

Canestrari, F., Mariani, E., Ingrassia, L.P. (2024) Use of Wehner-Schulze machine to evaluate pavement skid resistance: A review, Journal of Traffic and Transportation Engineering (English Edition), available online.

Mahmoud, A. F. F., & Bahia, H. (2004). *Using gyratory compactor to measure mechanical stability of asphalt mixtures.* Wisconsin Highway Research Program.

Milad, A., Babalghaith, A. M., Al-Sabaeei, A. M., Dulaimi, A., Ali, A., Reddy, S. S., ... & Yusoff, N. I. M. (2022). A comparative review of hot and warm mix asphalt technologies from environmental and economic perspectives: towards a sustainable asphalt pavement. *International Journal of Environmental Research and Public Health, 19*(22), 14863.

Picado-Santos, L. G., Capitão, S. D., & Neves, J. M. (2020). Crumb rubber asphalt mixtures: A literature review. *Construction and Building Materials*, *247*, 118577.

Puccini, M., Leandri, P., Tasca, A. L., Pistonesi, L., & Losa, M. (2019). Improving the environmental sustainability of low noise pavements: comparative life cycle assessment of reclaimed asphalt and crumb rubber based warm mix technologies. *Coatings*, *9*(5), 343.

Wang, H., Liu, X., Apostolidis, P., & Scarpas, T. (2018). Review of warm mix rubberized asphalt concrete: Towards a sustainable paving technology. *Journal of cleaner production*, *177*, 302-314.

Yu, J., Yu, X., Gao, Z., Guo, F., Wang, D., & Yu, H. (2018). Fatigue resistance characterization of warm asphalt rubber by multiple approaches. *Applied Sciences*, *8*(9), 1495.

Ziari, H., Naghavi, M., & Imaninasab, R. (2018). Performance evaluation of rubberised asphalt mixes containing WMA additives. *International Journal of Pavement Engineering*, *19*(7), 623-629.

Production of recycled plastic modified bitumen- Effect of base bitumen

S. Deb, P. Kumar, & N. Saboo
Department of Civil Engineering, Indian Institute of Technology Roorkee, Uttarakhand, India

ABSTRACT: In this study, two different viscosity grade base bitumen (VG10 and VG30) and 3 dosages (2%, 3%, and 4%) of recycled low-density polyethylene (RLDPE) were selected for the preparation of the recycled plastic modified bitumen (RPMB). All modified bitumen were evaluated for physical, morphological, and rheological properties. Results state that the softening point of RPMB increases by 8 °C-18 °C depending on the dosage and type of base bitumen. The dispersion of RLDPE, measured by mean particle size, remains unaffected by the dosage of waste plastic and the type of base bitumen. However, the storage stability of RPMB is primarily governed by the density difference between the base bitumen and RLDPE, and is not influenced by the type of base bitumen.

1 INTRODUCTION

The pavement industry is advancing to meet the demand for durable, high-performance roads by improving the quality of bitumen and asphalt mixtures. Enhancing bitumen properties with polymers has become a preferred method globally. Elastomers and thermoplastics are the most common polymer types used for bitumen modification. Among these, use of recycled plastics is gaining popularity in the recent years. Utilizing recycled plastics not only improves the quality of the pavement but also promotes the environmental sustainability (Kumar et al. 2023).

Incorporation of recycled plastic (RP) in base bitumen can be carried out through dry and wet processes. Wet method of bitumen modification is more popular due to its ability to achieve a more uniform dispersion of polymers within the bitumen (Yin et al. 2020).

Literature review indicates that a wide range (0.3-12% by weight of base bitumen) of RP have been used for wet modification of bitumen. The blending is done at temperatures between 150°C and 180°C, using a high-shear mixer that operates at 200–20,000 rpm for 5–3600 minutes. For effective modification, the RP's melting point should preferably be lower than the modified bitumen's production temperature (Rafiq et al. 2021).

Numerous studies have found that modifying the base bitumen with RP significantly enhances the physical, rheological, and mechanical properties of the modified bitumen (Kumar et al. 2023). Low-density polyethylene (LDPE) is one of the preferred choices to modify the base bitumen (Rafiq et al. 2021; Wahhab et al. 2017). However limited research has focused on the influence of various base bitumen types on the preparation of recycled plastic modified bitumen (RPMB) using RP. The dispersion properties of the RPMB are largely influenced by the compatibility between the RP and base bitumen matrix. The selection of base bitumen grade is critical, as it can affect the overall quality and functionality of RPMB. As a result, the blend's homogeneity and performance under different circumstances may change. Understanding these interactions are essential for optimizing the formulation and performance of RPMB. The purpose of this research is to evaluate the effect of grade of base bitumen on the morphological, rheological, and physical characteristics of RPMB. Variations in the viscosity of the base bitumen could influence the degree of interaction with RP. Morphological analysis will help to evaluate the dispersion and distribution of RP within the base bitumen. Rheological testing will provide insights into the flow behaviour and temperature susceptibility of the RPMB.

2 EXPERIMENTAL

2.1 *Materials*

In this study, two different viscosity grade (VG) bitumen, viz. VG10 and VG30, were selected as base bitumen. Their properties were evaluated in

accordance to IS 73:2013 (BIS 2013). Recycled low-density polyethylene (RLDPE) was used with three different dosages (2%, 3%, and 4%; by the weight of bitumen) for the preparation of RPMB. The blending operation was carried out using a high shear mixer at 1000 rpm for 60 minutes at 170 ±5 °C (Rafiq et al. 2021).

2.2 Experimental protocols

2.2.1 Physical property

To study the phase change properties of the base bitumen after modifying with RLDPE, softening point test was conducted as per ASTM D36/D36M−14 (ASTM 2008).

2.2.2 Fluorescence microscopy (FM)

The dispersion characteristics of RPMB was studied using fluorescence microscopy. Drop method (Deb et al. 2025) was used to prepare sample glass slides, and fluorescence images were analysed at 10x magnification level.

2.2.3 Storage stability test

The phase separation behaviour of modified bitumen under high-temperature storage is critical for road construction applications. In this test, samples were conditioned in aluminium tubes (25.4 mm diameter, 136.7 mm length) at 163±5°C for 48±4 hours, followed by freezing at 6.7±5°C for 4 hours to solidify the material and limit dynamic movement (BIS 15462 : 2019 2019). The tube was divided into three portions after solidification, and samples from the top and bottom sections were examined using a standard DSR at 10°C intervals between 40°C and 70°C (0.1% strain, 10 rad/sec frequency). The separation ratio index (SR) was computed using the complex shear modulus (G*) values. To ensure phase stability the value of SR should be between 0.8 to 1.2. (Wahhab et al. 2017).

3 RESULTS AND DISCUSSION

3.1 Softening point analysis

The base bitumen modification with different dosages of RLDPE resulted in 16–40% average increase in the softening point of RPMB. This increase in the softening point was attributed to the viscosity of different grades of base bitumen which influence the softening point of RPMB relative to base bitumen. The increase in softening point of VG10 ranged between 11.2 °C to 17.8 °C, while for VG30 it was between 8 °C to 14 °C. This

difference in the increase may be attributed to the variation of interaction between the RLDPE and the bitumen matrix.
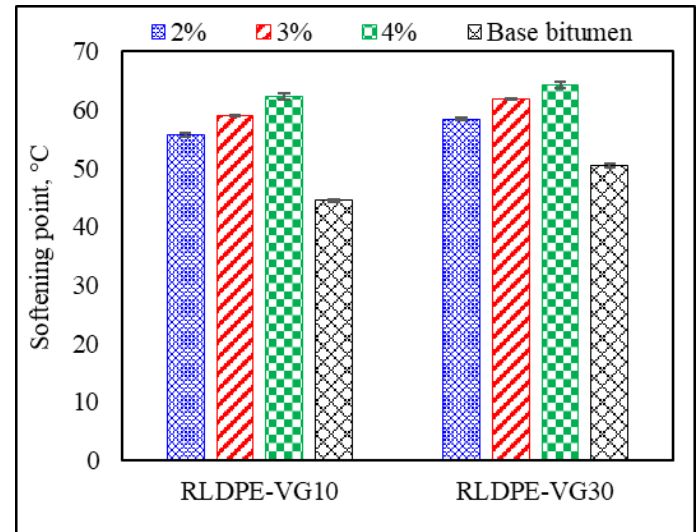
Figure 1: Softening point results of the modified bitumen

3.2 Mean particle size (MPS) analysis

The size of the dispersion RLDPE within the base bitumen was quantified by analysing the mean particle sizes of the dispersed polymers. The evaluation of the MPS was carried out by using java based software 'ImageJ' developed by US National Institutes of Health (NIH) (Schneider et al. 2012). The conversion of the RGB images to binary images calculated the MPS of the polymers in the modified bitumen, as shown in Figure 2.
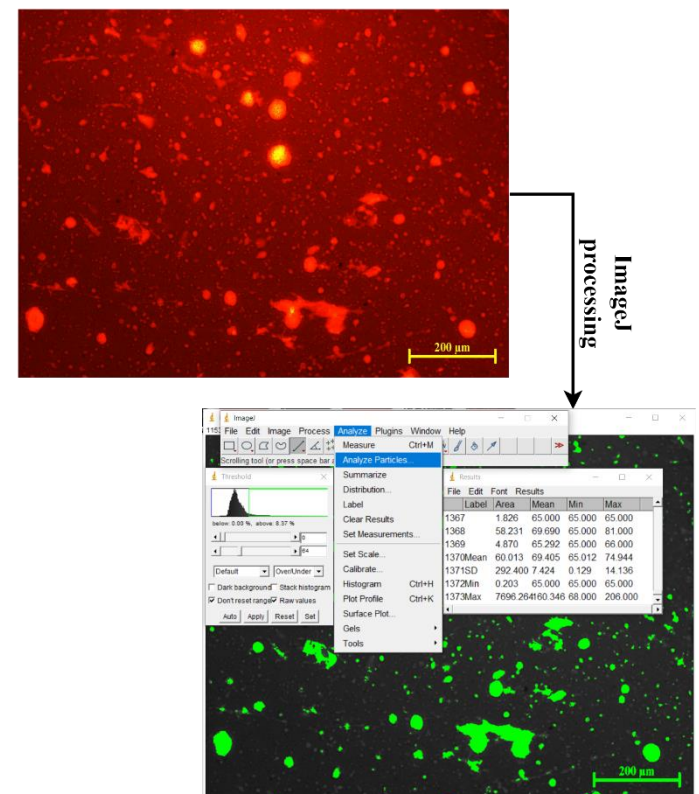
Figure 2: FM image processing by ImageJ

Figure 3 presents the MPS measurements for varying dosages of RLDPE used as a modifier for VG10 and VG30 base bitumen. The results indicate that the MPS of the polymers is independent of the dosage of waste plastic added to the base bitumen. Although slight variations in MPS are observed between the two base bitumen types; these differences are likely attributable to adjustments in the threshold limits applied during image processing by the ImageJ software (Hao and Wang 2021).
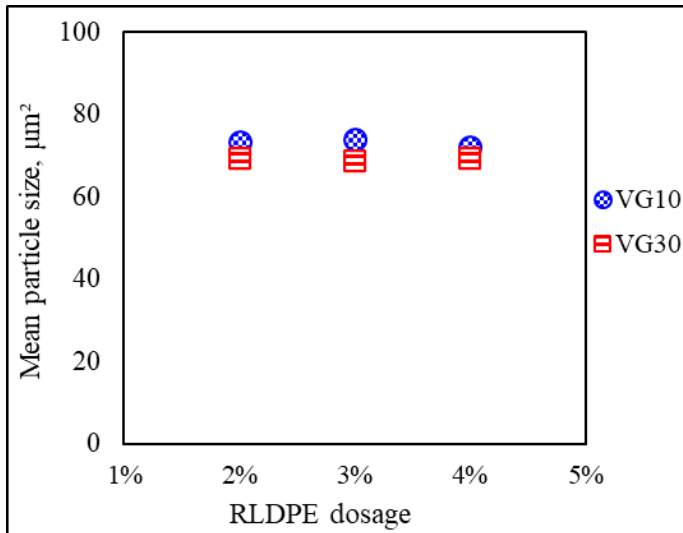
Figure 3: MPS of modified bitumen at different dosages

A statistical analysis (Table 1) was conducted to evaluate the influence of base bitumen type and waste plastic dosage on the dispersion characteristics of RLDPE modified bitumen, using softening point and fluorescence microscopy results. Analysis of variation (ANOVA) was performed at 95% (p-value>0.05) confidence level to determine the significance of these factors on the dispersion behaviour.

Table 1: ANOVA results

Parameter	Variable	p-value	Level of significance
ΔSP	Type of base bitumen	0.245	No
MPS	Dosage of RLDPE	0.963	No

Based on Table 1, the p-values of the analyzed variables exceed 0.05, indicating that the type of base bitumen and the dosage of RLDPE are independent factors in the modification of base bitumen using recycled waste plastics.

3.3   *Phase separation characteristics*

The results of the separation index (SR) are represented in Figure 4 and 5. At lower temperatures (40°C), the binder remains stiff,

minimizing its flow and resulting in stable SR values for both top and bottom specimens. As the temperature increases (>50°C), the binder's flowability rises, amplifying the impact of polymer content. The SR value of the modified bitumen in the top of the separation tube were higher than the values obtained for the lower part. This is in agreement to the results obtained by Wahhab et al. (Wahhab et al. 2017). This phenomenon was found almost identical for both RLDPE modified VG10 and VG30 bitumen. It was found that at 2-3% RLDPE dosage, the SR values of the modified bitumen remain within the recommended limit (0.8-1.2) for all the test temperatures. At 4% dosage, phase separation was observed in the modified bitumen (both VG10 and VG30). This suggests that the choice of base bitumen does not significantly influence the storage stability of the RLDPE-modified bitumen.
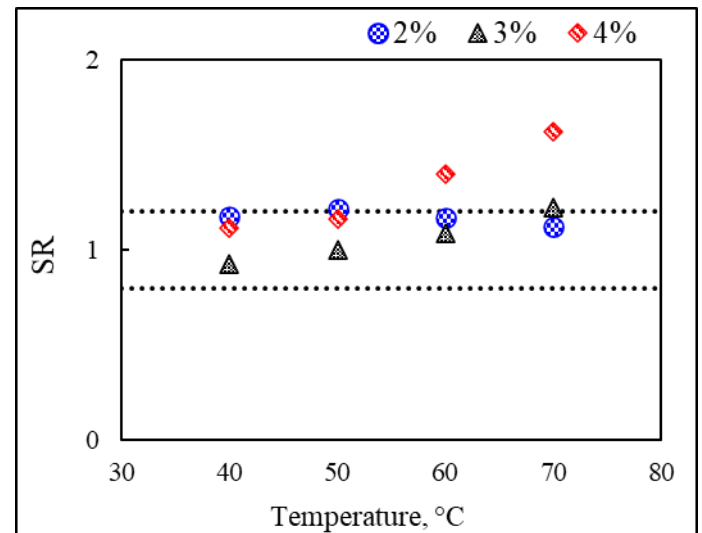
Figure 4: SR results for the RLDPE-VG10 modified bitumen
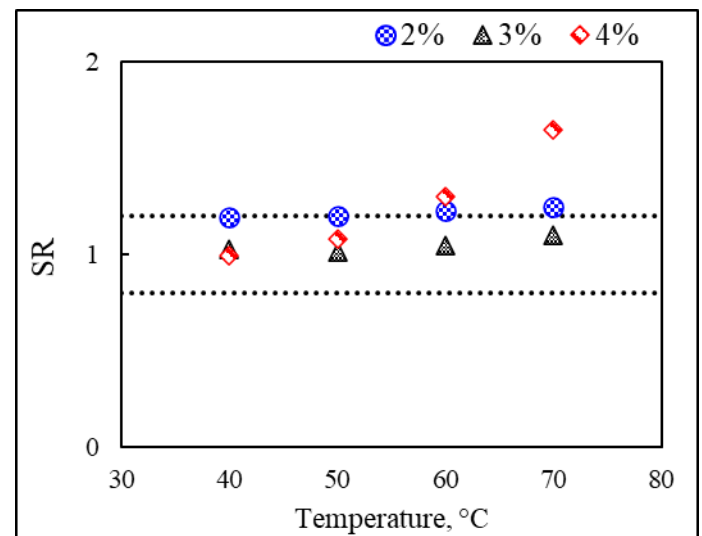
Figure 5: SR results for the RLDPE-VG30 modified bitumen

4 CONCLUSION

In this study, two different grades of base bitumen were used to understand the dispersion characteristics of RPMB. Based on the results and analysis, following conclusions were drawn:

- Inclusion of RLPDE leads to varying degree of increase in softening point of the base bitumen. With VG10 as the base bitumen, the increase in SP ranged between 11.2 °C to 17.8 °C, while for VG30 it was between 8 °C to 14 °C.
- The dispersion of RLDPE polymers into the base bitumen, quantified by mean particle size, was found independent of both the dosage of waste plastic and the type of base bitumen.
- The storage stability of PMB is primarily influenced by the density difference between the base bitumen and RLDPE. The influence of the type of base bitumen was not evident.

REFERENCES

ASTM D36/D36M − 14. 2008. *Standard Test Method for Softening Point of Bitumen (Ring-and-Ball Apparatus)*.

BIS 15462 : 2019. 2019. "POLYMER MODIFIED BITUMEN (PMB) ― SPECIFICATION." *Bur. INDIAN Stand.*

Bureau of Indian Standards (BIS). 2013. *IS 73 : 2013 Paving bitumen — Specification*.

Deb, S., P. Kumar, and N. Saboo. 2025. "Use of Recycled Waste Plastic for Wet Modification of Bitumen." *J. Mater. Civ. Eng.*, 37 (1).

Hao, G., and Y. Wang. 2021. "3D Reconstruction of Polymer Phase in Polymer-Modified Asphalt Using Confocal Fluorescence Microscopy." *J. Mater. Civ. Eng.*, 33 (1): 1–10.

Kumar, P., A. Sreeram, X. Xu, and P. Chandrasekar. 2023. "Closing the Loop : Harnessing waste plastics for sustainable asphalt mixtures – A comprehensive review." *Constr. Build. Mater.*, 400 (August): 132858. Elsevier Ltd.

Rafiq, M., P. Mikhailenko, Z. Piao, M. Bueno, and L. Poulikakos. 2021. "Analysis of waste polyethylene (PE) and its by-products in asphalt binder." *Constr. Build. Mater.*, 280: 122492.

Schneider, C. A., W. S. Rasband, and K. W. Eliceiri. 2012. "NIH Image to ImageJ: 25 years of image analysis." *Nat. Methods*, 9 (7): 671–675. Nature Publishing Group.

Wahhab, H. I. A., M. A. Dalhat, and M. A. Habib. 2017. "Storage stability and high-temperature performance of asphalt binder modified with recycled plastic." *Road Mater. Pavement Des.*, 0629 (18:5): 1117–1134.

Yin, F., M. Raquel, and A. Anurag. 2020. "Recycled plastics in asphalt part B: Literature Review." *Natl. Asph. Pavement Assoc.*

Characterization of asphalt mixture containing bio-extended bituminous binder with spherical indentation test

H. Fadil & D. Jelagin
Department of Civil and Architectural Engineering, KTH Royal Institute of Technology, Stockholm, Sweden

J. Zhu & A. Ahmed
Swedish National Road and Transport Research Institute (VTI), Linköping, Sweden

ABSTRACT: Replacing petroleum-based bitumen with alternative bio-based binders in asphalt mixtures is a promising solution for green transition of road construction industry. The mechanical performance of bio-extended bituminous binders and asphalt mixtures is not yet fully understood, in particular with respect to dynamic mechanical behavior due to traffic and environmental exposures. As bio-binders differ in their chemical compositions, their physical properties and mechanical behavior may vary and differ significantly from bitumen-based materials. This paper aims to contribute to this important topic by evaluating a spherical indentation test as a quasi-nondestructive tool for viscoelastic characterization of the asphalt mixture containing bio-extended bituminous binder. Asphalt indentation tests are more sensitive to the binder phase properties as compared to standard macro-scale asphalt tests and may thus be a potentially useful tool for monitoring binder properties from the measurements performed on asphalt mixtures without extracting the binder.

1 INTRODUCTION

The asphalt pavements constitute a major part of global road network. The petroleum-based bitumen, used as a binder in the asphalt mixtures, has a relatively high environmental impact and carbon footprint. Accordingly, the use of bio-based binders in asphalt mixtures, manufactured from renewable resources such as plant-based biomass, is a promising solution for green transition of road construction industry (He et al., 2023). While a number of promising results have been obtained in this field so far, certain fundamental aspects of material behavior of bio-extended bituminous binders and asphalt mixtures are still not fully understood. In particular, the dynamic mechanical performance is of profound importance as bio-based binders have different chemical compositions compared to bitumen and they may affect mixture durability and performance in a different way as compared to bitumen. This paper aims to contribute to this important topic by evaluating a spherical indentation test as tool to characterize the properties of asphalt mixture containing bio-binder with measurements performed on the asphalt mixture without extracting the binder.

Spherical indentation test for characterization of asphalt mixtures has recently been proposed by Fadil et al. (2021, 2022). The test allows to determine the shear relaxation function $G(t)$ from the measured indentation force $P(t)$ and depth $h(t)$ at arbitrary non-decreasing load history. Indentation measurements allow capturing local mechanical properties of the specimen, as they are primarily influenced by the material properties in the direct vicinity of the indenter-specimen contact point. The spherical indentation test is thus a promising tool for monitoring changes in the binder phase of the material, from measurements performed on asphalt mixtures, as shown by Fadil et al. (2021, 2022) for the conventional mastic asphalts and asphalt concrete mixtures. The indentation test applicability to bio-asphalt, however, has not been evaluated yet.

2 EXPERIMENTAL STUDY

2.1 Materials

Two bituminous binders of penetration grade 160/220 were used to prepare dense graded asphalt mixtures: typical Swedish base course mixtures AG16. The mix design procedure was the same and the basic characteristics such as aggregate gradation and volumetric parameters of mixtures were kept as close as possible between the bio-extended variant (BIO) and reference counterpart (REF). The binder content was 4.5% for both mixtures, and the target air void was 4.2%.

Table 1. Binder properties.

Binder	Penetration @25°C [1/10 mm]	Softening point [°C]
REF	196	38.8
BIO	193	40.4

Figure 2. Photo of the indentation test setup.

2.2 Rheological characterization

The binder samples were subjected to laboratory ageing protocols, with the Rolling Thin Film Oven Test (RTFOT) according to EN 12607-1:2024 to simulate the short-term ageing. The dynamic shear moduli, G^* of the binders were measured with the Dynamic Shear Rheometer (DSR), according to EN 14770:2023. For the compacted asphalt mixture specimens, their dynamic moduli, E^*, were measured according to EN 12697-26:2018+A1:2022 (Annex F cyclic indirect tensile test).

2.3 Spherical indentation tests

A schematic of the indentation test setup is shown in Figure 1, along with the main test parameters. The photo of the test setup used is shown in Figure 2. In the test, a spherical indenter is pushed into the specimen with a specific indentation depth history, $h(t)$, resulting in a reaction force, $P(t)$. Both $P(t)$ and $h(t)$ are measured as a function of time for the duration of the test.

The viscoelastic solution for the spherical contact problem, derived by Fadil et al. (2018) is shown in Equation (1):

$$P(t) = \frac{8}{3(1-v_o)}\sqrt{R}\int_0^t G(t-\tau) \times \frac{dh^{\frac{3}{2}}(\tau)}{d\tau}d\tau \qquad (1)$$
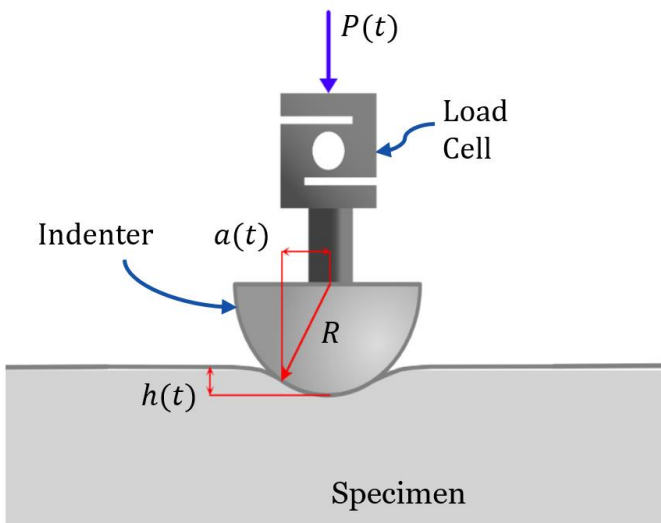
Figure 1. A schematic showing the parameters of the indentation test.

where R is the radius of the indenter (Figure 1), while τ is a dummy integration variable. The validity of Equation (1) is constrained to arbitrary non-decreasing loading. By giving $G(t)$ the form of a Prony series as Equation (2), Equation (1) is solved numerically for $G(t)$ using linear programming.

$$G(t) = G_\infty + \sum_{i=1}^N G_i \cdot e^{-t/\tau_i} \qquad (2)$$

where N is the number of branches in the Prony series, G_∞ is the equilibrium shear modulus, τ_i is the relaxation time for branch i and G_i is the shear relaxation strength for branch i.

As presented in detail in Fadil et al. (2021, 2022), the $G(t)$ measured with spherical indentation test is representative for viscoelastic properties of material in the immediate vicinity of the indenter-specimen contact point. The size scale of the region characterized in the test is proportional to the size of the contact area, a. As shown in Fadil et al. (2022) for the case of standard asphalt, performing the tests in grid pattern on the specimen surface, results in wide range of measured $G(t)$. This is expected, due to varying distribution of asphalt mixture components in the vicinity of the indentation point, resulting in some measurements being dominated by the mastic phase properties, while others are dominated by the aggregates. Accordingly, a statistical method was proposed by Fadil et al. (2022) to separate the test measurements into two clusters: mastic-dominated and aggregate-dominated. The average of $G(t)$ measurements was found to correlate linearly to the asphalt shear relaxation modulus measured with the conventional tests. At the same time, the mastic-dominated results were found to capture the mastic properties.

In this study, the spherical indentation test is applied to characterize REF and BIO asphalts. The tests were performed on laboratory-manufactured asphalt cores of 150 mm diameter. The surfaces were prepared by cutting approximately 5 mm from each side and therefore the specimens had thicknesses of 37-40 mm. Two specimens were used for each mixture. The test setup used a steel spherical indenter with a curvature radius $R = 15.875$ mm. The test rig was an MTS

810 servo-hydraulic load frame with a 10 kN load cell. The tests were performed in depth controlled mode, applying the maximum indentation depth, h_{max} = 0.3 mm in 0.1 s ramp, and keeping it constant for 200 s. This corresponds to a maximum contact area radius of a_{max}= 2.51 mm. The surfaces of each sample was divided into grid with 25 squares each with side edge size of 2 cm. One indentation test was performed close to the center of each grid square, resulting in 50 tests per specimen in total. That ensures that the distance between each indentation is no less than $10 \times a$. This is to avoid that the effect of indentation in one location interferes with the other measurements. The tests were performed at 0°C.

Figure 3. Complex moduli of RTFOT-aged binders, T_{ref} = 0°C.
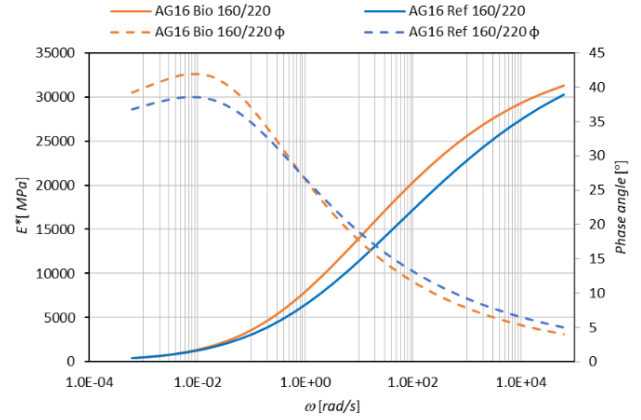
Figure 4. Complex moduli of AG16 BIO and REF mixtures, T_{ref} = 0°C.

3 RESULTS AND DISCUSSION

The $G^*(\omega)$ measured with the DSR for RTFOT-aged REF and BIO binders are presented in Figure 3. As seen the BIO binder is somewhat stiffer compared to the REF at reference temperature 0°C. The maximum $G^*(\omega)$ difference between the materials is approximately 50% and it is diminishing with the frequency to about 30%. It should be pointed out, however, that the measured difference is comparable to the measurement scatter seen in Figure 3.

The dynamic moduli of AG16 REF and AG16 BIO asphalt mixtures at reference temperature 0°C are presented in Figure 4 along with their phase angles. It is observed that, within the frequency range where the binder phase dominates mixture behavior (intermediate to high frequencies), the somewhat stiffer binder in the case of AG16 BIO asphalt results in higher dynamic modulus for the mixture as well. In contrast to the results in Figure 3, however, there is no clear trend in stiffness differences with respect to frequency, which is likely due to the impact of the aggregate phase. The maximum difference in dynamic moduli of the two asphalts reaches approximately 20%. It must be pointed out that, as reported by Zhu et al. (2024), the REF and BIO binders are basically identical in terms of their penetration grade. The difference observed in Figures 3 and 4 are thus attributed to the different dynamic mechanical performance of the two materials. This illustrates importance of controlling dynamic mechanical properties of asphalt materials due to traffic and environmental exposures.

The interconversion method proposed by Park & Schapery (1999) is used to convert the $G(t)$ measured on asphalt mixtures with the spherical indentation tests to $G^*(\omega)$ to facilitate comparison with the results presented in Figures 3 and 4. In Figure 5 the average mixture $G^*(\omega)$ obtained from the indentation test measurements are presented along with their 95% confidence intervals. As may be seen, the average $G^*(\omega)$ obtained from the indentation are significantly smaller as compared to the E^* values presented in Figure 4. For instance, for $\omega = 1$, the indentation measurements result in $G^*(\omega) = 0.8$ and 1.1 GPa for the REF and BIO asphalts correspondingly. This may be compared to the respective E^* values of 6.0 and 8.0 GPa, presented in Figure 4. Even after considering the Poisson's ratio (approximately 0.5 at low temperatures and high frequencies), the shear modulus obtained from indentation test is still relatively low. Similar observation has previously been reported by Fadil et al. (2022) for the tests performed on the conventional asphalt concrete. This discrepancy is attributed to the localized nature of the indentation test, which possibly leads to not capturing fully the effect of the aggregate skeleton on the asphalt mixture properties. At the same time, both in Figures 4 and 5 the BIO asphalt is approximately 30% stiffer as compared to the REF one, which indicates that indentation tests capture the relative differences in the materials and their ranking correctly.
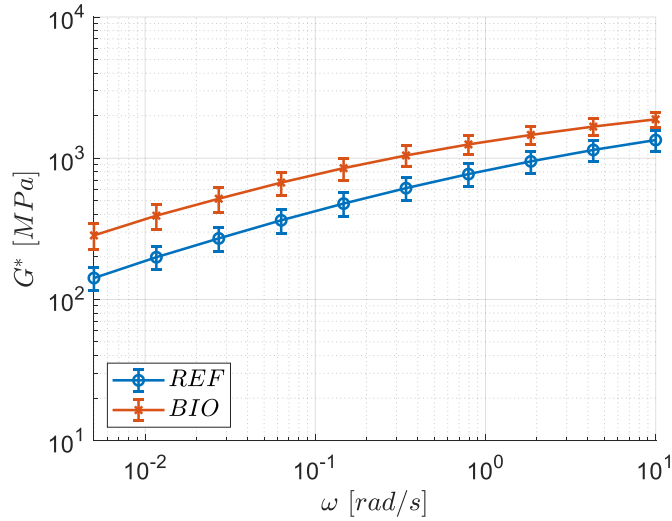
Figure 5. Average mixture $G^*(\omega)$ measured with indentation test on AG16 REF and BIO, $T = 0°C$.

Focusing on mastic-dominated measurements improves the indentation test sensitivity to the binder phase properties further, as illustrated in Figure 6 where average $G^*(\omega)$ obtained from the mastic-dominated measurements are presented together with the 95% confidence boundaries. $G^*(\omega)$ values in Figure 6 are both lower in magnitude and are accompanied by significantly less scatter as compared to the results presented in Figure 5. In Figure 6, the difference in $G^*(\omega)$ between REF and BIO measurements is within similar range as the DSR results presented in Figure 3, i.e. 40-100%. Accordingly, the results obtained in this study demonstrate feasibility of using indentation test for monitoring evolution of the bio-extended bituminous binders from the measurements performed on asphalt specimens.
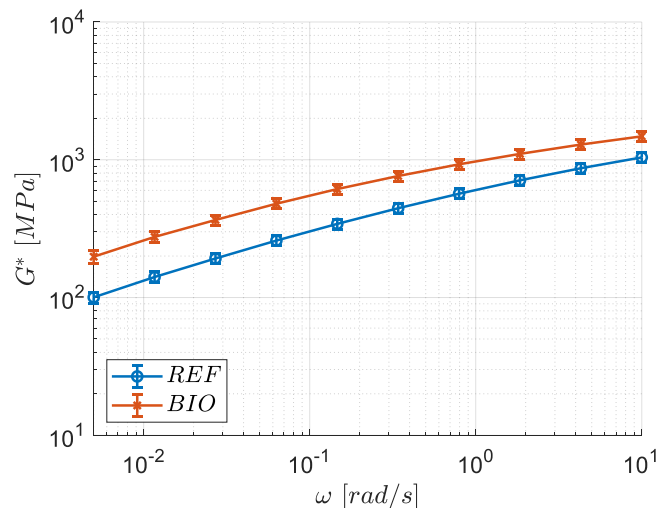
Figure 6. Average mastic-dominated $G^*(\omega)$ measured with indentation test on AG16 REF and BIO, $T = 0°C$.

4 CONCLUSIONS

Spherical indentation testing has been evaluated in this study as an alternative method for measuring the viscoelastic properties of asphalt mixture with bio-based binder. The increase in the modulus of asphalt mixture resulting from the incorporation of bio-oil, as measured through indentation tests under the specified conditions, showed good agreement with results from the conventional asphalt testing method. Applying a statistical analysis procedure to identify mastic-dominated indentation measurements further enhanced the test's sensitivity to binder properties and significantly reduced measurement variability. The experimental results suggest that the indentation test is a viable alternative for the viscoelastic characterization of bio-asphalts and their binders. Moreover, this method shows great potential for further development to enable in situ monitoring of changes in the viscoelastic properties of the binder phase due to environmental exposures.

5 REFERENCES

Fadil, H., Chen, F., Jelagin, D., Partl, M. N. (2021). The viscoelastic characterisation of asphalt mixtures using the indentation test. Road Mater Pavement Des 22(S1), 411–424

Fadil, H., Jelagin, D., & Larsson, P. L. (2018). On the Measurement of two Independent Viscoelastic Functions with Instrumented Indentation Tests. Exp Mech 58, 301–314

Fadil, H., Jelagin, D., & Partl, M. N. (2022). Spherical indentation test for quasi-non-destructive characterisation of asphalt concrete. Mater Struct 55, 102

He, L., Tao, M., Liu, Z., Cao, Z., Zhu, J., Gao, J., … Ma, Y. (2023). Review of Biomass valorization toward sustainable asphalt pavements : Progress and prospects. Waste Management, 165, 159–178.

Park, S. W., & Schapery, R. A. (1999). Methods of interconversion between linear viscoelastic material functions. Part I - A numerical method based on Prony series. International Journal of Solids and Structures, 36(11), 1653–1675.

Zhu, J., Ahmed, A., Dinegdae, Y., & Waldemarson, A. (2024). Investigation on Ageing Behaviour of Bio-Extended Bituminous Binders and Asphalt Mixtures for Sustainable Road Infrastructure. In Transport Research Arena (TRA), Dublin, Ireland, 15-18 April 2024.

Impact of Influencing Factors on Stribeck Curve Measurement for bituminous Binders

V.G. Gayathri, M. Rochlani, J. Murali Krishnan
Indian Institute of Technology Madras, Tamil Nadu, India

ABSTRACT: Bitumen and aggregates are blended to produce the bituminous mixture at a specific mixing temperature. During the mixing stage, the binder coats the aggregate particles. The efficiency of the coating is influenced by the interfacial friction at the aggregate-binder interface. During the compaction process, the temperature reduces, leading to an increase in viscosity. Such an increase in viscosity also influences the ease with which the mixture can be compacted, and this is again influenced by the friction between the binder-coated aggregate particles. Quantifying the extent of friction, usually characterized by the Stribeck curve, can provide a significant understanding of the compaction mechanics. This study investigates the tribological properties of unmodified binders, focusing on their lubrication characteristics under specific temperatures and normal forces. The study focuses on two typical temperatures, 80 °C, and 160 °C, and two normal forces, such as 3N and 10N, with varying sliding speeds. The Stribeck curves are generated, and the influence of the testing parameters on the generation of the Stribeck curve is discussed in detail.

1 INTRODUCTION

The bituminous mixture is produced by mixing bitumen with aggregate particles. The bitumen and aggregate particles are heated to obtain a mixture in which the aggregates are entirely coated with the binder. The rheological properties of bitumen in the mixing and compaction temperature regime play a critical role in achieving a consistent mixture.

The interaction between the aggregate and bitumen, along with an understanding of friction reduction, obtain a workable mixture. The viscosity of the binder and the friction between the aggregates and the binder influence it to a large extent. At high temperatures, the binder behaves like a Newtonian fluid, but as compaction progresses and as the temperature reduces, the material's response becomes non-Newtonian. In this temperature range, while viscosity plays a critical role in providing lubrication, it is unclear whether the viscosity of the binder has a direct one-to-one relationship with interfacial friction.

Researchers have recently investigated the lubricating behavior of bituminous binders to determine the reduction in friction and improvement in workability of bituminous material (Hanz et al., 2010; Hanz and Bahia, 2013; Ingrassia et al., 2018). Mannan and Tarefder (2018) underlined the importance of interfacial properties at the binder-aggregate interface. Comparable studies have been conducted for a wide variety of materials such as foamed bitumen (Bairgi et al., 2019a, 2019b), WMA additives (Baumgardner et al., 2012), polymer modified binder (Emami and Khalegian, 2019).

Demarcation of the various stages of friction development is depicted using the Stribeck curve. In an ideal scenario, four stages are seen: boundary regime, mixed regime, elasto-hydrodynamic regime, and hydrodynamic regime (Bhushan, 2013). Figure 1 shows

the classical Stribeck curve with all four regimes generated under specific testing conditions in this study, and the details are described in Section 3.

During the reduced sliding velocity, the boundary regime (a) showcases maximum friction, primarily attributed to the interaction between surface asperities. Transitioning to the mixed regime (b), a portion of the surface becomes coated with lubricant while other areas maintain contact, initiating the lubricant's effects, which reduces the coefficient of friction. In the elasto-hydrodynamic lubrication (EHL) regime (c), the lubricant forms a thin film between surfaces, resulting in minimal friction. Finally, in the hydrodynamic regime (d), friction escalates with sliding speed due to viscous drag (Bhushan, 2013).
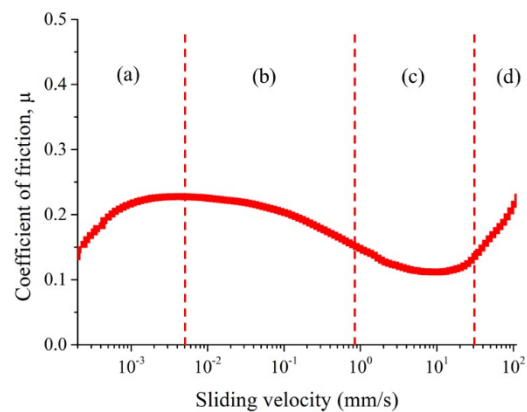
Figure 1. Stribeck curve: Coefficient of friction as a function of sliding speed.

Researchers working with binders (Hanz and Bahia, 2013) use the four-ball testing geometry as per ASTM: D5183 (2021) and the ball-on-three-plate geometry (Baumgardner and Reinke, 2012; Mannan and

Tarefder, 2018), connected with a Dynamic Shear Rheometer (DSR).

In bitumen tribology studies, most researchers have followed a normal force of 5N and 10N (Baumgardner and Reinke, 2012; Mannan and Tarefder, 2018). For silicone oil, it can be 1N (Zhang et al., 2020), and for tribology, testing of different polymers such as polytetrafluoroethylene and polyethylene, a normal force of 1-100N is applied (Myshkin and Kovalev, 2018). The tribological characteristics of bitumen have been tested at various temperatures, ranging from 25 °C to a maximum of 160 °C (Bairgi et al., 2019). Mannan and Tarefder (2018), using ball-on-three-plate geometry, discussed the frictional characteristics of three grades of PG binders at temperatures of 25, 50, and 135 °C. Studying viscosity and the Stribeck curve to see the change in the characteristics of lubrication is crucial for investigating the tribological properties of a material as the studies show that (Hanz et al., 2010) the increase in viscosity reduces the material's ability to coat the surface.

The coefficient of friction measured is not a single constant value; rather, it's a function of sliding speed. The range of sliding velocities at which each material exhibits a four-stage Stribeck curve varies depending on the material and the lubricant used. For SAE30 lubricant oil used in journal bearings (Lu and Khonsari, 2007), sliding velocities ranging from 1 to 1000 rpm yield a four-stage Stribeck curve. In the case of bitumen, sliding speeds ranging from 0.0001 to 1000 rpm produce a complete Stribeck curve (Ingrassia et al., 2018; Bairgi et al., 2019).

From the above discussion, it is understood that the lubrication characteristics demonstrated through the Stribeck curve analysis are influenced by various factors such as temperature and normal force. The main objective of the study is to investigate the tribological properties of bituminous binders under various temperatures and normal forces. Additionally, the research aims to understand how the viscosity of binder influences its lubrication properties, which are applicable to the bituminous binder during the production process of bituminous mixtures.

2 EXPERIMENTAL INVESTIGATION

An unmodified binder, viscosity grade 30 (VG30) as per Indian Standards (IS 73, 2018) was used for this study. The materials were tested at 80 and 160 °C with normal forces of 3N and 10N. Viscosity data were collected by conducting shear rate sweep tests on unaged conditions at testing temperatures using Anton Paar DSR 302. The tribology experiments used a ball-on-three plate geometry (Figure 2) attached to the Anton Paar DSR 702. After fixing all the plates in the holder, a sample of around 1.5 gms is filled in the sample holder.

Figure 2. Three plate geometry sample holders.

A ball with radius R (6.35 mm) is placed on three plates in this experimental set-up and subjected to normal force. The sliding speed used in the study was varied from 0.0001 mm/s to 1000 mm/s on a logarithmic scale. The trial was repeated five times for repeatability. Based on the applied normal force and resulting friction force, the coefficient of friction was computed at the interface between the ball and the plate using geometric calculations (Ingrassia et al., 2018).

3 RESULTS AND DISCUSSION

3.1 Binder Viscosity

The variation of apparent viscosity as a function of shear rate is shown in Figure 3. The material exhibits only the first two regimes in the apparent viscosity curve. At 80 °C, the binder exhibits a shear-thinning behavior. At 160 °C, the material shows a shear thinning at a lower rate, and hence, it is assumed to be a Newtonian fluid at this higher temperature.
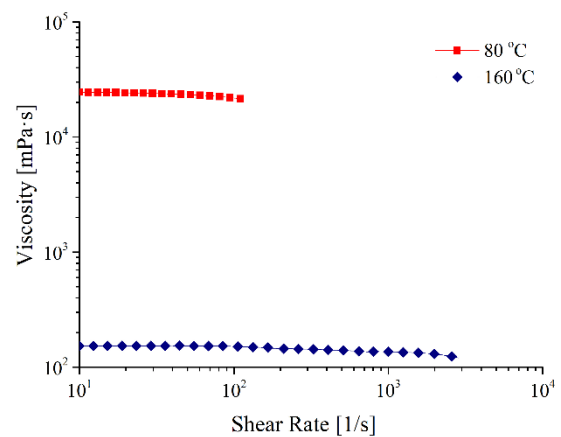
Figure 3. The apparent viscosity of unmodified binder at 80 and 160 °C.

3.2 Influence of temperature and normal force on Friction

The variation in the coefficient of friction with increasing sliding velocity indicates the transition between different lubrication regimes. The derivative curve of a Stribeck curve can identify the inflection points where the trend reverses. Figure 4 shows the Stribeck curve for VG30 tested at 80 °C with a 10N normal force, illustrating the transitions between different regimes, whereas Figure 1 shows the same data

for a 3N normal force. The minimum coefficient of friction in the EHL regime provides maximum lubrication to the system. The variations in the coefficient of friction values across two temperatures, such as 80 and 160 °C, are shown in Figure 5. At higher temperatures, where the material exhibits Newtonian behavior, the influence of normal force becomes negligible.
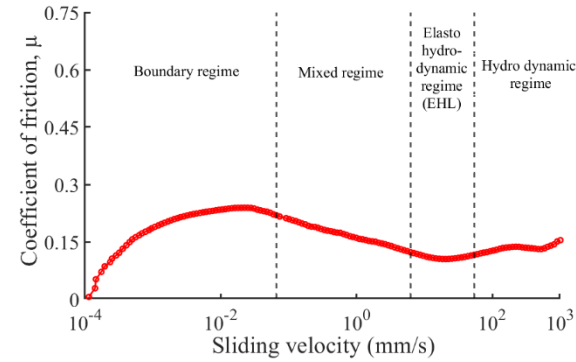
Figure 4. Stribeck curve generated for VG30 binder at two temperatures and two normal forces
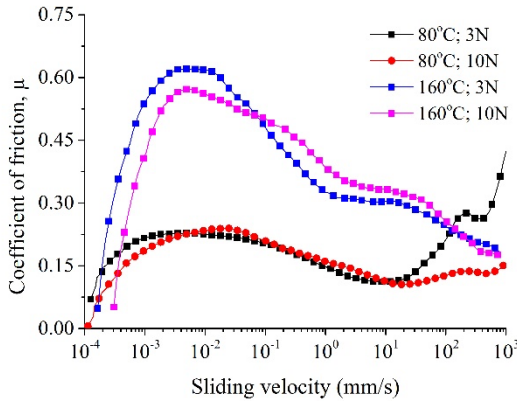
Figure 5. Stribeck curve generated for VG30 binder at two temperatures and two normal forces

The Stribeck curve exhibits a clear and distinct pattern with a decreased coefficient of friction in the EHL regime for 80 °C when tested at 3N and 10N. In the boundary regime, where asperity contact predominates, a lower coefficient of friction results from the flattening of the surface's asperities under relative motion as the normal force increases from 3N to 10N. Additionally, the EHL regime shows the maximum effect of lubrication with a minimal coefficient of friction when tested at 10N normal force. The complete Stribeck curve is obtained only when the material is tested at 80 °C with 3N and 10N normal forces. As the temperature increases, the coefficient of friction in the boundary regime also increases.

At the higher temperature of 160°C for both the normal forces, such as 3N and 10N, only two regimes exist in the Stribeck curve: boundary and mixed regime, with no EHL and hydrodynamic regime present. It is also observed that the Stribeck curve shifts to the left as the temperature increases, indicating that the mixed regime persists for a longer duration and

extends beyond the maximum limit of sliding velocity. The binder exhibits lower viscosity at higher temperatures, transitioning to Newtonian behavior, which results in minimal viscous drag. This allows the material to continue reducing friction without exhibiting an increased resistance.

3.3 Influence of Viscosity on Friction

It was observed that as the temperature increased from 80 to 160 °C, viscosity significantly reduced. All the stages of the Stribeck curve were observed during the tribological testing at 80 °C for both 3N and 10N normal forces, and the minimum coefficient of friction at the EHL regime could be determined. However, determining the minimum coefficient of friction in the EHL regime under high temperature was challenging, as the sliding velocity level exceeded the instrument capacity, and the curve continued in the mixed regime. In the present study, the EHL regime was not observed during the testing at 160 °C for both 3N and 10N. The role of the viscosity related to the development of the Stribeck curves is yet to be demonstrated in a convincing manner for bituminous materials.

The Stribeck curve can be used to relate the coefficient of friction with the Hersey number. It is a dimensionless number (Hersey, 1935), also known as the Stribeck parameter (Gallego et al., 2016). The Hersey number is used to describe the collective influence of lubricant viscosity (η), entrainment speed (U), and the contact load per unit of contact radius (F). Therefore, the Hersey number takes into account the influence of fluid viscosity and the contact load (provided the film thickness remains constant by change of load) and displays the influence of speed change on frictional forces. It is expressed by the equation (1).

$$H_n = \frac{\eta U}{F} \tag{1}$$

where H_n=Hersey number; η = dynamic viscosity of the lubricant (mPa.s); U= sliding velocity (mm/s); and F = normal force (N).

Figure 6 shows the variation in the Stribeck curve plotted with Hersey's number for VG30 binder 3N normal force. By normalizing the effect of sliding velocity, viscosity, and normal force into a single parameter, a generalized view of friction variation can be observed. It was observed that the VG30 binder at 80 °C exhibited the EHL regime when the Hersey number ranged between 10^4 and 10^5, whereas at 160 °C, the same binder showed only the mixed regime within the same range. This facilitates the comparison of the lubrication properties of materials with different viscosities.
.
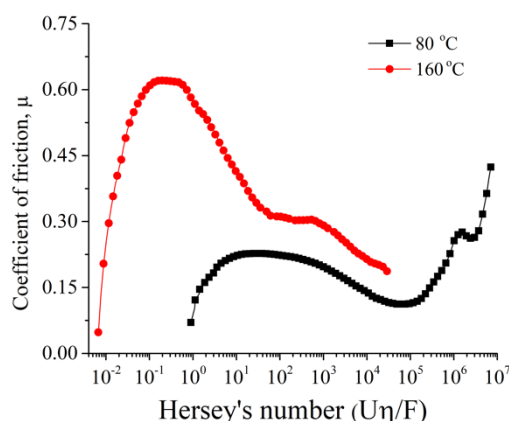
Figure 6. The variation of the coefficient of friction as a function of Hersey's number for VG30 binder at 3N normal force.

4 CONCLUSION

This study investigated the challenges of conducting tribological tests on bitumen binders, specifically focusing on generating a four-stage Stribeck curve with an emphasis on the EHL regime. The research found that increasing normal force smoothens surface asperities, reducing the coefficient of friction in the boundary regime. In the EHL regime, higher loads further decrease friction, thereby enhancing lubrication. Temperature also plays a crucial role; as the temperature rises, the critical coefficient of friction decreases, and the Stribeck curve may show fewer stages at higher temperatures (e.g., only two stages at 160 °C). At higher temperatures, the EHL regime diminishes, complicating the identification of the minimum friction point. The study underscores the importance of determining the optimal normal force and temperature to understand lubrication properties in bituminous binders.

5 REFERENCES

Ajimotokan, H.A. 2024. Principles and applications of tribology. In *Springer Briefs in Applied Sciences and Technology, Manufacturing and Surface Engineering.* Springer Nature Switzerland AG.

ASTM D5183-21a. 2021. Standard test method for determination of the coefficient of friction of lubricants using the four-ball wear test machine, tribometer. *ASTM International*, West Conshohocken, PA.

Bairgi, B.K., Mannan, U.A. & Tarefder, R.A. 2019. Influence of foaming on tribological and rheological characteristics of foamed asphalt. *Construction and Building Materials*, 205, 186-195.

Baumgardner, G.L. & Reinke, G.R. 2012. Lubricity properties of asphalt binders used in hot-mix and warm-mix asphalt pavements. In Proceedings of the 5th Eurasphalt & Eurobitume Congress, Istanbul, Turkey, June 13-15.

Bhushan, B. 2013. Introduction to tribology (2nd ed.). New York: John Wiley & Sons Inc.

Emami, A. and Khaleghian, S., 2019. Investigation of tribological behavior of Styrene-Butadiene Rubber compound on asphalt-like surfaces. *Tribology International*, 136, pp. 487-495.

Gallego, R., Cidade, T., Sánchez, R., Valencia, C., & Franco, J. M. 2016. Tribological behaviour of novel chemically modified biopolymer-thickened lubricating greases investigated in a steel–steel rotating ball-on-three plates tribology cell. *Tribology International*, 94, 652-660.

Hanz, A.J. and Bahia, H.U., 2013. Asphalt binder contribution to mixture workability and application of asphalt lubricity test to estimate compactability temperatures for warm-mix asphalt. *Transportation Research Record*, 2371, pp. 87–95.

Hanz, A.J., Faheem, A., Mahmoud, E. and Bahia, H.U., 2010. Measuring effects of warm-mix additives: Use of newly developed asphalt binder lubricity test for the dynamic shear rheometer. *Transportation Research Record*, 2180.

Hersey, M.D., 1935. A short account of the theory of lubrication. II. Film thickness, film pressure and load capacity. *Journal of the Franklin Institute*, 220(1), pp. 93-119.

Hirani, H., 2016. *Fundamentals of Engineering Tribology with Applications*. Cambridge University Press, New Delhi.

Ingrassia, L.P., Lu, X., Canestrari, F. and Ferrotti, G., 2018. Tribological characterisation of bituminous binders with warm mix asphalt additives. *Construction and Building Materials*, 172, pp. 309–318.

IS 73 2018. Indian standard for paving bitumen. *Bureau of Indian Standards*, New Delhi.

Lu, X. and Khonsari, M.M., 2007. An experimental investigation of dimple effect on the Stribeck curve of journal bearings. *Tribology Letters*, 27(2), pp. 169–176.

Mannan, U.A. and Tarefder, R.A., 2018. Tribological and rheological characterisation of asphalt binders at different temperatures. *Road Materials and Pavement Design*, 19(2), pp. 445–452.

Myshkin, N.K. and Kovalev, A., 2018. Polymer mechanics and tribology. *Industrial Lubrication and Tribology*, 70(4), pp. 764–772. Emerald Group Publishing Ltd.

Woydt, M. and Wäsche, R., 2010. The history of the Stribeck curve and ball bearing steels: The role of Adolf Martens. *Wear*, 268(11–12), pp. 1542–1546.

Zhang, X., Jing, H., Tian, Y. and Meng, Y., 2020. Thermodynamics model for Stribeck curve and experiments: The role of interfacial interactions. *Journal of Tribology*, 142(8), pp. 081801.

Influence of Additives on Rheological Behavior and Structure Evolution of Cement Asphalt Mortar

Vinayakumar Gopika, T. Divya Darsini, S. P. Atul Narayan, J. Murali Krishnan, Manu Santhanam
Department of Civil Engineering, Indian Institute of Technology Madras

ABSTRACT: Cement Asphalt Mortar (CAM) is a composite organic-inorganic material, composed of cement, emulsified asphalt, river sand, and various admixtures. It is used in ballastless track systems of high-speed railways to damp vibrations. The rheology of the mortar in its fresh state is mainly characterized by the constituents and their proportions. This study investigates the effect of different constituents such as asphalt emulsion, calcium sulfoaluminate, aluminium powder, and defoamer on the rheological properties and structural development of CAM in its fresh state. Time sweep tests were conducted in a coaxial cylinder geometry in a dynamic shear rheometer to assess structure development. Shear rate sweep tests were conducted to obtain rheological properties. The results illustrate the critical impact of additives on the early strength, hydration rates, and rheological properties of CAM.

1 INTRODUCTION

Cement asphalt material (CAM) is a composite material made with cement, asphalt emulsion, sand water, and other additives. Cement gives strength to the mixture whereas bitumen provides it dissipative characteristics. It is primarily used in ballastless track systems for high speed railway for damping load-induced vibrations. Its properties are primarily regulated by the proportion of asphalt to cement (A/C ratio), water to cement ratio (W/C ratio), and sand to cement ratio (S/C ratio). The interaction between cement hydration and asphalt emulsion is crucial. As the cement hydrates, it creates an environment for faster breaking of asphalt emulsion, with asphalt droplets forming a film around cement grains. This slows but does not halt hydration, creating a plasticizing effect and enhancing the fresh mortar's mechanical behaviour. The modulus of the mortar depends on the interparticle bond strength and the shape and surface area of the C3S and hydrated particles like C-S-H (Nachbaura et al., 2001). The evolution of the internal structure of cement-asphalt mortar is studied by conducting oscillatory tests and observing the evolution of viscoelastic properties like dynamic modulus (Baldino et al., 2014).

In addition to the main ingredients of the mortar, many additives are used, such as calcium sulfoaluminate for early strength gain, defoamers to prevent the emulsion from causing foaming, superplasticizers for better flow characteristics, alumnium powder for aeration, etc. Calcium sulfoaluminate is added for early strength gain. The effect of these additives on cement mortar has been investigated previously by many researchers (Nagataki & Gomi., 1998; García-Maté et al., 2012; Telesca et al., 2014; Randal&Kenneth, 2019; Yuan et al., 2020; Wang et al., 2020). But the effect of these additives on the evolution of internal structure in the mortar and the rheological characteristics has received less attention.

In this study, the fresh properties of cement-asphalt mortar with different additives are investigated and com-pared with that of a similar cement mortar. The additives considered for the investigation are calcium sulfoaluminate, a silcon-based defoamer, and aluminimum poweder. The evolution of the internal structure is investigated through time sweep tests. The rheological behavior is investigated through shear-rate sweep tests.

2 MATERIALS

An Ordinary Portland cement 53 grade as per IS 269, calcium sulfoaluminate admixture (CSA), a locally available sand with particles finer than 1.18mm, a cationic slow-setting asphalt emulsion (SS2) with a residue content of 63%, water, an organic silicon-based defoamer (DF) and aluminium powder (AL) were used in the study. Initial tests were conducted on the cationic slow setting (SS2) emulsion as per IS 8887:2018 and on the cement as per IS 12269:2013.

Three systems were prepared for the analysis – a cement paste (CP) (W/C-0.5), a cement mortar (CM) (W/C-0.8, S/C-1.8), and a cement asphalt mortar (CAM) (W/C-0.8, A/C-0.8, S/C-1.8). Calcium sulfoaluminate was added at a dosage of 9% of the total cementitious material, the defoamer (DF) at 0.25% of the emulsion, and aluminum powder (AL) at 0.01% of the total cementitious material.

3 EXPERIMENTAL PROCEDURE

Rheological studies were performed in a concentric cylinder geometry with profiled walls in a Dynamic Shear Rheometer (DSR 302). Tests were conducted at a constant temperature of 25°C immediately after mixing for 1 minute.

Table 1. Test matrix

Systems	Additives	Tests
Cement paste(CP)	calcium sulfoaluminate admixture (CSA)	Time sweep
Cement mortar (CM)	Aluminium (AL)	Shear rate sweep
Cement asphalt mortar (CAM)	Defomear (DF)	

Twelve different systems were used in this study - Cement paste (CP), Cement mortar (CM), Cement asphalt mortar (CAM), CP+CSA, CP+AL, CP+DF, CM+CSA, CM+AL, CM+DF, CAM+CSA, CAM+AL, CAM+DF, where CSA, AL, and DF, refer to calcium sulfoaluminate, defoamer, and aluminium powder, respectively. The time-sweep test is carried out for about 2 hours at a constant strain of 0.01% and a frequency of 1Hz. Data points were collected at 10s intervals. Shear rate sweep tests were performed after a pre-shear of 20 s^{-1}. In this test, the shear rate is increased from 20 to 120 s^{-1} in a step-wise manner and then decreased to 20 s^{-1}. To ensure that a steady state is reached, each shear rate is applied for a duration of 10 seconds (Jayasree et al, 2011). The shear is applied in two blocks and the down ramp of the second block is used for the computation of apparent viscosity. To ensure repeatability, a minimum of two trials were conducted for each system.

4 RESULT AND DISCUSSIONS

Structure development is investigated by analyzing the evolution of linear viscoelastic properties with time through time-sweep tests. Figures 1 and 2 show the variation of the dynamic modulus of cement paste and cement mortar systems during the time-sweep tests. As expected, the viscoelastic properties of the fresh paste and mortar evolve with time in such a way that the dynamic modulus increases. The variation of phase angle with time during the time sweep test is shown in Figure 3 and Figure 4.
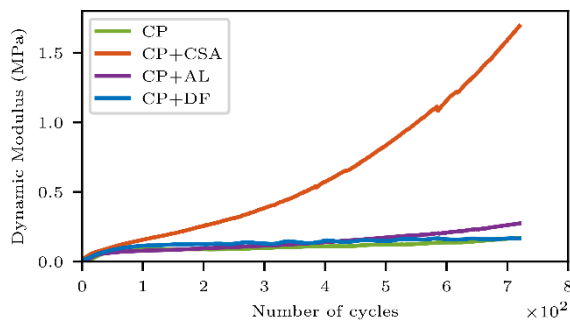
Figure 1. Dynamic modulus of cement paste systems
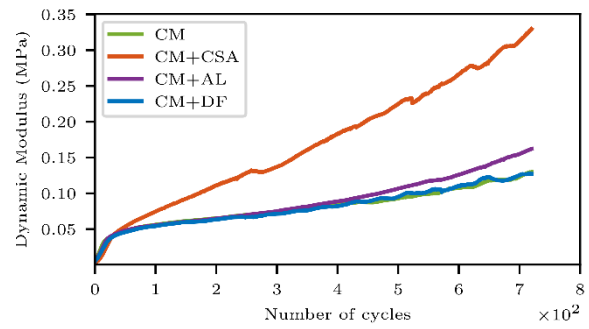
Figure 2. Dynamic modulus of cement mortar systems
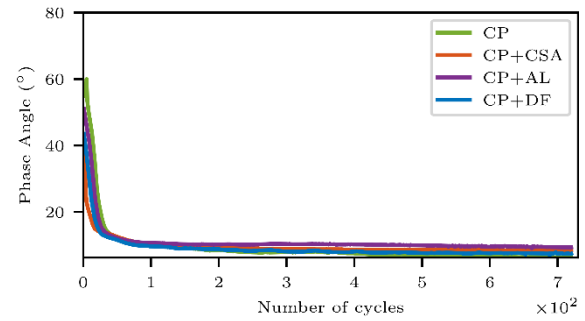
Figure 3. Phase angle variation of cement mortar systems
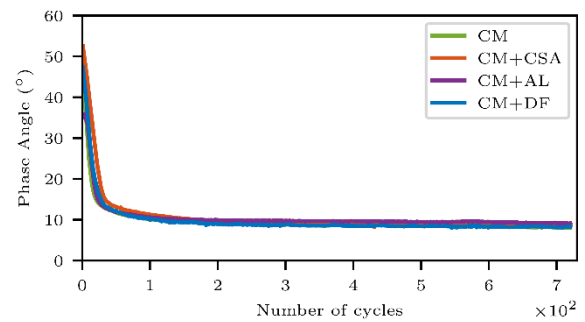
Figure 4. Phase angle variation of cement mortar systems

The phase angle is seen to decrease from a relatively large value to a value lower than 10°. The point at which the phase angle crosses 45° is the point at which the elasticity of the material dominates over its dissipative characteristics. This appears to happen within the first few cycles for all the systems.

Additionally, the cement paste and mortar with the calcium sulfoaluminate admixture appear to harden and form structures faster than those with other additives. All others have a similar trend in structural development. The addition of aluminium or defoamer does not affect the strength gain or formation of structures (Figures 1 and 2).

The increase in the dynamic modulus ($|G^*|$) and the decrease in the phase angle (δ) can be attributed to the formation of interconnected particles and flocs by van der Waals forces, indicating a transition from a more liquid to a more structured state. These modulus increases are characterized by the increase in contact points and interconnected points which facilitated the transmission of stresses with lower delay, enhancing the rigidity of the formed network.
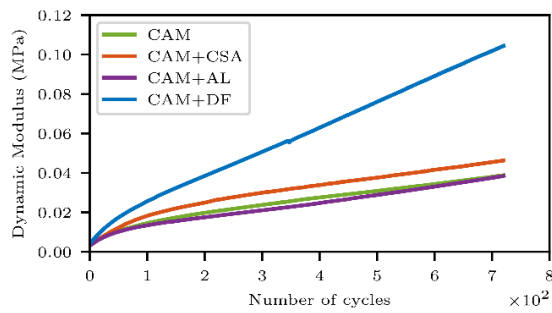
Figure 5. Dynamic modulus of cement asphalt mortar systems

Figure 6. Phase angle variation of CAM systems

Figure 5 presents the variation of dynamic modulus with time for the CAM systems. There is an increase in dynamic modulus in CAM systems as well. However, the increase in modulus in CAM systems is due to emulsion breaking rather than structural formation by flocculation of cement particles and hydration. This is evident from the evolution of the modulus for the CAM+CSA system. Unlike CM+CSA, the evolution of modulus in the CAM+CSA system did not progress at a high rate. The reaction of the admixture was masked by the presence of asphalt emulsion and hence there was not much difference in the evolution of the moduli between systems with and without the calcium sulfoaluminate admixture. The modulus value of CAM+DF is larger than other systems. This is because the presence of a defoamer reduces the foam from emulsion. CAM+AL has the least modulus because the aluminium reaction with cement has not happened here.

The evolution of the phase angle of CAM systems is shown in Figure 6. The initial phase angle of the CAM systems is similar to the CM systems. But unlike the CM systems, the phase angle of the CAM systems does not decrease significantly. In some cases, the phase angle appears to increase. This suggests that the evolution of viscoelastic properties is more influenced by the breaking of the emulsion in these systems than the flocculation and hydration of cement particles. Moreover, the phase angle of the CAM systems is seen to remain above 45°, which indicates that the CAM systems do not possess similar elastic characteristics compared to the CM systems. Structures similar to those observed in CM systems are not formed in the CAM systems. This can again be attributed to the breaking of the asphalt emulsion.

Comparing CM to CAM systems (Figure 7), fresh cement mortar systems exhibited higher modulus than the corresponding CAM system. The storage modulus of CAM is only about 1/10th of the CM. Moreover, for the CM system exhibited a storage modulus greater than the loss modulus ($G' > G''$) at the tested strain level and frequency. But cement asphalt mortar showed a more viscous behaviour with the loss modulus higher than the storage modulus ($G'' > G'$).
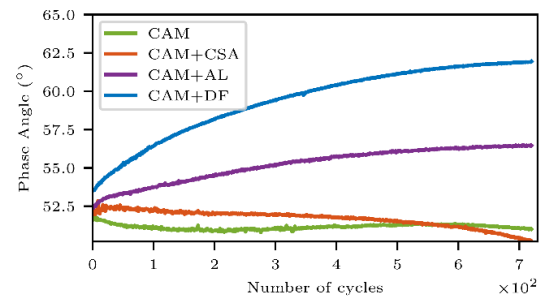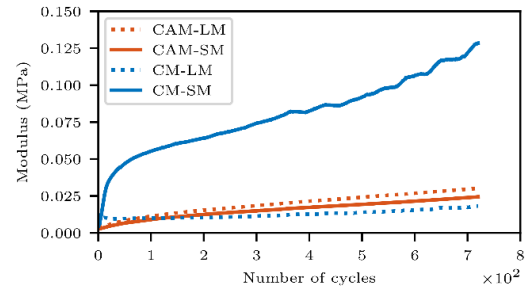
Figure 7. Comparison of CAM and CM modulus values

The shear stress vs. shear rate for different systems from the shear sweep tests are presented in (Figures 8 and 9). All systems are observed to behave as yield stress fluids. However, the yield stress appears to be higher for the CM systems compared to the CAM systems. All systems are also observed to show shear thinning behaviour beyond the yield stress.
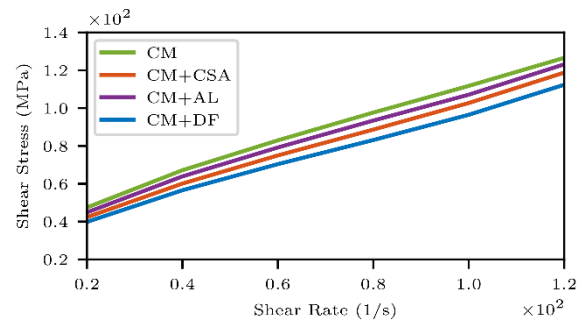
Figure 8. Shear stress vs. shear rate plots of CM
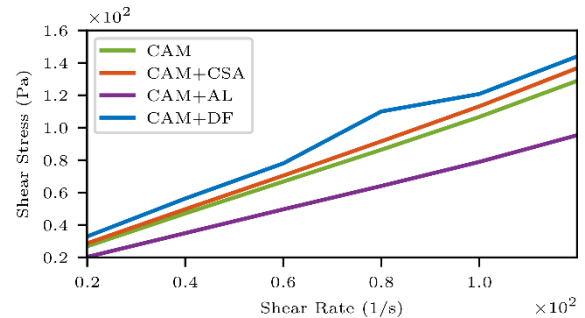
Figure 9. Shear stress vs. shear rate plots of CAM

The apparent viscosity vs. different shear rates is shown in Figures 10 and 11. In CAM systems, the CAM+DF is again seen to exhibit higher viscosity than the other systems. This again indicates that the breaking of the asphalt emulsion is affecting the rheology of the material more than the flocculation/hydration of the cement.
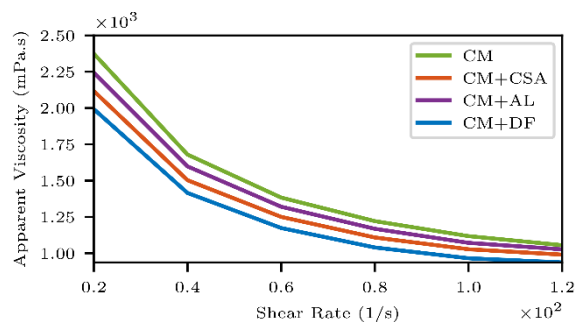
Figure 10. Apparent viscosity vs. shear rate plots of CAM
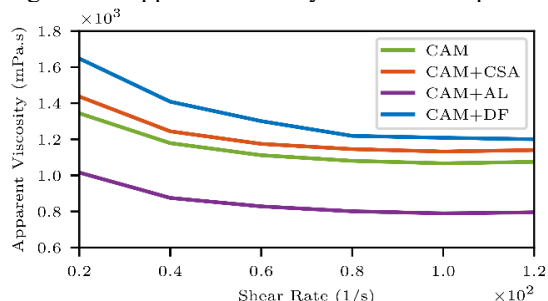
Figure 11. Apparent viscosity vs. shear rate plots of CAM

The apparent viscosity of the CAM system is in general lower than the CM systems at a given shear rate. But the decrease in apparent viscosity with any increase in shear rate appears to be higher for the CM systems compared to the CAM systems.

5 SUMMARY AND CONCLUSION

This study explored the structure formation in cement asphalt mortar (CAM) and the rheology of CAM in its fresh state and compares it to that of cement mortar. The effect of different additives on the mechanical behaviour was also investigated. It was shown that CAM shows shear-thinning behaviour. Additives have a significant impact on the early strength of CAM, rate of hydration, and viscoelastic characteristics. Key findings include:

1. The breaking down of the asphalt emulsion influences the early evolution of the dynamic modulus in CAM. The complex internal structures created through the interaction of asphalt droplets and cement particles provide CAM with its distinct mechanical characteristics. In comparison, the structure development in CM systems was dominated by flocculation and hydration of cement particles.

2. CAM systems had $G'' > G'$ whereas CM systems had $G' > G''$. CAM systems also exhibited a relatively lower modulus than CM systems. Both are indicative of slower structure development in CAM systems.

3. CAM systems exhibited yield-stress fluid behaviour similar to CM systems. Their apparent viscosity was also lower than the corresponding CM systems. Beyond the yield stress, CAM systems showed shear-thinning behaviour.

This study emphasizes the importance of understanding the interaction between cement hydration and asphalt emulsion breaking in developing advanced composite materials with tailored properties for specific engineering needs.

6 REFERENCES

Baldino, N., Gabriele, D., Lupi, F. R., Seta, L., & Zinno R., 2014. Rheological behaviour of fresh cement pastes: Influence of synthetic zeolites, limestone, and silica fume. *Cement and Concrete Research*, 63, 38–45.

García-Maté, M., Santacruz, I., Ángeles, G., León-Reina, L., & Aranda, M. A., 2012. Rheological and hydration characterization of calcium sulfoaluminate cement pastes. *Cement and Concrete Composites*, 34(5), 684-691.

Jayasree, C., Murali Krishnan, J., & Gettu, R., 2011. Influence of superplasticizer on the non-Newtonian characteristics of cement paste. *Materials and structures*, 44(5), 929-942.

Lesueur, D., & Potti, J. J., 2004. Cold mix design: a rational approach based on the current understanding of the breaking of bituminous emulsions. *Road Materials and Pavement Design*, 5(sup1), 65-87.

Nachbaura L., Mutina J.C., Nonata A., & Choplinb L., 2001. Dynamic mode rheology of cement and tricalcium silicate pastes from mixing to setting. *Cement and Concrete Research* 31 183 ± 192.

Nagataki, S., & Gomi, H., 1998. Expansive admixtures (mainly ettringite). *Cement and Concrete Composites*, 20(2-3), 163-170.

Peng, J., Deng, D., Liu, Z., Yuan, Q., & Ye, T., 2014. Rheological models for fresh cement asphalt paste. *Construction and Building Materials*, 71:254–262.

Qiang, W., Peiyu, Y., Ruhan, A., Jinbo, Y., & Xiangming, K., 2011. Strength mechanism of cement-asphalt mortar. *Journal of Materials in Civil Engineering*, 23(9), 1353-1359.

Randal, M., & Kenneth, C., 2019, Silicone Polymers for Foam Control. Silicone Surfactants, 159.

Ren, J., juan, H., lan Li, X., pei Cai, S., jie Deng, J., Wang, & W. Du., 2020. Viscoelastic deformation behaviour of cement and emulsified asphalt mortar in China railway track system I prefabricated slab track. *Journal of Zhejiang University- Science A*, 21 (4): 304–316. Zhejiang University. https://doi.org/10.1631/jzus.A1900525 (2020).

Telesca, A., Marroccoli, M., Pace, M. L., Tomasulo, M., Valenti, G. L., & Monteiro, P. J. M., 2014. A hydration study of various calcium sulfoaluminate cements. *Cement and Concrete Composites*, 53, 224-232.

Umar, H. A., Zeng, X., Lan, X., Zhu, H., Li, Y., Zhao, H., & Liu, H., 2021. A review on cement asphalt emulsion mortar composites, structural development, and performances. *Materials*, 14(12), 3422.

Wang, F., Liu, Z., & Hu, S., 2010. Early age volume change of cement asphalt mortar in the presence of aluminium powder. *Materials and structures*, 43(4), 493-498.

Yang, J., Yan, P., Kong, X., & Li, X., 2010. Study on the hardening mechanism of cement asphalt binder. *Science China Technological Sciences*, 53(5), 1406-1412.

Yuan, Q., Zuo, S., & Deng, D., 2020. Early-age deformation of cement emulsified asphalt mortar with aluminium powder and expansive agent. *Construction and Building Materials*, 260, 120484.

Zhang, Y., Kong, X., Hou, S., Liu, Y., & Han, S., 2012. Study on the rheological properties of fresh cement asphalt paste. Construction and Building Materials, 27(1), 534-544.

Viscoelastic aging characterization of asphalt materials: a computational approach

Mahmoud Khadijeh, Aikaterini Varveri, Cor Kasbergen, Sandra Erkens
Delft University of Technology, Faculty of Civil Engineering and Geosciences, Structural Engineering Section

ABSTRACT: The viscoelastic behavior of bituminous materials is significantly influenced by aging mechanisms. These mechanisms affect the long-term performance of pavements. This study introduces a computational approach to characterize the rheological properties of bitumen and mastic under short-term and long-term aging using an advanced viscoelastic model. A user-defined material subroutine was developed to capture time-dependent responses through a carbonyl area-based aging index. The model integrates a multi-term Prony series with an exponential aging mechanism to accurately quantify the material stiffness evolution. Finite element models are proposed to simulate the dynamic shear rheometer tests (DSR) on bitumen and mastic. The models proposed can effectively capture the progressive stiffening and microstructural changes due to thermal and oxidative aging, providing a robust framework for predicting age-dependent viscoelastic behavior and enhancing pavement design methodologies.

1 INTRODUCTION

Asphalt materials experience continuous physico-chemical transformations throughout their service life, a process known as aging, which fundamentally alters their mechanical and rheological properties. This complex phenomenon is primarily driven by oxidative and thermal aging mechanisms that contribute to material deterioration. Oxidative aging occurs when asphalt binders interact with atmospheric oxygen. This process leads to significant chemical modifications of complex organic molecules through oxidation (Jing et al. 2019) . The key transformations include formation of polar functional groups such as carbonyls and sulfoxides. Chemical crosslinking increases the molecular weight of the binder. These changes result in progressive stiffening of the binder's microstructure and reduce its viscoelastic performance. The carbonyl index, typically measured through infrared spectroscopy, serves as a quantitative indicator of oxidative aging intensity. Asphalt aging progresses through distinct stages: short-term aging (STA) during production and initial compaction, and long-term aging (LTA) occurring throughout the pavement's service life (Pipintakos et al. 2021). Computational methods like Finite Element Modeling (FEM) have emerged as powerful tools for investigating material aging phenomena (Khadijeh et al. 2025). These advanced numerical techniques provide the capability to simulate complex physicochemical transformations, allowing researchers to predict material behavior across multiple temporal and spatial scales. In this research, a novel computational framework is developed to model the viscoelastic behavior of bituminous materials under aging conditions. The study employs a user-defined material (UMAT) subroutine with a carbonyl area-based aging index to simulate the rheological evolution of bitumen and mastic. The research introduces a robust methodology that

combines multi-term Prony series representation with an exponential aging mechanism, enabling precise quantification of material stiffness changes during short-term and long-term aging processes. Finite element simulations of the DSR tests demonstrate high accuracy in comparison with experimental tests, presenting a sophisticated predictive tool for understanding material degradation due to the aging process.

2 METHODOLOGY

2.1 *Maxwell model for viscoelasticity*

The Maxwell model describes a linear viscoelastic material behavior using a generalized formulation based on the Prony series (Kraus et al. 2017). In this work, the Maxwell model is extended to incorporate material aging effects, which are modeled through a carbonyl area-based aging index. The methodology integrates viscoelastic relaxation with time-dependent material property evolution, allowing for the accurate simulation of aging-induced changes in mechanical behavior.

In the Maxwell model, the total stress σ is expressed as the sum of the volumetric and deviatoric stress components:

$$\sigma = \sigma_{vol} + \sigma_{dev} \qquad (1)$$

where the volumetric stress is given by:

$$\sigma_{vol} = 3K\epsilon_{vol}I \qquad (2)$$

with $\epsilon_{vol} = 1/3\ tr(\epsilon)$ representing the volumetric strain, K is the bulk modulus, and I is the identity tensor.

The deviatoric stress accounts for both long-term elastic and time-dependent relaxation effects and is expressed as:

$$\sigma_{dev} = 2G(G_\infty \epsilon_{dev} + \sum_{i=1}^{N} s_m^i) \qquad (3)$$

where G is the shear modulus G, $\epsilon_{dev} = \epsilon - \epsilon_{vol}I$ is the deviatoric strain, $G_\infty = 1 - \sum_{i=1}^{N} G_i$ is the long-term modulus ratio, and s_m^i represents the stress contribution from each Prony term.

The stress memory term s_m^i for the i-th Prony element is computed incrementally using exponential integration:

$$S_m^{i,new} = e^{(-\frac{\Delta t}{\tau_i})} S_m^{i,old} + \frac{2G_i}{1+\frac{\Delta t}{\tau_i}} \Delta \epsilon_{dev} \qquad (4)$$

where Δt is the time increment, τ_i, is the relaxation time, and $\Delta \epsilon_{dev}$ is the deviatoric strain increment.

2.2 Incorporating of aging effects

The aging process is modeled through a time-dependent scaling of the material stiffness, governed by the carbonyl area $CA(t)$. The evolution of $CA(t)$ is described as:

$$CA(t) = CA_0 + CA_\infty(1 - e^{-R_t t}) \qquad (5)$$

where CA_0 is the initial carbonyl area, CA_∞ is the asymptotic value at long times, and R_t is the reaction rate controlling the rate of carbonyl accumulation.

The aging index $A(t)$ is defined as:

$$A(t) = 1 + k.CA(t) \qquad (6)$$

where k is a scaling factor that quantifies the sensitivity of the material properties to aging. The Young's modulus at time t, $E_{aged}(t)$ is then computed as:

$$E_{aged}(t) = E_0.A(t) \qquad (7)$$

where E_0 is the initial Young's modulus before aging. This modification affects both the bulk modulus K and shear modulus G, which are updated as:

$$K = \frac{E_{aged}}{3(1-2\nu)} \qquad (8)$$

$$G = \frac{E_{aged}}{2(1+\nu)} \qquad (9)$$

where ν is the Poisson's ratio. The aging also impacts the relaxation times τ_i, which are scaled inversely with the aging index:

$$\tau_i^{aged} = \frac{\tau_i}{A(t)} \qquad (10)$$

In each time increment, the UMAT subroutine computes the updated stress and internal state variables. The stress memory terms S_m^i are recalculated for each Prony term, incorporating the aged relaxation times. The state variables are updated to store the stress memory terms, the current carbonyl area $CA(t)$, the aging index $A(t)$, and the aged Young's modulus E_{aged}.

The material Jacobian D, or tangent stiffness matrix, is derived to ensure numerical stability. The effective shear modulus G_{eff}, incorporating both elastic and viscoelastic contributions, is computed as:

$$G_{eff} = G(G_\infty + \sum_{i=1}^{N} \frac{G_i}{1+\frac{\Delta t}{\tau_i}}) \qquad (11)$$

The tangent stiffness matrix is then assembled, including contributions from both the bulk modulus K and G_{eff}.

2.3 Model construction

The computational model is designed to simulate the behavior of the binder and mastic materials under controlled loading conditions. The binder and mastic sample is modeled as a cylindrical structure with a diameter of 8 mm and a thickness of 2 mm. Within the mastic sample, the volume fraction of fillers embedded in the binder is set at 28%, replicating the microstructural composition of the mastic material with a Young's modulus equals to 70 GPa. To mimic the experimental test setup, the sample is positioned between two parallel plates, which are modeled as rigid bodies. The interaction between the rigid plates and the sample is defined using cohesive stiffness contact properties, ensuring proper load transfer without penetration or separation artifacts during the simulation. A logarithmic sinusoidal load is applied to replicate the experimental loading conditions. This load type is chosen for its ability to introduce controlled cyclic deformation while capturing the time-dependent mechanical response of the sample.

The material properties used in this study were extracted from Ren et al. 2022 for the binder models and from Granular et al. (2019) for the mastic properties. An optimization process, utilizing the Python tool provided by (Khadijeh et al. 2025), was conducted to determine the Prony series parameters. For fresh conditions, both the initial Carbonyl area (CA_0) and the long-term carbonyl area (CA_∞) were set to 0. Under STA conditions, CA_0 was set to 0 and CA_∞ to 0.8. For long-term aging conditions, CA_0 was set to 0.8 and CA_∞ to 1.2. The parameters k and R_t were set to 1.2 and 0.1, respectively.

In the mastic model, the fillers are assumed to be fully merged with the binder, forming a homogenous composite material. This approach simplifies the representation of the filler-binder interactions while retaining the bulk mechanical behavior observed in real

mastic samples. Figure 1 illustrates the overall modeling framework, including the geometric setup and loading configuration.
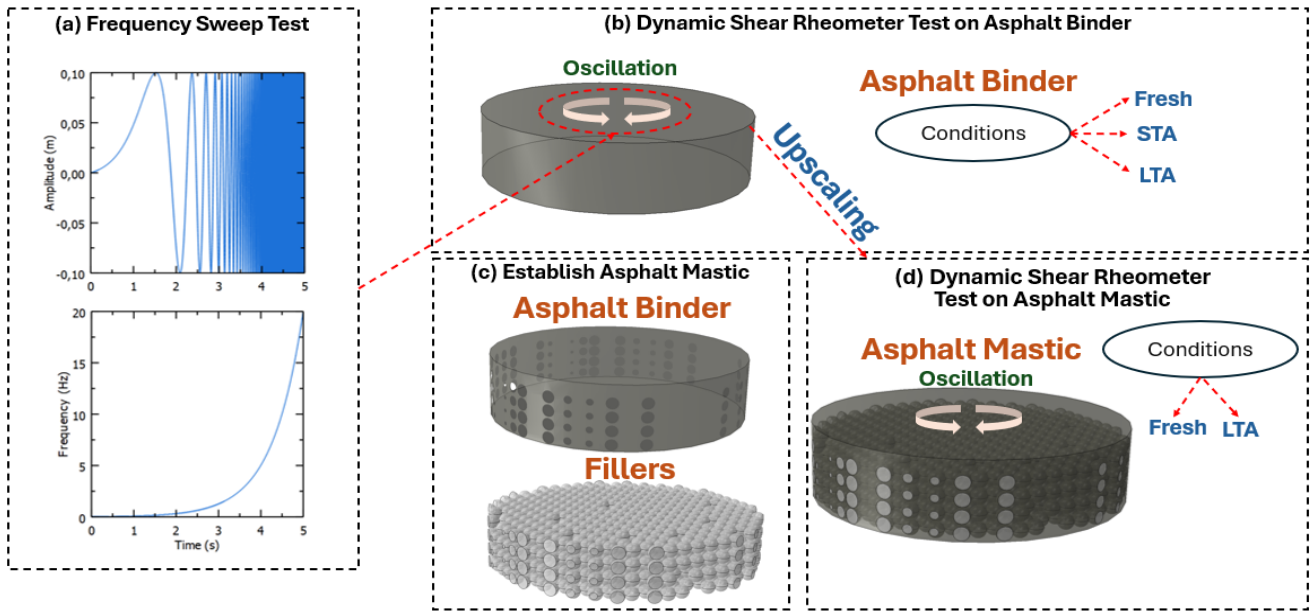
Figure 1 Overview of the experimental framework for asphalt binder and mastic characterization. (a) Frequency sweep test setup (b) DSR test performed on asphalt binder under different conditions: fresh, short-term aged (STA), and long-term aged (LTA), (c) schematic representation of the asphalt mastic model, and (d) DSR test applied to asphalt mastic under fresh and LTA conditions.

3 RESULTS

3.1 *Asphalt binder results*

Figure 2 presents the comparison between experimental tests and FEM predictions for G^* as a function of frequency. Three distinct cases are analyzed: (a) fresh asphalt binder, (b) short-term aged (STA) asphalt binder, and (c) long-term aged (LTA) asphalt binder. Across all cases, G^* increases with frequency, reflecting the viscoelastic nature of asphalt binders, where higher frequencies correspond to stiffer responses. Aging significantly increases G^*, with STA and LTA binders exhibiting progressively higher stiffness compared to the fresh binder due to the stiffening effects of oxidation and chemical hardening. The FEM predictions closely replicate the experimental trends, particularly at mid-to-high frequencies, demonstrating the model's effectiveness in capturing both frequency dependence and aging effects. Minor deviations are observed at lower frequencies, especially for the long-term aged binder, likely due to limitations in capturing aging-induced microstructural changes and relaxation mechanisms. Overall, the results confirm that the proposed numerical framework accurately reflects the viscoelastic and aging behavior of asphalt binders.

3.2 *Asphalt mastic results*

Figure 3 illustrates the complex shear modulus G^* as a function of frequency for asphalt mastic in its fresh state (a) and LTA state (b), comparing experimental results with FEM predictions. Similar to the asphalt binder results, G^* increases with frequency, indicating the viscoelastic stiffening behavior of asphalt mastic under higher loading rates. Aging leads to a significant increase in stiffness, with the LTA mastic exhibiting higher G^* values compared to the fresh mastic due to the presence of fillers and the effects of long-term oxidation. The FEM predictions align well with the experimental results, particularly at mid-to-high frequencies, confirming the model's ability to capture both the viscoelastic and aging behavior of the mastic. Slight discrepancies are observed at lower frequencies, where relaxation mechanisms and filler interactions may be more pronounced. Overall, the results demonstrate the accuracy and robustness of the numerical framework in simulating the frequency-dependent and aging responses of asphalt mastic.
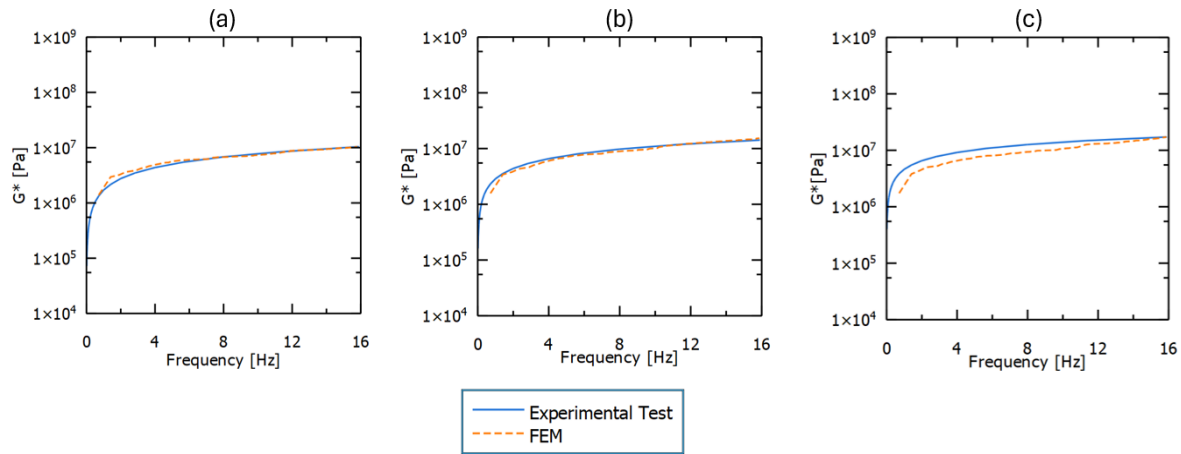
Figure 2 Comparison of experimental and FEM results for G^* of asphalt binders. (a) Fresh asphalt binder, (b) STA asphalt binder, and (c) LTA asphalt binder.
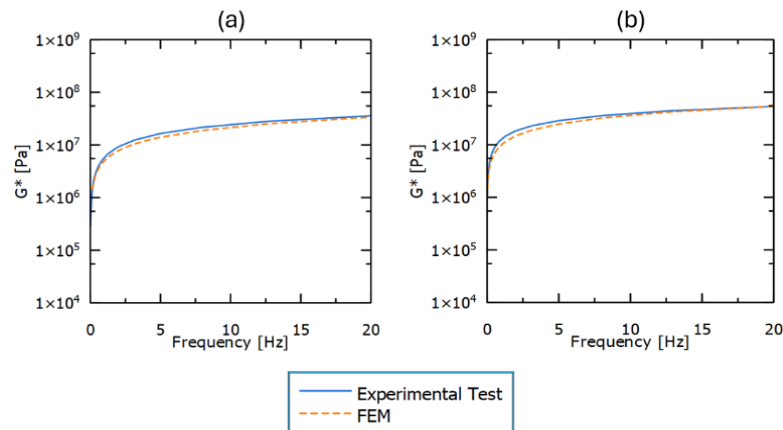
Figure 3 Comparison of experimental and FEM results for G^* of asphalt mastics. (a) Fresh asphalt mastic, (b) LTA asphalt mastic.

4 CONCLUSION

This research enhances our understanding of bituminous materials by developing a computational framework that illuminates the complex viscoelastic behavior of asphalt binders and mastics under aging conditions. The study introduces an advanced user-defined material (UMAT) subroutine with a carbonyl area-based aging index, offering researchers and engineers a powerful tool for examining the intricate physicochemical transformations that occur throughout an asphalt material's lifecycle.

The FE models accurately predicted how asphalt materials change over time and frequency. These simulations closely matched real-world experimental results across different stages of material aging, from newly created to extensively aged samples.

5 REFERENCES

Jing, R., Varveri, A., Liu, X., Scarpas, A. & Erkens, S., 2019, 'Laboratory and Field Aging Effect on Bitumen Chemistry and Rheology in Porous Asphalt Mixture', 2673(3), 365–374.

Khadijeh, M., Kasbergen, C., Erkens, S. & Varveri, A., 2025, Exploring the roles of numerical simulations and machine learning in multiscale paving materials analysis: Applications, challenges, best practices, Computer Methods in Applied Mechanics and Engineering, 433.

Kraus, M.A., Schuster, M., Kuntsche, J., Siebert, G. & Schneider, J., 2017, 'Parameter identification methods for visco- and hyperelastic material models', Glass Structures and Engineering, 2(2), 147–167.

Pipintakos, G., Soenen, H., Ching, H.Y.V., Velde, C. Vande, Doorslaer, S. Van, Lemière, F., Varveri, A. & bergh, W. Van den, 2021, 'Exploring the oxidative mechanisms of bitumen after laboratory short- and long-term ageing', Construction and Building Materials, 289, 123182.

Ren, S., Liu, X., Lin, P., Jing, R. & Erkens, S., 2022, 'Toward the long-term aging influence and novel reaction kinetics models of Toward the long-term aging influence and novel reaction kinetics models of bitumen', International Journal of Pavement Engineering, (January), 1–16.

Residue Recovery of Asphalt Emulsion and Cutback Asphalt Using Vacuum Oven

Satyavati Komaragiri
Indian Institute of Science

Hui Chen, Fujie Zhou
Texas A&M Transportation Institute

Zahra Sotoodeh-Nia, Pravat Karki, Enad Mahmoud
Texas Department of Transportation

Darren Hazlett, Amit Bhasin
The University of Texas at Austin

ABSTRACT: Typical applications of asphalt emulsions and cutbacks are surface preservation treatments and as a bonding layer between pavement layers in a pavement structure during pavement construction. Cutback and emulsion residues are routinely evaluated for quality control purposes to ensure its performance. Current standard methods for residue recovery of materials are distillation-based methods which require large equipment footprint is less productive. A new method was developed by the authors in their earlier work which offers high throughout and requires less material as well as equipment. The method exhibited good repeatability between two laboratories. The present study advances the previous research by examining the robustness of this test method by performing a round robin testing of various grades of cutbacks and emulsions with six participating laboratories. The mass loss during the residue recovery and G*/sin δ obtained from the Dynamic Shear Rheometer (DSR) testing of residue were used to examine repeatability. The results show very good repeatability between the participating laboratories which further demonstrates the potential use of this method for routine screening of asphalt emulsions and cutbacks.

1 INTRODUCTION

Asphalt emulsions and cutbacks are widely used in surface treatments, as tack coat between pavement layers and in cold-mix technologies as they are liquid at room temperatures. These liquids are produced by mixing asphalt binder and water with the help of emulsifying agent in the case of emulsions, and petroleum solvent is mixed with asphalt binder in the case of cutbacks. The water/solvent in these materials need to evaporate in the field after application to ensure desired performance. These materials are routinely screened in the laboratory by testing the residue to ensure desired field performance. Tests on the residue indicate the state of the emulsion or cutback after evaporation of water or solvent in the field after application, respectively.

Currently, the standard test methods used to obtain the cutback or emulsion residue in the laboratory are distillation-based methods in the state of Texas: (i) AASHTO T78 (2022) for cutbacks and (ii) AASHTO T59 (2022). These test methods typically involve very high temperatures which is a safety concern and is also not a representative of field temperatures. These test methods also require high operators' time as well as a lot of time in sample preparation and cleanup. To address these limitations, in a previous research, authors developed a new test method to obtain residues from emulsions and cutbacks using a vacuum oven and demonstrated the feasibility of the method for routine screening by examining the repeatability of the test between two laboratories (Komaragiri et al., 2024).

Other test methods were also evaluated using evaporative techniques for emulsions such as AASHTO T59 evaporation method, AASHTO R78 (2022) ASTM 7404 (2019). However, very high temperatures were used in these tests which are not a representative of field conditions and high temperatures used in the tests reportedly damage the polymer network in the polymer modified emulsions and caused aging (Wasiuddin et al., 2013; King et al., 2010; Reinke et al., 2013;Motamed et al., 2014). The test method developed by the authors in the previous research addresses these issues. The new method requires a small quantity of emulsion or cutbacks for residue recovery as the residue obtained from this test method is evaluated using a DSR which requires a very small quantity of sample for testing. Due to this reason, residue recovery for eight cutback samples or six emulsion samples can be performed at the same time showing a huge potential of this test method for routine screening of cutbacks and emulsions. Note that this method is not intended to provide a detailed compositional breakdown, as is the case with the distillation-based methods. More details of this test can

be found elsewhere (Komaragiri et al., 2024). The present study advances the previous research work by performing a broader round-robin testing.

2 SCOPE

Previous study by the authors developed test methods to obtain residues from cutbacks and emulsions (Komaragiri et al., 2024). The main goal of this study was to advance this research by demonstrating the robustness of the method by performing a broad round-robin testing. This round-robin testing involved six participating labs from the state of Texas both from industry and academia.

3 MATERIALS

The materials used in this study are as follows:
- RC-250 cutback from two suppliers
- MC-30 cutback from 2 suppliers
- CRS-2P emulsion from two suppliers
- HFRS-2P emulsion from one supplier

Note that these materials were selected in the study as these cutbacks and emulsions are used the most in the state of Texas. The same material was split and sent to all participating laboratories of round-robin testing.

4 TESTING

The vacuum oven-based test method developed in previous research for residue recovery of cutbacks and emulsions was used in the present study. Mass loss during the residue recovery was also recorded. The DSR test protocol that was used to develop the residue recovery procedures in the previous research was also used to test the recovered residue from the aforementioned cutbacks and emulsion in this study. The DSR procedure is reiterated here for the sake of completeness: G*/sin δ parameter was recorded at 64°C at 10% strain rate and 10 rad/s frequency. This parameter was obtained as the average of the last five cycles out of the recorded ten cycles. The same test protocol was followed in all participating laboratories.

5 RESULTS

Data obtained from the round-robin testing conducted in various industrial and research laboratories is summarized in the next subsections. Note that this round-robin study had different equipment (vacuum ovens, vacuum pumps and dynamic shear rheometers) and different operators.

5.1 Emulsions

CRS-2P emulsion from two suppliers and HFRS-2P from one supplier was used for the round-robin testing. Figure 1 shows the mass loss data obtained from the six participating laboratories. It must be noted that four out of six laboratories conducted testing on two replicates and the remaining two laboratories conducted testing on one replicate. In the case of two replicates, the average of the two replicates is reported in the figure. It can be observed that the mass loss data is very repeatable between the six labs and average mass loss was around 33% for all the emulsions which is approximately the amount of water present in these emulsions based on the information obtained from the producers.
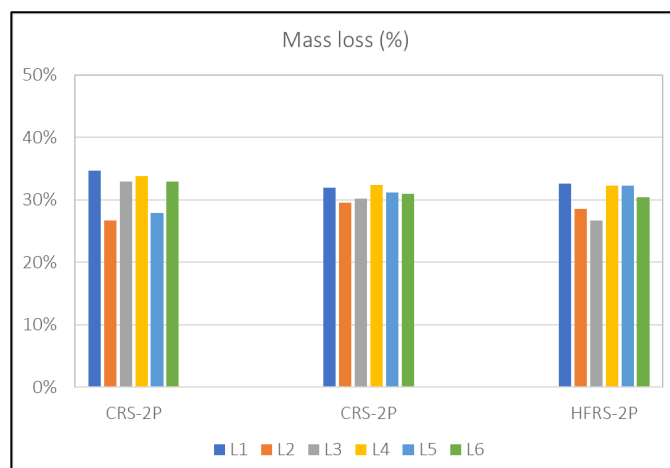
Figure 1. Mass loss data obtained from the six laboratories participated in the round robin testing

Figure 2 shows the G*/sin δ parameter from DSR obtained from the six labs. It should be noted that each replicate in the figure is shown as a separate data point. Base binders were also obtained from the producers for reference. It can be observed from this figure that the DSR parameter shows very good repeatability between the six participating labs. More variability can be observed for HFRS-2P emulsion as compared to CRS-2P emulsions. However, even with a higher variation the DSR parameter from all six labs lies in the range of 1 to 1.6. This shows that even though the repeatability of HFRS-2P is lower compared to that of the CRS-2P emulsions, the overall repeatability is still very good. It can also be seen from the figure that base binders of these emulsions are less stiff than the emulsion residue recovered by the developed procedure. Authors found out from the producers that the base binders used for the production of these emulsions were not polymer modified. In fact, these polymer-modified emulsions (both CRS-2P and HFRS-2P) were obtained by the addition of the polymer during the emulsification process.
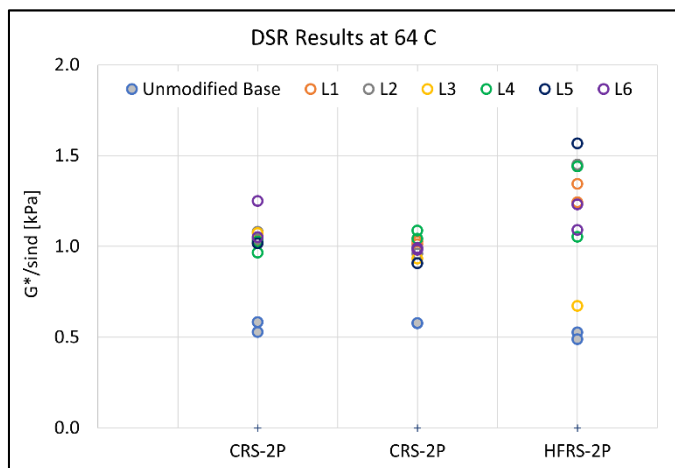
Figure 2. G*/sin δ data obtained from the six labs participated in the round-robin testing

Figure 3. Mass loss data obtained from the six laboratories participated in the round-robin testing for cutback residue recovery

5.2 Cutbacks

MC-30 and RC-250 cutbacks from two different suppliers were used for the round-robin testing. Figure 3 shows the mass loss data obtained from the six participating laboratories during the residue recovery procedure. It can be observed from the figure that the mass loss data is very repeatable across the six laboratories. The mass loss for the MC-30 cutback obtained from both the suppliers was around 40% and the mass loss for RC-250 cutback was around 20%. Based on the information obtained from the producers, this is the approximate amount of solvent that is used to produce these cutback grades. It must be noted here that only one replicate was tested in two out of the six laboratories and two replicates were tested in the remaining four laboratories, in which case the average of the two replicates is reported in the figure.

Figure 4 shows the G*/sin δ parameter at 64°C from the six participating labs. It must be noted that each replicate is shown as a separate data point in the figure. Base binders for the cutbacks were also obtained from the producers to get a reference. It can be observed that the DSR parameter was repeatable for three cutbacks (two RC-250s and one MC-30) and there was a lot of variability in the results for one MC-30. The reason for variability was observed to be because of unusually stiff base (G*/sin δ parameter is around 60 at 64°C) of the cutback. Overall, this exercise demonstrated the robustness of the developed method and its immediate applicability to the industry for routine screening purposes.

Figure 4. G*/sin δ data obtained from the six labs participated in the round-robin testing

6 SUMMARY AND CONCLUSIONS

In a previous study, authors developed a test method for residue recovery of cutbacks and emulsion using vacuum oven (Komaragiri et al., 2024). This new procedure needs a smaller equipment footprint, increases overall throughput, requires less material and cleaning as compared to the standard test method that is currently used for residue recovery. The feasibility and potential of this method for routine screening of cutbacks and emulsions was demonstrated based on the data obtained from two different laboratories which had different operators and equipment. This study builds on the previous study by performing a broader round-robin testing on the developed test procedure for residue recovery with six participating laboratories. These laboratories include various research and industry laboratories in the state of Texas. Six participating laboratories had different operators, vacuum ovens, vacuum pumps and DSRs.

Various cutback and emulsion grades were used in the round-robin testing. Mass loss data during the residue recovery test and G*/sin δ parameter obtained from the DSR test on residue sample were recorded in this study. Results from the round-robin testing show very good repeatability between all six participating laboratories both in mass loss data and G* G*/sin δ data with one exception of MC-30 cutback which had an unusual base with very high stiffness. This study further demonstrates the robustness of the residue recovery procedure developed in the previous study with respect to different operators, different brands of vacuum ovens, vacuum pumps and DSRs. This study further exhibits the potential and readiness of using this test method for routine screening of cutbacks and emulsions.

7 ACKNOWLEDGEMENTS

8 DISCLAIMER

The contents of this paper reflect the views of the authors who are solely responsible for the facts and accuracy of the data presented herein and do not necessarily reflect the official views or policies of any agency or institute. This paper does not constitute a standard, specification, nor is it intended for design, construction, bidding, contracting, tendering, certification, or permit purposes. Tradenames were used solely for information purposes and not for product endorsement, advertisement, promotions, or certification.

9 REFERENCES

AASHTOR78. (2022). Standard method of test for recovering residue from emulsified asphalt using low-temperature evaporative techniques. In *AASHTOR78*. American Association of State Highway and Transportation Officials.

AASHTOT59. (2022). Standard method of test for emulsified asphalts. In *AASHTOT59*. American Association of State Highway and Transportation Officials.

AASHTOT78. (2022). Standard method of test for distillation of cutback asphalt products. In *AASHTOT78*. American Association of State Highway and Transportation Officials.

ASTM:7404. (2019). Standard Practice for Determination of Emulsified Asphalt Residue by Moisture Balance Analyzer. *Annual Book of American Society for Testing Materials: ASTM Standards*.

King, G. N., King, H., Galehouse, L., Voth, M. D., Lewandowski, L. H., Lubbers, C., & Morris, P. (2010). Field validation of performance-based polymer-modified emulsion residue tests: The FLH study. *First International Conference on Pavement PreservationCalifornia Department of TransportationFederal Highway AdministrationFoundation for Pavement Preservation*.

Komaragiri, S., Chen, H., Hazlett, D., Sotoodeh-Nia, Z., Mahmoud, E., Zhou, F., & Bhasin, A. (2024). Evaluation of Using Vacuum Oven for Residue Recovery of Asphalt Emulsion and Cutback Asphalt for Routine Screening. *Journal of Materials in Civil Engineering*, *36*(10), 4024315. https://doi.org/10.1061/JMCEE7.MTENG-17594

Motamed, A., Salomon, D., Sakib, N., & Bhasin, A. (2014). Emulsified asphalt residue recovery and characterization: Combined use of moisture analyzer balance and dynamic shear rheometer. *Transportation Research Record*, *2444*(1), 88–96.

Reinke, G., Ryan, M., Engber, S., & Herlitzka, D. (2013). Techniques for Accelerating Recovery of Asphalt Emulsion Residues at 60 C by Using Thin Film Procedures and Test Methods Suited to the Limited Amount of Residue Obtained to Characterize the Recovered Binder. *Progress Toward Performance-Graded Emulsified Asphalt Specifications*, 90.

Wasiuddin, N. M., Salehi Ashani, S., Kabir, M. S., Abadie, C., King Jr, W., & Mohammad, L. N. (2013). *Rheology of Asphalt Emulsion Residues and Its Relationship to Elastic Recovery in AASHTO T301*.

Advancements in lightweight deflectometer testing and strain modeling for subgrade evaluation

Dina Kuttah

Senior researcher at the Swedish National Road and Transport Research Institute, VTI, Pavement technology division, Olaus Magnus väg 35, SE-581 95, Linköping, Sweden, dina.kuttah@vti.se

ABSTRACT: This study investigates the modeling and prediction of permanent strains in subgrade soil using repeated lightweight deflectometer (LWD) testing. The research focuses on understanding the relationship between applied stress, recoverable strain, water content, and accumulated permanent strains, specifically in silty sand subgrade soils. In-situ LWD tests were conducted at different stress levels (50, 100, and 200 kPa) and water contents (8%, 10%, and 15%) to measure both permanent and recoverable deformations. A developed model, designed to predict permanent strains utilizing recoverable strains in road materials under various conditions, was compared with LWD results and evaluated for accuracy. While discrepancies were observed at higher water contents and certain stress levels using this model, the regression models demonstrated strong predictive capabilities, with R² values exceeding 0.91 for most testing conditions. This study underscores the potential of in-situ repeated LWD testing as a reliable tool for assessing subgrade behavior for pavement design.

1 INTRODUCTION

Permanent strain in unbound granular materials used in road construction is a critical factor affecting pavement performance and longevity. Several models have been proposed to relate permanent strains in these materials to the number of load applications and other influencing factors. These models aim to predict the permanent deformation behavior of unbound layers in flexible pavements (Lekarp and Dawson, 1998).

One of the earliest simple models proposed to relate plastic strains to the number of load applications and other influencing factors is the model by Monismith et al. (1975), as presented in Eq. (1) below:

$$\varepsilon_p = a. N^b \qquad \text{......................} \quad (1)$$

where:

ε_p = Accumulated plastic strain (%)

N = Number of load applications

a, and b = Parameters that represent the influence of other factors.

Puppala et al. (2009) conducted a comprehensive research study to measure permanent deformation properties of subgrade soils under repeated loading cycles, contributing to the understanding of these relationships. Among the developed models used to predict permanent strain, the one suggested by Rahman et. al. (2021) has been verified against LWD permanent strain data in this study. This model con

siders the resilient strain (ε_r) to predict the permanent strain as given in Eq. 2 below:

$$\varepsilon_p = a. \varepsilon_r . N^{b\ \varepsilon_r} \qquad \text{..........................} \quad (2)$$

where ε_r is the resilient (elastic) strain during one load cycle.

In this study, a model for accumulated permanent strains was evaluated to align with the permanent strains measured during single-stage in-situ repeated LWD tests. The model incorporates the number of load cycles (N) and recoverable strain, and its applicability was assessed for water contents up to 15%. Additionally, regression models were developed to represent the data obtained from the series of single-stage repeated LWD tests conducted in this research. The development, application, and evaluation of these models are discussed comprehensively in the following sections. Further details on using the single-stage lightweight deflectometer to measure permanent deformations can be found in Kuttah (2020, 2021, and 2024).

2 TESTING METHODOLOGY

Field tests were conducted on compacted silty sand subgrade soil using repeated lightweight deflectometer (LWD) tests to evaluate elastic and plastic deformations under varying stress levels (50 kPa, 100 kPa, and 200 kPa) and moisture conditions (8%, 10%, and 15%). The study, carried out at VTI's

backyard in Linköping, involved preparing a controlled test pit with compacted subgrade soil classified for its physical and mechanical properties. The testing process simulated real-life vehicle stress impacts on paved and unpaved roads. The newly developed LWD includes a control beam with a central LVDT to measure plastic deformations at the centerline of loading, alongside a central geophone for total deformation. The LVDT directly measures plastic deformations through the steel plate, ensuring accuracy and overcoming integration errors associated with geophone measurements, see Figure 1. The test pit was equipped with a roof panel for environmental control and a water system to regulate moisture conditions. LWD tests were conducted systematically at marked points on the compacted soil, with moisture levels adjusted through drying or wetting processes. Data on deformation, field density, and relative compaction were collected using NDG tests and oven-dried methods, providing insights into the subgrade's performance under varying stress and moisture conditions.
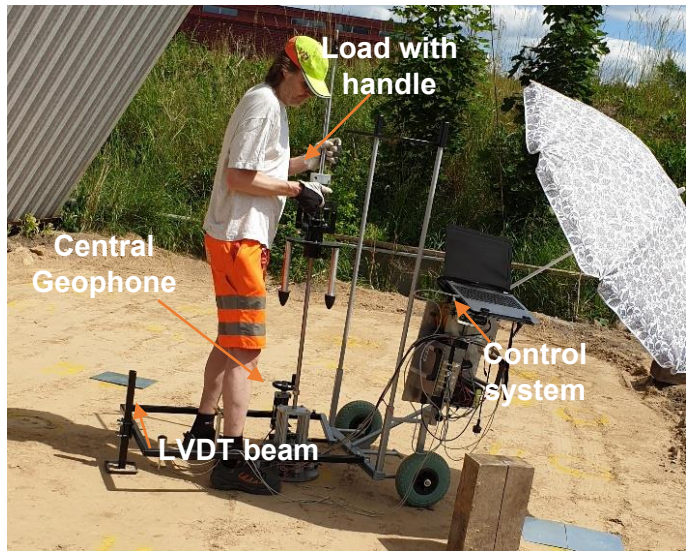
Figure 1. The developed lightweight deflectometer, capable of separately measuring the permanent and recoverable deformations of the tested soil.

3 TESTED SOIL PROPERTIES

A silty sand subgrade soil was selected for testing in this study, and a series of laboratory tests were performed to determine its physical properties, including particle size distribution, clay fraction, soil classification, specific gravity, liquid and plastic limits, and compaction characteristics. The particle size distribution test was carried out according to SS-EN 933-1 (2004), which showed that about 40% of the soil passed through a 0.063 mm sieve. The clay content was measured using VTI's laser diffraction method (10 nm - 2 mm) and found to be 5%. The specific gravity was determined according to SS-EN 1097-6 (2013), annex G, and was found to be 2.64. The liquid and plastic limits were measured at SGI

following SS-EN ISO 17892-12 (2018), revealing a liquid limit of 18% and a plastic limit of 14.3%, resulting in a plasticity index of 3.7%. The compaction characteristics were determined using the modified Proctor test (ASTM D1557, 2012), which involved compacting soil samples at varying moisture contents between 0% and 16%. The results showed a maximum dry density of 2.03 g/cm³ at an optimum moisture content of 8.2%.

4 MODELING PERMANENT STRAINS MEASURED DURING REPEATED LWD TESTING

It is clear that the models shown in Eq. 2 requires the permanent strains while in the developed repeated LWD test, the permanent deformations can be measured. To convert these measured deformations into strains, specifically the recoverable strains required in Eq. 2, the LWD's zone of influence must be estimated. Nazzal (2003) and Tompai (2008) found that the LWD's zone of influence typically ranges from 1 to 2 times the plate diameter, which is consistent with the findings of Elhakim et al. (2014). In this study, the zone of influence of the LWD was assumed to be 1.5 times the plate diameter of 20 cm, resulting in a zone of influence of 30 cm, in depth.

The model in Eq. 2 was used to predict the accumulated permanent deformations measured during in-situ repeated LWD tests. To achieve the best fit for each specific water content and stress level group, nonlinear parameters, denoted as a and b, were determined separately for each case and are shown in Figures 2 and 3. The parameter "a" for points tested at the same stress level was plotted against water content (W), as illustrated in Figure 2. The results indicate that "a" follows a power function of W within the study's water content range. The values of "a" for different stress levels, along with the corresponding R^2 values, are provided in Figure 2.
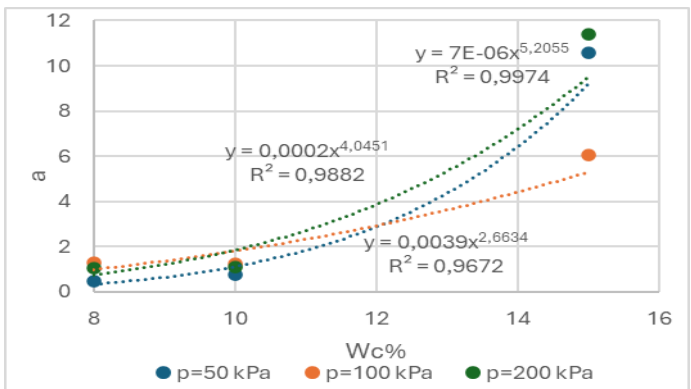
Figure 2. Parameter a (Eq. 2) as a function of the water content for different applied stress levels.

Similarly, the parameter "b" was plotted against W for points tested at the same stress level, as shown

in Figure 3. The results suggest that "b" can be expressed as a linear function of W within the studied ranges, with the corresponding values and R² values displayed in Figure 3.
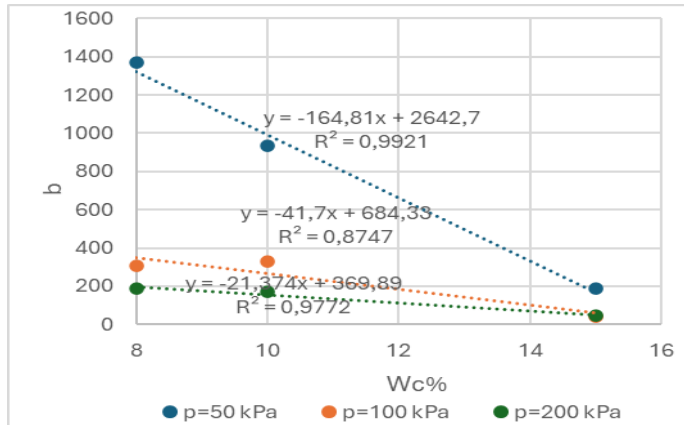
Figure 3. Parameter b (Eq. 2) as a function of the water content for different applied stress levels.

Figures 4, 5, and 6 show a comparison between the measured and predicted accumulated permanent strain, using Eq. 2 as a function of N for the tested soil at different stress levels and water contents (8%, 10%, and 15%).
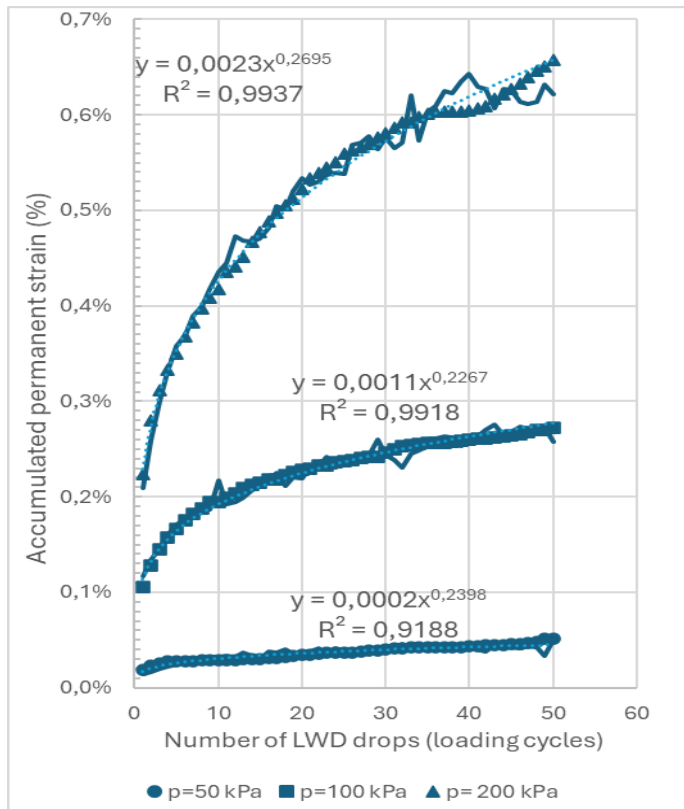
Figure 4. Measured and modelled accumulation of permanent strain using Eq. 2 for W=8%.

These figures also present the measured versus modeled accumulated permanent strain based on regression analysis for different stress levels and moisture contents, along with the R² values.

From Figures 4 to 6, it is evident that the model from Eq. 2 fits well with the in-situ repeated LWD measured permanent strains, except for cases at p = 100 kPa and 200 kPa at 15% water content, and for N > 20 drops at p = 200 kPa and 10% water content. In these instances, the model fails to provide a reliable prediction due to excessive accumulated permanent strains that cannot be accurately represented.
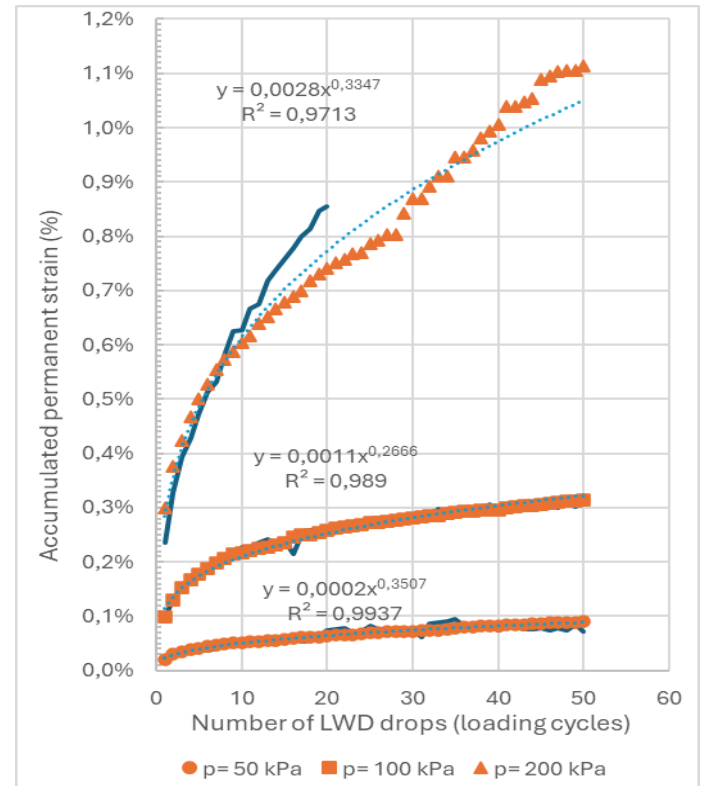
Figure 5. Measured and modelled accumulation of permanent strain using Eq. 2 for W=10%.
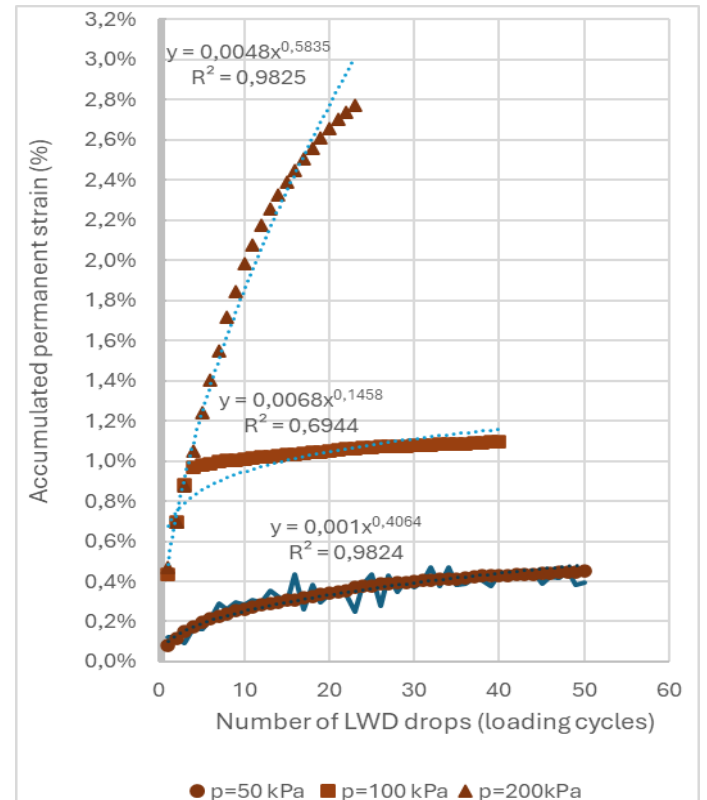
Figure 6: Measured and modelled accumulation of permanent strain using Eq. 2 for W=15%.

As for the regression fitting, Figures 4 to 6 demonstrate that the power function used in the regression provides a good fit, with R² values greater than 0.91 for most cases, except for p = 100 kPa at 15% water content. The discrepancy in this curve is attributed to the loss of plastic deformation data for one of the testing points. Consequently, the curve was extended using the available data from another test point on the same location.

5 CONCLUSIONS AND RECOMMENDATIONS

In conclusion, this study successfully applied the model presented in Eq. 2 to predict the accumulated permanent deformations of subgrade soil measured during repeated LWD tests under various stress levels and moisture contents. The nonlinear parameters "a" and "b" were determined for each stress level and water content group, and their relationships with water content were found to be a power function for "a" and linear for "b". The model showed a good fit with the measured data in most cases, demonstrating the ability to predict accumulated permanent strains under typical testing conditions. However, discrepancies were observed for certain stress levels and moisture contents, particularly at higher water contents and larger numbers of drops, where the model could not reliably predict the observed strains. Despite these limitations, the regression fitting provided a high level of accuracy with R² values above 0.91 in most cases. The findings underscore the importance of considering moisture content and stress levels in predicting subgrade soil behavior, while also highlighting areas for further refinement of the model to improve its applicability in extreme conditions. It is important to note that the models developed in this study are specific to the tested materials and conditions, and when applied to other materials or conditions, a combination of prior experience and engineering judgment should be used. Further studies on other road materials are recommended to expand the application of in-situ repeated LWD testing for modeling accumulated permanent strains.

6 REFERENCES

- ASTM D1557. 2012. *Standard test methods for laboratory compaction characteristics of soil using modified effort (56,000 ft-lbf/ft3-2,700 kN-m/m3)*. ASTM International, West Conshohocken, PA, United States.
- Elhakim, A. F.; Elbaz, K.; and Amer, M. I. 2014. The use of light weight deflectometer for in situ evaluation of sand degree of compaction. *Housing and Building National Research Center HBRC Journal*, 10, 298-307 http://ees.elsevier.com/hbrcj.
- Kuttah, D. 2020. Simple and quick evaluation of unbound materials bearing capacities that could be used as input data in Mechanistic-Empirical Pavement Design. *VTI report* 1054, ISSN 0347-6030, in Swedish, VTI rapport 1054 (diva-portal.org).
- Kuttah, D. 2021. Determining the resilient modulus of sandy subgrade using cyclic light weight deflectometer test. *Transportation Geotechnics*, Volume 27,100482, ISSN 2214-3912, https://doi.org/10.1016/j.trgeo.2020.100482.
- Kuttah, D. 2024. Optimizing Geotechnical Data Input Based on Light Weight Deflectometer for Road Design and Performance Analysis. Transp. *Infrastruct. Geotech*. 11, 3783–3804. https://doi.org/10.1007/s40515-024-00430-6
- Lekarp F, Dawson A. 1998. Modelling permanent deformation behaviour of unbound granular materials. *Constr Build Mater*.;12:9–18.
- Monismith CL, Ogawa N, Freeme CR. 1975. Permanent deformation characteristics of subgrade soils due to repeated loading. *Transp Res Rec*; 537:1–17.
- Nazzal, D. M. 2003. *Field evaluation of in-situ test technology for QC/QA during construction of pavement layers and embankments*. (Master's thesis), Louisiana State University, Baton Rouge.
- Puppala AJ, Saride S, Chomtid S. 2009. Experimental and modeling studies of permanent strains of subgrade soils. *Geotech Geoenviron Eng*,135:1379–89.
- Rahman, M.; Erlingsson, S.; Ahmed, A. and Dinegdae, Y. 2021. A model for the permanent deformation behavior of the unbound layers of pavements. *Proceedings Eleventh International Conference on the Bearing Capacity of Roads, Railways and Airfields*: Volume 1, Edited by Inge Hoff, Helge Mork & Rabbira Saba, London: CRC Press, 277-287.
- SS-EN 1097-6 2013. *Tests for mechanical and physical properties of aggregates*. Part 6 "Determination of particle density and water absorption", SIS, Swedish Standards Institute, Stockholm, Sweden.
- SS-EN 933-1 2004. *Tests for geometrical properties of aggregates*. Part 1 "Determination of particle size distribution – sieving method", SIS, Swedish Standards Institute, Stockholm, Sweden.
- SS-EN ISO 17892-12 2018. *Geotechnical investigation and testing - Laboratory testing of soil* - Part 12: Determination of liquid and plastic limits. ISO, the International Organization for Standardization.
- Tompai, Z. 2008. Conversion between static and dynamic load bearing capacity moduli and introduction of dynamic target values. *Periodica Polytechnica, Civil Engineering,* Hungary, 52–2: pp. 97-102.

7 ACKNOWLEDGEMENT

Field and numerical study of transverse crack in JPCP with misalignment and non-greased dowels

M. Lazarowicz & P. Jaskula
Gdansk University of Technology, Faculty of Civil and Environmental Engineering, Gdansk, Poland

L. Khazanovich
University of Pittsburgh, Anthony Gill Chair Professor, Department of Civil and Environmental Engineering USA

ABSTRACT: This study investigates the effects of dowel lubrication and positioning on the performance of Jointed Plain Concrete Pavements (JPCPs) through field evaluations, laboratory experiments, and numerical modeling. Field observations of a JPCP section revealed transverse cracking near a bridge transition zone, attributed to the absence of dowel lubrication and misalignment. Laboratory pull-out tests demonstrated that unlubricated dowels exhibited significantly higher friction, restricting movement within the joint, which inhibited natural slab expansion and contraction. In contrast, lubricated dowels allowed smoother movement, reducing pull-out forces and enhancing joint performance. The findings emphasize that dowel lubrication has a more substantial impact on joint functionality than misalignment, especially during the early stages of pavement life when concrete is less stiff and more prone to cracking.

1 INTRODUCTION

1.1 Background

A characteristic feature of Jointed Plain Concrete Pavements (JPCPs) is the division of the pavement into slabs by transverse and longitudinal contraction joints. This design minimizes the formation of randomly located shrinkage cracks by creating a series of interconnected slabs. However, jointed concrete pavements are often susceptible to distresses that either originate at the joints or result from improper joint design, construction, or maintenance. Common joint-related distresses include faulting, pumping, spalling (caused by various mechanisms), corner breaks, blowups, and mid-panel cracking, which can occur due to excessive joint spacing or inadequate joint construction (FHWA 2019).

The use of dowels enhances load transfer capacity between the loaded and unloaded slabs during vehicle traffic while allowing horizontal slab movement due to daily and seasonal variations in temperature and moisture conditions (Huang 2004).

To minimize the risk of premature deterioration during the pavement's service life, several measures should be implemented from the construction stage. These include making contraction cuts promptly and ensuring that dowels are correctly positioned and properly lubricated before installation (Lazarowicz et al. 2023). Improper joint construction can lead to premature pavement failures and significantly compromise long-term pavement performance.

1.2 Objective and Scope

This study aims to examine the effects of dowel lubrication and positioning within contraction joints on the performance of concrete pavements, as observed during field evaluations.

2 MATERIALS

2.1 Field Observations

The evaluated JPCP was constructed using slip-form paving technology in March 2019. It consists of two lanes and an emergency lane. Transverse joints were spaced at 5-meter intervals, while the longitudinal spacings were 3.9, 3.9, and 2.2 meters. Polymer-coated steel dowels $\phi = 0.025$ m were embedded in the transverse joints at 0.25 m intervals, and steel tie bars $\phi = 0.02$ m were placed in the longitudinal joints at 1.0 m intervals. The dowels were not lubricated before installation using the dowel bar inserter.

After several months, transverse cracking was observed across the entire width of the road, splitting the 5-meter-long concrete slabs into fragments approximately 1.5 and 3.5 meters in length. At the time of observation (June 7, 2019), the crack measured 0.5 to 0.8 mm wide and ran parallel to the contraction joints in which the dowels were embedded. The cracked slab was the transition slab where the JPCP connects to the asphalt pavement, located near the access to the bridge. Due to the design of the technological connection between the two pavement types,

the concrete slab exhibited varying thickness in the region where the crack occurred.

During the field investigations, local excavations were conducted to assess the extent of the cracks and the condition of the contraction joints. Diagrams illustrating this case are shown in Figures 1 and 2.
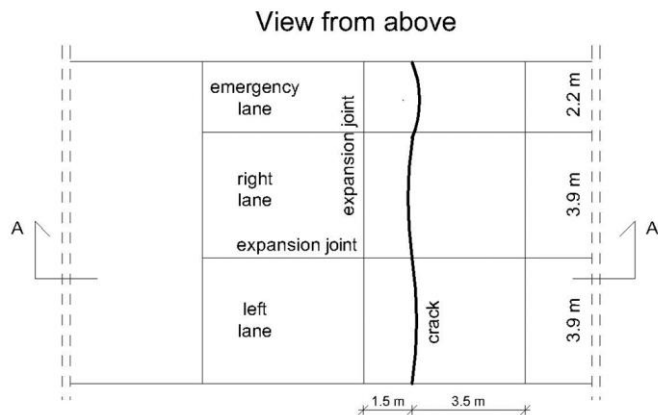
Fig. 1. Diagram of the analysed pavement.
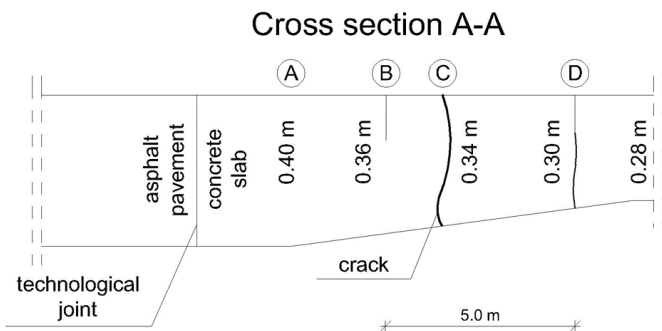
Fig. 2. Cross-section of the analysed pavement.

The excavation revealed that while joint D was properly formed, propagating through the entire thickness of the concrete slab, joint B did not propagate as intended. Additionally, a random crack, labeled as crack C, was found to have propagated through the full thickness of the slab.

The positions of the dowels in joints B and D were examined using the MIT-Scan2-BT device. A statistical summary of the results is presented in Tables 1 and 2.

Tab. 1. Positions of the dowels at point B.

Parameter	Min. value [mm]	Max. value [mm]	Mean value [mm]
Vertical translation	-2	100	42
Transverse translation	177	283	251
Longitudinal translation	-45	0	-13
Horizontal skew	-18	16	3
Vertical tilt	-11	12	2

Tab. 2. Positions of the dowels at point D.

Parameter	Min. value [mm]	Max. value [mm]	Mean value [mm]
Vertical translation	-23	32	-1
Transverse translation	221	273	250
Longitudinal translation	-26	48	-4
Horizontal skew	-24	9	-7
Vertical tilt	-19	17	2

2.2 Documentation analysis

Based on the analysis of the execution documentation, the layout of the pavement structure in the area of the transverse cracking (point C) was determined. Due to the variable thickness of the concrete slab, two sections within the contraction joints, representing the extremities of the cracked slab, were identified. Details of both sections are provided in Table 3.

Tab. 3. Road surface properties at points B and D.

Material	Young's Modulus [MPa]	Poisson ratio	Thickness [cm]	
			Point B	Point D
Cement Concrete C 35/45	35 000	0.16	36	30
Geotextile	-	-	0.2	
Cement Bound Base C 8/10	3 000	0.3	10	16
Cement Bound Base C 5/6	2 000	0.3	15	
Cement Bound Subbase C 1.5/2	200	0.3	20	
Subgrade G1	80	0.35	30	

The analyzed pavement section was constructed on March 20, 2019. Archived weather reports from the nearest weather station to the assessed section were used to compile Table 4, which summarizes the daily minimum and maximum air temperatures for one week following the pavement's construction. Using this data, the positive and negative temperature gradients in the concrete slab during this period were calculated, as described by (Szydło et al. 2013).

Tab. 4. Air temperatures and temperature gradients in the concrete slab during the first week after construction of the test section.

Date	Min. Air Temp. [°C]	Max. Air Temp. [°C]	Negative concrete gradient [°C]	Positive concrete gradient [°C]
20.03.2019	-6,0	9,0	-5,1	11,2
21.03.2019	4,0	11,2	-4,5	7,9
22.03.2019	-2,0	14,0	-5,1	11,6
23.03.2019	-5,0	14,1	-5,3	12,9
24.03.2019	1,0	12,0	-4,8	9,5
25.03.2019	-2,0	9,0	-4,8	9,5
26.03.2019	-1,0	7,0	-4,6	8,2

3 LABORATORY TESTS

3.1 Specimen preparation

The pull-out test of the dowels was conducted on short samples, defined as those with an adhesion length between three and five diameters of the dowel. This configuration allows for necessary simplifications, ensuring linear strain changes along the dowel's axis during measurement. Additionally, adhesion stresses remain constant, corresponding to the smooth surface of the dowels (Burdziński et al., 2024).

The tests were performed on polyethylene-coated steel dowels produced by the same manufacturer as those used in the pavement section under study. Two sets of samples were prepared: dowels lubricated with SAE 30 oil, as recommended by (Snyder 2011), and unlubricated dowels. Each set consisted of three samples.

The dowels tested were 500 mm long and embedded in cubic concrete specimens measuring 150 × 150 × 150 mm. The contact length between the dowel and the concrete was set to four times the dowel diameter (100 mm). The remaining length of the dowel was isolated from the concrete using a protective sponge, which was removed after the concrete hardened.

The concrete used for the specimens was class C35/45, meeting the requirements for concrete slabs subjected to the heaviest traffic loads, as specified in national guidelines. No spiral transverse reinforcement was included in the specimens to avoid additional restraint on the dowels and reduce the likelihood of concrete splitting.

The objective of the test was to replicate, as closely as possible, the working conditions of dowels in concrete slabs, where spiral reinforcement is typically absent.

3.2 Test procedure

The test procedure followed the provisions of ISO 1040-1, Clause 7, and the methodology described by (Burdziński et al. 2024). After the concrete had cured for at least 28 days, the specimen was placed in the testing machine with the free end of the dowel fixed securely. The concrete cube was positioned in a specially designed steel cage, which allowed a vertical force to be applied, causing upward movement. The displacement rate of the specimen was set at 1 mm/min, as recommended by (Khazanovich et al. 2009). A schematic of the test setup is shown in Fig. 3.
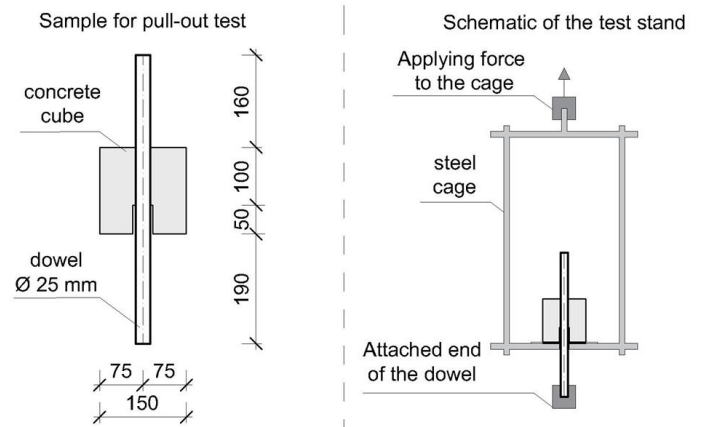
Fig. 3. View of the sample and schematic of the pull-out test apparatus.

3.3 Results of pull-out tests

The maximum pull-out forces for the dowels from the concrete specimens are shown in Fig. 4. The average force required to pull out the lubricated dowels was 8.9 kN, approximately half the pulling force of the unlubricated dowels (17.5 kN). These results align well with findings from other studies; for instance, (Saxena et al. 2009) reported that the absence of lubrication can increase pull-out forces by more than 2.5 times. This indicates that high friction between the concrete slab and the unlubricated dowels restricts their free movement within the joint, hindering the natural expansion and contraction of the concrete slabs.
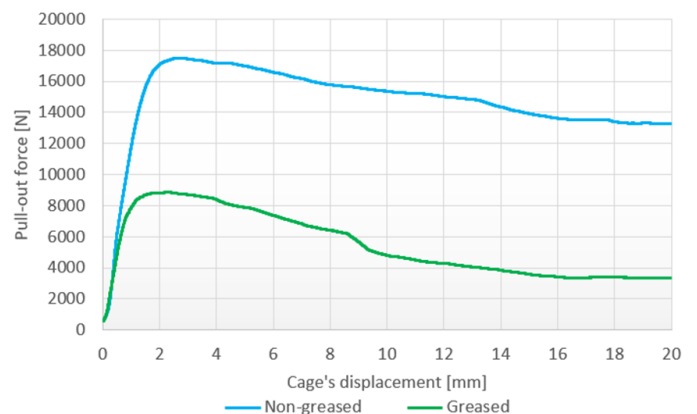
Fig. 4. Pull-out forces of lubricated and unlubricated dowels in the pull-out test.

4 DISCUSSION

While dowel misalignment has traditionally been associated with joint lockup and related distresses, this study, as well as the United States National Cooperative Research Program 10-69 study (Khazanovich et al. 2009), demonstrates that dowel-concrete friction primarily influenced by the presence or absence of grease might have a more significant detrimental effect on joint performance than dowel misalignment. Ungreased dowels experience much higher friction with the surrounding concrete,

leading to a substantial increase in the force required to pull them out. In contrast, dowel misalignment led to only a marginal increase in pull-out force and often resulted in a decrease. These findings are supported by other laboratory studies, which have often been misinterpreted (Prabhu 2007; Al-Humeidawi and Mandal 2018). Although previous studies observed a significant increase in pull-out forces due to dowel misalignment, they simulated unrealistically high joint openings. For smaller, more realistic joint openings, no significant increase in pull-out forces was observed.

The results of finite element modeling reported by (Saxena et al. 2009) also showed that high friction between ungreased dowels and surrounding concrete generates significantly higher stresses in the concrete. These stresses, primarily tensile, concentrate near the dowel and can easily exceed the concrete's tensile strength, making it susceptible to cracking and spalling, which compromises the pavement's structural integrity and leads to premature deterioration.

It should be noted, however, that previous experimental and laboratory studies primarily investigated the effect of dowel greasing and misalignment on relatively mature concrete pavements, i.e., after the concrete has reached substantial strength and stiffness. The effect of these factors may be even more pronounced immediately after concrete placement. At early ages, when concrete stiffness is low, ungreased dowels may provide significant reinforcement against crack formation, which would increase the effective slab length and contribute to random cracking in the slab. This, in combination with the slow rate of concrete strength gain due to cold ambient temperatures, a stiff foundation, and high friction with the base layer, could cause premature cracking.

5 SUMMARY

This study highlights the critical role of dowel lubrication and positioning in the performance of Jointed Plain Concrete Pavements (JPCPs). The findings demonstrate that unlubricated dowels experience significantly higher friction with the surrounding concrete, leading to increased pull-out forces and restricting the dowel's movement within the joint. This impedes the natural expansion and contraction of the concrete slabs, potentially contributing to premature pavement distress. In contrast, lubricated dowels reduce friction and allow for greater dowel mobility, improving long-term joint performance. The results align with previous research, emphasizing that dowel lubrication has a more significant impact on joint function than dowel misalignment.

The field and laboratory tests also revealed that dowel misalignment, while traditionally associated with joint lockup and related distresses, has a rela-

tively minor effect on pull-out forces compared to the impact of lubrication. Additionally, the study suggests that the effects of dowel lubrication and misalignment may be more pronounced immediately after concrete placement, when the slab is less stiff and more susceptible to cracking. To enhance the durability and performance of JPCPs, it is essential to ensure proper dowel lubrication and alignment during construction, and to implement regular inspection and maintenance practices.

6 REFERENCES

Al-Humeidawi, B. H., & Mandal, P. (2018). Experimental investigation on the combined effect of dowel misalignment and cyclic wheel loading on dowel bar performance in JPCP. *Engineering Structures*, *174*, 256-266.

Burdzinski, M., Niedostatkiewicz, M. 2024, Experimental analysis of the effect of bar anchorage length on bond behavior in pull-out test, *Inżynieria i Budownictwo*, 3-4/2024, 115-120

Federal Highway Administration (FHWA). "Concrete Pavement Joints," *FHWA Technical Advisory 5040.30. Federal Highway Administration*, Washington, DC, 2019

Huang Y. H. 2004, *Pavement analysis and design*, Upper Saddle River, Pearson Prentice Hall.

Khazanovich, L., Hoegh, K., Snyder, M. B. 2009. *NCHRP Report 637: Guidelines for Dowel Alignment in Concrete Pavements*, Washington, Transportation Research Board.

Lazarowicz, M., Krzeminski, J., Jaskula, P. 2023, Evaluation of the impact of selected material and technological parameters of dowel bars on the behavior of Portland Cement Concrete pavement, *Inżynieria i Budownictwo*, 11-12/2023, 594-598.

Prabhu, M., Varma, A. H., & Buch, N. (2007). Experimental and analytical investigations of mechanistic effects of dowel misalignment in jointed concrete pavements. *Transportation research record*, *2037*(1), 12-29.

Saxena, P., Hoegh, K., Khazanovich, L., & Gotlif, A. (2009). Laboratory and finite element evaluation of joint lockup. *Transportation research record*, *2095*(1), 34-42.

Snyder, M. B. 2011. *Guide to dowel load transfer systems for jointed concrete roadway pavements*, Technical Report, Ames, Institute for Transportation Iowa State University.

Szydlo, A., Mackiewicz, P., Wardega, R., Krawczyk, B. 2013, Aktualizacja katalogu typowych konstrukcji nawierzchni sztywnych Etap III, Technical Report, Wroclaw, Wroclaw University of Technology and Science

Asphalt pavement compaction evaluation by Dielectric Profiling System

H.B. Muslim & S.W. Haider
Michigan State University, USA

F. Kaseer & E. Akerly
Michigan Department of Transportation, USA

ABSTRACT: The compaction quality achieved during construction significantly affects the performance of asphalt pavements and its longitudinal joints. Traditional quality assessment procedures rely primarily on pavement cores; coring is a surface-destructive, time-consuming, and costly process. More importantly, it provides limited coverage. Dielectric Profiling System (DPS) provides continuous compaction coverage and accurately predict as-constructed air voids non-destructively. This study highlights the benefits of DPS adoption for compaction assessment. DPS's can highlight low-density areas within a pavement lane both longitudinally and laterally. Such in-depth analysis enable highway agencies in accurately estimating pavement service lives. It can also enable optimization of maintenance needs focused on locations identified with compaction issues within a pavement lane. Using DPS for compaction quality assessment would encourage utilization of high-quality construction practice resultantly achieving durable and high performing asphalt pavements without risking overpayments for substandard quality.

1 INTRODUCTION

As-constructed air void content (or density) of the asphalt layer is a key indicator of the long-term performance of new and resurfaced flexible pavements. The impact of the achieved compaction levels during construction on asphalt mix performance has been researched since the 1960's (Goode and Owings, 1961). Previous studies have shown that a 1% decrease in as-constructed air voids is associated with an 8 to 44% improvement in fatigue performance and a 7 to 66% increase in rutting resistance of the asphalt layer (Aschenbrener et al., 2018). Every 1% increase in air void content of the compacted asphalt mat beyond 7% is estimated to reduce the pavement's service life by 10% (Linden et al., 1989). Thus, compaction is the most important construction-related factor directly related to achieved air voids and can enhance the durability of asphalt pavements (Hughes, 1989).

State highway agencies (SHAs) traditionally assess construction quality by determining the achieved compaction using pavement cores extracted in the field. However, this coring process is surface-destructive, labor-intensive, and costly. Using density gauges (nuclear and non-nuclear) provides a non-destructive way of assessing the achieved density. However, both cores and density gauges provide limited coverage. Either of these methods involves random sampling, increasing the risk of missing areas with compaction issues or reporting density from non-representative areas.

Density profiling system (DPS), a ground-penetrating radar (GPR) based device, has recently gained popularity due to its ability to assess asphalt compaction non-destructively during construction. DPS measures its dielectric values when rolled over a freshly laid asphalt layer, which can be directly related to as-constructed air voids (density). As opposed to the limited coverage of the traditional compaction assessment methods, DPS provides continuous dielectric profiles recording a value every 6 inches. Thus, it provides the equivalent of about 100,000 cores per mile compared to the spot tests (core or density gauges), aiding better monitoring and evaluation of as-constructed pavement density (Hoegh et al., 2020).

This paper demonstrates the benefits of using the DPS for pavement compaction assessment during the construction of asphalt pavements. It highlights the importance of the continuous coverage provided by the DPS and its possible usage in identifying critical locations for predicting pavement service lives and future maintenance requirements.

2 DATA SYNTHESIS

This study uses DPS dielectric data collected from four pavement projects constructed in Michigan be-

tween 2022 and 2023. The study used a PaveScan rolling density meter (RDM) v2.0 developed by Geophysical Survey Systems Inc. (GSSI) that used three GPR sensors mounted on a wheeled cart. The cart was strolled along 1000 ft sections at each project, measuring three dielectric profiles simultaneously with varying offsets from the centerline longitudinal joint. Testing at each pavement section typically involved three DPS passes measuring at least nine dielectric profiles along the width of the pavement lane on the surface asphalt layers. Table 1 shows the asphalt layer thicknesses and the mix details.

Table 1. Surface asphalt layer thickness and mix details.

Project	Surface layer thickness (in) & NMAS (mm)	Surface mix G_{mm}	Surface mix binder type & content (%)
US-23	1.5, 9.5 (SMA)	2.426	PG70-28P, 6.77
M-89	1.5, 9.5	2.455	PG64-28, 6.46
I-69	1.5, 9.5	2.505	PG64-28, 5.99
M-61	2.0, 9.5	2.477	PG64-28, 5.94

Note: NMAS= Nominal maximum aggregate size, P=Polymer modified, SMA=Stone Matrix Asphalt.

3 COMPACTION ASSESSMENT

3.1 DPS calibration

The recorded dielectric values require calibrating a model for converting into air voids. This study used the core-free calibration method developed by Hoegh et al., which requires compacting gyratory pucks in the laboratory (Hoegh et al., 2019). Using an empirical model from a recent study (Eqn. 1), the dielectric-air void relationship was calibrated for each project's asphalt mix (Haider et al., 2023). Figure 1 shows the calibrated relationships for US-23 and M-61. The figures display the 95% confidence (CB) and prediction bands (PB) for the model (Av-P) and measured puck air voids (Av-O). It also shows measured air voids of the pavement cores extracted during testing for validation. The horizontal error bars display the allowable ±0.08 dielectric measurement variability per AASHTO PP98-19 (AASHTO, 2019). The vertical error bars indicate a 1% air void measurement tolerance per MDOT quality assurance procedures (MDOT, 2020). The figure shows that the coreless calibration predicts air voids with reasonable accuracy as represented by the core data.

$$AV = \frac{0.20}{1 + \left(\frac{e}{c}\right)^b} + \frac{0.0008}{(e-1)} \qquad (1)$$

where AV = air voids (%); ε = asphalt dielectric value; and b,c = regression coefficients.
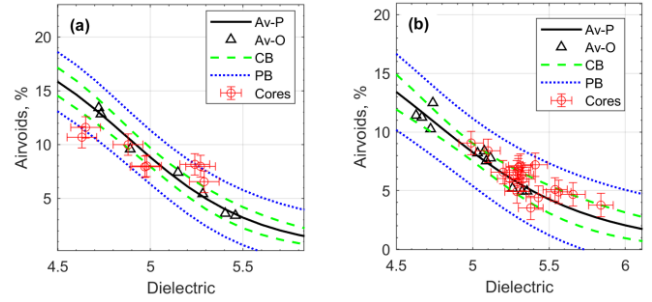
Figure 1. The calibrated dielectric-air voids relationship and its core validation is (a) US-23 SMA and (b) M-61.

3.2 As-constructed compaction evaluation

Figure 2 compares dielectric values at various offsets from the longitudinal joint on US-23. DPS measurements covered the full 1000 ft lane's width on the unconfined side and a shorter segment (142 m) on the confined side. Dielectric values on the unconfined side are mostly 5.6 or lower, with many below 4.8 at a 0.5 ft offset, indicating lower compaction. Conversely, the confined side shows values mostly between 4.8 and 5.6. This highlights the impact of joint type and construction conditions on compaction, with unconfined joints having lower values.

Examining the asphalt mat's dielectric data (excluding the two outer offsets) along the pavement lane reveals significantly lower dielectric values across the width in the final 400 ft section (right side of the plot). This suggests that the latter portion of the pavement was not compacted as consistently as the first half. This compaction difference is translated into significant air void differences, as illustrated in Figure 3. The mat's air voids range between 8% to over 12%, while the unconfined joint (i.e., at 0.5 ft offset) has over 12% air voids for the majority of the sections' length. The air voids are below 8% on the confined side of the joint, with limited data showing void content between 8% and 12%.

Figures 4 and 5 display box plots of the dielectric and predicted air voids data for US-23. These figures demonstrate that the paving conditions and type of joint affect the achieved compaction, as shown in Figures 2 and 3. While the dielectric values next to the pavement edges are lower for the unconfined side of the joint, they are relatively higher on the confined side. Consequently, the confined joint side has lower air voids and better compaction than the unconfined side. For a joint to be acceptable, its air voids must be within 2% of the mat's density (Kandhal and Mallick, 1996). This corresponds to a dielectric difference of about 0.14 (mat minus joint) based on the US-23 project-specific calibration model, given that 8% air voids in the mat are considered acceptable, yielding a dielectric of 5.057. Hence, 10% air voids are acceptable in the joint, corresponding to a 4.921 dielectric value. However,

dielectric values for the unconfined joint show a significantly greater difference than the 0.14 threshold compared to measurements farther from the joint.

Lateral variations in pavement compaction within the lane are evident from the mat's dielectric values. Although these values are consistently higher than those at the unconfined joint, the measurements at 8.5 ft and 12.5 ft offsets exceed the acceptable dielectric threshold of 5.057 for 8% air voids. Such detailed compaction analysis is crucial for identifying critical areas of lower density that may affect the pavement's long-term performance and require focused periodic maintenance.

Figures 6 and 7 show the boxplots for predicted air void values for the M-89 and I-69 projects. Similar to the compaction on US-23, the confined joint on M-89 shows air voids comparable to the asphalt mat. For this project, a 5.141 dielectric value corresponds to 8% air voids; 4.956 equals 10% air voids. Figure 6 indicates that air voids remain below 8% throughout the lane across all offsets. The compaction variability reveals that, aside from the outer shoulder joint (14.5 ft offset), most air void levels seen in Figure 6 are between 5% and 7%.
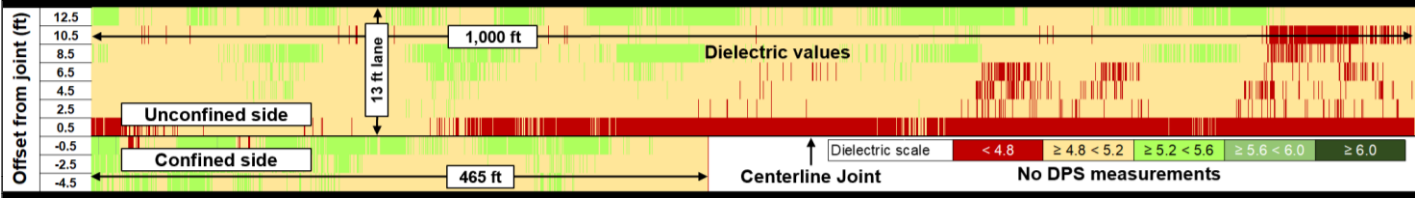
Figure 2. Recorded dielectric data heat maps at different offsets from the centerline joint on either side – US-23 SMA project
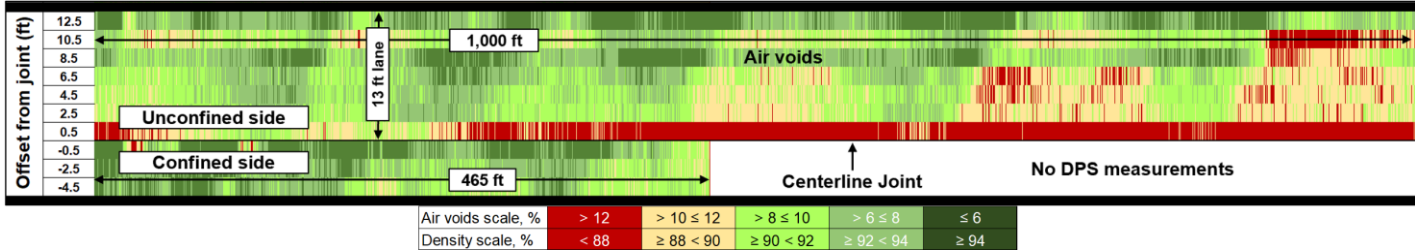
Figure 3. Predicted air void heat maps at different offsets from the centerline joint on either side – US-23 SMA project.
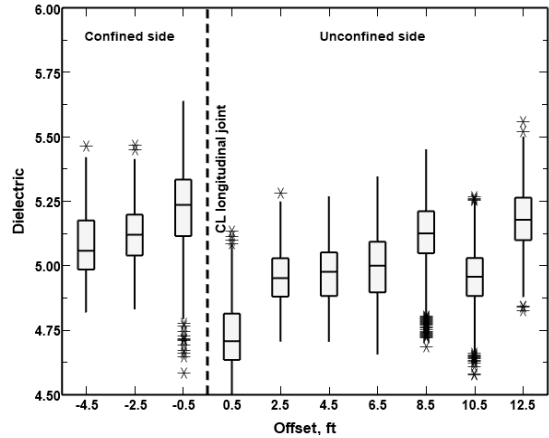
Figure 4. Box plots displaying recorded dielectric values at varying offsets on US-23.
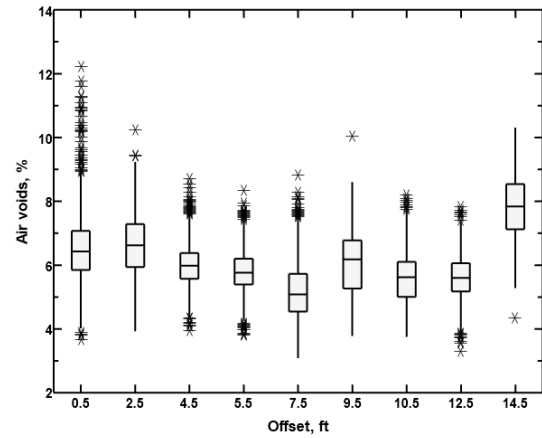
Figure 6. Box plots displaying predicted air voids at varying offsets on M-89 (confined centerline joint).
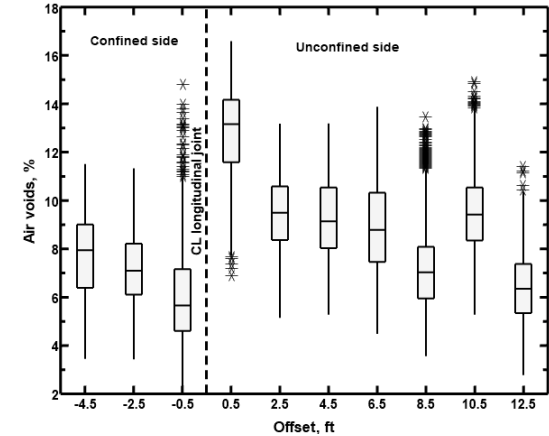
Figure 5. Box plots displaying predicted air voids at varying offsets on US-23.
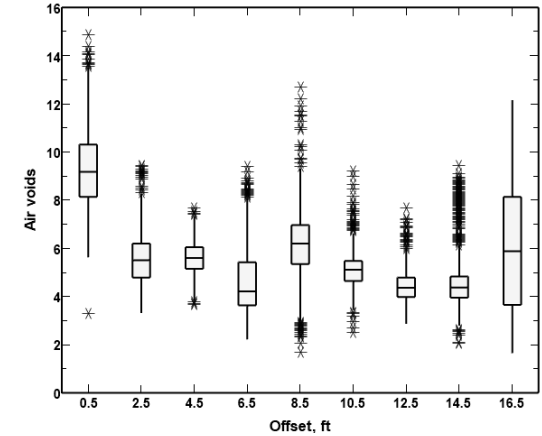
Figure 7. Box plots displaying predicted air voids at varying offsets on I-69 (Echelon-paved).

The I-69 project was constructed using the echelon paving method. Except for the dielectric values measured 0.5 ft from the shoulder joint, all the other values surpassed 5.110 (i.e., 8% air voids), indicating air voids between 4% and 8% throughout the 1000 ft lane on the I-69 project (Fig. 7). This consistency reflects the echelon paving method's effectiveness in achieving proper and consistent compaction; maintaining acceptable air void levels across the lane.
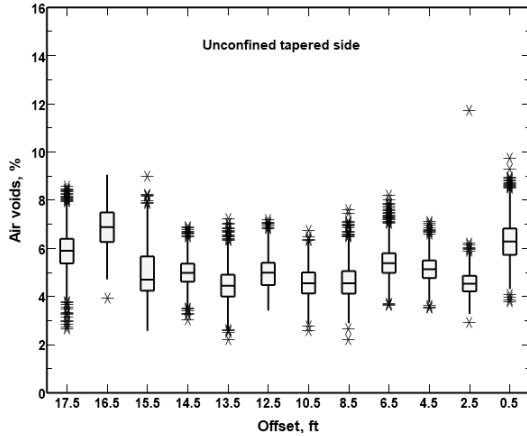
Figure 8. Box plots displaying predicted air voids at varying offsets on M-61.

Figure 8 shows the predicted air voids for the M-61 project that was constructed with a notched wedge/tapered centerline joint. For this project's asphalt mix, 8% of the air voids result from a 5.027 dielectric value, and 10% of the air voids align with a dielectric value 4.828. The tapered construction method resulted in higher compaction, reflected by elevated dielectric values. The predicted air voids consistently ranged between 4% and 6% across both lanes on either side of the joint. Figures 2 through 8 demonstrate the benefit of the DPS's continuous compaction coverage capability, allowing for extensive air voids (density) analysis, which is impossible with conventional spot-test-based methods. With such a detailed compaction analysis, one can predict future pavement performance variations. Additionally, highway agencies can identify locations with sub-par compaction levels within a pavement that may require focused preventive maintenance throughout the pavement's service life.

4 CONCLUSIONS AND RECOMMENDATIONS

Asphalt pavement and longitudinal joint quality are significantly impacted by as-constructed air voids (density) achieved in the field. Traditional compaction quality assurance processes primarily rely on cores that offer limited spatial coverage, risking overpayment for sub-par quality in the field. The DPS is a better alternative to the spot-test-based compaction assessment procedures since it provides continuous, comprehensive compaction coverage and accurately estimates as-compacted air voids.

This study highlighted the benefits of DPS's usage for compaction quality evaluation. These are as follows:
- DPS provides thorough compaction coverage and can highlight under-compacted and low-density areas across the pavement lane longitudinally and laterally.
- Such in-depth compaction assessment enables SHAs to estimate pavement service lives accurately.
- It can also aid SHA in optimizing maintenance efforts by focusing on identified locations with compaction issues.
- Given the critical role of compaction quality in asphalt pavement performance, quality assurance methods should transition from current spot-test-based approaches to DPS.
- Adopting DPS will promote high-quality construction practices, enabling the achievement of durable asphalt pavement with longer-lasting performance without risking overpayments for substandard quality.

5 REFERENCES

AASHTO 2019. Asphalt Surface Dielectric Profiling System Using Ground Penetrating Radar, PP98-19. Washington, D.C.: AASHTO.

Aschenbrener, T., Brown, E. R., Tran, N. & Blankenship, P. B. 2018. The FHWA's demonstration project for enhanced durability of asphalt pavements through increased in-place pavement density. *Transportation Research Record,* 2672, 57-67.

Goode, J. F. & Owings, E. P. 1961. A laboratory-field study of hot asphaltic concrete wearing course mixtures. *Public roads.*

Haider, S. W., Muslim, H. B., Khazanovich, L., Kutay, M. E. & Cetin, B. 2023. BMP For Issues with Asphalt Centerline Joint and Intelligent Compaction for Local Agencies. Minnesota. Department of Transportation. Office of Research & Innovation.

Hoegh, K., Roberts, R., Dai, S. & Zegeye Teshale, E. 2019. Toward core-free pavement compaction evaluation: An innovative method relating asphalt permittivity to density. *Geosciences,* 9, 280.

Hoegh, K., Steiner, T., Zegeye Teshale, E. & Dai, S. 2020. Minnesota Department of Transportation case studies for coreless asphalt pavement compaction assessment. *Transportation Research Record,* 2674, 291-301.

Hughes, C. S. 1989. National Cooperative Highway Research Program Synthesis of Highway Practice 152: Compaction of Asphalt Pavement. Washington, D.C.

Kandhal, P. S. & Mallick, R. B. 1996. Study of longitudinal-joint construction techniques in hot-mix asphalt pavements. *Transportation Research Record,* 1543, 106-112.

Linden, R. N., Mahoney, J. P. & Jackson, N. C. 1989. Effect of compaction on asphalt concrete performance. *Transportation Research Record.*

MDOT 2020. HMA Production Manual. Lansing, MI: Construction Field Services, Michigan Department of Transportation.

A VECD Model Integrating Viscoelasticity and Damage Evolution in Asphalt Concrete

V Navjot and S P Atul Narayan
Indian Institute of Technology, Madras

ABSTRACT: Viscoelastic-Continuum Damage (VECD) models are developed for asphalt concrete to describe the damage it undergoes due to repeated loading and the evolution of viscoelastic properties because of the damage. These models consider the material as a continuum and use a damage parameter that evolves based on the deformation history to capture the damage behavior. Traditional VECD models, which utilize Schapery's work potential theory and the elastic-viscoelastic correspondence principle, impose constraints on how viscoelastic properties evolve with damage. This study introduces a new VECD model that couples viscoelasticity and damage characteristics within a Helmholtz-potential-based thermodynamic framework, ensuring thermodynamic consistency and eliminating the constraints prevalent in traditional VECD models. The model captures the sudden decrease in modulus towards the end of the fatigue life of the material. It also allows for the phase angle to evolve without constraint, because of which it can increase, decrease, or remain constant with any increase in fatigue damage.

1 INTRODUCTION

In pavement design, the fatigue of asphalt concrete is a critical factor in the design process. However, the models currently used to predict pavement fatigue life are predominantly regression-based (AASHTO-321, 2017; Austroads, 2016; Wang et al. 2016). There is a growing need to replace these models with mechanistic models that can provide more accurate and reliable predictions. One of the mechanistic models that has been developed for asphalt concrete considers the material to be a continuum and characterizes the extent of damage with the help of a damage parameter. These models are called Viscoelastic-Continuum Damage (VECD) models. In these VECD models, the relationship between the stress and strain histories is assumed to depend on a damage parameter, and the damage parameter, in turn, is prescribed an evolution equation depending on the deformation history of the material (Daniel & Kim, 2002; Kutay & Lanotte, 2018; Lee et al. 2000; Lee & Kim, 1998; Park et al. 1996; Underwood et al. 2006).

Most VECD models that are developed for asphalt concrete are based on Schapery's work potential model (Schapery, 1990) along with Schapery's elastic-viscoelastic correspondence principle (Schapery, 1984). The VECD models based on Schapery's work use pseudo strain to separate the viscoelastic part of the response and the damage part of the response. This constrains the storage modulus and the loss modulus to evolve in a coupled manner. Furthermore, for VECD models developed through this approach, the phase angle exhibited by damaged material when subjected to small amplitude oscillations is the same as the phase angle exhibited by an undamaged material.

However, experimental observations have shown that the phase angle can decrease with the number of repetitions (Abhijith & Narayan, 2022). This suggests that the phase angle (at small amplitude oscillations) also evolves with damage (Abhijith & Narayan, 2020).

In a VECD model following Schapery's framework, a quantity known as pseudo-strain is defined based on the anticipated viscoelastic response of the material:

$$\varepsilon_r(t) := \frac{\sigma_{ve}(t)}{E_r}, \tag{1}$$

where $\sigma_{ve}(t)$ is the stress response predicted by a viscoelastic model, and E_r is a reference modulus. The constitutive equations are subsequently derived from the work potential, which is expressed as a function of this pseudo-strain and a damage parameter α:

$$W = \widehat{W}(\varepsilon_r, \alpha). \tag{2}$$

The constitutive equations are then derived as

$$\sigma = \frac{\partial W}{\partial \varepsilon_r} \tag{3a}$$

$$\frac{d\alpha}{dt} = K\left(-\frac{\partial W}{\partial \alpha}\right)^n, \tag{3b}$$

where K and n are model parameters. The first equation defines the stress-strain relationship depending on the damage parameter. The second describes the evolution of the damage parameter with the deformation of the material. However, the fundamental framework of these models includes the use of pseudo-strain to separate the viscoelasticity of the material from the damage mechanics.

There is a need for the development of a model that allows for all aspects of viscoelasticity to evolve with damage and for the apparent storage modulus and apparent loss modulus to evolve independently of each other. This study proposes developing viscoelastic damage models for asphalt concrete based on a Helmholtz-potential-based thermodynamic framework. Unlike traditional VECD models based on Schapery's work potential model, the model developed in this study does not constrain the evolution of the apparent loss modulus with the evolution of the apparent storage modulus.

2 MODEL DEVELOPMENT

In this study, a viscoelastic continuum damage model is developed within a Helmholtz-potential-based thermodynamic framework of Rajaopal & Srinivasa, 2000, starting with the reduced dissipation equation for isothermal conditions:

$$\sigma\dot{\varepsilon} - \dot{\psi} = \xi \geq 0, \tag{4}$$

where σ is the one-dimensional stress and ε is the one-dimensional linearized strain. The method of developing constitutive relations involves assuming specific functional forms for the Helmholtz potential and the rate of dissipation and then determining constitutive relations that satisfy the reduced dissipation equation. The model is developed for asphalt concrete in a similar manner to that of Rajagopal et al. 2007 by assuming the Helmholtz potential and the rate of dissipation to be functions of the strain history of the material, along with a damage parameter α and its material time derivative in the following way:

$$\psi = \int_{-\infty}^{t} E(t-s,\alpha)[\varepsilon(t)-\varepsilon(s)]\dot{\varepsilon}(s)ds, \tag{5}$$

$$\xi = \mu[(\dot{\alpha})^2]^{\frac{p+1}{2}}$$
$$- \int_{-\infty}^{t} \frac{\partial E}{\partial t}(t-s,\alpha)[\varepsilon(t)-\varepsilon(s)]\dot{\varepsilon}(s)ds. \tag{6}$$

Substituting the form for $\dot{\psi}$ and ξ in the reduced dissipation equation, it becomes

$$\sigma\dot{\varepsilon}(t) - \int_{-\infty}^{t} \frac{\partial E}{\partial t}(t-s,\alpha)[\varepsilon(t)-\varepsilon(s)]\dot{\varepsilon}(s)ds$$
$$- \left[\int_{-\infty}^{t} \frac{\partial E}{\partial \alpha}(t-s,\alpha)[\varepsilon(t)-\varepsilon(s)]\dot{\varepsilon}(s)ds\right]\dot{\alpha}$$

$$- \int_{-\infty}^{t} E(t-s,\alpha)\dot{\varepsilon}(t)\dot{\varepsilon}(s)ds = \mu[(\dot{\alpha})^2]^{\frac{p+1}{2}}$$

$$- \int_{-\infty}^{t} \frac{\partial E}{\partial t}(t-s,\alpha)[\varepsilon(t)-\varepsilon(s)]\dot{\varepsilon}(s)ds \geq 0. \tag{7}$$

By rearranging the terms, the final form of the reduced dissipation equation can be written as

$$\left(\sigma - \int_{-\infty}^{t} E(t-s,\alpha)\dot{\varepsilon}(s)ds\right)\dot{\varepsilon}(t)$$

$$- \left(\int_{-\infty}^{t} \frac{\partial E}{\partial \alpha}(t-s,\alpha)[\varepsilon(t)-\varepsilon(s)]\dot{\varepsilon}(s)ds\right)\dot{\alpha}$$

$$= \mu(\dot{\alpha})^{p+1} \geq 0. \tag{8}$$

Since the above inequality needs to hold for all values of $\dot{\varepsilon}(t)$, it is necessary that:

$$\sigma = \int_{-\infty}^{t} E(t-s,\alpha)\dot{\varepsilon}(s)ds. \tag{9}$$

The inequality (8) will be satisfied if

$$\mu(\dot{\alpha})^p = - \int_{-\infty}^{t} \frac{\partial E}{\partial \alpha}(t-s,\alpha)[\varepsilon(t)-\varepsilon(s)]\dot{\varepsilon}(s)ds. \tag{10}$$

Equation (9) is the stress-strain relation, and the evolution equation for α is given by

$$\dot{\alpha} = \left[-\frac{1}{\mu} \int_{-\infty}^{t} \frac{\partial E}{\partial \alpha}(t-s,\alpha)[\varepsilon(t)-\varepsilon(s)]\dot{\varepsilon}(s)ds\right]^{\frac{1}{p}}. \tag{11}$$

Equation (9) together with equation (11), form the constitutive equations for the material. To ensure that the damage parameter α remains real, $\frac{\partial E}{\partial t}(t,\alpha)$ must be non-positive for all values of α. That is, $E(t,\alpha)$ should be decreasing with respect to α. The functional form of $E(t,\alpha)$ with respect to t should be such that it is non-negative, its first derivative with respect to time is non-positive, and its second derivative is again non-negative for all t. Similarly, the functional form of $E(t,\alpha)$ in terms of α should be such that $\frac{\partial E}{\partial \alpha}$ is non-positive, and its derivative with respect to time is non-negative for all times and α. Also, the evolution equation for the damage parameter requires that the parameter $p > 0$. The model developed in this study couples the evolution of the damage parameter to the viscoelastic characteristics. When the model is subjected to repeated loading, the damage parameter changes monotonically.
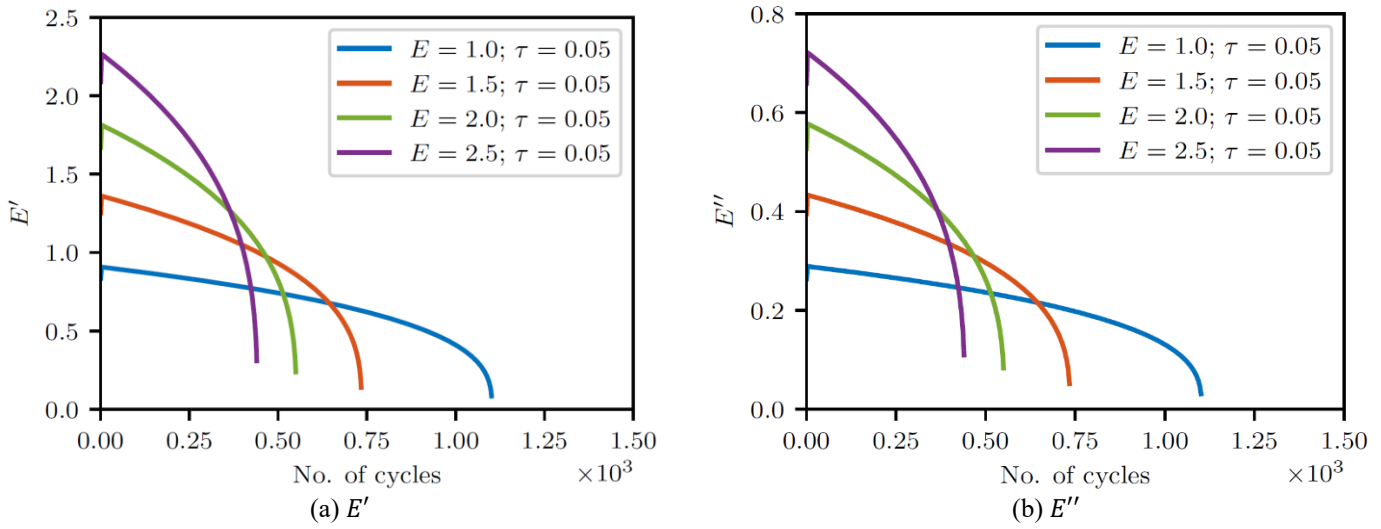
Figure 1. Variation of E' and E'' with cycles for different values of E
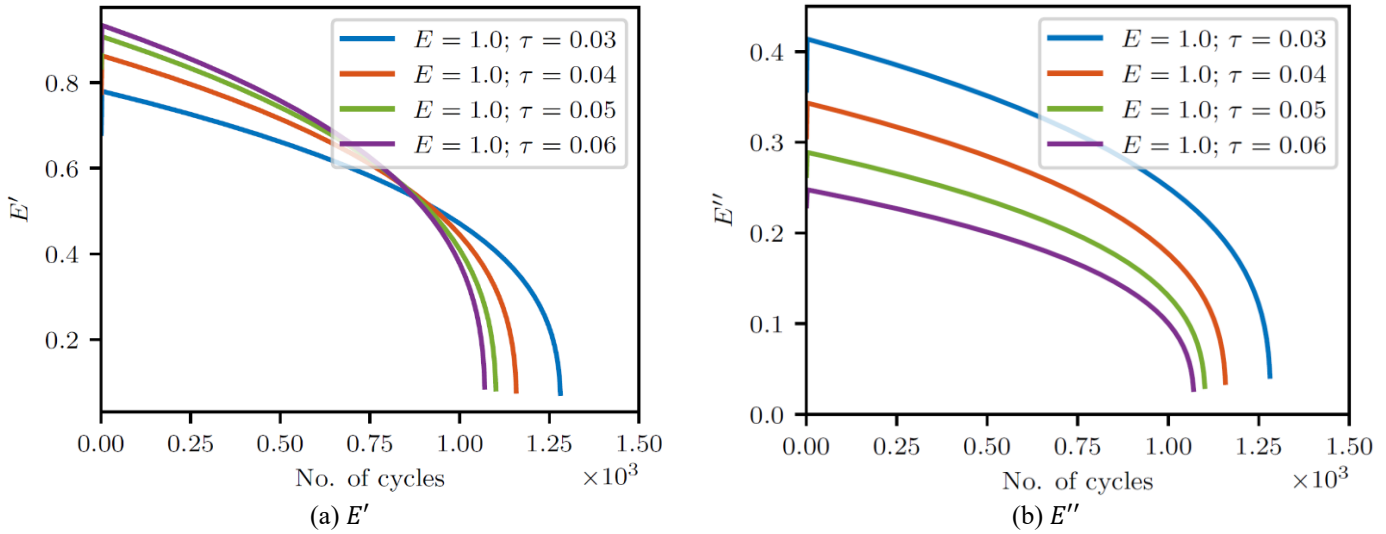
Figure 2. Variation of E' and E'' with cycles for different values of τ

3 COUPLING OF VISCOELASTICITY AND DAMAGE EVOLUTION

The coupling of the damage evolution with the viscoelasticity of the model is illustrated with a simplified model by assuming a form for $E(t, \alpha)$ as

$$E(t, \alpha) = E_0(1 - \alpha)^n e^{-\left(\frac{t}{\tau(1-\alpha)^k}\right)}, \quad (12)$$

where E_0, τ, n, and k are model parameters. As α increases from 0 to 1, the terms $(1 - \alpha)^n$ decreases. Therefore, the modulus of the asphalt concrete reduces progressively as α increases from 0 to 1. Therefore, the damage parameter corresponding to a virgin material is taken to be zero, and that corresponding to a fully damaged material is one.

The coupled governing equations were solved numerically using MATLAB for repeated strain loading:

$$\varepsilon = \varepsilon_0 \sin \omega t. \quad (13)$$

From each cycle of the stress response, the in-phase component of the first harmonic was divided by the strain amplitude to get the apparent storage modulus, E'. Similarly, the out-of-phase component of the first harmonic was divided by the strain amplitude to obtain the apparent loss modulus, E''.

To demonstrate the coupling between viscoelasticity and fatigue, the viscoelastic properties, specifically the elastic modulus, E and the relaxation time, τ, were first varied, and their impact on fatigue life was analyzed. The variation in the response when the parameter E was varied while keeping the parameter τ constant is shown in Figure 1. Figure 2 shows the variation in the response with changes in the parameter τ, while E was kept constant. Changes in viscoelastic properties, E and τ, are observed to cause changes in the rate of decrease in modulus and the shape of the E' and E'' curves.

The model can also show different variations in the evolution of phase angle in repeated loading tests. With changes in the parameter, k, the phase angle can increase, decrease, or remain constant.

This is illustrated in Figure 3 through numerical simulations while varying k and keeping all the other parameters constant. When $k > 0$, the phase angle increases with the number of cycles. It decreases when $k < 0$. Such a coupling between viscoelastic properties and the damage parameter is not observed in traditional VECD models.
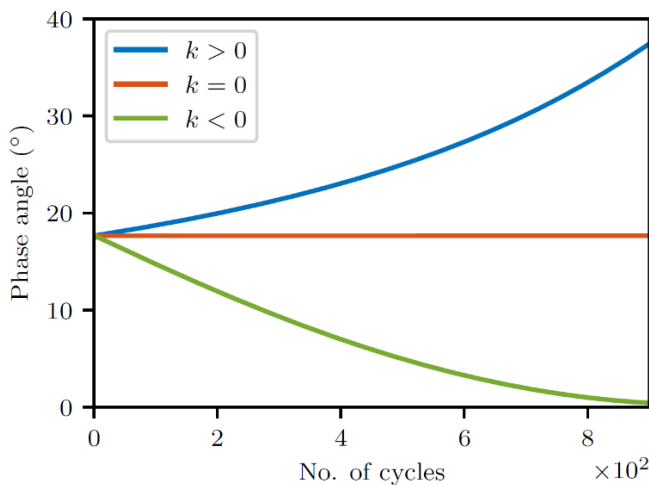
Figure 3. Influence of k on phase angle

4 CONCLUSION

This study introduces a VECD model for asphalt concrete that addresses the limitations of traditional models based on Schapery's work potential and elastic-viscoelastic correspondence principles. Traditional VECD models, which decouple viscoelasticity from damage mechanics using a pseudo-strain, impose constraints on the evolution of the viscoelastic properties during fatigue testing. This study presents a new VECD model that fully couples the material's viscoelasticity with its damage characteristics through a Helmholtz-potential-based thermodynamic framework, ensuring consistency with the laws of thermodynamics. The developed model effectively couples the evolution of the damage parameter with viscoelastic properties. This coupling illustrates how both viscoelastic properties and damage evolve together during fatigue tests, highlighting the model's ability to reflect the interconnected nature of viscoelastic behavior and damage progression.

5 REFERENCES

AASHTO, T. 321. 2017. standard method of test for determining the fatigue life of compacted asphalt mixtures subjected to repeated flexural bending. *American Association of State and Highway Transportation Officials*: Washington, DC, USA.

Abhijith, B., Atul Narayan, S. 2022. Evolution of complex modulus and higher harmonics of stress response of asphalt concrete in strain-controlled four-point beam fatigue tests. *International Journal of Pavement Engineering* 23(13), 4487–4503.

Abhijith, B., Narayan, S.A. 2020. Evolution of the modulus of asphalt concrete in four-point beam fatigue tests. *Journal of Materials in Civil Engineering* 32(10), 04020310.

Austroads.2016 Characterisation of flexural stiffness and fatigue performance of bituminous mixes.

Daniel, J.S., Kim, Y.R. 2002. Development of a simplified fatigue test and analysis procedure using a viscoelastic continuum damage model (with discussion). *Journal of the Association of Asphalt Paving Technologists* 71.

Kutay, M.E., Lanotte, M. 2018. Viscoelastic continuum damage (vecd) models for cracking problems in asphalt mixtures. *International journal of pavement engineering* 19(3), 231–242.

Lee, H.J., Daniel, J.S., Kim, Y.R. 2000. Continuum damage mechanics-based fatigue model of asphalt concrete. *Journal of Materials in Civil Engineering*12(2), 105–112.

Lee, H.J., Kim, Y.R. 1998. Viscoelastic constitutive model for asphalt concrete under cyclic loading. *Journal of engineering mechanics* 124(1), 32–40.

Park, S.W., Kim, Y.R., Schapery, R.A. 1996. A viscoelastic continuum damage model and its application to uniaxial behavior of asphalt concrete. *Mechanics of materials* 24(4), 241–255.

Rajagopal, K., Srinivasa, A., Wineman, A. 2007. On the shear and bending of a degrading polymer beam. *International Journal of Plasticity* 23(9), 1618–1636.

Rajagopal, K.R., Srinivasa, A.R. 2000. A thermodynamic framework for rate type fluid models. *Journal of Non-Newtonian Fluid Mechanics* 88(3), 207–227.

Schapery, R. 1990. A theory of mechanical behaviour of elastic media with growing damage and other changes in structure. *Journal of the Mechanics and Physics of Solids* 38(2), 215–253.

Schapery, R.A. 1984. Correspondence principles and a generalized j integral for large deformation and fracture analysis of viscoelastic media. *International journal of fracture* 25, 195–223.

Underwood, B.S., Kim, Y.R., Guddati, M., Pellinen,T., Rongzong, W., King, G., Kluttz, R., Gibson,N. 2006. Characterization and performance prediction of alf mixtures using a viscoelastoplastic continuum damage model. In: *Association of Asphalt Paving Technologists-Proceedings of the Technical Sessions 2006 Annual Meeting*. pp. 577–636.

Wang, Y., Norouzi, A., Kim, Y.R. 2016. Comparison of fatigue cracking performance of asphalt pavements predicted by pavement me and lvecd programs. *Transportation Research Record* 2590(1), 44–55.

Experimental Study on the Influence of Out-of-Band Gradations and Ageing on Fracture Properties of Asphalt Concrete using IDEAL-CT Test

Sachin Gowda M K[1], Nikhil Saboo[2], Gottumukkala Bharath[1] and Aakash Gupta[1]

[1]*CSIR-Central Road Research Institute (CRRI), New Delhi, India-110025.*

[2]*Indian Institute of Technology (IIT) Roorkee, Roorkee, India- 247667*

ABSTRACT: The need to enhance the cracking resistance of asphalt mixes under varying conditions of aging and traffic loads has become increasingly critical for sustainable pavement performance. This study explores the impact of aggregate gradation, volumetrics, and aging on the cracking potential of asphalt mixes, evaluated using the Bailey method and IDEAL-CT test. Three gradations were considered, and the mixes were subjected to unaged (UA), short-term aged (STA), and long-term aged (LTA) conditions. Gradation-2 showed the best cracking resistance, as reflected by the highest CT-Index values, though significant reduction was noted after LTA. IDEAL-CT parameters such as $|m_{75}|$, fracture energy (G_f), and Asphalt Flexibility Ratio (AFR) revealed the complex interplay between stiffness, flexibility, and aging effects. The findings underline the importance of selecting optimal aggregate gradation and binder content for enhancing long-term durability and resistance to cracking in asphalt pavements.

1 INTRODUCTION

Cracking is one of the most critical distresses in bituminous pavements, driven by various factors such as repeated heavy traffic, thermal stresses, and aging effects, all of which contribute to pavement deterioration and shortened service life. To mitigate these effects, considerable attention has been directed toward improving the cracking resistance of bituminous mixtures during the design phase. While traditional volumetric-based mix designs were once sufficient for ensuring adequate pavement performance, the increased complexity of modern bituminous mixtures due to incorporating recycled materials, modifiers, and warm-mix technologies has complicated this process. As a result, volumetric evaluation no longer guarantees an optimal mix, necessitating the integration of performance-based tests to accurately assess these modern mixes' cracking potentials. Zhou et al. [1] developed the Indirect Tensile Asphalt Cracking Test (IDEAL-CT) as a practical method for assessing the intermediate-temperature cracking resistance of bituminous mixtures. The test's simplicity and effectiveness have led to its widespread adoption, particularly in the United States, where multiple Departments of Transportation have incorporated it into their specifications for asphalt mix design.

The IDEAL-CT test quantifies cracking resistance using the Cracking Tolerance Index (CT-Index), which is calculated based on key parameters such as fracture energy (G_f), post-peak displacement at 75% of the peak load (l_{75}), and the absolute value of the post-peak slope ($|m_{75}|$). These parameters are sensitive to essential mixture components such as air voids, aging, binder type, and aggregate gradation, all of which influence cracking resistance. Previous studies have demonstrated the utility of CT-Index in differentiating bituminous mixtures based on their cracking potential under various conditions [2]. However, limited research has explored the combined effects of aggregate gradation, binder content, and aging on cracking resistance [3]. Therefore, the current study seeks to address this gap by investigating how out-of-band aggregate gradations, volumetric properties, and aging levels impact critical performance parameters such as CT-Index, $|m_{75}|$, G_f, and the L_{75}/m_{75} ratio in bituminous concrete mixes. The outcomes will help refine the mix design process by incorporating performance-based specifications, thereby enhancing the long-term durability of flexible pavements.

2 OBJECTIVES

This study aims to investigate the influence of aggregate gradation, volumetric properties, and aging on the cracking resistance of bituminous concrete mixes. Specifically, it assesses the effects of out-of-band gradations (using the Bailey method), air void content, binder content, and volumetrics on key performance indicators such as the CT-Index, $|m_{75}|$, G_f, and L_{75}/m_{75} ratio. Additionally, the study examines the impact of various aging conditions, such as unaged, STA, and LTA, on cracking performance to establish performance-based design guidelines for enhancing flexible pavements' durability and cracking resistance.

3 MATERIALS USED

3.1 *Bitumen*

This study utilized a viscosity-graded binder (VG-40), and its physical properties were tested following standard guidelines. The results showed a softening point of 51.90°C (ASTM D36-14), ductility greater than 100 cm (ASTM D113-17), a penetration of 42.0 mm (ASTM D5M-20), specific gravity of 1.06 (ASTM D70-21), and a viscosity of 454 cSt at 135°C (ASTM D4402-15). These values confirm the binder's suitability for use in asphalt mixtures.

3.2 *Conventional Aggregates*

The physical properties of the aggregates used in this study were tested according to standard guidelines. The combined index (flakiness and elongation) was 31.04% (IS 2386 Part 1:1963), the aggregate impact value was 18.63% (IS 2386 Part 4:1963), and the Los Angeles abrasion value was 27.1% (IS 2386 Part 4:1963). These results ensure the aggregates meet the required criteria for use in the asphalt mix.

3.3 *Aggregate Gradations*

The aggregate gradation conforming to Bituminous Concrete Grade 2 (BC-II) [4], which is widely used as a wearing course for Indian highways, was utilized in this study. Gradations, including those outside the specified limits, were considered to assess the cracking characteristics of asphalt mixtures, as illustrated in Figure 1.
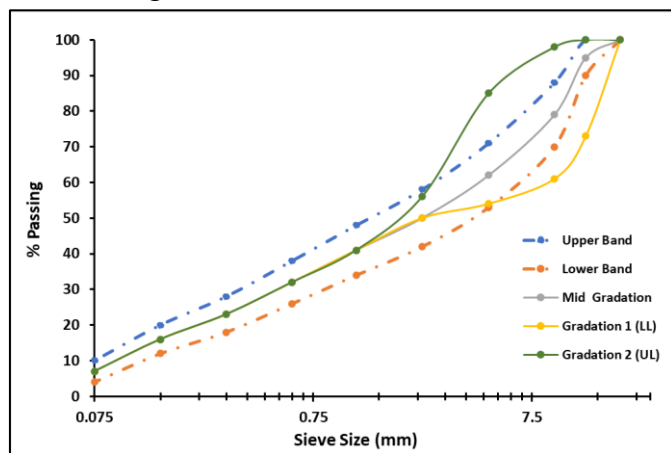
Figure 1. Aggregates Gradations Considered for the Study

3.4 *Ratios for Evaluating Gradation*

The Bailey method provides a systematic approach for evaluating the gradation of aggregates by breaking down the gradation into ratios that reflect different portions of the aggregate structure. The Coarse Aggregate Ratio (CAR) evaluates the packing density of the coarse aggregate by controlling the volume of coarse particles, ensuring that the voids are well-structured for optimal performance. The CAR typically ranges between 0.30 and 0.95 for balanced mixtures, avoiding excessive voids or over-packing. The Fine Aggregate Coarse Ratio (FA_c) reflects how the coarser portion of the fine aggregate interacts with the finer portion, and should remain below 0.50 to prevent tender mixes prone to early failure. Similarly, the Fine Aggregate Fine Ratio (FA_f) assesses the finest portion of the blend, and it is also recommended that it be below 0.50 for dense-graded mixes [5]. In this study, using Bituminous Concrete Grade 2 (BC-II), the calculated ratios are listed in Table 1.

Table 1. Ratios for Evaluating Gradation

Gradation	CAR	FA_c	FA_f
Mid Gradation	0.32	0.64	0.50
Gradation 1	0.09	0.64	0.50
Gradation 2	1.93	0.57	0.50

4 EXPERIMENTAL PROGRAM, RESULTS, AND DISCUSSION

The three different aggregate gradations, as shown in Figure 1, were blended with varying binder contents to determine the Optimum Binder Content (OBC) corresponding to a target air void of 4% [6]. The associated volumetric properties were then analyzed. The mixes were produced at the OBC under three aging conditions: unaged, short-term aged [6], and long-term aged [7], and were tested using the IDEAL-CT test at a target air void of 7%.

4.1 *Volumetrics*

The Bailey method offers a structured approach to analyzing aggregate gradation using volumetric properties, which is important in optimizing asphalt mixtures. This study analyzed three different gradations, resulting in varying optimum binder contents (OBC) and volumetric parameters. For the mid-gradation, the OBC was determined to be 5.80%, with a void in mineral aggregates (VMA) of 15.52% and voids filled with bitumen (VFB) of 69%. Gradation-1 yielded a lower OBC of 5.10%, with a VMA of 14.75% and a higher VFB of 73%, indicating a better fill of voids with asphalt. Conversely, Gradation-2 required a higher OBC of 6.90%, achieving a VMA of 15.85% and a VFB of 75%. These findings highlight the importance of maintaining an optimal balance of air voids and binder content to enhance the performance of asphalt mixes, particularly in relation to durability and resistance to aging under different conditions. All three gradations resulted in the marshall stability greater than 15KN and flow value less than 4mm at their corresponding OBC.

4.2 Marshall Stability and Flow

Figure 2 highlights the effects of MSWI-BA replacement on Marshall Stability and Flow. The mix with 10% MSWI-BA showed a slight improvement in stability compared to the control mix (CM), but stability declined as MSWI-BA content increased further, attributing the decline to increased binder film thickness and smoother MSWI-BA particles, which reduce interparticle friction and bonding. Flow values mostly remained acceptable, except for mixes with 40% and 50% replacement, where flow exceeded 5 mm, indicating a potential for increased rutting susceptibility.

4.3 IDEAL-CT Test

The IDEAL-CT test is crucial in this study as it evaluates the cracking resistance of asphalt mixtures, providing insights into their performance under real-world conditions. Given the variations in aggregate gradations and binder content, the IDEAL-CT test is an effective method for assessing how these factors influence the fracture characteristics of the asphalt mixes. By targeting specific air void contents of 7% in this case, the test helps determine the optimal balance between durability and flexibility in the asphalt mixes. The outcomes of the IDEAL-CT test will inform the suitability of the evaluated gradations and binder contents, guiding future mix designs to enhance resistance to cracking and extend the service life of pavements, especially under varying aging conditions.

The various parameters derived from the IDEAL-CT test, including the CT-Index, $|m_{75}|$, G_f (N/m²), and Asphalt Flexibility Ratio (AFR), play a crucial role in analyzing the cracking potential of asphalt mixes. The CT-Index provides insight into the material's performance at intermediate temperatures, indicating its susceptibility to cracking. The $|m_{75}|$ parameter measures the slope of the load-displacement curve, reflecting the stiffness of the asphalt mix. At the same time, G_f quantifies the energy required to propagate a crack, thereby assessing the material's toughness. L_{75}/m_{75} offers a ratio of loading at the critical point, which helps evaluate the mix's resistance to deformation, and the AFR highlights the balance between flexibility and strength in the mix [2]. Collectively, these parameters enable a comprehensive assessment of the material's ability to withstand thermal and mechanical stresses, ensuring long-term durability. Literature indicates that mixes exhibiting favourable IDEAL-CT results, characterized by optimal values across these parameters, tend to demonstrate enhanced resistance to cracking. Thus, understanding and optimizing these parameters is essential for developing asphalt mixes that maintain pavement integrity over time, particularly given the influence of variations in aggregate gradations and binder contents on

performance. The IDEAL-CT test results are tabulated in Table 2.

Table 2. IDEAL-CT test results

Gradation	Ageing	CT-Index	$|m_{75}|$	G_f (Nm⁻²)	AFR
Mid Gradation	UA	13.9	6.0	3976.8	0.35
	STA	14.7	7.1	4445.8	0.33
	LTA	11.8	8.1	4410.5	0.27
Gradation 1	UA	10.8	7.8	3986.8	0.28
	STA	20.2	6.3	5455.0	0.38
	LTA	7.1	10.7	3745.4	0.20
Gradation 2	UA	30.0	5.0	4821.8	0.63
	STA	24.4	5.3	4907.9	0.51
	LTA	14.4	6.8	4449.4	0.33

The IDEAL-CT test results comprehensively analyze the cracking performance of asphalt mixes, revealing strengths and limitations across different gradations and aging conditions. The mid-gradation exhibits a CT-Index of 13.9 for the UA sample, indicative of moderate resistance to cracking. This value increases to 14.7 under STA, suggesting a beneficial impact of initial binder hardening. However, the subsequent drop to 11.8 in LTA raises concerns about durability. This decline suggests that while the mix may perform adequately initially, prolonged exposure to environmental factors leads to brittleness and cracking susceptibility. The $|m_{75}|$ values, which reflect the material's stiffness, show an increasing trend from UA (6.0) to LTA (8.1), reinforcing that as the mix ages, it becomes stiffer, diminishing its ability to withstand thermal stresses.

In contrast, Gradation-1 presents a more complex picture. The CT-Index peaks at 20.2 under STA, indicating exceptional resistance to cracking, likely due to the optimal binder content that enhances the mix's ductility. However, this impressive performance is short-lived; the LTA sample drops to 7.1, suggesting that while the mix initially demonstrates high resistance, it becomes increasingly brittle over time. This inconsistency in performance under varying aging conditions indicates that the mix may not be well-suited for long-term applications without additional modifications to enhance durability. The $|m_{75}|$ values for Gradation-1 remain relatively high across aging conditions. Yet, the G_f values reinforce a concerning trend: they peak at 5455.0 N/m² under STA but drop significantly to 3745.4 N/m² under LTA, indicating a reduced energy absorption capacity that compromises the mix's resilience against cracking.

Gradation-2 shows the most alarming results. The UA sample boasts a CT-Index of 30.0, signaling excellent cracking resistance. However, the corresponding low $|m_{75}|$ value of 5.0 suggests that this mix may have inadequate stiffness despite its toughness in resisting deformation effectively. The CT-Index decreases to 14.4 as aging progresses, signaling a

significant performance loss. The increasing $|m_{75}|$ value to 6.8 under LTA indicates a trend toward increased stiffness but raises questions about the mix's ability to adapt to stress without failing. This contrast between high toughness and low stiffness is particularly troubling, as it suggests that while the mix may initially resist cracking, it could become overly brittle with time.

The L_{75}/m_{75} ratio across the gradations further complicates the analysis. The low and consistent ratio across aging states suggests ineffective stress distribution for mid-gradation, likely leading to localized failure. In Gradation-1, the ratio shows variability that hints at improved load distribution under STA but deteriorates under LTA, indicating a loss of balance in the aggregate structure as aging occurs. Gradation-2, despite its high initial CT-Index, demonstrates a potential imbalance with low $|m_{75}|$, which can result in a brittle failure mechanism due to an inability to distribute applied loads effectively.

The AFR is an essential metric for evaluating the flexibility-to-strength balance within each mix. Mid-gradation maintains an AFR between 0.25 and 0.35, suggesting a marginal balance vulnerable to aging-induced failures. Gradation-1 increasing AFR under STA indicates a temporary balance between flexibility and strength; however, the significant drop to 0.18 under LTA underscores the mix's compromised ductility as it ages. In contrast, Gradation-2 exhibits a high AFR, particularly in the UA condition (0.59), reinforcing its initial flexibility. Yet, the decline to 0.31 under LTA suggests an alarming shift toward brittleness, raising concerns about its long-term viability.

Overall, while the IDEAL-CT parameters provide valuable insights into the cracking potential of asphalt mixes, they also reveal critical vulnerabilities that must be addressed in the design process. The data indicate that mixes that perform well under initial conditions can become severely compromised with aging, underscoring the need for a multifaceted approach in the mix design. This necessitates careful consideration of gradation, binder content, and aging effects to ensure the long-term durability and performance of asphalt pavements. Without such considerations, premature cracking and structural failure risk increases significantly, exposing the pavement system to danger or risking its integrity.

5 CONCLUSIONS

This study highlights the critical role of aggregate gradation, aging, and IDEAL-CT parameters in determining the cracking resistance of asphalt mixes. Using the Bailey method, it was found that optimized gradation improves aggregate packing and volumetric properties. Gradation-2, with the best packing structure, exhibited the highest initial cracking resistance but significantly declined under LTA.

Gradation-1 performed well under STA but became brittle with LTA, as reflected by its reduced CT-Index and AFR.

Aging effects were significant across all gradations, with STA improving cracking resistance while LTA led to increased stiffness (higher $|m_{75}|$ values) and reduced flexibility. This was evident in reduced fracture energy (G_f) and CT-Index for all mixes under LTA, highlighting the need to balance stiffness and flexibility in mix designs carefully. The study underscores the importance of optimizing aggregate gradation and binder content and accounting for aging effects to achieve durable asphalt pavements with balanced cracking resistance and flexibility.

6 ACKNOWLEDGMENTS

7 REFERENCES

[1] Zhou, F., Development of an IDEAL Cracking Test fo Asphalt Mix Design, Quality Control and Quality Assurance. NCHRP IDEA Project 195, Texas Department of Transportation, 2019.

[2] Leavitt, A., Epps Martin, A., & Arámbula, E. (2024). Model for Evaluating Cracking Performance of Asphalt Pavements with Field Aging Based on IDEAL-CT Parameters. Transportation Research Record, 0(0). https://doi.org/10.1177/03611981241231806

[3] Shaikh, S., & Gupta, A. (2024). Assessing cracking resistance and threshold limits of bituminous mixtures with IDEAL-CT and predictive modeling techniques. Construction and Building Materials, 449. https://doi.org/10.1016/j.conbuildmat.2024.138349

[4] MoRTH, Specifications for Road Bridge Works 5th Revision, 2013.

[5] Vavrik, W. R., Pine, W. J., & Carpenter, S. H. (n.d.). Aggregate Blending for Asphalt Mix Design, Transportation Research Record 1789, Paper No. 02-3629.

[6] Asphalt Institute, MS-2, Asphalt Mix Design Methods, 7th Edition, Asphalt Institute, USA, 2014.

[7] AASHTO R 30-2, Standard Practice for Mixture Conditioning of Hot Mix Asphalt (HMA)

Quantification of Self-Healing in Warm Mix Asphalt Binders using Linear Amplitude Sweep Test

Sunny Kumar Yadav
CSIR-CRRI, New Delhi-110025

Deepa Sasidharan
Scientist, CSIR-CRRI, New Delhi-110025

Bharat Gottumukkala
Senior Scientist, CSIR-CRRI, New Delhi-110025

Sampath Kumar
Senior Scientist, CSIR-CRRI, New Delhi-110025

ABSTRACT: Discrepancies between laboratory-based predictions and field performance of asphalt mixes in terms of fatigue life can be reduced by taking into account the self-healing characteristics of asphalt in experimental protocols. In this study, the healing potential of an unmodified binder is quantified both in the presence and absence of a warm mix additive (WMA). During the test, rest periods of varied durations (10 and 30 minutes) are introduced at 25% and 75% of damage levels prior to reaching failure to examine their influence on the further evolution of damage. It was observed that the addition of the WMA resulted in an improved healing index of the unmodified binder at different damage levels pre-failure. The results suggest the potential of WMA additives to enhance the healing of bituminous mixes in addition to their established benefits in lowering temperatures.

1 INTRODUCTION

Significant energy consumption is involved during the production of bituminous mixtures mainly from oil refineries and asphalt mixing plants, making it the second most energy-intensive industry (Zapata & Gambatese, 2005). Higher bitumen production temperatures result in considerable energy demand for heating aggregates and binders, leading to high greenhouse gas emissions. By lowering production and compaction temperatures by 30 to 50°C compared to conventional hot mix asphalt (HMA), WMA not only reduces emissions but also improves workability, minimizes aging and facilitates cold weather paving (Milad et al., 2022).

Fatigue cracking is one of the major modes of distress in bituminous pavements (IRC 37, 2018). The healing potential of asphalt mixtures refers to their ability to repair cracks during rest periods between traffic loads. Self-healing is a process by which the micro-cracks caused due to the traffic gradually close and restore the material's properties without external intervention (Pronk, 1997; Wang et al., 2018). This results in improved stiffness and fatigue resistance in the pavement.

Discrepancies between laboratory-based predictions and field performance of bituminous mixes generally happen due to various reasons such as differences in loading mode, moisture susceptibility, environmental conditions and construction aspects. One critical reason for the underestimation of fatigue life in laboratory settings is the failure to incorporate the self-healing properties of asphalt binders. Introduc-ing a rest period during the fatigue test has been found to expedite damage recovery in bituminous material (Xie et al., 2017). This also replicates the intermittent loading conditions experienced in the field and thus better captures the stiffness modulus which correlates well with field performance.

Gupta et al. (2023) explored the healing potential of reclaimed asphalt pavement (RAP) binders blended with different rejuvenators using the Linear Amplitude Sweep test, both with and without rest periods. It was observed that the inclusion of rest periods significantly enhanced the healing potential of the binders. A study by Yue et al., (2021) on Sasobit and polymer modifiers on asphalt binders reported that healing potential varied depending on the binder's composition. Pang et al. (2012) explored the self-healing capabilities of asphalt binders and determined that aging and SBS modification had a notable impact on healing. The study also observed that extended rest periods delayed the crack formation and subsequently increased the service life.

Despite significant advancements in evaluating the fatigue performance of warm mix asphalt binders, investigating their self-healing potential remains relatively underexplored. The present study aims to evaluate the healing potential of an unmodified binder blended with a WMA additive. For this purpose, the conventional LAS test has been modified to incorporate rest periods of varying durations. This approach will allow a quantification of the relative healing behavior of the binder with and without WMA additive.

2 EXPERIMENTAL INVESTIGATION

This study is carried out on a VG-40 binder (IS 73, 2013), and this base binder is blended with a chemical warm mix additive in order to prepare the warm mix binder. Prior to the addition of the WMA additive, the base binder was heated at 120°C in the oven for 30 minutes. Further, 0.1% of WMA additive by the weight of the binder was added and the mix was blended at a constant speed in a shear mixture at 120°C for 10 minutes. The binders, viz, VG-40 and VG-40+0.1% WMA additive, are further referred to as VG-40 and VG-40+WMA, respectively. Table 1 and Table 2 show the properties of the WMA additive and the bituminous binders respectively.

Table 1. Properties of the WMA additive

Properties of WMA additive	Values
Physical State	Liquid
Color	Pale Yellow
Odour	Slight Aromatic
Melting Point (^{0}C)	-10
Boiling Point (^{0}C)	200
Density (g/cm^3)	1.03
Water Solubility	Soluble

Table 2. Physical Properties of Binders

Tests	Binders	
	VG-40	VG-40 + WMA additive
Specific gravity	1.03	1.03
Softening point (◦C)	53	52
Penetration grade at 25◦C (0.1 mm)	51	49
Rotational viscosity (@135 ◦C) (cP)	625	500

2.1 Continuous LAS test

The LAS test was conducted in accordance with AASHTO TP 101 (2014) wherein, the fatigue endurance of bituminous binders was estimated under the application of a continuous linearly ramping strain amplitude. In this investigation, the LAS tests were carried out using an Anton Paar MCR 302 dynamic shear rheometer (DSR) with an 8 mm parallel plate geometry and 2 mm gap setting at the intermediate temperature of 25°C.

The LAS test was performed on long-term aged binders. During the LAS test, the binder was subjected to oscillatory shear loading, and the strain amplitude increases linearly from 0 to 30% over 3,100 cycles. During the test, peak stress and strain are captured every 10 cycles, and the dynamic shear modulus and phase angle are calculated for all these cycles.

Before the LAS test, a frequency sweep was performed to obtain information on the undamaged material parameters, such as the complex shear modulus. A frequency sweep test was conducted by applying an oscillatory shear at 0.1% strain amplitude across a range of frequencies that range from 0.2 to 30 Hz at 25°C.

2.2 LAS test with rest periods

The healing-based LAS test procedure comprises two distinct steps. Initially, a standard continuous LAS test is conducted without any interruption. The damage accumulation in the material is denoted as the damage level (S), with Sf representing the critical threshold for failure. Further, rest periods are introduced at 25% and 75% of Sf, respectively, prior to reaching failure to examine their impact on the further evolution of damage. Varied rest periods (10 and 30 minutes) are tested at each damage level to analyze their effects on the binder response.

2.3 Data Analysis

The viscoelastic continuum damage (VECD) concept is used to analyze the LAS test data (Bhasin et al., 2008; Karki et al., 2017). As per AASHTO TP 101, the damage accumulation in the sample is determined using Equation 1,

$$D(t) = \sum_{i=1}^{N} [\pi \gamma_0^2 (C_{i-1} - C_i)]^{\frac{\alpha}{1+\alpha}} (t_i - t_{i-1})^{\frac{1}{1+\alpha}} \quad (1)$$

where $C(t)$ is given by Equation 2.

$$C(t) = \frac{|G^*|(t)}{|G^*|(initial)} \quad (2)$$

Pseudo stiffness ($C(t)$) is calculated as the ratio of the dynamic shear modulus $|G^*|$ at time, t, and the "undamaged" initial modulus ($|G^*|$). γ_0 is the applied strain for each data point (% strain), and 'α' is obtained from the frequency sweep test. As seen from Equation (1), the total damage at 30% stain is the summation of the damage occurring in the material at each strain increment. The relationship between $C(t)$ and $D(t)$ is modeled using a power law function given by Equation 3.

$$C(t) = C_0 - a(D)^b \quad (3)$$

where C_0 takes the value 1, and a, b are constants. The value of $D(t)$ at failure is denoted by D_f and is computed as Equation 4.

$$D_f = \left(\frac{C_0 - C_{peak\ stress}}{a}\right)^{1/b} \quad (4)$$

The plot of Damage (D) vs Pseudo stiffness (C) is referred to as the damage characteristic curve (DCC).
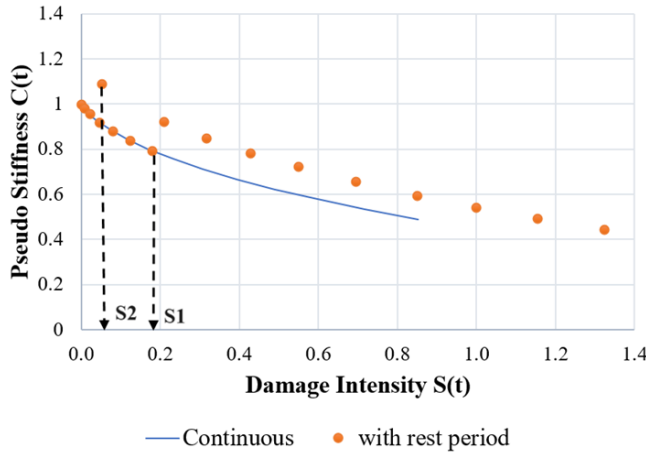
$$\%H = \left(\frac{S_1 - S_2}{S_1}\right) * 100 \qquad (5)$$

The calculation of healing (%*H*), involves the damage (S) values before (*S1*) and after (*S2*) the rest period and is given in Equation 5.

3 RESULTS AND DISCUSSIONS

3.1 Continuous LAS test

Figure 2 shows the Damage Characteristic Curve (DCC) for the binders in a continuous LAS test. It can be observed that the addition of a WMA additive to an unmodified binder has improved the stiffness of the binder at higher damage levels.
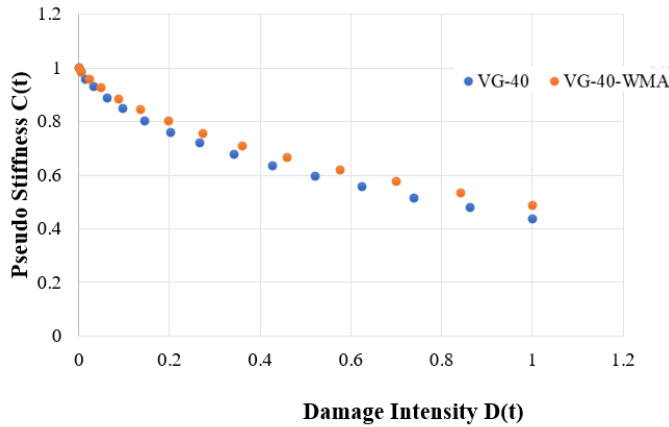
Figure 2. Damage Characteristic Curves for binders

3.2 LAS test with rest periods

Figure 3 shows the results of the continuous LAS test and the LAS test with a rest period for both VG40 and VG40+WMA. Here, the rest period is applied at 25% Sf. It can be observed that when rest periods are applied at an early stage of damage (25%Sf), there is a complete recovery in the damage in both binders. Notably, the extent of stiffness recovery increases with the length of the rest periods.
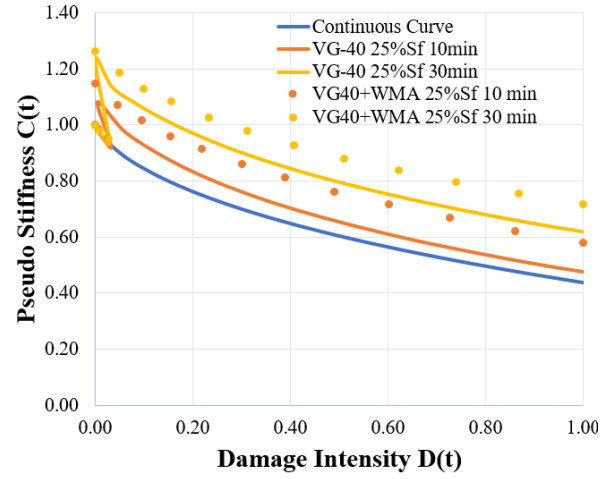
Figure 3. DCC at 25% Sf

It can be noted that the damage recovery has improved by adding a WMA additive to the VG40. The stiffness (C) in the WMA blended VG40 has also improved. At the same damage intensity, VG40+WMA has better stiffness as compared to an unmodified binder.
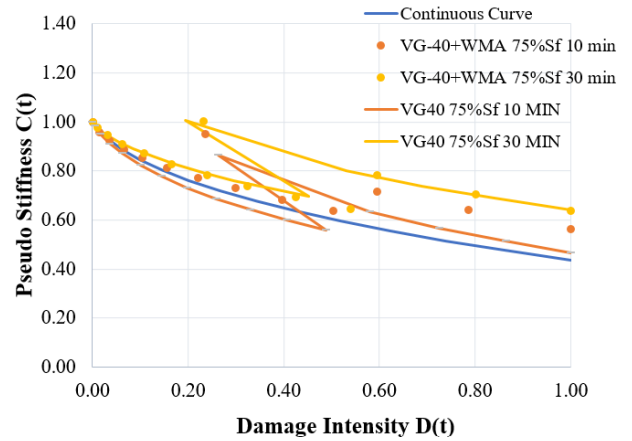
Figure 4. DCC at 75% Sf

It is observed from Figure 4 that the application of rest periods at higher damage levels (75% Sf) has a lesser impact on the healing of the binders. When rest period is given at 75% Sf, stiffness recovery is lower than that at 25% Sf. Also, the damage recovery is much lower. It can be noted that the rest period duration is also less significant at higher damage levels. The addition of WMA has resulted in better stiffness and damage recovery even at 75% Sf. This underscores the potential of WMA additives to enhance the healing of binders in addition to their well-known benefits in reducing working temperatures.

3.3 Calculation of healing Index

The healing index (%) was evaluated for VG40 and VG40+WMA at two different damage levels (25%, and 75% Sf) and rest periods (10 and 30 minutes) as presented in Table 3.

Table 3. Healing Index

Healing Index (%)			
Binder	%Sf	Rest period (minutes)	
		10	30
VG40	25	85	100
	75	46	57
VG40+ WMA	25	100	100
	75	53	57

The healing percentage shows that the ability of the binder to heal, diminished with an increase in the damage levels, possibly due to excessive internal damage that cannot be reversed during the given rest periods. Also it can be observed that incorporating WMA additives into VG40 improved its healing performance across all damage levels.

4 CONCLUSIONS

- Application of rest periods during the LAS test results in binder healing and enhanced stiffness during the rest of the test.
- It is understood that the application of rest periods at higher levels of damage has a reduced effect on the healing of binders.
- The addition of the WMA additive has improved the healing index of VG40 at all the damage levels pre-failure.
- The results highlight the potential of WMA to enhance healing in binders, in addition to its established benefits in lowering working temperatures.

5 REFERENCES

[1] AASHTO TP 101-14 (2014) Estimating Damage Tolerance of Asphalt Binders Using the Linear Amplitude Sweep. American Association of State Highway and Transportation Officials, Washington D.C., USA

[2] Gupta, A., Sasidharan, D., Gottumukkala, B., & Kar, S. S. (2023). Evaluation of healing performance of blended reclaimed asphalt binders with rejuvenators based on rheological and chemical properties. *Sādhanā*, 48(3), 139.

[3] IS: 73-13, (2013). Specification for paving bitumen. New Delhi: Bureau of Indian Standards.

[4] IRC: 37 (2018) Guidelines for design of flexible pavements. Indian Road Congress. New Delhi, India

[5] Milad, A., Babalghaith, A. M., Al-Sabaeei, A. M., Dulaimi, A., et.al. (2022). A Comparative Review of Hot and Warm Mix Asphalt Technologies from Environmental and Economic Perspectives: Towards a Sustainable Asphalt Pavement. *International Journal of Environmental Research and Public Health*, 19(22), 14863.

[6] Pang, L., Jiang, H., Wu, S., & Wu, S. (2012). Self healing capacity of asphalt binders. *Journal of Wuhan University of Technology-Mater. Sci. Ed*., 27(4), 794–796.

[7] Pronk, A. C. (1997). Healing during fatigue in 4 point dynamic bending tests. *Report: W-DWW-97-095*, DWW, Delft, The Netherlands.

[8] Wang, C., Xie, W., & Underwood, B. S. (2018). Fatigue and healing performance assessment of asphalt binder from rheological and chemical characteristics. *Materials and Structures*, 51(6), 171.

[9] Xie, W., Castorena, C., Wang, C., & Richard Kim, Y. (2017). A framework to characterize the healing potential of asphalt binder using the linear amplitude sweep test. *Construction and Building Materials*, 154, 771–779.

[10] Yue, M., Yue, J., Wang, R., & Xiong, Y. (2021). Evaluating the fatigue characteristics and healing potential of asphalt binder modified with Sasobit and polymers using linear amplitude sweep test. *Construction and Building Materials*, 289, 123054.

[11] Zapata, P., & Gambatese, J. A. (2005). Energy Consumption of Asphalt and Reinforced Concrete Pavement Materials and Construction. *Journal of Infrastructure Systems*, 11(1), 9–20.

Considering realistic soil behaviour in numerical simulations of the road

S. Ullmann & I. Herle
Institute of Geotechnical Engineering, Technische Universität Dresden, Germany

ABSTRACT: The subsoil beneath the road pavement is often simplified as a linear-elastic material, although real soils can behave in a non-linear and inelastic manner. This study presents a numerical analysis of a road pavement behaviour under repeated tyre loads, focusing on incorporating realistic soil behaviour for the subsoil. A three-dimensional finite element model of the road pavement is employed, featuring a typical pavement structure that includes the asphalt, the frost protection layer and the subsoil, which is modelled using an advanced hypoplastic model. The results show that during repeated wheel loads, the soil's state variables undergo only minor changes, implying that the stiffness of the subsoil does not change significantly. Consequently, a simplified surrogate soil model can be used to effectively replicate the deformation predictions of the advanced hypoplastic model.

1 INTRODUCTION

Numerical investigations of the structural behaviour of road pavements are frequently subject of research. Many of the studies primarily focus on detailed modelling of the pavement-tyre interaction or the realistic modelling of the pavement surface materials, usually asphalt. On the contrary, the subsoil, as an essential part of the road pavement, is typically simplified as a linear-elastic material. In reality, however, the behaviour of the soil is highly inelastic and non-linear. Under cyclic loading, for instance, plastic deformations may accumulate in the soil, potentially contributing to a damage in the road pavement.

In this study a numerical analysis, in which the subsoil is incorporated into a holistic FE model of the road pavement using an advanced material model, is used to analyse the influence of the soil behaviour on the deformation of the pavement surface. Based on the obtained results, a simplified surrogate soil model is calibrated and subsequently compared with the results of the advanced model.

2 FINITE ELEMENT MODEL

2.1 *Geometry*

A three-dimensional FE model was created to realistically model a truck tyre crossing a section of a road pavement. The model dimensions and the mesh were determined in advance in a parameter study and are

shown in Figure 1, along with the selected boundary conditions and the geometry of the road pavement.

The road pavement was designed in accordance with the German guideline for the standardization of the road pavement for traffic areas (RSt0, 2012). An asphalt construction method with an asphalt base course on a frost protection layer of the load class BK100, which is commonly used for heavily trafficked motorways, was chosen for the road pavement. According to the RSt0 (2012), this construction method requires an asphalt layer with a total thickness of $d_1 = 0.34$ m and a frost protection layer of at least $d_2 = 0.31$ m.
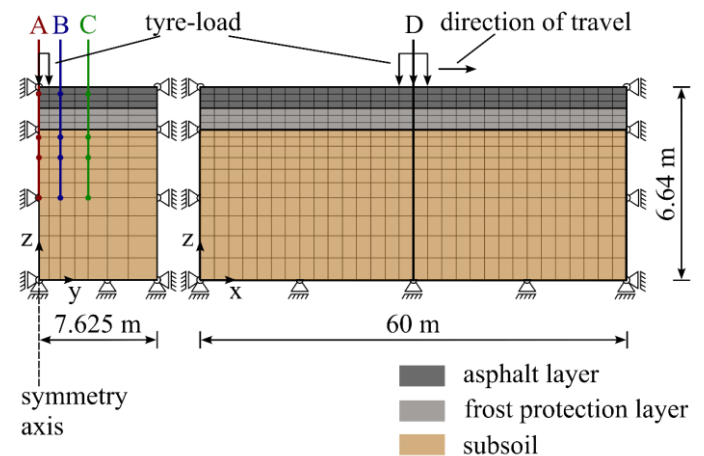
Figure 1. Dimensions, mesh and boundary conditions for the 3D finite-element model in the cross and longitudinal section. The mesh consists of 73,440 linear hexahedral elements and 82,422 nodes.

2.2 Modelling the tyre-pavement interaction

A simplified approach was chosen to model the load caused by a rolling tyre. Instead of modelling the whole tyre, the contact stresses between the tyre and pavement were applied in the FE model, similar to the study by Hu & Walubita (2011). Both the vertical and horizontal contact stresses that occur while driving were taken into account, see Figure 2. According to Hu & Walubita (2011), the horizontal contact stresses $\sigma_{h,x}$ and $\sigma_{h,y}$ correspond to 12% and 30% of the vertical contact stress σ_v, respectively. The vertical contact stress was calculated to $\sigma_v = 400$ kPa, assuming a tyre load of $F = 50$ kN and a contact area of 0.25 x 0.50 m.
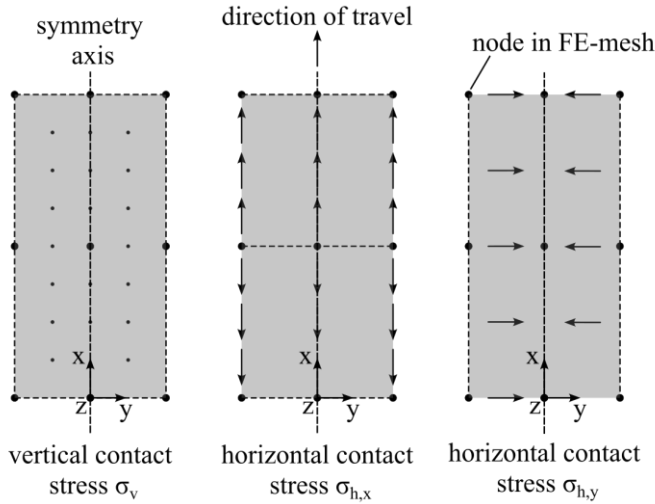
Figure 2. Simplified modelling approach for the contact stresses between tyre and pavement, illustrating vertical and horizontal contact stresses acting along and transverse to the direction of travel, based on Hu & Walubita (2011).

2.3 Material models

The investigation focuses on the material behaviour of the subsoil beneath the road pavement rather than the material behaviour of the individual layers. Therefore, the asphalt and frost protection layers were modelled as isotropic linear-elastic materials. The elasticity parameters for asphalt depend on variety factors, including composition, temperature and load frequency. According to the study by Leutner et al. (2006), the Young's modulus of asphalt can be assumed as 10,000 MPa with a Poisson's ratio of 0.3. The elastic parameters for the frost protection layer were defined as E = 150 MPa and ν = 0.3.

The hypoplastic material model proposed by von Wolffersdorff (1996) with the extension of the Intergranular Strains by Niemunis & Herle (1997) and the modification by Wegener & Herle (2014) was used to realistically model the subsoil behaviour under cyclic loading. The material parameters for the basic hypoplastic model were calibrated in advance for a sand-fines mixture using standard classification tests, as well as oedometer and triaxial compression tests. The parameters for the Intergranular Strain extension

were adopted from Abdelkadr (2023), who calibrated a similar soil with comparable grain size distribution. A summary of all used material parameters is given in Table 1.

Table 1. Summary of the used material models and parameters

Layers	Value	Unit
Asphalt*		
Density	2500	kg/m^3
Thickness	0.34	m
Young's modulus E	10,000	MN/m^2
Poisson's ratio ν	0.3	-
Frost protection		
Density	2200	kg/m^3
Thickness	0.30	m
Young's modulus E	150	MN/m^2
Poisson's ratio ν	0.3	-
Subsoil		
Density (dry)	1900	kg/m^3
Thickness	6.0	m
Hypoplastic model parameters (Wolffersdorff 1996)		
φ_c	34.3	°
e_{i0}	1.332	-
e_{c0}	1.110	-
e_{d0}	0.476	-
h_s	8300	kPa
n	0.329	-
α	0.11	-
β	4.80	-
*Intergranular Strain Extension (Niemunis & Herle 1997)***		
R	1x10^{-4}	-
m_R	4.0	-
m_T	2.8	-
β_r	0.05	-
χ	1.0	-
*Extension by Wegener & Herle (2014)***		
υ	10.0	-

* Asphalt material parameters adopted from Leutner et al. (2006)
** Intergranular Strain parameters adopted from Abdelkadr (2023)

2.4 Initial state and calculation procedure

The mechanical behaviour of the soil highly depends on its state variables such as the soil's void ratio and the effective stresses. These quantities need to be prescribed. For this reason, a calculation step was carried out in which the gravity was gradually increased to generate the initial stress state with the defined weights of the overlaying pavement. The void ratio at the start of the calculation was specified so that the soil reaches a relative density of $I_D = 0.95$ after the increase in gravity, representing a realistic density of the soil after compaction prior to the construction of the actual road pavement. The simulations were carried out using the finite element code TOCHNO Professional by Roddemann (2022).

3 RESULTS

3.1 *Stress evolution and propagation*

The stresses in the subsoil and the road pavement caused by a passing tyre are shown in Figure 3. In Figure 3a it can be seen, that as the tyre travels over the road pavement the principle stress state undergoes a rotation, which is characterized by the development of shear stresses. The change of the stress state in the subsoil is mainly caused by the change in the vertical stress, while the changes in the horizontal and shear stresses are small. This indicates that the asphalt layer functions as a load distributing layer, significantly reducing the impact of the tyre load on the frost protection layer and the subsoil, see Figure 3b.
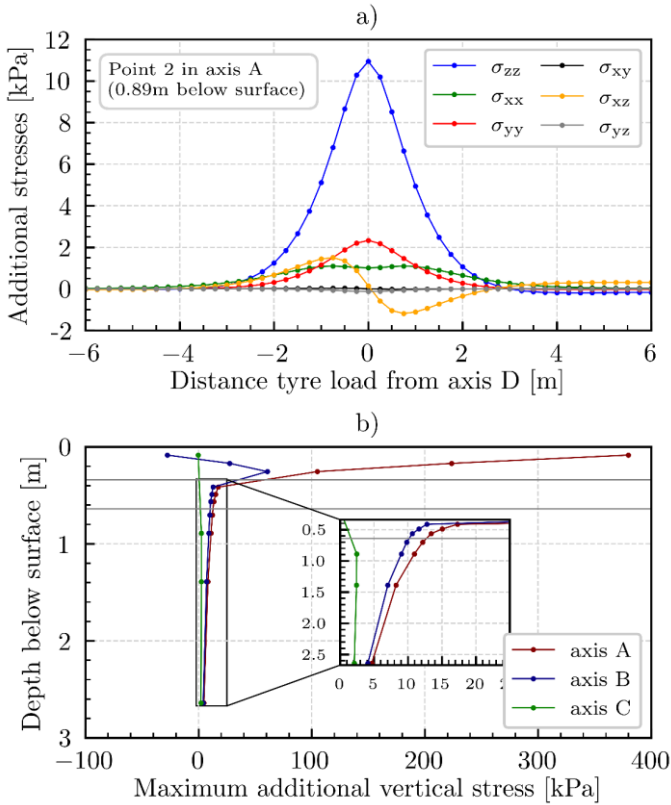
Figure 3. Stresses in a road pavement caused by a passing tyre: a) Evolution of additional stresses in the subsoil and b) the maximum additional vertical stress in the road pavement along axis A (directly under the tyre load) and axis B and C (located 0.25 m and 0.75 m away from the tyre load, respectively).

3.2 *Evolution of state variables*

In addition to the mechanical stresses, the density – expressed by the void ratio – plays an important role in the mechanical behaviour of the soil. Laboratory tests have shown that soil tends to densify when subjected to cyclic shearing. Since shear stresses occur in the subsoil, the evolution of the void ratio caused by multiple tyre passages is shown in Figure 4a. The diagram illustrates that there is indeed a compaction of the soil, as the void ratio decreases with an increasing number of cycles. However, the change in the void ratio is negligible when compared to the limits e_{c0} and

e_{d0} given in Table 1. This indicates that, for a low number of cycles, the void ratio can be assumed to remain constant.

Figure 4b shows the evolution of the intergranular strain tensor expressed by the state variable ρ, which can be interpreted as the mobilization of the intergranular strains. ρ ranges between 0 and 1 and significantly influences the stiffness of the subsoil. The blue curve represents the evolution of ρ starting from an initial state that resulted from a gradual increase in gravity. In contrast, the red curve shows the evolution of ρ when the initial state was reset to zero after the increase in gravity but before the cyclic loading begins. Both curves tend to converge towards a quasi-static state after two cycles, which means that the intergranular strain tensor remains constant and therefore the stiffness of the soil does not change with the strain increments anymore. This effect is independent of the initial state of the intergranular strain tensor.
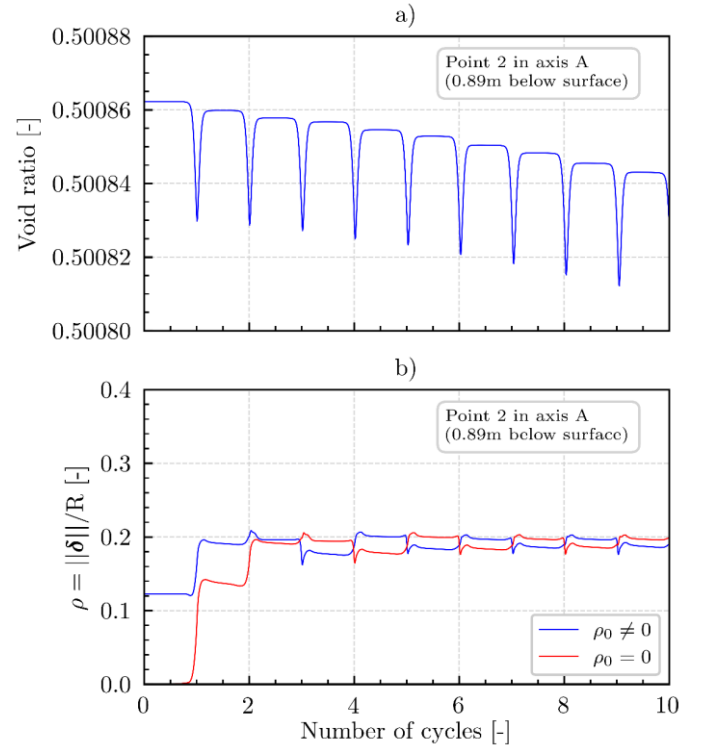
Figure 4. Evolution of state variables in the subsoil over the course of 10 tyre passages: a) void ratio and b) mobilization of the intergranular strain tensor.

3.3 *Surrogate soil model*

In the previous sections it has been shown that, the state variables do not change much after two cycles and therefore the stiffness of the soil can be considered constant. It is convenient to model the soil behaviour as a linear elastic material with a constant Poisson's ratio and a stress dependent Young's modulus E, which can be calculated from Equation 1.

$$E = E_{\text{ref}} \left(\frac{p'}{p'_{\text{ref}}} \right)^{\alpha} \tag{1}$$

The parameters of this stress dependent linear elastic model were calibrated using the results of the FE simulation with the hypoplastic model. For this purpose simulations of one-dimensional compression tests (oedometer test) with the hypoplastic model and the linear-elastic model were performed. The state variables after the ninths cycle were used as initial conditions for the oedometer tests. The parameters of the linear elastic model were adjusted to reproduce the stiffness calculated by the hypoplastic model with special emphasis to the low stress levels that the soil experiences underneath the road pavement, see Figure 5.
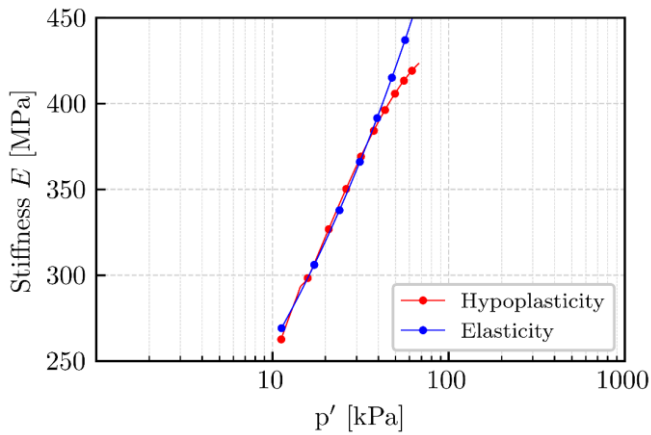
Figure 5. Calibration of the stress dependent linear elastic model parameters using oedometer tests ($\nu = 0.3$, $E_{ref} = 320,000$ kPa, $p'_{ref} = 20$ kPa and $\alpha = 0.3$).
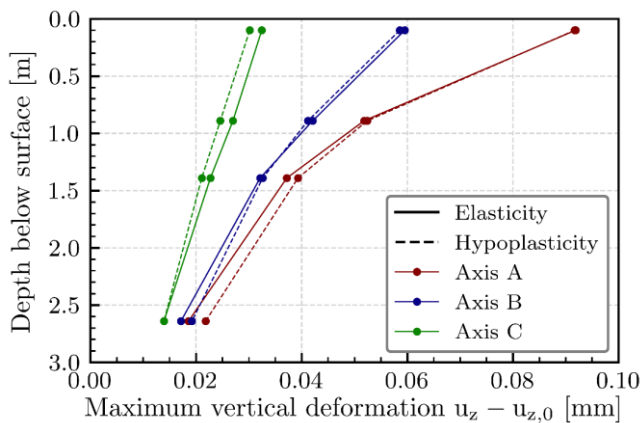
Figure 6. Comparison of the maximum vertical deformations in one cycle along the axes A, B, C calculated by the hypoplastic model and the stress dependent linear elastic model after modification of the parameters.

After calibrating the parameters of the elastic model, another simulation of the road pavement was performed. Figure 6 shows the maximum vertical deformation predicted by both the hypoplastic and elastic models. The elastic model was able to replicate the deformation behaviour in one cycle along the axes A,B, C quite well, after slightly adjusting the parameters to: $\nu = 0.3$, $E_{ref} = 240,000$ kPa, $p'_{ref} = 20$ kPa and $\alpha = 0.2$.

4 CONCLUSION

This study presented a numerical analysis of the road pavement behaviour, focusing on the integration of a realistic soil behaviour using an advanced hypoplastic material model for the subsoil.

The evolution of the state variables in the hypoplastic model under repeated wheel loading was evaluated. It was observed that, although the void ratio decreased, indicating compaction, the density change was minimal. Additionally, the intergranular strain tensor reached a quasi-static state after a few cycles and showed minimal variation thereafter. From these observations, it can be concluded that the stiffness of the subsoil can be effectively represented using a linear elastic model, provided that only a limited number of cycles are considered and the changes of the state variables remain small.

Using the results from the advanced hypoplastic model, a simplified surrogate soil model was calibrated, effectively replicating the deformation predictions of the hypoplastic model.

5 ACKNOWLEDGEMENTS

6 REFERENCES

Abdelkadr, A. O. (2023). Cyclic behaviour and liquefaction potential of silty sand: experimental and numerical investigations. PhD thesis, Universität Kassel.

Forschungsgesellschaft für Straßen und Verkehrswesen Arbeitsgruppe Infrastrukturmanagement (2012). Richtlinie für die Standardisierung des Oberbaus von Verkehrsflächen, RStO 12.

Hu, X. & Walubita L. F. (2011). Modeling mechanistic responses in asphalt pavements under three-dimensional tire-pavement contact pressure. Journal of Central South University of Technology 18 (1): 250-258.

Leutner, R. & Lorenzl, H. & Schmoeckel, K. (2006). Stoffmodelle zur Voraussage des Verformungswiderstandes und Ermüdungsverhaltens von Asphaltbefestigungen. BASt-Bericht S45.

Niemunis, A. & Herle, I. (1997). Hypoplastic model for cohesionless soils with elastic strain range. Mechanics of Cohesive-frictional Materials 2(4): 279-299.

Roddemann, D. (2022): TOCHNOG PROFESSIONAL User's manual, Version 14–02–2022.

Wegener, D. & Herle, I. (2014). Prediction of permanent soil deformations due to cyclic shearing with a hypoplastic constitutive model. geotechnik 37(2): 113-122.

Wolffersdorff, P.-A. (1996). A hypoplastic relation for granular materials with a predefined limit state surface. Mechanics of Cohesive-frictional Materials 1(3): 251-271.

Reintroducing the poker chip direct tension test for asphalt concrete mixtures

Abhilash Vyas
University of Illinois Urbana-Champaign

Ramez M. Hajj
University of Illinois Urbana-Champaign

ABSTRACT: Mode I fracture in flexible pavements occurs due to the inability of asphalt concrete (AC) mixtures to resist tensile stresses. At binder scale, microcracks nucleate and gradually coalesce into macrocracks at mixture scale. Various laboratory test procedures have been developed to simulate cracking behavior. This study reintroduces the AC poker chip test to evaluate cracking mechanisms in three AC mixes with varying Recycled Asphalt Pavement (RAP) content and compares the energy dissipated curves with two additional test methods: Indirect Tensile Test (IDT) and Illinois Flexibility Index Test (I-FIT). The results indicate that the AC poker chip test is a useful test geometry, as it allows for total energy dissipation into crack initiation and propagation. Specimens with higher aspect ratios were better suited for testing due to more uniform stress distributions. Finally, a unified energy-based characterization revealed that high RAP mixtures require greater energy for crack initiation but exhibit brittle crack propagation behavior.

1 INTRODUCTION

Cracking is a prevalent distress in asphalt concrete (AC) pavements, arising from tensile forces induced either by vehicular loads or temperature variations. While AC withstands compressive stresses well, it is inherently weak under tensile loading, leading to mode I fracture at critical tensile strain regions, such as the bottom of the AC layer. Cracks nucleate at the binder scale, where microcracks coalesce into macrocracks. Traditional dynamic shear rheometer (DSR) tests evaluate binders within the linear viscoelastic (LVE) range but fail to capture higher, nonlinear strain behavior (Hajj *et al.* 2018). To address this, the poker chip test has emerged as a reliable method for evaluating cracking resistance, offering realistic ductility measurement compared to bulk testing (Vyas *et al.* 2023). Though effective at the binder scale, its application at the fine aggregate matrix (FAM) and AC scales remains underexplored, with the only known study taking place more than 40 years ago (Bynum, 1979).

Various tests have been developed to evaluate asphalt concrete (AC) cracking resistance at intermediate temperatures. Strength-based tests, such as the Indirect Tensile Strength (IDT) and IDEAL-CT, assess cracking potential by applying compressive loads to cylindrical specimens, inducing tensile stresses along the horizontal diameter. However, concerns remain regarding the efficacy of these tests for ductile AC mixtures, as they produce non-uniform strain distribution and permanent deformation beneath the loading strip (Al-Qadi *et al.* 2022). The Illinois Flexibility Index Test (I-FIT) (Ozer *et al.* 2016), a notch-based SCB fracture test, effectively captures crack propagation but places less emphasis on crack initiation. Studying crack initiation effectively requires evaluating AC properties in an undamaged state, free from notch-induced effects. Additionally, energy dissipated during testing should be solely attributed to crack initiation and propagation, necessitating a testing mechanism involving pure tensile loading.
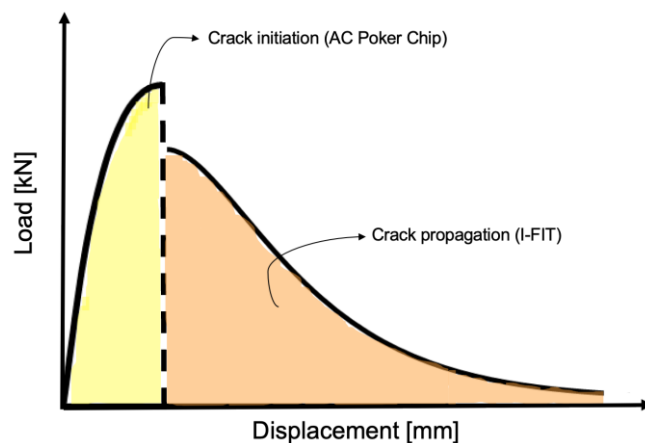
Figure 1. Isolating crack initiation and propagation.

To isolate the crack initiation process, a Direct Tension (DT) test, hereafter referred to as the Asphalt Concrete (AC) poker chip test, was employed. The test involves applying uniaxial tension to an AC specimen sandwiched between two metal plates under displacement control. Initially used during the SHRP studies in the 1990s, the DT test faced challenges with eccentric loading and complex specimen preparation. However, this test holds potential for studying crack initiation and total energy dissipation, if conducted diligently. This study reintroduces the AC poker chip test (Bynum 1979), evaluating different aspect ratios

and analyzing stress distribution using finite element modeling (FEM), aiming to develop a unified energy-based characterization (Figure 1) by combining crack initiation and propagation mechanisms. This creates a framework for further studies of the direct tensile behavior of AC mixes and the use of a triaxial state of stress in evaluating combined tensile/shear cracking in AC.

2 MATERIALS AND MIX DESIGN

A U.S. Federal Aviation Administration P-401 mix, designed using Type 2 gradation, was obtained from an airport paving contractor. Component materials—aggregates, binder, and anti-strip additives—were collected. Two additional AC mixtures were designed by incorporating 10% and 30% RAP into the control P-401 mix with no RAP. Figure 2 presents aggregate gradation curves within FAA specification limits.
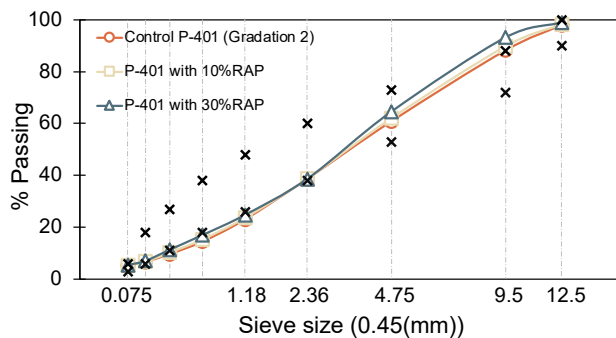
Figure 2. Gradation curves.

Aggregates were dried at 110°C for 24 hours, while recycled materials were dried at 50°C for 72 hours with periodic stirring. A Performance Grade (PG) 76-28 binder, modified with Styrene-Butadiene-Styrene (SBS), was used. To enhance adhesion and prevent stripping, a 0.4% liquid anti-strip additive (by binder weight) was added. Mixing and compaction temperatures were 173°C and 163°C, respectively. Short-term aging (STA) was performed at compaction temperature for one hour. Specimens were compacted using 75 gyrations with a Superpave Gyratory Compactor (SGC) to achieve 3.5% air voids and ≥15% Voids in Mineral Aggregates (VMA), per P-401 standards. The volumetric compositions of the mixes are shown in Table 1.

Table 1. Mix design parameters.

Mix type	Control P-401	P-401(10%RAP)	P-401(30%RAP)
Binder	PG 76-28	PG 76-28	PG 76-28
P_b (%)	6.2	6.2	6.2
Anti-strip	0.4%	0.4%	0.4%
ABR (%)	0	9.65	28.97
V_a (%)	3.46	3.53	3.51
VMA (%)	15.84	15.73	15.47

* P_b = Percent binder, ABR = Asphalt Binder Replacement, V_a = Air voids, VMA = Voids in Mineral Aggregates.

3. AC POKER CHIP TEST

3.1 Specimen preparation

AC cylindrical specimens with dimensions of 150 mm in diameter and 180 mm in height were prepared. Specimens were cored from the center and saw-cut into dimensions of 100 mm in diameter and 150 mm in thickness, ensuring that air voids met the requirement of 7 ± 1%. Subsequently, these specimens were further saw-cut at the midpoint to produce two specimens with dimensions of 100 mm × 50 mm and 100 mm × 25 mm. Two replicates were prepared for each mixture. Prior to the gluing process, all specimens were dried under a fan for a minimum of 24 hours to eliminate surface moisture. A high-strength epoxy was used for gluing. Steel plates with grooves were employed to prevent bonding failures between the epoxy and steel. A gluing jig was utilized to attach the top and bottom steel plates to the specimens, applying 40 g of epoxy to each side. To minimize the risk of eccentric loading during testing, diligent care was taken during the sawing process to ensure that the average diameter and thickness of the specimens were within ±1 mm tolerances.

3.2 Testing and results

A Universal Testing Machine (UTM) was employed for the tensile testing. Each specimen was securely mounted onto the testing frame, and a displacement-controlled load was applied at a constant rate of 0.5 mm/min to the top plate. The results were analyzed by plotting the load-displacement curves. The area under the curve represents the work done or the energy dissipated during the test.
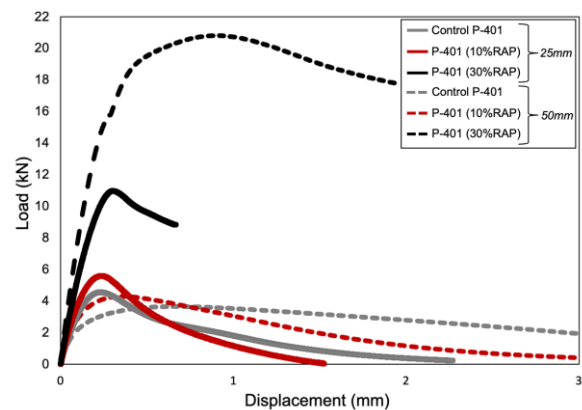
Figure 3. AC Poker chip output.

Figure 3 presents the load-displacement curves for the specimens. For both 50-mm and 25-mm specimens, it can be observed that an increase in RAP content consistently resulted in higher peak loads. Additionally, the post-peak behavior appeared significantly more brittle compared to the Control P-401. 25-mm specimens exhibited higher peak loads for both the Control P-401 and P-401 (10% RAP).

However, the opposite trend was observed for the P-401 (30% RAP), where the 50-mm specimen demonstrated a higher peak load. It is important to note that only one replicate was tested for the P-401 (30% RAP) 50-mm configuration, and testing is ongoing. Based on these preliminary results, it can be inferred specimens with a higher aspect ratio exhibited more brittle behavior and rapid crack propagation. The stress distribution in the 50-mm specimens appeared to be non-uniform, as indicated by an observed diagonal failure slope, whereas the failure plane in the 25-mm specimens was predominantly horizontal. These observations align well with the load-displacement data, and theory of edge effects. Furthermore, it can be postulated that while the mix without RAP exhibited ductile behavior during crack propagation, as evidenced by the gradual post-peak slope, the load required to initiate the crack was relatively low.

3 DIFFERENCES IN ENERGY DISTRIBUTION

Load-displacement curves were analyzed for three test setups: IDT test, I-FIT, and AC poker chip test. For the IDT test, three SGC specimens were prepared for each P-401 mixture. The specimens were compacted to dimensions of 95 mm in thickness and 150 mm in diameter, ensuring compliance with the air voids requirement of 7 ± 1%. The test involved applying a displacement-controlled diametrical load at a rate of 50 mm/min until specimen failure. The I-FIT was conducted following the AASHTO T 393-22 protocol. For each mixture, two SGC specimens were compacted with a diameter of 150 mm and a height of 160 mm. Each SGC specimen was then saw-cut into four SCB specimens, ensuring that the air voids satisfied the 7.0 ± 1% requirement. Load and displacement data were collected for both the IDT and I-FIT procedures. As observed in Figure 4, the area under the load-displacement curve for the IDT test is significantly larger compared to the I-FIT and AC poker chip tests. This inflated curve is primarily attributed to energy dissipation dominated by plastic deformation under the loading strip, with limited energy directed toward crack initiation and propagation. Consequently, the IDT test overestimates the energy associated with fracture formation, as it primarily captures the plasticity component rather than the energy dissipated exclusively for crack formation and propagation. In contrast, the area under the load-displacement curve for the I-FIT is comparatively smaller, reflecting its focus on measuring energy dissipation during crack propagation. The I-FIT is explicitly designed as a fracture test, with a loading scheme that minimizes energy dissipation toward plasticity and crack initiation. The inclusion of a notch effectively reduces plastic deformation energy, channeling the majority of the energy toward crack propagation. This makes the I-FIT particularly effective in distinguishing between brittle mixtures, where cracks propagate rapidly, and ductile mixtures, where crack growth is more gradual.
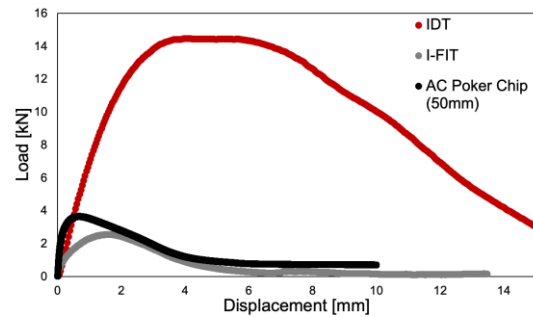
Figure 4. Avg. load-displacement curve for Control P-401.

However, while the I-FIT efficiently measures crack propagation, the presence of the notch limits its ability to capture crack initiation. The notch acts as a stress concentrator, bypassing the natural crack initiation process, which involves the nucleation and coalescence of microcracks from an undamaged state. The load-displacement curve from the AC poker chip test presents potential for an ideal setup, where the entire energy dissipation is associated with crack initiation and propagation. However, due to the randomness in crack formation, the energy dissipated toward crack propagation may not be as effectively captured as in the I-FIT, where the fracture is much more channelized. To address this limitation, the pre-peak portion of the AC poker chip test curve and the post-peak portion of the I-FIT curve were used to isolate the mechanisms of crack initiation and propagation, respectively.

4 EFFECT OF ASPECT RATIO

To evaluate the effect of aspect ratio on stress distribution, a simplified 3D AC specimen was modeled using the ABAQUS Finite Element Modeling (FEM) software. Three specimen thicknesses, all with a diameter of 100 mm, were simulated: 50 mm, 25 mm, and 3.125 mm, corresponding to aspect ratios of 2, 4, and 32, respectively. Although the 3.125 mm specimen is practically challenging to produce, it was included to examine the effects of a very high aspect ratio. The specimens were assigned viscoelastic properties and assumed to be homogeneous for the purposes of the simulation. The bottom face was constrained with an encastre boundary condition, restricting all structural degrees of freedom, while the top face was subjected to uniform tension at a displacement rate of 0.5 mm/min. The specimens were meshed using standard linear elements. Figure 5 shows the top view of the maximum principal (absolute) stresses on the top plate. The results indicate that an increase in aspect ratio leads to a more uniform stress distribution, corroborating the laboratory

findings from the AC poker chip test presented in Section 3. However, in this study, the aspect ratio was not further increased due to the nominal maximum aggregate size (NMAS) of the AC mixtures being 12.5 mm. Bynum (1979) demonstrated the feasibility of conducting tests on specimens with higher aspect ratios in mixtures with smaller NMAS.
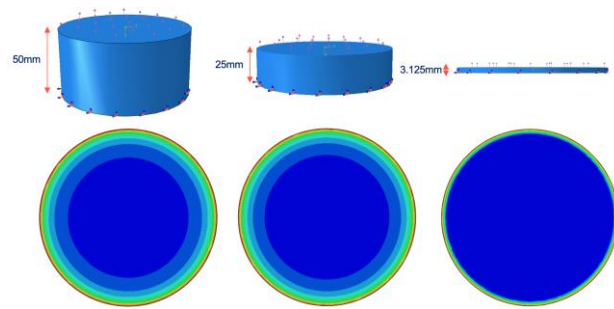
Figure 5. FEM results.

5 UNIFIED ENERGY-BASED ANALYSIS

The load-displacement curves from the AC poker chip test and the I-FIT were combined into a single curve to isolate the mechanisms of crack initiation and propagation (Figure 6). The pre-peak region from the AC poker chip test was used to represent crack initiation, while the post-peak region from the I-FIT was used for crack propagation. These two regions were merged into one curve to analyze the energy dissipated during each phase.
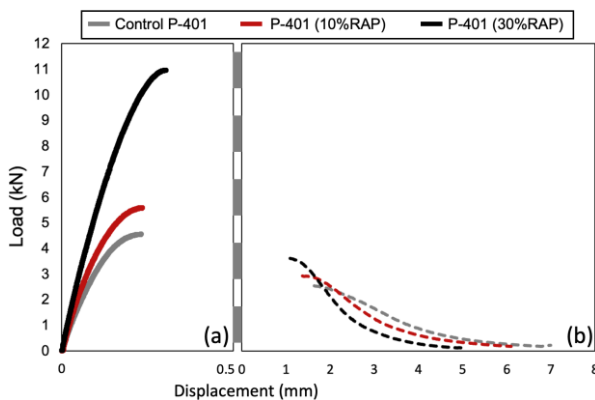
Figure 6. (a) Pre-peak AC poker chip, and (b) Post-peak I-FIT.

The results showed that the energy dissipated (or work done) to initiate cracking, as obtained from the AC poker chip test curve, was higher than that observed in a typical I-FIT output (Figure 6a). This difference is attributed to the presence of a notch in the I-FIT specimens, which bypasses the natural crack initiation process that begins from an undamaged state. However, the I-FIT setup is well-suited for studying crack propagation behavior, as seen in the post-peak region (Figure 6b). Compared to the control mix, the results indicate that while a larger amount of work is required to initiate a crack, the crack propagation is brittle, as evidenced by the steep slope of the post-peak curve when more RAP is included.

6 CONCLUSION

This study aimed to reintroduce the AC poker chip test as a method for evaluating cracking resistance in AC mixtures. Three airfield AC mixtures containing 0%, 10%, and 30% RAP were prepared and tested using IDT, I-FIT, and the AC poker chip test. The primary focus was on analyzing the load-displacement curves obtained from each testing procedure. It was observed that the IDT test tends to overestimate the energy associated with fracture formation, as it primarily captures the plasticity component rather than isolating the energy dissipated for crack initiation and propagation. In contrast, the I-FIT curve, which represents energy dissipation during crack propagation, yielded a smaller area under the curve. The presence of a pre-existing notch in the I-FIT limits its capability to evaluate crack initiation. AC poker chip test demonstrated significant potential as an ideal setup for evaluating crack initiation and propagation, as the entire energy dissipation could be directed solely toward these mechanisms. Results indicated that an increase in the aspect ratio (or a decrease in specimen thickness) led to a more uniform stress distribution, which was further validated through finite element modeling. Finally, a unified energy-based characterization approach was introduced. This approach revealed that, for high RAP mixtures, a larger amount of work is required to initiate a crack, while the crack propagation behavior is brittle, as indicated by the steeper post-peak slope. Future studies will explore higher aspect ratios to generate more shear and a triaxial stress state in the proposed test.

7 REFERENCES

Al-Qadi, I. L., Said, I. M., Ali, U. M., & Kaddo, J. R. (2022). Cracking prediction of asphalt concrete using fracture and strength tests. *International Journal of Pavement Engineering*, *23*(10), 3333-3345.

Bynum, D. (1979). Poker chip tests on bituminous concrete. *Matériaux et Construction*, *12*, 193-199.

Hajj, R., & Bhasin, A. (2018). The search for a measure of fatigue cracking in asphalt binders–a review of different approaches. *International Journal of Pavement Engineering*, *19*(3), 205-219.

Ozer, H., Al-Qadi, I. L., Lambros, J., El-Khatib, A., Singhvi, P., & Doll, B. (2016). Development of the fracture-based flexibility index for asphalt concrete cracking potential using modified semi-circle bending test parameters. *Construction and Building Materials*, *115*, 390-401.

Vyas, A., Wang, Y., Hajj, R., & Jahns, E. (2023). Investigation of factors affecting modified asphalt binder development and performance using the poker chip test. *Construction and Building Materials*, *403*, 133037.

A novel approach to predict aging performance of asphalt mixtures through oxygen diffusion analysis

Yi Wu

School of Highway, Chang'an University, Xi'an, China
Department of Civil, Chemical, Environmental and Material Engineering (DICAM), University of Bologna, Bologna, Italy

Yong Wen & Rui Li, Xuesong Wang

School of Highway, Chang'an University, Xi'an, China

ABSTRACT: This study investigated the relationship between oxygen diffusion and the aging performance of asphalt mixtures. The results showed as aging temperatures and porosity increased, the creep stiffness (S), creep rate (*m-value*), and creep recovery (R) values increased as well while the non-recoverable creep compliance (J_{nr}) and complex shear modulus at peak stress ($\Delta|G^*|_{peak}$) decreased. There was aging gradient along the depth, with deeper depths showing less severe aging. The R, S, and *m-value* increased with the increase of oxygen diffusion coefficient (D_s), while the Jnr and $\Delta|G^*|_{peak}$ decreased. The most significant correlations were found between the D_s and the R at 0.1kpa, the J_{nr} at 3.2kpa, and $\Delta|G^*|_{peak}$. The prediction model of the aging behavior of the asphalt mixtures was developed based on these indicators. The root mean square error of prediction models for $R_{0.1}$、 $\Delta|G^*|_{peak}$ and $J_{nr3.2}$ were 1.816, 0.0383, and 0.0309, respectively.

1 INSTRUCTION

The asphalt aging is one of major contributors to the decrease in the performance of asphalt pavement. Among various aging factors, oxygen plays a critical role. It can react with various asphalt constituents, destroying the original structure and changing the properties of asphalts (Somé et al., 2023).

The oxygen initially reacts with asphalt at the pavement's surface, and the rate of this reaction is highly dependent on pavement temperature and oxygen concentration (Xie et al., 2023). Subsequently, oxygen gradually diffuses into the interior of asphalt pavement through its pores (Petersen and Harnsberger, 1998). The concentration of oxygen form a gradient in the depth direction of the pavement (Chen et al., 2023, Sun et al., 2023). The process of oxygen diffusion is related to the oxygen diffusion coefficient (D_s) (Malinowski, 2023). The D_s represents the rate at which oxygen diffuses through a specific material, with higher values indicating a faster diffusion rate within the material. The reaction between oxygen and asphalt is then highly dependent on pavement temperature and oxygen concentration (Xie et al., 2023). The higher the value of D_s, the more oxygen penetrates the pavement, and becomes available to react with asphalt binders. Understanding oxygen diffusion behavior in asphalt pavement is key to studying asphalt aging in asphalt pavements.

Most studies have focused on oxygen diffusion behavior in base asphalt (Darabi et al., 2017, Chen and Wang, 2024, Sun et al., 2023). However, research on oxygen diffusion in modified asphalts remains limited. While SBS-modified asphalt is increasingly prevalent in practical engineering applications (Xu et al., 2022). Further insight is needed into the oxygen diffusion behavior within modified asphalt mixtures to improve their applicability in practical engineering. Additionally, the correlation between oxygen diffusion behavior and the aging behavior of asphalt mixtures requires further investigation.

This study investigated the aging behavior and oxygen diffusion behavior of SBS-modified asphalt binders. Oxygen diffusion tests and rheological properties tests were conducted on the asphalt binders extracted from the asphalt mixtures after being aged at different temperatures and porosity. A correlation analysis between the aging characteristics and the D_s was then conducted. The indicators that are significantly correlated with the D_s were used to develop an aging prediction model for the modified asphalt mixture.

2 MATERIALS AND METHODS

2.1 *Materials*

Base asphalt (penetration grade 70, Table 1) from Shnopec Maoming Petrochemical Company was used in this study to prepared for SBS modified asphalt binders. The SBS modifier is 1401, and the aggregate and mineral powder used were limestone.

The lignin fiber was selected to optimize the void distribution of the specimen.

Table 1. Technical specifications of base asphalt.

Technical Specifications	Unit	Testing results
Penetration (25°C, 100g, 5s)	0.1mm	67
Ductility (5cm/min, 10°C)	cm	48
Softening point	°C	24

2.2 Specimen Preparation

SBS-modified asphalt was prepared using a high-speed shearing machine, with an SBS modifier dosage of 5% by weight, and 0.1% sulfur was added as a stabilizer. The asphalt mixture (SMA-13) was prepared using aggregates with a maximum nominal size of 13 mm and an asphalt content of 5.8% by weight of the aggregate. The asphalt mixture specimens were prepared using the rotary compaction method, with target porosities of 4%, 6%, and 8% at 35°C, 45°C, and 55°C.

2.3 Testing Methods

2.3.1 Oxygen diffusion test

The diffusion test was conducted using a self-developed apparatus. The oxygen diffusion test equipment consists of a closed double-chamber device, an oxygen sensor, a constant temperature insulation cabinet, and a data acquisition instrument (Figure 1(a)). The tests were performed on specimens with porosities of 4%, 6%, 8%. at 35°C, 45°C, and 55°C.
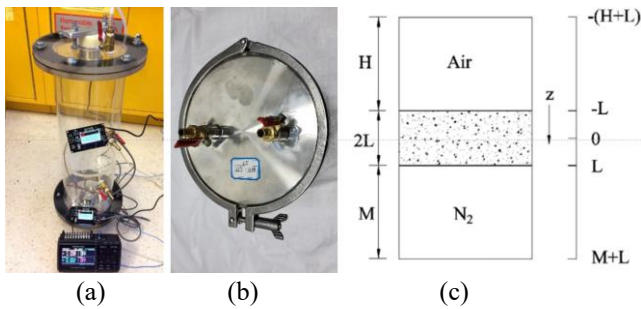
Figure 1. Test devices: (a) oxygen diffusion test device, (b) long-term aging test device, (c) double air chamber closed device.

2.3.2 Long-term aging test

An oxygen-enriched environment was used to accelerate the aging process to simulate the aging conditions of asphalt pavement under different environmental temperatures. A customized aging container was developed for indoor long-term aging tests on specimens with porosities of 4%, 6%, and 8%, which were subjected to temperatures of 35°C, 45°C, and 55°C for four weeks.

2.3.3 Rheological Properties

The SMA-13 mixtures with different aging degrees were cut into four slices along the radial direction, and the aged asphalt binders were then extracted from the slices for subsequent rheological tests.

The frequency sweep test was conducted to investigate the viscoelastic properties of the SMA-13 mixtures after being aged at 40°C, 52°C, 64°C, and 72°C. The multi-stress creep recovery (MSCR) test was performed at the asphalt PG high temperature under shear stresses of 0.1 kPa and 3.2 kPa respectively. (Liu et al., 2021, Zhang et al., 2015). The average recovery rates ($R_{0.1}$ and $R_{3.2}$) and irrecoverable creep compliance ($J_{nr0.1}$ and $J_{nr3.2}$) were selected to investigate the high-temperature performance of the SMA-13 mixtures after aging. The linear amplitude sweep test (LAS) was performed under 10 Hz frequency. The $\Delta|G^*|_{peak}$ was used to evaluate the fatigue performance of asphalt after aging (García Mainieri et al., 2021). The DSR-based asphalt low-temperature performance test method was explored by Sui et al. (Sui et al., 2011). The creep stiffness modulus S characterizes the low-temperature deformation capacity of asphalt, and the creep rate m-value characterizes the low-temperature stress relaxation capacity of asphalt.

2.4 Determination of D_s

The D_s was calculated using the finite volume method (Wen and Wang, 2018). The equations for the two-chamber diffusion system are shown in Equation 1 (SallamJury and Letey, 1984). The boundary conditions were set according to Equation 2-4, and the initial conditions were set according to Equation 5-7.

$$\frac{\partial C_g(z,t)}{\partial t} = D_g \frac{\partial^2 C_g(z,t)}{\partial z^2} \tag{1}$$

$$\frac{\partial C_g(z,t)}{\partial z} = 0 \ (z = -(L+H) \text{、} \ z = L+M) \tag{2}$$

$$C_g(z,t) = C_s(z,t)(Z = \pm L) \tag{3}$$

$$-D_g \frac{\partial C_g(z,t)}{\partial z} = -D_s \frac{\partial C_s(z,t)}{\partial z}(Z = \pm L) \tag{4}$$

$$C_g(z,0) = C_0(-(L+H) < z < -L) \tag{5}$$

$$C_g(z,0) = 0(-L < z < L) \tag{6}$$

$$C_g(z,0) = 0(L < z < L+M) \tag{7}$$

where C_g = air chamber gas concentration, kg/m³ of air; t = time, s; z = distance along chamber, cm; D_g =

gas diffusion coefficient in air, cm³/min; H = length of air chambers, cm; L = one-half length of soil chamber, cm; C_s = asphalt mixture gas concentration, kg/m³ of air; D_s = oxygen diffusion coefficient in asphalt mixture, cm²/min; M = molecular weight, gm/mol.

3 RESULTS AND DISCUSSION

3.1 Oxygen diffusion coefficient

The calculated D_s results are shown in Figure 2. It can be seen from the figure that D_s values increased with the increase of the testing temperature and the specimen porosity. The results show that the rate of D_s growth increased more rapidly when the temperature increased by 436% from 35°C to 45°C. Porosity also caused a considerable rise in D_s, D_s increased by 820% from 6% to 8% porosity at 45°C. A similar trend was found at 35°C and 55°C. These findings suggest that porosity has a greater impact on D_s than temperature.
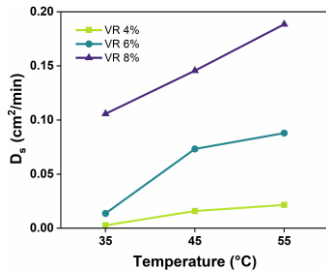
Figure 2. D_s with different temperatures and void ratios

3.2 Rheological properties

Figure 3 (a) shows the results of aging indicators under different temperatures and porosity. The results show that $R_{0.1}$ and $R_{3.2}$ exhibited a positive correlation with both testing temperature and porosity. The $J_{nr0.1}$ and the $J_{nr3.2}$ both decreased significantly with increasing temperature from 35°C to 55°C, by -33.78% and -29.07%, respectively. Regarding the effect of porosity, the $J_{nr0.1}$ and $J_{nr3.2}$ exhibited an overall reduction of -13.08% and -27.34% when porosity increased from 4% to 8%, respectively. The $\Delta|G^*|_{peak}$ also showed a negative correlation with both temperature and porosity. The S exhibited low sensitivity to external factors, with only a slight increase of 1.46% under varying temperatures and porosity. The m-value was highly sensitive to temperature changes, decreasing significantly by -36.65% with rising temperature from 35°C to 55°C. These results suggest that asphalt aging becomes more severe at higher aging temperatures and higher mixture porosity.

Figure 3 (b) shows the aging index results at different depths. As the aging depth increased, $R_{0.1}$ showed a slight increase while $R_{3.2}$ increased steadi-

ly with aging depth. $J_{nr0.1}$ and $J_{nr3.2}$ decreased by -9.59% and -33.65% with increasing aging depth, respectively. The $\Delta|G^*|_{peak}$ increased at layer 4 after initially declining slightly. The S value remained relatively stable, but the m gradually decreased with depth. These findings highlighted the aging gradients in the depth direction of the asphalt mixture and demonstrated that aging is less severe at lower aging depths.

(a)   (b)
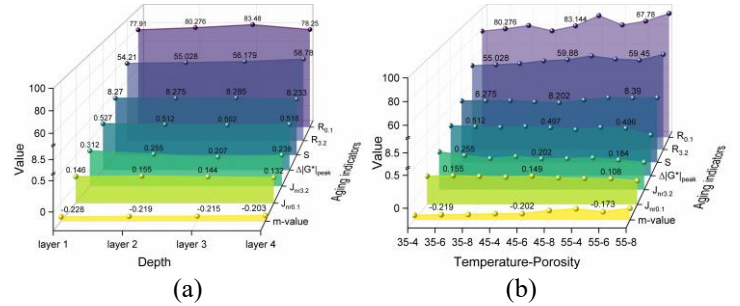
Figure 3. (a) Aging indicators under different temperatures and porosity; (b) Aging indicators under different depth
* The x-axis label '35-4' represents a mixture with 4% porosity aged at 35°C, Other labels follow the same pattern; The depths from layer 1 to layer 4 are 10mm, 20mm, 30mm, and 40mm respectively.

3.3 Correlation between D_s and Aging indicators

The correlation coefficients between the aging indices and D_s of $R_{0.1}$、$\Delta|G^*|_{peak}$, $J_{nr3.2}$, $R_{3.2}$, $J_{nr0.1}$, m-value, S were 0.92, -0.88, -0.82, 0.76, -0.65, 0.57, and 0.39, respectively. Among these variables, $R_{0.1}$、$\Delta|G^*|_{peak}$ and $J_{nr3.2}$ exhibited the highest correlation coefficients with D_s. Therefore, these three indicators were selected to develop a predictive model with aging temperature (T) and aging time (t). The predictive model was then developed using nonlinear regression analysis, as shown in Equations (8)-(10).

$$R_{0.1} = 108.54D_s^2 - 0.026831t^2 - 0.016122T^2 + 37.951D_s + 1.8591t + 1.7802T + 3.4624 \qquad (8)$$

$$J_{nr3.2} = 1.592D_s^2 + 0.00015079t^2 - 0.84655D_s - 0.011821t - 0.0027383T + 0.59622 \qquad (9)$$

$$\Delta|G^*|_{peak} = -0.038551D_s^2 - 0.00021032t^2 + 0.00043122T^2 + 0.32759D_s + 0.014309t - 0.035841T + 8.7632 \qquad (10)$$

The D_s and corresponding aging index data were incorporated into the prediction model to obtain the predicted values of the aging index, as shown in Figure 4. The data points were evenly distributed on both sides of the 45° line, with $R_{0.1}$ values being the closest to the line. This indicates excellent agreement between the predicted and observed values for $R_{0.1}$. The Coefficient of Determination (R^2) values for the prediction equations of $R_{0.1}$, $\Delta|G^*|_{peak}$, and $J_{nr3.2}$ were 0.9611, 0.8394, and 0.7654, respectively, further confirming that the predictive equations for SBS-modified asphalt binders is reliable.
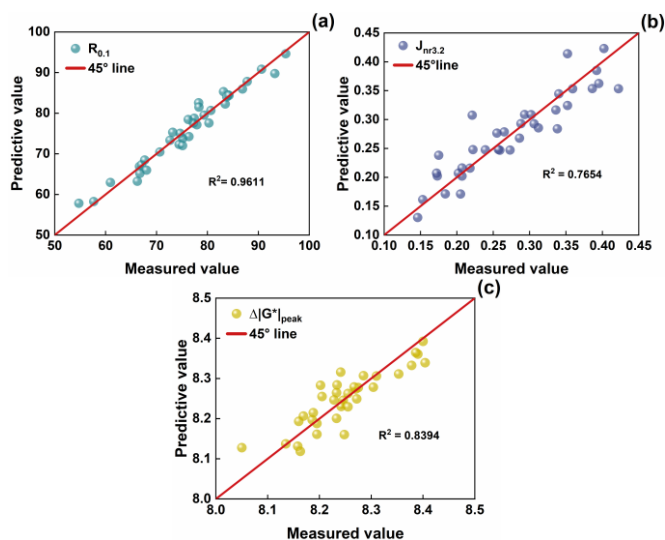
Figure 4.   The distribution plots of predicted value and measured values for (a) $R_{0.1}$, (b) $\Delta|G^*|_{peak}$, (c) $Jnr_{3.2}$.

4 CONCLUSIONS

This study investigates the aging behavior of the SMA-13 mixture using oxygen diffusion tests and rheological proper-ties tests. The following conclusions can be drawn:

1. The D_s exhibits positive correlation with $R_{0.1}$, $R_{3.2}$, *m-value*, and S, and negative correlations with $\Delta|G^*|_{peak}$, $J_{nr3.2}$, and $J_{nr0.1}$. Among these indexes, $R_{0.1}$, $\Delta|G^*|_{peak}$, and $J_{nr3.2}$ demonstrate the strongest correlations with D_s.

2. The R, S, and *m-value* exhibit positive correlations with aging temperatures and porosity while showing negative correlations with J_{nr} and $\Delta|G^*|_{peak}$ values. Distinct aging gradients were observed along the aging depth profile, characterized by decreasing R-values, increasing J_{nr} *values*, and $\Delta|G^*|_{peak}$ at deeper aging depths, indicating reduced aging severity.

3. The calculated values from aging indices prediction equations closely matched the measured values, with data points closely aligning along the 45° line. There are no significant deviations were observed. The R^2 values for the predicted models for the aging performance indicators represent high accuracy.

5 REFERENCES

CHEN, X. & WANG, Y. Quantitative Evaluation of the Oxygen Retarding Efficiency of Pavement Preventive Maintenance Using the Oxygen Diffusion Coefficient of Asphalt Mixtures.   International Conference on Maintenance and Rehabilitation of Pavements, 2024. Springer, 295-301.

CHEN, X., WANG, Y., WEN, Y., CHENG, H. & HAO, G. 2023. Oxygen diffusion coefficients of asphalt mixtures and their impacts on mixture aging.

Transportation Research Record, 03611981221143117.

DARABI, M. K., RAHMANI, E., LITTLE, D. N., MASAD, E. A. & RUSHING, J. F. 2017. A computational-experimental method to determine the effective diffusivity of asphalt concrete. *Journal of Engineering Mechanics,* 143, 04017076.

GARCíA MAINIERI, J. J., SINGHVI, P., OZER, H., SHARMA, B. K. & AL-QADI, I. L. 2021. Fatigue tolerance of aged asphalt binders modified with softeners. *Transportation Research Record,* 2675, 1229-1244.

LIU, H., ZEIADA, W., AL-KHATEEB, G. G., SHANABLEH, A. & SAMARAI, M. 2021. Use of the multiple stress creep recovery (MSCR) test to characterize the rutting potential of asphalt binders: A literature review. *Construction and Building Materials,* 269, 121320.

MALINOWSKI, S. 2023. Aromatisation process as part of bitumen ageing in the light of electronic structure and further oxidation of its components. *Construction and Building Materials,* 366, 130198.

PETERSEN, J. C. & HARNSBERGER, P. M. 1998. Asphalt aging: dual oxidation mechanism and its interrelationships with asphalt composition and oxidative age hardening. *Transportation Research Record,* 1638, 47-55.

SALLAM, A., JURY, W. & LETEY, J. 1984. Measurement of gas diffusion coefficient under relatively low air-filled porosity. *Soil Science Society of America Journal,* 48, 3-6.

SOMé, S., KOUEVIDJIN, A., MOUILLET, V., FEESER, A., BARTHéLéMY, J.-F. & BEN DHIA, H. 2023. Evaluation of effects of short and long-term thermo-oxidative aging on chemo-rheological and mechanical properties of asphalt concretes. *Road Materials and Pavement Design,* 24, 2827-2856.

SUI, C., FARRAR, M. J., HARNSBERGER, P. M., TUMINELLO, W. H. & TURNER, T. F. 2011. New low-temperature performance-grading method: Using 4-mm parallel plates on a dynamic shear rheometer. *Transportation Research Record,* 2207, 43-48.

SUN, L., GU, X., WEN, Y., DONG, Q. & HU, D. 2023. Investigation of oxygen diffusion behavior in asphalt mixtures using molecular dynamics simulations and laboratory test. *Journal of Materials in Civil Engineering,* 35, 04023300.

WEN, Y. & WANG, Y. 2018. Determination of oxygen diffusion coefficients of compacted asphalt mixtures. *Construction and Building Materials,* 160, 385-398.

XIE, H., LIU, Y., LONG, Z., XU, F., YOU, L., TANG, X., ZHU, C. & DING, Y. 2023. Micro-characterization of the adhesion properties and mechanisms at the asphalt-silica aggregate interface under combined thermal-oxygen aging and chloride salt erosion. *Construction and Building Materials,* 401, 132818.

XU, X., SREERAM, A., LENG, Z., YU, J., LI, R. & PENG, C. 2022. Challenges and opportunities in the high-quality rejuvenation of unmodified and SBS modified asphalt mixtures: State of the art. *Journal of Cleaner Production,* 378, 134634.

ZHANG, J., WALUBITA, L. F., FARUK, A. N., KARKI, P. & SIMATE, G. S. 2015. Use of the MSCR test to characterize the asphalt binder properties relative to HMA rutting performance–A laboratory study. *Construction and Building Materials,* 94, 218-227.

Identification on Blending Zone and Qualitative Analysis of Blending Degree in Recycled Asphalt Based on ESEM-EDX Analysis

Rui Wu[1], Yi Li[1, *], Xueyan Liu[1,*], Sandra Erkens[1], Arjan Thijssen[2]

1. Delft University of Technology, Faculty of Civil Engineering & Geosciences – Section of Pavement Engineering, Stevinweg 1, 2628 CN Delft, The Netherlands

2. Delft University of Technology, Faculty of Civil Engineering & Geosciences - Department of Materials & Environment, Stevinweg 1, 2628 CN Delft, The Netherlands

ABSTRACT: Recycled Asphalt (RA) offers economic and environmental benefits in pavement construction in Netherlands, but also faces a high potential for premature cracking, especially when it is used in porous asphalt. One main reason is the blending of aged and fresh material components will lead to complex internal microstructure in RA, which is the weak zone where cracking is initiated. However, preliminary research was not systematically describing blending zones at the microscale. This study utilized ESEM-EDX testing to characterize and analyze the internal structure of RA. An identification method was developed by converting EDX element mapping results into internal morphology maps. This method, incorporating boundary recognition, threshold segmentation, and data interpolation, successfully classified the internal structure of RA into six components: fresh mastic, aged mastic, blended mastic, aggregate, filler, and epoxy. Qualitative analysis of the blending degree using this method revealed that fresh aggregates achieve a more thorough blending state than RAP aggregates, as evidenced by the absence presence of aged mastic attachment. This research advances the understanding of RA's internal structure and blending behavior, laying a solid foundation for future quantitative analysis of blending degrees in RA.

1 INTRODUCTION

With increasing emphasis on sustainability in pavement construction, particularly supported by the Circular Economy Action Plan in Europe, Recycled Asphalt (RA) is becoming a preferred choice due to its economic and environmental benefits. However, incorporating Reclaimed Asphalt Pavement (RAP) into RA introduces challenges, especially in raveling failure when used in porous asphalt (Zaumanis and Mallick, 2015). Raveling is significantly caused by weak zones prone to cracking initiation and propagation due to the incomplete blending of aged bitumen with fresh bitumen (Xing et al., 2023). Therefore, accurately identifying the blending degree of aged and fresh bitumen is crucial for evaluating the performance of asphalt mixtures and getting reliable road materials design.

Microscopic testing methods have proved the feasibility in observing the asphalt microstructures. Among various methods, Environmental Scanning Electron Microscopy (ESEM) is particularly suited for analyzing oily and non-conductive asphalt samples (Mazumder et al., 2018). Aggregates and mastics can be distinguished in ESEM based on the differences in the detected atomic weights of their elemental components. However, fresh and aged mastic areas, which exhibit overlapping elemental compositions, are difficult to distinguish using ESEM. Energy Dispersive X-ray Spectroscopy (EDX) analysis is typically used for differentiation.

Preliminary research has demonstrated the feasibility of ESEM-EDX test techniques for distinguishing the fresh and aged mastic within RA with different indicators. For example, in research using TiO_2 as a tracer, Abdalfatta employed the Ti/S peak area ratio in EDX results as an indicator to evaluate the blending degree at pre-selected points (Abdalfattah et al., 2021). Similarly, Jiang used the Ti/S as an indicator to evaluate the blending degree in limited regions (Jiang et al., 2018). Castorena selected the Ti/C ratio as an indicator, successfully analyzed blending degree at pre-selected points(Castorena et al., 2016).

Although current studies have confirmed the multiphase structure within the blending zone, consisting of aged mastic, fresh mastic, and blended mastic, they assume that blended mastic was a homogeneous phase. As a result, they rely on values of single point or localized areas to estimate the blending degree of the entire microstructure, which fails to capture the heterogeneity of the blending zone in RA (Bowers et al., 2014).

To make a more intuitive description of blending zone and reliable analysis of blending degree, this research develops a methodology to identify the blending zone and visualize the distribution of aged, blended and fresh mastics in RA, based on ESEM-EDX test methods and successfully performs a qualitative analysis of the blending degree within RA.

2 MATERIALS

Two types of samples were tested for ESEM-EDX in this experiment: stone-mastic samples and artificial RA samples. These samples are separately used in Step 1 and Step 2, as introduced in Chapter 3.

Stone-mastic samples were developed to analyze the elemental content of individual components, providing a theoretical basis for qualitative analysis. These samples were prepared by immersing aggregates in aged and fresh mastic, both made with bitumen and filler in a 1:1 mass ratio. Fresh mastic used 70/100 penetration bitumen (Total Energy Netherlands), while aged mastic was produced by aging fresh bitumen according to AASHTO R28 (PAV) procedures, extended to 40 hours (2PAV) to simulate 10 years of field pavement aging (Singhvi et al., 2022). To distinguish fresh mastic, 12% of the filler (by mass) was replaced with TiO_2.

RA samples were designed to study blending zones during RA production. They were prepared in the lab to ensure precise control, using the same aged and fresh mastic as the stone-mastic samples. RAP was created by mixing aged mastic with 8 mm aggregates, and RA was produced by combining RAP with 4 mm aggregates and fresh mastic, with a RAP content of 50%.

All test samples will be stabilized with epoxy and cut into small thin pieces. After the grinding and polishing processes, samples' surface came smooth, which is a necessary requirement in ESEM-EDX test. Micro-morphology was analyzed using an FEI Quanta FEG 650 ESEM, equipped with a silicon drift Thermo Fischer EDX detector.

3 RESEARCH METHEDOLOGY

This research consists of two main steps. The first step focuses on establishing the visualization process in element mapping from EDX results. The second step is identifying the blending zone based on visualization processing.

3.1 *Step 1: Visualization Process Decision*

In Step 1, as previously mentioned, microscopic images obtained from ESEM cannot distinguish between fresh and aged mastic. Therefore, to visualize all components-epoxy(E), aggregate(A), fresh mastic(FM), aged mastic(AM) and blended mastic(BM), and their distribution, element mapping from EDX is required. Thus, the visualization process means classifying the scattered data points into different components. There are two methods: one is based on boundary identification, and the other is based on chemicals indicator selection.

The E and A components can be classified by boundary identification because their boundaries are distinct in the ESEM microscopic images. Boundary recognition is typically achieved through digital image processing (DIP) techniques, with the workflow shown in Figure 1. Typical DIP steps(Coenen et al., 2012) involves following operations: include: a) image smoothing; b) selecting an H_{max} (maximum gray value); c) applying watershed transformation; d) identifying epoxy and aggregate components; e) marking and exporting boundaries.
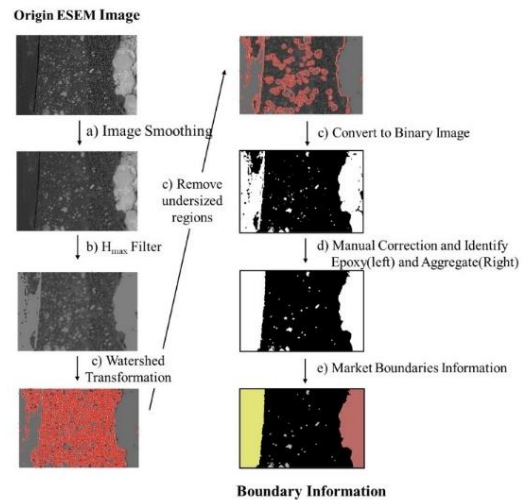
Figure 1 Illustration of DIP Operations

Since ESEM cannot distinguish between different mastic components, AM, BM and FM can only be classified by their chemical contents' values. Therefore, the choice of element type and the threshold value used as classification criteria determine the accuracy of their identification. Because stone-mastic samples only consist of AM and FM, by analyzing the characteristic elements and their threshold values in the AM and FM regions, a more accurate classification scheme on AM, FM, and BM can be developed.

3.2 *Step 2: Blending Zone Identification*

After completing the visualization process by stone samples, it was applied to RA samples that underwent the mixing process. Aggregates originating from RAP and newly added aggregates were selected for qualitative analysis and to identify morphological information of AM, FM, BM in the blending zone.

4 RESULTS AND DISCUSSION

4.1 *Boundary Identification*

There are four types of stone samples in step 1. Their internal multi-layer structure from left to right are listed: E-FM-A, E-AM-A, E-FM-AM-A, E-AM-FM-A. According to the DIP techniques, the boundaries of different phases were successfully identified. Taking E-AM-FM-A for example, the elements distribution is shown in Figure 2.

In Figure 2, three lines from left to right represent the boundaries of epoxy, mastic, and aggregate from DIP technology. In Figure 2(b), a sharp change in 'S' content occurs at the identified E and A boundaries. In the actual material composition, the epoxy and aggregate are also significantly having lower 'S' than mastics. This indicates that the boundaries of epoxy and aggregate from DIP align with the actual component boundaries. Furthermore, the 'Ti' distribution in Figure 2(a) shows that only the FM, which contains TiO_2 tracer, exhibits a significantly higher Ti content. This confirms the accuracy of the mastic boundary. So, Figure2 shows the accuracy of all three boundaries identification.

Figure 2 Element Mapping in EDX (weight percentage) of E-AM-FM-A sample: a) Ti; b) S; c) O; d) Si; e) K; f) Fe.

4.2 Indicator and its threshold

The quantitative analysis results of four samples are shown in Figure 3. The average value of all data points is taken as the representative value for that component.
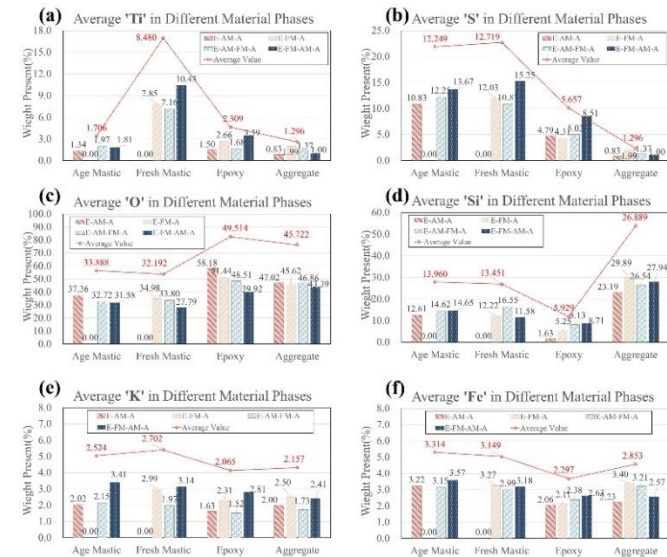
Figure 3 Contents of Different Elements in Samples and Their Average Value Comparison: a) Ti; b) S; c) O; d) Si; e) K; f) Fe.

As shown in Figure 3, the elemental distribution characteristics of the four samples align with the E-FM-AM-A. For elements 'S' and 'O', their concentrations in AM and FM differ significantly from those in E and A. 'Si' exhibits the highest concentration in A, while 'K' and 'Fe' are relatively evenly distributed among the four components. However, for the most critical AM and FM phases, these five elements did not exhibit significant differences. Only 'Ti' showed a clear distinction between AM and FM. Therefore, the average 'Ti' content is chosen as the indicator to represent the characteristic element of AM and FM. Specifically, the characteristic 'Ti' content is 8.0 for AM, 2.0 for FM.

4.3 Identification of Blending Zone in RA

After deciding the visualization steps, they are applied to the morphology identification of microstructure in RA. This requires two additional supplementary steps.

The first step is recognizing the boundaries of fillers, as shown in Figure 4. Different from stone-mastic samples (200x), the ESEM-EDX analysis of RA samples is conducted at a much higher magnification (3000x), which needs to take account of filler particles' influence. So, the filler regions within the mastic are individually marked.

Figure 4 DIP Techniques and Its Results in RA Samples: a) Original ESEM Image; b) Image with Identified Particles, yellow for epoxy, red for aggregate, grey for fillers; c) epoxy and aggregate boundaries; d) filler boundaries

The second supplementary step involves performing data interpolation. Because 'Ti' is distributed in the mastic form of discrete particles, resulting in a discontinuous distribution.

Figure 5 shows the results when applying the visualization process mentioned in Sections 4.1 and 4.2 to identify the bending zone. Ti weight percentages of 8.0 and 2.0 represent AM and FM, respectively, dividing the mastic area into three parts: 0–2.0 for AM, 2.0–8.0 for BM, and 8.0–10 for FM. Using boundaries and indicator thresholds, the original Ti element map in Figure 6(a) is visualized in Figure 6(b). In Figure 6(b), there is a substantial presence of blank points, which are incorrectly identified as AM. To fill these blank points with appropriate values, median, mean, and Gaussian filters were applied, with results shown in Figures 6(c), (d), and (e). The Gaussian

filter proved to be the most suitable for achieving a continuous distribution of mastic components, as shown in Figure 6(e), and is thus chosen for data processing.
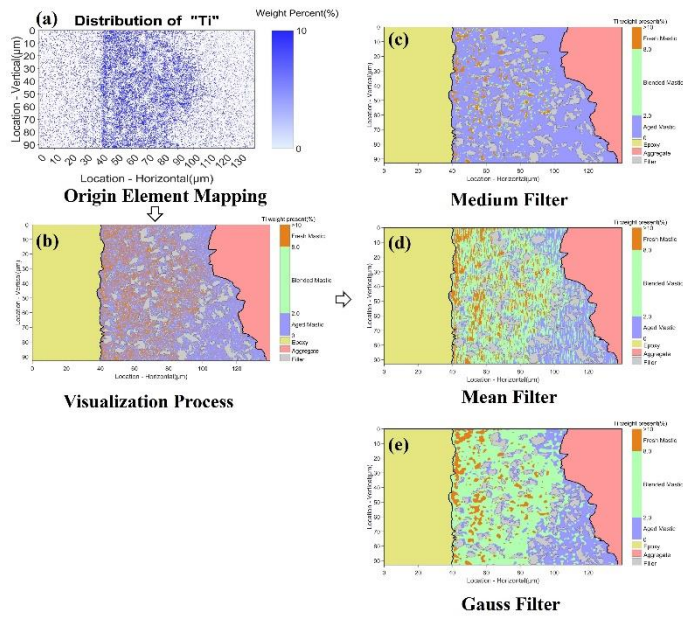
Figure 5 Visualization of Ti Element Distribution in RA Samples: a) Original element map; b) Dataset after boundary identification and threshold segmentation; c) Median filter applied; d) Mean filter applied; e) Gaussian filter applied.

4.4 Blending Degree in RA

Using the visualization approach described above, the mastic region in RA was successfully divided into AM, FM, and BM components, enabling the characterization of blending zone morphology. Two stones—one from RAP(8mm) and one from fresh aggregate(4mm)—were selected for observation. The results are shown in Figure 6. After mixing, the RAP-origin stone retains a coating of aged mastic, while the stone from fresh aggregate is surrounded by a more uniform layer of blended mastic.
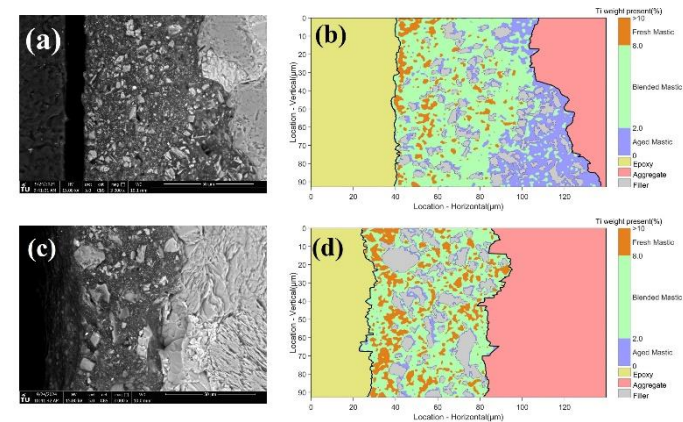
Figure 6 Micro-morphology of Aggregate in RA and Their Visualization Map: (a)(b) RAP; (c)(d) fresh aggregate

5 CONCLUSIONS

This research demonstrates a set of analysis tools to visualize the blending zone in RA using TiO$_2$ as the tracer, with ESEM-EDX characterization. This visualization approach effectively illustrates the multi-layer structure aged-blended-fresh mastics, and directly reveals the different blending conditions between the aggregate from RAP and fresh aggregates. This research provides a reliable methodology for quantitative analysis of the blending degree in RA.

ACKNOWLEGEMENT

REFERENCE

ABDALFATTAH, I. A., MOGAWER, W. S. & STUART, K. 2021. Quantification of the degree of blending in hot-mix asphalt (HMA) with reclaimed asphalt pavement (RAP) using Energy Dispersive X-Ray Spectroscopy (EDX) analysis. *Journal of Cleaner Production,* 294**,** 126261.

BOWERS, B. F., HUANG, B., SHU, X. & MILLER, B. C. 2014. Investigation of Reclaimed Asphalt Pavement blending efficiency through GPC and FTIR. *Construction and Building Materials,* 50**,** 517-523.

CASTORENA, C., PAPE, S. & MOONEY, C. 2016. Blending Measurements in Mixtures with Reclaimed Asphalt: Use of Scanning Electron Microscopy with X-Ray Analysis. *Transportation Research Record,* 2574**,** 57-63.

COENEN, A. R., KUTAY, M. E., SEFIDMAZGI, N. R. & BAHIA, H. U. 2012. Aggregate structure characterisation of asphalt mixtures using two-dimensional image analysis. *Road Materials and Pavement Design,* 13**,** 433-454.

JIANG, Y., GU, X., ZHOU, Z., NI, F. & DONG, Q. 2018. Laboratory Observation and Evaluation of Asphalt Blends of Reclaimed Asphalt Pavement Binder with Virgin Binder using SEM/EDS. *Transportation Research Record,* 2672**,** 69-78.

MAZUMDER, M., AHMED, R., WAJAHAT ALI, A. & LEE, S.-J. 2018. SEM and ESEM techniques used for analysis of asphalt binder and mixture: A state of the art review. *Construction and Building Materials,* 186**,** 313-329.

SINGHVI, P., MAINIERI, J. J. G., OZER, H., SHARMA, B. K., AL-QADI, I. L. & MORSE, K. L. 2022. Impacts of Field and Laboratory Long-Term Aging on Asphalt Binders. *Transportation Research Record,* 2676**,** 336-353.

XING, C., LI, M., LIU, L., LU, R., LIU, N., WU, W. & YUAN, D. J. J. O. C. P. 2023. A comprehensive review on the blending condition between virgin and RAP asphalt binders in hot recycled asphalt mixtures: Mechanisms, evaluation methods, and influencing factors. 398**,** 136515.

ZAUMANIS, M. & MALLICK, R. B. 2015. Review of very high-content reclaimed asphalt use in plant-produced pavements: state of the art. *International Journal of Pavement Engineering,* 16**,** 39-55.

First-year asphalt mixture results from a European in situ Ageing Consortium (EurIAC)

G. Jacobs[1], W. Van den bergh[1], C. Vuye[1], A. Singh[2], A. Varveri[2], M. Zaumanis[3], L. Poulikakos[3*], E. Freitas[4], J. Mirwald[5], B. Hofko[5], E. Manthos[6] & G. Pipintakos[1]

[1]*University of Antwerp, SuPAR Research Group, Groenenborgerlaan 171, Antwerp 2020, Belgium*
[2]*Delft University of Technology, Pavement Engineering, Stevinweg 1, Delft 2628 CN, Netherlands*
[3]*EMPA, Überlandstrasse 129, Dubendorf 8600, Switzerland*
[4]*University of Minho, Campus de Azurém, Guimarães 4800-058, Portugal*
[5]*Christian Doppler Laboratory for Chemo-Mechanical Analysis of Bituminous Materials, Institute of Transportation, TU Wien, Lilienthalgasse 14, Wien 1030, Austria*
[6]*Aristotle University of Thessaloniki, Highway Engineering Laboratory, Thessaloniki 54124, Greece*
emerita

ABSTRACT: Ageing of asphalt pavements is an inevitable phenomenon that reduces the overall lifespan of the road network. Typically, this process is simulated in the lab, however several climatic factors are often overlooked in such simulations. To evaluate the ageing effects more realistically, a network of universities in six Western-European countries was established in the summer of 2023. This paper reports the first-year results of in situ climatic conditioning and their effect on a reference asphalt mixture. Asphalt slabs were assessed for their mechanical performance via indirect tensile strength and resilient modulus. The findings depict slight differences between the participating labs concerning these properties, with the majority of them pointing to slightly increased modulus values ascribed to ageing. The extent of mix properties changes, yet in the early stages of long-term ageing, is still insignificant. Finally, a weak positive correlation was found between the two asphalt mixture properties which can collectively explain the regional differences across Europe in the near future. Correlations with the changes at the binder level will also be considered as well as the linkage to the climatic history, as additional results will become available over extended time intervals.

1 INTRODUCTION

Ageing of asphalt mixture is one of the governing factors that affects the service life of pavements (Cavalli et al., 2018). Typically, bitumen is the binding medium of asphalt mixtures and due to its organic nature, it is prone to degradation under climatic conditioning (Pipintakos et al., 2024). Hence, considerable efforts have been made to simulate the in situ climatic conditions in the laboratory. A variety of ageing protocols persist at both binder (i.e. pressure ageing vessel) and mixture levels (i.e. ageing of loose or compacted asphalt mixtures), including testing under different temperatures and atmospheric conditions (Jacobs et al., 2023; Ma et al., 2022; Mirwald et al., 2020). However, most of these attempts are rather accelerated simulations of in situ conditions and the exact history of the climatic conditions, such as solar radiation, humidity and temperature, is challenging to be considered. Additionally, a few studies have investigated the influence of realistic field conditions with a primary focus on quantifying the effects of ageing gradients, air void percentage, and film thickness (Jing et al., 2021; Song et al., 2022; Zhang et al., 2022). Despite these efforts, a factor that is often missing for a thorough understanding and fair comparison of the effects of climatic conditions is the incorporation of a reference mixture into the experimental matrix, considering the different climatic regions.

Inspired by the paradigm of ongoing international efforts at a global scale (Adwani et al., 2023), current joint efforts in Europe, by means of a European in situ Ageing Consortium (EurIAC), try to elucidate these effects. This is realised by taking into account the specific climatic conditions, such as temperature, moisture, and UV/VIS history, among others, for a reference and local mixtures exposed to various climatic regions, assessed at different time intervals. The assessment of climatic data was performed on both binder and asphalt mixture levels, with an optimum future goal to link the changes in performance with the climatic data that will be recorded for a total duration of seven years in six European countries. Moreover, a European ageing model will be developed as an output of this collaborative work. This work reports on the first set of reference mixtures.

2 MATERIALS & METHODS

2.1 *Participating laboratories*

Six laboratories are participating in this study, as shown in

Table 1. Climate classifications according to Köppen system are also included, from which it can be seen that the majority of them are classified as temperate

oceanic climate (Cfb) regions, which is representative of a significant part of Europe (Beck et al., 2006).

Table 1: Overview of participating laboratories and their climate classification

Laboratory	Köppen Climate classification
University of Antwerp	Cfb
TU Delft	Cfb
EMPA	Cfb
TU Wien	Cfb/Dfb
University of Minho	Csb
Aristotle University of Thessaloniki	Bsk/Bsh

The results in this paper are anonymised, thus the order of the labs in Table 1 does not necessarily correspond to the order of the graphs in the results section.

2.2 Materials
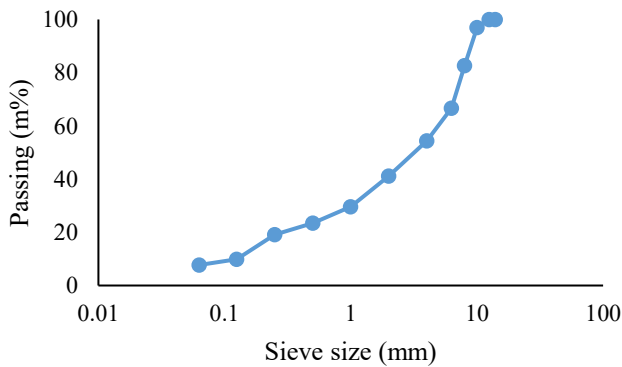
Figure 1: Gradation of the AC10 surface mixture

The reference mixture was a typical dense-graded asphalt concrete surface layer (hereafter referred as AC10) prepared with 5.8% (in total mixture) of 50/70 penetration grade binder, having a design air void content of 5.6%. The aggregates used for the mixture were porphyry (2/4, 4/6 and 6/10) limestone (0/2) and natural, round sand (0/1). Figure 1 shows the gradation of the AC10 surface mixture.

The mixture was produced in one of the laboratories in accordance with EN 12697-35 using an automatic mixer to avoid variations due to slightly different lab mixture production procedures, which could influence the results. Afterwards, the mixture was compacted in slabs of 60x40x5 cm as per EN 12697-33. Each laboratory received three slabs, having similar average air void contents, determined using the geometrical method. The slabs were placed outside on a flat surface in the summer of 2023 (between July and September), and were subjected to the local environmental conditions (no cover from precipitation or solar radiation) as shown in Figure 2.

2.3 Experimental Methods

2.3.1 Coring

Figure 2: In situ slabs of all participating partners

Each participating partner is asked to drill four cores of 100 mm diameter at regular time intervals of 0.5, 1, 2, 3, 5, and 7 years. A minimum distance of 40 mm was maintained between the cores and the slab edges as well as between two cores to minimise the impact of ageing from sides and of the other cores. In addition, each laboratory received four cores of 100 mm diameter, cored at the mixture-producing lab, which were tested to obtain reference results (0m) corresponding to short-term ageing. After coring, the specimens were dried to constant mass at room temperature and the mass alongside the dimensions of each specimen was measured.

2.3.2 Resilient modulus

The stiffness (resilient modulus) of the samples was assessed for 4 replicates per ageing time interval according to EN 12697-26, annex C (IT-CY) at 15 °C. The test was performed with a load rise time of 80 ms with a maximum allowable horizontal deformation of 6.5 μm. Further, two readings were obtained per replicate as proposed in the test standard. The average resilient modulus and corresponding standard deviation were determined for each laboratory based on these 8 measurements (four samples, each tested in two directions).

2.3.3 Indirect Tensile Strength

After the non-destructive stiffness test, the indirect tensile strength (ITS) was determined as per EN 12697-23 by applying a loading rate of 50 mm per minute at 15 °C. The peak load P, together with the average height H and diameter D, were used to calculate the ITS value according to Equation 1.

$$ITS = \frac{2P}{\pi DH} \qquad (1)$$

3 RESULTS & DISCUSSION

3.1 *Resilient modulus*

The resilient modulus results obtained in different laboratories are presented in Figure 3. As shown in Figure 3, two measurements were made by the participating organisations, where 0m refers to results without in situ ageing and acts as the t=0 time interval, while 6m corresponds to in situ ageing at t=6 months. However, laboratory C performed the tests after 9 months instead of 6, whereas the values for 0m were similar for A and B since the mixture testing was performed at the same laboratory due to limitations of testing facilities. Samples after in situ ageing were shipped between these two labs.
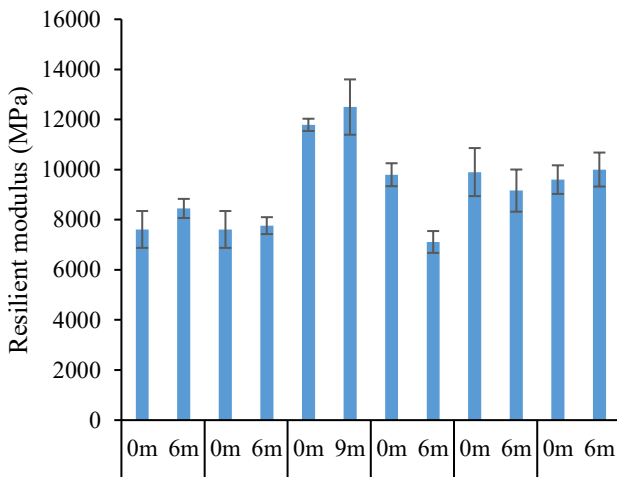
Figure 3: Resilient modulus results for all labs and time intervals 0 and 6 months

In general, considering the standard deviations, the differences between the average resilient modulus of the reference and aged mixtures after 6 months, were rather limited. Nevertheless, some differences can be observed. Laboratory C obtained a higher resilient modulus compared to all other labs. Further, the difference before and after 6 months of ageing was significant in laboratory D, with a drop in average resilient modulus of over 2500 MPa. The majority of the laboratories (A, B, C and F) showed a slight increase in average resilient modulus, as can be expected after in situ ageing.

3.2 *ITS*

Figure 4 shows the ITS results for labs A to E, since for laboratory F this test was not performed. Similarities between the resilient modulus and ITS results were noticed with some exceptions within the testing repeatability for labs A, B, and E. A significant drop in ITS after 6 months of ageing was recorded by laboratory D, corroborating with the resilient modulus results and clearly depicting a change in mixture performance. Based on these observations, it is likely that the properties of the drilled asphalt cores at t=0 differed significantly from the cores extracted at laboratory D after 6 months.

The ITS values of laboratory C were slightly higher compared to others but not to the same extent as can be seen in the resilient modulus results. The similarities and trends observed between ITS and resilient modulus results led to a more in-depth exploration of the potential correlation between the two tests, which is elaborated in the next subsection.
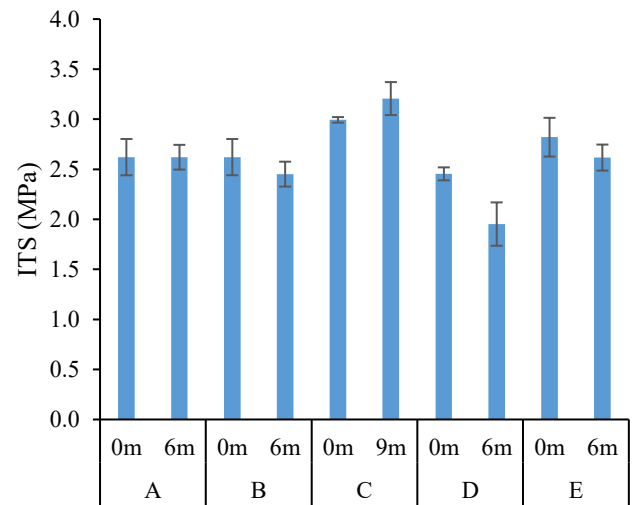
Figure 4: ITS results for labs A-E and time intervals 0 and 6 months

3.3 *Correlation between modulus and ITS*

Figure 5 displays the resilient modulus and ITS of the individual samples for laboratories A to E. This allows a visual assessment of the correlation between the two parameters and the variance in testing results. The dashed line is a linear trendline ($R^2 = 0.563$) that confirms a positive, though weak, correlation between the resilient modulus and ITS. However, the graph shows individual differences and trends for different labs, that may be generated by the sample size and test type, which supports the use of both tests.
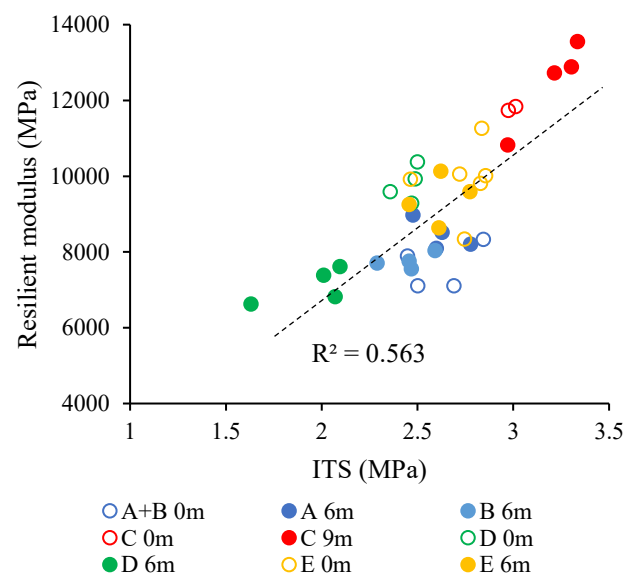
Figure 5: Resilient modulus vs ITS for labs A-E

The first apparent observation from Figure 5 is that despite expectations the correlation for the 0m results was not better. In the same graph, one can observe

that laboratory C clearly distinguishes itself with relatively high values for ITS and resilient modulus, while maintaining increased ITS values after in situ ageing. On the other hand, labs D and E showed slightly decreased ITS and resilient modulus values after 6 months of in situ ageing. Finally, the results for labs A and B were similar before and after ageing. Therefore, it can be concluded that the trends are diverse and that future testing at multiple time intervals can help in establishing a clear relationship between the effects of ageing duration, climatic conditions, and mechanical performance.

4 CONCLUSIONS & RECOMMENDATIONS

This paper reports the results of the first-year in situ ageing at the asphalt mixture level of a collective effort of six European countries. The conclusions and recommendations are summarised herein.

- The effect of climatic conditions in different European regions is rather negligible for both ITS and resilient modulus after 6 months in situ.
- Four out of six participating laboratories showed a slight increase in resilient modulus, while the same increase was less obvious in the ITS results.
- Possible performance deviations at t=0 may have been introduced by testing device calibration errors.
- A weak positive correlation exists between the ITS and resilient modulus results when accounting for both ageing time intervals.
- The differences between the asphalt specimens of the participating laboratories can be better highlighted via the correlation between ITS and resilient modulus.
- The consideration of both parameters to capture trends and understand testing deviations is crucial for the next in situ years.

During the forthcoming ageing time intervals of this project, the consortium will carefully assess possible testing device deviations and the origin of them. Moreover, correlations with the climatic data will be performed. Ongoing investigations of EurIAC will include extraction and recovery of bitumen at different depths for a chemomechanical evaluation of the ageing gradients in order to potentially link them with the mixture performance and the climatic data.

5 REFERENCES

Adwani, D., Sreeram, A., Pipintakos, G., Mirwald, J., Wang, Y., Hajj, R., Jing, R., & Bhasin, A. (2023). Interpreting the effectiveness of antioxidants to increase the resilience of asphalt binders: A global interlaboratory study. *Construction and Building Materials*, *366*(December), 130231. https://doi.org/10.1016/j.conbuildmat.2022.130231

Beck, C., Grieser, J., Kottek, M., Rubel, F., & Rudolf, B. (2006). *Characterizing global climate change by means of Köppen climate classification*.

Cavalli, M. C., Zaumanis, M., Mazza, E., Partl, M. N., & Poulikakos, L. D. (2018). Aging effect on rheology and cracking behaviour of reclaimed binder with bio-based rejuvenators. *Journal of Cleaner Production*, *189*, 88–97. https://doi.org/10.1016/j.jclepro.2018.03.305

Jacobs, G., Pipintakos, G., Van den Buijs, X., Kalama, D. M., & Van den bergh, W. (2023). Chemo-rheological equivalence of bitumen between different lab ageing procedures: from binder to mixture. *Road Materials and Pavement Design*, 1–16. https://doi.org/10.1080/14680629.2023.2170271

Jing, R., Varveri, A., Liu, X., Scarpas, A., & Erkens, S. (2021). Differences in the ageing behavior of asphalt pavements with porous and stone mastic asphalt mixtures. *Transportation Research Record*, *2675*(12), 1138–1149. https://doi.org/10.1177/03611981211032218

Ma, L., Varveri, A., Jing, R., Kasbergen, C., & Erkens, S. (2022). Thermodynamics and kinetics of moisture transport in bitumen. *Materials & Design*, *222*, 111028. https://doi.org/https://doi.org/10.1016/j.matdes.2022.111028

Mirwald, J., Maschauer, D., Hofko, B., & Grothe, H. (2020). Impact of reactive oxygen species on bitumen aging – The Viennese binder aging method. *Construction and Building Materials*, *257*, 119495. https://doi.org/10.1016/j.conbuildmat.2020.119495

Pipintakos, G., Sreeram, A., Mirwald, J., & Bhasin, A. (2024). Engineering bitumen for future asphalt pavements: A review of chemistry, structure and rheology. *Materials & Design*, 113157. https://doi.org/10.1016/j.matdes.2024.113157

Song, S., Liang, M., Hou, F., Gao, H., Bi, Y., Zhang, H., & Guo, M. (2022). Analysis of Natural Aging Behavior of Asphalt Binder in Cold and Arid Region. *Advances in Materials Science and Engineering*, *2022*, 1–9. https://doi.org/10.1155/2022/2425976

Zhang, H., Soenen, H., Carbonneau, X., Lu, X., Robertus, C., & Zhang, Y. (2022). Experimental and Statistical Analysis of Bitumen's Field Ageing in Asphalt Pavements. *Transportation Research Record: Journal of the Transportation Research Board*, 036119812210798. https://doi.org/10.1177/03611981221079823

Impact of Virgin Binders on IDEAL-CT Results of RAP Asphalt Mixtures

[a]Fan Yin, [a]Raquel Moraes, [a]Madhav Verma, [b]Juliana Montanez, [a]Nam Tran, [b]Amy Epps Martin, [b]Edith Arambula-Mercado

[a]*National Center for Asphalt Technology at Auburn University;* [b]*Texas A&M Transportation Institute*

ABSTRACT: This study evaluated the impact of virgin binders on the Indirect Tensile Asphalt Cracking Test (IDEAL-CT) results of asphalt mixtures containing reclaimed asphalt pavement (RAP). A total of 14 RAP mixtures were tested, covering two U.S. climate zones, four mix designs, and six virgin binders. Each virgin binder underwent rheological characterization at three aging conditions: unaged, rolling thin film oven (RTFO) plus 20-hour pressure aging vessel (PAV) aging, and RTFO plus 40-hour PAV aging. The test results showed that using a softer virgin binder improved the IDEAL-CT results, whereas using a polymer modified asphalt binder did not show similar benefits. The impact of binder source on the IDEAL-CT results was found to vary depending on the RAP mix design. Furthermore, the modified Glover-Rowe (G-R) parameter at 15°C and 10 Hz after 40-hour PAV aging exhibited a very strong correlation to the IDEAL-CT results, highlighting its potential as a mix design tool to screen virgin binders for the cracking resistance of RAP mixtures.

1 INTRODUCTION

The asphalt pavement industry in the United States is committed to achieving net-zero carbon emissions by 2050 [1]. One key strategy to meet this goal is to increase the use of RAP in asphalt mixtures. Although this approach provides significant economic and environmental benefits, it also presents pavement performance challenges as RAP mixtures can be susceptible to cracking and durability issues due to increased binder stiffness and brittleness. To address these challenges, many state highway agencies are considering the implementation of a laboratory cracking test to evaluate the cracking resistance of RAP mixtures as part of the mix design and production acceptance process. Among many mixture cracking tests developed over past decades, the Indirect Tensile Asphalt Cracking Test (IDEAL-CT) has gained increasing popularity [2]. This test is favored for its practicality in specimen preparation, simplicity in providing results quickly, and relevance in providing a reasonably strong correlation to field cracking performance [3-4]. Meanwhile, the asphalt pavement industry is actively exploring mix design strategies to improve IDEAL-CT results. One of the most common strategies is to change the source, grade, or type of virgin binder in RAP mixtures. However, limited guidance exists on selecting virgin binders to improve the cracking resistance of RAP mixtures.

2 STUDY OBJECTIVE

The objectives of the study were twofold: (1) to determine the impact of virgin binders on the long-term cracking resistance of RAP asphalt mixtures, as measured by the IDEAL-CT after aging; and (2) to relate binder rheological properties to mixture IDEAL-CT results.

3 EXPERIMENTAL PLAN

3.1 *Materials*

This study included four RAP mix designs, including two from a northern state and two from a southern state in the United States. The RAP content of the mix designs varied from 20% to 41%, corresponding to a recycled binder ratio (RBR) of 0.16 to 0.37. Table 1 summarizes the key mix design variables. More detailed information is available elsewhere [5].

Table 1. RAP Mix Design Summary

Mix Design ID	Climate Zone	NMAS	Aggregate Type	RBR	Asphalt Content
Northern 25% RAP	Northern State	9.5mm	Granite Dolomite	0.21	5.95
Northern 41% RAP	Northern State	9.5mm	Granite Dolomite	0.37	5.61
Southern 20% RAP	Southern State	9.5mm	Granite	0.16	5.79
Southern 35% RAP	Southern State	9.5mm	Granite	0.29	5.75

The RAP mix designs were evaluated using different virgin asphalt binders to assess mixture cracking performance. The virgin binders included five unmodified performance grade (PG) binders (PG 52-34, two PG 58-28, and two PG 64-22 binders) and a PG 76-22 styrene-butadiene-styrene (SBS) polymer-modified asphalt (PMA) binder. The PG 58-28 and PG 64-22 asphalt binders were sourced from different crude oils and, despite meeting the same PG requirements per AASHTO M 320, were expected to have notably different rheological properties.

3.2 *Virgin Binder Testing*

Each virgin binder was tested using a Dynamic Shear Rheometer (DSR) and Bending Beam Rheometer (BBR) to verify Superpave PG. In addition, the DSR frequency sweep test was conducted for rheological characterization at three aging condi-

tions: unaged, RTFO plus 20-hour PAV, and RTFO plus 40-hour PAV. The frequency sweep test was performed across a temperature range of 10°C to 90°C (10°C increments) and an angular frequency range of 0.1 to 30 Hz. The results were analyzed using RHEA™ software to determine a battery of rheological parameters, including the phase angle (δ) at a complex shear modulus ($|G^*|$) of 8.967 MPa and 15°C (variable frequency), δ at $|G^*|$ of 10 MPa and 10 rad/s (variable temperature), crossover frequency (ω_c), crossover modulus (G_c), crossover temperature (T_{Gc}), Glover-Rowe (G-R) parameter at 15°C and 0.005 rad/s, modified G-R parameter at 15°C and 10 Hz (other temperature and frequency combinations were also included, but the results are not included in the paper due to space limitations), and R-value. The R-value results were obtained from DSR master curve analysis utilizing the Christensen-Anderson model at a reference temperature of 15°C with variable glassy modulus G_g and $|G^*|$ greater than 10^5 Pa.

3.3 RAP Mixture Testing

The study included fourteen RAP mixtures prepared with different mix design and virgin binder combinations. Each mixture was tested for intermediate-temperature cracking resistance using the IDEAL-CT per ASTM D8225. To account for the impact of asphalt aging, the IDEAL-CT was conducted after long-term aging. The aging procedure involved short-term aging of loose mixtures for 4 hours at 135°C, followed by long-term aging for 6 or 8 hours at 135°C for PG 52-34, PG 58-28, and PG 64-22 binders, and 5 days at 95°C for the PG 76-22 binder. The 95°C aging procedure was used for the PG 76-22 binder to prevent the potential thermal degradation of SBS polymer at an elevated aging temperature, but it was expected to provide an equivalent level of asphalt aging as the 135°C aging procedure according to the $|G^*|$ aging kinetics model by Kim et al [6]. Shorter aging times (6 hours) were applied to the two northern mix designs, while longer aging times (8 hours or 5 days) were applied to the southern mix designs. These aging procedures were expected to simulate approximately 5 to 6 years of surface aging for asphalt pavements in the United States [7].

4 TEST RESULTS AND DISCUSSIONS

4.1 Rheological Characterization of Virgin Binders

Figure 2 summarizes the virgin binder continuous PG temperatures and ΔT_c results, determined in accordance with ASTM D7643 (AASHTO M 320).

All binders met their as-supplied PG requirements. The two PG 58-28 binders from different crude sources showed a 1.6°C difference in ΔT_c, despite having nearly identical continuous grading temperatures. Among the two PG 64-22 binders, Source 2 was slightly softer but exhibited significantly better relaxation properties, as indicated by a 2.7°C higher ΔT_c compared to Source 1. Overall, the virgin binders evaluated in the study covered a wide range of PG and ΔT_c results.

	52-34	58-28 Source 1	58-28 Source 2	64-22 Source 1	64-22 Source 2	76-22 SBS
High	53.6	59.6	60.3	65.7	65.0	77.4
Low	-35.5	-28.6	-28.8	-25.3	-26.4	-24.6
DTc	2.5	0.4	2.0	-1.4	1.3	-1.0
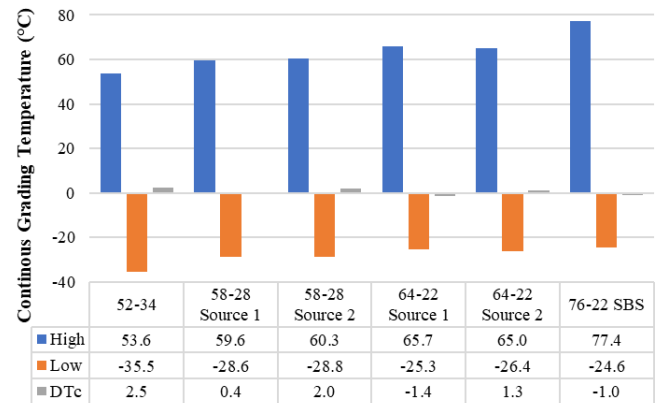
Figure 2. Virgin Binder Continuous PG Temperatures and ΔT_c Results

Tables 2 through 4 summarize the rheological parameters of the virgin binders, determined from the DSR frequency sweep test at three aging conditions. The softer virgin binders (PG 52-34, PG 58-29 Source 1, PG 58-28 Source 2) exhibited lower G-R parameter values (at 15°C and 0.005 rad/s and 15°C and 10 Hz) than the PG 64-22 Source 1, PG 64-22 Source 2, and PG 76-22 PMA binders across all aging conditions. Even after extended aging, the softer binders did not enter the cracking damage zone (i.e., G-R parameter criteria of 180 kPa at 15°C and 0.005 rad/s). Only the PG 64-22 Source 1 binder exceeded the criterion for visible surface cracking (i.e., G-R parameter criteria of 600 kPa at 15°C and 0.005 rad/s) after RTFO plus 40-hour PAV. Among the unmodified binders, PG 64-22 Source 1 exhibited the highest change in G-R parameters, indicating greater susceptibility to aging. Caution is advised when interpreting the G-R parameter (and possibly the R-value) for the PG 76-22 PMA binder, as polymer modification can significantly increase failure strain at a given binder modulus. As expected, as aging progressed for all binders, a decrease in the crossover frequency (ω_c) and crossover modulus (G_c) and an increase in the crossover temperature (T_{Gc}) and R-value were observed.

Table 2. Virgin Binder Rheological Parameter Results at Unaged Condition

Asphalt Binder Properties	52-34	58-28 Source 1	58-28 Source 2	64-22 Source 1	64-22 Source 2	76-22
R-value	1.8	1.7	1.6	1.7	1.7	1.9
δ at $|G^*|$ = 8.967 MPa, 15°C (°)	55.5	51.5	56.3	52.0	52.9	49.9
δ at $|G^*|$ = 10 MPa, 10 rad/s (°)	54.4	50.4	55.6	51.4	52.3	49.0
ω_c (rad/s)	7.28E+03	1.09E+02	6.90E+02	6.23E+01	8.54E+01	2.31E+01
G_c (Pa)	3.96E+07	1.86E+07	3.28E+07	1.97E+07	2.14E+07	1.53E+07
T_{Gc} (°C)	−8.2	7.3	1.4	8.4	7.2	11.6
G-R$_{15°C,0.005rad/s}$ (kPa)	0.007	0.3	0.1	0.7	0.7	8.2
G-R$_{15°C,10Hz}$ (kPa)	5.55E+02	8.98E+03	3.42E+03	1.43E+04	1.24E+04	2.20E+04

Table 3. Virgin Binder Rheological Parameter Results at RTFO plus 20-hour PAV Aging Condition

Asphalt Binder Properties	52-34	58-28 Source 1	58-28 Source 2	64-22 Source 1	64-22 Source 2	76-22
R-value	2.6	2.3	2.1	2.2	2.1	2.1
δ at $|G^*|$ = 8.967 MPa, 15°C (°)	44.1	40.7	45.3	39.8	43.7	42.3
δ at $|G^*|$ = 10 MPa, 10 rad/s (°)	43.4	39.9	44.8	39.4	43.2	41.9
ω_c (rad/s)	2.52E+01	1.76E+00	5.92E+00	2.34E-02	1.69E+00	2.61E-01
G_c (Pa)	6.77E+06	4.74E+06	8.91E+06	3.83E+06	6.93E+06	5.53E+06
T_{Gc} (°C)	10.7	20.7	15.7	34.6	19.9	25.8
G-R$_{15°C,0.005rad/s}$ (kPa)	4.2	21.7	16.3	205.8	47.0	191.6
G-R$_{15°C,10Hz}$ (kPa)	8.47E+03	2.79E+04	2.69E+04	6.70E+04	4.03E+04	7.66E+04

Table 4. Virgin Binder Rheological Parameter Results at RTFO plus 40-hour PAV Aging Condition

Asphalt Binder Properties	52-34	58-28 Source 1	58-28 Source 2	64-22 Source 1	64-22 Source 2	76-22
R-value	2.8	2.4	2.4	2.9	2.2	2.5
δ at $|G^*|$ = 8.967 MPa, 15°C (°)	39.4	37.1	41.7	35.6	41.7	38.8
δ at $|G^*|$ = 10 MPa, 10 rad/s (°)	38.8	36.4	40.9	35.1	41.3	38.4
ω_c (rad/s)	1.52E+00	2.23E-01	5.88E-01	4.57E-03	2.35E-01	2.50E-02
G_c (Pa)	3.17E+06	2.69E+06	5.03E+06	1.36E+06	4.81E+06	2.84E+06
T_{Gc} (°C)	20.7	26.6	24.2	40.2	26.4	34.2
G-R$_{15°C,0.005rad/s}$ (kPa)	30.3	111.3	88.3	966.8	189.2	736.9
G-R$_{15°C,10Hz}$ (kPa)	1.81E+04	3.66E+04	5.02E+04	9.66E+04	7.07E+04	1.05E+05

4.2 IDEAL-CT Testing of RAP Mixtures

Figure 3 presents the IDEAL-CT results of RAP mixtures using different mix design and virgin binder combinations. The columns and error bars represent the average and standard deviation, respectively, of the cracking tolerance index (CT$_{Index}$). The letters represent statistical groupings for individual mix designs according to the Tukey-Kramer test. For all RAP mix designs, using a softer virgin binder increased the CT$_{Index}$, suggesting improved cracking resistance. While the degree of improvement varied across different mix designs, it was statistically significant in all cases except for the northern 25% RAP mix design with PG 58-28 Source 2 binder and the northern 41% RAP mix design with PG 58-28 Source 1 binder.

For the two southern RAP mix designs, using a PG 76-22 SBS modified binder or changing the PG 64-22 binder source did not statistically affect the CT$_{Index}$, when the test variability was considered. However, changing the PG 58-28 binder from Source 1 to Source 2 (with a 2.7°C lower ΔT_c) increased the CT$_{Index}$ of the two northern mix designs, but the improvement was not statistically significant for the 41% RAP mix design according to the statistical grouping letters.
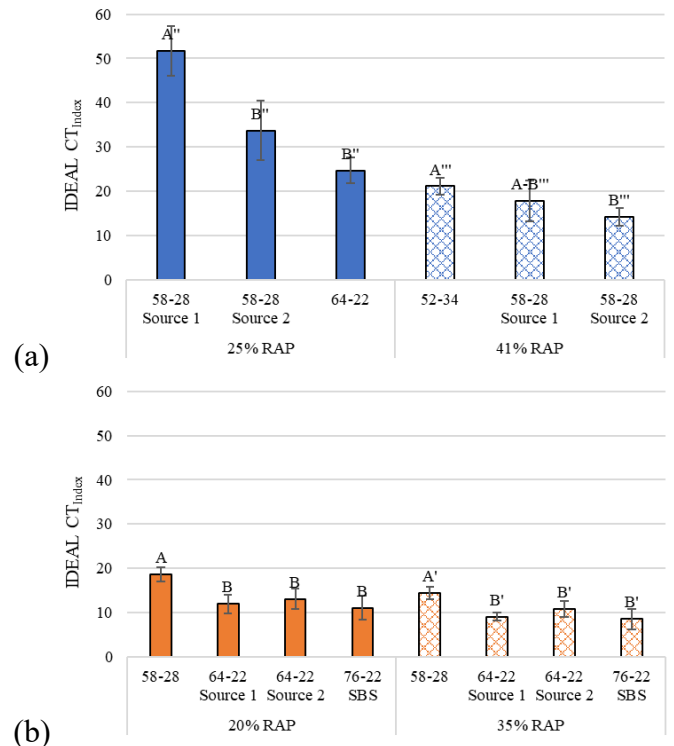
Figure 3. RAP Mixture IDEAL-CT Results: (a) Northern Mix Designs, (b) Southern Mix Designs

4.3 Relating Virgin Binder Rheological Parameters to Mixture IDEAL-CT Results

Pearson correlation analysis was conducted to relate the rheological properties of virgin binders to the IDEAL-CT results of RAP mixtures. The analysis focused on RAP mixtures using the same mix design but with different virgin binders, allowing for the isolation of potential confounding impacts of other design variables, such as RAP content, aggregate type, and aggregate gradation. Furthermore, the analysis was conducted separately for each binder aging condition, and the Pearson correlation coefficient (r) results are summarized in Figure 4.

(a)

(b)

(c)
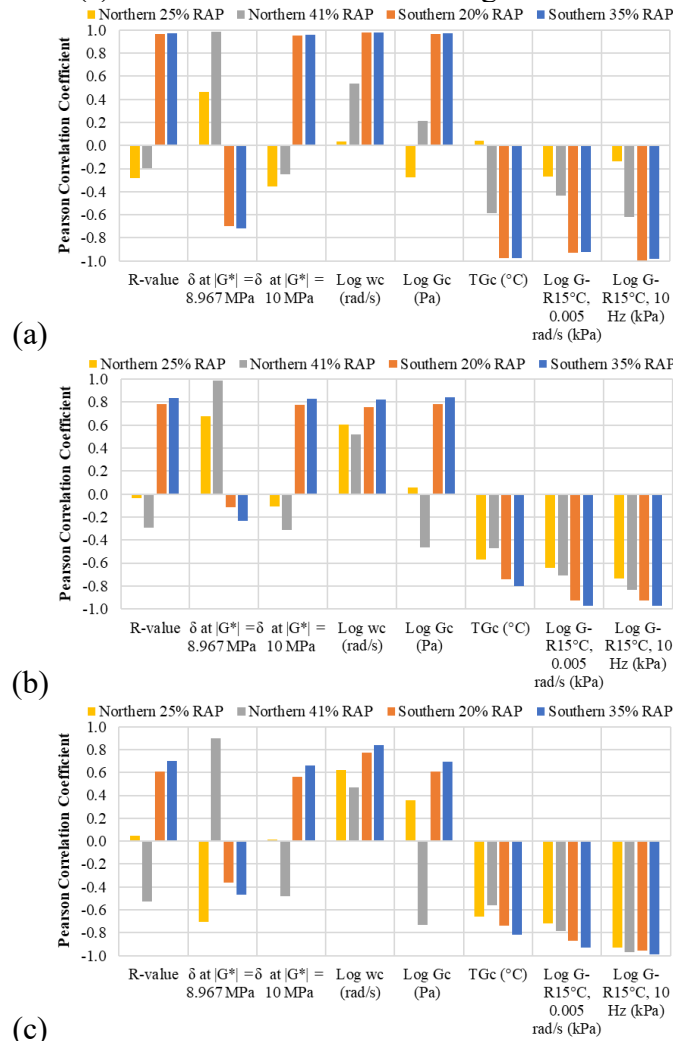
Figure 4. Pearson Correlation Coefficients for CT_{Index} versus Binder Rheological Parameters: (a) Unaged, (b) RTFO plus 20-hour PAV Aging, (c) RTFO plus 40-hour PAV Aging

Among all the rheological parameters evaluated in the study, only ω_c and G-R showed consistent trends (either positive or negative correlations) with the IDEAL-CT results across all RAP mix designs and binder aging conditions. For both G-R parameters, the correlation to CT_{Index} improved as binder aging increased, especially from unaged to 20-hour PAV aging. After 40-hour PAV aging, the modified G-R parameter at 15°C and 10 Hz exhibited a strong correlation with CT_{Index}, with an $|r|$ value exceeding 0.9 across all RAP mix designs, as shown in Figure 5. This suggests that the modified G-R parameter

can serve as a potential mix design tool for screening virgin binders to enhance the IDEAL-CT results of RAP mixtures.
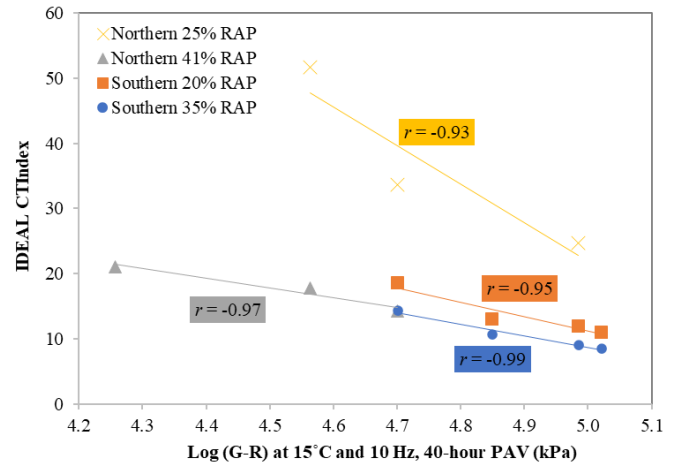
Figure 5. Correlation of Modified G-R Parameter at RTFO plus 40-hour PAV Aging to IDEAL-CT

5 FINDINGS AND CONCLUSIONS

This study found that using a softer virgin binder effectively improved the IDEAL-CT results of RAP mixtures, while using a PMA binder did not show similar benefits. The impact of changing the binder source on the IDEAL-CT results was inconclusive. Among the various binder rheological parameters evaluated, the modified G-R parameter at 15°C and 10 Hz after RTFO plus 40-hour PAV aging exhibited the strongest correlation with the IDEAL-CT results. Therefore, this parameter shows potential as a mix design tool for screening virgin binders to improve the cracking resistance of RAP mixtures, but further verification with additional data for mixtures with different virgin binder sources, RAP sources, and aggregate types is warranted.

6 REFERENCES

[1] National Asphalt Pavement Association. The Road Forward, accessed on December 6, 2024.

[2] National Asphalt Pavement Association. Balanced Mix Design Resource Guide, accessed on December 6, 2024.

[3] Zhou et al. (2017). Development of an Ideal Cracking Test for Asphalt Mix Design and QC/QA. Road Materials and Pavement Design, 18(sup4).

[4] West et al. (2021). Phase VII (2018-2021) NCAT Test Track Findings. NCAT Report 21-03.

[5] Epps Martin et al. (2024). Capturing Durability of High Recycled Binder Ratio (RBR) Asphalt Mixtures. NCHRP Research Report 1130.

[6] Kim et al., (2021). Long-Term Aging of Asphalt Mixtures for Performance Testing and Prediction: Phase III Results. NCHRP Research Report 973.

[7] Chen et al. (2022). Preliminary Validation of the Critical Aging Protocol for NCAT Top-down Cracking Experiment. Journal of the Association of Asphalt Paving Technologists, Vol. 89.

Microwave deicing performance and low-temperature cracking resistance evaluation of asphalt mixture incorporating graphene-coated functional aggregates

Shaowei Zhang
Department of Civil and Environmental Engineering, The Hong Kong Polytechnic University, Hong Kong Special Administrative Region.

Zhen Leng[*]
Department of Civil and Environmental Engineering, The Hong Kong Polytechnic University, Hong Kong Special Administrative Region.

ABSTRACT: Ice/snow on pavements is a constant threat to traffic safety and needs to be removed efficiently. Graphene as novel carbon nanomaterial have excellent microwave-absorbing and mechanical properties, making it the most favorable candidate for heating-generation composites. But there is a problem of uneven dispersion when introducing them through traditional processes. This research aims to fabricate graphene-coated functional aggregate (FLG@FA) to boost pavement deicing via a new coating method and high-temperature curing process. Microwace deicing and Low-temperature SCB test at low-LLD rates were conducted to evaluate the ice-melting and the low-temperature performance. Results show that deicing velocity of FLG@FA could be enhanced to 29.6 g/min (~64%↑). It also demonstrated an enhanced level of low-temperature cracking resistance (~31.4%↑), and an improved method for calculating fracture work (W_f) was proposed.

1 INSTRUCTIONS

Ice/snow on transportation infrastructure is a constant threat to traffic safety and needs to be removed efficiently to maintain normal operations (Sun et al., 2018, Wu et al., 2005). There are multiple deicing approaches, such as removal techniques, ice-melting chemicals, the hydronic pipe method, and self-healing technology (Qiu and Nixon, 2008). Among them, chemical agents like salt and mechanical means have been most prevalently utilized. Nevertheless, the overuse of salt commonly results in environmental pollution and corrosion issues. Meanwhile, removal methods exhibit low work efficiency and are liable to cause damage to the pavement surface. The hydronic pipe method is also favored, but its application is relatively costly and complex, alters the internal pavement structure, and poses potential risks to durability. Thus, it is of great significance to investigate efficient and eco-friendly ice-melting technologies.

Nowadays, self-healing heating technology has become a research hotspot. It is closely related to the road surface temperature. Electromagnetic induction and microwave heating are used in self-healing technology, and microwave heating has more advantages like uniform heating and high efficiency (Wang et al., 2022). Scholars have conducted a large number of studies on microwave snow and ice-melting asphalt pavements. For example, Sun et al. studied the heating rate of steel fiber-modified asphalt pavements under microwave radiation (Sun et al., 2023). Arabzadeh et al. used carbon fiber-modified asphalt concrete for anti-icing and deicing (Arabzadeh et al., 2019). Gao et al. verified the feasibility of steel slag for microwave deicing (Gao et al., 2017). Microwave deicing technology has advanced, but its use is restricted as current magnetic substitutes underperform in deicing, leading to low efficiency and weak competitiveness. Immediate material and technical upgrades are essential to enhance its practicality and competitiveness.

Nano-carbon materials like graphene have excellent abilities in absorbing electromagnetic waves and conductivity and also possess many excellent mechanical properties (Tan et al., 2023). Incorporating them into asphalt pavement can solve related limitations (Kim et al., 2015). However, nanomaterials are prone to form agglomerates due to the high van der Waals force among themself, making it difficult for graphene to be effectively dispersed in a high-viscosity asphalt binder. Using nano-carbon materials as coating materials to prepare functional aggregates for microwave deicing can overcome the dispersion problem and improve the insufficient electromagnetic wave absorption ability. However, there is still a research gap regarding the application of this technology.

This research aims to creatively fabricate the graphene-coated functional aggregates (FLG@FA) for improved deicing efficiency of asphalt pavement via a novel coating method. The microwave ice-melting performance of the FLG@FA group was investigated. Meanwhile, the evaluation of deicing asphalt mixture's low-temperature performance is of great significance for mitigating transverse thermal cracking and preventing traffic accidents. Low-temperature SCB tests at a slow load-line displacement (LLD) rate of 0.5 mm/min and an improved calculation method of W_f will be conducted for the evaluation of low-temperature cracking resistance.

2 MATERIALS AND METHODOLOGY

2.1 Materials

Raw materials of few-layer graphene (FLG) dispersion and nanoceramic resin were selected to prepare the functional ink before coating. Well-dispersed functional ink (FLG ink) was synthesized by thorough shear mixing of FLG dispersion with ceramic resin using a dispersion disc and mixer equipment at 1000 rpm for 30 min at ambient temperature. The fundamental properties of FLG ink are presented in Table 1. In addition, raw granite aggregates (RA) and an asphalt binder with a performance grading (PG76/22) provided by a supplier in Hong Kong, K. Wah Asphalt Limited, were selected in this study.

Table 1. Fundamental properties of FLG ink.

Properties	FLG ink
Ingredients	FLG, isopropyl alcohol, ceramic resin, dispersing agents
Solid content	2.5%
State	Liquid
Color	Grey
Odor	Acetone-like
Density (25 °C)	1.08 g/cm^3
Viscosity (25 °C, Pa·s)	1.095

2.2 Preparation of graphene-coated FA (FLG@FA)

FLG ink and RA were used to fabricate FLG@FA through the flip-spraying method and high-temperature curing process. In the flip-spraying method, FLG ink was sprayed onto one side of RA using a spray gun and an air pump. Subsequently, two pieces of foam were employed to clamp aggregates and then flip them over, after which their other side was also sprayed, ensuring the uniform application of FLG ink onto the aggregate surface. During the curing process, FA with the ink on its surface initially needed to be left at room temperature for 30 minutes to enable the evaporation of alcohol solvent. Thereafter, it was heated in an oven at 190 °C for 30 minutes. Following spraying and curing procedures, FLG@FA with a uniformly and firmly coated FLG film on the surface was successfully obtained.

2.3 Preparation of test specimens with FLG@FA

FLG@FA was used to prepare asphalt mixture specimens with PG 76/22 asphalt and filler. A porous asphalt mixture with a nominal maximum aggregate size of 13.2 mm (PA-13), an optimum asphalt-aggregate content of 4.1%, and a target void ratio of (20 ± 0.5) % were selected. The aggregates were preheated in an oven at 105 °C for more than 4 hours until reaching a constant weight and then further heated at 190 °C to ensure complete heating. Subsequently, they were mixed with hot asphalt binder heated at 170 °C following JTG E20-2011. It should be noted that after the heating procedures, the curing process of FA did not necessitate additional high-temperature treatment. After mixing and compacting, asphalt mixture specimens incorporating FLG@FA were obtained and were ready for further investigation.

2.4 Microwave deicing test

A microwave deicing test was conducted to evaluate the ice-melting efficiency. In this test, standard Marshall specimens (Φ101.6 mm × 63.5 mm) were used and an ice layer with a thickness of 10 mm was frozen on their surface (Figure 1). Those deicing specimens were initially maintained at a temperature of around -33 °C. Subsequently, their melting performance was examined through microwave heating at a power of 800 W. The specimen was heated for 30 s and then allowed to rest for 10 s alternately. The intermission time within the heating intervals was employed to document the mass of the ice and the surface temperature of the ice layer under ambient temperature conditions (15 °C). The average ice-melting velocity (v) was adopted to assess the melting efficiency, which is defined as follows:

$$v = \frac{m_2 - m_1}{t}$$

(1)

where m_1 is the mass of test specimen before testing, m_2 is the mass after testing, and t is the heating time.
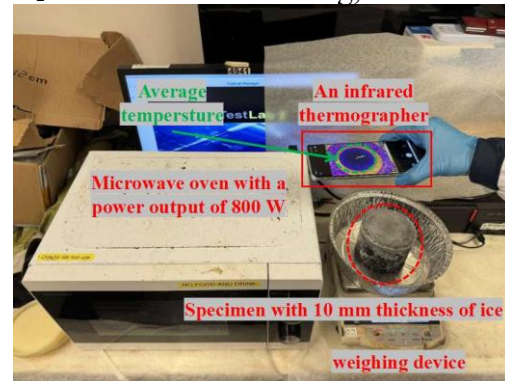
Figure 1. Experimental setup of ice-melting.

2.5 SCB test at lowPG+10 °C

The low-temperature cracking resistance was evaluated utilizing the SCB strength test under AASHTO TP105. Superpave gyratory compactor (SGC) specimens were shaped (Φ150 mm × 170 mm) and then sectioned into four semi-circular specimens (R150 mm × 50 mm). A notch (15 mm × 1.0 mm) was cut into the central bottom of each semi-circular specimen, aiming to ensure the cracking mode. Before testing, the specimens were subjected to a pre-conditioning treatment within a temperature-

controlled chamber at a temperature of lowPG+10 (specifically -12) °C for a duration of 4 h using a DTS-30 universal testing machine. An LLD-controlled configuration facilitates a more accurate acquisition of the fracture energy, as its measurement aligns with the direction of load application (Son et al., 2019). Subsequently, the SCB test was executed at a slow LLD rate of 0.5 mm/min. Final analysis was performed by using the load-LLD curves and fracture energy (G_f), which can be calculated using the following equation

$$G_f = \frac{W_f}{A_{lig}}$$
(2)

$$A_{lig} = (r - l) \times t$$
(3)

$$W_f = \int_{u_0}^{u_p} P_1(u)du + \int_{u_p}^{u_f} P_2(u)du$$
(4)

where W_f is the fracture work (J); Alig is the ligament area (m^2); r is the height of the specimen (mm), l is the depth of the notch (mm), and t is the thickness of the specimen (mm).

The flexibility index (FI), proposed by Ozer et al., serves as a crucial parameter for ascertaining the damage potential of asphalt mixture. It is indicative of the process zone size or other property combinations and exhibits a strong correlation with the crack growth speed (Al-Qadi et al., 2015). FI can be calculated from the parameters obtained using the load–LLD curve.

$$FI = \frac{G_f}{|m|} \times a$$
(5)

where G_f is the fracture energy (J/m^2), m is the post-peak load slope at the inflection point (kN/mm), and a is a factor (equal to 0.01).

According to experimental results, differences were found between load-displacement curves under the low-temperature condition and typical outcomes of the SCB test. Specifically, the curve under low temperature exhibits unique patterns as shown in Figure 2. Compared with the typical curve (left), it is evident from the right curve that a pronounced and linear downtrend is observable immediately after attaining the peak load. This phenomenon can be attributed to the transformation of the asphalt mixture from a viscoelastic material to a completely brittle one under low temperatures. After reaching the peak load, specimens snapped suddenly. As this material property changed, the test controlled by LLD mode failed to capture the post-peak slope, which is an essential factor for the calculation of FI. In addition, the area of the fracture work necessitated adjustment to the area of the curve ranging from the initial point (u_0) to the point corresponding to the peak load (u_p) since the specimen underwent brittle

fracture after reaching the peak load. The modified calculation is shown as follows:

$$W_f = \int_{u_0}^{u_p} P(u)du$$
(6)

where u_0 is the displacement at the contact load of 0.1 kN (mm) and u_p is the displacement at the peak load (mm).
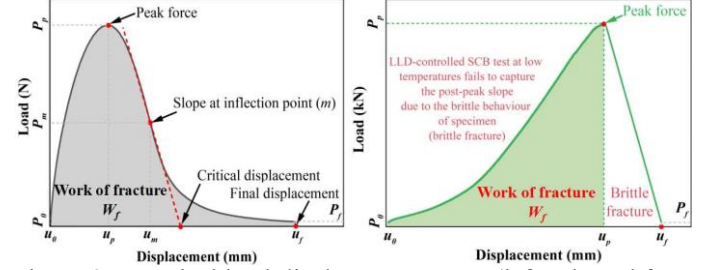
Figure 2. A typical load-displacement curve (left, adapted from (Al-Qadi et al., 2015)) and a load-displacement curve at lowPG+10 °C (right).

3 TEST RESULTS AND ANALYSIS

3.1 *Microwave deicing behavior*

Figure 3 presents the alterations in the average temperature of the ice surface on the specimen. The specimen with FLG@FA exhibits a considerably higher temperature increase rate compared to RA. FLG@FA curtailed the time of three microwave heating cycles (i.e., 90 s) to melt an ice layer with a thickness of 10 mm at an initial temperature of around -33 °C. After 150 s of microwave heating, the ice layer was entirely melted, and the average surface temperature of the ice layer reached 32.1 °C, which is higher than that of RA (30.2 °C). Notably, RA demanded a longer heating duration of 240 s. Despite the complete melting, the extended time implies that the ice absorbs and transforms microwave energy into heat inefficiently, thereby emphasizing the feeble responsiveness to microwave heating. As depicted in Figure 4, FLG@FA attained an ice-melting velocity of 29.6 g/min (an enhancement of ~64%) in comparison to RA (18.1 g/min) for melting the ice layer, thus manifesting the remarkable microwave deicing capacity of FLG@FA.
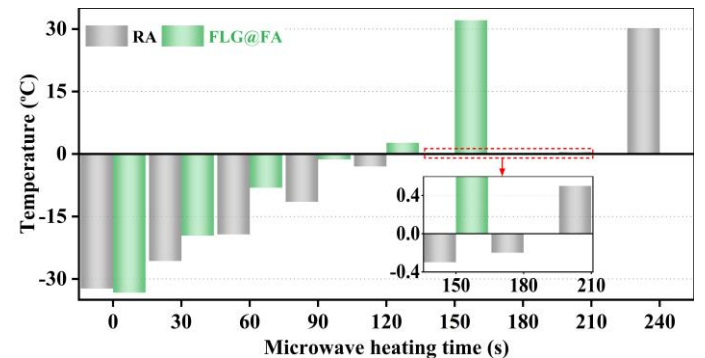
Figure 3. The average surface temperature on the ice layer.
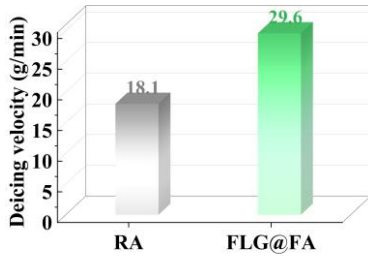
Figure 4. Deicing velocity results of specimens.

3.2 *Low-temperature cracking resistance*

The load-displacement curves obtained from the low-temperature SCB test are illustrated in Figure 5. The low-temperature curves exhibit unique patterns as previously mentioned (left). A distinct and linear downward trend was discernible after reaching the peak load (brittle behavior). The load-displacement curve of FLG@FA exhibited a higher peak load of 6.4 kN in contrast to that of RA, which was 6.1 kN. Simultaneously, it is observable that the W_f of RA (depicted by the gray area) ranging from u_0 to u_p is smaller than that of FLG@FA (green area). Subsequently, the G_f was determined by conducting integrations and calculations based on modified Equation 6 and Equation 2. The resultant values are illustrated in Figure 5 (right). Compared to the control group with a G_f value of 306.1 J/m^2, FLG@FA augmented its G_f value to 402.2 J/m^2, showing a substantially enhancing effect on low-temperature cracking resistance, with an improvement rate of approximately 31.4%.
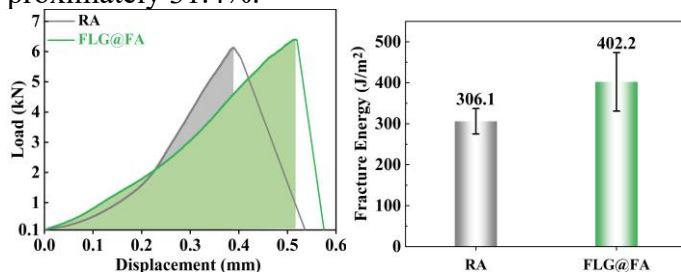
Figure 5. Modified fracture work results (left) and fracture energy results of SCB test at lowPG+10 ºC (right).

4 CONCLUSIONS

The following conclusions can be drawn according to the results and analysis:

1. Functional aggregates evenly coated with graphene film on the aggregate surface could be achieved through the flip-spraying method.
2. FLG@FA could significantly improve the microwave ice-melting performance. Its ice-melting velocity to melt an ice layer with a 10 mm thickness at about -33 ºC could be enhanced from 18.1 g/min to 29.6 g/min (~64%↑).
3. An improved method of calculating fracture work (W_f) was proposed and low-temperature SCB test results show that FLG@FA manifested an enhanced level of low-temperature cracking resistance (~31.4%↑) when compared with RA.

REFERENCES

AL-QADI, I. L., OZER, H., LAMBROS, J., KHATIB, A. E., SINGHVI, P., KHAN, T., RIVERA-PEREZ, J. & DOLL, B. 2015. Testing protocols to ensure performance of high asphalt binder replacement mixes using RAP and RAS.

ARABZADEH, A., NOTANI, M. A., KAZEMIYAN ZADEH, A., NAHVI, A., SASSANI, A. & CEYLAN, H. 2019. Electrically conductive asphalt concrete: An alternative for automating the winter maintenance operations of transportation infrastructure. *Composites Part B: Engineering,* 173**,** 106985.

GAO, J., SHA, A., WANG, Z., TONG, Z. & LIU, Z. 2017. Utilization of steel slag as aggregate in asphalt mixtures for microwave deicing. *Journal of Cleaner Production,* 152**,** 429-442.

KIM, M. S., JANG, D. U., HONG, J. S. & KIM, T. 2015. Thermal modeling of railroad with installed snow melting system. *Cold Regions Science and Technology,* 109**,** 18-27.

QIU, L. & NIXON, W. 2008. Effects of Adverse Weather on Traffic Crashes: Systematic Review and Meta-Analysis. *Transportation Research Record Journal of the Transportation Research Board,* 2055**,** 139-146.

SON, S., SAID, I. M. & AL-QADI, I. L. 2019. Fracture properties of asphalt concrete under various displacement conditions and temperatures. *Construction and Building Materials,* 222**,** 332-341.

SUN, Y., WU, S., LIU, Q., HU, J., YUAN, Y. & YE, Q. 2018. Snow and ice melting properties of self-healing asphalt mixtures with induction heating and microwave heating. *Applied Thermal Engineering,* 129**,** 871-883.

SUN, Y., ZHENG, L., CHENG, Y., CHI, F., LIU, K. & ZHU, T. 2023. Research on maintenance equipment and maintenance technology of steel fiber modified asphalt pavement with microwave heating. *Case Studies in Construction Materials,* 18**,** e01965.

TAN, Y., WANG, W., XU, Y., XING, C., LIANG, Z. & ZHANG, J. 2023. Investigation on preparation and properties of carbon fiber graphite tailings conductive asphalt mixture: A new approach of graphite tailings application. *Construction and Building Materials,* 402**,** 133057.

WANG, F., ZHU, H., SHU, B., LI, Y., GU, D., GAO, Y., CHEN, A., FENG, J., WU, S., LIU, Q. & LI, C. 2022. Microwave heating mechanism and self-healing performance of asphalt mixture with basalt and limestone aggregates. *Construction and Building Materials,* 342**,** 127973.

WU, S., MO, L., SHUI, Z. & CHEN, Z. 2005. Investigation of the conductivity of asphalt concrete containing conductive fillers. *Carbon,* 43**,** 1358-1363.

3.1

CHEMO-MECHANICAL AND OTHER TOOLS FOR PERFORMANCE EVALUATION OF ASPHALT BINDERS

On the use of DMT modulus distribution for quantifying the efficacy of recycling agent

L. Abinaya
Research Scholar, Department of Civil Engineering, Indian Institute of Technology Madras, Chennai, India.

K. Lakshmi Roja
Assistant Research Scientist, Department of Mechanical Engineering, Texas A&M University at Qatar, Doha, Qatar.

Wubulikasimu Yiming
Assistant Manager, Central Materials Facility, Texas A&M University at Qatar, Doha, Qatar.

M. R. Nivitha
Assistant Professor, Department of Civil Engineering, PSG College of Technology, Coimbatore, India

Eyad Masad
Professor, Department of Mechanical Engineering, College of Science and Engineering, Hamad Bin Khalifa University, Doha, Qatar

J. Murali Krishnan
Professor, Department of Civil Engineering, Indian Institute of Technology Madras, Chennai, India.

ABSTRACT: Quantifying the efficacy of recycling agents (RA) is crucial to determine the optimal dosage for recycling Reclaimed Asphalt Pavement (RAP) materials. Atomic Force Microscopy (AFM) is used to capture the microstructure of binders and observe the dispersing effect of RA. However, the extent to which the dispersion effect impacts the aged binder properties remains unclear. To address this and identify the limiting RA dosage in terms of dispersion efficacy, the Derjaguin-Muller-Toporov (DMT) modulus and its frequency distribution obtained from AFM are analyzed in this investigation. Laboratory-aged binders are blended with different RA dosages, and the microstructure images revealed that the dispersion effect plateaued beyond 10% RA. Frequency distribution of DMT modulus showed reduced mean and increased skewness with RA addition. Results suggest that RA facilitates dispersion and softening up to a 10% threshold dosage, beyond which its dispersion efficacy reduces and RA contributes to softening primarily by introducing low-modulus fractions.

1 INTRODUCTION

Utilization of higher proportions of Reclaimed Asphalt Pavement (RAP) material necessitates recycling the aged binder to mitigate the effects of its increased „stiffness". Recycling agents are added to RAP to reduce the „stiffness" of the aged binder and achieve target rheological properties in the final recycled blend. Different types of recycling agents are available, and the interaction mechanism between the aged binder and the recycling agent, which governs the changes in rheological properties, can vary depending on the composition of the recycling agent (Fini et al., 2020). Literature hypothesizes the interaction effects of RA to be one or a combination of the following: reducing „stiffness" (softening effect) through the addition of lighter hydrocarbons, balancing asphaltene-maltene proportions, and dispersing the polar asphaltenes associations (Martin et al., 2020).

The extent of these interactions depends on the composition of RA and aged binder, which determines the RA dosage required to achieve target rheological properties (Abdelaziz et al., 2022). While continued addition of RA may reduce the „stiffness"

of aged binder due to the low molecular weight hydrocarbons present in RA, it is uncertain whether the dispersion and asphaltenes-maltene balancing effects remain consistent across incremental dosages. Therefore, it is necessary to quantify the efficacy of RA in terms of its interaction effects at different dosages to identify the threshold dosage beyond which its influence diminishes.

To capture the influence of RA, studies have used various experimental techniques such as Dynamic Shear Rheometer (DSR), Atomic Force Microscopy (AFM), Fourier Transform Infrared (FTIR) Spectroscopy, and polarity-based fractionation. Studies often use specification compliance parameters, such as penetration, softening point, apparent viscosity and performance grade, to quantify the influence of recycling agents, while some assess rheological responses under varying frequencies and aging conditions (Karkhi & Zhou, 2016; Samara et al., 2022; Abdelaziz et al., 2022). For changes in chemical composition, carbonyl and sulfoxide indices are calculated to determine how RA addition influences oxidation functional groups present in aged binders (Karkhi & Zhou, 2016; Abdelaziz et al., 2021).

To evaluate the dispersing effect of RA, studies often qualitatively analyze the topographical images obtained from AFM (Holleran et al., 2021; Abe et al., 2023). In addition to making inferences based on images, it is essential to consider quantifiable measurements at micro-scale to assess the influence of RA. For this purpose, studies used mechanical properties measured using PeakForce Quantitative Nanomechanical Mapping (PFQNM) mode in AFM (Holleran et al., 2021; Abdelaziz et al., 2021). This technique generates force-displacement curves by applying a controlled peak force on an oscillating tip, allowing computation of mechanical properties such as adhesion, dissipation, and DMT modulus from the approach and retraction curves. This paper focuses on using DMT modulus to quantify the efficacy of RA in terms of softening and dispersion effects.

Studies have compared the frequency distribution of DMT modulus and its mean value for blends with varying RAP binder proportions and different recycling agents (Roja et al., 2020; Abdelaziz et al., 2022; Masad & Roja, 2024). Abdelaziz et al. (2022) found that mean DMT modulus reduced, and the distribution became narrower with RA addition. However, the DMT modulus and its distribution have not been further explored to quantify the influence of varying RA dosages. A reduction in DMT modulus with RA addition could arise from the dispersion of polar associations or through the softening effect facilitated by addition of lighter fractions. It will thus be interesting to identify characteristics representing the distribution and relate them to the microstructure to obtain insights into the interaction between RA and aged bitumen at different RA dosages.

The objective of this study is to use DMT modulus, obtained from PFQNM mode in AFM, to quantify the softening and dispersion effects of the recycling agent on the aged binder at the micro-scale. Here, different dosages of RA are added to a laboratory-aged binder such that the recycled blends bracket the high-temperature PG of the unaged binder. DMT modulus images of aged and recycled binders are analyzed, and the characteristic properties (mean, full-width half maximum, and skewness) of their corresponding frequency distributions are computed. The characteristics of the DMT modulus distribution are used to identify a critical RA dosage beyond which the efficacy of RA in dispersing the polar associations decreased.

2 MATERIALS AND METHODS

2.1 Materials

An unmodified bitumen meeting Viscosity Grade 30 (VG30) as per Indian Standards (IS 73: 2018) is used as the base binder for the study. Table 1 lists the properties of the VG30 binder as per IS 73: 2018.

Table 1. Characteristics of unaged VG30 binder

Characteristics	Result
Penetration at 25 °C, 100 g, 5 s, 0.1 mm	56
Absolute viscosity at 60 °C, 300 mm Hg vacuum, Pa.s	279.1
Softening point (R&B), °C	50

The RAP binder was obtained through laboratory aging, wherein the VG30 binder was spread to 1 mm film thickness and subjected to aging in a forced draft oven. The binder was aged at 120 °C for 86 hours, following the procedure outlined by Abinaya et al. (2023). The continuous high-temperature PG of the binders is listed in Table 2. A tall oil-based recycling agent named Evoflex CA 21, manufactured by Ingevity Corporation (Ingevity, 2024), was used in the study. Different dosages of the recycling agent, namely 5%, 10%, and 15% by weight of the aged binder, were added such that the recycled binders bracket the high-temperature PG of the VG30 binder.

Table 2. Continuous high-temperature PG of binders

Binder	PG (°C)	Nomenclature
Unaged VG30	64.4	VG30
86 hours aged binder	82.4	86H
86H + 5% RA	74.7	86H+5%RA
86H + 10% RA	66.7	86H+10%RA
86H + 15% RA	61.8	86H+15%RA

2.2 Atomic Force Microscopy

The specimen for AFM imaging was prepared using the heat-cast method, which involves heating 0.2 g of bitumen on a glass slide in an oven at 140 °C for 5 minutes to achieve an approximately 400 μm thick film with a smooth surface. The tests were conducted at least 24 hours after specimen preparation. The microscopic imaging was carried out using Dimension Icon AFM manufactured by Bruker Corporation, Germany. The topography images and mechanical properties were captured in PeakForce Quantitative Nano-mechanical (PFQNM) property imaging mode in air. The scans were conducted using the RTESPA 300 Bruker AFM silicon probe, which has a nominal frequency of 300 kHz, a nominal tip radius of 30 nm, and a spring constant of 55.1 N/m. The probe calibration and sample analysis were performed through Bruker NanoScope Analysis 3.0 software (NanoScope, 2022). The samples were scanned with a constant peak force of 30 nN at a frequency of 1 kHz, using 256 data points per line and 256 scan lines over a 10 μm scan size.

2.3 Derjaguin-Muller-Toporov (DMT) modulus

DMT modulus is computed by fitting the Derjaguin-Muller-Toporov (DMT) model, shown in Equation 1 (Derjaguin et al., 1975; NanoScope, 2022) to the re-

traction curve of the force-displacement plot. Here, the DMT modulus (E) depends on the force required to indent the sample surface and the extent to which the sample deforms under this force.

$$F - F_{adhesion} = \frac{4}{3} E\sqrt{R(d - d_o)^3} \qquad (1)$$

F is the force on the tip, $F_{adhesion}$ is the adhesion force, R is the tip-end radius, $d - d_o$ is the deformation of the sample.

3 RESULTS AND DISCUSSION

3.1 Influence of recycling agent on microstructure

The two-dimensional images indicating the spatial distribution of the DMT modulus of the binders under investigation are presented in Figure 1.

(a) VG30

(b) 86H

(c) 86H+5%RA

(d) 86H+10%RA

(e) 86H+15%RA
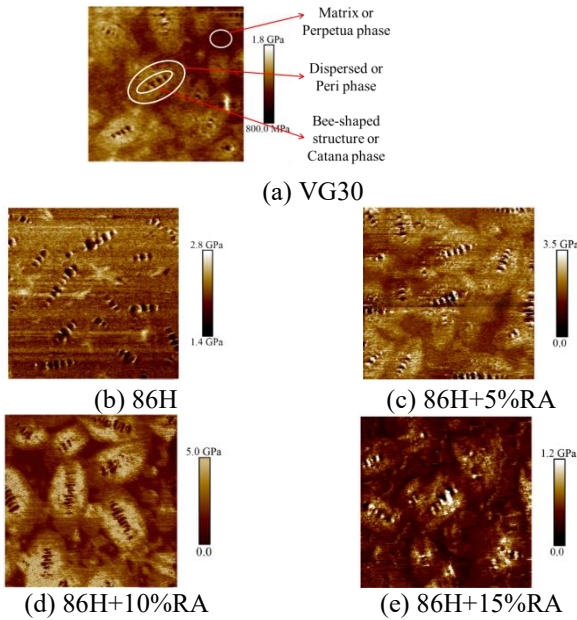
Figure 1. DMT modulus images

The following observations are made from the microstructure images.

- The DMT modulus image of VG30 binder contains three phases, as described in the literature (Masson et al., 2006). The bee-shaped structure, or the catana phase, consists of alternating high-modulus and low-modulus regions. The catana phase is surrounded by the peri phase, which exhibits a lower modulus than the peaks in the catana phase. Both catana and peri phases are dispersed in a continuous, lower-modulus medium, known as the perpetua or matrix phase.
- DMT modulus image of 86H binder shows that aging increases the number of catana and peri phase associations, resulting in the disappearance of the matrix phase.
- Adding 5 and 10% recycling agent (Figures 1c and 1d) disperses the catana and peri phase asso-

ciations and increases the region occupied by the matrix phase.
- A further increase in RA dosage to 15% (Figure 1e) did not show major changes in dispersion, indicating that the RA does not promote dispersion beyond a certain level.

3.2 Frequency distribution of DMT modulus

To quantify the influence of recycling agent, the frequency distribution of DMT modulus across the 2D image (Figure 1) is presented in Figure 2.
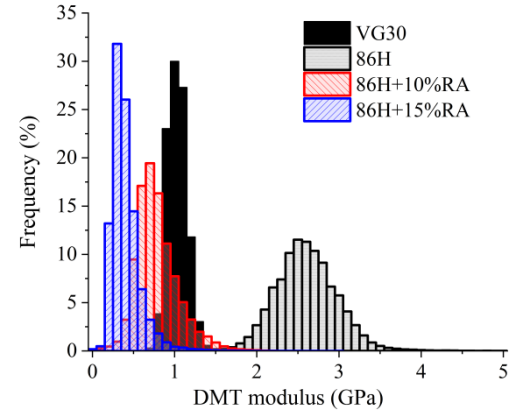
Figure 2. DMT modulus distribution

Here, the distribution is approximated to be Gaussian-shaped, and the characteristics that quantify the shape and spread of the DMT modulus distribution are listed in Table 3. Full-width half maximum (FWHM) represents the width of the curve at half the height of maximum frequency. FWHM quantifies the spread of the distribution, indicating the extent to which DMT modulus varies in the binder. The skewness of the distribution was calculated using Pearson's coefficient of skewness. A positive or right skewness indicates that a higher proportion of material exhibits lower DMT modulus, and a smaller proportion (peaks in catana phase) exhibits significantly higher modulus values.

Table 3. Characteristics of DMT modulus distribution

Binder	Mean (GPa)	FWHM	Skewness
VG30	1.08	0.24	0.194
86H	2.47	0.74	0.026
86H+5%RA	1.79 (27%)	0.62 (16%)	0.354 (1261%)
86H+10%RA	0.93(48%)	0.41 (34%)	0.505 (42%)
86H+15%RA	0.45 (51%)	0.23 (44%)	0.699 (38%)

The following findings were obtained from Figure 2 and Table 3.
- Aging increased the mean DMT modulus and FWHM, with a decrease in skewness, reflecting an increase in the proportion of high-modulus regions (catana and peri phases) in Figure 1b.
- Adding the recycling agent decreased the mean DMT modulus and FWHM, indicating that the extent of variation in DMT modulus reduced with RA addition. Also, the skewness value in-

creased, suggesting an increase in the proportion of low-modulus fractions.

- The percent differences are calculated for every 5% increment in RA dosage in Table 3 (shown in brackets) to quantify the relative influence of RA dosages. The percent difference in mean and FWHM increased with higher RA dosage, indicating that the efficacy of RA in softening persists at higher dosages.

- The percent difference in skewness decreased with an increase in RA dosage. Relating this to the minimal variations in the dispersion of polar associations observed at higher RA dosages (beyond 10%), it can be inferred that beyond a certain dosage, RA primarily contributes to a reduction in the DMT modulus by increasing the proportion of low-modulus fractions, while its efficacy in promoting dispersion diminishes.

4 CONCLUSIONS

The current investigation relates the microstructure images from AFM and the corresponding DMT modulus distribution to obtain insights into the softening and dispersion effects of the recycling agent. The microstructure images show that RA addition resulted in the dispersion of associated phases (catana and peri phases), while no change in dispersion was seen beyond a specific dosage (10%). The influence of varying RA dosages was quantified based on the characteristics of the DMT modulus distribution (mean, FWHM, and skewness). The percent difference in these characteristics shows that as RA dosage increases, the change in mean and FWHM continue to increase, and the change in skewness decreases. The findings suggest that RA promotes softening and dispersion up to a certain dosage, after which the softening effect becomes predominant. The changes in dispersion effect from microstructure and skewness of the DMT modulus distribution can be examined to assess the efficacy of RA in dispersing the polar associations, thereby allowing for the identification of a threshold RA dosage.

The study highlights that analyzing the microstructure and skewness of the distribution is useful when comparing the efficacy of different recycling agents in terms of their relative influence in softening and dispersing effects. Future research should focus on exploring various recycling agents and RAP binders to confirm the plausible explanations provided in this paper.

REFERENCES

Abdelaziz, A., Masad, E., Martin, A. E., Mercado, E. A., and Bajaj, A. (2021). Multiscale characterization of aging and rejuvenation in asphalt binder blends with high RAP con-
tents. *Journal of Materials in Civil Engineering*, 33(10):04021287.

Abdelaziz, A., Masad, E., Martin, A. E., Mercado, E. A., and Bajaj, A. (2022). Thermal, microscopic, and rheological characterization of rejuvenated asphalt binders. *Materials and Structures*, 55(3): 98.

Abe, A. A., Rossi, C. O., Eskandarsefat, S., Porto, M., Loise, V., Venturini, L., and Caputo, P. (2023). Reclaimed asphalt recycling agents: Looking into the blueprint of their mechanisms of action. *Construction and Building Materials*, 363:129843.

Abinaya, L., Thirumalavenkatesh, M., Nivitha, M. R., and Krishnan, J. M. (2023). Influence of aging on the rheological response of bitumen. In *Advances in Materials and Pavement Performance Prediction III*. CRC Press, Hong Kong, China.

Derjaguin, B. V., Muller, V. M., and Toporov, Y. P. (1975). Effect of contact deformations on the adhesion of particles. *Journal of Colloid and interface science*, 53(2):314–326.

Dhasmana, H., Hossain, K., and Karakas, A. S. (2021). Effect of long-term ageing on the rheological properties of rejuvenated asphalt binder. *Road Materials and Pavement Design*, 22(6):1268–1286.

Fini, E., Rajib, A. I., Oldham, D., Samieadel, A., and Hosseinnezhad, S. (2020). Role of chemical composition of recycling agents in their interactions with oxidized asphaltene molecules. *Journal of Materials in Civil Engineering*, 32(9):04020268.

Holleran, I., Masad, E., Holleran, G., Wubulikasimu, Y., Malmstrom, J., and Wilson, D. (2021). Nano-mechanical mapping of rejuvenated asphalt binders. *Road Materials and Pavement Design*, 22(11):2478–2497.

Ingevity (2024). Evoflex CA. https://www.ingevity.com/uploads/market-pdfs/EvoFlex-CA.pdf. Accessed: 13-12-2024.

IS 73: 2018 (2018). Paving Bitumen - Specification. Indian standards, Bureau of Indian Standards, New Delhi, India.

Karki, P. and Zhou, F. (2016). "Effect of rejuvenators on rheological, chemical, and aging properties of asphalt binders containing recycled binders." *Transportation research record*, 2574(1), 74–82.

Martin, A. E., Kaseer, F., Mercado, E. A., Bajaj, A., Cucalon, L. G., Yin, F., Chowdhury, A., Epps, J., Glover, C., and Hajj, E. Y. (2020). Evaluating the effects of recycling agents on asphalt mixtures with high RAS and RAP binder ratios. NCHRP Report 927, National Cooperative Highway Research Program and Transportation Research Board, Washington, DC.

NanoScope (2022). NanoScope Analysis, Version 3, Bruker Corporation, Massachusetts, United States.

Masad, E., and Roja, K. L. (2024). Assessment of aging behaviour of reclaimed asphalt binders: multi-scale mechanical and microstructural characterization. *Road Materials and Pavement Design*, 1–21.

Masson, J.-F., Leblond, V., and Margeson, J. (2006). Bitumen morphologies by phase detection atomic force microscopy. *Journal of microscopy*, 221(1):17–29.

Roja, K. L., Masad, E., Vajipeyajula, B., Yiming, W., Khalid, E., and Shunmugasamy, V. C. (2020). Chemical and multi-scale material properties of recycled and blended asphalt binders. *Construction and Building Materials*, 261:119689.

Samara, M., Offenbacker, D., Mehta, Y., Ali, A., Elshaer, M., and Decarlo, C. (2022). "Performance evaluation and characterization of extracted recycled asphalt binder with rejuvenators." *Transportation Research Record*, 2676(12): 714–727.

Evaluating bitumen long term cracking susceptibility: Chemical & rheological insight

P. Aeron & D. Singh
Indian Institute of Technology Bombay, Mumbai, Maharashtra, India

ABSTRACT: Fatigue cracking is a critical distress mechanism in pavements, driven by environmental exposure that reduces binder flexibility, causing brittleness and cracks. Variability among same-grade binders due to differing aging susceptibilities further complicates cracking resistance. This study evaluates 12 binders from diverse sources under long-term aging simulated using a Pressure Aging Vessel (20, 40, and 60 hours). Tests included SARA fractionation, softening point, fatigue factor, Linear Amplitude Sweep (LAS), and Double Edge Notched Tension (DENT). Results showed that prolonged aging amplified variability in aging susceptibility. Conventional parameters like fatigue factor and fatigue life were unable to correlate with chemical and physical properties, whereas DENT parameters exhibited strong correlations, even under extended aging. These findings emphasize the limitations of existing parameters and highlight DENT testing as a superior tool for assessing binder performance under various aging conditions.

1. INTRODUCTION

Aging is an inevitable phenomenon in bituminous pavements, influenced by environmental factors and construction practices. It begins during mixing, compaction, and transportation, referred to as short-term aging, and continues throughout the pavement's service life as long-term aging (Bi et al., 2020). Aging induces chemical changes in the bitumen matrix, notably an increase in asphaltene content at the expense of maltenes. Rheologically, this shift enhances the elastic component at the cost of the viscous component, while physically, it increases stiffness and the aging index (Qin et al., 2014).

Short-term aging can improve rutting resistance by hardening the binder, but prolonged aging adversely affects fatigue and fracture cracking resistance, posing challenges to pavement durability. Laboratory simulations of aging typically employ the Rolling Thin Film Oven Test (RTFOT) for short-term aging and the Pressure Aging Vessel (PAV) test for long-term aging. Standard PAV protocols involve exposing RTFO-aged samples to 100°C and 2.1 MPa for 20 hours, simulating approximately five to ten years of field aging. (Bredenhann et al.2019)

In tropical regions, where elevated temperatures accelerate aging, standard aging protocols may fall short in replicating field conditions. Extended aging durations of 40 and 60 hours have been proposed to better assess long-term performance under these conditions (Gholami et al., 2024). Moreover, aging susceptibility varies significantly among same-grade binders from diverse sources due to differences in chemical composition and reaction kinetics. This highlights the need for a deeper understanding of binder variability and its influence on aging behavior (Roopashree & Singh, 2020).

To evaluate cracking resistance, various chemical and physical tests, such as the softening point test and SARA analysis, provide insights into binder hardness and cracking potential. Precise predictive methods, including the fatigue factor, Linear Amplitude Sweep (LAS) test, and Double Edge Notched Tension (DENT) test, further assess fatigue and fracture resistance (Zhou et al., 2013). However, the reliability of these evaluations depends on correlations among various parameters.

This study investigates the effects of source variability and extended aging on binder crack resistance using chemical, physical, rheological, and advanced test methods. It also analyzes the inter-correlations of these parameters to identify the most reliable

indicators of cracking resistance under various long-term aging conditions. By addressing the limitations of existing evaluation methods and proposing the most effective approach, the study aims to improve the predictive capability for binder durability across different aging scenarios.

2. MATERIAL

In this study, viscosity-grade 40 (VG 40), a widely used unmodified binder in India, was chosen as the test material. Samples were produced from six domestic sources (Sources 1 to 6) and six international sources (Sources 7 to 12) to assess property variability. Since the samples were collected from ongoing projects, the analysis also considers additional variability arising from differences in project conditions, source locations, and refinery processes.

3. EXPERIMENTAL PLAN

The experimental plan involved simulating short-term aging through the Rolling Thin Film Oven Test (RTFOT) in accordance with ASTM D2872, followed by long-term aging of the RTFO-aged binder using the Pressure Aging Vessel (PAV) as per ASTM D6521. Chemical analysis was performed using SARA fractionation, while physical properties were evaluated using the softening point test (ASTM D36). Rheological properties were assessed with a Dynamic Shear Rheometer (DSR) to determine the Superpave fatigue factor and conduct the Linear Amplitude Sweep (LAS) test (AASHTO TP101). Additionally, the Double Edge Notched Tension (DENT) test was performed to evaluate binder performance under fracture conditions.

4. RESULT AND DISCUSSION

4.1. *Chemical properties of bitumen*

The chemical analysis in this study was conducted using SARA analysis, which categorizes bitumen, based on polarity, into four components: saturates, aromatics, resins, and asphaltenes. The proportions of these components determine the overall hardness of bitumen. While various parameters have been used in literature, the Gaestel Index (I_c), as shown in Equation 1, was found to be the most appropriate for assessing bitumen hardness. Binders with I_c values between 0.22 and 0.5 are considered stable, those above 0.5 are classified as hard, and values below 0.22 indicate soft binders (Paliukaite et al.2014 and Kleizienė et al. 2019)

$$I_c = (Saturates + Asphaltenes) / (Resins + Aromatics)$$

(1)
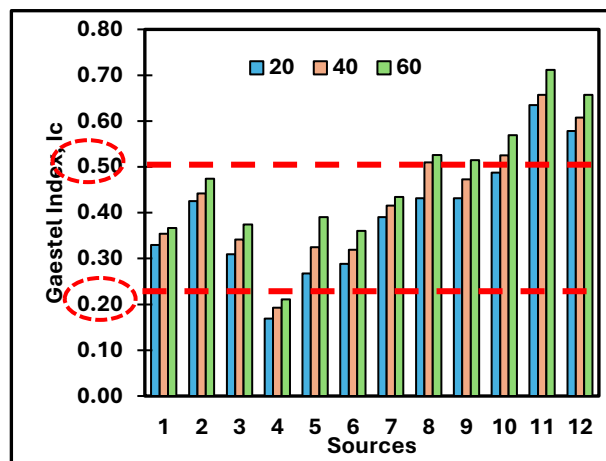
Figure 1. Chemical analysis of various binders

In this study, long-term aged data was analyzed using the I_c value, revealing significant variability among binders of the same grade, as shown in Figure 1. This variability became more pronounced with extended aging durations of 40 and 60 hours. Prolonged aging resulted in increased binder stiffness and reduced fatigue crack resistance. These findings highlight the importance of considering both aging duration and source variability when evaluating binder durability. However, the rate of aging varied across sources, indicating that different binders of the same grade can exhibit distinct chemical kinetics based on their aging susceptibility. The observed decline in crack resistance with aging is further supported by correlations with other parameters, offering additional insights into binder behavior under prolonged long-term aging conditions.

4.2. *Correlation of softening point with Gaestel Index (I_c)*

As aging progressed, both the binder's hardness and softening point increased, which can be attributed to oxidation-induced molecular agglomeration and the formation of condensed aromatic rings (Saha Chowdhury et al., 2022).

Although the softening point increased with prolonged aging duration, the graph has been omitted for brevity, and instead, the correlation with the chemical parameter is presented for better clarity in understanding their relationship. As expected, the softening point values exhibited a positive correlation with the I_c, as shown in Figure 2. This correlation further supports the reliability of I_c as a robust predictor of aging and the resulting stiffening of binders. Both parameters show promise as reliable indicators for assessing crack resistance across various binder sources and aging conditions. Therefore, they are anticipated to correlate with other critical parameters as well, enhancing the overall understanding of binder performance.
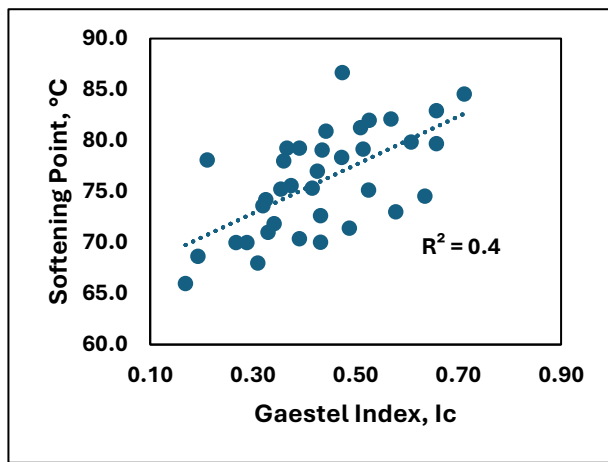
Figure 2. Correlation of Softening point with Gaestel Index

Figure 3. Correlation of Fatigue factor with Gaestel index and softening point

4.3. *Cracking performance using Superpave fatigue parameter and LAS*

In this section, two rheological parameters were evaluated: the Superpave fatigue factor and fatigue life (Nf), calculated using the LAS test. As anticipated, aging led to an increase in binder stiffness, which resulted in reduced fatigue resistance. This was reflected by an increase in the fatigue factor and a decrease in N_f over 20, 40, and 60 hours of aging.

However, when correlating the chemical parameter (on the primary axis) and physical parameters (on the secondary axis) with the fatigue factor (Fig. 3) and fatigue life (Fig. 4), the results did not align with expectations. Specifically, the fatigue factor was expected to show a positive correlation, and N_f was expected to show a negative correlation, with both the Gaestel Index (I_c) and the softening point (SP). The absence of these anticipated relationships raises concerns about the reliability of these rheological parameters. They fail to align with chemical and physical properties, which are governed by similar stiffness principles, thus questioning their accuracy as indicators of crack resistance.

This discrepancy emphasizes the need for a more reliable and robust crack resistance parameter—one that consistently correlates with multiple properties and offers more accurate insights into binder crack resistance across various aging conditions.

Figure 4. Correlation of Fatigue life with Gaestel index and softening point

4.4. *Cracking performance using Double-Edge Notched Tension (DENT) test parameter:*

The limitations of previous parameters were addressed by evaluating Crack Tip Opening Displacement (CTOD), derived from the DENT test. CTOD assesses both crack initiation and propagation, making it a robust indicator of fracture crack resistance. However, the test's applicability is limited to aging durations of up to 40 hours, which meant it was only evaluated for 20 and 40 hours of long-term aging.

A higher CTOD value indicates greater resistance to fracture cracking. Therefore, with prolonged aging, the CTOD value decreased, as expected.

Through correlation studies, it was anticipated that CTOD would exhibit a positive correlation with N_f and a negative correlation with the fatigue factor, softening point (SP), and Gaestel Index (I_c). However, as shown in Figure 5, when fatigue factors (primary axis) and N_f (secondary axis) were correlated with CTOD, they did not align with the expected correlations. In contrast, Figure 6 shows that when Ic

(primary axis) and SP (secondary axis) were correlated with CTOD, strong and expected correlations were observed, reaffirming its reliability for predicting crack resistance, even under prolonged long-term aging conditions.

Moreover, in the absence of DENT test results, the strong correlation between I_c (chemical parameter) and SP (physical parameter) with CTOD suggests that these parameters can serve as indirect indicators of fracture crack resistance for binders across various long-term aging scenarios.
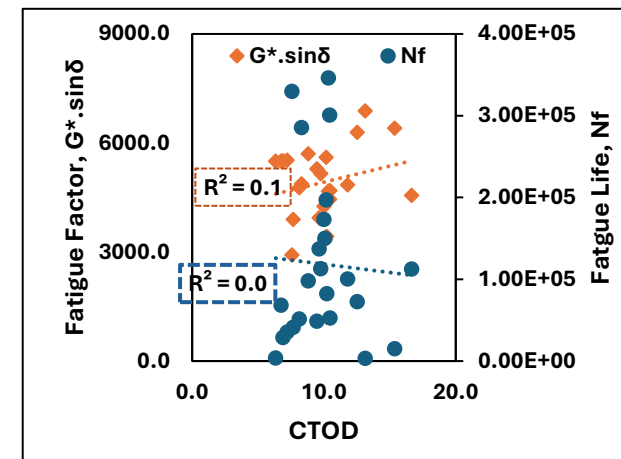
Figure 5. Correlation of CTOD with Fatigue factor and Fatigue life
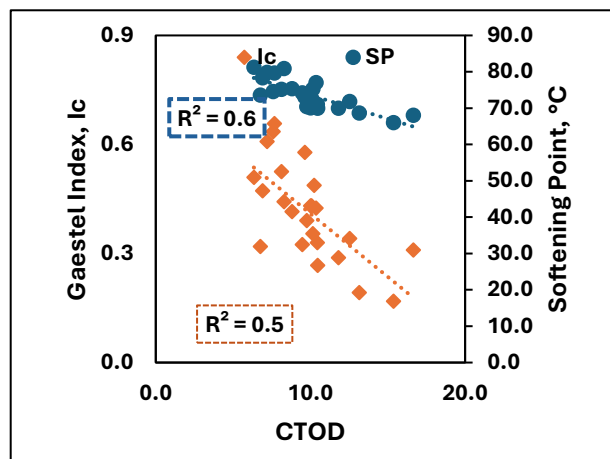
Figure 6. Correlation of CTOD with Gaestel index and softening point

5. CONCLUSION

The following conclusions can be drawn based on the above findings

I_c was identified as the most reliable parameter for predicting binder stability and hardness, effectively accounting for the polarity-based distribution of bitumen components.

The softening point proved to be a robust physical parameter, providing consistent results even under prolonged long-term aging conditions.

The positive correlation between I_c and SP confirmed the applicability and reliability of the chemical parameter in assessing binder aging and stiffness.

Rheological parameters, including $G^*.\sin\delta$ and N_f, did not exhibit the expected correlations with I_c and SP, highlighting their limitations in predicting crack resistance.

The CTOD from the DENT test demonstrated strong correlations with both I_c and SP, establishing itself as the most reliable parameter for evaluating crack resistance, even in extended aging scenarios.

In the absence of DENT test results, I_c and SP can serve as practical predictive tools for assessing fracture crack resistance due to their strong correlation with CTOD.

This study highlights the need for integrating advanced testing methods like CTOD with chemical and physical parameters to enhance the assessment of binder performance under aging conditions.

REFERENCE

Bi, Y., Wu, S., Pei, J., Wen, Y., & Li, R. (2020). Correlation analysis between aging behavior and rheological indices of asphalt binder. Construction and Building Materials, 264, 120176.

Bredenhann, S. J., Myburgh, P. A., Jenkins, K. J., O'Connell, J. S., Rowe, G. M., & D'Angelo, J. (2019). Implementation of a performance-grade bitumen specification in South Africa. Journal of the South african institution of civil engineering, 61(3), 20-31.

Gholami, M., Khodaii, A., & Hajikarimi, P. (2024). Long-term aging simulation of asphalt mixture: A comparative experimental study. Construction and Building Materials, 435, 136856.

Kleizienė, R., Panasenkienė, M., & Vaitkus, A. (2019). Effect of aging on chemical composition and rheological properties of neat and modified bitumen. Materials, 12(24), 4066.

Paliukaite, M., Vaitkus, A., & Zofka, A. (2014). Evaluation of bitumen fractional composition depending on the crude oil type and production technology. In Environmental engineering. Proceedings of the international conference on environmental engineering. ICEE (Vol. 9, p. 1). Vilnius Gediminas Technical University, Department of Construction Economics & Property.

Qin, Q., Schabron, J. F., Boysen, R. B., & Farrar, M. J. (2014). Field aging effect on chemistry and rheology of asphalt binders and rheological predictions for field aging. Fuel, 121, 86-94.

Roopashree, M. S., Singh, D., & Showkat, B. (2020). A comprehensive study on source dependency of conventional, chemical and rheological properties of asphalt binder. Construction and Building Materials, 258, 120338.

Saha Chowdhury, P., Mullapudi, R. S., & Reddy, M. A. (2022). An investigation on the effect of aging on chemical and mechanical properties of asphalt binders. Journal of Materials in Civil Engineering, 34(10), 04022252.

Zhou, F., Mogawer, W., Li, H., Andriescu, A., & Copeland, A. (2013). Evaluation of fatigue tests for characterizing asphalt binders. Journal of Materials in Civil Engineering, 25(5), 610-617.

Evaluating the compatibility between bitumen and bio-additives using Hansen Solubility Parameter (HSP)

Yongping Hu, Anand Sreeram & Gordon D. Airey
Nottingham Transportation Engineering Centre (NTEC), Faculty of Engineering, University of Nottingham, Nottingham, NG7 2RD, United Kingdom

ABSTRACT: The rising demand and increasing environmental concerns necessitate the urgent exploration of alternative, sustainable resources as partial or full replacement for bitumen. One of the promising approaches is the use of bio-based alternatives as bitumen substitutes. This study utilised solubility science to assess the fundamental physicochemical compatibility between bitumen and two bio-based additives. Tall oil (bio-additive-1) and waste cooking oil (bio-additive-2) were employed as bio-sourced additives. The Hansen solubility parameters (HSP) of bitumen, its subfractions and bio-additives were measured. Frequency sweep tests and bending beam rheometer (BBR) tests were also carried out. Bio-additive-1 showed better performance and efficiency compared to bio-additive-2 in improving the low-temperature performance and durability of bio-bitumen. The HSP of bio-additive-1 was closer to those of bitumen and its subfractions compared to bio-additive-2, which likely contributes to increased compatibility. The overlapping ratios of Hansen spheres and bitumen subfractions were positively correlated with the rheological properties of the bio-bitumen.

1 INTRODUCTION

The continuous increase in bitumen consumption will ultimately lead to energy shortages (He et al., 2019). Additionally, modern refining processes are more efficient in extracting high-value products from crude oil, leaving less high-quality residue for bitumen production (Lapidus et al., 2018). Moreover, the production of bitumen results in excessive CO_2 emissions and energy consumption, which increases environmental concerns (Thives and Ghisi, 2017). These concerns necessitate the urgent exploration of alternative, eco-friendly resources for bitumen. One of the ways to make the pavement industry more sustainable is using bio-based alternatives to partially replace bitumen (Espinosa et al., 2024). However, although the use of bio-bitumen offers a sustainable option, the selection of bio-additives is currently arbitrary. Mixing bitumen with less suitable bio-additives may lead to incompatibility issues and thereby adversely affect the performance of bio-bitumen.

One promising approach to evaluate compatibility is using solubility science. Hansen solubility parameter (HSP) is one of the most used solubility-based models (Hansen, 1969). The HSP consists of three parts influencing a given material's solubility, namely dispersion forces (δ_D, in MPa$^{1/2}$), polar interactions (δ_P, in MPa$^{1/2}$), and hydrogen bonding (δ_H, in MPa$^{1/2}$) (Hansen, 1969). Materials which have similar values of HSPs are believed to be soluble and compatible with each other (Hansen, 2007).

However, there are no established methods to scientifically characterise the compatibility between bio-additives and bitumen (Yang et al., 2017). Current approaches are primarily based on trial and error, lacking scientific basis and fundamental understanding of physicochemical interactions in these complex mixes. In this regard, this study will evaluate compatibility of bio-additives and bitumen using HSP approach. This approach will investigate the fundamental physiochemical interactions in bio-bitumen and is envisaged to lead to a necessary understanding in terms of the influence of compatibility on the physical performance of bio-bitumen.

2 MATERIALS AND METHODS

2.1 Materials

A PG 64-22 neat bitumen with a penetration of 81 (0.1mm) and softening point of 45.5 °C, and two bio-additives, namely tall oil and recycled cooking oil were employed in this study. The HSPs of bitumen and bio-additives were measured using 33 different chemicals with a wide range of known HSPs.

2.2 Testing methods

Bitumen and its subfractions, namely asphaltenes and maltenes, as well as bio-additives were dissolved by the solvents in glass vials. Then the solutions were stored at fume hood for 24 hours. For solvents that could dissolve bitumen or its subfractions, homogeneous solutions were observed. For solvents that could not dissolve bitumen or its subfractions, bitumen or its subfractions precipitated at the bottom of the containers. Regarding the solubilities of bio-additives, if the bio-additives and solvents were mutually soluble, homogeneous blends were observed. If they were insoluble, distinct boundaries between the materials were observed. Based on the

solubility tests, the HSP values of each material could be computed using the HSPiP software.

Frequency sweep tests were carried out for examining the rheological performance of bitumen. The frequencies ranged from 0.1 rad/s to 100 rad/s, and the temperatures ranged from 10 °C to 70 °C in 10 °C intervals, with a strain level of 0.2%, and two replicates were tested. For the BBR tests, two replicates were tested at -12 °C, -18 °C, and -24 °C

3 RESULTS AND DISCUSSION

3.1 *Hansen Solubility Parameters*

The Hansen spheres of two bio-additives and maltenes as well as asphaltenes are shown in Figure 1. The visualised HSPs of two bio-additives were significantly different. The Hansen sphere of asphaltenes was almost entirely covered by that of bio-additive 1 while partially covered by that of bio-additive 2. In terms of the Hansen sphere of maltenes, it overlapped partially with both bio-additive 1 and bio-additive 2. The overlapping ratio of the Hansen spheres of asphaltenes and maltenes was 96.99%. Moreover, it was observed that asphaltenes were more soluble in bio-additives compared to maltenes. The overlapping ratios of Hansen sphere of

asphaltenes with bio-additive 1 and bio-additive 2 were 97% and 52.81%, respectively, which were 45.9% and 35.2% higher than the overlapping ratios of maltenes and bio-additives. It should be noted that the Hansen radius of maltenes was greater than that of asphaltenes, indicating that maltenes were more soluble than asphaltenes, which explained why the overlapping ratios between maltenes, and bio-additives were relatively smaller. However, the overlapping ratios between maltenes and bio-additives were still reasonably high, indicating that the affinity and compatibility between maltenes and bio-additives to be adequate.

Previous studies have postulated that bitumen is considered compatible with modifiers and additives when their Hansen spheres partially overlap (Sreeram et al., 2022, Hu et al., 2024). Therefore, given that the Hansen spheres of both maltenes and asphaltenes were significantly overlapped with those of bio-additives, it can be assumed that the bio-additives used in this study were theoretically compatible with bitumen to a large extent. However, it is noteworthy that bio-additives used in this study had different compatibilities with bitumen fractions. This is expected to be reflected in their rheological performance.
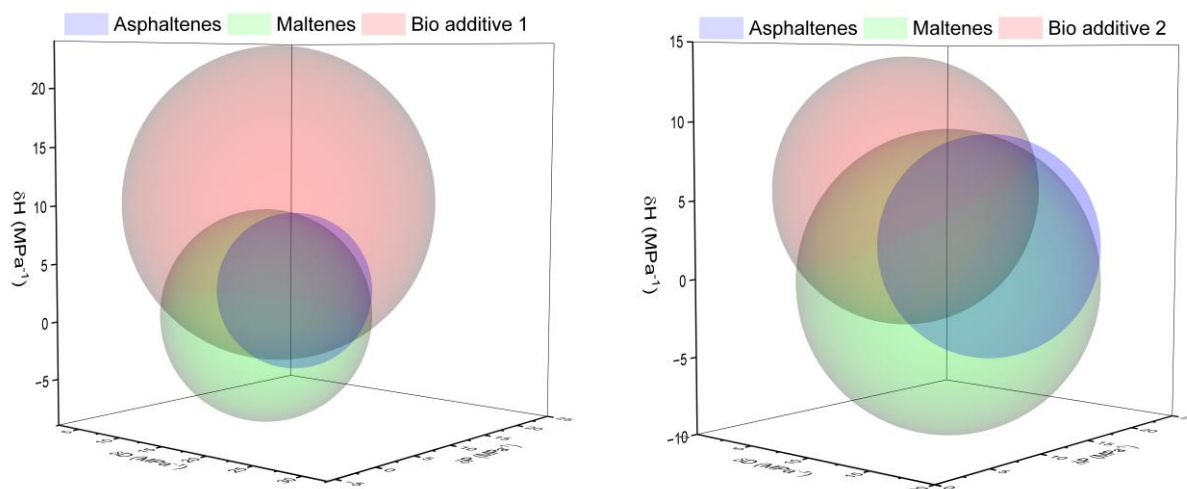
Figure 1 Hansen spheres of bio-additives and bitumen subfractions

3.2 *Master curves and black space diagrams*

The master curves and black space diagrams were plotted based on the frequency sweep tests. As shown in Figure 2(a), the incorporation of bio-additives significantly softened bitumen as the master curves for complex modulus moved downwards after the addition of the bio-additives. It was also noted that the addition of bio-additives had more pronounced impact on the complex modulus at low-frequency (high-temperature) range. Two bio-additives showed similar effect on the complex modulus of bio-bitumen as the master curves of the two bio-bitumen were almost parallel, though bio-

additive 1 showed higher efficiency compared to bio-additive 2 as bio-bitumen 1 was softer than bio-bitumen 2. When it comes to the master curves for phase angle, it was observed that the bio-bitumen was more viscous than the control bitumen as the master curves for phase angle moved upwards. It was noteworthy that bio-additives had more significant impact on the phase angle at high-frequency (low-temperature) range, which was opposite to the impact on complex modulus. It has been reported that higher phase angle at low-temperature is beneficial for the relaxation properties of bitumen (Primerano et al., 2023), therefore, the incorporation of bio-additives could significantly improve the ther-

mal cracking resistance of bio-bitumen. The impact of bio-additive 1 was more pronounced than bio-additive 2 in terms of increasing the phase angle of bio-bitumen, which was consistent with that for complex modulus. As the bio-bitumen was softer and more viscous than control bitumen, its high-temperature performance might be compromised. Therefore, these bio-additives were more suitable to be used as softeners or rejuvenators for softening the aged bitumen to recover its performance.

(a) Master curves   (b) Black diagrams
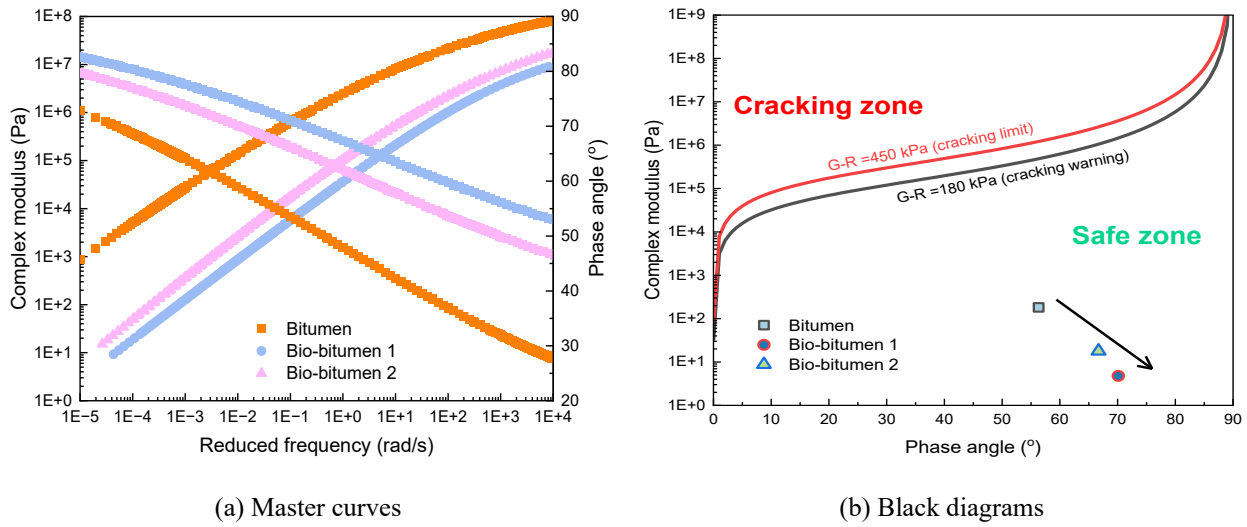
Figure 2 Rheological properties of bitumen

G-R parameter is proven to be highly correlated with the durability of asphalt pavements (Rowe et al., 2014). A lower value of G-R parameter suggests that the bitumen is more durable and less susceptible to fatigue cracking. The observation from Figure 6(b) indicated that both control bitumen and bio-bitumen fell within the "safe zone", suggesting that these materials were less likely to encounter durability issues. Being in the "safe zone" implied that the properties and performance characteristics are within acceptable limits. Notably, the addition of bio-additives lowered the G-R parameters of the bio-bitumen, indicating better durability. Furthermore, bio-additive 1 showed more pronounced effectiveness. The observations from Figure 2 aligned with the HSP results. The improvement or lack of detrimental effect in term of rheological properties could be reflected by the high compatibility between bio-additives and bitumen subfractions. Moreover, bio-additive 1 was more compatible with bitumen subfractions compared to bio-additive 2, therefore, the rheological properties of bio-bitumen 1 were seemingly superior to those of bio-bitumen 2.

3.3 Low-temperature performance of bitumen with bio-additives

The critical temperatures and ΔT_c of bio-bitumen and control sample are shown in Figure 3. The incorporation of bio-additives significantly improved the low-temperature performance (thermal cracking resistance) of bitumen. For the control sample, its performance grade (PG) was PG 64-22, while for the two types of bio-bitumen, their performance grades were PG 64-40 and PG 64-34, which improved three and two grades, respectively. The incorporation of

bio-additives also improved the relaxation properties of bitumen, denoted by the shifting of lower PG from m-value controlled to stiffness controlled. More negative values of ΔT_c are correlated with higher susceptibility to thermal cracking (Asphalt Institute, 2019). It is evident from Figure 3 that after the modification, the bio-bitumen was less susceptible to thermal cracking. Therefore, the incorporation of bio-additives improves the low-temperature performance of bitumen in two ways: lowering the critical temperature and reducing the cracking susceptibility. Overall, the incorporation of bio-additives effectively improved the thermal cracking resistance of bitumen at low-temperature. This observation was conducted on unaged samples, further testing is required for aged samples.
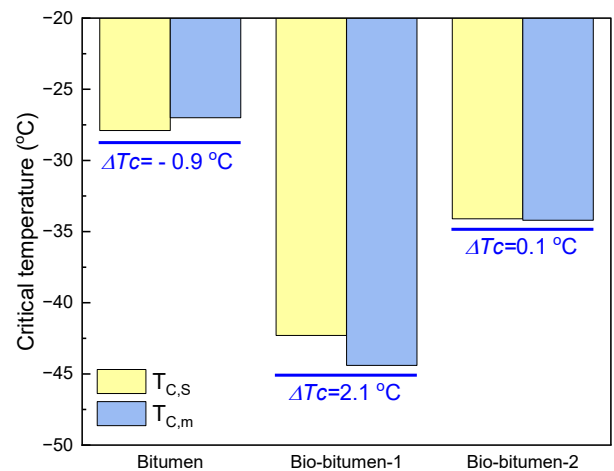
Figure 3 Low-temperature properties of bitumen

It was also observed that bio-additive 1 was more effective than bio-additive 2 in terms of improving the thermal cracking resistance of bitumen. Combining the low-temperature performance of bio-bitumen

and the results of Hansen solubility parameters, it could be assumed that HSP is correlated with low-temperature performance of bio-bitumen, as the overlapping ratios of Hansen spheres were positively correlated with the low-temperature performance. When the same dosage of bio-additives was added to bitumen, the bio-additive with higher Hansen sphere overlapping ratio could improve the thermal cracking resistance of bitumen more significantly. It is likely that although adding higher dosage of bio-additives could improve the low-temperature performance of bitumen due to a softening effect, incompatibility issues might arise. Therefore, it is believed that bio-additives with higher overlapping ratio could be more efficient and compatible in terms of material chemistry. In relation to this, the HSP-based solubility science could potentially be used to select highly effective additives or extenders for bio-based bitumen.

4 CONCLUSIONS

This study investigates the use of solubility science to evaluate fundamental physicochemical interactions and compatibility between bitumen and bio-additives. Based on the results conducted on representative bio-additives, the following findings and conclusions could be drawn.

• Bio-based additives could improve the low-temperature performance of bitumen by lowering the critical temperatures and reducing cracking susceptibility. The addition of bio-additives lowered the complex modulus of bio-bitumen while increasing its phase angle, which benefits the relaxation properties of bio-bitumen, thereby improving its durability.

• Bio-additive 1 significantly outperformed bio-additive 2 in enhancing bitumen performance at identical modification levels. Specifically, the G-R parameter and thermal cracking resistance of bio-bitumen 1 were 438% and 200% greater than those of bio-bitumen 2, respectively. This superior performance was attributed to the higher overlapping ratios of Hansen spheres between bio-additive 1 and maltene and asphaltenes, which were 45.9% and 35.2% greater than those between bio-additive 2 and bitumen subfractions.

• Solubility science, specifically Hansen solubility parameter (HSP) could be used as a fundamental basis for selecting the most optimum materials for partially substituting conventional bitumen. Overlapping ratios between bio-additives and bitumen or its subfractions were positively correlated with the rheological properties of bio-bitumen.

• The application of HSP could identify the fundamental mechanisms of interaction between bio-additives and bitumen. Highly efficient bio-additives have similar HSP with bitumen and its subfractions.

The overlapping ratio could be used as an indicator for the compatibility.

REFERENCES

– *Asphalt Institute. 2019. State-of-the-Knowledge: Use of the Delta Tc Parameter to Characterize Asphalt Binder Behavior.*

– *Espinosa L. V., Vasconcelos K., Alvarez A. E., Bhasin A. & Bernucci L. 2024. Moisture damage susceptibility of a wood-based bio-binder for total replacement of asphalt binders. Road Materials and Pavement Design, 25, 45-55.*

– *Hansen C. M. 1969. The Universality of the Solubility Parameter. Industrial & Engineering Chemistry Product Research and Development, 8, 2-11.*

– *Hansen C. M. 2007. Hansen solubility parameters: a user's handbook, Boca Raton, CRC press.*

– *He M., Tu C., Cao D. W. & Chen Y. J. 2019. Comparative analysis of bio-binder properties derived from different sources. International Journal of Pavement Engineering, 20, 792-800.*

– *Hu Y., Sreeram A., Xia W., Wang H., Zhou L., Si W. & Airey G. D. 2024. Use of Hansen Solubility Parameters (HSP) in the selection of highly effective rejuvenators for aged bitumen. Road Materials and Pavement Design, 1-19.*

– *Lapidus A. L., Kerimov V. Y., Mustaev R. N., Movsumzade E. M., Salikhova I. M. & Zhagfarov F. G. 2018. Natural Bitumens: Physicochemical Properties and Production Technologies. Solid Fuel Chemistry, 52, 344-355.*

– *Primerano K., Mirwald J., Bhasin A. & Hofko B. 2023. Low-temperature characterization of bitumen and correlation to chemical properties. Construction and Building Materials, 366, 130202.*

– *Rowe G. M., King G. & Anderson M. 2014. The Influence of Binder Rheology on the Cracking of Asphalt Mixes in Airport and Highway Projects. Journal of Testing and Evaluation, 42, 1063-1072.*

– *Sreeram A., Filonzi A., Komaragiri S., Lakshmi Roja K., Masad E. & Bhasin A. 2022. Assessing impact of chemical compatibility of additives used in asphalt binders: A case study using plastics. Construction and Building Materials, 359.*

– *Thives L. P. & Ghisi E. 2017. Asphalt mixtures emission and energy consumption: A review. Renewable and Sustainable Energy Reviews, 72, 473-484.*

– *Yang X., Mills-Beale J. & You Z. 2017. Chemical characterization and oxidative aging of bio-asphalt and its compatibility with petroleum asphalt. Journal of Cleaner Production, 142, 1837-1847.)*

Impact of SBS structure on modified binder morphology during PAV ageing

S.S. Islam
Contractual Faculty, National Institute of Technology Hamirpur, Hamirpur, India, ssohelislam@ce.iitr.ac.in

A. Ghosh
Research Associate, Indian Institute of Technology Roorkee, Roorkee, India

G.D.R.N Ransinchung
Professor, Indian Institute of Technology Roorkee, Roorkee, India

S.S Ravindranath
Associate Professor, Indian Institute of Technology Roorkee, Roorkee, India

ABSTRACT: This research investigates the impact of SBS copolymer molecular structure and vinyl content on the morphological behavior of modified binders during PAV ageing. Four SBS copolymers—linear (L-SBS), high vinyl (HV-SBS), radial (B-SBS), and di-block (DB-SB)—were used to formulate polymer-modified binders (PMBs). The binders' morphology was analyzed before and after PAV ageing using Atomic Force Microscopy (AFM) and Fluorescent Microscopy (FM). AFM results showed a significant increase in bee phase percentage for L-SBS (30%) and B-SBS (19%) binders post-ageing, whereas HV-SBS and DB-SB showed smaller increases. FM indicated polymer network fragmentation in L-SBS and B-SBS due to polybutadiene dissolution. The study concludes that binders with lower vinyl content are more susceptible to degradation than those with higher vinyl content.

1 INTRODUCTION

1.1 *General*

The use of Styrene-butadiene copolymer (SBS)-modified binders has gained prominence for improving pavement strength and performance (Airey, 2003; Zhang et al., 2014). SBS polymers, including linear, high vinyl, and radial types, display varying molecular structures and styrene/butadiene content, which influence binder performance (Hernández et al., 2006). Radial/branched SBS polymers exhibit superior softening points, complex viscosity, and rutting resistance compared to linear types (Han et al., 2014). However, branched polymers often face phase separation and poor dispersion issues (Bulatovic et al., 2014). Polymers with high vinyl content show enhanced thermal stability (Luksha et al., 2006). Despite these advantages, SBS binders exhibit thermo-oxidative instability during ageing, influenced by UV rays, oxygen, heat, and rain (Chen & Qian, 2003). This study examines how molecular structure impacts SBS binder morphology during unaged and PAV-aged conditions using Atomic Force Microscopy (AFM) and Fluorescence Microscopy (FM). AFM has enabled researchers to identify the microstructure of binders, revealing two phases: a dispersed elliptical bee phase within the matrix. Wang et al. (2015) found that PAV ageing enhances the cohesive and adhesive strength of the binder, increasing spatial variation.

Hofko's study demonstrates a relationship between the occurrence of bee structures and the presence of asphaltene (Hofko et al. 2016). The findings of this research will provide deeper insights into the ageing behaviour of SBS-modified binders, guiding the development of more durable and efficient materials for asphalt pavements. Understanding the microscale changes under different ageing conditions will contribute to better performance predictions and optimization of modified binder formulations for long-term infrastructure sustainability.

2 MATERIALS AND METHODOLOGY

2.1 *Materials*

In this study, VG-10 was used as a base binder for the preparation of polymer-modified binders (PMBs). Moreover, to produce the modified binders, four distinct commercially available SBS polymers (L-SBS, B-SBS, HV-SBS, and DB-SB) were procured, which was distinguished by their molecular structure and chemical composition. The characteristics of the studied polymers along with the physical properties of the base binder are depicted in Table 1.

2.2 *Experimental plan*

2.2.1 Preparation of modified binders
To prepare the modified binder, the SBS content was set at 4.5 wt.%, with the selected polymer being

supplied in pellet form. Mixing of the SBS polymer into the bitumen was conducted in the laboratory using the Silverson L4RT high-shear mixer, followed by further blending at 600 rpm for 90 minutes using a low-shear mixer. To prevent phase separation of the polymer, 0.12 wt.% of sulfur was added during the homogenization process.

2.2.2 Ageing of modified binder

The main objective of this research is to ascertain how four different SBS copolymers impact the degree of property deterioration in SBS-modified binders when subjected to heat and air, mirroring conditions encountered during road construction.

To replicate actual site conditions, the modified binders underwent laboratory short-term aging using the rolling thin film oven (RTFO) and thereafter long-term aging in the pressure aging vessel (PAV), following ASTM guidelines

Table 1. Physio-chemical properties of base binder and different SBS copolymer used

Base Binder properties	Test value	Properties	SBS copolymer			
			L-SBS	B-SBS	HV-SBS	DB-SB
Penetration @ 25 °C	92	Molecular Structure	Linear	Radial	Linear	Linear
Softening point (°C)	48	Copolymer type	Tri-block	Tri-block	Tri-block	Di-block
viscosity @ 60 °C (Poise)	920	Styrene/Butadiene ratio	≈ 30/70	≈ 30/70	≈ 30/70	≈ 30/70
PG upper temperature (°C)	58	Vinyl content (%)	≤ 15	≤ 15	≥ 30	≥ 30

2.3 Methodology

Samples for Atomic Force Microscopy (AFM) were prepared using the heat casting method, where asphalt was heated, cooled, and stored before imaging with a Bruker Dimension Icon AFM. Surface topography and bee phase structures were analyzed using Gwyddion 2.3 software. Fluorescent Microscopy (FM) was employed to examine polymer particle dispersion before and after ageing, with samples viewed at 40X magnification on a Thermo-Fisher microscope.

3 RESULTS AND DISCUSSION

3.1 Characterization of polymers

The rheological characteristics of the PMBs are significantly influenced by the molecular weight distribution (Mw) of the polymers, which were evaluated using the Gel permeation chromatography (GPC) test, as depicted in Figure 2(a). Analyzing the GPC results for the four polymers reveals that L-SBS and HV-SBS share a similar molecular weight (Mw) owing to their identical linear triblock molecular structure. In contrast, B-SBS exhibits the highest Mw, while the di-block polymer demonstrates a notably lower molecular weight compared to the other three polymers. Thermogravimetric analysis (TGA) was conducted to determine the initial and final degradation points, along with the residual mass, for the four SBS

polymers. Notably, polymers with higher branching exhibited higher susceptibility to degradation compared to linear polymers. These results underscore the impact of branching and molecular weight distribution on thermal stability. As depicted in Figure 2(b), it is evident that the B-SBS polymer undergoes abrupt degradation at 450 °C, followed by subsequent combustion in comparison to its linear counterparts.

3.2 AFM analysis

To analyze the micromechanics and morphology of SBS-modified binders before and after ageing, the PFQNM mode of AFM was employed. AFM images (Figure 2) show the distinct bee phase and relatively flat matrix phase. Figures 2(a-d) depict unaged L-SBS, B-SBS, HV-SBS, and DB-SB samples, while Figures 2(e-h) show the PAV-aged samples. The results indicate that the bee phase increased for all modified binders after PAV ageing, with L-SBS and B-SBS showing a more significant increase (30% and 19%, respectively), as presented in Table 3. This increase suggests binder hardening and disruption of intermolecular networks during long-term ageing. In contrast, the increase in bee phase for HV-SBS and DB-SB was minimal (8% and 7%), indicating higher thermal stability due to their higher vinyl content. Additionally, ageing caused a decrease in the length of the bee structures, particularly in B-SBS and L-SBS. the binder matrix remains unaffected. Therefore, the unaffected SBS network can retain the performance properties even after long term ageing.
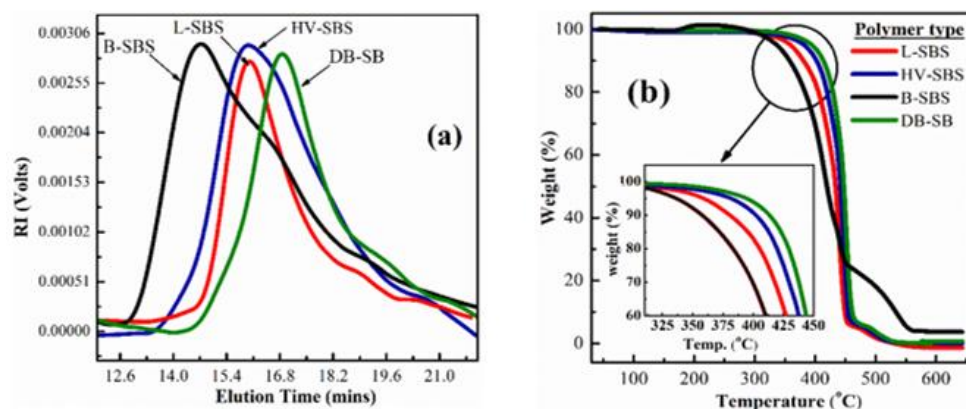
Figure 1. (a) GPC and (b) TGA analysis of studied SBS copolymers properties even after long-term ageing.
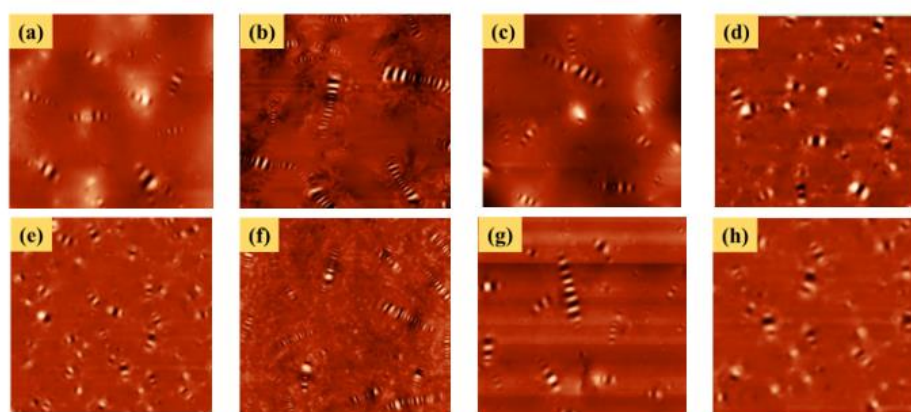
Figure 2. Two-dimensional AFM images of different SBS-MB samples before and after PAV ageing (a, e) L-SBS, (b, f) B-SBS, (c, g) HV-SBS (d, h) DB-SB

Table 3. Nano morphology parameters of AFM images

Polymer type	Ageing type	Nano-parameters of AFM study			
		Proportion of bee (%)	Length of bee (μm)	Area of bee (μm²)	Standard deviation of bee area
L-SBS	Fresh	37	2.66	2.42	0.78
	PAV	48	2.08	2.16	0.95
B-SBS	Fresh	42	3.3	3.14	0.69
	PAV	49	2.74	2.67	0.8
HV-SBS	Fresh	36	2.72	2.51	0.72
	PAV	39	2.76	2.58	0.55
DB-SB	Fresh	40	2.2	2.3	0.48
	PAV	43	2.25	2.34	0.62

3.3 *FM analysis*

To comprehend the effect of long-term ageing on the morphological behaviour of the modified binders with different SBS copolymers, FM study was conducted. Since the rheological and chemical characterization of the binder shows maximum property deterioration after long-term ageing, FM images have not been captured for short-term aged samples. Figure 3(a, b, c, d) depicts the FM images of unaged modified binders prepared with L-SBS, B-SBS, HV-SBS and DB-SB polymer, respectively. Whereas, Figure 3

(e, f, g, h) highlights the FM micrographs of PAV aged samples of the respective binders. It can be observed that at unaged condition SBS particles are homogeneously dispersed in the binder matrix for all the studied SBS copolymers. At the unaged condition, due to similar molecular structure, L-SBS and HV-SBS produced alike FM images with a filamentous appearance. B-SBS depicted a star-shaped formation due to the branching of strong polymer network density, whereas DB-SB showed a droplet-like structure with a homogeneous distribution. However, after long-term ageing, the polymer network density was fragmented for binders modified with B-SBS and L-

SBS polymers. Due to longer ageing, the SBS molecule might have been susceptible to thermal oxidative degradation, which in turn affected the strength of the polymer network structure. As a result, the polymer particles become less distinct or disappear altogether. In contrast, such degradation was not observed for HV-SBS and DB-SB modified binders after PAV ageing. Figure 3(f) and Figure 3(h) show the presence of ample polymer network density even after longer ageing. The results clearly illustrate that SBS polymers with higher vinyl content exhibit better thermal stability. An increase in the vinyl content increases the number of C=C bonds as the side group in the butadiene segment. The thermally induced cleavage of the C=C bonds present as the side group will not reduce the overall length (molecular weight) of the SBS polymer, so the network created by the SBS polymer in the binder matrix remains unaffected. Therefore, the unaffected SBS network can retain the performance properties even after long term ageing.
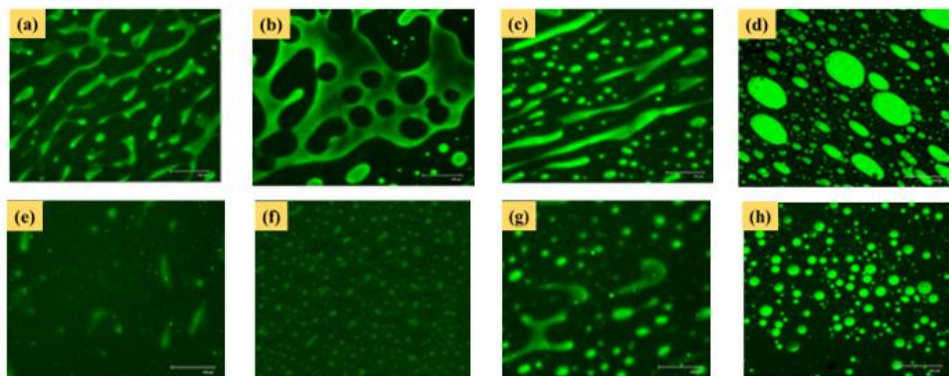
Figure 3. Fluorescent microscopy images of unaged and PAV aged binder (a, e) L-SBS, (b, f) B-SBS, (c, g) HV-SBS (d, h) DB-SB

CONCLUSION

The crucial finding of this research is summarized below.

• Surface topographical AFM images highlight the augmentation of a higher proportion of bee phase for binders modified with L-SBS and B-SBS. Such a result emphasizes binder hardening and SBS degradation effect due to PAV ageing. However, HV-SBS and DB-SB polymer modified showed negligible changes in such parameters after long-term ageing.

• Study also finds that B-SBS and L-SBS modified binders depict substantial deterioration in SR value, which highlights lower self-healing properties against long-term ageing. However, such a detrimental effect was not visible for high vinyl polymers used in this study

• FM study shows that after long-term ageing, the polymer network density was fragmented for binders modified with B-SBS and L-SBS polymers, and that was due to the ageing of modified binder, which dissolves the insoluble polybutadiene segment into matrix and disappearance of polymer particles occurs.

• The findings suggest that while L-SBS, HV-SBS, and DB-SB share a common linear molecular chain structure of SBS, the presence of higher vinyl content in the polymer renders HV-SBS and DB-SB less susceptible to oxidative thermal degradation.

4 REFERENCES

Airey, G. D. 2003. Rheological properties of styrene-butadiene-styrene polymer modified road bitumens. *Fuel*, 82, 1709–1719.

Bulatovic, V. O., Rek, V., & Markovic, K. J. 2014. Effect of polymer modifiers on the properties of bitumen. *Journal of Elastomers and Plastics*, 46, 448–469. https://doi.org/10.1177/0095244312469964.

Chen, F., & Qian, J. 2003. Studies on the thermal degradation of polybutadiene. *Fuel Processing Technology*, 67, 53–60.

Han, S., Niu, D. Y., Liu, Y. M., Chen, D., & Liu, D. W. 2014. Analysis on the impact of the type and content of SBS on the performance of the modified asphalt mixture. *Advanced Materials Research*, 919–921, 1079–1084.

Hernández, G., Medina, E. M., Sánchez, R., & Mendoza, A. M. 2006. Thermomechanical and rheological asphalt modification using styrene-butadiene triblock copolymers with different microstructure. *Fuels*, 20, 2623–2626.

Hofko, B., Eberhardsteiner, L., Füssl, J., Grothe, H., Handle, F., Hospodka, M., Großegger, D., Nahar, S., Schmets, A., & Scarpas, T. 2016. Impact of maltene and asphaltene fraction on mechanical behavior and microstructure of bitumen. *Materials and Structures*, 49(3), 829–841.

Luksha, O. V., Opanasenko, O. N., Krut'ko, N. P., & Loboda, Y. V. 2006. Modification of oxidized bitumen with styrene-butadiene-styrene copolymers of various structures. *Russian Journal of Applied Chemistry*, 79, 1021–1024. https://doi.org/10.1134/s1070427206060280.

Wang, P. E. Y., Zhao, K., Glover, C., Chen, L., Wen, Y., & Chong, D. 2015. Effects of aging on the properties of asphalt at the nanoscale. *Construction and Building Materials*, 80, 244–254.

Zhang, Q., Wang, T., Fan, W., & Ying, Y. 2014. Evaluation of the properties of bitumen modified by SBS copolymers with different styrene-butadiene structure. *Journal of Applied Polymer Science*, 131, 1–7.

Hygrothermal aging of mastic samples

S. Khalighi, L. MA, R. Koning, & A. Varveri
Delft University of Technology, Netherlands

ABSTRACT: This study examines the aging behavior of mastic samples subjected to hygrothermal conditions in a pressure aging vessel (PAV) for 10, 20, and 40 hours, as well as to reactive oxygen species and humidity in Vienna Binder Aging (VBA-WET). Fourier-transform infrared spectroscopy (FTIR) was used to analyze the chemical aging processes, and principal component analysis (PCA) was applied to differentiate mastic types and evaluate the efficacy of indices versus spectral data. Results show that W60k mastic has lower carbonyl and sulfoxide indices, indicating greater resistance to oxidative degradation compared to W mastic. PCA effectively differentiates the mastic types and confirms that both FTIR indices and full spectra distinguish between mastic types. These findings highlight the impact of filler composition on aging behavior and suggest directions for future research on material performance in practical applications.

1 INTRODUCTION

The aging process of bituminous binders is crucial for the longevity of asphalt pavements, as excessive aging can significantly impair the durability of asphalt mixtures. Aging occurs in two phases: short-term aging during storage, mixing, and paving, and long-term aging that occurs in service (Petersen 2009). Key mechanisms such as oxidation, evaporation of volatile components, and steric hindrance drive these processes, with oxidative aging having a particularly pronounced impact on long-term pavement performance. Standard aging protocols, including the Rolling Thin Film Oven (RTFO) and Pressure Aging Vessel (PAV), have been established to simulate these conditions (Nagabhushanarao and Vijayakumar 2021, Koyun et al. 2022). However, these aging protocols have been proven to be not accurate enough in simulating field asphalt pavement aging (Singhvi et al. 2022). To improve laboratory protocols and better mimic field conditions, it is essential to understand the effect of mineral fillers and the effects of environmental factors such as pressure, moisture, and reactive oxygen species (ROS) (Khalighi et al. 2024a, Khalighi et al. 2024b).

Fillers significantly influence the aging behaviour of asphalt binders, affecting both their chemical and physical properties. Previous studies indicate that fillers like hydrated lime can retard aging more effectively than other materials, limiting oxygen diffusion and reducing viscosity and softening point increases (Gubler et al. 1999, Alfaqawi et al. 2022). Additionally, environmental factors, including pressure and moisture, also play a vital role in the aging process, with the combination of these elements requiring careful examination to develop more representative aging protocols. This study aims to investigate the responses of mastics containing hydrated lime and limestone to hygrothermal aging in PAV (Khalighi et al. 2024c, Khalighi et al. 2024a) and VBA (Khalighi et al. 2024b), utilizing Fourier-transform infrared spectroscopy (FTIR) (Khalighi et al. 2024d) and principal component analysis (PCA) (Ma et al. 2023) to assess and compare aging behaviours at the mastic level.

2 MATERIALS AND METHODS

2.1 *Materials and sample preparation*

In this study, one PEN 70/100 bituminous binder was evaluated, named as Q, which has a softening point between 43-51 °C. Its complex shear modulus at 1.6 Hz and 60 °C is 1.8 kPa, with a phase angle of 88° under the same conditions. The elemental composition includes nitrogen (0.59%), carbon (79.19%), hydrogen (10.81%), sulfur (4.47%), and oxygen (2.25%).

Binder samples were prepared by pouring 50 grams of fresh binder into pans, forming films of 3.2 mm thickness. Short-term aging was conducted at 163°C for 5 hours per EN 12607-2 (EN 12607-2 2014). Portions of the aged binders were then transferred to glass petri dishes to achieve a uniform 1 mm thickness by reheating at 163°C for 3 minutes. For mastics, two types were prepared using different fillers: Wigro (limestone) and Wigro60k (hydrated lime), with a filler-to-bitumen ratio of 1:1. The specifications for fillers can be found in (Khalighi et al. 2024a). Both components were preheated to 130 °C for one hour, then mixed and stirred for five minutes. The mixture was then oven-cured at 130°C for 30 minutes and manually stirred for even distribution of filler.

2.2 *Long-term aging conditions*

The LTA conditions involved PAV treatment at 85°C for varying durations (10, 20, 40 hours) and

99% relative humidity, using 1000 grams of demineralized water to achieve this (Khalighi et al. 2024a). Additionally, the Viennese Binder Aging (VBA) method was employed, exposing samples to air with 25 ppm NO_2 and 4 g/m^3 ozone at $85 \pm 1°C$ for three days, along with 75 g/m^3 humidity (VBA-Wet) (Mirwald et al. 2020). Naming conventions include "W"/"W60k" for Wigro/Wigro60k, "VBA-W" for hygrothermal aging in VBA, and "W-10H" for hygrothermal aging in PAV for 10 hours.

2.3 Fourier-transform infrared spectroscopy (FTIR)

Chemical changes in mastic samples during aging were analysed using ATR-FTIR spectroscopy. Samples (~1 g) were heated to 110°C, stirred, and deposited on silicon foil for analysis with a Nicolet iS5 Thermo Fisher Scientific instrument, generating four spectra per aging state in the 4000–400 cm^{-1} range. Pre-processing included an 8-point baseline correction and normalization via the NMO method (Khalighi et al. 2024d). Table 3 lists the wavenumber ranges of main functional groups identified for mastic samples. Functional group indices were calculated using the equation:

$$index = A_x / A_{Total} \quad (1)$$

$$A_{Total} = A_{810} + A_{1030} + A_{1376} + A_{1460} + A_{1600} + A_{1700} + A_{2953} + A_{3400} \quad (2)$$

Where A_x represents the tangential peak area under the curve within specified ranges from Table 1.

Table 1. Main functional groups of mastic in FTIR spectra (Khalighi et al. 2025).

Area groups	Vertical band limit (cm^{-1})	Functional
A810	680-912	$(CH_2)_n$, thiols, CO_3^{2-}
A1030	930-1120	S=O, silicate
A1376	1350-1395	Branched aliphatic structures
A1460	1395-1525	CH_3 and CH_2, CO_3^{2-}
A1600	1550-1660	Aromatic structure, C=C
A1700	1660-1735	Carbonyl, C=O
A2953	2820-2990	Aliphatic structures
A3400	3100-3700	Hydroxyl stretching, OH, NH

2.4 Principle component analysis (PCA)

PCA is a crucial method for transforming datasets with many variables into uncorrelated components, aiding in dimensionality reduction. The scores for target samples are calculated using $\mathbf{Y} = \mathbf{X} \times \mathbf{W}$, where $\mathbf{X}$ is the dataset of m samples across l categories and n variables. The matrix $\mathbf{W}$, an $n \times p$ loading matrix, indicates the selected principal components, while $\mathbf{Y}$ forms an $m \times p$ score matrix projecting $\mathbf{X}$ into a p-dimensional feature space. $\mathbf{W}$ is derived from the eigenvectors and eigenvalues of the covariance matrix of the spectral dataset, with the largest eigenvalues selected to construct $\mathbf{W}$. PCA loadings are further analyzed to identify significant regions for cluster formation (Ma et al. 2023). The dataset for PCA included FTIR results, encompassing all indices listed in Table 1, and an additional analysis utilized the entire FTIR spectra for comparison.

3 RESULT AND DISCUSSION

3.1 Effect of Aging on Mastic Samples using FTIR

Figure 1 shows the pre-processed FTIR spectra of mastic samples subjected to hygrothermal aging in PAV and VBA. Notably, certain spectral regions, particularly the fingerprint region, exhibit an upward shift with aging. To quantify these changes, the areas under the key peaks will be analysed according to the regions specified in Table 1. Previous studies have identified the carbonyl, sulfoxide, hydroxyl, and long-chain indices in the 680-734 cm^{-1} and 783-838 cm^{-1} regions as significant for mastic differentiation and aging (Khalighi et al. 2025). Consequently, these indices will be the primary focus of the analysis.
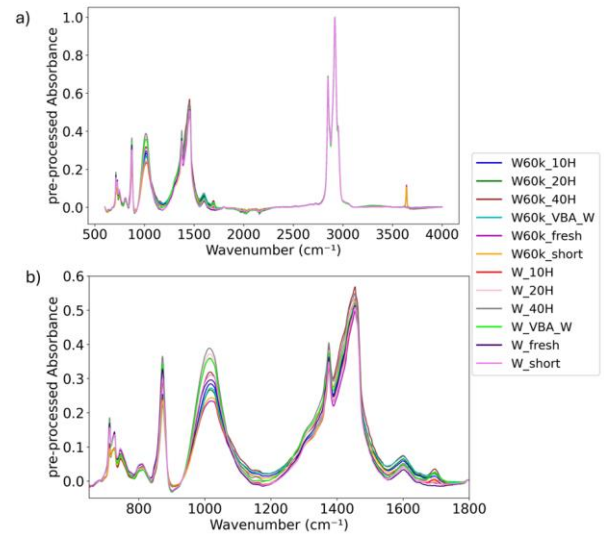
Figure 1- FTIR spectra of fresh, short-term aged, and long-term aged mastics under various hygrothermal aging conditions in PAV (10, 20, and 40 hours) and VBA-WET: a) pre-processed spectra; c) variations in the 650-1800 cm^{-1} fingerprint region.

Figure 2a illustrates the carbonyl index, which increases with long-term aging, indicating the formation of oxidative products. Notably, hygrothermal aging under PAV conditions, particularly at 40 hours, results in a more significant increase in the carbonyl index compared to 72 hours of VBA-WET aging, underscoring the role of high pressure in oxidative degradation. Figure 2b presents the sulfoxide index, which remains relatively stable across various aging conditions but shows a slight increase during long-term aging (LTA). The pronounced sulfoxide peak can be attributed to the presence of sulfur- or silicate-containing groups in the fillers. Figure 2c

depicts the hydroxyl index, which also rises with aging, indicating an accumulation of oxidative products. Longer PAV aging increases this index more than VBA-WET aging for W mastic, although the trend is similar for W60k mastic. Figures 2d and 2e display the long-chain index, which exhibits minimal changes under most aging conditions. However, a decrease is observed in the 783-838 cm^{-1} region for W mastic during LTA, while the W60k sample remains relatively stable. The slight variations in the long-chain index may be influenced by the carbonate content in fillers such as limestone and carbonated hydrated lime.
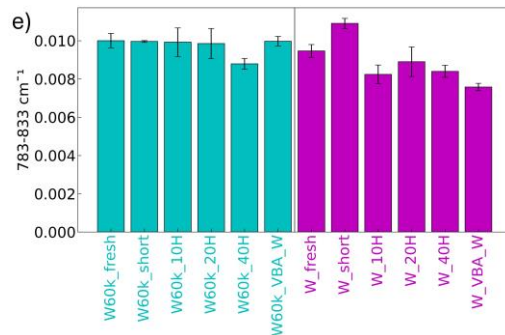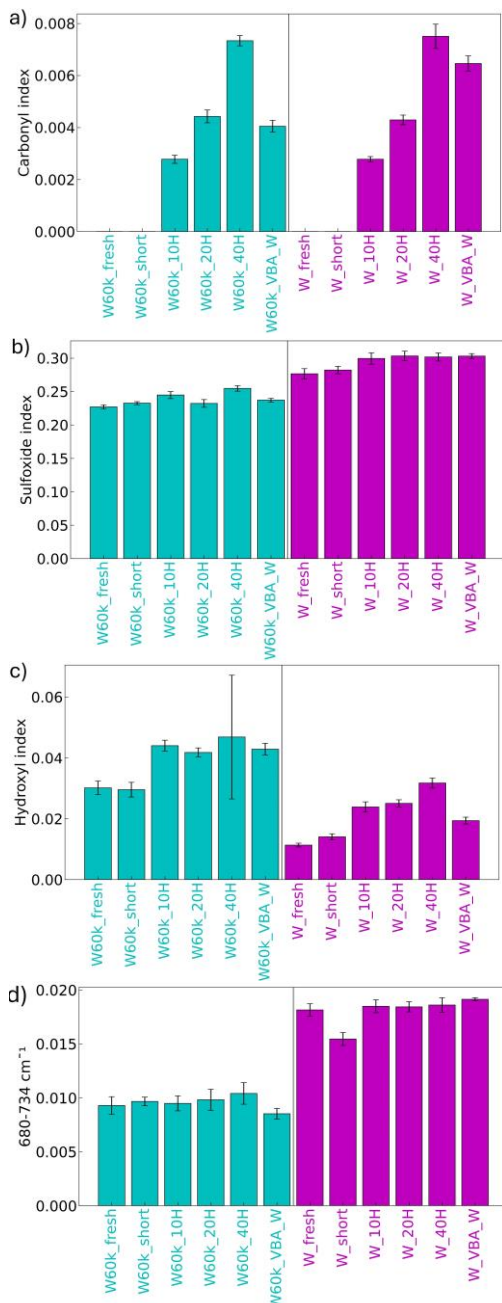
Figure 2- FTIR results for all samples: a) carbonyl index, b) sulfoxide index, c) hydroxyl index, d) 680-734 cm^{-1}, and e) 783-833 cm^{-1}, showing the effects of long-term aging under various conditions, including PAV (10, 20, and 40 hours) and VBA-WET aging.

3.2 Comparison of Mastic types

The comparison of W (limestone) and W60k (hydrated lime) mastics reveals significant differences in their aging behavior. For the carbonyl index (Figure 2a), both mastics exhibit similar trends under PAV aging; however, under VBA-WET conditions, W60k displays a lower carbonyl index, suggesting reduced oxidative aging due to the protective properties of hydrated lime. Regarding the sulfoxide index (Figure 2b), W60k consistently shows lower values compared to W mastic, likely attributable to differences in filler formulations. The hydroxyl index (Figure 2c) indicates a distinct peak for W60k mastic, reflecting the presence of OH functional groups in the filler, which is absent in W mastic. In the 680-734 cm^{-1} region (Figure 2d), the long-chain index is generally higher for W mastics, likely due to the greater carbonate content in limestone. Conversely, in the 783-838 cm^{-1} region (Figure 2e), W60k mastic exhibits greater stability, with less degradation over time compared to W mastic, particularly under long-term aging and VBA-WET conditions. This suggests that W60k mastic is more resistant to oxidative and long-term aging. Further research is needed to validate these findings.

3.3 Mastic type analysis using PCA with indices vs. spectral data

This step aimed to compare the effectiveness of FTIR indices versus the entire FTIR spectra for analysing aging trends and sample classification. PCA was conducted separately on the FTIR indices and full spectra. The first two principal components explained over 80% of the variance for the indices and more than 70% for the spectra. A two-dimensional plot of PC1 versus PC2 (Figure 3) effectively represents the data. Figure 3 shows a clear distinction between W and W60k mastic samples in both FTIR indices and spectra-based PCA results, indicating that the preprocessing and index calculations retain

essential information about sample type and aging behaviour. Both PC1 and PC2 are critical for differentiating the samples and tracking the aging process, with consistent aging trends observed in both analyses, characterized by a shift toward higher PC1 and lower PC2 values.
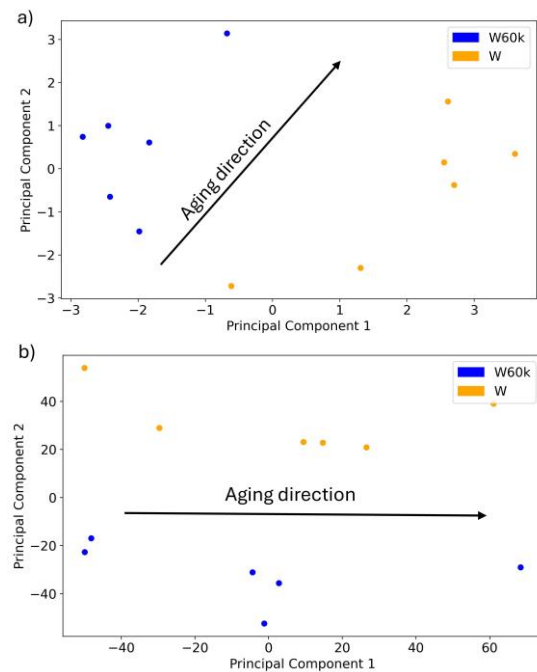
Figure 3- PCA plot of a) FTIR indices and b) FTIR spectra for fresh, short-term aged, and long-term aged mastic samples subjected to hygrothermal aging in PAV (10, 20, and 40 hours) and VBA-WET aging.

4 CONCLUSION

In conclusion, this study highlights the distinct aging behaviors of W (limestone) and W60k (hydrated lime) mastics, as revealed through FTIR analysis and PCA. The results demonstrate that W60k exhibits greater resistance to oxidative aging, particularly under VBA-WET conditions, as evidenced by lower carbonyl and sulfoxide indices. Additionally, the hydroxyl index indicates the presence of OH functional groups in W60k. The PCA results effectively illustrate the differentiation between the two mastic types, confirming that both FTIR indices and spectra retain critical information about sample aging and classification. Overall, these findings suggest that the choice of filler significantly impacts the aging behavior of mastics, and further research is warranted to explore the underlying mechanisms and implications for material performance in real-world applications.

6 REFERENCE

Alfaqawi, R. M., et al. 2022. Effect of hydrated lime and other mineral fillers on stiffening and oxidative ageing in bitumen mastic. *Construction and Building Materials* 315: 125789.

EN 12607-2, C. 2014. 12607-1: Bitumen and Bituminous Binders—Determination of the Resistance to Hardening under Influence of Heat and Air—Part 1: RTFOT Method. *European Committee for Standardization: Brussels, Belgium*

Gubler, R., et al. 1999. Investigation of the system filler and asphalt binders by rheological means. *Journal of the Association of Asphalt Paving Technologists* 68

Khalighi, S., et al. 2024a. Accelerated laboratory simulations to mimic field aging of bituminous binders and mixtures: A multivariant analysis on environmental aging effects. *Available at SSRN: https://ssrncom/abstract=4995141*

Khalighi, S., et al. 2024b. The Impact of Reactive Oxygen Species Coupled with Moisture on Bitumen Long-Term Aging.

Khalighi, S., et al. 2024c. Exploring the impact of humidity and water on bituminous binder aging: a multivariate analysis approach (TI CAB). *Road Materials and Pavement Design*: 1-25.

Khalighi, S., et al. 2024d. Evaluating the impact of data pre-processing methods on classification of ATR-FTIR spectra of bituminous binders. *Fuel* 376: 132701.

Khalighi, S., et al. 2025. Multi-scale analysis of ageing behaviour in bituminous materials.

Koyun, A., et al. 2022. Rheological, spectroscopic and microscopic assessment of asphalt binder ageing. *Road Materials and Pavement Design* 23(1): 80-97.

Ma, L., et al. 2023. Chemical characterisation of bitumen type and ageing state based on FTIR spectroscopy and discriminant analysis integrated with variable selection methods. *Road Materials and Pavement Design*: 1-15.

Mirwald, J., et al. 2020. Impact of reactive oxygen species on bitumen aging–The Viennese binder aging method. *Construction and Building Materials* 257: 119495.

Nagabhushanarao, S. S. and A. Vijayakumar 2021. Chemical and rheological characteristics of accelerate aged asphalt binders using rolling thin film oven. *Construction and Building Materials* 272: 121995.

Petersen, J. C. 2009. A review of the fundamentals of asphalt oxidation: chemical, physicochemical, physical property, and durability relationships. *Transportation research circular*(E-C140)

Singhvi, P., et al. 2022. Impacts of field and laboratory long-term aging on asphalt binders. *Transportation Research Record* 2676(8): 336-353.

Potentials for the quantification of the chemical microstructure of modified bitumen

Miomir Miljković

University of Niš, Faculty of Civil Engineering and Architecture, 18000 Niš, Serbia
Email: miomir.miljkovic@outlook.com, ORCID: 0000-0002-1821-4651

Virginie Mouillet

Cerema, Université Gustave Eiffel, UMR MCD, 13100 Aix-en-Provence, France
Email: virginie.mouillet@cerema.fr, ORCID: 0000-0003-2450-9875

Jean-Christophe Molinengo

Cerema, Université Gustave Eiffel, UMR MCD, 13100 Aix-en-Provence, France

ABSTRACT: This research investigated the potential for quantifying the microstructural features of montmorillonite-modified bitumen by Fourier-transform infrared (FTIR) microscopy. The analysis was based the successive thresholding of the micrographs representing integrals of the FTIR spectra from 960 to 1100 cm^{-1}. The characterisation included size distributions and spatial arrangements of peak-value regions, and the local thickness distributions of the surrounding space. The arrangement of regions of modifier's high concentration was mostly randomly heterogeneous, while the thresholded area fraction barely affected the assessment of agglomeration. In agglomerated areas, the local peaks seemed to repel each other. Microstructural manifestations of ageing were recognised to be the most promising application of this approach. Moreover, there is a huge potential for evaluating interfacial chemical interactions like diffusion in polymer-modified bitumens.

1 INTRODUCTION

The continuous advancement and innovation in materials science-based experimental techniques refocuses the evaluation of bitumen performance towards determining more intrinsic physicochemical phenomena [1]. As a component of this development, coupling microscopic features of bitumen with its chemical composition is essential for acquiring deep knowledge about the interactions and processes causing the macroscopic manifestations.

The microscopic analysis of the spatial distribution of chemical tracers by Fourier-transform infrared (FTIR) enables the chemical identification of the microphases present within heterogeneous materials such as polymer-modified bitumens [2, 3]. The combination of a spectrometer and a FTIR microscope provides spectral characteristics (and their spatial distribution) on the specimen's surface by determining an infrared spectrum for each pixel of the two-dimensional image's raster. To obtain this image, the sample to be analysed must be placed on a motorised stage under the objective. The infrared spectrometer generates a beam of infrared light which reaches the specimen's surface after passing through a system of reflective optics. The reflected beam is being received by an array detector cooled by liquid nitrogen. The attenuated total reflectance (ATR) imaging infrared microscopy technique provides high-resolution spectral maps of two-dimensional surfaces [3, 4].

The potentially high spatial and temporal heterogeneity of modified bitumen's microstructure due to the phase separation under various factors like composition and ageing is the main are among the main tasks of the microscopic analysis. Nevertheless, there is still little scientific knowledge beyond the common qualitative characterisation. This is even more important knowing that bitumen's bulk thermo-mechanical properties are intrinsically dependent on its component's interfacial morphology and chemical interactions. Therefore, it is particularly important to provide comprehensive understanding on the influence of modification and thermo-oxidative ageing on the microstructure of bitumen, as well as to interpret its effects on the behaviour of the entire system.

The objective of this research was to investigate the potential for quantifying the microstructural features with indistinct interfaces of montmorillonite-modified bitumen based on the FTIR microscopy.

2 MATERIALS AND METHODS

2.1 *Materials*

The base bitumen used in this research had the penetration grade of 50/70 (according to NF EN 12591), with the penetration of $58 \cdot 10^{-1}$ mm and the softening point of 49.6 °C. The base bitumen was modified by organo-modified montmorillonite previously subjected to surface treatment by a quaternary ammonium salt and dimethyl dihydrogenated tallow.

The modified bitumen was prepared using a high-shear mixer. Initially, 400 g of base bitumen was

(a) Original

50 μm

(b) Original

50 μm
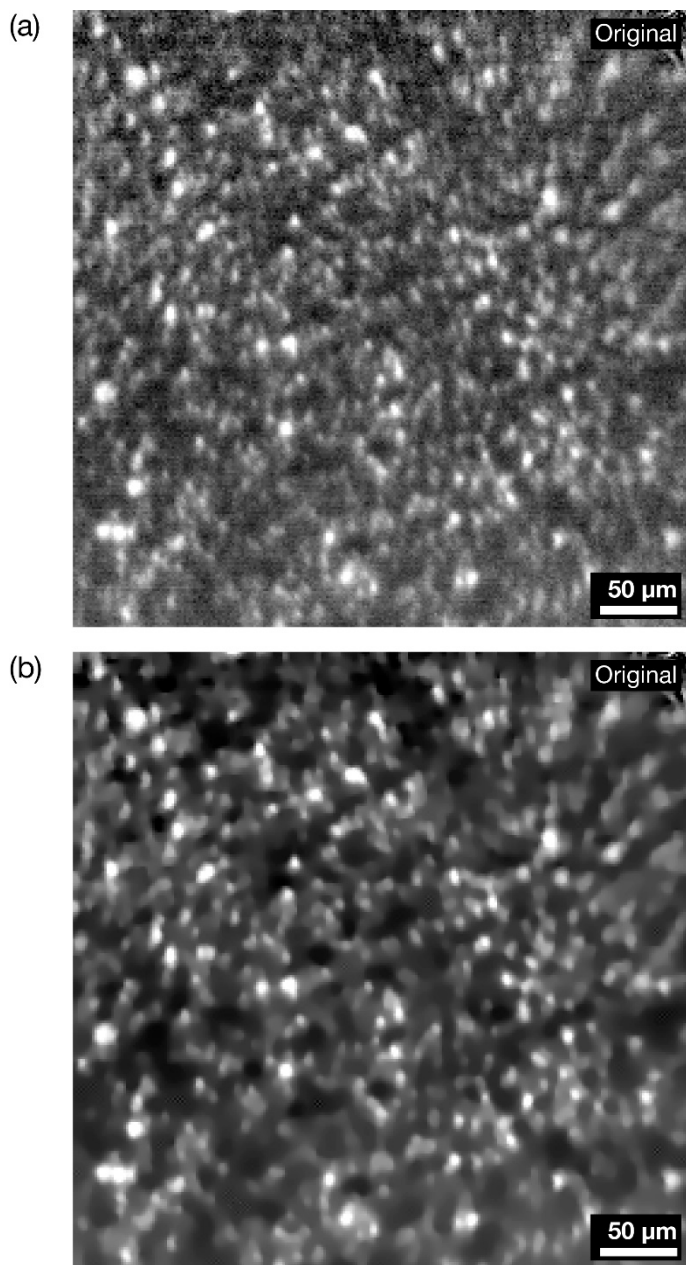
Figure 1. Micrograms representing the values of $I_{960-1100}$ of the bitumen specimen: (a) original micrograph of bitumen and (b) micrograph of bitumen after the reduction of noise.

heated at (140 ± 5) °C in a 2000 ml spherical flask until it become a well-melted fluid. Afterwards, the mass fraction of 3 % of organo-modified montmorillonite (steamed for 3 h at 105 °C before the use) was added into bitumen and mixed for 60 min at the rate of 3000 min^{-1} to homogenise the dispersion, and afterwards left to cool to room temperature for 48 h.

2.2 Specimen preparation and measurement

The measurements were performed by placing a few grams of on the microscope's observation stage. The images were obtained using ATR with germanium crystal having the refraction index of 4.01 and the contact area of approximately 600 μm of diameter. The images had the field of view of 400 by 400 μm and the effective pixel size of 1.56 by 1.56 μm. The analysis covered the domain of wavelengths from 960 to 1100 cm^{-1} to include the peak of Si–O at 1050 cm^{-1}

as a tracer of montmorillonite, so the image pixel values represented the integral on this range, $I_{960-1100}$.

2.3 Postprocessing and analysis of micrographs

To minimise the misjudgement of pixel values originating from the image noise (common for this type of microscopy) the noise reduction was necessary. This was done by 20 iterations of an anisotropic diffusion-based algorithm [5, 6] which favoured the diffusion along contours and suppressed it orthogonally. The output of noise removal is shown in Figure 1.

To obtain regions representing different characteristic areas under the FTIR spectra in the range from 960 to 11100 cm^{-1}, the postprocessed micrographs were successively thresholded by fixing the lower threshold at $I_{960-1100}$ of 0, while the upper threshold was gradually increased from 1.0 to 4.0 with the increment of 0.2. A series of output binary images represented regions with different maximal values of $I_{960-1100}$, while their inversion defined discrete (i.e. peak) regions including the local maxima of $I_{960-1100}$, as shown in Figure 2. The morphology of the latter discrete regions was characterised for area (size) distributions and for the spatial arrangement (F- and G-functions) [6], while the former regions were characterised by local thickness distributions [6].

3 RESULTS

3.1 Size distribution of peak regions

Diagrams of the area-weighted cumulative distributions of peak region areas for different lower threshold values of $I_{960-1100}$ are shown in Figure 3. It could be observed that the areas of peak regions almost continuously reduced with increase in the lower threshold. Thus, with the relatively low thresholds of up to about 2.0, the evolution was drastic with no noticeable consistency. Nevertheless, this trend got gradually stabilised above the $I_{960-1100}$ of 3.0, so the evolution taking place up to 4.0 became minor.

3.2 Spatial arrangement of peak regions

Diagrams of the F- and G-functions of peak regions for the lower threshold values of $I_{960-1100}$ corresponding to the thresholded area fractions of 0.01 and 0.1 are shown in Figure 4. It was noticeable that both functions mainly differed due to different total number of peak regions, while their overall shape was similar. In both cases, the F-functions suggested random global arrangement across the field of view (and were even partially within the confidence intervals of the CSR), with symbolic tendency towards the regu-
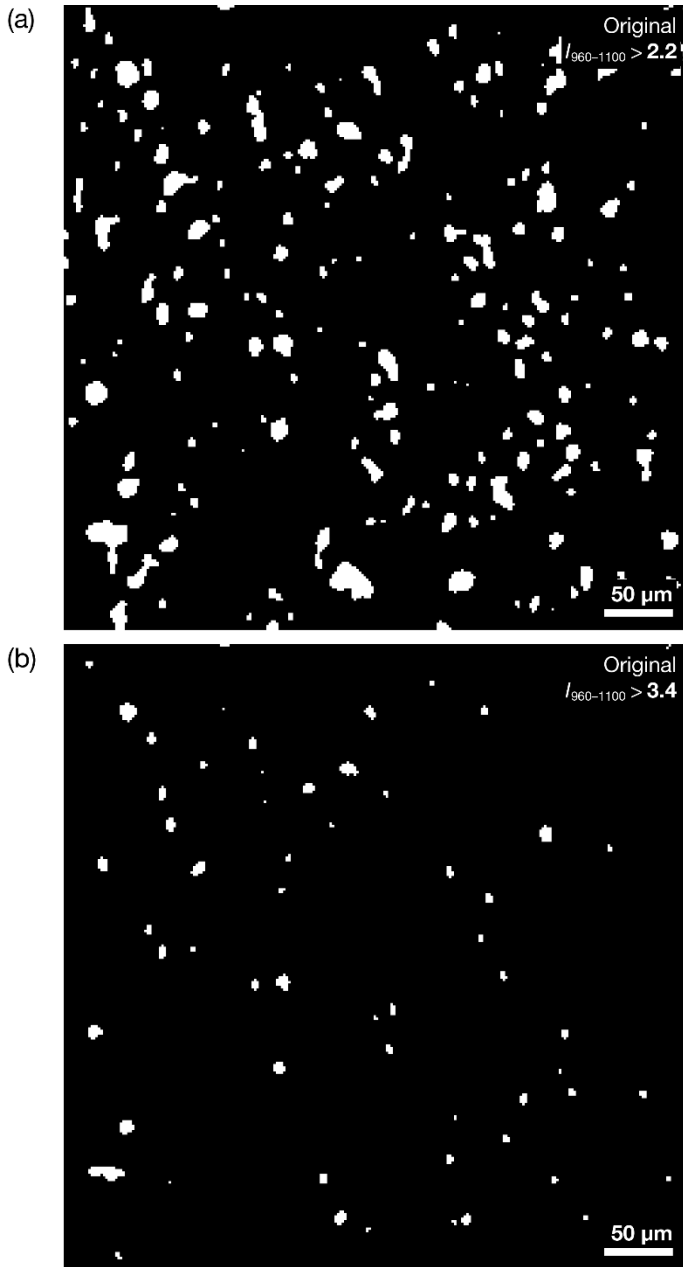
Figure 2. Examples of inverted cumulative thresholding of the values of $I_{960-1100}$ of the original bitumen for two characteristic values of lower thresholds (i.e. peak regions): (a) $I_{960-1100}>2.2$ and (b) $I_{960-1100}>3.4$.

Figure 3. Area-weighted cumulative distributions of peak region areas for different lower threshold values of $I_{960-1100}$.
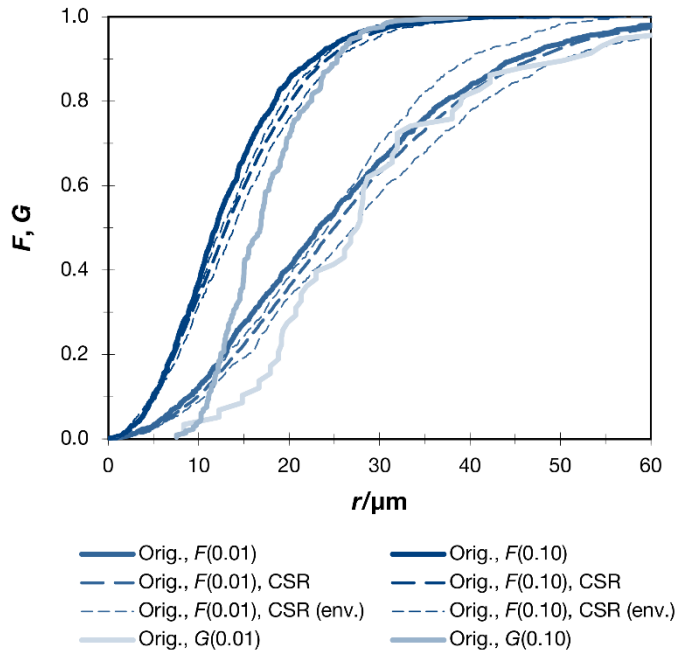
Figure 4. Spatial arrangement functions of peak regions for the lower threshold values of $I_{960-1100}$ corresponding to the thresholded area fractions of 0.01 and 0.10.

lar arrangement. This was confirmed by the G-functions which were predominantly rightwards of the CSR, especially in lower half of their domain.

3.3 Local thickness distributions

Colour maps of local thicknesses for different upper thresholds of $I_{960-1100}$ and the diagrams of local thickness distributions of the thresholded regions are shown in Figures 5 and 6, respectively. The colour maps indicated the high interconnectivity of the intermediate zones around the peak regions with only negligible presence of throats around the upper threshold of 2.8, which was not visible at other thresholds. The continuous distribution of local thicknesses was maintained at all thresholds and drastically evolved until reading mostly steady state above the threshold

of 3.0. Consequently, the median diameter changed from the initial value approximately 3 μm to about 100 μm where it was stabilised for the range of upper thresholds of $I_{960-1100}$ from 3.0 to 4.0. In that domain, the distributions had extremely high uniformity, so that $d_{0.1}$ and $d_{0.9}$ were approximately 80 and 150 μm.

4 CONCLUSIONS

This research demonstrated a high potential of the experimental and analytical methodology based on infrared microscopy to comprehensively quantify the heterogeneous microstructure of montmorillonite-modified bitumen. It could be concluded that the
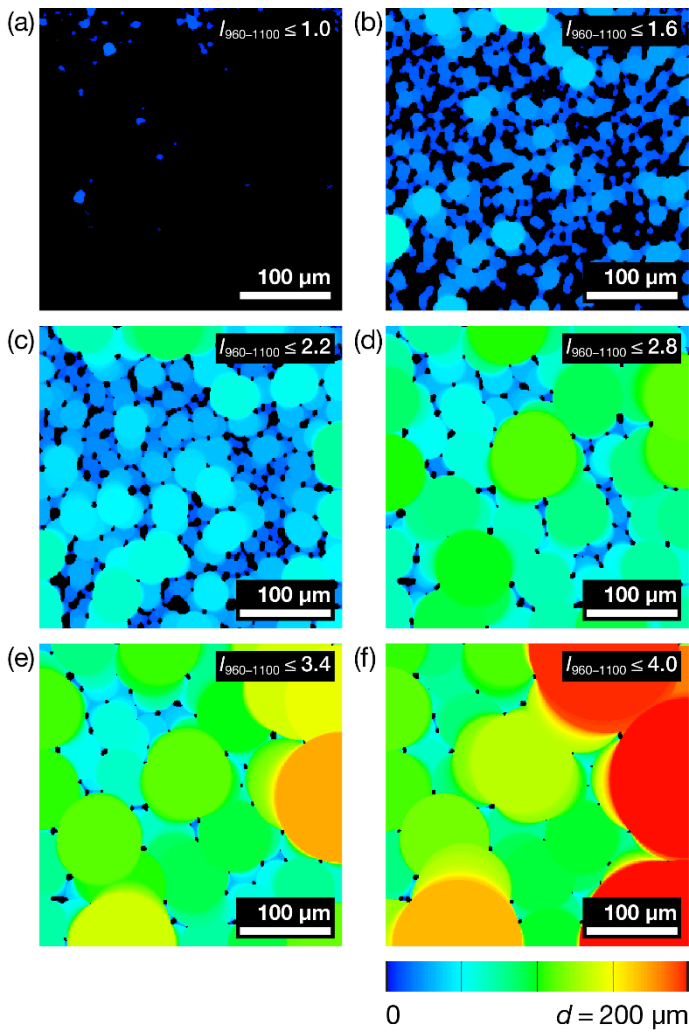
Figure 5. Colour maps of local thicknesses (expressed by diameters) for different upper thresholds of $I_{960-1100}$: (a) $I_{960-1100} \leq 1.0$, (b) $I_{960-1100} \leq 1.6$, (c) $I_{960-1100} \leq 2.2$, (d) $I_{960-1100} \leq 2.8$, (e) $I_{960-1100} \leq 3.4$, and (f) $I_{960-1100} \leq 4.0$.
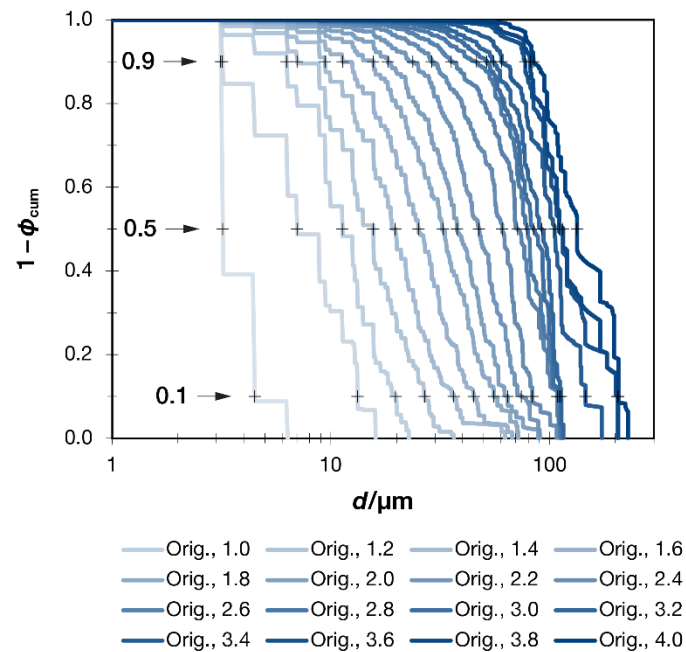
Figure 6. Local thickness distributions of the thresholded regions for different upper threshold values of $I_{960-1100}$.

modification of bitumen led to mostly randomly heterogeneous microstructure with notable peakedness of the regions of modifier's high concentration.

The area distributions of peak regions indicated that the gradients of $I_{960-1100}$ were the largest in the in the closest vicinities of the local maxima, as these regions were the least sensitive to the successive thresholding. Quite the opposite, the intermediate regions had typically low gradients. The consideration of different of 0.01 and 0.1 did not considerably affect the conclusions about these regions' agglomeration. It was found that the local peaks seemed to repel each other in the areas of their higher agglomeration, which gradually diminished on a larger scale.

The most promising application of this approach is the microstructural characterisation of ageing, which should be prioritised in the future research. Moreover, the quantitative morphological analysis of infrared micrographs reveals huge potential for evaluating interfacial chemical interactions (like diffusion) typical for polymer-modified bitumen.

REFERENCES

[1] Zhu, X., Miljković, M., Wang, Y., Hao, G., 2023. Property transitions of neat and styrene-butadiene-styrene (SBS)-modified asphalt binders from small, medium to large-amplitude oscillatory shears. *Int. J. Pavement Eng.*, 24 (2), 2068548. https://doi.org/10.1080/10298436.2022.2068548

[2] Mouillet, V., Lamontagne, J., Durrieu, F., Planche, J.P., Lapalu, L., 2008. Infrared microscopy investigation of oxidation and phase evolution in bitumen modified with polymers. *Fuel,* 87, 1270–1280. https://doi.org/10.1016/j.fuel.2007.06.029

[3] Lamontagne, J., Durrieu, F., Planche, J.P., Mouillet, V., Kister, J., 2001. Direct and continuous methodological approach to study the ageing of fossil organic material by infrared microspectrometry imaging: application to polymer modified bitumen. *Anal. Chim. Acta*, 444 (2), 241–250. https://doi.org/10.1016/S0003-2670(01)01235-1

[4] Lopes, M., Mouillet, V., Bernucci, L., Gabet, T., 2016. The potential of Attenuated Total Reflection imaging in the mid-infrared to study recycled asphalt mixtures. *Constr. Build. Mater.*, 124, 1120–1131. https://doi.org/10.1016/j.conbuildmat.2016.08.108

[5] Zhu, X., Wang, Y., Miljković, M., Li, R., and Hao, G., 2024. Effects of polymer structure on the physicochemical and performance-related properties of SBS-modified asphalt binders subjected to short-term aging. *Constr. Build. Mater.*, 411, 134446. https://doi.org/10.1016/j.conbuildmat.2023.134446

[6] Miljković, M., Wu, C., Jelagin, D., Xie, H., 2024. Microstructural analysis of the phase separation of epoxy-modified bitumen. *Constr. Build. Mater.*, 451, 138596. https://doi.org/10.1016/j.conbuildmat.2024.138596

Impact of Warm-Mix Additives on Viscosity Reduction in Virgin and Aged Bitumen with Polymer Modification

Shisong Ren [1,2], Ahmed Majeed [2], Wim Van den bergh [1], Aikaterini Varveri [2]
1. SuPAR group, University of Antwerp, Belgium. 2. Delft University of Technology, the Netherlands.

ABSTRACT: Combining warm-mixing and recycling technologies in asphalt pavement is essential for reducing energy consumption, lowering greenhouse gas emissions, and decreasing material costs, providing both economic and environmental benefits. This study examines how warm-mix additive types and dosages, bitumen aging levels, and bio-oil addition impact the viscosity of virgin bitumen, polymer-modified bitumen (PMB), and their aged binders. The results indicate that wax-based and chemical-based warm-mix additives impact viscosity differently: Wax-based additive reduces viscosity in virgin bitumen more effectively, while chemical-based additive lower viscosity in PMB significantly. Polymer presence increases viscosity compared to virgin bitumen, but PMB demonstrates superior aging resistance, especially beyond 40h aging. Moreover, bio-oil consistently provides a greater viscosity reduction than Sasobit, which tends to be less effective in aged virgin bitumen but becomes more effective in aged PMB over time. Using a warm-mix additive with a bio-rejuvenator is an effective way to rejuvenate aged bitumen, though the effectiveness of each additive depends on the presence of polymer and the aging level of the bitumen.

Keywords: Warm-mixing agents; Viscosity reduction; Bio-rejuvenator; Aging level; SBS-modified bitumen

1 INTRODUCTION

Bitumen is an important material in road construction, serving as the primary binder in asphalt mixtures [1, 2]. However, its high viscosity at typical production temperatures poses challenges in mixing and compaction, often necessitating elevated temperatures during asphalt production. While this practice ensures workability, it also leads to high energy consumption and greenhouse gas emissions, raising environmental concerns [3].

To address these issues, warm-mix asphalt (WMA) technologies have emerged as a sustainable alternative, allowing asphalt production and paving at lower temperatures without sacrificing performance [4, 5]. This is achieved through the use of warm-mix additives, which reduce the viscosity of bitumen, making it easier to mix and compact at reduced temperatures. These additives offer the potential to lower emissions, conserve energy, and enhance the long-term performance of asphalt pavement [6].

While warm-mix additives have been shown to improve workability, their effects on bitumen viscosity, particularly in aged or polymer-modified bitumen, require further exploration [7, 8]. Aged bitumen often experiences increased stiffness due to oxidation, while polymer-modified bitumen, known as its enhanced durability and deformation resistance, presents additional viscosity challenges [9]. Understanding how warm-mix additives influence both virgin and aged bitumen, with and without polymer modification, is crucial for optimizing WMA technologies.

This study aims to study the impact of warm-mix additives on viscosity reduction of virgin and aged bitumen, both with and without polymer modification. By comparing these effects, the research seeks to provide valuable insights into the use of warm-mix technologies in the high-efficient rejuvenation process of bituminous materials.

2 MATERIALS AND METHODS

2.1. Bitumen and warm-mixing additives properties
A 70/100 grade bitumen was chosen with its fundamental properties detailed in Table 1. Two commercial warm-mixing agents, Sasobit (wax-based) and Rediset (chemical-based), were utilized to prepare the warm-mix bitumen. The characteristics of these two WMA additives are presented in Table 2.

Table 1 Chemo-physical properties of bitumen

Properties		value
25°C Penetration (1/10 mm)		91
Softening point (°C)		48
Chemical fractions (wt%)	Saturate, S	3.6
	Aromatic, A	51.6
	Resin, R	30.2
	Asphaltene, As	14.6
Element compositions (wt%)	Carbon, C	80.1
	Hydrogen, H	10.9
	Oxygen, O	0.6
	Sulfur, S	3.5
	Nitrogen, N	0.9

Table 2 Basic property of warm-mix additive [10, 11]

Properties	Sasobit	Rediset

Appearance			
25°C Density (g/cm³)	0.900		-
20°C Solubility in water	Insoluble		-
40°C viscosity (cP)	-		135
40°C Density (g/cm³)	-		0.962
Flash point (°C)	285		230
Initial boiling point (°C)	271		215

Meanwhile, the bio-oil was used as rejuvenator for performance recovery of aged bitumen. The bio-oil is the rapeseed oil with a pale-yellow color. Its density and viscosity at 25°C are 0.911 g/cm³ and 50 cP, respectively. The main molecular components of the bio-oil are methyl oleate, methyl linoleate, and methyl palmitate [13].

2.2. Preparation of polymer modified bitumen

The Styrene-Butadiene-Styrene (SBS) modified bitumen was produced using 70/100 penetration grade bitumen as the base binder, with 4% by weight of Kraton D1102 SBS added. The SBS polymer is a linear block copolymer containing 28.5% styrene [12]. It should be noted that the abbreviation of virgin bitumen and aged bitumen is VB and PMB, respectively.

2.3. Aging protocols

In this study, both bitumen and SBS-modified bitumen were subjected to short-term and long-term aging to prepare the aged binders. The Thin-Film Oven test (TFOT) and Pressure Aging Vessel (PAV) were used to age the samples. The temperature and duration of TFOT test is 163°C and 5 hours. The PAV test was run at 100°C and 2.1MPa with variable aging times of 20h, 40h, and 80h to investigate the effect of aging level. The abbreviations for aged bitumen are 1PB, 2PB, and 4PB, while the abbreviations of aged SBS-modified bitumen are 1PMB, 2PMB, and 4PMB.

2.4. Preparation of warm-mix and rejuvenated bitumen

The virgin bitumen and SBS-modified bitumen were heated in an oven at 140°C to ensure flowability. Afterwards, the warm-mixing additives (Sasobit and Rediset) are added in bitumen. The Sasobit dosages were 0%, 1%, 2%, and 4% by weight of bitumen, while the Rediset concentration was 0%, 0.3%, 0.6%, and 0.9%. To obtain a homogenous warm-mixing bitumen binder, the bitumen and the added warm-mix additives were mixed at 140°C for 30min.

In addition, the aged bitumen and aged polymer modified bitumen were mixed with Sasobit additive (4wt%) first at 140°C for 30min, and then the bio-oil rejuvenator (10wt%) was incorporated to prepare the warm-mixing rejuvenated binders.

2.5. Viscosity measurement

The rotational viscometer (RV) was utilized to measure the dynamic viscosity values of all bitumen binders according to the standard of AASHTO T316-13. The temperature was set as 120°C and the rotor spinning rate was 20 rad/s.

3 RESULTS AND DISCUSSION

3.1. Effect of WMA additives on viscosity of bitumen and PMB

The viscosity variations of fresh and polymer modified bitumen as a function of WMA dosage are displayed in Fig.1. It is evident that increasing the dosage of WMA additives leads to a substantial reduction in viscosity, which is consistent with the goal of these additives in improving workability at lower temperatures. For all bitumen, the viscosity shows a linear reduction trend as the increase in Rediset dosage, while an exponential decline law is observed for the Sasobit case. Compared to Rediset, Sasobit appears to be more effective in achieving a sharper drop in viscosity in virgin bitumen.
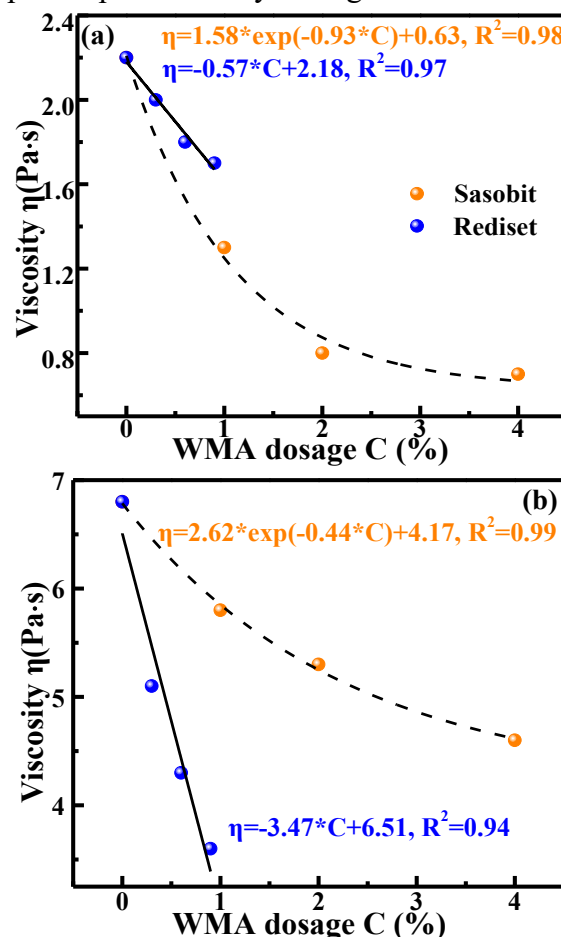
Fig.1. Influence of WMA additives on viscosity of bitumen (a) and PMB (b)

For polymer modified bitumen (PMB), all viscosities are higher than the virgin bitumen due to the presence of SBS polymer. An opposite phenomenon can be observed in the reduction of viscosity of PMB compared to virgin bitumen that the addition of Rediset has a greater impact on the reduction compared to the addition of Sasobit in PMB. The

phenomenon may be attributed to the effective reduction function of Rediset on the surface tension between polymer and bitumen, and thus improving the flowability of whole PMB. Moreover, the addition of Sasobit can reduce the viscosity of PMB, but less effective than virgin bitumen. Therefore, the Sasobit is more useful for the warm-mixing production of virgin bitumen, while the Rediset is more effective for PMB case. From the results, the need for selection of WMA additives, based on the specific type of bitumen and desired workability during construction, should be considered carefully.

3.2. Aging effect on viscosity of bitumen and PMB

Figure 2 illustrates the effect of aging on the viscosity of virgin and SBS-modified bitumen. The relationship between aging time and viscosity is captured through exponential equations, highlighting how both materials respond to oxidative aging. The viscosity of virgin bitumen increases significantly with aging time. The steep rise in viscosity, particularly at longer aging times (80 h), suggests that virgin bitumen undergoes substantial hardening due to oxidation. This result underscores the susceptibility of virgin bitumen to aging, which can lead to reduced flexibility and potential cracking in pavement over time.

In contrast, the viscosity of PMB increases more gradually. Initially, PMB has a higher viscosity (6.8 Pa·s) compared to VB, due to the presence of polymers. Even after 80h aging, the viscosity of PMB only reaches 16.2 Pa·s, a much smaller increase compared to VB. The result highlights the superior resistance of PMB to aging, likely due to the stabilizing effect of the polymer, which mitigates the hardening process.
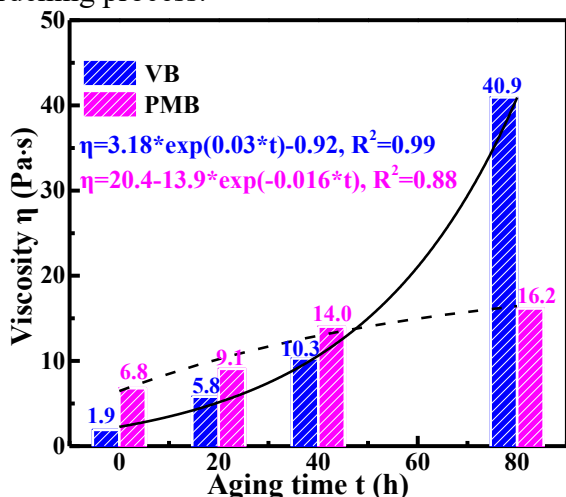
Fig.2. Aging effect on viscosity of bitumen and PMB

3.3. Effect of WMA and bio-oil rejuvenator on viscosity of aged bitumen and PMB

Sasobit and bio-oil were added to aged bitumen and aged polymer-modified bitumen (PMB) with varying aging durations to achieve the dual objectives of warm-mixing and rejuvenation. Fig.3 shows the changes in viscosity after the addition of Sasobit

(WMA) and a Sasobit/bio-oil blend (WMA-BO). The results indicate that both Sasobit and bio-oil effectively reduce the viscosity of both virgin and aged bitumen, with bio-oil consistently achieving a greater percentages reduction than Sasobit. This trend holds true for both VB and PMB, although the relative effectiveness of these additives decreases with increasing aging, especially for Sasobit. Notably, the impact of Sasobit on viscosity reduction in virgin bitumen declines as the aging level rises. At an aging level of PAV80h, the reduction efficiency is only 9.1%. For PMB, the effectiveness of Sasobit first increase slightly and then declines. Although the initial effect of Sasobit on viscosity reduction is lower in PMB than in VB, it becomes relatively more effective for PMB after prolonged aging, particular at 20-hour and 40-hour aging intervals.
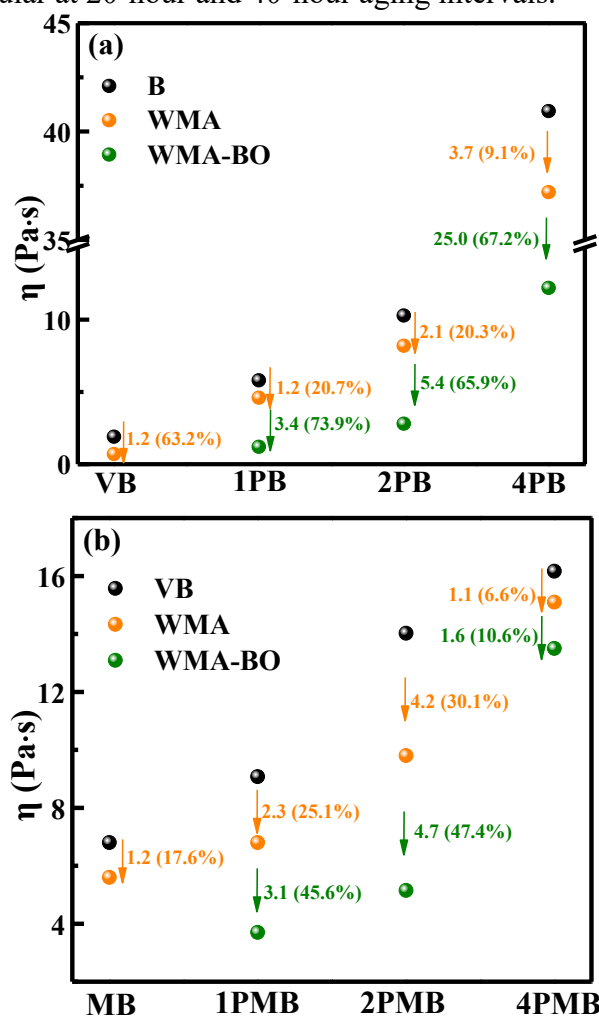
Fig.3. Effect of Sasobit and bio-oil on viscosity of bitumen (a) and PMB (b) with various aging levels

In highly aged bitumen and PMB, the superior performance of bio-oil suggests it may be more effective for restoring workability in severely-aged binders. This makes bio-oil a potentially more versatile and efficient rejuvenator for aged bitumen and PMB, contributing to improved long-term sustainability and performance in asphalt pavements. Based on viscosity reduction percentages, the impact of bio-oil on aged bitumen is more pronounced than on

aged polymer-modified bitumen. Overall, combining a warm-mix additive with a bio-rejuvenator provides an effective approach to achieving warm-mixing rejuvenation of aged bitumen. However, their effects are highly dependent on the aging level of both bitumen and polymer-modified bitumen.

4 CONCLUSIONS

This study investigates the effects of warm-mix additive types and dosages, aging level of bitumen, and bio-oil on the viscosity property of bitumen, polymer-modified bitumen, and their corresponding aged binders. The main findings are drawn as follows:

(1) The two warm-mix additives, Sasobit and Rediset, have distinct effects on reducing the viscosity of both virgin bitumen and polymer-modified bitumen. Sasobit shows a more pronounced viscosity-reducing effect on virgin bitumen, whereas the addition of Rediset results in a significant viscosity reduction in polymer-modified bitumen.

(2) Compared to virgin bitumen, the presence of polymer increases the viscosity of modified bitumen. However, the rate of viscosity increase due to aging is considerably lower in polymer-modified bitumen than in virgin bitumen, due to its superior aging resistance, particularly when aging time exceeds 40 hours.

(3) Both Sasobit and bio-oil reduce the viscosity of virgin and aged bitumen, with bio-oil consistently achieving a greater reduction. The impact of Sasobit lessens in virgin bitumen as aging progresses, but it becomes more effective for polymer-modified bitumen after 20h and 40h aging.

(4) Combining a warm-mix additive with a bio-rejuvenator offers an effective method for achieving warm-mix rejuvenation of aged bitumen. However, the selection of warm-mix agent and its effectiveness on viscosity reduction is highly dependent on the presence of polymer and aging level of bitumen.

ACKNOWLEDGEMENTS

REFERENCES

[1] A. Behnood. A review of the warm mix asphalt (WMA) technologies: Effects on thermo-mechanical and rheological properties. Journal of Cleaner Production. 2020. 259, 120817.

[2] M. Pouranian, M. Notani, M. Tabesh, B. Nazeri, M. Shishehbor. Rheological and environmental characteristics of crumb rubber asphalt binders containing non-foaming warm mix asphalt additives. Construction and Building Materials. 2020, 238, 117707.

[3] G. Cheraghian, A. Falchetto, Z. You, S. Chen, Y. Kim, J. Westerhoff, K. Moon, M. Wistuba. Warm mix asphalt technology: An up to date review. Journal of Cleaner Production. 2020, 268, 122128.

[4] M. Ameri, A. Afshin, M. Shiraz, F. Yazdipanah. Effect of wax-based warm mix additives on fatigue and rutting performance of crumb rubber modified asphalt. Construction and Building Materials. 2020, 262, 120882.

[5] C. Li, H. Wang, C. Fu, S. Shi, G. Li, Q. Liu, D. Zhou, L. Jiang, Y. Cheng. Evaluation of modified bitumen properties using waste plastic pyrolysis wax as warm mix additives. Journal of Cleaner Production. 2023, 405, 136910.

[6] A. Jamshidi, M. Hamzah, Z. You. Performance of warm mix asphalt containing Sasobit: State-of-the-art. Construction and Building Materials. 2013, 38, 530-553.

[7] Z. Cao, M. Chen, X. Han, J. Yu, R. Wang, X. Xu. Evaluation of viscosity-temperature characteristics and rheological properties of rejuvenated SBS modified bitumen with active warm additives. Construction and Building Materials. 2020, 236, 117548.

[8] P. Xu, D. Zhang, Z. Liu, J. Tang, S. Xu. Quantifying the blending efficiency of warm mix asphalt-synchronous rejuvenated SBS-modified asphalt through a dynamic shear rheometer (DSR) testing approach. Construction and Building Materials. 2024, 449, 138183.

[9] Z. Hossain, S. Lewis, M. Zaman, A. Buddhala, E. O'Rear. Evaluation for warm-mix additive-modified asphalt binders using spectroscopy techniques. Journal of Materials in Civil Engineering. 2013, 25(2), 149-159.

[10] S. Rosyidi, B. Idiajir, N. Akhir, S. Rahmad, N. Lestari, V. Widoanindyawati, A. Al-Sabaeei, A. Milad, N. Mashaan, N. Yusoff. Physical, chemical, thermal properties of palm oil boiler ash/Rediset-modified asphalt binder. Sustainability. 2022, 14(5), 3016.

[11] B. Kheradmand, R. Muniandy, L. Hua, A. Solouki. A laboratory investigation on the rheological properties of aged and unaged organic wax modified asphalt binders. Petroleum Science and Technology. 2015, 33, 757-764.

[12] L. Ma, A. Variveri, R. Jing, S. Erkens. Chemical characterisation of bitumen type and ageing state based on FTIR spectroscopy and discriminant analysis integrated with variable selection methods. Road Materials and Pavement Design. 2023, 24(S1), S506-S520.

[13] S. Ren, X. Liu, S. Erkens, P. Lin. Y. Gao. Multi-component analysis, molecular model construction, and thermodynamics performance prediction on various rejuvenators of aged bitumen. Journal of Molecular Liquids. 2022, 360, 119463.

Identification and Quantification of HDPE, LDPE, and PP in Asphalt Binders using DSC

Shahjalal Selim
Doctoral Student, Department of Civil Engineering, Louisiana Tech University, Ruston, LA, USA

Nazimuddin M Wasiuddin
Professor, Department of Civil Engineering, Louisiana Tech University, Ruston, LA, USA

Andrew Peters
Associate Professor, Department of Chemical Engineering, Louisiana Tech University, Ruston, LA, USA

ABSTRACT: The use of plastics in road construction has gained significant traction in recent years, and identifying the type and quantity of plastic in asphalt blends is important for quality control. Previously the authors demonstrated that the Fourier Transform Infrared Spectrometer (FTIR) can only identify polypropylene (PP), while neither FTIR spectrometer nor Dynamic Shear Rheometer (DSR) with Sentmanat Extensional Rheometer (SER) can detect polyolefin plastomers like high-density polyethylene (HDPE) and low-density polyethylene (LDPE). This study presents a Differential Scanning Calorimetry (DSC)-based method to identify and quantify HDPE, LDPE, and PP in asphalt-plastic blends using a calibration curve. The curve was developed using enthalpy and plastic percentage data from HDPE, LDPE, and PP-modified PG 67-22 and PG 58-28 binders. The calibration was validated with PG 64-22 binder modified with the same plastics. The results confirm that DSC is a reliable and efficient technique for accurate and precise identification and quantification of HDPE, LDPE, and PP plastics in asphalt binders.

1 INTRODUCTION

Plastic production has grown rapidly, from 2 million metric tons (MT) in 1950 to 460 MT in 2019, and is projected to reach 540 MT by 2040, with polyethylene (PE) and polypropylene (PP) comprising a significant share (Sharma et al., 2023). To reduce plastic waste, countries such as the USA, UK, Canada, India, and others have begun incorporating it into asphalt for road construction (Mashaan et al., 2021). For quality assurance in road construction, detecting polymers is crucial to minimize the use of lower-quality materials (Diefenderfer et al., 2006). The FTIR-based AASHTO T302 test method, however, is limited to determining concentrations of Styrene-Butadiene-Rubber (SBR), Styrene-Butadiene (SB), and Styrene-Butadiene-Styrene (SBS) in polymer-modified asphalt (Diefenderfer et al., 2006). (Hossain et al., 2019) used a dynamic shear rheometer (DSR) with a Sentmanat extensional rheometer (SER) fixture to assess the type of modifier in asphalt. The SER test results showed that the first peak elongation force (F_1) reflects the binder's stiffness, while the second peak elongation force (F_2) indicates the type of modifier in the asphalt-polymer blend. Their findings revealed that HDPE-modified binders exhibited an F_1 value but lacked an F_2 value, suggesting that HDPE plastic cannot be identified in

HDPE-modified binders using the SER test. (Islam & Wasiuddin, 2022) employed a hand-held FTIR device to identify HDPE, LDPE, and PP plastics in their respective modified binders. While they were able to detect PP plastic in the blend, no significant changes in FTIR peaks were observed for HDPE and LDPE, making it difficult to identify these plastics. In this study, we employed a DSC-based approach to identify and quantify HDPE, LDPE, and PP plastics in plastic-modified asphalt binders. A calibration curve was developed using enthalpy vs. plastic percentage data for PG 67-22 and PG 58-28 binders modified with varying amounts of HDPE, LDPE, and PP. The calibration curve was then validated with PG 64-22 binder modified with the same types of plastics.

2 MATERIALS AND EXPERIMENTAL PLAN

2.1 *Materials*

Neat asphalt binders, PG 67-22 and PG 58-28, were modified with varying percentages of HDPE, LDPE, and PP plastic pellets obtained from Sigma-Aldrich. Additionally, a separate binder, PG 64-22, was modified with the same plastics for experimental validation purposes. For each asphalt-plastic modified

binder, three replicate samples were prepared for the DSC test. Detail test factorial is provided in Table 1.

Table 1. Test factorial

Binder	Added Plastic	Percentages	Total Samples
PG 67-22	HDPE, LDPE, PP	3,9,15,30	36
PG 58-28	HDPE, LDPE, PP	3,6,15,30	36
PG 64-22	HDPE*, LDPE, PP	3,6	24*

* PG 64-22+9% HDPE and PG 64-22+6% PP (SW) samples were also prepared. SW represents solid waste.

2.2 Sample preparation

The asphalt binder was modified with HDPE, LDPE, and PP pellets using a high-shear mixer operating at 4000–5000 rpm for 150–180 minutes. Upon completion of mixing, a 1–2 g sample was carefully extracted using a spatula. The sample was then placed between two silicon mats, with a 5–10 lb weight applied to form a thin film. A small portion (2–10 mg) of this sample was subsequently transferred to a DSC Tzero pan, sealed with a Tzero Hermetic Lid, and prepared for testing. Figure 1 outlines the sample preparation process.
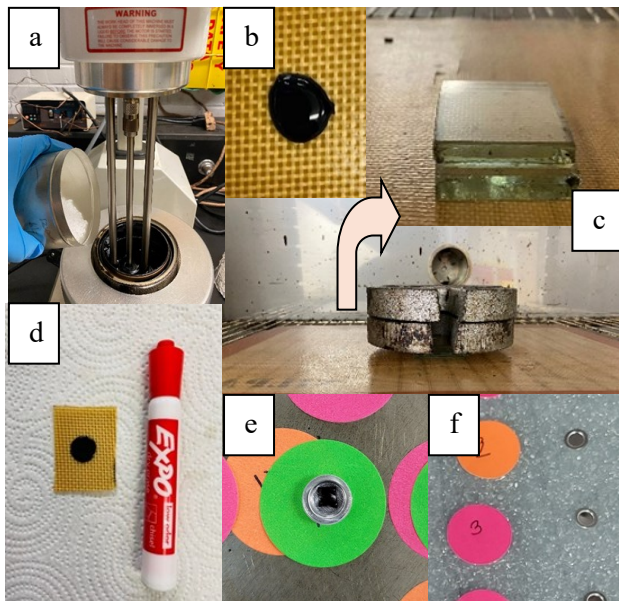
Figure 1. a) Asphalt-plastic blend mixed in high shear mixer, b) 1-2 g sample poured on mat, c) sample pressed under another mat with glass and weight, d) thin film formed, e) film cut to size, f) sample placed in DSC pan.

2.3 DSC test protocol

TA Instrument's DSC 2500 with an RCS cooling unit was used for DSC experiments. The DSC test utilized a standard heat-cool-heat protocol, with a temperature range of -80 °C to 170 °C. The heating or cooling rate was kept at 10°C/min. Test protocol steps are given below:
   i) Equilibrate to 25 ° C

ii) Isothermal 10 min
iii) Ramp 10 ° C/min to -80 ° C
iv) Isothermal 10 min
v) Ramp 10 ° C/min to 170 ° C
vi) Isothermal 5 min
vii) Ramp 10° C/min to -80° C
viii) Isothermal 10 min
ix) Ramp 10° C/min to 170° C

3 RESULT AND DISCUSSIONS

3.1 Melting point temperature (T_m) and enthalpy (H_m)

Melting point temperature (T_m) and enthalpy (H_m) data of all the plastic modified binders were taken from the second heating cycle of the DSC thermogram and given in Table 2.

Table 2. Thermal properties of LDPE, HDPE, and PP modified asphalt binders

Binder	Plastic	Plastic Percent	T_m (°C)	H_m (J/g)
PG 67-22	LDPE	3	102.61±0.20	2.55±0.38
		9	100.99±1.25	8.62±1.53
		15	104.31±0.19	14.16±1.26
		30	104.66±0.25	23.00±2.04
	HDPE	3	119.16±0.86	4.85±1.82
		9	117.97±0.38	14.71±0.89
		15	119.27±0.72	20.33±4.29
		30	119.44±0.52	45.61±3.46
	PP	3	150.55±0.22	1.39±0.58
		9	150.09±0.78	6.16±1.05
		15	150.47±0.34	7.65±0.89
		30	151.31±0.06	20.99±1.98
PG 58-28	LDPE	3	101.75±0.69	2.46±0.62
		6	98.84±0.36	5.41±2.58
		15	99.22±0.28	11.02±1.34
		30	100.87±0.3	31.42±6.22
	HDPE	3	117.14±0.09	5.41±0.94
		6	117.13±0.27	10.82±0.86
		15	119.03±0.14	29.23±4.42
		30	120.17±0.74	49.63±5.99
	PP	3	156.47±0.39	1.38±0.38
		6	156.98±1.18	4.17±1.23
		15	148.96±1.07	8.44±0.43
		30	150.42±0.32	20.17±1.88

T_m value of all the asphalt-plastic blends were clustered around mean. Ideally T_m should increase with the increase in plastic percent, however, factors such as heating rate effects polymer crystal's ability to adjust their fold periods, which may cause irregularity of the T_m value (Harrison & Runt, 1979). Additionally, factors such as polymer structure, molecular weight, crystallite size, chemical composition, and thermal history may contribute to variability in the T_m data (Farrow, 1963), (Hatakeyama & Quinn,

1999). The typical melting points for pure LDPE, HDPE, and PP are 108–123°C, 135°C, and 160°C, respectively (Lesueur, 2009). The melting points of the plastic-modified asphalt binder samples were found to be lower than those of the corresponding pure plastic components. The HDPE-asphalt blend demonstrated an average melting temperature ranging from approximately 98°C to 105°C, while the LDPE-asphalt blend exhibited a range of 116°C to 121°C, and the PP-modified binder showed a range from 150°C to 158°C.

The melting enthalpy (H_m) of the modified PG 67-22 and PG 58-28 binders increased as the plastic content increased (Table 2). Binders with HDPE showed a higher melting enthalpy compared to those with LDPE and PP, due to the higher crystallinity of HDPE pellets. A higher degree of crystallinity requires more heat for polymer melting (Kong & Hay, 2003). Figure 2 shows the DSC thermograms of all plastic-modified PG 67-22 binder, superimposed in a single plot. Multiple endothermic peaks observed in DSC thermograms (Figure 2) have been linked to variations in crystal types and sizes by several researchers. (Passingham et al., 1990) observed that thinner lamellae within isotactic polypropylene (IPP) melt at lower temperatures and recrystallize into thicker lamellae, resulting in two melting peaks: the first peak represents smaller, loosely packed crystals, while the second peak reflects larger, more densely packed crystalline regions (Miao et al., 2018). The melting temperature was determined using the highest point of the melting peak, in accordance with the guidelines from the International Conference of Thermal Analysis and Calorimetry (ICTAC) (Menczel et al., 2009).
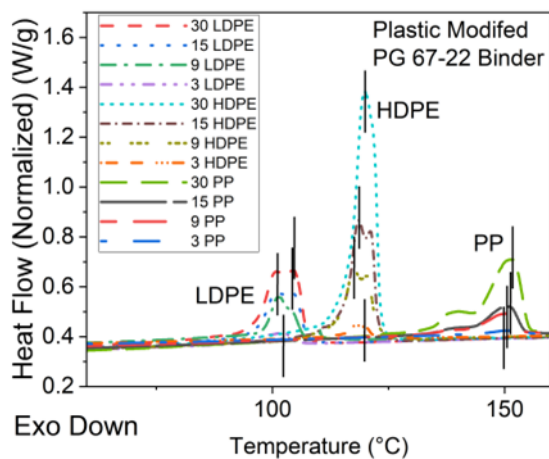
Figure 2. DSC thermograms of plastic modified PG 67-22 binder

3.2 Identification and quantification of plastic from DSC thermogram

Differential scanning calorimetry (DSC) serves as a valuable method for identifying plastic type and determining plastic content in binders by using an enthalpy vs. plastic percentage calibration curve. This curve was developed from experimental data on plastic-modified asphalt binders PG 67-22 and PG 58-28. Figure 3 illustrates the relationship between enthalpy and plastic content for both binders, revealing a strong correlation between plastic percentage and enthalpy (H_m). The HDPE-modified binder shows a notably steeper slope than the other plastic-modified binders, with an R^2 value of 0.993. The linear equations derived for HDPE, LDPE, and PP modified binders are $y = (1.642 \pm 0.048)x$, $y = (0.832 \pm 0.035)x$, and $y = (0.584 \pm 0.025)x$, respectively. These equations can be used in conjunction with the melting point temperature ranges of HDPE, LDPE, and PP to facilitate identification and quantification.
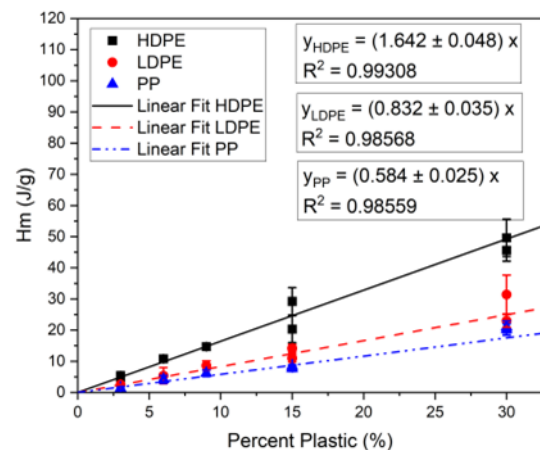
Figure 3. Enthalpy Vs. Plastic percentage curve for HDPE, LDPE, and PP. These curves were developed from data of PG 67-22 and PG 58-28 binders for quantification of plastic percentage of unknown binders.
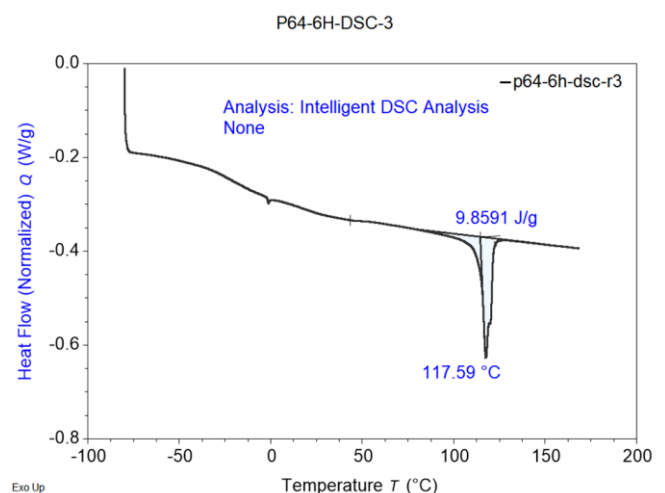
Figure 4. DSC thermogram of 6% HDPE modified PG 64-22 binder

As an example of how this calibration curve is applied, a DSC thermogram was obtained for a 6% HDPE-modified PG 64-22 binder, shown in Figure 4. The melting point temperature for this blend was

determined to be 117.59°C, with an enthalpy value of 9.86 J/g. Observed melting point temperature ranges for HDPE, LDPE, and PP modified PG 67-22 and PG 58-28 binders were 116.88–120.89°C, 98.44–104.84°C, and 147.73–157.74°C, respectively. The temperature of 117.59°C falls within the HDPE-asphalt blend range, confirming HDPE as the modifying plastic in this binder. Using the enthalpy value of 9.86 J/g in the equation y = (1.642 ± 0.048)x yields an x value of 6.001, closely matching the plastic content in the binder. Results for other PG 64-22 plastic-modified binders are presented in Table 3. Table 3 shows that the calibration curve accurately predicted the plastic content in HDPE- and LDPE-modified PG 64-22 binders, with minimal error. However, predictions for PP-modified binders were less precise than for HDPE and LDPE, though the method remains effective. Additionally, we tested a 6% PP (SW)-modified PG 67-22 binder using the calibration curve, with this PP sourced from solid waste, and found the curve provided a reasonable quantification of plastic content.

Table 3 Quantification of plastic percentage from DSC data

Binder	Avg T_m (°C)	Avg H_m (J/g)	Plastic Type	Plastic percent in blend
PG 64-22+3% HDPE	119.64	5.47	HDPE	3.33
PG 64-22+6% HDPE	117.65	10.09	HDPE	6.15
PG 64-22+9% HDPE	117.44	14.41	HDPE	8.77
PG 64-22+3% LDPE	102.69	2.46	LDPE	2.96
PG 64-22+6% LDPE	102.62	4.80	LDPE	5.77
PG 64-22+3% PP	150.58	2.32	PP	3.97
PG 64-22+6% PP	156.98	3.18	PP	5.45
PG 67-22+6% PP (SW)	156.42	3.77	PP	6.43

4 CONCLUSIONS

This study developed a DSC-based calibration curve using melting point temperature and enthalpy data from HDPE, LDPE, and PP-modified PG 67-22 and PG 58-28 binders, validated with PG 64-22, to effectively identify and quantify plastics in asphalt blends. Key findings are as follows:

- A standardized DSC test protocol was established for plastic and plastic-modified asphalt binders to determine melting point temperature and melting enthalpy. The consistency and repeatability of test results demonstrated the reliability of this method across all binders and plastic types.

- DSC proved to be an effective tool for identifying plastic type and quantifying plastic content in asphalt binders based on the enthalpy vs. plastic percentage calibration curve developed in this study.

REFERENCES
Diefenderfer, S. D., Virginia Transportation Research Council (VTRC), Virginia. Dept. of Transportation, & United States. Federal Highway Administration. (2006). *Detection of polymer modifiers in asphalt binder.* (FHWA/VTRC 06-R18). https://rosap.ntl.bts.gov/view/dot/19731

Farrow, G. (1963). Crystallinity, 'crystallite size' and melting point of polypropylene. *Polymer*, 4, 191–197. https://doi.org/10.1016/0032-3861(63)90025-9

Harrison, I. R., & Runt, J. (1979). The heating rate dependence of polymer melting points. *Journal of Polymer Science: Polymer Physics Edition*, 17(2), 321–328. https://doi.org/10.1002/pol.1979.180170211

Hatakeyama, T., & Quinn, F. (1999). *Thermal analysis: Fundamentals and applications to polymer science.* [sl].

Hossain, R., Arafat, S., & Wasiuddin, N. M. (2019). Identification and Evaluation of the Elastomeric, Plastomeric, and Chemical Modifiers in Asphalt Binders. *Airfield and Highway Pavements 2019*, 255–265. https://doi.org/10.1061/9780784482469.026

Islam, M. R., & Wasiuddin, N. (2022). *Identification of Low Density Polyethylene, High Density Polyethylene, and Polypropylene in Asphalt Binder with a Handheld FTIR Spectrometer* (p. 15). https://doi.org/10.1061/9780784484609.002

Kong, Y., & Hay, J. (2003). The enthalpy of fusion and degree of crystallinity of polymers as measured by DSC. *European Polymer Journal - EUR POLYM J*, 39, 1721–1727. https://doi.org/10.1016/S0014-3057(03)00054-5

Lesueur, D. (2009). The colloidal structure of bitumen: Consequences on the rheology and on the mechanisms of bitumen modification. *Advances in Colloid and Interface Science*, 145(1), 42–82. https://doi.org/10.1016/j.cis.2008.08.011

Mashaan, N. S., Chegenizadeh, A., Nikraz, H., & Rezagholilou, A. (2021). Investigating the engineering properties of asphalt binder modified with waste plastic polymer. *Ain Shams Engineering Journal*, 12(2), 1569–1574. https://doi.org/10.1016/j.asej.2020.08.035

Menczel, J. D., Judovits, L., Prime, R. B., Bair, H. E., Reading, M., & Swier, S. (2009). Differential Scanning Calorimetry (DSC). In *Thermal Analysis of Polymers* (pp. 7–239). John Wiley & Sons, Ltd. https://doi.org/10.1002/9780470423837.ch2

Miao, W., Zhu, H., Duan, T., Chen, H., Wu, F., Jiang, L., & Wang, Z. (2018). High-density polyethylene crystals with double melting peaks induced by ultra-high-molecular-weight polyethylene fibre. *Royal Society Open Science*, 5(7), 180394. https://doi.org/10.1098/rsos.180394

Passingham, C., Hendra, P. J., Cudby, M. E. A., Zichy, V., & Weller, M. (1990). The re-evaluation of multiple peaks in the DSC melting endotherm of isotactic polypropylene. *European Polymer Journal*, 26(6), 631–638. https://doi.org/10.1016/0014-3057(90)90219-T

Sharma, S., Sharma, V., & Chatterjee, S. (2023). Contribution of plastic and microplastic to global climate change and their conjoining impacts on the environment—A review. *Science of The Total Environment*, 875, 162627. https://doi.org/10.1016/j.scitotenv.2023.162627

Characterisation of aged rejuvenated bitumen using master curve approach

Minnu Shaji, Prof. Dr. Steffen Riedl, Kim Rodiger
Department of Civil Engineering, University of Applied Sciences, Erfurt, Germany

Prof. Dr. Ronny Sorge
Department of Civil Engineering, University of Applied Sciences, Erfurt, Germany

Arbin Raj
Department of Civil Engineering, Indian Institute of Technology Madras, Chennai, India

ABSTRACT: Reclaimed asphalt pavement (RAP) materials contain aged binders that require recycling to achieve optimal rheological properties. To accomplish this, rejuvenators are introduced to "soften" the aged binders, enabling them to meet specific performance targets. Current practices involve using virgin bitumen of particular grades, with or without rejuvenators, based on the proportion of RAP being recycled. It is crucial to determine the appropriate dosage of rejuvenator to maximize RAP utilization and obtain desired binder properties. This study evaluates the rheological characteristics of both unmodified and polymer-modified binders under varying aging conditions and rejuvenator contents (0 to 12%) using a dynamic shear rheometer. Findings reveal that aging can affect the mechanical properties of bitumen, which can be mitigated by the addition of rejuvenators, as viscosity decreases with higher rejuvenator content. Therefore, it is evident that both binder aging and rejuvenators significantly influence the rheological properties of bitumen, highlighting the importance of optimal rejuvenator application in RAP recycling.

1 INTRODUCTION

Bitumen, also referred to as asphalt or bituminous binder, is a complex mixture of hydrocarbons obtained through the distillation of crude oil. Over time, exposure to environmental factors leads to changes in the chemical and physical properties of bitumen, a phenomenon known as aging (Airey, 2011). This aging process causes bitumen to become brittle and lose its elasticity, often resulting in pavement issues such as cracking. Recycling asphalt is increasingly recognized as a sustainable and environmentally friendly approach to road construction and maintenance (Sengoz & Oylumluoglu, 2013). It involves incorporating reclaimed asphalt pavement (RAP) - obtained from deteriorated or decommissioned pavements - into new asphalt mixtures, thereby conserving natural resources and reducing the need for virgin materials.

To address the challenges posed by aged bitumen, rejuvenators are commonly used. These chemical agents restore the properties of oxidized or aged bitumen found in RAP. Rejuvenators, which can be classified as bio-based or petroleum-based, are integral to asphalt recycling and pavement preservation. Research indicates that the effectiveness of rejuvenators in altering the chemical and rheological properties of RAP binders varies based on their type (Rathore et al. 2022) (Zhang et al., 2020). On a broader scale, the use of rejuvenators has been shown to decrease the absolute shear modulus and increase the phase angle of asphalt mixtures (Elkashef et al. 2020). However, concerns have been raised regarding the long-term performance of rejuvenators, particularly at higher dosages (Dhasmana et al., 2021) (Haghshenas et al., 2018) (Karki & Zhou, 2016) (Ongel & Hugener, 2015).

This study focuses on the application of a plant-based rejuvenator to restore the properties of both road-grade bitumen (70/100) and polymer-modified bitumen. The bitumen samples are subjected to aging using the Braunschweig Aging (BSA) method, after which varying amounts of the rejuvenator are added. Using a Dynamic Shear Rheometer (DSR), under stress- controlled oscillation, master curves are generated to evaluate the performance of the rejuvenated bitumen under different aging conditions. In rheology and materials science, determining master curves is a crucial process, especially for describing the viscoelastic behaviour of materials over a large range of frequencies or temperatures. Master curves (Ren et al. 2023) are used to describe a material's complex modulus (G*) or other rheological characteristics as a function of a condensed time variable, enabling comparison and prediction of the behavior of the material under various circumstances. The main parameter of the test is the complex modulus, which refers to a fundamental rheological characteristic that describes the material's overall stiffness under dynamic conditions.

2 EXPERIMENTAL INVESTIGATION

2.1 *Sample nomenclature*

Two different types of bitumen were used in the test: conventional road bitumen 70/100 and a polymer-modified bitumen (PMB). Both unmodified and modified bitumen are produced from Total Bitumen Deutschland GmbH. The unmodified bitumen is referred to as AZALT 70/100 DE and Polymer modified bitumen is referred to as Styrelf 40/100-65A.

The sample used in this study is named as a combination of one alphabet followed by two numerical for the identification purpose. The first part of the name is an alphabet, indicate the type of bitumen in which A represents an unmodified binder and B as a modified binder. The second and third part of the name is a numerical which represents the aging state of bitumen and amount of rejuvenator added, respectively. Unaged bitumen is designated as 0, single aged bitumen is designated as 1 and double aged bitumen is designated as 2. In the case of rejuvenator content, bitumen with 0% rejuvenator is denoted as 0, 4% mass of rejuvenator based on test specimen is denoted as 1, 8% mass of rejuvenator based on test specimen is denoted as 2 and 12% mass of rejuvenator based on test specimen is denoted as 3. For example A01 represents unaged unmodified bitumen with 4% of rejuvenator and B12 represents single aged modified bitumen with 8% of rejuvenator.

2.2 *Sample preparation*

For unaged sample, 40g of bitumen is mixed with specified amount of rejuvenators before testing. In the case of single aged samples, 40g of bitumen is kept in oven maintained at a temperature of 85 °C for 96 hours and later the specified mass of rejuvenator is added to obtain the sample for testing. For long term or double aging of bitumen, Braunschweig method was used. Bitumen is subjected to aging at a temperature of 85 °C for 96 hours, two times. After the second aging, rejuvenators are added in the required quantity. A propeller mixing process is used to mix the rejuvenator with the bitumen samples. For ensuring the homogeneity and to maintain pouring temperature, rejuvenator is continuously stirred and tempered. In this study, the rejuvenator used is derived from a plant, to regain the properties of road bitumen 70/100 and polymer modified bitumen. Once the sample is mixed, these are shifted to silicon molds for resting and cooling period in accordance to DIN EN 14770. According to DIN EN 14770, for the unmodified bitumen of the 70/100 class, a minimum storage period of two hours is required and for polymer-modified bitumen, however, needs a minimum of 12 hours of storage time.

2.3 *Master Curve using DSR*

In this study, DSR with a parallel plate geometry having a diameter of 8 mm (PP8) and a gap setting of 2 mm is used. The sample undergoes oscillation in the stress-controlled mode, also known as the CS mode, at a temperature range from 60 °C to -10 °C under stress and strain control. The frequency is varied 16 times in the range of 0.1 Hz to 70 Hz, for each temperature step ($\Delta T = 10$ K) at a shear stress of 50 Pa.

3 RESULTS AND DISCUSSION

The analysis of the measurement data is carried out using Microsoft Excel and Matlab. The isotherms of the derived master curve can be shifted along the abscissa towards the frequency axis using the horizontal shift factor logαT.

3.1 *Master curves for unmodified 70/100 bitumen*

The baseline of the test is specimen A00 which is unaged, non-rejuvenated conventional unmodified bitumen 70/100. Figure 1, Figure 2, and Figure 3 shows the master curves for the unaged, single aged and double aged unmodified bitumen, respectively, with different rejuvenator content.
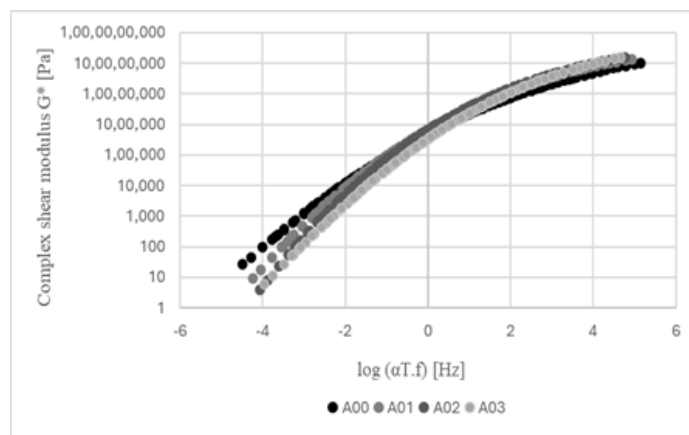
Figure1. Master curve for unmodified unaged bitumen
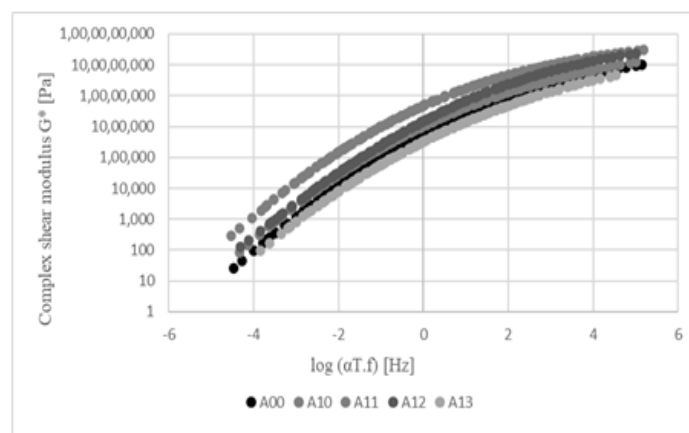
Figure 2. Master curve on single aged unmodified bitumen

In the case of unmodified unaged bitumen, in the low reduced frequency values, the baseline variant has higher complex shear modulus when compared to rejuvenated samples, but with increase in the values, the complex modulus of the rejuvenated samples is increased. In case of single aged bitumen, the samples A10 and A11 are shifted above the reference sample whereas the sample A13 shift below A00 and the sample A12 with 8% rejuvenator content shows more approach to the virgin bitumen sample A00.
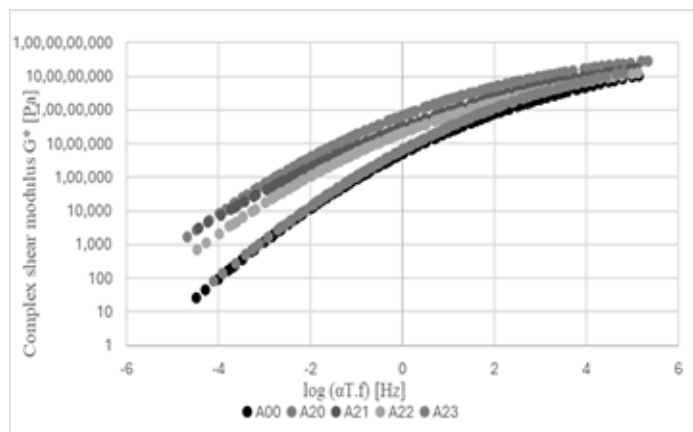
Figure 3. Master curve on double aged unmodified bitumen

For double aged variants, when compared to the unaged reference sample A00, there is a noticeable change in the aged variants' master curves and the deviation for the samples with double aging is big. However, by adding more rejuvenator, the sample almost reached the values of the baseline variant. Therefore, as the aging increases, a high amount of rejuvenation is required to bring down the complex shear moduli.

3.2 *Master curves for polymer modified bitumen*

The baseline of the test is the specimen B00 which is unaged, non-rejuvenated polymer modified bitumen. Figure 4, Figure 5, and Figure 6 shows the master curves for the unaged, single aged and double aged polymer modified bitumen, respectively, with different rejuvenator content.
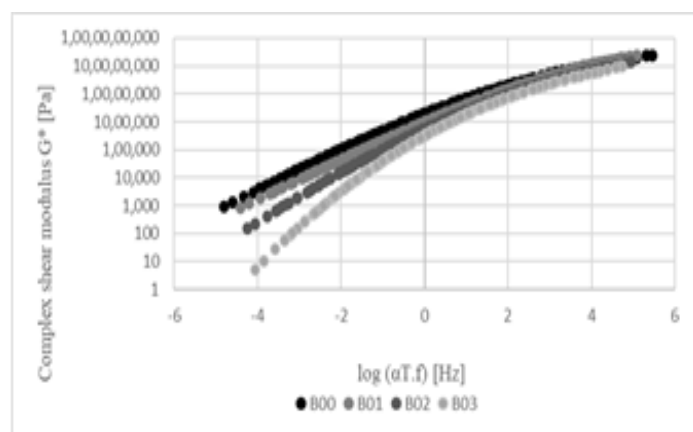
Figure 4. Master curve on unaged PMB

In the case of unaged PMB, the results show that all the variations shows an approach to the reference with increase in the reduced frequency values. However, the sample BO3 with most rejuvenation shows the lower complex shear modulus than other samples. For single aged bitumen, the variant without rejuvenation, B10, moves above the B00 reference curve and exhibits noticeably greater complex shear moduli. With the addition of 4% rejuvenator, the B11 curve is nearly equal to the B00 reference variation and corresponds to the ideal. Although the master curve B12 is similar to the B00 curve, it displays smaller complex shear moduli at low frequencies. With the addition of 12% rejuvenator, curve B13 exhibits the biggest shift. The sample B13 falls below the reference variant indicating that less rejuvenator may be needed to attain the measurement results of the sample B00. When compared to the unaged reference variety, there is a noticeable change in the aged variants' master curves, especially in the low frequency areas.
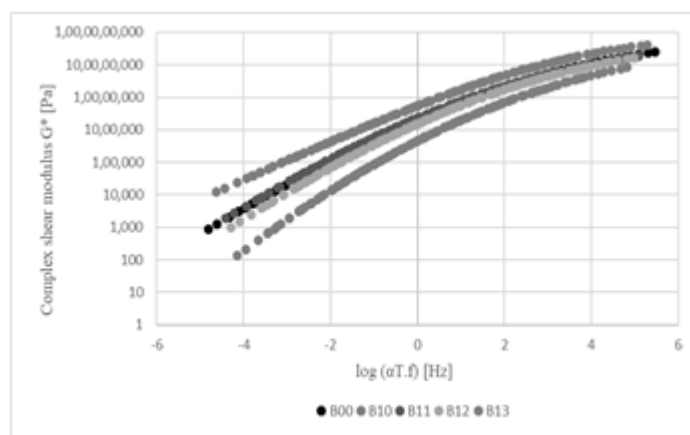
Figure 5. Master curve on single aged PMB
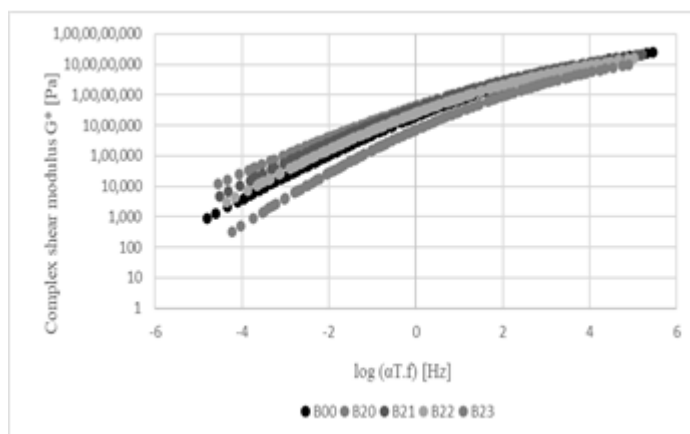
Figure 6. Master curve on double aged PMB

For double aged bitumen the complex shear moduli of variants B20 and B21, which underwent a shift above the reference curve, are noticeably greater. The measurements of the B00 master curve match the curve B22 almost exactly, even though there is a slight variation in the low frequency zone. However samples B20 and B21 also becomes ideal with B00 as the frequency increases. The least complex shear moduli are displayed on variant B23's curve and has

a noticeable down shift. This depicts the sample doesn't need 12% rejuvenation to regain the properties.

3.3 *Interpretation of Master Curves*

The impact of rejuvenation on the aging processes and the impact of aging on bitumen is taken into account in the examination of the master curves that are displayed. The aim of using a rejuvenator is to rejuvenate and improve the properties of aged bitumen, bringing it closer to the characteristics of virgin bitumen, with the potential for enhancing its overall performance. When complex moduli increase for a bitumen, the flexibility of bitumen decreases and its capacity to absorb and dissipate energy decreases. This makes it more vulnerable to cracking. The bitumen samples without rejuvenation, but with aging and also the samples treated with rejuvenator show a shift in relation to the reference variants. The deviation from the reference is more for polymer modified bitumen than for conventional road bitumen. However, both aged variations strongly differ from the unaged sample in the low-frequency band but gradually converge as the frequency rises. When compared to the two reference versions, the unaged but modified variants show a move towards lower complex shear moduli. But with increase in frequency, it moves above reference for variant A and it becomes ideal to reference for variant B. The increase in complex moduli with increase in reduced frequency is due to the dominancy of elastic behavior over viscous behavior and vice versa. In the low reduced frequency values (<1), the baseline variant has higher complex shear modulus when compared to rejuvenated samples. However, with the high reduced frequency values (>1), the complex modulus of the rejuvenated samples is shifted. This implies the rejuvenation has improved the mechanical properties of bitumen.

4 CONCLUSION

This investigation was carried out to check the effect of a plant derived rejuvenator on the rheological properties of bitumen and how it could reduce the effects of aging. Specimens were made using BSA aging and with different amount of rejuvenators varying from 0 to 12% for polymer modified and unmodified bitumen. Tests were done using DSR and results were obtained and compared. Bitumen undergo deterioration and change in its properties due to aging. Polymer modified bitumen shows more evident results when compared to conventional road bitumen. The polymer modified bitumen is modified with certain additives that enhances its performance and hence has higher complex shear modulus compared to conventional road bitumen. The increase

and decrease in the values of complex shear modulus always provides merits and demerits. Bitumen with high complex shear modulus is more useful in cold areas as it can withstand rutting during freezing conditions due to its high stiffness. In terms of fatigue behavior and rutting, the bitumen characteristics improved with increase in the complex moduli. However, increased stiffness would lead to reduced flexibility which can lead to distress. The use of rejuvenators can reduce the high dependency on virgin bitumen. Aged bitumen can be reclaimed with a rejuvenator, but the amount depends totally on what extend the material is aged. It is also evident that the rejuvenator enhances the bitumen's rheological characteristics but cannot stop the aging process from occurring. In conclusion, it has been established that rejuvenator addition and BSA aging both affect the rheological characteristics of bitumen.

REFERENCES

Airey, G. D. 2011. Factors affecting the rheology of polymer modified bitumen (PMB). *In Polymer modified bitumen*: 238-263. Woodhead Publishing.

Dhasmana, H., Hossain, K. & Karakas, A.S. 2021. Effect of long-term ageing on the rheological properties of rejuvenated asphalt binder. *Road Materials and Pavement Design* 22(6): 1268–1286.

Elkashef, M., Elwardany, M.D., Liang, Y., Jones, D., Harvey, J., Bolton, N.D. & Planche, J.P. 2020. Effect of using rejuvenators on the chemical, thermal, and rheological properties of asphalt binders. Energy & Fuels 34(2): 2152–2159.

Haghshenas, H.F., Kim, Y.R., Kommidi, S.R., Nguyen, D., Haghshenas, D.F. & Morton, M.D. 2018. Evaluation of long-term effects of rejuvenation on reclaimed binder properties based on chemical and rheological tests and analyses. *Materials and Structures* 51: 1–13.

Karki, P. & Zhou, F. 2016. Effect of rejuvenators on rheological, chemical, and aging properties of asphalt binders containing recycled binders. *Transportation Research Record* 2574(1): 74–82.

Ongel, A. & Hugener, M. 2015. Impact of rejuvenators on aging properties of bitumen. *Construction and Building Materials* 94: 467–474.

Rathore, M., Haritonovs, V., Meri, R.M. & Zaumanis, M. 2022. Rheological and chemical evaluation of aging in 100% reclaimed asphalt mixtures containing rejuvenators. Construction and Building Materials 318: 126026.

Ren, S., Liu, X., Varveri, A., Khalighi, S., Jing, R., & Erkens, S. 2023. Aging and rejuvenation effects on the rheological response and chemical parameters of bitumen. *Journal of materials research and technology*. 25: 1289-1313.

Schwettmann, K., Nytus, N., Radenberg, M., & Stephan, D. 2023. Bitumen reuse: Physical and chemical approach to investigate the effectiveness of rejuvenators. Road Materials and Pavement Design 24(4): 1130-1157.

Sengoz, B., & Oylumluoglu, J. 2013. Utilization of recycled asphalt concrete with different warm mix asphalt additives prepared with different penetration grades bitumen. Construction and Building Materials 45: 173-183.

Zhang, J., Sun, C., Li, P., Jiang, H., Liang, M., Yao, Z., Zhang, X. & Airey, G. 2020. Effect of different viscous rejuvenators on chemical and mechanical behavior of aged and recovered bitumen from RAP. Construction and Building Materials 239: 117755.

Assessing the Influence of Stress Levels on the Creep and Recovery Behavior of LDPE-Modified Bitumen

Aakash Singh[1], Ankit Gupta[2]

[1]Research Scholar, Department of civil engineering, Indian Institute of Technology (BHU), Varanasi, India-221005, aakashsingh.rs.civ21@iitbhu.ac.in, ORCID Id: 0000-0002-2014-7064

[2]Associate Professor, Department of civil engineering, Indian Institute of Technology (BHU), Varanasi, India-221005, ankit.civ@iitbhu.ac.in, ORCID Id: 0000-0003-1789-9502

ABSTRACT: This study analyses the influence of stress levels and rest periods on the creep and recovery behaviour of plastic-modified (LDPE) bitumen. The modified bitumen is prepared by incorporating varying proportions of LDPE and sulphur. Non-standard multiple stress creep and recovery (MSCR) tests are conducted at a controlled temperature of 70°C to evaluate non-recoverable creep compliance (J_{nr}) and percentage recovery (R). The findings reveal that the addition of plastic significantly enhances the resistance to permanent deformation of the bitumen. Furthermore, viscoelastic behaviour of bitumen improves with an increase in plastic content, as characterized by R. The stiffness of the bitumen increases with the addition of plastic, with R initially increasing up to an optimal plastic content (i.e., 4.5%) and then reducing with increment in plastic content. These findings offer valuable insights for the development of resilient and high-performing bituminous pavements.

1 INTRODUCTION

Polymer modification of bitumen has gained significant global attention due to its ability to enhance bitumen's performance. Elastomeric polymers, such as styrene-butadiene-styrene (SBS), are particularly effective, improving rutting resistance, cracking performance, durability, and reducing aging susceptibility. However, the high cost and limited availability of virgin polymers often discourage widespread adoption, especially in developing countries like India (García Mainieri et al., 2024). Waste and recycled plastics have emerged as a cost-effective and environmentally sustainable alternative, addressing both economic constraints and plastic waste management challenges. Among these, low-density polyethylene (LDPE), a major type of waste plastics, preferred due to its high production volume and limited recycling potential (Singh & Gupta, 2024a).

Recycled LDPE, when mixed and dispersed in micronized form under optimized conditions, can significantly influence the rheological properties of bitumen. However the compatibility between LDPE and bitumen is a concern, this has been addressed by the researchers with the use of compatibilizers and crosslinkers such as maleic anhydride and sulfur, with sulfur being widely preferred for its availability and ability to improve storage stability. Polymer-modified bitumen (PMB) typically forms a biphasic system, where stress levels govern its linear and non-linear viscoelastic behavior. PMB's shows delayed elastic response and stress dependent behaviour. This stress-dependent behavior, influenced by polymer type, content, and modification process. This behaviour becomes pronounced at higher temperatures (Polacco et al., 2015). Additionally, it has been reported that the polymers yield under higher stress levels thus higher stress levels better characterize the performance of PMB's (Behnood & Olek, 2017a). The Multiple Stress Creep and Recovery (MSCR) test is extensively used to evaluate PMB's resistance to permanent deformation under stress conditions that simulate in-service performance (Stempihar et al., 2017).

This experimental research study primarily focusses on assessing the high temperature permanent deformation and viscoelastic response of LDPE modified bitumen when subjected to higher stress levels. As per the best of authors knowledge none of the research studies have evaluated the response of LDPE modified bitumen under such conditions. This study aims to fill a critical knowledge gap, offering new insights into the stress-dependent viscoelastic behavior of LDPE-modified bitumen, which is essential for optimizing its use in high temperature domain.

2 MATERIALS AND EXPERIMENTAL PROGRAM

2.1 Materials

Present study used a viscosity-graded (VG 30) bitumen as a virgin bitumen with an absolute viscosity ranging from 2400 – 3600 poises. The bitumen was modified using low-density polyethylene (LDPE) plastic as modifier and sulfur as a crosslinker. Waste LDPE was obtained from local recycler in pellets form, and the elemental sulfur was procured from industry with 98% purity. The weight fractions of combined modifiers were set at 75% LDPE and 25% sulfur; the combination of both is referred to as plastic modifier or simply the modifier throughout this

study. The bitumen was modified with varying weight fractions of the modifiers, namely 0%, 1.5%, 3%, 4.5%, 6%, and 7.5%. The base bitumen and modified bitumen produced were labelled as B - 0 and B - xx, respectively, where xx indicates the weight fraction of modifier. For instance, B - 1.5 represents the base bitumen modified with a 1.5% modifier. To check the phase separation of modified bitumen prepared, this study followed the standard IS 15462 – 2019 for storage stability test of the modified bitumen. The ratio of LDPE and sulfur was optimized in lab and all the modified bitumen with different proportions of LDPE and sulfur used in this study was found to be storage stable and higher proportions than 7.5% were unstable. Table 1 illustrates the index properties of base bitumen and modified bitumen. In this study, sulfur was used to improve the storage stability of modified bitumen. From the previous literature, sulfur is among the most favourable compatibilizers that crosslinks the bitumen and polymers. The detailed description on the bitumen modification has not been discussed here but can be found in other literature (Singh et al., 2023; Singh & Gupta, 2024a, 2024b).

Table 1 Basic properties of modified and unmodified bitumen

Bitumen with modifications	Properties of bitumen			
	Penetration (dmm)	Softening point (°C)	Performance grade (High temperature) (°C)	Failure temperature (°C)
B – 0	65	48.5	64	65.4
B – 1.5	51	59	82	82.7
B – 3	48	63	82	84.4
B – 4.5	41	66	88	88.1
B – 6	39	68	88	89.6
B – 7.5	32	74	94	95.9

2.2 Experimental program

The MSCR test was performed on short-term aged bitumen, both modified and unmodified bitumen were aged using the universal simple aging test (USAT) procedure (Farrar et al., 2014). This research focuses on conducting the MSCR tests under controlled conditions at a temperature of 70 °C. The rationale for choosing this specific temperature is to cover the highest in-service temperature observed in the Indian environment and ensure that the material's behavior is studied within non-linear domain with practical relevance. During the MSCR test, four distinct stress levels were applied: 0.1, 3.2, 6.4, and 12.8 kPa. These stress levels were selected to encompass a wide range of loading scenarios, providing valuable insights into the material's response under various conditions. Stress higher than 12.8 kPa was not selected because except B-7.5 all other bi-

tumen was spilled out during testing, which reports erroneous results. Also, stress levels equal to or higher than 15 kPa is not recommended in the literatures (Stempihar et al., 2017). To avoid any potential carry-over effects and ensure the accuracy of results, each combination of stress levels was necessitated using separate samples. The testing protocol was similar to standard MSCR test, only different stress levels were used.

3 RESULTS AND DISCUSSION

The MSCR test results were analysed using J_{nr} and R parameters. Figure 1 illustrates the variation of the J_{nr} parameter with stress level for both modified and unmodified bitumen. Among the modified bitumen samples, B - 4.5 exhibits the highest recovery and the lowest J_{nr} values at higher stress levels, indicating its superior resistance to permanent deformation at non-linear stress levels. The modification of bitumen with plastics leads to a reduction in stress sensitivity. For B - 0 bitumen, an increase in stress level up to 3.2 kPa increases the slope in the J_{nr} vs. stress level, indicating a higher stress-sensitive bitumen. However, beyond a stress level of 6.4 kPa, the B - 0 bitumen shows a remarkable increase in stress sensitivity, accompanied by an increase in the J_{nr} value. This phenomenon can be attributed to a 100% increase in applied stress, which leads to an increase in accumulated strain by 36% and a consequent 113% increase in J_{nr} value. This jump in J_{nr} was primarily due to the non-recoverable deformation. The sudden increase in $J_{nr\text{-}slope}$ beyond stress level of 6.4 kPa shows the yielding of polymer network present in the LDPE modified bitumen and in unmodified bitumen this can be attributed to relatively large deformations resulted from increment of stress level at very high temperature (higher than PG of bitumen).

Among the various modified bitumen samples, B - 4.5 exhibited lowest J_{nr} value. The $J_{nr\text{-}slope}$ of B - 6 is the smallest compared to other modified bitumen samples. These findings suggest that modified bitumen have reduced stress sensitivity, leading to improved resistance against permanent deformation. The observed reduction in J_{nr} values in modified bitumen can be attributed to the incorporation of plastic. Plastic within the bitumen enables it to stretch when subjected to load, thus contributing to its improved ability to withstand deformation (Joohari & Giustozzi, 2020). The increment in plastic content beyond 4.5% is associated with an increase in both J_{nr} values and stress sensitivity of the bitumen. Since, both B - 6 and B - 7.5 fall within the category of highly polymer-modified bitumen. Under the in-

fluence of oscillatory loading, the plastic phase becomes the dominant phase. As the applied stress level increases, the polymer networks entangles and break, which can be observed by the increase in deformation, resulting in higher J_{nr} values. Furthermore, with increased stress levels, the mobility of these polymer particles within the bitumen matrix also increases, contributing to the overall increased stress sensitivity.
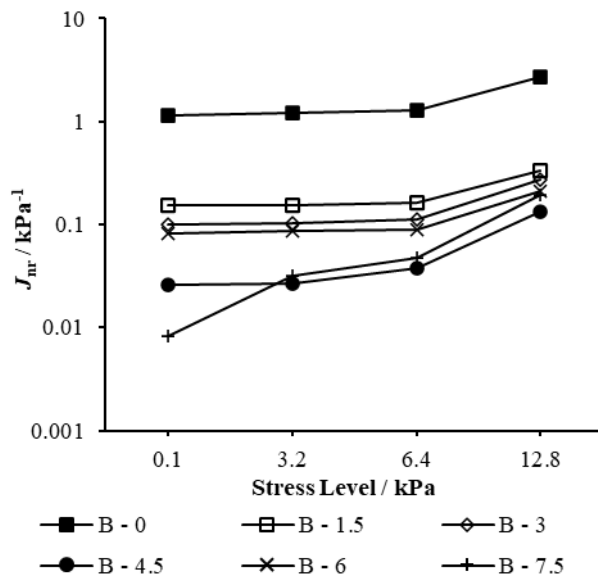
Figure 1 J_{nr} calculated from MSCR test

The viscoelastic behavior of bitumen was evaluated by plotting percentage recovery (R) versus the stress level. Recovery was calculated for each cycle, and the average recovery of ten cycles was reported for each stress level. Figure 2 illustrates the average R value of both modified and unmodified bitumen over the different stress levels. It was clearly observed that addition of plastic improves the recovery of bitumen, regardless of stress level. However, the elastic recovery of bitumen varies among the different modified bitumen samples. Moreover, a consistent result was observed: as stress level increases, the recovery of bitumen decreases, irrespective of the modifier content. Upon increasing the stress level from 0.1 kPa to 3.2 kPa, the highest decrease in R-value was observed in B - 7.5. Although the slope of R versus stress level curve decreases, the reduction in R values with incremental stress levels remains consistent. B - 3 and B - 6 show nearly similar R values, while B - 4.5 exhibited the highest R values at higher stress levels (3.2 kPa and above). The decrease in slope of recovery versus stress level was more pronounced in case of modified bitumen, with the highest slope observed for B - 7.5. At a stress level of 0.1 kPa, the observed elastic recovery was highest, indicating that the polymer network present in modified bitumen due to the addition of waste plastic.

From Figure 2, the negative recovery at higher stress levels was observed; Behnood & Olek, (2017b) attributed negative recovery to the inability of rheometers to remove load instantly. Liu et al., (2020) associated negative recovery with accumulated strain that had not recovered during the previous cycle's rest period. Conversely, Jafari et al. (2015) linked the negative recovery to very high strain values resulting from the application of high stresses, causing bitumen to flow from the parallel plates of rheometer. In this study, the unmodified bitumen shows negative recovery even at 0.1 kPa stress level because the sample's integrity was not preserved at 70 °C. The test temperature significantly exceeded the softening point (48 °C) and the high-temperature performance grade (PG 64). Consequently, upon applying the load, the sample might have flowed out of the plates, leading to higher deformations and negative recovery. For modified bitumen, negative recovery was observed beyond the stress level of 6.4 kPa. B - 1.5 specifically exhibited negative recovery due to the inertia of instrument, due to the limitation of rheometer from instantaneously removing load at the end of creep cycle.
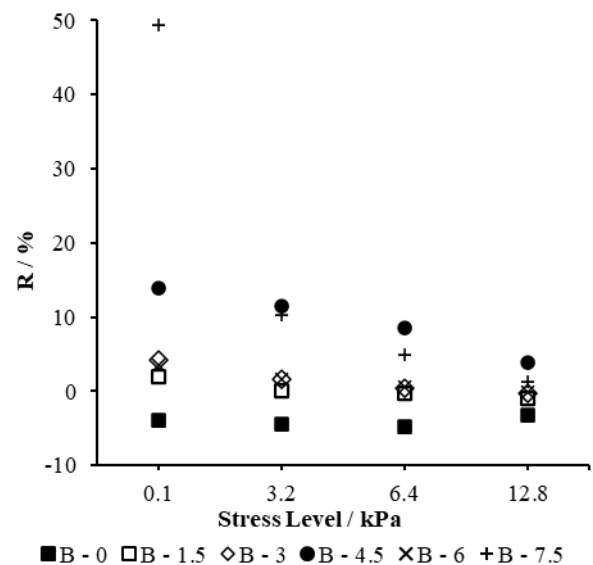
Figure 2 J_{nr} calculated from MSCR test

4 CONCLUSIONS AND FUTURE SCOPE OF RESEARCH

In this study, viscosity-graded base bitumen (VG 30) was modified with LDPE plastics to evaluate its resistance to permanent deformation. The experimental findings demonstrate that plastic-modified bitumen exhibits lower J_{nr} values and higher R values compared to unmodified bitumen, indicating superior resistance to permanent deformation. Notably, bitumen samples with similar performance grades can exhibit significant variations in J_{nr} and R values,

highlighting the influence of plastic modification on performance. The study also reveals that plastic modification enhances the stress sensitivity of bitumen, as evidenced by a reduced J_{nr} -slope. Furthermore, the viscoelastic behavior of the bitumen improves with plastic modification, as reflected in increased R values. These improvements in J_{nr} and R values are particularly pronounced at higher plastic content levels, emphasizing the potential of LDPE modification to enhance the high-temperature performance of bitumen.

The conclusions presented in this paper are based on the outcomes of MSCR test conducted during this research study. Ideally, the findings from bitumen test should be corroborated with those from bituminous mixtures and field test sections. Future research needs to gather more data from the field and the rutting evaluation of bituminous mixtures made with these plastic-modified bitumen. This additional data will be instrumental in proposing a comprehensive MSCR testing protocol for plastic-modified bitumen.

5 REFERENCES

Behnood, A., & Olek, J. (2017a). Rheological properties of asphalt binders modified with styrene-butadiene-styrene (SBS), ground tire rubber (GTR), or polyphosphoric acid (PPA). *Construction and Building Materials*, *151*, 464–478. https://doi.org/10.1016/J.CONBUILDMAT.2017.06.115

Behnood, A., & Olek, J. (2017b). Stress-dependent behavior and rutting resistance of modified asphalt binders: An MSCR approach. *Construction and Building Materials*, *157*, 635–646. https://doi.org/10.1016/J.CONBUILDMAT.2017.09.138

Farrar, M. J., Planche, J.-P., Grimes, R. W., & Qin, Q. (2014). The Universal Simple Aging Test (USAT): Simulating short- and long term hot and warm mix oxidative aging in the laboratory. In R. Y. Kim (Ed.), *Asphalt Pavements* (1st ed., Vol. 1, pp. 103–112). CRC Press. https://doi.org/10.1201/B17219-18

García Mainieri, J. J., Al-Qadi, I. L., & Ghabchi, R. (2024). Effects of waste high-density polyethylene (HDPE) on asphalt binder and airfield mixes. *International Journal of Pavement Engineering*, *25*(1). https://doi.org/10.1080/10298436.2024.2303661

Jafari, M., Babazadeh, A., & Aflaki, S. (2015). Effects of Stress Levels on Creep and Recovery Behavior of Modified Asphalt Binders with the Same Continuous Performance Grades. *Transportation Research Record: Journal of the Transportation Research Board*, *2505*, 15–23. https://doi.org/10.3141/2505-03

Joohari, I. B., & Giustozzi, F. (2020). Chemical and high-temperature rheological properties of recycled plastics-polymer modified hybrid bitumen. *Journal of Cleaner Production*, *276*, 123064. https://doi.org/10.1016/J.JCLEPRO.2020.123064

Liu, J., Asce, S. M., Liu, J., Asce, M., Zhu, ; Anyou, & Saboundjian, S. (2020). Evaluation of Multiple Stress-Creep Recovery Test on Alaskan Asphalt Binders. *Journal of Materials in Civil Engineering*, *32*(10), 04020302. https://doi.org/10.1061/(ASCE)MT.1943-5533.0003337

Polacco, G., Filippi, S., Merusi, F., & Stastna, G. (2015). A review of the fundamentals of polymer-modified asphalts: Asphalt/polymer interactions and principles of compatibility. *Advances in Colloid and Interface Science*, *224*, 72–112. https://doi.org/10.1016/J.CIS.2015.07.010

Singh, A., & Gupta, A. (2024a). Effect of Variability in Sources of Low-Density Polyethylene on the Intermediate Temperature Fatigue Performance of Modified Bitumen. *Lecture Notes in Civil Engineering*, *523* LNCE, 489–497. https://doi.org/10.1007/978-3-031-63584-7_47

Singh, A., & Gupta, A. (2024b). Mechanical and economical feasibility of LDPE Waste-modified asphalt mixtures: pathway to sustainable road construction. *Scientific Reports 2024 14:1*, *14*(1), 1–18. https://doi.org/10.1038/s41598-024-75196-5

Singh, A., Gupta, A., & Miljković, M. (2023). Intermediate- and high-temperature damage of bitumen modified by HDPE from various sources. *Road Materials and Pavement Design*, 1–14. https://doi.org/10.1080/14680629.2023.2181017

Stempihar, J., Akshay Gundla, ;, Underwood, B. S., & Asce, A. M. (2017). Interpreting Stress Sensitivity in the Multiple Stress Creep and Recovery Test. *Journal of Materials in Civil Engineering*, *30*(2), 04017283. https://doi.org/10.1061/(ASCE)MT.1943-5533.0002153

Aging and moisture effect of asphalt binder on adhesion properties

Zheng Wang
Rutgers University, Piscataway, NJ, USA, 08854

Bingyan Cui
Rutgers University, Piscataway, NJ, USA, 08854

Hao Wang
Corresponding author, Email: hwang.cee@rutgers.edu
Rutgers University, Piscataway, NJ, USA, 08854

ABSTRACT: This study explores the effects of oxidative aging and moisture on adhesion properties of asphalt binders using atomic force microscopy (AFM) tests and molecular dynamics (MD) simulations. The results Long-term aging substantially reduces asphalt binder adhesion at both dry and wet conditions, weakening asphalt-aggregate bonding. Asphalt binder after longer time of water immersion exacerbates the reduction in adhesion, with aged asphalt experiencing more pronounced decrease compared to asphalt. MD simulations and AFM tests show consistent trends of aging effect. However, the asphalt model with diffused water shows limitations in fully capturing the effect of moisture content on adhesion

1. INTRODUCTION

Asphalt pavements are continuously subjected to traffic loads and environmental factors, resulting in progressive degradation of field performance. Distresses such as potholes, stripping, and cracking are exacerbated by using reclaimed asphalt pavement (RAP) content, which lowers the resistance of asphalt to moisture-induced damage (Aguiar-Moya et al. 2015). Moisture-induced damage, primarily due to adhesion loss between asphalt and aggregate caused by aging and water intrusion, remains a critical challenge. To address this issue, it is crucial to understand the complex effects of aging and moisture on asphalt-aggregate adhesion properties.

Numerous studies have highlighted that molecular compositions and physical structures of asphalt binders influence asphalt-aggregate adhesion performance. Theories of interfacial adhesion include mechanical interlocking, chemical bonding, and surface energy compatibility (Tan & Guo, 2013). Advances in experimental and simulation methods, such as atomic force microscopy (AFM) and molecular dynamics (MD) simulations have enabled detailed analysis of adhesion forces at the micro- and nanoscale levels. AFM offers high-resolution measurement of adhesive forces (Yu et al. 2013), while MD simulations provide insights into molecular-level interactions that govern adhesion strength (Xu & Wang 2016).

Despite these advances, gaps remain in correlating experimental and simulation data to comprehensively understand the impact of asphalt aging and moisture effect on adhesion properties. This study aims to evaluate adhesion properties of asphalt-aggregate interfaces under varying conditions of aging and moisture. Combining MD simulations and AFM experiments, this study aims to provide comprehensive understanding of adhesion behavior with the following objectives:

- Investigate the relationship between asphalt adhesion properties obtained through MD simulations and AFM tests.
- Examine the effects of oxidative aging and moisture content on adhesion properties at the asphalt–aggregate interface.

2. ASPHALT BINDER AND AFM TESTS

The virgin asphalt binder used for this study was PG64-22. The aged asphalt binder samples were prepared using 40-hr pressure aging vessel (PAV) in accordance with ASTM D6521, which represents long-term aging behavior.

Atomic Force Microscopy (AFM) was used to measure adhesive forces between the silicon tip and asphalt binder at the nanoscale. Customized containers with a diameter of 10 mm and a thickness of 2.5 mm were employed to ensure uniform sample flatness and thickness. Asphalt binders were poured into these containers, annealed at 110°C for 10 minutes to achieve a flat surface, and then cooled in a glass box at 25°C for 24 hours before testing.

To evaluate moisture effects on adhesion properties, AFM tests were performed on asphalt samples after water immersion. Following established methods (dos Santos et al., 2014; Hung et al., 2017), the samples were annealed, cooled at room temperature for 24 hours, and then immersed in deionized water for 4 and 24 hours. After immersion, the samples were dried with a nitrogen gun at room temperature and prepared for testing.

Micromechanical properties were assessed using the peak force tapping quantitative nanomechanical (PFT-QNM) mode of a Bruker Dimension Icon AFM, with a scanning area of 20μm × 20μm. Considering that the Young's modulus of most asphalt is less than 2GPa (Gong et al., 2017), an RTESPA-150 silicon tip with medium stiffness was used to obtain Force-Separation curves. Adhesive force, as shown in Figure 1, was calculated as the difference between the baseline and the lowest point of the retracting curve. Using the PFT-QNM mode, force-separation curves for all test points (512 × 512) were collected, and the overall adhesive force was determined as the average value across all data points.
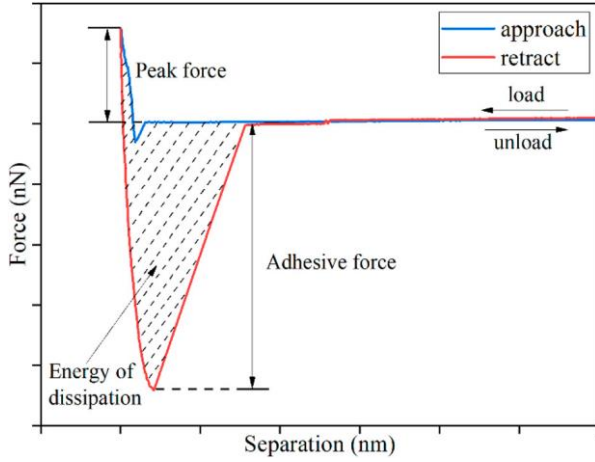
Figure 1. The Force-Separation Curve Measured with AFM.

The work of adhesion (W_{ad}) between asphalt and silicon, a critical indicator of the resistance of asphalt-aggregate interfaces to adhesive failure, was calculated with the adhesion force based on the Johnson, Kendall, and Roberts (JKR) model, as expressed in Equation (1) (Leite et al., 2012).

$$W_{ad} = 2F_{ad}/3\pi R \qquad (1)$$

where, F_{ad} is the adhesive force between the sample and AFM tip; R is the equivalent radius of AFM tip.

3. MOLECULAR DYNAMICS SIMULATTION

3.1 Average Molecular Model of Asphalt

The 4-component average molecular models were utilized to simulate the asphalt binders tested in the AFM experiment. The molecular model for virgin binder was derived based on element analysis, nuclear magnetic resonance (NMR), and gel-permeation chromatography (GPC) tests. For the 40-hour PAV-aged binder, the molecular model was developed based on Fourier transform infrared spectroscopy (FTIR) measurements and validated with ReaxFF molecular dynamics (MD) simulations. More details on the derivation and validation of molecular models can be found in the authors' previous work (Cui & Wang, 2023).

The number of molecules within each SARA fraction was determined for virgin and aged binders, as

shown in Table 1 and 2. The results indicate that the asphalt model accurately captures the SARA fraction, with deviations of less than 0.6%.

Table 1 Molecular compositions of virgin asphalt binder

Component	Saturate	Aromatics	Resin	Asphaltene
Formula	$C_{37}H_{72}$	$C_{41}H_{60}S$	$C_{44}H_{59}NOS$	$C_{62}H_{63}NO_2S_2$
Molecule Mass	517	585	650	918
No of Molecules	7	31	17	5
Modeled Proportion	9.7%	48.5%	29.5%	12.3%
Measured Proportion	10%	48%	30%	12%

Table 2 Molecular compositions of 40-hr PAV aged asphalt binder

Component	Saturate	Aromatics	Resin	Asphaltene
Formula	$C_{37}H_{72}$	$C_{41}H_{60}OS$	$C_{44}H_{56}NO_3S$	$C_{62}H_{64}NO_7S_2$
Molecule Mass	517	601	679	989
No of Molecules	7	27	19	7
Modeled Proportion	9.1%	40.9%	32.5%	17.5%
Measured Proportion	9.3%	40.9%	32.2%	17.6%

3.2 Asphalt-Aggregate Interface Models

Molecular dynamics (MD) simulations were performed using the CVFF force field in Materials Studio to calculate interaction energies and work of adhesion under both dry and wet conditions. The simulation system included models of asphalt binders and silica (SiO_2) surfaces, which replicate the mineral composition of basalt and granite aggregates. Additionally, since the AFM tip used in experiments was made of silicon, an interface model featuring silicon was constructed to validate MD simulation results against AFM test data.

To create aggregate surface, the crystal unit cell of SiO_2 was cleaved along the (0,0,1) plane to form a mineral surface with a thickness exceeding the cutoff distance. The confined layers of asphalt and aggregate were then constructed to generate the asphalt-aggregate interface model by attaching the asphalt layer to the aggregate layer, as shown in Figure 2.

Once the models were constructed, simulations were performed at 298K to achieve the equilibrium state under natural conditions. The equilibrium process was carried out in two steps:

1. Canonical Ensemble (NVT): The first simulation step utilized the canonical ensemble, maintaining a constant number of atoms, volume, and temperature for 700 ps.
2. Isothermal-Isobaric Ensemble (NPT): Following this, the isothermal-isobaric ensemble was employed to maintain a constant number of atoms, pressure, and temperature for an additional 700 ps.
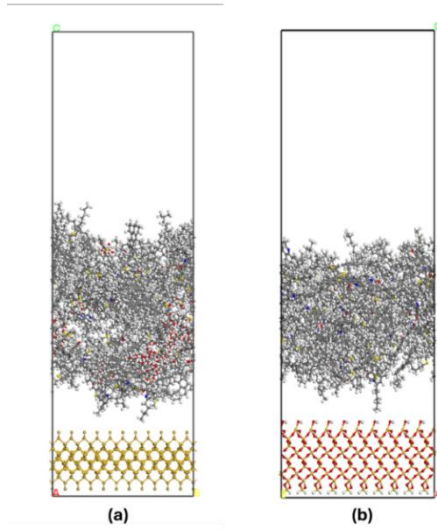
Figure 2. Molecular Dynamic Models for (a) Asphalt-Silicon Tip and (b) Asphalt-Aggregate Interface

The equilibrium state of the model was achieved, as shown in Figure 3. During the simulations, a time step of 1 fs, Van der Waals interactions and atom-based summation method with a cutoff distance of 15.5 Å was applied, ensuring accuracy and consistency throughout the process.

Moisture diffusion in asphalt cluster can be described using the complex water transportation kinetic process, where the diffusion of water varies with relative humidity, temperature, asphalt binder properties, and time (Ma, 2024). The moisture content within asphalt was measured through Gravimetric testing. At 25°C, under conditions of 100% relative humidity or immersion in liquid water, experimental studies indicated that the maximum moisture absorption rate of asphalt is approximately 6% to 7% (Nguyen et al. 1992; Chen et al. 2022). In this study, moisture was assumed to be present within the asphalt with random distribution of water molecules to simulate wet conditioned asphalt in the experiment.

3.3 Calculation of Work of Adhesion in MD

The primary interactions between asphalt binder and aggregate include van der Waals forces, electrostatic interactions, and hydrogen bonds. Molecular dynamics (MD) simulations provide a powerful method for calculating energy changes, offering detailed insights into adhesion properties.

The work of adhesion is defined as the energy required to separate asphalt from aggregate surface (Bhasin et al., 2007), which is calculated using the interaction energy between asphalt and aggregate, as shown in Equation 2. A higher magnitude of W_{ad} indicates stronger bond strength and greater resistance to adhesive failure (Moraes et al., 2017).

$$W_{ad} = \Delta E_{\text{interface}}/A = (E_{total} - E_a - E_{agg})/A \quad (2)$$

Where, W_{ad} represents the work of adhesion, $\Delta E_{\text{interface}}$ is the interfacial energy between asphalt binder and aggregate, E_{total} is the total potential energy of the asphalt-aggregate system, E_a is the potential energy of the asphalt binder, E_{agg} is the potential energy of the aggregate, and A is the contact area of the interface.

4. RESULLT AND DISCUSSION

Figure 3 presents the work of adhesion between asphalt binder and silicon for virgin and aged binder. The results indicate that after 40 hours of PAV aging, the work of adhesion at dry condition significantly decreases from both AFM measurements and MD simulation. However, the MD results are greater than the one from AFM measurements although at the same scale. It is found that MD results are affected by the model size and further analysis is needed to find the representative model size.

From AFM test results, the virgin binder consistently exhibits higher work of adhesion than the aged binder at wet conditions, indicating that oxidative aging degrades adhesion. The degradation is particularly evident under 24-hour immersion, where the adhesion of aged binder shows sharper decline as compared to the one of virgin binder. This suggests that oxidative aging exacerbates the detrimental effects of moisture on adhesion.
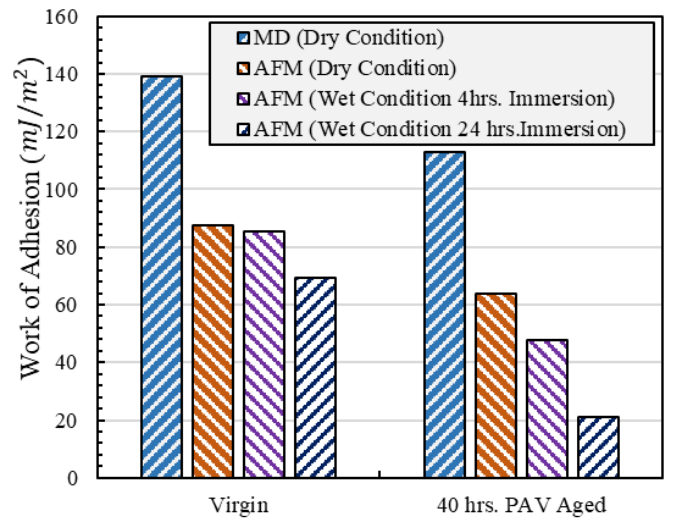
Figure 3. Comparison of the work of adhesion of asphalt-silicon tip interface from MD simulation and AFM tests.

Figure 4 shows the work of adhesion of asphalt-aggregate interface from MD simulations. Like the asphalt-silicon interface results from FM tests, virgin asphalt consistently exhibits higher work of adhesion than the aged asphalt at both dry and wet conditions. While the adhesion decreases with the increased moisture content, a sharp decline is not observed in the results from MD simulations. This indicates that while MD simulations effectively capture the degradation in adhesion properties due to aging, the current asphalt model with diffused water molecules face limitations in fully representing the combined effects of aging and moisture.
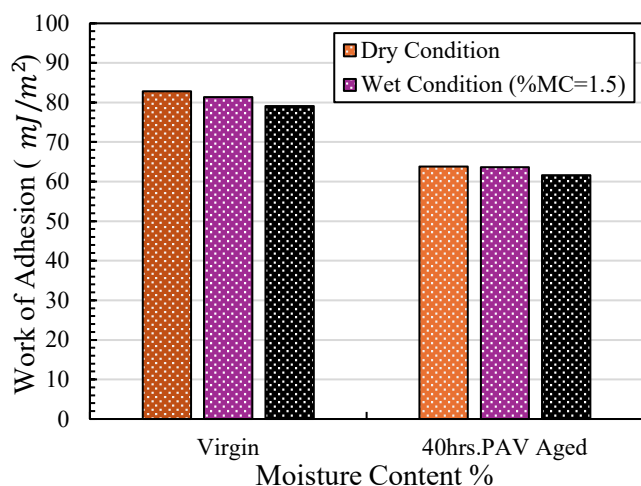
Figure 4. The work of adhesion of asphalt-aggregate interface at different aging levels and moisture contents from MD simulations

5. CONCLUSIONS

This study investigates the effects of aging and moisture on adhesion properties of asphalt binders. Measurements from AFM tests were utilized to evaluate the reliability of MD simulations for asphalt-silicon interaction. Subsequently, the work of adhesion at asphalt-aggregate interface was analyzed under dry and wet conditions. The following conclusions can be drawn:

- MD simulations and AFM tests show consistent trends, confirming MD as a reliable tool for assessing moisture and aging effects.
- Long-term aging substantially reduces asphalt binder adhesion at both dry and wet conditions, weakening asphalt-aggregate bonding.
- Asphalt binder after longer time of water immersion exacerbates the reduction in adhesion, with aged asphalt experiencing more pronounced decrease compared to asphalt.
- MD simulations using the asphalt model with diffused water show limitations in fully capturing the effect of moisture content on adhesion.

Further investigation is needed to explore the combined effect of aging and moisture effect on adhesion properties of asphalt binder. MD simulation models need be improved to provide deeper insights into asphalt-aggregate interactions under real-world conditions.

6. REFERENCES

Aguiar-Moya, J. P. et al. 2015. Effect of aging on adhesion properties of asphalt mixtures with the use of bitumen bond strength and surface energy measurement tests. *Transportation Research Record, 2505(1), 57–65.*

Bhasin, A., Little, D. N., Vasconcelos, K. L., & Masad, E. (2007). Surface free energy to identify moisture sensitivity of materials for asphalt mixes. *Transportation Research Record, 2001*(1), 37–45.

Chen, G., et al. (2022). Diffusion of moisture and oxygen in bitumens using electrochemical impedance spectroscopy. Fuel, 315, 123212.

Cui, B., & Wang, H. (2023). Oxidative aging mechanism of asphalt binder using experiment-derived average molecular model and ReaxFF molecular dynamics simulation. *Fuel, 331, 125678.*

dos Santos, S., Partl, M. N., & Poulikakos, L. D. (2014). Newly observed effects of water on the microstructures of bitumen surface. *Construction and Building Materials, 71, 618–627.*

Gong, M. Et al. (2017). Evaluation of bio-binder modified asphalt's adhesion behavior using sessile drop device and atomic force microscopy. *Construction and Building Materials, 145, 42–51.*

Hung, A. M., Goodwin, A., & Fini, E. H. (2017). Effects of water exposure on bitumen surface microstructure. *Construction and Building Materials, 135, 682–688.*

Leite, F. L., Bueno, C. C., Da Róz, A. L., Ziemath, E. C., & Oliveira, O. N. (2012). Theoretical models for surface forces and adhesion and their measurement using atomic force microscopy. *International Journal of Molecular Sciences, 13(10), 12773–12856.*

Ma, L.L. (2024). Interactions of moisture and oxidative ageing mechanisms in paving binders, PhD dissertation, Delft University of Technology, The Netherland

Nguyen, T., Byrd, W. E., Bentz, D., & Seiler Jr., J. (1992). Development of a technique for in situ measurement of water at the asphalt/model siliceous aggregate interface. *Strategic Highway Research Program.*

Tan, Y., & Guo, M. (2013). Using surface free energy method to study the cohesion and adhesion of asphalt mastic. *Construction and Building Materials*, 47, 254–260.

Xu, G., & Wang, H. (2016b). Study of cohesion and adhesion properties of asphalt concrete with molecular dynamics simulation. Computational Materials Science, 112, 161–169.

Yu, X., Burnham, N. A., Mallick, R. B., & Tao, M. (2013). A systematic AFM-based method to measure adhesion differences between micron-sized domains in asphalt binders. *Fuel*, 113, 443–447.

Improved FTIR method for quantifying elemental changes of asphalt

Xin Xiao
Key Laboratory of Road and Traffic Engineering of Ministry of Education, Tongji University, Shanghai, China

Feipeng Xiao*
Key Laboratory of Road and Traffic Engineering of Ministry of Education, Tongji University, Shanghai, China

ABSTRACT: In current pavement engineering practice, the operational complexity of elemental analyzer poses a challenge for simply and effectively characterizing elemental changes in asphalt, which is not conducive to optimizing chemo-mechanical performance, diagnosing aging conditions, and guiding regeneration. In this study, an improved Fourier-Transform Infrared Spectroscopy (FTIR) method was proposed to improve the quantification capabilities of Attenuated Total Reflectance (ATR) mode by integrating quantitative Transmission (TR) mode. The results showed that TR- and ATR-FTIR have analytical potential in quantifying alkyl and semi-quantifying functional group content, respectively. The spectral index from improved FTIR method shows a promising correlation with the element indexes, namely atomic H/C ratio and heteroatom content (S (%), N (%), and O (%)), with relatively high R^2 values of 0.97, 0.45, 0.84, and 0.73. The obtained findings and proposed indices have quantitative effect for more precise elemental analysis of asphalt.

1 INTRODUCTION

Asphalt, a preferred binder material in pavement construction, especially for high-grade road, is largely composed of carbon (C, 80–88%), hydrogen (H, 8–12%), and functional groups containing sulfur (S, 0–9%), nitrogen (N, 0–2%), and oxygen (O, 0–2%), as well as trace amounts of metals. The diverse elemental composition of asphalt necessitates precise identification of the constituent to elucidate the correlations between chemical properties and mechanical behaviors. Theoretically, low-grade hard asphalt and aged asphalt exhibit higher C/H ratios and increased concentration of heteroatoms. The C/H ratio is intrinsically linked to the compositional ratio of alkanes, naphthenes, and aromatics within the matrix, and the heteroatoms contribute significantly to asphalt polarity (Wang, Wang et al. 2022).

Characterizing elemental changes in asphalt is beneficial for optimizing chemo-mechanical performance, diagnosing aging conditions, and guiding asphalt regeneration. For instance, during the aging process, concentrations of S, N, and O increase with time exposed to the external environment. However, the current elemental analyzer (EA) is technically intricate with rigorous test requirements, which poses challenges for engineers in practical applications in the pavement field.

Attenuated Total Reflectance Fourier-Transform Infrared Spectroscopy (ATR-FTIR) has emerged as a pivotal tool for non-destructive and rapid semi-qualitative chemical characterization of asphalt, including asphalt performance analysis, oil source identification, and aging evaluation (Hou, Lv et al. 2018). For example, carbonyl (C=O) and sulfoxide (S=O), identified through the integrated peak areas within the spectral ranges of 1750-1660 cm^{-1} and 1050-990 cm^{-1}, respectively, serve as typical aging indices. However, the quantitative accuracy of ATR-

FTIR in asphalt analysis needs to be improved. The limitation mainly arises from the non-compliance with the "Lambert-Beer" law of the ATR mode and other errors such as baseline drift, which undermine the linear relationship between intensity of functional group and their actual concentrations in asphalt. Multiple trials, baseline calibration, and reference area method, have been employed to achieve a semi-quantitative analysis. However, these methods are unable to fundamentally improve the quantitative effect of chemical information, leading to significant variations in reported values in different studies.

Transmission Fourier-Transform Infrared Spectroscopy (TR-FTIR) is employed as a test method to comply with the "Lambert-Beer" law and offers quantitative analytical advantages in chemical analysis. It allows the quantitative characterization of functional group content in asphalt solutions with suitable solvents such as carbon tetrachloride and carbon disulfide. However, the application of TR-FTIR is hindered by the solvent absorption effect, which makes it difficult to acquire complete molecular structural information of asphalt.

In this study, an improved FTIR method was proposed to enhance the quantification capabilities of ATR mode by integrating quantitative TR-FTIR. The method leverages the strengths of both modes to achieve more accurate and reliable element quantification in asphalt. First, original and aged asphalt as well as asphalt component samples were collected. Subsequently, elemental analysis and spectral characterization were conducted. Finally, limitations of single FTIR method and synergistic enhancement of the hybrid approach were validated. This improved FTIR method offers a promising methodological basis for more precise elemental analysis, paving the way for quantitatively regulating elemental composition and properties of asphalt.

2 MATERIALS AND METHODS

2.1 Materials

High-quality samples are the basis of elemental and spectral analysis. To begin with, five original binders (OB) were collected, including one #30, one #50, two #70 and one #90 asphalt.

Based on OB, three aging methods, including ultraviolet aging (UV), weather aging (WA) and pressure aging vessel (PAV), were used to simulate the aging effect of various environmental conditions: (1) 2-mm asphalt film was prepared and subjected to UV aging with radiation intensity of 50 mW/cm^2 for 12 days; (2) 2-mm film was weather aged for 90 days (Shanghai, Jul.16-Oct.16); (3) The PAV tests were carried out to simulate the asphalt aging after 5 to 10 years of pavement operation according to the JTG E20-2011 specification.

In addition, the asphalt can be divided into four broad chemical groups called saturates, aromatics, resins and asphaltenes (SARA). Since asphalt is an organic SARA composition with different contents, an improved SARA analysis method proposed by our research group was applied to separate the above asphalt to obtain sufficient SARA samples in batches (Xiao, Wang et al. 2024). The original and aged asphalt as well as SARA samples essentially cover the distribution range of asphalt element content.

2.2 Methods

First, the Elementar UNICUBE elemental analyzer was used to quantify the elemental composition of asphalt. Carbon, hydrogen, nitrogen, sulfur and oxygen (CHSN/O) of the samples were quantitatively analyzed by applying CHNS and O analysis mode in oxygen and helium environment, respectively. The accuracy of the instrument was CHSN < 0.1% and O < 0.2%. The content of each element was determined after two parallel tests and the average value was taken as the final results.

The TR-FTIR spectra were then determined using a Bruker ALPHA II FTIR spectrometer equipped with a 0.1-mm fixed liquid cell. Considering the solubility and absorbance requirements, carbon disulfide (CS$_2$) was selected as the solvent to prepare a 0.04 g/ml solution for TR-FTIR analysis, so that the absorbance value of the samples was kept within an appropriate range.

Subsequently, the ATR-FTIR tests were carried out by applying an attenuated total reflection (ATR) diamond accessory. The samples were analyzed after coating and pressing on the crystal position.

During the FTIR tests, spectra were collected from 600 cm^{-1} to 4000 cm^{-1} with a resolution of 4 cm^{-1} and scan times of 16 times. Three replicates were tested for each sample and the spectra were averaged as the final result after an automated baseline calibration in the BRUKER OPUS software.

3 RESULTS AND DISCUSSION

3.1 Elemental composition of asphalt

Figure 1(a) depicts the elemental composition of 70# asphalt and its fractions, including saturate (Sa), aromatic (Aro), resin (Re), and asphaltene (As). It is evident that the content of C and H gradually decreases, while the content of heteroatoms (S, N, and O) increases accordingly. The elemental composition of original binder (OB) is between aromatic and resin. The observations were a direct consequence of the fact that saturate primarily comprises long aliphatic chains, and asphaltene consists mainly of polyaromatic rings and functional groups, with aromatic and resin falling between these two frictions.

Figure 1(b) presents the elemental changes after exposure to UV, WA, and PAV aging. The content of C and H decreases progressively, while the content of heteroatoms increases with the aging degree increasing sequentially. This trend is consistent with the reported aging behavior, which primarily attributed to volatilization, oxygen absorption, dehydrogenation, and condensation of asphalt, leading to the reduction of lighter components and the conversion of aromatic and resin to asphaltene.

The C/H ratios and concentrations of heteroatoms (S, N, and O) have a decisive influence on the physicochemical properties of asphalt. Therefore, the changes in the H-to-C atomic ratio (n(H/C)) and the content of S, N, and O were focused and the distribution is presented in Figure 1(c). The values for n(H/C) and O content were enlarged fivefold for better visualization. The indices approximately follow a normal distribution and cover the element content range, providing a basis for validating the effectiveness of the improved FTIR method in quantifying elemental changes.
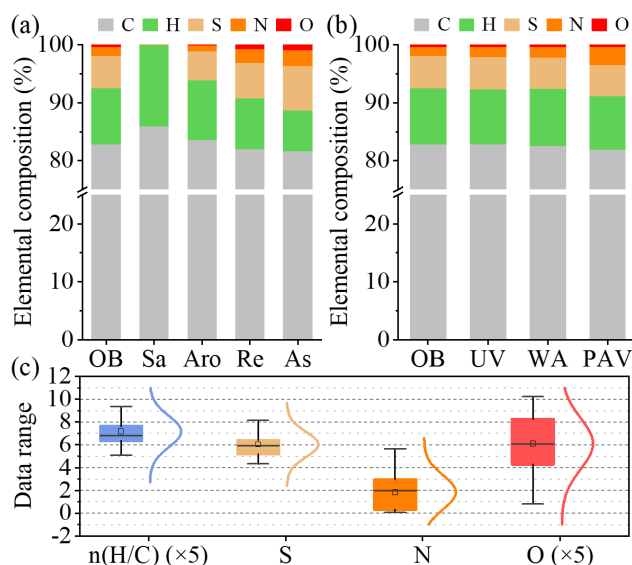
Figure 1. Elemental analysis results, (a) Elemental changes of asphalt component, (b) Elemental changes during asphalt aging, (c) Data distribution range of element related indices.

3.2 Improved FTIR evaluation results

The quantitative performance of TR-FTIR was first verified by evaluating the capability of distinguishing SARA characteristics and aging process. Figure 2(a-b) indicate the absorbance changes in the wavenumber range of 3000~2800 cm⁻¹ available for analysis. The spectra have the same peak positions with varied peak values, which indicate the presence and content of methyl and methylene groups in asphalt.

In Figure 2(a), the absorbance decreases with the order of saturate, aromatic, original binder, resin, and asphaltene. Figure 2(b) depicts the changes with the sequential increased aging degree, and the absorbance decreases with the order of original, and UV, WA, PAV aged binder. The change trends of the peak value showed good agreement with the content change of C and H from the EA results.

Based on the observation, quantitative analysis of absorbance was further carried out by integrating the peak areas of the TR- and ATR-FTIR spectra using two-point area extraction method (Hou, Lv et al. 2018). The peak positions and the integral range of functional groups associated with the elemental changes are listed in Table 1. Note that the baseline correction was performed in the preprocessing process, making the peak area an index to quantify the change of the functional groups.

Table 1. Analyzed functional group in FTIR results.

Functional group	Peak centered at /cm⁻¹	Peak range/cm⁻¹
Vas(-CH3)	2960±5	3000-2910
Vas(-CH2-)	2925±5	2965-2890
Vs(-CH3)	2875±5	2950-2850
Vs(-CH2-)	2855±5	2890-2830
V(C=O)	1690	1730-1670
V(C=C)	1605	1665–1540
V(S=O)	1030	1070–983

Figure 3 summarizes the integral area changes of functional groups with different SARA fractions and asphalt aging degrees. It could be observed that TR-FTIR can better identify the change of alkane content in asphalt. The content of long-chain and saturated alkanes in Sa, Aro, Re and As decreased sequentially, and the alkane content in OB was similar to that in Re and slight lower than that in Aro; Regarding the aging process, the alkane content decreased with the aging degree of asphalt.

It could be concluded that ATR-FTIR could reflect the molecular structure changes such as heteroatom content and aromatic ring content, which was consistent with instrument capability. However, the ATR-FTIR results in terms of alkane group were not consistent with the content in SARA fractions and the trend of content change caused by aging.

Figure 2. Spectra changes, (a) TR-FTIR results of SARA, (b) TR-FTIR results of aged asphalt, (c) ATR-FTIR results of SARA, (b) ATR-FTIR results of aged asphalt.

The ATR-FTIR analysis was further performed to evaluate its analytical capability. Figure 2(c-d) shows the spectra changes with varied SARA fractions and asphalt aging degree. The spectra difference was distinguished for SARA. In term of various aging degree, it could be observed from Figure 2(d) that the functional group changes correlated with heteroatoms of S, N, and O was significant, while the change trends of alkyl group ranges were less obvious. The observations outlined the analytical potential of ATR-FTIR in semi-quantifying functional group content.

Figure 3. Integral area changes of functional groups, (a) With different SARA fractions, (d) Asphalt aging degrees.

Herein, to enhance the capabilities in quantifying elemental changes of asphalt, an improved FTIR method was proposed based on quantitative characteristics of TR-FTIR regarding alkane groups and semi-quantitative characteristics of ATR-FTIR in terms of functional groups containing heteroatom. The formula is as follows, the ATR-FTIR results of alkanes are used as a reference area for functional group areas, and the TR-FTIR results are used to improve the quantification of elemental changes:

$$I(E) = (A(E)_{ATR}/A(-CH-)_{ATR}) \times A(-CH-)_{TR} \quad (1)$$

In which, $I(E)$ was spectral index for elemental changes, $A(E)_{ATR}$ was functional group areas from ATR mode, $A(-CH-)_{ATR}$ and $A(-CH-)_{TR}$ were area of alkane group from ATR and TR mode, respectively.
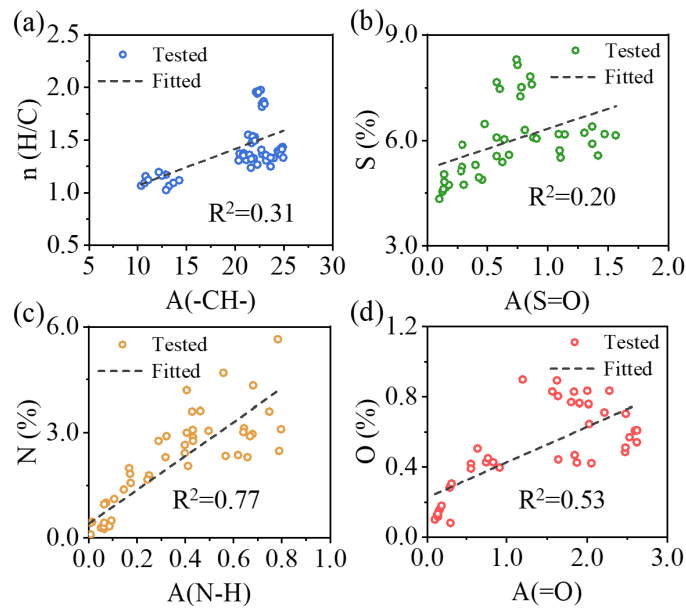
Figure 4. Correlation analysis between integral areas of ATR-FTIR and element related indices.
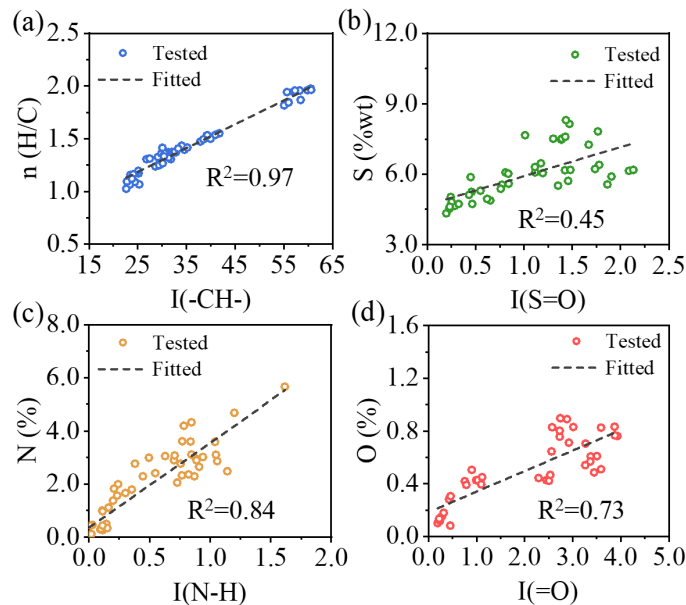
Figure 5. Correlation analysis between proposed spectral indexes regarding elemental changes and element related indices.

Figure 4(a-d) shows the correlation analysis results between integral functional group areas and n(H/C) as well as the heteroatom content (S (%), N (%), and O (%)). The R^2 values are 0.31, 0.20, 0.77, and 0.53, respectively. It can be concluded that the ATR-FTIR peak area has a certain semi-quantitative effect, which is consistent with the previous conclusions. Among them, A(=O) is equal to A(C=O) plus A(S=O). A(-CH-) index and n(H/C) have a positive correlation, which is mainly due to the fact that A(-CH-) is mainly related to the content of alkane group. Generally, the higher the content of saturated alkane group indicated the relative increase of H element content and the increase of n(H/C).

Figure 5(a-d) shows the correlation analysis results between spectral index from improved FTIR method and element indexes, with relatively higher R^2 values of 0.97, 0.45, 0.84, and 0.73, respectively. It could be concluded that the proposed improved FTIR method based on the physical basis of TR- and ATR-FTIR has better quantitative effect for more precise elemental analysis. However, a large number of experiments are further needed to establish a complete prediction model of elemental changes.

4 CONCLUSIONS

Overall, the findings from this study contribute to a deeper understanding of the elemental composition changes in asphalt. TR- and ATR-FTIR have analytical potential in quantifying alkyl and functional group content, respectively. The proposal and validation of the improved FTIR method offers a promising tool for quantitative analysis of elemental variations in asphalt with relatively high R^2 values, facilitating more accurate assessments of asphalt aging and the development of effective mitigation strategies. It is necessary to further optimize the findings and the proposed method based on a larger amount of data, which provides insights into the physicochemical alterations and their implications for asphalt performance.

5 REFERENCES

Hou, X., S. Lv, Z. Chen and F. Xiao (2018). "Applications of Fourier transform infrared spectroscopy technologies on asphalt materials." Measurement 121: 304-316.
Wang, Y., W. Wang and L. Wang (2022). "Understanding the relationships between rheology and chemistry of asphalt binders: A review." Construction and Building Materials 329.
Xiao, X., J. Wang, T. Wang, S. N. Amirkhanian and F. Xiao (2024). "Linear visco-elasticity of asphalt in view of proportion and polarity of SARA fractions." Fuel 363: 130955.

3.2

SELF-HEALING/REJUVENATION METHODOLOGIES FOR EXISTING PAVEMENT STRUCTURES

Effect of encapsulated pyrolytic rejuvenator derived from end-of-life mining tyres on the self-healing properties of aged bitumen

J.L. Concha & M. Chávez-Delgado
LabMAT, Department of Civil and Environmental Engineering, Universidad del Bío-Bío, Concepción, Chile

E. Alpízar-Reyes & L.E. Arteaga-Pérez
Department of Wood Engineering, Universidad del Bío-Bío, Concepción, Chile

J. Norambuena-Contreras
Materials and Manufacturing Research Institute, Department of Civil Engineering, Faculty of Science and Engineering, Swansea University, Bay Campus, SA1 8EN, United Kingdom

ABSTRACT: This study aimed to evaluate the use of biopolymeric capsules based on alginate and a pyrolytic rejuvenator derived from end-of-life mining tyres to enhance the self-healing properties of aged bitumen in asphalt pavements. Capsules were produced using the jet vibrating technique settled with nozzle sizes of 300, 450, 750 µm and $CaCl_2$ hardening solutions at 2%, 5%, and 8% wt. Their morphological, thermal, and mechanical properties were analysed. Self-healing performance was evaluated by incorporating 0.5%, 1.0%, and 2.0% wt. capsules into long-term aged bitumen and testing healing efficiency through cyclic fracture-healing tests over 6 and 24-hour periods. The main results showed that capsules presented mechanical and thermal stability for the paving conditions. An optimal capsule design was achieved using a 750 µm nozzle size and 2% wt. $CaCl_2$ solution. Finally, a dosage of 1% wt. of the optimal capsule design optimised the self-healing property.

1 INTRODUCTION

The oxidative damage of asphalt bitumen, driven by environmental factors and traffic conditions, presents a significant challenge to the long-term durability of asphalt pavements. This challenge has spurred advancements in technologies designed to enhance the extrinsic self-healing of bituminous materials through the use of encapsulated rejuvenators (Gonzalez-Torre and Norambuena-Contreras 2020).

Encapsulated rejuvenators are typically spherical additives, such as polynuclear or core-shell capsules, which enclose asphalt rejuvenating liquids (oils). These capsules are incorporated into asphalt mixtures to restore the original physical and rheological properties of aged bitumen (Xu et al., 2018).

During the service life of asphalt pavements, the bitumen undergoes oxidation due to traffic loads and environmental exposure, leading to microcrack formation and propagation. When a microcrack intersects with a capsule or is subjected to pressure from traffic loads, the capsule can rupture or deform, releasing the rejuvenator. The rejuvenator subsequently diffuses into the cracked area, softening the aged bitumen, which then flows and seals the microcrack (Al- Mansoori et al., 2018). The success of this healing process depends on factors such as the duration of healing time and the number of activated capsules.

Recent research has emphasised the sustainable synthesis of polynuclear biocapsules as rejuvenators, promoting the use of biopolymers like alginate and rejuvenating agents derived from industrial waste, including pyrolytic oils (PO) from End-of-Life tyres (ELTs) (Norambuena-Contreras et al., 2021). Studies, such as those by Xu et al., 2019, suggest that capsules with polynuclear morphology allow a controlled release of rejuvenators, supporting multiple healing cycles in the bituminous material. Additionally, Chávez-Delgado et al., 2024a concluded that the addition of 3% wt. of PO derived from ELTs in long-term aged bitumen restored its rheological properties to an unaged bitumen state. Chávez-Delgado et al., 2024b explored the pyrolysis of ELTs from mining tyres to produce asphalt rejuvenators. So, its encapsulation could be used for asphalt self-healing purposes.

Despite these advancements, several research gaps remain regarding the encapsulation of pyrolytic rejuvenators, particularly their thermal and mechanical stability and their impact on the self-healing performance of aged bituminous materials. This study evaluates the effect of varying dosages of a novel encapsulated pyrolytic rejuvenator (under patent) and rest periods on the self-healing capacity of long-term aged bitumen. Polynuclear biopolymeric capsules were synthesised and analysed for their thermal and mechanical properties. Laboratory experiments quantified the healing efficiency of long-term aged bitumen samples, incorporating these capsules at different dosages with the new pyrolytic liquid.

2 MATERIALS AND METHOD

2.1 *Materials*

The polymeric structure of the capsules consisted of low-viscosity sodium alginate (density 1.02 g/cm^3,

viscosity ≤ 300 mPa·s in a 2% wt. solution), provided by Buchi (Switzerland) and calcium-chloride dihydrate (CaCl$_2$•2H$_2$O) at 77% purity, provided by Winkler (Chile). The pyrolytic oil (PO) presented density 0.86 g/cm^3, viscosity 1.7 mPa·s and pH 8.9. Virgin asphalt bitumen specified as CA-24 (PG 64-22) was long-term aged using the Pressure Air Vessel (PAV) method, according to ASTM D 6521-19.

2.2 Synthesis and characterisation of the capsules

Capsules with polynuclear internal morphology were synthesised based on the ionic gelation principle by electrostatic interactions between sodium alginate and the Ca^{2+} ions form the Calcium solution, following the method proposed by Concha et al., 2024. First, a 2% wt. sodium alginate solution was prepared by using a magnetic stirrer (SCI550-S) at 250 rpm for 24 h. Next, the PO was incorporated in the alginate solution at a biopolymer:oil mass (B:O) ratio of 1:5, resulting in a stable emulsion. Then, the emulsion was pumped using an encapsulator Buchi (B-390) through nozzles of 300, 450, and 750 μm diameter. The emulsion was then separated into droplets and collected in CaCl$_2$·2H$_2$O hardening solution prepared at three concentrations: 2%, 5%, and 8% wt. Finally, the capsules were filtered from the CaCl$_2$ solution and rinsed with deionised water later dried in an oven at 30ºC for 24h.

The morphological, physical, thermal, and mechanical properties of the capsules were determined as proposed by Norambuena-Contreras et al., 2021. The diameter of 100 random capsules was measured using an optical microscope (Leica EZ4) with 35x magnification and the software ImageJ®. The physical property of encapsulation efficiency (EE), i.e., the proportion of PO encapsulated, was determined. Thermogravimetric analysis (TGA) was carried out using a NETZSCH STA 409 PC equipment in a range of temperatures 20-600ºC, and constant N$_2$ flow of 50 mL/min. Compressive mechanical tests were performed using a Universal Testing Machine (UTM) Zwick/ Roell Z005 with a load cell of 1kN and a load speed of 0.2 mm/min. Capsules were tested at preconditioning temperatures of 20, 50, 80, 120, and 150ºC.

2.3 Self-healing measurement of PAV-aged bitumen incorporating capsules

The effect of the PO capsule dosage (0.5%, 1.0%, and 2.0% wt. of bitumen) on the self-healing ability of PAV-aged bitumen samples was evaluated on ductility samples through a mechanical cyclic process of 3 steps described as follows. *Step 1. Conditioning.* Ductility samples were conditioned at -5°C for 2 h (Figure 1(a)), ensuring a brittle fracture. *Step 2. Fracture.* The samples were fractured into two pieces at 5°C under uniaxial tensile test using a Zwick/Roell Z05 universal testing machine with 1 kN load cell and a loading

speed of 5 mm/min (Figure 1(b)). *Step 3. Healing.* The fractured pieces were placed back into the mould and secured with bolts at the ends of the sample. The fractured samples were conditioned at 20°C in a thermal chamber for two healing (rest) times: 6h and 24h, (Figure 1(c)). After this step, steps 1 and 2 were repeated, determining a healing level (*HL*) as:

$$HL\ (\%) = \left(\frac{F_h}{F_i}\right) \times 100 \qquad (1)$$

Where F_i and F_h are the maximum forces resisted by a sample before and after the healing process, respectively. For each healing time, an effective average healing level (*HL$_e$*) was calculated by comparing the maximum average *HL* of each test sample (*HL$_{po}$*) with capsules and the ones without capsules (*HL$_{ref}$*):

$$HL_e = HL_{po} - HL_{ref} \qquad (2)$$
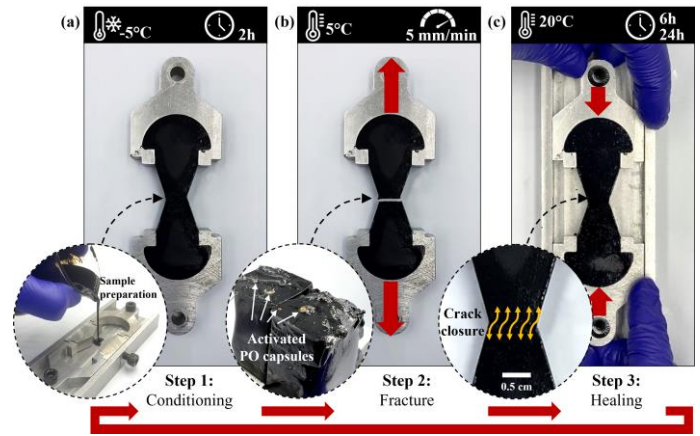
Figure 1. Healing test method on bitumen samples showing the steps of: (a) Conditioning, (b) Fracture, and (c) Healing.

Finally, statistically significant differences in the morphological, physical, and mechanical properties were evaluated by Analysis of Variance (ANOVA) with a significance of 95% (α:0.05) and the Tukey's pairwise mean comparisons.

3 RESULTS AND DISCUSSION

3.1 Characterisation of the biopolymeric capsules

Figure 2 shows representative optical microscopy images for each of the PO capsule designs. Overall, the capsules presented average values of size ranging from 0.61–1.1 mm and EE values between 96.5%–98.9%. Additionally, ANOVA and Tukey tests revealed that the higher the nozzle diameter, the higher the capsule size was. Nonetheless, the nozzle size had no effect on the EE. In terms of the CaCl$_2$ content, ANOVA and Tukey tests revealed no statistical differences for both size and EE. From these results, it can be primary selected a capsule design with low CaCl$_2$, reducing the use of this raw material.

Figure 2. Optical images for each capsule design, showing their representative average sizes and encapsulation efficiency.

Figure 3 shows the average results of compressive strength for each capsule design, ranging between 5.1–15.1 MPa. Overall, these values were higher than the maximum compacting pressure during paving (Sac) of 0.7 MPa (Delgadillo et al., 2008) or the contact pressure for light-duty truck, around 1.0 MPa (Yu et al., 2022). These high compressive strength values could make capsule activation difficult. Consequently, to decide a proper capsule design, ANOVA revealed that the lower compressive strength values were reached for the capsule designs of 750 µm - 8% CaCl$_2$ (5.1 MPa) < 300 µm-8% CaCl$_2$ (7.5 MPa) < 750 µm-2% CaCl$_2$ (8.8 MPa). Based on these results and the previous selection of capsule designs based on 2% CaCl$_2$, the optimal capsule design was that based on a nozzle diameter of 750 µm and 2% CaCl$_2$.
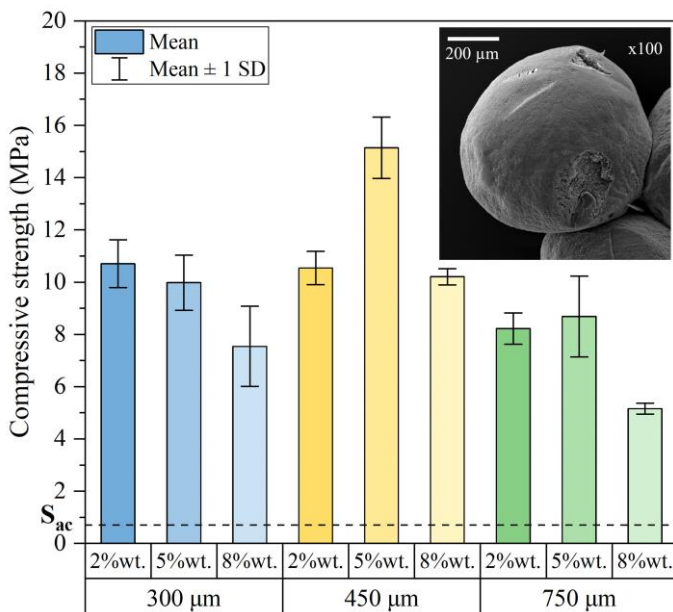
Figure 3. Average results of compressive strength depending on the nozzle size (300, 450, 750 µm) and CaCl$_2$ concentration (2%, 5%, 8% wt).

Figure 4 shows the effect of thermal degradation on the average compressive strength of the optimal capsule design. Overall, the compressive strength was reduced with the temperature increase from 20°C to 150°C (temperature of asphalt mixing) resulting in average values between 8.2 MPa and 2.1 MPa, respectively. It can be noticed that, at 150°C, the compressive strength of the optimal capsule design is higher than the Sac, potentially ensuring their stability during paving. The high mechanical stability of the capsule at this temperature can be explained by its low thermal degradation as proved by the TGA analysis, where the optimal capsule design presented a mass loss lower than 5% at 150°C, mostly attributed to the loss of initial moisture and partial damage on the alginate matrix structure of the capsule, not compromising their mechanical stability.
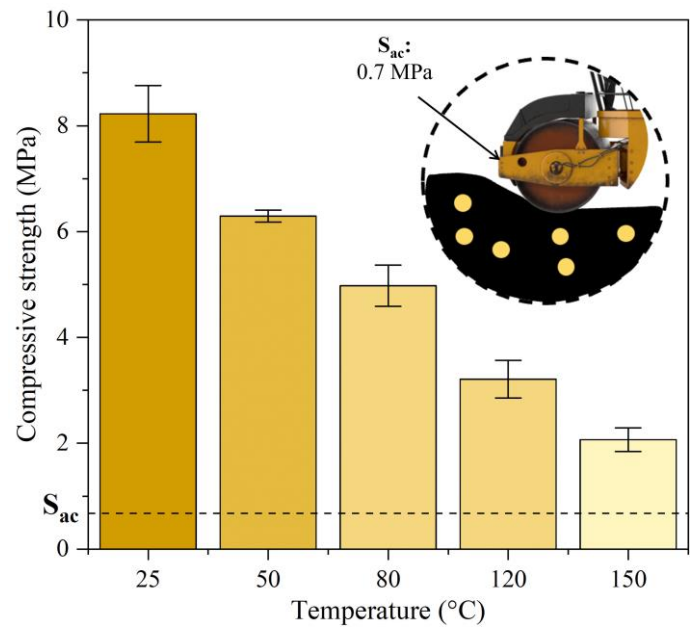
Figure 4. Average results of compressive strength test depending on the conditioning temperature for the optimal capsule design (nozzle diameter of 750 µm and CaCl$_2$ of 2% wt.).

Based on these results, it is concluded that the optimal capsule design was a mechanically and thermally stable additive to be incorporated into bituminous materials for asphalt self-healing purposes. These Ca-alginate PO capsules can be potentially activated by fatigue damage during the service life of the asphalt pavement similarly as proposed by García-Hernandez et al., 2020 in alginate capsules with sunflower oil.

3.2 *Effect of capsule addition on the self-healing properties of aged bitumen*

Figure 5 presents the average results of *HL* depending on the capsule content and the healing time. Overall, the *HL* was increased with the capsule addition, healing time and temperature. ANOVA analysis developed on each individual variable showed statistically significant differences for i) the healing time of 6 h (*HL*: 32.1%) and 24 h (*HL*: 61.7%), and ii) the

capsule dosage of 0%, 0.5%, 1%, and 2%, with average *HL* values of 28.5%, 44.3%, 55.3%, and 59.5%, respectively. These results suggest that higher *HL* values are obtained with a healing time of 24 h, and a capsule content of 2% wt.

With respect to the combined analysis of each factor on the *HL*, Figure 5 revealed that, at low healing time of 6h, no statistically significant effect was detected for samples with 0.0%, 0.5% and 1% capsule content. Consequently, the *HL* evaluated at shorter healing times was only sensitive to a capsule content of 2%. While, for a healing time of 24 h, 0.5% of capsule dosage showed statistically significant differences with respect to a reference sample. Capsule contents of 1% and 2% did not yield statistically significant differences in the *HL*.
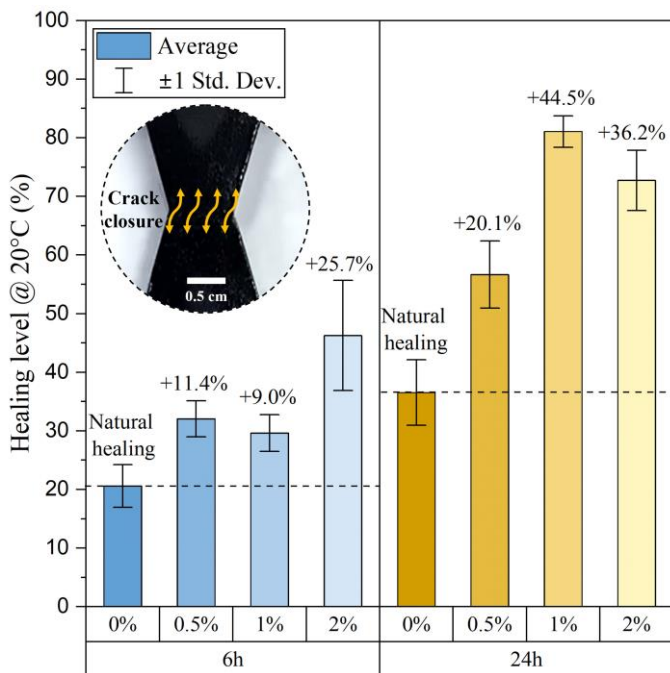
Figure 5. Average HL results for bitumen samples depending on the capsule dosage (0, 0.5, 1, 2 %) and healing time (6, 24 h).

Additionally, the effective healing provided by effect of the capsule (*HL_e*) are shown above each healing bar. It is observed that capsule contents of 1% or higher, combined with a healing time of 24 h, resulted in *HL_e* values exceeding 30%. Specifically, for 24 h healing, a 1% capsule content led to an increase of 44.5%. Since no statistically significant differences were observed in the *HL* between 1% and 2% capsule contents, it can be concluded that long healing times using a capsule content of 1% optimised the healing level of the asphalt binder is used in the production of asphalt mixtures. Future research proposes the use of a capsule design based on 750 um and 2% $CaCl_2$.

4 CONCLUSIONS

- The synthesised capsules designs containing pyrolytic liquid derived from end-of-life mining tyres presented high encapsulation efficiency, over 95% and mechanical stability. The optimal design was a capsule synthesised with a nozzle size of 750 µm and 2% wt. $CaCl_2$.
- The optimal polynuclear capsule design provided mechanical stability and thermal stability, effectively withstanding mixing, compaction, and traffic loads throughout the pavement's service life.
- A capsule content of 1.0% wt. and 24-hour healing time optimised self-healing properties in PAV-aged bitumen, resulting in an effective healing level of up to 44.5%.

6 REFERENCES

Al-Mansoori, T., Norambuena-Contreras, J., Micaelo, R., & Garcia, A. 2018. Self-healing of asphalt mastic by the action of polymeric capsules containing rejuvenators. *Construction and Building Materials*, 161, 330–339.

ASTM D6521-19 Standard Practice for Accelerated Aging of Asphalt Binder Using a Pressurized Aging Vessel (PAV), West Conshohocken, PA, USA, 2019.

Chávez-Delgado, M., Concha, J.L., Arteaga-Pérez, L.E., Norambuena-Contreras, J. 2024a. Rejuvenator based on pyrolysis of waste tyres to improve aged asphalt rheological properties. *2nd Int. Workshop on the Use of Biomaterials in Pavements.* Switzerland: Springer

Chávez-Delgado, M., Colina, J., Segura, C., Álvarez, C., Osorio-Vargas, P., Arteaga-Pérez, L.E., Norambuena-Contreras, J. 2024b. Asphalt pyro-rejuvenators based on waste tyres: An approach to improve the rheological and self-healing properties of aged binders. *Journal of Cleaner Production* 452, 142179.

Concha, J.L., Sáez-Gutiérrez, M., Norambuena-Contreras, J. 2024. Mechanical activation assisted of biobased encapsulated rejuvenators to promote asphalt self-healing. *Materials Today Communications* 38, 107735.

Delgadillo, R., Bahia, H.U. 2008. Effects of temperature and pressure on hot mixed asphalt compaction: field and laboratory study *Journal of Materials in Civil Engineering* 20.

García-Hernandez, A., Salih, S., Ruiz-Riancho, I., Norambuena-Contreras, J., Hudson-Griffits, R, Gomez-Meijide, B. 2020. Self-healing of reflective cracks in asphalt mixtures by the action of encapsulated agents. *Construction and Building Materials* 252, 118929.

Gonzalez-Torre, I., Norambuena-Contreras, J. 2020. Recent advances on self-healing of bituminous materials by the action of encapsulated rejuvenators. *Construction and Building Materials* 258, 119568.

Norambuena-Contreras, J., Arteaga-Pérez, L-E., Concha, J.L., & Irene Gonzalez-Torre. 2021. Pyrolytic oil from waste tyres as a promising encapsulated rejuvenator for the extrinsic self-healing of bituminous materials. *Road Materials and Pavement Design* 22, S117-S133.

Xu, S., García, A., Su, J., Liu, Q., Tabaković, A., & Schlangen, E. 2018. Self-Healing Asphalt Review: From Idea to Practice. *Advanced Materials Interfaces* 5, 1–21.

Xu, S., Tabaković, A., Liu, X., Palin, D., & Schlangen, E. 2019. Optimisation of the calcium alginate capsules for self-healing asphalt. *Applied Sciences* 9.

Yu, L., Hu, J., Li, R., Yang, Q., Guo, F., Pei, J. 2022. Tire-pavement contact pressure distribution analysis based on abaqus simulation. *Arabian Journal for Science and Engineering* 47, 4119-4132.

Microcapsules-Encapsulated Rejuvenators for Asphalt Self-Healing: Effects on Pavement Performance

Mahadevapura Krishnegowda Sachin Gowda, Ambika Behl and Aakash Gupta
CSIR-Central Road Research Institute (CRRI), New Delhi, India-110025.

Kadhiravan Shanmuganathan
CSIR-National Chemical Laboratory (NCL), Pune, India- 411008.

ABSTRACT: Encapsulating rejuvenators in asphalt offers a promising approach to extend pavement lifespan. This study synthesized calcium alginate capsules containing rejuvenator oil, achieving a compressive strength of 18 N and a 75.83% weight loss at 900°C. Capsules were added to asphalt mixes at 0%, 0.5%, and 1% by weight of aggregates. Laboratory tests on unaged, short-term aged (STA), and long-term aged (LTA) samples showed that capsule inclusion did not affect volumetric properties or significantly alter rutting, ITS, or resilient modulus. However, SARA fractionation revealed a 9.4% increase in aromatics content in LTA samples with 1% capsules, indicating enhanced bitumen properties through gradual rejuvenator release.

1 INTRODUCTION

Creating long-lasting asphalt pavements requires timely maintenance and durable bituminous mixtures. Traditionally, bitumen's durability is enhanced by modifiers to improve rheology, adhesion, and aging resistance. Recently, enhancing asphalt's self-healing capability through encapsulated rejuvenators has been explored. Bitumen naturally self-heals by wetting and interdiffusion at damaged sites, but this is slow at service temperatures and less effective as bitumen ages. Encapsulated rejuvenators release healing agents when cracks occur, softening the mastic and restoring strength [1]. Methods like porous sand, sodium alginate gelation, and urea-formaldehyde polymerization have been developed to encapsulate rejuvenators [2, 3]. Calcium-alginate beads show promising results, enhancing self-healing without compromising rutting or moisture resistance. These rejuvenators release under traffic loads, softening bitumen and aiding crack repair, thus significantly restoring aged bitumen. The right rejuvenating agent is crucial for reducing costs and environmental impact [4]. This study focuses on commercial rejuvenator oil in capsules, highlighting the need for innovative methods to improve asphalt self-healing efficiency.

2 OBJECTIVES

The study aims to evaluate the effect of adding microcapsule-encapsulated rejuvenators on asphalt mix performance. Microcapsules will be incorporated at 0.5% and 1% dosages by aggregate weight, and tests for fatigue resistance, rutting resistance, moisture sensitivity, and SARA analysis will be conducted under unaged, short-term aged (STA), and long-term aged (LTA) conditions. The goal is to ensure the capsules do not alter the initial mix properties but activate only when exposed to oxidative aging and repeated loading.

3 MATERIALS USED

3.1 *Bitumen*

This study utilized a viscosity-graded binder (VG-40), and its physical properties were tested following standard guidelines. The results showed a softening point of 51.6°C (ASTM D36-14), ductility greater than 100 cm (ASTM D113-17), a penetration of 42.44 mm (ASTM D5M-20), specific gravity of 1.06 (ASTM D70-21), and a viscosity of 463 cS at 135°C (ASTM D4402-15). These values confirm the binder's suitability for use in asphalt mixtures.

3.2 *Aggregates*

The physical properties of the aggregates used in this study were tested according to standard guidelines. The combined index (flakiness and elongation) was 31.04% (IS 2386 Part 1:1963), the aggregate impact value was 18.03% (IS 2386 Part 4:1963), and the Los Angeles abrasion value was 26.3% (IS 2386 Part 4:1963). These results ensure the aggregates meet the required criteria for use in the asphalt mix.

3.3 *Microcapsule-Encapsulated Rejuvenators*

Rejuvenator capsules were synthesized in the lab using ionic gelation, where sodium alginate was cross-linked with calcium ions (Ca^{2+}). A 2% weight/volume aqueous solution of sodium alginate was stirred for 24 hours and then emulsified with rejuvenator oil. This mixture was pumped at 2 mL/min through a syringe into a calcium chloride ($CaCl_2$) solution, which acted as a hardener. The hardener solution was stirred continuously at 300 rpm. Once the

capsules formed, they were filtered and dried at 40°C. The resulting calcium alginate capsules ranged from
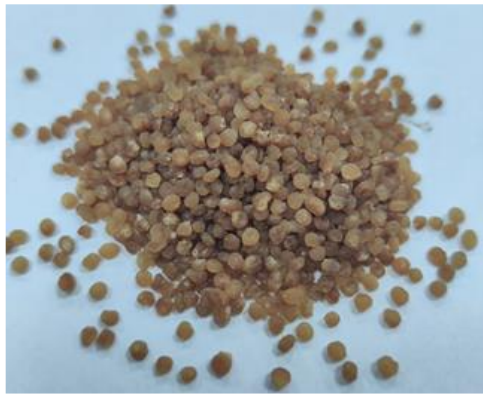
2 to 3 mm in diameter.
Figure 1. Laboratory Synthesized Calcium Alginate Capsules.

4 METHODOLOGY

The study used Bituminous Concrete Grade-2 (BC-II) mix gradation (Figure 2) according to MoRT&H specifications [5], with Marshall mix design conducted per the Asphalt Institute MS-2 manual. The optimum binder content (OBC) was determined to achieve 4% target air voids with 75 blows on each side of the Marshall specimen. Aggregates and bitumen were heated separately and mixed at a specified temperature, and rejuvenator capsules were added and blended for uniformity before compaction.

Specimens were prepared in three conditions: unaged, short-term aged (STA), and long-term aged (LTA). STA specimens were conditioned at 135°C for 4 hours, while LTA specimens were aged at 85°C for five days. Performance tests, including Marshall stability, moisture sensitivity, indirect tensile strength (ITS), resilient modulus (MR), dynamic creep, and SARA analysis, assessed the impact of the microcapsule-encapsulated rejuvenators on asphalt mixes.
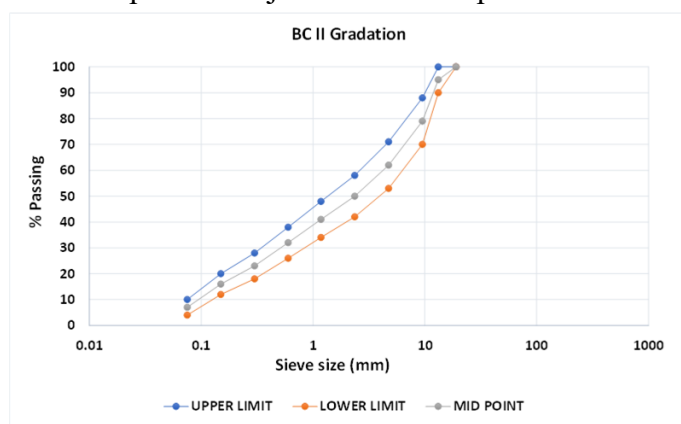
Figure 2. Gradation for BC-II Mix.

5 LABORATORY EXPERIMENTS, RESULTS AND DISCUSSIONS

5.1 *Preparation of Bituminous Mix*

The coarse and fine aggregates were first proportioned according to the gradation shown in Figure 2. The preheated aggregates and bitumen were mixed at the specified mixing temperature. Then, the microcapsules were added to the mix and blended uniformly. The mixture was compacted in Marshall moulds with 75 blows on each face.

5.2 *Mechanical strength and Thermal stability of Microcapsules*

Calcium alginate capsules are integrated into asphalt mixtures to assess their impact on performance and self-healing capabilities. Their mechanical strength is evaluated through a uniaxial compression test, where a compressive force is applied until the yield point is reached. The load-displacement curve reveals that the capsules initially behave elastically but undergo permanent deformation beyond the yield point, increasing the risk of rejuvenator leakage. The capsules demonstrated a maximum force of 18 N before crushing, with previous research indicating that a compressive strength above 10 N ensures their integrity during mixing and compaction [1].

To assess thermal stability, thermogravimetric analysis (TGA) was conducted to measure mass loss at elevated temperatures, confirming that the capsules remain stable with less than 5% mass loss up to 200 °C (Figure 3). This indicates that the capsules will not melt at the mixing and compaction temperatures of asphalt mixtures, ensuring their effectiveness in enhancing self-healing properties without compromising the mix's integrity.
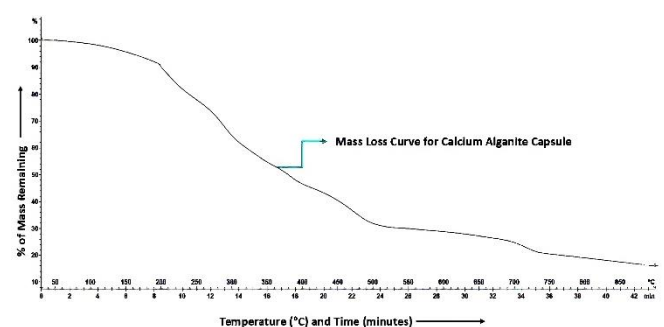
Figure 2. TGA results of calcium-alginate microcapsule.

5.3 *Influence of microcapsules on volumetrics of asphalt mixes*

The asphalt mix design followed the MS-2 procedure, determining the optimum binder content (OBC) to be 5.80% for target air voids of 4%. The measured values for Marshall stability, flow value, bulk density, voids in mineral aggregates (VMA), and voids filled with bitumen (VFB) were 1750 kg, 3.7 mm, 2.41

g/cc, 15.58%, and 74%, respectively. Although adding microcapsules can theoretically increase air voids and reduce the percentage of voids filled with asphalt, laboratory experiments showed that incorporating 0.5% to 1% of microcapsules did not significantly affect the asphalt mix's volumetrics, which are crucial for its performance.

5.4 *Influence of microcapsules on ITS and moisture-sensitivity of asphalt mixes*

The ITS and TSR (AASHTO T-283) tests on unaged, STA, and LTA specimens with 0%, 0.5%, and 1% capsule additions showed no significant changes in values. While ITS values slightly decreased with increased capsule content, these variations were minimal, and TSR values exhibited minor fluctuations without a clear trend. This suggests that capsule additions up to 1% do not significantly affect the mechanical properties or moisture damage resistance of the mix. The variations in ITS and TSR values are illustrated in Figures 4 and 5, respectively.

5.5 *Influence of microcapsules on Resilient modulus of asphalt mixes*

The resilient modulus (MR) tests (ASTM D4123-20) on unaged, STA, and LTA specimens with 0%, 0.5%, and 1% capsule additions indicated a marginal decrease in MR values with higher capsule dosages. Specifically, MR values dropped from 3137 MPa at 0% to 2913 MPa at 1% for unaged specimens, with similar trends observed in STA and LTA specimens (Figure 6). This decrease may be linked to capsule breakage during loading, affecting stress distribution and the material's ability to recover after deformation. The results suggest that the capsules alter the elastic properties of the asphalt-capsule mixtures due to mechanical interactions under repeated loading.
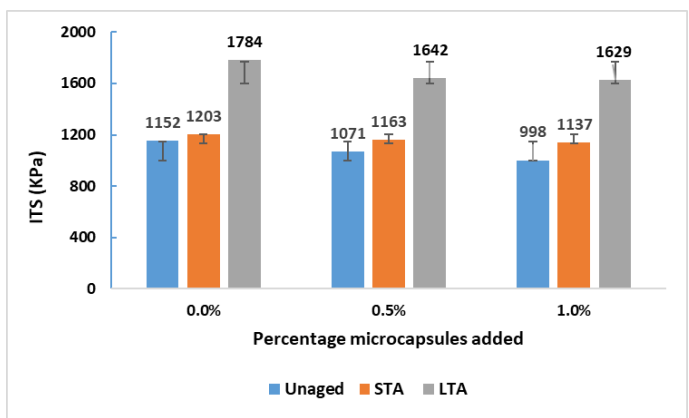
Figure 4. Variation of ITS (in Kpa) with a percentage increase in microcapsules addition.
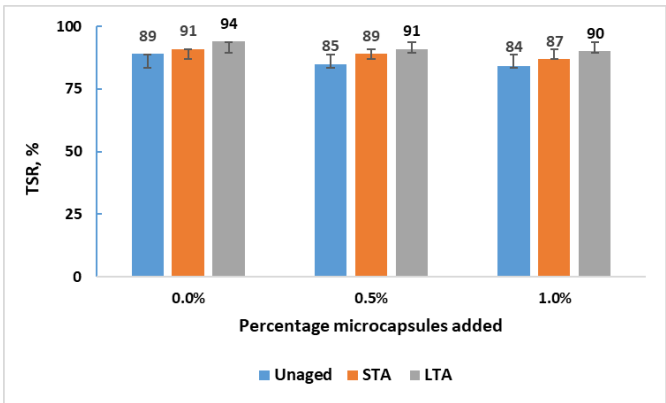
Figure 5. Variation of TSR (in %) with a percentage increase in microcapsules addition.
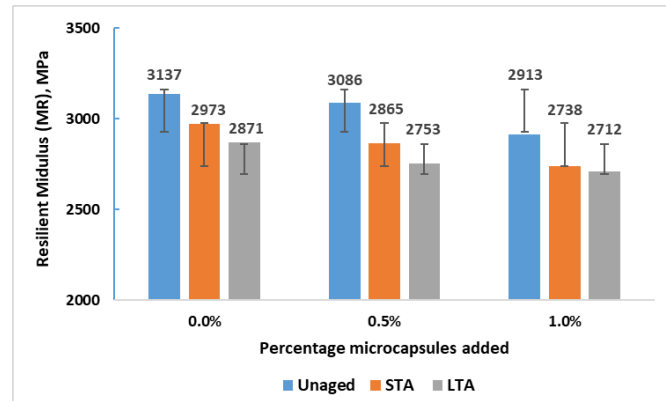
Figure 6. Variation of Resilient Modulus (in MPa) with a percentage increase in microcapsules addition.

5.6 *Influence of microcapsules on rutting behaviour of asphalt mixes*

Dynamic creep test (EN 12697-25) results for unaged, STA, and LTA samples with varying microcapsule additions (0%, 0.5%, and 1%) reveal significant trends in asphalt behavior (Figures 7). Permanent strain accumulation decreases as samples age, attributed to increased asphaltene content and reduced maltene content, leading to a stiffer binder that resists deformation under repeated loading. Although there is a negligible rise in permanent strains with higher microcapsule percentages, this is due to the reorientation of microcapsules during loading, causing slight increases in plastic deformation. The addition of microcapsules influences mechanical behavior across all aging conditions, but rutting performance remains largely unaffected. Increased microcapsule dosage in STA and LTA specimens results in a slight rise in permanent strain, likely due to rejuvenator release under cyclic loading and oxidative aging. SARA fractionation results confirm that some microcapsules break during testing, increasing aromatic content and enhancing elasticity. The mix can accommodate microcapsule additions without substantial performance loss, even with microcapsule strength at only 18 N.
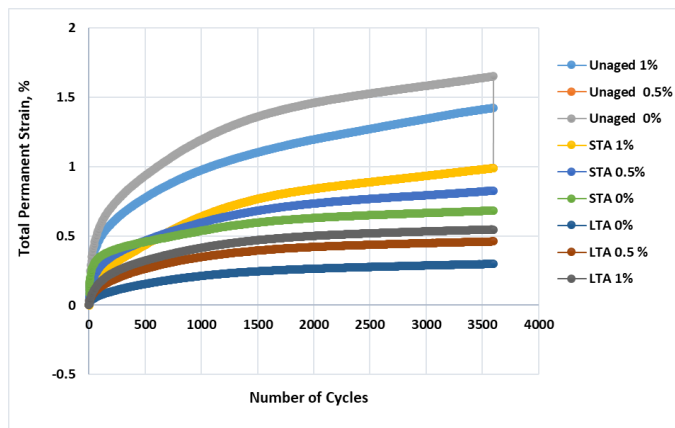
Figure 7. Dynamic creep test results for unaged, STA and LTA asphalt mixes with 0%, 0.5%, and 1% of microcapsules

5.7 Influence of microcapsules on SARA components

SARA analysis results for unaged, STA, and LTA specimens with 0%, 0.5%, and 1% microcapsule additions indicate several trends (Figure 8). For unaged specimens, increased microcapsule content leads to higher levels of saturates and aromatics while decreasing asphaltenes, a trend also observed in STA specimens but with more modest changes. LTA specimens show a notable increase in saturates and resins, particularly at higher microcapsule content. This enhancement is likely due to rejuvenating oil being released from microcapsules during repeated dynamic loading, which helps rejuvenate bitumen properties, restoring flexibility and resilience.
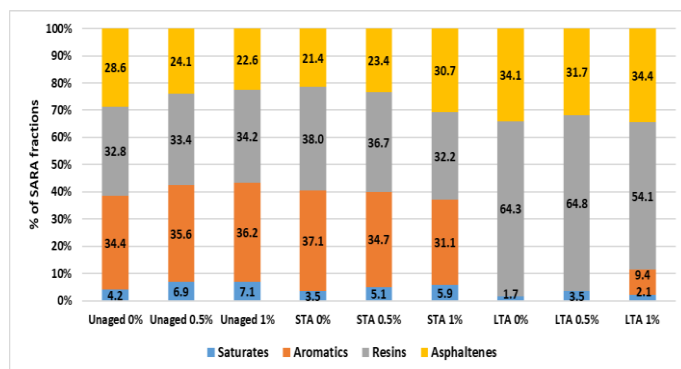
Figure 8. Comparison of SARA fractions for Unaged, STA, and LTA samples with 0%, 0.5%, and 1% microcapsule addition.

The increased maltene components across all aging conditions suggest improved bitumen performance, especially in LTA specimens where resin levels rise significantly. Conversely, higher microcapsule additions decrease asphaltene content, indicating a breakdown of heavier components into lighter fractions. Overall, the results demonstrate the effectiveness of microcapsules in improving bitumen properties through the gradual release of rejuvenating agents during mechanical stress.

6 CONCLUSIONS

This study examined the effects of microcapsule-encapsulated rejuvenators on asphalt mix performance. Calcium alginate capsules containing rejuvenator oil were synthesized and added to asphalt mixes at dosages of 0%, 0.5%, and 1% by weight. Various tests, including ITS, moisture resistance, resilient modulus, dynamic creep, and SARA fractionation, were conducted on unaged, STA, and LTA mixes. Key findings indicate that the capsules have a uniaxial compressive strength of 18 N and can withstand temperatures up to 200°C without rupture. The microcapsules did not significantly affect volumetric properties or moisture resistance, but increased dosage slightly decreased resilient modulus due to potential capsule breakage under load. SARA analysis showed improved bitumen properties with increased maltene components and decreased asphaltenes, enhancing flexibility and resilience. Dynamic creep tests indicated that while permanent strain accumulation increased with more microcapsules, rutting performance remained largely unaffected. In conclusion, microcapsule-encapsulated rejuvenators can enhance the self-healing properties of asphalt by gradually releasing rejuvenating agents, supporting future research to optimize capsule formulations for improved pavement lifespan.

7 ACKNOWLEDGMENTS

8 REFERENCES

[1] Garcia A ´, Schlangen E, van de Ven M, Sierra-Beltra´nG (2010) Preparation of capsules containing rejuvenators for their use in asphalt concrete. J Hazard Mater 184:603–611. https://doi.org/10.1016/j.jhazmat.2010.08.078

[2] Al-Mansoori T, Micaelo R, Artamendi I, Norambuena Contreras J, Garcia A (2017) Microcapsules for self-healing of asphalt mixture without compromising mechanical performance. Constr Build Mater 155:1091–1100. https://doi.org/10.1016/j.conbuildmat.2017.08.137

[3] A. García, E. Schlangen, M. van de Ven, Properties of capsules containing rejuvenators for their use in asphalt concrete, Fuel 90 (2) (2011) 583–591.

[4] Micaelo R, Al-Mansoori T, Garcia A (2016) Study of the mechanical properties and self-healing ability of asphalt mixture containing calcium-alginate capsules. Constr Build Mater 123:734–744. https://doi.org/10.1016/j.conbuildmat. 2016.07.095

[5] MoRTH, Specifications for Road Bridge Works 5th Revision, 2013.

Rheological effects of chemo-rejuvenators on aged SBS modified bitumen

B. Li

Civil Engineering and Geosciences, Delft University of Technology, Delft, The Netherlands

CD Laboratory for Chemo-Mechanical Analysis of Bituminous Materials, Institute of Transportation, TU Wien, Wien, Austria

P. Lin & X. Liu

Civil Engineering and Geosciences, Delft University of Technology, Delft, The Netherlands

Y. Hung

Bitumen Research team, TotalEnergies, Centre de recherche de Solaize, Solaize, France

A. Tolboom

Latexfalt B.V., Koudekerk aan den Rijn, The Netherlands

ABSTRACT: Aging of Styrene-Butadiene-Styrene (SBS) modified bitumen leads to polymer network degradation and existing commercial rejuvenators mainly replenish light components but fail to restore this network. The present paper introduces an innovative rejuvenator that not only supplements these light components, but also mends the compromised SBS polymer network through specially designed chemical connecting agents.

1 INTRODUCTION

The aging mechanism of SBS modified bitumen cannot be simply divided into base bitumen aging or SBS polymer degradation. The mutual protection between the two significantly slows the aging rate of polymer and bitumen together compared to either of them separately (Chen et al., 2021). During aging, bitumen undergoes molecular weight increases, while SBS polymer degrades into copolymer particles dispersed within the bitumen. These combined effects of bitumen oxidation and polymer degradation influence the rheological properties (Wei et al., 2020). Thus, it is important to take both bitumen and SBS polymer into consideration when designing rejuvenators for aged SBS modified bitumen.

There are some studies that have focused on rejuvenating the degraded polymers. For instance, a rejuvenator comprising 75% aromatic oil and 25% SBS polymer was applied to reclaimed asphalt pavement (RAP) binders, significantly softening the binder as well as improving low-temperature cracking and high-temperature rutting resistance (Eltwati et al., 2022). Another rejuvenator, containing aromatic oil, light oil, corn oil, and SBS polymer, demonstrated remarkable improvements in the ductility, elasticity, and cracking resistance of the aged bitumen (Cong et al., 2020). Beyond the aforementioned polymer restoration through physical interaction, chemical reaction rejuvenation has also been explored. Some active oxidative functional groups like hydroxyl and carboxyl will appear at the fracture sides of the broken SBS polymer segments as they degrade, and specific chemical compounds can react with these functional groups thereby reconnecting the degraded SBS polymer (Cao et al., 2020). For example, rejuvenators containing 1, 4-butanediol diglycidyl ether (BUDGE)

and trimethylolpropane triglycidyl ether (TMPGE) have been shown to improve low-temperature ductility and cracking resistance, with FTIR and fluorescence microscopy confirming chemical reactions between the terminated reactive groups on epoxy molecules and the reactive functional groups on polymer (Xu et al., 2017). Similarly, epoxidized soybean oil (ESO) with triphenyl phosphine (TPP) as the catalyst was used to restore polymer networks, with FTIR analysis confirming that TPP opened epoxy groups in ESO, allowing them to react with degraded SBS segments to reconnect them (Wei et al., 2020).

For both approaches, however, the problems are apparent. Adding fresh SBS polymers is efficient but neglects the reuse of degraded polymers. Chemical rejuvenation utilizes existing polymers but fails to fully restore the original polymer network, as reactive compounds can only reconnect broken polybutadiene segments. To address these issues, this paper proposes an innovative rejuvenator that not only softens the aged bitumen phase but also integrates fresh polymers and repairs the SBS polymer network using a specially designed chemical connecting agent.

2 MATERIALS AND METHODS

2.1 *Rejuvenators preparation*

Liquid Resin (LS oil), a by-product of the kraft process, was employed as a pure oil rejuvenator for reference and as the base oil for other rejuvenators. A physical rejuvenator (LS-L), consisting of LS oil and low content of SBS polymer, was blended in the lab using a high shear mixer for 40 minutes, followed by stirring with an overhead stirrer for 2 hours. Additionally, a reactive chemical compound, M, was chosen to produce the chemical rejuvenators.

2.2 Binder samples preparation

The SBS modified bitumen was provided by TotalEnergies Bitumen. The Thin Film Oven Test (TFOT) was performed according to EN 12607-2 (CEN, 2014) to simulate short-term aging and the Pressure Aging Vessel (PAV) test was performed for 80 hours according to EN 14769 (CEN, 2023) to simulate long-term aging.

Rejuvenated bitumen samples were prepared by first dividing long-term aged bitumen into small containers. The rejuvenators were then added to these containers at the designed dosage. A hand-held mixer was used to blend the rejuvenator and aged bitumen thoroughly at 170°C for 15 minutes.

The reactive chemical compound M was used as a standalone reference rejuvenator (10% M). It was also combined with the pure oil rejuvenator to create a chemo-oil rejuvenator (10% X_iM + LS) and with the physical rejuvenator to produce chemo-physical rejuvenators (10% X_iM + LS-L). The addition ratio of M is represented by the factor X_i, with i ranging from 1 to 3, corresponding to addition ratios varying from 0.2% to 1%.

2.3 Rheological properties analysis methods

An Anton Paar Modular Compact Rheometer 502 was utilized for the rheological tests. Frequency sweep tests were conducted in accordance with EN 14770 (CEN, 2012) at temperatures of 0, 15, 30, 40, 60, and 80°C, with frequencies ranging from 0.1 to 10 Hz. The Multiple Stress Creep and Recovery Test (MSCRT) was performed at 70°C following EN 16659 (CEN, 2015). The Linear Amplitude Sweep (LAS) test was carried out at 20°C as per AASHTO TP 101-14 (AASHTO, 2014). Additionally, a creep-relaxation test was conducted at 0°C using an 8 mm diameter parallel plate and a 2 mm gap. During this test, the sample was subjected to 1% shear strain within 0.1 seconds, followed by a 100-second relaxation period under constant strain, with shear stress recorded throughout the process (Jing et al., 2020).

The complex modulus master curves were built with the Sigmoidal model from the National Cooperative Highway Research Program (NCHRP) Project A-37A (Yusoff et al., 2013). The Kramers-Kronig relations were applied to construct the phase angle master curves (Lin et al., 2021). The equations used for plotting the master curves are provided below.

$$\log|G^*| = \upsilon + \frac{\alpha}{1+e^{(\beta+\gamma \log \omega)}} \tag{1}$$

$$\delta = 90 \times \frac{d\log G^*}{d\log \omega} = -90 \times \alpha\gamma \frac{e^{(\beta+\gamma \log \omega)}}{[1+e^{(\beta+\gamma \log \omega)}]^2} \tag{2}$$

where $|G^*|$ is the complex modulus (Pa), δ is the phase angle (degree), ω is the reduced frequency at the reference temperature (rad/s), υ is the lower asymptote, α is the difference between the values of the upper and lower asymptote, β and γ define the shape between

the asymptotes and the location of the inflection point (inflection point obtained from $10^{(\beta/\gamma)}$).

The master curves were constructed with a reference temperature of 30°C.

3 RESULTS AND DISCUSSION

The master curves of complex modulus and phase angle for rejuvenated bitumen binder samples are shown in Figures 1-2. Compared to the unaged sample, the aged PMB exhibits increased stiffness in the complex modulus and a loss of the downward trend and plateau region in the phase angle, indicating degradation of the polymer network structure within the binder (Asgharzadeh et al., 2013).
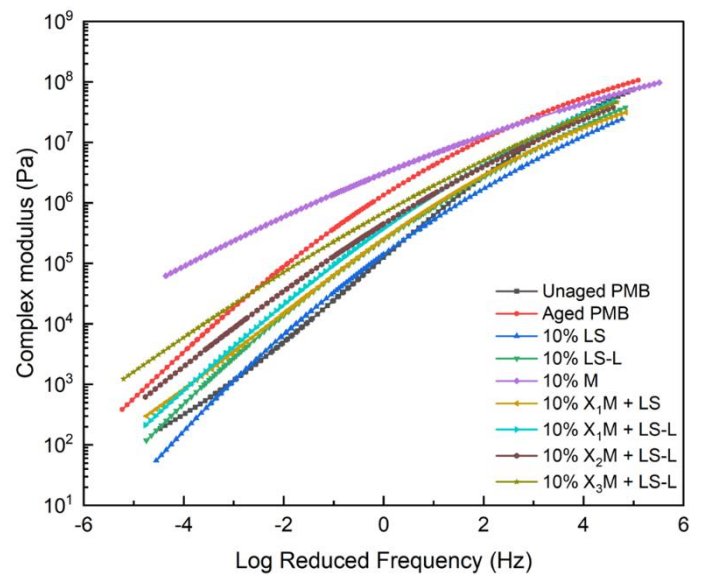
Figure 1. Complex modulus master curves.
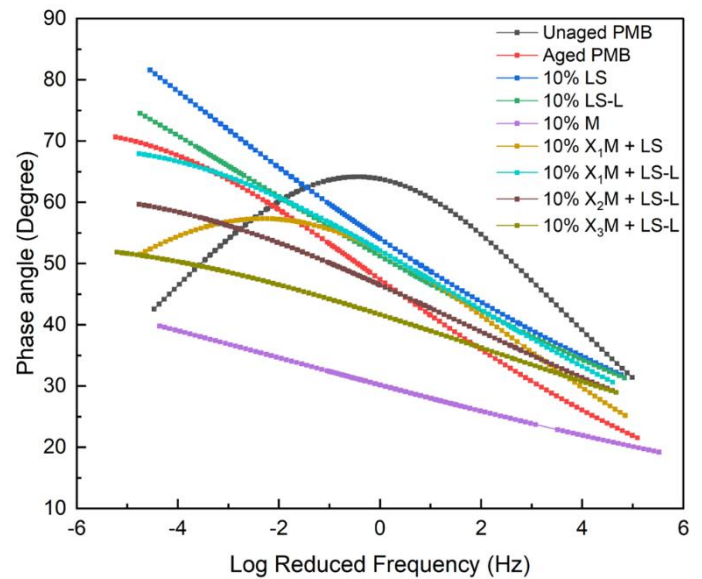
Figure 2. Phase angle master curves.

Rejuvenating aged bitumen with pure oil or the physical rejuvenator significantly softens the binder. However, due to the presence of SBS polymer in the physical rejuvenator, the softening effect is slightly less pronounced than with pure oil alone. In contrast, the use of the pure reactive chemical compound M substantially increases stiffness and elasticity, resulting in a brittle rejuvenated binder. When the chemical compound is combined with the pure oil rejuvenator, the elasticity introduced by the chemical phase and the viscosity from the oil phase are effectively balanced. The joined use of chemical and physical rejuvenating components achieves similar effects, with higher proportions of the chemical compound introducing more elasticity to the rejuvenated binder.

Figure 3 presents the average percent recovery value R after a 3.2 kPa shear stress from MSCRT. The use of pure oil and physical rejuvenators decreases the R-value, as the oil component reduces elasticity by increasing the binder's viscosity. In contrast, the pure chemical compound significantly enhances percent recovery, even exceeding that of unaged PMB, due to its exceptional elasticity recovery ability. In the chemo-oil rejuvenator, the opposing effects of the chemical and oil components on elasticity recovery balance each other. At the given addition ratio of the chemical compound, the oil component counteracts the elasticity-enhancing effects of the chemical compound, resulting in no significant change in the R-value compared to aged bitumen. For chemo-physical rejuvenators, the percent recovery increases with higher addition ratios of the chemical compound M, confirming its positive contribution to the high-temperature performance of rejuvenated bitumen.
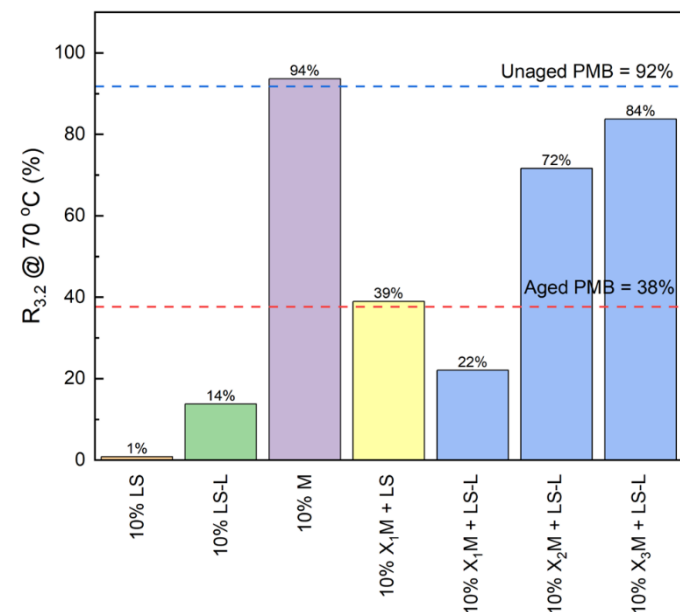
Figure 3. Average percent recovery value from MSCRT.

The fatigue life of the rejuvenated binders at 5% applied strain from the LAS test is presented in Figure

4. Both pure oil and physical rejuvenators greatly enhance fatigue life, surpassing that of unaged PMB. However, the presence of polymer in the physical rejuvenator has a negative effect on fatigue life. The pure chemical compound M, on the other hand, makes the rejuvenated binder excessively stiff and brittle, resulting in an extremely low fatigue life. In contrast, rejuvenated bitumen with the chemo-oil rejuvenator outperforms unaged PMB in the fatigue life test. For chemo-physical rejuvenators, the combined influence of polymer and the chemical compound has limited effectiveness in improving fatigue life.
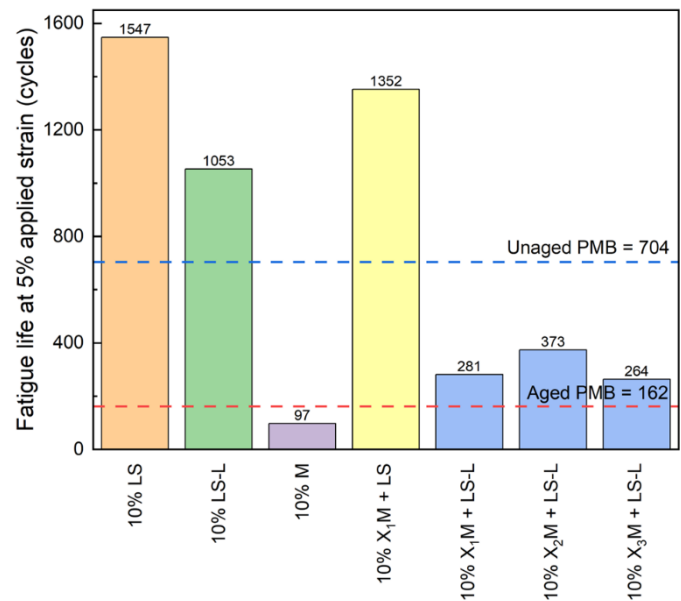
Figure 4. Fatigue life at 5% applied strain.

Figure 5 demonstrates the time for stress reduced 50% from the maximum of different rejuvenated bitumen samples in the creep-relaxation tests. Pure oil and physical rejuvenators significantly reduce the time required for stress relaxation compared to aged PMB, with the additional SBS polymer in the physical rejuvenator having little impact on the time reduction compared to the pure oil rejuvenator. However, introducing the pure chemical compound dramatically increases the required time, leading to greater stress accumulation and heightened vulnerability to crack at low temperatures. By adding extra oil, the chemo-oil rejuvenator can let the rejuvenated binder have the same performance as unaged PMB. Chemo-physical rejuvenators also reduce stress relaxation time, though less effectively than the chemo-oil rejuvenator due to the added polymer. Nonetheless, both chemo-modified rejuvenators outperform aged bitumen and show time results similar to their respective base rejuvenators (pure oil and physical rejuvenators), indicating that the additional chemical compound does not introduce a considerable detrimental effect.
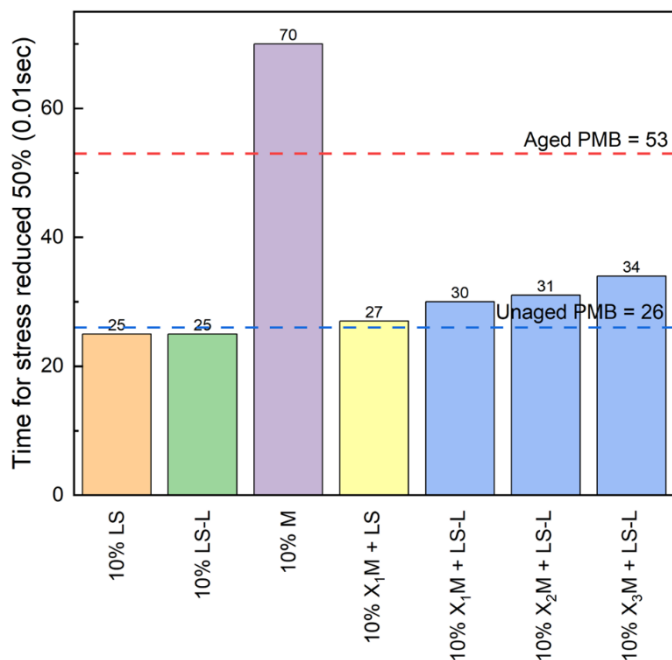
Figure 5. Time for stress reduced 50% from the maximum in creep-relaxation test.

4 CONCLUSIONS

In conclusion, different types of rejuvenators were compared in this paper based on the rheology of rejuvenated SBS modified bitumen. Experiments show that:

- Pure oil rejuvenator effectively replenishes light components and softens aged bitumen, improving low-temperature cracking resistance and fatigue life. However, it reduces the high-temperature elasticity.
- The physical rejuvenator, containing SBS polymer, provides fewer light components, resulting in inferior fatigue life compared to the pure oil rejuvenator. Meanwhile, the extra SBS polymer does not help a lot in elasticity restoration.
- The pure chemical compound significantly improves elasticity but lacks light components, leading to poor low-temperature and fatigue performance, even worse than aged PMB.
- Reactive chemical modified rejuvenators, however, offer a balanced solution, replenishing light components to improve low-temperature properties while introducing fresh SBS polymer and reactivating existing polymers to restore the polymer network structure.

REFERENCES

AASHTO 2014. TP 101 Standard Method of Test for Estimating Damage Tolerance of Asphalt Binders Using the Linear Amplitude Sweep.

ASGHARZADEH, S. M., TABATABAEE, N., NADERI, K. & PARTL, M. 2013. An empirical model for modified bituminous binder master curves. *Materials and Structures,* 46**,** 1459-1471.

CAO, Z., CHEN, M., YU, J. & HAN, X. 2020. Preparation and characterization of active rejuvenated SBS modified bitumen for the sustainable development of high-grade asphalt pavement. *Journal of Cleaner Production,* 273**,** 123012.

CEN 2012. EN 14770 Bitumen and bituminous binders - Determination of complex shear modulus and phase angle - Dynamic Shear Rheometer (DSR).

CEN 2014. EN 12607-2 Bitumen and bituminous binders - Determination of the resistance to hardening under influence of heat and air - Part 2: TFOT method.

CEN 2015. EN 16659 Bitumen and Bituminous Binders - Multiple Stress Creep and Recovery Test (MSCRT).

CEN 2023. EN 14769 Bitumen and bituminous binders - Accelerated long-term ageing conditioning by a Pressure Ageing Vessel (PAV).

CHEN, M., GENG, J., XIA, C., HE, L. & LIU, Z. 2021. A review of phase structure of SBS modified asphalt: Affecting factors, analytical methods, phase models and improvements. *Construction and Building Materials,* 294**,** 123610.

CONG, P., GUO, X. & MEI, L. 2020. Investigation on rejuvenation methods of aged SBS modified asphalt binder. *Fuel,* 279**,** 118556.

ELTWATI, A., AL-SAFFAR, Z., MOHAMED, A., ROSLI HAININ, M., ELNIHUM, A. & ENIEB, M. 2022. Synergistic effect of SBS copolymers and aromatic oil on the characteristics of asphalt binders and mixtures containing reclaimed asphalt pavement. *Construction and Building Materials,* 327**,** 127026.

JING, R., VARVERI, A., LIU, X., SCARPAS, A. & ERKENS, S. 2020. Rheological, fatigue and relaxation properties of aged bitumen. *International Journal of Pavement Engineering,* 21**,** 1024-1033.

LIN, P., LIU, X., APOSTOLIDIS, P., ERKENS, S., ZHANG, Y. & REN, S. 2021. ESEM observation and rheological analysis of rejuvenated SBS modified bitumen. *Materials & Design,* 204**,** 109639.

WEI, C., ZHANG, H. & DUAN, H. 2020. Effect of catalytic-reactive rejuvenator on structure and properties of aged SBS modified asphalt binders. *Construction and Building Materials,* 246**,** 118531.

XU, X., YU, J., XUE, L., ZHANG, C., HE, B. & WU, M. 2017. Structure and performance evaluation on aged SBS modified bitumen with bi- or tri-epoxy reactive rejuvenating system. *Construction and Building Materials,* 151**,** 479-486.

YUSOFF, N. I. M., JAKARNI, F. M., NGUYEN, V. H., HAININ, M. R. & AIREY, G. D. 2013. Modelling the rheological properties of bituminous binders using mathematical equations. *Construction and Building Materials,* 40**,** 174-188.

Improving rheological and self-healing properties of aged asphalt binders using rejuvenators derived from waste tyre thermal conversion

J. Norambuena-Contreras
Materials and Manufacturing Research Institute, Department of Civil Engineering, Faculty of Science and Engineering, Swansea University, Bay Campus, SA1 8EN, United Kingdom

R. Delgadillo
Departamento de Obras Civiles, Universidad Técnica Federico Santa María, Valparaíso, Chile

J.L. Concha & M. Chávez-Delgado
LabMAT, Department of Civil and Environmental Engineering, Universidad del Bío-Bío, Concepción, Chile

L.E. Arteaga-Pérez & E. Alpízar-Reyes
Department of Wood Engineering, Universidad del Bío-Bío, Concepción, Chile

C. Segura
Unidad de Desarrollo Tecnológico, Universidad de Concepción, Coronel, Chile.

Y. Casas-Ledón
Department of Environmental Engineering, Environmental Sciences Faculty and Center EULA-Chile, Universidad de Concepción, Concepción, Chile.

ABSTRACT: This study investigates the development and application of asphalt rejuvenators derived from waste tyres through pyrolysis process. Two several products were produced and evaluated: an optimised Pyrolytic Liquid Rejuvenator (PLR) and Biopolymeric Polynuclear Capsules (BPC) encapsulating PLR for self-healing asphalt mixtures. Rheological and self-healing properties of aged asphalt binders were examined using dynamic shear rheometer and tensile fracture-healing tests. Main results demonstrated that PLR significantly reduced the stiffness of aged binders, achieving properties comparable to unaged binders at 15% dosage by weight. BPCs enhanced self-healing, with a maximum Effective Healing Level (EHL) of 44.5% achieved at 1% dosage after 24 hours. The results indicate that pyrolytic rejuvenators and encapsulated formulations offer effective and environmentally sustainable solutions for enhancing the durability of recycled asphalt pavements.

1 INTRODUCTION

The increasing necessity for improving our road infrastructure has implied the use of several innovative techniques, such as recycling asphalt pavements and alternative asphalt rejuvenators, as potential solutions to produce more sustainable and durable asphalt pavements. Even though asphalt recycling is a sustainable road solution, this technique requires rejuvenating agents to improve the chemo-mechanical properties of aged binder in Recycled Asphalt Pavement (RAP) aggregates (Zaumanis et al., 2014).

Asphalt rejuvenators are lubricating and extender additive oils with a high proportion of aromatic and light aliphatic molecules used to reconstitute the chemical composition of asphalt binders (Loise et al., 2021). Rejuvenators are used to reduce the asphalt binder's softening point, viscosity, and complex shear modulus $|G^*|$ and increase the penetration and phase angle (δ). Rejuvenating agents can also be encapsulated to promote the extrinsic self-healing properties in conventional and recycled asphalt mixtures (Gonzalez-Torre & Norambuena-Contreras, 2020). Despite this, asphalt rejuvenators are commercial products mainly derived from petroleum, and their extended use on roads could have environmental impacts. Recently, several efforts have been developed to produce pyrolytic liquid and encapsulated asphalt rejuvenators (Norambuena-Contreras et al., 2021; Chávez-Delgado et al., 2024) based on waste tyres, refers to discarded or end-of-life tyres. These critical wastes often accumulate in landfills or storage areas, posing significant environmental hazards.

This paper describes a case study of a research project developed in Chile in partnership with six several companies and three local universities. This interdisciplinary project aimed to develop asphalt rejuvenators based on functional liquids obtained from the waste tyres pyrolysis. The study involved producing, chemically optimising, and validating the capacity of functional pyrolytic liquids to improve the rheological and self-healing properties of asphalt binders.

2 MATERIALS AND METHOD

2.1 *Asphalt binders and rejuvenator products based on waste tyres*

A virgin bitumen CA-24 (PG 64-22) with a penetration grade of 50/70, a softening point of 51°C and a density of 1.034 g/cm³ was used for asphalt rejuvenating tests. This virgin bitumen was subjected to a

short-term ageing process using the standardised Rotary Thin Film Oven (RTFO) test according to ASTM D 2872-19. RTFO sample was then subjected to a long-term ageing process in a Pressurised Air Vessel (PAV) according to ASTM D 6521-19. Reclaimed bitumen CA-24 from a RAP material with a 10-year service life was extracted according to ASTM D2172/D2172M using a centrifuge extractor and trichloroethylene as the solvent. It was then recovered from the solvent according to ASTM D 5404/D 5404M. Both PAV and RAP binders were mixed with the rejuvenators.

The first asphalt rejuvenator product was an optimised *Pyrolytic Liquid Rejuvenator* (PLR in Figure 1(a)) produced from mining waste tyres pyrolysis. PLR can be applied on the surface of aged asphalt pavements and as an additive in asphalt mixtures containing RAP material. The pyrolytic asphalt rejuvenator contains 74% wt. of aromatic and terpenic compounds, which gives it antioxidant capacity, the potential to replace the aromatic/asphaltene fraction, and over 90% stability to oxidative ageing. Likewise, its low viscosity (2.49 cP), density (0.856 g/cm^3), and water content (<3% wt.) are in the same order as commercial competitors. The pyrolytic asphalt rejuvenator was obtained from an autothermal process with a carbon footprint equivalent to -1.85 kgCO$_2$/kg of rejuvenator.

The second asphalt rejuvenator product of the project was *Biopolymeric Polynuclear Capsules* (BPC in Figure 1(b)), which store the optimised PLR inside them and add it as an additive into self-healing asphalt mixtures. The BPCs consisted of spherical particles of 1.06 mm, constituted by a porous microstructure generated from sodium alginate. BPCs were produced using the jet-vibrating encapsulation of an oil-in-water emulsion with a stable biopolymer-to-rejuvenator ratio. BPCs showed an encapsulation efficiency of 97% and a compressive mechanical strength of 8.23 MPa at 20°C, a cumulative mass loss of 5.9% at 150°C, proving their ability to survive asphalt hot mixing without thermal degradation and mechanical resistance to asphalt mixing processes.
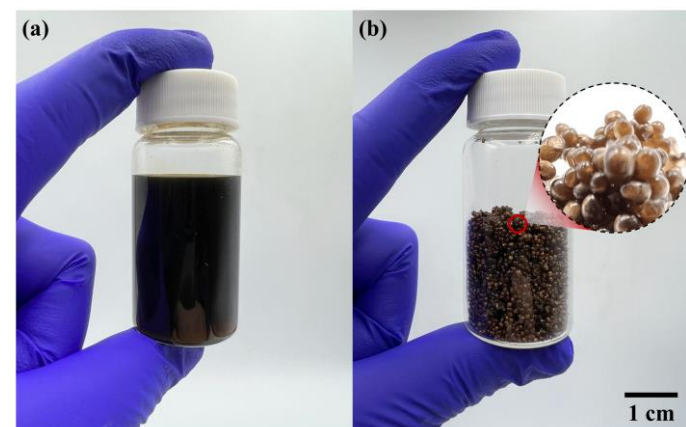
Figure 1. Asphalt rejuvenators based on waste tyres produced during the research project: (a) Pyrolytic Liquid Rejuvenator (PLR), and (b) Biopolymeric Polynuclear Capsules (BPC).

2.2 Rheological properties of asphalt binders with optimised PLR

The rheological characterisation of the asphalt binders (Unaged, PAV, RTFO and RAP with PLR doses of 0%, 9%, 12% and 15% by wt. binder) was carried out with frequency and temperature sweep tests according to ASTM D7175. A Dynamic Shear Rheometer (DSR), Anton Paar model MCR 301, with Anton Paar RheoCompass® software was used. The test frequencies were varied between 100 and 0.1 [rad/s] and the temperatures between 5 and 40°C, with 5°C steps. Plates with 8 mm diameter and 2 mm gap were used. Dynamic shear modulus ($|G^*|$) and phase angle (δ) were obtained. The master curves of both variables were constructed for each material at a reference temperature of 25°C.

2.3 Self-healing properties of PAV asphalt binder with BPCs

The Healing Level (HL) in PAV binder tensile test samples (produced using the ductility mould) containing different capsule doses was quantified. The capsules were incorporated at three different contents: 0.5%, 1.0%, and 2.0% by wt. of 80 g PAV binder heated at 150°C and stirred at 300 rpm for 15 minutes. The HL of the test samples with and without capsules was measured based on a cyclic process of 3-steps that includes: I) sample conditioning at -5°C for 2 hours, Figure 2(a), II) tensile fracture at a loading speed of 5 mm/min, Figure 2(b), and Figure III) the healing process of the fractured pieces thermally conditioned at 20°C for healing time of 6 and 24 hours, Figure 2(c). After healing, steps I and II were repeated, determining the HL as the ratio between the maximum forces resisted by a test sample before and after the healing process, respectively. The Effective Healing Level (EHL) has been calculated by subtracting the HL of samples without capsules from the average HL obtained from those with capsules.
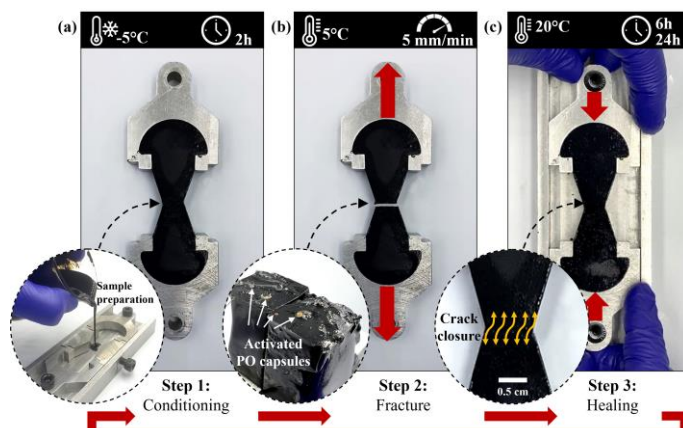
Figure 2. Healing test method on bitumen samples considering the steps of (a) Conditioning, (b) Fracture, and (c) Healing.

After tests, statistically significant differences in morphological, physical, and mechanical properties

were assessed using Analysis of Variance (ANOVA) at a 95% significance level (α = 0.05) and Tukey's pairwise mean comparisons.

3 RESULTS AND DISCUSSION

3.1 *Effect of the PLR dosage on the rheological response of PAV-aged bitumen*

The |G*| and δ master curves for all asphalt binders are presented in Figure 3 and Figure 4, respectively. Regarding |G*| master curves, they show increased stiffness for all frequencies as the bitumen is subjected to ageing. The |G*| master curve for the RAP is even stiffer than the PAV one, indicating that the recovered binder had a degree of ageing superior to the one simulated by the PAV procedure. Applying PLR to the RAP binder diminished its stiffness, with higher PLR doses resulting in lower stiffness.
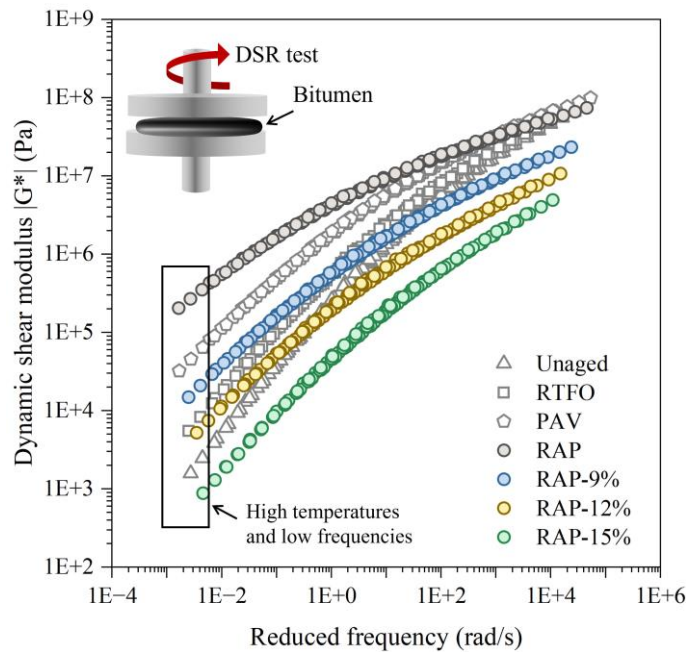
Figure 3. Average master curve of |G*| for the asphalt binders with and without PLR.

Dosages of 9% and 12% by weight of binder (RAP-9% and RAP-12%) resulted in stiffnesses at low frequencies (high temperatures) similar to those observed in the RTFO and unaged binders, respectively. The effect at higher frequencies (lower temperatures) was more pronounced, achieving lower |G*| values than the unaged binder at those conditions, which is beneficial for lowering the susceptibility to cracking. Figure 4 displays the δ master curves. The viscous part decreases when the asphalt binder is subjected to ageing through RTFO and PAV.
Compared with the PAV one, the RAP binder's higher ageing level is confirmed by its lower δ value at all frequencies. The rejuvenating effect of the PLR is less significant in δ than in |G*|. A dosage of 9% brings the RAP binder only to δ levels similar to a PAV binder. With a 15% dose, the δ values are returned to

levels similar to those of an RTFO, but the viscous part is not recovered to levels comparable to those of the unaged binder, except at the highest frequency range.
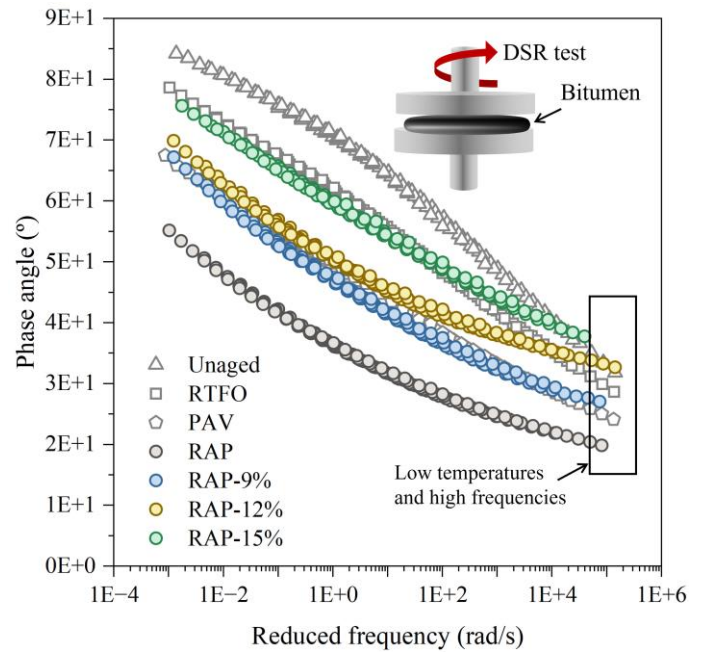
Figure 4. Average master curve of δ for the asphalt binders with and without PLR.

3.2 *Effect of the BPC addition on the self-healing properties of aged bitumen*

Figures 5 and 6 show the average HL and EHL results for the PAV samples with BPCs at temperatures of 20 and 25ºC, respectively. Overall, results show that the HL in the PAV samples increased with the capsule addition and healing time. When evaluating only the effect of the temperature, ANOVA revealed statistically significant differences at 20°C (HL: 46.9%) and 25°C (HL: 52.8%).
In term of healing time, the ANOVA showed statistically significant differences (p-value < 0.05) for 6 hours and 24 hours, with average HL values of 35.7% and 64.0%, respectively. Furthermore, when evaluating only the effect of capsule content on healing level, ANOVA followed by Tukey's mean comparison analysis revealed statistically significant differences for each capsule content, with average values of 33.7%, 42.9%, 58.4%, and 64.4% for capsule contents of 0%, 0.5%, 1%, and 2%, respectively. As a result, the self-healing properties of crack-damaged bituminous materials were enhanced at higher healing temperatures (25°C), extended healing times (24 hours), and increased capsule dosages (2% by weight).
Furthermore, to evaluate the pure effect of the capsules, Figures 5 and 6 show the EHL above each bar (see % values in bars). In this regard, it is concluded that these healing levels depended on the percentage of capsules and the healing times. For example,

capsule contents of 1% or higher and healing times of 24 hours resulted in HL above 30%. Specifically, for 24 hours and 20°C, a capsule content of 1% resulted in a 44.5% increase. Since no statistically significant differences were observed between 1% and 2% capsule content, it is possible to conclude that a capsule content of up to 1% optimised the capsule dosage to achieve a high healing level. Future research will explore the physical, mechanical, and self-healing properties of recycled asphalt mixtures containing 1% capsule content.
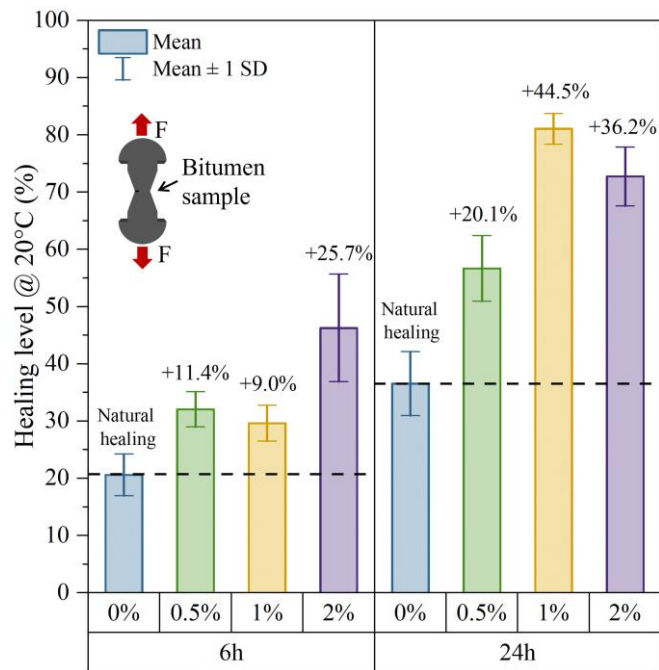
Figure 5. Average results of healing level for the bitumen samples depending on the capsule dosage (0%, 0.5%, 1%, 2% wt.) and healing time (6 h, and 24 h) at 20°C.
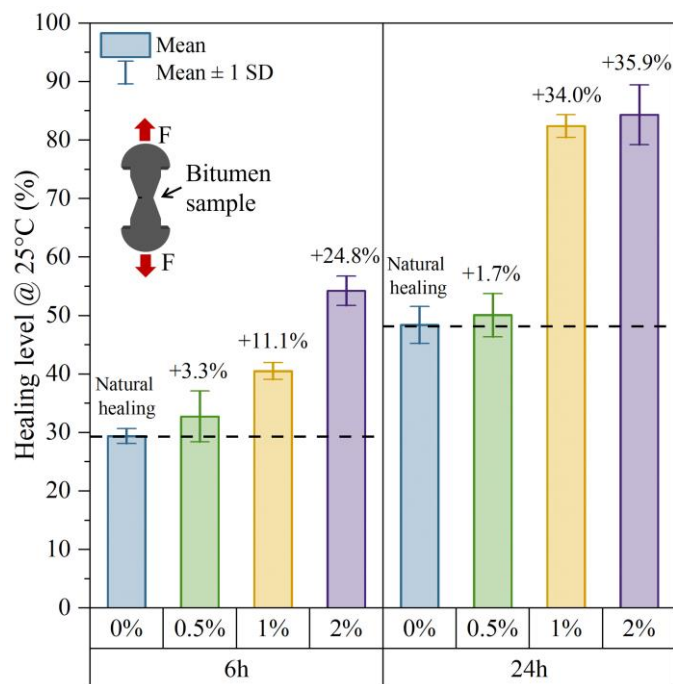
Figure 6. Average results of healing level for the bitumen samples depending on the capsule dosage (0%, 0.5%, 1%, 2% wt.) and healing time (6 h, and 24 h) at 25°C.

4 CONCLUSIONS

The following conclusions can be established:

- The Pyrolytic Liquid Rejuvenator (PLR) based on waste tyres successfully rejuvenated the rheological properties of the RAP asphalt binder.
- The rejuvenating effect was more significant on the |G*|, achieving stiffnesses like an unaged binder with dosages of 15% PLR by weight of the binder. For δ, the same dosage achieved rejuvenating effects similar to an RTFO asphalt binder.
- Additionally, the Healing Levels (HL) values depended on the percentage of Biopolymeric Polynuclear Capsules (BPCs) added to the PAV binder and healing times.
- As no statistically significant differences were observed between 1% and 2% capsule contents for a 24-hour healing time, the study recommends a capsule content of 1% to achieve an Effective Healing Level (EHL) of 44.5% in PAV binders.

5 ACKNOWLEDGMENTS

6 REFERENCES

ASTM D 2872-19. Standard Test Method for Effect of Heat and Air on a Moving Film of Asphalt (Rolling Thin-Film Oven Test), West Conshohocken, PA, USA, 2019.

ASTM D6521-19. Standard Practice for Accelerated Aging of Asphalt Binder Using a Pressurized Aging Vessel (PAV), West Conshohocken, PA, USA, 2019.

ASTM D2172/D2172M. Standard Test Methods for Quantitative Extraction of Asphalt Binder from Asphalt Mixtures, West Conshohocken, PA, USA, 2024.

ASTM D 5404/D 5404M Standard Practice for Recovery of Asphalt Binder from Solution Using the Rotary Evaporator.

Chávez-Delgado, M., Colina, J. R., Segura, C., Álvarez, C., Osorio-Vargas, P., Arteaga-Pérez, L.E., Norambuena-Contreras, J. 2024. Asphalt pyro-rejuvenators based on waste tyres: An approach to improve the rheological and self-healing properties of aged binders. *Journal of Cleaner Production* 452, 142179.

Gonzalez-Torre, I., Norambuena-Contreras, J. 2020. Recent advances on self-healing of bituminous materials by the action of encapsulated rejuvenators. *Construction and Building Materials* 258, 119568.

Loise, V., Calandra, P., Abe, A.A., Porto, M., Oliviero Rossi, C., Davoli, M., Caputo, P. 2021. Additives on aged bitumens: What probe to distinguish between rejuvenating and fluxing effects?. *Journal of Molecular Liquids* 339, 11674.

Norambuena-Contreras, J., Arteaga-Pérez, L. E., Concha, J. L., Gonzalez-Torre, I. 2021. Pyrolytic oil from waste tyres as a promising encapsulated rejuvenator for the extrinsic self-healing of bituminous materials. *Road Materials and Pavement Design* 22, 117-133.

Zaumanis, M., Mallick, R. B., Frank, R. 2014. 100% recycled hot mix asphalt: a review and analysis. *Resources, Conservation and Recycling* 92, 230–245.

Assessing repeated recycling capacity of 100% RAPM binder using mustard oil

P. Rai, P. Kumar, & N. Saboo
Indian Institute of Technology Roorkee, Uttarakhand, India, 247667

ABSTRACT: This study evaluates the effectiveness of mustard oil (MO) in restoring the properties of a 60 h PAV aged binder across multiple recycling cycles. Two recycling cycles were conducted with 100% aged binder, and the changes in rheological and performance characteristics were assessed using Dynamic Shear Rheometer (DSR). Results indicated that MO effectively restores binder properties in the first recycling cycle (FRC); however, complete restoration in the second cycle (SRC) is not achievable with the same dosage. This indicates a diminishing effectiveness of mustard oil (MO) with successive recycling cycles. Additionally, MO-rejuvenated binders demonstrated reduced sensitivity to re-aging and subsequent re-rejuvenation. LAS test results confirmed that fatigue resistance can be sustained even after multiple aging and recycling cycles. Overall, the findings suggest that while RAPM can be recycled multiple times, selecting an appropriate rejuvenator is essential for restoring and maintaining binder performance across successive cycles to ensure sustainable pavement solutions.

1 INTRODUCTION

Asphalt mixtures used in road construction have a limited lifespan, primarily influenced by factors like traffic, environmental conditions, natural aging, etc. Consequently, it becomes necessary to replace or rehabilitate these mixtures after a certain period, leading to the generation of large quantities of reclaimed asphalt pavement materials (RAPM). Since this material is produced after its first use, it is referred to as first-generation RAPM. Many pavements have been and are still being constructed using this first-generation RAPM, either with or without the addition of rejuvenating agents (RAs). As these pavements approach the end of their service lives, their maintenance and rehabilitation will result in the large quantity of waste materials termed as second generation RAPM. Recycling these second-generation RAPM and furthermore generations is known as re-recycling or repeated recycling. It supports environmental and economic sustainability by reducing land pollution, carbon footprint, conserving natural resources (virgin aggregates and bitumen), and lowering construction and maintenance costs.

Although re-recycling is essential for sustainable pavement practices, re-recycled pavements (constructed with second-generation RAPM) must demonstrate performance equal to or better than conventional pavements to justify widespread adoption. The primary concern with the re-recycled RAPM is the cumulative aging process, which leads to increased stiffness and greater susceptibility to cracking. This increased stiffness limits the interaction between aged binders and RA, making it diffi-cult for RA to fully restore the binder's original properties, thereby making it unsuitable for repeated recycling processes. To address these concerns, efforts have been made to evaluate the feasibility of repeated recycling and its impact on RAPM performance.

In 1995, Yoshikane introduced the use of second-generation RAPM and evaluated the performance of re-recycled RAPM through 15-year field investigation (Yoshikane 1995). The study found that re-recycled RAPM performed satisfactorily compared to single-recycled RAPM and conventional HMA, demonstrating that re-recycling of RAPM is a feasible and effective option. Similarly, Petho and Denneman (2016) concluded that RAPM can be re-cycled multiple times without compromising the performance. However, Kriz et al. (2017) concluded that the virgin binder type, a high recycling rate, and type of RAs might reduce the number of viable cycles significantly and thus make recycling unsustainable in the future. Further, Koudelka et al. (2019) used a variety of rejuvenators to restore the properties of first and second generation RAPM and found that most rejuvenated asphalt blends in the second cycle of rejuvenation did not meet the performance requirements. Additionally, Rodrigues et al. (2024) investigated the effects of repeated recycling on the fatigue and rutting resistance of asphalt binders, focusing on how multiple cycles influence their performance characteristics. The findings indicated that asphalt binders could be effectively re-recycled up to three cycles while maintaining satisfactory performance.

Most of the previous studies have primarily focused on the single recycling of RAPM in HMA, with or without recycling agents. These studies concluded that some RAs are effective in preserving the performance of recycled asphalt binder after a single reuse (Koudelka et al. 2019, Rai et al. 2024). However, there is still the issue of the effectiveness of RAs in allowing repeated recycling processes without compromising the performance. Repeated recycling of RAPM is not common, and limited research and information are available on this topic. Therefore, the role of RAs in restoring the characteristics of RAPM over multiple recycling cycles must be evaluated.

The objective of this study was to evaluate the effectiveness of mustard oil (MO) as a RA in restoring the properties of RAPM across multiple recycling cycles. Two recycling cycles were performed with 100% RAPM content, and the changes in rheological and performance characteristics were assessed using Dynamic Shear Rheometer (DSR) testing.

2 MATERIALS AND METHODS

2.1 *Materials*

The asphalt binder used in this study was VG30 with penetration of 45dmm and softening point of 52.3°C. Its performance grade was PG 70-XX. Mustard oil (MO), derived from mustard seeds, was used as the RA. MO used in this study was obtained locally from a grocery store. The density and viscosity (at 60°C) of MO was found to be 0.92 g/cm³ and 40.12 cP, respectively.

2.2 *Methods*

2.2.1 *Experimental process design*
Asphalt binder was aged in the laboratory and then rejuvenated using MO. The rejuvenated asphalt binder was then re-aged and re-rejuvenated again. This process continued for two cycles of aging and rejuvenation, as shown in the flow diagram in Figure 1. Comprehensive rheological tests, including frequency sweep (FS), true high fail temperature (TFT), multiple stress creep and recovery (MSCR), and linear amplitude sweep (LAS) were conducted using a DSR to thoroughly assess the performance of asphalt binder after each aging and rejuvenation cycle. The results were then analyzed to evaluate the changes in the rheological and performance characteristics at all the selected MO dosages.

2.2.2 *Aging and rejuvenation procedure*
The asphalt binder was short-term aged in the laboratory using universal simple aging test (USAT) at

150°C for 50 mins. The residue was subsequently subjected to pressure aging vessel (PAV) at 110°C and 2.1 MPa for 60h. For long-term aging, instead of standard aging time of 20h, 60h was adopted to replicate severely aged binder in tropical countries (Rai et al. 2024). The binder obtained after the first aging cycle (FAC) is called as the first generation of RAPM binder, labelled as RAP[1]. The first recycling cycle (FRC) involved mixing of RAP[1] with MO at three dosages: 10%, 20%, and 30% by weight of the aged binder. The mixture was blended for 15 minutes at a speed of 700-1000 rpm. The resulting binders were labelled RAP[1] + 10%, RAP[1] + 20%, and RAP[1] + 30%, respectively. Following this, the optimal MO dosage (30%) was determined using a rational procedure, the details of which can be found elsewhere (Rai et al. 2024). The first rejuvenated binder (FRB) was prepared by incorporating the optimal MO dosage in RAP[1]. The FRB underwent second aging cycles (SAC) to generate the second generation of RAPM (RAP[2]). Subsequently, it was subjected to second recycling cycles (SRC) to produce the second rejuvenated binder (SRB). The aging and rejuvenation process in the second cycle was kept similar to the first cycle.
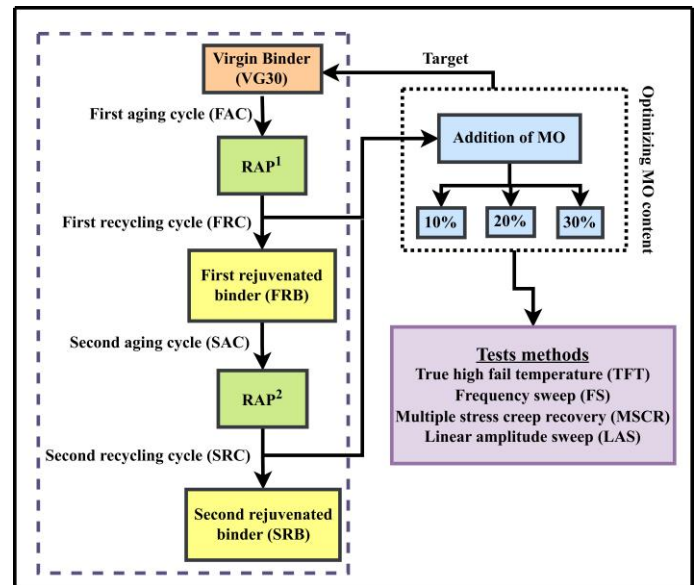
Figure 1. Design methodology and experimental plan

3 RESULTS AND DISCUSSIONS

3.1 *True high fail temperature (TFT)*

Figure 2 illustrates the TFT of aged and rejuvenated asphalt binders obtained for FRC and SRC. In the first cycle (FAC + FRC), Figure 2(a) shows that the TFT of VG30 increased by approximately 51% after aging, indicating significant stiffening of asphalt binder. Following rejuvenation, the binder softened, and the TFT decreased. At FMO dosage of around

30%, the TFT of rejuvenated binder closely aligned with that of VG30, suggesting effective restoration during FRC.

In the second cycle (SAC + SRC), a similar trend was observed: aging increased the TFT, while rejuvenation reduced it. However, during SAC, 42.3% increase in the TFT was observed, which is notably lower than the increase observed in the FAC. This indicates that the stiffness of RAP[2] was significantly lower than that of RAP[1], demonstrating that the presence of MO slowed down the aging process.

Although RAP[2] exhibited lower stiffness than RAP[1], the 30% dosage of MO used in the SRC was insufficient to fully restore the binder property of RAP[2] (to match with VG30). This suggests that higher dosages or alternative rejuvenators may be required for further recycling cycles. Therefore, the concept that less stiffened binder required low rejuvenator dosages is not valid for repeated aging and recycling process. This conclusion is based on the selected RA and the aged binder used in this study. However, further research is necessary to validate these findings and explore their applicability across a broader range of aging conditions, binder types, and RA types.

To determine the exact dosages required to achieve comparable properties, a plot of TFT versus MO content was generated as shown in Figure 2(b) for both recycling cycles. The linear regression equations, shown in the graphs for each cycle, were then used to calculate the required dosage. The results indicate that during the FRC, a dosage of approximately 33% MO was sufficient to restore the TFT similar to VG30. However, in the SRC, a substantially higher dosage of around 62% was necessary to achieve similar TFT. This significant increase in the required dosage underscores the reduced effectiveness of MO in second recycling cycles. This may be due to reduced binder reactivity, attributed to re-aging or the reduced capacity of the MO to diffuse and soften the RAP[2].
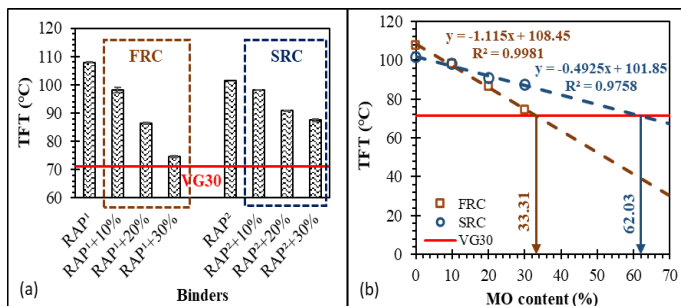
3.2 Complex modulus (G*) master curve

For the first cycle, as shown in Figure 3, it was observed that after aging, the G* of asphalt binder increased significantly. After rejuvenation, the binder softened, and the value of G* reduced in the entire domain of reduced frequency. However, the reduction in G* due to rejuvenation was found to be more prominent at lower reduced frequencies. It can also be observed that none of the rejuvenated binder master curves exactly match the virgin binder master curve. As observed, aligning the G* curve of rejuvenated binders in the low-frequencies range (corresponding to high temperatures) can result in a lower G* value compared to virgin binders in the high-frequencies range (corresponding to lower temperatures). This indicates that rejuvenated binders exhibit reduced stiffness at lower temperatures while maintaining comparable or improved stiffness at higher temperatures. In other words, the rejuvenation process enhances the low-temperature performance of the aged asphalt binder. Similar trends have been reported in a previous study (Hugener and Kawakami 2017).

In the second cycle, as shown in Figure 3, complex modulus (G*) increased after aging and reduced after rejuvenation, following trends similar to the first cycle. The increase in stiffness due to aging was lower in the second cycle compared to the first, suggesting that the binder became more resistant to aging-induced stiffening. Despite this, MO effectively softens the binder, as evidenced by the reduction in G* with increase in dosage. However, the differences in the G* master curves across various rejuvenator dosages were less pronounced, particularly in the lower frequencies range, indicating reduced sensitivity of the asphalt binder to rejuvenation. Furthermore, rejuvenated binders exhibit lower values of G* at higher frequencies and higher values at lower frequencies, compared to VG30. This indicates that MO (up to 30%) was unable to fully restore the stiffness characteristics of the rejuvenated binder, particularly in the low-frequencies domain.

Figure 2. (a) TFT of aged and rejuvenated binder, (b) Linear regression of TFT versus MO dosage for FRC and SRC.
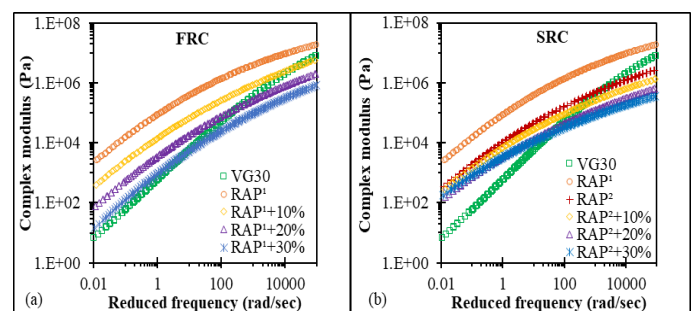
Figure 3. Complex modulus (G*) master curve at 60 °C for (a) FRC (b) SRC

3.3 Rutting and fatigue performances

The MSCR test was conducted at 60°C to evaluate the rutting performance, while the LAS test was performed at 20°C to assess the fatigue characteristics of the asphalt binders. Non-recoverable creep compliance (J_{nr}) and fatigue life (N_f) were the primary parameters obtained from these tests. Lower Jnr and higher N_f values indicate better rutting and fatigue resistance in the binder. Previous studies have suggested that Jnr at a stress level of 3.2kPa ($J_{nr,3.2}$) and fatigue life at 5% strain ($N_{f,5}$) may be used to study the effects of aging and rejuvenation process. The results obtained in this study are shown in Figure 4.

Figure 4 (a) shows the $J_{nr,3.2}$ values for the virgin binder and rejuvenated binder after each aging and rejuvenation cycle. Aging reduces $J_{nr,3.2}$, indicating improvement in the resistance to rutting. Conversely, adding MO increases $J_{nr,3.2}$, thus softening the binder. The increase in $J_{nr,3.2}$ with the increase in MO content in FRC was more prominent than SRC. In FRC, MO successfully restored $J_{nr,3.2}$ of aged binder to similar level of VG30 at 30% MO dosage. However, in the SRC, the same dosage was insufficient to achieve a comparable $J_{nr,3.2}$ indicating a diminished rejuvenation effect in subsequent cycles. This reduction in effectiveness could be attributed to MO's inability to significantly reduce the G* of RAP[2] up to the 30% dosage, as discussed in the previous section.

Figure 4 (b) shows that the fatigue life of the binder decreased after aging but improved with the incorporation of MO in both recycling cycles. All rejuvenated binders exhibited greater fatigue resistance than the virgin binder in both cycles. However, the reduction in fatigue life after FAC was more significant compared to SAC, indicating that MO also acts as an anti-aging agent. Additionally, the fatigue life of the binders increased progressively with successive recycling cycle. The improvement was attributed to the lower G* of rejuvenated binder compared to VG30 at lower temperatures, as discussed in section 3.2.
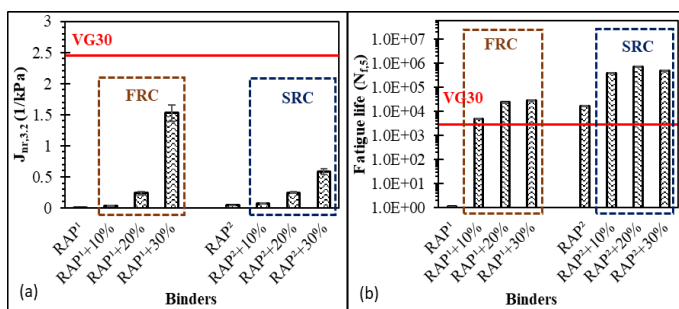
4 CONCLUSIONS

Based on the test results, the following conclusions can be drawn.

- MO is effective in restoring the original properties of the aged binder during the FRC, its effectiveness significantly diminishes with subsequent aging and recycling, requiring higher MO dosages in SRC.
- High temperature performances can be recovered during FRC but recovery during SRC using similar dosage is not achievable.
- The MO rejuvenated binder appeared to be less sensitive to both re-aging and the subsequent re-rejuvenation process, as seen by the lesser increase and decrease in stiffness caused by aging and rejuvenation in the second cycle compared to the first cycle.
- The LAS test result indicates that fatigue resistance can be maintained even after multiple aging and recycling cycles. Moreover, the fatigue life of the binders progressively improved with each successive recycling cycle.
- Overall, RAPM can be recycled multiple times, but selecting the right rejuvenator is essential for restoring and maintaining its performance.

5 REFERENCES

Hugener, M., and A. Kawakami. 2017. "Simulating repeated recycling of hot mix asphalt." *Road Mater Pavement Des*, 18 (May): 76–90. https://doi.org/10.1080/14680629.2017.1304263.

Koudelka, T., P. Coufalik, J. Fiedler, I. Coufalikova, M. Varaus, and F. Yin. 2019. "Rheological evaluation of asphalt blends at multiple rejuvenation and aging cycles." *Road Mater Pavement Des*, 20 (sup1): S3–S18. https://doi.org/10.1080/14680629.2019.1588150.

Kriz, P., B. J. Tardiff, S. R. S. Maria, and R. D. Shirts. 2017. "Asphalt Re-recycling." *Can Tech Asph Assoc*.

Petho, L., and E. Denneman. 2016. "Maximising the Use of Reclaimed Asphalt Pavement in Asphalt Mix Design Field Validation". *Austroads Research Report AP-R517-16*.

Rai, P., P. Kumar, and N. Saboo. 2024. "Effectiveness of rejuvenating agents (RAs): Analysis of mechanical restoration and long-term aging effects." *Constr Build Mater*, 456 (July): 139308. Elsevier Ltd. https://doi.org/10.1016/j.conbuildmat.2024.139308.

Rodrigues, J. A., K. L. Vasconcelos, A. E. Martin, E. Arámbula-Mercado, and E. Masad. 2024. "Effects of multiple recycling on the performance characteristics of asphalt binder using different recycling agents." *Road Mater Pavement Des*, 25 (8): 1680–1693. https://doi.org/10.1080/14680629.2023.2268744.

Yoshikane, T. 1995. "Investigation of deterioration of recycled hot-mixed asphalt concrete pavement and a trial rerecycling of asphalt concrete." *Dispos Recycl Org Polym Constr Mater Proc*, 27: 210–221.

Figure 4. (a) Rutting resistance and (b) fatigue life of asphalt binders during repeated aging and recycling cycles

Postcarbone road: Limits and possibilities of cyclic bitumen rejuvenation

S.A. Schröder & S. Weigel
Federal Institute for Materials Research and Testing, Berlin, Germany

N. Nytus, J. Dominik & M. Radenberg
Ruhr-Universität Bochum, Bochum, North Rhine-Westphalia, Germany

K. Schwettmann, M. Cheng & D. Stephan
Technische Universität Berlin, Berlin, Germany

ABSTRACT: In road construction, the reuse of reclaimed asphalt depends on the addition of large quantities of fresh binder. Bio-based rejuvenators can represent a sustainable alternative to this, but their performance concerning multiple reuses has yet to be investigated. For this study, fresh 50/70 bitumen was subjected to up to four ageing and rejuvenation cycles using eight commercially available rejuvenators (five bio- and three petroleum-based). The rheological and chemical evaluation of the raw materials and resulting products was carried out using a dynamic shear rheometer and Fourier transform infrared spectrometer. Through examination of the infrared spectra, the rejuvenators were divided into three groups based on similar chemical composition. Further, evaluated optimum dosage quantities required to rejuvenate aged binder indicate that bio-based rejuvenators are more resource-efficient than their petrol-based counterparts. Finally, a most promising bio-based rejuvenator candidate was found, allowing up to four reuse cycles.

1 INTRODUCTION

Like any organic construction material, asphalt is subject to natural deterioration processes, which affect its performance in the long term. Particularly when used as a road pavement, asphalt can experience a comparatively rapid deterioration in material properties, especially with high traffic volumes and harsh weather conditions. The maximum service life of asphalt pavements in Germany is therefore set at 30 years, depending on the type of use (FGSV, 2012). While in the distant past, most reclaimed asphalt pavement (RAP) was sent to landfill, the scarcity of resources during the oil crisis in the 1970s led to an increase in the reuse of RAP for road construction (Copeland, 2011). Nowadays, the use of RAP is well established in Germany, with around 87 % of reclaimed asphalt being reused in 2022 (EAPA, 2022).

By using rejuvenators, it is possible to counteract the effects of ageing in RAP by restoring specific performance properties. Rejuvenators make the binder softer, more flexible, less brittle, and partially restore the original viscoelastic structure of the aged asphalt (Shen et al., 2007). Various petrol-based rejuvenators have been intensively investigated in recent decades to optimise their effectiveness in recycling processes (Carey and Paul, 1980, NMT, 1985, Behnood, 2019). They mainly replenish fractions lost due to the ageing process. In contrast, biobased rejuvenators are said to change the chemical properties of the old binder, making them even more effective (Fang et al., 2021).

Considering the increasing shortage of primary resources, especially crude oil, and concerning sustainability, bio-based rejuvenators could be seen as a game changer for sustainable road construction. However, this raises the question of where the limits lie for rejuvenators. Asphalt has been systematically reused in Germany since the late 1970s (DAV, 2011). As a result, more and more RAP containing recycled materials are being produced. In the future, we will face the challenge of using RAP after multiple reuse cycles. Particularly regarding successive cycles of paving, ageing, and rejuvenation of the asphalt, it must be clarified whether rejuvenators can meet the requirements from a chemical and rheological viewpoint without any performance loss. In addition, it must be clarified how often this cycle can be repeated and whether endless reuse is possible (Schwettmann et al., 2023).

The project "Postcarbone road - The endless cycle of bitumen reuse" has provided the basis for clarifying this topic by investigating the impact of eight different rejuvenators on three partly cyclically aged bitumen of the 50/70 grade. By using a dynamic shear rheometer (DSR) and Fourier transform infrared spectroscopy (FTIR), for instance, it was possible to gain insights from a rheological and chemical

perspective into which factors limit endless rejuvenation of bitumen.

The following article presents some of the project's findings regarding the effects and efficiency of rejuvenators on bitumen and the limits of multiple reuses. Furthermore, a brief insight is given into the follow-up project "Postcarbone road - The endless cycle of asphalt reuse."

2 MATERIALS AND METHODS

2.1 *Materials*

The exemplary results presented in this article include investigations on paving grade bitumen 50/70 and eight commercially available rejuvenators (R1-R8). The rejuvenators R2, R6, and R7 are petroleum-based, whereas the rejuvenators R1, R3, R4, R5, and R8 are bio-based and, according to the manufacturers, were obtained from sustainable raw materials.

2.2 *Aging and rejuvenation*

Based on preliminary investigations, a program was selected for artificial ageing, according to which the rheological properties of the aged binder are comparable to those of RAP (Schwettmann et al., 2022). This involved short-term ageing using the rolling thin oven test (RTFOT) according to EN 12607-1 (CEN, 2015) and 2x long-term ageing using a pressure aging vessel (PAV) according to EN 14769 (CEN, 2023a). For rejuvenation, the bitumen was first heated to 160 °C and then added under constant stirring using a flight wheel mixer. After adding the rejuvenator, stirring continued for another 10 min. Single aging and rejuvenation was carried out with R3, R4, R6, and R7. Cyclic rejuvenation was simulated with R1, R2, R5, and R8.

2.3 *Rheological investigations*

The rheological investigations of the samples were carried out using a DSR according to EN 14770 (CEN, 2023b). The calculated optimal dosages of the rejuvenators were determined using the equi-stiffness temperature $T(|G*|=15$ kPa$)$, whereby the target values corresponded to the properties of fresh bitumen (Radenberg et al., 2021).

2.4 *Chemical characterization*

The chemical characterisation of the samples was carried out through FTIR using the attenuated total reflectance (ATR) technique equipped with a zinc selenide (ZnSe) crystal (25x reflection). For the measurement, the samples were previously dissolved in a mass ratio of 1:3 with cyclohexane, applied to the ZnSe crystal, and then the solvent was allowed to evaporate for at least 15 min. For each sample, 32 scans were performed, with a spectral wavenumber range of 4000 cm⁻¹ to 600 cm⁻¹ and a resolution of 4 cm⁻¹. The resulting reflectance spectra were then converted to absorbance spectra, standardised using standard normal variate (SNV) transformation and averaged.

3 RESULTS AND DISCUSSION

3.1 *Impact and functionality of rejuvenators on bitumen*

The project aimed to investigate the possibilities of cyclic reuse of bitumen at the binder level. Initially, the first characterisation of the eight selected rejuvenators was carried out using FTIR spectroscopy. This revealed that the rejuvenators could be divided into three groups based on their distinct chemical composition (Figure 1) (Schwettmann et al., 2020): The biobased rejuvenators (R1, R3, R4, R5, R8) can be divided into two groups based on the FTIR spectra (Figure 1(a) and (b)), indicating two different groups of sources. Within the groups, however, the sources of the rejuvenators appear to be similar. In contrast, the petroleum-derived rejuvenators R2, R6, and R7 show more bitumen-like FTIR spectra (Figure 1(c)).
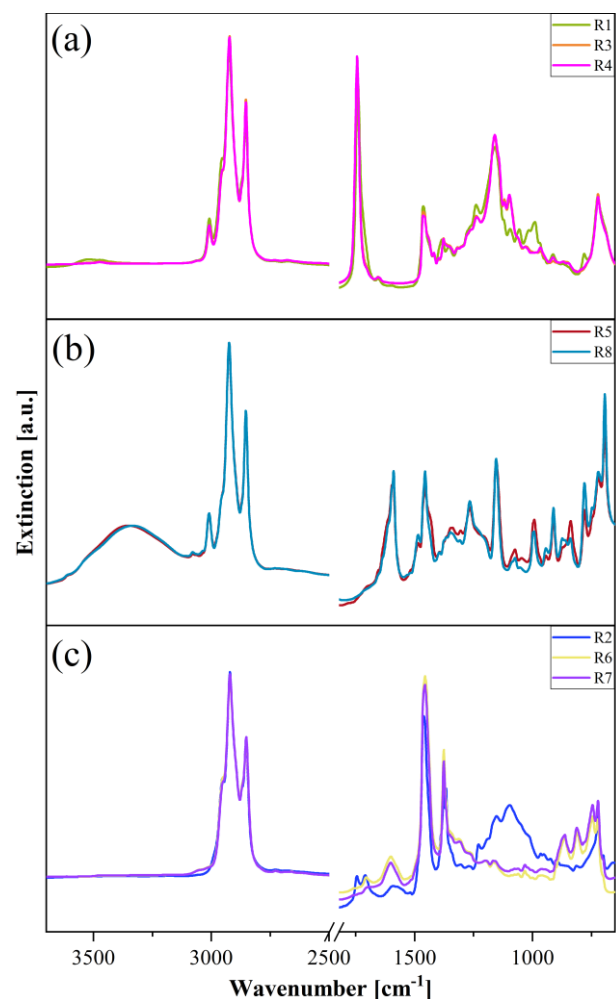
Figure 1. SNV-standardised FTIR spectra of the rejuvenators used: (a) R1, R3, R4 and (b) R5, R8 biobased rejuvenators; (c) R2, R6, R7 petroleum-derived rejuvenators.

The separation of the bio-based rejuvenators into two groups is also evident in the effects of the rejuvenators on the rheology of the fresh 50/70 bitumen. DSR investigations of the bitumen-rejuvenator mixtures show viscoelastic properties that can be attributed to the distinct chemical composition of the rejuvenators. While the addition of R1, R3, and R4 only caused a decrease in the equi-shear modulus temperature, an additional increase in the phase angle can be recorded for R5 and R8.

Regarding the estimation of the rejuvenators' efficiency, further rheological tests were carried out to investigate the required optimum dosage of the rejuvenators. For the aged bitumen, the optimum rejuvenator dosage rates required to achieve the complex shear modulus of an unaged 50/70 bitumen were calculated. This was done using the equi-shear modulus temperatures based on the results of the temperature sweep (T-sweep) over a temperature range of -20 to 150 °C (Figure 2). This made it possible to determine the required dosage of the rejuvenators for the relevant temperature range of -20 to 40 °C (Radenberg et al., 2021). In general, the required dosage for all rejuvenators increases with increasing temperature from -20 to 40 °C but remains virtually constant beyond this point. However, individually, the dosage quantities vary considerably. While the bio-based rejuvenators with a dosage of up to approx. 15 wt.-% manage to achieve the performance of fresh bitumen, the petroleum-based rejuvenators R2, R6, and R7 with a dosage of around 20, 40, and 50 wt.-% are severely limited regarding individual resource efficiency.
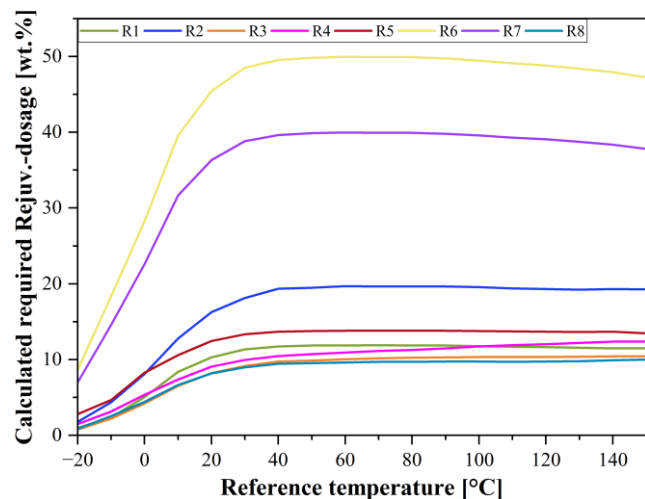
Figure 2. Calculated optimal dosages of rejuvenators R1 to R8 depending on the respective reference temperature for a 50/70 bitumen (bio-based: R1, R3, R4, R5, R8; petroleum-based: R2, R6, R7).

3.2 Multiple reuses of bitumen and its limitations

The Black diagram in Figure 3 illustrates the changes in the equi-shear modulus temperature T(G*= 15 kPa) and the corresponding phase angle δ for four rejuvenation cycles using R8. The diagram visualis-

es how the rheological properties of the bitumen-rejuvenator mixture change through successive ageing and rejuvenation: As the number of cycles increases, the viscoelastic deformation components gradually shift towards the elastic component. After the fourth ageing cycle, the phase angle is significantly reduced, and almost no change can be achieved even through subsequent rejuvenation. Due to the low phase angle and high equi-shear modulus temperature, the reuse of the binder is no longer possible without problems.
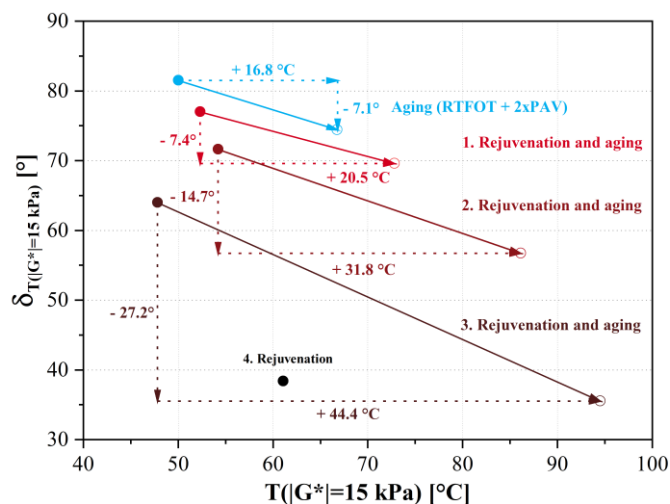
Figure 3. Change in rheological properties in the various reuse cycles exemplified for the bio-based rejuvenator R8 and a 50/70 bitumen.

The limits of reuse also become apparent visually. Figure 4 shows an example of observable phase separation of the bitumen-rejuvenator mixtures (critical state), which occurred at the latest after four rejuvenation cycles and subsequent ageing.
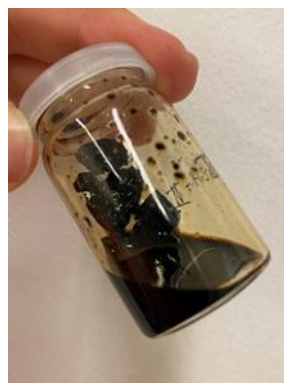
Figure 4. Image of a heterogeneous bitumen sample dissolved in cyclohexane.

In general, the chemical analyses indicate no reactions between the rejuvenators and the bitumen. Figure 5 compares exemplarily the FTIR spectra of the pure R8, the fresh bitumen C, and the respective bitumen-rejuvenator mixture after three reuse cycles. Only mixing between the bitumen and the rejuvenator occurred, which resulted in the FTIR spectrum of the bitumen becoming more similar to that of the pure rejuvenator after each new rejuvenation step.
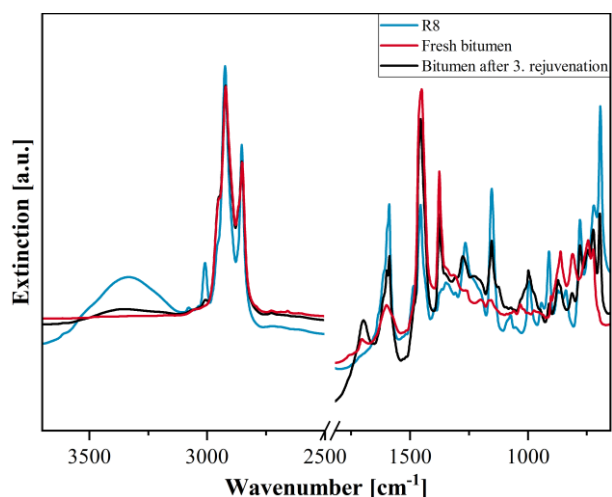
Figure 5. SNV-standardised FTIR spectra of the bio-based rejuvenator R8, fresh 50/70 bitumen, and 50/70 bitumen after the third rejuvenation cycle.

3.3 *Multiple reuses of asphalt*

In the follow-up project, "Postcarbone road - The endless cycle of asphalt reuse," the identified limits will be resolved or shifted. To this end, the bio-based rejuvenator will be specifically modified so that the bitumen can undergo more than four reuse cycles. The rejuvenator's impact will be investigated at the binder, mastic, and asphalt levels. On the asphalt level, the adhesion behaviour, and the degree of mixing between the binder and rejuvenator will also be considered, whereby the development of two novel method concepts based on FTIR spectroscopy is planned for the latter. The results of this project are intended to show a fundamental way of realising endless or rather multiple reuses of asphalt by rejuvenators.

4 SUMMARY

The exemplary results of the project "Postcarbone road - The endless cycle of bitumen reuse" presented in this article are intended to show the possibilities of cyclic reuse of asphalt at the binder level. Based on chemical and rheological investigations, it was shown that bio-based rejuvenators are the most promising candidates for this task. A rejuvenator was identified that requires low dosages on the one hand and enables up to four rejuvenation cycles on the other hand. In the follow-up project, the "Postcarbone road - The endless cycle of asphalt reuse", the knowledge gained will now be transferred to the asphalt level.

5 FUNDING

6 REFERENCES

EAPA, 2022. *Asphalt in Figures.* Available at: https://eapa.org/asphalt-in-figures-2022-view/.

Behnood, A. 2019. Application of rejuvenators to improve the rheological and mechanical properties of asphalt binders and mixtures: A review. *Journal of Cleaner Production,* 231**,** 171-182.

DOTD, 1980. *Effects of asphalt cement rejuvenating agents.* Available at: https://rosap.ntl.bts.gov/view/dot/21944.

R&D, 2011. *Reclaimed Asphalt Pavement in Asphalt Mixtures: State of the Practice.* Available at: https://highways.dot.gov/media/841.

DAV, 2011. *Recycling of Asphalt.* Available at: https://www.asphalt.de/fileadmin/user_upload/International Publications/2011_recycling_of_asphalt.pdf.

Fang, Y., Zhang, Z., Yang, J. & Li, X. 2021. Comprehensive review on the application of bio-rejuvenator in the regeneration of waste asphalt materials. *Construction and Building Materials,* 295.

FGSV, 2012. *Richtlinien für die Standardisierung des Oberbaus von Verkehrsflächen*. Cologne: FGSV.

NMT, 1985. *Recycling Agent Selection and Tentative Specification.* Available at: https://apps.dtic.mil/sti/tr/pdf/ADA153529.pdf. Radenberg,

M., Nytus, N., Stephan, D. & Schwettmann, K. 2021. Bestimmung der optimalen Dosierung und Wirksamkeit. *Asphalt,* 2**,** 8.

Schwettmann, K., Nytus, N., Radenberg, M. & Stephan, D. 2022. Bitumen reuse: physical and chemical approach to investigate the effectiveness of rejuvenators. *Road Materials and Pavement Design,* 24**,** 1130-1157.

Schwettmann, K., Nytus, N., Weigel, S., Radenberg, M. & Stephan, D. 2023. Effects of rejuvenators on bitumen ageing during simulated cyclic reuse: A review. *Resources, Conservation and Recycling,* 190.

Schwettmann, K., Weigel, S., Stephan, D., Nytus, N. & Radenberg, M. 2020. Postcarbone road - The endless cycle of bitumen reuse.

Shen, J., Amirkhanian, S. & Tang, B. 2007. Effects of rejuvenator on performance-based properties of rejuvenated asphalt binder and mixtures. *Construction and Building Materials,* 21**,** 958-964.

CEN, 2015. *EN 12607-1: Bitumen and bituminous binders–determination of the resistance to hardening under the influence of heat and air—part 1: RTFOT method*. Brussels: CEN.

CEN, 2023a. *EN 14769: Bitumen and bituminous binders - Accelerated long-term ageing conditioning by a Pressure Ageing Vessel (PAV)*. Brussels: CEN.

CEN, 2023b. *EN 14770: Bitumen and bituminous binders - Determination of complex shear modulus and phase angle - Dynamic Shear Rheometer (DSR)*. Brussels: CEN.

Effect of in-situ treatment on porous asphalt durability and ravelling

A. Singh[1], F. Mastoras[2], M. Moenielal[2], and A. Varveri[1]

[1]*Pavement Engineering Section, Department of Engineering Structures, Delft University of Technology, 2628 CN, Delft, The Netherlands.*
[2]*Netherlands Organization for Applied Scientific Research, TNO, Molengraaffsingel 8, 2629 JD, Delft, The Netherlands.*

ABSTRACT: This study evaluated the durability of in-situ treated porous asphalt pavement surface (ZOAB) layers using surface treatment agents, both with and without rejuvenating effects. Field cores were extracted from four highway sections before and after treatment to analyze their impact on durability and raveling resistance. Fourier Transform Infrared Spectroscopy showed that the application of these agents led to reduction of carbonyls and sulfoxides without the formation of additional chemical functional groups. Further, micro-computed tomography revealed no significant changes in void distribution or material phases. The rotating surface abrasion test demonstrated that treated sections exhibited 67–82% lesser aggregate loss compared to control, attributed to the effects of applied treatment agents. Overall, the study highlighted that in-situ surface treatments, both rejuvenating and non-rejuvenating, are promising approaches for sustainable pavement maintenance.

1 INTRODUCTION

Porous asphalt is an engineered mixture comprising very little to no fine particles such that the minimum design air void content is 20% (CROW, 2000). Due to high porosity, the use of porous asphalt mixtures (also referred to as ZOAB in The Netherlands) in the surface layer is an effective strategy to reduce traffic noise and the risks of hydroplaning during wet weather. However, the high air void content makes the surface susceptible to deterioration under the actions of traffic and environment. Raveling is one of the most common distresses in ZOAB (Hagos, 2008). The open-graded structure is exposed to oxygen, moisture, temperature variations, and ultraviolet radiations that accelerate material ageing, thereby increasing bitumen viscosity and resulting in stiffer mixtures that are prone to aggregate loss from the pavement's surface.

Therefore, it is important to restore the properties of aged bitumen and use maintenance measures that can preserve the pavement condition and extend its service life. In-situ rejuvenation has emerged as one of the promising approaches that extends the service life of pavements as they have the potential to restore the original asphaltene to maltene ratio (Karlsson & Isacsson 2006). It involves spraying a compound over the existing pavement's surface, targeted at immediate diffusion into asphalt concrete to re-store the properties of the aged binder. The first investigation in the United States reported that the rejuvenator penetrated to a depth of about 9.5 mm into the dense asphalt surface, and softened the binder as confirmed by penetration and viscosity measurements of extracted binder (Brown & John-son 1976). Another study recommended that in-situ rejuvenation must be conducted on pavements having void content higher than 7% to allow the product to penetrate to a depth of 9.5 mm from the surface and rejuvenate the oxidized binder (Estakhri & Agarwal 1991). Computed tomography scans have detected the presence of rejuvenators within 9-20 mm depth of field extracted ZOAB cores, with porosity values still being higher than 20% (Zhang et al. 2015).

Some researchers have highlighted that surface treatments, involving the application of a thin layer of asphalt or other materials, can effectively preserve pavement surfaces (Herrington & Alabaster 2007; Qian & Lu 2015). For example, porous epoxy-modified asphalt mixtures demonstrated superior cohesive properties compared to standard open-graded porous mixtures at 10°C (Herrington & Alabaster, 2007). These mixtures also offer excellent resistance to moisture damage, maintain desired permeability, enhance sound absorption, and improve the durability of ZOAB. Additionally, the use of surface treatment agents, both with and with-out rejuvenating effects, can yield significant economic benefits by extending pavement service life (Singh & Varveri, 2024; Zuniga-Garcia et al., 2018).

Based on the literature, it may be stated that although multiple studies have explored the effects of surface treatment on aged bitumen and asphalt mixture properties, limited efforts have been made to investigate the durability of in-situ treated ZOAB. Thus, the objective of this research was to investigate the durability and raveling resistance of ZOAB before and after in-situ treatments, including a rejuvenator and preservative agent. The results of this study are part of an ongoing investigation that is aimed at evaluating the service life extension of ZOAB and test methods to capture the influence of these treatments on Dutch highway network.

2 METHODOLOGY

The pavement sections investigated in this research were constructed between the years 2011 and 2014, and since then they have been continuously exposed to the natural environmental conditions and traffic loads. One treatment has been conducted on these field sections. Multiple field cores of 150 mm diameter were drilled from the different pavement sections right before the in-situ treatment (15-30 cores) and about 2-3 months after treatment (12-18 cores). Sections A, B, and D received in-situ treatments with rejuvenation effects, while section C underwent a non-rejuvenating surface treatment. It is worth mentioning that the objective of this research is not to investigate the mechanism of treatment agents but explore their influence on durability of ZOAB.

2.1 *Chemical analysis*

To identify the development of additional chemical functional groups due to in-situ treatment, Fourier transform infrared spectroscopy (FTIR) was used in attenuated total reflection mode. From the field specimens, the top slice was cut having a thickness varying from 10-15 mm, and the bitumen was extracted in accordance with International standards (EN 12697-3+A1, 2018). The characteristic peaks and FTIR spectral regions such as sulfoxides, carbonyls, and aromatics were used for analysis. FTIR spectra (two independent measurements) were obtained in the mid-infrared range of 4000 to 650 cm^{-1} with 16 scans per specimen and a resolution of 4 cm^{-1} to identify functional groups present in the samples. The carbonyl and sulfoxide indices were expressed as the ratio of area of specific bands of spectrum to the sum of area under aliphatic bands using Equations 1 and 2.

$$Carbonyl\ index = \frac{A_{1700}}{A_{1460}+A_{1376}} \quad (1)$$

$$Sulfoxide\ index = \frac{A_{1030}}{A_{1460}+A_{1376}} \quad (2)$$

where, A_{1700} = area under the spectrum, tangential baseline between wavenumbers 1750 and 1610 cm^{-1}; A_{1030} = area under the spectrum, tangential baseline between wavenumbers 1030 and 924 cm^{-1}; A_{1460} = area under the spectrum, tangential baseline between wavenumbers 1525 and 1395 cm^{-1}; and A_{1376} = area under the spectrum, tangential baseline between wavenumbers 1390 and 1350 cm^{-1}.

2.2 *Micro-computed tomography*

The internal microstructure of the ZOAB field cores and the presence of different material phase (due to in-situ treatment) were investigated using micro-computed tomography (micro-CT). The imaging was performed on 45 mm diameter cylinders before and after treatment. All the micro-CT scans were performed under identical spatial resolution (voxel size of 90 μm). The projection images were post-processed using a non-commercial software and the images were segmented into different phases based on thresholds of greyscale pixel intensity.

2.3 *Rotating surface abrasion test*

The ravelling resistance of the control, i.e. untreated, and treated sections was evaluated using rotating surface abrasion test (RSAT). Though RSAT measurements are typically performed at 20°C, past Dutch experience has shown that raveling becomes more severe at low temperatures (CEN/TS 12697-50, 2018; Houben & Van De Ven 2014). Hence, the test temperature of 5°C was used. Three drill cores of 150 mm diameter were used to create an RSAT plate (see Fig. 1) and the specimens were subjected to 86,600 wheel passes. A minimum of three replicates were tested for each section, with an exception of one test section, for which only two replicates were tested for the treated mixtures, due to the absence of suitable drill-cores to produce a third test plate. The weight of aggregates larger than 2 mm lost during the test was recorded at various time intervals (1, 4, 8, 12, 16 and 20 h) as well as after the completion of the test (24 h).
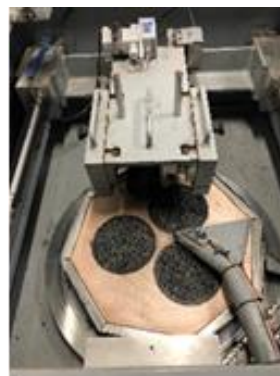
Figure 1. Arrangement of RSAT plates and test setup.

3 RESULTS AND DISCUSSIONS

3.1 *Chemical analysis*

The FTIR spectra (enlarged image of the spectral region critical for bitumen ageing) for the control (denoted as Ctrl in Fig. 2) and treated (denoted as Treat in Fig. 2) pavement sections (denoted as A, B, C, and D) indicated that the in-situ treatment did not result in formation of additional chemical functional groups. It is important to mention that strong unanticipated peaks (nitro compounds) were observed at wavenumbers 1578 and 1540 cm^{-1}. However, these peaks were not due to the in-situ treatment as they were also found in the FTIR spectra of control specimens.

Further, the average (3 replicates per highway section except D where 5 control and 2 treated replicates were tested) carbonyl and sulfoxide indices are presented in Figure 3. The results indicated that the carbonyl and sulfoxide indices of treated sections were relatively lower than those of control (untreated) sections, except for highways C and D, where the ageing indices were almost similar. For both treated and untreated sections, a higher proportion of sulfoxides were formed compared to carbonyls attributed to the higher reactivity of sulfur with oxygen than carbon. Other studies have also mentioned that the generation of carbonyls due to ageing of bitumen is slower compared to sulfoxides (Jing et al. 2019).
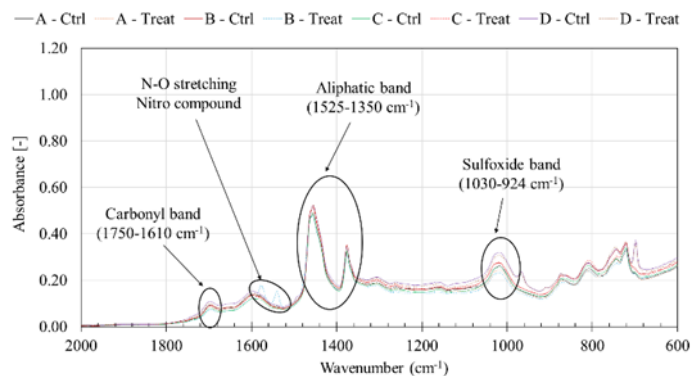
Figure 2. FTIR spectra of critical region for untreated and treated sections.
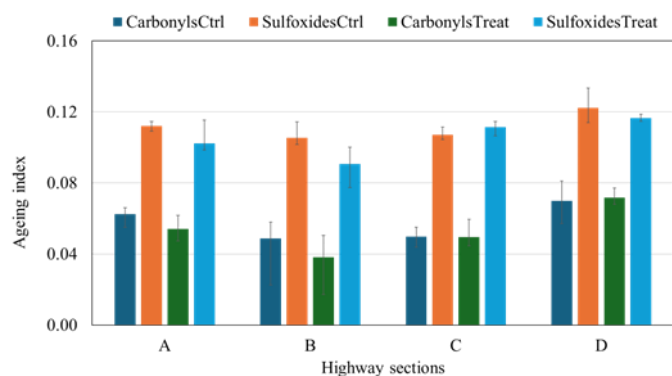
Figure 3. Carbonyl and sulfoxide indices for the four highway sections before and after in-situ treatment.

It is worth mentioning that though the peak intensity of FTIR spectra for the in-situ treatment agents (confidential data not plotted) was different compared to the binders, their corresponding wavenumbers were similar to those for the control and treated sections. Thus, it may be stated that the chemical composition of these agents was similar to that of bitumen. Consequently, the presence of treatment agents did not result in major differences in the chemical composition. This indicates that the they did not affect the chemical bonds or functional groups but rather led to rearrangement of polar/nonpolar molecular components. The lower ageing indices can also be due to the availability of additional fresh bitumen-like products after treatment. Therefore, the effectiveness of applied products is unclear based on the existing FTIR data. Future research will focus on collecting more data and exploring additional tests that can help in capturing the influence of in-situ treatment on bitumen composition.

3.2 *Micro-computed tomography*

The peak histogram phase detection method was employed to detect the presence of treatment agents. The histogram curves for the treated ZOAB did not show any additional peaks, which could indicate the presence of different material phases other than aggregates, asphalt mortar, and voids. A typical histogram of the treated sections is shown in Figure 4. The possible reason for the non-appearance of surface treatment agents could be that they either diffused in the mortar or their density was similar to that of bitumen, which did not caused a dramatic changes in the density of treated mixtures. Further, no clear trends were observed in terms of void reduction across the depth of ZOAB and the application of treatment agents did not lead to reduction of air voids.
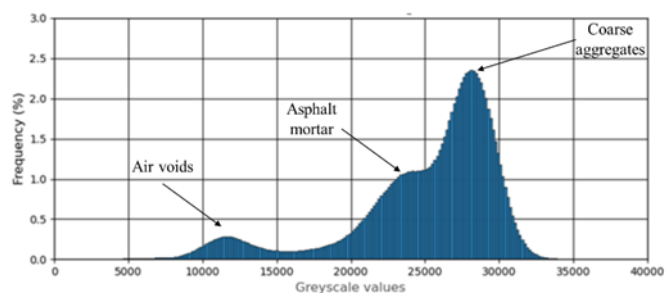
Figure 4. Greyscale histogram for treated sections.

3.3 *Rotating surface abrasion test*

As illustrated in Figure 5, the average aggregate loss for the treated sections was lower than control by approximately 67-82%. Ageing typically increases the asphaltene fraction and reduces maltenes, which causes a reduction in the effective contact area between the bitumen and aggregate bridges, thereby

increasing the risk of adhesive failure (Yuan et al. 2020). Note that the FTIR results confirmed that the in-situ treatment did not create additional chemical functional groups in the aged binder, and possibly, physically diffused into the aged material. This physical diffusion provided additional fresh binder, strengthening the mastic and bitumen bridges as well as restoring bitumen properties, thereby reducing the stiffness of mixture. Consequently, the bond strength between the binder and aggregates increased as also reflected by the lower aggregate loss of treated mixtures compared to control.
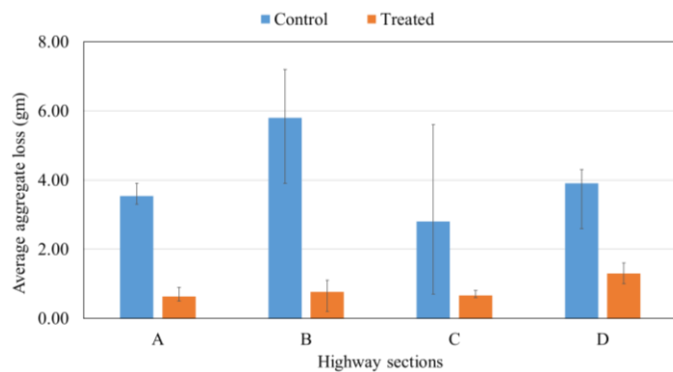
Figure 5. Average aggregate loss in the four highway sections before and after in-situ treatment.

4 CONCLUSIONS AND RECOMMENDATIONS

In this study, different investigations were undertaken to analyze the durability and raveling resistance of in-situ treated ZOAB mixtures. The major conclusions and recommendations are:

- FTIR analysis indicated that in-situ treatment reduced ageing indices by physically diffusing into binder without forming new chemical functional groups, indicating the preservation or restoration of binder properties.
- Micro-computed tomography detected no distinct material phases, indicating that treatment agents either diffused into the binder or had a density similar to bitumen, causing minimal changes within the mixtures.
- The in-situ rejuvenation reduced the aggregate loss by up to 82%, attributed to the reduced stiffness of the mixture.

Future research will focus on incorporating advanced performance characterization methods to better understand and quantify the effects of in-situ treatments, both with and without rejuvenating effects, on aged binder properties and pavement service life. In-situ treatment, already a mainstream maintenance pavement preservation technology in the Netherlands, is a promising method to extend asphalt service life, with potential for wider global adoption as a sustainable practice.

5 REFERENCES

Brown, E. R. & Johnson. R. R. 1976. *Evaluation of rejuvenators for bituminous pavements*. Tyndall Air Force Base, Florida: Air Force Civil Engineering Centre.

CEN/TS 12697-50. 2018. Bituminous mixtures - Test methods - Part 50: Resistance to scuffing. European Standard.

CROW. 2000. Specifications, the Technology Platform for Transport, Infrastructure and Public Space (CROW). Standard RAW provisions. The Netherlands.

EN 12697-3+A1. 2018. Bituminous mixtures - Test methods - Part 3: Bitumen recovery: Rotary evaporator. European Standard.

Estakhri, C. K. & Agarwal, H. 1991. *Effectiveness of fog seals and rejuvenators for bituminous pavement surfaces*. Texas A&M University, Texas.

Hagos, E. T. 2008. The effect of aging on binder properties of porous asphalt concrete. Doctoral thesis. The Netherlands: Delft University of Technology.

Herrington, P. & Alabaster, D. 2007. Epoxy modified open-graded porous asphalt. Road Materials and Pavement Design, 9: 481-498. https://doi.org/10.1080/14680629.2008.9690129.

Houben, L.J.M. & Van de Ven, M.F.C. 2014. *Samenvattend rapport resultaten LVO 2010-2014*. Infraquest: 2014-41. Delft: Infraquest.

Jing, R., Varveri, A., Liu, X., Scarpas, A., & Erkens, S. 2019. Laboratory and field aging effect on bitumen chemistry and rheology in porous asphalt mixture. Transportation Research Record, 2673 (3): 365–374. SAGE Publications Inc. https://doi.org/10.1177/0361198119833362.

Karlsson, R. & Isacsson, U. 2006. Material-related aspects of asphalt recycling—state-of-the-art. Journal of Materials in Civil Engineering, 18 (1): 81–92. American Society of Civil Engineers. https://doi.org/10.1061/(ASCE)0899-1561(2006)18:1(81).

Qian, Z. & Lu, Q. 2015. Design and laboratory evaluation of small particle porous epoxy asphalt surface mixture for roadway pavements. Construction and Building Materials, 77: 110-116. https://doi.org/10.1016/j.conbuildmat.2014.12.056.

Singh, A. & Varveri, A. 2024. Quantification of lifecycle costs for porous asphalt life-extension maintenance methods under managerial uncertainties. International Journal of Pavement Engineering, 25: 2376221. https://doi.org/10.1080/10298436.2024.2376221.

Yuan, Y., Zhu, X., & Chen, L. 2020. Relationship among cohesion, adhesion, and bond strength: From multi-scale investigation of asphalt-based composites subjected to laboratory-simulated aging. Materials & Design, 185: 108272. https://doi.org/10.1016/j.matdes.2019.108272.

Zhang, Y., Verwaal, W., Van de Ven, M. F. C., Molenaar, A. A. A., & Wu, S. P. 2015. Using high-resolution industrial CT scan to detect the distribution of rejuvenation products in porous asphalt concrete. Construction and Building Materials, 100: 1–10. https://doi.org/10.1016/j.conbuildmat.2015.09.064.

Zuniga-Garcia, N., Martinez-Alonso, W., Smit, A.F., Hong. F., & Prozzi, J.A. 2018. Economic Analysis of Pavement Preservation Techniques. 2672: 10-19. https://doi.org/10.1177/0361198118768515.

Self-healing capacity of asphalt mortars with encapsulated rejuvenators using fatigue tests under strain- and stress-controlled conditions

A. Viana-Sepulveda & S. Caro
Department of Civil and Environmental Engineering, Universidad de los Andes, Bogotá, Colombia

J. Norambuena-Contreras
Materials and Manufacturing Research Institute, Department of Civil Engineering, Faculty of Science and Engineering, Swansea University, Bay Campus, SA1 8EN, United Kingdom

ABSTRACT: A recent self-healing technique in asphalt mixtures involves adding biopolymer capsules with rejuvenation agents during the fabrication of the mix. Several laboratory tests have been proposed to assess the effectiveness of this technique. Among these, fatigue-healing tests are of particular interest, as fatigue damage is a primary source of crack initiation and propagation. There are two experimental approaches for performing fatigue testing: under strain- or stress-controlled mode. The selection of the mode is crucial when assessing self-healing mixtures, as it impacts the potential activation of the capsules (i.e., the actual release of the internal healing agent). This study evaluates the self-healing capacity of long-term aged asphalt mortars with capsules using fatigue-healing-fatigue tests under strain- and stress-controlled conditions with a resting period of 3 hours at 22°C and 45°C. The results show that the capsules enhance the healing capacity of asphalt mortars when tested under a stress-controlled mode and high temperatures, while under other conditions, no significant differences were observed compared to the control mortar.

1 INTRODUCTION

Fatigue in asphalt materials is a primary degradation process that causes the initiation and propagation of cracks and significantly reduces the service life of asphalt pavements. It is characterized in the laboratory using two approaches: strain-controlled and stress-controlled modes. In the stress-controlled mode, a cyclic loading signal with a constant stress amplitude is applied to the material. As a result, the deformation increases as damage progresses, leading to an increase in the dissipated energy per applied cycle. Conversely, in the strain-controlled mode, a cyclic signal with a constant strain amplitude is applied. In this case, the stress magnitude within the material decreases with damage, resulting in a reduction of the dissipated energy in each applied cycle. Consequently, strain-controlled tests yield longer fatigue lives (i.e., number of cycles to failure).

Significant efforts have been made to unify these two methods, although no consensus has been reached on which one is more representative of the actual field conditions (Masad et al., 2008; Braham, 2016). Some studies suggest that using fatigue strain-controlled tests as an appropriate field representation for asphalt mixtures layers thinner than 5 cm, and stress-controlled tests for thicker layers (Cheng et al., 2022).

The selection of the fatigue mode is particularly important when assessing the self-healing capacity of asphalt mixtures with encapsulated rejuvenators. This technique consists of adding capsules that contain healing agents –typically oils– during the fabrication of the asphalt mixture. It is expected that high-stress concentrations during propagation of cracks could break or compress the capsules, causing the release of the agent and its diffusion in the aged binder surrounding the cracks, thereby enhancing the natural self-sealing capacity of the binder (Gonzalez-Torre & Norambuena-Contreras, 2020).

In this context, it can be hypothesized that fatigue testing under stress-controlled conditions might promote capsule activation due to the increased deformation and dissipated energy per loading cycle within the asphalt material. This might explain why most existing studies used stress-controlled conditions to evaluate the self-healing capacity of asphalt materials (Xue et al., 2017; Zhang, 2020; Li et al., 2022; Wang et al., 2022). However, it is important to comprehend the efficiency of this technique under all possible field scenarios.

It should be also noted that most studies have evaluated the healing capacity of mixtures with capsules under short-term aged or unaged conditions (Xue et al., 2017; Zhang, 2020; Yamaç et al., 2021; Yao & Xu, 2023), while fatigue cracking occurs in a later

stage of the service life of pavements, where the asphalt binder is severely aged. Under this state, the natural healing capacity of the binder and the impact of a rejuvenator agent to increase such capacity are more limited.

The objective of this study is to evaluate the self-healing capacity of long-term aged asphalt mortars, with and without capsules, under both fatigue evaluation modes (i.e., strain– and stress–controlled), using resting periods of 3 hours at 22 and 45 °C. The results will permit a better characterization of the self-healing response of the material across a wide range of scenarios, contributing to identify the impact of stress and healing conditions to promote capsules' activation and healing processes.

2 MATERIALS AND METHODS

2.1. *Materials*

In this study, the asphalt mortar is defined as the compacted mix of aggregates smaller than 1.18 mm (passing sieve No. 16) and the asphalt binder. The mortars used correspond to a dense-graded asphalt mixture with a nominal maximum aggregate size (NMAS) of 12.5 mm and it follows the gradation in Table. The binder corresponds to an unmodified asphalt classified as Pen 60/70 (1/10mm), and the optimum binder content was 9.75% by total weight.

Table 1. Gradation of the aggregates (less than 1.18mm)

Sieve no.	Sieve size (mm)	% Passing
No°16	1.18	100.0
No°40	0.42	65.0
No°80	0.17	41.7
No°200	0.075	13.4

The specimens were fabricated with an air void content, V_a, of 10% ± 0.6%. This void content was selected based on previous studies on this material (e.g., Montañez et al., 2020). The selected morphology of the capsules is polynuclear, with a biopolymer structure of calcium alginate and sunflower oil as healing agent. They are 1.5 mm of diameter and were added at a dosage of 0.5% by weight of the total material, following the recommendations of previous studies (Norambuena-Contreras et al., 2019; Xu et al., 2018).

2.2. *Fabrication of asphalt mortar specimens*

The aggregates were preheated at 160 °C for 8 hours and the asphalt binder for 10 min. The materials were mixed at this temperature. In the case of the mortars with capsules, these were added at the final stage of mixing to ensure appropriate distribution and to prevent oil release during the process (Norambuena-Contreras et al., 2018; Kargari et al., 2022;).

The resulting mixes were subjected to two aging conditions: (i) short-term aging (STA), where the material was heated in an oven for 2 hours ± 5 minutes at 140°C (AASHTO R 30, 2019), and (ii) long-term aging (LTA), where the material was kept in the oven for 8 days at 95°C following the STA procedure (Kim et al., 2017).

Then, a cylindrical metal mould was used to compact each mortar individually. The compaction process involved applying a constant pressure of 0.8 MPa using a pneumatic piston for 45 ± 5 minutes (Caro et al., 2015). This process was calibrated to ensure the final target air void content (V_a). The resulting compacted cylindrical mortar had an average diameter of 14 mm and a height of 50 mm. Figure 1 illustrates the primary steps of the procedure for fabricating the specimens.
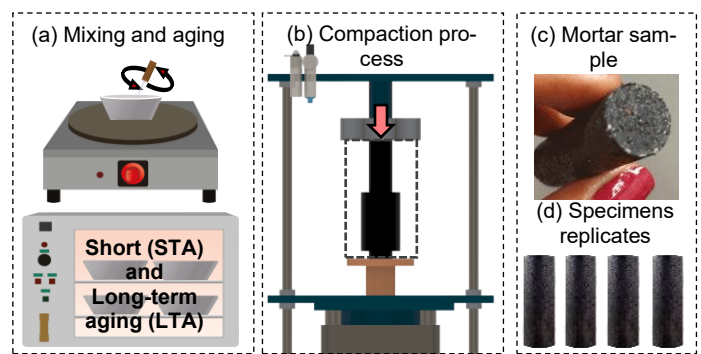
Figure 1. Fabrication of asphalt mortars specimens: (a) mixing and aging processes, (b) compaction, (c) compacted specimen, and (d) replicates

2.3. *Methods and cases of study*

In this study, the procedure used to measure the self-healing capacity of asphalt mortars is named fatigue-healing-fatigue tests and they were performed using the solid geometry of a Discovery HR 30 rheometer. This experimental protocol consisted of an oscillatory fatigue test under: i) strain-controlled of 0.1% angular strain, and ii) stress-controlled at a torsion value of 0.25 MPa. These loading conditions were selected after performing strain and stress sweep tests. All tests were performed at room temperature and using a loading frequency of 10 Hz. The parameter obtained during this phase was the initial dynamic shear modulus ($|G^*|_{initial}$). In each case, the test was stopped when the modulus decreased by 45% relative to its initial value ($|G^*|_{45\%}$). Then, the specimen was left resting for 3 hours at an intermediate and a high temperature of 22°C or 45°C, respectively. Three replicates were tested per type of mortar and for each healing condition.

After the resting period, a second fatigue stage was conducted, resuming the fatigue test for 30 additional minutes under the same testing (i.e., strain– or stress–controlled) and temperature conditions as in the first stage. The parameter obtained during this second phase was the peak modulus upon resuming the test ($|G^*|_{healed}$). Based on this procedure, and following

existing approaches to compute the healing capacity of asphalt mixtures with these capsules (Li et al., 2022; Sun et al., 2019; Wang et al., 2022), a Healing Index (*HI*) was computed to represent the relative recovery of the dynamic modulus after the resting period, as follows:

$$HI = \frac{|G^*|_{healed} - |G^*|_{45\%}}{|G^*|_{initial} - |G^*|_{45\%}} \qquad (1)$$

Figure 2 summarizes the experimental fatigue-healing-fatigue test protocol and the respective parameters. This curve corresponds to a strain-controlled fatigue test.
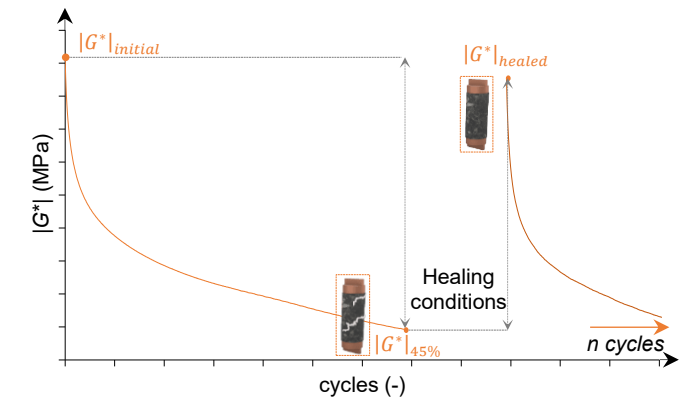
Figure 2. Experimental fatigue-healing-fatigue protocol.

3 RESULTS AND DISCUSSION

Figure 3 presents the results of *HI* for both types of tests. Error bars present ± one standard deviation. As expected, the mean values show a general increment in this index with the increase in resting temperatures from 22 to 45 °C for asphalt mortars with and without capsules. To better assess the significance of the differences from the results obtained, One-way Analysis of Variance (ANOVA) tests among the healing indexes for these mortar specimens were performed. All the statistical analyses in this study used a significance level (α) of 0.05.

Table 2 presents the results. Data in this table indicate that there are no significant differences between *HI* in the mortars with and without capsules when using strain-controlled tests. This result suggests that the addition of capsules did not enhance the natural healing capacity of the asphalt binder under these specific testing and recovery conditions evaluated. As mentioned in the introduction, this could be associated with the fact that strain-controlled conditions are unfavourable for promoting the activation of the capsules due to the reduction in the stress conditions within the specimen with the progression of the fatigue test.
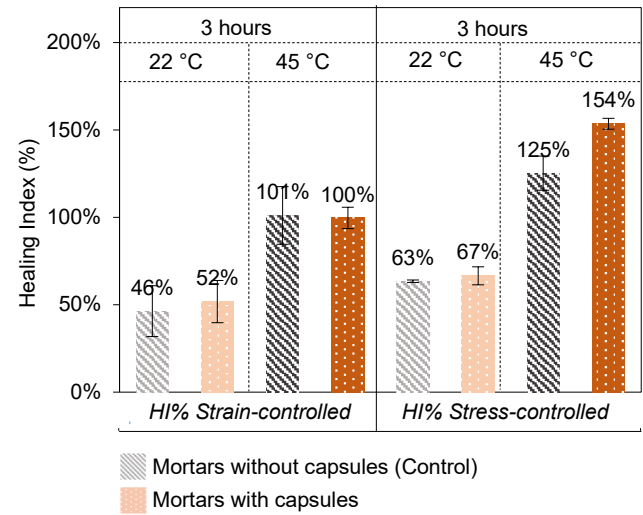
Figure 3. Healing Index (HI) under strain and stress-controlled for the long-term aged asphalt mortars with and without capsules

Table 2. One-way ANOVA *p*-value results on HI under strain and stress-controlled.

	Healing Index (HI)			
	Strain-controlled		Stress-controlled	
Control vs. Capsules	Statistically significant?	*p*-value	Statistically significant?	*p*-value
3 hours 22°C	No	0.64	No	0.36
3 hours 45°C	No	0.90	Yes	0.01

On the other hand, data in Table 2 show that capsules enhanced the self-healing capacity of asphalt mortars only in the case of 3 hours and high temperatures (45°C) under stress-controlled conditions. This test mode is more favourable to activate the capsules because the stress demands within the microstructure of the specimen increase over time. Under this scenario, it is more likely that a crack path would intersect a capsule or that capsules would be subjected to high compressive deformations, promoting the release of the healing agent. Also, at higher temperatures, the release agent will diffuse faster into the aged asphalt binder, so that the rheological and self-healing properties of the rejuvenated binder in the crack zone will be enhanced.

It is noteworthy that, although no significant differences were found at intermediate temperatures under stress-controlled conditions, it is necessary to evaluate recovery periods longer than 3 hours to determine the effectiveness of using capsules under this temperature condition.

Future work will focus on assessing the healing capacity of the material under a broader variety of test conditions (i.e., recovery times and temperatures).

4 CONCLUSIONS

This study evaluated the self-healing capacity of long-term aged asphalt mortars with and without capsules through a fatigue-healing-fatigue testing protocol under strain– and stress–controlled conditions.

The resulting Healing Index shows that the mortars with capsules subjected to stress-controlled conditions at high temperatures (45°C) enhanced the natural self-healing capacity of the binder. This is attributed to the increased mechanical demands within the microstructure of the material under this testing mode. Results under strain-controlled conditions and stress-controlled at intermediate temperatures (22°C) showed no significant differences between mortars with and without capsules, suggesting that these conditions were not sufficient to promote capsule activation.

5 REFERENCES

AASHTO R 30. (2019). Standard practice for mixture conditioning of hot mix asphalt. *American Association of State and Highway Transportation Officials*, *02*(2019), 1–5.

Braham, A. (2016). *State of the Art and Practice in Fatigue Cracking Evaluation of Asphalt Concrete Pavements*.

Caro, S., Sánchez, D. B., & Caicedo, B. (2015). Methodology to characterise non-standard asphalt materials using DMA testing: application to natural asphalt mixtures. *International Journal of Pavement Engineering*, *16*(1), 1–10. https://doi.org/10.1080/10298436.2014.893328

Cheng, H., Sun, L., Wang, Y., Liu, L., & Chen, X. (2022). Fatigue test setups and analysis methods for asphalt mixture: A state-of-the-art review. *Journal of Road Engineering*, *2*(4), 279–308. https://doi.org/10.1016/j.jreng.2022.11.002

Gonzalez-Torre, I., & Norambuena-Contreras, J. (2020). Recent advances on self-healing of bituminous materials by the action of encapsulated rejuvenators. *Construction and Building Materials*, *258*, 119568. https://doi.org/10.1016/j.conbuildmat.2020.119568

Kargari, A., Arabani, M., & Mirabdolazimi, S. M. (2022). Effect of palm oil capsules on the self-healing properties of aged and unaged asphalt mixtures gained by resting period and microwave heating. *Construction and Building Materials*, *316*(November 2021), 125901. https://doi.org/10.1016/j.conbuildmat.2021.125901

Kim, Y. R., Castorena, C., Elwardany, M., Rad, F. Y., Underwood, S., Gundha, A., Gudipudi, P., Farrar, M. J., & Glaser, R. R. (2017). Long-Term aging of asphalt mixtures for performance testing and prediction. *Long-Term Aging of Asphalt Mixtures for Performance Testing and Prediction*. https://doi.org/10.17226/24959

Li, J., Ji, X. ping, Fang, X. zheng, Hu, Y. lin, Hua, W. long, Zhang, Z. ming, & Shao, D. ye. (2022). Self-healing performance and prediction model of microcapsule asphalt. *Construction and Building Materials*, *330*(December 2021), 127085. https://doi.org/10.1016/j.conbuildmat.2022.127085

Masad, E., Castelo Branco, V. T. F., Little, D. N., & Lytton, R. (2008). A unified method for the analysis of controlled-strain and controlled-stress fatigue testing. *International Journal of Pavement Engineering*, *9*(4), 233–246. https://doi.org/10.1080/10298430701551219

Montañez, J., Caro, S., Carrizosa, D., Calvo, A., & Sánchez, X. (2020). Variability of the mechanical properties of Reclaimed Asphalt Pavement (RAP) obtained from different sources. *Construction and Building Materials*, *230*. https://doi.org/10.1016/j.conbuildmat.2019.116968

Norambuena-Contreras, J., Liu, Q., Zhang, L., Wu, S., Yalcin, E., & Garcia, A. (2019). Influence of encapsulated sunflower oil on the mechanical and self-healing properties of dense-graded asphalt mixtures. *Materials and Structures/Materiaux et Constructions*, *52*(4), 1–13. https://doi.org/10.1617/s11527-019-1376-3

Norambuena-Contreras, J., Yalcin, E., Garcia, A., Al-Mansoori, T., Yilmaz, M., & Hudson-Griffiths, R. (2018). Effect of mixing and ageing on the mechanical and self-healing properties of asphalt mixtures containing polymeric capsules. *Construction and Building Materials*, *175*, 254–266. https://doi.org/10.1016/j.conbuildmat.2018.04.153

Sun, D., Li, B., Tian, Y., Lu, T., Zhu, X., Sun, G., & Gilabert, F. A. (2019). Aided regeneration system of aged asphalt binder based on microcapsule technology. *Construction and Building Materials*, *201*, 571–579. https://doi.org/10.1016/j.conbuildmat.2018.12.167

Wang, Y. Y., Tan, Y. Q., Lv, H. J., & Han, M. Z. (2022). Evaluation of rheological and self-healing properties of asphalt containing microcapsules modified with graphene. *Construction and Building Materials*, *357*(August), 129287. https://doi.org/10.1016/j.conbuildmat.2022.129287

Xu, S., Tabaković, A., Liu, X., & Schlangen, E. (2018). Calcium alginate capsules encapsulating rejuvenator as healing system for asphalt mastic. *Construction and Building Materials*, *169*, 379–387. https://doi.org/10.1016/j.conbuildmat.2018.01.046

Xue, B., Wang, H., Pei, J., Li, R., Zhang, J., & Fan, Z. (2017). Study on self-healing microcapsule containing rejuvenator for asphalt. *Construction and Building Materials*, *135*, 641–649. https://doi.org/10.1016/j.conbuildmat.2016.12.165

Yamaç, Ö. E., Yilmaz, M., Yalçın, E., Kök, B. V., Norambuena-Contreras, J., & Garcia, A. (2021). Self-healing of asphalt mastic using capsules containing waste oils. *Construction and Building Materials*, *270*. https://doi.org/10.1016/j.conbuildmat.2020.121417

Yao, X., & Xu, T. (2023). Fatigue fracture and self-healing behaviors of cold recycled emulsified asphalt mixture containing microcapsules based on semicircular bending test. *Journal of Cleaner Production*, *410*(February), 137171. https://doi.org/10.1016/j.jclepro.2023.137171

Zhang, H. (2020). Self-healing property and road performance of asphalt binder and asphalt mixture containing urea-formaldehyde microcapsule. In *Eco-efficient Pavement Construction Materials* (pp. 171–196). LTD. https://doi.org/10.1016/B978-0-12-818981-8.00009-6

4.1

PAVEMENT SURFACE CHARACTERISTICS FOR SAFETY

Texture and skid resistance of asphalt mixtures with crumb rubber for safety roads

Freddy R. Apaza[a], Federico Gulisano, Damaris Cubilla, Gustavo Boada, Rafael Jurado, Juan Gallego.

Department of Transport Engineering, Territory and Urban Planning, Universidad Politécnica de Madrid
Profesor Aranguren 3, 28040 Madrid, Spain.
Corresponding author: email: fr.aapaza@upm.es, [a]

ABSTRACT: The skid resistance of asphalt pavements is influenced by their texture. While macrotexture has been more extensively studied due to easier measurement methods, microtexture also plays a significant role. Incorporation of crumb rubber (CR) from end-of-life tires into asphalt mixtures has shown potential for improving in skid resistance, though its effects remain underexplored. This study evaluated three types of mixtures (semi-dense AC, stone matrix asphalt SMA, and open-graded BBTM) with varying CR content (0.0%, 0.75%, and 1.5%). The mixtures were subjected to wear and polishing in successive stages, with macrotexture and microtexture analyzed using a laser profilometer and skid resistance measured via the British Pendulum Test (BPN). Predictive models revealed that microtexture revealed that microtexture have a more substantial impact on BPN values compared to macrotexture. Additionally, the presence of CR enhanced skid resistance in SMA and BBTM mixtures.

1 INTRODUCTION

Road accidents are a global issue influenced by human, road-related, vehicle-related, and environmental factors. Addressing these factors effectively reduces accidents. Skid resistance is a critical pavement property that helps prevent accidents caused by tire sliding. It depends on two primary frictional forces: adhesion and hysteresis *(Serigos et al. 2014)*. Adhesion arises from molecular interactions between the tire and pavement but is reduced by presence of water. Hysteresis results from the tire's deformation energy during contact the pavement. Both forces are affected by road texture, tire-pavement conditions, and speed. Pavement texture, comprises macrotexture (λ = 0.5–50 mm) and microtexture (λ < 0.5 mm), significantly impacts skid resistance *(Chen* et al. *2019)*. Macrotexture facilitates water drainage, reducing hydroplaning risks, while microtexture related to fine aggregate asperities and resistance to polishing *(Ueckermann* et al. *2015a)*.

In this study, an accelerated wet abrasion polishing machine was used to simulate traffic-induced wear under wet and contaminated conditions. The machine, a modified version of the Wet Traction Abrasion Tests (WTAT) equipment, was adapted for studying the polishing of hot asphalt mixtures for wearing courses. Skid resistance was evaluated using the British Pendulum Number (BPN), and pavement texture was analyzed with a laser texturometer (LTS) .Measurements were conducted during three wear stages : the initial state (with macrotexture obscured by binder), an intermediated

state (with significant microtexture wear and minimal macrotexture change).

2 MATERIALS

2.1 *Aggregates*

The aggregates used for the asphalt mixtures were porphyry (of magmatic origin) with a specific gravity of 2.80 g/cm3 (EN 1097-6), Los Angeles (LA) abrasion resistance of 15 % (EN-1097-2) and an Accelerated Polishing Value (PSV) of 56 (EN-1097-8). The filler consists of calcium carbonate. With these aggregates, the particle size distributions shown in Figure 1 have been obtained.
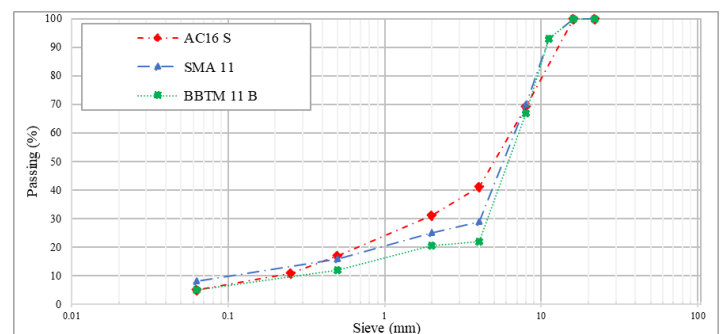
Figure 1. Aggregate gradation curves are used for asphalt mixtures.

2.2 *Crumb rubbers and binder*

The crumb rubber (CR) used in this research had a maximum particle size of 0.6 mm by total weight of the mixture. In the three types of asphalt mixtures (AC,SMA and BBTM). Three rubber contents have been used: 0.0 % (reference), 0.75 % and 1.50% in relation to the total weight of the mixture.

The bituminous binder was 50/70 penetration grade bitumen with penetration of 63 dmm and softening point of 47.6°C (EN-1427).

2.3 Experimental methodology

The research was conducted in four phases, as shown in figure 2.

-In phase 1, Asphalt mixture samples were fabricated in the laboratory, consisting of AC,SMA and BBTM with added CR contents of 0.0 %, 0.75 % and 1.50 %. This resulted in nine distinct mixtures. Table 1 outlines the mixtures of compositions and manufacturing temperatures.

-Phase 2, Surfacing scanning, the pavement texture was measured using a Laser Texture Scanner (LTS) (figure 2 b), portable device capable of scanning the surface along straight parallel lines with high precision (0.001mm).Each sample was scanned with 150lines of 101.6 mm and 0.00635 mm point spacing.

-Phase 3 Data collection: Texture and skid resistance measurements were performed at various wear stages, starting from the initial state to the residual state.

-Phase 4 Analysis: A database was created containing wear stage , texture parameters and skid resistance (BPN) for each sample. Predictive models of skid resistance were developed using mixture type, CR content, and texture variable as explanatory factors.
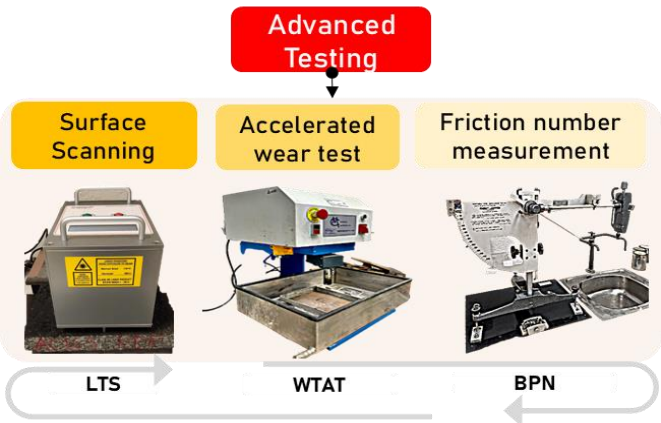
Figure 2. Caption of a typical figure. Photographs will be scanned by the printer. Always supply original photographs.

Table 1. Margin settings for A4 size paper and letter size paper.

Mixtures	CR (%)	G_{mm} (g/cm)^3	G_{mb} (g/cm)^3	V_a (%)
AC16S	0.00	2.540	2.406	5.27
	0.75	2.487	2.357	5.23
	1.50	2.479	2.310	6.83
SMA 11	0.00	2.517	2.349	6.66
	0.75	2.483	2.316	6.73
	1.50	2.445	2.280	6.75
BBTM 11B	0.00	2.643	2.148	18.72
	0.75	2.634	2.140	18.76
	1.50	2.632	2.135	18.87

2.4 Surface Scanning

The texture is obtained using the Laser Texture Scanner (LTS) produced by AMES (Figure 4a,b), which is a lightweight, portable device that scans the pavement surface using a laser sensor that moves along straight parallel lines. Each line can have a

2.5 Accelerated wear test equipment

The WTAT test originally consists of applying an abrasive wear process to the surface of in cold asphalt slurries samples by means of a rubber cylinder rotating at a speed of 150 revolutions per minute while rubbing the sample with a contact pressure of approximately 2.533 MPa EN 12274-5:2003. The test provides as a result the percentage loss in mass of the sample for different time intervals or wear cycles previously established.

Table 2 Abrasive material dosage and wear time

ABRASIVE	--	RUBBER							COARSE GRINDER		FINE GRINDER			RUBBER			
STAGE	I	II							III		IV			V			
WEAR SET	1	2	3	4	5	6	7	8	9	10	11	12	13	14	15	16	17
TIME (min)	0	.5	1	2	3	4	5	6	10	10	10	10	10	10	10	10	10
Accumulated gyros	0	5	150	300	450	600	750	900	1500	3000	4500	6000	7500	9000	10500	12000	13500

Figure 3 illustrates the hypothesis assumed that the contact zone on the macro texture. To overcome this drawback the discrete wavelet transform is used (Li et al. 2021).
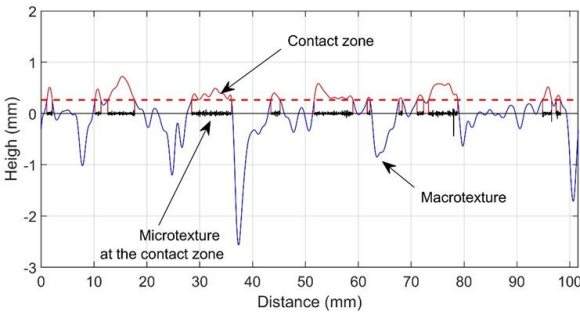
Figure 3. Profile microtexture and macrotexture

3 RESULT AND ANALYSIS

3.1 Texture characterization

Texture signals were decomposed into five octave bands, representing microtexture components (wavelengths 0.0127-0.05 mm) and an approximation level representing macrotexture (wavelengths 0.5 mm) (Sengoz *et al.* 2012) .The roughness average (Ra) quantified the mean absolute deviation of the microtex-

ture and macro texture profile, respectively , as shown in Equation 1.

$$R_a = \frac{1}{N} \sum_{i=1}^{N} |h_i| \qquad (1)$$

Where : h_i: represents the height of the profile considered (microtexture or macrotexture) measured at point i in mm. N: is the total number of measurement points along the sample length.

3.2 Experimental results

The study produces 51 observations for each parameter: macrotexture (Rama), microtexture roughness (Rami) BPN and CR content 0, 0.75, and 1.50%. Tables 3, 4 and 5 present average results of Rama, Rami and BPN for each mixture.
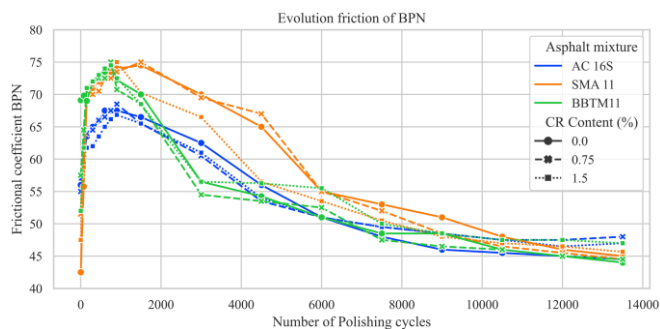
Figure 4. Evolution of the friction measurement BPN

Table 2. Results of the surface properties of the AC 16 S mixtures

	AC	BBTM	SMA
Mean BPN	57	60	60
Rami	0.014	0.0152	0.013
RMSmi	0.018	0.0197	0.016
MPDmi	0.039	0.0419	0.035
Rskmi	0.031	0.0339	0.03
Rkumi	2.996	3.09	2.96
Rama	0.412	0.6964	0.73
RMSma	0.579	0.906	0.79
Rskma	-1.598	-1.3041	-1.298
Rkuma	5.609	4.6711	4.663
MPDma	0.648	1.1261	0.965

3.3 Prediction models

Table 5 summarizes the predictive models for BPN, showing their goodness of fit (R^2 and $R^2\_$ adj).
For AC mixtures, the best-performing model (R^2=0.90) included only texture parameters (Rami , Rama) as the CR content was found to be non-significant. In contrast, significantly   influenced BPN in SMA rsely, in the case of SMA and BBTM mixtures, all three variables, Rama, Rami, and CR

content, were determined to have a significant impact on BPN. Consequently, models with R^2 values of 0.82 and 0.95 were obtained for SMA and BBTM mixtures, respectively.

Table 3. correlation coefficients R2 and adjusted R2 for AC, SMA and BBTM asphalt mixtures.

AC			SMA			BBTM		
Model	R^2	R^2_{adj}	Model	R^2	R^2_{adj}	Model	R^2	R^2_{adj}
Rama	0.76	0.75	Rama	0.30	0.29	Rama	0.51	0.50
Rama,CR*	0.77	0.76	Rama, CR	0.56	0.55	Rama, CR	0.76	0.75
Rami	0.84	0.84	Rami	0.64	0.64	Rami	0.91	0.91
Rami, CR	0.86	0.86	Rami, CR	0.78	0.77	Rami, CR	0.92	0.92
Rama, Rami	0.90	0.90	Rama, Rami	0.65	0.63	Rama*,Rami	0.92	0.91
Rama,Rami,CR*	0.91	0.90	**Rama,Rami, CR**	0.82	0.81	**Rama,Rami, CR**	0.95	0.94

For AC mixtures, the best-performing model (R^2=0.90) considered only the surface texture parameters, Rama and Rami, as the CR content was found to be non-significant. Conversely, in the case of SMA and BBTM mixtures, all three variables, Rama, Rami, and CR content, were determined to have a significant impact on BPN. Consequently, models with R^2 values of 0.82 and 0.95 were obtained for SMA and BBTM mixtures, respectively.

Table 1. Estimates of the BPN model for the AC mixture

Variable	Unstandardized β	Std. Error	Standardized β	t	p-value
Constant	9.235	2.562		3.605	<0.001
Rami	1899.789	228.851	0.603	8.301	<0.001
Rama	54.348	9.847	0.401	5.519	<0.001
R^2	0.901				
R^2_{adj}	0.897				

$$BNP = 9.235 + 1899.789\ Rami + 54.348\ Rama \qquad (3)$$

Table 2. Estimates of the BPN model for the SMA mixture

Variable	Unstandardized β	Std. Error	Standardized β	t	p-value
Constant	-91.573	13.586		-6.740	<0.001
CR	10.938	1.611	0.595	6.790	<0.001
Rami	6547.885	792.930	0.761	8.258	<0.001
Rama	81.599	23.355	0.407	3.494	0.001
R^2	0.822				
R^2_{adj}	0.811				

$$BNP = -91.573 + 10.938\ CR + 6547.885\ Rami + 81.599\ Rama \qquad (4)$$

Table 3. Estimates of the BPN model for the BBTM mixture

Variable	Unstandardized β	Std. Error	Standardized β	t	p-value
Constant	-194.201	41.840		-4.641	<0.001
CR	4.787	0.906	0.264	5.282	<0.001
Rami	2926.585	226.568	0.747	12.917	<0.001
Rama	296.675	63.277	0.333	4.689	<0.001
R^2	0.947				
R^2_{adj}	0.943				

$$BNP = -194.201 + 4.787\ CR + 2926.585\ Rami + 296.675\ Rama \qquad (5)$$

All the coefficient obtained in the models (Equations 3, 4 and 5) had positive signs, indicating that the Rami, Rama and CR content tend to increase the BPN value. To evaluate the sensitivity of the BPN value to changes in the explanatory variables within the observed intervals and to compare these sensitiv-

ities the values of the standardized beta coefficients (Table 7, 8, and 9) were analyzed. As expected, an increase in the aggregate asperity (Rami) of the asphalt mixture results in an increase in the BPN value.

Figure 13 confirms that BBTM mixtures exhibit a better slope in the model compared to SMA and AC. To demonstrate the predictive capability of the multivariate linear regression model, a validation process is conducted by comparing the data predicted by the model-predicted data with the laboratory-measured data. After fitting a linear model to the data for each type, the mixture type, the prediction errors, calculated as root mean square errors (RMSE) were as follows : 2.54% for AC mixtures, 4.94% for SMA mixtures, and 2.67% for BBTM mixtures. This indicates that, on average, the model predictions have an error of approximately less than 5 units compared to the actual average BPN values. A commonly accepted criterion for a good model fit based fit is that the RMSE should not exceed 10% (Karunasingha 2022). Therefore, the model fit can be considered acceptable. The model demonstrated a linear fit with robust coefficient for AC mixtures (R^2 = 0.91) and BBTM mixtures (R^2 = 0.950). SMA mixtures, while showing a slight lower correlation coefficient R^2 = 0.82), still display a significant correlation. This result indicated a strong relationship between the measurement variables. strong relationship between the variable measurements. The grey line in the graph represents the 45-degree line, and the model's accuracy improves as the data point approaches this line. In this case, the models showed a strong fit.
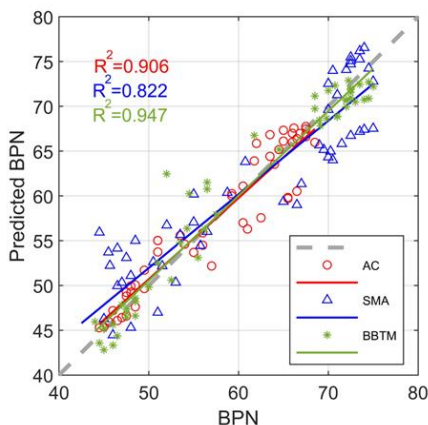
Figure 4. Comparison between Predicted BPN and measured BPN

4 CONCLUSIONS

This study aims to develop models for predicting the skid resistance of asphalt mixtures based on microtexture, macrotexture, and crumb rubber (CR) content. The main findings are as follows:

- Skid resistance, measured by the British Pendulum Test (BPN), can be effectively predicted through models that incorporate microtexture, macrotexture (quantified by roughness average), and CR content.

- For all mixtures studied (Dense AC16S, SMA 11, and BBTM 11 B), microtexture and macrotexture contribute to skid resistance. CR content influences skid resistance in SMA 11 and BBTM 11 B but not in AC mixtures.

- The models, developed using data from various wear stages in the laboratory, may remain valid throughout the pavement's service life.

5 PREFERENCES

Serigos, P.A., Buddhavarapu, P., Gorman, G.M., Hong, F., and Prozzi, J.A., 2016. Project title : Effect of Aggregate Micro- and Macro-texture on Pavement Skid Resistance ii, 7 (2).

Chen, S., Gong, F., Ge, D., You, Z., and Sousa, J.B., 2019. Use of reacted and activated rubber in ultra-thin hot mixture asphalt overlay for wet-freeze climates. Journal of Cleaner Production, 232, 369–378.

UNE, 2020. UNE-EN 12274-5:2020 - Lechadas bituminosas. Métodos de ensayo. Parte 5: Determinación del contenido mínimo de ligante y resistencia al desgaste. [online]. Available from: https://www.une.org/encuentra-tu-norma/busca-tu-norma/norma/?c=norma-une-en-12274-5-2003-n0029487 [Accessed 23 Aug 2022].

Sengoz, B., Topal, A., and Tanyel, S., 2012. Comparison of pavement surface texture determination by sand patch test and 3D laser scanning. Periodica Polytechnica Civil Engineering, 56 (1), 73–78.

Li, F., Ablat, G., Zhou, S., Liu, Y., Bi, Y., Weng, Z., and Du, Y., 2021. 2D-wavelet based micro and macro texture analysis for asphalt pavement under snow or ice condition. Journal of Infrastructure Preservation and Resilience, 2 (1).

Karunasingha, D.S.K., 2022. Root mean square error or mean absolute error? Use their ratio as well. Information Sciences, 585, 609–629.

Development and verification of a laser profilometer for microtexture assessment of pavement surfaces

G. Baimukhametov
University of the Sunshine Coast, Sippy Downs, Queensland, Australia

G. White
University of the Sunshine Coast, Sippy Downs, Queensland, Australia

S. Jamieson
University of the Sunshine Coast, Sippy Downs, Queensland, Australia

ABSTRACT: Surface friction is one of the most important aspects of safety for runway pavements. Consequently, accurate friction assessment can inform safe aircraft operations. One of the ways to increase the accuracy of friction assessment is to use texture tests. The aim of this study is to develop and verify a simple profilometer and profile picture processing algorithm for microtexture assessment. Such parameters as smothering coefficient and angle between laser, camera and surface were optimized. Laser profilometer testing results correlate well with the stylus-based roughness tester ($R^2 = 0.99$). The proposed assessment technique can be used for the microtexture assessment during runway friction surveys.

1 INTRODUCTION

1.1 *Surface friction*

Surface friction is one of the most important parameters of pavement affecting runway safety. The friction between a tire and a pavement directly affects the braking performance and maneuverability of aircraft. The coefficient of friction is a complex value that mostly depends on the hysteresis and adhesion effect between two surfaces. Adhesion, however, has a smaller influence on the friction due to the presence of moisture, dust, and other contaminants. Hysteresis effect, due to its nature, mostly depends on surface texture (Ueckerman et al., 2015). Additionally, surface texture lowers the risk of contact loss (hydroplaning) by providing contact patch drainage and reducing the water film thickness on a pavement surface (White, 2024).

Surface friction is generally measured by continuous friction measuring equipment (CFME) (AAA, 2017). However, due to the complexity of the friction phenomena, direct friction measurements by imitating the contact between a tire and a surface usually have low accuracy and repeatability. Changes in humidity, surface temperature, wear of the sliders and tires of the CFME, and the influence of speed make the reliability of the friction measurements poor, which could lead to serious friction-related accidents (Dardano & Wickham, 2005). Consequently, one of the ways to improve the friction management of runways is to add microtexture measurement to the tools for conducting friction surveys on runway pavement surfaces.

1.2 *Surface texture and friction*

Surface texture is a set of surface irregularities. Texture is usually divided into four classes depending on the wavelength; microtexture (up to 0.5 mm), macrotexture (0.5 to 50 mm), megatexture (50 mm to 500 mm), and unevenness (greater than 500 mm). However, only macrotexture and microtexture are important for the braking performance and maneuverability of aircraft. Megatexture and unevenness are usually eliminated due to noise and vibration during aircraft movement (Chen et al., 2022).

Microtexture and macrotexture affect the friction differently at different speed. At high speed, dynamic hydroplaning is the main reason for friction loss, with increased macrotexture lowering the risk by improving water drainage. Microtexture, on the other hand, provides good friction at lower speed, by reducing the thickness of the water film and increasing the hysteresis effect (Xiao et al., 2024).

There are a number of studies, with theoretical and empirical models being used, for the friction prediction based on a surface texture (Li et al., 2020). Some of the studies use artificial neural networks to predict surface friction with high accuracy (Yang et al., 2018). Some of the models were used during the development of the International Friction Index system (Wambold et al., 1995).

1.3 *Surface texture measurements*

Macrotexture measurements are usually simple due to the larger size of the surface irregularities. Differ-

ent methods are standard for the macrotexture measurements, such as profilometry and volumetric methods, which are widely used in engineering practice (White et al., 2021). Microtexture testing, however, is more challenging, and in current practice, there is no widely accepted method of microtexture assessment.

In research practice, different methods of microtexture assessment can be used, which can be divided into contact and non-contact methods. Contact methods include such methods as the mechanical stylus test and different wear tests. Non-contact methods are used more often and include laser profilometry, image texture analysis, stereoscopy, computed tomography scanning, 3D scanning, and simpler microscopy assessment methods, such as the straightedge shadow method (Chen et al., 2022).

The most precise and simple method is laser profilometry, which is based on the geometrical measurement of a projection of the laser beam on a surface (Martín-Béjar et al., 2023). However, there is no standard laser profilometer equipment for pavement testing. Suitable models are usually expensive, which makes it impossible to use them for pavement microtexture assessment.

The aim of this study is to introduce the design of a cheap and simple laser profilometer for pavement testing, including a profile picture analysis algorithm, and to verify it.

2 MATERIALS AND METHODS

2.1 *Testing surfaces*

To avoid the macrotexture influence, the verification was performed using plain surfaces with different textures, which include polished metal plates, sandpaper, and a mill file. A total of eight tests were performed by assessing an average roughness (Ra) of the surface, which can be found as an average deviation of the profile point coordinate.

2.2 *Profilometer verification*

Reference surface texture measurements were performed using the Intra Touch roughness tester with 4 nm vertical and 0.5 µm horizontal resolution. This roughness tester is based on the stylus test and provides a precise microtexture measurement. However, the vertical range of that tester allows use only with plain surfaces.

2.3 *Laser profilometer*

A laser profilometer was designed using widely accessible and economically available components (Fig. 1). The total price of profilometer components, excluding the price of the mount, which is made of 3 mm metal sheet, was equal to 36 AUD (24 USD).

The resolution of the camera was equal to 6.09 µm. Vertical resolution can vary by changing the angle between the camera and a laser. The pro-

filometer mount allows a change in the angle between the laser, camera and surface. The resulting profile is registered as a picture, allowing analysis in the VBA application for Excel.
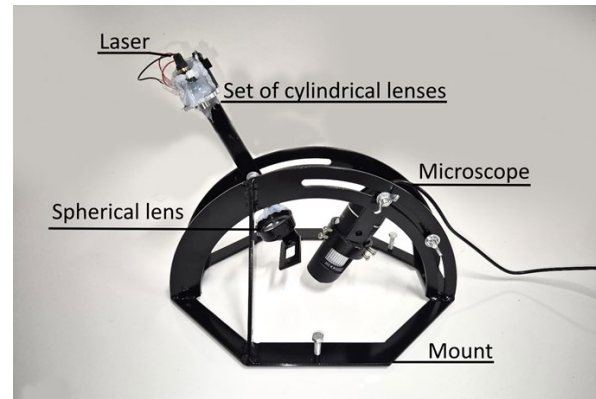
Figure 1. Laser profilometer model

3 RESULTS AND DISCUSSION

3.1 *Profilometer design*

A laser profilometer consists of two main parts; a camera or sensor, and a laser. Depending on the construction of a profilometer, a laser requires a set of lenses to project the laser line on a surface. The profilometer scheme is shown in Figure 2.
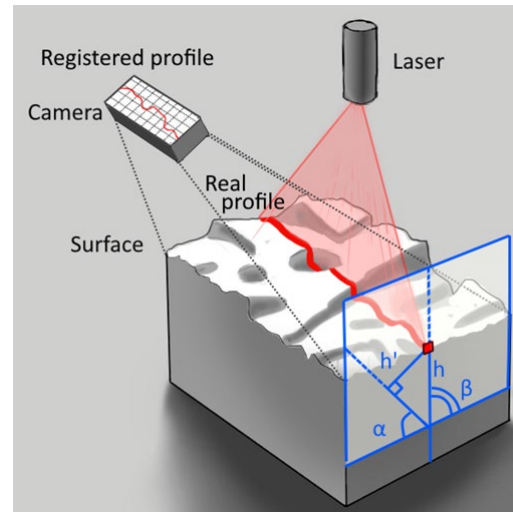
Figure 2. Laser profilometer scheme

The relative height of the profile point on surface and, on registered profile in Figure 2, are related via the Equation (1):

$$h = h' \times \sin \beta / \sin (180 - \alpha - \beta) \qquad (1)$$

where h is a real height of the point on a profile, h' is a height of the point on a registered profile, α is an angle between camera and surface, and β is an angle between laser and surface.

In most of the commercial laser profilometers used for materials testing, the β angle is equal to 90° (Mitaľ et al., 2019). The reason for that is a distortion of a profile line if that angle is less than 90° (Fig. 3). However, as seen in Equation 1, that reduc-

es the vertical resolution of a profilometer. For the purpose of pavement surface analysis, the straightness of the profile is inconsequential because the pavement surface is usually irregular anyway, so the slope angle change in not as important, since the height difference is still accurate.
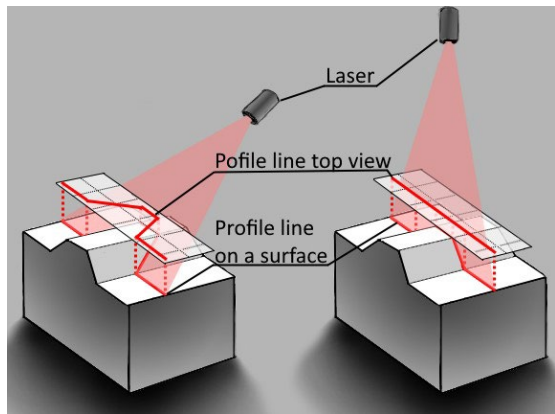
Figure 3. Distortion of a profile line

Lowering the angle increases the vertical resolution of a profilometer until the asperity slope and bottom cannot be reached by the camera and laser. In the case of a cone-shaped asperity (Fig. 4), the asperity wall and bottom can be seen on a profile only if both the camera (α) and laser (β) angles are greater than the angle of an asperity slope (γ). Overwise, the profile picture will contain discontinuities, which will add a significant error to the readings. Due to that reason, it is important to be able to change the angle to control the accuracy of the profilometer in a stage of profilometer verification.
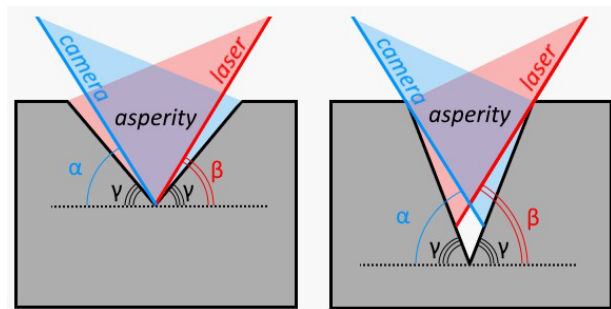
Figure 4. Distortion of a profile line

3.2 Processing algorithm

For this study, a data processing algorithm was also designed. It consisted of the following steps; profile registration, fine smothering, macrotexture filtration, texture parameter calculation.

The profile photo first needs to be processed to obtain a texture profile. First, pixel brightness is calculated as well as the profile line brightness threshold. After that, points on a profile were calculated by finding the centre of brightness of each column of pixels. A registered profile then needs to be smothered to remove any errors. After that, a macrotexture

filtration needs to be performed. During that step, profile leveling was also obtained. Macrotexture filtration was not done during the verification of a profilometer since the data from the roughness tester was not filtrated. However, the same algorithm was used for profile leveling by increasing the approximation range. An example of a processed profile is shown in Figure 5. S' and S are fine smothering and filtration coefficients.
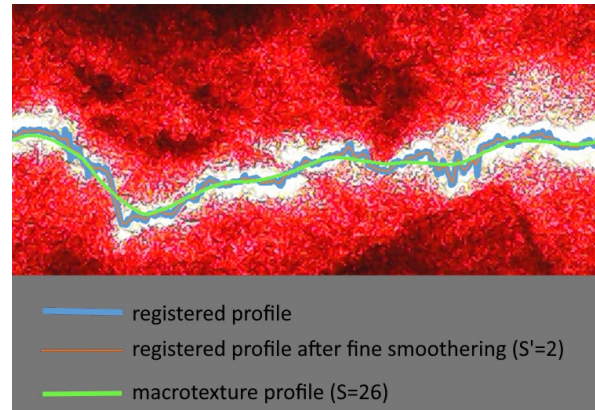
Figure 5. Processing of the photo of a profile (concrete texture)

For the fine smothering and filtration, an algorithm based on linear approximation, based on the method of least squares, was used. This algorithm approximates the line for each point based on the S-points before and after the point. Accordingly, the smothering coefficient is named S', and the filtration coefficient is named S. The part of that line becomes the profile after smothering or a macrotexture profile line near the point. Microtexture was calculated as a distance between a point and the approximated line. The advantages of this linear approximation are simplicity and efficiency.

Conventional filtration algorithms, based on the Fourier transformation, the Butterworth filter, the Gaussian smoothing filter, or other frequency-based algorithms, calculate the microtexture as a height difference between a point and a macrotexture, which leads to an error (Edjeou et al., 2020). Algorithms based on the polynomial approximation can lead to "overfitting," and they usually do not consider curved surfaces to be part of a microtexture, which is inappropriate for friction assessments because the overall grip is better on those surfaces. Plain surfaces, on the other hand, have the worst grip, and a polynomial approximation does not fit well to a straight line.

3.3 Laser profilometer verification

The laser profilometer verification was performed with different angles between the camera, laser, and a surface. The angle optimization was performed with the optimization of S' coefficient. The results of the optimization are presented in Table 1. In all sets of tests, the R^2 value between the roughness tester and laser profilometer results was calculated.

Table 1. Sets of tests for profilometer verification

| Number of sets of tests | The angle between | | Theoretical vertical resolution of the profilometer, um | Coefficient of determination between the roughness tester and profilometer (R²) |
	camera and surface (α), °	laser and surface (β), °		
1	45	45	4.31	0.92
2	45	90	8.61	0.95
3	60	90	12.18	0.89
4	60	60	6.09	0.99

As shown in Table 1, the optimal angle between the surface and both the laser and camera is equal to 60°. Although the lower angle increases the resolution of the profilometer, the profile discontinuities lower the total accuracy. It can be seen that profile distortion with the change of an angle between laser and surface does not affect the accuracy that much compared to the reduction of vertical resolution.

As shown in Figure 6, where the results of the fourth set of tests are presented, the designed laser profilometer model's vertical resolution is much lower than the vertical resolution of the roughness tester, which leads to an error in the case of polished metal plates. However, proportionality of the results for polished metal plate was still obtained.
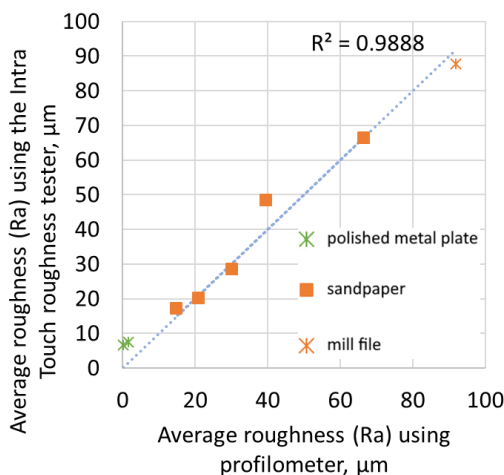
Figure 6. Profilometer verification results

4 CONCLUSION

The profile image assessment methodology presented in this paper can be used for the microtexture assessment. The smothering algorithm based on the linear approximation is simple and more suitable for friction assessment. Laser profilometry testing equipment for friction assessment can be cheap and reliable since friction assessment requires an analysis of texture wavelengths up to 0.5 mm. The laser profilometer model presented in this study is designed using cheap and common components and has a maximum vertical and horizontal resolution equal to 6 μm. Obtained results were verified with the stylus-based roughness tester; the R^2 coefficient is equal to 0.99.

5 REFERENCES

AAA. 2017. *Airport Practice Note 12 – Airfield Pavement Essentials.* Australia: Australian Airports Association.

Chen, S., Liu, X., Luo, H., Yu, J., Chen, F., Zhang, Y., Ma, T. & Huang, X. 2022. A state-of-the-art review of asphalt pavement surface texture and its measurement techniques. *Journal of Road Engineering*. 2(2):156–180. doi.org/10.1016/j.jreng.2022.05.003.

Dardano, J. & Wickham, G. 2005. *Australia's National Friction Testing Programme*. Available from: https://www.nzta.govt.nz/assets/resources/surface-friction-conference-2005/6/docs/australia-national-friction-testing-programme.pdf [Accessed 24 February 2022].

Edjeou, W., Cerezo, V., Zahouani, H. & Salvatore, F. 2020. Multiscale analyses of pavement texture during polishing. *Surface Topography: Metrology and Properties*. 8(2):024008. doi.org/10.1088/2051-672X/ab8f1b.

Li, Q.J., Zhan, Y., Yang, G. & Wang, K.C.P. 2020. Pavement skid resistance as a function of pavement surface and aggregate texture properties. *International Journal of Pavement Engineering*. 21(10):1159–1169. doi.org/10.1080/10298436.2018.1525489.

Martín-Béjar, S., Cañero-Nieto, J.M., Solano Martos, J.F. & Sevilla Hurtado, L. 2023. Laser Profilometry Application in Welding Geometrical Characterization. *Key Engineering Materials*. 960:65–72. doi.org/10.4028/p-2EHBlY.

Mitaľ, G., Dobránsky, J., Ružbarský, J. & Olejárová, Š. 2019. Application of Laser Profilometry to Evaluation of the Surface of the Workpiece Machined by Abrasive Waterjet Technology. *Applied Sciences*. 9(10):2134. doi.org/10.3390/app9102134.

Ueckermann, A., Wang, D., Oeser, M. & Steinauer, B. 2015. Calculation of skid resistance from texture measurements. *Journal of Traffic and Transportation Engineering (English Edition)*. 2(1):3–16. doi.org/10.1016/j.jtte.2015.01.001.

Wambold, J.C., Antie, C.E., Henry, J.J., Rado, Z., Descornet, G., Sandberg, U., Gothie, M. & Huschek, S. 1995. *International PIARC Experiment to Compare and Harmonize Texture and Skid Resistance Measurements*. Available from: https://www.piarc.org/ressources/publications/1/3832,01-04-T.PDF [Accessed 24 February 2022].

White, G. 2024. Comparison of bituminous surface options for regional airport runway pavements. In: *Bituminous Mixtures and Pavements VIII*. London: CRC Press. 355–363. doi.org/10.1201/9781003402541-42.

White, G., Ward, C. & Jamieson, S. 2021. Field evaluation of a handheld laser meter for pavement surface macro texture measurement. *International Journal of Pavement Engineering*. 22(8):950–959. doi.org/10.1080/10298436.2019.1654103.

Xiao, S., Xi, C., Xu, L., Li, J. & Tan, Y. 2024. Effects of road particulate contaminants on pavement skid resistance. *Road Materials and Pavement Design*. 25(4):874–887. doi.org/10.1080/14680629.2023.2229921.

Yang, G., Li, Q.J., Zhan, Y., Fei, Y. & Zhang, A. 2018. Convolutional Neural Network–Based Friction Model Using Pavement Texture Data. *Journal of Computing in Civil Engineering*. 32(6). doi.org/10.1061/(ASCE)CP.1943-5487.0000797.

Advancement in Pavement safety assessments

J. Daleiden
ARRB SYSTEMS, Texas, United States of America

V. Balaram
ARRB SYSTEMS, Melbourne, Australia

ABSTRACT: Transportation Safety continues to evolve as a significant area of interest and concern. As a result, evaluation of safety from pavement surface characteristics is also attracting more interest recently. Historically, pavement safety assessments have focused on friction assessments. Curiously, common technology for conducting such assessments has not changed much in the past half century. With significant changes in automotive braking systems, exploration of alternative methodologies for pavement surface assessment are gaining interest. Not surprisingly, current methodologies continue to involve test tyres assessing frictional resistance. Interest has always existed in exploring the relationship between texture and friction, in part, because texture can be assessed with non-contact technologies. Unfortunately, neither friction nor texture were previously collected with sufficient density and precision to establish any meaningful relationships. With the availability of these more comprehensive assessments, more detailed investigations are now more feasible.

1. INTRODUCTION

Low friction surfaces are rarely the sole cause of crashes, which typically involve multiple contributing factors. While friction can play a role, understanding pavement safety requires considering parameters such as traffic load, surface wear, and water dispersion. Areas with inherently low or irregular friction may result from design, materials, or wear over time, varying significantly across locations. Continuous, network-wide assessments are essential for identifying high-risk areas, determining intervention levels, and taking proactive action. As technology advances, authorities face challenges in effectively implementing data to identify segments needing treatment.

2. TECHNICAL APPROACH

The testing methodology for a locked-wheel skid tester (LWST) device requires the test wheel to be progressively braked over a time up to the fully locked state, before releasing again ready for the next test. The full lock/release requirement means that measurements can only be recorded periodically over short intervals of time typically resulting in less the 2% of the pavement surface being tested intermittently, and often without repeatability. With the difficulty of aligning of spot tests within short curves and intersections, it is common that these areas of high friction demand are not tested.

In comparison, a sideway force coefficient device (SFC) measures 100% of the surface, continuously, with reporting intervals as granular as 0.1m.

Continuous sampling is particularly important on those discrete localised sections within a network that have high demand for friction, such as curves and intersections. These areas typically have the highest levels of aggregate polishing and surface wear due to action of traffic manoeuvres in these high-risk locations, and ironically are where high friction is needed the most.

To provide a complete picture of road safety, with all the data needed for comprehensive friction and safety evaluations, continuous friction needs to be collected simultaneously with macrotexture from surface texture (Mean Profile Depth, MPD) data, as well as rutting and geometry data for potential water ponding, rainfall surface flow determination, and digital imagery for visual road safety risk assessments.

2.1 Continuous Friction Sideway Force Coefficient Concept

A SFC device measures the traction availability of the road surface. These measurements can be made of a road network in both wheel paths (Figure 2.1) continuously, capable of collecting far more data than traditional locked wheel or other small trailer based continuous friction measuring equipment (CFME). Sideway Force Coefficient (SFC) measurement devices use an instrumented measuring wheel angled to the line of the chassis in the wheel path. The test tyre is freely rotating with no restriction, however as it is set at an angle the tyre is compelled to slip over the pavement surface as the vehicle moves forward. The sideway slip resistive force can then be measured through the wheel axle via a load cell. The measurements are continuous while the vehicle is moving, as side slip friction resistive forces are always being generated by the forward motion. The angle of the wheel is chosen to be enough to generate this sideways force while unaffected by typical road curvature. To determine SFC the variables measured are the vertical downwards force on the test wheel - nominally 2.0kN - and the sideways (horizontal) force on the test wheel (Figure 1).

The friction parameters derived from the measurements are:
  1.) Sideway-force coefficient (SFC) which is the ratio of the sideways force to the vertical force, and

  2.) Sideway-force ratio (SR) which is the SFC x 100 (effectively a %)
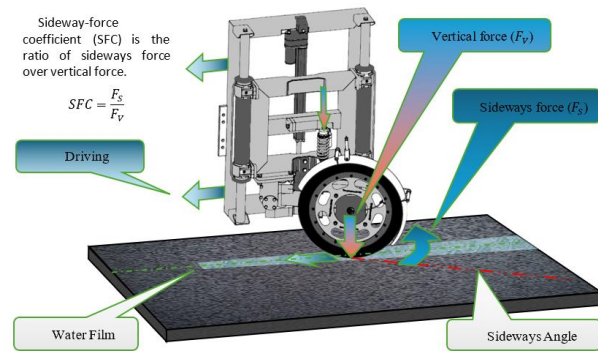
Figure 1: Sideways Force Coefficient concept (PD Sanders and C Browne,2020

2.2 Surface texture (macrotexture)

Macrotexture of the pavement surface is collected using three non-contact 32 kHz lasers. The speed of the laser is sufficient that height measurements are made every 1 mm or less at speed of 100km/h. The three texture lasers are situated in each wheel path at 950 mm as well as along the centre of the vehicle. for comparison purposes.

2.3 Rut Measurement

Laser Rut Measurement System (LRMS) are used to digitise transverse sections of the pavement. Transverse profile of the pavement is documented from 1280 points over a nominal 4-meter width. Custom optics and high-power pulsed laser line projectors allow the system to operate in full daylight or in night-time conditions.

With a 150 Hz sampling rate, this equates to one transverse profile being recorded every mm of longitudinal travel per km/h of travel speed (i.e., every 100mm at 100km/h). It does this with a nominal transversal resolution of ±2 mm with a nominal depth accuracy ±1 mm.

2.4 Spatial referencing
2.4.1 Distance measurement

Calibrated distance measuring devices provide linear referencing. Conducting appropriate calibrations prior to the commencement of each survey provides greater confidence in the positioning of the data and findings. Having calibration routines within the acquisition software facilitate the calibration process.

2

2.4.2 Spatial Positioning System

Global Navigation Satellite Systems (GNSS) and Inertial Navigation Systems (INS) provide sub-metre spatial accuracy and precise road geometry data. This includes grade, crossfall (±15%), and horizontal/vertical curvature, sampled every 2 meters and reportable at intervals of 10 meters or more.

2.5 Imaging

Digital imaging cameras capture high-quality, distortion-free images of pavement and road assets, with all cameras calibrated for precise linear and geospatial referencing. These systems ensure calibration accuracy through continuous alignment checks and are housed in the cab to prevent fogging. Images are tied to road location data (chainage) and GPS coordinates, allowing for accurate defect identification and asset mapping. Additionally, the captured images enable inventory data collection with unique GPS tagging, providing valuable information for future asset assessment or condition analysis, even if not immediately required.

2.6 Synchronization of Data

To ensure precise synchronisation of all collected data, all data streams and reference measurements are recorded from the same original source of odometer Distance Measurement Instrument (DMI) and GPS receiver (spatial coordinates) and are aligned through a high precision software module to synchronise output data at desired road location referencing intervals. Acquisition navigation functionality can deliver faster project completion times, accurate location referencing and reduced error through GIS based referencing, real-time survey route planning.

3. CASES

From experiences to date, several common scenarios are observed when gathering a more thorough set of safety parameters, continuously. The following representative cases depict how these scenarios practically impact strategic maintenance planning.

For the purposes of this discussion, pavement sections are categorized into cases with conditions as follows:

1.) Low friction and/or low texture, but all other metrics are within acceptable tolerances.
2.) Low friction and/or low texture, with conditions that impact surface moisture (. i.e. transverse profile concerns, geometric transitions, abnormal precipitation).
3.) Acceptable friction and/or texture but similar conditions that impact surface moisture.

2.1 Case 1

When conducting comprehensive safety assessments, it is possible to identify locations where the friction and/or texture is truly the only cause of concern.

1.) Without comprehensive safety assessments, it is possible these cases may go undetected.
2.) Without geometric concerns or the presence of moisture (from transverse profile issues or drainage concerns), such cases may not present the greatest of safety hazards.
3.) With only friction testing, these cases may be planned for treatments that may not be entirely necessary.

2.2 Case 2

In instances where low friction and/or texture are present along with conditions that impact surface moisture.

1.) Geometric concerns or the presence of moisture (from transverse profile issues or drainage concerns), typically necessitate more extensive remediation.
2.) With only friction testing, these other concerns may go undetected.
3.) Surface treatments may not necessarily address these cases, depending on the severity of the other concerns.
4.) Comprehensive safety assessments help to establish if more than just surface treatments are needed to truly reduce the safety risk.
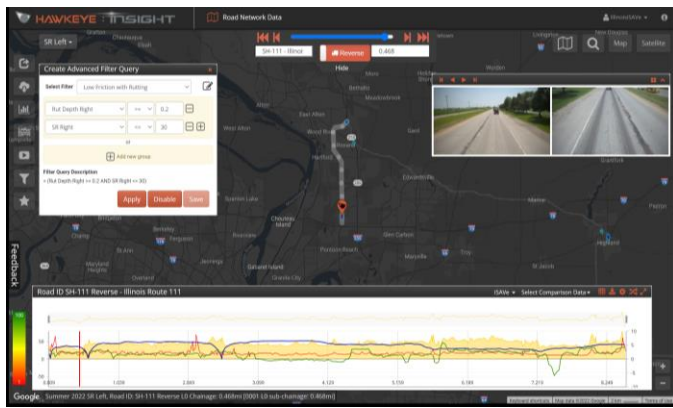
Figure 2: Low Friction, but other metrics provide greater cause concern (Case 2). (Arrb Systems, 2024)

2.3 *Case 3*

As most recognize, there are instances when acceptable friction and texture may be present, but other conditions may exist that impact safety.

1.) Transverse profile (rutting) and/or other geometric issues that create issues with the presence of surface moisture can create significant safety hazards, regardless of other conditions.

2.) Similarly, adverse geometrics (in horizontal or vertical curvature) can also present significant causes for concern.

3.) Comprehensive safety assessments help to identify/confirm these occurrences and provide for appropriate remediation.
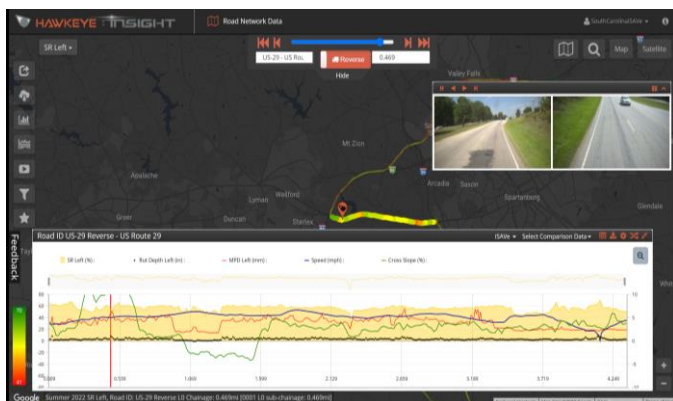
Figure 3: Friction assessment acceptable, but other metrics show cause for concern (Case 3). (Arrb Systems, 2024)

Continuous data allows for more detailed project-level assessments, enabling accurate identification and treatment of critical sections rather than relying on average conditions. This approach improves decision-making by leveraging network-level data

to inform project-specific needs. However, inconsistencies in relationships between parameters like friction and macrotexture, as observed with line laser data, highlight the need for further research. These additional assessments are essential to enhance understanding of safety parameters and improve road safety outcomes.

4. CONCLUSION

Historically, assessing pavement conditions has been challenged by limitations in traditional methods, resulting in a gap between network assessments and the design of specific treatment applications. Common issues with traditional safety assessment approaches include insufficient sampling, an inability to assess multiple factors at once, difficulty in proactively identifying areas in need, and high costs. As a result, there is increasing interest in new methods that collect data on friction, texture, and other functional parameters continuously, leading to more comprehensive safety assessments and project-level applications. Though the full impact of these methods is still uncertain, many are optimistic about their potential.

Most agencies are embracing network-level assessments and focusing on how to integrate this data into existing management systems. Project-level treatment applications are still being developed, with data being used to identify specific road sections that require special attention, such as targeted surface repairs, geometric changes, or other safety measures. These comprehensive assessments can enhance the optimization and application of pavement funds. However, challenges remain, such as the inconsistency of relationships between friction and macrotexture, which suggests the need for further research. Continuing assessments are essential to deepen understanding of these parameters and improve the ability to create safer roads.

5. REFERENCES

Arrb Systems, 2024,
https://us.hawkeyeinsight.com/app#/dataviewer
PD Sanders, C Browne, July 2020, Characterising the measurements made by
sideways-force skid resistance, TRL, Sept 2024

4

Building transition matrices for network-level projection of road pavement condition measurements

D. Castillo
Research Associate, Michigan State University

M.E. Kutay
Professor, Michigan State University

J. Bryce
Assistant Professor, West Virginia University

S.W. Haider
Professor, Michigan State University

ABSTRACT: This paper summarizes the development of transition matrices to forecast road pavement conditions. These conditions are commonly described via indices or measurements such as the International Roughness Index (IRI), Rutting (RUT), Faulting (FLT) and Cracking (CRK). Transition matrices allow for a versatile approach to forecasting pavement conditions, because (1) they describe the deterioration of the pavements, and (2) they facilitate the evaluation of the expected effect of planned interventions. Consequently, this method may potentially be a valuable tool for decision making.

OVERVIEW

This paper describes the development of transition matrices for network-level modeling of road pavement condition measurements. These matrices can be built from historical data on condition and maintenance record for a group of road sections of interest. Transition matrices can be used to forecast condition measurements such as IRI, RUT, FLT, or CRK (known collectively as General Condition Ratings, GCRs) across the road network over time. Using transition matrices allows for projecting the percentages of pavement in good, fair, and poor condition across a network, accounting for both (1) natural deterioration and (2) the effects of planned interventions by a transportation agency.

To generate these projections, a set of transition matrices for a given GCR are combined and weighted according to planned interventions (e.g., chip seals, cold mill & resurface, joint sealing, etc.). Projections are conducted starting from an initial condition, representing the state of the network in a specific year.

The input data for building the transition matrices should contain two types of information:

- A detailed record of the maintenance (date and fix type) performed on the road sections, and
- Measurements of the GCRs of the sections, ideally over an extensive range of conditions and along several years, for the same group of road sections.

Only data from sections with a known maintenance record should be used when building the transition matrices, because the GCR records are expected to reflect the impact of certain maintenance activities.

This study used data from 2,376 Flexible (FLX) and 783 Rigid (RIG) road sections collected between 1998 and 2019 in Michigan, USA. Annually, a measured length of 2,000 to 5,000 miles was available for analysis.

The process of building the transition matrices may be divided into three steps:

- *Step 1.* Compile the maintenance record of the road sections.
- *Step 2.* Compile the record of GCRs (i.e., IRI, RUT, FLT, CRK…) over time for the same road sections.
- *Step 3.* Combine the information from the maintenance and GCR records to build the transition matrices.

The output of this process is a set of transition matrices for each GCR. Finally, the transition matrices, the planned improvements, and the "starting point" (network status on year 0 of the projection) are used as inputs to perform the projection.

BUILDING THE TRANSITION MATRICES

Step 1. Maintenance record

The first step is to compile a detailed record of all intervention (maintenance) activities performed over the life of each section. This record is essential because the transition matrices will later use this data to reflect two key aspects: (1) how the section deteriorates after various interventions and (2) the impact and effectiveness of those interventions.

The maintenance record for the sections of interest was compiled from data provided by the Michigan Department of Transportation (MDOT). The data

contains a list of the maintenance activities performed on the sections over the years, their BMP/EMP and job numbers, among other fields. All maintenance activities are identified with a label. The labels were standardized and grouped into three fix categories: Capital Preventive Maintenance (CPM), Reconstruction (RCN), and Rehabilitation (RHB). A visualization of the maintenance record for two road sections of flexible pavement is presented in Figure 1.
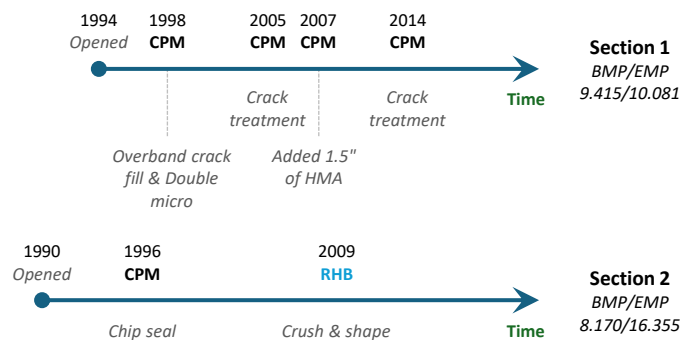
Figure 1. Maintenance record of two sections, including Beginning and Ending Mile Post (BMP/EMP).

Step 2. GCR record

The GCR records were built based on 0.1-mile measurements across the pavement network. To create the GCR history for a specific section, the corresponding data was retrieved over multiple years using the section's identification information (ID, beginning/end mileposts). Once the relevant data range is accessed, the GCR is characterized by its average value (excluding zeroes) and the extent of miles classified as Good, Fair, or Poor based on GCR-specific thresholds. This information is recorded in the section's GCR record. Additional considerations about the GCR data are as follows:

- The GCRs had a Left and Right wheel-path measurement. IRI and RUT use the average of the Left/Right data. FLT uses only the Right-side data.
- Entries with a negative average Left/Right GCR were not used. A few values were extremely high, likely due to issues during the measurement. Thus, the data above a maximum limit is "topped off."
- The range of GCR values will be discretized into equally sized bins when building the matrices.

The GCR record was compiled for all FLX and RIG sections. Figure 2 displays plots of IRI and RUT records over time for one FLX section.

Step 3. Building the transition matrices

The maintenance and GCR records of the sections provide the necessary foundation for developing the transition matrices:

- The GCR record for each section is divided into intervals, or pairs of consecutive data points. Each

interval is composed of a "present" (earlier) value and a "future" (later) value.
- A matrix is two-dimensional, with one dimension corresponding to present values and the other to future values.
- Both dimensions of the matrix are segmented into bins, which discretize the range of possible GCR values.

To populate a *precursor* matrix for a specific GCR, all GCR records of the sections are processed to identify the present and future bins for each data interval. Each interval is then added to the precursor matrix by accumulating the section length. As a result, the precursor matrix represents miles of road that have transitioned between GCR values. The precursor matrix is normalized across the rows to convert it into a **transition matrix**. Each row in the transition matrix lists the probabilities of a set of miles with a representative present GCR value (bin) of transitioning to a future GCR value (bin).

Two types of transition matrices were prepared:

- *Deterioration matrices* contain the intervals that describe the deterioration of the sections. Since the rate of deterioration may differ after a CPM, RCN, or RHB intervention, three separate deterioration matrices are created.
- *Improvement matrices* contain the intervals where maintenance activities took place. For instance, an interval associated with the reconstruction of a section is added to a RCN-specific improvement matrix. Given the three types of maintenance (CPM, RCN, and RHB), there are three corresponding improvement matrices as well.
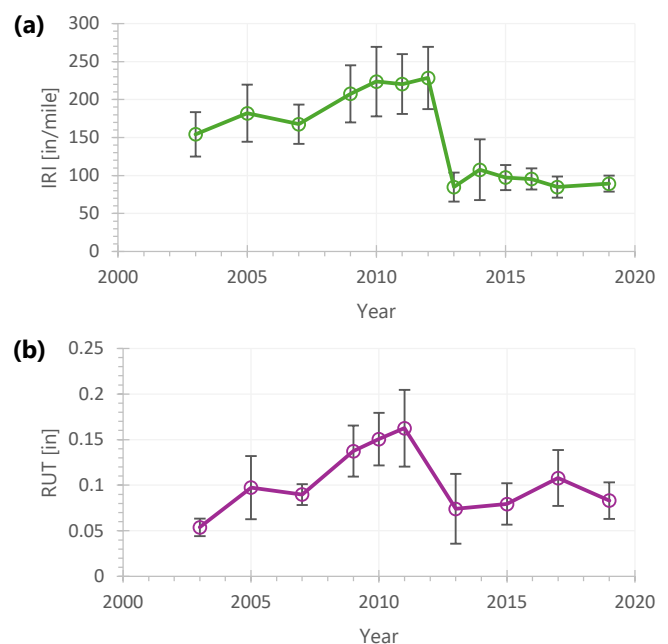
Figure 2. GCR records for a FLX section: (a) IRI, and (b) RUT. Maintenance record for this section: crack treatment (2002), overband crack fill (2005), HMA reconstruction (2012).

By associating each interval of the GCR record with the interventions occurring simultaneously, it can be ensured that each interval is added to the appropriate matrix. This approach results in six matrices per GCR, separately capturing (a) the deterioration of the GCR following each type of intervention and (b) the immediate impact of each intervention on the GCR. Once built, the transition matrices can be used to project the evolution of a given GCR at the network level under normal environment deterioration and planned improvements.

A full set of transition matrices for one GCR (RUT) is presented in the lower part of Figure 3. Some differences can be observed between deterioration and improvement matrices. Deterioration matrices have higher probabilities along their diagonals, indicating that present data generally remains similar or changes only slightly over time. In contrast, improvement matrices have higher probabilities in the left-most columns, signifying that regardless of the present value, future values are more likely to shift toward a fixed, improved range. This behavior aligns with the expected effect of an intervention, which is to restore the GCRs to a "Good" range.

Special considerations at this point include:

- The matrices are assigned a weighted interval length based on the number of 1-yr and 2-yr-wide intervals added. Intervals with gaps of 3 years or longer are excluded.
- So-called 'prior' matrices are smooth, "ideal" versions of the transition matrices used to compensate for lack of data in some rows or outlier data points. A prior matrix is constructed row by row, fitting the rows with the most miles to a Weibull probability distribution to determine its parameters A and B:

$$f(x; A, B) = \frac{B}{A}\left(\frac{x}{A}\right)^{B-1} e^{-\left(\frac{x}{A}\right)^{B}} \qquad (1)$$

  where f is the Weibull probability density function, x is the variable, and A and B are constants (scale and shape parameter, greater than 0).
- These parameters are then used for interpolating or extrapolating A and B values for rows with fewer miles. The definitive matrices used for projection are a weighted combination of the transition and prior matrices.

USING TRANSITION MATRICES TO FORECAST PAVEMENT CONDITIONS

The process of projecting the GCRs integrates three key elements: transition matrices, planned interventions, and a starting point.

Transition matrices describe the probability of a set of miles in a present state (with GCR values within a specific range or bin) transitioning into a future state over a specified time step (i.e., years). Matrices can be of a *deterioration* or *improvement* type.

Planned interventions are the network-wide CPM, RCN, and RHB maintenance activities planned by the transportation agency, expressed as percentages of the network to be intervened. Table 1 presents the sample values that were used in this study.

Table 1. Planned percentages of the network to be intervened with CPM, reconstruction (RCN), and rehabilitation (RHB).

Year	CPM [%]	RCN [%]	RHB [%]
2023	3.62	0.65	1.74
2024	2.78	0.45	0.56
2025	3.58	1.00	0.88
2026	3.09	0.34	0.20
2027	3.30	0.31	0.6
2028	3.14	0.29	0.52
2029	3.72	0.22	0.50
2030	2.94	0.31	0.93

Starting points represent the current state of the network, indicating the number of miles within each GCR bin for a specific year. A historical record of bin miles can be compiled to facilitate projections beginning from any chosen year.

The projection for the next time step is obtained by multiplying the starting point (a vector of miles) by a combined transition matrix. This combined matrix is a weighted blend of the six transition matrices for the GCR: three deterioration matrices and three improvement matrices. The weighting values are derived from the intervention percentages planned for the years within the current time step. The combined matrix is obtained as follows:

- Weight the *Improvement* matrices using the planned intervention percentages for the years within the time step (noted P_{CPM_i}, P_{RCN_i} and P_{RHB_i}).
- Weight the *Deterioration* matrices. These weights account for the deterioration of the non-intervened fraction of the network (noted P_{CPM_0}, P_{RCN_0} and P_{RHB_0}). They were estimated from historical intervention data, to reflect the most likely last intervention for the non-intervened segments.
- Build the combined matrix by weighting the previous two matrices with the total percent improved (PI) and the total percent deteriorated (PD).

The following equation describes the calculation of the combined transition matrix:

$$CTM =$$
$$PI \cdot \left(P_{CPM_i} \cdot \boldsymbol{I_{CPM}} + P_{RCN_i} \cdot \boldsymbol{I_{RCN}} + P_{RHB_i} \cdot \boldsymbol{I_{RHB}}\right) + \qquad (2)$$
$$PD \cdot \left(P_{CPM_0} \cdot \boldsymbol{D_{CPM}} + P_{RCN_0} \cdot \boldsymbol{D_{RCN}} + P_{RHB_0} \cdot \boldsymbol{D_{RHB}}\right)$$

where:

CTM = Combined transition matrix
PI = Total percent improved, $P_{CPM_i} + P_{RCN_i} + P_{RHB_i}$
PD = Total percent deteriorated, 100% - PI

P_{CPM_i} = Percent of CPM-improved miles in this time step

P_{RCN_i} = Percent of RCN-improved miles in this time step

P_{RHB_i} = Percent of RHB-improved miles in this time step

$\mathbf{I_{CPM}}$ = Improvement transition matrix for CPM

$\mathbf{I_{RCN}}$ = Improvement transition matrix for RCN

$\mathbf{I_{RHB}}$ = Improvement transition matrix for RHB

P_{CPM_0} = Percent of miles last intervened with CPM

P_{RCN_0} = Percent of miles last intervened with RCN

P_{RHB_0} = Percent of miles last intervened with RHB

$\mathbf{D_{CPM}}$ = Deterioration transition matrix after CPM

$\mathbf{D_{RCN}}$ = Deterioration transition matrix after RCN

$\mathbf{D_{RHB}}$ = Deterioration transition matrix after RHB

The projection process for a single step is summarized visually in Figure 3. First, the starting point data, representing the bin miles for the starting year of the specific GCR, is retrieved and stored in a vector, referred to as **A**. Then, the combined transition matrix is obtained as previously described. Finally, the projection is completed by multiplying the miles-bin vector (**A**) by the combined matrix for the current time step. The result of this vector-matrix multiplication represents the projected distribution of miles across bins for the next time step.

Projections are carried out stepwise, using the time step associated with the transition matrices, which may not always be an integer. The results are then interpolated to represent whole years and presented annually, in terms of percentages of Good/Fair/Poor miles. Projections were conducted separately for sets of miles exclusively FLX or RIG because the transition matrices were built based on separate FLX/RIG data; planned intervention percentages should be adjusted accordingly. Projections for IRI (FLX) are presented in Figure 4, forecasting three scenarios: no work (deterioration only), planned work, and double the planned work.

CONCLUSION

This paper described the development of transition matrices based on maintenance and GCR records of road sections. These matrices encapsulate and describe (1) deterioration trends, as well as (2) the effects of various improvements over the pavement condition measurements. Because of these features, they can prove useful to forecast scenarios and to assess the potential network-level benefits of different intervention strategies.
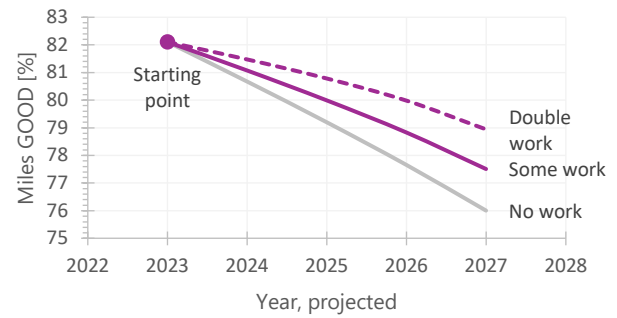
Figure 4. Projections for IRI (FLX).
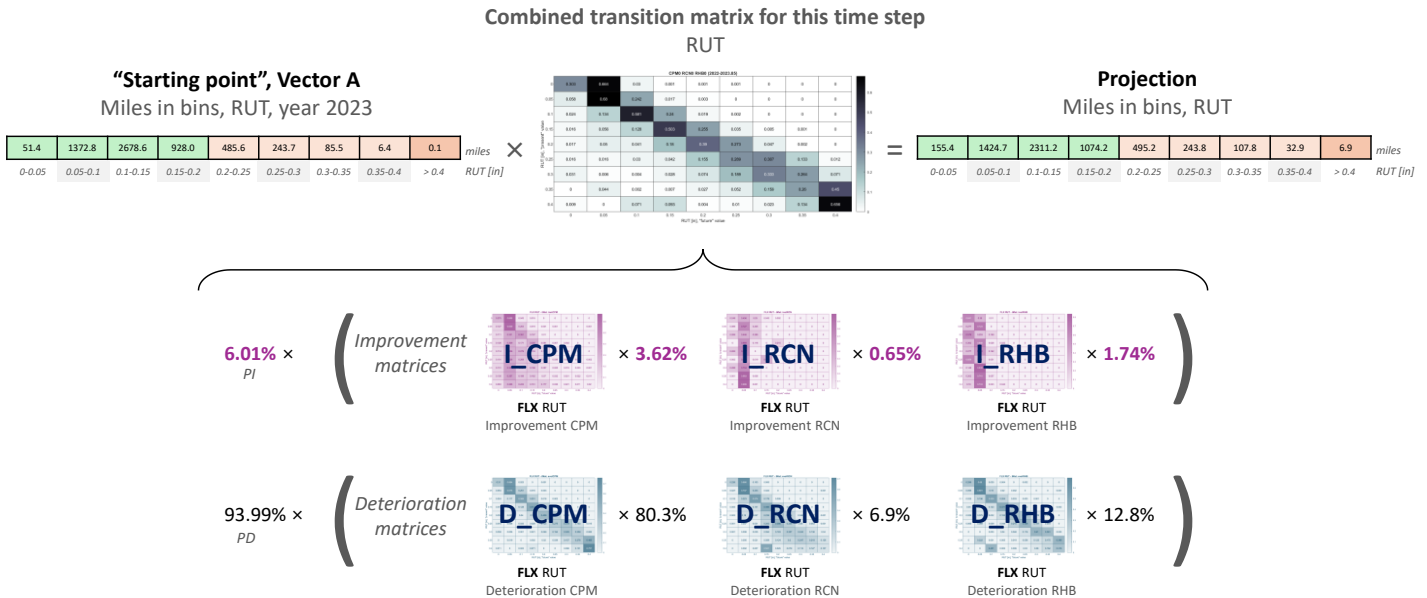
Figure 3. Simplified process of projection, one time step. Example for RUT.

Predicting Asphalt Pavement Macrotexture Depth in Discrete Element Method

Jiaqi Jiang & Maurizio Crispino

Department of Civil and Environmental Engineering, Politecnico di Milano, Piazza Leonardo da Vinci 32, 20133 Milan, Italy

ABSTRACT: Pavement macrotexture plays an important role in determining tire-pavement frictional characteristics, which is critical for considering road safety from pavement functional use point of view. This study introduces a numerical modelling to simulate asphalt mixture based on Discrete Element Method (DEM), thus predicting surface macrotexture depth under various mix conditions. The proposed model incorporates comprehensive parameters of asphalt mixture, including aggregate gradation, percentage of bitumen, density of aggregates and bitumen, and air voids. Model validation was conducted using on-site measurements of Height of Sand (HS). The comparisons of macrotexture depth between on-site HS and numerical prediction out of the proposed model showcase the robustness and reliability of this approach. The findings highlight the model's potential to analyze pavement macrotexture depth effectively, with enhanced precision over empirical formula by integrating sufficient parameters of asphalt mixture.

1 INTRODUCTION AND LITERATURE REVIEW

Skid resistance represents the ability of pavement surface to resist skidding or sliding of vehicles, which significantly contributes to road safety. Inadequate skid resistance will lead to higher road accidents especially during rainy days. Wet pavement surface will cause loss of skid resistance, thus lead to longer braking distance (Jiang et al., 2024). Pavement engineers usually design the wearing course with appropriate microtexture and macrotexture depth to satisfy the required skid resistance level. The Permanent International Association of Road Congress (PIARC) classified pavement microtexture and macrotexture by wavelengths of the deviations. Microtexture refers to the surface roughness of single aggregate, with wavelengths ranging from 0 mm to 0.5 mm, which is typically affected by the mineralogical composition of aggregates. Macrotexture is typically formed by the shape and arrangement of aggregate particles, with wavelengths ranging from 0.5 mm to 50 mm, which is dependent on the aggregate gradation, maximum aggregate size, binder content and compaction effort (Kogbara et al., 2016).

Pavement surface characteristics can only be measured by the on-site tests instead of the laboratory slabs or samples, due to different compaction methods accounting for large-scale on-site pavement and small samples in the lab. Laboratory measurements usually give a lower value of macrotexture depth, which can't be considered to evaluate pavement macrotexture on the field. Therefore, pavement engineers need to do large field experiments of wearing course to test their functional characteristics before construction. However, traditional experiments are quite time-consuming, labor-intensive and economically-cost. Moreover, there are also inevitable errors in setting up experiments. Motivated by these challenges, this study aims to seek a numerical modelling to predict pavement macrotexture depth instead of field experiments.

The existing empirical formula for predicting Mean Profile Depth (MPD) of asphalt pavement is primarily based on aggregate gradation, without sufficiently accounting for other critical parameters of asphalt mixture. The aggregate gradation curve is widely modelled by two-parameter Weibull distribution: $F(x,k,\lambda) = 1 - \exp[-(x/\lambda)^\wedge k]$, k and λ are known as shape and scale parameters of Weibull function, x is the sieve size [mm], F is the cumulative passing rate of aggregates. Rezaei et al., (2011) proposed a method to predict MPD using the following formula: $MPD = 1.8 - 3.041/\lambda - 0.382/k^2$, $R^2 = 0.90$. While this empirical formula brings a step forward, it still fails to incorporate adequate key

parameters of asphalt mixture, thereby limiting its precision and applicability.

To overcome the limitations inherent in field experiments and enhance the empirical formula for predicting MPD, this study introduces an innovative approach to simulate asphalt mixture in 2-dimensinal Discrete Element Method (DEM) for predicting pavement macrotexture depth. The numerical modelling will be conducted in PFC2D 7.00 software. This approach currently incorporates the following: 1) aggregate gradation, 2) percentage of bitumen, 3) density of aggregates and bitumen, 4) air voids. Figure 1 illustrates the framework of this study.
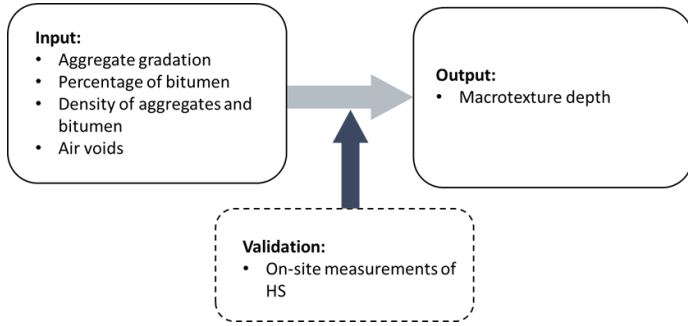
Figure 1. Framework of this study.

2 MODEL DEVELOPMENT

Asphalt mixture consists of aggregates, bitumen and air voids. Depending on the functional and structural requirements of different road types, aggregate gradation is adjusted to meet the various demands. Figure 2 illustrates the gradation curves adopted in Section 4. The critical factors to simulate asphalt mixture in DEM are the volume percentages of each component as illustrated in Figure 3. The volume percentage of each fraction of aggregates and bitumen can be calculated in detail as the Equation 1-6. Owing to the limitations of software, the aggregates finer than 0.5 mm, bitumen and air voids will be collectively transformed into porosity. The porosity directly governs the spatial distribution and density of aggregates, acting as a determining role in simulating asphalt mixture. In summary, the combined effects of aggregate gradation, percentage of bitumen, density of aggregates and bitumen govern the distribution and arrangement of particles, which in turn have a fundamental impact on the macrotexture depth of the pavement.

Density of aggregates: ρ_a; Mass of aggregates: m_a; Volume of aggregates: V_a

Density of Bitumen: ρ_B; Mass of Bitumen: m_B; Volume of Bitumen: V_B

Total volume of asphalt mixture: V_T; Air voids in asphalt mixture: V_V

Percentage of bitumen:

$$\alpha = \frac{m_B}{m_a} = \frac{\rho_B * V_B}{\rho_a * V_a} \tag{1}$$

Percentage of aggregate volume to the total volume of asphalt mixture:

$$V_T * (1 - V_V) = V_B + V_a = \frac{\alpha * \rho_a * V_a}{\rho_B} + V_a \tag{2}$$

$$= V_a * (\alpha * \frac{\rho_a}{\rho_B} + 1)$$

$$\frac{V_a}{V_T} = (1 - V_V) / (\frac{\alpha * \rho_a}{\rho_B} + 1) \tag{3}$$

Percentage of the ith volume fraction to the total volume of aggregates: P_i, $i = 1, 2, \ldots, n$.

$$P_1 + P_2 + \ldots + P_n = 1 \tag{4}$$

Percentage of the ith volume fraction of aggregates to the total volume of asphalt mixture:

$$V_a^i / V_T = P_i * \frac{V_a}{V_T} \tag{5}$$

Percentage of volume of bitumen to the total volume of asphalt mixture:

$$\frac{V_B}{V_T} = \frac{\alpha * \rho_a}{\rho_B} * (1 - V_V) / (\frac{\alpha * \rho_a}{\rho_B} + 1) \tag{6}$$
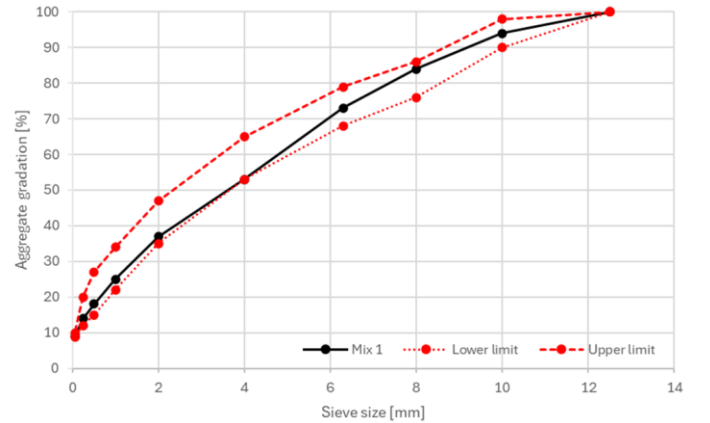
Figure 2. Illustration of aggregate gradation of AC 12.5.
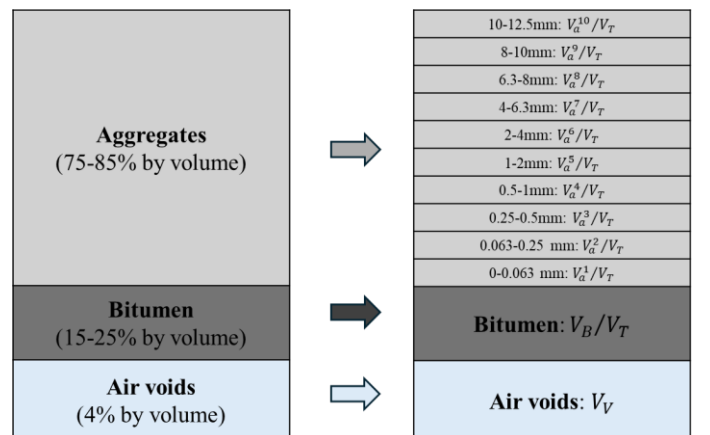
Figure 3. Illustration of volume fraction of asphalt mixture, consisting of aggregates, bitumen and air voids.

At the first stage to generate model, the rectangular wall (100 mm ×40 mm) of the numerical specimen was established. Then the software would generate the balls according to the specified aggregate gradation, with the target porosity controlling the ball generation. The porosity could be derived according to the previous equations.

There are elastic, viscoelastic and viscous performances in asphalt mixture under different circumstances of temperature and tire loads. Various contact models have been used in previous literature depending on the aim of applications. The linear elastic model is hereby adopted to characterize the contact between aggregate and aggregate. The Young's modulus of aggregates in road pavements range typically from 40 to 80 GPa. For particle-particle contacts in the PFC2D 7.00 software, an effective modulus of 55.5 GPa is selected, and the friction coefficient is set to 0.35. Additionally, the normal-to-shear stiffness ratio of aggregate particles is specified as 4.

Once the numerical specimen with specified gradation and target porosity is generated, the balls will be replaced by the irregular polygons, each having the same diameter as the corresponding ball. This procedure is crucial to better represent the irregular shape of real aggregate in asphalt mixture. Figure 4 illustrates the crucial steps to generate numerical modelling of asphalt mixture in DEM.

(a)

(b)
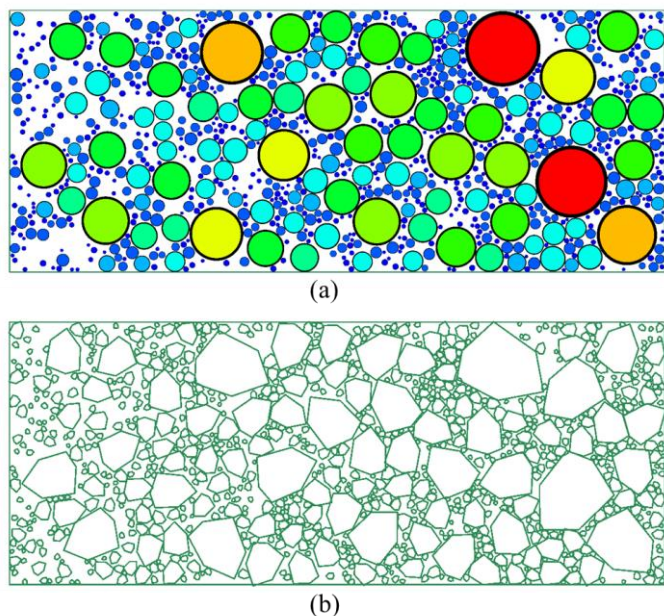
Figure 4. Numerical modeling of asphalt mixture in DEM. (a) generating particles according to aggregate gradation and calculated porosity; (b) replicating the balls into irregular shape subsequently.

3 MODEL VALIDATION

The validity of the proposed approach for predicting macrotexture depth of a given asphalt pavement was evaluated by comparing its results with the on-site measurements of Height of Sand (HS). HS is obtained by the volume of sand divided by the area of the sand, which is a conventional experiment used to measure the pavement macrotexture depth as shown in Figure 5b. To minimize the inevitable manual errors, 5 measurements were conducted at each road site, and their average value was used as the representative result. In the PFC2D 7.00 software, the numerical modelling can be exported as a .dxf file. The .dxf file subsequently can be converted into a .csv file to perform further data processing and analysis. The road profile is a series of vertical elevations along with the longitudinal axis of the road, as illustrated in Figure 5a. The profile data is captured with an incremental step of 0.1 mm in MATLAB software, starting from 0 mm to 100 mm. The Mean Texture Depth (MTD) of the numerical modelling is computed as the average vertical difference between the captured surface profile and the reference wall. After comparison, the proposed model in this study demonstrates a high degree of agreement with the filed test results, confirming its capability to reliably predict the macrotexture depth of asphalt pavements. These findings validate the proposed approach and highlight its potential for practical applications in pavement texture analysis.

(a)

(b)
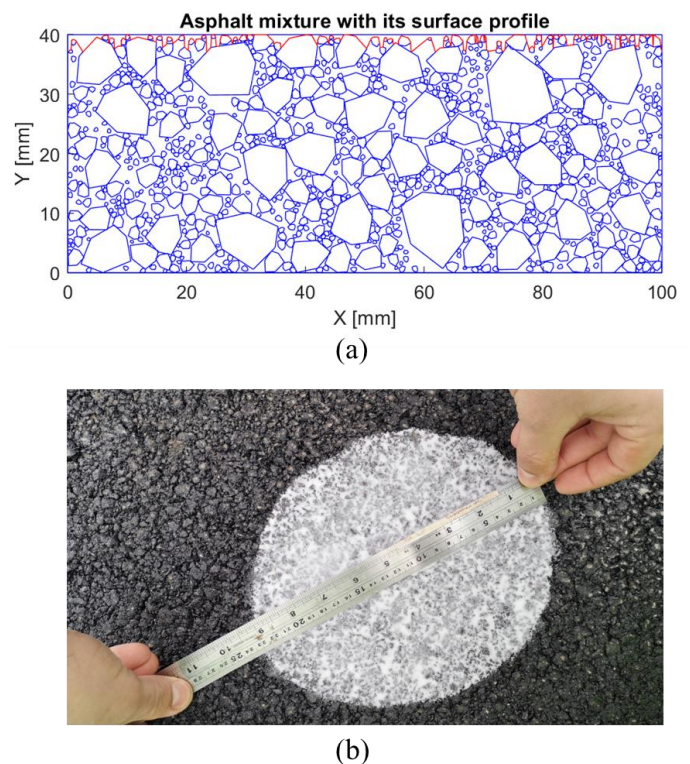
Figure 5. Illustration of model validation (a) extracting surface profile from numerical simulation of asphalt mixture in DEM; (b) on-site measurements of HS.

4 MODEL APPLICATION AND RESULT ANALYSIS

One case study was conducted to set up the boundary conditions of one on-site road to simulate the proposed numerical modelling in this study. The input parameters utilized in the simulation are outlined in Table 1. In order to minimize the inevitable errors of each individual measurement, 5 models were generated randomly to obtain the average value for predicting MTD, the results are listed in Table 2. Both the output from the empirical formula and the proposed model in this study for predicting macrotexture depth were compared with the on-site measurements of HS. The comparisons indicate that the proposed model can improve the empirical formula to analyze macrotexture depth considering more input parameters with a better accuracy as shown in Table 3.

Table 1. Boundary conditions to simulate asphalt mixture

Sieve size [mm]									
0.063	0.25	0.5	1	2	4	6.3	8	10	12.5
Gradation [%]									
9	14	18	25	37	53	73	84	94	100

ρ_B [g/cm3]	1.03
ρ_a [g/cm3]	2.7
α	5.78 %
V_V	4 %
V_B / V_T	12.63%
V_a^1 / V_T	7.50 %
V_a^2 / V_T	4.17 %
V_a^3 / V_T	3.33 %
Porosity	31.63 %

Table 2. Simulated results of MTD from the proposed model in this study

MTD [mm]					
1st	2nd	3rd	4th	5th	Average
0.85	0.76	0.76	0.76	0.79	0.78

Table 3. Comparisons of macrotexture depth between on-site measurements and empirical formula; Comparisons of macrotexture depth between on-site measurements and numerical modelling in DEM

Measurements (HS)	0.72 mm
Empirical formula (Rezaei et al., 2011)	0.61 mm
Difference between measurements and empirical prediction	-15.3 %
Prediction (DEM)	0.78 mm
Difference between measurements and numerical prediction in DEM	8.3 %

5 CONCLUSIONS

This study investigates simulating asphalt mixture from a DEM perspective, aiming at predicting asphalt pavement macrotexture depth under various mix conditions. The proposed model considers various mix parameters, including aggregate gradation, percentage of bitumen, density of aggregates and bitumen, and air voids. The outcomes of this model highlight the following points:

• Detailed computations of volume percentage of bitumen and particle fraction to the total asphalt mixture. These calculations are derived using formulas based on critical parameters of asphalt mixture.

• An advanced numerical modelling for asphalt mixture in DEM, which takes into account the irregular shape of aggregates and the stochastic nature of particle distributions.

• Accurate predictions for asphalt pavement macrotexture depth considering a wider range of input parameters than empirical formulas, exhibiting its potential for practical applications in pavement design.

REFERENCES

Jiang, J., Ketabdari, M., Crispino, M., & Toraldo, E. (2024). Estimating vehicle braking distance over wet and rutted pavement surface through back-propagation neural network. Results in Engineering, 21, 101686.

PIARC World Road Association. (1987, September). Report of the committee on surface characteristics. In Proceeding of XVIII World Road Congress (pp. 13-19).

Kogbara, R. B., Masad, E. A., Kassem, E., Scarpas, A. T., & Anupam, K. (2016). A state-of-the-art review of parameters influencing measurement and modeling of skid resistance of asphalt pavements. Construction and Building Materials, 114, 602-617.

Rezaei, A., Masad, E., & Chowdhury, A. (2011). Development of a model for asphalt pavement skid resistance based on aggregate characteristics and gradation. Journal of transportation engineering, 137(12), 863-873.

Simulation of Pavement Texture and Skeleton Characteristics of the Wearing Layer using Discrete Element Method

X.Y. Liu, S.Y. Cao, S.Y. Chen, S.Q. Wang, T. Ma, & X.M. Huang
School of Transportation, Southeast University, Nanjing 211189, China

ABSTRACT: To explore the texture and skeletal characteristics of the wearing layer, discrete element 3D models of the wearing layer were established. The texture characteristics were analyzed by different texture parameters, such as Estimate Mean Texture Depth (EMTD). The skeleton structure was analyzed based on contact force analysis, average coordination, and normal contact force distribution. This study indicated that the proportion of coarse and fine aggregates determines the texture and skeletal characteristics. The dense-graded mixture has the smallest texture structure, while the EMTD of gap-graded and open-graded mixture increased by 60% and 100% compared to dense-graded mixture respectively. EMTD decreases by approximately 10-20% for each level of nominal maximum size of aggregates decrease. Mixtures with a larger proportion of coarse and fine aggregates have better skeleton stability. Therefore, it is necessary to further explore and consider design indicators related to the ratio of coarse and fine aggregates during the design process.

1 INSTRUCTIONS

As the service life of roads increases, both skid resistance and durability gradually decline (Huang & Zheng 2019). The application of the wearing layer technology in asphalt pavement significantly enhances these properties and is therefore widely adopted (Fwa 2021). The texture of the wearing layer critically influences skid resistance, while its skeletal characteristics determine durability (Liu et al. 2024). Therefore, it is imperative to conduct further studies on the texture and structural composition of the wearing layer to optimize its performance.

The skid resistance and durability of the wearing layer have been studied from different perspectives. For texture characteristics of the wearing layer, the 3D texture of the pavement is mainly obtained through the high-resolution laser scanner (Liu et al. 2023a) and the digital image processing technology (Ji et al. 2024). Liu et al. (2023a) collected fine-grained texture data of over 800 pavement sections with various anti-skidding abilities using laser scanning technology and proposed an automated pavement friction estimation model using deep neural networks. Ding et al. (2021) achieved 3D image reconstruction and segmentation of pavement texture using digital image processing technology,

demonstrating that the effective texture depth for road friction is 2 mm. For the skeleton structure of the wearing layer, the skeleton mechanics analysis is mainly evaluated by photoelastic experiment (Taniguchi et al. 1996), discrete element method (DEM) (Xue et al. 2024), finite element method (FEM) (Pei et al. 2023), and coupled discrete element finite element method (DEM-FEM) (Liu et al. 2023b). Wang et al. (2023) evaluated the impact of grain size composition on the mechanical performance requirements for aggregate of each size and investigated the mechanical properties of the asphalt mixture. Liu et al. (2020) developed a 2D DEM model of asphalt mixture by simplifying aggregates into balls, defining the skeleton main force chain, and comparing the force chain characteristics of dense-suspended and dense-skeleton types asphalt mixtures. Kumar et al. (2024) analyzed the response of asphalt concrete pavement under different conditions using FEM model. Ge et al. (2023) analyzed the evolution of particle force chain, displacement and velocity distributions, and particle force characteristics within asphalt mixtures using the DEM-FEM coupling algorithm.

However, there are still some limitations in the current research on the texture and skeleton of the wear layer. While significant work has been done on the texture, there is a gap in understanding the correlation between material composition and pavement texture from a mechanical perspective,

hindering a comprehensive understanding of the relationship between the mixture skeleton and pavement texture. Additionally, simulating aggregates as spherical particles oversimplifies the mechanical behavior of the skeleton and does not accurately reflect its true composition. The inherent randomness and discreteness of the DEM align well with texture simulation. Our research group has developed a 2D DEM model for the wearing layer, but notable differences exist between this model and the actual layer. Therefore, investigating the feasibility of a 3D DEM model for the wearing layer is crucial for better analyzing skid resistance and skeleton stability.

2 METHODOLOGY OF DEM SIMULATION

2.1 *Gradation types and the 3D simulation method*

To analyze the texture parameters and corresponding skeleton state of different gradation types of wearing layer, 3D DEM models were established, including single size gradation, dense gradation, gap gradation, and open grading. The gradation details are shown in Figure 1. Among them, single size gradation, AC-13, SMA-13, and OGFC-13 were used to analyze the differences in various graded mixture with the same Nominal Maximum Size of Aggregates (NMSA). SMA-13, SMA-10, SMA-8, and SMA-5 were used to analyze the differences in the same gradation types with different NMSA.
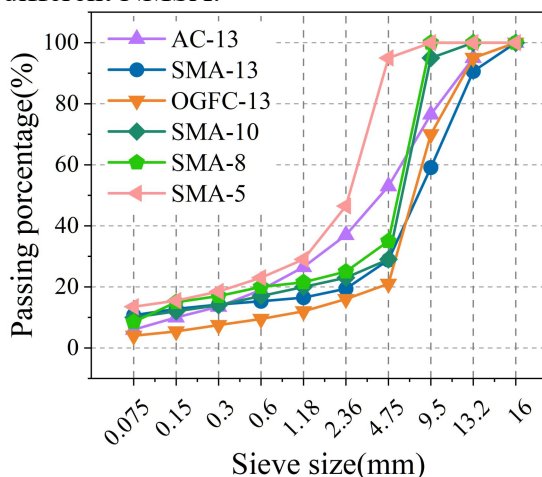
Figure 1. Gradation types: (a) Different skeleton types with same NMSA; (b) Same skeleton types with different NMSA.

The modeling of the wearing layer is established by DEM software. The modeling process mainly includes aggregates reconstruction, aggregates generation, and compaction process.

Accurate aggregate modeling is crucial for analyzing texture characteristics in wearing layer reconstruction. However, detailed modeling reduces computational efficiency. Aggregates larger than 2.36 mm are classified as coarse aggregates, providing support through interlocking, while aggregates smaller than 2.36 mm are fine aggregates, used for filling and compacting. Coarse aggregates are modeled with pebbles, while fine aggregates are represented by spheres to balance model accuracy and computational efficiency. The ratio is 0.2, and the distance is 110 during pebble generation. To improve realism, 10 representative coarse aggregates from the test were scanned to obtain their morphology as a reference for pebble reconstruction. During the aggregate generation process, spheres of various sizes are randomly placed in the mold based on gradation data. Small spheres larger than 2.36 mm are replaced with pebbles reconstructed from real aggregate scans. The mold dimensions are 100 mm×100 mm×40 mm.

During SMA-13 construction, the compaction process involved 2 initial passes, 4 recompaction passes, and 2 final passes. For simulation, this was simplified to 8 total rolling passes. A compaction force of 120 kN and a steel wheel radius of 550 mm, matching the roller used in actual construction, were applied. The wearing layer models of different types are shown in Figure 2.

2.2 *Installation of Contact Properties*

The DEM model presented includes five categories of contacts between particles, as detailed in Table 1. The contact model parameters were calculated based on the macro-properties of the materials and were subsequently adjusted to fit laboratory results. The DEM model presented includes five categories of contacts between particles, as detailed in Table 1. The contact model parameters were calculated based on the macro-properties of the materials and were subsequently adjusted to fit laboratory result.

3 RESULTS AND DISCUSSIONS

3.1 *Pavement texture*

The simulated texture from the 3D DEM model was compared with the actual texture of SMA-13. A 3D portable laser scanner (3D-PLS) was utilized to measure the real texture, with scanned point cloud data stored in ASC format and a scanning precision of 0.05 mm. The real texture and simulated texture of SMA-13 are shown in Figure 3.

The simulated texture was measured by a program for texture extraction and the calculation of texture characteristics was compiled in Matlab software. The texture was categorized into three categories, including: Amplitude-Related Parameters, Such as Estimate Mean Texture Depth (EMTD), Arithmetic Average Roughness (R_a), Root Mean Square (R_q), Skewness (R_{sk}), Including Arithmetic Mean Wavelength (λ_a), Root Mean Square Wavelength (λ_q), and Peak Ratio (*PR*).

Aggregates Grain Size

- 🟩 0.6-2.36 mm
- 🟦 2.36-4.75 mm
- 🟫 4.75-9.5 mm
- 🟪 9.5-132. mm
- ⬜ 13.2-16.0 mm

(a) Single size (b) AC-13 (c) SMA-13 (d) OGFC-13 (e) SMA-10 (f) SMA-8 (g) SMA-5
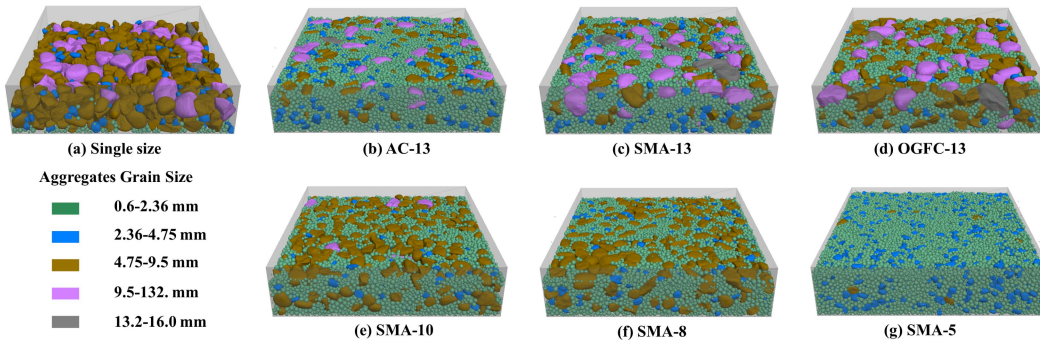
Figure 2. Wearing layer models with different types.

Table 1. Micromechanical Properties of DEM model.

Contact type	Ball-ball	Ball-pebble	Pebble-Pebble	Ball-facet	Pebble-facet
Model Type	Linear Parallel Bond Model			Linear model	
Normal Stiffness/(N·m-1)	9.0×10^8	9.0×10^8	5.0×10^8	9.0×10^8	9.0×10^8
Shear Stiffness/(N·m-1)	9.0×10^8	9.0×10^8	5.0×10^8	9.0×10^8	9.0×10^8
Friction Coefficient	0.05	0.10	0.15	0.05	0.05
Normal Critical Damping Ratio	0.2	0.2	0.2	0.2	0.2
Radius Multiplier	1.0	1.0	1.0	-	-
Normal Stiffness/(N·m-1)	2.0×10^5	2.0×10^5	2.0×10^5	-	-
Shear Stiffness/(N·m-1)	2.0×10^5	2.0×10^5	2.0×10^5	-	-
Tensile Strength/(pa)	1.2×10^6	1.2×10^6	1.2×10^6	-	-
Cohesion/(pa)	3.5×10^5	3.5×10^5	3.5×10^5	-	-
Friction Angle/(°)	40	40	40	-	-
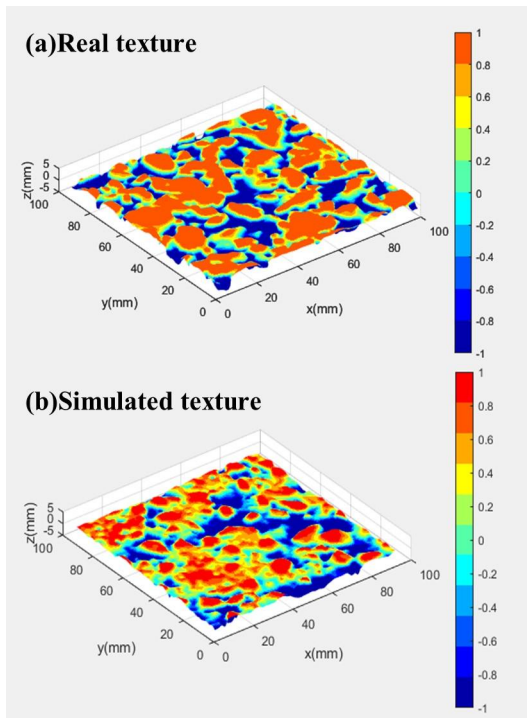
Figure 3. The pavement texture of SMA-13: (a) Real texture; (b) Simulated texture.

Shape-Related Parameters, Such as Mean Slope (Δ_a), Root Mean Square Slope (Δ_q), and Developed Interfacial Area Ratio (S_{dr}). These parameters of DEM model and actual pavement texture were calculated respectively and compared in Figure 4.

According to Figure 4, the texture parameters of simulated texture are similar to those of real texture. For amplitude-related parameters, EMTD, and R_{ku} are more accurate than other parameters, and the

accuracy of the simulation exceeds 90%. Where, the similarity of R_{sk} is relatively low, which may be due
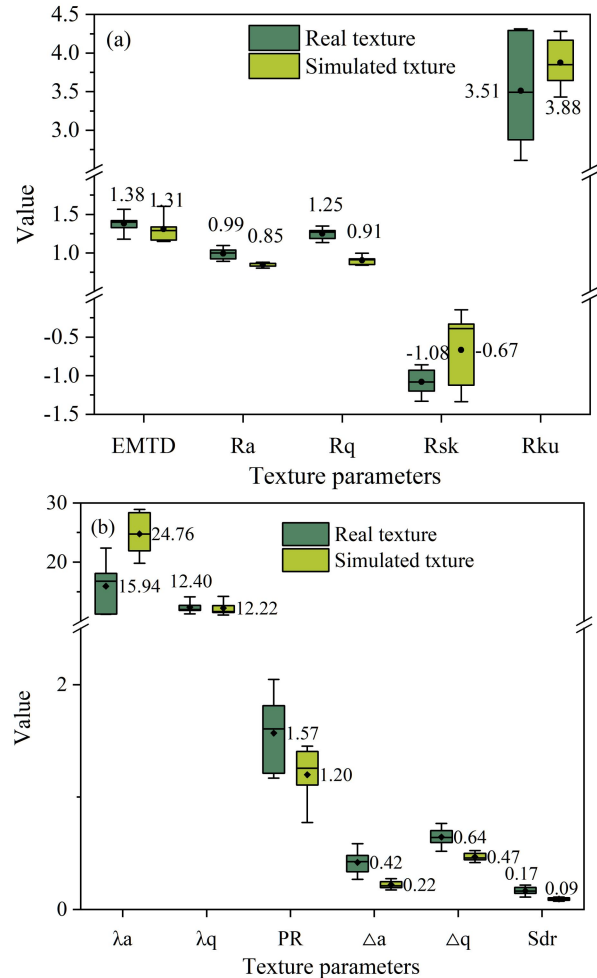
Figure 4. The texture parameters of SMA-13: (a) Amplitude-related parameters; (b) Wavelength-related and shape-related parameters.

to aggregates are considered rigid and the influence of asphalt is ignored during the simulation process, therefore the DEM model is uneasily compacted than the real pavement. For wavelength-related parameters, λ_q and PR shows a higher correlation to real texture, which is higher than 75%. For shape-related parameters, only Δ_q show a higher correlation to real texture, which is higher than 70%, where Δ_a and Sdr show a relatively low correlation to real texture, which is less than 60%. In addition, the similarity of the amplitude-related texture parameters is generally higher, so the DEM model is more suitable for the simulation of the amplitude-related parameters. Therefore, the two parameters with higher correlation in each category were selected for further study, including EMTD, R_{ku}, λ_q, PR, Δ_q, and S_{dr}.

3.2 Verification of Voids in Mineral Aggregate (VMA)

The *VMA* of the 3D DEM model is calculated by Equation (1), The *VMA* of the model was calculated to be 20.34%. The *VMA* of real pavement is 18.18%, which is higher than 17.0% meets the Technical Specifications for Construction of Highway Asphalt Pavements (JTG F40-2004).

$$VMA = 1 - \frac{V_{agg}}{V_{tot}} \times 100\% \tag{1}$$

The pavement texture and *VMA* of the actual mixture and simulation model are consistent. Therefore, the simulation model can be used for the research of texture parameters and corresponding skeleton composition.

4 CONCLUSIONS

This method demonstrates the feasibility of using the 3D DEM model for simulating pavement texture. Specifically, for the EMTD simulation, the accuracy exceeds 90%, while the simulation results for VMA are also within an acceptable range. These findings confirm that the approach is effective in capturing the significant effects of gradation type and NMSA on both the texture and skeletal structure of the wear layer. The 3D DEM model highlights the crucial role of the coarse-to-fine aggregate ratio in influencing the wear layer characteristics. This insight provides valuable guidance for optimizing mix design and improving the performance of the wearing layer.

5 ACKNOWLEDGEMENTS

6 REFERENCES

Ding, S. H., Wang, K. C. P., Yang, E. H. & Zhan, Y. 2021. Influence of effective texture depth on pavement friction based on 3D texture area. *Construction and Building Materials,* 287, 123002.

Fwa, T. F. 2021. Determination and prediction of pavement skid resistance–connecting research and practice. *Journal of Road Engineering,* 1, 20.

Ge, H., Quezada, J. C., Le Houerou, V. & Chazallon, C. 2023. Three-dimensional FEM-DEM coupling simulation for analysis of asphalt mixture responses under rolling tire loads. *Construction and Building Materials,* 369, 130615.

Huang, X. M. & Zheng, B. S. 2019. Research Status and Progress for Skid Resistance Performance of Asphalt Pavements. *China Journal of Highway and Transport,* 32, 32-49.

Ji, X., Zhu, S., Sun, Y., Li, H., Chen, Y. & Chen, Y. 2024. Reconstruction and evolution of 3D model on asphalt pavement surface texture using digital image processing technology and accelerated pavement testing. *Road Materials and Pavement Design,* 25, 1694-1719.

Kumar, A., Gupta, A., Anupam, K. & Wagh, V. P. 2024. Finite element-based framework to study the response of bituminous concrete pavements under different conditions. *Construction and Building Materials,* 417.

Liu, C., Xu, N., Weng, Z., Li, Y., Du, Y. & Cao, J. 2023a. Effective pavement skid resistance measurement using multi-scale textures and deep fusion network. *Computer-Aided Civil and Infrastructure Engineering,* 38, 1041-1058.

Liu, G., Han, D., Zhao, Y. & Zhang, J. 2020. Effects of asphalt mixture structure types on force chains characteristics based on computational granular mechanics. *International Journal of Pavement Engineering.*

Liu, G., Qian, Z. D., Wu, X. Y. & Zhang, X. F. 2023b. Stress responses analysis of asphalt mixture particles based on average principle during the rolling compaction process of weld SBDP. *Construction and Building Materials,* 400.

Liu, X. Y., Luo, H. Y., Chen, C., Zhu, L. Y., Chen, S. Y., Ma, T. & Huang, X. M. 2024. A technical survey on mechanism and influence factors for asphalt pavement skid-resistance. *Friction,* 12, 906-918.

Pei, Z., Yi, J., Mao, Q., Feng, D. & Wang, D. 2023. DEM analysis of the evolution of reflection cracks in old cement concrete pavement with an ATB layer. *International Journal of Pavement Engineering,* 24, 2049263.

Taniguchi, T., Inaba, Y., Murai, S. & Nishizawa, T. 1997. Mechanism of ice debonding on an asphalt mixture containing rubber particles. 3rd International Conference on Snow Engineering, 1996 Sendai, Japan. 379-386.

Wang, S., Miao, Y. & Wang, L. 2023. Effect of grain size composition on mechanical performance requirement for particles in aggregate blend based on photoelastic method. *Construction and Building Materials,* 363.

Xue, B., Que, Y., Pei, J. Z., Ma, X. Y., Wang, D., Yuan, Y. & Zhang, H. 2024. A state-of-the-art review of discrete element method for asphalt mixtures: Model generation methods, contact constitutive models and application directions. *Construction and Building Materials,* 414, 134842.

4.2

MODELING AND MONITORING TECHNIQUES FOR VEHICLE-PAVEMENT INTERACTION

Cost-Effective Pavement Roughness Assessment: Implementation and Validation of Solid-State LiDAR for IRI Measurement

A. Behzadian
Ph.D. Student, University of Missouri-Columbia, Columbia, Missouri, United States of America

Y. Adu-Gyamfi
Associate Professor, University of Missouri-Columbia, Columbia, Missouri, United States of America

W.G. Buttlar
Professor, University of Missouri-Columbia, Columbia, Missouri, United States of America

ABSTRACT: This study investigates the potential of solid-state LiDAR (SSL) technology for measuring the International Roughness Index (IRI) as an alternative to inertial profilers. Using a Livox HAP SSL sensor mounted on a vehicle alongside a reference SSI inertial profiler, measurements were conducted on a 100-meter road section exhibiting varying roughness conditions. Point cloud data from the SSL was processed to extract elevation profiles at 30-centimeter intervals, and IRI values were calculated using the quarter-car model. Comparative analysis revealed acceptable agreement between SSL and inertial profiler, with an R^2 of 0.821, MAE of 1.3 (m/km), and RMSE of 1.7 (m/km). While the SSL system showed some limitations in high-roughness zones, the overall results demonstrate its potential as a cost-effective alternative for pavement condition assessment, particularly in moderate roughness conditions.

1 INTRODUCTION

The International Roughness Index (IRI) serves as a standardized roughness measurement that characterizes the longitudinal profile of a road's surface. This critical metric has become the global standard for evaluating road surface conditions, playing a vital role in pavement management systems and maintenance decision-making processes. Transportation agencies worldwide rely on IRI measurements to assess road quality, plan maintenance schedules, and allocate resources effectively, as road surface conditions directly impact vehicle operating costs, safety, and user comfort (Sayers, 1995).

IRI measurements are primarily conducted using inertial profilers equipped with high-frequency laser sensors. These systems combine precise laser measurements with accelerometer data to generate accurate road profile measurements while compensating for vehicle dynamics. The laser-based inertial profilers have demonstrated high accuracy and reliability in measuring road roughness, making them the industry standard for pavement condition assessment (Chang et al., 2006). However, these systems come with significant limitations that restrict their widespread adoption, particularly among smaller transportation agencies and contractors. The primary constraints include substantial initial investment costs, ongoing maintenance requirements, and operational expenses. Furthermore, these systems require spe-cialized training and certified operators, adding to the overall cost and complexity of implementation.

In recent years, researchers have begun exploring alternative technologies for IRI measurement to address these limitations (Fares and Zayed, 2023). Various sensing technologies, including RGB-D sensors, depth cameras, and LiDAR systems, have emerged as potential solutions for road roughness measurement (Zhang et al., 2024). These technologies offer promising advantages in terms of cost-effectiveness and ease of use. However, their application in IRI measurement requires further investigation to validate their accuracy and reliability compared to traditional inertial profilers.

This study aims to evaluate the potential of solid-state LiDAR technology, one of the latest advancements in LiDAR systems, for IRI measurement. Solid-state LiDAR represents a significant technological evolution, offering advantages such as no moving parts, compact size, and potentially lower costs compared to traditional mechanical LiDAR systems. The research focuses on developing and validating a methodology for IRI measurement using solid-state LiDAR, with particular emphasis on comparing its accuracy against conventional inertial profiler measurements. By investigating this emerging technology, this study seeks to contribute to the development of more accessible and cost-effective solutions for road condition assessment while maintaining acceptable levels of accuracy for pavement management applications.

2 METHODOLOGY

2.1 Data Collection

The data collection process involved a comprehensive setup combining solid-state LiDAR with traditional inertial profiling equipment for validation purposes. The primary sensor used in this study was a Livox HAP solid-state LiDAR (SSL), which represents the latest generation of LiDAR technology without moving mechanical components. The SSL device was mounted on the rear of the vehicle using a secure suction cup mounting system, oriented in a top-down configuration to capture detailed point cloud data of the pavement surface. This mounting position was specifically chosen to optimize the sensor's field of view and ensure consistent data capture of the road surface profile.

To enhance the data collection process and provide additional contextual information, a GoPro camera was installed directly above the SSL unit. This camera served dual purposes: capturing high-resolution images of the pavement surface for visual reference and documentation, while simultaneously recording GPS coordinates. The GPS data was particularly crucial as it allowed for precise spatial registration of the SSL point cloud data, enabling accurate correlation between different measurement systems and facilitating subsequent data analysis.

For validation purposes, this study employed an SSI inertial profiler, which represents the current industry standard for IRI measurement. The inertial profiler was mounted on the same vehicle to ensure simultaneous data collection under identical conditions, allowing for direct comparison between the SSL measurements and the established reference measurements. Figure 1. shows the data collection equipment and setup.

The field testing was conducted on a carefully selected 100-meter road section in Columbia, Missouri. This test section was specifically chosen for its diverse range of surface conditions, exhibiting IRI values ranging from low to high. The variability in surface roughness within this single test section provided an ideal environment for evaluating the SSL system's performance across different roughness conditions. This strategic selection of the test section enabled the research team to assess the accuracy and reliability of the SSL-based measurements across a broad spectrum of pavement conditions within a controlled testing environment.
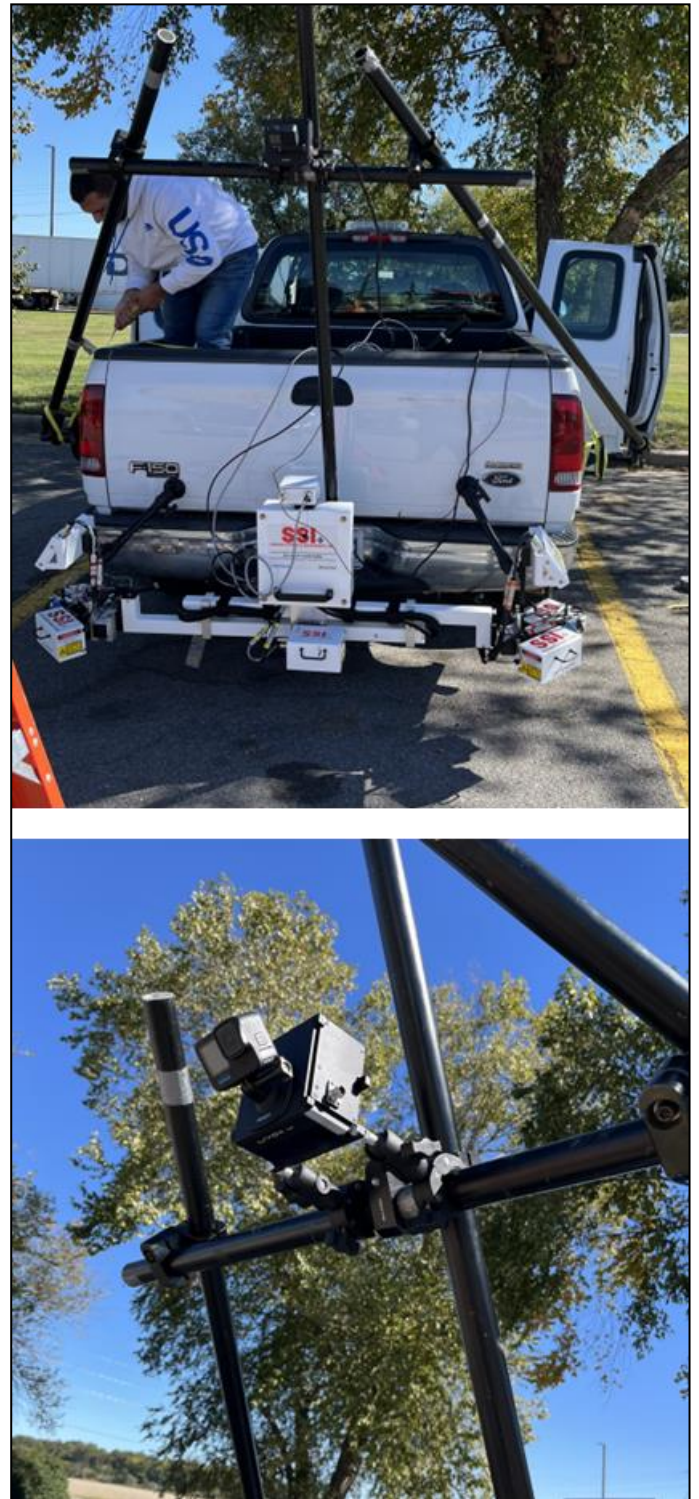
Figure 1. Data collection equipment and setup.

2.2 Longitudinal Profile Extraction

The extraction of longitudinal profiles from the collected point cloud data required a systematic approach to transform raw SSL data into meaningful elevation measurements suitable for IRI calculation. The process began with the temporal synchronization of the GoPro camera and SSL data streams, which allowed for the precise mapping of GPS coordinates to each point cloud frame. This synchronization was crucial as it enabled the transformation of the SSL's local coordinate system measurements into global coordinates, providing a standardized reference frame for the entire dataset.

Following the coordinate transformation, a thresholding approach was implemented to isolate the relevant points corresponding to the wheel path on the pavement surface. This selective extraction was essential for focusing the analysis on the specific path that influences vehicle response and ride quality. The thresholding process effectively filtered out peripheral data points while retaining the critical elevation measurements along the wheel path.

To facilitate IRI calculation, which requires regularly spaced elevation measurements, this study established a fixed sampling interval of 30 centimeters (equivalent to 1 foot) along the longitudinal profile (ASTM., 2005). At each sampling point along the longitudinal profile, elevation values were extracted from the point cloud data, creating a discrete elevation profile suitable for subsequent IRI computation.

2.3 IRI Measurement

Place The IRI is calculated using a mathematical model known as the quarter-car model, which simulates the dynamic response of a simplified vehicle suspension system traveling over a road surface. The quarter-car model consists of four primary components that work together to simulate vehicle dynamics. The sprung mass (representing one-quarter of the vehicle body mass), the unsprung mass (representing the wheel assembly), a spring element (simulating the primary suspension system), and a damper (representing the shock absorber) (Sayers, 1995).

The model processes road profile data by simulating the vehicle's response while traveling at a standardized speed of 80 kilometers per hour (50 mph). During this simulation, the system's response to road surface variations is governed by a set of differential equations that describe the dynamic interaction between the vehicle components and the road profile. These equations incorporate specific mechanical parameters that have been standardized worldwide, including precise spring rates, damping coefficients, and mass ratios. The IRI value is ultimately derived from the accumulated suspension motion, calculated as the sum of the relative displacement between the sprung and unsprung masses, normalized by the distance traveled.

For analysis and verification purposes, IRI measurements were obtained through two methods. First, the reference IRI values were extracted directly from the SSI inertial profiler measurements of the test section. Second, a Python script was used to calculate IRI values using the elevation data extracted from the SSL point clouds, implementing the quarter-car model to process these measurements (Šroubek et al., 2021). This dual approach enabled direct comparison between the inertial profiler measurements and the SSL-based results.

3 EXPERIMENTAL RESULTS

The experimental results demonstrate a strong correlation between IRI measurements obtained from the solid-state LiDAR (SSL) system and the reference SSI inertial profiler. The comparison of these two measurement systems was conducted through both longitudinal profile analysis and statistical correlation assessment.

The overall IRI comparison, illustrated as Figure 2., shows the IRI values measured by both systems along the 100-meter test section. The profile reveals that both systems captured similar patterns of road roughness variations throughout the section. The SSL measurements (shown in red) closely tracked the SSI measurements (shown in blue), with mean IRI values of 7.09 m/km and 7.77 m/km respectively. This difference in mean values indicates that the SSL system typically produced slightly lower IRI measurements than the reference system, but the overall difference remained relatively small at 0.68 m/km.

The IRI values show particularly higher agreement in sections with moderate roughness (between 4-8 m/km). Notable variations between the two systems were observed in areas of high roughness, particularly around the 40-meter and 80-meter marks, where IRI values peaked above 14 m/km. In these high-roughness zones, the SSL measurements sometimes underestimated the peak values compared to the SSI system, though they still captured the general pattern of roughness variation.

The statistical correlation analysis, presented in Figure 3., provides a quantitative assessment of the agreement between the two measurement systems. The analysis yielded an R-squared value of 0.821, indicating an acceptable positive correlation between the SSL and SSI measurements. This high correlation coefficient suggests that approximately 82% of the variance in SSL measurements can be explained by the SSI reference measurements, demonstrating reliability of the SSL system.
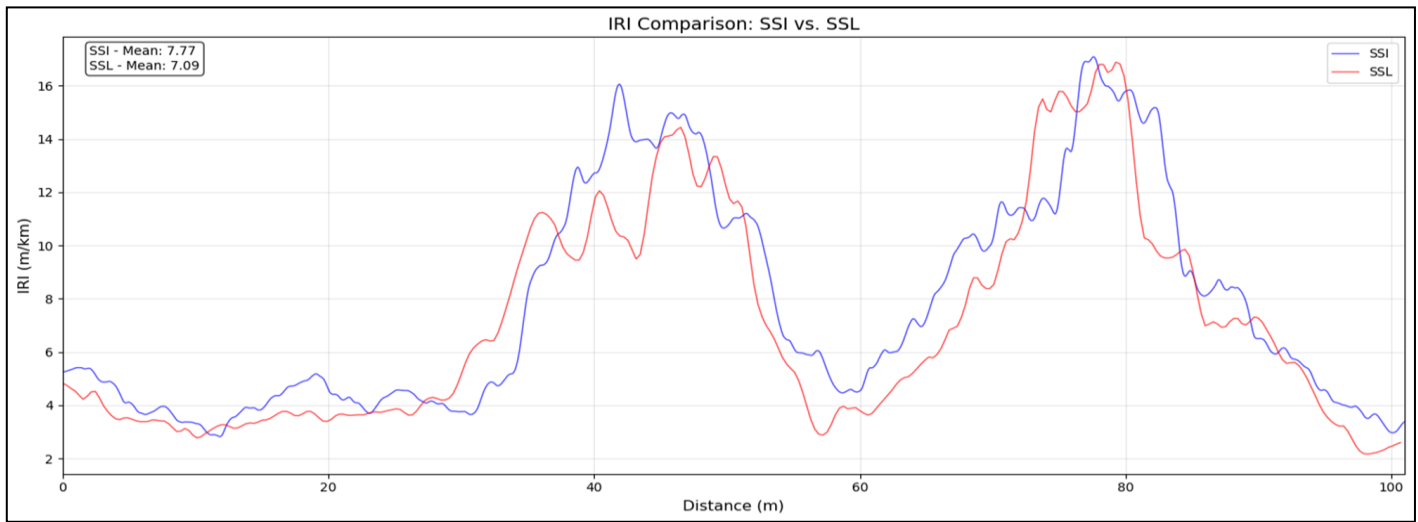
Figure 2. IRI comparison of SSL vs. SSI for the test road section.
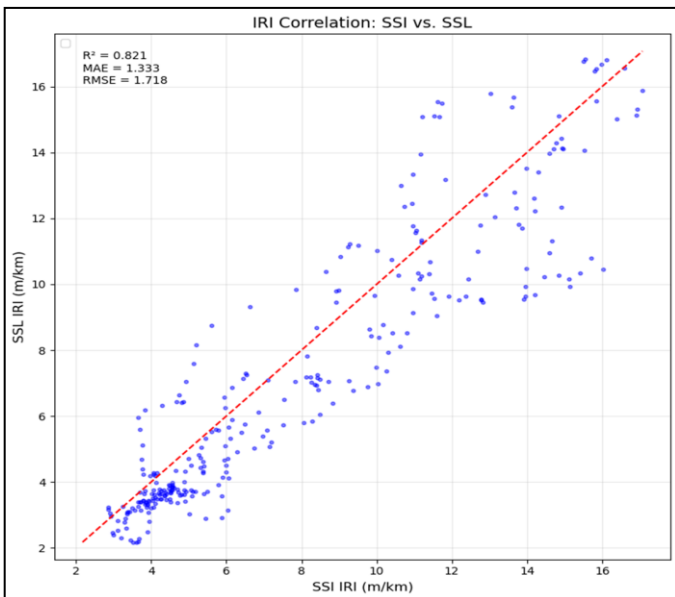
Figure 3. Statistical correlation analysis between SSI and SSL.

The accuracy of the SSL system was further quantified through error metrics. The Mean Absolute Error (MAE) of 1.333 m/km indicates the average magnitude of measurement differences between the two systems. The Root Mean Square Error (RMSE) of 1.718 m/km, being slightly higher than the MAE, suggests the presence of some larger discrepancies, particularly in the high-roughness regions as observed in the IRI profile. These error metrics, while indicating potential for further improvement, demonstrate promising performance for the SSL system, especially considering the complexity of road roughness measurement and the innovative nature of the technology.

4 CONCLUSION

This study demonstrates the potential of solid-state LiDAR technology as a viable alternative for measuring IRI in pavement condition assessment. Through field testing and analysis, the research validates that SSL-based measurements can achieve ac-

ceptable levels of accuracy when compared to inertial profiler systems, with a correlation coefficient of 0.821 between the two measurement methods.

The SSL system showed particularly promising performance in sections with moderate roughness levels (4-8 m/km), where it consistently tracked the reference measurements with high fidelity. While some discrepancies were observed in high-roughness regions, where the SSL measurements typically underestimated peak IRI values, the system successfully captured the overall patterns of surface roughness variation. The relatively small difference in mean IRI values between the SSL and SSI systems (0.68 m/km) further supports the potential of this technology for practical applications.

The results suggest that solid-state LiDAR could offer a more accessible alternative to traditional inertial profilers, potentially addressing the significant barriers of high cost and operational complexity that currently limit widespread adoption of road condition monitoring systems.

REFERENCES

ASTM. 2005. Standard test method for measuring road roughness by static level method. *E1364-95*.

CHANG, J.-R., CHANG, K.-T. & CHEN, D.-H. 2006. Application of 3D laser scanning on measuring pavement roughness. *Journal of Testing and Evaluation,* 34**,** 83-91.

FARES, A. & ZAYED, T. 2023. Industry-and academic-based trends in pavement roughness inspection technologies over the past five decades: A critical review. *Remote Sensing,* 15**,** 2941.

SAYERS, M. W. 1995. On the calculation of international roughness index from longitudinal road profile. *Transportation Research Record*.

ŠROUBEK, F., ŠOREL, M. & ŽÁK, J. 2021. Precise international roughness index calculation. *International Journal of Pavement Research and Technology***,** 1-7.

ZHANG, A. A., SHANG, J., LI, B., HUI, B., GONG, H., LI, L., ZHAN, Y., AI, C., NIU, H. & CHU, X. 2024. Intelligent pavement condition survey: overview of current researches and practices. *Journal of Road Engineering*.

Evaluating in-situ pavement deflection using geophone and accelerometer signal processing: A case study of the E16 motorway in Sweden

M.A. Bidgoli[a,b] & S. Erlingsson[a,b,c]

[a] *Swedish National Road and Transport Research Institute (VTI), Linköping, Sweden*
[b] *KTH Royal Institute of Technology, Stockholm, Sweden*
[c] *University of Iceland, Reykjavík, Iceland*

ABSTRACT: This research investigates the use of geophones and accelerometers for real-time pavement deflection monitoring under heavy vehicle loads. Traditional methods, such as the Falling Weight Deflectometer (FWD), are effective but costly and limited in both spatial and temporal applicability. In contrast, embedded geophones and accelerometers offer continuous deflection measurements, capturing vertical velocity and acceleration data that can be processed to derive pavement deflection values. In this study, field tests were conducted on the E16 motorway north of Borlänge in Sweden, with data processed through filtering, frequency transformations, and signal integration. Results indicate that sensor-based measurements align closely with theoretical deflections calculated via the elastic response software ERAPave, validating these sensors as cost-effective, scalable tools for pavement health monitoring. This approach demonstrates potential for continuous pavement assessment, supporting maintenance planning and promoting the durability of road networks.

1 INTRODUCTION

Monitoring pavement deflection is a critical component in assessing the structural strength and long-lasting durability of road infrastructure. Traditionally, methods like the Benkelman beam and Falling Weight Deflectometer (FWD) have been widely used to measure pavement deflection, but these approaches are often costly and limited to periodic, point-specific measurements. Recent advancements in sensor technology, including geophones and accelerometers, offer new opportunities for cost-effective, easy-to-install, and continuous monitoring, (Bahrani et al., 2019; 2020a; 2020b, Duong et al., 2020). These technologies offer a promising alternative for capturing real-time pavement deflection under actual traffic conditions.

This study explores the use of geophones and accelerometers as potential instruments for measuring pavement deflection in real-world conditions under heavy vehicle loads. Geophones measure vertical velocity, while accelerometers capture vertical acceleration. Through specific signal processing techniques, these sensors provide indirect deflection measurements. Geophone signals are integrated once to yield deflection, while accelerometer signals require double integration to derive displacement values, providing accurate and continuous data on pavement performance.

2 RESEARCH BACKGROUND

Previous studies have primarily focused on measuring pavement deflection using geophones and accelerometers in controlled laboratory environments (Bahrani et al., 2020b, Duong et al., 2020, Arraigada et al., 2007). Laboratory tests were initially conducted using vibrating tables to simulate pavement deflections, enabling a controlled analysis of sensor responses. Following these tests, APTs (accelerated pavement tests) were carried out under heavy vehicles and controlled loading scenarios to further assess sensor accuracy against standard reference deflection sensors. To ensure reliable deflection measurements, advanced signal processing techniques, including various filtering and transformation methods, were utilized to correct raw signals and reduce errors, particularly addressing issues of noise and integration drift.

The use of geophones and accelerometers for pavement monitoring has emerged as a promising and validated approach for obtaining real-time deflection measurements (Bahrani et al., 2020a). This study extends these evaluations to real-world field conditions, specifically in cold climates, further validating the practical implications of these sensors. In doing so, this research contributes to the growing body of knowledge on effective, scalable methods for pavement health monitoring and maintenance.

3 METHODOLOGY

The approach for measuring pavement deflection under heavy vehicle loads involves processing signals from embedded geophones and accelerometers. These sensors capture pavement vibrations induced by vehicle loads, which are then converted into deflection measurements through key signal-processing steps. Figure 1 outlines the process, which includes:

- Data collection: Using geophones and accelerometers to capture raw vibration data.
- Signal preprocessing: Filtering and cleaning the raw signals to remove noise and isolate relevant frequency components.
- Transfer function: Applying transformations and transfer functions to model dynamic pavement responses.
- Signal amplification: Adjusting signals based on sensor sensitivity and vehicle speed.
- Signal integration: Converting geophone (velocity) and accelerometer (acceleration) data into displacement via single and double integration, respectively.
- Deflection envelope: Detrending and applying the Hilbert Transform to extract the pavement deflection envelope.
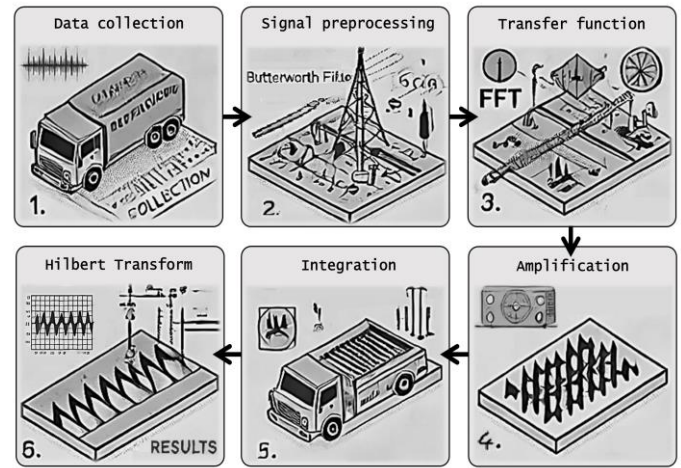
Figure 1. Flowchart of methodology for processing geophone and accelerometer signals to calculate vertical displacements.

To evaluate how well the processed geophone and accelerometer signals measure pavement deflections, we compared them with deflections calculated using the Multilayer Elastic Response Analysis of Pavements software (ERAPave), developed by Erlingsson and Ahmed (2013). Table 1 provides an overview of the pavement layer properties at the project site, which were used as inputs for the ERA-Pave model.

Table 1. Pavement layer properties.

Layers	Material	Thickness (cm)	E-Modulus (MPa)	Poisson's ratio
Layer 1	Surface course	4.0	5000	0.35
Layer 2	Binder course	5.5	5000	0.35
Layer 3	Road base	6.5	5000	0.35
Layer 4	Unbound base	8.0	400	0.35
Layer 5	Subbase	42.0	400	0.35
Layer 6	Protection layer	45.0	300	0.35
Layer 7	Subgrade	---	120	0.35

3.1 Data Collection

Real-time signals from geophones and accelerometers are recorded as vehicles pass the measurement site on the E16 motorway north of Borlänge, Sweden. Geophones capture voltage variations proportional to velocity (m/s), while accelerometers record acceleration (m/s²), both sampled at 1000 Hz. The setup includes two sets of five geophones and three accelerometers positioned in the first (slow) lane, installed at depths of 7.0 cm and 2.5 cm, respectively, as shown in Figure 2.

As a case study, signals were recorded under an 8-axle heavy vehicle weighing 45,550 kg and moving at 81 km/h. Table 2 presents the wheel load configuration on the right side of the heavy vehicle, obtained from a WIM (weigh-in-motion) system installed prior to the sensor setup. This loading configuration was also used for import into the ERA-Pave model.
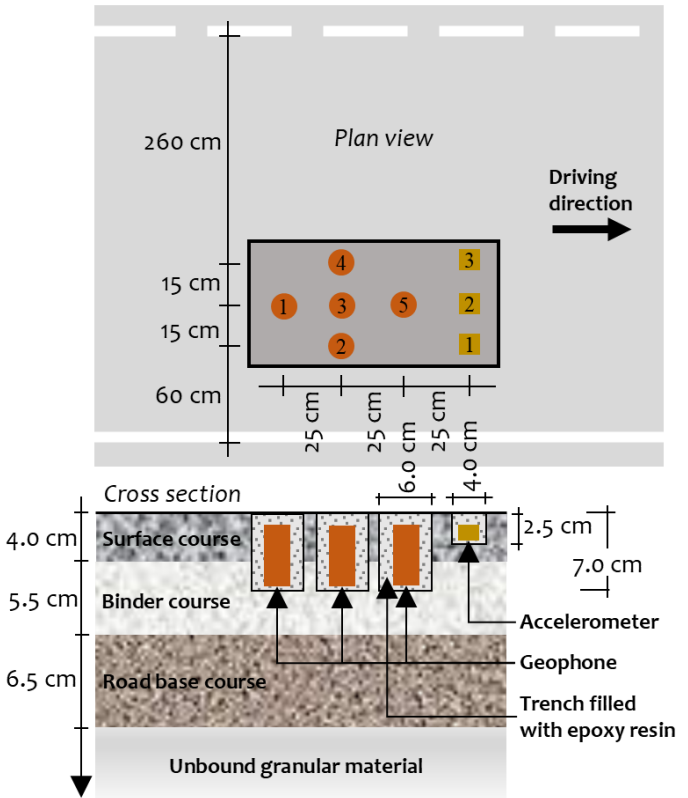
Figure 2. Plan view and cross section showing the positions of geophones and accelerometers embedded within the pavement.

3.2 Data Processing

The procedures for processing data were carried out to compute pavement surface displacements using signals from geophones and accelerometers. Displacement measurements from each sensor type are presented in Figures 3 and 4, illustrating the progression from raw signals (Figs 3a and 4a) to the final displacement results (Figs 3d and 4e) for the research case study.

Table 2. Wheel load configuration.

X (cm)	Y (cm)	Tire type*	Wheel load (kN)	Contact pressure (kPa)
0	0	S	41.97	1192
471	0	D	58.64	547
606	0	D	37.66	527
1114	0	S	18.04	867
1250	0	S	18.14	820
1842	0	S	16.97	932
1973	0	S	15.30	750
2104	0	S	15.98	683

* S and D represent single and dual tire types, respectively.
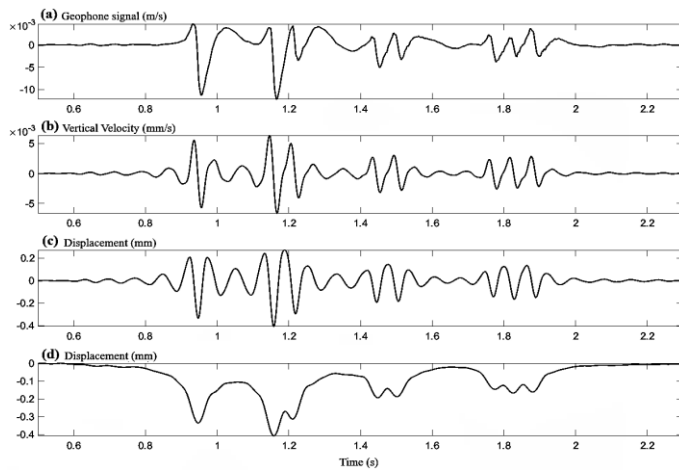
Figure 3. Displacement computation through geophone signals: a) the original signal; b) the filtered velocity signal (bandpass, 13-50 Hz cutoff); c) the displacement signal (transferred, amplified, and integrated); and d) the final displacement (Hilbert Transform).
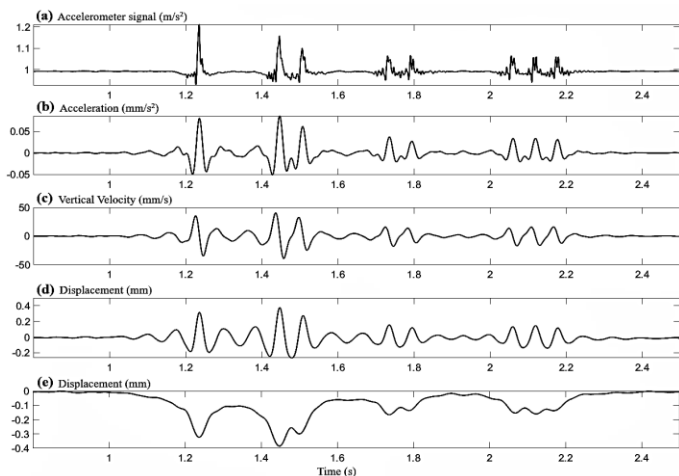
Figure 4. Displacement computation through accelerometer signals: a) the original signal; b) the filtered acceleration signal (bandpass, 13-50 Hz cutoff); c) the velocity signal (transferred, amplified, and first integrated); d) the displacement signal (second integration); and e) the final displacement (Hilbert Transform).

3.2.1 Signal Preprocessing

A 6th-order Butterworth bandpass filter (13-50 Hz) is applied to remove noise and isolate frequencies associated with pavement deflection (Mitra, 2001). This filter range is selected based on the vehicle's speed to capture relevant frequency content effectively.

3.2.2 Frequency Domain Transformation and Transfer Function

Signals are converted to the frequency domain using the Fast Fourier Transform (FFT), allowing the application of transfer functions to model pavement dynamics under heavy loads (Hons and Stewart, 2006). For geophone signals, a transfer function converts velocity to displacement, while accelerometer signals undergo a transfer function to convert acceleration to displacement. The frequency response model, defined by natural angular frequency (ω_0) and damping ratio (λ), adjusts the signal to reflect the actual pavement response, as given by, $TF(\omega) = \omega^2 / (\omega_0^2 - \omega^2 + 2i\lambda\omega_0\omega)$. After applying these functions, an inverse FFT returns the signals to the time domain (Figs 3b and 4b).

3.2.3 Amplification and Integration

The signal is amplified to align with real-world pavement deflection. Geophone data is integrated once to obtain displacement, as shown in Figure 3c. Accelerometer data undergoes double integration to achieve displacement, as illustrated in Figures 4c and 4d. Amplification and integration ensure that signals from both sensors reflect the pavement's actual deflection.

3.2.4 Detrending and Hilbert Transform

To remove drift and unwanted oscillations, the displacement signal is detrended, and the Hilbert Transform is applied for envelope extraction (Bahrani et al., 2020a). This transform shifts the signal phase to extract the envelope amplitude, giving a clearer measure of maximum deflection and smoothing out oscillations, as given by, $E(t) = \sqrt{(s^2(t)+\dot{s}^2(t))} =|S_e(t)|$, where s(t) represents the real part of the signal and $\dot{s}(t)$ is the imaginary part of the signal, both used to extract $S_e(t)$ as the envelope amplitude of the signal.

These final processed signals (Figs 3d and 4e) accurately represent true pavement deflection, removing noise and drift for clearer analysis.

4 RESULTS AND DISCUSSIONS

The processed averages of geophone and accelerometer measurements Bunts were compared with theoretical deflections calculated using ERAPave, as illustrated in Figures 5 and 6. These visual analyses provide detailed insights into the pavement response to the dynamic loading of an 8-axle, 446 kN heavy vehicle

moving at 81 km/h. The ERAPave model was configured to compute deflections along each centimeter of the x-axis at depths of 6 cm and 3 cm, corresponding to the installation depths of the geophones and accelerometers, respectively.

Figure 5 presents a time-series comparison between the calculated deflections from ERAPave and the averaged geophone measurements, while Figure 6 shows a similar comparison for accelerometer measurements. The alignment between sensor data and ERAPave calculations indicates that both geophones and accelerometers can effectively capture real-time pavement deflections, closely matching the model's predicted values at each sensor depth.

This analysis provides valuable insights into the pavement's behavior under heavy vehicle loads, demonstrating the ability of sensor-based monitoring to assess pavement responses accurately. Minor discrepancies between ERAPave calculations and sensor measurements, observed under specific load configurations, suggest areas for further refinement. Possible adjustments include calibrating the signal processing parameters, such as modifying cutoff frequencies, amplification factors, or filter order in the Butterworth filter. These refinements could enhance the accuracy of field measurements and improve the model's predictive alignment with observed data.
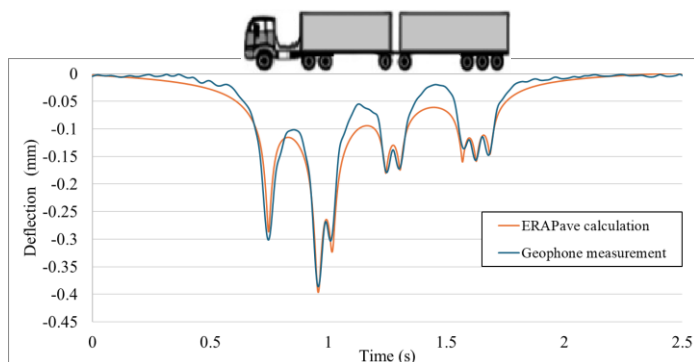
Figure 5. Comparison of deflections between ERAPave calculations and geophone measurements.
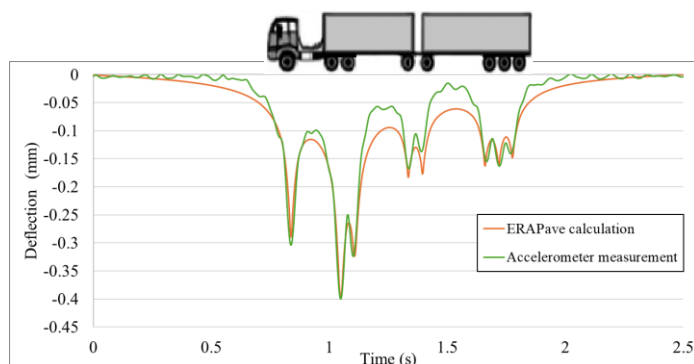
Figure 6. Comparison of deflections between ERAPave calculations and accelerometer measurements.

5   CONCLUSIONS

This study confirms the viability of a sensor-based approach using geophones and accelerometers to measure pavement deflection under heavy vehicle loads. We obtained real-time deflection data by utilizing 10 geophones and 6 accelerometers, which we compared with ERAPave-calculated deflections. The close alignment of sensor data with the model outputs supports the potential of this approach for reliable infrastructure monitoring. Minor discrepancies between ERAPave results and field measurements suggest that enhancing the model's precision could further improve accuracy, potentially through adjustments for material-specific characteristics and refinements in signal processing techniques.

Overall, this study provides field-based validation for deploying geophones and accelerometers as effective tools in real-time pavement monitoring. The findings underscore the benefits of incorporating advanced sensor technology with computational models to enhance the accuracy of pavement performance assessments. Beyond providing timely insights into pavement health, this approach shows promise for applications such as vehicle type and speed detection and back-calculating pavement layer properties, all of which contribute to the design and maintenance of more durable road infrastructure.

6   ACKNOWLEDGEMENTS

7   REFERENCES

Arraigada, M., Partl, M. N. & Angelone, S. 2007. Determination of Road Deflections from Traffic Induced Accelerations. *Road Materials and Pavement Design,* 8, 399-421.

Bahrani, N., Blanc, J., Hornych, P. & Menant, F. Pavement instrumentation for condition assessment using efficient sensing solutions. International Conference on Smart Infrastructure and Construction, 2019. 471-480.

Bahrani, N., Blanc, J., Hornych, P. & Menant, F. 2020a. Alternate method of pavement assessment using geophones and accelerometers for measuring the pavement response. *Infrastructures,* 5, 25.

Bahrani, N., Blanc, J., Hornych, P. & Menant, F. Evaluation of the use of geophones and accelerometers for monitoring pavement deflections, using accelerated pavement tests. Lecture Notes in Civil Engineering, 2020b. 526-535.

Duong, N. S., Blanc, J., Hornych, P., Menant, F., Lefeuvre, Y. & Bouveret, B. 2020. Monitoring of pavement deflections using geophones. *International Journal of Pavement Engineering,* 21, 1103-1113.

Erlingsson, S. & Ahmed, A. 2013. Fast layered elastic response program for the analysis of flexible pavement structures. *Road Materials and Pavement Design,* 14, 196-210.

Hons, M. S. & Stewart, R. R. 2006. Transfer functions of geophones and accelerometers and their effects on frequency content and wavelets. *CREWES Res. Rep,* 18, 1-18.

Mitra, S. K. 2001. *Digital Signal Processing: A Computer-Based Approach*, McGraw-Hill Higher Education.

Fourier-finite element analysis of pavements incorporating high precision tire footprint measurements

G. Canon Falla, S. Leischner & A. Zeißler
Institute of Pavement Engineering, Technische Universität Dresden, Dresden, Germany

V. Yordanov
Institute for Automotive Engineering, RWTH Aachen, Aachen, Germany

ABSTRACT: This paper presents a numerical model, the Fourier-Assisted Finite Element Method (FSAFEM), for the efficient calculation of pavement responses under traffic loads. The model was employed to determine the in-pavement stresses and strains of a mill-and-overlay pavement, focusing on the asphalt surface overlay layer. High-precision tire footprint measurements of a truck tire at different tire inflation pressures were incorporated into the simulations, along with variations in the interlayer bond conditions. The results showed the significance of precise numerical models capable of integrating such detailed inputs, particularly for analyzing pavement distresses that originate near the surface.

1 INTRODUCTION

In recent years, the concept of digital twins has emerged in pavement engineering, emphasizing the need for precise modeling of pavement responses to realistic loading conditions. This precision is particularly critical near the pavement surface, where stresses are highest and the upper asphalt layer houses valuable sensor equipment. Traditional modeling techniques, such as three-dimensional finite element modeling (3D FEM), have been widely used to simulate tire-pavement interactions. However, these methods often require very fine meshing to capture the details of the tire pressure distributions in the tire contact patch (further referred to as tire footprints), leading to substantial computational time and resource constraints. The limitations of conventional 3D FEM in this context highlight the need for alternative modeling approaches that can speed up the delivery of results without compromising their quality.

This paper introduces the Fourier Series Assisted Finite Element Method (FSAFEM). With FSAFEM, it is feasible to utilize high-precision measurements of the tire footprint to determine pavement responses. By effectively accounting for the detailed geometry and pressure distribution within the tire-pavement contact area, FSAFEM achieves pavement response predictions comparable to those of 3D FEM methods while requiring only a fraction of the computational time.

The paper begins with an overview of the mathematical background of FSAFEM and its implementation into an in-house developed software, Dromos.

Next, an application case is presented where Dromos is employed to simulate the responses in the surface layer of an hypothetical mill-and-overlay asphalt pavement. The simulations were conducted using tire footprint measurements of a truck tire at three different inflation pressures. The interlayer bond between the surface and the underlying asphalt layer was also varied (considering both full bond and no bond conditions). Finally, the key findings are discussed, along with potential applications into a digital twin of the road.

2 FOURIER SERIES ASSISTED FINITE ELEMENT METHOD (FSAFEM)

The FSAFEM (Potts 2001) is a numerical approach that combines the computational efficiency of analytical methods with the geometrical modeling versatility of FEM. This method is particularly well-suited for pavements, as it approximates the calculation domain as straight and infinite in the longitudinal (traffic) direction. Such an approximation is valid for most pavements geometries, where the length and radius of curvature greatly exceed their thickness and width.

The core concept of FSAFEM is to perform Fourier analysis in the longitudinal direction while using finite elements to model the cross-section of the pavement. The cross-section plane (x-y plane) is discretized with a 2D finite element mesh, where field variations within this plane are represented using nodal values and shape functions. Assuming that (1) the material properties remain constant in the traffic

direction and (2) the materials exhibit linear behavior, a Fourier transform can be applied to all special dependent variables (i.e. displacement, stress and strain) in the traffic direction (z-coordinate). Additionally, if it is further assumed that the load is periodic, the Fourier transform can be replaced by a Fourier series.

By applying this transformation, the analysis reduces to the solution of a 2D boundary value finite element problem for each wavenumber in the Fourier series. The results, obtained in the wavenumber domain, must then be inverse Fourier transformed to retrieve the solution in the spatial domain. A detailed description of the mathematical background of FSAFEM is provided in Canon (2021).

In a nutshell, the pavement responses under measured tire contact pressures using FSAFEM are determined as follows:

1. Compute the Fourier transform (Fourier series) of the tire footprint measurements in the traffic direction.
2. Create a 2D finite element mesh of the pavement cross-section. The finite element discretization within the loading region shall match the spatial dimensions of the tire footprint measurements.
3. Solve the 2D finite element boundary value problem in the wavenumber domain for each Fourier term representing the tire footprint measurements.
4. Apply the inverse Fourier transform to obtain displacements, stresses, and strains in the spatial domain.

The FSAFEM was programmed in Fortran 90 into an in-house developed software, *Dromos*, by the Institute of Pavement Engineering at TU Dresden. The software was designed in a modular manner, comprising three main modules: The Preprocessing Module defines the data structures for the problem. It includes a mesh generator and a load generator. The mesh generator creates the 2D finite element mesh of the pavement cross-section using 4-node isoparametric finite elements. The interfacial deformation at the interlayer zone is modeled using the zero-thickness element proposed by Goodman (1977). Figure 1 shows a schematic representation of the 2D finite element mesh and both types of elements. The load generator computes the Fourier coefficients of the load, representing the tire footprint pressure. The Processing Module is responsible for computational tasks such as assembling stiffness matrices and force vectors for each Fourier harmonic. It solves the finite element boundary value problem in the wavenumber domain. The Post processing Module handles the transformation from the wavenumber domain back to the spatial domain. The postprocessor also generates output files compatible with the

open-source visualization tool *ParaView* for easy analysis and visualization.
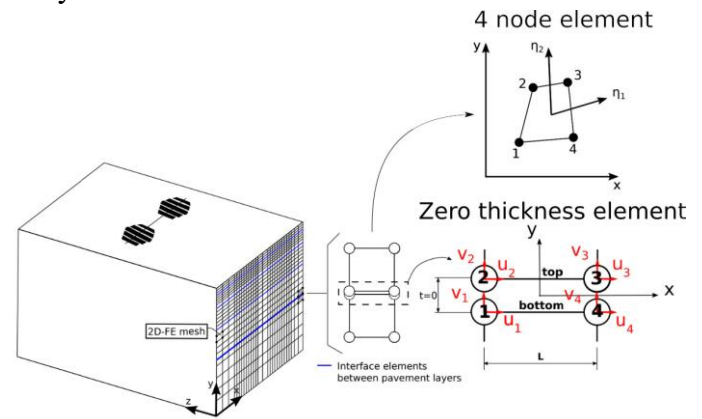
Figure 1. Schematic representation of the 2D finite element mesh.

The implementation and accuracy of *Dromos* were verified by comparing its results with those obtained from commercial 3D finite element software, such as Abaqus, across several benchmark cases. The validation demonstrated the potential of *Dromos* to significantly reduce computation time compared to Abaqus, particularly when simulating pavement structures with non-fully bonded layers. *Dromos* employs the Goodman element to account for such scenarios directly. In contrast, Abaqus requires the use of a contact formulation with slave and master surfaces, which substantially increases computation time.

3 TIRE FOOTPRINT MEASUREMENTS

In this paper, the tire footprints were measured utilizing the tire stiffness test rig (SteiReP) developed at the Institute for Automotive Engineering (ika), RWTH Aachen University (Fig. 2). The test rig offers the flexibility to use various surfaces for the assessment of stiffness characteristics as well as a dedicated truck tire pressure-mapping sensor surface for collecting contact pressures. The truck tire used in this study, is Pirelli - ST:01T with dimensions 385/55R22.5 and carcass construction 160K.
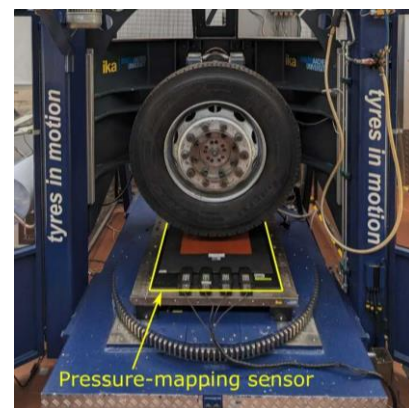
Figure 2. Tire Stiffness Test Rig (SteiReP).

Utilizing load control operation mode of the test rig, footprints of the tire, shown in Figure 3, were measured at a constant vertical load of 35.3 kN and three inflation pressures: 6 bar, 8 bar and 10 bar. The measurements show that the loaded area is slightly decreasing with increase of the inflation pressure. On the other hand, the maximum and average local contact pressures are significantly increasing with increase of the inflation pressure. This highlights the concentration of the load towards the centre of the contact patch and thus potentially increase the local stresses transferred to the road surface.
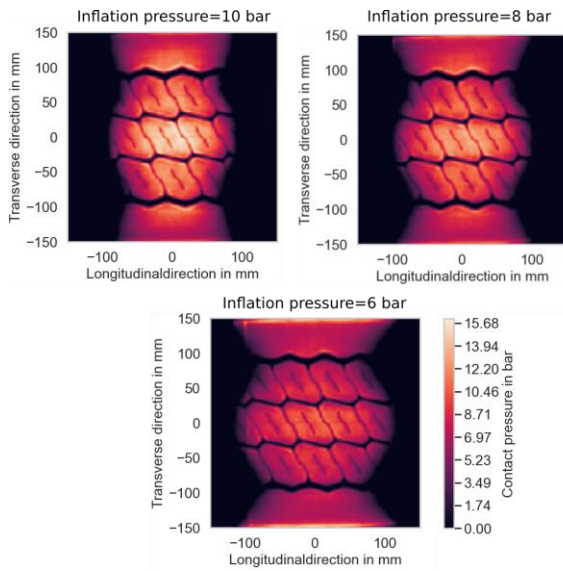
Figure 3. Measured tire footprints for three different inflation pressures.

4 APPLICATION AND SIMULATION RESULTS: EFFECTS OF INFLATION PRESSURE AND INTERLAYER BOND

Simulations were performed on a hypothetical mill-and-overlay pavement where the top surface layer was replaced with an asphalt overlay. Within the context of digital twin road, this asphalt overlay is a smart asphalt layer that interact with the digital twin. Accurately determining the in-pavement stresses of this smart layer is crucial, as it hosts valuable sensors whose functionality supports the operation of the digital twin system. Furthermore, the service life of this layer largely dictates the overall lifespan of the digital twin. Consequently, it is essential to accurately predict key pavement responses associated with common distresses to estimate the layer's durability.

The pavement structure consists of a 40 mm asphalt overlay (Elasticity modulus, E=3000 MPa, Poisson's ratio, ν=0.35) placed over a 240 mm asphalt concrete layer (E=5000 MPa, ν=0.35), underlain by a 320 mm unbound base course (E=400 MPa, ν=0.4) and 400 mm unbound subbase (E=120 MPa,

ν=0.4). The subgrade (E=45 MPa, ν=0.2) was modeled with a thickness of 2000 mm. At its current stage of development, *Dromos* models all materials as linear elastic. However, future enhancements are planned to account for the viscoelastic behavior of asphalt materials.

Figure 4 illustrates the calculation domain, which comprises a 2D finite element mesh representing the transverse cross-section of the pavement. A width of 6 m is assumed to eliminate the influence of boundary conditions. The results along the longitudinal direction are obtained by evaluating the nodal variables of the mesh at various positions along the z-coordinate. Within the loading area, a fine mesh discretization of 1.56 mm is employed, matching the resolution of the tire footprint measurements.
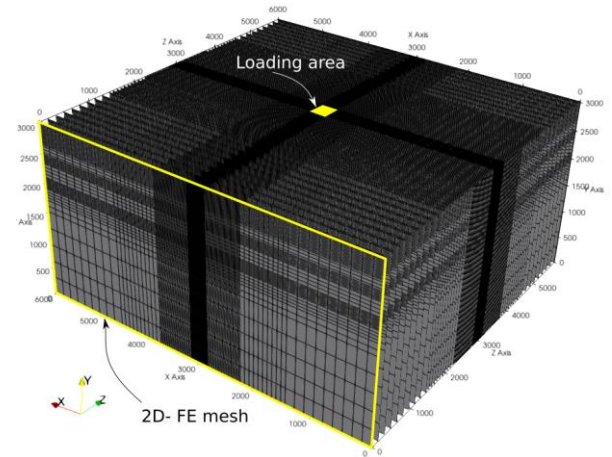
Figure 4. *Dromos* calculation domain.

The tire footprint measurements were transformed in the longitudinal direction using a Fourier series with 400 harmonics and a period of 6 m. Figure 5 presents the histogram of the goodness-of-fit (R-square) values from the Fourier transformation compared to the original measurements. The histogram shows that the majority of R-square values are concentrated near 1, indicating an excellent fit between the Fourier-based regression and the measured data. However, a small number of lower R-square values highlight cases where the regression may not perform as well. An example of such a case is detailed in the figure, which occurs when the measurements exhibit high variability with sharp peaks.
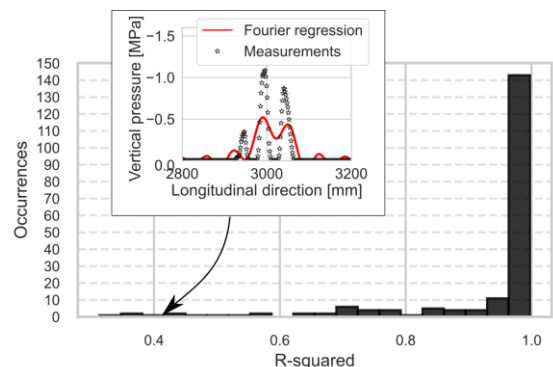
Figure 5. *Histogram of goodness-of-fit (R-square)*

Figure 6 shows the simulation results in terms of stress distribution within the pavement at the cross-section beneath the tire footprint. The results clearly indicate that the asphalt overlay is subjected to high localized stresses, which increase with the magnitude of the inflation pressure. The stress concentration is particularly critical at the center of the tire footprint under the 10 bar inflation pressure. In contrast at the 6 bar inflation pressure, the stresses are more evenly distributed throughout the entire contact patch area.
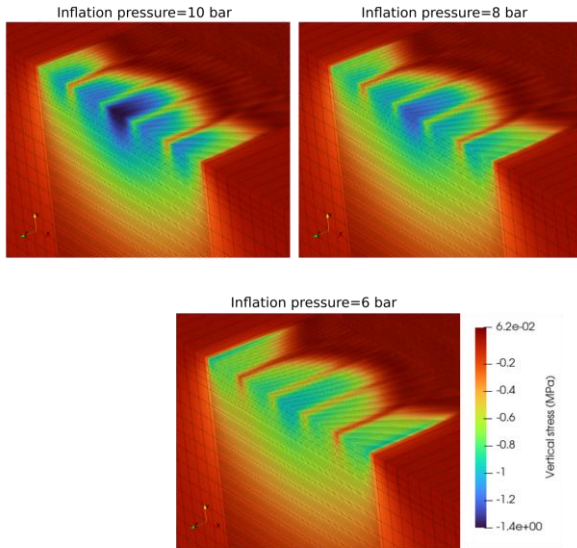
Figure 6. *In pavement vertical stresses*

The interlayer bond between asphalt layers significantly influences the service life of the pavement. When the bond breaks, the asphalt structure behaves as a laminated composite, leading to tensile strains emerging at the bottom of the layers where the bond failure occurs. Under repeated traffic loads, these strains can initiate cracking that propagates and result in fatigue damage. This phenomenon is evidenced in Figure 7, which illustrates the longitudinal strains at the pavement cross-section for both interlayer conditions: full bond and no bond. Under the full bond condition, the bottom of the asphalt overlay experiences compressive strains. However, when the bond fails (no-bond condition), significant tensile strains develop at the bottom of the overlay.
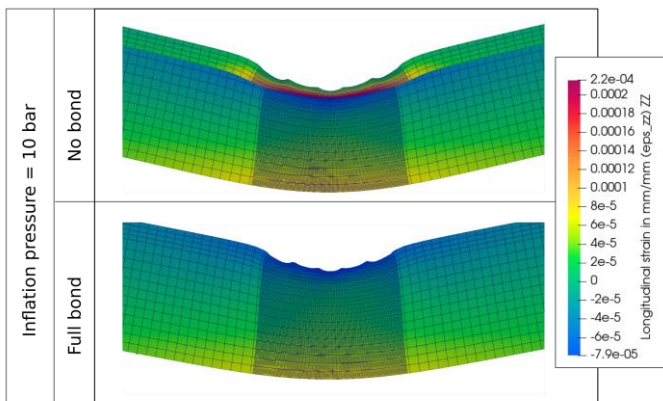
Figure 7. *In-pavement Longitudinal strains.*

Figure 8 presents the magnitude of the longitudinal strains at the bottom of the overlay and at the bottom of the asphalt. The magnitude of the tensile strains is an indicator used in empirical formulas to determine the fatigue resistance of the layer. Thus, it is evident that both the inflation pressure and the interlayer bond significantly affect the service life of the overlay. High-performance asphalt materials are crucial to accommodate off-design scenarios where the interlayer bond fails, leading to substantial tensile strains near the load.
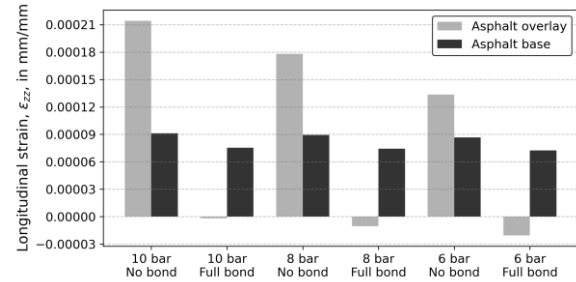
Figure 8. Longitudinal strains at the bottom of the asphalt layers.

5 CONCLUSIONS

This paper presents an efficient numerical alternative to 3D-FEM, the FSAFEM, for accurately determining pavement responses to realistic traffic loads. The following conclusions can be drawn:

- FSAFEM efficiently incorporates high-precision tire footprint measurements and varying interlayer bond conditions, offering significant computational advantages over traditional 3D-FEM methods.
- Tire inflation pressure strongly affects stress and strain magnitudes at the surface layer. For digital twin roads, which host expensive sensors near the loads, it is crucial to use high-performance asphalt materials to handle such stress/strain conditions.

6 ACKNOWLEDGEMENTS

7 REFERENCES

Canon Falla, G. 2021. Characterization and modeling of asphalt concrete from micro-to-macro scale. PhD Thesis, Technische Universität Dresden.

Goodman, J., Wilson, E.L., and Isenberg, J. 1977. Finite element for rock joints and interfaces. Journal of Soil Mechanics and Foundations Division, ASCE.

Potts, D.M. 2001. Finite Element Analysis in Geotechnical Engineering: Theory and Application. ICE Publishing.

Transportation infrastructure contrition evaluation via connected vehicles: a case study

M.S. Entezari

Department of Civil and Environmental Engineering, Amirkabir University of Technology, Tehran, Iran

A. Golroo

Department of Civil and Environmental Engineering, Amirkabir University of Technology, Tehran, Iran
Faculty of Information Technology and Electrical Engineering, University of Oulu, Oulu, Finland

M. Rasti

Faculty of Information Technology and Electrical Engineering, University of Oulu, Oulu, Finland

ABSTRACT: Gathering pavement data has always been a tedious task for highway agencies. Researchers and Practitioners have always looked for a cost-effective and continuous method for pavement monitoring. With vehicles being equipped with Information and Communication Technologies (ICT), Connected Vehicles (CVs) are now available in the market. In this paper an architecture for CV-based pavement evaluation was proposed. Next a model was developed for distress detection and implemented on vehicle using a raspberry pi. The model was capable of detecting 8 different pavement distresses with a Mean Average Precision (mAP) of 58.8%, a precision of 74.2%, and a recall of 52.1%. Due to the low computation time, the model could be run on the onboard mini-computer to detect anomalies in real time. It was concluded that the model could be used on vehicles to gather condition data.

1 INTRODUCTION

Highways, as strategic and essential infrastructures, allow for the social development in a country. However, factors such as traffic loads, temperature, and moisture will result in the degradation of highway pavements, consequently bringing about large economic losses (Li et al. 2019). For instance, pavement distresses impose $ 130 billion of additional vehicle repair costs to US motorists (ASCE, 2019). It is therefore important periodically assess pavement condition and then develop pavement maintenance scenarios. If the maintenance operations are carried out in the right time and without delay, budget expenditures of the road authorities are reduced (Ji et al. 2020).

The current practice in pavement evaluation involves using vehicles equipped with high-tech sensors such as laser scanners, black-box cameras, and accelerometers. Along with the technical equipment, Deep Learning (DL) algorithms such as Convolutional Neural Networks (CNNs) are employed to automatically analyze the collected data (Gopalakrishnan, 2018). The collected information includes inventory data (road geometrics and amenities such as drainage) and condition data (pavement distresses, roughness, and skid resistance) (Sholevar et al. 2022). Although automatic road surveyors offer many advantages, there are challenges in using them for network-wide monitoring. Provision, maintenance, and operation of the equipment impose high expenses to the highway agencies. Thus, the agen-

cies can only afford to provide one or two automatic profilers and implement them on limited areas of the network. The other shortcoming is long inspection periods. With the small number of surveyors available, road authorities are not able to cover all the network and can only concentrate on major roads (Chen et al. 2022). As relying on Road Surface Profilers (RSPs) for pavement monitoring is not feasible and cannot provide timely data, researchers have tried to devise alternative health monitoring systems with commercial-grade tools and capable of automatic evaluation in short time.

In this regard, Linton & Fu 2016 proposed a structure for winter road surface condition evaluation using CVs. Bridgelall et al. 2019 concentrated on the enhancement of CV signals and improvement of distress localization. Entezari & Golroo 2023 conducted a thorough review on the applications of CVs in pavement evaluation. According to the research, evaluation of many pavement distresses (including raveling, weathering, potholes, alligator cracks, along with manholes and faded markings) have not been investigated in a CV-environment by taking advantage of computer vision techniques. In the present article, YOLOv8 object detection algorithm is used to detect pavement distresses in a CV environment.

In the following sections of the present article, first an architecture for CV-based pavement evaluation is proposed based on Edge computing. Then, the case study carried out based on the architecture

is discussed. Finally, the strategies for future research are proposed.

2 METHODOLOGY

The system architecture in an Intelligent Transportation System (ITS) is presented in Figure 1. In such a system, data obtained from vehicles is stored on a backend server. Data could be transmitted to the data processing center through Roadside Units (RSUs). Each vehicle is equipped with an Onboard Unit (OBU) to send, receive, or process data (Jadaan et al. 2017).
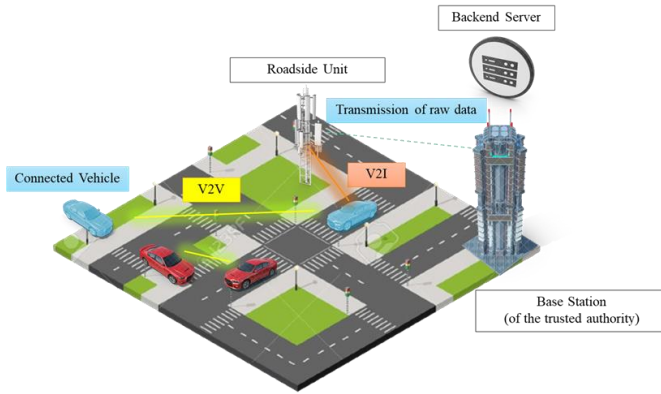
Figure 1. The architecture and components in an intelligent Transportation System

To grasp more deeply how such an architecture could be deployed to assess pavement condition, the details of the architecture is demonstrated in the workflow in Figure 2. According to the workflow, first, vehicles traverse the roads and gather data by different sensors, including visual sensors such as the rear-view camera. The data are processed by onboard computer which is programmed to analyze the input data. The obtained information is then sent to RSUs. Subsequently, the data is transferred to the data processing center from RSUs. Various information obtained from the fleet of vehicles such as pavement distresses could then be used to have an understanding of the asset condition. The information can be used by experts to calculate pavement performance indices and address the required maintenance operations.
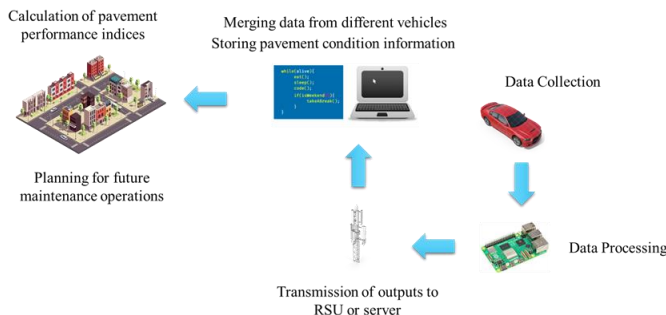
Figure 2. Pavement monitoring and maintenance planning in a CV environment

In the architecture presented in this article, the OBU is advised to be made of two main parts. The first part is a radio communication unit which broadcasts messages to other CVs or the RSUs. The information sent to the RSUs will finally reach the backend server in order to fulfill the authority's database. The second part of the OBU is a processing unit which performs data analysis models on the collected data. To automatically process the data, the application of DL models is necessary.

In order to comply with the essence of Edge computing, a pavement distress detection model was developed in this research and implemented on Raspberry pi 3B+ device. To develop the model, YOLOv8 algorithm was used. YOLO is a one-stage object detection model based on Convolutional Neural Networks (CNNs) which is run on Python and installed using a PIP package (Zheng et al. 2024).

To train the model, a dataset of 600 pavement images were gathered and annotated[1]. The distresses labeled on the images included linear cracks, alligator cracks, lane shoulder drop-off, weathering, raveling, patching, and potholes. Also, faded lane markings were labeled in the dataset.

The available data were divided into 3 different groups of training data (70%), validation data (15%), and Testing data (15%). Google Colab platform was used for model training. In order to evaluate the model, 3 performance indices were investigated: Recall, Precision, and mAP. The formulations of the first two are presented in Equations 1 and 2:

$$Recall = \frac{TP}{TP+FN} \tag{1}$$

$$Precision = \frac{TP}{TP+FP} \tag{2}$$

where TP = True Positive; FN = False Negative; and FP = False Positive.

The formulation of mAP is also presented in Equation 3:

$$mAP = \frac{1}{n}\sum_{k=1}^{k=n} AP_k \tag{3}$$

where AP_K = Average Precision of the Kth group; and n = number of groups.

3 RESULTS AND DISCUSSION

The performance indices obtained for the distress detection model after a 300-epoch training process were an mAP of 58.8% (Fig. 3), a Precision of 74.2%, and a Recall of 52.1% (Fig. 4).

---

[1]https://universe.roboflow.com/dissertation-ac1jd/saleh/dataset/1
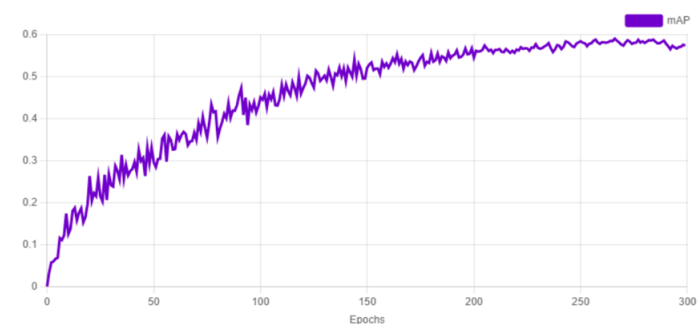
Figure 3. The increase in model's mAP through 300 iterations of the training process
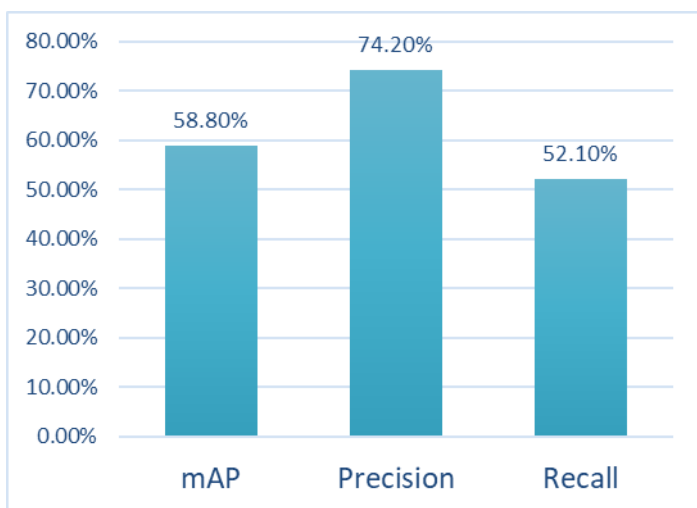
Figure 4. Obtained performance indices for the distress detection model

It is presumed that the low mAP is perhaps due to the low number of instances for each category. It could also be attributed to the quality of crowdsourced cameras, not fully capturing the texture of the pavement and making it hard to detect weathering defects. As the model merits from a high precision index, but has a low recall, it can be realized that the model misses some of the distresses, but correctly classifies the ones that it detects. The Average Precision obtained for each group is presented in Table 1.

Table 1: Average Precision obtained by the model for the 8 detected classes

Distress	Average Precision
Linear crack	55.5%
Alligator crack	61%
Weathering	59.5%
Shoulder drop-off	71%
Patching	50%
Raveling	66%
Pothole	33%%
Faded Marking	74.5%

To make sure whether the presented solution is compatible for a CV-environment, the duration of analysis for each picture on the raspberry pie was evaluated. As the videos were first preprocessed and then sent to the model, the analysis period of each frame was about 2 seconds. A sample analyzed frame is presented on Figure 5.
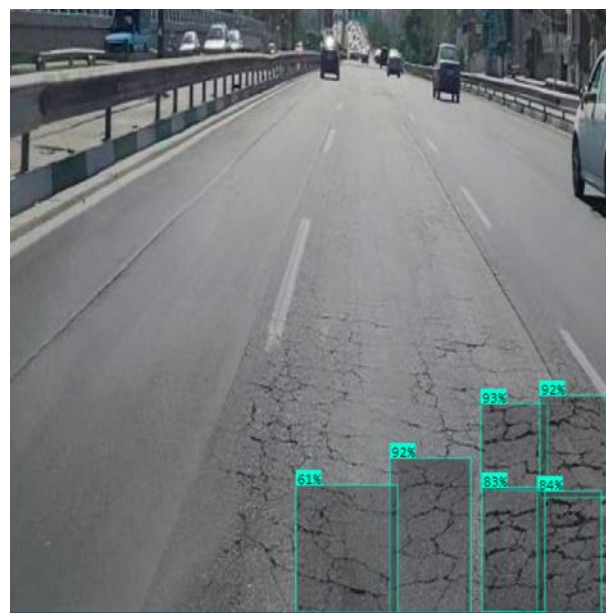
Figure 5. A sample frame analyzed by the distress detection model

4 CONCLUSION

Pavements are adversely affected by axle loadings, environmental factors and interaction with underneath layers. As a result, the serviceability of the infrastructure is lowered by the appearance of distresses (such as linear cracks, alligator cracks, weathering, and faded markings) and roughness. Thus, road authorities continuously monitor pavements of the wide road network. The collected information includes condition data and inventory data. Automatic pavement surveyors such RSPs are the current technology implemented by highway agencies to collect pavement data. For this purpose, they traverse road segments by the surveyor vehicles. As the equipment is highly expensive, each agency can afford to purchase very few automatic surveyors. As it is not possible to traverse the whole network by the available vehicles, road agencies can only concentrate on major roads and even these high-priority roads are evaluated only once a year. In such a system maintenance planning is difficult as the data is delayed and timely data is not at hand. To come up with a new framework for pavement evaluation, connected vehicles have proven to fulfill the requirements of a pavement health monitoring system. These vehicles consistently move in the network and evaluate pavement using cost-effective sensors. As the vehicles are able to communicate with each other and with the infrastructure, the obtained data can be used to both complete the database of the road authority and to alert drivers of intense distresses. In

this article an architecture was proposed for evaluating pavement by CVs and a specific design for the OBU was suggested. Next, as a case study, pavement distress detection was performed on the vehicle, detecting 8 different pavement anomalies including linear crack, alligator crack, raveling, weathering, shoulder drop-off, patching, pothole, and faded marking. The case study included collection and annotation of 600 pavement images, training a distress detection model using Yolo V8 algorithm, and implementing the model on a raspberry pie. The model reached an mAP of 58.8%, a precision of 74.2%, and a recall of 52.1%. It was concluded that pavement distress detection could be applied on vehicles. It was suggested that the developed system could be improved in future research by implementing radio communication technologies for broadcasting the results, increasing the number of instances in the model for higher accuracy, and comparing the performance of other detection models such as SSD with the current model.

5 ACKNOWLEDGMENT

6 REFERENCES

American Society of Civil Engineers (ASCE). 2017. *Infrastructure Report Card: Roads*, Virginia: American Society of Civil Engineers (ASCE).

Bridgelall, Raj, Leonard A. Chia, Bhavana Bhardwaj, Pan Lu, Denver D. Tolliver, and Neeraj Dhingra. 2019. Enhancement of signals from connected vehicles to detect roadway and railway anomalies. *Measurement Science and Technology* 31 (3): 035105.

Chen, Cheng, Hyungjoon Seo, and Yang Zhao. 2022. A novel pavement transverse cracks detection model using WT-CNN and STFT-CNN for smartphone data analysis. *International Journal of Pavement Engineering* 23 (12): 4372-4384.

Entezari, Mohammad Saleh, and Amir Golroo. 2023. A review on the impacts of connected vehicles on pavement management systems. *International Journal of Pavement Engineering* 24 (1): 2246093.

Gopalakrishnan, Kasthurirangan. 2018. Deep learning in data-driven pavement image analysis and automated distress detection: A review. *Data* 3 (1): 28.

Jadaan, Khair, Sana Zeater, and Yazan Abukhalil. 2017. Connected vehicles: an innovative transport technology. *Procedia Engineering* 187: 641-648.

Ji, Ankang, Xiaolong Xue, Yuna Wang, Xiaowei Luo, and Weirui Xue. 2020. An integrated approach to automatic pixel-level crack detection and quantification of asphalt pavement. *Automation in Construction* 114: 103176.

Li, Zhiqiang, Chengqi Cheng, Mei-Po Kwan, Xiaochong Tong, and Shaohong Tian. 2019. Identifying asphalt pavement distress using UAV LiDAR point cloud data and random forest classification. *ISPRS International Journal of Geo-Information* 8 (1): 39.

Linton, Michael A., and Liping Fu. 2016. Connected vehicle solution for winter road surface condition monitoring." *Transportation Research Record* 2551 (1): 62-72.

Sholevar, Nima, Amir Golroo, and Sahand Roghani Esfahani. 2022. Machine learning techniques for pavement condition evaluation." *Automation in Construction* 136: 104190.

Zheng, Lu, Junchao Yi, Pengcheng He, Jun Tie, Yibo Zhang, Weibo Wu, and Lyujia Long. 2024. Improvement of the YOLOv8 Model in the Optimization of the Weed Recognition Algorithm in Cotton Field. *Plants* 13 (13): 1843.

Optimizing storage for real-time road monitoring with dual-camera systems

N. Gholipoor
Centre for Wireless Communications, University of Oulu, Finland

A. Kharbouch
Centre for Wireless Communications, University of Oulu, Finland

M. Rasti
Faculty of Information Technology and Electrical Engineering, University of Oulu, Oulu, Finland

A. Golroo
Civil and Environmental Engineering Department, Amirkabir University of Technology, Tehran, Iran,
Faculty of Information Technology and Electrical Engineering, University of Oulu, Oulu, Finland

ABSTRACT: Efficient and accurate road surface distress detection is essential for enhancing road safety and optimizing maintenance strategies. A significant challenge in pavement distress detection lies in developing an optimized data collection approach. This paper introduces a real-time road surface distress detection system utilizing a dual-camera setup mounted on a vehicle. The system incorporates an RGB camera at the front and an RGB-D (stereo vision) camera at the rear, both capturing videos stored in temporary buffers. When the front camera detects anomalies, e.g., cracks or potholes, the corresponding frames from both cameras are saved. Depth-enabled frames from the rear camera facilitate precise assessment of distress dimensions. To optimize storage, only event-related frames are retained along with pre- and post-event context. This selective strategy significantly reduces storage requirements while preserving critical data for analysis. Simulations validate the system's efficiency, demonstrating substantial storage savings compared to continuous recording methods while maintaining effective road condition monitoring.

1 INSTRUCTION

With the increasing emphasis on Intelligent Transport Systems (ITS), real-time road condition monitoring has become essential for improving road safety and ensuring efficient maintenance practices. Detecting road surface distress such as cracks and potholes can significantly reduce risks associated with vehicle damage and accidents (Koch & Brilakis, 2011). Various sensing technologies, including vibration sensors, LiDAR, and accelerometers, have been explored for road surface monitoring. While these approaches offer valuable insights, they are often limited by high deployment costs (Ranyal et al., 2022). In contrast, camera-based solutions have gained attraction due to their ability to capture detailed visual data and provide actionable insights for road distress detection (Chambon & Moliard, 2011).

Buffer management in wireless sensor networks (WSNs) has been extensively studied as a means of reducing packet loss during data transmission and maintaining data integrity (Joshi & Ranjan, 2011). Adaptive flow control and energy-aware buffer management strategies have been proposed to optimize data handling in these systems (Jayarajan et al., 2020). By managing buffers and storing specific data, the amount of stored data can be reduced, which results in decreased processing units and processing time, thereby reducing processing energy. While buffer management in wireless networks primarily focuses on minimizing packet loss, the focus here shifts towards storage optimization. Minimizing storage in cloud environments is crucial, and techniques such as data compression play a significant role. Effective storage optimization not only reduces the storage footprint but also enhances processing efficiency and energy consumption. Despite these advancements, limited research has addressed the integration of storage optimization with high-resolution image capture systems for vehicular road monitoring, leaving a critical gap in the field.

Moreover, recent advancements in smart sensing and artificial intelligence have significantly improved road condition monitoring systems. For instance, vision-based AI methodologies have been employed to evaluate, classify, and localize pavement distresses using high-resolution images captured by cameras mounted on vehicles. These systems leverage deep learning algorithms to detect and analyze road surface anomalies such as potholes, cracks, and other forms of distress (Ranyal et al., 2022). Additionally, ITS have integrated real-time detection technologies to enhance traffic management and safety. Advanced techniques such as Convolutional Neural Networks (CNNs) have been employed to automate the detection of surface anomalies from video streams (Gopalakrishnan et al., 2017). While these advancements
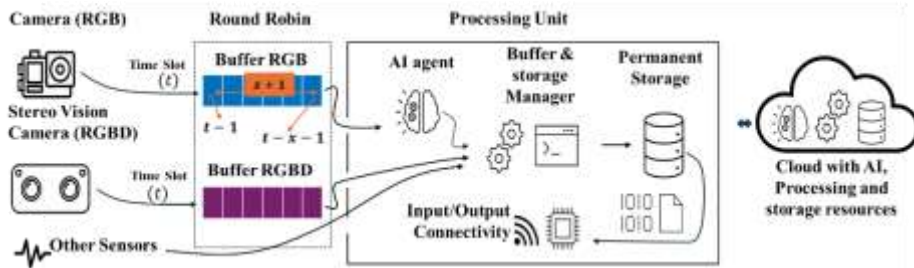
Figure 1. Proposed System Model.

enhance detection accuracy, they often neglect challenges such as optimizing storage and managing critical data under resource-constrained environments.

Existing research primarily focuses on real-time detection of road surface anomalies, often overlooking the critical challenges associated with optimized pavement condition data collection in terms of storage efficiency and data prioritization in vehicular systems. One significant gap is the lack of effective storage management, as many systems store all captured data, including information that may not be relevant to road distress detection. This indiscriminate storage approach leads to excessive use of processing units, increased processing time, and higher energy consumption. Additionally, the lack of data prioritization in current systems prevents them from efficiently handling large volumes of high-resolution images. Furthermore, current camera-based road monitoring systems fail to incorporate efficient storage mechanisms that selectively retain critical data for comprehensive analysis. This gap highlights the need for an integrated approach combining dual-camera setups with advanced buffer management strategies, which can address the dual challenges of data fidelity and resource optimization, allowing for long-distance monitoring with a limited storage capacity.

To address these gaps, this paper introduces a novel dual camera vehicular monitoring framework with a priority-based buffer management strategy for storage optimization. The system comprises a front RGB camera for continuous monitoring of the road surface and a rear RGB-D stereo vision camera for capturing depth-enabled images of detected pavement distress. Using stereo vision technology, the system provides detailed depth information about anomalies, such as the depth and width of cracks, facilitating more precise and actionable analysis. To address storage constraints, the framework employs selective storage, retaining only the critical frames associated with detected anomalies and their surrounding context. This approach optimizes storage utilization while maintaining data fidelity, enabling the monitoring of extended road distances without compromising the quality of analysis.

In addition to addressing storage limitations, the proposed system integrates advances in smart sensing and artificial intelligence (AI) to improve road condition monitoring. Vision-based AI methodologies, coupled with real-time detection technologies, have proven to be effective in assessing, classifying, and localizing pavement distress (Ranyal et al., 2022).

Using these technologies, the proposed model not only improves resource efficiency, but also provides accurate and timely information for ITS and infrastructure maintenance.

2 SYSTEM MODEL

This section outlines the proposed system model, which integrates a dual-camera configuration and buffer management mechanisms to optimize storage and ensure reliable data retention. The system involves a probe vehicle equipped with two cameras: a front camera and a rear camera. The front camera operates continuously to capture the road surface and uses a real-time algorithm (e.g., MobileNet) to detect distress events such as potholes or cracks. Concurrently, the rear camera captures high-resolution images of the same road segment for detailed analysis to recognize distress severity and density. However, due to storage constraints, not all high-resolution images can be permanently stored. To address this limitation, the system utilizes two temporary buffers that stores images for a limited duration. If the front camera identifies a distress event, the system preserves the associated high-resolution images from the rear camera. In contrast, non-critical images are discarded to save storage. This approach ensures that critical data is effectively preserved while optimizing storage utilization. Additionally, the system integrates GPS data to provide precise geolocation information for each detected distress, aiding infrastructure maintenance.

2.1 Buffer Management

The buffer management system is a core component of the proposed model, designed to handle the temporary buffers and permanent storage of high-resolution images captured by the cameras. As illustrated in Figure 1, the system includes two temporary buffers—one for the rear camera and one for the front camera—and a permanent storage unit, defined as follows:

1) *Temporary Buffers*: Initially, captured videos are stored in the temporary buffers for each camera, organized into two distinct parallel buffers. At time t, when a distress event is detected using the frames from the RGB buffer, the system retains x frames before and x frames after the event in permanent storage. To achieve this, the buffer must be of size $L^{Temp} = x + 1$, allowing the system to capture a new frame at time t while deciding whether to discard or store the frame located at $t - x - 1$. If a distress event is detected between $t - 2x - 1$ and t (which will be

discussed in the next section), the frame at $t - x - 1$ is transferred to permanent storage; otherwise, it is discarded.

2) *Permanent Storage*: For each frame in the temporary buffers, the system determines whether it belongs to the context of a distress event. If a distress is detected within the window $[t - 2x - 1, t]$, the frame at $t - x - 1$ is transferred to permanent storage. If no distress is detected within this window, the frame at $t - x - 1$ is discarded to optimize permanent storage.

2.2 Temporary Buffers

We assume that, upon detecting a distress event, it is necessary to store x frames of data before and after the detected distress. Consequently, the detection event, $a(t)$, is defined as:

$$a(t) = \begin{cases} 1, & \text{If distress is detected at time } t, \\ 0, & \text{Otherwise.} \end{cases} \quad (1)$$

The rear camera captures data at a rate of R_R frame/s. The buffer state for rear camera at time slot t, denoted as $Q_R^{Temp}(t)$, evolves according to the following equation:

$$Q_R^{Temp}(t) = \max\{0, Q_R^{Temp}(t-1) + R_R - O_R^{Temp}(t) - T_R^{Temp}(t)\}, \quad (2)$$

where $O_R^{Temp}(t)$ represents the data discarded from the buffer of rear camera, and $T_R^{Temp}(t)$ corresponds to the amount of data transmitted to permanent storage from the buffer of rear camera during the time slot t. Similarly, the front camera captures data at a rate of R_F frame/s. The buffer state for the front camera at time slot t, denoted as $Q_F^{Temp}(t)$, evolves based on the following equation:

$$Q_F^{Temp}(t) = \max\{0, Q_F^{Temp}(t-1) + R_F - O_F^{Temp}(t) - T_F^{Temp}(t)\}, \quad (3)$$

where $O_F^{Temp}(t)$ represents the data discarded from the buffer of front camera, and $T_F^{Temp}(t)$ denotes the amount of data transmitted to permanent storage from the buffer of front camera during the time slot t. An auxiliary variable, $b(t)$, captures the history of distress detection over a window of $[t - 2x - 1, t - x]$:

$$b(t) = \max_{t-2x-1 \leq t' \leq t-x} a(t'). \quad (4)$$

The data transmitted to permanent storage from the buffer of front camera, $T_R^{Temp}(t)$, is calculated as:

$$T_R^{Temp}(t) = \begin{cases} R_R, & \text{If } b(t) = 1, Q_R^{Temp}(t) = L_R^{Temp}, \\ 0, & \text{If } Q_R^{Temp}(t) < L_R^{Temp}. \end{cases} \quad (5)$$

and

$$O_R^{Temp}(t) = \begin{cases} R_R, & \text{If } b(t) = 0, Q_R^{Temp}(t) = L_R^{Temp}, \\ 0, & \text{If } Q_R^{Temp}(t) < L_R^{Temp}. \end{cases} \quad (6)$$

where L_R^{Temp} is the size of rear camera buffer. Similarly, the amount of data transmitted to permanent storage from the buffer of the front camera, $T_F^{Temp}(t)$, is calculated as:

$$T_F^{Temp}(t) = \begin{cases} R_F, & \text{If } b(t) = 1, Q_F^{Temp}(t) = L_F^{Temp}, \\ 0, & \text{If } Q_F^{Temp}(t) < L_F^{Temp}. \end{cases} \quad (7)$$

and

$$O_F^{Temp}(t) = \begin{cases} R_F, & \text{If } b(t) = 0, Q_F^{Temp}(t) = L_F^{Temp}, \\ 0, & \text{If } Q_F^{Temp}(t) < L_F^{Temp}. \end{cases} \quad (8)$$

where L_F^{Temp} is the size of front camera buffer.

These formulas ensure an efficient buffer management strategy by dynamically adjusting the buffer state based on the incoming data rate, the data transmitted to permanent storage, and the discarded data. By maintaining the buffer state within the defined limits, the model supports seamless data flow while minimizing the risk of overflow or data loss, ensuring the system's operational requirements are met.

2.3 Permanent Storage

The permanent buffer state, $Q^{Perm}(t)$, evolves as follows:

$$Q^{Perm}(t) = Q^{Perm}(t-1) + T_R^{Temp}(t) + T_F^{Temp}(t). \quad (9)$$

To prevent frame loss in the temporary buffers and ensure sufficient space for critical data to be stored in permanent storage, the constraint is expressed as:

$$Q^{Perm}(t) + L_R^{Temp} + L_F^{Temp} \leq L^{Perm}, \quad (10)$$

where L^{Perm} represents the total capacity of the permanent storage.

3 SIMULATION RESULTS

To evaluate the performance of the proposed system model, we conduct a series of simulations using realistic parameters and configurations. The key parameters considered in our simulations are summarized in Table I. For each frame, the probability of distress is denoted as P. The simulation environment is designed to replicate real-world conditions, including varying vehicle speeds and road types. Speeds of 50 km/h and 120 km/h are selected to represent typical driving conditions in Finland, corresponding to the speed limits in built-up areas and on motorways, respectively, in accordance with standard traffic regulations. The values $x = 0$ and $x = 4$ correspond to scenarios with no additional context frames and retaining four context frames, respectively. The cameras are configured to capture video at 30 frames per second (FPS) with a resolution of 1280×720 pixels. The front camera's vision range extends from 2 to 3 meters, while the RGBD rear camera, installed at a height of 0.5 to 1.5 meters, faces the road surface. Additional configurations include:

• The permanent storage of RGBD images from the stereo vision camera might be nothing or two images (stereo) per each captured RGB image from the front camera, this is due to the fact that the distress might be at the edge of the road or out of vision range of the rear camera.

• The storage of RGB images is always at least one for each detected distress. The front camera is configured to store 1 min video frames in the buffer and then processed with the AI agent while the other video is still in record. That is to say, a 1 min processing time is ensured for the AI agent to detect the distress, map the detected frame to the RGBD images and store them in the permanent storage to free the buffer.

Table 1. Considered parameters in simulation.

Parameters	Value
Vehicle speed	50 km/h, 120 km/h
RGBD camera video frames	30 Frames Per Second
RGB Resolution	1280 × 720 (pixels)
Vision range	2 m to 3 m
RGBD Depth Resolution	1280 × 720 (pixels)
RGBD Maximum Range	10 m
Size per frame	0.259 MB
Other sensors data, GPS + Encoder +Accelerometer	maximum 25KB/minute (JSON format)
Distress Probability in the road	up to 50% of 100Km

Figure 2 illustrates the required permanent storage for 100 km of road monitoring at different distress probabilities and vehicle speeds. The results show that the proposed algorithm significantly reduces the required storage compared to storing all data continuously. At a vehicle speed of 50 km/h and a distress probability of 0%, the required permanent storage is minimal. As an example, at a distress probability of 5% and a speed of 50 km/h, the proposed algorithm uses only one-third of the storage when x = 4 and as little as one-twentieth of the storage when x = 0, compared to continuous storage. Moreover, as the distress probability increases, the storage requirement also increases but remains lower than the case in which all data stored. For higher vehicle speeds (e.g., 120 km/h), the storage requirements are slightly reduced due to fewer frames being captured per unit distance. The simulation results demonstrate the effectiveness of the proposed buffer management strategy in optimizing storage utilization. By selectively storing high-resolution images of detected distress events and discarding non-critical data, the system can monitor longer road distances without exceeding storage limits. Future research will explore strategies to eliminate duplicate frames and optimize processing by correlating vehicle speed with the pausing of processing and recording when the vehicle is stationary.

4 CONCLUSION

In this paper, we introduced a real-time road surface distress detection system designed to enhance road safety and optimize data storage for efficient infrastructure maintenance. The proposed model employs a dual-camera setup, with an RGB camera at the front for continuous anomaly detection and an RGB-D
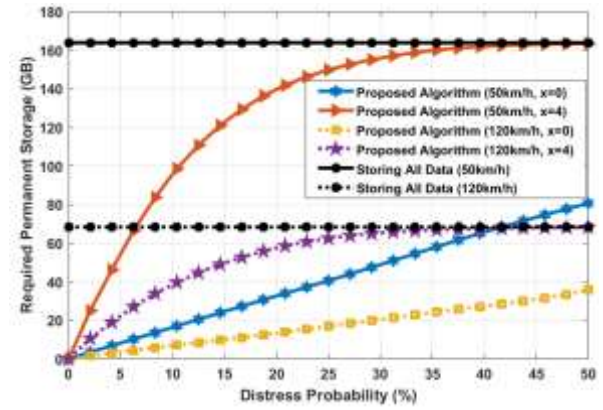
Figure 2. Required Permanent Storage for 100 Km vs. Distress Probability

camera at the rear to capture depth-enabled images of distress events. By leveraging a buffer management strategy, the system selectively stores only event-related frames along with pre- and post-event context, significantly reducing storage requirements without compromising critical data. This approach enables the analysis of extended road distances while maintaining comprehensive road condition monitoring. The model effectively addresses challenges in data fidelity, latency, and storage optimization, making it a valuable tool for ITS. Future work will focus on integrating advanced machine learning techniques, such as generative AI, to enhance detection accuracy and efficiency. Additionally, real-world deployments will provide insights to further refine the system for practical applications.

5 REFRENCES

Chambon, S. & Moliard, J.-M. 2011. Automatic road pavement assessment with image processing: Review and comparison. *International Journal of Geophysics* 2011(1): 989354.

Gopalakrishnan, K., Khaitan, S.K., Choudhary, A. & Agrawal, A. 2017. Deep convolutional neural networks with transfer learning for computer vision-based data-driven pavement distress detection. *Construction and Building Materials* 157: 322–330.

Jayarajan, P., Kanagachidambaresan, G., Sundararajan, T., Sakthipandi, K., Maheswar, R. & Karthikeyan, A. 2020. An energy-aware buffer management (EABM) routing protocol for WSN. *The Journal of Supercomputing* 76(6): 4543–4555.

Joshi, G. & Ranjan, P. 2011. Optimizing power and buffer congestion on wireless sensor nodes using coordinated adaptive power (Cap) management technique. *International Journal of Wireless & Mobile Networks* 3(2).

Koch, C. & Brilakis, I. 2011. Pothole detection in asphalt pavement images. *Advanced Engineering Informatics* 25(3): 507–515.

Ranyal, E., Sadhu, A. & Jain, K. 2022. Road condition monitoring using smart sensing and artificial intelligence: A review. *Sensors* 22(8): 3044.

Impact of Pavement Surface Roughness on WIM Sensors Performance

Muhamad Munum Masud
Associate Professor, National University of Sciences and Technology (NUST), Risalpur-24080. Pakistan

Syed Waqar Haider
Professor, Civil and Environmental Engineering, Michigan State University, East Lansing, MI 48824, USA

ABSTRACT: Weigh-in-motion (WIM) systems are vital for collecting accurate and consistent vehicle weight and axle load data, which is essential for highway planning, pavement and bridge design, and freight studies. WIM system accuracy can be influenced by vehicle dynamics, sensor types and layouts, and site-specific factors such as pavement roughness. This study examines the impact of pavement roughness on WIM measurement accuracy using the WIM Roughness Index (WRI), calculated for 24 high-quality WIM sites from the Long-Term Pavement Performance (LTPP) Specific Pavement Studies (SPS) experiment. WRI thresholds, based on AASHTO M331-17 standards, were used to evaluate roughness levels across sites equipped with Quartz Piezo (QP) and Bending Plate (BP) sensors. Results indicate that no significant relationship between WRI and WIM measurement precision or total error based on the available data, suggesting that pavement roughness alone may not be a critical determinant of WIM accuracy. These findings underscore the need for further research to identify alternative factors influencing WIM measurement variability and improve system reliability under diverse road conditions.

1 INTRODUCTION

Weigh-in-motion (WIM) is a primary technology for monitoring and collecting vehicle weights and axle loads on roadways. State and other highway agencies collect WIM data for many reasons, including highway planning, pavement and bridge design, freight movement studies, motor vehicle enforcement screening, and vehicle size and weight regulatory studies. Therefore, the data collected must be accurate and consistent with so many potential uses.

Vehicle, site, and sensor characteristics can influence WIM accuracy considerably. These factors have an individual and a combined effect on the WIM measurements (Burnos and Rys 2017). The European road specification reports that WIM site characteristics influence vehicle motion behavior and may cause significant discrepancies between the impact forces and corresponding static loads (Glover and Newton 1991; Jacob 2000; Jacob and O'Brien 1998; Jacob et al. 2000). Several other studies documented that regardless of the WIM system calibration, the WIM accuracy can deteriorate over time due to several factors, including temperature, pavement roughness, and fatigue of load sensors (Burnos and Gajda 2016; Burnos and Rys 2017; Papagiannakis et al. 2001; Rys 2019).

Pavement roughness, quantified through measures like the International Roughness Index (IRI), influences the dynamic interaction between vehicles and WIM sensors, potentially introducing errors in axle weight and gross vehicle weight measurements. The Weigh-in-Motion (WIM) Roughness Index (WRI) is an important parameter used to evaluate the impact of pavement roughness on the accuracy and reliability of WIM systems. The WRI, introduced in standards such as AASHTO M331-17, serves as a specialized metric to assess the suitability of WIM installation sites and their likelihood of producing accurate data. Lower WRI values indicate smoother pavement sections that facilitate stable sensor performance, while higher values often correlate with increased variability in measurement precision and bias (AASHTO M331-17 Standard Specification 2017).

Numerous studies have investigated the relationship between pavement roughness and WIM accuracy. For instance, data from Long-Term Pavement Performance (LTPP) studies reveal that smoother pavements generally exhibit lower error margins in WIM measurements. In contrast, rougher pavements exacerbate inaccuracies due to dynamic vehicle-sensor interactions (Selezneva and Wolf 2017). Furthermore, site-specific analyses have shown that WIM systems installed on rough pavements are more prone to weighing errors, necessitating more frequent calibration and maintenance (FHWA, 2018). These findings underscore the im-

portance of evaluating pavement roughness during WIM site selection and system design to ensure data quality.

WRI has emerged as an effective tool for identifying and managing these challenges. By defining thresholds for acceptable and unacceptable levels of pavement roughness, the WRI enables engineers to predict the potential impact of road conditions on WIM system performance and to optimize sensor placement and calibration strategies (Guide 2021).

2 SCOPE

This paper explores the relationship between pavement roughness and WIM (Weigh-in-Motion) measurement accuracy using the WIM Scale Roughness Index (WRI). The study utilizes data from 24 high-quality WIM sites included in the Long-Term Pavement Performance (LTPP) Specific Pavement Studies (SPS) Experiment, with Quartz Piezo (QP) and Bending Plate (BP) sensors. The WRI values for these sites were calculated using the ProVAL OWL module and categorized into thresholds specified by AASHTO M331-17 standards.

3 PAVEMENT SURFACE ROUGHNESS AND SENSOR TYPE

The pavement surface roughness data collected in the vicinity of the WIM sites were used to analyze the effect of road roughness on the variability of WIM measurement errors. The longitudinal profile data for 600 ft (400 ft before and 200 ft after the WIM location) were used to calculate IRI values to investigate its impact on WIM accuracy. Table 1 shows the descriptive statistics for IRI by sensor type and climate. Compared to AC pavements with quartz piezo sensors, higher average IRI values are observed for PCC pavements with bending plate sensors.

Table 1. Descriptive statistics of IRI by sensor type and climate

Variable	Factor	N	Mean	SD	Minimum	Maximum
Max IRI (in/mile)	BP	11	271.7	42.9	139.0	513.0
	QP	13	253.3	67.4	50.0	743.0
	Dry	11	196.8	32.4	77.0	429.0
	Wet	13	316.7	67.6	50.0	743.0

Note: All bending plate sensors were installed on PCC pavements.

4 WIM SCALE ROUGHNESS INDEX AND SENSOR TYPE

The WRI indicates whether or not the pavement roughness will likely result in an acceptable level of weighing error (AASHTO M331-17 Standard Specification 2017). These indices were computed for the SPS WIM dataset using the Ride Quality and Optimum WIM Locator (OWL) modules of the Pro-Val software (ProVAL User's Guide 2001) using the available longitudinal profile data collected at WIM site locations. The WRI values were computed for the 40-meter (131 feet) WIM scale approach area and compared against the lower and upper threshold values for the Type I WIM scales specified in AASHTO M331-17 standard specification (AASHTO M331-17 Standard Specification 2017). The OWL software has been utilized for LTPP SPS TPF and SPS 10 sites since 2016. Lower and upper threshold values for the index for Type I WIM scales are 1.34 m/km (84.8 in./mi.) and 2.70 m/km (171.1 in./mi.), respectively. Lower threshold values of WRI are those below which a system is likely to produce an acceptable level of weighing error. The upper threshold value of the index is above which a WIM system is expected to deliver an unacceptable level of weighing error. Values between the threshold values may or may not produce an unacceptable level of weighing error.

For LTPP SPS TPF and SPS 10 sites, 1673 profile sample points were collected at a sampling rate of 25 mm within the 40-meter WIM scale approach area for each of the pavement profiler runs. These data were uploaded to ProVal, and the OWL module was used to compute WIM Scale Roughness Indices for the left and right wheel paths for each profile run. Average WRI values and maximum index values for each profile run's left and right wheel path were calculated and compared to the acceptable threshold values. Additionally, the percentages of WRI values that exceed the lower and upper thresholds within the 40-meter section were calculated. The location of the maximum index was also obtained from each longitudinal profile data, and the distance between WIM location and the maximum WRI location was determined. The following variables related to WRI were used to evaluate their impact on WIM accuracy parameters:

- Average WRI (m/km)
- Maximum WRI (m/km)
- Location difference between maximum WRI and WIM sensor (m)
- Percentage of points >1.34 m/km WRI (%)
- Percentage of points > 2.7 m/km WRI (%)

Table 2 presents the descriptive statistics of the above five variables by sensor type based on the available data for high-quality LTPP WIM sites. It should be noted that WIM data measurement error variability for high-quality sites could be related to the variations in these WRI variables. Higher average and maximum values of WRI were observed on WIM sites with bending plates compared to quartz piezo sensors. These higher values of WRI are asso-

ciated with pavement types since all the bending plates are on PCC pavements, while quartz piezo sensors are installed in AC pavements.

Table 2. Descriptive statistics of WRI related variables by sensor type

Variable	Sensor	N	Mean	Minimum	Maximum
Avg. WRI (m/km)	BP	11	2.94	1.38	7.00
	QP	13	2.09	0.94	8.49
Max. WRI (m/km)	BP	11	6.14	2.30	15.03
	QP	13	5.10	1.78	27.84
Loc. Diff. (m)	BP	11	23.25	0.97	39.62
	QP	13	15.22	3.38	32.14
P>1.34 (%)	BP	11	0.87	0.47	1.00
	QP	13	0.50	0.05	0.89
P>2.7 (%)	BP	11	0.37	0.00	1.00
	QP	13	0.10	0.00	0.49

Note: All BP are installed in PCC pavements, all QP are installed in AC pavements.

The average and maximum WRIs were categorized into three ($\leq$1.34, >1.34, and <2.7, $\geq$ 2.7) and two (<2.7 and $\geq$ 2.7) ranges, respectively. Figure 1 shows the 95% CI for standard deviation and total WIM error within different WRI categories. The results in Figure 1 show that average or maximum WRI does not significantly impact WIM precision and total error. Figure 2 presents the 95% CI for precision and total error based on WRI categories with an average percentile of the points less than or greater than 50 for the lower and upper WRI thresholds of 1.34 and 2.7 m/km. Based on the available data, the results show no significant difference in precisions and total errors for different categories of WRI, at least for the sample of sites used in the analysis. Consequently, WRI may not explain the accuracy of WIM measurement based on the available data.

The effects of WRI on WIM accuracy, as mentioned above, were further examined within each sensor type and different climates, as shown in Figure 3. The results show that the average and maximum WRI for different sensor types and climates do not significantly impact the WIM precision, at least for the sample of sites used in the analysis. Based on available data, no consistent relationship between WIM measurement variability and WRI were observed for different sensor types and climates.

(c) Precision (d) Total error
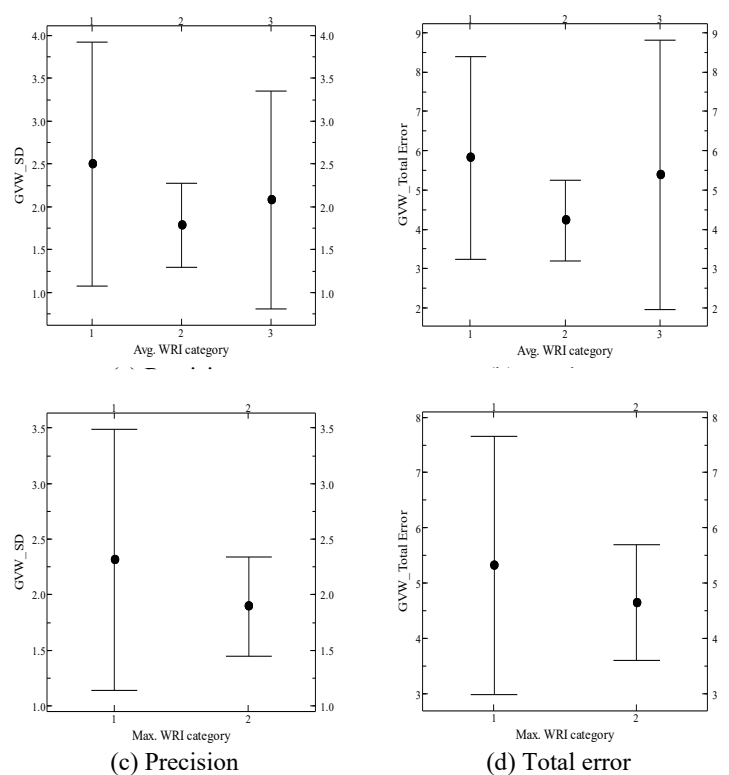
Figure 1. Impact of average and maximum WRI on WIM accuracy

(c) Precision (d) Total error
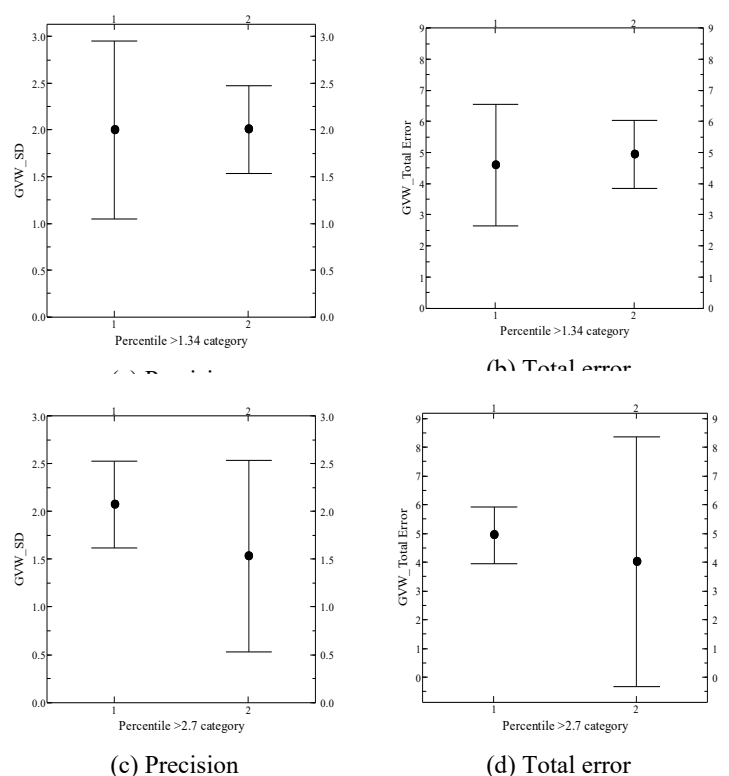
Figure 2. Impact of low and high WRI percentile on WIM accuracy

5 CONCLUSION

In conclusion, this study highlights that while variations in pavement roughness, as measured by the WIM Scale Roughness Index (WRI), exist across different sensor and pavement types, WRI does not significantly impact WIM measurement precision or

total error, at least for the WIM sites analyses in this study. These findings suggest that pavement roughness alone may not be a critical determinant of WIM accuracy. The study emphasizes the need for further research to identify alternative parameters or factors that could better explain WIM measurement variability and improve the reliability of WIM data under varying road conditions.
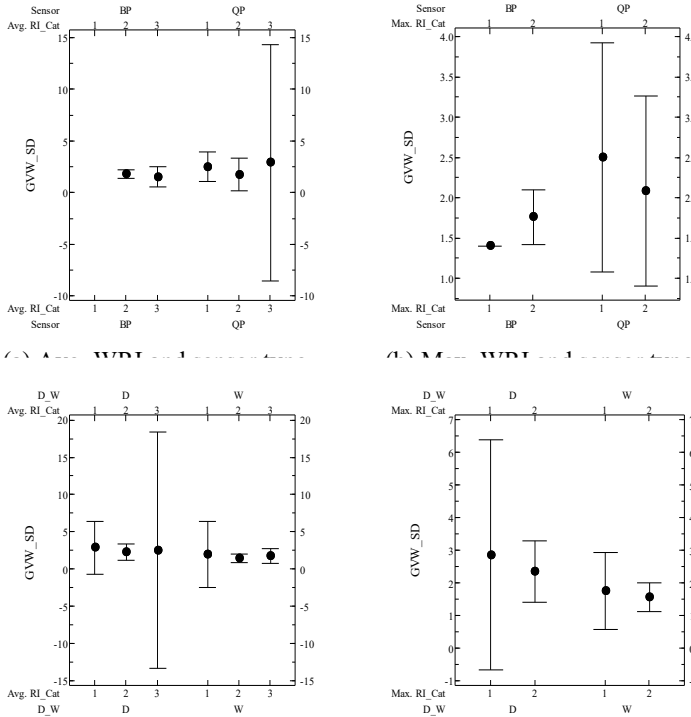
(c) Avg. WRI and climate   (d) Max. WRI and climate

Figure 3. Impact of WRI on WIM accuracy by sensor type and climate [D: Dry, W: Wet]

6 REFERENCES

AASHTO M331-17 Standard Specification (2017). "Smoothness of Pavement in Weigh-in-Motion Systems." American Association of State Highway and Transportation Officials, Washington, D.C.

Burnos, P., and Gajda, J. (2016). "Thermal property analysis of axle load sensors for weighing vehicles in weigh-in-motion system." *Sensors*, 16(12), 2143.

Burnos, P., and Rys, D. (2017). "The Effect of Flexible Pavement Mechanics on the Accuracy of Axle Load Sensors in Vehicle Weigh-in-Motion Systems." *Sensors*, 17(9), 2053.

Glover, M., and Newton, W. (1991). "Evaluation of a Multiple-sensor Weigh-in-motion System."

Guide, P. U. s. (2021). "ProVAL User's Guide - Ride Quality and Optimum WIM Locator (OWL) Modules."

Jacob, B. (2000). "Assessment of the Accuracy and Classification of Weigh-in-Motion Systems Part 1: Statistical Background." *International Journal of Heavy Vehicle Systems*, 7(2-3), 136-152.

Jacob, B., and O'Brien, E. J. "European Specification on Weigh-in-Motion Of Road Vehicles (COST323)." *Proc., Second European Conference on Weigh-In-Motion of Road Vehicles, Held Lisbon, Portugal 14-16 September 1998*.

Jacob, B., O'Brien, E. J., and Newton, W. (2000). "Assessment of the Accuracy and Classification of Weigh-in-Motion Systems. Part 2: European Specification." *International Journal of Heavy Vehicle Systems*, 7(2-3), 153-168.

Papagiannakis, A., Johnston, E., and Alavi, S. (2001). "Fatigue performance of piezoelectric Weigh-in-Motion sensors." *Transportation research record*, 1769(1), 87-94.

ProVAL User's Guide (2001). "Profile Viewing and Analysis Software."

Rys, D. (2019). "Investigation of weigh-in-motion measurement accuracy on the basis of steering axle load spectra." *Sensors*, 19(15), 3272.

Selezneva, O., and Wolf, D. (2017). "Successful Practices in Weigh-in-Motion Data Quality with WIM Guidebook Vol 1."

Investigation of electrical signals induced in a piezoelectric axle load sensor mounted in asphalt mixture

Dawid Ryś [a], Przemysław Więckowski [a], Magdalena Złotowska [b], Paweł Tutka [b]

a)Gdańsk University of Technology, Faculty of Civil and Environmental Engineering

b) Warsaw University of Technology, Faculty of Civil Engineering

ABSTRACT: This paper describes a laboratory test stand and a dedicated FEM model, both specifically designed to study the impact of stress distribution, acting on the axle pressure sensor, on the electrical signal delivered, which is then processed and converted into the vehicle's wheel load. A linear relationship between maximum voltage and applied stress was observed in both laboratory tests and numerical analyses. However the voltage change signal differs between FEM models and laboratory test measurements, what is probably caused with the capacitor discharge or other electric circuit effects.

1 INTRODUCTION

1.1 Background

Weigh in Motion (WIM) systems have been developing in order to improve the efficiency of traffic loads control. They may contribute to reduction of the number of overloaded vehicles and minimalize an adverse effect caused by vehicle overloading to road infrastructure, which was discussed by Rys et. al. (2015). Although WIM technology has been in use for several years, its full potential has yet to be fully realized. The primary challenge remains the gradual loss of measurement accuracy over time (Adresi et al. 2024, Masud et al. 2023). The phenomenon arise from temperature variations (Rys et.al., 2024) and the overly simplified treatment of stresses acting on the pressure sensor under the load of vehicle wheels (Burnos &Rys, 2017).

The problem solution needs a deeper investigation of electrical signals induced in a piezoelectric axle load sensor mounted in asphalt mixture, which is the subject of this paper. Despite there are some previous studies presenting full-scale experimental testing of WIM sensors (Hornych et al., 2016) and WIM sensor modeling (Otto et al., 2017), there is still gap in laboratory-scale testing of asphalt mixture-load sensor systems and system modelling.

1.2 Objective and Scope

The paper presents preliminary tests of the newly developed laboratory stand of axle load sensor-asphalt mixture system. The main aim is to develop a numerical model of the stand, perform computer simulations of the laboratory test and compare them with laboratory measurements.

2 STAND FOR LABORATORY TESTING

The experimental stand included an asphalt mixture sample embedded with a Weigh-In-Motion sensor. Initially, the asphalt mixture (AC16, containing neat bitumen of grade 35/50) was placed in wooden molds and compacted using a roller. The resulting beam measured 1800 mm in length, 340 mm in width, and 120 mm in thickness. After demolding, a groove measuring 72 mm in width and 70 mm in depth was cut along the center axis of the beam for WIM sensor installation. The sensor, of 1750 mm length, 44 mm width and 52 mm depth, was installed in the cleaned groove, with the remaining gaps filled using a resin-silica sealing compound. The sample is placed on a steel plate of 10 mm thickness, matching the remaining dimensions of the asphalt beam. The WIM sensor was connected to computers with specialized software allowing for signal processing and data gathering. The Universal Testing Machine UTM-130, which is equipped with hydraulic actuator was used to load the system. Figure 1 presents a view on the laboratory stand.
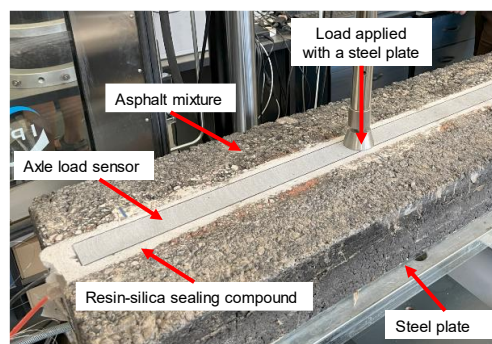
Figure 1. A view on a laboratory stand of axle load sensor – asphalt mixture system under loading in UTM-130 hydraulic press.

The tests aimed to measure the voltage induced in the WIM sensor when subjected to a load transmitted on the asphalt specimen with the sensor. The results discussed in this paper have been obtained through loading transmitted from the hydraulic press to the asphalt specimen using a round steel stamp of 109.2 mm diameter. Three stress levels have been tested – 700, 800 and 900 kPa. The loads were applied in series (for each stress level) of sinusoidal impulses with a duration of 100 ms and a rest interval of 11 s.

3 FEM MODELING OF THE SENSOR-ASPHALT MIXTURE SYSTEM

The numerical model of the experimental stand was created using the Finite Element Method (FEM) and the software Abaqus. The geometry of the model corresponds to the specimen (beam) used in the laboratory test. Half of the beam was modelled using the symmetry of the system with respect to the *x-z* plane. The model consists of several elements - an asphalt layer, an axle load sensor made of piezoelectric material, and a resin-silica sealing compound mass in which the sensor is embedded (Figure 2). A steel plate on which the asphalt mix beam is placed was also modelled. The possibility of sliding between the steel plate and the asphalt mix layer was assumed, and the defined contact prevents the surfaces of these elements from penetrating. Full continuity of displacement between the elements was assumed for the sealing compound, the sensor and the asphalt mixture. The steel stamp that the beam is loaded with has also been modelled with respect to the symmetry conditions.
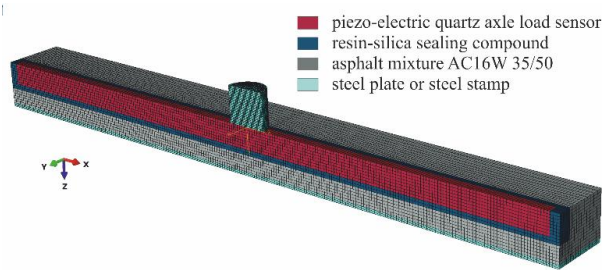
Figure 2. FEM model of Axle Load Sensor – Asphalt Mixture System.

The WIM (Weigh-In-Motion) sensor operates based on the unique piezoelectric properties of quartz-like materials, which couple mechanical and electromagnetic phenomena. Specifically, the piezoelectric effect enables the material to convert mechanical stress into an electrical response, and conversely, an applied electric field induces mechanical strain. This dual functionality is described by the linear piezoelectric constitutive equations, where the stress tensor σ_{ij} and strain tensor ε_{ij} are directly linked to the electric field E_i and electric displacement field q_i.

The mechanical and electromagnetic coupling is expressed through the piezoelectric constants, which define the material's response to external stimuli. Under mechanical loading, stress generates an electric displacement field q_i, which is proportional to the magnitude and direction of the stress. Simultaneously, the induced strain can alter the electric field distribution within the material. These interactions are governed by the linear relationships:

$$\sigma_{ij} = C_{ijkl}\left(\varepsilon_{kl} - d_{mij}E_m\right) \qquad (1)$$

$$q_i = g_{ijk}\varepsilon_{jk} + D_{ij}E_j \qquad (2)$$

where σ_{ij} – stress tensor [MPa], C_{ijkl} – stiffness tensor at zero voltage [MPa], ε_{kl} – strain tensor [-], d_{ij} – piezoelectric strain coefficient tensor [C/N], E_m – electric field vector [V/m], q_i – electric induction vector [C/m^2], g_{mij} – piezoelectric stress coefficient tensor [C/m^2], D_{ij} – dielectric constant tensor [F/m].

These equations highlight the interplay between the mechanical and electromagnetic domains, essential for accurate modeling of WIM sensors. The mechanical properties of the material are defined by the tensor C_{ijkl}. The tensors d_{ijk} and g_{ijk} describe the piezoelectric properties of the material, the values of these tensors being mutually dependent. The material's mechanical properties are assumed to be isotropic and the electrical permeability is assumed to be isotropic, and the piezoelectric properties occur only in the *z*-axis direction, induced by vertical stresses and horizontal stresses along the *x*-axis.

Table 1. Material properties of the WIM sensor.

E [MPa]	Poisson Coefficient [-]	ρ [kg/m3]	d_{zzz} [C/N]	d_{zxx} [C/N]	D [F/m]
210000	0.3	7850	8x10^{-13}	-3.2x10^{-13}	1.77x10^{-8}

The deviatoric part of the stiffness tensor of the asphalt mixture was modeled as viscoelastic, while the spherical part was modeled as elastic. The viscoelastic properties were considered using a five-branch generalized Maxwell model, which is implemented as a Prony series. The deviatoric part of the stiffness tensor was assumed to exhibit viscoelastic behavior, and the spherical part was modeled as elastic. To determine the model parameters, stiffness master curves for the test section were used, assuming a constant temperature for the asphalt layers in each segment of the pavement. The relationship between the complex modulus and loading frequency is expressed by Equation (3).

$$E^*\left(\omega\right) = E_\infty + \sum_{i=1}^{n}\frac{E_i\omega^2\tau_i^2}{1+\omega^2\tau_i^2} + i\left(\sum_{i=1}^{n}\frac{E_i\omega\tau_i}{1+\omega^2\tau_i^2}\right) \qquad (3)$$

In Abaqus, the Maxwell model is defined using the dimensionless parameters g_i and τ. The relationship between these parameters and the quantities of a Prony series is presented by Equations (4) - (6). The obtained parameter values and the root mean square error from fitting the master curve are presented in Table 2. To describe the temperature dependence, the Williams–Landel–Ferry model was used. The data were obtained from stiffness measurements at three temperatures (6°C, 20°C, and 40°C). A reference temperature T_r of approximately 20°C was adopted, and the parameters C_1 of 9.436 and C_2 of 55.338°C were determined.

$$E_0 = E_\infty + E_1 + E_2 + E_3 + E_4 \quad (4)$$

$$\tau_i = \frac{\eta_i}{E_i} \quad (5)$$

$$g_i = \frac{E_i}{E_o} \quad (6)$$

Table 2. Maxwell Model parameters assumed for Asphalt Mixture.

E_0 [MPa]	g_1 [1]	g_2 [1]	g_3 [1]	g_4 [1]
17051	0.292	0.206	0.182	0.257
ρ [kg/m3]	τ_1 [s]	τ_2 [s]	τ_3 [s]	τ_4 [s]
2450	0.0002	0.2969	9.5496	0.0183

Linear elastic properties are assumed for filler mass and steel. The material properties are summarised in Table 3.

Table 3. Material parameters for Hooke's Model.

Lp.	Name	Elastic Modulus [MPa]	Poisson Coefficient [-]	ρ [kg/m3]
1	Steel	210000	0.3	7850
2.	Resin-silica sealing compound	75000	0.3	2450

Following the experiment, the beam was loaded with a steel stamp positioned at the center of the specimen. A sinusoidal time-varying load with a period of 100.0 ms and a maximum stress from 700 to 900 kPa was assumed as in the experiment.

A boundary condition specifying zero electric field potential on the lower surface of the WIM sensor is applied. The support has a width of 0.65 m and its center is under the load axis. The boundary conditions of symmetry with respect to the *x-z* plane were also applied in the system.

The calculations were performed using the Dynamic Implicit procedure available in Abaqus, which considers the time variability resulting from the movement of the load and the viscoelastic material properties. C3D8R and C3D8E finite elements were used.

4 COMPARISON OF NUMERIC ANALYSIS TO INITIAL LABORATORY TESTS

The numerical calculations provided the distribution of the electric field potential on the upper surface. The difference in potential between the lower and upper surfaces represents the electric voltage across individual points. The resulting potential distribution and the

obtained vertical stresses for a pressure value of 900 kPa are shown in Figure 3.
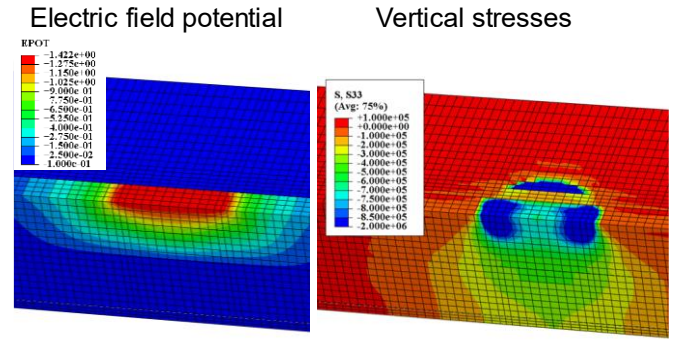
Figure 3. Electric field potential and vertical stresses on the upper surface of WIM sensor.

In practical measurement systems, signal processing circuitry often averages the observed electric potential to determine the effective voltage across the sensor. This simplification facilitates the interpretation of sensor outputs and ensures consistency with the overall response of the measurement system.

To calculate the averaged electric potential, the potential distribution over the top surface of the piezoelectric material was integrated. The resulting integral was divided by the total surface area of the electrode, yielding the area-averaged electric potential. This averaged value represents the effective voltage between the upper and lower surfaces of the piezoelectric material, where the lower surface potential is fixed at zero as a boundary condition.

The computation of the averaged voltage utilized the electric potential values obtained from the nodes on the upper surface of the sensor. Each node was assigned the surface area closest to its location, effectively partitioning the electrode surface. The averaging process involved calculating the sum of the products of the potential values at each node and their corresponding surface areas. This sum was then normalized by dividing it by the total surface area of the electrode.

This approach is particularly justified in scenarios where the readout system inherently integrates spatial variations due to its design or during subsequent signal processing. Averaging also reduces the influence of local anomalies in the potential distribution, providing a robust and representative measure of the sensor's overall response. The values of the averaged voltage over time, obtained from numerical calculations, are presented in Figure 4.
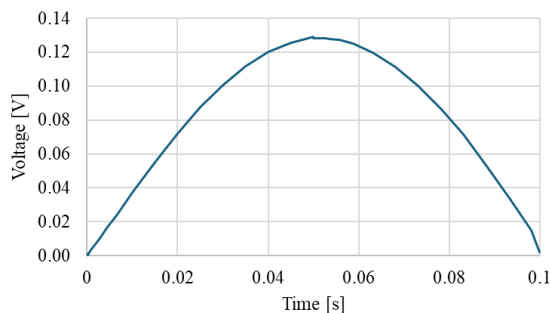
Figure 4. Average value of the electric field potential on the upper surface of the WIM sensor as a function of time at 900 kPa.

As for the laboratory testing, the voltage in time values were obtained directly from the computer, being a part of the measuring system. For each loading cycle, there was a separate file containing voltage and time information. An example of laboratory-measured voltage in function of time is shown in Figure 5.
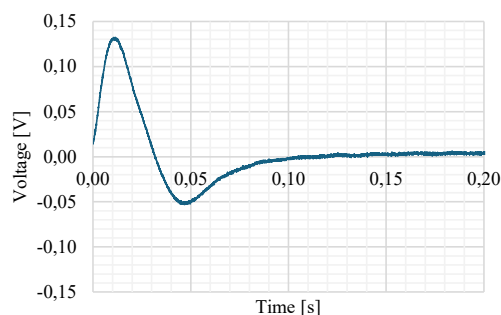
Figure 5. Example of measured voltage in function of time from laboratory testing of WIM sensor at 900 kPa.

Due to the linear physical model, the shape of the voltage curve as a function of time closely resembles the shape of the applied load. The model does not account for the discharge of capacitors in the electrical circuit, which occurs in real measurement systems.

Figure 6 illustrates the relationship between the maximum recorded or calculated voltage value and applied stress. The results obtained from numerical analysis show a very high degree of agreement with experimental measurements, also maintaining a linear characteristic of the relationship.
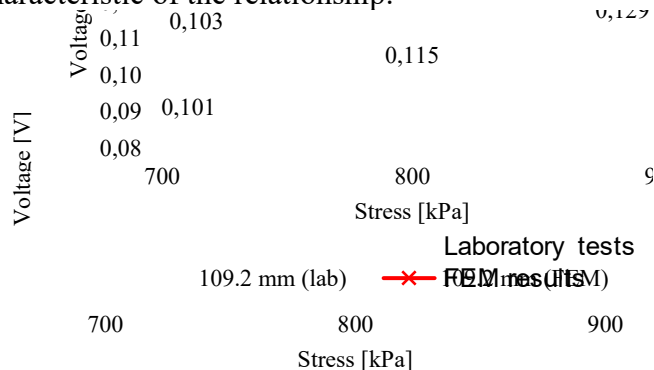
Figure 6. A comparison between maximum voltage values and stress relation from laboratory testing of WIM sensor and corresponding relation resulting from numerical analysis.

5 CONCLUSIONS

This paper provides a comprehensive representation of the axle load sensor system embedded in a mineral-asphalt mixture, along with a comparison of electrical signal measured in experimental results with FEM analysis outcomes.

The voltage change signal exhibits distinct characteristics depending on whether it is derived from the FEM model or actual measurements. The FEM model produces results as an integrated electric potential field, whereas the axle load sensor measurement system reflects a more complex response, primarily influenced by a discharge of capacitors in the electrical circuit.

Nevertheless, the linear relationship between maximum values of voltage and applied stress were found both for laboratory testing results and corresponding numerical analysis.

The developed model and research stand have great potential for conducting further research, including the assessment of the influence of various factors, such as road surface temperature, contact stress at the tire-road interface or system fatigue.

6 REFERENCES

Adresi, M., Abedi, M., Dong, W., & Yekrangnia, M. 2024. A review of different types of weigh-in-motion sensors: State-of-the-art. *Measurement*, 225, 114042.

Burnos, P., & Rys, D. 2017. The effect of flexible pavement mechanics on the accuracy of axle load sensors in vehicle weigh-in-motion systems. *Sensors*, 17(9).

Hornych , P., Simonin , J. M., Piau , J. M., Cottineau , L. M., Gueguen , I., & Jacob , B. 2016. Evaluation of weight in motion sensors on the IFSTTAR accelerated testing facility. *The roles of accelerated pavement testing in pavement sustainability: Engineering, environment, and economics* (pp. 671–684).

Masud, M. M., Haider, S. W., Selezneva, O., & Wolf, D. J. 2023. Representative weigh-in-motion (WIM) system accuracy and guidelines for equipment selection based on sensor, site, and calibration-related factors. *International Journal of Pavement Research and Technology*, 17, 732–749.

Otto, G. G., Simonin, J.-M., Piau, J. M., Cottineau, L. M., Chupin, O., Momm, L., & Valente, A. M. 2017. Weigh-in-motion (WIM) sensor response model using pavement stress and deflection. *Construction and Building Materials*, 156, 83–90.

Rys, D., Więckowski, P., Wasilewska, M., & Dołęga, C. 2024. Impact of accuracy of weigh-in-motion data for pavement analysis and design: influence of temperature variations. *Road Materials and Pavement Design*, 1–18.

Rys, D., Judycki, J., & Jaskula, P. 2015. Analysis of effect of overloaded vehicles on fatigue life of flexible pavements based on weigh in motion (WIM) data. *International Journal of Pavement Engineering*, 17(8), 716–726.

Low-cost sensing system for measuring tire width, wheel wander & vehicle classification

R. Tariq, S.W. Haider, K. Chatti, & N. Lajnef
Department of Civil and Environmental Engineering, Michigan State University, East Lansing, MI, USA

ABSTRACT: This paper presents a low-cost, pressure sensor-based system designed for real-time monitoring of tire widths, vehicle classifications, and wheel wander in highway traffic. By integrating sensors encased in rubber strips across lanes, the system captures voltage signals generated by the tires of passing vehicles. These signals facilitate tire width estimation, axle-based vehicle classification, and wheel wander measurement. Tested on US127 in Mason, MI, the system demonstrated high accuracy in vehicle classification, showing minor errors compared to Weigh-in-Motion (WIM) data and achieving a weighted error of 1.54%. This innovative approach provides essential data for pavement analysis and traffic monitoring, offering a reliable, minimally invasive solution adaptable for continuous traffic data collection.

1 INTRODUCTION

This paper presents the development and testing of a low-cost, novel sensing system designed to detect and classify wide-base tire (WBT) types, determine their distributions, and estimate the tire widths and wheel wander of passing vehicles. The system's usefulness in data collection for pavement analysis and design applications is also demonstrated. The focus of this work is on the development of the sensor within the context of WIM systems, leveraging piezoelectric sensors. The principle of piezoelectricity, discovered by Pierre and Jacques Curie in the late 19th century, as noted by Mason (1981), enables these sensors to generate electrical signals in response to mechanical pressure, as described by More & Kapusetti (2017). When a vehicle passes over the sensor, the weight of its tires compresses the piezoelectric elements, producing unique electrical signals. These signals, characterized by features such as amplitude and duration, reflect the force and weight exerted by the tires. Falconi (2019) notes that these sensors collect real-time data on vehicle weight, speed, and axle configuration when embedded within the road surface. As a vehicle traverses the WIM system, it records portions of the load and converts these into electrical voltage signals, as outlined in ASTM E1318 (2009). Piezoelectric sensors are ideal for precise measurements, given their high sensitivity to mechanical force.

Similar to conventional WIM systems, this new sensor is designed to operate at highway speeds, minimizing traffic disruptions compared to static systems, as noted by Sivakumar et al. (2011). Piezoelectric sensors often face harsh environmental conditions and wear, and to enhance their longevity and reliability, they are typically protected with methods such as rubber shielding. This approach involves covering the sensors with materials that provide insulation against mechanical shocks and environmental factors. Patrick & Maher (2009) emphasize that choosing rubber material is crucial for ensuring adequate protection.

While WIM systems classify vehicles based on axle count, axle spacing, and vehicle weight, conventional vehicle classifiers use only axle count and spacing for classification, as Hallenbeck et al. (2014) highlighted. Similarly, the developed system effectively classifies vehicles using axle count and spacing alone.

The Traffic Monitoring Guide (TMG, 2022) recommends collecting vehicle classification counts for at least 48 continuous hours. Extending counts beyond 48 hours is even more beneficial, providing a more comprehensive dataset on traffic volumes by vehicle class.

This work aims to design and develop a system that measures dynamic tire forces, tire widths, vehicle classification, and wheel wander within a lane. The design incorporates piezoelectric sensors in rubber strips positioned in each traffic lane. These sensors detect voltage fluctuations caused by tire pressure on each axle, enabling accurate estimation of tire widths, wheel wander, and vehicle classification.

2 DATA COLLECTION

The design incorporates a pressure sensor encased within a protective rubber strip in each traffic lane. This encasement shields the sensors from direct traffic loads and safeguards them against various environmental conditions, such as moisture, temperature fluctuations, and debris, thereby enhancing sensor longevity and accuracy. The system ensures consistent data collection for accurate traffic monitoring and vehicle classification.

An array of pressure sensors encased in rubber is positioned along the anticipated wheel path in the outer highway lane. When vehicle tires contact the strip, the mechanical force activates the sensors, generating a voltage output that peaks when the tire is fully positioned on the strip. As the tire gradually moves off the rubber contact area, these voltages decrease, ultimately returning to zero, as shown in Figure 1, which depicts the passage of a 5-axle vehicle. When tires make contact, multiple sensors are activated. By counting the number of activated sensors for each tire, the tire width can be estimated by multiplying this count by the sensor width and the spacing between sensors. Wheel wander is assessed by measuring the distance from the lane edge to the first sensor activated by the tires of the passing vehicle.
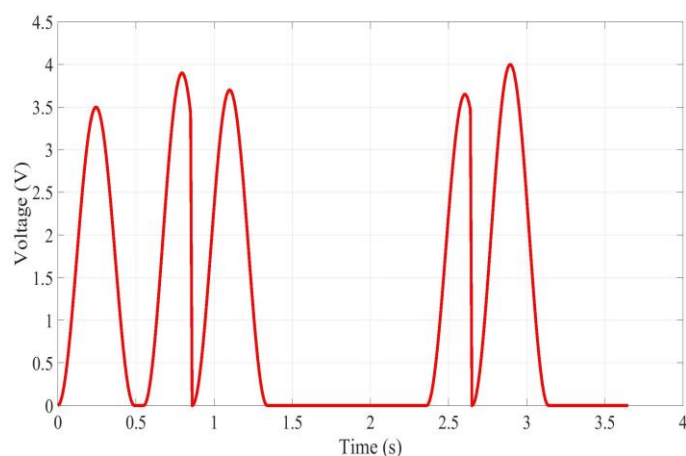
Figure 1. Voltage output for 5-axle vehicle.

The refined LTPP WIM rule set, proposed by Hallenbeck et al. (2014), was used for vehicle classification. The LTPP classification rules utilize axles, spacing, gross vehicle weight (GVW), and front axle weights to differentiate between certain vehicle classes. However, the FHWA report states that vehicle classification can also be performed based solely on axle count and spacing, as discussed by Hallenbeck et al. (2014).

For the collection of the data, a 40-foot-long strip was installed adjacent to a WIM site on US127 in Mason, MI, across the road width for five days, as illustrated in Figure 2, to collect vehicle passage data for classification based on axle count, wheelbase, and wheelbase ranges, along with tire width and wheel wander estimation. The sensors were connected to a PCB linked to a Raspberry Pi-based device, and a portable solar power source powered the entire system. The adhesive was used to secure the strip firmly to the road surface to minimize noise in the voltage outputs. Data from the WIM system was used to verify the sensor's accuracy in classifying vehicles.

Figure 2. Strip laid across the road width at US 127, Mason, adjacent to a WIM system.

3 DATA ANALYSIS

The collected voltage data was processed using a developed algorithm that applies the refined LTPP classification rule set for vehicle classification while estimating tire widths and wheel wander for passing vehicles.

3.1 *Tire Width*

Figure 3 illustrates the distribution of tire widths among passing vehicles. The data shows that 58.9% of vehicles had tire widths between 4 and 10 inches, 12.9% between 10 and 12 inches, 22.1% between 12 and 15 inches, 6.1% between 15 and 17 inches, and only 0.1% exceeded 17 inches. The high concentration of vehicles with tire widths primarily within the 4-10 inch range suggests a predominance of passenger cars and small trucks in the observed traffic flow. These findings align with general traffic patterns on similar road types, where lighter, narrower-tired vehicles constitute the majority of traffic, providing valuable insights for infrastructure planning and pavement wear analysis.
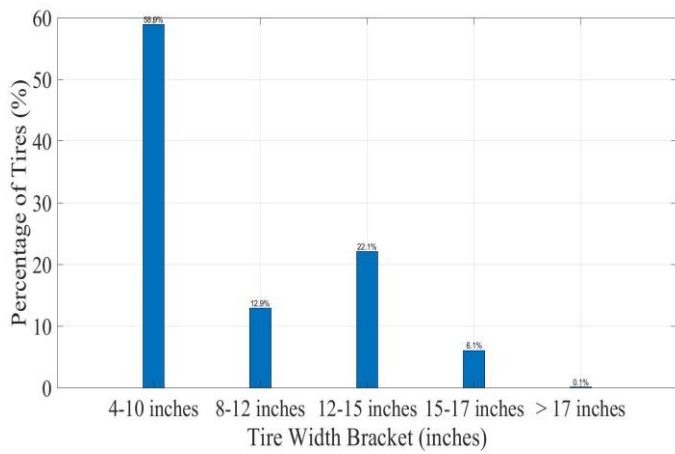
Figure 3. Tire width distribution.

The model also demonstrated its ability to classify tire widths within Class 9 vehicles, distinguishing wide-base tires from standard options. This level of detail in tire width classification is essential for accurate vehicle profiling and further analysis. As shown in Figure 4, the results indicate that a majority, 80.4%, of identified tires fall within the 10–15 inch width range, while 19.1% are wide-base tires in the 15–17 inch range, representing a smaller segment with intermediate widths. Notably, only 0.5% of classified tires exceed 17 inches, underscoring the rarity of such broad tires within this vehicle class. This categorization highlights the model's effectiveness in refining the tire dimension classification framework, which could be integral to enhancing vehicle type assessments and related applications in transportation studies.
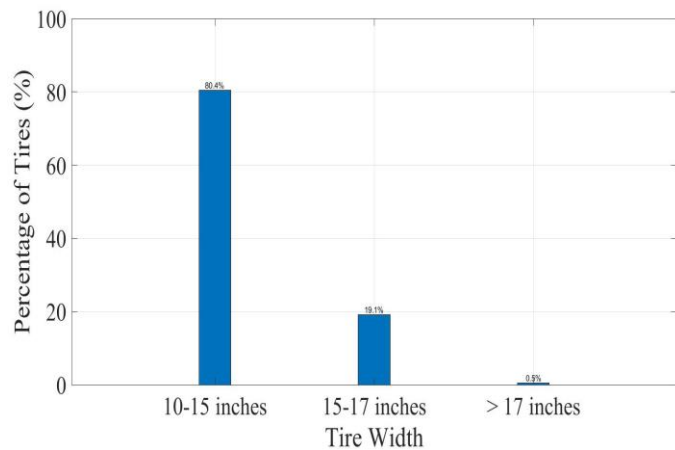
Figure 4. Tire width distribution for class 9 vehicles.

3.2 Vehicle Classification

The model further categorized vehicles based on axle count and wheelbase ranges. Out of 20,499 identified vehicles, 69.23% were classified as Class 2, 8.59% as Class 5, 10.63% as Class 9, and 1.73% as Class 13, among other classifications. Vehicles classified as Class 5 and above were compared to the WIM data. Figure 5 shows the vehicle classification distribution according to the WIM system and the

prototype sensor. A comparative analysis of data from both sources, presented in Table 1, reveals minor misclassifications for primary classes, including Class 5, Class 9, Class 10, Class 12, and Class 13. However, significant classification errors occurred in Class 7, resulting in an overall weighted error rate of 1.54%.
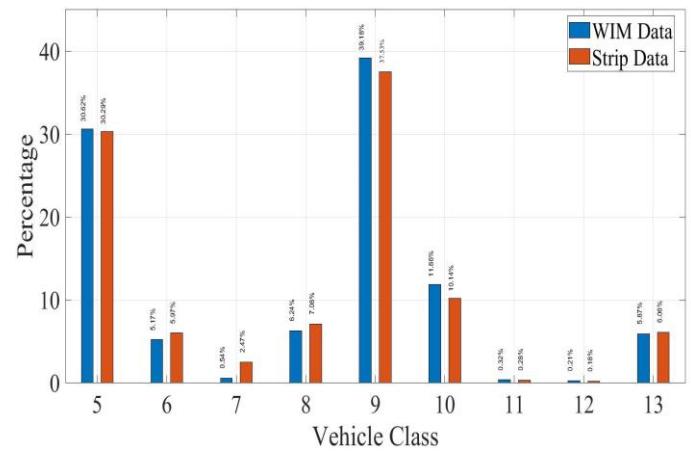
Figure 5. WIM & sensor data.

Table 1. Comparison of WIM & sensor data.

Type	WIM Data	Sensor Data	Error (%)
Class 5	1720	1712	0.14
Class 6	339	289	1.03
Class 7	140	30	9.04
Class 8	402	349	1.08
Class 9	2131	2191	1.03
Class 10	576	663	1.33
Class 11	16	18	0.03
Class 12	10	12	0.03
Class 13	344	328	0.03
Total	5678	5592	1.54

The model was also implemented for daily vehicle classification, enabling continuous monitoring and categorization of traffic. The classification outcomes were compared to data obtained from the WIM system to validate its performance. The analysis revealed a high degree of alignment between the model's classifications and the WIM data, with only minimal discrepancies observed across daily classifications. These minor deviations underscore the model's accuracy and reliability in replicating WIM's established classifications. Figure 6 provides a detailed illustration of these deviations, showing the extent of alignment and highlighting the model's robustness in maintaining classification accuracy over an extended period. The strong correlation between the model's results and the WIM data underscores this approach's potential for scalable, real-time vehicle classification in traffic management and analysis.
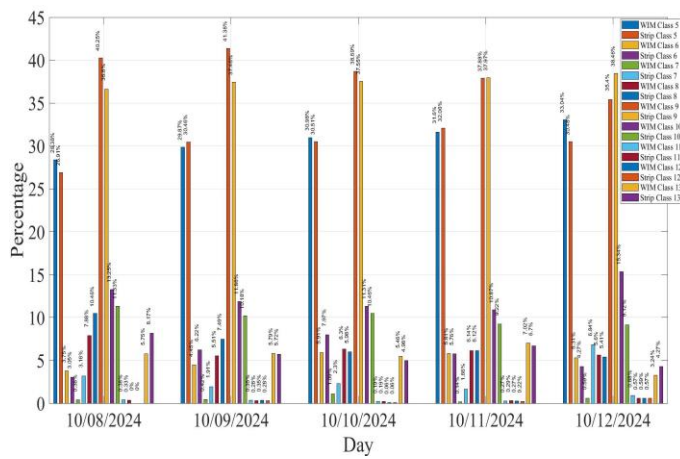
Figure 6. WIM & sensor data (per day).

3.3 Wheel Wander

The model also calculated wheel wander for all vehicles relative to the edge of the road, revealing deviations from the anticipated wheel path, as shown in Figure 7. The mean deviation was 28.95 inches, with a standard deviation of 7.95 inches. This distribution pattern, approximating a normal distribution, suggests that most vehicles adhered closely to the anticipated wheel path, with only minor deviations. These findings indicate relatively stable and predictable driving behavior among the observed vehicles.
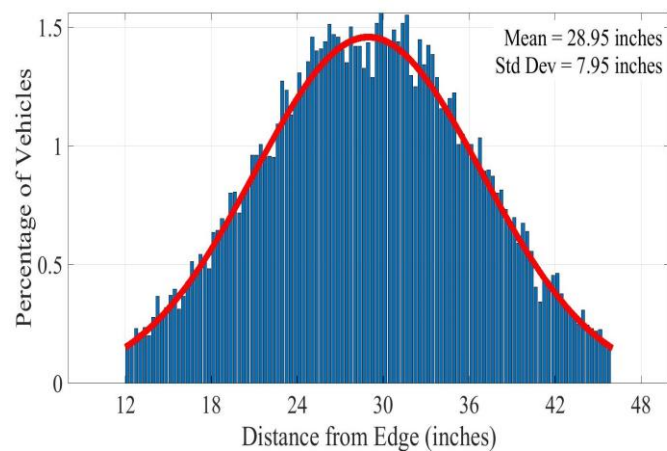
Figure 7. Distribution of wheel wander.

4 SUMMARY OF THE RESULTS

This study presents a cost-effective system utilizing pressure sensors to monitor tire widths, vehicle classifications, and wheel wander in real time. Installed in traffic lanes, these sensors generate voltage signals as tires pass over them, providing valuable data for vehicle classification and pavement analysis. Tested on US127 in Mason, MI, the system effectively classifies vehicles based on axle count and spacing, with minimal deviations from conventional WIM data and a weighted error rate of 1.54%. Results indicate that most vehicles maintain stable

wheel paths, with minimal wheel wander observed. Tire width data reveals a predominance of smaller tires, with larger widths primarily found in Class 9 vehicles. This system offers a reliable alternative to WIM for continuous traffic data collection, which is especially advantageous for high-speed, minimally invasive monitoring.

The developed system effectively captures accurate traffic data at a low cost, supporting its potential for extended monitoring of vehicle characteristics on highways. Integrating pressure sensors with a protective rubber casing enhances durability, while solar power enables self-sustaining functionality. For future improvements, we recommend increasing sensor resolution to reduce classification errors, particularly among closely grouped classes. Additionally, incorporating vehicle weight in the classification process could enhance accuracy. Expanding the system to cover multiple lanes would provide a more comprehensive traffic dataset. To optimize robustness and accuracy across diverse regions and climates, broader field testing is suggested under varying traffic and environmental conditions.

5 REFERENCES

ASTM E1318. 2019, Standard Specification for Highway Weigh-in-Motion (WIM) Systems with User Requirements and Test Method 1. In *2007 Annual Book of ASTM Standards*, ed. ASTM Committee E17-52 on Traffic Monitoring. USA: ASTM International.

Falconi, W. 2019. Piezoelectric nano transducer. *Nano Energy* 59: 730-744. doi: 10.1016/j.nanoen.2019.03.027.

Federal Highway Administration. 2022. *Traffic Monitoring Guide*. Report No. FHWA-PL-022-026.

Hallenbeck, M.E., Selezneva, O.I. & Quinley, R. 2014. Verification, Refinement, and Applicability of Long-Term Pavement Performance Vehicle Classification Rules. Report No. FHWA-HRT-13-091.

Mason, W.P. 1981. Piezoelectricity, it's history and applications. *Journal of the Acoustical Society of America* 70(6): 1561-1566. doi: 10.1121/1.387221.

More, N. & Kapusetti,m G. 2017. Piezoelectric material-A promising approach for bone & cartilage regeneration. *Med Hypothesis* 108; 10-16. doi: 10.1016/j.mehy.2017.07.021.

Patrick, S. & Maher, A. 2009. Implementation of Weigh-in-Motion (WIM) Systems.

Sivakumar, B., Ghosn, M. & Moses, F. 2011. NCHRP REPORT 683—Protocols for Collecting and Using Traffic Data in Bridge Design. *Transportation Research Board.*

Study on passenger-vehicle coupling vibration response for autonomous driving

Dawei Wang*

Corresponding author: School of Transportation Science and Engineering, Harbin Institute of Technology, 73 Huanghe Rd., Nangang District, Harbin 150090, China. Email: dawei.wang@hit.edu.cn

Zepeng Fan

School of Transportation Science and Engineering, Harbin Institute of Technology, 73 Huanghe Rd., Nangang District, Harbin 150090, China. Email: zepeng.fan@hit.edu.cn

Yifan Wang

School of Transportation Science and Engineering, Harbin Institute of Technology, 73 Huanghe Rd., Nangang District, Harbin 150090, China. Email: yifanwang@stu.hit.edu.cn

Yulin He

Department of Civil and Environmental Engineering, The Hong Kong Polytechnic University, Kowloon, Hong Kong, China. Email: yulin.he@polyu.edu.hk

ABSTRACT: Autonomous driving is a crucial area of research. Beyond ensuring safety, it is important to enhance the ride comfort of autonomous vehicles (AVs) and minimize the risk of vibration-induced damage. Therefore, an 18-degree-of-freedom (DOF) 3D passenger-vehicle coupled vibration model was developed, which takes into account various components of both the passenger and the vehicle. The study examined the conditions related to comfort, motion sickness, and potential vibration damage to different organs during AV operations. The results showed that maintaining surface roughness at Level A and limiting speed to 100 km/h were optimal for passenger comfort and health. The conclusions offer valuable insights for autonomous cars operation from the passengers' perspective.

1 INTRODUCTION

Autonomous driving technology is extensively researched across various disciplines, including vehicle engineering, transportation engineering, and computer science. In recent years, the focus of autonomous driving research has primarily been on AV design, navigation and localization, external environment sensing, path planning, and vehicle dynamics control (Parekh et al., 2022). However, studies addressing the comfort and health aspects of autonomous driving have been relatively limited. To enhance ride comfort and mitigate the risk of motion sickness and potential vibration damage to humans, it is crucial to guide and control the movement of AVs from the perspective of the passengers.

Human-vehicle coupling models are essential for studying ride comfort, motion sickness, and the potential vibration-related damage to human organs during travel. Desai (Desai et al., 2021) created a 12-DOF seated human-nonlinear seat cushion-full vehicle model and explored the sensitivity of a multi-compression damper with an inclined damper-seat suspension system. Song (Song et al., 2023) developed a fully coupled human-vehicle model using CarSim software and MATLAB/Simulink, and assessed ride comfort through the generalized polynomial (gPC) method. While extensive research has been conducted on the dynamics of both human and vehicle models, most studies primarily focused on evaluating ride comfort and its impact on vehicle motion. For passengers, assessing ride comfort alone is inadequate.

In summary, for advanced autonomous driving technology, it is essential to further explore ride comfort, motion sickness, and the potential risk of vibration-related injuries from the passenger's perspective to guide AV operation. To address this, an 18-DOF 3D passenger-vehicle coupled vibration dynamics model was developed. This study offers a theoretical foundation for intelligent decision-making and control of AVs with a focus on passenger well-being.

2 THEORETICAL DERIVATION AND MODEL CONSTRUCTION

2.1 *Modeling 3D passenger-vehicle coupling vibration*

To accurately represent the human vibration during the ride, a 3D passenger-car coupling vibration model was developed by integrating the vibrations of various parts of the seated human body and the entire vehicle, as shown in Figure 1.

A 3D elastic roller contact tire model was employed (Wang et al., 2023). The system's vibration equations were derived from classical structural dynamics theory, as shown in Equation 1.

The central difference method was used to solve these equations. Parameters for both the passenger

and the car were based on previous studies (Wang et al., 2023, Taskin et al., 2018).
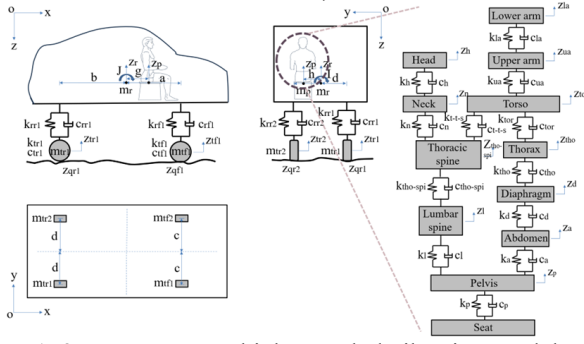
Figure 1. 3D passenger-vehicle coupled vibration model.

$$MÜZ + CŻ + KZ = F \qquad (1)$$

where M = mass matrix; C = damping matrix; K = stiffness matrix; U = Unknown matrix. F = External Force Matrix.

2.2 Ride comfort model and evaluation index

The ride comfort calculation method followed the international standard ISO 2631-1 (ISO, 1997). Overall Vibration Total Value (OVTV) was selected as the evaluation index and the comfort threshold was derived from existing research (Wang et al., 2023).

2.3 Motion sickness model and evaluation index

According to the ISO 2631-1 standard, the motion sickness index (MSI) was used to assess passenger motion sickness. MSI is expressed in percentage, representing the proportion of individuals in a population likely to experience vomiting due to motion sickness.

2.4 Analysis and Evaluation Methods of Potential Vibration Damage to Human Organs

During the driving process, passengers will be exposed to vibrations, and if the vibration frequency matches or closely resembles the natural frequency of human organs, resonance will occur, amplifying the risk of potential vibration-related damage. By analyzing the time-domain vibration curves of different organs, the power spectrum was calculated using the direct method to obtain the vibration response in the frequency domain. By comparing the external vibration frequency of different parts of the human body with the natural frequency, the impact of vibration on human organs could be analyzed. The natural frequencies of each organ were derived from existing research (WIĘCKOWSKI, 2012, Ruoxun et al., 2019, Fan et al., 2021).

3 RESULTS AND DISCUSSION

3.1 Model comparison and verification

To verify the accuracy of the 3D passenger-vehicle coupled vibration model, a traditional 3-DOF quarter vehicle model (Wang et al., 2023) was used.

The condition involved two vehicles traveling at 80km/h on a Class C roughness pavement, and the vehicle vibration responses are shown in Figure 2.
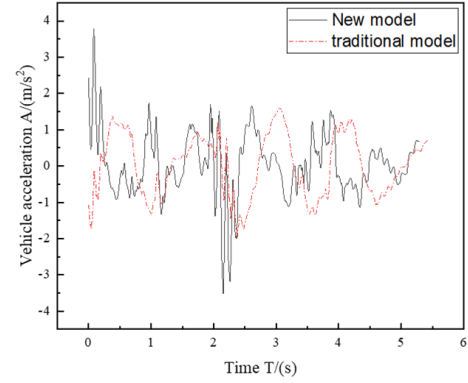
Figure 2. The verification of vehicle vibration response.

As shown in Figure 2, the time-domain curves of vehicle vertical acceleration obtained from both models were highly consistent, fluctuating within the range of $-4\sim4$m/s^2. The root-mean-square value of vehicle vibration acceleration calculated using the 3D model was 0.865m/s^2, while the root-mean-square value of the traditional model was 0.8685m/s^2, yielding a relative error of only 0.4%. Therefore, the accuracy of the model proposed in this study could be proved.

3.2 Ride comfort analysis

Using the comfort indicators OVTV and corresponding thresholds, the results of the ride comfort evaluation are shown in Figure 3.
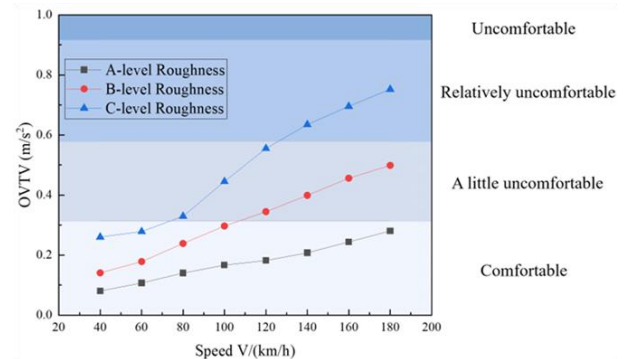
Figure 3. Ride comfort evaluation.

As could be seen from Figure 3, the influence of pavement roughness and speed on comfort was obvious. During autonomous driving, to ensure optimal ride comfort, it should be crucial to adjust the driving speed according to the condition of the road sur-

face. It is recommended to maintain the pavement roughness at Class A to enhance passenger comfort.

3.3 *Motion sickness analysis*

Motion sickness is influenced by pavement roughness, driving speed, and travel time. The analysis of passenger motion sickness under different conditions of pavement roughness, speed, and travel time is shown in Figures 4~6.
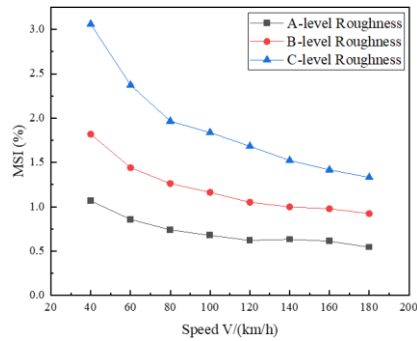
Figure 4. Motion sickness evaluation with different pavement roughness.
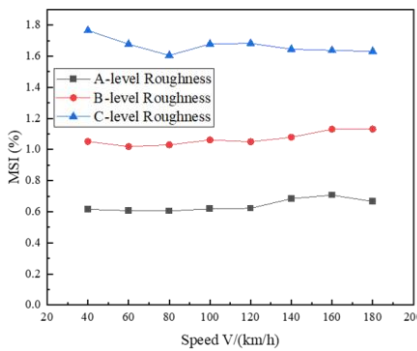
Figure 5. Motion sickness evaluation with different driving speeds.
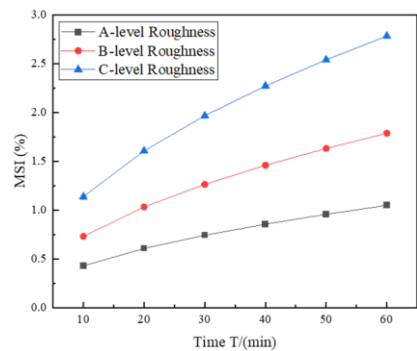
Figure 6. Motion sickness evaluation with different travel times.

As shown in Figure 4, when the road length and speed were held constant, the worse the pavement roughness was, the more likely it was to cause motion sickness in humans. Additionally, the lower the speed, the more obvious the motion sickness caused by pavement roughness.

As can be seen from Figure 5, driving speed had little impact on motion sickness, indicating that speed was not a direct contributor to motion sickness.

It could be seen from Figure 6, that the MSI had a linear relationship with travel time at a given speed.

3.4 *Analysis of potential vibration damage to human organs*

The results of the vibration power spectrum for each human organ under varying pavement roughness and different speeds are shown in Figures 7~9.
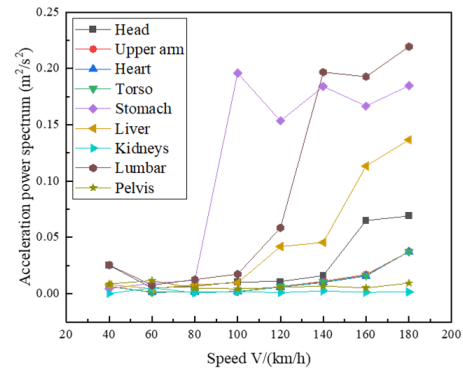
Figure 7. Acceleration power spectrum for A-level pavement roughness.
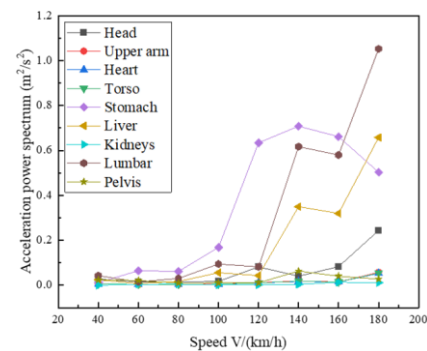
Figure 8. Acceleration power spectrum for B-level pavement roughness.
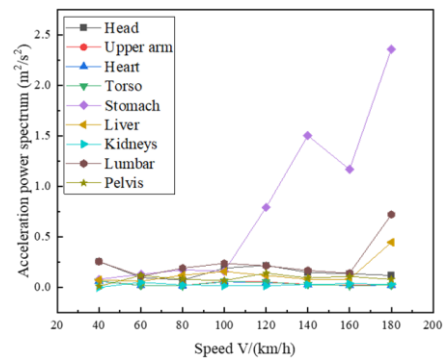
Figure 9. Acceleration power spectrum for C-level pavement roughness.

As could be seen from Figures 7~9, the power spectrum of different parts of the human body changed in the corresponding natural frequency range with the increase in speed and the deterioration of pavement roughness. Organs including the upper arm, heart, lungs, torso, kidneys, and pelvis showed minimal changes. In contrast, the head, stomach, liver, and lumbar spine experienced more noticeable changes, especially the biggest impact on the stomach, followed by the lumbar spine. For vari-

ous pavement roughness, the power spectrum value would increase significantly when the speed exceeded 100km/h. Therefore, it is recommended to maintain the driving speed below 100km/h to minimize the risk of vibration-related damage to human organs.

4 CONCLUSIONS

(1) Ride comfort was primarily influenced by pavement roughness and driving speed. Therefore, during autonomous driving, a suitable driving speed should be chosen based on the pavement roughness.

(2) Motion sickness was affected by pavement roughness and driving time, but not significantly by speed. Therefore, the duration of the ride should be adjusted according to the road surface condition during autonomous driving to reduce the risk of motion sickness.

(3) Vibration had a great significant impact on the head, stomach, liver, and lumbar spine, with the stomach and lumbar spine being the most affected.

(4) Based on the analysis of ride comfort, motion sickness, and potential vibration damage to human organs, it was recommended to maintain the pavement roughness at Class A and control the driving speed below 100 km/h during autonomous car operation.

(5) In further investigations, the impact of AVs changing speed based on detecting road surface defects on ride comfort and motion sickness should be further considered. This would enhance the applicability and generalizability of the findings.

5 PREFERENCES

DESAI, R., GUHA, A. & SESHU, P. 2021. Modelling and simulation of an integrated human-vehicle system with non-linear cushion contact force. *Simulation Modelling Practice and Theory,* 106.

FAN, R., LIU, J. & LIU, J. 2021. Prediction of the natural frequencies of different degrees of degenerated human lumbar segments L2-L3 using dynamic finite element analysis. *Computer Methods and Programs in Biomedicine,* 209.

ISO 1997. Mechanical vibration and shock—Evaluation of human exposure to whole-body vibration. Part I: General requirements. ISO. 2631-1: Geneva: ISO.

PAREKH, D., PODDAR, N., RAJPURKAR, A., CHAHAL, M., KUMAR, N., JOSHI, G. P. & CHO, W. 2022. A Review on Autonomous Vehicles: Progress, Methods and Challenges. *Electronics,* 11.

RUOXUN, F., JIE, L., JUN, L. & WEIJUN, W. 2019. Presentation of an Approach on Determination of the Natural Frequency of Human Lumbar Spine Using Dynamic Finite Element Analysis. *Applied Bionics and Biomechanics,* 2019, 1-8.

SONG, B.-G., BAE, J.-J. & KANG, N. 2023. Uncertainty Quantification of Ride Comfort Based on gPC Framework for a Fully Coupled Human–Vehicle Model. *Applied Sciences,* 13.

TASKIN, Y., HACIOGLU, Y., ORTES, F., KARABULUT, D. & ARSLAN, Y. Z. 2018. Experimental investigation of biodynamic human body models subjected to whole-body vibration during a vehicle ride. *International Journal of Occupational Safety and Ergonomics,* 25**,** 530-544.

WANG, C., WANG, D., LIU, P., HE, Y. & OESER, M. 2023. Study on Vehicle Vibration Response under the Condition of 3D Tire–Pavement Contact for Unmanned Driving. *Journal of Transportation Engineering, Part B: Pavements,* 149.

WIĘCKOWSKI, D. 2012. An attempt to estimate natural frequencies of parts of the child's body. *Archiwum Motoryzacji***,** 61-74.

5.1

SUSTAINABLE AND RESILIENT PAVEMENTS AND MATERIALS

Redefining HiMA: An Approach to Performance Based Characterization

M. Bhardwaj, P. Kumar, & N. Saboo
Indian Institute of Technology, Roorkee, Uttarakhand, India

ABSTRACT: Highly Modified Asphalt (HiMA) represents an advanced evolution of Polymer-Modified Asphalts (PMAs), engineered to meet the demands of high-stress pavement applications. Incorporating higher dosages of Styrene-Butadiene-Styrene (SBS) polymer, HiMA offers enhanced resistance to rutting, fatigue, and thermal degradation, surpassing the performance of conventional SBS-modified PMAs. Traditional methods of identifying HiMA, such as Fluorescence Microscopy (FM), rely on detecting phase reversal but fail to encompass broader performance attributes relevant to real-world applications.This study proposes a more holistic approach to HiMA classification, focusing on measurable parameters like softening point, penetration values, and Performance Grading (PG) under various aging conditions. By quantifying the SBS content necessary for significant PG shifts, the research establishes a clearer understanding of the transition from PMA to HiMA. These insights provide a robust framework for correlating SBS content with asphalt performance, bridging gaps in scenarios where only PG temperatures are specified, and enhancing the practical application of HiMA.

1 INTRODUCTION

The use of PMAs has significantly improved pavement performance by enhancing the mechanical and thermal properties of asphalt binders. Polymers, when added to asphalt, improve their elasticity, reduce brittleness, and increase its resistance to deformation, leading to more durable pavements (Airey 2003). Among these polymers, SBS is one of the most commonly used due to its ability to simultaneously increase the elasticity and stiffness of the asphalt. This combination makes SBS particularly effective in improving the binder's resistance to cracking, rutting, and temperature-induced stresses, making it suitable for regions with diverse weather conditions and high traffic volumes (Huang and Tang 2015; Jiang et al. 2017).

Despite their proven effectiveness, conventional SBS-modified PMAs, which typically contain 3-5% polymer by weight of asphalt, sometimes fall short in more demanding applications, such as heavily trafficked expressways, ports, airports and areas with extreme weather conditions (Greene et al. 2014; Rajan et al. 2023). To address these limitations, researchers developed HiMA, which is characterized by a higher polymer content (>7% by weight of asphalt) (Fournier 2010).

HiMA has emerged as a transformative material in the field of pavement engineering, offering superior resistance to fatigue, rutting, and thermal degradation, making it a more robust solution for high-demand pavement applications (Diefenderfer et al. 2018; Habbouche et al. 2020). Its enhanced properties not only extend pavement service life but also significantly reduce maintenance requirements.

Traditionally, HiMA has been characterized and identified primarily through FM imaging, where the occurrence of phase reversal - a distinctive morphological change indicating a high degree of polymer modification - served as the defining criterion (Vargas-Nordcbeck and Musselman 2021). While FM imaging provides valuable insights into the microstructural behavior of asphalt, this approach does not fully capture the broader performance attributes and practical implications of HiMA in real-world applications.

This study aims to redefine the classification and characterization of HiMA by incorporating a more comprehensive set of measurable properties, including softening point, penetration values, and PG Grading under both unaged and short-term aged (STA) conditions. By analyzing these performance-based parameters, the research examines the specific SBS content or range of SBS content at which PMA transitions into HiMA, offering a deeper and more

comprehensive understanding rather than relying solely on FM.

The study also establishes a quantitative relationship between SBS content and PG shifts, addressing critical questions such as the amount of SBS required to achieve a 6°C change in PG grade or determining the PG value that corresponds to a specific SBS content in the modified asphalt. This approach helps bridge the gap in cases where only PG temperature is specified, rather than the SBS content, ensuring a more comprehensive understanding of asphalt properties.

2 MATERIALS AND SAMPLE PREPARATION

2.1 Materials

The materials used in this study include VG40 bitumen, a viscosity grade binder commonly used for highway paving in India, sourced from Tiki Tar and Shell Bitumen Industries. For modification, a linear SBS polymer (SBS LG-501 S) from LG Chem Industries and a locally sourced sulfur additive were employed to enhance the binder's performance and facilitate polymer cross-linking. Physical properties of VG40 are shown in Table 1.

Table 1. Properties of base binder, VG40.

Property	Value
Penetration, 25°C, 0.1 mm	38
Softening Point, °C	55.3
Absolute Viscosity, 60°C, Pa-s	389.6
High Temperature PG	PG 70
True High Fail Temperature, °C	74.6

2.2 PMA Preparation

In this study, SBS copolymer was incorporated into the base binder to produce SBS-modified asphalt. The SBS copolymer was added at dosages of 2%, 4%, 6%, 8%, 10% and 12% by weight of the base binder. Mixing occurred at a binder temperature of 180°C with a shear rate of 4200 rpm for 90 minutes, followed by a period of low shear (288 rpm) for another 90 minutes. Additionally, Sulphur (0.15% by weight of base binder) was introduced at the beginning of the low shear mixing phase to prevent phase separation of polymer and asphalt. Sulphur has a cross-linking property that connects polymer molecules, enhancing the stability of modified asphalt.

3 METHODOLOGY

The methodology adopted in this study is illustrated in Figure 1.
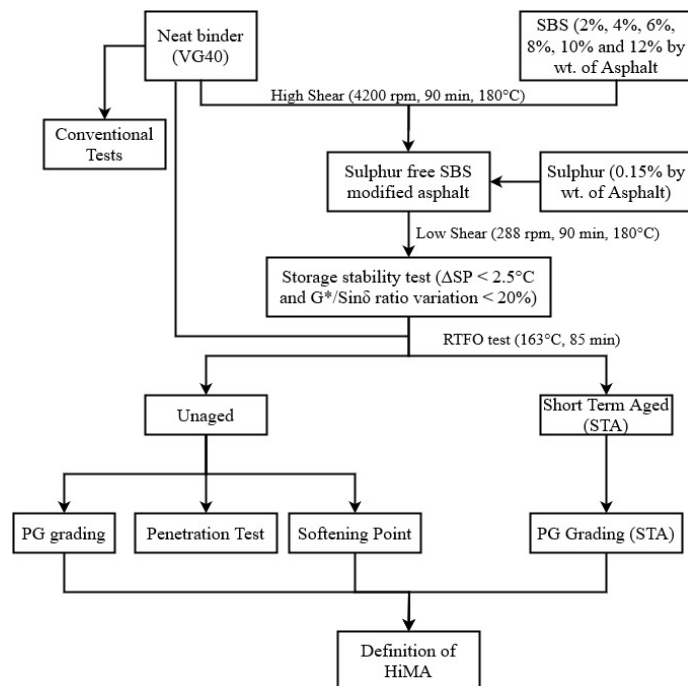
Figure 1. Methodology chart of the study.

4 EXPERIMENTAL PROGRAM

4.1 Storage Stability

The storage stability of SBS-modified asphalt was evaluated as per ASTM D7173, using 32 mm × 160 mm aluminum tubes stored vertically at 163 °C for 48 hours. After freezing and sectioning the samples, Softening point difference (ΔSP) and G*/Sinδ ratio between the top and bottom sections were measured, with stability criteria of ΔSP < 2.5°C and 0.8 < G*/Sinδ ratio < 1.2.

4.2 Tests on Modified Asphalt

Conventional tests, including softening point and penetration, were conducted on unaged SBS-modified samples, along with High PG Grading tests using Dynamic Shear Rheometer (DSR) on both unaged and short-term aged (STA) samples. PG grading failure was observed when G*/Sinδ fell below 1 kPa for unaged samples and 2.2 kPa for STA samples.

5 RESULTS AND DISCUSSIONS

5.1 Storage Stability

The storage stability testing of SBS-modified VG40 binders demonstrated uniform polymer dispersion at all tested doses. Both lower and higher SBS dosages (10% and 12%) showed ΔSP and G*/Sinδ ratio within acceptable limits (ΔSP < 2.5°C and 0.8 < G*/Sinδ ratio < 1.2), confirming good storage stability and compatibility as shown in Figure 2 and Figure 3. These findings indicate effective blending and dispersion of SBS polymer without any phase separation. This

compatibility arises from the similar chemical nature of SBS and the base binder, enabling stable intermolecular interactions and uniform distribution.
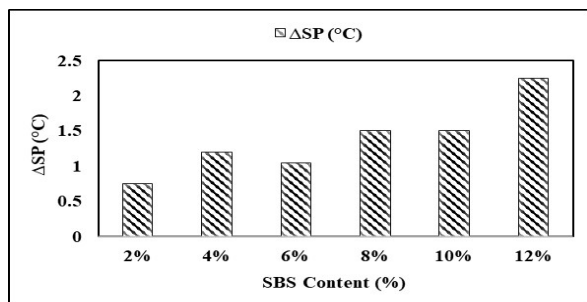
Figure 2. Softening point difference (ΔSP)
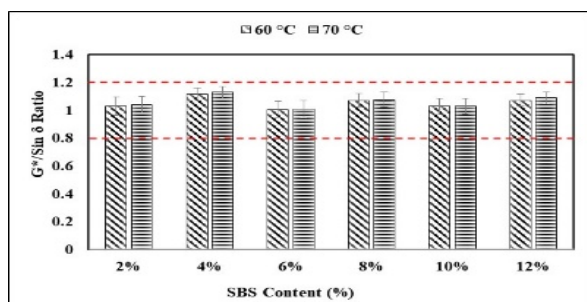
Figure 3. G*/Sinδ ratio values.

5.2 Conventional Tests

Penetration and softening point tests were performed on both modified and unmodified asphalt samples. At 25°C, penetration decreased with increasing SBS content, with a less pronounced reduction observed in the 6% to 8% range due to the formation of a spatial network structure that limits asphalt flow as shown in Figure 4. This phase marks the transition from conventional SBS-modified asphalt to HiMA. Beyond 8% SBS content, penetration decreased more significantly due to the enhanced stiffness and elasticity provided by HiMA.
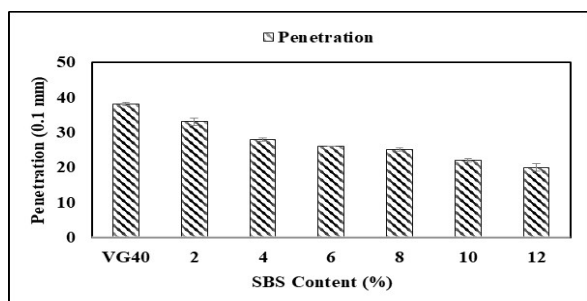
Figure 4. Penetration test results.

The addition of SBS modifier raises the softening point of asphalt binders, improving their high-temperature performance and stability as shown in Figure 5. At lower SBS dosages (<6%), the improvement in softening point values is minimal because the asphalt phase remains continuous, and the SBS phase is dispersed within it. As SBS content increases to 6–8%,

the softening point rises moderately due to the emergence of a critical co-continuous phase, where both SBS and asphalt phases coexist. However, this state is unstable as the proximity between SBS particles and asphalt micelles reduces, weakening the interface layer. Beyond 8% SBS content, the structure transitions to a continuous SBS polymer phase with asphalt dispersed within, significantly increasing softening points due to SBS-dominated properties. This transition phase (>8% SBS content) with significant softening point enhancement can be classified as HiMA.
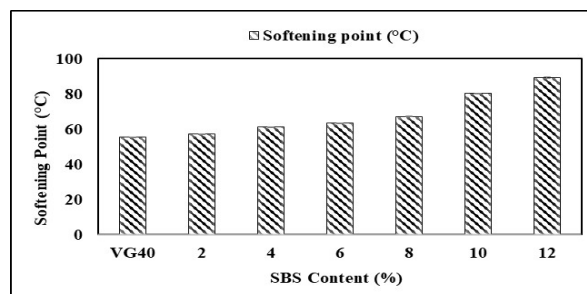
Figure 5. Softening point test results.

5.3 PG Grading Test

PG grading tests were performed on both unaged and STA samples to evaluate their performance. For the unaged samples, an increase in SBS content was observed to correspond with a rise in the pass/fail temperature as illustrated in Figure 6. However, within the transition phase (6-8% SBS content), this increase became stagnant. This stagnation is consistent with observations from the softening point and penetration tests, which suggest a weakening of the interface layer.
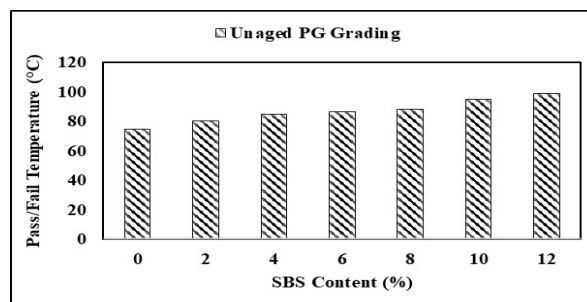
Figure 6. Unaged PG Grading results.

Beyond the transition phase, a steep increase in the pass/fail temperature was noted for SBS contents exceeding 8% as seen from Figure 7. This significant improvement suggests that the phase beyond the transition can be classified as HiMA.

Figure 7 also reveals that for SBS content up to 4%, a 6°C change in pass/fail temperature requires the addition of 2% SBS. However, during the transition phase, the pass/fail temperature increase becomes constant. Once the HiMA phase is reached (8% SBS content), the first 2% increase in SBS content results

in a steep rise of 7°C in pass/fail temperature, which then returns to a 6°C rise for a subsequent 2% SBS
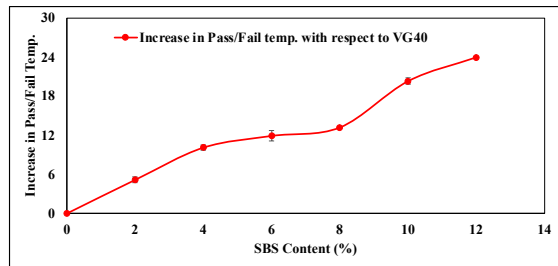
Figure 7. Increase in Pass/Fail temperature for unaged samples.

additions. This result can be used to determine the appropriate amount of SBS to add in order to achieve a desired PG value.

PG grading tests conducted on STA samples showed a consistent increase in pass/fail temperature with rising SBS content, as illustrated in Figure 8. This trend aligns with the observations from earlier tests. However, at 12% SBS content, a decline in pass/fail temperature was observed compared to 10% SBS, indicating that STA contributes to the degradation of SBS polymers. This highlights the existence of an optimal SBS content limit. To improve the performance and longevity of HiMA binders, further research should focus on their aging behavior and resistance to degradation.
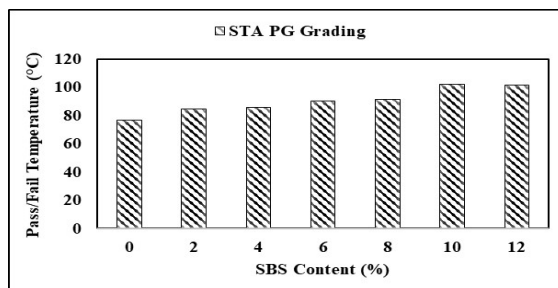
Figure 8. STA PG Grading results.

6 CONCLUSIONS

Based on the analysis of the results, the following conclusions can be drawn:

- All SBS-modified asphalts were found to be storage stable, with each meeting the acceptable limits for softening point difference and $G^*/Sin\delta$ ratio. This indicates good dispersion and compatibility of SBS with asphalt.
- As SBS content increased, penetration decreased and the softening point increased. However, during the transition phase (6-8% SBS content), the changes in penetration and softening point values became stagnant, signaling the transition from conventional SBS-modified asphalt to HiMA.
- PG grading results for unaged samples also revealed a transition phase (6-8% SBS content),

after which the pass/fail temperature increased significantly, indicating the formation of HiMA. This aligns with the findings from the penetration and softening point tests.

- A 6°C increase in pass/fail temperature was observed for every 2% increase in SBS content, excluding the transition phase from conventional SBS-modified asphalt to HiMA. This conclusion will be helpful in determining the optimal SBS content required to achieve the desired PG value.
- For STA samples, the pass/fail temperature increased, consistent with the results of other tests. However, at 12% SBS content, a decrease in pass/fail temperature was observed, likely due to SBS degradation. This highlights the need for further investigation into the aging behavior of HiMA.

REFERENCES

Airey, G. D. 2003. "Rheological properties of styrene butadiene styrene polymer modified road bitumens." *Fuel*, 82 (14): 1709–1719. https://doi.org/10.1016/S0016-2361(03)00146-7.

Diefenderfer, S. D., B. K. Diefenderfer, and B. F. Bowers. 2018. *Evaluation of highly polymer-modified asphalt mixtures: Phase I.* Virginia Transportation Research Council.

Fournier, P. 2010. "Georgia DOT chooses highly modified asphalt for busy intersection." *Dixie Contactor Edition*, 849 (10).

Greene, J., S. Chun, and B. Choubane. 2014. *Evaluation and Implementation of a Heavy Polymer Modified Asphalt Binder through Accelerated Pavement Testing.*

Habbouche, J., E. Y. Hajj, P. E. Sebaaly, and M. Piratheepan. 2020. "A critical review of high polymer-modified asphalt binders and mixtures." *International Journal of Pavement Engineering*, 21 (6): 686–702. Taylor and Francis Ltd. https://doi.org/10.1080/10298436.2018.1503273.

Huang, W., and N. Tang. 2015. "Characterizing SBS modified asphalt with sulfur using multiple stress creep recovery test." *Constr Build Mater*, 93: 514–521. Elsevier Ltd. https://doi.org/10.1016/j.conbuildmat.2015.06.041.

Jiang, Z., C. Hu, S. M. Easa, X. Zheng, and Y. Zhang. 2017. "Evaluation of physical, rheological, and structural properties of vulcanized EVA/SBS modified bitumen." *J Appl Polym Sci*, 134 (21). John Wiley and Sons Inc. https://doi.org/10.1002/app.44850.

Rajan, B., A. Suchismita, and D. Singh. 2023. "Rutting Resistance Evaluation of Highly Polymer-Modified Asphalt Binder and Mixes Using Different Performance Parameters." *Journal of Materials in Civil Engineering*, 35 (8). American Society of Civil Engineers (ASCE). https://doi.org/10.1061/jmcee7.mteng-15194.

Vargas-Nordcbeck, A., and J. A. Musselman. 2021. *Highly Modified Asphalt Florida Case Study.* United States. Federal Highway Administration. Office of Preconstruction

Characterization of gasifier condensate as a potential replacement of asphalt binder

Bhaswati Bora & Nikhil Saboo & Praveen Kumar & Sonal K. Thengane
IIT Roorkee, Roorkee, UK, India

ABSTRACT: Biobased materials and byproducts of bio refineries are explored as alternative materials to replace the fossil fuel-based binders. Biomass or biowaste are processed and chemically treated to a compatible form to blend with asphalt binder homogeneously. In this study, gasifier byproduct of pine needle biomass was investigated as a potential replacement of asphalt binder. Replacement up to 20 % was studied and the binders were chemically characterized using FTIR and TGA. Correlations were developed between the chemical indices and the physical properties. For morphological analysis, imaging studies were performed using AFM. It was found that the gasifier bio-condensate has some potential for use as a replacement for asphalt binders. The bio-condensate also showed a rejuvenation effect, as observed from chemical and morphological studies.

1 INTRODUCTION

Life cycle assessment of asphalt binder shows significant CO_2 and GHG emissions. Lignocellulosic biomass and biowaste have been explored as alternative sustainable resources for asphalt binder replacement that can substantially reduce these emissions. Biomass is initially chemically treated to convert into compounds with a similar composition as that of the asphalt binder. The thermochemical conversion process is the most effective method for converting biomass into biobased carbonaceous materials. Past studies have performed pyrolysis and hydrothermal liquefaction on plant-based and waste biomass to obtain bio-oil as a replacement for asphalt binder. Literature survey indicates mixed performance results of bio-asphalt binder (with a replacement up to 40%). Due to the softening of the base binder with the use of higher dosage of bio-oil, polymer modification of the bio-asphalt has also been explored in a few studies (He et al. 2020; Al-Sabaeei et al. 2020).

Biomass condensate obtained from a gasifier facility was used in this study as a partial replacement of asphalt binder. In general, a gasifier facility is used for syngas production from biobased feedstock such as lignocellulosic, bio-waste, or other carbonaceous resources. They are sustainable production systems for producing clean and green alternative forms of energy over fossil fuel-based natural resources. The gasifier operates at high temperatures of 800°C to 1100°C for biomass conversion into sustainable renewable energy in the presence of oxygen. The feedstock is initially pretreated for moisture removal. The gasifier operates through a series of physico-chemical processes occurring inside the reactor, such as combustion reaction, pyrolysis, cracking, reforming, oxidation, and reduction producing gas and char as primary products. Other than syngas and char production, higher production temperatures lead to the formation of a byproduct. This condenses on the reactor bed after cooling the gasifier. Gasifier condensate is a combination of heavy metals, oil, fly ash, tar, and low-carbonaceous materials. The condensate is recovered as a mixture of water during the cleaning process of the gasifier. The composition of the gasifier condensate is widely dependent on feedstock source, operating conditions, and gasifier type. In this study, gasifier condensate of pine needle biomass was investigated as a potential replacement for asphalt binder. The bio-asphalt binders were prepared by replacing the base binder with 5%, 10%, 15%, and 20% bio-condensate (by weight of the base binder). The bio-condensate and the prepared bio-asphalt binder were characterized using Fourier Transform Infrared (FTIR) spectroscopy to identify the chemical composition of the condensate and the bio-asphalt binder. Thermal stability, mass loss, and residue analysis were performed on the prepared bio-asphalt using Thermogravimetric Analyzer (TGA). The aging performance of the bio-asphalt binder was further investigated using physical, rheological, and chemical analysis. Finally, morphological investigations were performed using AFM to understand the interaction between base binder and bio-condensate at different aging conditions.

2 EXPERIMENTAL STUDIES

2.1 *Bio-asphalt production*

A VG-40 binder, as per IS 73-2013, was used as the base binder in this study. The condensate obtained from the gasification process was heated initially at a controlled temperature of 150°C to remove water. Volatiles and lightweight compounds also get removed with water at this temperature. The recovered condensate had a homogeneously viscous oily texture. The dewatered bio-condensate was added to the preheated asphalt binder at 135°C. (Zhang et al. 2020). The condensate and the asphalt binder were

mechanically mixed with a stirrer rotating at 1500 rpm for 20 mins to prepare the bio-asphalt binder. Low blending temperatures were considered for bio-asphalt production to ensure that the inherent properties are not affected by the production temperatures. The homogeneity of the produced bio-asphalt binder was assessed visually.

2.2 FTIR analysis

FTIR spectroscopy can be used to evaluate the functional groups and compounds present in any material. The quantification of the compounds present in the asphalt binder is typically performed by calculating the indices of the functional groups and compounds. Carbonyl (C=O) and sulfoxide (S=O) indices are generally used to quantify aging in the asphalt binder (refer to Equations 1 and 2). The samples in this study were tested using the KBr pellet method. Sample solutions were prepared using CS_2 as a solvent and 10 microliters of the sample solution was drop casted on the KBr pellet to test using the FTIR spectroscopy (Bora & Das 2020, 2021). 32 scans were performed per sample to obtain the absorbance spectra. 4 cm^{-1} resolution was used during the experiment.

$$I_{C=0} = \frac{I_{1700}}{I_{REF}}$$ (1)

$$I_{S=0} = \frac{I_{1600}}{I_{REF}}$$ (2)

2.3 TGA analysis

The temperature stability and mass loss of the bio-asphalt binder can be analyzed using a thermogravimetric analyzer. The decomposition kinetics and the degradation behaviors of asphalt binders at higher temperatures were investigated using the TGA. For TGA analysis, around 10 mg of binder sample was tested from 30°C to 800°C under inert conditions at a heating rate of $(10°C)/min$.

2.4 AFM analysis

Images of the base binder and the bio-asphalt binder were captured using the PeakForce Quantitative Nanomechanics (QNM) mode of scanning. Catanaphase, periphase, and paraphase are the three phases of asphalt binder identified using the AFM. Sometimes waxes are identified as a fourth phase and are observed as a bright phase on the AFM images. In this study, AFM imaging was performed on the base binder and bio-asphalt binders to identify the wax content and the phase changes on modification and aging (Das et al. 2016, Yu et al. 2016). A force of 272μN was applied on the cantilever probe

having a spring constant 40.41 N∕m and a tip radius of 64.56 nm for the QNM mode of scanning.

2.5 Physical properties

The softening point (SP) (ASTM D36/D36M-14) and the high-temperature true fail (T/F) temperature (AASHTO 2017) of the binders were evaluated for the unaged binder, short-term aged (STA) binder, and long-term aged (LTA) binder. The short-term aging index (STAI) was calculated using the values of SP and T/F temperatures. Long-term aging index (LTAI) was also determined using the SP values. The mathematical definition of the aging index is presented through Equation (3). Similarly, the FTIR chemical indices were used to study the susceptibility of the binders to aging.

$$Aging\ index\ (AI) = \frac{Parameter\ value\ after\ aging}{Parameter\ value\ before\ aging}$$ (3)

3 ANALYSIS AND RESULTS

The values of SP and the T∕F temperatures are presented in Table 1 and Table 2, respectively. In general, with aging, the SP of all the binders increased. Irrespective of the type of binder, the increase in SP after STA and LTA was found to be approximately 5°C and 18°C, respectively. Addition of bio-condensate led to marginal reduction in the SP. With increase in the dosage of the bio-condensate, the SP values were found to reduce. Interestingly, these results of T/F temperature were not in agreement with the results of SP. At 15% and 20% replacement, the bio-asphalt binder showed significant increase in stiffness after STA. In other words, at higher replacement dosages, the bio-asphalt binder may be more prone to aging. More studies are required to explain the difference in the results of SP and T/F temperature.

Table 1. Softening point (SP) of binders.

	VG-40	5% rep	10% rep	15% rep	20% rep
Unaged (UA)	52.5	51	50.9	50.8	50.8
STA	58.5	59.1	58.4	57.1	55.6
LTA	71.2	70.4	70.2	69.1	69.3

Table 2. High temperature PG and T/F temperature.

		VG-40	5% rep	10% rep	15% rep	20% rep
UA	Fail Temp	82	76	76	76	76
	P/F Temp	76.3	72.4	72.2	72.1	70.7
STA	Fail Temp	82	82	82	118	118
	P/F Temp	80.5	81	80.4	117.9	117

Figure 1 represents the peaks in the fingerprint region of the FTIR spectra of the 5% bio-asphalt binder in different aging conditions. Similar peaks pre-

sent in the bio-oil was observed in the bio-asphalt binder. However, amines, ester, ether, anhydrides, and substituted aromatic compounds were not observed in the asphalt binder. Also, the -OH groups and the compounds formed due to presence of the hydroxyl compounds are absent in the bio-asphalt binder (refer to Figure 1). S=O formation, which typically occurs on aging, is observed at 1060 cm^{-1}. Cyclic compounds such as cyclic alkenes, cyclic amides, and aromatic compounds with C=O groups i.e., amide, lactam, and carboxylic acid are observed to be present in both bio-asphalt binder and bio-oil. On short-term aging no peak degradation is observed in peaks between 1560 cm^{-1} and 1760 cm^{-1}. However, on long-term aging the peaks due to the cyclic compounds, amides, acids, unsaturated ketones decompose. -OH compounds also decompose on aging observed form the peak at 3440 cm^{-1}. On the contrary, no degradation is observed in the alkene peaks at 1647 cm^{-1} and 1654 cm^{-1} on aging.
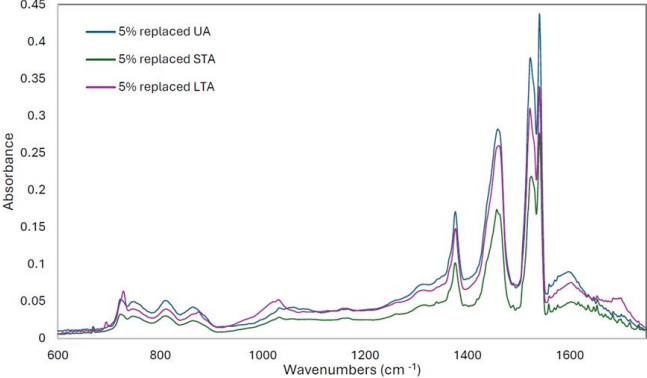
Figure 1. 5% bio-asphalt binder spectra on aging.

Figure 2 shows the C=O indices of the bio-asphalt binders and VG-40. C=O generally increases on aging, as observed for all the binders. The C=O values of 5% bio-asphalt binder are higher than VG-40 and decrease with the increase in the bio-condensate percentage. The decrease in C=O values is the rejuvenation effect of the bio-asphalt binder. The unsaturated ketones, amides, and acids containing C=O decompose on biomodification using gasifier bio-condensate, leading to occurrence of such effect. Similar results were observed for long-term aged S=O, as presented in Figure 3. The S=O decomposes for the higher bio-condensate percent, i.e., the bio-condensate reduces S=O formation after STA and LTA. However, an increase in S=O was observed with the percent increase in bio-condensate.
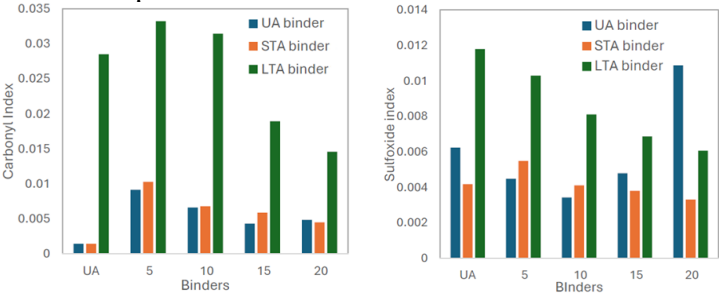
Figure 2. C=O index of bio-asphalt binder.

Figure 3. S=O index of bio-asphalt binder.

3.1 Aging Index

The chemical indices obtained using FTIR were correlated with the binder's physical properties. Good correlation is observed between the SP and C=O index after STA. Similarly, good correlation between T/F temp and C=O index after STA was seen. Good correlation is observed between SI and SP for STA samples, but a poor correlation was obtained between the SI and SP after LTA. This is due to S=O decomposition reactions at higher temperatures. Additionally, poor correlation between the SI and the T/F temp is observed after STA. The R^2 value for all the correlation analysis is presented in Table 3. Inconsistencies in correlations under different aging conditions and between different material properties require further investigations.

Table 3. Correlation values R^2 of the chemical indices with the physical properties.

	STAI	LTAI
CI vs SP	0.94	0.80
SI vs SP	0.98	0.83
CI vs PG	0.92	-
SI vs PG	0.80	-

3.2 TGA analysis

Figure 4 represents the TGA decomposition graph of the base binder and the bio-asphalt binders. A two-step decomposition graph was observed for the bio-asphalt binder whereas, a one-step decomposition graph was seen for the base asphalt binder. The mass loss observed for all the asphalt binders follows a similar reaction path and is found to vary from 85% to 88%. The first stage decomposition was observed at 116°C for the 5% bio-binder, which decreases to 110°C for the 20% bio-binder. The decomposition for the base asphalt binder was found to be approximately 239°C for the base asphalt binder. The second stage decomposition temperature increased on asphalt replacement to 291°C and decreased with the bio-condensate replacement percentage to 275°C. Similar results were observed with the final decomposition temperatures at both the decomposition stages for all the binders.
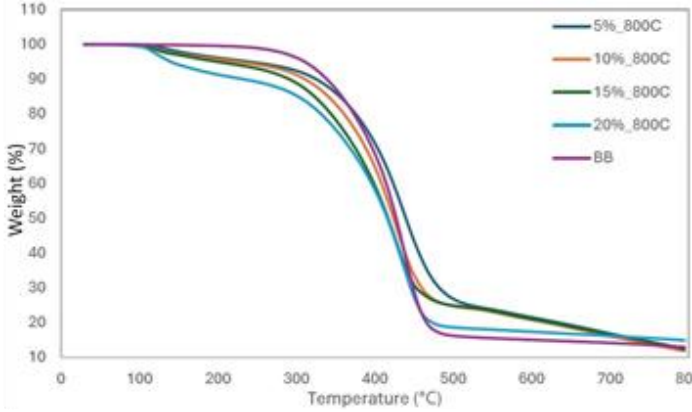
Figure 4. Thermogravimetry (TGA) graph

3.3 *AFM analysis*

The AFM images of the base asphalt binder showed three distinct phases on the binder surface (refer Figure 5). The three phases observed in asphalt binder, i.e., catena phase (bee structures), periphase, and paraphase can be identified distinctly on the base asphalt binder surface. Bee structure agglomeration can be observed for the LTA binders due to the increase in the asphaltene structures. In the case of the bio-asphalt binders only two phases can be identified. Also, the bee structures appear to dissolve in the periphase. This is due to the increase in the lighter components in the bio-asphalt binder due to the presence of bio-condensate. Also, asphaltene deagglomeration occurs in the bio-asphalt binder as the periphase and the catanaphase disintegrate due to the rejuvenation effect of the bio-asphalt binder. The restoration effect is also indicated by the C=O indices, which decrease with the increase in replacement percentage. Morphologically, the base binder structure is affected due to the replacement with the gasifier bio-condensate. Further investigations are required to assess the effect of the morphological changes on the binder performance.

Unaged VG 30   STA   LTA

Unaged 5% rep.   5% rep. STA   5% rep. LTA
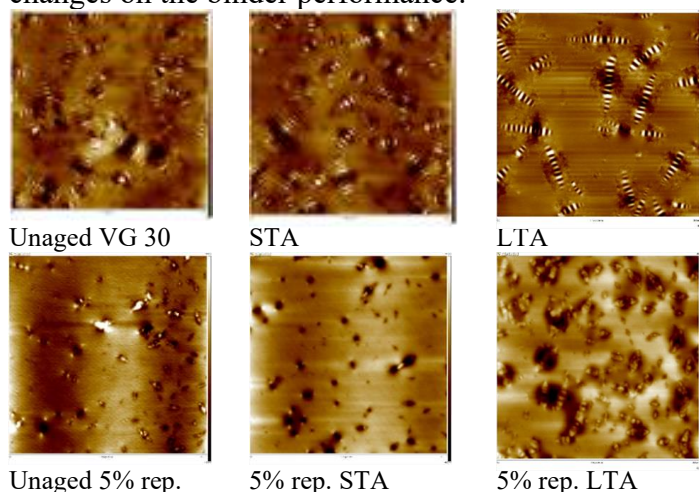
Figure 5. Morphological images of the binders through AFM.

4 CONCLUSIONS

This study investigated the characterization of bio-condensate replaced asphalt binder chemically using FTIR and TGA. Physical properties were measured and correlated with the chemical indicators. Also imaging studies were performed to investigate the morphological changes due to the addition of bio-condensate. Following conclusions were drawn:

- The SP reduced by 2°C on replacement up to 20% using gasifier bio-condensate. Similarly, the high temperature PG reduced by one grade up to 20% replacement.
- The CI and SI aging indices from FTIR showed a good correlation with the aging indices of the physical properties.

- Although moisture decomposition is observed in the TGA graphs from the bio-condensate replaced binders, the thermal stability of all the bio-condensate replaced binders increased.
- Removal of moisture occurs from the bio-asphalt binders on aging. This was observed from the -OH values and from TGA graphs. This is due to higher -OH compounds in the bio-condensate.
- The bio-condensate also has a rejuvenation effect, decreasing the C=O index. This was observed from the bee structure deagglomeration images from AFM morphological studies.

This study establishes the use of condensate from gasifier as a potential biobased material for asphalt binder replacement. The characterization studies on bio-condensate replaced binders up to 20% shows a potential for replacement of asphalt binder with the pine needle gasifier condensate. Further investigations on bio-asphalt binder rheology and performance evaluation of the bio-condensate replaced asphalt mixtures are required to explain the potential of gasifier condensate as a sustainable replacement of asphalt binders in the future. In addition, the potential for the use of gasifier condensate as a recycling agent for RAP binders can be further explored.

REFERENCES

Al-Sabaeei A. M., et al. 2020. A systematic review of bio-asphalt for flexible pavement applications: Coherent taxonomy, motivations, challenges and future directions, J. Clean. Prod., 249, 119357

ASTM D36/D36M-14. (2014). *Standard test method for softening point of bitumen.* ASTM International.

AASHTO M 320. 2017. *Standard Specification for Performance-Graded Asphalt Binder*. Washington, DC.

Bora B., & Das A. 2020. Estimation of binder quantity in binary mixture of asphalt binders. *Transp. Res. Proc.*, 48, 3756–3763.

Bora B., & Das A. 2021. Blending of RAPM samples with virgin binder: A study using FTIR spectroscopy. *IOP Conf. Ser.: Mat. Sci. and Engg.*, Malaysia, 1075, 012016.

He L. et al. 2023. Biomass valorization toward sustainable asphalt pavements: progress and prospects, *J. Waste Manag.*, 165, 159–178.

IS:73. 2013. *Paving bitumen - specification. New Delhi, India, Bur. Indian stand*. Indian standards institution, (1–4).

Rosyidi S.A.P et al. 2022. Physical, chemical and thermal properties of palm oil boiler ash/rediset-modified asphalt binder, *Sustain.*, 14(5), 3016.

Das P. K., Baaj H., Tighe S., & Kringos N. 2016. Atomic force microscopy to investigate asphalt binders: A state-of-the-art review. *Road Mater. Pavement*, 17(3), 693–718.

Yu X., Burnham N. A., & Tao M. 2015. Surface microstructure of bitumen characterized by atomic force microscopy, *Adv. Coll. Int. Sci.*, 218, 17–33.

Zhang X. et al. 2020. Preparation of bio-oil and its application in asphalt modification and rejuvenation: A review of the properties, practical application and life cycle assessment, *Constr. Build. Mater.*, 262, 120528.

Reuse of Asphalt as a Contribution to More Sustainability in Maintenance Management - Case Study of a Major German City

A. Prof. Dr.-Ing. Alexander Buttgereit
Jade University of Applied Sciences, Oldenburg, Germany

B. Dr.-Ing. Daniel Gogolin
Engineering Company PTM Dortmund mbH, Germany

C. MBA Diploma Stefan Gomolluch
Civil Engineering and Mobility department, City of Münster, Germany

ABSTRACT: Financial resources for road maintenance are regularly among the largest expenditure items in public budgets. For this reason, a sustainable asset management system has been set up in the Münster Department of Mobility and Civil Engineering for several years in order to make objective and sustainable decisions. In view of the impending climate changes and the resulting reduction in the service life of asphalt roads, the question arises as to how far today's asphalt roads will meet future requirements and how far today's assumptions for forecasts in maintenance management will hold up in the future. An important component is to increase the reuse rates in asphalt road construction beyond the current set of regulations without reducing the service life of the road. This is because the more reclaimed asphalt used in production, the poorer the quality of the resulting bitumen in the asphalt. For this purpose - based on bitumen and asphalt tests in the laboratory - various test sections in asphalt construction with a total of 20 different asphalt mix variants in asphalt wearing courses, asphalt binder courses and asphalt base courses on service roads, residential and access roads as well as on main roads have been successfully realized. Some results of laboratory, control, and performance testing are presented here, as well as implications for maintenance management.

1 INTRODUCTION

The resource relevance of the construction industry in Germany is considerable. According to previous experience, a fundamental renewal of the municipal road is necessary approximately every 30 to 60 years, depending on the road category. Asphalt surface courses have the shortest service life of up to 20 years. However, it can be assumed that the renewal cycles and service live will become shorter in the future due to increasing stresses on the road surface (e.g. increased volume of heavy traffic, climate change) [1]. Due to its thermoviscous properties, asphalt as a construction material is excellently suited for reuse or recycling. The technical regulations required for this are available in principle with corresponding limits for the addition of asphalt granulate (AG).

However, the authors are not satisfied with these limits and therefore want to investigate, among other things, the question: How much more reuse of asphalt beyond the current German regulations is possible in practice today and in the future? Since the reuse of asphalt (granulate) has already been an integral part of the asphalt cycle for many years, it is foreseeable that rejuvenators will represent an important building block in the reuse of asphalt in the future, which will also enable the highest possible reuse rates with consistently high quality in the long term [2].

Within the scope of previous projects and contributions about rejuvenators [3] [4], a large number of positive aspects have already been identified. Further questions have subsequently arisen from the results of the projects to date:

• Is it possible to increase the amount of AG added without negatively affecting the quality?
• Does it generally make sense to use rejuvenators - even with low amounts of AG?
• Can the use of rejuvenators generally improve the quality or extend the service life?

These questions should be answered practically in several construction projects.

2 PREPARATION (PLANNING STEPS)

In January 2020, the idea of building test sections with an increased addition of asphalt granulate in the asphalt base course and the asphalt surface course was discussed for the first time between the construction company and the city of Münster. This will only succeed if there is close coordination between all parties involved in the project (construction company, asphalt mixing plant, test laboratory, client). In the initial meeting between the asphalt mixing plant, the testing laboratory and the client in March 2020,

the project objectives and implementation were discussed and fixed. With regard to the objectives, a concept was developed to carry out comparative tests on an asphalt base course AC 22 TN and on an asphalt surface course AC 11 DN with varying proportions of asphalt granulate and in each case with and without rejuvenator.

Two roads (1-Feuerstiege, 2-Hartmannsbrook) have been selected as pilot sections by the Department for Mobility and Civil Engineering of the City of Münster. The construction length in both cases is approx. 2 km. While up to 50 % asphalt granulate was used in the asphalt surface course (3 cm, AC 8 DN) of the Feuerstiege with and without the addition of a rejuvenator, the proportion of asphalt granulate in the asphalt base course (6 - 8 cm, AC 22 TN) of the Hartmannsbrook was increased to up to 80% - also with and without the addition of a rejuvenator.

3 TESTING METHODOLOGY AND TESTING PROGRAMME

At the beginning of April 2020, suitable asphalt granulates were available from the asphalt mixing plant in sufficient quantities for the project. Analogous to the preparation of the preliminary initial tests by the asphalt mixing plant, the base bitumen and the asphalt granules were tested in the laboratory of Engineering Company PTM Dortmund mbH.

Within the scope of these tests, the addition quantity of the rejuvenator was to be determined and specified by means of physical and rheological binder tests for the different variants of the asphalt wearing course AC 8 D N and the asphalt base course AC 22 T N by laboratory methods:

• Asphalt base course AC 22 T N with 50 % asphalt granulate
• Asphalt base course AC 22 T N with 80 % asphalt granulate
• Asphalt top layer AC 11 D N with 20 % asphalt granulate
• Asphalt top layer AC 11 D N with 50 % asphalt granulate.

A road bitumen 70/100 was specified as an addition binder for all variants and a road bitumen 50/70 as the target binder. VIATOP® plus RC was used as rejuvenator. For the determination of the individual binder proportions, i.e. addition binder 70/100, recovered binder from asphalt granulate and rejuvenator, reference was made to the preliminary initial tests and to the previous findings of the mode of action of the rejuvenator (Additive 2.0 from [5]).

For the project, different asphalt granulates were used for each of the two asphalt wearing courses AC 8 D N and the asphalt base course AC 22 T N. The addition of the rejuvenator was determined based on the preliminary initial tests. The addition quantity was determined classically via softening point ring and ball and rheologically via the BTSV method.

Based on the bitumen analyses carried out, the addition quantities of the rejuvenator were determined for the individual asphalt mix variants and incorporated into the corresponding initial tests.

4 RESULTS

Due to the limited number of pages, only a small excerpt of the results is presented here.

4.1 *Performance Control Tests and initial interpretation of the results*

During the control tests, four asphalt cores were taken from each test area or asphalt variant and analysed in the laboratory together with the corresponding asphalt mix sample (bucket sample).

The evaluation of the control tests of the trial patches regarding the asphalt wearing course variants shows that compaction levels of ≥ 98 % could be determined at all five test points/test patches of the asphalt wearing course. Due to the uniformly high values (between 99.6 % and 100.6 %) of the variants with asphalt granules, the sole consideration of the compaction degrees does not allow a meaningful differentiation. In contrast, variant 5 of the asphalt surface courses (without asphalt granulate), with 98.0%, shows sufficient compaction according to the regulations, but is clearly below the other variants in the overall assessment. The results for the void content of the paved layers are analogous to the compaction levels.

For the evaluation of the binder parameters softening point ring and ball, the limit values of ZTV Asphalt-StB 07/13 (recovered binder) and (informatively) the limit values according to TL Bitumen-StB 07/13 (fresh binder) were used. Based on the results, both the influence of the asphalt granulates, and the influence of the rejuvenator used can be identified. Basically, it can be stated that all variants are within the limits for a road bitumen 50/70 as defined in ZTV Asphalt-StB 07/13. A more differentiated analysis of the results shows that the variants with 0 % asphalt granulate, with 20 % asphalt granulate and Rejuvenator and the variant with 50 % and Rejuvenator all lie within the grade range of a fresh road bitumen 50/70. The tested equi-stiffness temperatures T further support this fact. The phase angle δ is also positively influenced by the Rejuvenator used in the direct comparison of the variants.

If the results of the asphalt base course are considered, a very high level of compaction of greater than 100% is shown overall across all six test patches. A direct influence by the Rejuvenator could not be detected at this point, i.e. purely measured by the final compaction. The increased proportion of asphalt granules, on the other hand, leads to a slight foamed bitumen effect, which in turn has a positive

effect on the compaction properties of the asphalt mixture, partly due to the higher residual moisture.

In relation to the limit values of ZTV Asphalt-StB 07/13, the softening points ring and ball are clearly exceeded in the variants with 80 % and 50 % asphalt granulate (box 3.2). Especially for variant 2 (80% AG with rejuvenator), the effect of the rejuvenator can be clearly seen by the reduction of the softening point ring and ball by 10.6°C. Based on the two variants with 50 % asphalt granules and the one with 60% asphalt granules, it is also possible to recognize the sometimes very high fluctuations in the binder qualities of the asphalt granules. At this point, too, the classical binder characteristic is again confirmed by the rheological investigations (here equi-stiffness temperature T). At higher addition rates of asphalt granules, the positive influence of the rejuvenator on the phase angle is also evident. For the asphalt variants with 50 % and 80 % asphalt granules, the phase angle is increased on average between 1.3° and 3.3°.

4.2 Performance-Tests

On each variant, the test variables compliance Jnr and recovery R were determined using the MSCR test according to the AL DSR test (MSCRT). For all asphalt variants, a higher addition of asphalt granules leads to a higher percentage recovery R. This is due to the higher degree of hardening of the bitumen. This is due to the higher degree of hardening of the bitumen, as the corresponding bitumen are still primarily assigned to the visco-elastic range regarding the deformation behavior at the test temperature of 60°C. The addition of the rejuvenator results in a higher percentage recovery R for all asphalt variants. The addition of the rejuvenator reduces the proportion of recovery, so that the deformation behavior increasingly shifts into the viscous range and the proportion of yielding Jnr or plastic deformations increases. The test results therefore show an approximation of both test variables to the properties of the recovered base bitumen 50/70 (test field 5 of the test section "Feuerstiege") when using the rejuvenator. This does not show any recovery (R = 0 %), since in the test temperature range the plastic aggregate state has already been reached and a completely viscous behavior with a compliance of Jnr = 2.956 kPa-1 is present.

From the test results it can be deduced that, on the one hand, a higher addition quantity of asphalt granules leads to a larger recovery R and, on the other hand, that this effect can be compensated by the addition of the rejuvenator. In this case, the recovery R decreases and the compliance Jnr increases. Thus, the expected development towards the rheological behavior of the pure reclaimed road bitumen can be deduced, which, according to the present comparative investigations, exhibits a recovery R → 0.0%. Furthermore, it can be seen from the test results that

the effect of the rejuvenator and thus the associated influence on the reclaim/yield increases up to a certain point with the addition percentage of the asphalt granulate. Thus, for the AC 8 D N, a reduction in recovery R of ≈ 22% at 20% AG and of ≈ 80 % at 50 % AG was determined. The bituminous binder from the asphalt base courses shows a reduction of the deformation between approx. 80 % and 90 % for the variants with 50 % to 80 % AG.

5 CONSEQUENCES FOR MAINTENANCE MANAGEMENT, CASE STUDY MÜNSTER

A maintenance strategy for the Münster road network has been developed from the German regulations and the experience of the Münster construction administration. The useful lives of asphalt pavements are shown separately by layer, and these values can be used to estimate the time periods for rehabilitation measures. The service lives of the unbound base courses determine the total service life of the pavement. In addition, considering the maintenance work listed in the regulations, the costs for road maintenance over the life cycle are as follows. If depreciation is also considered from the costs of the initial or replacement investment, the price for providing the road is obtained (cf. [8, 9]).

Figure 1: Price development with constant and variable total useful life

The price is very dependent on the length of the service life, so that the road authorities should be interested in using high should be interested in using high-quality and durable construction methods for the respective type of use or stress. As an example, it is assumed that the service lives of the layers can be increased by improved material properties of the asphalt by 25%, 50%, 100%, 150%. The effect of these service life extensions is represented by the resulting price changes for the provision of the road.

Figure 1 compares the effects of a constant total service life of 40 years on the one hand and an extension of the total service life of up to 80 years corresponding to the extension of the service life of the individual layers on the other hand. With constant total useful life (GND), the price can be reduced by up to 34%, which results only from the reduction in repair costs due to the elimination of repair measures because of longer useful lives of the layers. In the case of variable total useful life, the price can be reduced by up to 54%, which results from the reduc-

tion in repair costs and from the distribution of repair costs and production costs (depreciation) over a longer total useful life.

The example calculation illustrates that extending the service life of individual layers or the entire road system has a significant impact on finances. In terms of finances, longer service lives can lead to reinvestments being stretched, annual road maintenance funds being reduced and balance sheet depreciation also being reduced. Positive effects from an environmental point of view are, for example, decreasing carbon dioxide emissions, less traffic disruption due to a smaller number of construction sites, and less noise emissions due to defective roads, construction work, or congestion caused by construction sites. If one adds up the above statements and draws a conclusion, one concludes that the measures and fields of action described together serve all three pillars of sustainability - ecology, economy and socio-cultural concerns. It is therefore entirely justified to speak of sustainable asset management.

To this end, it is necessary to set up an urban material flow management system, if possible, in accordance with BIM standards, and to link it with the existing databases in order to know in good time the quantities and qualities of asphalt granulate that will be produced and to minimize the additional administrative work involved.

6 CONCLUSION AND OUTLOOK

Based on the test sections and the corresponding laboratory tests, it could be shown that with the technical possibilities already available today, it is possible in practice to significantly increase the proportion of RAP without reducing the service life of the road.

The results presented so far show very emphatically that, with the use of suitable rejuvenators, it is quite possible to reuse high quality asphalt granulate in large proportions in the asphalt mix. Based on these findings, it is also possible to make specific statements on the quality of this construction method and, based on aging and load simulations carried out, to make far-reaching forecasts on durability and sustainability. These findings have a direct influence on the maintenance cycles of a road, for example, and can in turn be used effectively for maintenance management, e.g., in estimating future financial requirements.

The results from the pilot sections have shown that the sustainable use of larger quantities of asphalt granulate is economically feasible. The basic requirement for overall environmental reduction when using high rates of RAP is the use of "green" rejuvenators. In this context, only products with a low ecological footprint and basically high environmental compatibility should be used.

In these cases, the quality of the construction work was so good that initially no adjustment of the maintenance strategy is required. The example calculation illustrates that extending the service life of individual layers or the entire road system has a significant impact on minimizing financial requirements. In terms of finances, longer service lives can lead to reinvestments being stretched, annual road maintenance funds can be reduced, and balance sheet depreciation is also reduced. Positive effects from an environmental point of view are, for example, decreasing carbon dioxide emissions, less traffic disruption due to a smaller number of construction sites, and less noise emissions due to defective roads, construction work, or congestion caused by construction sites. If one sums up the above-mentioned statements and draws a conclusion, one concludes that it is therefore quite justified to speak of sustainable asset management in Münster.

Further investigations in the coming years will analyze and describe the development of the asphalt under traffic. However, it is already becoming apparent that in the future significantly more asphalt granulate can be returned to the material cycle if suitable rejuvenators are used, i.e. downcycling is minimized, and thus the asphalt granulate can be used for at least one further maintenance cycle. Since the rejuvenator used here is a green product derived from natural raw materials (not hazardous to water), its reuse is currently possible in an environmentally compatible manner. Consequently, a significant contribution to resource conservation can be made by this course of action.

7 REFERENCES

[1] Knappe, F. et al: Substitution von Primärrohstoffen im Straßen- und Wegebau durch mineralische Abfälle und Bodenaushub, Heidelberg, Dezember 2015

[2] Sonderrundschreiben 07/2020 vom 28.08.2020 und Technisches Informationspapier des Deutschen Asphalt-verbands (DAV) e.V. „Verwendung von Rejuvenatoren bei der Wiederverwendung von Asphalt" Stand August 2020

[3, 4, 5] Wirksamkeit und Performance von Rejuvenatoren, Fachzeitschrift asphalt; Teil 1 Heft 2/2019, Teil 2 Heft 4/2019 und Teil 3 Heft 6/2019

Lifecycle costs of in-situ rejuvenation and warm-mix porous asphalt technologies

M.H. Celebi, A. Singh, A. Varveri

Department of Engineering Structures, Delft University of Technology, Stevinweg 1, 2628 CN, Delft, South Holland, The Netherlands

ABSTRACT: This study evaluated the lifecycle costs associated with in-situ rejuvenation and the use of warm-mix porous asphalt mixtures (WM-ZOAB) and compared them with traditional resurfacing maintenance. The results indicated that the economic impacts of in-situ rejuvenation maintenance strategies were lower by about 6% compared to their counterpart resurfacing. Further, the sensitivity analysis suggested that the gasoline prices, traffic growth rate, discount factor, milling costs, and asphalt mix prices were the most influential factors affecting the lifecycle costs. In addition, the study highlighted that the WM-ZOAB alternatives must function satisfactorily for a design life of at least about 13 years in order to be recognized as cost-effective pavement solutions. The research findings support the transition towards sustainable pavement technologies, while emphasizing the importance of comprehensive economic assessments in decision-making.

1 INTRODUCTION

Lifecycle cost analysis (LCCA) has historically served as a structured methodology in engineering and economics, enabling the estimation of costs associated with a project or facility throughout its lifecycle. This approach ensures a comprehensive assessment of both initial investments and long-term operational costs, supporting informed decision-making (Durairaj, 2002). Recent government mandates aimed at promoting sustainable infrastructure development further emphasize the necessity of incorporating LCCA into project management and tendering processes. Consequently, LCCA has become integral to evaluating and comparing pavement alternatives, ensuring their economic feasibility over time (Walls, 1998).

In alignment with the sustainability goals, road administrations have adopted strategies such as increasing the use of reclaimed asphalt pavement (RAP) and other recycled materials (Qiao et al., 2019), adopting low-emission material production such as warm mix asphalt (WMA) (Binnenlands Bestuur, 2024), and prioritizing pavement preservation measures such as in-situ rejuvenation (Thé et al. 2016). These practices not only enhance the cost-effectiveness but also impart broader sustainability benefits including reduced environmental impacts and increased social benefits.

An investigation has shown that the Dutch roadway systems on average comprise 50 % RAP (Solids, 2023). Typical practice is to use about 20-30% RAP to design a durable porous asphalt surface layer (also regarded as DZOAB in the Netherlands) with much higher proportion of recycled materials in the underlying layers (Tsakoumaki et al. 2024). Research has shown that partial and/or complete substitution of virgin aggregates with RAP in asphalt mix reduces the road agency costs, thereby making it a cost-effective material (Qiao et al. 2019).

In-situ rejuvenation, a life-prolonging pavement maintenance technique, is extensively used on Dutch highway network to extend the service life of pavements (Thé et al. 2016). Researchers have shown that in-situ rejuvenation leads to 13% lower lifecycle costs compared to traditional resurfacing maintenance (Singh & Varveri, 2024).

Furthermore, WMA being an energy-efficient and environmental-friendly technology (Ma et al. 2019) is known to reduce the fuel costs by 11-35% compared to traditional hot-mix asphalt (Tutu & Tuffour, 2016). However, other researchers have claimed that the lower fuel costs may not be large enough to offset the capital costs and require further investigation (Anderson & May, 2008). In line with these advancements, Dutch asphalt producers have committed to reducing production temperatures, with a collective decision to cease the production of asphalt exceeding 140 ºC starting January 1, 2025 (Binnenlands Bestuur, 2024).

Therefore, Netherlands is witnessing a significant push towards integrating sustainable technologies, namely, WMA, RAP, and in-situ rejuvenation, into road construction and maintenance. While in-situ rejuvenation has shown promise in extending pavement service life, and WMA is being evaluated as a viable alternative to traditional hot-mix asphalt, there is a lack of historical input data and comprehensive research on the economic feasibility of these methods over their entire lifecycle. Additionally, there is uncertainty regarding the minimum service life WMA must achieve to be considered a sustaina-

ble and cost-effective option. Addressing these gaps is critical to ensuring informed decision-making. This work is part of a larger stochastic analysis aimed at assessing the risks associated with these maintenance methods.

Therefore, the primary objective of this research is to evaluate the economic impacts of in-situ rejuvenation and the use of WMA in DZOAB mixtures and compare them with traditional resurfacing maintenance. The study also aims to identify key financial uncertainty factors and determine the desired service life that WMA must meet to be recognized as a cost-effective solution.

2 METHODOLOGY

2.1 Goal & Scope

The goal of this research is to assess the economic feasibility of four different pavement construction and maintenance alternatives as below:

- Resurfacing: removal of DZOAB layer having 50 mm thickness comprising 30% RAP having a service life of 12 years (typical for right lane in The Netherlands) (van der Kruk & Overmars, 2022).
- Rejuvenation: a bituminous emulsion is applied on the pavement surface in years 5 and 10 after the construction (Thé et al. 2016). Each rejuvenation treatment prolongs the service life of road by 3 years, with two activities resulting in 6 year life-extension. Therefore, the first resurfacing maintenance (50 mm DZOAB thickness with 30% RAP) will occur in year 18.
- Resurfacing with WMA: this strategy is similar to resurfacing, with the only difference being that the DZOAB is now constructed with WMA comprising 30% RAP.
- Rejuvenation of warm-mix DZOAB (WM-DZOAB) layer: this strategy follows the same maintenance plan as in-situ rejuvenation, with the only difference being that the DZOAB is constructed with WMA comprising 30% RAP.

The timeline of different pavement alternatives is shown in Figure 1. Based on discussions with roadway stakeholders in the Netherlands, it is anticipated that WM-DZOAB possess a higher durability and may achieve a service life approximately five years longer than conventional DZOAB. Other researchers have also suggested that the durability of WMA is higher than conventional HMA (Rodríguez-Fernández et al. 2020; Gaarkeuken et al. 2016). However, given the limited availability of scientific research to substantiate this hypothesis, a conservative approach was adopted. Accordingly, the initial design life of WM-DZOAB scenarios was aligned

with that of conventional DZOAB. Sensitivity analyses was subsequently conducted to determine the minimum service life required for WM-DZOAB to be recognized as a cost-effective alternative.

The analysis period was 36 years, determined in accordance with International guidelines (Walls, 1998) and the functional unit was a single lane ZOAB having dimensions 1000 m × 3.5 m × 0.5 m (Rijkswaterstaat, 2019). Further, the different processes considered in this research are presented in Figure 2. The end-of-life costs were not taken into account due to the lack of appropriate data for modelling this phase.
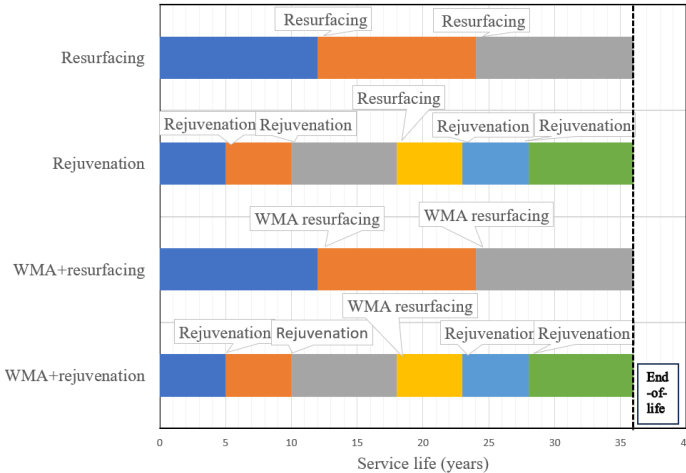
Figure 1. Timeline for all four strategies.
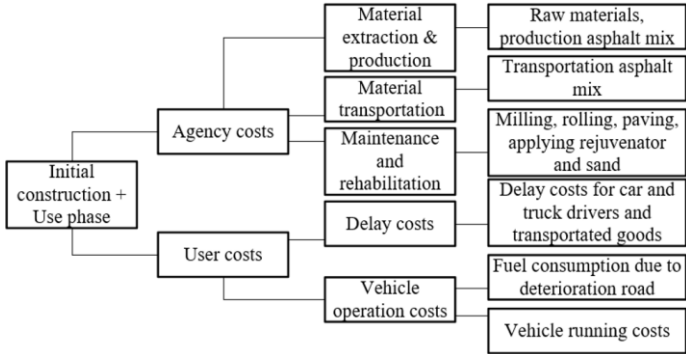
Figure 2. Processes and system boundaries for LCCA.

2.2 Lifecycle inventory

The lifecycle cost inventory was generated by collecting the data from primary and secondary sources. The primary data comprised material and activity costs collected through interviews and online meetings with Dutch roadway contractors and material suppliers. Further, secondary data sources comprised national statistics board (CBS - Statistics Netherlands, 2018), Eurostat's database (Eurostat, 2022a, 2022b, 2022c), standard Dutch maintenance guidelines (Koster, 2013) and other available literature (Silva, 2013, Decò & Frangopol, 2011). The most important input parameters used in the LCCA are presented in Table 1 and others can be found elsewhere (Singh & Varveri, 2024).

Table 1. Most important input parameters.

Input parameters	Value	Source*
DZOAB 30%RAP (€/t)	82	P
WMA DZOAB 30%RAP (€/t)	83	P
Average detour speed (km/h)	50	P
Rejuvenation cost (€/sq.m)	1,96	P
Sand spraying cost (€/sq.m)	0,16	P
Detour during rejuvenation (days)	0,33	P
Design speed (km/h)	90	P
Traffic growth rate (%)	3	P and S
Discount rate (%)	2	P and S
Milling charges (€/sq.m)	10,57	P and S
Average running cost of cars (€/km)	0,08	P and S
Annual average daily traffic (vehicle/h)	2300	S
Initial MPD (mm)	1,7	S
MPD change rate (mm/year)	0,041	S
Initial IRI (m/km)	0,8	S
IRI growth rate (m/km)	0,08	S
Gasoline price (€)	1,96	S

Source: P = primary source and S= secondary source

2.3 Lifecycle cost assessment

In the context of pavement LCCA, costs are typically categorized as agency and road user costs. Agency costs encompass all expenses directly incurred by the managing road agency to ensure the pavement meets the required service level. On the other hand, road user costs represent the costs borne by the public during the operation and use of vehicles (Walls, 1998).

Road user costs were calculated as the sum of vehicle operating costs (VOC) and delay costs (DC). VOC account for increased fuel consumption caused by pavement deterioration over the analysis period and vehicle running costs (VRC) is given by Equation 1. The DC reflect the economic impact of delays resulting from reduced speeds during maintenance activities and computed using Equation 2 (Decò & Frangopol, 2011, Khakzad & Gelder, 2016).

$$VRC = \left[C_{Run,Car}\left(1 - \frac{T}{100}\right) + C_{Run,Truck}\left(\frac{T}{100}\right) \right] \times D \times A(t) \times d \tag{1}$$

$$DC = \left[C_{AW}O_{Car}\left(1 - \frac{T}{100}\right) + (C_{ATC}O_{Truck} + C_{Goods})\frac{T}{100} \right] \times \frac{D \times A(t) \times d}{S} \tag{2}$$

Where, T = average daily truck traffic (%), $C_{Run,car}$ = average running costs for cars (€/km), $C_{Run,truck}$ = average running cost for trucks (€/km), D = detour length (km), A(t) = average daily traffic, d = duration of the detour, C_{AW} = average wage of car driver (€/h), C_{ATC} = average wage of truck driver (€/h), C_{Goods} = time value of goods transported (€/h), O_{Car} = average vehicle occupancy of cars, O_{truck} = average vehicle occupancy for trucks, and S = average detour speed (km/h).

The increased fuel consumption was computed using the MIRIAM models (Hammarström, 2012). The economic impacts were determined using the net

present value (NPV) (see Equation 3) as it provides a direct monetary value, making it easier to compare and rank alternatives with different lifespans or costs (Moins et al. 2020).

$$NPV = Initial\ costs + \sum_{k=1}^{Q} Future\ cost \frac{1}{(1+d)^n} - Residual\ value \frac{1}{(1+d)^n} \tag{3}$$

Where, n = year into the future cash flow activity and d = discount rate.

2.4 Results, interpretation, and sensitivity analysis

The lifecycle cost for the four pavement maintenance alternatives is provided in Figure 3. As observed in Figure 3, the traditional resurfacing maintenance strategies both with and without WMA resulted in higher NPV compared to their counterpart in-situ rejuvenation maintenance. This is mainly attributed to the higher agency costs associated with the resurfacing (milling and laying) which encompassed three cycles compared to rejuvenation where only two resurfacing activities were undertaken. The life-extension maintenance delayed the resurfacing timeline and as a consequence of the discounting effect, resulted in lower NPV. Further, the contribution of costs due to fuel consumption was highest and accounted for about 63-68% of the total NPV. As the timeline of rejuvenation maintenance was lower than resurfacing, it resulted in lower VRC and DC, consequently lower NPV. Furthermore, the production cost of WM-DZOAB mixture was higher (due to higher initial plant investments) resulting in a greater NPV for the WMA alternatives.
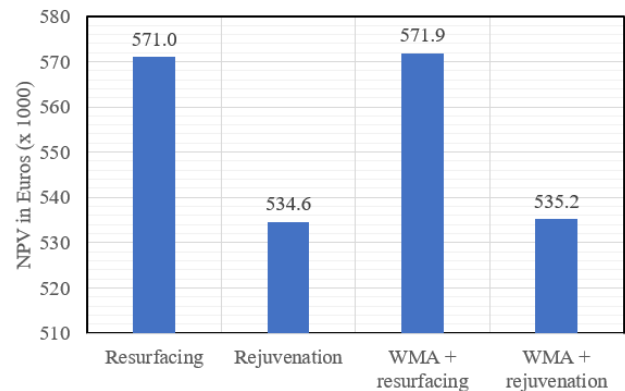
Figure 3. NPV results for the deterministic LCCA.

A one factor at-a-time sensitivity test was conducted by varying 18 input variables by a magnitude of ±50% and the results are presented in Figure 4. It revealed that the NPV was most sensitive to gasoline prices, traffic growth rate, discount factor, milling charges, asphalt mix price, and detour speed.

Furthermore, the service life of pavement alternatives was varied by 5 years to identify the required minimum service life of WM-DZOAB to be recognized as sustainable solutions. The results indicated

that the pavement alternatives designed with WMA and undergoing resurfacing must possess a service life of atleast 12.39 years to be cost-effective. On the other hand, the in-situ rejuvenation of WM-DZOAB is the preferred choice if the pavement serves a minimum life of 12.68 years.
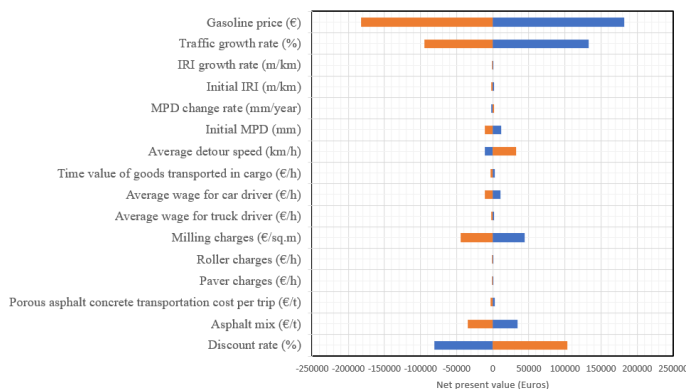
Figure 4. Sensitivity analysis for resurfacing.

3 CONCLUSION & RECOMMENDATION

This study investigated the lifecycle costs associated with four different pavement alternatives and the major findings are summarized below:

- Maintenance strategies involving in-situ rejuvenation yielded lower lifecycle costs (by about 1.07 times) compared to conventional resurfacing.
- NPV was highly sensitive to gasoline prices, traffic growth rates, discount factor, asphalt prices, and milling charges.
- WMA alternatives had higher costs than conventional systems due to higher initial investments required at plants for production.
- WMA-based pavements demonstrate financial viability when coupled with service life extension (in addition to the typical 12 year life of DZOAB) of at least 0.39 years for resurfacing and 0.68 years for rejuvenation.

Future research must focus on developing predictive models for estimating the service life of WM-DZOAB and progression of distresses in these systems. While LCCA is an important tool, it cannot be solely used for decision making as such processes are also based on environmental and social benefits. Thus, policymakers should prioritize options that align with the three pillars of sustainability.

4 REFERENCES

Anderson, R. M., Baumgardner, G., May, R., & Reinke, G. 2008. Engineering properties, emissions, and field performance of warm mix asphalt technologies. *Interim Report*, 9-47.

Binnenlands Bestuur. 2024. *Asfaltsector werkt planmatig aan duurzame wegverharding*. Retrieved from: https://www.binnenlandsbestuur.nl/ruimte-en-milieu/duurzame-infra-en-seb/asfaltsector-werkt-aan-verduurzaming

CBS - Statistics Netherlands, 2018. *Trends in the Netherlands 2018*. Retrieved from: https://longreads.cbs.nl/trends18-eng/society/figures/traffic/

Decò, A., & Frangopol, D. M. 2011. Risk assessment of highway bridges under multiple hazards. *Journal of Risk Research*, *14*(9), 1057-1089.

Durairaj, S., Ong, S., Nee, A., & Tan, R. 2002. Evaluation of life cycle cost analysis methodologies. *Corporate Environmental Strategy*, 9(1), 30-39.

Eurostat, 2022. *Passenger Mobility Statistics: Average Passenger Car Occupancy for Urban Mobility on all Days*. Retrieved from: https://ec.europa.eu/eurostat/statistics-explained/index.php?title=File:Average_passenger_car_occupancy_for_urban_mobility_on_all_days_v2.png#file

Gaarkeuken, G., Oosterveld, M., Sprenger, M., & Voskuilen, J. 2016. LEAB-PA, A Half Warm Porous Asphalt Can Increase the Lifetime. *In 8th RILEM International Symposium on Testing and Characterization of Sustainable and Innovative Bituminous Materials*, (pp. 215-227).

Hammarström, U., Eriksson, J., Karlsson, R., & Yahya, M. R. 2012. *Rolling resistance model, fuel consumption model and the traffic energy saving potential from changed road surface conditions*. Statens väg-och transportforskningsinstitut.

Rodríguez-Fernández, I., Lizasoain-Arteaga, E., Lastra-González, P., & Castro-Fresno, D. 2020. Mechanical, environmental and economic feasibility of highly sustainable porous asphalt mixtures. *Construction and Building Materials*, *251*, 118982.

Koster, I.W., 2013. Factsheets levensduurverlengende technieken voor asfaltverhardingen.

Ma, H., Zhang, Z., Zhao, X., & Wu, S. 2019. A comparative life cycle assessment (LCA) of warm mix asphalt (WMA) and hot mix asphalt (HMA) pavement: A case study in China. *Advances in Civil Engineering*, *2019*(1), 9391857.

Moins, B., France, C., & Audenaert, A. 2020. Implementing life cycle cost analysis in road engineering: A critical review on methodological framework choices. *Renewable and Sustainable Energy Reviews*, 133, 110284

Qiao, Y., Dave, E., Parry, T., Valle, O., Mi, L., Ni, G., ... & Zhu, Y. 2019. Life cycle costs analysis of reclaimed asphalt pavement (RAP) under future climate. *Sustainability*, *11*(19), 5414.

Silva, M.D., 2013. *The Relationship between Road Surface Properties and Environmental Aspects (Master of Science Thesis)*. Delft University of Technology, The Netherlands.

Singh, A., & Varveri, A. 2024. Quantification of lifecycle costs for porous asphalt life-extension maintenance methods under managerial uncertainties. *International Journal of Pavement Engineering*, 25(1), 2376221.

Solids. 2023. *Op weg naar 100% ¬circulair asfalt*. Retrieved from : https://solidsprocessing.nl/artikel/op-weg-naar-100-circulair-asfalt/

Thé, P., Voskuilen, J., & Van de Ven, M. 2016. *Life-prolonging preventive maintenance techniques for porous asphalt*. Rijkswaterstaat.

Tsakoumaki, M., & Plati, C. 2024. A Critical Overview of Using Reclaimed Asphalt Pavement (RAP) in Road Pavement Construction. *Infrastructures*, *9*(8), 128.

Tutu, K. A., & Tuffour, Y. A. 2016. Warm-mix asphalt and pavement sustainability: A review. Open Journal of Civil Engineering, 6(2), 84-93.

Walls, J. 1998. *Life-cycle cost analysis in pavement design: in search of better investment decisions*. US Department of Transportation: Federal Highway Administration.

Preliminary environmental impact assessment of plant-based oils as fossil-based bitumen alternatives based on Dutch Environmental Cost Indicator (ECI) scoring method

C.G. Daniel
Copernicus Institute of Sustainable Development, Utrecht University, the Netherlands

B. Corona
Copernicus Institute of Sustainable Development, Utrecht University, the Netherlands

R. Hoefnagels
Copernicus Institute of Sustainable Development, Utrecht University, the Netherlands

M. Junginger
Copernicus Institute of Sustainable Development, Utrecht University, the Netherlands

ABSTRACT: This study serves as a preliminary environmental impact assessment of 10 plant-based oils to substitute fossil-based bitumen used in road construction in the Netherlands using life cycle assessment based on EN 15804 +A1 and the CML midpoint impact category method, where the outcome is monetized using the environmental cost indicator (ECI) score governing in the Netherlands. Inventories of the products are obtained from the combination of available databases (EcoInvent and Agri Footprint 5) and existing research papers. The outcome shows that excluding the biogenic carbon dioxide storage capacity in the bio-based feedstocks causes their ECI scores per 1 ton of material as the functional unit to be higher than the fossil-based bitumen, with the exception of used cooking oil, when compared with bitumen from the EcoInvent database (€52 vs €94.1/ ton). Including biogenic carbon storage leads to the materials cooking oil, tall oil pitch and rosin scoring lower than bitumen (-€95.4 and -€91.2/ton). The total scores are dominated by the human toxicity, marine aquatic eco-toxicity, and global warming potential impact categories. Thus, the feedstocks with the lowest total ECI scores are used cooking oil, tall oil pitch, and tall oil rosin.

1 INTRODUCTION

In the construction industry, bitumen is widely used as a binder component in a bituminous mix for road structures as an alternative to cementitious materials. There has been a growing concern over time about the environmental impact of fossil-based bitumen usage, where its production consumes an enormous amount of energy of about 0.33 GJ/ton in the Netherlands (Oliveira & Silva, 2022) with the carbon footprint intensity recorded at 53.7 kg CO_2-eq/ton, one-four of the annual emission of a one-person vehicle (Shacat et al., 2024). Therefore, alternative bio-binder materials have been proposed throughout the years.

The application of bio-based materials in road construction has been popular in recent decades. The application of the bio-binder constituents yields mixed outcomes in terms of performance. Most oil seeds, including linseed, rapeseed, castor and soybean oils are reported to increase the penetration and decrease the softening point of the binder mix, leading to a softer binder with marginal rutting resistance. Meanwhile, corn oil enhances rutting resistance and viscosity but also increase cracking and moisture susceptibilities, and tall oil resin produces a more resistant material at

high and low temperatures. In addition, waste cooking oil is often reported to act as a rejuvenator owing to its psycho-chemical composition, which allows it to soften aged bitumen (Awogbemi et al., 2019; da Silva et al., 2022; Quan et al., 2024). This study intends to evaluate the environmental impact of 10 bio-based materials to substitute the fossil-based bitumen in the Dutch context based on the preliminary research conducted in the CircuRoad consortium, a knowledge-based group in the Netherlands established to support the national goal of reaching net-zero carbon state in 2050. The products analysed herein are castor oil, Jatropha oil, linseed oil, rapeseed oil, corn oil, soybean oil, tall oil pitch, tall oil rosin, tall oil rosin ester, and used cooking oil.

2 METHOD

2.1 *Goal and Scope*

This study contains the outcome of the screening-phase life cycle assessment (LCA) to provide a preliminary comparison of the environmental impact of the 10 plant-based oils considered to replace fossil-based bitumen. The list of materials is based on their technical performance and

compatibility in the asphaltic mixture and availability in the Netherlands, as provided by the preliminary literature study conducted within the CircuRoad consortium. The current scope of this report is the **cradle-to-production gate** of each constituent, which accounts for the **A1 stage only**. The functional unit used in this stage is **1 ton of binder materials used in the asphalt mixture for road construction**. The geographical scope in this study is the Netherlands. However, the inventory data is taken from the country from which the material is exported to the Netherlands according to World Bank database (*freely accessible from* https://wits.worldbank.org/trade/comtrade/en/country/NLD/year/2023/tradeflow/Imports/partner/ALL/product/150790).

2.2 *Inventory*

The inventory data combines the generic databases of EcoInvent and Agri Footprint 5 (which are available directly in SimaPro) and research papers. In general, there are two available streamlines for the plant-based oils. Firstly, the oil can be considered a co-product in the system, where the whole impact is calculated from the cultivation activities at farm. There are some extra steps included in several materials, such as drying of rapeseed and maize grain, steeping and de-germ processing of wet maize grain, and retting and scutching for linseed oil. On the other hand, tall oil and used cooking oil are considered waste product, where their system boundary exclude the impact from the stages prior to the first processing stage at the plant, which is part of the cut-off principle applied in the Eurocode.

The biogenic carbon dioxide content of each material is taken either from the existing information in the database or calculated based on EN 16449 about the calculation rule of biogenic carbon content in plant-based product and conversion to carbon dioxide. Moreover, only mass allocation is considered in this study, as preferred in the Eurocode to deal with multifunctionality issue.

Lastly, the transportation distance from the farm to the extraction plant is assumed to be 50km for each case.

2.3 *Impact Assessment*

In this phase, all relevant inventories from the reference flow adjusted to the functional unit are grouped and converted according to the impact categories associated with each item in the list. The EN 15804 +A1 norm specifies the CML 2001 midpoint method to be used in the impact assessment, which generates 11 impact categories. Furthermore, the outcome will be weighted using the environmental cost indicator system developed

in the Netherlands to describe the shadow cost from the environmental impacts, known as the Environmental Cost Indicator (ECI, or *Milieukosten Indicator* – MKI in Dutch). The conversion factors to the ECI score are governing for all impact categories from the CML method, and are given in (CE Delft, 2020). However, the ECI score does not contain a specific value to account for the biogenic carbon dioxide intake, since the global warming potential impact category includes the total of biogenic carbon intake (usually taken into account with negative characterization factor) and other types of greenhouse gases (usually with positive factor).

3 RESULTS AND DISCUSSION

3.1 *ECI score of bio-based oils*

The total ECI scores for all of the evaluated materials according to EN 15804 +A1 are shown in Figure *1*.
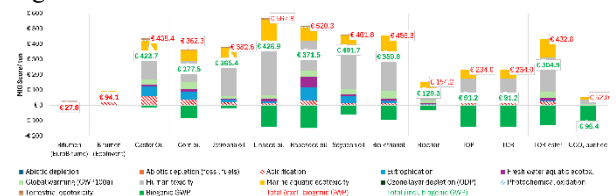
Figure 1. Total ECI score (including vs excluding biogenic CO_2 uptake) of the evaluated bio-based oils

Upon excluding the biogenic carbon dioxide uptake (numbers given in black), it is evident from (numbers are written in black, whereas the baseline – bitumen is written in red) that given the ECI scoring system based on EN 15804 +A1, three impact categories become the primary contributors in general. The most significant factor herein is **human toxicity (HTP),** with a relative contribution of 40 – 60% of total ECI scores in all the materials. The second most influential impact category is **marine aquatic eco-toxicity** potential **(MAETP)**, with the relative contribution ranging from 17 – 40% for all materials. Lastly, **global warming potential (GWP)** is considered a significant impact category with the relative contribution ranging from 5 – 22% for 12 materials, excluding castor oil, soybean oil, rapeseed oil, and jatropha oil.

Finally, when excluding the biogenic climate change impact, it is apparent that **linseed oil** yields the highest score by €567.8/ ton oil. The ECI score of bitumen from the Eurobitume inventory **(€28/ton)** is evidently lower than all the evaluated alternatives, whereas only the purified used cooking oil yields a lower score than the bitumen derived from EcoInvent database **(€94.1/ton)**. Comparing the score of bitumen with that of Kraft

lignin used in another bio-binder study in the Netherlands also shows that the lignin product produced using the energy from natural gas will yield the score of €250/ ton, placing it in the middle position of the list (Moretti et al., 2022). However, including the effect of biogenic carbon dioxide uptake will change the outcome (numbers given in green), where both tall oil pitch and rosin also have lower ECI scores than bitumen (EcoInvent). Hence, the three products with the lowest ECI scores are **purified used cooking oil (€52 and -€95.4/ton), tall oil pitch, and tall oil rosin (€234 and €91.2/ton)**.

3.2 *Process contribution for three most dominant impact categories*

The contribution of each production stage of the evaluated materials associated with the three most dominant impact categories based on the ECI score is illustrated in *Figure 2*.
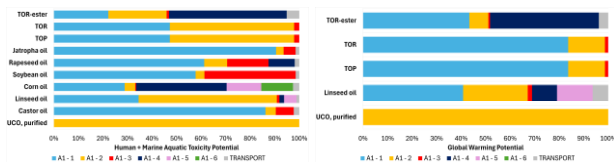
Figure 2. Process contribution associated with (left) human toxicity and (right) global warming potential

The first production phase (**A1 – 1**) is the primary contributor to the toxicity categories in 4 materials, such as jatropha oil, rapeseed oil, soybean oil, and castor oil, all of which resemble the cultivation stage of these materials. Among all the inputs in this phase, the **use of fertiliser** and **agricultural activities**, i.e. harvesting and ploughing, which introduce diesel fuel consumption, are the common causes of this impact. Both the impact from agricultural activities and urea fertiliser are derived from the production of the machineries, which utilizes coke derived from coal. The production of coke is found to emits carcinogenic compounds such as cadmium and arsenic (Institute, n.d.). The phosphate fertiliser production in the plant potentially emits heavy metal compounds, such as lead and cadmium, that leech to the aquatic environment and pose significant harm to it (Noli et al., 2024).

The second production stage (**A1 – 2**) is the main contributor to the toxicity impacts of linseed oil, used cooking oil, and tall oil products. Both the coke derived from coal production to **produce the infrastructure for the electricity** and **natural gas** supply to derive the energy and equipment for **retting and extraction** activities of the linseed oil and used cooking oil production chains. Lastly, the **crude tall oil production** involves sulfuric acid. The production of sulfur emits toxic substances

such as sulfur dioxide and benzene, which become the major cause of human toxicity potential due to its ability to induce potential breathing issue that can be lethal (Agency for Toxic Substances and Disease Registry, n.d.)

Other two classifications of production processes (**A1 – 3 and A1 – 4**) are the major factors for corn oil and tall oil rosin ester. In the corn oil production, coke production involved in the infrastructure process to produce electricity is the major factor for the **drying** activity**.** Meanwhile, pentaerythritol, an alcohol substance commonly employed in the **esterification process** in tall oil rosin ester (TOR-ester) manufacturing, is synthesised from formaldehyde, the substance that becomes the main driver of the human toxicity potential score herein.

In summary, both the **coke production involved in the infrastructure process** related to energy source production (natural gas) or equipment that emits carcinogenic compounds, and the formaldehyde emission from the alcohol compound production used in the esterification process are the major factors in the toxicity impact categories. The relationship between coke and infrastructure in this case is mostly that coke is used in the steel manufacturing, where the steel is used to construct supporting infrastructures, such as pipeline for natural gas transmission, agricultural machinery, or furnace.

Lastly, the global warming potential generally stems both from the greenhouse gas emissions directly recorded during the cultivation practices (**A1 – 1**) and indirect emissions from the of energy sources generation, such as natural gas or heavy fuel, used in the oil production processes. The natural gas production process emits an enormous amount of methane.

Based on the preliminary LCA conducted in this study, it is evident that toxicity impacts become the primary concern in the outcome. This circumstance even occurs despite a relatively low ECI weighing factor given to those categories, all below 10 cents/ kg of impact category. Such phenomena have been previously reported as part of uncertainties, where the fate of substances contributing to the impact categories are considered infinite. Conversely, other impact categories, such as global warming potential, commonly consider 100 years as its fate, yielding a difference in the outcome (Frischknecht et al., 2007). However, this method has not accounted for land use, which is a critical factor for plant-based products. While EN 15804 +A2 has attempted to cover this aspect, an updated ECI value also needs to be established to adapt with the updated Eurocode. Moreover, since this analysis

has been primarily carried out using generic database as the input (taking into account various geographical and temporal scopes for each), it will increase the uncertainty of the outcome. Hence, more extensive research needs to be conducted to produce the outcome more relevant to the scope of the Netherlands using primary and updated data. Lastly, while comparison can be made within this scope, a cradle-to-grave analysis needs to be performed furthermore to take into account the effect of incorporating the alternative materials into the asphalt mixture, which might result in different properties and durability compared with the conventional mixture made of fossil bitumen.

4 CONCLUSION

This study aims to compare the environmental impact of 10 plant-based oils as alternatives to replace fossil-based bitumen for road construction in the Netherlands. The evaluation is carried out using the CML midpoint impact category method in accordance with EN 15804 +A1, and weighted using the Environmental Cost Indicator (ECI) factors developed in the Netherlands to describe the shadow environmental cost of the oil products. Evidently, the cost of all plant oils exceed the fossil bitumen (calculation based on Eurobitume inventory) when excluding the biogenic carbon dioxide uptake, ultimately for linseed oil. In contrast, only used cooking oil has a lower score than bitumen (calculation based on EcoInvent database). Tall oil pitch and rosin will also have lower ECI score than the baseline bitumen when taking into account the biogenic carbon dioxide storage. Three major impact categories herein are human toxicity, marine aquatic eco-toxicity, and global warming potential. The toxicity impacts can be traced back to the emission of toxic materials from the production of coke related to the supporting infrastructure, such as steel manufacturing used for the pipeline for natural gas distribution and agricultural machinery. Meanwhile, global warming potential is derived from the direct emission of greenhouse gases during the cultivation practice and indirect emission from the production of energy source for the production stage. Hence, the three materials with the lowest ECI scores are **purified used cooking oil, tall oil pitch, and tall oil rosin**, and they specifically have lower ECI scores than the standard bitumen when accounting for the biogenic carbon dioxide storage potential.

5 REFERENCES

Agency for Toxic Substances and Disease Registry. (n.d.). *Sulfur Trioxide & Sulfuric Acid | Public Health Statement | ATSDR*. Retrieved November 22, 2024, from https://wwwn.cdc.gov/TSP/PHS/PHS.aspx?phsid=254&toxid=47

Awogbemi, O., Onuh, E. I., & Inambao, F. L. (2019). Comparative study of properties and fatty acid composition of some neat vegetable oils and waste cooking oils. *International Journal of Low-Carbon Technologies*, *14*(3), 417–425. https://doi.org/10.1093/ijlct/ctz038

CE Delft. (2020). *Milieuprijzen als weegfactor in de bepalingsmethode milieuprestatie bouwwerken*. www.ce.nl

da Silva, C. C. V. P., Melo Neto, O. de M., Rodrigues, J. K. G., Mendonça, A. M. G. D., Arruda, S. M., & de Lima, R. K. B. (2022). Evaluation of the rheological effect of asphalt binder modification using *Linum usitatissimum* oil. *Matéria (Rio de Janeiro)*, *27*(3), e20220138. https://doi.org/10.1590/1517-7076-RMAT-2022-0138

Frischknecht, R., Jungbluth, N., Althaus, H.-J., Bauer, C., Doka, G., Dones, R., Hischier, R., Hellweg, S., Köllner, T., Loerincik, Y., Margni, M., & Nemecek, T. (2007). *Implementation of Life Cycle Impact Assessment Methods*. http://www.ecoinvent.org/fileadmin/documents/en/03_LCIA-Implementation.pdf

Institute, N. C. (n.d.). *Coke Oven Emissions*. Retrieved October 23, 2024, from https://www.cancer.gov/about-cancer/causes-prevention/risk/substances/coke-oven

Moretti, C., Corona, B., Hoefnagels, R., van Veen, M., Vural-Gürsel, I., Strating, T., Gosselink, R., & Junginger, M. (2022). Kraft lignin as a bio-based ingredient for Dutch asphalts: An attributional LCA. *Science of the Total Environment*, *806*. https://doi.org/10.1016/j.scitotenv.2021.150316

Noli, F., Sidirelli, M., & Tsamos, P. (2024). The impact of phosphate fertilizer factory on the chemical and radiological pollution of the surrounding marine area (seawater and sediments) in northwestern Greece. *Regional Studies in Marine Science*, *73*, 103458. https://doi.org/10.1016/J.RSMA.2024.103458

Oliveira, C., & Silva, C. X. (2022). *DECARBONISATION OPTIONS FOR THE DUTCH ASPHALT INDUSTRY*. www.pbl.nl/en.

Quan, X., Chen, C., Ma, T., & Zhang, Y. (2024). Performance evaluation of rapeseed oil-based derivatives modified hard asphalt binders: Towards greener and more sustainable asphalt additives. *Construction and Building Materials*, *411*, 134657. https://doi.org/10.1016/J.CONBUILDMAT.2023.134657

Shacat, J., Willis, R., & Ciavola, B. (2024). *The Carbon Footprint Of Asphalt Pavements: A Reference Document For Decarbonization*.

Case study: Evaluation of cool pavement surface treatments in the City of San Antonio, Texas

S. Dessouky, N. Debbage, W. Zhai, E. López Ochoa, and R. Lee
University of Texas at San Antonio, San Antonio, Texas, USA

ABSTRACT: Extreme heat is one of the most pressing climate hazards that urban areas face. Elevated temperatures threaten public health, the environment, and urban infrastructure. One mitigation strategy that has gained increasing popularity across cities is the usage of cool pavement. The City of San Antonio, Texas, as part of its broader climate action and adaptation plan, conducted a cool pavement pilot program in 2023. The pilot program evaluated the effectiveness of four cool pavement treatments across San Antonio districts during the summer of 2023. For each product, Skid resistance, friction, bonding strength, and meteorological measurements were collected across the cool pavement sites and representative control sites. The findings indicated that the performance of the cool pavement applications varied across the products tested. In terms of Texture and friction properties, the GuardTop experienced the most reduction while GAF experience the most reduction over the control. In terms of metrological data, the SealMaster displayed the most consistent and statistically significant reductions in surface temperatures with an average reduction of 4°F during the afternoon testing period.

INTRODUCTION

The city of San Antonio (COSA) installed cool pavement surface treatment application on each of its ten districts from April to July of 2023. The map presented in Figure 1 (Dessouky et al. 2024) shows the approximate locations of the treated sections in each District. The selection of cool pavement sites was based on an analytical approach utilizing a series of data sets consisting of; urban heat index, equity score, energy burden, urban tree canopy, pavement condition, and population. The COSA used heat and equity data to identify candidate census tracts with high scores of temperatures, and poverty. COSA selected roads that were in adequate pavement condition and had minimal tree canopy. Finally, each District decided on two locations from the candidate list as shown in Figure 1.

COOL PAVEMENT PRODUCTS

Four cool pavement products were evaluated:
Seal Master (SolarPave®) is a polymer emulsion coating manufactured with UV resistant, reflective light-colored mineral pigments to provide minimum solar reflectance of 0.33. It is blended with ant-slip aggregate to increase surface texture.

GAF Streetbond (DuraShield®) is a two-component waterborne epoxy-modified acrylic coating blended with silica aggregates. The coating is formulated using ultraviolet reflective technology to provide an initial solar reflectance of 0.33.

GuardTop (CoalSeal®) is a water-based asphalt emulsion sealcoat. It has fine aggregate and asphalt content of at least 32% and 10% by weight, respectively. It has a Solar Reflectance of 0.33 and a final cured grey color.

Pave Tech (PlusTi®) is a TiO2-based asphalt rejuvenating/sealing agent. It is composed of a petroleum resin oil base uniformly emulsified with water. With its Photo Catalytic Technology, it enables removal of volatile organic compounds, and exhaust pollutants. Aside from the other three products, PlusTi® penetrates into the pavement surface and does not change the surface color and characteristics. Except Pave Tech, all products are applied in one coat with application rate varied among products and depending on existing pavement conditions and age, traffic volume, and expected outcome from the treatment.
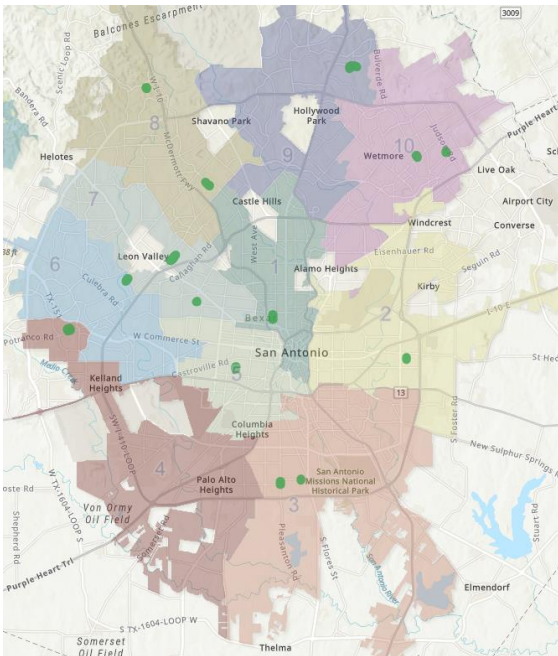
Figure 1. Cool pavement project locations by District

FIELD TESTING

Four field tests were conducted to evaluate pavement texture, friction, bonding strength, and metrological properties. Pavement surface texture was measured with the Nippo Sangyo CT Meter. a laser-based device that reports texture as mean profile depth (MPD) in accordance with ASTM E 1845. Friction was measured with the Nippo Sangyo DF Tester that uses three rubber sliders mounted to a disk that spins parallel to the surface. Friction is measured based on torque as the disk rotational velocity decreases to zero due to friction between the rubber slides and surface (ASTM E1911). The adhesive strength between the applied treatment and existing pavement was measured using the Pull-off tester to assess bond strength (ASTM D 4541). The strength is determined by the maximum tensile pull-off force of coating away from pavement using hydraulic pressure. The metrological data includes; surface temperature, air temperature, and albedo measured with Fluke and NR01 Net Radiometer.

MEASUREMENT PLAN

Five measurements were made in the wheelpath, and two measurements were made outside of the wheelpath to capture any potential variations in texture and friction due to traffic wear (Figure 2). Example of cool pavement product is shown in Figure 2.

Figure 2. Typical measurement locations relative to traffic direction and photo cool pavement treatment (GuardTop).

Summary of Texture Measurements

Figure 3 presents the MPD for control and treated sites at wheelpath and outside wheelpath. Data suggests that the applications of cool pavement treatment reduced on average the surface texture for the Seal Master and GuardTop sites at and outside wheelpath to 10 and 20%, respectively. The drop in texture is consistent with other studies which depict the change to the application of surface emulsion layer that reduces the MPD with the treated surface. It is also noticed that the reduction in texture is more pronounced in these two treatments than in GAF and Pave Tech.
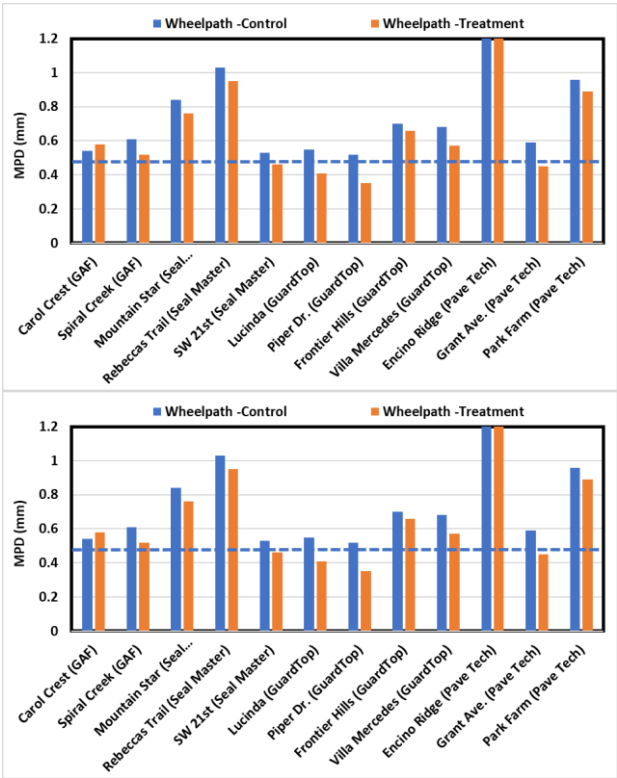
Figure 3. Texture measurements.

Summary of Friction Measurements

Figure 4 presents the Friction data (DFT_{20}) for control and treated sites at wheelpath and outside wheelpath. Figure 4 provides the change in surface friction at and outside wheelpath due to applied treatment. Results suggest that Seal Master and GuardTop have significantly reduced surface friction by 52 and 84% at wheelpath and outside wheelpath after less than 90 days of application, respectively. The friction reduction in the treated surface in the wheelpath is lesser degree than in outside wheelpath by 50 and 21% for Seal Master and GuardTop, respectively.
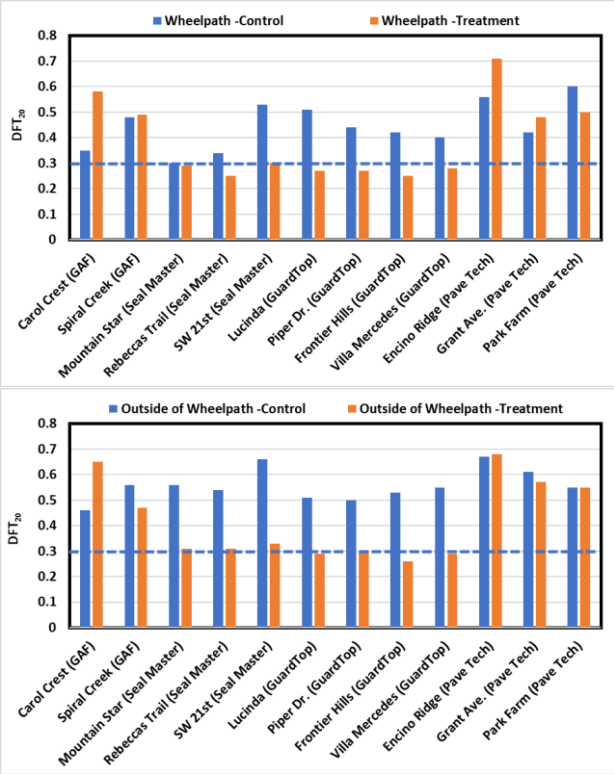
Figure 4. Friction measurements

Bonding Strength

It is suggested that traffic will deteriorate the adhesion strength of the treated layer over time. As shown in Figure 5, all sites experienced a reduction in the adhesion. The data suggests that SealMaster has the least reduction in adhesion while GuardTop has the highest reduction over the performance period. It was not determined to calculate the adhesion strength of Pave Tech due to the nature of the applied penetrating treatment.

Product	Reduction in adhesion due to traffic	Performance period (days)
GAF	30%	193
Seal Master	22%	173
GuardTop	36%	177
Pave Tech	zero	150
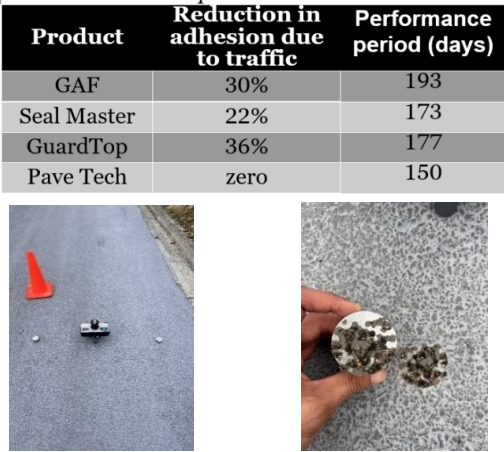
Figure 5. Traffic effect on adhesion of cool pavement

Metrological Data

The surface temperature differences between the treated and control sites were modest in the morning and never exceeded +/- 1°F. By noon, differences in the surface temperatures were more pronounced. The largest negative difference occurred with the PlusTi product was 4°F cooler than the control site. At one site but 12°F warmer than the control in another site. This is attributed to the road surface differences between treated and control site. Example of surface difference is shown in Figure 6.
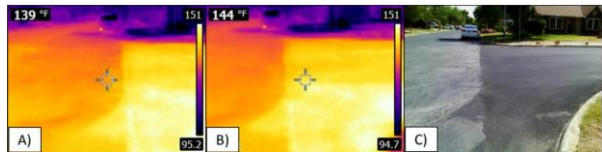
Figure 6. Temperature differences observed at cool and conventional pavement

The albedo measurements, which evaluated the reflectivity of the surfaces, revealed several differences between the various products (Table 1). The SolarPave material displayed the largest increase (0.06) in albedo relative to the control. The cool pavement at Mountain Star reflected 28% of the shortwave radiation whereas the control street reflected only 22%. The GAF product increased the albedo by 0.02. The control sites generally exhibited high albedo values. For example, the albedo for fresh asphalt typically ranges between 0.06 and 0.08.5 This suggests that due to wear and tear as well as exposure to the natural elements typical streets in San Antonio may often have albedo values that are more analogous to cool pavement surfaces than fresh asphalt.

Table 1. Albedo data for three cool pavement products (Debbage et al. 2024).

	Carol Crest (Durashield)	Grant Ave. (PlusTi)	Mountain Star (SolarPave)
Cool Pavement	0.18	0.14	0.28
Control	0.16	0.21	0.22

SUMMARY:

GuardTop experienced a higher reduction (20%) in texture followed by Seal Master (10%). This represents the average reduction among the sites treated with this specific product. GAF showed a decrease in texture by 4% at wheelpath but an increase of 13% outside wheel path. In the case of Pave Tech, an average texture increases of 5% was measured across the surface.

In terms of friction properties and with respect to control sections: GuardTop experienced higher reduction (66%) in friction followed by Seal Master (39%) in the wheel path, while Pave Tech and GAF experienced increase in friction of 5 and 21%, respectively.

In terms of adhesion strength with respect to exposure to traffic (wheelpath and outside wheelpath), Seal Master experienced the least reduction, followed by GAF and GuardTop after 5-6 months of installation. No difference in adhesion strength was noticed in the case of Pave Tech due to the lack of a coating layer.

Overall, the findings highlighted a clear potential for cool pavement to reduce surface temperatures. This was particularly true for the SolarPave product, which displayed consistent reductions in surface temperatures during the daytime at both sites. The results for the other temperature metrics (i.e., air temperature and WBGT) were more inconclusive in nature due to the small magnitude of the differences between the cool pavement and control sites as well as the accuracy of the instruments used during the fieldwork.

REFERENCES

- Debbage N., Zhai W. Ochoa E.L., Lee R.J., et al. (2024) "Evaluating the Urban Heat Mitigation Potential of the San Antonio Cool Pavement Pilot Program" Report for City of San Antonio
- Dessouky, S. Masad A., Tallon R., and Merritt D. "Evaluation of Cool Pavement Surface Treatments Using Friction, Texture and Adhesion Properties" Report for City of San Antonio

ACKNOWLEDGMENTS

Warm-mixed-asphalt in construction sites: determination of the void structure

M.Sc. Jasmin Elzer, M.Sc. David Kempf, M.Sc. Leandro Harries, Dr.-Ing. Stefan Böhm, Prof. Dr.-Ing. Jia Liu
Technical University Darmstadt, Institute for Transportation Infrastructure Engineering, Darmstadt, Hesse, Germany

ABSTRACT: Warm mix asphalt (WMA) is a promising approach to do both: Reduce the energy consumption of the asphalt production and mitigate the exposure of asphalt workers to fumes and aerosols. WMA pavements should have the same quality and performance like conventional hot mix asphalt (HMA) pavements. The void structure of asphalt pavements is an important parameter to determine the quality of an asphalt pavement. In this research, the visual method of asphalt petrology was used to determine the void structure of WMA asphalt drill cores. It could be found out that the quality of the void structure was satisfying. Though, the gathering of voids on the upper and lower margins of the asphalt layers was an observation that generates further research needs.

1 INTRODUCTION

Hot mix asphalt is the main material used for paving roads in Europe. The material is temperature dependent and therefore has different viscosities at different temperatures. To pave a road, the material has to be heated to high temperatures (~150°C-200°C) which induces a low viscosity and makes the material workable on the construction site. However, this heating process includes two major drawbacks: Firstly, there is a high energy consumption necessary to reach the required temperatures. Secondly, the high temperatures lead to evaporation of easily volatile particles in the asphalt which can be harmful to the workers at the construction sites. (EAPA, 2024)

Both drawbacks are not in accordance with the goals of the European countries to reduce the greenhouse gas emissions and to regulate the exposure level to asphalt fumes. A possibility to tackle these challenges is the use of WMA for paving asphalt constructions. Due to lower mixing and paving temperatures up to 130 °C, energy consumption and exposure level can be reduced. (EAPA, 2024)

Research works have already been conducted to examine the properties of WMA, the void structure in particular (Alvarez et al., 2011; Ren et al., 2019), Though, further analysis of the void structure is necessary to get a better understanding of the performance of WMA. The Institute of Transportation Infrastructure Engineering of the Technical University Darmstadt conducted three case studies with samples of construction sites to get further insights in the void structure of WMA.

2 METHODOLGY

2.1 *Construction sites and materials*

Three construction sites were available for examination of the asphalt pavement void structure. Drill cores were taken from the sites and further analyzed in the laboratory. The following table gives an overview of the analyzed materials and layers. Construction site 3 included two sections with different layer compositions. In section 2, a combination of surface and base layer (s&b layer) was paved in one layer. Zeolite was used as an additive on all three construction sites to improve the viscosity of WMA. Also, reclaimed asphalt pavement (RAP) was used.

Table 1. Overview of the analyzed materials

Site	built layers	asphalt	material	RAP [%]
Site 1	base layer	AC 22	W&HMA	30&40
	binder layer	SMA 16	W&HMA	30&30
	surface layer	SMA 8	W&HMA	-
Site 2	base layer	AC 32	WMA	50
	binder layer	AC 16	WMA	35
Site 3-1	base layer	AC 22	WMA	60
	binder layer	AC 16	WMA	40
Site 3-2	s&b layer	AC 16	WMA	75

2.2 Asphalt petrology

Asphalt petrology was used to determine the void structure. It is a 2-D imaging technique that allows the analysis of location and distribution of voids in asphalt sections. The method has been continuously used at the Institute of Transportation Infrastructure Engineering in Darmstadt. To prepare an asphalt petrology specimen, a drill core or a comparable specimen has to be cut in prisms with a diamond-tipped high precision saw. After cutting and drying, the air voids in the produced asphalt prisms are filled with a fluorescent epoxy resin. After the hardening process, the supernatant resin is ground off so that the structure of the voids is finally visible under UV-light. With an adapted scanner, the surface of the prisms can be turned into a high-resolution picture. Those get visually examined and parameters like void content, void distribution or void sizes can be calculated. The method has already been used successfully in several research projects. (Harries et al., 2023; Middendorf, Kempf, et al., 2023; Middendorf, Umbach, et al., 2023)

3 RESULTS

3.1 Construction site 1

Both HMA and WMA were applied on construction site 1. The other boundary conditions on this construction site are identical. It is therefore possible to directly compare the paving quality of the two construction materials.

The base layer was built in two steps. In the following figures, the comparison between the WMA and HMA are depicted for the layers.
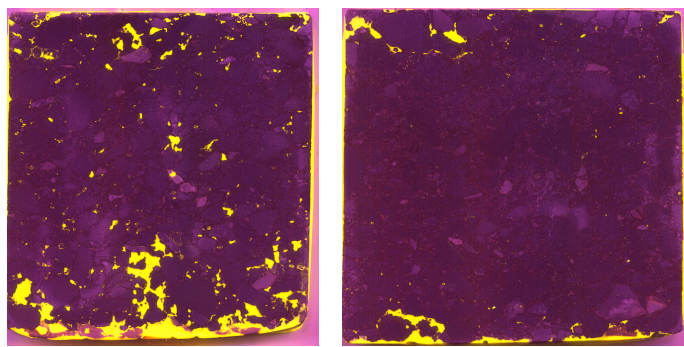
Figure 1. Asphalt petrology prisms for base layer 1. Left: HMA, right: WMA.
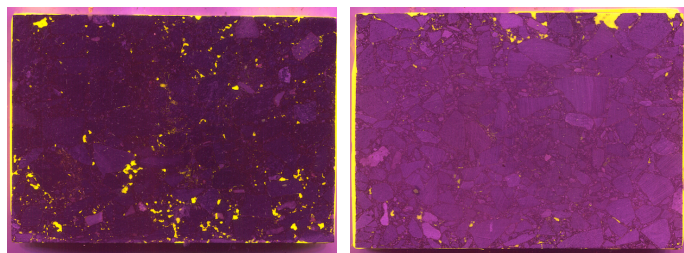
Figure 2. Asphalt petrology prisms for base layer 2. Left: HMA, right: WMA.
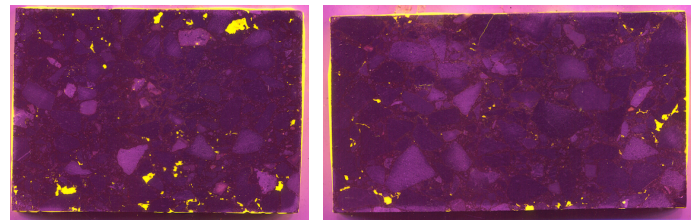
Figure 3. Asphalt petrology prisms for the binder layer. Left: HMA, right: WMA.
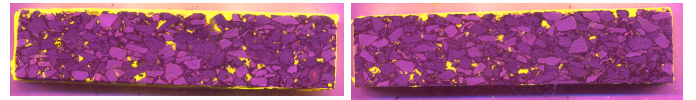
Figure 4. Asphalt petrology prisms for the surface layer. Left: HMA, right: WMA.

Also, the void content and the void distribution are calculated. The results of the void content and one example of the void distribution are depicted in the following pictures.
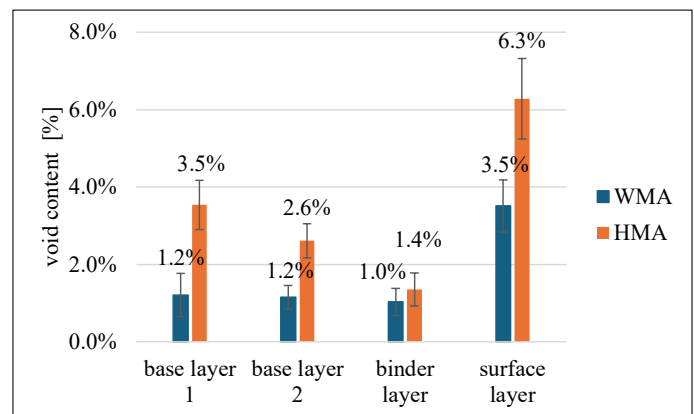
Figure 5. Comparison of the void contents
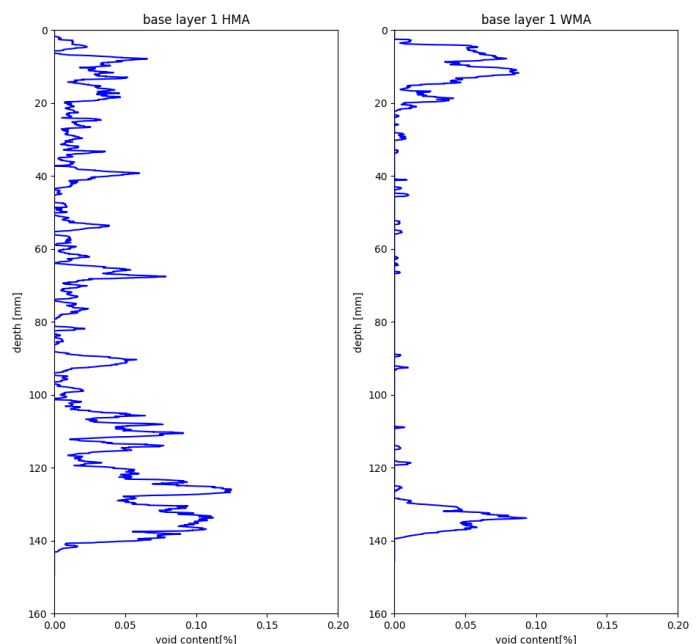
Figure 6. Void distribution for base layer 1. Left: HMA, right: WMA.

The visual impression of the WMA layers having a lower void content than the HMA in Figures 1-4 is confirmed when looking at the void contents in

Figure 5. For all layers, the WMA have lower void contents than the HMA. Analyzing the void distribution, for the base layer, the voids gather at the top and bottom of the layer. That can be seen exemplary in Figure 6.

The so-called void distribution homogeneity is introduced to simplify the evaluation of the void distribution. This parameter calculates the deviation between an optimal linear vertical void distribution and the distribution of the analyzed sample. Optimal linear vertical distribution means a constant inclination of the void content sum with growing depth of the sample. In the depicted Figure 6 a straight vertical line would appear. For all layers this parameter was calculated. The results for the void distribution homogeneity are depicted in Figure 7.
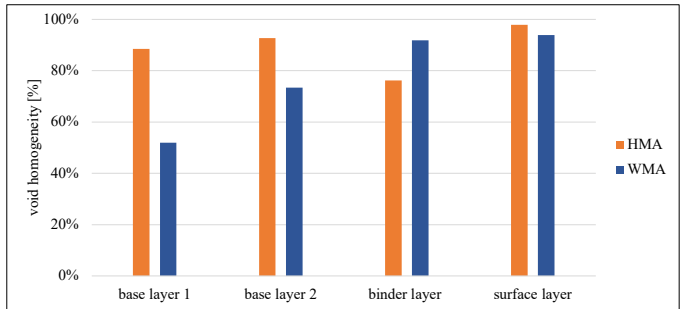
Figure 7. void distribution homogeneity of the layers in construction site 1

3.2 Construction site 2

Drill cores were taken at two locations of the construction site. The void content and the distribution homogeneity of the voids in the WMA binder and base layers are depicted in Figures 8 and 9.
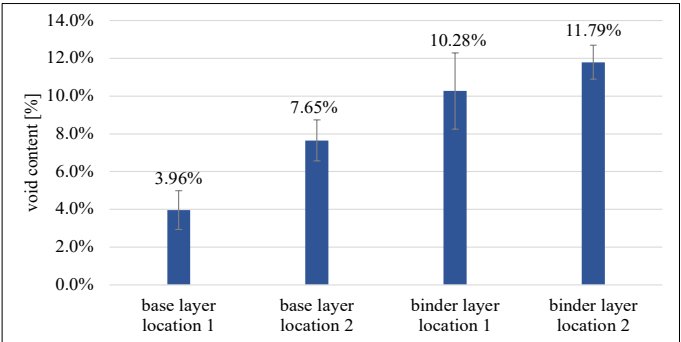
Figure 8. Void contents of the layers in construction site 2
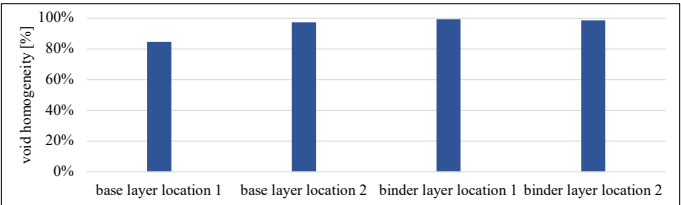
Figure 9. void distribution homogeneity of the layers in construction site 2

3.3 Construction site 3-1

With the same method of construction site 2, the results of construction site 3-1 are depicted in figures 10 and 11.
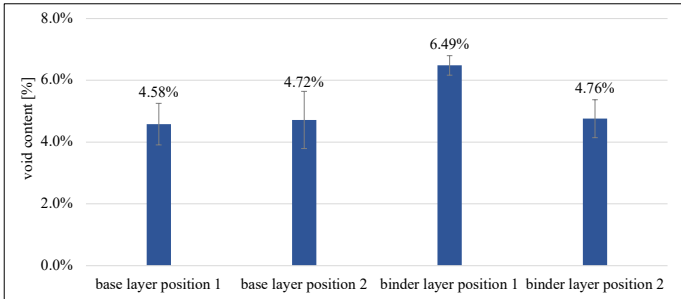
Figure 10. Void contents of the layers in construction site 3-1
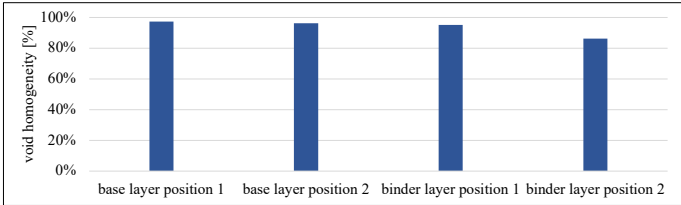
Figure 11. void distribution homogeneity of the layers in construction site 3-1

3.4 Construction site 3-2

With the same method of construction site 2, the results of construction site 3-2 are depicted in Figures 12 and 13. Here, there are three analyzed locations for the s&b layer.
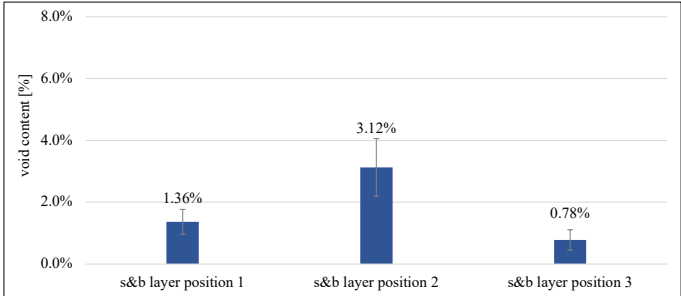
Figure 12. Void contents of the layers in construction site 3-2
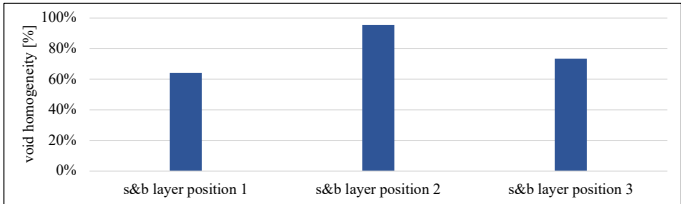
Figure 13. void distribution homogeneity of the layers in construction site 3-2

4 DISCUSSION

The results of construction site 1 show that the void structure of the WMA layers is comparable to the structure of the HMA samples. There is less void content in all samples. This could lead to a better performance and finally to a longer service life, though a

too dense structure can mitigate the durability. Therefore, the condition of the pavement must be observed regularly. The tendency of voids gathering at the top or at the bottom of the WMA layers is an important finding of this site.

Analyzation of sites 2 and 3 focused on WMA asphalt layers. Taking the void distribution into account, in site 2 the void content of the base layer fulfills the requirements of the German regulations. Some voids gather at the vertical edges. The permissible void content in the binder layer was exceeded. The void distribution was inhomogeneous. This could be confirmed with the conventional method of determining the void content in the laboratory. It can be concluded that the construction work did not show a sufficient quality for the binder layer, as the temperature of the asphalt mixture was too low and the construction logistic chain took too long to deliver fresh asphalt material.

In construction site 3-1 and 3-2, the void content fulfills the requirements of the German regulations. Also here, there are gatherings of voids at the layer boundaries.

5 SUMMARY AND CONCLUSIONS

Several drill cores from three construction sites using WMA have been analyzed in 2024 at the institute of Transportation Infrastructure Engineering at the Technical University of Darmstadt. With the method of asphalt petrology, the parameters void content and void distribution of the WMA layers could be analyzed.

This method delivers the following relevant insights in the layer structures:
Firstly, the void structure of WMA is satisfying. Secondly, for the most WMA drill cores, a gathering of voids at the upper and lower margins of the layers was observed.

That seems to be a common contemplation for WMA. It could depend on the fact that the temperature of the mixture cools down too fast on the vertical edges of the layers.

The formation of so called "edge voids" could depend on the faster cooling rate at the margins of the layers and is an important finding that should be analyzed more detailed in the future. Furter research should be conducted to assess and correlate the findings regarding the void structure with the performance and service life of WMA layers.

6 REFERENCES

Alvarez, A. E., Macias, N., & Fuentes, L. G. 2011. *Analysis of connected air voids in warm mix asphalt*. DYNA (Colombia). 79. 29-37

EAPA. 2024. *Recommendations for Road Authorities to optimise paving sustainability, health & safety, and quality through the use of Warm Mix Asphalt*. European Asphalt Pavement Association.

Harries, L., Schütz, M., Kempf, D., & Liu, J. 2023. *Methods of Asphalt Petrology: Determination of Permeability*. International Journal of Civil Infrastructure. 6. 41-50

Middendorf, M., Kempf, D., & Böhm, S. 2023. *Influence of the Application Method of Bitumen Emulsion on the Layer Bond*. International Journal of Pavement Research and Technology.

Middendorf, M., Umbach, C., Böhm, S., Liu, J., & Middendorf, B. 2023. *Comparative Study of 2D Petrographic and 3D X-ray Tomography Investigations of Air Voids in Asphalt*. Materials 16(3). 1272.

Ren, J., Xing, C., Tan, Y., Liu, N., Liu, J., & Yang, L. 2019. *Void Distribution in Zeolite Warm Mix Asphalt Mixture Based on X-ray Computed Tomography*. Material*s*. 12(12). 1888.

Electric Vehicles Induced Damage on Flexible Pavement in Arid Climates

M.Y. Fares
Department of Civil and Environmental Engineering, Michigan State University, East Lansing, MI, USA

M. Lanotte
Department of Civil and Environmental Engineering, Michigan State University, East Lansing, MI, USA

ABSTRACT: The transition to Electric Vehicles (EVs), particularly in regions like the United Arab Emirates (UAE), presents both environmental benefits and unique challenges for transportation infrastructure. This study examines the impact of heavy-duty EV adoption on flexible pavements in the UAE, where increased axle loads from EV battery weights are expected to accelerate pavement deterioration. Using the Mechanistic-Empirical (ME) design method, the effects of partial replacement of Class 5 Internal Combustion Engine (ICE) vehicles with Class 5 EVs on pavement performance are analyzed. Results indicate that the increased load demands of EVs lead to premature fatigue cracking and a shorter pavement lifespan. Enhanced asphalt mixtures, such as high polymer and rubber-modified binders, were tested to improve pavement durability, showing that both options could extend service life with minimal additional thickness. Findings suggest that while polymer-modified materials provide significant durability improvements, cost-benefit analysis is necessary to optimize binder choice for long-term infrastructure sustainability.

1 INTRODUCTION

The global transition to sustainable transportation is growing, with Electric Vehicles (EVs) emerging as a pivotal alternative to reduce carbon emissions, improve air quality, and address the climate crisis. Many countries, including the United Arab Emirates (UAE), are integrating EVs into their transportation networks as part of broader environmental goals (International Energy Agency, 2023; Seitz et al., 2024). Recognized as a regional leader in e-mobility, the UAE has implemented ambitious strategies, including the UAE Energy Strategy 2050 and the Green Mobility Strategy 2030, to guide the nation toward a sustainable future. These frameworks aim to replace many ICE vehicles with EVs, setting goals for 50% of all vehicles to be electric or hybrid by 2050 (Maddren, 2024; Seitz et al., 2024).

The rapid adoption of EVs presents specific challenges for the UAE's infrastructure, particularly its flexible pavement roads, which are widely used due to their cost-effectiveness and ease of construction. EVs exert unique and often heavier loads on pavement surfaces due to the weight of their battery packs, which can weigh several hundred kilograms. Unlike ICE vehicles, where the load is distributed differently, EVs concentrate greater weight on specific pavement areas (Fares et al., 2024; Zhou et al., 2024). This additional stress can accelerate wear and tear, potentially leading to increased rutting, cracking, and a reduction in pavement lifespan—especially in hot climates like the UAE, where high temperatures exacerbate pavement deterioration (Fares et al., 2024; Seitz et al., 2024).

Given these challenges, it is essential to explore pavement design and material solutions tailored to the demands of EVs. Pavement materials and structural design play a critical role in determining the durability of roads under varying loads and environmental conditions. This study starts by investigating the effects of introducing EVs to the currently used pavement structures in the UAE. Next, solutions to mitigate EV-induced damage on flexible pavements, including using modified asphalt materials for the UAE's unique environment. Additionally, this paper concludes with policy recommendations and regulatory measures that could support the sustainable integration of EVs without compromising infrastructure longevity.

In sum, the UAE's journey toward a sustainable transport sector requires technological and policy advancements and proactive measures to ensure that infrastructure can withstand the evolving demands of EVs. By addressing these concerns, this study aims to contribute to the UAE's vision of a resilient and eco-friendly transportation network, ultimately fostering a sustainable future for the region.

2 METHODOLOGY AND MATERIALS

In this study, a typical pavement section commonly used for high-demand highways is investigated. The actual vehicle class distribution of the road segment (Fig. 1) showed that most vehicles belong to class 5 (Salameh, 2020). Although all classes of the current heavy ICE vehicle fleet are expected to be partially or fully replaced with EVs over time, it is reasonable to assume that significant effects will be noticed when corresponding Class 5 EVs replace Class 5 ICE vehicles. The analysis was performed by replacing a percentage of Class 5 ICE vehicles with the Volvo FL Electric (Volvo, 2024). A 45/55 weight split between the front and rear axles of the Volvo FL was assumed in the analysis (Fares et al., 2024). Figure 2 represents the difference in weight between

a typical Class 5 vehicle with two axles and the Volvo FL Electric.
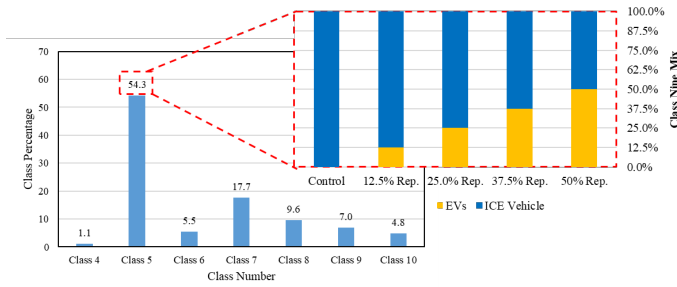
Figure 1. Typical vehicle class distribution in the UAE
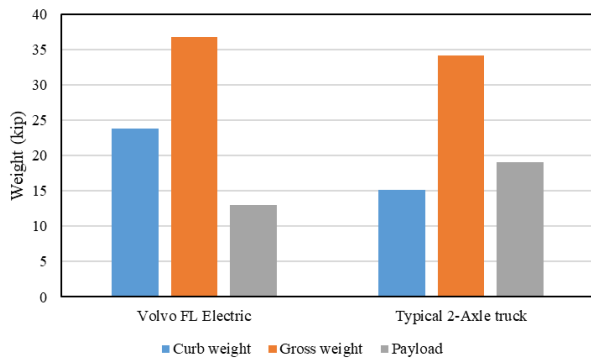
Figure 2. Estimated EVs' weights for Class 5 vehicles.

Table 1 shows the traffic inputs collected for the case study. The Average Annual Daily Truck Traffic (AADTT) is 21,211 vehicles (Salameh, 2020). In the design case, the following scenarios were evaluated:

- Control – All ICE vehicles.
- 12.5% Class 5 replacement: 12.5 % of the Class 5 ICE vehicles (54.3 % of the traffic mix) are replaced with Class 5 Volvo FL EVs.
- 25.0%, 37.5%, & 50.0% Class 5 replacement.

Figure 3 illustrates the cross-section of the pavement structure and the material properties used in the analysis. While the material type for the unbound base and subgrade layers are fixed, the HMA Wearing Course (WC) layer changes as the paper progresses. First, all the scenarios are evaluated using a Dense Graded HMA mixed with a 60/70 Neat Binder (DG-NB). This material is typical for flexible pavements in the UAE. Two more HMAs with the same gradation but different binders are evaluated. The first is a High Polymer Modified Binder (PMB), while the other is a Terminally Blended Rubberized Binder (TBRB) (Ibrahim et al., 2024). Both binders are produced in the UAE and are currently used in a limited number of projects with special performance requirements.

2.1 NCHRP 1-37A mechanistic-empirical method

The mechanistic-empirical analysis was conducted using the MEAPA (Mechanistic-Empirical Asphalt Pavement Analysis) web application using the climatic data of the UAE (Kutay & Lanotte, 2020). Asphalt Concrete (AC) rutting and bottom-up fatigue cracking were compared. All these flexible pavement-related distresses were evaluated using the mixture-specific calibration coefficients obtained by conducting Repeated Load Permanent Deformation (RLPD) Testing and Push-Pull (PP) Testing (AASHTO TP 79, 2012; Kutay & Lanotte, 2018). Additionally, the viscoelastic properties of the asphalt binders and mixtures were obtained from laboratory testing (AASHTO M 320-17, 2017; AASHTO TP 79, 2012). Table 2 presents the materials-specific coefficients alongside general inputs for the ME analysis.

Table 1. General traffic input values for the evaluated design case.

General Traffic Input	UAE Design Case
Two-way AADTT	21,211
Number of lanes	2
Trucks in design direction [%]	58
Trucks in design lane [%]	95
Operational speed [km/h]	100
Reliability [%]	95
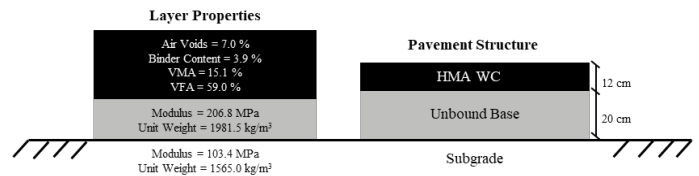
Figure 3. Pavement cross-section and layer properties

Table 2. MEAPA, analysis data input

Parameter	Mix ID		
	DG-NB	DG-TBRB	DG-PMB
Bottom-up fatigue coefficients (β_{r1}, β_{r2}, β_{r3})	(1.43E-5, 1.726, 1.877)	(1.02E-2, 1.671, 2.059)	(5.87E53, 1.749, 1.941)
AC Rutting (β_{r1}, β_{r2}, β_{r3})	(3.00E-3, 1.0, 0.616)	(6.54E-3, 1.0, 0.418)	(8.70E-3, 1.0, 0.357)

General Details	Value
Analysis duration	20 years
Groundwater table	30.48 meters
MERRA2 Station Latitude	24.355003
MERRA2 Station Longitude	54.579152

3 RESULTS AND DISCUSSION

Figure 4 shows the number of Equivalent Single Axle Loads (ESALs) calculated for all the scenarios analyzed. The values from "All ICE vehicles" are obtained using the traffic information for the pavement structures under evaluation. Hence, they represent the design traffic. The percent increase obtained by replacing 12.5% of Class 5 ICE vehicles with Class 5 EVs is more than 18%. As the replacement percentage increases, the difference can reach more than 70% of the original amount.
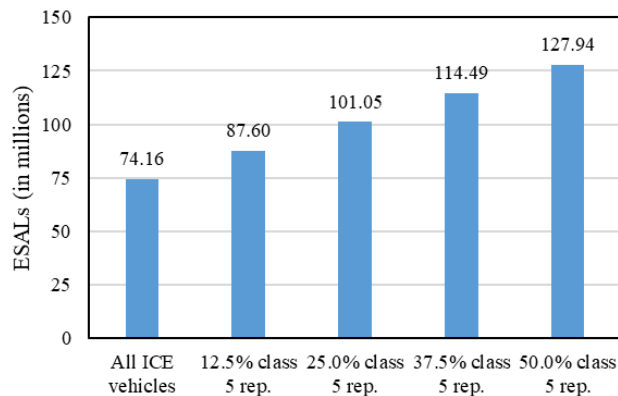
Figure 4. ESAL outcome for each scenario

The ME analysis showed that the leading distress is the bottom-up fatigue cracking (Fig. 5). The analysis indicated minimum rutting (>0.5 mm), which goes along with observations made in the field where design practices suggest the use of a low binder percentage (i.e., 3.9%) to account for the dominant arid climate in the UAE. Meanwhile, it can be noticed that with the "All ICE vehicles" scenario, the pavement structures fail within six years of service life. Moreover, the replacement of class 5 vehicles resulted in accelerated failure, with the pavement structure failing within 42 months for the 50% replacement case.

When the wearing course material was changed to PMB and TBRB, results showed that both materials performed significantly better than the currently employed low penetration grade binder (i.e., 60/70). Instead of failing within the first six years, the DG-PMB fails after 15 years, while the DG-TBRB fails after 16 years. This outcome shows that the DG-TBRB outperforms the DG-PMB, which is also reinforced as an outcome when comparing the 50% class 5 replacement, where the DG-TBRB service life extends to 131 months, and the DG-PMB fails within 123 months of service.

Even though using polymer-modified binders could enhance the performance of pavement structures and extend their service life, they have yet to meet a 20-year design life, and optimization of the pavement structure thickness is required.

Table 3 presents the pavement cross-section thicknesses for the control scenario and the 50% class 5 replacement.
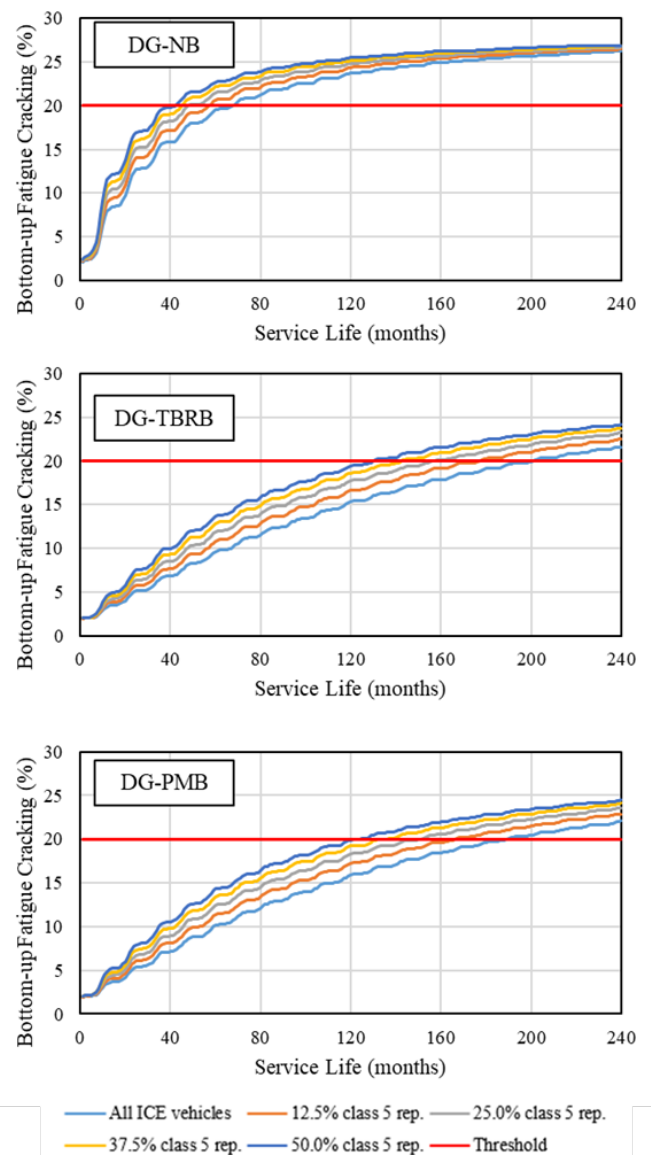
Figure 5. Results of the Mechanistic-Empirical Pavement Structural Analysis

The outcomes indicate that an increase of 2.5 cm (1 inch) is essential for the DG-NB WC to withstand the full design life, while both the DG-TBRB and -PMB require an additional 0.5 cm to pass the 20 years of design life with the "All ICE vehicles" scenario. Moreover, for the 50% class 5 replacement, a 16 cm thick wearing course is needed using DG-NB, and 14.5 cm for modified materials. This change in thickness leads to additional costs. Table 3 shows the difference in the expected material cost if the polymer-modified binders are used instead of the neat binder. Due to their higher cost, it can be observed that the DG-PMB costs $1839 per lane per km in comparison to the DG-NB, while the DG-TBRB costs an additional $901 per lane per km. These costs are related to the material costs; however, to obtain a more complete picture, the cost of the construction and maintenance should be factored into the analysis.

Table 3. Additional material cost due to the 50% class 5 replacement

	DG - NB	DG - TBRB	DG - PMB
Optimized cross-section thickness (All ICE vehicles) [cm]	14.5	12.5	12.5
Optimized cross-section thickness (50% class 5 rep.) [cm]	16	13.5	13.5
Difference in thickness [cm]	1.5	1.0	1.0
HMA density [kg/m^3]	2528	2513	2527
Mass per lane (3.6 m) per km [ton]	136.5	135.7	136.5
Unit price [$/ton]	60.0	67.0	73.5
Additional Material Cost [$]	8,191	9,092	10,030

4 CONCLUSION

This study evaluates the potential impact of light-duty EVs on road networks. Compared to traditional ICE vehicles, the findings reveal that the increased EVs' weight accelerates pavement deterioration.

The primary design method followed in the UAE is AASHTO 1993. However, previous studies showed the inadequacies of the technique in accurately designing pavement structures (Fares et al., 2024). The ME analysis results indicate that the pavement sections analyzed failed within the first six years for fatigue cracking, which is close to field observations (5 years, fatigue cracking as lead distress) (Marini & Lanotte, 2021).

Replacing class 5 ICE vehicles with class 5 EVs increases the traffic load on the structure. However, the growth is not as significant as in other case studies (e.g., Michigan, Fares et al., 2024) due to the dominant vehicle class being class 5 with lower gross vehicular weight.

The ME analysis showed that the dominant distress is bottom-up fatigue cracking with no asphalt concrete rutting occurring. A balanced mixed design could be used in the region to enhance the fatigue cracking performance but only slightly increase rutting potentials.

The use of PMBs and TBRBs can extend the service life of the pavement structure without changing the thickness of the wearing course layer. Of the two options evaluated, the TBRB is preferable since it slightly overperforms the PMB asphalt mixture.

The optimization of the pavement structure design to serve satisfactorily for 20 years with the EVs present showed that the change of thickness varies between 1.0-1.5 cm compared to the control scenario. The outcome showed that DG-NB would cost less than the other two binders from a material cost point of view, yet the addition of the construction and transportation costs could likely change the outcome where the DG-TBRB can be the best solution (Ibrahim et al., 2024).

5 REFERENCES

AASHTO M 320-17. (2017). AASHTO M 320: Standard Specification for Performance-Graded Asphalt Binder. In *Standard Specifications for Transportation Materials and Methods of Sampling and Testing and Provisional Standards*.

AASHTO TP 79. (2012). *Standard Method of Test for Determining the Dynamic Modulus and Flow Number for Hot Mix Asphalt (HMA) Using the Asphalt Mixture Performance Tester (AMPT)*.

Fares, M. Y., Albdour, A., & Lanotte, M. (2024). Evaluation of potential electric vehicles load-induced damage on flexible pavements. *Transportation Research Part D: Transport and Environment*, *136*(August), 104475. https://doi.org/10.1016/j.trd.2024.104475

Fares, M. Y., Marini, S., & Lanotte, M. (2024). Multiple Stress Creep Recovery of High-Polymer Modified Binders: Consideration of Temperature and Stress Sensitivity for Quality Assurance/Quality Control Policy Development. *Transportation Research Record*, 1–17. https://doi.org/10.1177/03611981241240765

Ibrahim, H., Marini, S., Farina, A., & Lanotte, M. (2024). Integrating Mechanistic-Empirical Pavement Analysis in the Life Cycle Assessment Use Phase and Monetization of Environmental Impacts to Promote Low Carbon Transportation Materials. *Transportation Research Record*. https://doi.org/10.1177/03611981241253576

International Energy Agency. (2023). Global EV Outlook 2023. *Geo*, *Geo*, 9–10. https://www.iea.org/reports/global-ev-outlook-2023

Kutay, M. E., & Lanotte, M. (2018). Viscoelastic continuum damage (VECD) models for cracking problems in asphalt mixtures. *International Journal of Pavement Engineering*, *19*(3), 231–242. https://doi.org/10.1080/10298436.2017.1279492

Kutay, M. E., & Lanotte, M. (2020). *Formulations of the Pavement Performance Prediction Models in the Mechanistic-Empirical Asphalt Pavement Analysis (MEAPA) Web Application*.

Maddren, E. (2024). *Emobility in the United Arab Emirates: Understanding opportunities for New Zealand exporters* (Issue May).

Marini, S., & Lanotte, M. (2021). Waste rubber from end-of-life tires in 'lean' asphalt mixtures—a laboratory and field investigation in the arid climate region. *Polymers*, *13*(21). https://doi.org/10.3390/polym13213802

Salameh, A. (2020). *Characterization of Truck Traffic towards Implementation of Mechanistic-Empirical Pavement Design Guide in Northern Emirates of the UAE* (Issue May). University of Sharjah.

Seitz, H., Gupta, S., Wussow, J., & Bev, S. (2024). *The future is electric: A strategy for EV adoption in the UAE*.

Volvo. (2024). *Volvo FL Electric*. https://www.volvotrucks.com/en-en/trucks/electric/volvo-fl-electric.html

Zhou, Q., Ramakrishnan, A., Fakhreddine, M., Okte, E., & Al-Qadi, I. L. (2024). Impacts of heavy-duty electric trucks on flexible pavements. *International Journal of Pavement Engineering*, *25*(1). https://doi.org/10.1080/10298436.2024.2361087

Evaluation RAP Cluster Dissociation under Different Breakdown Modes

W.L.G. Ferreira
Universidade Federal Rural do Semi-Árido (UFERSA), Campus Caraúbas - Caraúbas/Brasil
K. Vasconcelos
Universidade de São Paulo (USP), Escola Politécnica, São Paulo/Brasil
I.S. Bessa
Universidade Federal do Ceará (UFC), Campus do Pici - Bloco 703 – Fortaleza/Brasil
V.T.F. Castelo Branco
Universidade Federal do Ceará (UFC), Campus do Pici - Bloco 703 – Fortaleza/Brasil

ABSTRACT: The presence of RAP clusters (particles that are agglomerated as a single aggregate) is one of the main factors to increase RAP heterogeneity. During hot mixture asphalt (HMA) production, only part of the RAP binder might be activated, and part of the RAP clusters might be dissociated. The objective of this study is to evaluate the RAP cluster dissociation under two different breakdown modes. First, stages of binder extraction were performed to simulate different levels of cluster dissociation. Second, the Micro-Deval (MD) was used to induce cluster dissociation by combining temperature and mixing time. The RAP particles gradation and shape properties were analyzed. The results indicated that there was a significant impact of the partial cluster dissociation on the RAP aggregate characteristics (gradation and shape properties). Besides, the abrasion time was more relevant than the mixing temperature to breakdown RAP clusters.
Keywords: RAP, Micro-Deval, temperature, aggregates' shape properties, binder activation

1 INTRODUCTION

The reclaimed asphalt pavement (RAP) is obtained after the milling process carried out in the field and it allows the reuse of aggregates and asphalt binder, two of the main consumed materials in asphalt paving services. However, the presence of RAP (even in fractionated stockpiles) clusters, or agglomerates of small particles, lead to another source of variability (Xu et al., 2019; Ferreira et al., 2021). A coarse RAP particle could be a cluster of several small particles connected appearing as a single aggregate. The nature of these clusters is controlled by the type of milling process (including parameters such as speed and cut thickness), and the mixture characteristics that are being milled (asphalt binder type and content, aggregate gradation, aging level). The cluster dissociation occurs during the asphalt mixture production (because of high temperature and mixing time) and compaction in the field.

The AASHTO M 323 (2022) standard mentions that the RAP binder should be fully extracted from the RAP using solvent extraction or the ignition oven. Then, the aggregate gradation and shape properties requirements should be determined. In this scenario, the RAP aggregates properties are determined considering that all RAP binder is activated, clusters are fully dissociated and disregards the possibility of partial RAP binder activation and cluster dissociation, as commented by Lo Presti el al. (2019).

Overall, it is common to characterize RAP as having 0% of binder activation (i.e., black rock with clusters undissociated), usually for cold recycling, or 100% of binder activation (all clusters dissociated), for hot recycling. These extreme assumptions do not consider the reality, which is somewhere between the two situations and dictated by the RAP characteristics and the asphalt mixture production. There is still lack of research that treats the RAP aggregate as a material which changes alongside the asphalt mixture production, as the clusters are disintegrated.

In this context, this research investigates the RAP cluster dissociation under different breakdown modes: (i) asphalt binder extraction with solvent, and (ii) the use of the equipment Micro-Deval (MD). The two different laboratory methods were selected to partially breakdown the RAP clusters with the purpose to better understand how the cluster dissociation occurs, and which parameter (temperature and mixing time) is more relevant to disintegrate the agglomerations. This information is useful to design the recycled asphalt mixtures based on the RAP properties after cluster dissociation.

2 MATERIALS AND METHODS

Around 50kg of RAP was collected in the stockpile of an asphalt plant located in Maracanaú/CE, Brazil. The RAP was homogenized and spread on a flat surface for three days to eliminate moisture. Only coarse RAP particles were evaluated (19.0mm – 4.75mm). The RAP nominal maximum aggregate size (NMAS) is 19.0mm, and the asphalt binder content is 4.0% obtained by the centrifugation method. There is no information about the level of ageing of the RAP binder, but it was a 50/70 penetration grade virgin binder.

The first procedure (Figure 1) to induce cluster dissociation consisted in keeping the RAP sample

(around 1.0kg) immersed in solvent for 2 minutes, with the use of the centrifugation method (ASTM D2172, 2017) to separate the solution from the aggregates. While the RAP binder is activated, the RAP clusters are also dissociated. The degree of binder activation (DoA), after each stage of binder extraction, is cumulative, and it ranges from 0%, which represents the RAP before any binder extraction (cluster undissociated), to 100% after two or more binder extraction stages when all RAP binder is activated, and clusters are fully dissociated. This method has been used before in a previous study (Ferreira et al., 2021).
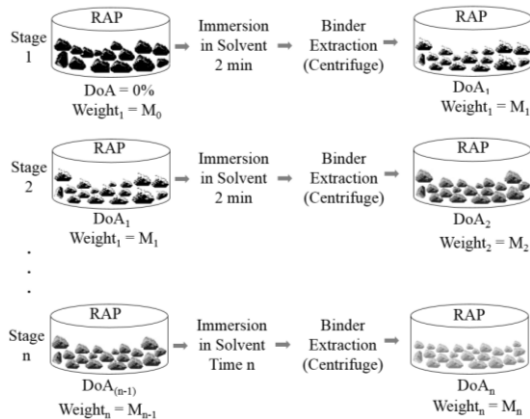
Figure 1. Illustration of the stages of RAP binder extraction.

In the second procedure (Figure 2), the MD equipment was used (ASTM D 6928, 2017) to breakdown the RAP clusters. This equipment is commonly used to assess aggregate polishing and breakage characteristics by the abrasion between coarse aggregates, and standardized metal spheres inside a rotating tambor. The standard MD test is performed using coarse aggregates (higher than 4.75mm) with a rotation of 100rpm during 2h.
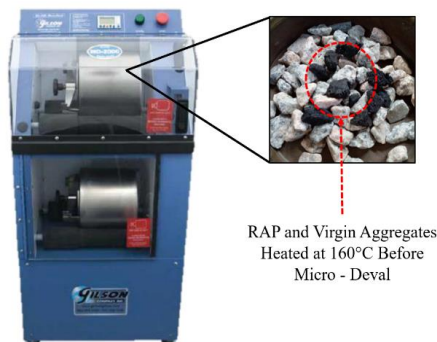
Figure 2. RAP with virgin aggregates before the MD test proposed in this study.

Three mixing times (5, 15, and 30min) were tested, and each RAP sample (around 1.0kg) was evaluated at room temperature (33°C, as a control sample), and heated at 140°C and 160°C (for 30 minutes in the oven before MD). In addition, 3.0kg of virgin aggregates (abrasive load, material retained at #25mm) was used instead of the metal spheres to be more re-

alistic comparing with the field conditions. The virgin aggregates were also heated at the same temperature of the RAP for 30min. As the virgin aggregates size is higher than the RAP particles, after the MD procedure it was possible to differentiate RAP particles from virgin aggregates by using sieve #25mm to retain the virgin aggregates. Besides, it was tested the MD only with virgin aggregates for 30 minutes to verify if the virgin aggregates breakdown, but no fine particles were observed. So, all fine particles after the MD come from the RAP.

For the stages of binder extraction and the MD procedure, only coarse RAP fractions (19.0mm – 4.75mm) were used since the MD equipment is developed for coarse particles. After each procedure, sieve analysis was performed and then each RAP fraction was evaluated using the Aggregate Imaging Measurement System (AIMS) to obtain the aggregates' shape properties following DNIT 432 – ME (2020). Two aggregates' shape properties (gradient of angularity - GA and surface texture - Tx) were evaluated.

3 RESULTS

Figure 3 presents the RAP aggregates size distribution after each asphalt binder extraction and after the MD test (160°C and 30min, highest temperature and longer time) as an example. The gray curve (DoA = 100%) represents the scenario where all RAP clusters are fully dissociated, while the black curve (DoA = 0%) is the opposite scenario, i.e., all clusters undissociated.
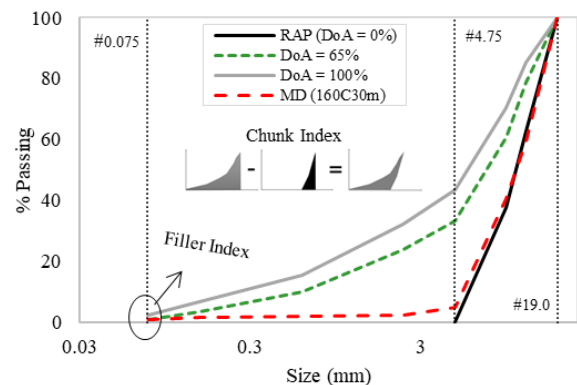
Figure 3. Size distribution for each Degree of activation (DoA) compared after Micro-Deval (MD) (160°C and 30min).

After the binder extraction and the MD, the clusters were dissociated and the presence of fine particles (below #4.75mm) increased. In the worst-case scenario, after complete binder extraction (white curve, DoA = 100%), around 40% of fine particles appeared coming from RAP clusters. Overall, the gradation curve tends to go up as the DoA increases because of the cluster dissociation. The gradation distribution after the MD (at 160°C after 30min) is

close to the gradation of the black curve (DoA = 0%) indicated less impact of the temperature and mixing time when compared with the stages of binder extraction. To quantify the RAP cluster dissociation, the chunk index and filler increased index proposed by Zaumanis et al. (2021) were calculated. The chunk index is obtained by the difference between the area below the white curve and black curve, as illustrated in Figure 3. In addition, it was also calculated the difference between the area below the curve after each scenario tested (stages of binder extraction and MD) and the black curve (DoA = 0%). Small values of chunk index (closer to zero) are desirable since it indicates that the two curves are closer which means fewer RAP particles as a cluster. The filler increased index indicates the percentage of filler generated after RAP cluster dissociation. It was calculated by the difference between the percentage of filler passing through the smallest sieve (#0.075mm) after each scenario tested and the black curve (DoA = 0%). A small filler increased index is also desirable meaning that less filler was generated after cluster dissociation. The results are presented in Figure 4. The legend MD33C5m means Micro-Deval test at 33°C for 5min, and so on.
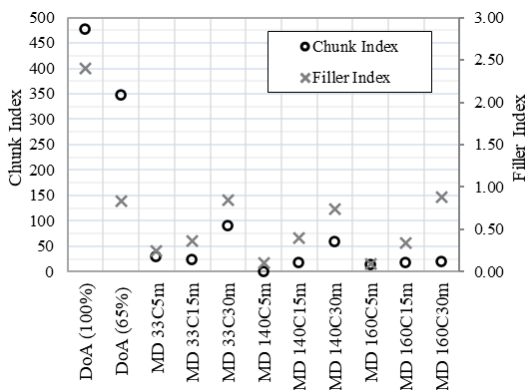
Figure 4. Chunk index and filler increased index proposed by Zaumanis et al. (2021).

As observed in Figure 4, the binder extraction seems to be more severe (higher values of indexes) to breakdown RAP clusters when compared with the MD procedure. The highest filler index (around 2.5) was observed for DoA = 100% (worst-case scenario), while for the rest, the filler index was less than 1.0. As the abrasion time increases (from 5min to 30min), both indexes increase as well, indicating the influence of the mixing time to dissociate the RAP cluster. Looking at the chunk index, the high temperature (160°C) induced less impact when compared to room temperature (33°C). At 160°C the hypothesis was that the RAP binder was partially activated but the RAP cluster still glued as a single particle now more resilient (because of the binder ef-

fect) to absorb the abrasion inside the MD chamber without breaking apart.

3.1 Shape Properties (using AIMS) versus MD Time and Temperature

Figure 5 presents the results of the aggregate shape properties for the fraction #4.75mm (passing through #9.5mm and retained at #4.75mm) as an example comparing angularity (Figure 5a) and surface texture (Figure 5b) values after each stage of binder extraction and after MD (160°C and 30min).

(a)

(b)
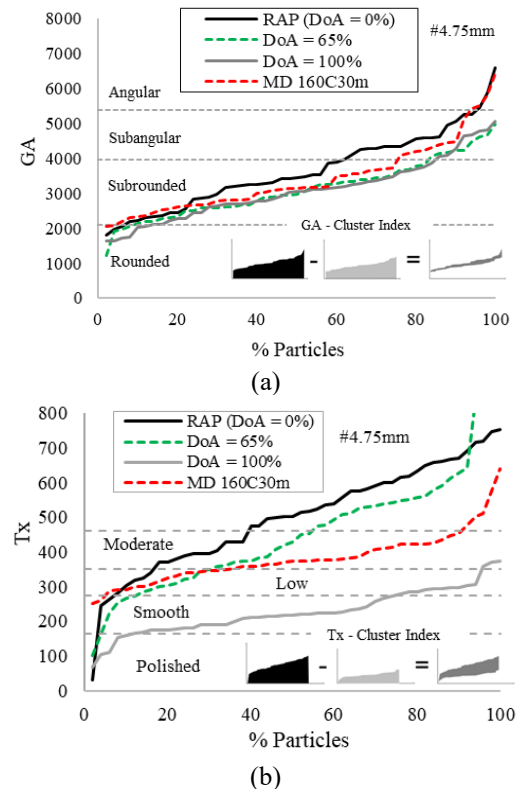
Figure 5. Results after each stage of binder extraction compared with the Micro-Deval (MD) test (160°C and 30min).

As observed in Figure 5a, the black curve (DoA = 0%) has more subangular and angular particles when compared with the curve (DoA = 100%). The GA tends to decrease as the clusters are dissociated and less angles/edges are presented in the particles. For texture, Figure 5b, as the aged binder/mastic/fine aggregate matrix (FAM) is removed, either by the solvent or by the abrasion and high temperature, the RAP particle surface tends to be smoother (white curve, DoA = 100%). To quantify the RAP cluster dissociation by the shape properties results, an adaptation of the chunk index calculated previously was obtained. The GA - cluster index (Figure 5a) and the Tx – cluster index (Figure 5b) were obtained by the difference between the area below the black curve (DoA = 0%) and each scenario tested (stages of binder extraction and MD). Smaller values (closer to zero) of the two indexes indicate that the RAP clus-

ter dissociation did not affect the shape properties. Figure 6a presents the results for angularity while Figure 6b presents the results for texture. In both cases, only two coarse fractions (#9.5mm and #4.75mm) were evaluated since it is necessary to have at least 50 particles to run the AIMS test, and there were not plenty of particles for #12.5mm and #19.0mm.

(a)

(b)
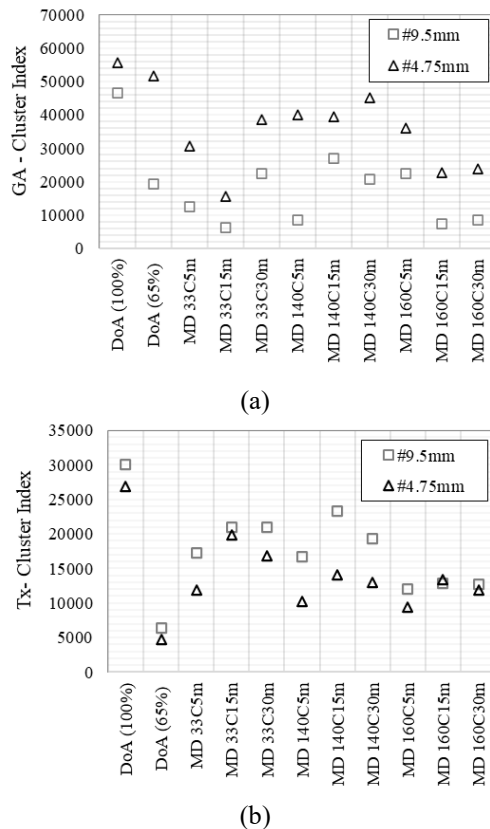
Figure 6. Gradient angularity (GA) cluster index (a) and Surface texture (Tx) cluster index (b).

Figure 6a shows that aggregate particles retained at the #9.5mm-sieve was less affected (smaller values) by the RAP cluster dissociation when compared to the #4.75mm-sieve particles, no matter the breakdown mode (binder extraction or MD). At 33°C and 140°C, the GA cluster index tends to increase as the mixing time increases for both fractions, which means a behavior closer to the white curve (DoA = 100%). However, at 160°C, as the mixing time increases, the GA cluster index decreases, meaning that the angularity values are closer to the values observed for the black curve (DoA = 0%). For texture, Figure 6b, the trend for both RAP fractions were similar in all scenarios evaluated. Sieve #4.75mm presents smaller values of Tx cluster index when compared with #9.5mm. At 160°C, the Tx cluster index is the smallest if compared with 33°C and 140°C indicating that the RAP particles texture values are closer to the black curve (DoA = 0%). These results could be explained by the fact that the RAP binder might be activated at 160°C, which introduc-

es another source of variability, as the presence of aged binder/mastic/FAM softened may help to keep the RAP cluster more resilient to abrasion, indicating less cluster dissociation. As a result, at 160°C, the RAP shape properties are closer to the black rock behavior (more angular and rougher). On the other hand, at 33°C, the RAP particles work like a traditional aggregate, which tends to be more polished and rounded after MD test.

4 CONCLUSIONS

The MD method used to breakdown the cluster formation by using temperature and mixture time was useful to the purpose of this study i.e., to examine RAP aggregates at different levels of cluster dissociation. To evaluate the scenario RAP clusters fully dissociated, the binder extraction seems to be more severe. Besides, at room temperature (33°C), the RAP may become smoother and rounded after the process using the MD equipment, closer to traditional mineral aggregate behavior. On the other hand, at 160°C, the main hypothesis is that part of the RAP binder (mastic or FAM) is activated, therefore, the RAP particles are more prone to abrasion without breaking apart, making the RAP particle rougher and more angular.

5 REFERENCES

Determining Aggregate Shape Properties by Means of Digital Image Analysis, DNIT 432 – ME (2020), (Brasilia, DF, Brazil).

Ferreira, W.L.G., Castelo Branco, V.T.F., Vasconcelos, K. and Bhasin, A. (2021). The Impact of the RAP Cluster Dissociation on Gradation and Shape Properties of Aggregates from Recycled Asphalt Mixtures, *J Test Eval 50*, no. 2, https://doi.org/10.1520/JTE20210155.

Lo Presti, D., Vasconcelos, K., Oreskovic, M., Pires, G.P., Bressi, S. (2019). On the Degree of Binder Activity of Reclaimed Asphalt and Degree of Blending with Recycling Agents, Road *Mat Pav Des* 21, no. 8. https://doi.org/10.1080/14680629.2019.1607537.

Standard Specification for Superpave Volumetric Mix Design, AASHTO M 323 – (2022) (Washington, D.C., U.S).

Standard Test Method for Quantitative Extraction of Asphalt Binder from Asphalt Mixtures, ASTM D2172 (2017), (West Conshohocken, PA, U.S).

Standard Test Method for Resistance of Coarse Aggregate to Degradation by Abrasion in the Micro Deval Apparatus, ASTM 6928 (2017), (West Conshohocken, PA, U.S).

Xu, G., Ma, T., Fang, Z., Huang, X. and Zhang, W. (2019). The Evaluation Method of Particle Clustering Phenomena in RAP. *Appl Sci* 9, no. 3, https://doi.org/10.3390/app9030424.

Zaumanis, M., Boesiger, L., Kunz, B., Mazzoni, H., Bruhin, P., Mazor, S., Poulikakos, L. (2021). Three Indexes to Characterise Crushing and Screening of Reclaimed Asphalt Pavement, *Inter Jour of Pav Eng*, no. 14, https://doi.org/10.1080/10298436.2021.1990287.

Recycling RAP in Geopolymer Concrete for Sustainable Pavement Solutions

A. Ghosh

Research Associate, Indian Institute of Technology Roorkee, Roorkee, India, a_ghosh@ce.iitr.ac.in

A. Sachdeva

PhD Scholar, Indian Institute of Technology Roorkee, Roorkee, India

S.I. Sk

Contractual Faculty, National Institute of Technology Hamirpur, Hamirpur, India

G.D.R.N Ransinchung & P. Kumar

Professor, Indian Institute of Technology Roorkee, Roorkee, India

ABSTRACT: This study investigates the potential of using coarse and fine Recycled Asphalt Pavement (RAP) fractions as substitutes for natural aggregates in paving-grade geopolymer concrete (GPC). Findings highlight that higher RAP content significantly impacts strength and durability, necessitating limitations on the proportion of RAP used. An optimal mix with 50% coarse RAP achieved a flexural strength of 4.72 MPa after 7 days of ambient curing while reducing carbon emissions by 56.16% compared to traditional concrete. Furthermore, fine RAP mixes exhibited a higher surface abrasion loss, with a maximum of 0.288 mm, indicating that coarser RAP fractions are more suitable for designing Pavement Quality Concrete (PQC). Furthermore, fine RAP mixes exhibited higher loss in surface abrasion depicting a maximum of 0.288mm suggesting the potential recycling of coarser RAP fractions for rigid pavement applications.

1 INTRODUCTION

1.1 *General*

Geopolymer Concrete (GPC) is emerging as a sustainable alternative to traditional Portland Cement Concrete (PCC), leveraging industrial by-products like Fly Ash (FA) and Ground Granulated Blast Furnace Slag (GGBS) as binders to reduce greenhouse gas emissions (Davidovits, 1988). Unlike PCC, GPC eliminates the need for cement clinkers, significantly lowering its carbon footprint. Despite extensive research on GPC for in building constructions, its potential in pavement construction, particularly for heavy traffic roads, remains underexplored. Reclaimed Asphalt Pavement (RAP) offers an additional opportunity to incorporate recycled materials, reducing the demand for natural aggregates. However, challenges such as reduced strength and workability due to adhered bitumen persist. By eliminating cement, GPC with RAP offers significant environmental advantages, including lower greenhouse gas emissions compared to PCC. This study focuses on integrating RAP into GPC for pavement applications, providing a sustainable solution that meets performance demands for heavy traffic infrastructure while enhancing environmental sustainability.

2 MATERIALS USED AND METHODOLOGY

2.1 *Materials*

This study investigated the use of Class F and GGBS as precursors for geopolymer concrete. The mechanical properties revealed a specific gravity of 2.21 for FA and 2.82 for GGBS, with respective specific surface areas of 395 m^2/kg and 424.01 m^2/kg. The XRF analysis in Table 1 indicates a Si/Al ratio of 2 for FA, confirming its suitability as a precursor, while the high Ca content in GGBS supports effective ambient curing.

For activation, 14M sodium hydroxide (NaOH) and sodium silicate (Na_2SiO_3) were used in a ratio of 0.5. Aggregates for the study were sourced from a local quarry, while RAP was obtained from a deteriorating section of the National Highway. The 20-year-old RAP was stockpiled for a year, leading to oxidation and stiffening of the asphalt. The RAP was then sieved into coarse (>4.75mm) and fine (<4.75mm) fractions, with bitumen content of 3.5% for fine RAP and 2.2% for coarse RAP. Natural aggregates included Zone II sand and coarse aggregates of 19mm and 10mm nominal sizes.

Table 1. Chemical composition of the studied wastes

Wastes	Chemical components (% by mass)									
	SiO_2	TiO_2	Al_2O_3	Fe_2O_3	CaO	SO_3	K_2O	P_2O_5	MgO	LOI (%)
GGBS	27.32	1.57	12.09	1.95	54.27	1.21	1.12	-	0.22	3
FA	56.70	3.51	26.31	7.17	1.54	0.11	2.82	1.10	-	1

*LOI- Loss on Ignition

2.2 *Methodology*

The water/geopolymer solid ratio was determined similarly to the water/binder ratio used in conventional concrete, while the alkaline activator-to-binder ratio was maintained below 0.45. To assess various substitution scenarios, natural aggregates were replaced with RAP aggregates—coarser fraction (RAP-C) and finer fraction (RAP-F)—at replacement levels of 25%, 50%, 75%, and 100%. All the considered design parameters have been based on the author's previous studies where the choice has been explicitly explained (Ghosh et. al, 2024)

The preparation of the geopolymer samples followed the process used for cement concrete mixes, starting with a dry blend of the materials, followed by a wet mixing phase. The activator solution was prepared 24 hours before casting to allow the heat generated from the sodium hydroxide and water reaction to dissipate. The samples were cured at ambient temperature to replicate real-world conditions, reflecting typical on-site curing practices.

3 RESULTS AND DISCUSSION

3.1 *Compressive strength*

The compressive strength of GPC mixtures, including those with and without RAP, was tested at 7, 28, and 90 days under ambient curing conditions (Fig. 1). Previous studies on traditional cement and geopolymer concrete (Debbarma et al., 2020) have shown that the mix using only natural aggregates consistently produced the highest strength at all measured time points. Incorporating RAP reduced compressive strength, with the RAP-F mix (fine RAP) showing less decline compared to the RAP-C mix (coarse RAP). The primary factor in this reduction was asphalt cohesion failure. Interestingly, RAP-F performed better in compression than RAP-C, despite having a higher asphalt content. At a 50% replacement rate, RAP-F reached a 7-day compressive strength of 46 MPa, outperforming RAP-C by 3.3%. In contrast, when for 100% RAP mixes, RAP-F experienced a strength reduction of 48%, whereas RAP-C saw a more significant decline of 57%. The 50% RAP-F mix met the required 40 MPa strength for PQC applications after 7 days (MoRTH, 2013), with the potential for up to 75% RAP replacement after 28 days.

The strength development of GPC follows a pattern similar to that of cement concrete, showing gradual improvement over time as Calcium-Silicate-Hydate and Calcium-Aluminate-Hydrate continue to form. The most substantial increase in strength happens within the first 28 days, after which the rate of growth significantly decreases. In conventional cement mixes, RAP's impact is more evident at 28 days, with failures attributed to asphalt cohesion. In contrast, GPC shows substantial strength development by 7 days, where failures are more related to poor bonding between RAP aggregates and the geopolymer matrix. This highlights the importance of optimizing RAP content and ensuring adequate interfacial bonding to achieve desired performance levels in GPC.

3.2 *Flexural strength*

The integration of RAP also led to a significant reduction in flexural strength, an observation similar to compressive strength decrement, regardless of the RAP type or replacement proportion (Fig 2). At all tested replacement levels and curing ages, the 25% RAP-C mix exhibited maximum flexural strength, followed by the RAP-F mixes. In contrast to the compression strength trend, RAP-C mixes performed better in flexural strength overall. At a 50% replacement level, RAP-C met the required minimum flexural strength of 4.5 MPa for PQC (MoRTH, 2013) at 7 days, while RAP-F mixes did not reach this threshold even at 28 days (4.43 MPa and 4.1 MPa, respectively). However, both RAP-F and RAP-C mixes showed satisfactory flexural strength at a 25% replacement level at both 7 and 28 days.

The 75% RAP-F mix met the required compressive strength but failed to satisfy the flexural strength requirements. This highlights the importance of flexural strength in pavement design, suggesting that coarse RAP offers superior performance compared to fine RAP when used in geopolymer concrete. The results emphasize the need for careful selection of RAP type to ensure optimal material properties for specific engineering applications.

3.3 Resistance to surface abrasion

Figure 3 presents the surface abrasion resistance, measured as wear depth (d) after 90 days of ambient curing. The control mix, which did not contain any RAP, exhibited the least wear depth at 0.05 mm. In contrast, incorporating RAP led to an increase in wear depth, suggesting a reduction in abrasion resistance. The finer RAP fraction (RAP-F) resulted in more pronounced abrasion, with the 100% RAP-F mix showing the highest wear depth of 0.288 mm. At lower replacement rates (up to 50%), the abrasion resistance across all mixes was comparable, with a mean wear depth of 0.081 mm. Although no specific standards for geopolymer mixes containing RAP exist, the results were benchmarked against conventional paver block standards, which allow a maximum wear depth of 1 mm for heavy traffic areas. This investigation underscores the feasibility of incorporating RAP into geopolymer concrete while also revealing that coarse RAP provides superior abrasion resistance.

3.4 Carbon emissions

The carbon emissions ($kgCO_2$ eq/kg) and embodied energy (MJ/kg) for materials used in both GPC and PCC were analyzed, as shown in Table 2. Due to limited regional data, insights from international studies were used, assuming they are applicable. The transportation phase was not considered, as it is assumed to be similar for both PCC and GPC. The analysis of carbon emissions and embodied energy during the production phase (Fig 4) revealed that the control GPC mix had the highest CO_2 emissions at 181.51 kg CO_2 eq./m³. Incorporating RAP significantly reduced emissions, with the 100% coarse RAP (100RAP-C) mix having the lowest emissions at 165.53 kg CO_2 eq./m³. The optimal 50% coarse RAP mix (50RAP-C) reduced emissions by 5% compared to the control mix and by 56.16% compared to PCC. Fine RAP mixes showed a less significant reduction in CO_2

emissions, likely due to the higher volume of coarse aggregates in the mix.

Energy consumption followed a similar pattern, with the control mix consuming 2282.43 MJ. The 100% fine RAP mix reduced carbon emissions and energy consumption by 8.8% and 2.71%, respectively, while 100% coarse RAP reduced emissions by 12.09% but energy use by only 2.23%. These results suggest that fine RAP is more effective in reducing energy consumption, while coarse RAP has a greater impact on reducing carbon emissions.

Table 2. Carbon and emission coefficients of studied materials

Material	Carbon Emission ($kgCO_2$ eq/kg)	Embodied Energy (MJ/kg)	Source
FA	0.01	0.1	Hammond & Jones (2008)
GGBS	0.066	0.64	Indian database, IFC (2017)
NaOH	0.625	10.8	Turner & Collins (2013)
Na_2SiO_3	0.445	5.3	Heath et al., 2014; Fawar et al., 1999
CA	0.017	0.3	Hammond & Jones (2008)
NA	0.009	0.11	Hammond & Jones (2008)
RAP	0.00209	0.0308	Lu et al. (2018)
Water	-	0.2	Hammond & Jones (2008)
Admixture	0.72	11.4	Nepune (2022); Flower & Sanjayan (2007)
Cement	0.91	6.4	Indian database, IFC (2017)
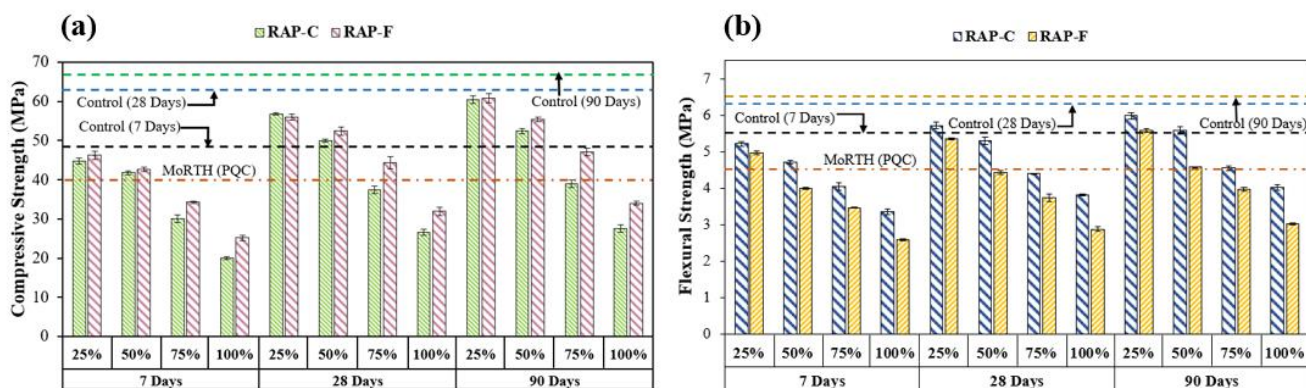
Figure 1. (a) Compressive strength and (b) flexural strength of the studied mixes at different curing periods
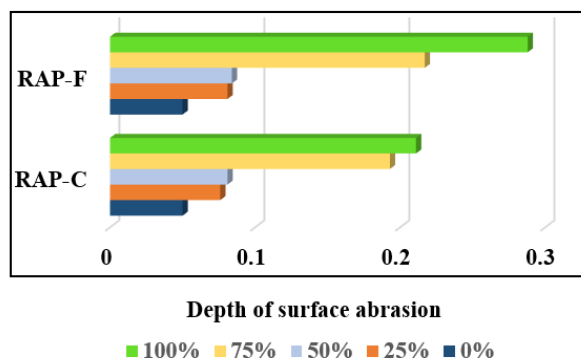
Figure 3. Resistance to surface abrasion of the different geopolymer concrete mixes
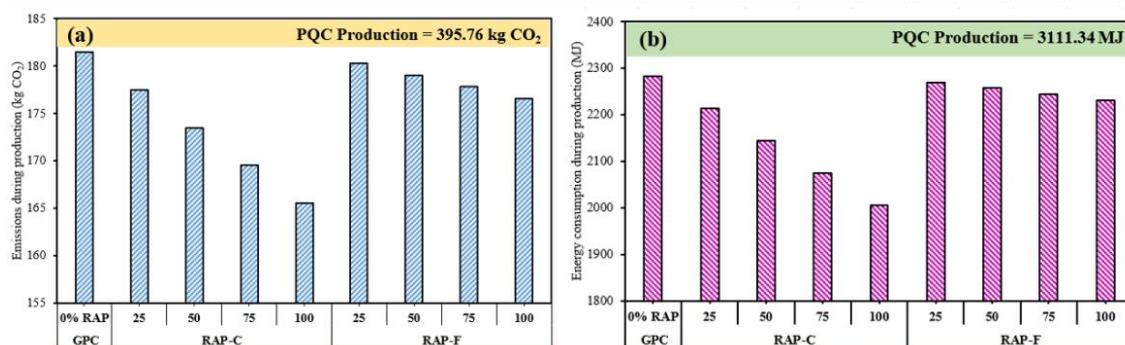
Figure 4. Carbon dioxide emissions and energy consumption during the production phase of concrete

4 CONCLUSION

This study demonstrated that coarse RAP aggregates outperformed fine RAP in flexural strength, while fine RAP provided superior compressive strength in geopolymer concrete. Replacing 50% of natural coarse aggregates with RAP in Pavement Quality Concrete (PQC) satisfied strength requirements after 7 days, achieving compressive and flexural strengths of 41.80 MPa and 4.72 MPa, respectively. Fine RAP replaced up to 25% of natural sand and up to 75% for compressive strength-focused applications. Geopolymer concrete with natural aggregates reduced carbon emissions by 50% compared to Portland cement, with a 54% reduction when 50% coarse RAP was used. Additionally, RAP-inclusive mixes exhibited strong resistance to surface abrasion.

5 REFERENCES

Davidovits, J. 1988. Geopolymer chemistry and properties. In J. Davidovits & J. Orlinski (eds.), *Proceedings of the 1st International Conference on Geopolymer* (pp. 25–48). Compiegne, France.

Debbarma, S. & Ransinchung, G. D. R. N. 2021. Achieving sustainability in roller compacted concrete pavement mixes using reclaimed asphalt pavement aggregates – state of the art review. *Journal of Cleaner Production*, 287, 125078.

Fawer, M., Concannon, M. & Rieber, W. 1999. Life cycle inventories for the production of sodium silicates. The International Journal of Life Cycle Assessment, 4(4), 207–217

Flower, D. J. M. & Sanjayan, J. G. 2007. Greenhouse gas emissions due to concrete manufacture. *International Journal of Life Cycle Assessment*, 12(5), 282–288.

Ghosh, A., Naga Gondaimei, R.R., & Kumar, P. 2024. Adopting sustainable practices in rigid pavement construction: Exploring geopolymer concrete with reclaimed asphalt pavement aggregates. Journal of Materials in Civil Engineering, 36(10), 04024317.

Hammond, G. P. & Jones, C. I. 2008. *Inventory of Carbon & Energy (ICE)*. University of Bath, Department of Mechanical Engineering.

Heath, A., Paine, K. & McManus, M. 2014. Minimising the global warming potential of clay-based geopolymers. *Journal of Cleaner Production*, 78, 75–83.

International Finance Corporation (IFC). 2017. Environmental Indicators for Materials: Methodology & Results, Version 1.0, India Construction Materials Database of Embodied Energy and Global Warming Potential. Retrieved from IFC.

Lu, Y., Wu, H., Liu, A., Ding, W. & Zhu, H. 2018. Energy consumption and greenhouse gas emissions of high RAP central plant hot recycling technology using life cycle assessment: Case study. *Pavement LCA Conference*.

Ministry of Road Transport and Highways (MoRTH). 2013. *Specifications for road and bridge works* (Fifth Revision). Indian Road Congress, New Delhi, India.

Nepune, K. 2022. Evaluation of environmental sustainability of one-part geopolymer binder concrete. *Cleaner Materials*, 6, 100138.

Turner, L. K. & Collins, F. G. 2013. Carbon dioxide equivalent (CO2-e) emissions: A comparison between geopolymer and OPC cement concrete. *Construction and Building Materials*, 43, 125–130.

Application of industrial treated wastewater in rigid pavement construction: Advancing towards sustainable infrastructure

Jallu Harishbabu
Research Scholar, Department of Civil Engineering, IIT Roorkee, Roorkee, INDIA- 247667, j_harishbabu@ce.iitr.ac.in

Nikhil Saboo
Associate Professor, Department of Civil Engineering, IIT Roorkee, Roorkee, INDIA- 247667, nikhil.saboo@ce.iitr.ac.in

Siksha Swaroopa Kar
Principal Scientist, Flexible Pavement Division, CSIR - Central Road Research Institute, New Delhi, INDIA-11002, siksha.crri@nic.in

ABSTRACT: Rigid pavement construction relies on freshwater for concrete production and subgrade compaction, contributing to the depletion of natural water resources. This highlights the urgent need for alternative water sources to reduce freshwater dependency in pavement construction. Thus, the current study investigates the use of paper and pulp industry treated secondary and tertiary wastewater in pavement quality concrete (PQC), dry lean concrete (DLC), and subgrade construction. The compaction characteristics and leaching potential of subgrade soil was assessed. Further, the mechanical and microstructural behavior of cement concrete were evaluated. Results indicated that treated wastewater marginally influenced the compaction properties of subgrade. Minerals in treated wastewater enhanced the CBR of subgrades, while metal concentrations remained within regulatory limits. The secondary treated wastewater (STWW) reduced the maximum dry density (MDD) of DLC approximately less than 5% and delayed ettringite formation in PQC. The study showed that treated wastewater from the paper and pulp industry can be a possible alternative for sustainable pavement construction practices.

Key words: Treated wastewater, pavement quality concrete, dry lean concrete, subgrade.

1 INTRODUCTION

Conventional rigid pavement construction relies on freshwater for both concrete production and subgrade compaction. The construction industry consumes 17% of the available fresh water and requires 500 liters to produce one cubic meter of concrete (De Brito and Saikia, 2013; Gagg, 2014). Excessive groundwater pumping beyond recharge rates depletes underground aquifers, making them harder to replenish. Energy consumption is inherent in all five stages of the water life cycle, including extraction, purification, transportation, utilization, treatment, and discharge (Zhou et al., 2020). Approximately 80% of freshwater extracted from natural sources is released into the environment as wastewater. However, effective treatment processes can assist in reclaiming around 70% of the discharged wastewater (Yi et al., 2011).

According to the Central Pollution Control Board, the estimated wastewater generation in India from urban sectors is nearly 72.4 million liters per day from municipal, industrial, and commercial activities. Only 28% was reused for different purposes after treatment, while the remaining treated wastewater was discharged into groundwater or rivers without further utilization (CPCB, 2021). The utilization of potable water is typically mandated in various provisions due to its well-regulated and known chemical composition.

However, where potable water is not easily accessible, alternative water sources can be effectively used in pavement construction (Kosmatka and Panarese, 1995). Several studies have investigated the use of treated wastewater in granular layer construction and concrete production (Chatveera and Lertwattanaruk, 2009; Mahdy and Kandil, 2012). However, the response of various layers in the rigid pavement, including PQC, DLC, and subgrade to non-potable water remains underexplored, leaving a need for further investigation. The scope of this study involved the use of paper and pulp industry treated wastewater at secondary and tertiary treatment levels in PQC, DLC, and in subgrade construction. The optimum dosage of treated wastewater for achieving the MDD and the corresponding mechanical properties were evaluated. The internal cement matrix was examined using scanning electron microscopy (SEM) to understand the behavior of cement at the microscopic level. Additionally, the toxicity leaching procedure assessed the potential for leaching to the ground surface.

2 MATERIALS AND PHYSICAL PROPERTIES

2.1 Cement

Ordinary Portland Cement (OPC) 43, conforming to IS:8112, (2013) was used in this study. The specific gravity and standard consistency were recorded as 3.16 and 29%, respectively.

2.2 Treated wastewater

Treated wastewater from paper and pulp industry ("Integrated Paper and Pulp Mill Ltd., Saharanpur – India") were collected at secondary and tertiary treatment levels. Chemical characterization secondary treated wastewater (STWW) and tertiary treated wastewater (TTWW) was conducted as per the American Public Health Association (APHA), (2012) guidelines shown in Table 1.

2.3 Mineral aggregates

The soil used for the experimental investigation was procured from Roorkee city, India. As per the grain size distribution (unified soil classification system), the soil was classified as silty sand (SM). Coarse aggregate of 20 mm nominal maximum aggregate size and coarse sand (Zone II) confirming to IS:383, (2002) was used for concrete production.

3 EXPERIMENTAL PROGRAM

The influence of STWW and TTWW were investigated on subgrade compaction characteristics (OMC and MDD) and strength characteristics determined by California Bearing Ratio (CBR) values. Toxicity characteristic leaching procedure (TCLP) was performed to evaluate the leaching characteristics of subgrade soil, following USEPA 1311 guidelines (USEPA, 1992). The performance of Dry Lean Concrete (DLC) was assessed based on OMC, MDD, and seven-day compressive strength as per IRC SP: 49, (2014). For PQC, the compressive strength was evaluated at 3, 7, 14, 28, 56, and 90 days of curing. Additionally, SEM analysis was conducted to assess the cement hydration.

4 RESULTS AND DISCUSSIONS

4.1 Geotechnical characterization

The OMC and MDD were determined using modified proctor density test in accordance with IS 2720 (Part 8) specifications. As shown in Figure 1, the OMC was slightly higher for STWW (9.8%) and TTWW (9.6%) compared to TW (9.5%) samples. Further, this could be attributed to the presence of suspended and dissolved solids (Table 1) in STWW act as catalyst for higher water absorption due to their spongy nature.
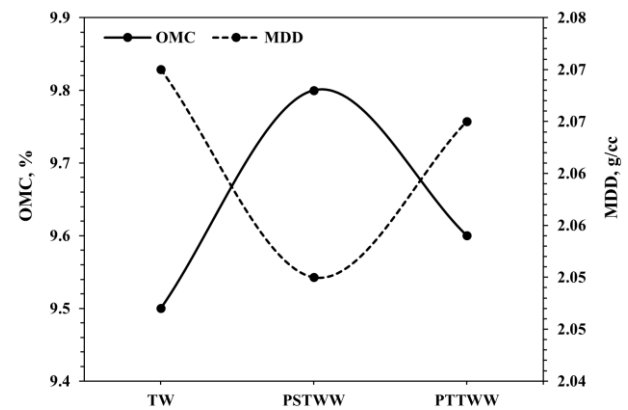
Figure 1. Compaction characteristics of TW and treated wastewater.

Similarly, the MDD of STWW and TTWW showed a marginal variation of less than 2% compared to the control sample. In the case of CBR, the soil bearing capacity increased by approximately 7% for STWW and 2% for TTWW. The improvement in CBR can be explained by the presence of minerals and nutrients in treated wastewater contributed to increasing the soil physical resilience.

4.2 TCLP

Table 2 presents the TCLP results of the subgrade prepared with TW and treated wastewater. Relatively, STWW has higher concentrations of arsenic, lead, and chromium compared to TW and TTWW. Variations in metal concentration could be due to the

Table. 1 Chemical analysis of TW and treated wastewater compared with standard guidelines.

Parameter	STWW	TTWW	TW	(ASTM 1602, 2012)	(IS 456, 2000)
pH	8.13	7.93	7.6	<3	≥ 6
Sulphate (mg/l)	7 63.5	692.5	26.67	<3000	<4000
Chloride (mg/l)	149	134	18	<0.05%	<2000
COD (mg/l)	72.4	61.2	5.2	-	-
BOD (mg/l)	42.3	31.4	0.74	-	-
TDS (mg/l)	1760	1732	198	<50,000	-
TSS (mg/l)	121	101	1	-	≤ 2000
NH_3-N (mg/l)	24.3	21.6	0.36	-	-
Total Hardness (as $CaCO_3$) (mg/l)	279	261	228.4	-	-
Turbidity (NTU)	28	16	0.4	-	-

industrial discharges, runoff, or the types of chemicals used in the treatment process. Chemical concentration in STWW may result from the accumulation of metals during wastewater treatment. However, all the water types (TW, STWW, and TTWW) have metal concentrations below the USEPA regulatory levels.

Table 2. TCLP results of subgrade soil prepared with TW and treated wastewater.

Elements	Tap water	STWW	TTWW	USEPA Reg. Level
Zinc	0.0924	0.1541	0.0724	-
Copper	0.0187	0.0190	0.0187	5
Nickle	0.0109	0.0127	0.0120	5
Arsenic	0.0546	0.0842	0.0444	5
Lead	0.0111	0.0256	0.0125	1
Chromium	0.0004	0.0342	0.0195	1
Zinc	0.0924	0.1541	0.0724	5

4.3 DLC

DLC samples (150×150×150 mm) were fabricated at different water contents ranging from 5-7%. The OMC for TW and TTWW was consistent at 6%, which can be attributed to the higher treatment quality of TTWW. However, the OMC for STWW was slightly higher at 6.5%. The MDD showed a reduction with STWW (2400 kg/m^3) compared to TW (2517 kg/m^3) and TTWW (2490 kg/m^3), indicating minor density loss with secondary treated wastewater. In terms of 7-day compressive strength, TW samples exhibited the highest value (16.5 MPa), followed by PSTWW (16 MPa) and PTTWW (15.5 MPa). These variations highlight the influence of water quality on the compaction and strength characteristics of DLC.

4.4 PQC

Figure 2 shows the compressive strength of TW and treated wastewater at different curing periods. The compressive strength results of PQC indicate that TW samples consistently achieved higher values across all the curing periods compared to STWW and TTWW. The reduction in strength could be attributed to the conversion of ettringite to monosulfate aluminate, which may disrupt the microstructure of the cement matrix. Further, residual impurities and variations in chemical composition from the treatment process may have impacted the cement hydration efficiency. However, the difference in compressive strength at 28 days of curing is approximately 6% for STWW and 7% for TTWW compared to TW.
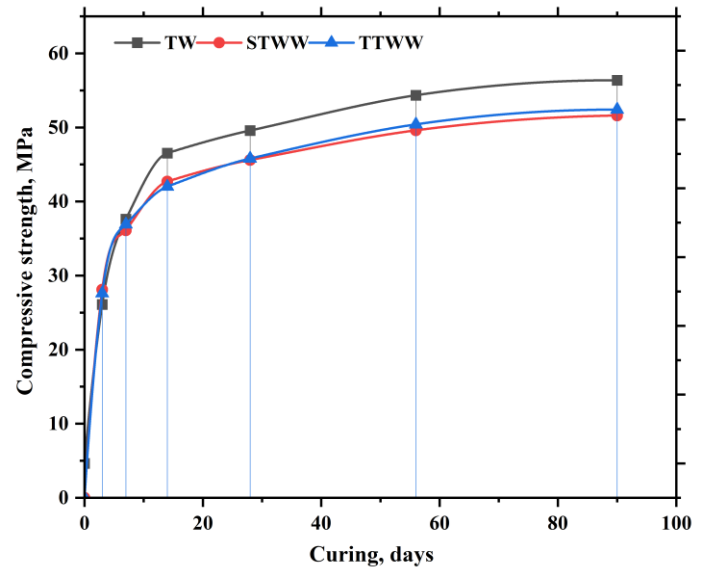
Figure 2. Variation in compressive strength of TW and treated wastewater at different curing periods.

4.5 SEM

The microstructure of PQC mixes with TW and treated wastewater at 28 days of curing can be seen in Figure 3.
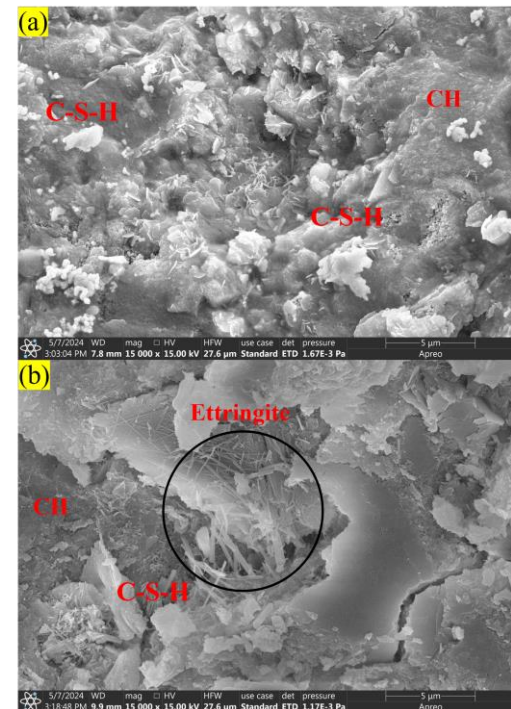
Figure 3 SEM image of PQC mix: a) TW sample at 28 days curing b) STWW at 28 days curing.

STWW was chosen for SEM image analysis due to its higher chemical concentration compared to TTWW. C-S-H gels and CH (portlandite) were evenly distributed in TW samples, indicating uninterrupted hydration.

In contrast, the presence of ettringite in the STWW PQC mix after 28 days may indicate delayed ettringite. This further leads to expansion or cracking within the cement matrix (Yan et al., 2023). In terms of density, both samples showed similar patterns. Both

samples exhibited similar microstructural patterns in terms of density and distribution of hydration products, suggesting better long-term durability.

5 CONCLUSIONS

a) Metal concentrations in STWW were relatively higher due to industrial discharges or chemical treatments but remained within USEPA regulatory limits.

b) Treated wastewater (STWW and TTWW) showed the marginal difference in compaction characteristics compared to the control sample, while the CBR improvement highlights the contribution of minerals and nutrients in treated wastewater.

c) STWW caused a slight reduction in MDD compared to TW and TTWW. Variations in compressive strength emphasize the effect of water quality on DLC properties.

d) Treated wastewater slightly reduced the compressive strength of PQC compared to TW. This reduction was possibly due to impurities interfering with the cement hydration process.

e) Delayed ettringite formation observed in STWW samples may lead to microstructural disruptions, while hydration products and density patterns suggest comparable long-term durability with TW.

6 REFERENCES

American Public Health Association (APHA), 2012. tandard Methods for the Examination of Water and Wastewater. Stand. Methods Exam. Water Wastewater 1496. https://doi.org/https://www.apha.org/

Chatveera, B., Lertwattanaruk, P., 2009. Use of ready-mixed concrete plant sludge water in concrete containing an additive or admixture. J. Environ. Manage. 90, 1901–1908. https://doi.org/10.1016/j.jenvman.2009.01.008

Ciancio, D., Beckett, C.T.S., Carraro, J.A.H., 2014. Optimum lime content identification for lime-stabilised rammed earth. Constr. Build. Mater. 53, 59–65. https://doi.org/10.1016/j.conbuildmat.2013.11.077

CPCB, 2021. Central Pollution Control Board, National Inventory of Sewage Treatment Plants March 2021.

De Brito, J., Saikia, N., 2013. Recycled Aggregate in Concrete: Use of Industrial, Construction and Demolition Waste. Green Energy Technol. 54. https://doi.org/10.1007/978-1-4471-4540-0

Gagg, C.R., 2014. Cement and concrete as an engineering material: An historic appraisal and case study analysis. Eng. Fail. Anal. 40, 114–140. https://doi.org/10.1016/j.engfailanal.2014.02.004

IRC SP: 49, 2014. Guidelines for the Use of Dry Lean Concrete as Sub-Base for Rigid Pavement , First Revision. ed. Indian Road Congress, New Delhi.

IS:383, 2002. Specification for Coarse and Fine Aggregates From Natural Sources For Concrete. Bur. Indian Stand. 24.

IS:8112, 2013. ORDINARY PORTLAND CEMENT, 43 GRADE — SPECIFICATION. Bur. Indian Stand. Second Rev, 17.

IS 2720 (Part 8), 1983. Determination of water content-dry density relation using heavy compaction. Bur. Indian Stand. New Delhi 3562–3577.

Kosmatka, Panarese, 1995. Mixing water for concrete." Design and control of concrete mixtures, 6th Canadian edn, Portland Cement Association.

Mahdy, H., Kandil, K., 2012. The use of reclaimed water in the compaction of granular materials, in: CICTP 2012: Multimodal Transportation Systems - Convenient, Safe, Cost-Effective, Efficient - Proceedings of the 12th COTA International Conference of Transportation Professionals. pp. 3295–3304. https://doi.org/10.1061/9780784412442.336

USEPA, 1992. United States Environmental Protection Agency (USEPA). Test Methods for Evaluating Solid Waste. pp. 1–35. https://doi.org/https://doi.org/https://www.epa.gov/hw-sw846/sw-846-test-method-1311-toxicity-characteristic-leaching-procedure

Yan, Y., Tang, J., Geng, G., 2023. Exploring microstructure development of C-S-H gel in cement blends with starch-based polysaccharide additives. Case Stud. Constr. Mater. 19, e02589. https://doi.org/10.1016/J.CSCM.2023.E02589

Yi, L., Jiao, W., Chen, X., Chen, W., 2011. An overview of reclaimed water reuse in China. J. Environ. Sci. 23, 1585–1593. https://doi.org/10.1016/S1001-0742(10)60627-4

Zhou, L., Xie, X., Wu, S., 2020. Use of the life cycle methodology to calculate energy consumption of Urban water cycle: A case study of Ordos city. Water (Switzerland) 12. https://doi.org/10.3390/W12092393

Low-temperature and fatigue performance of antioxidant-modified asphalt mixtures

Yongping Hu, Anand Sreeram & Gordon D. Airey
Nottingham Transportation Engineering Centre (NTEC), Faculty of Engineering, University of Nottingham, Nottingham, NG7 2RD, United Kingdom

ABSTRACT: The performance deterioration of asphalt pavements caused by oxidative ageing can theoretically be lowered by incorporating antioxidants in asphalt mixtures. In this study, zinc diethyldithiocarbamate (ZDC) was employed to evaluate its effect as an antioxidant to slow down the ageing related performance deterioration of asphalt mixtures. Both ZDC-modified and unmodified asphalt mixtures were subjected to short-term and long-term ageing. Subsequently, four-point bending (4PB) fatigue tests were carried out at 25 ºC, and indirect tensile asphalt cracking tests (IDEAL-CT) were carried out at 25 ºC and -10 ºC. The properties of long-term aged mixtures could be improved with the addition of ZDC. The ageing-mitigation efficiency of ZDC was more pronounced for the low-temperature performance (up to 69%) compared to fatigue performance (up to 44%).

1 INTRODUCTION

Bitumen within asphalt mixtures undergoes oxidation over time, leading to performance deterioration such as deteriorated fatigue and thermal cracking resistance (Petersen et al., 1996, Hu et al., 2022). One of the most promising methods to reduce the negative effects of bitumen ageing is incorporating additives termed as "antioxidants". Antioxidants are chemical additives that can theoretically slow down the rate of oxidation and extend the life of asphalt pavements. Several additives have been used as antioxidants, including Zinc diethyldithiocarbamate (ZDC), phenols, kraft lignin, quercetin (Haghshenas et al., 2021). Out of them, ZDC has been reported to be highly effective and promising (Adwani et al., 2024).

Although using antioxidants to inhibit the oxidation process in bitumen has proven to be a promising approach, a comprehensive understanding of its effectiveness remains limited. Moreover, most studies have only focused on the bitumen scale, without sufficient evidence of effectiveness at the mixture scale. In this regard, this study aims to investigate the low-temperature and fatigue performance of ZDC-modified asphalt mixtures. Such comprehensive performance evaluation can provide robust evidence for the extension of the application of antioxidants.

2 MATERIALS AND METHODS

2.1 Materials

The base bitumen used in this study was an unmodified PG 64-22 bitumen, with a penetration of 89 (0.1 mm) and softening point of 49 ºC. The aggregates were limestone, and the filler used was limestone powder. The binder content was 4.8%. The antioxidant ZDC provided by Shanghai Macklin Biochemical Technology Co., Ltd with a purity of 98%.

2.2 Test methods

The ZDC with dosages of 3 % and 5 % by mass of bitumen was blended with the neat bitumen using a propeller type mixer at 190 ºC for a period of 20 min followed by reduced temperature blending at 165 ºC for 40 min at 600 rpm. Then, the ZDC-modified bitumen was blended with aggregates and fillers to produce asphalt mixtures. The loose mixtures were conditioned in an oven at 135 ºC for two hours to simulate the short-term ageing as per AASHTO R30-22. Afterwards, the mixtures were separated into two sets. The first set was subjected to the manufacture of testing specimens. The second set was further conditioned in the oven at 95 ºC for 120 hours to simulate the long-term ageing as per NCHRP 09–54 report (Kim et al., 2021). Subsequently, the long-term aged loose mixtures were compacted.

Asphalt mixtures were compacted using a segmented rolling compactor as per ASTM D8079-23. The size of the slabs was 500 mm × 500 mm × 70 mm. Afterwards, the beams with a dimension of 380 mm × 63 mm × 50 mm were sawed from the slabs for four-point bending fatigue (4PB) tests. The cylindrical specimens were manufactured using a Marshall compactor as per ASTM D6926-20 for the Indirect Tensile Asphalt Cracking Tests (IDEAL-CT).

The 4PB fatigue tests were carried out at 25 ºC as per ASTM D8237-21 standard. Prior to testing, the specimens were placed into the environmental chamber at the same temperature for two hours of conditioning. The loading frequency was 10 Hz, and the loading strain amplitude was 500 με. The IDEAL-CT was carried out with loading rate of 50 mm/min at 25 ºC and 12.5 mm/min at -10 ºC as suggested in NCHRP Project D9-29 (Christensen and Bonaquist, 2004). Prior to testing, the specimens were placed into a freezer at the same temperature for four hours of conditioning.

2.3 Data analysis

In accordance with ASTM D8225-19, the work of failure (W_f) is calculated as the area under the load versus Load-Line Displacement (LLD) curve (Fig.1) through the quadrangle rule provided in Eq. (1).
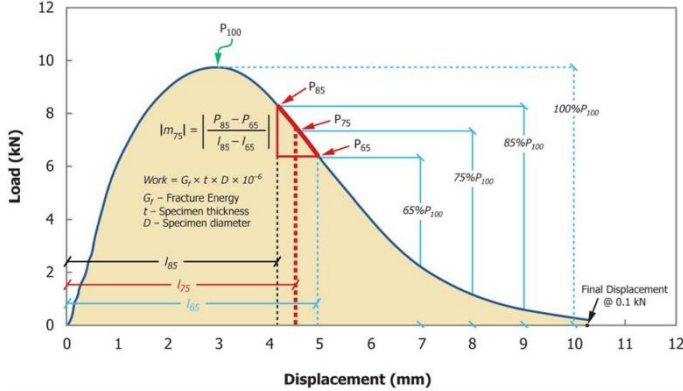
Figure 1. Load (P) versus Load-Line Displacement (LLD)

$$W_f = \sum_{i=1}^{n-1}\left[(l_{i+1} - l_i) \times P_i + \frac{1}{2} \times (l_{i+1} - l_i) \times (P_{i+1} - P_i) \right] \quad (1)$$

Where, P_i is the load at the i step, in kN, l_i is the LLD at the i step, in mm.

Failure energy (G_f) is calculated using Eq. (2).

$$G_f = \frac{W_f}{D \times t} \times 10^6 \quad (2)$$

Where, D is the diameter of specimen, in mm, and t is the thickness of specimen, in mm.

Cracking Tolerance index (CT_{index}) is calculated using Eq. (3).

$$CT_{index} = \frac{t}{62} \times \frac{l_{75}}{D} \times \frac{G_f}{|m_{75}|} \times 10^6 \quad (3)$$

Where, l_{75} is the displacement at 75% of the peak load after the peak, in mm, and $|m_{75}|$ is the absolute value of the post-peak slope, in N/m.

Cracking resistance index (CR_{index}) is calculated using Eq. (4):

$$CR_{index} = \frac{G_f}{P_{100}} \quad (4)$$

Where, P_{100} is the peak load of the tests.

Flexibility index (FI) is calculated using Eq. (5).

$$FI = \frac{G_f}{|m_{75}|} \times 0.01 \quad (5)$$

3 RESULTS AND DISCUSSION

3.1 Fatigue life

The fatigue life of each asphalt mixture is shown in Fig 2. It was seen that long-term ageing is significantly detrimental to the fatigue life of asphalt mixtures, as the fatigue life of neat long-term aged mixture was only one-fourth of that for neat short-term aged mixtures. The introduction of the antioxidant increased the fatigue life of long-term aged mixtures by around 30%, by likely mitigating the ageing-induced stiffening. Therefore, the asphalt pavements with antioxidants are expected to have longer service life and better durability. However, the difference between the fatigue lives of modified mixtures with varying dosages was insignificant, which suggested that the dosage had limited impact on the fatigue life of asphalt mixture as per this evaluation criteria.
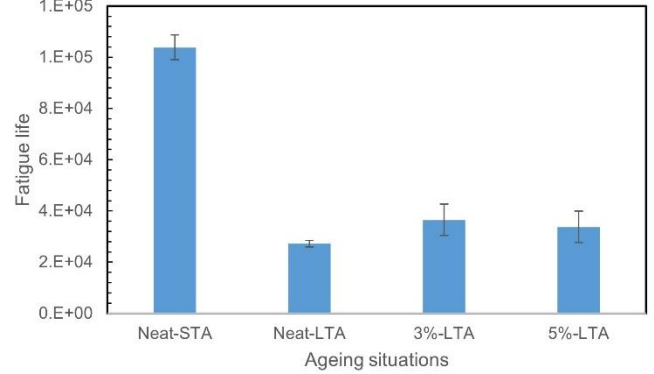
Figure 2. Fatigue life of asphalt mixtures

3.2 Cracking tolerance of asphalt mixtures at intermediate temperature

Based on the IDEAL-CT, various parameters could be derived and calculated from the raw data, such as failure energy (G_f), post-slope of load-displacement curve, indirect tensile strength (*ITS*), flexibility index (*FI*), cracking resistance index (*CR_index*), and cracking tolerance index (*CT_index*). The indices calculated for the tests at 25 °C are illustrated in Fig.3.

As shown in Fig.3 (a), the failure energies (G_f) of long-term aged asphalt mixtures were higher than that of short-term aged mixtures, indicating that more energy was required before the specimens were damaged. Interestingly, the G_f of modified mixtures after long-term ageing were even higher than that of the unmodified mixture at the same ageing levels. The correlation between G_f and cracking resistance of mixtures is controversial as previous studies have reported that G_f of long-term aged mixtures could be either higher or lower than that of short-term aged mixtures (Ling et al., 2017). Therefore, to avoid any arbitrary judgment of the antioxidant's effectiveness, G_f was used solely to illustrate changes in the properties of asphalt mixtures.

As depicted in Fig.3 (b), the slope of short-term aged mixture was the smoothest while that for the long-term unmodified mixture was the steepest. The slope of the long-term aged, modified mixtures was higher than that of short-term aged mixtures while lower than that of long-term aged unmodified mixture. A steeper slope represents that cracks could be developed quickly after the initial damage occurring (Nguyen et al., 2024). Therefore, the introduction of ZDC could effectively slow down the development of cracking during the long-term ageing process. Moreover, it was seen that the dosage of antioxidant did not

play a crucial role in the effectiveness of the effect of ZDC as the slope of mixtures modified with varying dosages of ZDC were almost identical.

For the indirect tensile strength of specimens, it was observed from Fig.3 (c) that the short-term aged mixtures had the smallest strength while the long-term aged unmodified mixture had the largest strength. The strengths of ZDC-modified mixtures after long-term ageing resided between the short-term aged and unmodified long-term aged mixtures. It has been reported in previous studies that after long-term ageing, increase in stiffness could result in the increase of strength. The introduction of the antioxidant can mitigate the stiffening effect caused by ageing, thereby reducing the strength of asphalt mixtures. When it comes to the three cracking-related indices, e.g. *FI*, *CR*~index~ and *CT*~index~, as illustrated in Fig.3 (d), (e), and (f), three indices followed identical evolution trend: short-term aged mixture had the best flexibility and cracking resistance/tolerance, while those for long-term aged unmodified mixture had the least.
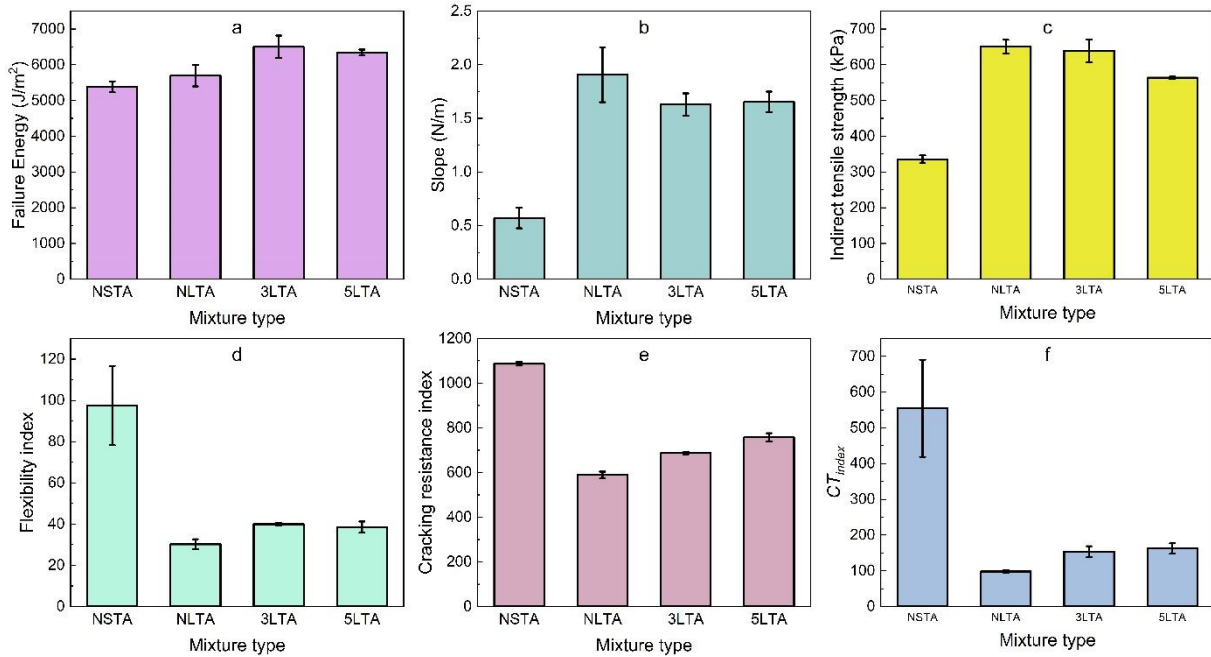
Fig.3 Indices for the IDEAL-CT at intermediate temperature: (a) Failure energy (G_f), (b) Post-peak slope of LLD curve, (c) Indirect tensile strength (*ITS*), (d) Flexibility index (*FI*), (e) Cracking resistance index (*CR*$_{index}$), and (f) Cracking tolerance index (*CT*$_{index}$)

3.3 Cracking tolerance of asphalt mixture at low temperature

Thermal cracking is the predominant distress in cold climates, causing transverse cracks perpendicular to the direction of traffic. The results of IDEAL-CT tests carried out at -10 °C are shown in Fig.4.

As illustrated in Fig.4 (a), at low temperature, e.g. -10 °C, the failure energies of mixtures showed opposite trends compared to those at intermediate temperature. As mentioned earlier, the failure energy is considered to be arbitrary and should not be correlated with the cracking resistance of mixtures (Ling et al., 2017).

For other parameters, the effect of the antioxidant on the low-temperature cracking resistance was identical with that at intermediate temperature. The primary difference between the low-temperature cracking resistance and intermediate temperature cracking resistance was that the antioxidant showed much higher effectiveness in mitigating the negative effect of ageing at low temperature. At intermediate temperatures, the incorporation of the antioxidant could improve the cracking resistance of asphalt mixture slightly, however, at low temperature, the cracking resistance of long-term aged asphalt mixture could be improved significantly. Some of the indices of the modified mixture after long-term ageing even were comparable to those for mixtures after short-term ageing. Therefore, the antioxidant could effectively mitigate the cracking-related distress of asphalt pavements in cold areas, thereby extending the service life of pavements.

The change in stiffness caused by ageing has a more significant influence on the low-temperature performance than on the intermediate-temperature performance of bitumen and asphalt mixtures. At low temperatures, asphalt mixtures tend to become very stiff and brittle, making them less able to resist loading and more prone to cracking. As mentioned earlier, the incorporation of ZDC could significantly reduce the stiffness of mixtures caused by long-term ageing, thereby improving the low-temperature performance more efficiently.
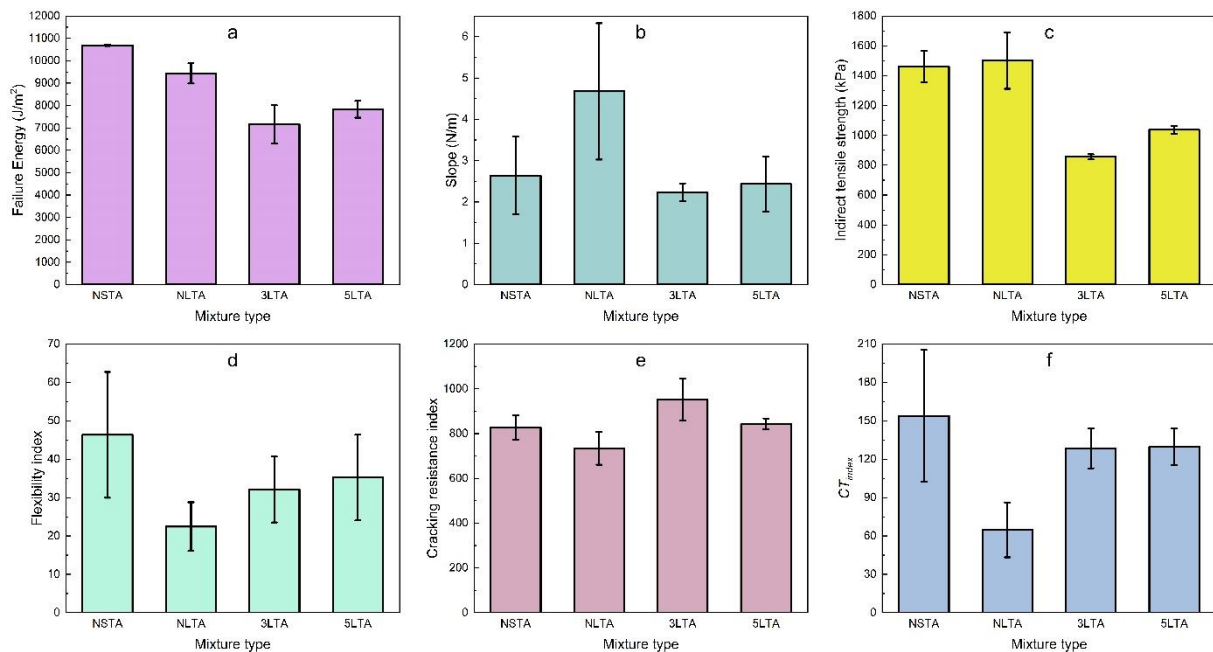
Fig.3 Indices for the IDEAL-CT at low temperature: (a) Failure energy (G_f), (b) Post-peak slope of LLD curve, (c) Indirect tensile strength (*ITS*), (d) Flexibility index (*FI*), (e) Cracking resistance index (CR_{index}), and (f) Cracking tolerance index (CT_{index})

4 CONCLUSIONS

This paper systematically characterised the ageing-mitigating effects for asphalt mixtures of ZDC-based antioxidant. Based on the results, the following conclusions could be drawn.

(1) The incorporation of ZDC could mitigate ageing effects, thereby slowing down the performance deterioration of asphalt mixtures. All properties of long-term aged asphalt mixtures measured at low temperature and intermediate temperature could be improved with the addition of ZDC.

(2) The ageing-mitigation efficiency of ZDC was more pronounced for the low-temperature performance of asphalt mixtures compared to the intermediate temperature performance.

(3) The dosage of ZDC was not directly correlated with the ageing-mitigation effectiveness of ZDC, as the lower dosage showed either higher efficiency of lower efficiency.

5 PREFERENCES

– *Adwani D., Pipintakos G., Mirwald J., Wang Y., Hajj R., Guo M., Liang M., Jing R., Varveri A., Zhang Y., Pei K., Xu X., Leng Z., Li D., Villamil W., Caro S., Chailleux E., Cantot J., Weigel S., Škultecké J., Tarsi G., Margaritis A., Wang H., Hu Y., Airey G., Sreeram A. & Bhasin A. 2024. Examining the efficacy of promising antioxidants to mitigate asphalt binder oxidation: insights from a worldwide interlaboratory investigation. International Journal of Pavement Engineering, 25, 2332363.*

– *Christensen D. W. & Bonaquist R. F. 2004. Evaluation of Indirect Tensile Test (IDT) Procedures for Low-Temperature Performance of Hot Mix Asphalt. Washington, DC: Transportation Research Board.*

– *Haghshenas H. F., Fini E., Rea R. & Khodaii A. 2021. Increasing the efficacy of recycling agents with simultaneous addition of zinc diethyldithiocarbamate as an antioxidant. Construction and Building Materials, 271.*

– *Hu Y., Si W., Kang X., Xue Y., Wang H., Parry T. & Airey G. D. 2022. State of the art: Multiscale evaluation of bitumen ageing behaviour. Fuel, 326, 125045.*

– *Kim Y. R., Castorena C., Saleh N. F., Braswell E., Elwardany M. & Rad F. Y. 2021. Long-Term Ageing of Asphalt Mixtures for Performance Testing and Prediction: Phase III Results. Washington, DC.*

– *Ling C., Swiertz D., Mandal T., Teymourpour P. & Bahia H. 2017. Sensitivity of the Illinois Flexibility Index Test to Mixture Design Factors. Transportation Research Record, 2631, 153-159.*

– *Nguyen L. N., Truong V. Q., Dao D. V., Nguyen M. H. & Tran T. 2024. Effects of rejuvenators and aging conditions on the properties of blended bitumen and the cracking behavior of hot asphalt mixtures with a high RAP content. Proceedings of the Institution of Mechanical Engineers, Part L: Journal of Materials: Design and Applications, 14644207241236901.*

– *Petersen J. C., Harnsberger P. M. & Robertson R. E. 1996. Factors affecting the kinetics and mechanisms of asphalt oxidation and the relative effects of oxidation products on age hardening. United States.*

Pavements through waste valorization: MSWI Bottom ash as viable fine aggregate alternative

Mahadevapura Krishnegowda Sachin Gowda, Aakash Gupta and Vasant G Havanagi
CSIR-Central Road Research Institute (CRRI), New Delhi, India-110025.

ABSTRACT: Despite growing interest in using Municipal Solid Waste Incineration Bottom Ash (MSWI-BA) in road construction, understanding its performance and environmental impact is crucial. With natural aggregates becoming scarce and the need for sustainable waste management increasing, this study examined replacing fine aggregates in Bituminous Concrete Grade-2 (BC-II) mixes with MSWI-BA at levels from 0-50%. Results showed that while MSWI-BA requires more binder due to its porosity, up to 20% replacement improved Marshall stability, stiffness, and moisture resistance. The 20% MSWI-BA mix achieved optimal performance, meeting MoRT&H specifications. Though higher replacement levels (up to 30%) showed slight increases in rutting susceptibility, they still performed satisfactorily. The TCLP confirmed the MSWI-BA was non-hazardous and effectively encapsulated. Thus, up to 20% MSWI-BA replacement in BC-II mixes is recommended for a balance of performance and environmental benefits.

1 INTRODUCTION

In 2022, India generated over 170,300 metric tonnes of municipal solid waste (MSW) daily, reflecting a 6% increase from the previous year [1]. Despite a high collection efficiency of 95.4%, 80-90% of MSW is still inadequately managed, leading to significant environmental pollution. The composition of MSW, largely biodegradable, inert, and recyclable materials, underscores the need for advanced waste management solutions. MSWI bottom ash, a byproduct of waste incineration, shows potential as a substitute for traditional aggregates in construction, though it requires treatment to address heavy metal contamination [2]. Successful applications in countries like the Netherlands and Germany demonstrate that, with proper regulations and quality controls, MSWI bottom ash can be effectively utilized in road construction, contributing to sustainability and reducing reliance on natural aggregates. Our research aims to explore MSWI bottom ash as a sustainable partial replacement for aggregates in bituminous mixtures, addressing landfill limitations and disposal challenges.

2 OBJECTIVES

This study evaluates the performance of MSWI-BA as a fine aggregate replacement in Bituminous Concrete Grade II (BC-II) mixes. It focuses on key properties such as Marshall Parameters, volumetrics, stiffness, moisture resistance, cracking susceptibility, and rutting susceptibility. The research will determine the optimal replacement percentage (0% to 50%) to enhance performance while meeting MoRT&H specifications. Additionally, it will assess the influence of MSWI-BA porosity on binder requirements, conduct leaching tests (TCLP) for environmental safety, and explore its potential as a sustainable alternative to natural aggregates in road construction, ultimately providing recommendations for its effective use in BC-II mixes.

3 MATERIALS USED

3.1 *Bitumen*

This study utilized a viscosity-graded binder (VG-40), and its physical properties were tested following standard guidelines. The results showed a softening point of 51.0°C (ASTM D36-14), ductility greater than 100 cm (ASTM D113-17), a penetration of 42.0 mm (ASTM D5M-20), specific gravity of 1.06 (ASTM D70-21), and a viscosity of 450 cS at 135°C (ASTM D4402-15). These values confirm the binder's suitability for use in asphalt mixtures.

3.2 *Conventional Aggregates*

The physical properties of the aggregates used in this study were tested according to standard guidelines. The combined index (flakiness and elongation) was 34.56% (IS 2386 Part 1:1963), the aggregate impact value was 17.71% (IS 2386 Part 4:1963), and the Los Angeles abrasion value was 27.1% (IS 2386 Part 4:1963). These results ensure the aggregates meet the required criteria for use in the asphalt mix.

3.3 *Physical characteristics of MSWI-BA*

The performance characteristics of the tested material reveal a specific gravity of 2.11 and an absorption rate of 15.02% (ASTM C 128 – 15). The liquid limit is 33.60%, while it shows non-plastic behavior at the plastic limit (AASHTO T 90 – 16). The modified Proctor density is measured at 17.06 KN/m³ with an optimum moisture content (OMC) of 14.04% (ASTM D1557 – 12). The California Bearing Ratio (CBR) is notably high at 100% (ASTM D1883 – 21),

indicating excellent strength, and the permeability is measured at 1.74 x 10⁻⁴ cm/sec (ASTM D2434 – 22), suggesting moderate drainage properties.

3.4 *Morphological characteristics of MSWI-BA*

The SEM analysis of MSWI-BA, as shown in Figure 1, revealed a complex and heterogeneous morphology characterized by irregularly shaped particles with a rough surface texture. The ash particles exhibited high porosity, with numerous voids and interconnected channels evident at higher magnification. Variations in grey levels across the particles may indicate compositional or density differences within the material. The observed morphology is consistent with the thermal history of MSWI-BA, where high incineration temperatures induce partial melting and subsequent solidification of various waste constituents, forming agglomerated and porous structures.
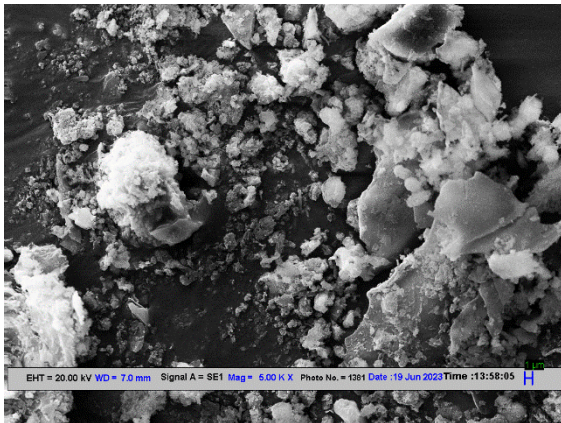
Figure 1. SEM images of MSWI-BA (Magnification = 10.0K X)

3.5 *Chemical Characterization of MSWI-BA*

The XRD results of MSWI-BA indicate a dominant presence of silica (SiO_2) at 54.3%, followed by calcium oxide (CaO) at 12.8%, and alumina (Al_2O_3) at 9.7%, along with other oxides such as iron oxide (Fe_2O_3), magnesium oxide (MgO), and potassium oxide (K_2O). The high silica content suggests potential pozzolanic properties that can enhance the strength and durability of asphalt mixes when used as a fine aggregate replacement. Additionally, the presence of CaO indicates potential cementitious reactions, improving aggregate-asphalt binder bonding and enhancing mechanical properties like stiffness and deformation resistance.

4 EXPERIMENTAL PROGRAM, RESULTS, AND DISCUSSION

The MSWI-BA was thoroughly dried and then incorporated into the mix by substituting the designated percentage of fine aggregates (from 0 to 50 % replacement for fine aggregates with 10% increments), meeting the gradation requirement of the BC-II mix [4]. Subsequently, bitumen, heated to a mixing temperature, was added to the aggregate-MSWI-BA blend, and the mixture was thoroughly mixed to ensure uniform coating of the constituent particles. Marshall Specimens were then prepared by compacting the mix using a Marshall compactor, applying 75 blows on each face of the specimen. The Marshall mix design method (ASTM D 6927, 2015) was employed to determine the OBC for each mix.

4.1 *Volumetrics*

As shown in Table 1, the optimum binder content (OBC) demonstrated a clear increasing trend with the percentage of MSWI-BA replacement. This trend is consistent with previous studies [3]] suggesting that the higher porosity and asphalt absorption capacity of MSWI-BA particles compared to conventional fine aggregates contribute to increased binder content.

Table 1. OBC for different mixes

Mix type	OBC (%)	VMA (%)	VFB (%)
Control Mix	5.73	16.75	76.12
10 % Replacement	5.95	14.17	71.06
20 % Replacement	6.16	14.21	71.12
30 % Replacement	6.36	14.58	71.52
40 % Replacement	6.70	15.08	72.93
50 % Replacement	7.40	15.41	74.04

4.2 *Marshall Stability and Flow*
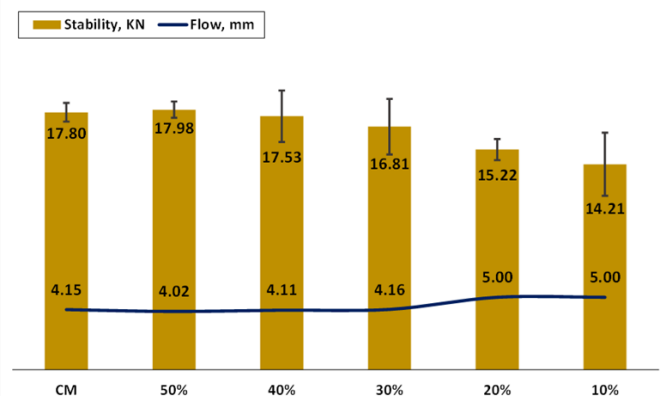
Figure 2 highlights the effects of MSWI-BA replacement on Marshall Stability and Flow. The mix with 10% MSWI-BA showed a slight improvement in stability compared to the control mix (CM), but stability declined as MSWI-BA content increased further, attributing the decline to increased binder film thickness and smoother MSWI-BA particles, which reduce interparticle friction and bonding. Flow values mostly remained acceptable, except for mixes with 40% and 50% replacement, where flow exceeded 5 mm, indicating a potential for increased rutting susceptibility.

Figure 2. Marshall Stability & Flow v/s % replacement of MSWI-BA

4.3 Moisture Susceptibility and Indirect Tensile Strength

The AASHTO T-283 indirect tensile test results (Figure 3) show that mixes with MSWI-BA exhibited higher ITS values compared to the control mix, which can be attributed to the increased binder content due to MSWI-BA's porous nature. This enhanced binder content improves the mix's cohesive forces, resulting in greater tensile strength. Additionally, the TSR values remained above the required 80%, indicating strong moisture resistance. The presence of SiO_2 (54.3%), CaO (12.8%), Al_2O_3 (9.7%), and Fe_2O_3 (5.4%) in MSWI-BA contributes to improved tensile strength, bonding, and durability. These oxides help preserve the mix's moisture resistance, making MSWI-BA a viable alternative to conventional aggregates in asphalt mixes without compromising performance.
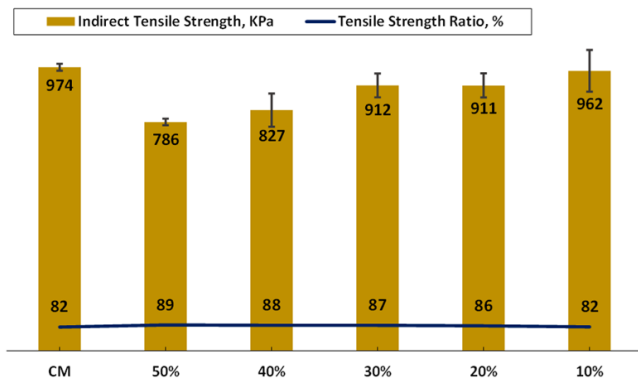
Figure 3. ITS & TSR Values for different mixes

4.4 Resilient Modulus

The MR test results, depicted in Figure 4, show that at 25°C, bituminous mixes with MSWI-BA demonstrated higher stiffness (MR values) than the control, with the 50% replacement mix achieving the highest stiffness (5713 MPa). This can be attributed to the increased binder content and the angular shape of MSWI-BA, which enhances interparticle friction and load distribution. The high silica (SiO_2 at 54.3%) and calcium oxide (CaO at 12.8%) content in MSWI-BA contributes to the improved stiffness and deformation resistance. However, as temperatures increased to 35°C, all mixes saw reduced MR values, indicating temperature sensitivity. This trend suggests that while MSWI-BA enhances stiffness at lower temperatures, it may reduce the mix's resistance to deformation at higher temperatures.

4.5 Rutting Evaluation (Dynamic Creep Test)

The dynamic creep test results, as shown in Figure 5, highlight the impact of MSWI-BA on the rutting resistance of bituminous mixes. While mixes with higher MSWI-BA replacement levels (40% and 50%) exhibited increased permanent deformation under repeated loading, indicating greater rutting susceptibility, mixes with lower MSWI-BA content (10%, 20%, and 30%) demonstrated improved resistance to deformation. The higher binder content required for MSWI-BA mixes, combined with the porous and angular nature of MSWI-BA, contributed to both softening at elevated temperatures and stress concentrations within the mix. However, the chemical composition of MSWI-BA, particularly its high SiO_2 and CaO content, plays a significant role in enhancing stiffness and bonding, which improves rutting resistance at lower replacement levels. This mixed behaviour suggests that while MSWI-BA can enhance pavement performance, the replacement percentage must be carefully optimized to balance stiffness, strength, and deformation resistance, particularly under the stresses and temperatures typical of heavy traffic loads.
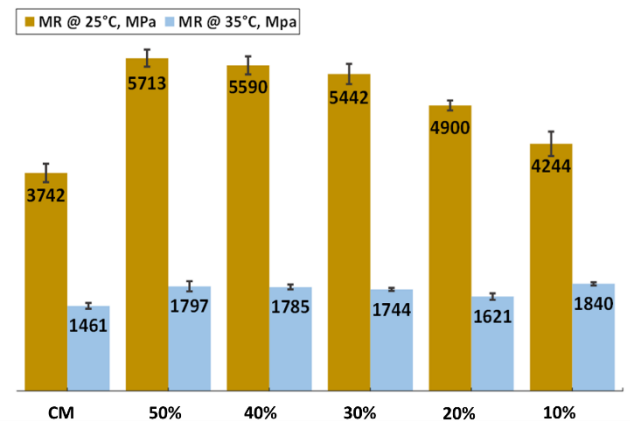
Figure 4. Resilient Modulus values at 25°C and 35°C
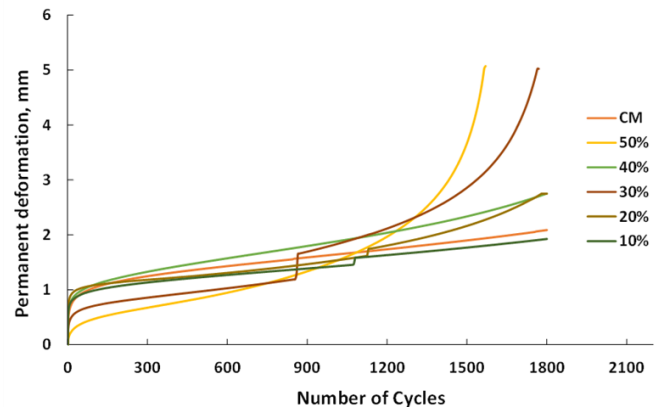
Figure 5. Permanent Actuator deformation for different mixes

4.6 IDEAL-CT Test

Key performance parameters—CT (Cracking Tolerance)-Index, |m75|, Fracture Energy (G_f), L75/m75 ratio, and AFR—are critical for evaluating asphalt mixtures cracking resistance and flexibility (ASTM D 8225, 2019). The IDEAL-CT test results show that MSWI-BA improves cracking resistance and flexibility at 10% to 40% replacement levels, attributed to CaO and Al_2O_3, which enhance bonding and toughness. Higher CT-Index, lower |m75|, and increased G_f values at these levels suggest balanced stiffness and

flexibility, improving stress distribution and crack resistance (Table 2). However, at 50% replacement, excessive stiffness and brittleness reduce performance due to high SiO_2 content, highlighting the need for optimal MSWI-BA dosage.
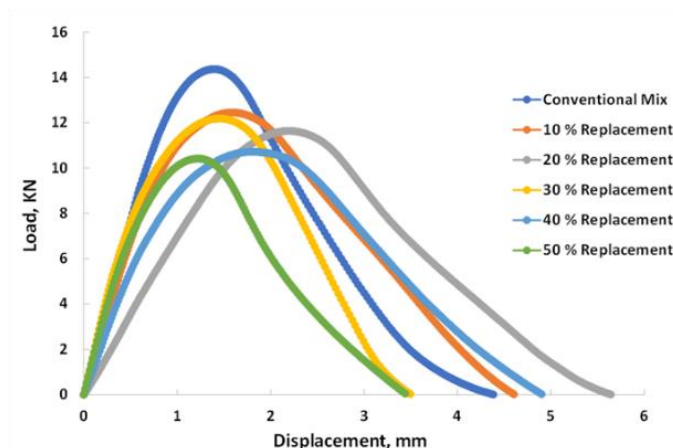
Figure 6. Load v/s Displacement Curves

Table 2. CT-Index test results

Mix type	CT-Index	$|m_{75}|$	G_f (N/m^2)	L_{75}/m_{75}
Control Mix	12.09	8.19	16.75	0.25
10 % Replacement	25.03	5.03	14.17	0.49
20 % Replacement	31.46	5.25	14.21	0.58
30 % Replacement	10.80	7.84	14.58	0.27
40 % Replacement	28.56	4.66	15.08	0.60
50 % Replacement	7.11	7.47	15.41	0.23

4.7 *Environmental Evaluation (TCLP)*

A comprehensive environmental evaluation was conducted to address concerns about the potential leaching of heavy metals from MSWI-BA, focusing on lead (Pb). The Toxicity Characteristic Leaching (TCLP) test, as per USEPA Method 1311, was performed on raw MSWI-BA and asphalt mixes containing MSWI-BA. Results indicated that lead concentrations in the leachate were well below the regulatory limit of 5.0 mg/L set by the CPCB of India. Specifically, raw MSWI-BA showed a lead concentration of 0.77 mg/L, which was reduced to 0.08 mg/L when incorporated into bituminous mixes. This reduction is attributed to the encapsulation properties of the bituminous binder, which immobilizes heavy metals, preventing their leachability. The oxides in MSWI-BA, such as CaO and SiO_2, likely stabilize lead by forming insoluble compounds. These findings, consistent with previous studies, suggest that using MSWI-BA in asphalt pavement does not pose significant environmental risks and is a sustainable alternative in road construction.

5 CONCLUSIONS

This study demonstrates the viability of using MSWI-BA as a sustainable alternative to conventional fine aggregates in BC-II mixes, enhancing key pavement performance metrics. While MSWI-BA requires a higher binder content due to its porosity, it improves Marshall Stability and stiffness, particularly at moderate replacement levels up to 30%, with 20% identified as optimal for balancing stability, flow, and volumetric properties. Performance tests show increased tensile strength, stiffness, and cracking resistance, though brittleness and rutting susceptibility rise at higher replacement levels. Environmental assessments via TCLP confirmed that MSWI-BA is non-hazardous, with heavy metal leaching well below regulatory limits, thanks to the encapsulation by the bituminous binder. Overall, MSWI-BA offers a sustainable and technically feasible alternative for BC-II mixes at levels up to 20%, contributing to resource conservation, waste valorization, and improved pavement performance, though careful consideration of higher replacement levels is necessary. Further studies on long-term field performance and environmental sustainability are recommended to unlock MSWI-BA's full potential in pavement construction.

6 ACKNOWLEDGMENTS

7 REFERENCES

[1] Municipal Solid Waste generated in India to increase 7 times next 30 years (factly.in)

[2] Rana, R., Ganguly, R. & Gupta, A.K. Physico-chemical characterization of municipal solid waste from Tricity region of Northern India: a case study. J Mater Cycles Waste Manag 20, 678–689 (2018). https://doi.org/10.1007/s10163-017-0615-3

[3] Colonna, P., Berloco, N., Ranieri, V., & Shuler, S. (2012). Application of bottom ash for pavement binder course. Procedia - Social and Behavioral Sciences, 53, 961-971. https://doi.org/10.1016/j.sbspro.2012.09.945

[4] MoRTH, Specifications for Road Bridge Works 5th Revision, 2013.

Effect of lignin-modification on the rheological properties of bitumen

S. Leischner, L. Tolsdorf, E. Kamratowsky, A. Mangalath Shine, A. Zeissler and G. Canon Falla

TU Dresden, Dresden, Saxony, Germany

ABSTRACT: This publication presents the outcome of a study which sought to evaluate the rheological behavior of lignin-modified bitumen (bitumen 50/70 with 20% lignin) using 3 different kinds of lignin. In particular, the properties of the lignin-modified bitumen are compared with those of a conventional bitumen (50/70). As part of the present study, the chemical composition of all bitumen was initially analyzed. In the laboratory study, the rheological properties of the bitumen were analyzed using the results of tests with the dynamic shear rheometer (DSR) and the corresponding properties were compared. Conclusions could be drawn regarding the rheology of the analyzed lignin-modified bitumen in comparison to the unmodified base bitumen.

1 INTRODUCTION

Since its inception, bitumen, a by-product of petroleum refining, has been the subject of considerable attention. The applications of bitumen have gradually expanded in line with the advancement of human understanding and technological progress. To date, asphalt has become a significant raw material in a number of industries, including road construction, civil engineering and roof waterproofing. A substantial proportion of the global annual production of bitumen is consumed in the construction and maintenance of roads, thereby confirming its dominant role in the use of bitumen in the construction industry. However, the non-renewable nature of bitumen, in conjunction with the reduction in global oil reserves and the influence of external factors, has resulted in consistently elevated bitumen prices. The current situation is having a significant impact on the pavement industry, where there is an increasing demand for the construction and maintenance of asphalt pavements. Consequently, there is also an increasing demand for bitumen. The growing contradiction between supply and demand makes it imperative to look at least for a partial replacement of crude oil based bitumen that is environmentally friendly, renewable and ensures a stable supply.

The use of lignin in flexible pavements is not a new concept, Terrel [1] presented a report related to the evaluation of wood lignin as a substitute or extender of asphalt. However, recently there has been a significant increase in interest in this topic as noted by Gaudenzi, et al. [2]. In particular, over the last decade there has been an exponential rise in research about the use of lignin in pavements. These studies explore different types of applications: as a bitumen modifier, extender or partial replacement of bitumen [3], and as an antioxidant additive [4]. The lignin has demonstrated the ability to act as a neutralizer, "hunter", stabilizer, and inhibitor of free radicals produced during oxidation processes. This antioxidant property is primarily due to the presence of phenolic groups that, given the presence of hydroxyls, have the ability to donate an electron to the free radical, affecting its reactivity and stabilizing it and thereby reducing their effects on the pavement material [4]. These multifunctional properties of lignin underscore its potential as a sustainable and effective practical bitumen replacement.

2 MATERIALS TESTED

In this research, a bitumen classified as 50/70 (1/10mm) penetration grade, commonly used in asphalt pavements in Germany, was selected as the base bitumen. The 3 types of lignin employed in this research and their chemical composition are listed below (Table 1). The chemical analysis of the lignin materials was carried out at the Pontifical Catholic University of Chile. While Kraftlignin and Organosolv-Lignin have similar chemical compositions, Lignosulfonate shows high sulfur and nitrogen content as well as low carbon content. To assess the ef-

fectiveness of bitumen incorporating lignin, bitumen samples were prepared with 20 M.-% lignin. The selected lignin percentage was chosen by prior experimental research [3]. Kraftlignin is sourced from Chile, while Organosolvlignin and Lignosulphonate are supplied from Germany.

Table 1. Main chemical components of the lignin variants.

Materials	N [%]	C [%]	H [%]	S [%]
Kraftlignin	0.20	63.6	5.7	1.40
Organosolv-lignin	0.17	63.2	5.9	0.37
Lignosulfonate	1.32	41.9	4.4	5.45

The production of a homogeneous mixture of lignin-modified bitumen presents a number of challenges, largely due to the hydrophilic nature of lignin. It was therefore essential to exercise strict control over the mixing parameters, including temperature and rotation speed of the high shear mixer used. The optimal parameters for the mixing process were a constant mixing temperature of 135°C, a mixing rotation speed of 5000 rpm, and a mixing duration of 60 minutes. To simulate the ageing process, the blends were subjected to short-term ageing in a laboratory setting, in accordance with the requirements of EN 12607-1 [5], using a rolling thin film oven (RTFO) at 163°C for a period of 75 minutes. Table 2 provides an overview of the different materials tested in this study.

Table 2. Sample labeling.

Sample	Modification	Aging Status
B50/70	base bitumen	unaged
B50/70-a	base bitumen	RTFO aged
B50/70 KL	20% Kraftlignin	unaged
B50/70 KL-a	20% Kraftlignin	RTFO aged
B50/70 OL	20% Organosolv	unaged
B50/70 OL-a	20% Organosolv	RTFO aged
B50/70 LL	20% Lignosulfonate	unaged
B50/70 LL-a	20% Lignosulfonate	RTFO aged

3 DSR TESTS

To evaluate the rheological properties of the materials, temperature frequency sweeps (TFS) were conducted within a temperature range of 70°C to -40°C at 10 K intervals. The tests were performed in a strain-driven mode, adjusting the strain level to stay within the linear viscoelastic range of the materials. The frequency sweeps covered a range from 0.152 to 15.92 Hz, with 10 frequencies per decade. Two samples were tested for each variant. With the results of the TFS, master curves were employed to describe the frequency-temperature dependency of the complex shear modulus (G*) and phase angle (δ). The shift factors were determined using the Williams-Landel-Ferry (WLF) function [6] to produce a continuous master curves. The reference temperature was chosen as 20°C. The results of the TFS were used to fit the 2S2P1D model [7] in conjunction

with the Time Temperature Superposition (TTS) principle.

4 DSR TEST RESULTS

4.1 *Rheology*

The outcomes of the TFS tests are illustrated in Figures 1 and 2. Firstly, the rheological data obtained from the TFS tests were employed to construct the master curves. Because smooth master curves could be constructed, all bitumen tested are thermo-rheological simple materials.
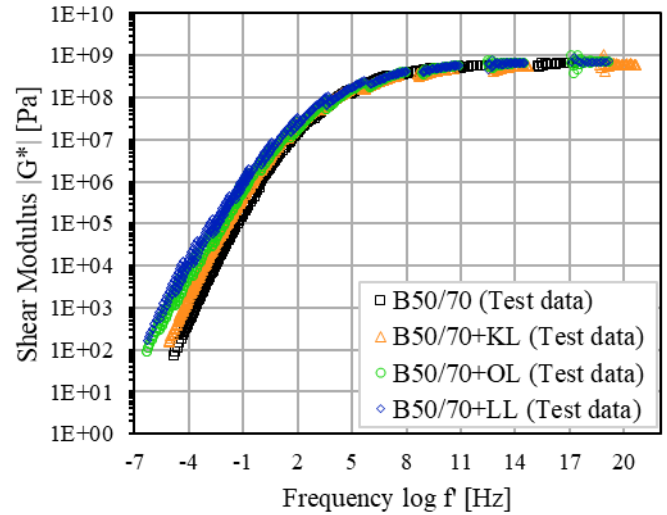
Figure 1. Master curves for the unaged materials tested (reference temperature = 20°C).

The incorporation of lignin into the bitumen results in a stiffening of the binder, as evidenced by the upward shift of the functions. Figure 2 presents the Cole-Cole plots of all materials tested in RTFO-aged condition.
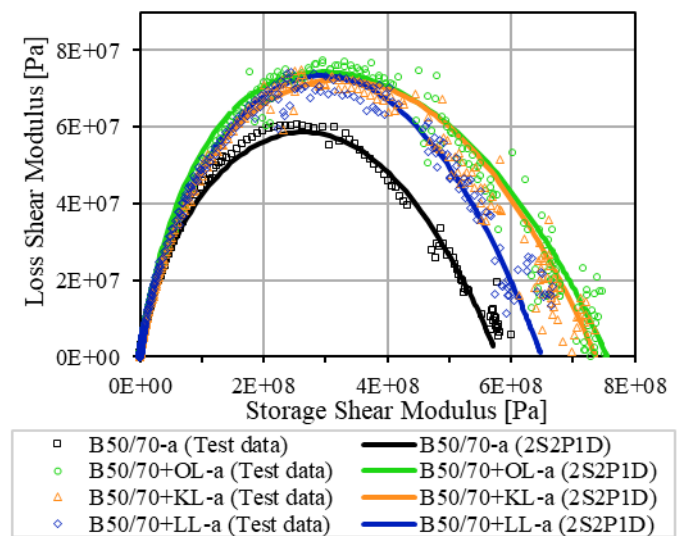
Figure 2. Cole-Cole plots of the RTFO-aged materials tested including 2S2P1D curves.

Analyzing the values of the base bitumen and the overall shape of each curve, all lignin-modified bitumen have higher G' and G'' values, which is owed to their higher stiffness. The B50/70+KL and B50/70+OL show similar Cole-Cole plots and hence

a similar rheological performance possibly due to the similar chemical composition of the lignin. The B50/70 LL is less stiff in aged condition at low temperatures compared to the other lignin modified bitumen. The shift factors utilizing the WLF method are presented in Table 3 and the 2S2P1D model parameters are listed in Table 4.

Table 3. WLF parameters.

Materials	WLF Parameters	
	C_1 [-]	C_2 [K]
B50/70	14	115
B50/70-a	21	163
B50/70 KL	14	105
B50/70 KL-a	20	130
B50/70 OL	20	130
B50/70 OL-a	20	130
B50/70 LL	20	130
B50/70 LL-a	19	150

Table 4. 2S2P1D model parameters, $\beta = 371$, $h = 0.58$.

Materials	2S2P1D Parameters					
	G_∞ [MPa]	α [-]	k [-]	τ_0 [s]	R^2_{G*} [−]	R^2_δ [−]
B50/70	640.87	2.64	0.23	2.65E-06	0.995	0.997
B50/70-a	578.22	3.60	0.24	1.44E-05	0.995	0.994
B50/70 KL	614.08	2.70	0.23	1.21E-05	0.998	0.986
B50/70 KL-a	736.87	3.15	0.23	6.87E-05	0.993	0.956
B50/70 OL	702.73	2.30	0.23	1.32E-05	0.992	0.968
B50/70 OL-a	755.75	2.50	0.21	2.89E-05	0.992	0.968
B50/70 LL	723.99	2.30	0.22	2.92E-05	0.992	0.986
B50/70 LL-a	649.75	3.15	0.26	3.21E-05	0.999	0.982

The Cole-Cole plots presented in Figure 2 demonstrate the actual data and the values predicted by the 2S2P1D model. A small gap between the actual and predicted data, which is also evidenced by the R^2 values shown in Table 4, indicates that the 2S2P1D model provides a good fit for the materials tested. It can be concluded that the 2S2P1D model is capable of adequately modelling the rheological behavior of the lignin-modified bitumen tested. As a result of the aging process, the value of the parameter α increases. The G_∞ values of the aged lignin-modified bitumen are larger than that of the B50/70-a, which indicates a higher stiffness at low temperatures. The k parameter is largest for the B50/70 LL-a which implies a rheological different performance at low temperatures compared to the other lignin-modified bitumen.

4.2 Aging performance

The change in relevant properties of bituminous materials due to aging can be assessed using an aging index, AI:

$$AI = P_{aged}/P_{unaged} \qquad (1)$$

where P_{unaged} - any physical property measured on the unaged bituminous materials, and P_{aged} - the same physical property measured under aged conditions.

To determine the aging index AI_{G*}, the complex shear modulus at 40°C down to -10°C at a frequency of 10 Hz was employed. A material with a low AI_{G*} is less susceptible to the effects of aging, and therefore exhibits fewer changes in comparison to unaged materials. Figure 3 illustrates the AI_{G*} for all materials.
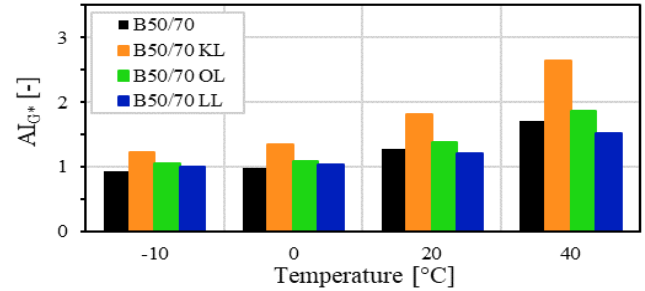
Figure 3: AI_{G*} at 10 Hz for the materials tested.

The findings indicate that the base bitumen B50/70 and the B50/70+LL exhibits reduced sensitivity to aging effects in comparison to the lignin-modified bitumen B50/70+KL and B50/70+OL. Among the lignin-modified bitumen, the B50/70 KL demonstrates the highest degree of aging susceptibility.

4.3 Modification Index

To present the lignin modification effects on the bitumen, the modification index (MI) was first calculated for the complex shear modulus at different temperatures at a frequency of 10 Hz (Figure 4). The formula used is as follows:

$$MI = M/B \qquad (2)$$

where M – the modified bitumen property and B – the corresponding base bitumen property. In general, the modification of lignin results in an increase in stiffness, in unaged and aged state.
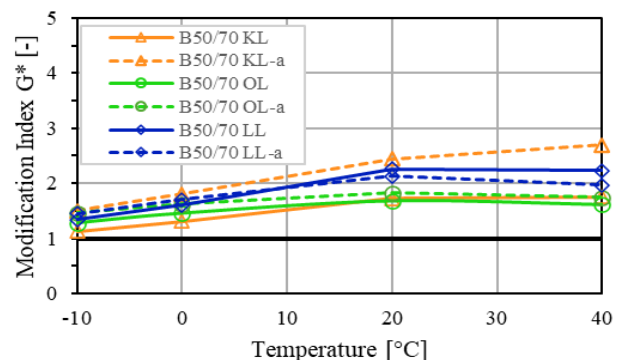
Figure 4. MI of complex shear modulus at 10 Hz for the materials tested.

In the aged state, the highest rise in stiffness is observed for B50/70 KL. Similar stiffening effects were observed in mastic samples [8], indicating that lignin may act also as a filler.

In order to provide a concise overview and evaluation of the findings related to the rheology of the

aged lignin-modified bitumen in comparison to the base bitumen, a spider diagram, was developed (Figure 5) for the MI on the basis of the following parameters: phase angle at 10 Hz and 20°C (representing the rheology at medium temperatures), Glass shear modulus (represents the response at low temperatures), complex shear modulus at 20°C and 10 Hz (representing the stiffness at medium temperature range), AI_{G*} and AI_δ at 20°C and 10 Hz (representing the aging at medium temperature range).
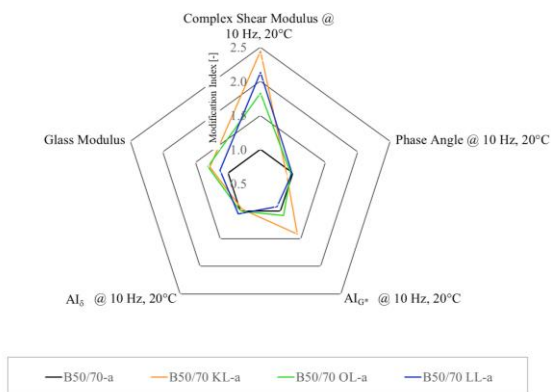
Figure 5. Modification indices.

The most significant effects of lignin modification are manifested in terms of a considerable increase in G* and a slight increase in G_∞. In the case of Kraft lignin-modified bitumen, a higher degree of aging susceptibility can be observed.

5 CONCLUSIONS

This article examines the impact of three different lignin on the performance of a bitumen, pen grade 50/70, at a representative quantity of 20 M.-%. The analysis was focused on rheological characterization with the objective of evaluating the potential antioxidant effect of lignin. The rheological performance was evaluated through a TFS test, which was employed to assess the viscoelastic properties. In light of the findings, the following conclusion can be drawn.

- It is possible to modify bitumen by adding lignin. The modification with lignin significantly impacts the bitumen performance.
- The chemical composition of lignin affects the rheological properties of lignin-modified bitumen. In the unaged and RTFO aged condition, there is an increase (1.5 to 2.5 times depending on the temperature and type of lignin) in stiffness for the lignin-modified bitumen compared to the base bitumen.
- Furthermore, the Kraft and Organosolv lignin-modified bitumen displays a heightened susceptibility to aging, manifested in stiffness, in comparison to the base bitumen. The Lignosulfonate-modified bitumen shows less sensitivity to aging at temperatures > 20°C than the base bitumen 50/70. That supports the hypothesis that lignin

could enhance the aging resistance of bitumen under certain conditions. However, the antioxidant effect of the lignin depends on the chemical composition of the lignin used.

It is essential to emphasise that the objective of this research was to analyse a limited number of lignin samples and only one percentage of lignin in short term aging condition. The bitumen should also be tested in long term aging conditions. The results are therefore preliminary. In order to evaluate the effect of lignin-modified bitumen on the asphalt mixture level, further performance tests on asphalt samples using lignin-modified bitumen should be undertaken.

6 ACKNOWLEDGMENTS

7 REFERENCES

[1] R. Terrell. Evaluation of wood lignin as a substitute or extender of asphalt, U.S. Department of Transportation - Federal Highway Administration, Washington DC, 1980.

[2] E. Gaudenzi, F. Cardone, X. Lu and F. Canestrari. The use of lignin for sustainable asphalt pavements: A literature review, Construction and Building Materials, vol. 362, no. 129773, 2023.

[3] W. Marquez, V. Fuentes and A. González, Use of forestry industry residue as a partial replacement of asphalt: Experience of the use of Lignin in Chile, in 14vo Congreso Internacional - PROVIAL 2023, Pucon, 2023

[4] P. Ortiz, R. van Sprunde, M. van Liesdonk, W. Van Hecke, R. Vendamme and K. Vanbroekhoven. Lignin as antioxidant: A review, Biorizon Community, 2020.

[5] EN 12607-1. Bitumen and bituminous binders - Determination of the resistance to hardening under influence of heat and air - Part 1: RTFOT method 2014.

[6] G.R. Dobson, The dynamic mechanical properties of bitumen Proc. Assoc. Asphalt Paving Technol, 38 (1969), pp. 123-135

[7] H. Di Benedetto, B. Delaporte and C. Sauzéat. Three-Dimensional Linear Behavior of Bituminous Materials: Experiments and Modeling. International Journal of Geomechanics, 7 (2), 2007.

[8] M. Rochlani, G. Canon Falla, S. Leischner and F. Wellner. Towards a unified performance based characterization of bitumen and mastic using the DSR. Road materials and pavement design 22, 2021.

Trinidad Oil Sand Sustainable Use in Asphalt Concrete for Light Traffic Roads

L. P. Leon
University of the West Indies

S. Hosein
University of the West Indies

D. Raghunanan
GroundTechnics TT Limited

ABSTRACT: Oil sands are bituminous sand deposits collected and processed to produce crude oil. While oil sands are primarily used in road construction for unbound pavement layers and temporary surfacing, they are also considered sustainable and environmentally friendly. Laboratory tests have examined the potential of using oil-contaminated sand as a sustainable alternative aggregate in asphalt concrete. The technique involved preparing asphalt mixtures with varying oil sands content (0, 10, 20, 30, 100) and conducting volumetric, moisture susceptibility, and performance tests. These mixtures were then evaluated against international standards. The results showed that bituminous mixtures containing less than 15% oil sand were suitable for use in secondary road layers, road beds, road subbases, impermeable landfill and containment layers, as well as steep embankment stabilizers. The research recommended an oil sand-based low-volume road mixture specification. Incorporating oil sand into asphalt concrete not only improves waste management but also reduces the environmental impact of road construction.

1 INTRODUCTION

The multibillion-dollar construction industry has significant environmental impacts. The rapid growth of the petroleum industry has increased waste production (Asim et al. 2021). To mitigate these effects, the industry must adopt sustainable waste management practices. One promising approach is using Oil-contaminated sands (OCS) in road construction. Oil sands, which contain high concentrations of bitumen or asphalt, can be used for oil extraction. These natural sands, with bitumen content ranging from 8% to 15% are typically low in load-bearing capacity (Anochie et al. 2008). For the past century, pavement surface development near oil reserves has involved using oil sand without guidelines (Vrtis & Romero 2015). This makes integrating these materials into pavement construction difficult.

The use of oil-contaminated sand in construction offers a realistic and cost-effective method for reducing environmental impact. However, it is essential to study how oil pollution affects the mechanical properties of sand. Abousnina et al. (2015) examined how petroleum-derived contaminants affected the water absorption, permeability, cohesion, friction angle, and shear strength of fine sand. They found that at optimal levels of light crude oil contamination, the mechanical properties of fine sand improved, suggesting potential for its use in construction. At the ideal contamination level, the sand exhibited high shear strengths, making it a viable substitute for fine sand in asphalt concrete mix design without compromising performance. This could result in mor durable and resilient pavement.

Al-Mutairi et al. (1997) researched methods for cleaning large quantities of oil-contaminated sand in Kuwait's desert, with the aim of restoring it to its natural state and exploring its potential use in asphalt concrete for secondary roads. Their findings indicated that crude oil-tainted sand could be incorporated into asphalt concrete, with laboratory tested asphalt mixes meeting international standards. These mixes are suitable for use in secondary roads, road beds, subbases, impermeable layers for landfills and hazardous locations, and steep embankment stabilizers. Zhou (2019) examined the potential of oil sands as both a foundational and surface material for gravel roads. His research showed that Lean Oil Sand, when mixed in appropriate ratios with gravel, helped reduced dust on unpaved roads and strengthened road layers.

To specify the appropriate use of oil sands in asphalt concrete, further testing is necessary. Without clear data on their mechanical properties, companies may find it difficult to incorporate materials into design specifications. Tar sand may eliminate the need for asphalt binder, offering both cost savings and promoting waste management innovation. However, the lack of technical support and guidelines from transportation agencies limits the widespread adoption of oil sand in pavement construction. Economic

studies by Gwilliam (2010) suggest that using oil sand in asphalt pavement could benefit private sector companies, as well as local and state governments. This study highlights the results of a comprehensive laboratory investigation aimed at developing tests to characterize the volumetric and mechanical properties of oil sands. These findings could lead to the establishment of standard specifications for oil sand asphalt concrete.

2 METHODS

2.1 Classification of Trinidad Oil Sand

Tar sand deposits have been present in southwest Trinidad since 1930 (Ransome 2014). The Oil Sand samples for the testing protocols were supplied by Stollmeyer's Oil Sand Quarry in Trinidad. Figure 1 compares a heavily contaminated dark sand sample with fine aggregates typically used locally. The OCS sample contained 10.1% hydrocarbon pollution. Sieve analysis was conducted, and according to the unified classification system the contaminated sand is classified as SM (silty sand).

Figure 1. Materials (a) contaminated oil sand – natural state (b) CS (c) limestone dust (d) sharp sand.

2.2 Laboratory prepared asphalt concrete mixes

This study developed asphalt mixtures for low-volume, medium-traffic highways using Marshall design criteria. The assessment focused on density, flow, percent of voids filled with asphalt (VFA), voids in mineral aggregates (VMA), and stability. The main components of the asphalt mixtures were natural aggregates (NA), including coarse aggregates, fine sand, dust, and bitumen. These samples were used as a reference base line for typical blends, allowing OS+NA (oil sand plus natural aggregates) and NA samples to be compared.

For the OS+NA mixtures, four mix designs were prepared with oil sand contents of 0, 10, 20, 30, and 100% as shown in Figure 2. The NA mixture, which included 20% sharp sand instead of oil sand, served as a control for evaluating the effects of oil sand. The mixture with 100% contaminated oil sand is referred to as OSM.
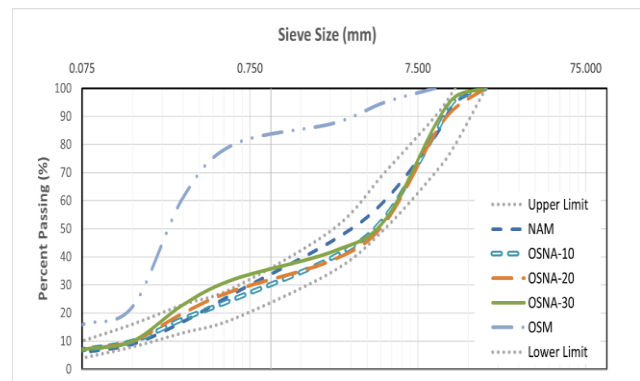
Figure 2. Study mixes designed according to dense grade specification.

3 RESULTS AND DISCUSSIONS

3.1 Density

Figure 3 shows that binder concentration increased with density in the normal mix without oil sand. However, increasing binder amount decreased density in oil sand combinations. As oil sand increased, density loss accelerated, as shown by the steeper slopes. This can be attributed to the low mass of oil sand, which consists primarily of sand, silt, water, and bitumen. The 100% oil sand sample, in particular, has a lower density than the other mixes. Adding lightweight ingredients like bitumen and water further reduces density. Water in oil sand causes buoyancy, further reducing its density. Even when crushed, oil sand retains air gaps. These spaces lower density by reducing mass per volume. These air-filled spaces indicate that the volume is not fully solid. It is also important to note that oil sand cannot be crushed beyond a certain air voids ratio. Despite efforts to compact the material, restrictions in particle arrangement prevent further increases in density.
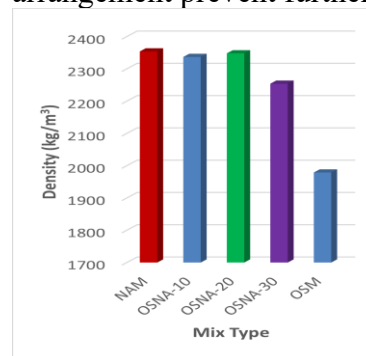
Figure 3. Effects of OS on Density.

3.2 VMA and VFA

Figure 4 shows how the presence of binder increases the Voids in Mineral Aggregate (VMA) in oil sand mixtures. The VMA of oil sand blends is consistent at 6% binder but varies at 4%. In the mixture without oil sand, an increase in binder concentration leads to a slight reduction in VMA. In contrast, some oil sand mixtures show a significant increase in VMA as binder content rises. More voids in asphalt

can negatively impact its performance, reducing its efficacy, pavement durability, moisture resistance, and resistance to deformation. Petroleum in oil sand affects aggregate adhesion. If bitumen is not evenly distributed or blended, it may have reduced cohesiveness, leading to voids. Oil sand mixtures failed to meet the VMA high traffic criterion of 15%. VMA increases with binder content, but the presence of additional oil sand leads to a smaller increase in Voids in the Filler (VFA). This is evident from the shallower gradients observed in the oil sand mixtures. The bitumen concentration and viscosity in oil sand influence the asphalt binder's ability to coat and cover aggregate voids. If the binder cannot sufficiently fill these cavities enough, it lowers the VFA, which in turn affects moisture resistance and durability. Lower VFA values can also impact the mechanical properties of the asphalt mixture, including moisture resistance and deformation.
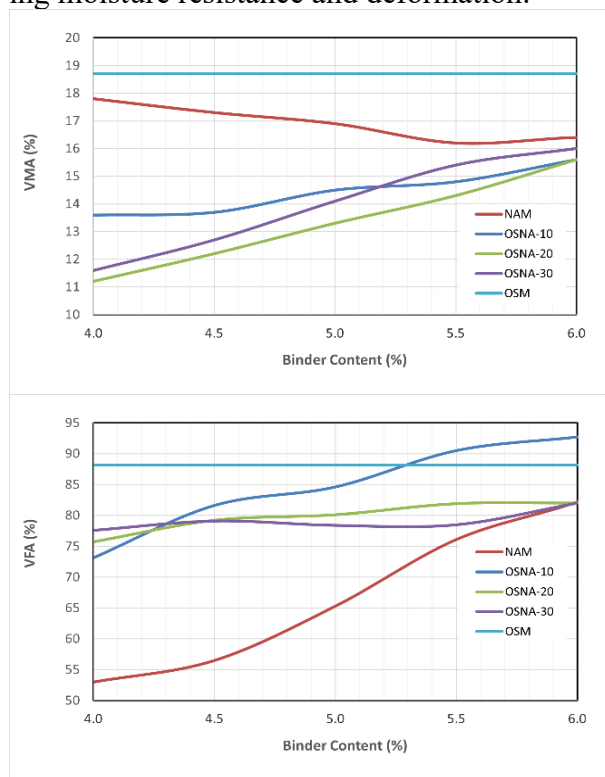
Figure 4. Effects of OS on VMA and VFA.

3.3 Stability and Flow

Figure 5 shows that the addition of binder reduces the stability of oil sand mixtures. Furthermore, the presence of oil sand itself reduces the stability of the combination. After adding 5.5% binder, the 20% oil sand blend proved unstable. Neither the 30% oil sand mixture nor the 100% oil sand sample exceeded the minimum stability requirements set by HMA standards. Similarly, Al-Mutairi et al. (1997) found that stability values were higher with a 27% oil sand blend, yielding 7.254 and 8611 kN respectively. However, their oil sands contained only 0.5% and 0.75% of the total blend, compared to the 3.03% used in this study. This study used a 10% mix with 1.01% oil contamination, which is comparable to the

27% mix used by Al-Mutairi et al. (1997). The stability of a 70% natural bitumen from sand and a 30% conventional binder blend examined by Ionita (2017) was stronger than that of the 20% oil sand mix in this study, which contained 24.19% oil sand and 7.2% bitumen (optimum binder concentration). This difference may be attributed to oil contamination characteristics. The irregular shapes and sizes of oil sand particles can negatively affect aggregate interlocking, thereby reducing stability. Poor interlocking leads to lower shear strength, which can lead to the likelihood of rutting. In contrast, well-coated aggregate particles improve the mélange cohesiveness and stability of the mixture.

Figure 8 shows that oil sand mixtures with higher bitumen content exhibit greater flow. The flow of the 30% oil sand blend surpassed the upper limit, which suggests excessive fluidity. Oil contamination can decrease aggregate friction, preventing stone-on-stone contact and allowing the particles to slip past each other, causing high flow. While the 100% oil sand sample demonstrated good flow, its low stability, makes making it unsuitable for surface courses. Conversely, the 0% oil sand blend showed the highest stability, while the 30% oil sand mix exhibited the least.
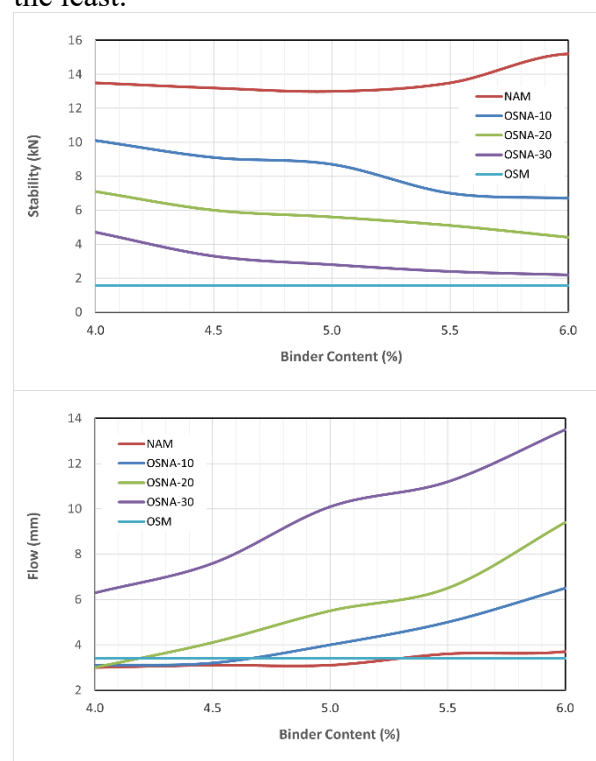
Figure 5. Effects of OS on stability and flow.

3.4 Elastic Modulus

As shown in Figure 6, the introduction of oil sand reduces the elastic modulus of the sample. The Stiffness of the 10% and 0% oil sand mixes is similar, but with 20% oil sand or more, the Indirect Tensile Stiffness Modulus (ITSM) decreases by approximately 50%. The layer might be thinner with higher surface stiffness. A decrease in ITSM would require

thicker pavement, which costs more. Oil sands influence asphalt binder viscosity, affecting elastic response. Oil sands also affect the viscosity of the asphalt binder, which in turn influences the elastic response. This lowers the elastic modulus at higher temperatures and improves the workability of the mixture.
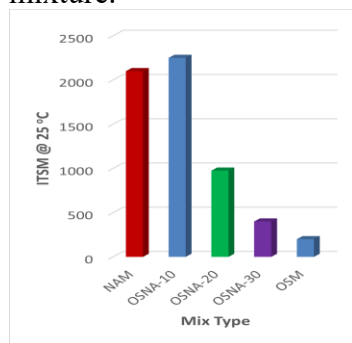
Figure 6. Oil Sand content vs ITSM.

3.5 Proposed specifications

Table 1 presents a specification for the use of asphalt concrete and oil sand. This is specification is essential for several reasons. First, it ensures consistency and quality in material performance, which is crucial for longevity and safety if infrastructure. Second, it facilitates effective communication among stakeholders, including engineers, contractors, and regulatory bodies, by providing clear guidelines and standards. Third, a well-defined specification helps in optimizing material properties, ensuring that the final product meets environmental regulations and sustainability goals. Lastly, it aids in cost management by minimizing the risk of project delays and material failures, ultimately leading to more efficient construction practices.

Table 1. Proposed specification for incorporating oil sand for light traffic roads

Criteria	Design Traffic 3000 - 7500 vpd	
	min	max
Stability, newtons	>5350	
Oil Sand	0	15
Virgin binder content	2	5
Voids in Mineral Aggregates (VMA)	>12	
Voids Filled with Asphalt (VFA)	65	80
Air voids content	3	5
Flow, mm	2	4
Bulk Specific gravity	>2.250	
ITSM @ 25°C, MPa	>2000	

4 CONCLUSIONS

The inclusion of oil sand in asphalt mixtures may necessitate adjustments to the mix design. Adjusting aggregate ratios or binder quantities may be needed to achieve the desired VMA and asphalt performance. This paper presents the results from a com-

prehensive laboratory investigation on three asphalt mixtures containing 10%, 20%, and 30% oil sand by weight. An improved laboratory testing technique was developed to determine the specific gravity of oil sand.

Asphalt concrete can be produced using oil-contaminated sand, and the laboratory's asphalt concrete mixes meet international standards. These mixes can be used for constructing secondary roads, road beds, subbases, impermeable layers for landfills and polluted areas, as well as steep embankment stabilizers. However, to prevent premature composite failure due to insufficient stability, flow, and elastic stiffness modulus, oil sand should be used in small quantities (<15%). Raw oil sand is too weak, leading to excessive rutting in pavement. The oil sand specifications, are most suitable for low-volume roads.

5 REFERENCES

Abousnina, R. M., Manalo, A., Shiau, J. & Lokuge, W. (2015). Effects of light crude oil contamination on the physical and mechanical properties of fine sand. Soil and Sediment Contamination: An International Journal, 24(8), 833-845.

Al-Mutairi, N. M. & Eid, W. K. (1997). Utilization of oil-contaminated sands in asphalt concrete for secondary roads. Materials and structures, 30, 497-505.

Anochie-Boateng, J., Tutumluer, E. & Carpenter, S. H. (2008). Permanent deformation behavior of naturally occurring bituminous sands. Transportation Research Record, 2059(1), 31-40.

Asim, N., Badiei, M., Torkashvand, M., Mohammad, M., Alghoul, M. A., Gasaymeh, S. S. & Sopian, K. (2021). Wastes from the petroleum industries as sustainable resource materials in construction sectors: Opportunities, limitations, and directions. Journal of Cleaner Production, 284, 125459.

Gwilliam, T. S. (2010). Economic feasibility of oil sand use in asphalt pavements. Utah Science, Technology, and Research Initiative, Salt Lake City, Utah.

Ioniţă, G. (2017). Bituminous sand road asphalt pavement. Buletinul Institutului Politehnic din Iasi. Sectia Constructii, Arhitectura, 63(3), 55-63.

Ransome, G. (2014). A Feasibility Study of Tar Sands Exploitation in Trinidad and Tobago. In SPE Latin America and Caribbean Petroleum Engineering Conference, p. D011S009R003.

Vrtis, M.C. & Romero, P. (2015). Creating a Performance-Based Asphalt Mix Design to Incorporate Oil Sand. In Airfield and Highway Pavements 2015, 53-61.

Zhou, B. (2019). Feasibility Study of Lean Oil Sand as Base and Surface Material on Gravel Roads in Alberta. Master's Thesis, University of Waterloo.

Effects of devulcanization temperatures on the properties of ground waste tire modified asphalt

Danni Li

Department of Civil and Environmental Engineering, The University of Tennessee

Email: dli48@vols.utk.edu

Hongyu Zhou

Department of Civil and Environmental Engineering, The University of Tennessee

Email: hzhou8@utk.edu

Qiang He

Department of Civil and Environmental Engineering, The University of Tennessee

Email: qianghe@utk.edu

Baoshan Huang

Department of Civil and Environmental Engineering, The University of Tennessee, Knoxville

Email: bhuang@utk.edu

ABSTRACT: Utilizing waste rubber in asphalt extends the lifespan of pavements and fosters the sustainable reuse of materials. This research explored how devulcanizing ground tire rubber (GTR) affects the qualities of rubber-modified asphalt. The study assessed their impact on flexibility, high-temperature and low-temperature performance, and storage stability by integrating devulcanized rubber at various temperatures and concentrations. Findings indicate that while devulcanization improves the compatibility of rubber with asphalt, it might diminish its performance at higher temperatures. Modifying the conditions of devulcanization could enhance the performance and stability of the binder.

1 INTRODUCTION

Addressing the effective recycling of waste tires is a significant environmental issue for numerous countries (Sienkiewicz et al., 2012). Each year, the disposal of tires exceeds approximately 1.5 billion, leading to environmental degradation, increased fire hazards, and heightened health risks (Hong et al., 2023). Around 40% of these tires are incinerated for energy recovery, while merely 5.5% are repurposed for civil engineering applications (Shu and Huang, 2014). Recycling waste Ground Tire Rubber (GTR) as a modifier in asphalt pavement materials can substantially improve road performance, lower construction expenses, and mitigate environmental impact (Ma et al., 2022).

Rubber-modified asphalt is recognized for its enhanced resistance to rutting and cracking. However, the swelling effect of rubber significantly increases the viscosity of the asphalt, presenting considerable challenges during handling, pumping, and compaction processes (Huang et al., 2017, Zhang et al., 2023). Additionally, the existence of insoluble rubber particles in the binder, which have different chemical and physical properties, exacerbates compatibility issues (Ma et al., 2021b). Therefore, it is essential to develop rubberized asphalt binders that are low in viscosity, homogeneous, and exhibit superior performance.

Devulcanization can promote the integration of rubber and asphalt. The degraded rubber hydrocarbons dissolve into the asphalt blender, resulting in an improved viscosity and compatibility of the binder. However, the devulcanization of the GTR elastomer leads to a loss of elastic properties and a sacrifice in the high-temperature performance (Meng et al., 2023). Effectively managing the devulcanization degree is a critical factor in obtaining a binder that exhibits desirable solubility, compatibility, and mechanical performance.

This research investigates the impact of varying levels of devulcanization on the characteristics of asphalt binders utilizing devulcanized GTR under different concentrations and conditions. By assessing the performance of asphalt, emphasizing the balance between enhanced low-temperature flexibility and the potential reduction in high-temperature stability, this investigation aims to improve application methods and increase the understanding of devulcanized rubber in road construction, ultimately contributing to the development of more durable and cost-effective solutions.

2 METHODOLOGY AND MATERIALS

2.1 *Rubber devulcanization*

GTR devulcanization was conducted using a twin-screw extruder, with temperatures strategically set as 240 °C, 260 °C, and 280 °C to break sulfur bonds.

2.2 Characterization of devulcanized GTR

In GTR, its composition includes natural rubber, synthetic rubber, carbon black, zinc oxide, sulfur, lubricating oils (acetone soluble), and fillers. To qualify the devulcanization degree of rubber, the Soxhlet extraction method separates the sol from the insoluble. After extraction, the compositions of the GTR and the sol fraction were determined using thermal gravimetric analysis (TGA).

Attenuated Total Reflection Fourier Transform Infrared (ATR-FTIR) spectroscopy was used to investigate the changes in the functional groups within the rubber during the devulcanization.

2.3 Preparation of modified asphalt

A high-speed shearing mixer was utilized to prepare the rubber-modified asphalt. Various parameters were set to investigate their effects on the properties of the asphalt, including different GTR contents (12%, 18%, 24%), and degrees of devulcanization of the GTR. PG 64-22 base asphalt binder was heated to 190 °C to ensure it became fluid. Adding the original and devulcanized GTR into the asphalt to make rubber-modified asphalt samples.

2.4 Storage Stability of modified Asphalt

The storage stability and phase separation of the modified asphalt were characterized according to ASTM D-7173. Dynamic Shear Rheometer (DSR) (ASTM D7175) test was applied for this purpose (Kim and Lee, 2013, Ma et al., 2021a).

2.5 Brookfield viscosity

The viscosity should be under 3000 cP at 135 °C, according to Typical Asphalt-Rubber Binder Specifications (Way, 2012). The viscosity asphalt binder samples were measured in accordance with AASHTO T-316.

2.6 Aging simulation

Short-term aging of the asphalt blends was simulated using the Rolling Thin-Film Oven (RTFO) according to AASHTO T-240. Long-term aging was simulated using the Pressure Aging Vessel (PAV) test, in accordance with AASHTO R28.

2.7 High-temperature performance

The oscillatory temperature sweep conducted using DSR in accordance with AASHTO T-315.

2.8 Permanent deformation resistance

The non-recoverable creep compliance (J_{nr}) and average percent recovery (R) were calculated following AASHTO T-350 based on Multiple Stress Creep Recovery (MSCR).

3 RESULTS AND DISCUSSION

3.1 Determination of rubber devulcanization degree

Table 1. Effects of extrusion temperature on sol fraction

Pretreatment Temperature (°C)	Devulcanization Degree (%)		
	Rubber	Natural Rubber	Synthetic Rubber
Untreated	5.054	6.460	2.086
240	15.950	16.085	13.159
260	20.970	25.521	17.380
280	27.524	31.432	26.615

The sol fraction of both natural and synthetic rubber increased with temperature. Notably, natural rubber consistently exhibited a higher sol fraction than synthetic rubber.

3.2 Characterization of chemical modification by ATR-FTIR
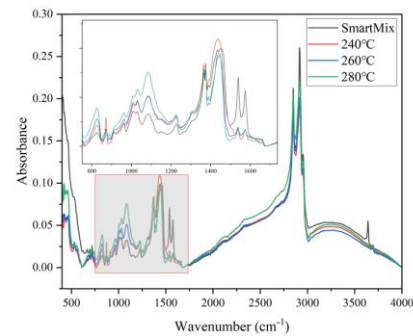
Figure 1. FTIR spectra of the devulcanized samples

With the increase of devulcanization temperature, the intensity ratio of S-S to S-O shows a trend of first slightly increasing and then decreasing, while the intensity ratio of C-S decreases slightly. The degree of bonding depends on the exposure of the sample to the devulcanization temperature, and the energy required to break each sulfur bond. The bond energies of S-S, S-O, and C-S are 268 kJ/mol, 226 kJ/mol, and 285 kJ/mol (Rooj et al., 2011). These results confirm that the devulcanization of GTR does occur at high temperatures and under the action of vacuum and that there may be non-uniform breaking and formation of different types of sulfur bonds.

3.3 Compatibility test
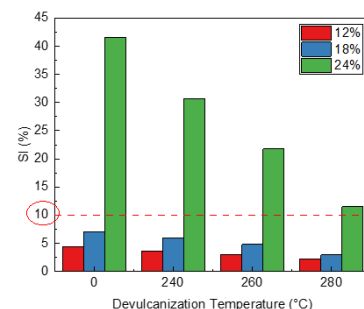
Figure 2. Separation Index (*SI*) of samples

The *SI* values of rubber-modified asphalt samples containing 12% GTR and 18% GTR are lower than 10%, which means that they can meet the ASTM requirements. As the GTR content increased from 12% to 24%, the SI also rose significantly, indicating reduced storage stability.

3.4 *Brookfield viscosity*
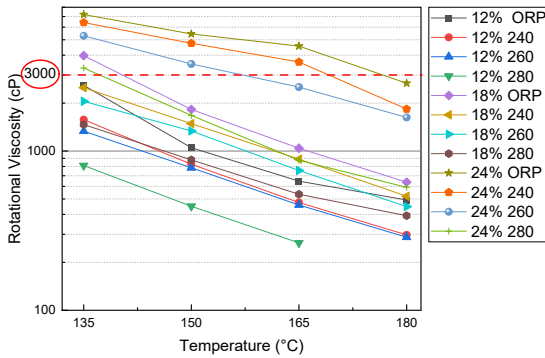
Figure 3. Brookfield viscosity profiles for various rubber-modified asphalt samples

At 12% rubber content, all asphalt binders have suitable processing viscosity. At 18% rubber content, the asphalt containing 18% untreated GTR exceeds the viscosity threshold at 135°C. At 24% rubber content, viscosities frequently approach or exceed the 3000 cP limit.

3.5 *Oscillation temperature sweep test*
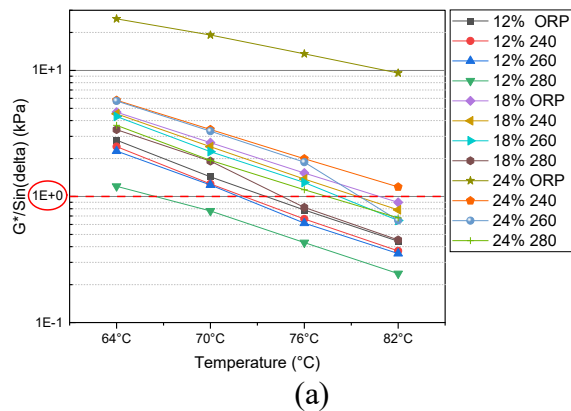
(a)
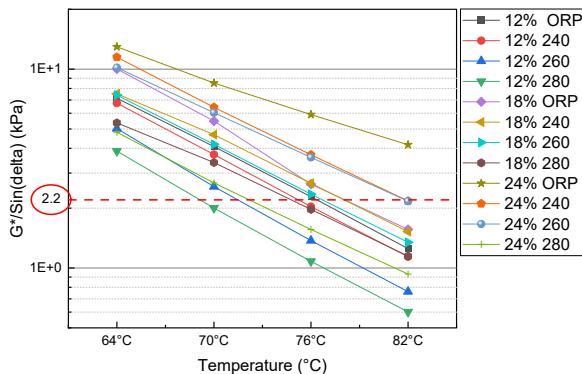
(b)

Figure 4. Results of Oscillation Temperature Sweep test: (a) original asphalt samples, (b) RTFO residues.

Figure 4 (a) reveals that most samples initially meet the minimum high-temperature performance standard of 1.0 kPa at 64 °C and 70 °C. As tempera-

tures rise, particularly at higher devulcanization temperatures, the values drop below this threshold, showing decreased effectiveness in rutting resistance with increased temperature.

In Figure 4 (b), samples with 12% rubber content at lower devulcanization temperatures show better high-temperature performance than the base asphalt. At a devulcanization temperature of 280 °C, performance under 70 °C does not meet the required standards. Increasing the rubber content enhances the $|G^*|/\sin\delta$ value, potentially raising the PG grade to 76 °C for 18% rubber and above 82 °C for 24% rubber when using original GTR. If devulcanization temperatures range from 240 °C to 260 °C with 18% or 24% rubber, the PG grade improves to 76 °C. At 280 °C, despite a slight increase in value, the grade remains unchanged.

3.6 *Multiple stress creep recovery test*

For rubber-modified asphalt, a stress level of 3.2 kPa is required to accurately simulate real traffic loads.
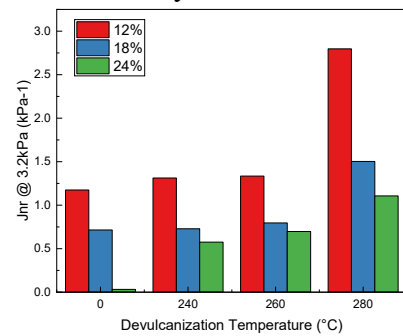
(a)
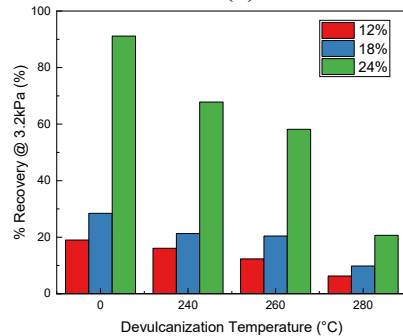
(b)

Figure 5. (a) Non-recoverable creep compliance, (b) Percent recovery.

Both $J_{nr,\,3.2}$ and $R_{3.2}$ results indicate that increasing the GTR dosage improves the elasticity and deformation resistance of the asphalt. The devulcanization process also plays a critical role in enhancing these properties. By breaking down the sulfur cross-links in rubber, devulcanization improves the compatibility between rubber and asphalt, leading to better stress distribution and reduced susceptibility to permanent deformation.

3.7 *Bending Beam Rheometer Test*

Table 2. BBR test results of rubber-modified asphalt samples

Sample	12% ORP	12% 240	12% 260	12% 280
S at -12 °C (MPa)	82.8	89.3	86.7	91.55
m-value at -12 °C	0.381	0.364	0.373	0.385
S at -18 °C (MPa)	187	189	194	189
m-value at -18 °C	0.330	0.334	0.314	0.331

Sample	18% ORP	18% 240	18% 260	18% 280
S at -12 °C (MPa)	54.4	63.6	55	58.3
m-value at -12 °C	0.387	0.381	0.393	0.372
S at -18 °C (MPa)	136	132	127	113
m-value at -18 °C	0.336	0.341	0.342	0.335

Sample	24% ORP	24% 240	24% 260	24% 280
S at -12 °C (MPa)	---	38.1	26.7	35.5
m-value at -12 °C	---	0.386	0.412	0.396
S at -18 °C (MPa)	62.9	76.6	56.8	91.3
m-value at -18 °C	0.346	0.340	0.366	0.371

The results show that both untreated and devulcanized GTR (at 240°C, 260°C, and 280°C) maintain the stiffness (S) values well below the 300 MPa threshold at -12°C and -18°C, with m-values consistently above 0.300 across all rubber contents (12%, 18%, and 24%). Notably, the S and m-values at 240°C and 260°C are similar, showing consistent performance, whereas at 280°C, a higher S hints at reduced flexibility at lower temperatures.

4 CONCLUSIONS

1. Changes of S-S, S=O, and C-S bonds confirmed the chemical degradation of sulfur cross-links due to devulcanization. Higher temperatures caused these bonds to break, making the rubber more reactive but less structurally sound.
2. The devulcanization procedure significantly improved the storage stability of asphalt binders by promoting a uniform distribution of rubber particles.
3. Incorporating rubber enhanced the rheological properties of asphalt, improving its resistance to deformations under cyclic loading. However, the devulcanization process tended to reduce the elastic response, which could potentially compromise the material's performance when subjected to stress.

5 REFERENCE

HONG, Y., GUAN, J., LIANG, C., HE, D., FAN, Y., WANG, L., NIE, F., LIU, J. & ZHANG, Q. 2023. Catalytic fast pyrolysis of waste truck-tire to aromatics production over metal-modified USY catalysts. *Journal of Analytical and Applied Pyrolysis,* 174, 106127.

HUANG, W., LIN, P., TANG, N., HU, J. & XIAO, F. 2017. Effect of crumb rubber degradation on components distribution and rheological properties of Terminal Blend rubberized asphalt binder. *Construction and Building Materials,* 151, 897-906.

KIM, H. & LEE, S.-J. 2013. Laboratory Investigation of Different Standards of Phase Separation in Crumb Rubber Modified Asphalt Binders. *Journal of Materials in Civil Engineering,* 25, 1975-1978.

MA, Y., WANG, S., ZHOU, H., HU, W., POLACZYK, P. & HUANG, B. 2021a. Potential Alternative to Styrene–Butadiene–Styrene for Asphalt Modification Using Recycled Rubber–Plastic Blends. *Journal of Materials in Civil Engineering,* 33.

MA, Y., WANG, S., ZHOU, H., HU, W., POLACZYK, P. & HUANG, B. 2022. Recycled polyethylene and crumb rubber composites modified asphalt with improved aging resistance and thermal stability. *Journal of Cleaner Production,* 334, 130102.

MA, Y., WANG, S., ZHOU, H., HU, W., POLACZYK, P., ZHANG, M. & HUANG, B. 2021b. Compatibility and rheological characterization of asphalt modified with recycled rubber-plastic blends. *Construction and Building Materials,* 270, 121416.

MENG, Y., YE, X., HE, F., CHEN, Z., HU, C. & LIN, P. 2023. Comprehensive study on the degradation progress of crumb tire rubber during the preparation of terminal blended rubberized asphalt binder. *Journal of Cleaner Production,* 417, 137916.

ROOJ, S., BASAK, G. C., MAJI, P. K. & BHOWMICK, A. K. 2011. New Route for Devulcanization of Natural Rubber and the Properties of Devulcanized Rubber. *Journal of Polymers and the Environment,* 19, 382-390.

SHU, X. & HUANG, B. 2014. Recycling of waste tire rubber in asphalt and portland cement concrete: An overview. *Construction and Building Materials,* 67, 217-224.

SIENKIEWICZ, M., KUCINSKA-LIPKA, J., JANIK, H. & BALAS, A. 2012. Progress in used tyres management in the European Union: A review. *Waste Management,* 32, 1742-1751.

WAY, G. B., KALOUSH, KAMIL E., PRAPOORNA BILIGIRI, KRISHNA 2012. Asphalt Rubber Standard Practice Guide. Chairman RPA Technical Advisory Board.

ZHANG, Z., YANG, W., MA, Y., ZHANG, C. & WANG, S. 2023. Effect of dynamic vulcanization on the performance of high content rubber modified asphalt. *Journal of Applied Polymer Science,* 140, e53889.

Investigation on performances of hot in-place recycling porous asphalt mixture

M. L. Li, J. Li, D.C.SUN, H. Wu, D. D. Han, R. F. Li
Research Institute of Highway Ministry of Transport, China

ABSTRACT: This study focuses on the performance of hot in-place recycled porous asphalt mixture, which is considered as a low-carbon maintenance technology of porous asphalt pavement using high-viscosity modified asphalt as the binder. Based on practical engineering project, the performance of aged high-viscosity modified asphalt was analyzed, and the effects of plant-based oil and petroleum-based rejuvenators at varying contents were compared. The influences of different proportions of new porous asphalt mixtures on recycled mixture performance and the impact of basalt fiber on asphalt leakage were also evaluated. Finally, observations from the field trial section were conducted to assess the performance of the recycled mixtures and pavement permeability. The results demonstrate that hot in-place recycling effectively restores the performance and permeability of porous asphalt mixtures, providing a sustainable maintenance method for porous asphalt pavements.

1 INTRODUCTION

Porous asphalt pavement is typical road surface used to enhance driving safety in rainy weather, mitigate traffic noise pollution and facilitate low-impact development. The surface layer is paved by porous asphalt mixture (PA) with a porosity of 18-25%. Research and applications both domestically and internationally indicate that the service life of the porous surface layer is generally 10-15 years [Nielsen. 2006, Takahashi. 2013]. Due to the limited contact area between coarse aggregates in porous asphalt pavement, the contact forces between particles become relatively high under load. Repeated traffic loading can lead to coarse aggregate detachment, known as raveling, caused by insufficient adhesion between asphalt and aggregate or mastic fracture [Manrique-Sanchez et al. 2016, De Visscher et al. 2017]. Once such disease occurs locally, it will accelerate aggregate raveling in adjacent areas and significantly impacting the pavement's service life, driving comfort, and safety. Currently, maintenance strategies for porous asphalt pavement at various service stages include: (1) preventive maintenance by spraying restorative and strengthening emulsion materials; (2) local damage repair using porous permeable resin materials;(3) overlaying thin layers for addressing medium aggregate loss over long sections [Chen et al. 2023, Li et al. 2021]. For porous asphalt pavement at the end of its service life, it is usually milled and the surface layer is repaved. Since the raw materials of porous asphalt mixture are mostly high-quality asphalt and mineral aggregates, material waste or downgrading use will inevitably cause great resource waste. Under the "carbon peaking and carbon neutrality" goals and promoting sustainable development, developing efficient, high-performance, and low-emission recycling methods for end-of-life porous asphalt mixtures has become one of the most pressing and significant challenges in the field of pavement engineering.

Hot In-Place Recycling (HIR), also known as on-site hot recycling or in-place hot recycling, is an efficient, rapid, and environmentally friendly asphalt pavement maintenance technology. Through the process of heating, scarifying, and repaving the asphalt pavement in place, it achieves 100% in-place recycling of the old pavement. Since the beginning of this century, the hot in-place recycling technology has developed rapidly in China. At present, key equipment such as heating and scarifying equipment, as well as recycling agent materials, have been domestically produced. HIR has become a critical pavement maintenance technology in some regions of China. Similarly, countries like the Netherlands and Japan, which have extensively adopted porous asphalt pavements, have validated the feasibility of HIR for porous asphalt through trial sections [van de Pol. 2019, Kayedi et al. 2017].

This study focuses on porous asphalt pavements in China constructed with high-viscosity modified asphalt (HVMA) as the binder. Investigation on characteristics of aged asphalt, recycled mixture, and pavement were carried out. Field application was also carried out to verify the practical effectiveness of HIR for porous asphalt mixtures. The achievements from this study provide foundational support for efficient and low-carbon maintenance of aged porous asphalt mixtures.

2 INVESTIGATION ON AGED BINDER

2.1 *Recycled asphalt*

This study focuses on the performance analysis of porous asphalt mixtures from G2513 Huai'an-Xuzhou Expressway. The porous asphalt pavement on this section was originally constructed in 2015, and samples were collected in 2023, which represents a service life of 8 years. Sampling was carried out to a depth of 4 cm, which is equal to the full thickness of the porous asphalt mixture. The collected mixture from the pavement was subjected to dust

removal. And the aged asphalt was extracted using rotary evaporation and centrifugal separation methods. The asphalt-aggregate ratio of the reclaimed asphalt mixture from the old pavement was measured at 4.74%, showing a slight reduction compared to the original pavement's ratio of 4.8%. Subsequently, the main performances of the aged asphalt were measured, with the results shown in Table 1. In this study, all tests for asphalt and asphalt mixtures were conducted in accordance with the "Standard Test Methods of Bitumen and Bituminous Mixtures for Highway Engineering." It finds that there are significant changes in the performances of the HVMA compared to its original state. Overall, the aged asphalt exhibited a pronounced trend of hardening and severe aging. Therefore, the use of rejuvenators is essential to restore the aged asphalt's performance properties effectively.

Table.1 Key performance indicators of old asphalt

Performance Indicators	Recycled bitumen	Original	Requirement*
25℃ Penetration/0.1mm	15.8	44	≥40
Softening Point/℃	＞117	98	≥80
5℃ Ductility/cm	Broken	35	≥30
Dynamic Viscosity/Pa•s	>1,000,000	440,806	≥50,000

*According to Chinese Transportation industrial specification "Technical Specifications for Design and Construction of Porous Asphalt Pavement" (JTG/T 3350-03-2020).

2.2 Effects of rejuvenator

The current heating process for hot in-place recycling typically requires a paving temperature of no less than 135°C. However, for porous asphalt mixtures, which have higher viscosity, the paving temperature generally needs to exceed 155°C. For better remixing, the liquid rejuvenators with warm-mix properties were used in this study. Comparative experiments were conducted using two types of rejuvenators: a plant-based oil rejuvenator RR18 and a petroleum-based PR-01.

Rejuvenators were added to aged asphalt at ratios of 2%, 4%, 6%, and 8%, and performance indicators such as penetration, softening point, and viscosity were measured. The test results are shown in Figure 1. Due to brittle fracture observed in most ductility tests, ductility results are not presented. Considering the practical emphasis on the workability of mixtures during in-place recycling, Brookfield viscosity tests at 170°C were also conducted. The results indicate that penetration increases with the addition of rejuvenators, while both softening point and Brookfield viscosity show a decreasing trend. This suggests that as the rejuvenator content increases, the performances of aged HVMA is restored to some extent, and the degree of recovery improved proportionally to the rejuvenator content. As to the two types of rejuvenators, the plant-based oil rejuvenator (RR18) demonstrated superior recovery effects on aged HVMA compared to the petroleum-based rejuvenator (PR-01). Consequently, RR18 was selected as the primary rejuvenator for subsequent mixture studies.

(a) 25℃ Penetration

(b) Softening point

(c) 170℃ Brookfield viscosity
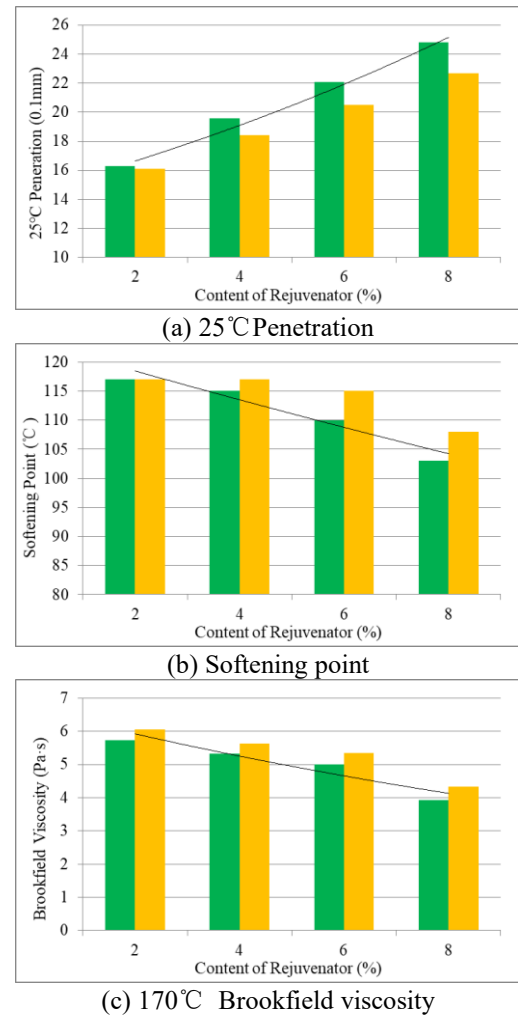
Figure 1.Effects of rejuvenator on performances of recycled asphalt.

3 INVESTIGATION ON RECYCLED MIXTURE

3.1 Influence of new mixture

In order to compensate for the loss of mixture caused by rutting, raveling etc., to recover the performance of porous asphalt mixture, and optimize the gradation of recycled asphalt mixture, it is necessary to add a portion of new asphalt mixture. In order to ensure the porosity of the recycled mixture, the newly added asphalt mixture is still a porous asphalt mixture. HVMA is used as the binder, with an optimal asphalt to aggregate ratio of 4.9%. The design voids content of the mixture is 22.0%. The blending percentage of the new porous asphalt mixture in the total mixture are set at 10%, 15%, and 20%, aiming for a final void ratio of 18.0% in the recycled mixture. The amount of RR18 rejuvenator was 4% in the

asphalt. Consequently, RR18 was selected as the primary rejuvenator for subsequent mixture experiments.

The performances of recycled porous asphalt mixtures with varying amounts of new material were measured, including raveling resistance, freeze-thaw splitting, low-temperature bending, and high temperature dynamic stability. The experimental results are shown in Figure 2.
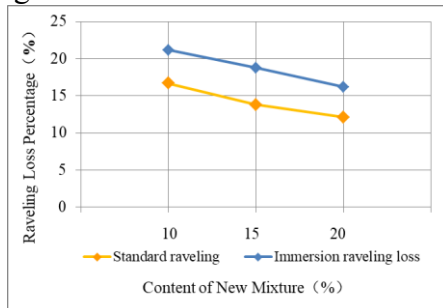
(a) Raveling loss percentage
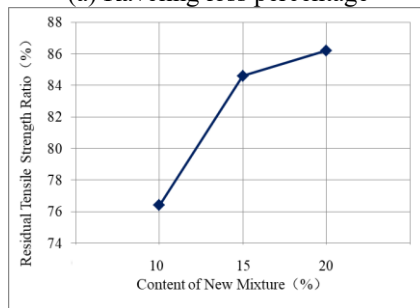
(b) Residual freeze-thaw split tensile strength ratio
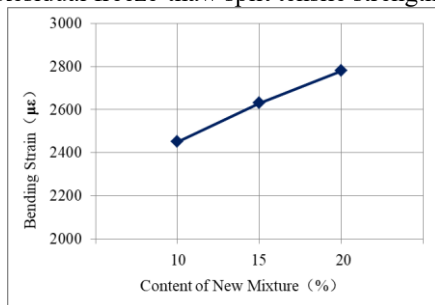
(c) Low temperature bending strain
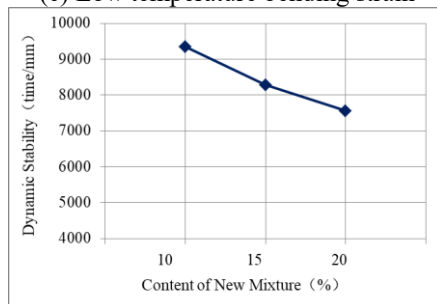
(d) 60℃ Dynamic stability

Figure 2.Effects of new mixture content on performances of recycled porous asphalt mixture.

As can be seen from the figure, with the increase of the new porous asphalt mixture ratio, the raveling loss percentages for both the standard and after immersion decrease, and the residual freeze-thaw splitting tensile ratio and low-temperature bending strain increase. This indicates that the resistance to raveling, water damage, and low-temperature damage of

the recycled asphalt mixture are improved. For the dynamic stability, it shows a decrease trend with increasing percentage of new mixture. It can be explained as that the addition of new asphalt mixture increases the proportion of fresh binder, softening the overall asphalt and slightly reducing rutting resistance. However, the dynamic stability remains above 6000 times/mm, reflecting a high performance of rutting resistance.

3.2 *Influence of fiber*

Porous asphalt mixtures, due to their high air void content, are susceptible to asphalt stripping from aggregate voids. The addition of fibers in asphalt mixtures can play an important role in absorbing and stabilizing the asphalt binder, thereby enhancing the adhesion between aggregates and reducing the stripping of asphalt binder from the voids. To improve the workability of mixtures during long-distance transportation, 0.3% basalt fiber by total mass was added into the new porous asphalt mixture. Asphalt drain-down tests were conducted on mixtures prepared with different asphalt-aggregate ratios, and the results are shown in Figure 3.

The findings demonstrate that the addition of 0.3% basalt fiber help to reduce the leakage loss of the porous asphalt mixture. At the optimal asphalt-aggregate ratio of 4.9%, the leakage loss percentage of the mixture without fiber was 1.2%, while it dropped to just 0.4% with the inclusion of basalt fiber. These results indicate that the addition of basalt fiber can enhance the workability of new porous asphalt mixtures during long-distance transportation by reducing binder leakage and maintaining material stability.
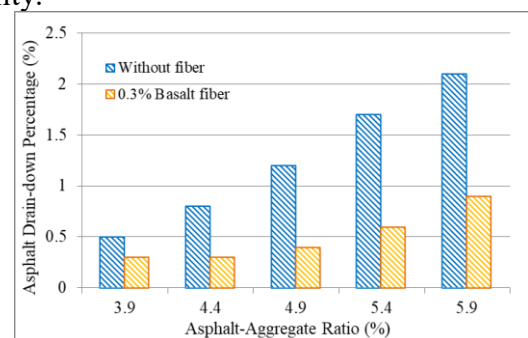
Figure 3. Asphalt drain-down percentage at different asphalt-aggregate ratio.

4 INVESTIGATION ON TRIAL SECTION

4.1 *Mixture performance*

The hot in-place recycling project for porous asphalt pavement was implemented on the G2513 Huai'an-Xuzhou Expressway. The construction process generally has six steps: cleaning voids on the old pavement, producing and transporting new asphalt mix-

ture, heating the pavement on site, loosening the mixture on site, mixing the recycled mixture, and paving and compacting the recycled mixture. Considering the economic feasibility of the project, the proportion of new porous asphalt mixture was set at 15%.

Samples were collected from the trial section, and performance tests were conducted on the recycled asphalt mixture, with the results presented in Table 2. According to the table, all performance indicators met the design requirements. The dynamic stability test results exceeded 8,000 time/mm, indicating excellent high-temperature rutting resistance of the recycled mixture. The residual stability and freeze-thaw splitting tensile strength were comparable to those of new porous asphalt mixtures. However, the raveling loss of the recycled mixture was higher than that of the new porous asphalt, indicating that asphalt ageing has adverse effect on the raveling resistance of the recycled mixture. It can be improved by adding suitable percentage of new mixture.

Table.1 Test results of performances of recycled porous asphalt mixture

Performance Indicators	Test Results	Design Target
Voids content（%）	17.4	≥16
Marshall stability（kN）	16.2	≥5
Drain-down percentage（%）	0.073	≤0.8
Standard raveling loss（%）	14.7	≤15
Immersion raveling loss（%）	18.0	≤20
Dynamic stability（time/mm）	8796	≥5000
Residual Mashall stability percentage（%）	87.9	≥85
Residual Freeze-thaw split tensile strength ratio（%）	87.5	≥80

4.2 *Permeability*

Permeability coefficients were tested on-site at ten locations before and after recycling, with the results shown in Figure 4.
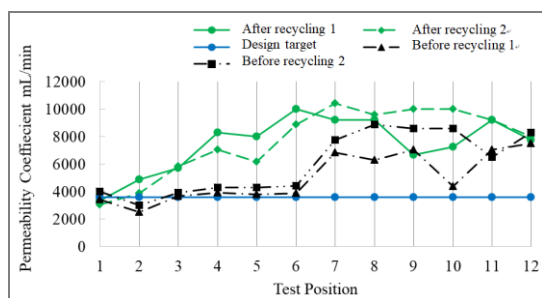
Figure 4. Permeability on the recycling section.

As indicated in the figure, except for location 1, the permeability coefficients at all other locations after recycling exceeded the design value of 3600 mL/min. Notably, locations 3 to 6, which initially

exhibited poor permeability, showed significant improvement in performance after recycling. This demonstrates that the hot in-place recycling process can effectively restore the permeability performance of porous asphalt pavements.

5 CONCLUSIONS

Following conclusions can be drawn from this study:

(1) The plant-based oil rejuvenator demonstrated superior recovery performance for aged HVMA. As the rejuvenator content increased from 2% to 8%, the light components in the asphalt were replenished, resulting in better softening of the binder.

(2) The addition of new porous asphalt mixture helps to improve the performance of the recycled asphalt mixture. As the proportion of new material increased, the recycled mixture exhibited enhanced resistance to raveling, improved water stability, and better low-temperature performance. Although dynamic stability decreased slightly, the rutting resistance remained satisfactory.

(3) Performance tests of recycled porous asphalt mixtures from the on-site trial section showed that all indicators met design requirements, and the permeability performance was successfully restored. These findings confirm that hot in-place recycling is a viable maintenance method for porous asphalt pavements.

6 REFERENCES

Nielsen, C. B. 2006. Durability of porous asphalt - international experiences. *Danish Road Institute Technical note 41*.

Takahashi, S. 2013. Comprehensive study on the porous asphalt effects on expressways in Japan: based on field data analysis in the last decade. *Road Materials and Pavement Design* 14(2):239-255.

Manrique-Sanchez, L., Caro, S. & Arámbula-Mercado, E. 2016. Numerical modelling of ravelling in porous friction courses (PFC). *Road Materials and Pavement Design* 19(3):1-22.

De Visscher, J. & Vanelstraete, A. 2017. Ravelling by traffic: Performance testing and field validation. *International Journal of Pavement Research and Technology* 10(1):54-61.

Chen, Li., Chen, J. & Li, M. et al. 2023. Study of fatigue performance of fiber reinforced high-viscosity asphalt mastic based on rheology. *Construction and Building Materials* 400:132784.

Li, M., Lu, H., & Li, J. et al. 2021. Performance study and application of porous ultra-thin wearing course for asphalt pavement maintenance, *IOP Conf. Series: Materials Science and Engineering* 1075: 012014.

van de Pol, C. 2019. Heating of porous asphalt for in-situ recycling: A contribution to the development of an asphalt recycling train in the Netherlands. *University of Twente*, the Netherlands.

Kayedi, D., Hosseini, M. & Mortazavi, R. 2017. Analysis of the strength of hot in-place recycled asphalt, its effecting factors and its comparison with conventional methods. *International Journal of Transportation Engineering* 4(4):351-358.

Mechanical performance, economic, and environmental assessment of bio-oil/RAP-based high-modulus mixtures with different RAP contents.

Zengyao Lin, Xinghai Peng, Chaoliang Fu, Pengfei Liu
Institute of Highway Engineering, RWTH Aachen University, Aachen 52074, North Rhine-Westphalia, Germany

ABSTRACT: The reuse of reclaimed asphalt pavement (RAP) offers a sustainable solution to reduce construction costs, energy consumption, and emissions. This study investigates bio-oil/RAP-based recycled asphalt pavements (BORAP) using bio-oil as a rejuvenator and graphene oxide (GO) to enhance mechanical performance, replacing high-modulus additives. Tests identified 70% RAP as the optimal content, achieving peak dynamic modulus and rutting resistance. A life cycle assessment revealed that 70% RAP reduced total embodied energy and greenhouse gas emissions by 41.48% and 41.59%, respectively, compared with hot-mix asphalt (HMA). BORAP provides a sustainable and high-performing alternative for pavement construction.

1 INTRODUCTION

Reclaimed asphalt pavement (RAP), generated during pavement reconstruction and rehabilitation, comprises aggregates and aged binder. Over time, the aged binder in RAP becomes hard and brittle due to long-term aging, exhibiting characteristics similar to low-grade hard asphalt. These properties make RAP a promising material for developing high-modulus mixtures, which are widely used in pavement construction (Miro et al., 2011). Furthermore, incorporating RAP offers a sustainable approach to reduce construction costs, total energy consumption (TEE), and greenhouse gas emissions (GHG) by minimizing the reliance on virgin materials (Mattinzioli et al., 2021). However, the stiffness of the aged binder increases the susceptibility of RAP mixtures to cracking under intermediate and low temperatures, posing challenges for its effective incorporation into new mixtures.

To address these limitations, bio-oil has emerged as a promising rejuvenator for RAP-based mixtures. Countries such as China generate millions of tons of bio-oil annually, highlighting its potential as a sustainable resource to mitigate environmental harm. Research has shown that bio-oil effectively restores the physical, rheological, and chemical properties of aged binder, making it comparable to virgin binder (Girimath and Singh, 2019). This enables higher RAP incorporation in asphalt mixtures while maintaining acceptable performance standards. The use of bio-oil, therefore, helps to develop the bio-oil/RAP-based recycled asphalt pavements (BORAP), offering a sustainable and high-performing alternative in pavement construction.

Building on these concepts, the objective of this study is to explore the feasibility and advantages of incorporating RAP in the development of BORAP. Specifically, the study evaluates the mechanical, economic, and environmental performances of BORAP mixtures with varying RAP contents (0%, 20%, 30%, 50%, 60%, 70%, and 80%). Customized rejuvenation schemes were designed to optimize binder properties and address the challenges posed by aged binder. By systematically assessing performance indicators such as dynamic modulus, rutting resistance, this study aims to identify the optimal RAP content and provide insights into the sustainable utilization of BORAP in pavement applications.

2 METHODOLOGY

2.1 *Materials*

In this study, basalt RAP material was sourced from the surface layer of the Changsha–Yongan highway in Hunan, China. The virgin asphalt, SBS-modified asphalt, was provided by Foshan Gaofu Asphalt Co., Ltd. The waste bio-oil, a by-product of the fatty acid distillation process, was sourced from Nantong Yuhao Chemical Technology Co., Ltd. Graphene oxide (GO), obtained from Henan Liugong Graphite Co., Ltd., was used in combination with sodium dodecyl sulfate, which served as a dispersing agent. GO enhanced the physical and rheological properties of the binder, significantly improving the mechanical performance of the mixture, including resistance to rutting, cracking, and aging.

2.2 *Synthetic gradation design of BORAP*

The gradation design for BORAP with different RAP contents was conducted to ensure compliance with the AC-13 mix design requirements. To achieve this, a portion of 9.5–13.5 mm basalt RAP aggregate was separately sieved as a single fraction for fine-tuning the gradation. The synthetic gradation was developed by adjusting the proportions of each fraction of new and aged aggregates, along with mineral powder. As a result, the gradation design for the bio-oil/RAP-based recycled asphalt mixture with 20% RAP content was finalized, and its synthetic gradation curve was plotted in Fig. 1.

Similarly, the proportions of RAP and new aggregates were adjusted to determine the synthetic gradation for mixtures with 30%, 50%, 60%, 70%, and 80% RAP content.
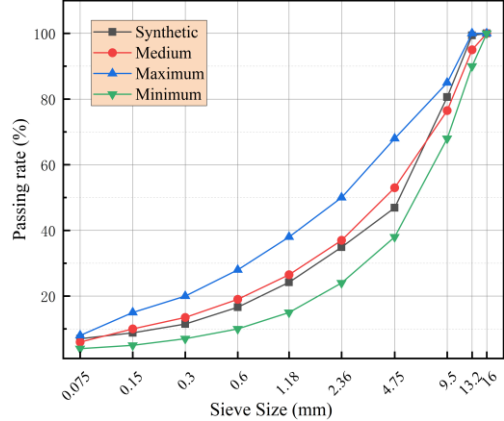
Fig. 1 Synthetic Gradation Curve of BORAP with 20% RAP.

The mixture composition ratios were determined based on the gradation curves and the optimized binder-aggregate ratio, as shown in Table 1.

Table 1. Composition and Proportion of BORAP.

| Material | HMA | Composition and proportion of BORAP (%) | | | | | |
		20% RAP	30% RAP	50% RAP	60% RAP	70% RAP	80% RAP
Bitumen	5.5	4.229	3.921	3.019	2.561	2.234	1.908
Aggregate	94.5	76.46	67.04	48.39	38.89	29.27	19.57
RAP	-	19.12	28.77	48.39	58.34	68.29	78.30
Bio-oil	-	0.167	0.173	0.176	0.183	0.189	0.195
GO	-	0.024	0.024	0.025	0.026	0.026	0.027

2.3 Mechanical performance assessment

BORAP with high RAP content is generally used as a high-modulus asphalt layer for base and intermediate courses. In this study, dynamic modulus testing and rutting performance testing were conducted to characterize the mechanical performance of BORAP mixtures with different RAP contents. The dynamic modulus tests for BORAP with varying RAP contents were conducted at temperatures of 20°C and 45°C, while the rutting tests were performed at a temperature of 60°C.

2.4 Environmental and economic assessment

A circular economy focuses on reusing materials to minimize environmental impact and enhance sustainability. Life Cycle Assessment (LCA) serves as a key methodology within this framework to quantify the environmental effects of material reuse. This study adopts a cradle-to-gate approach to evaluate the environmental impacts of optimal asphalt mixtures. In this study, the functional unit is defined as a 1.0 km long, 3.75 m wide, and 60 mm thick dual-lane recycled asphalt layer. The system boundaries define the modeling framework for assessing the to-

tal embodied energy (TEE) and greenhouse gas emissions (GHG) across the lifecycle phases, including raw material production, transportation to the mixing plant, manufacturing, delivery to the site, and the processes of compaction and laying.

The life cycle inventory (LCI) data for various stages were sourced from the 2015 China Energy Statistical Yearbook and relevant research studies. Models developed by White and further improved by Singh (Jain and Chandrappa, 2024) were utilized to quantify the TEE and GHG of BORAP, as shown in Equations 1 and 2.

$$TEE = \sum 1000 \times W (T \times Dn \times (Pe + Me + (Te \times Di)) + Ce) \quad (1)$$

$$GHG = \sum 1000 \times W (T \times Dn \times (Pg + Mg + (Tg \times Di)) + Cg) \quad (2)$$

Where W = road width (m); T = layer thickness (m); Dn = material density (kg/m³); Pe = material production value (MJ/kg); Pg = material production value (kg.CO_2eq./kg); Me = material mixing value (MJ/kg); Mg = material mixing value (kg.CO_2/kg) ; Te = transport from production site to application site (MJ/kg-km); Tg = transport from production site to application site (kg.CO_2eq./kg-km); Di = distance from material production site to mixing plant (km); Ce = compaction efforts (MJ/kg-km); and Cg = compaction efforts (kg.CO_2eq./kg-km)

Similar to the LCA, the construction cost for laying 1.0 km of asphalt layer was evaluated. The construction cost of BORAP can be categorized into three components: material cost (Mc), transportation cost (Tc), and construction cost (Cc). Material cost includes expenses for asphalt, aggregates, bio-oil, and GO. Transportation cost covers the delivery of raw materials to the mixing plant and asphalt mixtures to the construction site, or directly to the site for on-site mixing. Construction cost (Cc) includes expenses for asphalt mixture placement, equipment rental, and labor, as calculated in Equation 3.

$$C = \sum (T \times W \times (Mc + Tc + Cc)) \quad (3)$$

Where T = layer thickness (m); W = road width (m); M_c = Material cost (CNY/km/m²); T_c = Transportation cost (CNY/km/m²); C_c = Construction cost (CNY/km/m²).

3 RESULTS AND DISCUSSION

3.1 Mechanical performance

Fig. 2 and 3 illustrate the variation trends in the dynamic modulus of BORAP with different RAP contents. Compared to the virgin asphalt mixture (0% RAP), the mixtures with 20% and 30% RAP contents exhibit relatively lower strength. The reason is that, despite the addition of GO as a modifier, the bio-oil used as a rejuvenator significantly softens the aged asphalt. At these lower RAP levels, the softening and viscosity-reducing effects of the bio-oil outweigh the stiffening effects of the aged asphalt.

However, when the RAP content exceeds 50%, the situation reverses. The stiffening and elastic reinforcement effects of the aged asphalt become more prominent, coupled with the modifying effects of GO, resulting in a significant enhancement of the mechanical properties of the recycled asphalt mixtures. This dual effect greatly improves the cohesion of the recycled asphalt, leading to an increase in the mixture's overall strength.
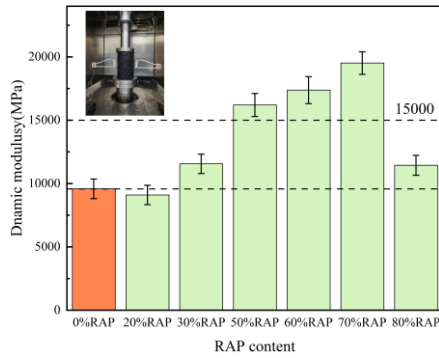
Fig. 2 Dynamic Modulus of BORAP under 20°C.
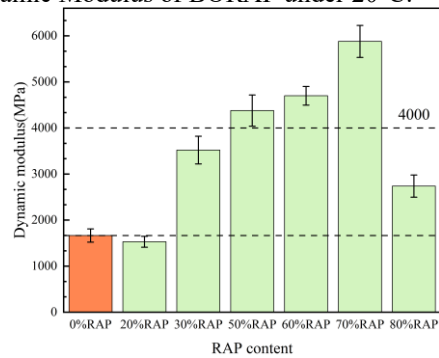
Fig. 3 Dynamic Modulus of BORAP under 45°C.

Although the strength increases with the RAP content, a declining trend is observed when the RAP content reaches 80%. Theoretically, the asphalt binder with 80% RAP content should meet the requirements of high-modulus asphalt mixtures. However, the strength of recycled asphalt mixtures is not solely determined by the cohesion of the binder; factors such as internal friction angle and gradation also play critical roles. As a result, mixtures with 80% RAP content may face challenges in ensuring stable bonding between the RAP and new bitumen during mixing and compaction, potentially leading to internal defects and overall decrease in strength. Therefore, from the perspective of dynamic modulus, 70% RAP can be considered the optimal content.

According to the rutting test results of BORAP shown in Fig. 4, the dynamic stability increases with the rise in RAP content. This is because the higher proportion of aged asphalt in the recycled asphalt mixtures enhances the high-viscosity and high-elasticity properties of the binder, thereby improving the overall resistance to permanent deformation. For BORAP with 20% RAP, 30% RAP, and 50% RAP, the dynamic stability is lower than that of the virgin

asphalt mixture. This is attributed to the significant softening effect of bio-oil on the aged asphalt, demonstrating that bio-oil is a scientifically reliable rejuvenator. For mixtures with 60% RAP, 70% RAP, and 80% RAP, the dynamic stability exceeds that of the virgin asphalt mixture. This indicates that at higher RAP contents, the softening and viscosity-reducing effect of bio-oil becomes limited, only partially restoring the performance of aged asphalt, and failing to bring the mixtures to the same level as the virgin asphalt mixture. Based on the data from the above test results, 70% is the optimal RAP content from the perspective of mechanical performance.
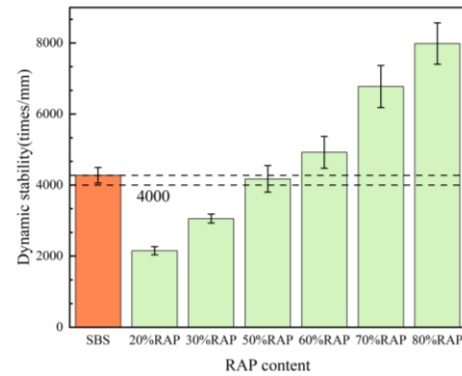
Fig. 4 Dynamic Stability of BORAP in Rutting Test.

3.2 TEE, GHG and cost comparisons

The material quantities for different recycling schemes were determined based on the mixture density, composition, and proportions. Using the LCI values, the energy consumption and emission values per unit mass of the mixture were obtained by calculating the weighted average of the mass proportions of the individual components. Finally, the TEE and GHG values were calculated from Eqs. (1) and (2) and the results were shown in Fig. 5 and Fig. 6. Compared to the HMA scheme, incorporating 30% RAP reduced the TEE of BORAP by 16.95% and GHG emissions by 16.18%. At 60% RAP content, the TEE decreased by 36.93%, while GHG emissions dropped by 35.88%. When the RAP content increased to 70%, the reductions reached 41.48% for TEE and 41.59% for GHG emissions. Although both TEE and GHG emissions decreased progressively with higher RAP content, the reduction rate slowed within the range of 60% to 80% RAP. Considering the mechanical performance and carbon reduction benefits, 70% RAP content is a reasonable choice for BORAP. Based on the calculation results, the main sources of TEE and GHG for BORAP are the material production and mixing stages. The TEE and GHG values during the transportation stage are influenced by both the RAP content and transportation distance. Reducing the transportation distance of RAP or increasing the RAP content can effectively lower these values. In contrast, the energy consumption and carbon emissions during the construction

stage are relatively low and less affected by the RAP content.
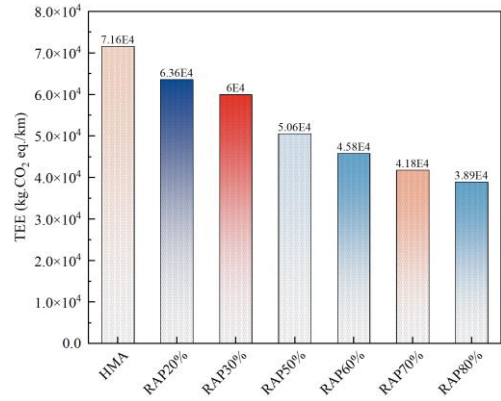
Fig. 5 TEE values for BORAP with different RAP contents.
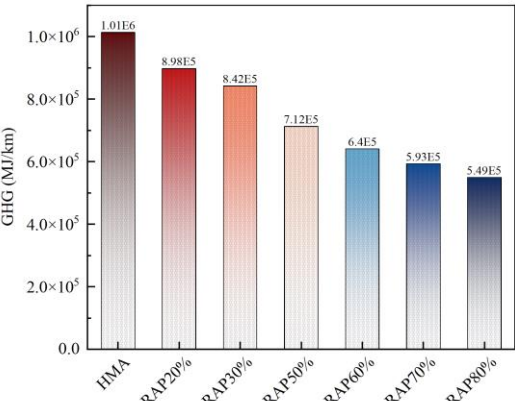
Fig. 6 GHG values for BORAP with different RAP contents.

The costs of different schemes were calculated based on the material quantities and their adjusted cost prices. The cost inventory was divided into three parts: material production costs, transportation costs, and construction costs. The cost data were derived from a comprehensive reference to JTG/T 3833-2018 *Specification*, JTG/T 3832-2018 *Specification*, quotes from material manufacturers, and price information provided by construction units. As shown in Table 2, as the RAP content increases, the total cost gradually decreases. The cost reduction becomes substantial when the RAP content reaches 50% or higher, significantly improving the economic efficiency of the project. Compared to the cost of HMA, the cost of BORAP with 70% RAP content is reduced by 37.16%, making it the most cost-effective option.

Table 2. Costs at Each Phase of BORAP.

Phase	Cost (CNY/1000)						
	HMA	20% RAP	30% RAP	50% RAP	60% RAP	70% RAP	80% RAP
Production	498	449	413	333	291	259	231
Transportation	81	104	99	89	84	79	75
Construction	68	68	68	68	68	68	68
Total	646	621	580	490	442	406	374

4 CONCLUSIONS

This study assesses the mechanical performance and the economic and environmental benefits of bio-oil/RAP-based high-modulus mixtures with different RAP contents. The main findings are as follows:

(1) The RAP content significantly affects the performance of BORAP. The dynamic modulus increases with the RAP content, reaching its peak at 70%, while the dynamic stability also improves as the RAP content increases. Based on a comprehensive analysis, the RAP content is recommended to be controlled at 70%.

(2) The utilization of RAP and bio-oil reduced the TEE and GHG values. Compared to the energy consumption and emissions of HMA asphalt mixture, the high-modulus asphalt mixture achieved a 41.48% reduction in TEE and a 41.59% reduction in GHG emissions, with the highest benefit ratio observed at 70% RAP content. When the RAP content reaches 70%, the cost of BORAP is reduced by approximately 37.16% compared to that of HMA.

5 ACKNOWLEDGEMENTS

6 REFERENCES

GIRIMATH, S. & SINGH, D. 2019. Effects of bio-oil on performance characteristics of base and recycled asphalt pavement binders. *Construction and Building Materials,* 227.

JAIN, S. & CHANDRAPPA, A. K. 2024. Performance and Life Cycle Assessment of Recycled Mixtures Incorporating Reclaimed Asphalt and Waste Cooking Oil as Rejuvenator: Emphasis on Circular Economy. *Journal of Materials in Civil Engineering,* 36.

MATTINZIOLI, T., SOL-SANCHEZ, M., DEL BARCO CARRION, A. J., MORENO-NAVARRO, F., DEL CARMEN RUBIO-GAMEZ, M. & MARTINEZ, G. 2021. Analysis of the GHG savings and cost-effectiveness of asphalt pavement climate mitigation strategies. *Journal of Cleaner Production,* 320.

MIRO, R., VALDES, G., MARTINEZ, A., SEGURA, P. & RODRIGUEZ, C. 2011. Evaluation of high modulus mixture behaviour with high reclaimed asphalt pavement (RAP) percentages for sustainable road construction. *Construction and Building Materials,* 25**,** 3854-3862.

Performance of bio-bitumen produced using sugarcane molasses

Dheeraj Mehta

Research Scholar, Department of Civil Engineering, Indian Institute of Technology Roorkee, Roorkee, INDIA-24766, d_mehta@ce.iitr.ac.in

Nikhil Saboo

Associate Professor, Department of Civil Engineering, Indian Institute of Technology Roorkee, Roorkee, INDIA- 247667, nikhil.saboo@ce.iitr.ac.in

ABSTRACT: Bio-bitumen has emerged as a sustainable alternative to petroleum bitumen. The renewable nature of bio-bitumen coupled with greener production has garnered significant attention in the pavement industry. This study presents the rheological and mixture performance of bio-bitumen produced using sugarcane molasses. Multiple stress creep recovery (MSCR) and linear amplitude sweep (LAS) tests were undertaken to evaluate the rheological performance, while mixture performance was assessed using wheel rut test and indirect tensile asphalt cracking test (IDEAL CT). The results of the investigation showed that the addition of SM lowered the accumulation of strain. The non-recoverable creep compliance (J_{nr}) was found to be lower in bio-bitumen as compared to conventional bitumen indicating enhanced rutting resistance. The number of cycles to failure (N_f) of bio-bitumen increased, indicating improved fatigue life. Overall, the mixture's performance against rutting and fatigue cracking was found to be satisfactory.

1 INTRODUCTION

The demand for crude oil derived bitumen is on steep rise due to rapid highway construction. The annual consumption of bitumen for the year 2022 stood at 122 million tonnes, as per the report of the International Bitumen Emulsion Federation (Asphalt Institute and Eurobitume 2022). From an Indian viewpoint, the consumption was 8.87 million metric tonnes. The non-renewable nature and ever-increasing price of crude oil generates search for sustainable paving materials. One such renewable material of interest is sugarcane molasses (SM).

SM is a viscous liquid obtained as a by-product of sugar production industry. Typically, SM is made up of sucrose, fructose, and glucose. Additionally, SM has few traces of minerals and has moisture in the range of 15 % - 25 %. SM is used in soil stabilization, as a retarder in concrete, and is being explored as a partial replacement of bitumen. Hareru and Ghebrab (Hareru and Ghebrab 2020) evaluated the rheological properties of sugarcane molasses modified binders. The results revealed that the addition of SM leads to improved rutting resistance. Phuc Le (Le 2021) studied the performance of sugarcane molasses replaced bituminous mixtures. The resistance against permanent deformation and moisture susceptibility was found to improve. Saboo et al. (Saboo et al. 2023a) explored the feasibility of using sugarcane molasses as a partial replacement of bitumen. Through a set of tests on bitumen and mixtures, they concluded that the incorporation of SM improved resistance against permanent deformation without compromising fatigue resistance. Mehta and Saboo (Mehta and Saboo 2024) assessed the effect of SM source on properties of physical and chemical properties of bio-bitumen. The findings showed that the SM source did not affect the properties of bio-bitumen. Based on the existing literature, it can be seen that limited studies are available on the performance of bio-bitumen. Therefore, the aim of the study is to evaluate the performance characteristics of bio-bitumen binders and mixtures against rutting and fatigue.

2 OBJECTIVES

- To assess the rutting and fatigue resistance performance of bio-bitumen blends using multiple stress creep recovery and linear amplitude sweep tests.
- To evaluate the performance of bio-bitumen mixtures against rutting and fatigue via wheel rut and indirect tensile asphalt cracking test (IDEAL-CT)

3 MATERIALS

Viscosity graded bitumen VG 40 which is widely used in Indian condition was used as a base binder in the study. Table 1 shows the properties of bitumen as per IS 73.

Table 1 Physical properties of VG 40

Properties	Results	Specifications
Penetration at 25°C, 100 g, 5 s, 0.1 mm	41	35*
Absolute viscosity at 60°C, Poises	4219	3200-4800
Flash point (Cleveland open cup), °C	285	220*
Solubility in trichloroethylene, percent	99.95	99*
Softening point (R&B), °C	52.4	50*
Ductility at 25°C, cm	>100	25*

* Minimum

Sugarcane molasses (SM) is a thick dark brown liquid obtained via sugar refining process. Figure 1 shows the appearance of SM. Table 2 represents the properties of SM.

Figure 1 Appearance of SM

Table 2 Basic properties of SM

Property	Value
°Brix	79
Moisture content, %	15.42
Specific gravity, g/cc	1.402
pH	4.72

4 OPTIMUM DOSAGE AND PRODUCTION PROCEDURE OF BIO-BITUMEN

4.1 Optimum dosage of SM

The selection pertaining to optimum dosage of SM was decided based on (a) change in the stiffness of the binder (true fail temperature), (b) flowability (tar viscometer), and (c) moisture sensitivity (10 min boiling test). At each dosage of SM (10 % to 40 % by weight of bitumen), all three criteria were checked sequentially. Until 30 % replacement, all the criteria were satisfied. At 40 % replacement, issues related to flowability were observed, limiting the pumpability of bio-bitumen. Based on the above criteria the optimum dosage was fixed at 30 % of SM by weight of bitumen. In the interest of brevity, the details regarding the criteria are not presented here and can be found elsewhere (Mehta and Saboo 2024; Saboo et al. 2023b; a).

4.2 Preparation procedure of bio-bitumen

Bio-bitumen was produced by heating the base binder (VG 40) to a temperature of 130 °C – 140 °C, followed by addition of SM. The blend of bitumen and SM is mixed with a low shear mixer at an rpm of 500 for a duration of 15 – 20 mins.

5 EXPERIMENTAL FLOWCHART

To accomplish the aforementioned objectives the following research plan was adopted as shown in figure 2
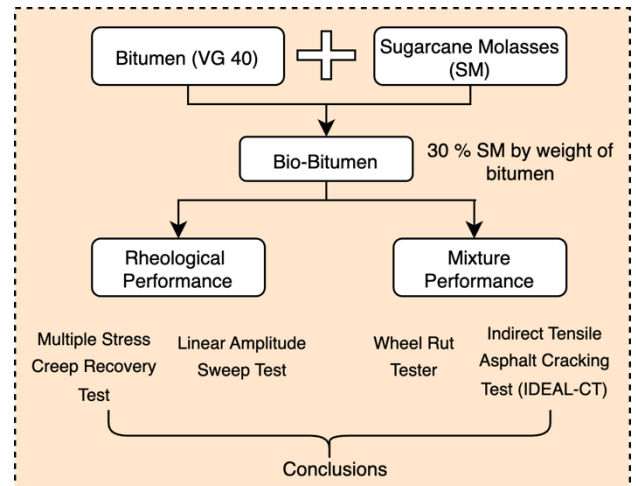
Figure 2 Research methodology flowchart

6 EXPERIMENTAL METHODS

6.1 Rheological Performance

The permanent deformation characteristics of bio-bitumen were evaluated using multiple stress creep recovery test as per AASHTO T350. The test was conducted at 50°C, 60 °C, and 70 °C. The range of temperature were considered to account for average maximum pavement temperature. Ten cycles of loading are given at each stress level (0.1 kPa and 3.2 kPa). A small non-recoverable creep compliance (J_{nr}) and higher percentage recovery (%R) are desired for enhanced rutting performance. The intermediate temperature performance of bio-bitumen was evaluated using linear amplitude sweep test (AASHTO TP 101). Intermediate test temperature 20 °C was considered. LAS is a two step wherein a frequency sweep test followed by an amplitude sweep test is performed. The obtained values are used as input to develop relation between number of cycles to failure (N_f) and strain (γ), as depicted in equation 1

$$N_f = A\gamma^B \qquad 1$$

Where A and B are model parameters.

6.2 Mixture Performance

The bio-bitumen mixtures were subjected to wheel rut test and IDEAL CT test to evaluate the resistance against rutting and fatigue. For wheel rut tester

samples were compacted to 7 % air voids wherein a wheel load of 700 N was made to pass back and forth over the specimen in accordance with EN 12697. The rut depth versus number of passes was recorded. IDEAL CT test was performed on the specimen prepared at 7 % air voids. A vertical load on diametrical axis of sample is applied to record the displacement versus load curve. CTindex and asphalt flexibility ratio (AFR), which is ratio of l_{75} by m_{75}. A higher AFR is an indication of better flexibility of the bituminous mixture.

RESULTS AND DISCUSSIONS

6.3 *Strain accumulation of bio-bitumen*

Figure 3 depicts the accumulated strains of bio-bitumen at 3.2 kPa^{-1} stress level for test temperatures of 60 °C and 70 °C. The results shown are average of three replicates. As seen, the addition of SM reduced the rate of strain accumulation in bio-bitumen compared to the base binder. At higher temperature, the smaller accumulation of strain ensures good rutting performance.
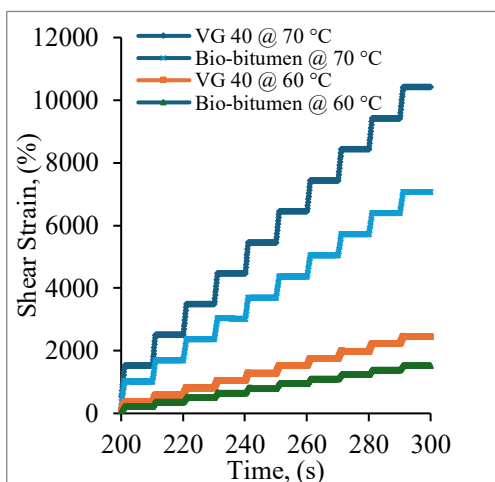
Figure 3 Strain accumulation of bio-bitumen

6.4 *Non recoverable creep compliance (J_{nr}) and percentage recovery (%R)*

The permanent deformation characteristics of bio-bitumen were quantified using non-recoverable creep compliance (J_{nr}) and percentage recovery (% R). A lower value J_{nr} indicates a small irrecoverable strain of bitumen. Figure 4 shows the variation of J_{nr} at 3.2 kPa stress level. It can be seen that the J_{nr} value increases with increase in test temperature whereas % R decreases (refer table 3). In general, regardless of the test temperature, the bio-bitumen showed better rutting resistance than the base binder. For instance, at 70 °C, the J_{nr} of bio-bitumen was found to be 32 % lower than VG 40. As seen, the %R value reduced with increase in temperature. At 50 °C and 60 °C, bio-bitumen showed equivalent or slightly better recovery

than base binders. However, at 70 °C no binder showed recovery. In summary, the enhanced rutting resistance could be linked to the chemical interaction between SM and bitumen leading to lower non-recoverable creep compliance.
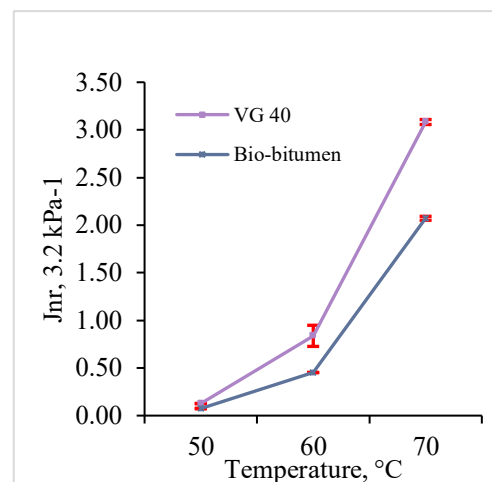
Figure 4. Non-recoverable creep compliance of bio-bitumen

Table 3 Percentage recovery of bio-bitumen

	@50 °C	@60 °C
VG 40	16.3 %	3.2 %
Bio-bitumen	21 %	5 %

6.5 *LAS*

The fatigue life of bio-bitumen was assessed using number of cycles versus strain as presented in figure 5. The fatigue life of bio-bitumen increased with the addition of SM. For bio-bitumen sample at 20 °C (5 % strain), the fatigue life increased by 3.55 %. The improvement in fatigue life can be attributed to gummy interaction imposed by SM to bitumen resulting in enhanced elasticity. Overall, it was found that the addition of SM led to improved intermediate temperature performance.
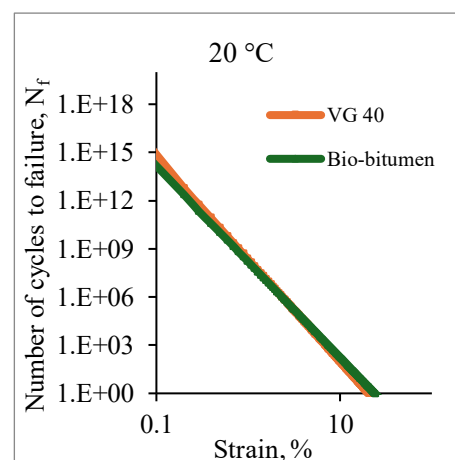
Figure 5 Variation of number of cycles to failure versus strain of bio-bitumen

6.6 Rutting resistance of mixtures

Figure 6 shows the variation of rut depth over the course of 2000 passes at 60 °C. As can be seen, the rut depth progression of bio-bitumen was lower than the base binder. At the end of 20000 passes, the rut depth of bio-bitumen and VG 40 was 4.91 and 5.58 mm, respectively. Overall, the incorporation of SM resulted in enhanced resistance against permanent deformation.
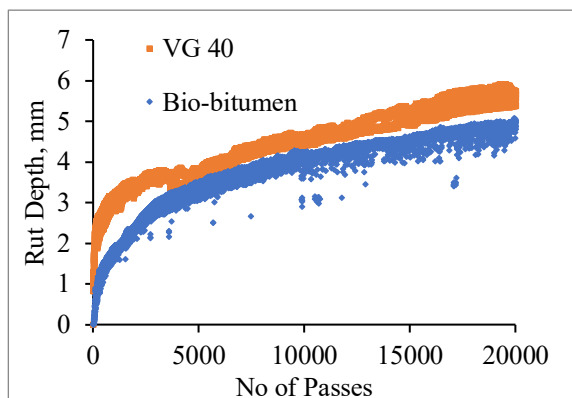
Figure 6 Rut depth versus number of passes of bio-bitumen

6.7 Fatigue resistance of mixtures

Figure 7 shows the IDEAL CT index and AFR of VG 40 and bio-bitumen mixtures. As can be seen, the incorporation of SM resulted in higher CT_{index} and AFR. The CT_{index} values of bio-bitumen were 20 % higher than control mixture. The higher values of AFR indicate improved cracking resistance of bio-bitumen.
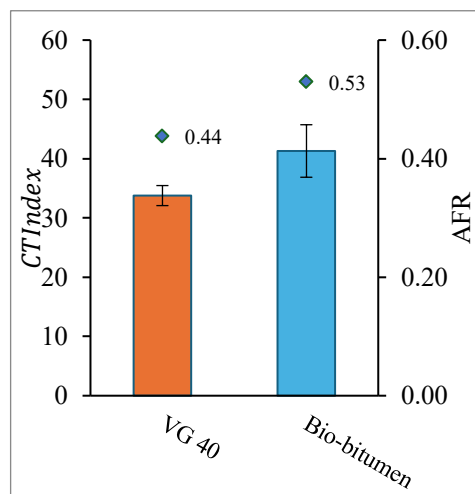
Figure 7 CTindex and AFR variation of bio-bitumen

7 CONCLUSIONS

This study evaluated the rheological and mixture performance of bio-bitumen against permanent deformation and fatigue resistance.

- The addition of SM through MSCR test results revealed that bio-bitumen had lower rate of strain accumulation and lower non recoverable creep compliance.
- The number of cycles to failure slightly increased, indicating an improved fatigue life of bio-bitumen in comparison to base binder.
- Through wheel rut testing, it was found that bio-bitumen mixture had lower rut depth compared to control mixtures.
- The bio-bitumen mixtures had 20 % CTindex than the control mixtures.

8 REFERENCES

Asphalt Institute and Eurobitume. 2022. *The bitumen industry-a global perspective*.

Hareru, W., and T. Ghebrab. 2020. "Rheological Properties and Application of Molasses Modified Bitumen in Hot Mix Asphalt (HMA)." *Applied Sciences 2020, Vol. 10, Page 1931*, 10 (6): 1931. Multidisciplinary Digital Publishing Institute. https://doi.org/10.3390/APP10061931.

Le, V. P. 2021. "Performance of asphalt binder containing sugarcane waste molasses in hot mix asphalt." *Case Studies in Construction Materials*, 15: e00595. Elsevier. https://doi.org/10.1016/J.CSCM.2021.E00595.

Mehta, D., and N. Saboo. 2024. "Use of sugarcane molasses for preparation of bio-asphalt: Effect of source." *Constr Build Mater*, 421: 135691. Elsevier. https://doi.org/10.1016/J.CONBUILDMAT.2024.135691.

Saboo, N., M. Sukhija, D. Mehta, K. Haswanth, A. Srivastava, and A. Patil. 2023a. "Use of raw sugarcane molasses as a partial replacement of asphalt binder: An experimental investigation." *Constr Build Mater*, 369: 130541. Elsevier. https://doi.org/10.1016/J.CONBUILDMAT.2023.130541.

Saboo, N., M. Sukhija, D. Mehta, M. Verma, and A. Patil. 2023b. "Production of bio-bitumen using sugarcane molasses: Perfromance and Application." *Journal of IRC*, 82–1: 26–34.

Mechanism analysis of bio-oil rejuvenated bitumen based on molecular dynamics simulation

Fei Pan
Institute of Highway Engineering, RWTH Aachen University, 52074 Aachen, Germany

Markus Oeser
Federal Highway Research Institute (BASt), Brüderstr. 53, 51427 Bergisch Gladbach, Germany

Pengfei Liu
Institute of Highway Engineering, RWTH Aachen University, 52074 Aachen, Germany

ABSTRACT: Bio-oil, a waste material, has been increasingly utilized to rejuvenate aged bitumen. This study employs molecular dynamics method to investigate how bio-oil enhances the performance and rejuvenates aged bitumen. The analysis was conducted on blended models with varying proportions of aged bitumen, virgin bitumen, and bio-oil to determine their density and zero-shear viscosity. Mean square displacement (MSD) and radial distribution function (RDF) analyses were used to elucidate the rejuvenation mechanisms of bio-oil in aged bitumen. The results demonstrate that adding bio-oil effectively reduces the density and zero-shear viscosity of aged bitumen. This enhancement is attributed to increased molecular diffusion and reduced asphaltene aggregation. These findings offer new insights into using bio-oil-rejuvenated bitumen in pavement engineering to enhance sustainability.
Keywords: Bio-oil; Aged bitumen; Molecular dynamics; Rejuvenation mechanism

1 INTRODUCTION

Energy generation, transportation, and manufacturing collectively account for the majority of global carbon emissions, with road transportation being a major contributor. To address this, asphalt pavement recycling technologies, particularly hot central plant recycling, have been widely adopted to reduce resource consumption and emissions in road construction. This method mixes reclaimed asphalt pavement (RAP) with virgin bitumen and rejuvenators under controlled conditions, though challenges like RAP variability and limited content persist. Utilizing waste products such as bio-oils, and engine oils as rejuvenators has shown significant potential for enhancing recycling efficiency and promoting waste utilization.

Recent studies have explored various bio-oils and waste products as rejuvenators for aged bitumen, yielding promising results. Daniel Oldham et al. demonstrated that esterifying WCO via transesterification reduces acidity and enhances resistance to water damage [1]. Lv et al. investigated WBO's rejuvenation effects on aged bitumen through rheological and microscopic analyses [2], while Wang et al. highlighted that bio-oil's rejuvenating effects vary with dosage, recommending levels below 10% [3]. Wang et al. found that WCO marginally restores self-healing properties, with temperature playing a critical role [4]. Ke et al. revealed that CFO improves fatigue resistance and recommended a 6% addition rate [5]. Yi et al. reviewed rejuvenation mechanisms, noting plant-based products restore through diffusion, while animal-based rejuvenators act on molecular forces [6].

On a molecular scale, Shisong Ren revealed that molecular mobility differences in rejuvenators influence the restoration of low-temperature relaxation properties [7]. While significant progress has been made, the underlying mechanisms of bio-rejuvenated bitumen remain unclear.

The aim of this study is to investigate the rejuvenating effect of bio-oil on aged bitumen and its underlying mechanisms. By modeling various proportions of aged bitumen, virgin bitumen, and bio-oil, the density, diffusion property, and asphaltene aggregation are evaluated. To elucidate the rejuvenation mechanisms, we analyzed MSD and RDF index during MD simulations.

2 MATERIALS AND METHODOLOGY

2.1 *Model Establishment*

Bitumen is a multifaceted organic mixture predominantly consisting of carbon, nitrogen, oxygen, and sulfur, derived from the petroleum refining process. Due to its intricate composition, it is nearly impractical to define a molecular model based on a single bitumen component. Instead, researchers typically segregate bitumen into four main fractions based on polarity and solubility: saturates, aromatics, resins, and asphaltenes (SARA). Li and Greenfield et al. devised the 12-component models reflecting these SARA classifications to depict the pristine bitumen composition [8]. Upon aging, FTIR analysis indicates a marked elevation in both the carbonyl index (ICO) and the sulfoxide index (ISO) [9]. By incorporating variable quantities of ketone and sulfoxide groups into the original 12-component models, re-

searchers can simulate the molecular structure of aged bitumen. Palmitic acid, oleic acid, linoleic acid, and stearic acid were chosen as the molecular structures of bio-oil. The molecular structures of the virgin bitumen, aged bitumen, and bio-oil are shown in Figure 1. The simulations utilize the OPLS-AA Force Field, specifically designed for organic small molecules, to effectively reproduce the physical properties of the bitumen system.
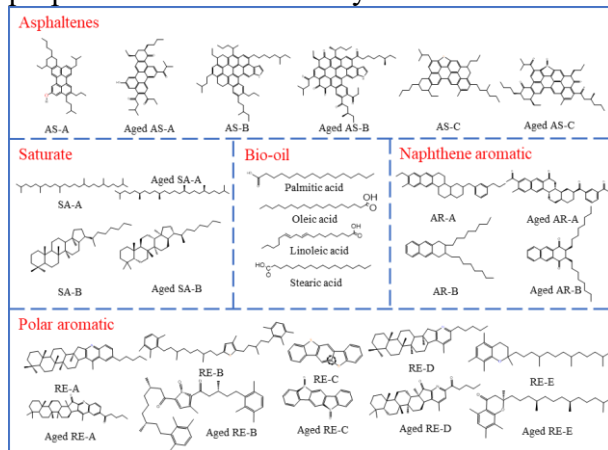
Figure 1. Structures of molecular structures of virgin bitumen, aged bitumen, and bio-oil.

MD simulations of various bitumen molecular configurations, including virgin and aged bitumen as well as bio-oil, were conducted in a periodic cubic box using the Gromacs software. Initial molecular models were constructed using Packmol software. Visualization of the molecular models was performed using the Visual Molecular Dynamics (VMD) software.

2.2 Simulation methods

2.2.1 Model equilibrium

After configuring the system, the model underwent further MD simulations with a simulation timestep of 1 fs. The equilibrium process for the system is detailed as follows:

1.Energy minimization: Initial relaxation of the system to remove any high-energy configurations.

2. Annealing at NVT ensemble: The temperature cyclically varied between 298.15 K and 598.15 K five times, each cycle lasting 10 ns, to enhance molecular mobility and achieve a more uniform distribution of molecular configurations.

3. Equilibration at Higher Temperature (NVT Ensemble): The system is equilibrated at 598.15 K for 10 ns to stabilize at this elevated temperature.

4. Annealing in NPT Ensemble: Similar to step 2, but under constant pressure, temperature is cycled between 298.15 K and 598.15 K five times, each for 10 ns.

5. Final Equilibration in NPT Ensemble: The system is brought to a final equilibrium at 298.15 K for 10 ns under constant pressure.

After 40 ns of total equilibration, the system is deemed to have reached equilibrium. The simulation then continues for an additional 1 ns at a constant temperature (NPT ensemble at 298.15 K), during which molecular trajectories and simulated states are recorded every 5 ps.

2.2.2 Shear viscosity

During asphalt pavement construction, the viscosity of bitumen plays an important role in the mixing as well as paving process. Among the various methods for monitoring bitumen viscosity in MD simulations, the Periodic Perturbation Method stands out as particularly effective. This method, a type of nonequilibrium molecular dynamics (NEMD), evaluates viscosity by examining the stress-strain relationship within the simulation model under cyclic perturbations. During simulation, a periodic external force is applied along the Z-direction to modulate the velocity field within the periodic system. Below are detailed steps for calculating zero-shear viscosity using the periodic perturbation method in MD simulations:

1. Initial Conformation: Start with a fully equilibrated conformation of the bitumen model as the initial state for viscosity calculations.

2. Equilibration in NPT Ensemble: Equilibrate the system at 408.15 K for 10 ns under NPT ensemble conditions to stabilize pressure and temperature.

3. Equilibration in NVT Ensemble: Further equilibrate the system at 408.15 K for 10 ns under NVT ensemble conditions to stabilize temperature while keeping volume constant.

4. NEMD Simulations: Perform NEMD simulations at a constant temperature of 408.15 K in the NVT ensemble. Apply different amplitudes of periodic perturbation (A = 0.01, 0.02, 0.03 nm/ps²) to the bitumen molecules over 1 ns.

5. Viscosity Calculation: Calculate the viscosity for each amplitude of the periodic perturbation and determine the standard deviation for these measurements.

6. Linear Fitting and Extrapolation: Employ linear fitting to extrapolate the viscosity values at different shear amplitudes to determine the zero-shear viscosity.

2.3 Analyzing indicators

2.3.1 Impact of bio-oil on diffusion behavior

Mean Square Displacement (MSD) is used to describe the motion of a molecule over a certain time interval and is especially important in the study of diffusion processes. MSD is obtained by calculating the average of the squares of the changes in the position of a particle over a specific time interval. The specific formula is shown in Equation (1):

$$MSD(\tau) = \langle |\mathbf{r}(t+\tau) - \mathbf{r}(t)|^2 \rangle \tag{1}$$

where $r(t)$ denotes the particle position at time t, τ is the time interval, ⟨...⟩ denotes the average over all particles and/or all possible times t. The MSD helps to understand the diffusion properties within a substance.

2.3.2 Impact of bio-oil on asphaltene aggregation

The radial distribution function (RDF), denoted as $g(r)$, is instrumental in describing the spatial distribution of particles. Specifically, it quantifies the ratio of the probability of locating another particle within a spherical shell at a specific distance r from a reference particle, relative to the probability of finding such a particle in an ideal gas state. This analysis is crucial for understanding the molecular aggregation and interaction dynamics induced by bio-oil in the bitumen. The RDF formula is given in Equation (2).

$$g(r) = \lim_{dr \to 0} (\rho(r))/(4\pi\rho\_bulk\, r^2\, dr) \quad (2)$$

where $g(r)$ is the RDF value, $\rho(r)$ is the average number of particles within the r and $r+dr$ shell layers, and ρ_bulk is the bulk density of the particles.

3 RESULTS AND DISCUSSION

3.1 Zero-shear Viscosity Analysis

Figure 2 illustrates the viscosity changes of aged bitumen at shear amplitudes of 0.01, 0.02, and 0.03 nm/ps², with varying proportions of virgin bitumen and bio-oil additions. Consistent with the shear-thinning effect, the viscosity of each bitumen model decreases as the shear amplitude increases. This phenomenon is attributed to the formation of nanoaggregates within the asphaltenes and aromatics components of the bitumen. To accurately determine the zero-shear viscosity, linear fits to the viscosity measurements at the three shear amplitudes were performed. The zero-shear viscosity for each model is identified at the intersection of the extrapolated line with the Y-axis, providing a precise measure of the model's inherent viscosity absent of shear forces. The shear viscosity measurements indicate that aged bitumen inherently possesses a higher viscosity compared to virgin bitumen. Upon the incremental addition of virgin bitumen to the aged mixture, a progressive decrease in shear viscosity is observed. This dilution effect is further enhanced by the incorporation of bio-oil. The results of the zero-shear viscosity simulation show the same trend as the viscosity lab-test results. Notably, the addition of bio-oil significantly reduces the viscosity of the aged bitumen, allowing it to approach the lower viscosity levels characteristic of virgin bitumen. This trend suggests that strategic formulations involving virgin bitumen and bio-oil can effectively modulate the rheological properties of aged bitumen, optimizing it

for specific application requirements and improving its workability during paving processes.
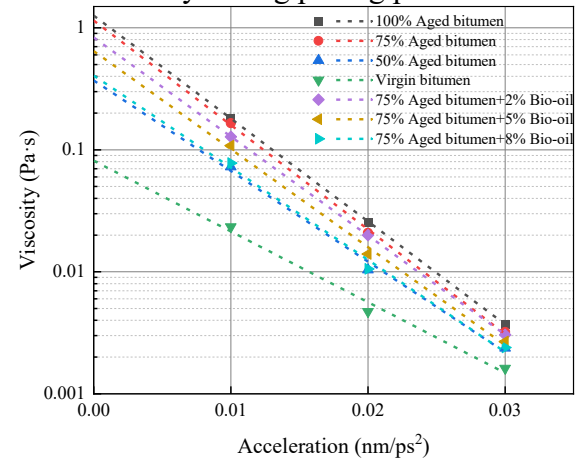
Figure 2. Density of each bitumen model.

3.2 Component diffusivity analysis

The rejuvenation effectiveness of aged bitumen is significantly influenced by the penetrative capacity of the rejuvenator. An increase in penetration ability of the rejuvenator typically correlates with a significant increase in the rejuvenation effect. In this study, MSD analysis was utilized to investigate the diffusion characteristics of bio-oil within the bitumen system. The MSD data were collected from simulations conducted at a constant temperature of 298.15 K over a duration of 1 ns under the NPT ensemble.

To mitigate the impact of initial fluctuations and ensure the system reached a steady state, the first and last 10% of the data collected during the simulation were excluded from the analysis.

Figure 3 presents the MSD curves for bitumen models with various dosages of virgin bitumen and bio-oil, all measured at 298.15 K. The analysis reveals that the self-diffusion rate of aged bitumen is inherently slower compared to that of virgin bitumen. However, the diffusion capability of the aged bitumen is enhanced with the addition of virgin bitumen. Notably, the introduction of bio-oil significantly boosts the overall self-diffusion ability of the bitumen system.
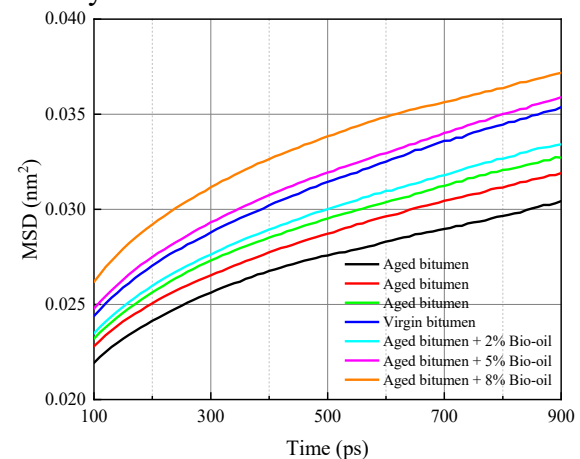
Figure 3. MSD curves for each bitumen model.

3.3 Structural analysis of bitumen models

This study employs RDF analysis to further investigate the structural changes of aged bitumen after the addition of virgin bitumen and bio-oil. Given that asphaltenes represent the most viscous component of bitumen, significantly contributing to its overall viscosity, this study focuses on the behavior of asphaltenes and their interactions within various components of virgin bitumen and bio-oil rejuvenated bitumen.

Figure 4 displays the RDF curves of asphaltene-asphaltene interactions within bitumen models rejuvenated by different dosages of bio-oil. The figure illustrates a clear trend: as the dosage of bio-oil increases, the peak values of the RDF curves decrease. This trend signifies an improvement in asphaltene dispersion within the bitumen with each incremental addition of bio-oil. The reduction in RDF peak heights indicates that bio-oil acts effectively to diminish the degree of asphaltene aggregation in aged bitumen. This molecular level disaggregation is crucial as it directly contributes to the rejuvenation of key performance characteristics of the bitumen, such as reduced viscosity and enhanced self-diffusion coefficients. By facilitating better dispersion of asphaltenes, bio-oil not only mitigates the stiffening effect inherent in aged bitumen but also enhances the material's overall workability and durability.
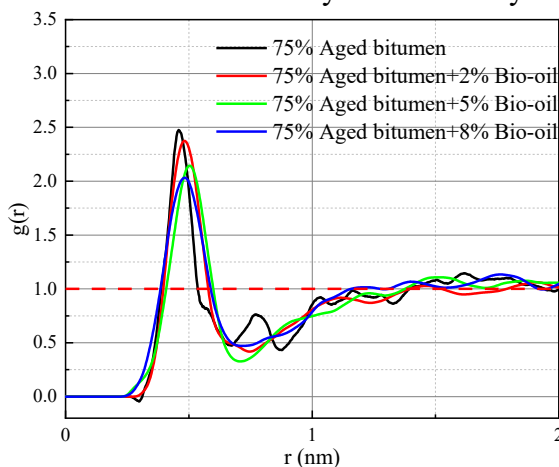
Figure 4. RDF curves for different bio-oil doping models.

4 CONCLUSIONS

In this study, molecular dynamics simulations were used to investigate the physical properties and nanoscale structural characteristics of aged bitumen, virgin bitumen, and bio-oil mixed models. The study aims to explore the rejuvenating of bio-oil as a rejuvenator for aged bitumen. The comprehensive simulations yielded the following conclusion: the incorporation of virgin bitumen and bio-oil into aged bitumen can effectively reduce zero-shear viscosity. The MSD index indicates that the incorporation of bio-oil can effectively improve the diffusion capacity of bitumen molecules. RDF analysis indicates that the addition of virgin bitumen and bio-oil can weak-

en the aggregation of asphaltenes, which is a key reason for their rejuvenation in aged bitumen.

REFERENCE

[1] D. Oldham, A. Rajib, K.P.R. Dandamudi, Y. Liu, S. Deng, E.H. Fini, Transesterification of Waste Cooking Oil to Produce A Sustainable Rejuvenator for Aged Asphalt, Resources, Conservation and Recycling 168 (2021) 105297.https://doi.org/10.1016/j.resconrec.2020.105297

[2] S. Lv, J. Liu, X. Peng, H. Liu, L. Hu, J. Yuan, J. Wang, Rheological and microscopic characteristics of bio-oil recycled asphalt, Journal of Cleaner Production 295 (2021) 126449.https://doi.org/10.1016/j.jclepro.2021.126449

[3] J. Wang, S. Lv, J. Liu, X. Peng, W. Lu, Z. Wang, N. Xie, Performance evaluation of aged asphalt rejuvenated with various bio-oils based on rheological property index, Journal of Cleaner Production 385 (2023) 135593.https://doi.org/10.1016/j.jclepro.2022.135593

[4] G. Sun, B. Li, D. Sun, J. Zhang, C. Wang, X. Zhu, Roles of aging and bio-oil regeneration on self-healing evolution behavior of asphalts within wide temperature range, Journal of Cleaner Production 329 (2021) 129712.https://doi.org/10.1016/j.jclepro.2021.129712

[5] K. Shi, Z. Fu, R.-m. Song, F.-l. Liu, F. Ma, J.-s. Dai, Waste chicken fat oil as a biomass regenerator to restore the performance of aged asphalt: rheological properties and regeneration mechanism, Road Materials and Pavement Design 24(1) (2023) 191-215.https://doi.org/10.1080/14680629.2021.2012505

[6] J. Yi, Y. Wang, Z. Pei, M. Xu, D. Feng, Mechanisms and research progress on biological rejuvenators for regenerating aged asphalt: Review and discussion, Journal of Cleaner Production 422 (2023) 138622.https://doi.org/10.1016/j.jclepro.2023.138622

[7] S. Ren, X. Liu, S. Erkens, Towards critical low-temperature relaxation indicators for effective rejuvenation efficiency evaluation of rejuvenator-aged bitumen blends, Journal of Cleaner Production 426 (2023) 139092.https://doi.org/10.1016/j.jclepro.2023.139092

[8] D.D. Li, M.L. Greenfield, Chemical compositions of improved model asphalt systems for molecular simulations, Fuel 115 (2014) 347-356.https://doi.org/10.1016/j.fuel.2013.07.012

[9] B. Hofko, M.Z. Alavi, H. Grothe, D. Jones, J. Harvey, Repeatability and sensitivity of FTIR ATR spectral analysis methods for bituminous binders, Materials and Structures 50(3) (2017) 187.https://doi.org/10.1617/s11527-017-1059-x

Evaluation of international sustainability certifications for road infrastructure

L. Rico, S. Caro, D. Borda-Cardozo, M. Sanchez-Silva, B. Caicedo
Department of Civil and Environmental Engineering. Universidad de los Andes, Bogotá D.C., Colombia

ABSTRACT: The construction sector is one of the most polluting industries because of its high resource consumption and related greenhouse gas emissions. To reduce these impacts, many countries have adopted sustainable practices for road infrastructure projects, which are major contributors to the industry's footprint. Over the past two decades, guidelines, technical specifications, and certifications have been developed to promote sustainability during different phases of these projects. These initiatives mainly focus on resource efficiency, biodiversity conservation, and community well-being. This study compares and analyzes how several international infrastructure sustainability certifications address the environmental impact of infrastructure projects. It also provides a preliminary evaluation of a Colombian public-private partnership road project using the Envision certification. The findings of this evaluation highlight opportunities to the project –and, on a major scale, to the country–, to enhance sustainability in the areas of materials, pavement design, energy use, and emissions.

1 INTRODUCTION

Sustainable infrastructure certification systems are tools to evaluate the compliance of a project to specific sustainability requirements. These certifications stand out for their ability to integrate economic, environmental, social, and governance dimensions, providing an overall rating that captures the level of sustainability of the project throughout its life cycle. The systems are based on specific indicators, and the final scores that deter-mine the level of sustainability are obtained through the direct sum of through a weighted system of partial scores, which allows to compare the results between different projects (León, 2018).

These certifications can be applied at all stages of infrastructure projects: from planning and design to implementation and dismantling, and they not only encourage the transition to low-carbon economies and promote sustainable solutions to environmental problems, but they also build trust among stakeholders such as governments, multilateral banks, and private investors (Losos & Fetter, 2022). Similarly, certifications serve as a vehicle to implement and communicate best practices in sustainability within the infrastructure industry.

The growing demand for sustainable infrastructure projects has driven the creation of certifications 'tailored' to specific contexts, ensuring that evaluation criteria address the particularities of the sector and environment (Bhattacharya et al., 2019). Existing experiences show that these certifications strengthen investor confidence by ensuring that projects meet high standards of quality and sustainability while considering the specific characteristics of each region and sector (León, 2018).

Existing certifications include BREEAM Infrastructure, created in the United Kingdom in 2003 as a pioneer in infrastructure sustainability. More recent efforts include FAST-Infra and Blue Dot Network. These newer certifications emphasize transparency and access to information while encouraging the mobilization of private capital towards sustainable and high-quality projects (Losos & Fetter, 2022). Additionally, certification systems like Envision, SURE, and IS-Scheme have broadened evaluation approaches by incorporating specific criteria related to resilience, biodiversity, and social equity. This approach has led certifications to become not only technical tools but also instruments of transformation towards more inclusive and responsible sustainable development models (Losos & Fetter, 2022).

In developing countries like Colombia, these certifications are especially relevant due to the need to align national standards with global sustainability demands. Although national regulations include basic sustainability-related aspects such as environmental licensing and project compensations, robust technical metrics and a comprehensive approach that also includes governance, resilience, and social justice

dimensions are still missing. For instance, international certifications address aspects such as resource efficiency, climate impact mitigation, and habitat protection, areas where Colombian regulations have significant limitations (Losos & Fetter, 2022).

Finally, certifications also play a crucial role in risk assessment and in the mobilization of financial resources. For example, for investors of public-private partnership road projects, the compliance with sustainability standards implies a reduction in risks associated with projects and ensures alignment with international agreements such as the Paris Agreement. This impact goes beyond the environmental area, as it also promotes practices that strengthen social equity, include vulnerable communities, and generate tangible benefits for populations affected by infrastructure projects (Sanchez, 2021; Losos & Fetter, 2022).

2 ENVIRONMENTAL CONSIDERATIONS AMONG CERTIFICATIONS

Understanding the environmental considerations of existing sustainable certifications is particularly important for pavement engineers, as they provide information to support decision-making processes related to material selection, pavement design, and construction and maintenance strategies, all of which can positively impact the sustainability of a project. Thus, the environmental aspects of the following nine international sustainability certifications that are applicable to road infrastructure projects were analyzed and compared: i) BREEAM Infrastructure, ii) GreenPave, iii) Green-LITES, iv) Greenroads, v) INVEST, vi) Envision, vii) IS-SCHEME, viii) SURE, and ix) FAST-Infra. The analysis focused on four main environmental topics: materials, energy and fuel, natural environment, and pollution. Within these, recurring patterns, less developed areas, and outstanding practices were identified.

2.1 Materials

After comparing all systems, seven subtopics were identified in this area: recycling, reuse, use of local materials, waste management, tools to measure environmental impact, durable designs and final disposal of materials. Figure 1 summarizes the findings. A value of '0' on the axes in this figure means that no certification considers this component, while a value of 9 means that all certifications evaluated take it into account.

It was found that recycling of materials is of particular interest in Greenroads and GreenPave, which are certification specifically for road infrastructure projects, and they include minimum recycling percentages based on the type of material and structure selected. In contrast, systems with a broader scope,

such as Envision and IS-SCHEME, address recycling in a more general way, although IS-SCHEME complements this evaluation with 'Type I environmental labels', facilitating the identification of materials with lower environmental impacts.

In terms of material reuse, certifications like Greenroads and INVEST prioritize resource conservation within the project, while BREEAM Infrastructure also focuses on reusing entire structures, highlighting their potential to minimize waste. Local materials are widely promoted in all systems as they reduce emissions related to transportation. However, only three certifications (GreenPave, Greenroads and SURE), specify usage percentages for these materials, revealing differences in how this aspect is evaluated.

Finally, the IS-SCHEME certification stands out in the area of 'materials' as it is the only one that addresses all seven subtopics.

Figure 1. Number of certifications that consider the different 'materials' components.

2.2 Energy and fuel

A total of four subtopics were identified in this area: reduction of energy consumption in the construction phase, reduction of energy consumption in the operation phase, use of alternative energies and reduction of the use of fossil fuels.

Reduction of energy consumption during operation is included in seven certifications. Reduction of energy consumption during construction and use of alternative energies are addressed by six certifications. However, only three systems include concrete goals to reduce fossil fuels. Among them, INVEST promotes the use of biofuels and similar efficient technologies. GreenPave recommends the use of warm-mix asphalt for flexible pavements, which significantly reduces energy consumption during the manufacturing stage. In terms of renewable energy, Greenroads and Envision are distinguished by

establishing minimum usage percentages for renewable sources (5% and 25%, respectively), and rewarding projects with energy surpluses.

Finally, Envision and INVEST were identified as the systems that more comprehensively address the different subtopics within the energy and fuel area.

2.3 Natural environment

The six subtopics identified in this area, which are illustrated in Figure 2, are: conservation of water resources, reduction of water consumption during the construction phase, reduction of water consumption during the operation phase, water resource management, preservation of areas with high ecological value and soil preservation.
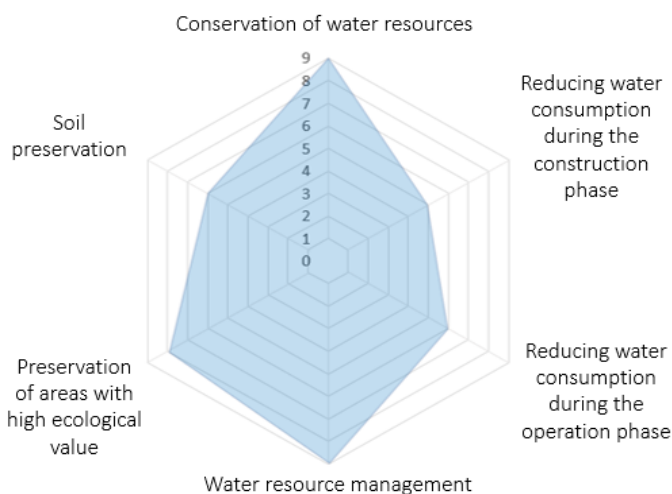
Figure 2. Number of certifications that consider the different 'natural environment' component.

In this case, Envision stands out for promoting connectivity between fragmented habitats and biodiversity monitoring plans, and Greenroads encourages the use of permeable pavements to control runoff and preserve sensitive areas. On the other hand, BREEAM Infrastructure and Envision are the only ones that include the restoration of areas affected after construction.

Envision, Greenroads, SURE, BREEAM Infrastructure and FAST-Infra include all the subtopics in the natural environment area.

2.4 Pollution

A total of five subtopics were identified in this area: water, noise, air, light and soil pollution. Eight certifications include aspects related with the first three, while light and soil pollution received less attention, and they are considered in only five certifications. Notably, Greenroads leads in water pollution with the recognition of specific techniques, such as biological filtration to remove heavy metals. Envision and Greenroads set goals to reduce embodied carbon in

materials, encouraging innovative practices to control air pollution. In terms of noise pollution, GreenPave introduces 'quiet pavements' that reduce urban noise by up to 7 dBA.

Envision, INVEST, SURE, BREEAM Infrastructure, and FAST-Infra address all five subtopics in this environmental area.

3 EVALUATION OF A CASE OF STUDY

As a first step to assess the current level of sustainability in major national road infrastructure projects in Colombia, a preliminary evaluation of the compliance of a 50 Km public-private partnership (PPP) project located on a mountainous area using the Envision certification was performed. These PPP are projects with investments exceeding $15.23 billion in Capex (EY, 2024). They consist of an agreement between a public entity, in this case the national government, and a private agent for the construction of public infrastructure and the provision of related services. In these types of contracts, the private partner assumes an important role in the management and mitigation of project risks. Road PPP projects have been developed over the last 25 years in Colombia, and they have been critical in developing a high-quality national road network.

The evaluation was performed using two scenarios: i) strict, and ii) flexible. In the strict scenario, only practices implemented with the required documentary evidence were considered, while in the flexible scenario, additional points were awarded for implemented practices that lack of complete documentation.

Envision has been proposed by the Institute for Sustainable Infrastructure (ISI) and the American Society of Civil Engineers (ASCE), and it evaluates five main categories: quality of life, leadership, resource allocation, natural environment, and climate and resilience. Scores awards projects the following levels depending on the total points obtained in percentage: Verified (20%), Silver (30%), Gold (40%), and Platinum (50% or more). This certification was selected as it has been widely promoted in North America and has the potential to be applied in Latin America as well.

Under the strict scenario, the results suggest that the project could obtain a score of 32%, reaching the Silver level. This result reflects strengths in the 'quality of life' category, which excelled in both scenarios (see Figure 3), achieving high scores due to efforts to improve community well-being, mobility, and accessibility. This reflects a strong focus on social sustainability as a key priority of the project.

However, categories related to environmental sustainability, such as 'energy', 'conservation', and 'ecology', scored low due to the absence of specific measures to reduce emissions, preserve sensitive

habitats, and optimize energy resource use. Specifically, within the 'natural environment' category, only one credit related to the preservation of undeveloped land scored points, highlighting significant opportunities to improve environmental conservation strategies.
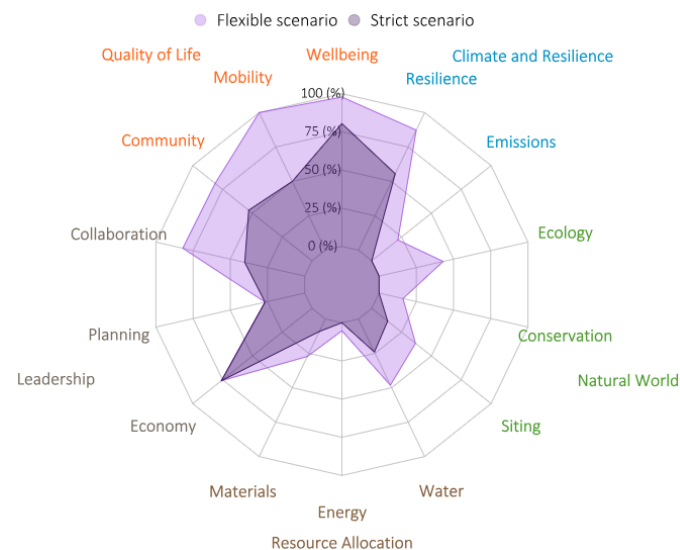
Figure 3. Results of the preliminary evaluation of a national PPP road project using Envision.

In the flexible scenario, the score increased to 56%, achieving the Platinum level. This improvement was primarily due to the recognition of implemented practices without complete evidence, especially in the categories of 'natural environment' and 'resource allocation'. Additional points were awarded for efforts in conserving undeveloped areas and for the initial use of recycled and local materials. However, these areas still showed limited performance compared to other categories, emphasizing the need to improve material management and environmental sustainability in the project.

It is hypothesized that a similar situation might occur in several other road projects in the country, which is valuable information to promote actions (e.g., material specification, public policy, contractual conditions) to strengthen these areas. Future work includes to perform a similar evaluation to other projects.

4 CONCLUSIONS

This work confirms that international certifications are interesting tools for assessing sustainability in infrastructure projects and they promote high standards and trust among stakeholders.

In terms of environmental sustainability, the certifications emphasize key areas such as material management, energy efficiency, natural environment conservation, and pollution reduction. They also encourage valuable practices like material recycling,

renewable energy adoption, and ecosystem protection. However, interesting opportunities were identified in some of the certification systems in areas such as long-lasting designs, tools to measure environmental impact, fossil fuel reduction, and soil preservation.

The preliminary evaluation of a major public-private partnership (PPP) road project in Colombia using Envision showed a strong commitment to social aspects, particularly in improving the living conditions of nearby communities and employees. The environmental sustainability areas received the lowest scores, highlighting opportunities to improve sustainable aspects, mainly in the areas of materials, energy and emissions.

6 PREFERENCES

Bhattacharya, A., Contreras Casado, C., Jeong, M., Amin, A.-L., Watkins, G., & Silva Zuniga, M. (2019). Attributes and Framework for Sustainable Infrastructure. https://doi.org/10.18235/0001723

Departamento Nacional de Planeación. 2024. Participación Privada en Proyecto de Infraestructura. Recovered from de https://tinyurl.com/ycxn3ctp

EY. 2024. Colombia: líder emergente en la gestión de las APPs para infraestructura. Recovered from https://tinyurl.com/zdycehve

León, K. (2018). Análisis de los diferentes sistemas de certificación en construcción sostenible a nivel mundial y sus perspectivas de aplicación y cumplimiento en Colombia. Monograph document. Universidad Militar Nueva Granada (Colombia).

Losos, E., & Fetter, R. (2022). Building a Common Approach: Global Infrastructure Standards. Nicholas Institute for Environmental Policy Solutions, Duke University. Recovered from: https://nicholasinstitute.duke.edu/sites/default/files/publications/Building-Common-Approach-Global-Infrastructure-Standards.pdf

Sanchez, P. (2021). Certificaciones sostenibles; Soluciones locales a un reto global. Monograph document. Universidad Politécnica de Madrid (Spain).

Multiscale evaluation of the effects of Organosolv lignin on asphalt materials

E.J. Rueda
Pontificia Universidad Católica de Chile, Escuela de Construcción Civil, Santiago, Chile

S. Caro
Universidad de los Andes, Department of Civil and Environmental Engineering, Bogotá, Colombia

R. Abedin-Zadeh
Universidad de los Andes, Department of Civil and Environmental Engineering, Bogotá, Colombia

J. Perdomo-Pacheco
Universidad de los Andes, Department of Civil and Environmental Engineering, Bogotá, Colombia

ABSTRACT: The increasing demand for road infrastructure, combined with the urgent need to reduce greenhouse gas emissions, has intensified the interest in sustainable alternatives for asphalt use, which currently accounts for approximately 6% of all industrial emissions. Among these alternatives, lignin—a natural biopolymer found in plans and a relevant byproduct of the paper industry—has demonstrated to have antioxidant and UV protection properties, which can extend the service life of asphalt mixtures. This work investigates the influence of Organosolv lignin on asphalt materials at two scales: i) asphalt binder (micro-scale), and ii) asphalt mortars (meso-scale). Linear viscoelastic properties of both materials at different ageing conditions were evaluated using different addition doses of lignin (0, 4, 8 and 12% by weight of the asphalt binder for asphalt modification and 0, 8 and 14% by weight of asphalt binder for mortars) at different ageing conditions, and a chemical characterization was conducted to assess the interactions between the lignin and the asphalt binder. The findings highlight the potential of this type of lignin as an additive for enhancing the response and durability of asphalt materials.

1. INTRODUCTION

There is an increasing concern about the pollution generated by flexible pavement projects, as more than 90% of road networks rely on asphalt binders –with a global demand that exceeds 18 million tons annually (Xie et al., 2017) –, and the fact that asphalt production contributes approximately with 6% of the total industrial greenhouse gas emissions (Lei et al., 2021). This situation has motivated the evaluation of more sustainable alternatives.

Biopolymers such as lignin have emerged as promising additives for the asphalt binder. This material is a natural component abundant in plants and wood, that has shown to exhibit antioxidant and stabilizing properties, making it an attractive candidate as an asphalt binder modifier (Boerjan et al., 2003). Previous studies have reported that the use of lignin in asphalt mixtures is related to the increase in the thermal and oxidation resistance of the material (Duarte Mendonça et al., 2023; Feng et al., 2023; Yu et al., 2021).

Despite these advances, there is still limited research on the use of different types of lignin. Also, most research has focused on evaluating the impact of lignin on the asphalt binder or in asphalt mixtures, but not on asphalt mortars, which is the mixture of asphalt binder and fine aggregate particles that constitutes a critical phase in the mechanical performance of asphalt mixtures. This study evaluated the use of Organosolv lignin as an asphalt binder modifier. The experimental plan included chemical testing of a lignin-modified asphalt binder, as well as a rheological evaluation of its impact at the micro (asphalt binder) and meso (asphalt mortar) scales, considering various addition doses and ageing conditions.

2. MATERIALS AND EXPERIMENTAL PLAN

Details of the materials and the experimental methodology applied at each scale is described next.

2.1. Materials and preparation of test specimens

The selected asphalt binder was an unmodified 60/70 (1/10 mm) penetration grade bitumen. The lignin was extracted from the Willow tree (Salix alba) using the Organosolv method and was acquired from China. The material is a brown powder with a purity of 85.9%. The aggregates used to prepare the mortars are sandstone and they are smaller than 1.18 mm (sieve No. 16).

2.1.1. Micro scale: asphalt binder specimens

To evaluate the effect of the lignin on the chemical and rheological properties of the asphalt binder, five binder blends were prepared: i) original unmodified asphalt (A-0%), ii) asphalt that has undergone the

mixing time and temperature conditions used for lignin modification but without adding the product (AL-0%), and ii) asphalt binder with 4% (AL-4%), 8% (AL-8%), and 12% (AL-12%) lignin by asphalt weight. The modification preparation procedure involved heating the asphalt to 120°C for one hour, the lignin during the final 20 minutes to remove moisture and mixing the materials at 1000 rpm for 40 minutes, using the procedure determined by Abedin-Zadeh (2018). Notice that AL-0% was included in the experimental plan, as the asphalt binder suffers ageing during the modification process, and it was important to capture such changes.

Within this stage of the research, the following ageing conditions were considered:

– Unageing: asphalt binder in its virgin state.
– Short-term ageing: simulated by subjecting the virgin binder to the Rolling Thin Film Oven (RTFO) test as per ASTM D2872.
– Long-term ageing: simulated by subjecting the binder to the Pressure Aging Vessel (PAV) test as per ASTM D6521.

2.1.2. Meso scale: asphalt mortar specimens

The asphalt mortars were fabricated using asphalt binder modified with lignin in proportions of 0%, 8% and 14%, by weight of the binder. The mortar design was based on the fine asphalt matrix of a regular dense graded hot-mix asphalt mixture with a nominal maximum aggregate size of 25mm. The asphalt content was 9.75% by total weight and the particle size distribution corresponded to that shown in Table 1.

Table 1. Gradation curve of asphalt mortar.

Sieve	Sieve [mm]	%Passing [%]
16	1.18	100
40	0.42	65
80	0.17	42
200	0.075	13
Passing 200	-	0

To fabricate the mortar specimens, both the asphalt binders and aggregates were preheated to 160°C for one hour prior to mixing. Testing included samples subjected to three different ageing conditions using one of the protocols proposed in NCHRP 09-54 (Kim et al., 2015):

– Short-term ageing (ST): 160°C for 90 minutes.
– Medium-term ageing (LT1): 135°C for 8 hours.
– Long-term ageing (LT2): 135°C for 24 hours.

After ageing, the mixtures were compacted into cylindrical specimens with 10 cm in diameter and in height using the Superpave Gyratory Compactor (SGC) at a target air void content of 10%, with a tolerance of ±0.7%. Small cylindrical specimens with 12mm in diameter and 50mm in height were cored from the SGC specimen.

2.2. Experimental plan

The experimental plan included the evaluation of the chemical properties of the modified asphalt binder using Fourier transform infrared spectroscopy (FTIR) and the analysis of the mechanical properties of the modified asphalt and of mortars prepared with these binders. The latter consisted of computing the dynamic shear modulus ($|G*|$) of the materials at the different lignin doses and ageing states.

2.2.1. Chemical characterization

The chemical characterization of the asphalt binder was performed using Fourier transform infrared spectroscopy (FTIR), with the aim of identifying the sulfoxide (S=O) and carbonyl (C=O) functional groups, whose increase is associated with asphalt ageing (Hou et al., 2018). For this purpose, asphalt samples in their original, short-term aged (RTFO) and long-term aged (PAV) states were analyzed.

2.2.2. Mechanical characterization

The dynamic shear modulus ($|G*|$) of the binders and mortars was measured under the different ageing conditions. To do so, a dynamic shear rheometer with a parallel plate system for testing the binders and the solid geometry for testing the mortars was used to conduct frequency and temperature oscillatory strain sweep tests in the linear viscoelastic range. At the two scales, frequency ranged between 1 and 30 Hz and temperature between 25°C to 75°C in 10°C increments.

3. RESULTS

Below are the results obtained from the chemical characterization on the asphalt binder and the mechanical characterization on the two scales.

3.1. Chemical characterization.

Figure 1 shows the FTIR results on the asphalt binder samples, highlighting a key difference in the 1000 and 1700 cm^{-1} band, corresponding to sulfoxide (S=O) and carbonyl (C=O) functional groups. In the virgin lignin-free asphalt (A-0%), a gradual increase in this band is observed from the unaged to RTFO state, with a marked peak at the PAV state, an expected increase since these groups increase with asphalt ageing (NCHRP 09-54). In contrast, in the binder modified with 12% lignin (AL-12%), the shift in the unaged and RTFO states is almost non-existent, and the peak at the PAV state is noticeably lower, when compared to the results for A-0%. This result demonstrates that this type of lignin controls the formation of these functional groups, confirming its anti-ageing effect on asphalt.
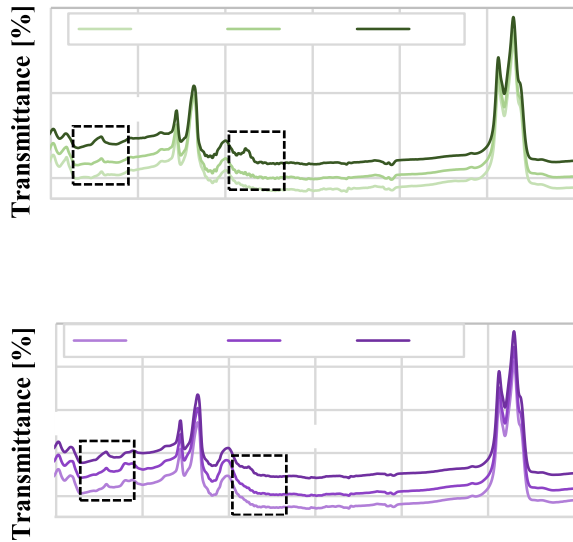
Figure 1. FTIR chemical characterization of asphalt binders (a) A-0% and (b) AL-12% in different ageing states.

3.2. Mechanical characterization.

The average results of |G*| were used to construct master curves of both materials at a reference temperature of 45°C. As an example of the results, Figure 2 shows the master curves of the asphalt binder and of the asphalt mortars with 0% and 8% lignin, grouped based on the ageing state.

At the asphalt binder level (micro scale, Figure 2.a), it is observed that the addition of lignin increases the stiffness of the material (i.e. increase in |G*|) in its original unaged state, as expected as the lignin acts as a filler additive. For example, at 45 °C and 1 Hz (Figure 2.a) |G*| increased by 19.93% and 42.39% between the asphalt binder without lignin and that with lignin at 4% and 8%, respectively.
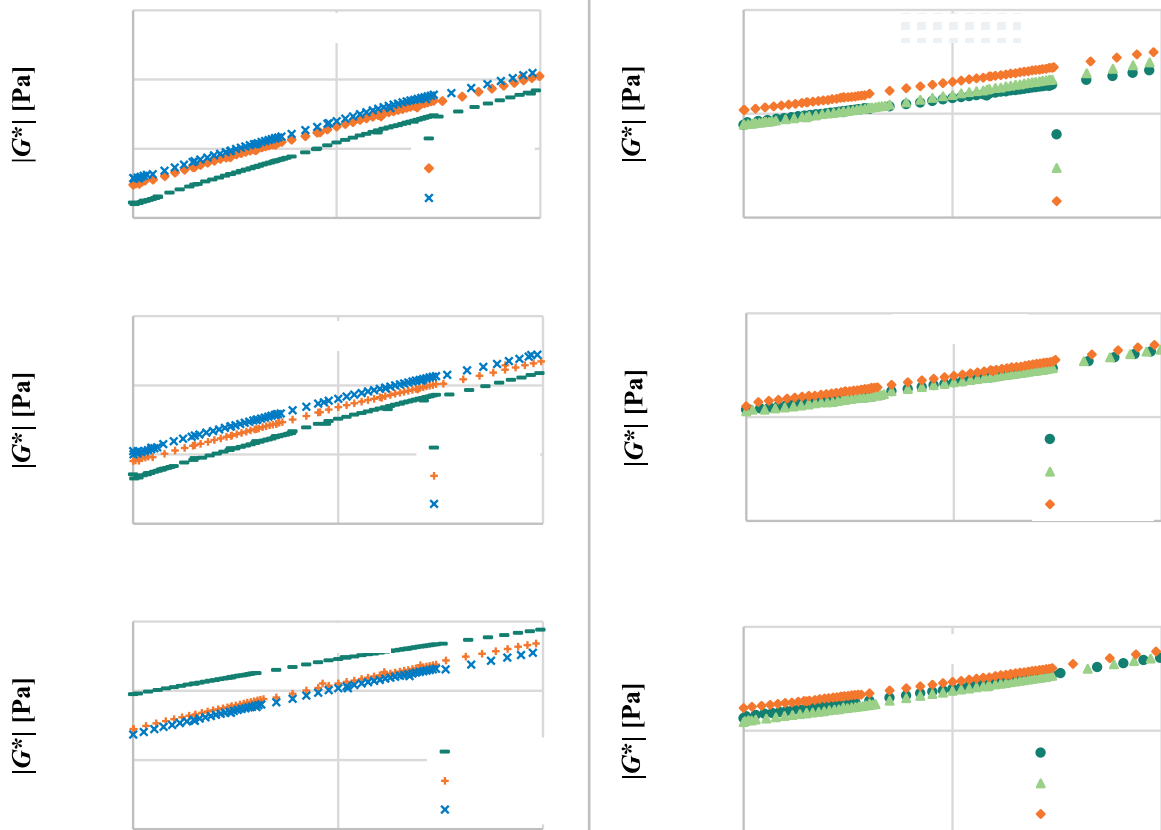
Figure 2. Master curves of |G*| at 45 °C for (a) asphalt binders, and (b) asphalt mortars at the different ageing states evaluated.

When comparing the impact of lignin addition in the increase in |G*| in the asphalt binder, it is observed that for the PAV ageing condition, the magnitude of |G*| is smaller as the lignin content increases. This, combined with the smaller differences in the increase of |G*| between ageing conditions in the binders with lignin, is evidence of the anti-ageing effect of lignin. For instance, at 45 °C and 10 Hz the modulus increased by 104.2% and 718.7% in the RTFO and PAV states for the binder with no lignin compared to

the unaged condition (Figure 3a), while these increases were of 101.7% in the RTFO state and 374.2% in the PAV state in the binder with 4% of lignin.

Although in asphalt mortars the addition of lignin produces larger values of $|G^*|$ is all ageing states (Figures 2b and 3b), the increase in $|G^*|$ between ageing states was smaller in the mortars with larger amounts of lignin. For example, at 1 Hz and 45 °C, the

magnitude of $|G^*|$ for the mortar without lignin increased by 61.6% between the ST and LT1 ageing states, while this increase was 93.8% in the LT2 state, (Figure 3b). In the asphalt mortar with 14% lignin, the increases in $|G^*|$ were only 21.4% and 49.3% when passing from the ST state to the LT1 and LT2 ageing states, respectively. This again shows the antioxidant effect of lignin in asphalt materials.
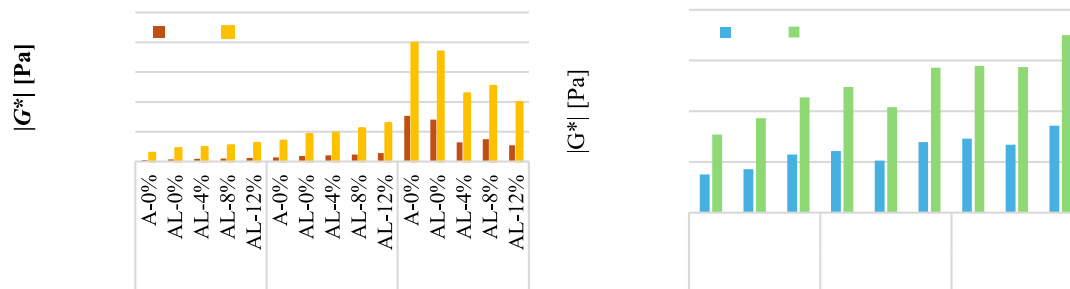
Figure 3. Magnitude of $|G^*|$ at 45 °C and 1 Hz and 10 Hz for (a) asphalt binder and (b) asphalt mortar.

4. CONCLUSIONS

This study investigated the impact of Organosolv lignin on the chemical and rheological properties of an asphalt binder and on the rheological properties of an asphalt mortar. The following are the main conclusions:

The addition of lignin increased the stiffness of both materials, due to the presence of an additional solid fraction. This effect was consistent in both materials across all ageing levels, except for the PAV conditions, where the unmodified binder had the largest value of $|G^*|$. In unaged conditions and during short-term ageing (simulated by RTFO for asphalt binders and ST for mortars), lignin caused an increase in the dynamic modulus in the order of 46 and 138%, respectively. However, in advanced ageing states (PAV for asphalt binder and LT1 y LT2 for mortars), the anti-ageing properties of the lignin controlled the progression of the stiffening effect in both materials.

These findings confirm previous studies on binders and mixtures that have shown the potential of lignin, in this case Organosolv, as an additive to control oxidative hardening caused with ageing. Thus, its use is associated with mixtures that are less fragile under severe ageing and, consequently, more durable.

Future studies are recommended to comprehensively evaluate the impact of this and other types of lignin on the long-term performance (i.e. rutting, fatigue cracking, low temperature cracking) on asphalts with different chemical compositions.

5. REFERENCES

Boerjan, W., Ralph, J., & Baucher, M. (2003). Lignin Biosynthesis. *Annual Review of Plant Biology*, *54*(1), 519–546. https://doi.org/10.1146/annurev.arplant.54.031902.134938

Duarte Mendonça, A. M. G., Melo Neto, O. de M., Rodrigues, J. K. G., Batista de Lima, R. K., Silva, I. M., & Marques, A. T. (2023). Characterisation of modified asphalt mixtures with lignin of pinus and eucalyptus woods. *Australian Journal of Civil Engineering*, *21*(2), 253–264. https://doi.org/10.1080/14488353.2022.2089376

Feng, L., Liu, J., & Hu, L. (2023). Rheological behavior of asphalt binder and performances of asphalt mixtures modified by waste soybean oil and lignin. *Construction and Building Materials*, *362*, 129735.

Kim R,, Castonera, C., Rad, F.; Elwardany, M Underwood. S., Farrar, M., and Glaser, R. (2015), Long-Term Aging of Asphalt Mixtures for Performance Testing and Prediction, *National Cooperative Highway Research Program* (NCHRP). The National Academies Press: Washington DC.

e , , Gu , D , h , Y , Zhe , B , , X , Me , J , … Tao, S. (2021). Adaptive CO2 emissions mitigation strategies of global oil refineries in all age groups. *One Earth*,*4*(8),1114–1126.
https://doi.org/10.1016/j.oneear.2021.07.009

Xie, S., Li, Q., Karki, P., Zhou, F., & Yuan, J. S. (2017). Lignin as Renewable and Superior Asphalt Binder Modifier. *ACS Sustainable Chemistry & Engineering*, *5*(4),2817–2823. https://doi.org/10.1021/acssuschemeng.6b03064

Yu, J., Vaidya, M., Su, G., Adhikari, S., Korolev, E., & Shekhovtsova, S. (2021). Experimental study of soda lignin powder as an asphalt modifier for a sustainable pavement material. *Construction and Building Materials*, *298*,123884. https://doi.org/10.1016/j.conbuildmat.2021.123884.

Performance Evaluation of Full Depth Reclamation (FDR) Mixes Containing Emulsified Asphalt

Rajan Tank[A],
Post Graduate Student, MS University

 Deepa Sasidharan [B]
Scientist, CSIR- Central Road Research Institute, New Delhi, 110025

Bharath Gottumukkala [C]
Sr. Scientist, CSIR- Central Road Research Institute, New Delhi, 110025

Sanjaykumar M Dave[D]
Faculty, MS University

ABSTRACT: Full Depth Reclamation (FDR) is a sustainable and cost-effective pavement rehabilitation technique that involves the in-place recycling of existing pavement materials. The current study evaluates the performance of FDR mixes treated with stabilizing agents such as cement and emulsion. The research compares three distinct gradations considering various in-service pavement compositions carrying different traffic volumes: (i) 100% RAP mix (ii) 50% RAP mix and (iii) 42% soil mixture. Mix design was performed and the performance characterization has been carried out for all three mixes. The performance was assessed through the indirect tensile cracking tolerance test. The results show that the increasing the cement content or the emulsion content can improve the indirect tensile strength of the FDR mixes. However, the increase in cement content can reduce the flexibility and cracking tolerance of the mix whereas increase in emulsion content can improve the flexibility of the FDR mix.

1 INTRODUCTION

The increasing demand on roadways over the past few decades, combined with shrinking budgetary allocations and the necessity to maintain a safe, efficient, and cost-effective transportation system, has created a pressing need to rehabilitate aging pavement infrastructure. In this context, asphalt recycling and reclaiming have gained significant attention as both technically and environmentally sustainable methods for pavement rehabilitation (ARRA, 2015). These techniques align with societal goals by providing safer and more durable roadways while reducing environmental impacts and energy consumption compared to traditional reconstruction methods.

Among the various recycling methods, Full Depth Reclamation (FDR) has emerged as a preferred rehabilitation technique (Smith & Braham, 2018). FDR involves pulverizing the entire thickness of the asphalt pavement, along with a portion of the underlying layers (such as base, subbase, and subgrade), to create a homogenous material (Ghanizadeh, et al., 2018). This reclaimed material can often serve as a stable base for a new surface layer. However, when necessary, mechanical, chemical, or bituminous stabilization methods are employed to enhance the structural and functional properties of the reclaimed material.

The depth of FDR typically ranges between 100 mm and 300 mm, depending on factors such as existing pavement thickness, soil characteristics, and traffic load repetitions (Mallick et al.). The use of FDR improves the pavement's bearing capacity, structural integrity, and longevity, thereby enhancing overall performance. By recycling existing materials, FDR minimizes environmental impact while offering a cost-effective solution for modern infrastructure development (Smith & Braham, 2018).

Full Depth Reclamation (FDR) materials treated with a combination of emulsion and cement demonstrate superior performance in submerged conditions compared to those treated with emulsion alone. The addition of cement enhances the mixture's durability and significantly increases its indirect tensile strength, ensuring improved structural integrity and long-term performance (González et al., 2016). The Indirect Tensile Strength (ITS) of bitumen-stabilized materials improves with increasing emulsion content at a constant cement dosage (Grilli et al., 2018). It has been reported that the stiffness modulus of bitumen-stabilized materials decreases with an increase in reclaimed asphalt content from 0% to 80%. However, this improved when cement dosage was increased from 1% to 2% at a constant emulsion content (Grilli et al., 2018). Studies showed that increase in the cement content in bitumen-stabilized materials (BSM) reduces the slope of fatigue lines, indicating a transi-

tion in material behaviour from asphalt mix to cement-treated materials (Modarres et al., 2011) Despite its advantages, FDR design in India faces challenges due to the lack of comprehensive guidelines.

2 OBJECTIVES

The current study aims to carry out a performance evaluation of FDR mixes with three distinct gradations corresponding to in-service pavement compositions carrying different traffic volumes, viz, (i) 100% RAP mix (ii) 50% RAP mix and (iii) 42% soil mixture. The 50% RAP mix and 42% soil mixes are indicative of roads carrying high and low traffic volume respectively. The FDR are mixes are subjected to indirect tensile test and their performance is evaluated by determining the Cracking Tolerance Index (CTI).

3 MATERIALS

3.1 *Cement*
Ordinary Portland Cement (OPC) 43-grade was utilized in this study. The Properties of Cement comply to IS Standards (IS: 269, 2015).

3.2 *Bituminous Emulsion*
A slow-setting bituminous emulsion (SS-2) containing 61.80% bitumen by weight was used (table 1).

3.3 *Virgin Aggregates*
Virgin aggregates of varying sizes, including 40 mm, 20 mm, 10 mm, 6 mm, and stone dust, were incorporated into the mix. The aggregates were graded in accordance with standard specifications to ensure proper particle size distribution for optimal performance.

Table 1. Properties of SS-2 emulsion

Properties	Result	Specifications	Test method
Penetration (residue) at 25∘C, 100 g, 5 s, 0.1 mm	65	60-350	IS8887
Residue 600 micron IS Sieve (% mass)	0.038%	Max 0.05	IS8887
Viscosity by Say bolt Furol Viscometer, Seconds	41	30-150	IS3117
Storage stability after 24 h, %	0.7	Max 2	IS8887
Miscibility with water (coagulation)	No Co-agulation	No Co-agulation	IS8887
Residue by evaporation, %	61.80%	Min 60	IS8887

3.4 *Reclaimed Asphalt Pavement (RAP)*
Reclaimed Asphalt Pavement (RAP) material containing 4.4% residual binder was used in the preparation of the samples.

4 GRADATION

The gradations were selected in such a way that they represent the actual reclaimed material during FDR of in-service pavements. The 100% RAP mix represents the scenario of reclaiming a thick asphalt layer (figure 1). The 50% RAP mix and 42% soil mixes are indicative of roads carrying high and low traffic volumes as shown in Figure 1. It has been ensured that the selected three gradations comply with the Technical Guideline 2 (TG2) for bituminous stabilized materials and Cement-Treated Base (CTB) gradation limits for FDR materials (MoRTH, 2013).
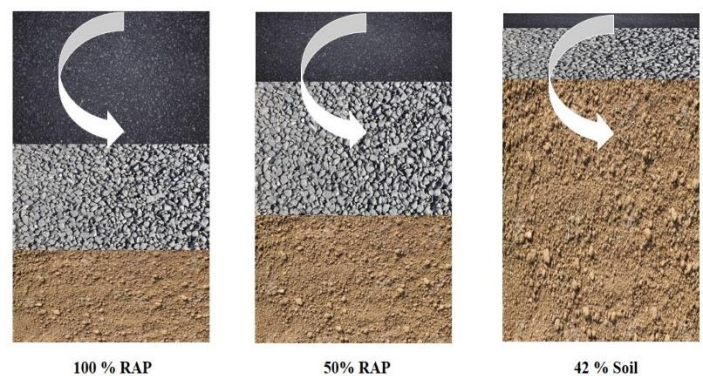
Figure 1. Criteria used for selecting FDR gradations

4.1 *High volume Road*

Trial and error exercises with different crust compositions corresponding to the available templates (1 to 8) in IRC 37: 2018 (based on standard axle road repetitions and California Bearing Ratio) were performed to arrive at the required graduation for high-volume roads. The thickness of the Full Depth Reclamation (FDR) material was limited to 300 mm. The overall reclamation thickness of 300 mm serves as the basis for calculating the contribution of each pavement layer to the overall gradation.

Blending was performed considering the gradation for the base course (WMM) as per MoRTH (2013), and the actual gradation of RAP milled from the wearing and binder courses. To represent those pavements that have been rehabilitated in the past with multiple overlays, 100% RAP mixes were considered in the study. In order to represent high-volume traffic roads, 50% RAP mixes were included, considering both RAP and granular layer (WMM).

4.2 Low Volume Road

For low-volume roads, the choice of gradation was based on the pavement design catalogues for gravel and granular bases/subbases outlined in IRC-SP-72:2015. Similar to high-volume roads, the thickness of the FDR layer is limited to 300 mm to analyse the contribution of the top layer of pavement. The gradation for layers such as Granular Subbase (GSB) and Gravel Base are obtained from the MORD (2014). A blending exercise is conducted for varying CBR values and traffic categories using the design templates from IRC-SP-72:2015.

Traffic category T2 with a CBR range of 7-9% was considered to arrive at the final FDR gradation. The final gradation for FDR was developed by blending the fractions from different layers, ensuring alignment with low-volume road performance requirements. Figure 2 shows the final gradation for a) 100% RAP, b) 50% RAP (high volume) and c) low volume roads. The upper and lower limits for cement-treated base material (IRC 37, 2018) are also included for reference.
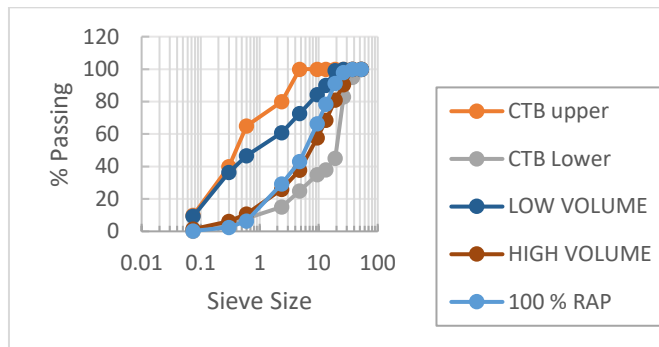
Figure 2. Final Gradation for the FDR mixes

5 MIX DESIGN FOR FDR MIXTURES

The mix design for Full Depth Reclamation (FDR) was performed considering three distinct mixtures: a) 100% RAP, b) 50% RAP + 50% fresh aggregates and, c) 41.7% soil and 58.3% fresh aggregates.

To stabilize these mixtures, bituminous emulsion at 3% and 4%, and cement at 1% and 2% were incorporated, resulting in a total of 12 combinations. The determination of the Optimum Moisture Content (OMC) for each mixture was performed, and the results are summarized in Table 2. The OMC included the pre-wetting water content and the water content of the emulsion.

Table 2. Optimum Moisture Content for Different Mixtures

Mixture Composition	Cement Content (%)	OMC (%)
100% RAP	1	3.70
	2	3.80
50% RAP + 50% Fresh Aggregate	1	3.90
	2	4.10
41.7% Soil + 58.3% Fresh Aggregate	1	4.00
	2	4.25

5.1 Sample Preparation and Compaction

Initially, the sample was prepared as per the required gradation to which the specific cement content (1, 2%) was added. Further, 1% pre-wetting water content was added to the mix, followed by the addition of emulsion. Further, the mix was cured at 40°C for 30 minutes in accordance with the guidelines provided by ARRA. The samples were further compacted using the Marshall Compaction method, where 75 blows were applied on both sides of the specimen to achieve the required density. After compaction, the specimens underwent post-compaction curing at 40°C for 72 hours. Following the curing process, the samples were subjected to a series of performance tests to evaluate their mechanical characteristics. The air void content in the sample ranges between 7- 13%.

5.2 Indirect Tensile Cracking Tolerance Test

The Indirect Tensile Cracking Tolerance test (IDEAL-CT) test was conducted at a temperature of 25°C to determine the cracking resistance of asphalt mixes (ASTM D8225-19). The load vs deformation curve gives an indication of the flexibility of the mixes. CT index is calculated as Eq (1)

$$CT_{index} = \frac{t}{62} \times \frac{l_{75}}{D} \times \frac{G_f}{|m_{75}|} \times 10^6 \qquad (1)$$

Where, $|m_{75}|$ = absolute value of the post-peak slope (N/m), D = Average diameter of the sample (mm), t = Average height of the sample (mm), G_f = Failure Energy (Joules/mm^2), and l_{75} = Displacement at 75 % of the peak load after the peak (mm).

6 RESULTS AND DISCUSSIONS

Figure 3 shows the ITS (indirect tensile strength) values of the FDR fixes at varying cement and emulsion dosages. Table 2 shows the Cracking Tolerance Index (CTI) of the different mixes.

It can be observed that increasing either cement or emulsion content leads to an increase in the ITS for all the mixes. However, at a constant emulsion content, an increase in cement dosage results in a decrease in the crack tolerance index (CTI). In contrast, increasing the emulsion content at a constant cement content results in an increase in both the ITS and the CTI of the mixes.
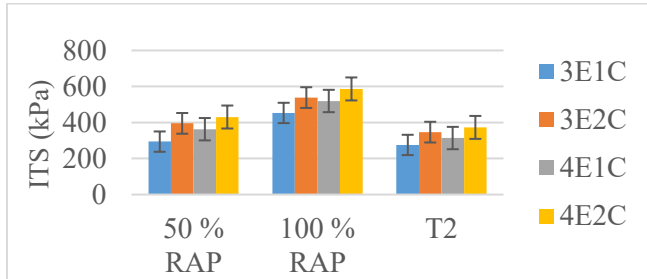
Figure 3. Indirect Tensile Strength (ITS)

Table 2: ITS strength And CT index of FDR mixture

Mix	Notation	Emulsion (%)	Cement (%)	ITS (kPa)	CTI
50 % RAP	50 R E3C1	3	1	296.9	25
	50 R E3C2	3	2	395.2	10
	50 R E4C1	4	1	362.8	33
	50 R E4C2	4	2	430.4	20
100 % RAP	100 R E3C1	3	1	453.1	43
	100 R E3C2	3	2	538.3	34
	100 R E4C1	4	1	519.5	66
	100 R E4C2	4	2	586.4	42
T2	T2 R E3C1	3	1	275.4	7
	T2 R E3C2	3	2	311.1	5
	T2 R E4C1	4	1	345.1	8
	T2 R E4C2	4	2	372.8	5

Figure 4 shows the load vs deformation curve for 100% and 50% rap mixes at specific cement and emulsion contents.
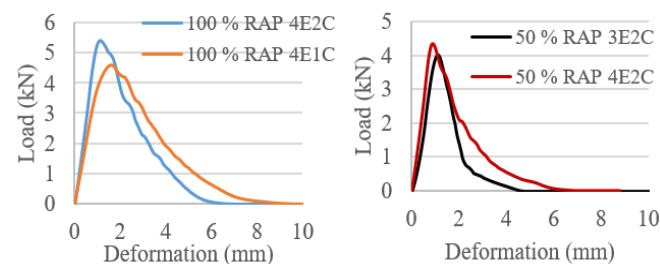
Figure 4. Load Vs Deflection Curve

Though the increase in cement content (1 to 2%) results in a higher peak load, the area under the curve significantly reduces. In contrast, an increase in emulsion content (3 to 4 %) improves the area under the curve and the overall flexibility of the mixes. It was observed that the soil mixes exhibited brittle behavior, failing suddenly without significant deformation.

7 CONCLUSIONS

The influence of emulsion on FDR mixes containing RAP is significant due to the improved flexibility and cracking resistance imparted by the bituminous emulsion. Though the increase in cement dosage can increase the indirect tensile strength, the flexibility of the mix is adversely affected. However, the addition of emulsion along with cement can improve the indirect tensile strength as well as the flexibility of the FDR mixes. The influence of emulsion on soil mixes is not significant and it was observed that the soil mixes exhibited brittle behaviour.

8 REFERENCES

1. ARRA (2015). Basic asphalt recycling manual, 2nd Edition.
2. Ghanizadeh, A. R., et al. (2018). The effect of cement and reclaimed asphalt pavement on the mechanical properties of stabilized base via full-depth reclamation. *Construction and Building Materials,* 161, 165–174.
3. González, Álvaro, Fernando Paniagua, Guillermo Thenoux, and Carlos López. 2016. "Evaluation of Additional Laboratory Tests for Design of Full-Depth Reclamation Mixtures Using Foamed Bitumen." *Transportation Research Record: Journal of the Transportation Research Board,* 2573
4. Grilli, Andrea, Fabrizio Cardone, and Edoardo Bocci. 2018. "Mechanical Behaviour of Cement-Bitumen Treated Materials Containing Different Amounts of Reclaimed Asphalt." *European Journal of Environmental and Civil Engineering,*
5. IRC: 37-2018, Guidelines for Design of Flexible Pavement.
6. IRC: 120-2015: Recommended practice for recycling of bituminous pavements.
7. IRC:SP-72-2015, Guidelines for the design of flexible pavements for low volume rural roads
8. Mallick et al. Laboratory Study of Full-Depth Reclamation Mixes. *Transportation Research Record,* 1813, Paper No 02-3139.
9. Modarres, A, Fereidoon M. N, et al., (2011). "A Parametric Study on the Laboratory Fatigue Characteristics of Recycled Mixes." *Construction and Building Materials.*
10. MoRTH, (2013). Specifications for road and bridge works (5th Rev.).Ministry of Road Transport and Highways, New Delhi.
11. MORD, (2014). Specifications for rural roads (1st Rev.).Ministry of Rural Development. Indian Roads Congress.
12. Smith, Sadie, and Andrew Braham. 2018. "Comparing Layer Types for the Use of PavementME for Asphalt Emulsion Full Depth Reclamation Design." *Construction and Building Materials 158 (January)*
13. TG 2. (2020). Technical guideline: Bitumen stabilized materials (3rd ed.).

Development of a Sustainable Semi-Flexible Pavement Composite Containing Recycled Asphalt Pavement

Sawarmal Sharma*, Prabin Kumar Ashish*[$], Debabrota Das*, Xing Cai[^], Zhifei Tan[#]

*Dept. of Civil Engg., Indian Institute of Technology Kanpur, India; [$]Corresponding author
[^]College of Transportation, Southeast University Mainland China
[#]Dept. of Civil and Environmental Engg., The Hong Kong Polytechnic University, Hong Kong

ABSTRACT: The purpose of this research is to investigate the feasibility of Recycled Asphalt Pavement (RAP) material in developing sustainable Semi-Flexible Pavement (SFP) composite material. While a lot of effort has been made in the last several years to explore the potential of RAP in bituminous and cement concrete pavement, such an attempt has not been made for emerging alternative pavement structure, such as SFP. SFP holds a unique ability to combine flexibility and rigidity which offers improved durability and performance. In this study, RAP material was integrated into the SFP mix to enhance sustainability while minimizing the dependance on virgin materials. Along with mix design part, different mechanical properties related to strength and durability of SFP composite were evaluated in the laboratory. Various RAP contents (0%, 25%, 50%, and 75% by weight) were assessed to understand their impact on performance. Results indicated that RAP significantly improved the sustainability component of the SFP while maintaining adequate mechanical performance. The findings demonstrate that this approach can potentially reduce the environmental footprint of road construction while providing a long-lasting pavement solution.

1. INTRODUCTION

Permanent deformation, moisture damage, etc., are some of the major concerns with asphalt pavement. Similarly, poor riding quality, heat generation due to friction, etc., are major concerns with cement concrete pavement. Nevertheless, both of these conventional pavements have their own advantages. Therefore, an attempt was made in the past to develop composite material that holds the advantages of asphalt as well as cement concrete pavement while addressing major drawbacks with respective pavement types. As a result of this thought process, Semi-Flexible Pavement (SFP) was developed, combining the benefits of asphalt and cement concrete pavement. SFP essentially consists of a porous asphalt skeleton filled with cementitious grout material. The asphalt mix part provided flexibility, while the cementitious grout phase provides strength to such composite material. Traditionally, the porous asphalt skeleton of SFP is prepared with the help of fresh asphaltic material. As a result, it holds serious environmental concerns. At the same time, it also provides an opportunity for researchers to look into alternative options for fresh asphalt mixtures to improve the sustainability quotient of SFP-based composite material. In this direction, one of the ways to address this problem could be the utilization of existing waste materials from the road sector, such as Recycled Asphalt Pavement (RAP) material in the construction of SFP composite.

It is important to note that reported research works on SFP have predominantly focused on enhancing the performance characteristics of SFP, such as deformation resistance, durability, and adaptability for heavy-load applications (Li et al., 2022, Zhao and Yang, 2022, Ling, et al. 2022). While research works on such performance-based parameters are extremely important, improving the sustainability of such composite material based pavement material is equally important. Unfortunately, very few researchers have attempted to improve the sustainability of SFP composite. For example, Cai et al. (2023) investigated the potential application of cold mix asphalt-based material for the porous asphalt part of SFP so that the heating requirement can be completely avoided and, hence, the sustainability part could be improved. However, to the best of the knowledge of the authors, none of the reported studies have explored the potential application of RAP material in developing SFP-based composite material. On the other hand, the use of RAP material in conventional asphalt mixture, cement concrete layer as well as in the aggregate layer of pavement structures has been explored extensively by several researchers over the last several years (Settari et al., 2015; Hong et al., 2014; Ghabchi et al., 2016; Leng et al., 2018).

Considering the motivation and research gap presented above, this research work aims to explore the suitability of RAP material in developing a porous asphalt skeleton of SFP composite. Along with the mix design of RAP-based porous asphalt structures, additional aspects such as formulating suitable cementitious grout material for subsequent grouting and the mechanical properties of the finally prepared SFP composite have been explored and discussed in this research work.

2. MATERIALS

The virgin asphalt binder (VG-30) utilized for this study was collected from IndianOil Total Pvt. Ltd. Recycled Asphalt Pavement (RAP) was obtained from milling operations on the Kanpur-Hamirpur highway, which is situated in the central part of India. The RAP material was initially processed using the Los Angeles Abrasion machine to minimize agglomerates and sieved to obtain particles with a specific size range suitable for use in the targeted porous asphalt mixture skeleton for subsequent cementitious grouting. Virgin aggregates were sourced from the NHAI site near Unnao Kanpur, India. The grout material was designed in the laboratory considering its flow and strength criteria to fill the voids in the porous asphalt concrete skeleton. The grout consisted of Ordinary Portland Cement (OPC), fine sand, silica fume, and fly ash to contribute to sustainability and carboxyl-based superplasticizers to achieve a flowable, high-strength material with enhanced durability.

3. MIX DESIGN OF SFP COMPONENTS

3.1. Mix Design of Porous Asphalt Mix Skeleton

The porous asphalt mix skeleton was designed with the objective of achieving 30% air voids to facilitate grout infiltration. Aggregate gradation was selected based on trial runs, ensuring optimal air void content with standard compaction efforts (Fig.1). The plot clearly indicates that the selected aggregate falls under uniform gradation category where the majority of the aggregate proportion is of similar size. The mix incorporated varying proportions of RAP: 0% RAP (control), 25% RAP, 50% RAP, and 75% RAP by weight of total aggregates. The binder content was optimized using the drain-down test as per ASTM D6390, ensuring that the drained binder content did not exceed the permissible limit of 0.30% by the total mix weight. Each mixture was compacted (only on one face using a Marshall compactor) and evaluated for air void connectivity through permeability tests to ensure sufficient voids for grout infiltration.
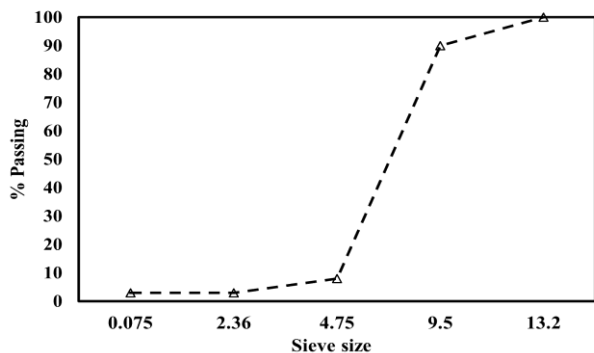
Fig.1: Selected aggregate gradation for porous asphalt mix skeleton

3.2. Mix Design of Cementitious Grout

The grout used in this study was designed to ensure adequate workability and strength for the final SFP composite. It was composed of Ordinary Portland Cement (OPC), fine sand, fly ash, silica fume, and a superplasticizer. The proportions of these components were optimized based on workability and strength through a series of laboratory experiments. Table 1 provides a summary of different grout combinations. Grout flowability was evaluated using a flow cone test as per ASTM C939, with acceptable flow times ranging from 10 to 16 seconds. Compressive strength was tested according to ASTM C109, targeting values more than 40 MPa, while flexural strength was measured per ASTM C348, ensuring a minimum value of 3 MPa. The material composition was thoughtfully varied to achieve flow and strength-based criteria, as highlighted above.

Table 1: Grout combinations

Grout Type	W/C	S/C	FA/C	SF/C	SP
A	0.35	0.2	0.1	0.025	0.01
B	0.4	0.2	0.1	0.025	0.01
C	0.45	0.2	0.1	0.025	0.01
D	0.5	0.2	0.1	0.025	0.01
E	0.4	0.2	0.1	0.025	0.5
F	0.45	0.2	0.1	0.025	0.5
G	0.35	0.2	0.2	0.025	0.01
H	0.4	0.2	0.2	0.025	0.01

4. PREPARATION OF SFP COMPOSITE

Once the mix design of the porous asphalt skeleton (with different RAP compositions, as mentioned before) and cementitious grout were over, the next step was to prepare the SFP composite by grouting the porous asphalt mix. For this purpose, several compacted porous asphalt skeletons were prepared using pre-identified binder content. Specially designed split moulds were fabricated for this research work. Subsequently, grouting was done with the selected grout composition. It was poured carefully into the pre-compacted porous asphalt skeleton. The whole setup was covered using a plastic sheet and was left undisturbed for 48 hours before de-moulding. The excess grout material on the top of the specimen was scrapped off using a sharp edge spatula after about 6-8 hours of grouting. Upon de-moulding, samples were wrapped using a moist cotton cloth and kept under an airtight zip-log bag for curing. The humidity level was measured within the bag and was consistently found to be in the range of 95-98% for all specimens during curing. The penetration of grout in the specimen till the bottom of the porous asphalt skeleton was not only ensured using visual observation but also through volumetric calculation on

available air void in the porous skeleton and the volume of the penetrated grout material. Specimens were also cut across the depth as well as across c/s at different depths to visually observe and confirm the maximum degree of grouting to the porous asphalt skeleton.

5. RESULTS AND DISCUSSION

5.1. Effect of RAP on Optimum Binder Content

Fig.2 shows the variation of optimal binder content for different porous asphalt mix skeletons (0%RAP to 75%RAP). It is evident from the plot that the additional virgin binder content required to satisfy the drain down-based criteria (max. 0.3% by the wt. of the porous asphalt mix) decreased from 4.62% to 3.67%. Such a response can be attributed to residual asphalt binder present in the RAP mix. Therefore, as the RAP content increased, the proportional requirement of additional binder content decreased to satisfy the drain down-based requirement. The authors also believe that the overall effective binder content (additional virgin binder plus residual binder in RAP) increased with the increase in RAP proportion.
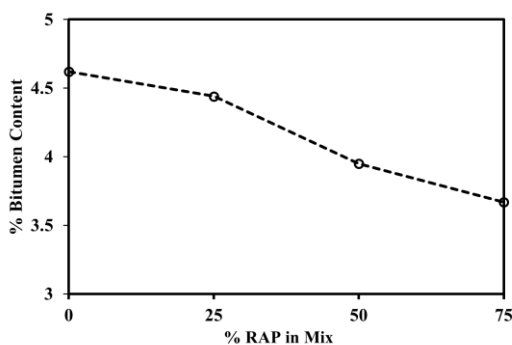
Fig.2: Optimum binder content

5.2. Influence of RAP on Compaction Effort

The number of Marshall blows required to achieve target air void for different mix combinations is presented in Fig.3. It is interesting to observe that the compaction effort required to achieve target air void substantially decreased from 75 blows for the control mix to about 21 blows for mix containing 75%RAP. Such a response could be believed due to a proportional increase in effective binder content in the RAP-based porous asphalt skeleton (i.e., the virgin binder plus residual binder content in the RAP), as highlighted in the previous section. As a result, the degree of lubrication effect proportionally increased with the increase in RAP proportion in the porous asphalt skeleton. This led to the need for proportionally lower compaction effort. Such a response is also important to look at from a sustainability angle because the amount of energy required to achieve the required degree of compaction will be reduced and, hence, a complimentary change along with the utilization of RAP waste.
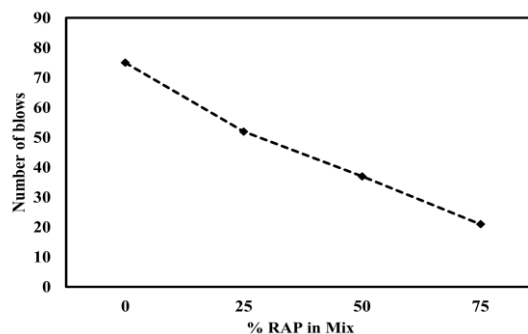
Fig.3: Plot for optimal compaction effort

5.3 Optimization of Grout Composition

The details of each grout composition, A through H, are provided in Table 1. In order to achieve the desired balance of flow time and compressive strength, different grout compositions were examined with adjustments in water-cement ratio, fly ash content, and a fixed sand cement ratio of 0.2. Flow time (with target value between 10 to 16 sec.) and compressive strength (min. 40 MPa for 28 days cured specimen) were measured for each grout composition. As shown in Fig.4(a) and 4(b), grout type B achieved optimal performance, with a flow time of 11 seconds and a compressive strength of 45 MPa. This balance indicates that grout type B provides both adequate workability and sufficient strength, making it suitable for semi-flexible pavement applications.
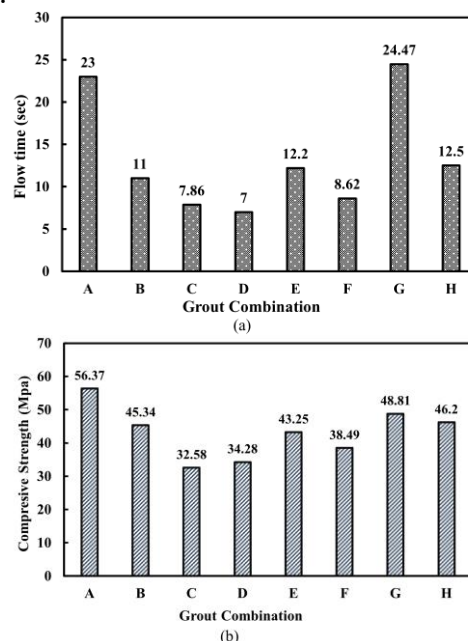
Fig.4: (a) Flow time, (b) compressive strength

Performance Evaluation of SFP Composite

Role of RAP in changing the ITS strength: The Indirect Tensile Strength (ITS) test was conducted to determine the tensile strength characteristics of SFP composite specimens. Fig.5 shows the variation of ITS of various sample combinations considered in this research work. Results showed that ITS values increased as RAP content increased, with ITS value increasing from 1.48 MPa for the 0% RAP mix to 1.691 MPa for the 75% RAP mix, indicating a mar-

ginal gain of approximately 12%. Such a response can be attributed to the relatively stiffer nature of RAP compared to the virgin mixture. Such a response clearly indicates that while cement grout is primarily responsible for imparting strength, incorporating RAP into porous asphalt skeleton will not hamper the strength parameter of SFP composite. These experimental results also highlight that the strength of SFP-based composite is significantly higher than that of conventional asphalt mixtures.
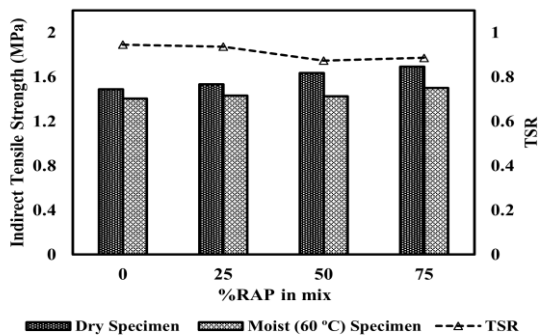
Fig.5: Indirect Tensile Strength and TSR value

Role of RAP in changing the moisture damage resistivity: The moisture damage resistivity of SFP composite was evaluated using the conventionally utilized ITS-based Tensile Strength Ratio (TSR) approach. The variation in TSR value is presented in Fig.5. The variation in TSR value reveals a slight decrease in TSR value as RAP content increased from 0.945 at 0% RAP to 0.886 at 75% RAP. It is important to note that the interface bond strength between the cementitious grout phase and the asphalt binder in the porous asphalt skeleton phase has an important role to play when it comes to the damage induced by such composite material in the presence of water. It is also reasonably known that the interface bond strength decreases with the increase in the degree of ageing of asphalt binder. The above discussion provides one of the possible justifications for a slight decrease in TSR value with an increase in RAP content in the SFE composite. Nevertheless, it is also evident that despite this decrease, the TSR value remained above the commonly accepted threshold of 0.80, commonly accepted for adequate moisture resistance. Such a response clearly indicates that the semi-flexible pavement mix retains sufficient tensile strength against moisture damage even at higher RAP contents.

Role of RAP in changing the durability-based property of SFP composite: The Cantabro abrasion loss test was conducted for this purpose. The experimental results of the Cantabro loss test indicated a slight increase in material loss with higher RAP content. Specifically, material loss rose from 16.37% in specimens with 0% RAP to 19.68% in specimens with 75% RAP. This marginal increase in Cantabro

loss indicates that although RAP content can slightly increase the abrasion susceptibility, the overall durability of the semi-flexible pavement will remain satisfactory. The slightly higher material loss with increased RAP may be attributed to the aged binder within RAP, which has a stiffer and potentially more brittle structure compared to the control SFP composite.

CONCLUSION

This study explores the feasibility of incorporating high proportions of Recycled Asphalt Pavement (RAP) into Semi-Flexible Pavement (SFP) systems to achieve sustainable and efficient pavement solutions. RAP inclusion significantly reduced the binder content and compaction efforts while preserving key mechanical properties. While higher RAP content introduced slight increases in abrasion susceptibility and lower Tensile Strength Ratio (TSR) under moisture conditions, these values were found to be within acceptable limits, affirming RAP's viability in SFP applications. Therefore, this research provides an initial indication for the utilization of RAP material in SFP systems.

REFERENCE

1. Zhao, W. and Yang, Q., 2022. Study on the applicability of asphalt concrete skeleton in the semi-flexible pavement. *Construction and Building Materials*, *327*, p.126923.

2. Li, G., Xiong, H., Ren, Q., Zheng, X., & Wu, L. (2022). Experimental Study and Performance Characterization of Semi-Flexible Pavements. *Coatings*, *12*(2), 241.

3. Ling, S., Chen, Z., Sun, D., Ni, H., Deng, Y., & Sun, Y. (2022). Optimal design of pouring semi-flexible pavement via laboratory test, numerical research, and field validation. *Transportation Research Record*, *2676*(11), 479-495.

4. Cai, X., Ashish, P. K., Leng, Z., Tan, Z., & Wang, H. (2024). Effects of residual water on mechanical properties of cold mix based semi-flexible pavement composite towards a sustainable paving material. *Journal of Cleaner Production*, *434*, 139857.

5. Settari, C., Debieb, F., Kadri, E. H., & Boukendakdji, O. (2015). Assessing the effects of recycled asphalt pavement materials on the performance of roller compacted concrete. *Construction and building materials*, *101*, 617-621.

6. Hong, F., Guo, R., & Zhou, F. (2014). Impact of recycled asphalt pavement material variability on pavement performance. *Road materials and pavement design*, *15*(4), 841-855.

7. Ghabchi, R., Barman, M., Singh, D., Zaman, M., & Mubaraki, M. A. (2016). Comparison of laboratory performance of asphalt mixes containing different proportions of RAS and RAP. *Construction and Building Materials*, *124*, 343-351.

8. Leng, Z., Sreeram, A., Padhan, R. K., & Tan, Z. (2018). Value-added application of waste PET based additives in bituminous mixtures containing high percentage of reclaimed asphalt pavement (RAP). *Journal of cleaner Production*, *196*, 615-625.

Rheological investigation of bio-modified bitumen with two types of bio-oil

J. Valentin
Czech Technical University in Prague, Prague, Czech Republic

S. Kalampokis & E. Manthos
Aristotle University of Thessaloniki, Thessaloniki, Greece

ABSTRACT: The present study focuses on the evaluation of the characteristic and rheological properties of bio-modified bitumen with two types of bio-derived oil (corn oil and sunflower seed oil). For each type of oil three different blends were produced (1%, 3% and 5% by weight of bitumen) utilizing a 35/50 reference bitumen. The characteristic properties were assessed via the Penetration, Softening Point, Elastic Recovery, Dynamic Viscosity and Storage Stability tests. The rheological properties were examined via the Dynamic Shear Rheometer (DSR). The fatigue cracking, rutting and permanent deformation resistance were investigated through the fatigue cracking factor, the rutting factor and the high critical temperature, respectively. Two rheological ageing indexes were calculated to examine the impact of bio-modifiers on the ageing susceptibility of bitumen. The two main observations were that the bio-derived oils enhance the resistance to fatigue cracking by softening the bitumen and also reduce its ageing sensitivity.

1 INTRODUCTION

Bitumen is the most common material used as a binding agent for flexible pavements. However, the rapid increase in the price of petroleum-based products along with their detrimental environmental impact led the research community to examine other materials as potential construction materials, such as the bio-materials (Ingrassia et al., 2020; Jiménez del Barco Carrión et al., 2023; Xie et al., 2022). Since bio-materials exist in abundance there are many additives that could be utilized as bio-modifiers. The origin, structure and processing method of the raw bio-materials will have a different impact on the subsequent bio-binder (Kalampokis et al., 2024a). Algae is a typical example of the above fact. On the one hand, algae powder has been found to improve the cohesion and consistency of bitumen by hardening it (Kalampokis et al, 2024b). On the other hand, a thermochemically-produced, algae-derived bio-oil can improve the fatigue life of bitumen (Duan et al., 2019). Other examples include materials from not only the marine world, but also the terrestrial, such as lignin, swine manure, date seed waste, rice husk, etc. (Zhang et al., 2019; Fini et al., 2011; Alattieh et al., 2020; Han et al., 2017).

Certain researchers have employed different types of bio-oils as rejuvenators in order to partially reverse the ageing of bitumen and thus increase the RAP content of the subsequent asphalt mixture and improve its performance (Ding et al, 2021; Elkashef

& Williams, 2017; Nogueira et al., 2019). These oils come from certain processes such as pyrolysis, hydrothermal liquefaction, acidulation, epoxidation etc. (Liu et al., 2020; Hosseinnezhad et al., 2020; Seidel & Haddock, 2014; Podolsky et al., 2020).

The present study focuses on two specific liquid-state bio-materials, namely corn oil and sunflower seed oil. The plant species where they originate from are widespread on a global scale and our knowledge about their properties is extensive. Consequently, they were selected to be investigated in regard to their characteristic, rheological and ageing properties as two potential bio-modifiers for the conventional, petroleum-based bitumen.

2 MATERIALS AND METHODS

2.1 *Materials*

A conventional, unmodified 35/50 penetration grade bitumen (noted as RB) was utilized as the reference bitumen and the virgin material for the production of the bio-modified blends. The two types of bio-derived oil used in this study were corn oil and sunflower seed oil, noted as CO and SSO, respectively. Figure 1 shows that the corn oil has a yellow color, whereas the sunflower seed oil is colorless. The two types of oil were incorporated into bitumen in three different contents (1%, 3% and 5% by weight of bitumen) using a high shear mixer of 2,500 rpm for 15 minutes at 150°C. Therefore, a total of six bio-

modified blends and a reference bitumen were examined. The temperature and time for the mixing of bitumen with the bio-derived oils were selected as mentioned above in order to avoid the excessive ageing of bitumen during the preparation stage by limiting the loss of its lightweight volatiles. The characteristic properties of the reference bitumen are displayed in Table 1.
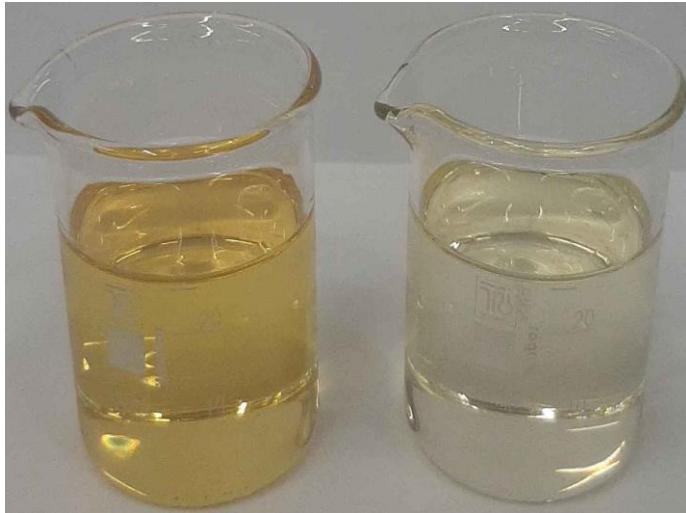
Figure 1. Corn oil (left) and sunflower seed oil (right).

Table 1. Characteristic properties of the 35/50 reference bitumen.

Property	Specification	Value
Penetration (dmm)	EN 1426	36
Softening Point (°C)	EN 1427	52.4
Elastic Recovery (%)	EN 13398	5
Cohesion Energy (J/cm^2)	EN 13703	3.40
Maximum Force (N)	EN 13703	51.6
Dynamic Viscosity* (Pa.s)	EN 13302	0.20

*Measured at 150°C via Brookfield viscometer

2.2 Methods

The blends were examined in terms of characteristic properties via the Penetration (Pen), Softening Point (S.P.), Elastic Recovery (El. Rec), Dynamic Viscosity (n) and Storage Stability tests. Additionally, the rheological properties and the ageing susceptibility were assessed with the Dynamic Shear Rheometer. The above tests were conducted before and after a short-term ageing protocol, namely the Rolling Thin Film Oven Test (RTFOT) in accordance with EN 12607-1. Based on the above test, the fatigue cracking and rutting factors were calculated along with the high critical temperatures. Furthermore, two rheological ageing indexes were calculated based on the fatigue cracking (noted as FCF) and rutting factors (noted as RF). In particular, the ratio of the RTFOT-aged over the unaged factor in each case was employed as a means of quantifying the ageing susceptibility of bitumen. A lower ageing index suggests lower ageing sensitivity and thus better behavior during the oxidative ageing of bitumen.

3 RESULTS AND DISCUSSION

3.1 Characteristic Properties

Tables 2-3 demonstrate the results of the characteristic properties. According to the penetration, softening point and dynamic viscosity tests, the oils had a softening effect on bitumen. In particular, CO-3 and CO-5 caused a change of penetration grade category from 35/50 to 50/70 in accordance with EN 12591 (54 and 62 pen, respectively). The ageing protocol resulted in bitumen hardening as demonstrated by the results of the RTFOT-aged samples. Furthermore, the bio-modifiers did not alter extensively the elastic recovery of bitumen. The ageing process caused a minor improvement of the above property. However, almost none of the blends exceeded the elastic recovery threshold of 10%. In terms of storage stability, the blends could be characterized as stable since the softening point difference between the top and the bottom parts of the tube in all cases was less than or equal to 2°C.

Table 2. Characteristic properties of the unaged blends.

Property	Pen (dmm)	S.P. (°C)	El. Rec (%)	ΔT (°C)	n* (Pa.s)
35/50	36	52.4	5	-	0.200
CO-1	45	51.4	7	1.0	0.200
CO-3	54	48.8	5	1.2	0.200
CO-5	62	48.2	5	1.8	0.175
SSO-1	40	51.8	10	1.8	0.175
SSO-3	43	49.4	10	1.8	0.175
SSO-5	46	48.4	10	2.0	0.150

*Measured at 150°C via Brookfield viscometer

Table 3. Characteristic properties of the RTFOT-aged blends.

Property	Pen (dmm)	S.P. (°C)	El. Rec (%)	n* (Pa.s)
35/50	11	55.8	9	0.300
CO-1	17	53.6	10	0.275
CO-3	20	52.4	6	0.250
CO-5	26	52.0	6	0.225
SSO-1	13	55.0	10	0.275
SSO-3	15	54.6	10	0.250
SSO-5	25	51.6	11	0.225

*Measured at 150°C via Brookfield viscometer

3.2 Rheological Properties (DSR)

Figure 2 depicts the results of the fatigue cracking factors (G*×sinδ) of the reference bitumen and the bio-modified blends at 20°C. In general, a lower fatigue cracking factor is linked to superior fatigue cracking resistance. It becomes obvious that an increasing content of bio-derived oil led to the reduction of the fatigue cracking factor regardless of the ageing state which means that both bio-modifiers upgraded the fatigue performance of bitumen by making the bitumen less brittle. Characteristically, the RTFOT-aged fatigue factors of RB, CO-5 and SSO-5 were 11,287, 3,085 and 3,108 kPa, respectively. The enhancement of the fatigue performance was more prominent for contents above 1% of bio-derived oil. Furthermore, the fatigue cracking factors of the RTFOT-aged samples were higher than their

unaged counterparts which was expected as oxidative ageing has a deteriorating impact on the fatigue cracking resistance of bitumen.
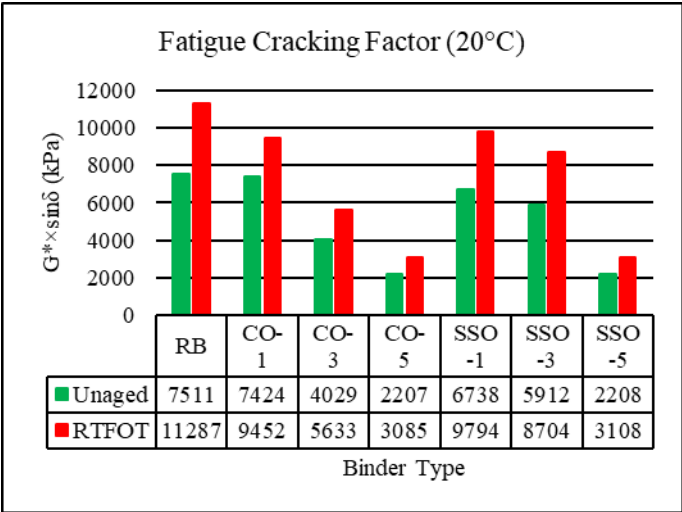
Figure 2. Fatigue cracking factors of the unaged and RTFOT-aged blends at 20°C.

Figure 3 presents the rutting factors (G*/sinδ) of the reference bitumen and the bio-modified blends at 70°C. A higher rutting factor translates into a higher rutting resistance. Although the bio-derived oils caused a decrease of the rutting factor and thus a reduced rutting resistance for both ageing states, the decline was insignificant for a content of 1% of bio-modifier. Specifically, the rutting factors of the unaged RB, CO-1 and SSO-1 samples were 1.60, 1.50 and 1.42 kPa, respectively. Furthermore, in all cases the rutting factor demonstrated an increment after the short-term ageing protocol due to the stiffening effect of oxidation on bitumen (Hofko et al., 2017; Pipintakos et al., 2022).
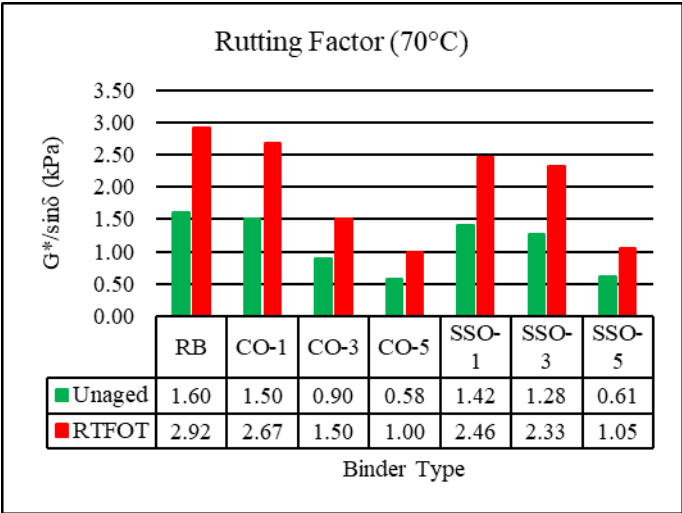
Figure 3. Rutting factors of the unaged and RTFOT-aged blends at 70°C.

Figure 4 portrays the high critical temperatures (Tc_{high}) of the reference bitumen and the bio-modified blends. The high critical temperature is re-

lated to the behavior of bitumen in the high-temperature domain and, more specifically, to the permanent deformation phenomena. A higher value for the critical temperature is associated with greater resistance against the aforementioned defects. Figure 4 shows that an increasing bio-modifier content had a negative effect on the high critical temperature. In particular, the high critical temperatures of CO-5 and SSO-5 reduced from 73°C (RB) down to 66°C before the ageing protocol. The decrease of the high critical temperatures was even more apparent for the RTFOT-aged samples. In particular, a drop of 10°C was manifested when 5% of corn oil or sunflower seed oil was mixed into the conventional bitumen which brought about a drop of the critical temperature from 72°C down to 62°C. These results align with the rutting factor results as the bio-derived oils had a softening effect on bitumen. However, the reduction of the high critical temperature was insignificant when the bio-modifier content did not exceed 1%. Therefore, a controlled dosage of bio-derived oil could limit the downgrade of the high temperature performance of bitumen.
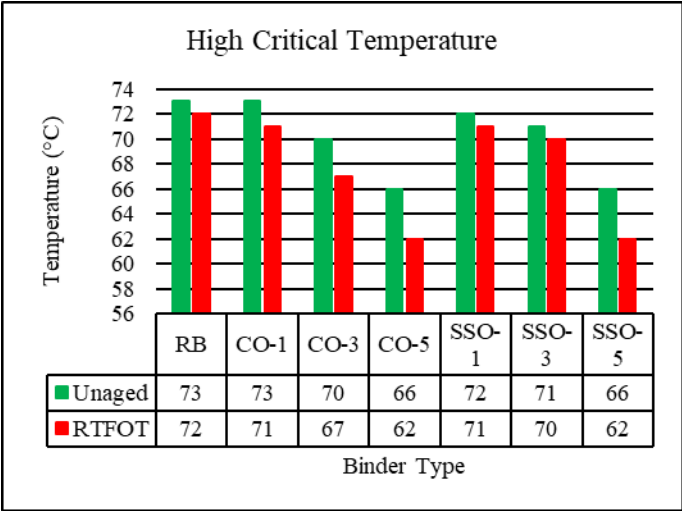
Figure 4. High critical temperatures of the unaged and RTFOT-aged blends.

3.3 Ageing Susceptibility

Figure 5 demonstrates the ageing indexes based on the fatigue cracking and rutting factors. It becomes evident that both of the ageing indexes of the RB were reduced after the incorporation of corn oil and sunflower seed oil into it. The reduction was more prominent in the case of corn oil-modified blends. This finding highlights the possible utilization of bio-derived oils as potential rejuvenating agents or antioxidants in bitumen as they seem to retard its oxidative ageing mechanism from a rheological point of view.
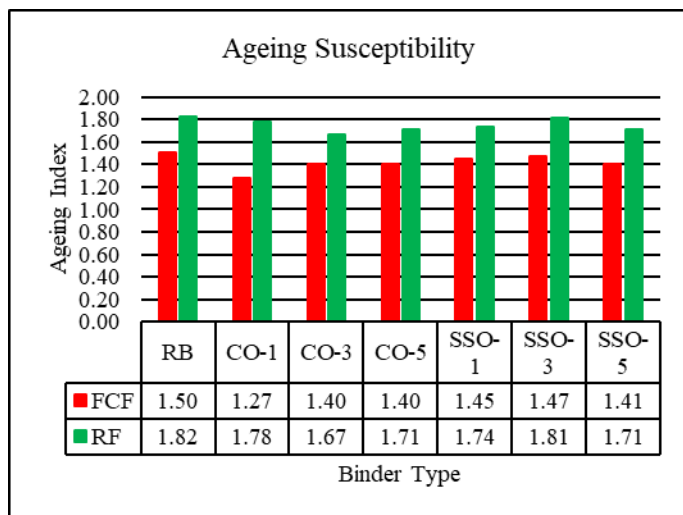
Figure 5. Ageing indexes based on rutting factors (70°C) and fatigue cracking factors (20°C).

4 CONCLUSIONS

1 Bio-derived oils had a softening effect on bitumen as demonstrated by the increased penetration and the reduced softening point and dynamic viscosity values.

2 The bio-modified blends did not present serious segregation phenomena when stored at elevated temperatures for extended periods of time.

3 The fatigue behavior of bitumen was improved by the addition of corn oil and sunflower seed oil.

4 The rutting and permanent deformation resistances of bitumen at elevated temperatures were downgraded extensively when exceeding a bio-modifier content of 1%.

5 Both types of oil improved the ageing susceptibility of bitumen as demonstrated by the reduced rheological ageing indexes.

6 Corn oil and sunflower seed oil could potentially be used as rejuvenators or antioxidants thanks to their ability to slow down the oxidative ageing mechanism of bitumen from a rheological standpoint.

REFERENCES

Allatieh, S., Al-Khateeb, G., Zeiada, W., & Shanableh, A. 2020. Performance assessment of bio-modified asphalt binder using extracted bio oil from date seeds waste. *International Journal Of System Assurance Engineering And Management* 11(6): 1260-1270.

Ding, H., Wang, H., Qu, X., Varveri, A., Gao, J., & You, Z, 2021. Towards an understanding of diffusion mechanism of bio-rejuvenators in aged asphalt binder through molecular dynamics simulation. *Journal of Cleaner Production* 299: 126927.

Duan, S., Muhammad, Y., Li, J., Maria, S., Meng, F., & Wei, Y. 2019. Enhancing effect of microalgae biodiesel incorporation on the performance of crumb Rubber/SBS modified asphalt. *Journal Of Cleaner Production* 237: 117725.

Elkashef, M., & Williams, R. 2017. Improving fatigue and low temperature performance of 100% RAP mixtures using a soybean-derived rejuvenator. *Construction And Building Materials* 151: 345-352.

Fini, E., Kalberer, E., Shahbazi, A., Basti, M., You, Z., Ozer, H., & Aurangzeb, Q. 2011. Chemical Characterization of Biobinder from Swine Manure: Sustainable Modifier for Asphalt Binder. *Journal Of Materials In Civil Engineering* 23(11): 1506-1513.

Han, Z., Sha, A., Tong, Z., Liu, Z., Gao, J., Zou, X., & Yuan, D. 2017. Study on the optimum rice husk ash content added in asphalt binder and its modification with bio-oil. *Construction And Building Materials*, 147: 776-789.

Hofko, B., Falchetto, A. C., Grenfell, J., Huber, L., Lu, X., Porot, L., Poulikakos, L. D., & You, Z. 2017. Effect of short-term ageing temperature on bitumen properties. *Road Materials and Pavement Design* 18: 108-117.

Hosseinnezhad, S., Hung, A., Mousavi, M., Sharma, B., & Fini, E. 2020. Resistance Mechanisms of Biomodified Binders against Ultraviolet Exposure. *ACS Sustainable Chemistry & Engineering* 8(6): 2390-2398.

Ingrassia, L. P., Lu, X., Ferrotti, G., & Canestrari, F. 2020. Chemical, morphological and rheological characterization of bitumen partially replaced with wood bio-oil: Towards more sustainable materials in road pavements. *Journal of Traffic and Transportation Engineering* 7(2): 192-204.

Jiménez del Barco Carrión, A., Lo Presti, D., Chailleux, E., & Airey, G. D.. 2023. Rheological investigation on the ageing performance of bio-recycled asphalt binders and mixtures. *Road Materials and Pavement Design* 24: 538-553.

Kalampokis S., Manthos E., Konstantinidis A., Kakafikas C., & Kalapouti A. 2024. Bio-Modified Bitumen: A Comparative Analysis of Algae Influence on Characteristic Properties. *Eng* 5(1): 417-432.

Kalampokis, S., Nikolaides, A., Manthos, E., & Kotopoulos, Y. Assessment of bio-modified bitumen incorporating different biomass powders. 2024. In *Bituminous Mixtures and Pavements VIII*. Thessaloniki: CRC Press Books.

Liu, Q., Wang, C., Fan, Z., Shi, S., Zhang, Z., & Oeser, M. 2020. Feasibility analysis of bio-binder as non-petroleum alternative for bituminous materials. *Materials Research Express* 6(12): 125115.

Nogueira, R., Soares, J., & Soares, S. 2019. Rheological evaluation of cotton seed oil fatty amides as a rejuvenating agent for RAP oxidized asphalts. *Construction And Building Materials* 223: 1145-1153.

Pipintakos, G., Lommaert, C., Varveri, A., & Van den Bergh, W. 2022. Do chemistry and rheology follow the same laboratory ageing trends in bitumen?. *Materials and Structures* 55(5): 146.

Podolsky, J., Saw, B., Elkashef, M., Williams, R., & Cochran, E. 2020. Rheology and mix performance of rejuvenated high RAP field produced hot mix asphalt with a soybean derived rejuvenator. *Road Materials And Pavement Design* 22(8): 1894-1907.

Seidel, J., & Haddock, J. 2014. Rheological characterization of asphalt binders modified with soybean fatty acids. *Construction And Building Materials* 53: 324-332.

Xie, M., Xu, L., Wu, K., Wen, Y., Jiang, H., & Jiang, Z. 2022. Rheology and Microstructure Properties of Asphalt Binder Modified by Spent Coffee Grounds. *SSRN Electronic Journal*.

Zhang, Y., Liu, X., Apostolidis, P., Gard, W., van de Ven, M., Erkens, S., & Jing, R. 2019. Chemical and Rheological Evaluation of Aged Lignin-Modified Bitumen. *Materials* 12(24): 4176.

Laboratory evaluation of antioxidant modified asphalt mixture

Muskan Verma
Research Scholar, Department of Civil Engineering, Indian Institute of Technology Roorkee, Roorkee, INDIA- 24766, muskan_v@ce.iitr.ac.in

Nikhil Saboo
Associate Professor, Department of Civil Engineering, Indian Institute of Technology Roorkee, Roorkee, INDIA- 247667, nikhil.saboo@ce.iitr.ac.in

ABSTRACT: Use of antioxidant is one of the effective alternatives to retard aging of binder, thereby enhancing the service life of asphalt pavements. Existing studies on the feasibility of antioxidants have demonstrated promising results at both macro and micro levels. Thus, to promote the wide application of antioxidant additives, it is imperative to evaluate the effect of modification at the mixture level. The present study focused on assessing the performance of a primary antioxidant (Irganox 1010) modified asphalt mixture. The critical characteristics, including stiffness, rutting, and fatigue were estimated by resilient modulus, wheel tracking, and indirect tensile cracking test (IDEAL-CT) tests. Laboratory findings revealed that addition of Irganox 1010 lowered the rate of long-term binder hardening of asphalt mixture. The modification enhanced the fatigue life of a control asphalt mixture by 10%, while ensuring satisfactory rutting resistance.

1 INTRODUCTION

The gradual changes occurring in the properties of asphalt binder and mixtures due to elevated temperature, UV radiation, or humidity is referred as aging. In general, the aging of binder starts at the mixing and paving stage due to volatilization of binder components, termed short-term aging (STA). This is followed by in-service oxidative aging of binder, known as long-term aging (LTA). With age, the binder becomes excessively stiff and brittle, increasing the cracking susceptibility of the asphalt mixture. This reduces the damage tolerance ability of binder leading to early distress formation in hot mix asphalt (HMA) pavement. Thus, necessitating the identification of effective age retarding methods. The incorporation of antioxidant (AO) additive in asphalt binder is one of the feasible alternatives to inhibit binder aging.

Antioxidants are reducing agents that prevent the formation of oxidation propagating compounds (free radicals) in the autooxidation reaction. They function either as peroxide decomposers or free radical scavengers to abate the binder aging process. In general, phenolic, amine, phosphate, and sulphide groups are major anti-aging agents. Several commercially available AO additives widely used in polymer industries have been explored to abate the rate of binder aging (Verma and Saboo 2024). Numerous studies at binder level have studied the efficacy of AO additive in increasing the aging re-sistance. The chemical and rheological evaluation of different AO modified binders reported decrement in the formation of carbonyl compounds and stiffness of aged asphalt binder, which is expected to improve the durability and service life of pavements. In order to translate the laboratory evaluation to the field it is imperative to explore the effect of AO at the asphalt mixture level. At present, limited studies have comprehended the performance characteristics of antioxidant modified asphalt mixtures. Therefore, the present study aims to examine the change in stiffness, rutting, and fatigue characteristics of asphalt mixture with and without AO.

2 MATERIALS

2.1 *Asphalt binder and aggregates*

In this study a viscosity graded (VG), VG-30 asphalt binder was selected as a base binder. The aggregates were obtained from a local quarry. The physical properties of procured binder and aggregates are presented in Table 1 and Table 2, respectively. The measured properties were observed to follow the desired specification (IS:73 2013; MoRTH 2013).

Table 1. Physical properties of VG 30

Tests	Result	Limit
Penetration Test	46.34	45 (min)

Softening point test (^{0}C)	50.9	47 (min)
Absolute viscosity (poises)	2899.3	2400 - 3600
Absolute viscosity (poises) RTFO aged bitumen	10876.6	-
Viscosity Ratio at 60 ^{0}C	3.75	4 (max)
Ductility at 25 ^{0}C, cm RTFO aged sample	> 100	40 (min)

* min: minimum; max: maximum

Table 2. Physical properties of mineral aggregates

Properties	Value	Limit
Aggregate Impact Value, %	17.95	27
Los Angeles Abrasion Value, %	29.86	35
Combined flakiness and elongation index, %	21.97	35
Water Absorption	0.27	< 2 %
Specific gravity (CA)	2.64	-
Specific gravity (FA)	2.54	-
Specific gravity (Filler)	2.54	-

2.2 Antioxidant additive

A sterically hindered phenolic compound, Irganox 1010 (pentaerythritol tetrakis 3-(3,5- di-tert-butyl 4-hydroxyphenyl) propionate) was used for binder modification. It is a type of primary antioxidant that mitigates the chain reaction of aging by the free radical scavenging mechanism. It is widely applied to prevent degradation of polymer and rubber made materials. Table 3 presents the general properties of the Irganox 1010 additive used in present work.

Table 3. Properties of Irganox (1010) additive

Melting point	110 – 125 °C	
Appearance	White powder form	
Purity	99 %	
Specific gravity (g/mm, 20 ^{0}C)	1.116	

3 SAMPLE PREPARATION

At first, the base binder was modified with 0.4% (by weight of binder) of Iragnox (1010). The following dosage was considered based on the literature re-

view. The existing studies have suggested that the dosage >1% softens the binder. Varying the dosage between 0.4% to 0.6% was observed to achieve optimum binder performance results (Apeagyei 2011). Therefore, the modified binder was prepared by blending the additive in the preheated binder at 125 °C for 30 minutes using a high-shear mixer at 1000 rpm speed.

Further, the asphalt mixtures were prepared with desired gradation of bituminous concrete (BC-1), as shown in Figure 1. BC-1 grading is employed as a wearing course in Indian highways. It is the most susceptible layer to get damaged due to aging. The Marshall mix design was carried out as per MS-2 (Asphalt Institute 2009) to determine the optimum binder content (OBC) of the mixtures. The OBC corresponding to 4% target air voids was found to be 5.21% (by weight of the mix). To assess the effect of antioxidant modification, both the modified (I(0.4)) and control mixtures (VG 30) were prepared at the same OBC. Subsequently, to simulate the STA and LTA aging state, the mixtures were laboratory conditioned following AASHTO R30 (AASHTO 2015).
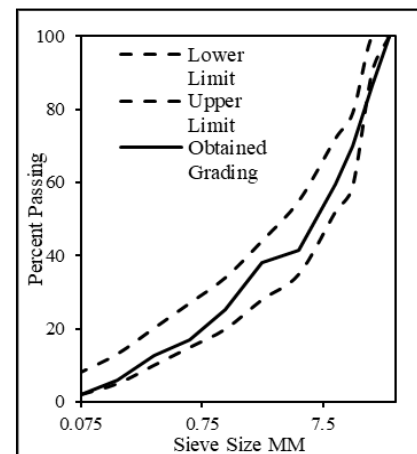
Figure 1. Selected aggregate gradation BC-1

4 METHODOLOGY

Laboratory experiments were conducted to estimate the effect of AO modification on the performance of HMA mixes. Figure 2 shows the comprehensive experimental program followed to address the objective of the study.
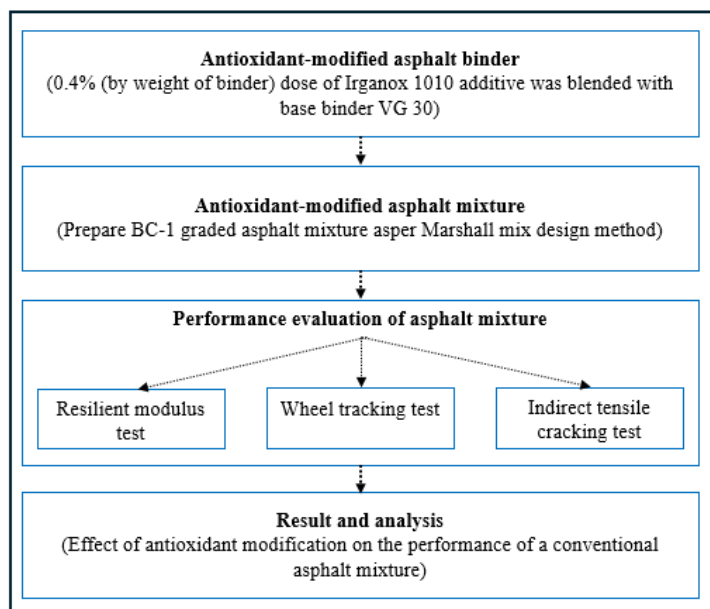
Figure 2. Methodology flow chart

4.1 Resilient modulus

Resilient modulus (M_r) is a parameter used to determine the stiffness characteristics of an asphalt mixture. To evaluate the effect of aging, the asphalt mixtures were tested at each aging condition. The repeated-load indirect tension test as per ASTM D4123 (ASTM 1995) was employed to evaluate Mr at 35°C. The cylindrical specimen was subjected to a haversine compressive loading for 0.1 seconds followed by a rest period of 0.9 seconds. The resulting recoverable horizontal deformation at the diametrical plane of the specimen was measured using two linear variable displacement transducers (LVDT's). Two replicates of each sample were tested to ensure repeatability.

4.2 Rutting resistance

Wheel tracking test was adopted to evaluate the rutting susceptibility of the asphalt mixtures (as per BSI EN 12697-35 (BS 2020). The test setup consists of a steel wheel and a modified Marshall sample of 150 mm diameter and 50 mm height, prepared at 7 ± 0.5% air void. A vertical load of 700 ± 10N was applied by a lever arm mechanism. The accumulated deformations at five different locations were recorded up to the limiting criteria of 12 mm total rut depth or 20,000 load passes is completed. The performance was measured for STA conditioned asphalt mixture at 60 °C, to simulate the maximum in-service pavement temperature.

4.3 Fatigue resistance

The indirect tensile cracking test (IDEAL-CT) is a simple test used to estimate the cracking resistance of asphalt mixture. The test was performed at an in-

termediate temperature of 25°C asper ASTM D8225 (ASTM 2019). The cylindrical Marshall specimen was prepared at 7% air void and long-term aged to surrogate the in-field pavement conditions. A vertical load was applied on the diametrical axis at a constant deformation rate of 50 ± 2 mm/min and a load versus displacement curve was plotted. The l_{75}/m_{75} (mm/kN) ratio was used to indicate the flexibility of asphalt mixture. It is found sensitive to field aging and thus considered a desirable parameter to simulate the field cracking performance of asphalt mixture (Leavitt et al. 2024). In general, with increasing aging severity the flexibility parameter, l_{75}/m_{75} ratio decreases. The l_{75}/m_{75} (mm²/kN) ratio is calculated from the post-peak analysis of the load-displacement curve. Wherein, l_{75} presents the displacement corresponding to 75% of peak load (mm) and m_{75} is the absolute value of the slope (N/m)

5. RESULTS AND DISCUSSION

5.1 Resilient modulus

The resilient modulus result describes the stiffness of asphalt mixtures under repeated load application. The M_r value of asphalt mixture increased with aging severity, as shown in Figure 3. At STA level, a slight increase of 2% in the stiffness was observed for I (0.4) mixes. Whereas, for LTA conditioned samples, the stiffness of modified mixture was decreased by 15%. The rate of stiffness increment from STA to LTA condition was 8% for AO modified mix and 30 % for the base binder, indicating improvement in aging resistance after modification. This could be attributed to the peptizing action of Irganox 1010 additive which inhibits the gelatinization of aged asphalt binder. It can therefore be concluded that the incorporation of antioxidant additive lowered the rate of aging, without affecting the stiffness at the initial STA level.
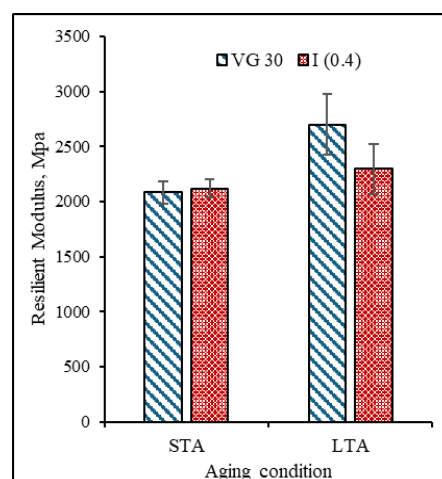
Figure 3. Resilient modulus results

5.2 Rutting

Rutting is a high temperature distress primarily observed in the early life of pavement. Therefore, it is imperative to evaluate the effect of AO modification on the rutting performance of asphalt mixture. Figure 4 shows the variation of rut depth with number of load passes. At the end of 20000 passes, the average total accumulated rut depth was recorded as 5.33 mm and 4.87 mm for VG 30 and I (0.4) asphalt mixtures, respectively. Thus, implying that rutting performance was not compromised due to antioxidant modification.
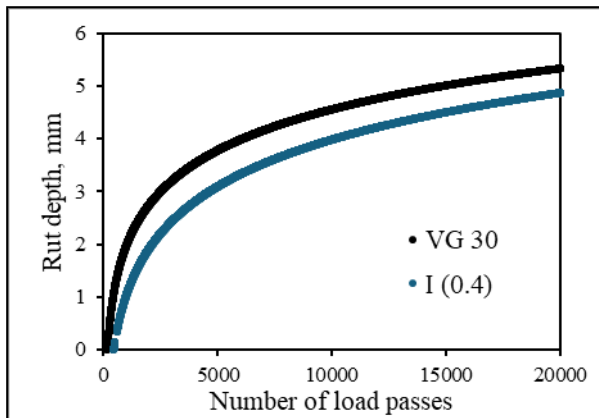
Figure 4. Rutting test results

5.3 Fatigue

Antioxidant additives inhibit aging of asphalt binder and are thereby expected to improve the cracking resistance of asphalt mixtures. Figure 5 presents the load-displacement curve of both VG 30 and I (0.4) asphalt mixes. As can be seen, compared to the control mix, a 10% increase in l_{75}/m_{75} parameter was observed after modification. This signifies that antioxidant modification elevates the flexibility and the fatigue performance of asphalt mixtures.
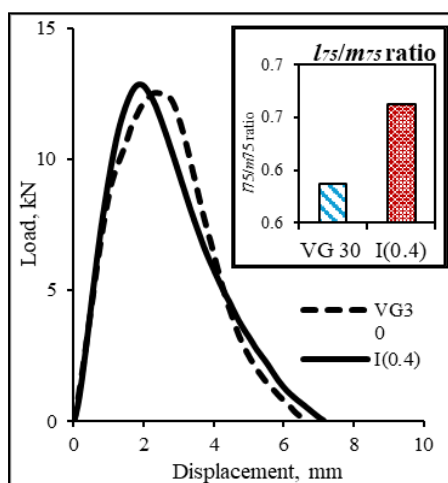
Figure 5. IDEAL-CT results

5 CONCLUSION

In summary, the results revealed that the incorporation of Irganox 1010 additive improved the long-term performance of asphalt mixes without negatively affecting its rutting performance. Based on the results, the following conclusions were drawn:

- In terms of stiffness, the addition of Irganox 1010 decreased the long-term stiffness of the control asphalt mixture by 15%.
- The stiffness increment due to aging was found to be 30% and 8% before and after AO modification, respectively. This implies lower binder hardening and better aging resistance.
- The rutting resistance of AO modified mixture was found comparable to the control mix.
- Compared to control mix, the l_{75}/m_{75} ratio was observed to increase by 10% after modification, exhibiting better fatigue performance.

6 REFRENCE

AASHTO. 2015. "AASHTO R30: Mix conditioning of hot mix asphalt (HMA), Washington, DC." *AASHTO*.

Apeagyei, A. K. 2011. "Laboratory evaluation of antioxidants for asphalt binders." *Constr. Build. Mater.*, 25 (1): 47–53. Elsevier Ltd. https://doi.org/10.1016/j.conbuildmat.2010.06.058.

Asphalt Institute. 2009. "MS-2 Asphalt Mix Design Methods." *ASTM Int.*, (111): 1–197.

ASTM. 1995. "ASTM D4123-20: Standard Test Method for Indirect Tension Test for Resilient Modulus of Bituminous Mixtures." *ASTM Int.*, 82: 2–5.

ASTM. 2019. "Astm D8225, Standard Test Method for Determination of Cracking Tolerance Index of Asphalt Mixture Using the Indirect Tensile Cracking Test at Intermediate Temperatures." *ASTM Int.*, 1–17.

BS. 2020. "EN 12967-22: Bituminous mixtures. Test methods. Part 22, Wheel tracking." *BSI*, 32.

IS:73. 2013. "Paving bitumen - specification. New Delhi, India,Bur.Indian Stand." (1–4).

Leavitt, A., A. Epps Martin, and E. Arámbula. 2024. "Model for Evaluating Cracking Performance of Asphalt Pavements with Field Aging Based on IDEAL-CT Parameters." *Transp. Res. Rec.* SAGE Publications Ltd. https://doi.org/https://doi.org//10.1177/03611981241231806.

MoRTH. 2013. *Specifications for Road Bridge Works 5th Revision.*

Verma, M., and N. Saboo. 2024. "Use of antioxidants to retard aging of bitumen: A review." *Environ. Sci. Pollut. Res. 2024 3136*, 31 (36): 48839–48863. Springer. https://doi.org/https://doi.org//10.1007/S11356-024-34431-2.

Evaluating the long-term cracking resistance of asphalt binder modified with bio-based softeners using poker-chip test

Ziyao Wei, Angelo Filonzi, & Amit Bhasin
Department of Civil, Architectural and Environmental Engineering, University of Texas at Austin, Austin, TX, USA

Gaylon Baumgardner
Paragon Technical Services, Inc., Jackson, MS, USA

ABSTRACT: Bio-based softeners, or bio-additives, are increasingly utilized as sustainable solutions for adjusting asphalt performance grading or rejuvenating aged binders in reclaimed asphalt pavements. However, comprehensive studies on the bio-based softener family remain limited, and their long-term effects on asphalt binder cracking performance are not well understood. This study evaluates four softeners with varying origins to examine their type- and dosage-dependent impacts on asphalt binder. Aging conditions, including RTFO, PAV20, PAV40, and PAV60, were employed to simulate long-term oxidative aging, while the poker-chip test was used to assess binder cracking performance. Results demonstrate the long-term effectiveness of bio-based softeners in enhancing cracking resistance, with significant improvements in poker-chip ductility under extended aging conditions. Additionally, the performance of bio-based softeners was found to be dosage-sensitive, with even a 1% dosage significantly improving cracking resistance, while higher dosages yielded further enhancements. This study highlights the potential of bio-based softeners as sustainable materials for significantly improving the long-term cracking performance of asphalt binders.

1 INTRODUCTION

Cracking is one of the most predominant distresses in asphalt pavement, which is accelerated by the oxidative aging of asphalt binder. It is widely recognized that long-term oxidative aging is detrimental to the service life of asphalt pavement, as it induces significant chemical transformations in the binder, including the polymerization and oxidation of its molecular structure, resulting in increased stiffness and brittleness. This stiffening compromises the binder's ability to relax stresses and accommodate deformations, thereby exacerbating the susceptibility of the pavement to cracking under thermal and mechanical loads. Consequently, maintaining adequate viscoelasticity and ductility in asphalt binders after long-term aging is essential for mitigating premature load-related and thermal cracking.

Since the introduction of the aging protocols and Performance Grading (PG) system by the Strategic Highway Research Program (SHRP), low-temperature PG grade has been used as a reliable predictor of thermal cracking performance of asphalt binders. Recognizing that regions with diverse climatic conditions and traffic loads require tailored PG specifications to ensure optimal pavement performance, asphalt binder producers have increasingly turned to modifiers and additives to achieve the desired low-temperature PG grade. Concurrently, the growing emphasis on sustainability and recyclability in pavement engineering has driven the widespread adoption of bio-based modifiers.

Bio-based softeners, or bio-additives, are additives derived from natural oils or synthesized from renewable resources and have been widely marketed and used to adjust and optimize the PG grades of asphalt binders. They can also be used as rejuvenators adding in Reclaimed Asphalt Pavement (RAP) and Recycled Asphalt Shingle (RAS) to soften the severely aged binders and restore the PG grades. Regardless of the mode of application, the main function of softeners is to improve the rheological and engineering properties of asphalt binder after long-term aging. In response to the growing demand for sustainable and recyclable materials in the pavement industry, bio-based softeners have increasingly been adopted for asphalt modification and rejuvenation.

Existing studies on bio-based softeners have primarily focused on individual softener types, lacking a comprehensive comparison across different softener types and dosages. Additionally, the influence of bio-based softeners on the intermediate-temperature cracking performance of asphalt binders remains unclear, largely constrained by the absence of a standardized and reliable fatigue cracking test for asphalt binders. Current fatigue cracking evaluation methods predominantly rely on rheological approaches, such as fatigue factors or the Glover-Rowe parameter (GRP) within the linear viscoelastic range, or shear strain fatigue tests like the Linear Amplitude Sweep (LAS). However, these methods have notable limitations: fatigue factors often fail to correlate with field cracking performance (Zhou, Karki and Im, 2017), GRP shows varying results with modified

binders (Glover *et al.*, 2005), and LAS-derived fatigue life can exhibit poor sensitivity to aging while being prone to edge flow issues (Gulzar *et al.*, 2024). Furthermore, fatigue cracking in asphalt pavements, typically driven by tensile loading, cannot be accurately captured in traditional DSR tests.

This study aims to characterize and understand the effects of bio-based softeners on the cracking performance of asphalt binders under long-term aging conditions. To achieve this, four bio-based softeners of varying origins were evaluated for their type- and dosage-dependent effects on asphalt binders. Aging durations from RTFO to PAV60 were used to simulate long-term oxidative aging, and the thin film direct tensile test, poker-chip test, was employed to assess cracking performance, providing a more representative evaluation of asphalt binder behavior under tensile loading conditions.

2 MATERIAL AND METHODS

2.1 *Raw Materials*

In this study, the unmodified asphalt binder with known performance grading, PG 67-22, was selected as the base binder. To fabricate the bio-based softener modified binders, four additives, including three commercially available bio-based softeners with diverse sources and compositions, as well as one petroleum-based softener, were employed. These additives, designated as S1 through S4, include various types of bio-based products, except for S1 which was a petroleum based product included as a reference.

2.2 *Blending and aging procedures*

Two blending strategies were employed to evaluate the long-term cracking and oxidation resistance of bio-based softeners. In the first strategy, the effect of different bio-based softeners was examined by modifying PG 67-22 with four softeners at similar dosage levels to achieve a target grade of PG 58-28. The second strategy investigated the influence of bio-based softeners dosage, where PG 67-22 was modified with S3 at four dosage levels (1%, 2%, 4%, and 6% by weight of binder). The details of all the binders, along with the corresponding nomenclature used in this study, are presented in Table 1. It is important to note that PG 58-28 S3 and PG 67-22 S3 4% refer to the same binder. Consequently, a total of eight binders were prepared for the following aging.

Table 1. Details of binders used in the study.

Name	Group	Nomenclature
PG 67-22	I, II	B1
PG 58-28 S1	I	B1-1
PG 58-28 S2	I	B1-2
PG 58-28 S3	I	B1-3
PG 58-28 S4	I	B1-4
PG 67-22 S3 1%	III	B1-1%
PG 67-22 S3 2%	III	B1-2%
PG 67-22 S3 4%	III	B1-4%
PG 67-22 S3 6%	III	B1-6%

Following blending, the binders were short-term aged using the rolling thin-film oven (RTFO) aging procedure at 163 °C for 85 min as per ASTM D2872. Subsequently, the pressure aging vessel (PAV) aging procedure at 100 °C for 20 h, 40 h, and 60 h, were used to simulate the long-term aging of asphalt binders, as per ASTM D652.

2.3 *Experimental methods*

The poker-chip test method (Filonzi *et al.*, 2022) consists of a two-part specimen mold and a simple loading frame, as shown in Figure 1.
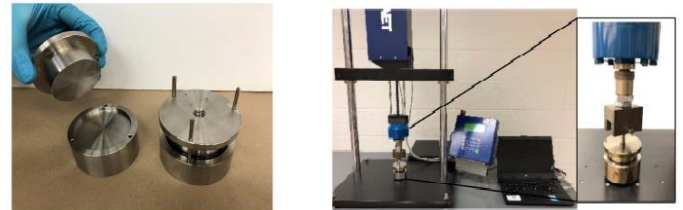
Fig. 1. Poker-chip mold (left) and simple loading frame (right)

A sample (4.5 ± 0.05 g) of the binder is poured into the bottom part of the mold that is preheated to approximately 165°C. Three dowel pins (1.589 ± 0.005 mm thick and 3.176 ± 0.25 mm long) are dropped in the binder to control the thickness of the specimen. The top of the mold (also preheated to 165°C) is then placed face down over the film of the asphalt binder. The top and bottom plates are aligned using three rods. The test specimens are allowed to cool to the test temperature, 25°C.

The poker-chip test is load-controlled and is performed by applying a constant loading rate of 2 N/s on a specimen that is 50.84 mm in diameter. This constant rate of load is applied after preloading the sample to 40 N. The test can be conducted using any feedback-controlled load frame that is capable

of applying a constant rate of load up to 3 kN and a motor that can displace at a rate of at least 160 mm/min. The load was applied until failure, and the load and displacement were recorded. The results from the test include: i) tensile strength of the binder, and ii) elongation or percentage strain of the binder when it reached 80% of post peak stress. In the context of this test and study, the second parameter is also referred to as ductility, which is used as the cracking parameter.

3 RESULTS AND DISCUSSIONS

The poker-chip test, a direct evaluation of binder cracking behavior, provides a ductility metric closely linked to field-scale pavement performance. A poker-chip ductility of 150% is regarded as the cracking threshold, with values above this benchmark signifying superior fatigue and thermal cracking resistance. In this section, poker-chip ductility was employed as the cracking index to evaluate the long-term cracking resistance of asphalt binders modified with bio-based softeners under two distinct mixing strategies

3.1 *Effect of different bio-based softeners on poker-chip ductility*

Fig. 2 illustrates the effect of different bio-based softeners on the long-term cracking performance of the non-modified base binder, B1. As shown, the poker-chip ductility of B1 decreases significantly with increasing aging duration, particularly from RTFO to PAV20, where a reduction of approximately 50% is observed, falling below the critical cracking threshold of 150%. This indicates that PAV20 already causes substantial loss of ductility and cracking resistance in the non-modified base binder. However, the addition of bio-based softeners substantially improves the ductility of the binder in two key aspects:

(1) Enhance the poker-chip ductility after long-term aging. While the ductility of modified binders remains similar to that of the base binder under RTFO aging, all bio-based softeners exhibit significant improvement effects under PAV20, PAV40, and PAV60 conditions, with nearly double the ductility observed compared to the base binder. Notably, all modified binders maintain ductility above the 150% threshold at PAV40, and B1-2 even retains this characteristic under PAV60. (2) Mitigation of early ductility loss. From RTFO to PAV20, bio-based softeners effectively prevent rapid ductility reduction. Several binders, such as B1-2, B1-4, and B1-5, maintain ductility levels at PAV20 comparable to or even higher than those observed under RTFO aging. These findings demonstrate that bio-based softeners, regardless of their source, significantly enhance the cracking resistance of asphalt binders. They effectively mitigate ductility loss under long-term aging, ensuring superior resistance to cracking even under extended aging conditions

3.2 *Effect of bio-based softener dosages on poker-chip ductility*

Fig. 3 illustrates the impact of bio-based softener dosage on poker-chip ductility. Generally, higher dosages result in greater ductility, particularly under long-term aging conditions. Under RTFO, the non-modified base binder (B1) exhibits minimal sensitivity to softener dosage, with a slight decrease in ductility at higher dosages. However, under long-term aging conditions, ductility is highly responsive to increased softener dosage. Even at a low dosage of 1%, the softener nearly doubles the ductility of B1 under PAV60. At higher dosages (B1-6%), the ductility of binders under PAV40 surpasses that of the base binder under PAV60, with PAV40 ductility reaching 164.6%, exceeding the critical cracking threshold of 150%. These results demonstrate the sensitivity of asphalt cracking performance to bio-
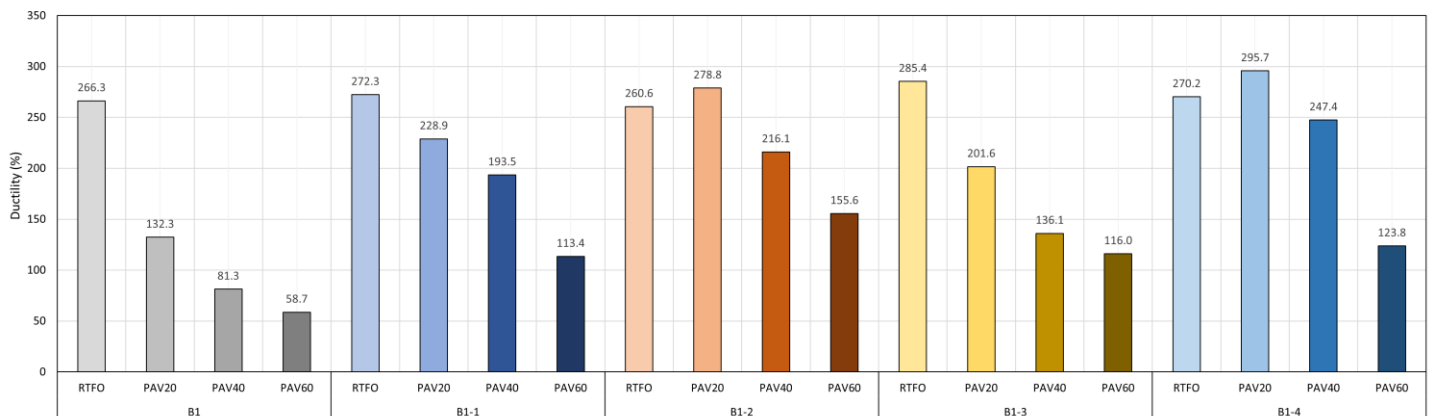
Fig. 2. Effect of different bio-based softeners on poker-chip ductility.
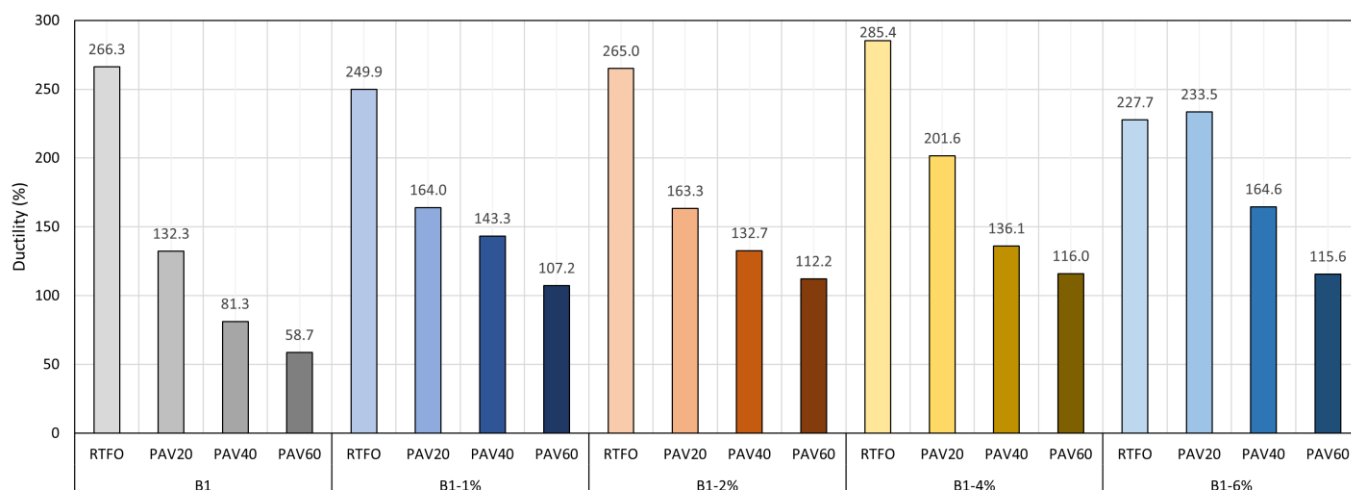
Fig. 3. Effect of bio-based softener dosages on poker-chip ductility.

based softener dosage, with higher dosages leading to significantly improved long-term cracking resistance

4 CONCLUSIONS

The poker-chip test demonstrates the effectiveness of bio-based softeners in improving the long-term cracking resistance of asphalt binders. They mitigate ductility loss during the transition from short-term to long-term aging and significantly enhance ductility under extended aging conditions. Moreover, the poker-chip ductility is highly sensitive to bio-based softeners dosage, with even small amounts significantly enhancing long-term cracking performance.

ACKNOWLEDGEMENTS

REFERENCES

Filonzi, A. *et al.* (2022) 'A method to evaluate the tensile strength and ductility of asphalt binders using a thin confined film', *International Journal of Pavement Engineering*, pp. 1–12. Available at: https://doi.org/10.1080/10298436.2022.2031194.

Glover, C.J. *et al.* (2005) *Development of a New Method for Assessing Asphalt Binder Durability with Field Validation*.

Gulzar, S. *et al.* (2024) 'Phenomenological modeling of aging and rejuvenation on asphalt binder fatigue characteristics', *Construction and Building Materials*, 425, p. 135929. Available at: https://doi.org/10.1016/j.conbuildmat.2024.135929.

Zhou, F., Karki, P. and Im, S. (2017) 'Development of a Simple Fatigue Cracking Test for Asphalt Binders', *Transportation Research Record: Journal of the Transportation Research Board*, 2632(1), pp. 79–87. Available at: https://doi.org/10.3141/2632-09.

A preliminary investigation of fungal-bound granular materials for pavement infrastructure

Yike Yin, Tian Wang, Alena Zhelezova, Lijuan Shi, Alexander Shapiro, & Eyal Levenberg
Technical University of Denmark, Kongens Lyngby, Denmark

Yike Yin
Visibuilt,Taastrup, Denmark

Oleksii Rebrov & Anna Guitó
Visibuilt,Taastrup, Denmark

ABSTRACT: This work was motivated by the desire to reduce the environmental footprint of asphalt pavements. A radically new binder category was explored in this context; one that is not bitumen-based and does not require aggregate heating and drying: mycelium of fungi. A specimen was prepared in the laboratory by mixing, at room temperature, aggregates with inoculated plant-based substrate. For a period of several weeks, as the mycelium metabolized the substrate, the specimen was imaged with X-ray computed tomography; also, the end-result was examined with optical microscopy. It is shown that mycelium permeated the substrate and grew around aggregates – tightly enveloping them – producing a binding effect at the bulk scale. It is concluded that the idea is viable and worthy of further investigation.

1 INTRODUCTION

Bitumen-bound granular layers exist in the vast majority of pavement infrastructures (Asphalt Institute 2019). From an environmental perspective, when the whole life cycle is taken into consideration, it is estimated that 65 kg of CO_2eq are emitted for every ton of such layers (EAPA 2024). This emission is mostly linked to the process of heating and drying aggregates and the environmental costs of producing bitumen.

The annual production of bitumen-bound materials in Europe is of the order of 300 million tons (EAPA 2022), which translates into almost 20 million tons of CO2eq per year. When extrapolated to a world scale, the estimated annual production of bitumen-bound granular materials is 1600 million tons with CO2eq emissions of the order of 100 million tons per year, i.e., about 0.25% of the entire world's annual CO2eq emissions.

This work is motivated by the desire to reduce the environmental footprint of bitumen-bound granular materials for pavements. A radically new binder category is explored in this context; one that does not require aggregate heating and drying, and can potentially serve as a bitumen alternative: mycelium of fungi.

Mycelium is part of a living organism composed of hyphae which has a three-dimensional topology of branching and interwoven thread-like filaments – each a few micrometers in thickness (Amobonye et al. 2023). Hyphae growth is achieved through metabolizing (i.e., digesting and consuming) biomass substrate which can be animal-based, organic waste, or plant-based (like wood dust, straw, or hay).

When aggregates are mixed with a substrate that is inoculated by fungal mycelium, hyphae growth takes place in the substrate itself; the hyphae also explore available void space. They end up closely enveloping the aggregates and constraining their ability to translate and rotate – producing a binding effect at the bulk scale. The growth process of mycelium can take place in the temperature range of 0 °C to 55 °C under moist conditions; thus, there is no requirement for a priori heating or drying of the aggregates; the ideal temperature range is about 20 °C to 30 °C (Maheshwari et al. 2000, Robinson 2001, Bueno & Silva 2014, Money 2024).

The objective of this work is to present results from a preliminary laboratory investigation of fungal-bound aggregates to provide intuition on the mechanism by which mycelium bounds aggregates. The investigation tools were X-ray Computed Tomography (CT) and optical microscopy.

2 TEST ON FUNGAL-BOUND AGGREGATES

2.1 *Specimen preparation*

One fungal-bound granular specimen was considered for this study with a total mass of 3 kg. It was prepared by mixing aggregates with a mycelium-inoculated plant-based substrate. The aggregates were a blend of four different sources: granite, silt-

stone, limestone, and quartzite. In terms of particle size distribution, all passed the 11.2 mm sieve and all were retained on the 5.6 mm sieve.

The inoculated substrate, named visiBIT, was produced by Visibuilt – a Danish startup company focusing on green solutions for the pavement industry. By weight percent, the final mix consisted of 85% aggregates, 10% visiBIT, and 5% water. The three ingredients were mixed at room temperature and placed without compaction in a clear plastic container for subsequent observation and testing. The container dimensions were 180 mm×180 mm×100 mm; it was placed uncovered inside a large clear polyethylene bag to prevent moisture loss.

Figure 1(a) shows the specimen ingredients before mixing, Figure 1(b) shows the specimen inside the plastic container immediately after mixing, and Figure 1(c) presents a saw-cut cross-sectional view of the mature specimen at an age of 50 days.

2.2 CT scanning of the specimen with evolving mycelium

After preparation, the specimen was imaged by a sequential CT scanner (Siemens Somatom Plus 4). In this CT device, the scan table moves stepwise to a desired scan location followed by the X-ray tube (voltage 120 kV, current 170 mA) rotating and acquiring a cross-section (slice). The specimen was placed on the scan table and remained there untouched for the entire duration of the scanning. Over a two-week period, 20 cross-section slices were scanned daily or every other day at 2 mm intervals, targeting the same portion close to the center of the plastic container. Each CT image contained a 512×512 matrix of square-shaped pixels with a side of 0.43 mm. A measure of the substance density in each pixel is a Hounsfield value, in the range of -1024 (air) up to +3071, where water is associated with a Hounsfield value of zero (Denotter & Schubert 2023).

Figure 2(a) shows part of a CT image 426×272 pixels in size. It was obtained by trimming the outer regions that did not include the specimen. This image was taken on Day 1, 12 h after the specimen was mixed, i.e., corresponding to a cross section in Figure 1(b). In this picture pure black represents Hounsfield of -1024 (i.e., air) and pure white corresponds to +3071. The aggregates can clearly be distinguished, characterized by pixel values exceeding +1000 whereas the substrate has pixel values between -900 to -100.

Figure 2(b) shows two pixel value histograms, one corresponding to Day 1 (blue bars) and another to Day 14 (orange bars). Both were calculated over three CT slices inside a frame with dimensions 360×180 pixels – refer to the red rectangular frame in Figure 2(a).
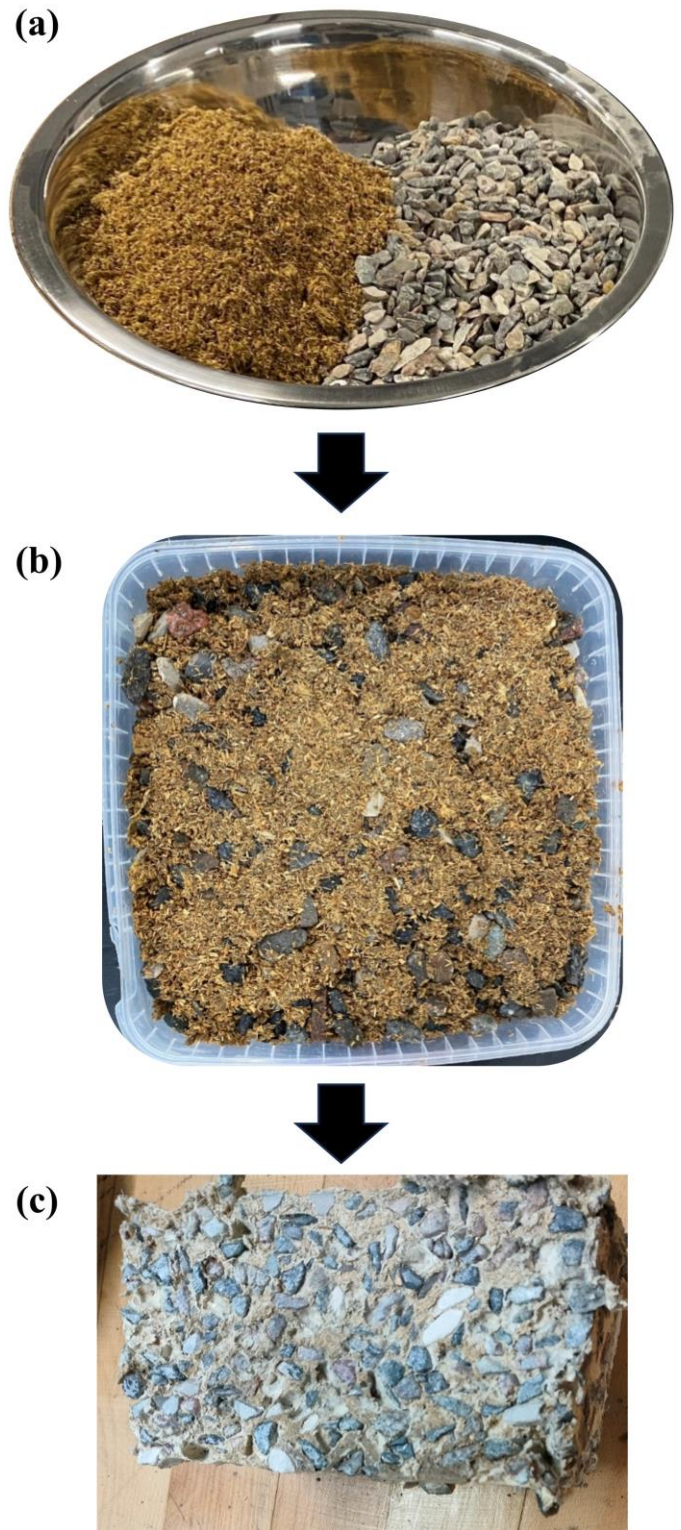
Figure 1. Pictures of a fungal-bound granular specimen: (a) aggregates and inoculated substrate (visiBIT) before mixing; (b) the specimen immediately after mixing; and (c) a saw-cut cross-sectional view at the age of 50 days.

As can be seen, the histograms do not display large differences between days with only minute changes in the proportion of pixel values. The slight drop in the -100 and +100 range may be attributed to water consumption and migration during hyphae growth. This is mainly compensated by an increase in the pixel value range over +1000 (especially around +2000), which constitutes the largest portion of the aggregates. Hyphae growth around the surfaces of aggregates (see also Subsection 2.3) could not

be observed in the images due to resolution limitations. The current CT scanner could not fully resolve layers that are several micrometers in thickness. This may explain the slight increase in pixel value proportions associated with aggregates. Mycelium, with its main compositions of chitin, glucans, and proteins (Mohseni et al. 2023), has similar compositions as the substrate. Therefore, the proportions for CT values between -900 and -100 stay largely unchanged.
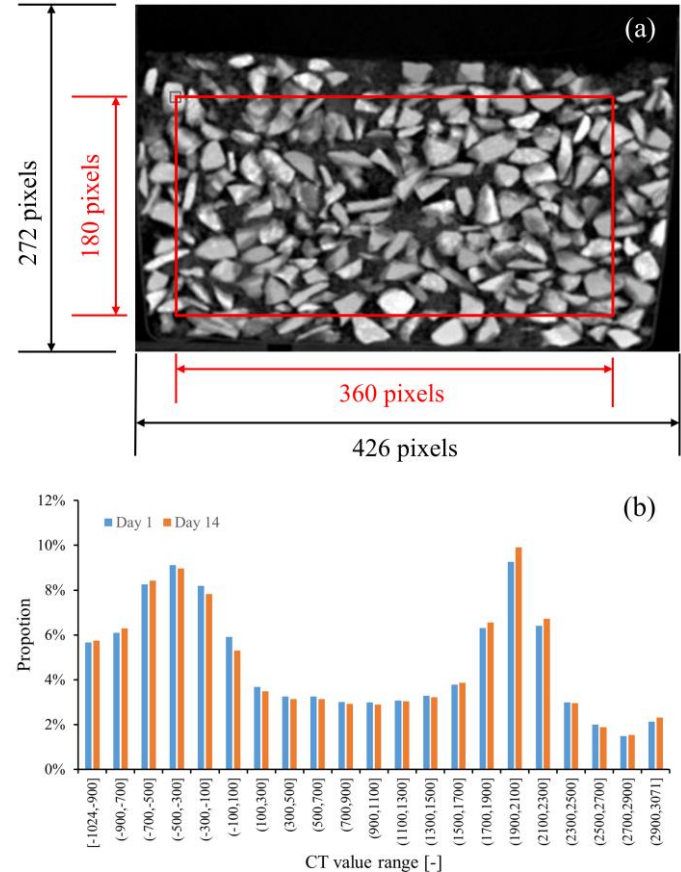
Figure 2. The results from CT scanning. (a) partial CT images taken on Day 1 as well as the calculating region enclosed by a red frame; (b) the proportion of pixels in certain CT value range on Day 1 and Day 14.

2.3 *Optical microscopy of the specimen with mature mycelium*

After 42 days the specimen was removed from the plastic container for further investigation. Small pieces of the specimen edges were manually sampled for a closer inspection in an optical stereo microscope (Nikon SMZ25). Three of the acquired images are presented in Figure 3; each contains a line scale (red color) indicating 1 mm. A view of dense mycelium with partially consumed substrate is shown in Figure 3(a). The mycelium looks like a white matrix of fibers while the substrate appears as a yellowish elongated particles.
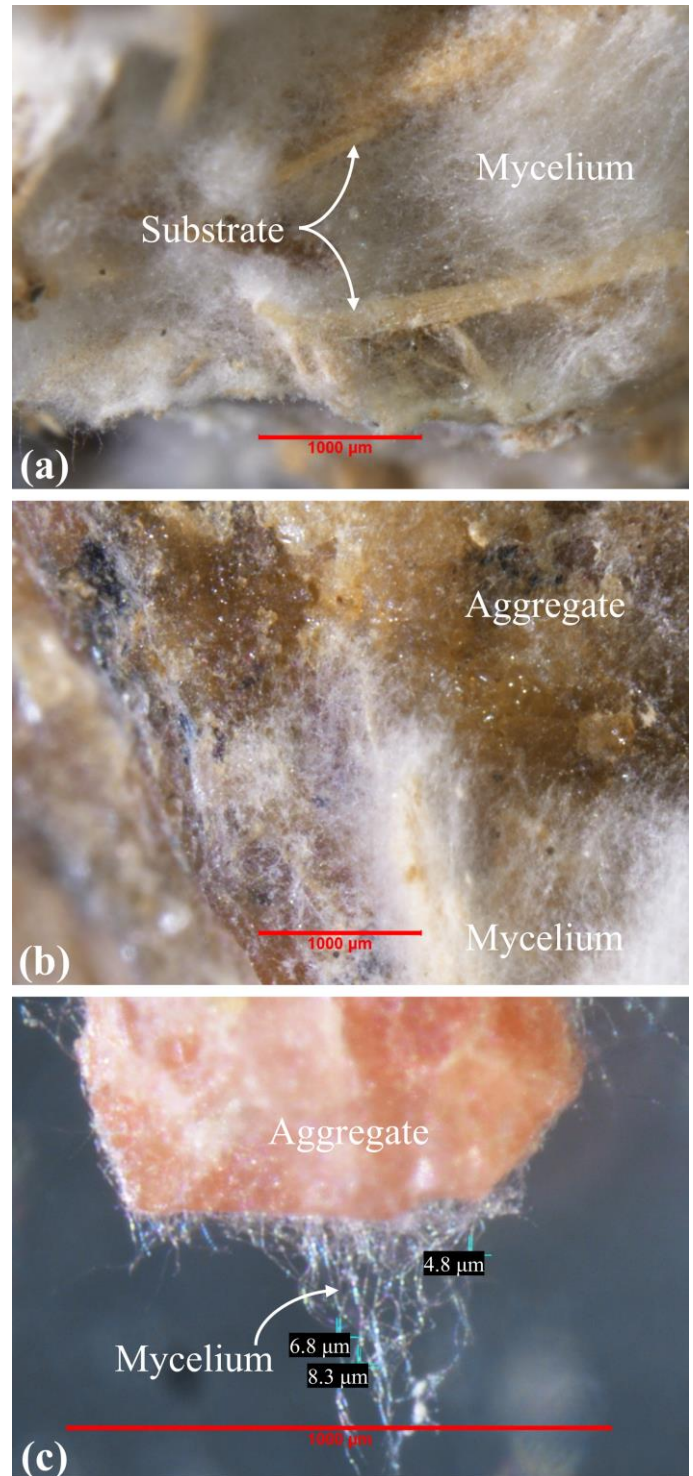
Figure 3. Magnified images of a mature fungal-bound granular material: (a) dense mycelium and substrate (not fully metabolized); (b) aggregate partially covered by dense mycelium; (c) aggregate wrapped by sparse mycelium.

Figure 3(b) offers a close view of an aggregate (brown-yellow color) that is partially covered by mycelium. Lastly, Figure 3(c) shows sparse mycelium, i.e., several hyphae, covering a pink-white colored aggregate. Hypha thicknesses were measured at three different locations, and were found to range from 4.8 μm to 8.3 μm.

3 CONCLUSION

A radically new binder category for granular pavement layers was explored in this study: mycelium of fungi. One fungal-bound granular specimen was prepared in the laboratory, CT scanned for 14 days during hyphae growth and inspected in an optical stereo microscope at the age of 42 days.

The CT scans revealed that the proportions of pixel values did not change much while the mycelium was developing inside the sealed specimen. This indicates no obvious change in average (bulk) density. From the microscopy inspection it was found that mycelium develops around aggregates, demonstrating the mechanism by which binding effect at the bulk scale is produced. It was also noticed that hyphae grow into a range of densities, from sparse to dense, and that the substrate may not be fully metabolized even after 42 days.

Overall, the idea of fungal-bound granular materials appears promising and worthy of further investigation. Future research will focus on improving the recipe of the mycelium-based binder to achieve a more uniform outcome, and quantifying the binding effect mechanistically under different temperature and moisture conditions.

REFERENCES

Amobonye, A., Lalung, J., Awasthi, M.K. & Pillai, S. 2023. Fungal mycelium as leather alternative: A sustainable biogenic material for the fashion industry. *Sustainable Materials and Technologies,* 38**,** e00724.

Asphalt Institute. 2019. *HOW MANY OF OUR U.S. ROADS ARE PAVED WITH ASPHALT?* [Online]. Available: https://www.asphaltmagazine.com/wp-content/uploads/2016/11/pavedroad_infographic.pdf [Accessed].

Bueno, D.J. & Silva, J.O. 2014. Fungi: The Fungal Hypha.

Denotter, T.D. & Schubert, J. 2023. *Hounsfield Unit,* StatPearls Publishing, Treasure Island ,FL, USA.

EAPA (EUROPEAN ASPHALT PAVEMENT ASSOCIATION). 2022. *Asphalt in Figures 2022* [Online]. Available: https://eapa.org/asphalt-in-figures/ [Accessed].

EAPA (EUROPEAN ASPHALT PAVEMENT ASSOCIATION). 2024. *Towards Net Zero: A Decarboni- sation Roadmap for the Asphalt Industry* [Online]. Available: https://horizoneuropencpportal.eu/sites/default/files/2024-06/eapa-towards-net-zero-2024.pdf [Accessed].

Maheshwari, R., Bharadwaj, G. & Bhat, M.K. 2000. Thermophilic fungi: their physiology and enzymes. *Microbiol Mol Biol Rev,* 64**,** 461-88.

Mohseni, A., Vieira, F.R., Pecchia, J.A. & Gürsoy, B. 2023. Three-Dimensional Printing of Living Mycelium-Based Composites: Material Compositions, Workflows, and Ways to Mitigate Contamination. *Biomimetics,* 8**,** 257.

Money, N.P. 2024. Fungal thermotolerance revisited and why climate change is unlikely to be supercharging pathogenic fungi (yet). *Fungal Biology,* 128**,** 1638-1641.

Robinson, C.H. 2001. Cold adaptation in Arctic and Antarctic fungi. *New Phytologist,* 151**,** 341-353.

Investigating the thermal-oxidative aging performance of waste rubbers in porous elastic road surface

Ke Zhong. Yuchun Li. Mingzhi Sun. Qi Wang.
Research of Institute of Highway Ministry of Transport, Beijing,China

ABSTRACT: The use of waste rubbers as partial aggregates in pavement is important for the lifetime of road, which are more susceptible to degradation from heat and oxygen exposure during the lifetime. The purpose of this work is to study the effect of thermal-oxidative aging of waste rubbers on the road performance and noise reduction ability of the porous elastic road surface (PERS) mixture. The impact of thermal-oxidative aging of waste rubbers on the water stability, dynamic stability at high temperatures, and maximum flexural strain at low temperatures of the PERS mixture was investigated, which were all decreased as aging time increased indicating. Additionally, the sound absorption ability of the PERS mixture initially increased but then decreased with aging time, ultimately falling below that of the unaged samples. It is hoped that this work can provide a new theory for long-life applications of waste rubbers in functional pavement.

1 INTRODUCTION

Waste rubbers as a vulcanized rubber are recycled by chemical methods to remove sulfur, which would also consume much energy(Zhong et al., 2024). In addition, they can be used as modifiers in pavement materials, while the applied amount is still limited. Now, part of aggregates is replaced with waste rubbers to form a functional pavement, which is regarded as the porous elastic road surface (PERS). Composed of polyurethane (PU) adhesive and open-graded aggregates, PERS exhibits superior sound absorption and vibration reduction ability(Cong et al., 2019, Wang et al., 2017). Besides, the impressive adhesion of PU at normal temperatures creates favourable conditions for constructing PERS at room temperatures, which consumes less energy compared to asphalt during the construction process.

However, the PU adhesive and waste rubbers as crosslinking polymers are prone to be attacked by light, heat, and oxygen during using life, resulting in the deterioration of noise reduction ability, the appearance of cracks, and the shortened use-life for the PERS mixture(Tan et al., 2022). Especially in the case of waste rubbers recycled from tires, the damage from stress, friction, and impact can affect their elastic properties (Li et al., 2021) . Additionally, the rubber crosslinking network formed by sulphur is also subject to change(Wright et al., 2019). It is reported that the mechanical properties of tires, including elastic modulus, elongation at break, and hardness, experienced a significant decline due to

the aging of rubber after driving a distance of 100,000 km(Salvi et al., 2023). After being introduced into PERS mixtures, the aged chains of waste rubbers would be rapidly destroyed by heat, oxygen, and light, contributing to road performance deterioration(Sandberg and Goubert, 2011). This is particularly evident in thermal-oxidative aging, where the high temperature generated by friction between the road and vehicles exacerbate the degradation process(Zhong et al., 2023). However, the aging influence of waste rubbers on the change in road performance of PERS has not been thoroughly studied, which limits its long-term application. Hence, exploring the thermal-oxidative aging performance of waste rubbers is essential to the long-life application of PERS. Furthermore, waste rubbers cannot be reprocessed to accurately evaluate their mechanical properties because of sulfurized structures, which poses a significant challenge in studying the effect of thermal-oxidative aging on the road performance of PERS mixtures.

2 METHODOLOGY

2.1 *Raw materials*

The single-component PU with a long curing time was selected from Wanhua Chemical Co., Ltd. to serve as the binder for the PERS mixture. Waste rubbers, sourced from Xinchen Chemical Co., Ltd. in China, were selected as natural rubbers for this study. The metals, fibres, and other additives in the

waste rubbers were removed, and the materials were then crushed into particles measuring 1.18 mm and 2.36 mm. The technical indexes of rubber particles are shown in Table 1.

Table 1. Technical indexes of rubber particles

Index	Unit	Test value
Relative density	/	1.14
Moisture content	%	0.2
Metal content	%	0.5
Slender and flat particles content	%	4.1

2.2 Specimen preparation

In this study, the rubber particles were aged at 100°C for varying times (0, 7, 14, 21, 28, and 35 days). Subsequently, a specific amount of aggregate, mineral filler, and unaged/aged rubber particles were prepared according to the selected gradation, and then heated in an oven at 100°C for 2 h until cooled to room temperature, and then they were mixed at room temperature. The mixture was then cured at 30°C and 80% humidity for 1 h, which were prepared by the standard Marshall specimens (Φ101.6 mm × 63.5 mm) according to the procedures outlined in Chinese standard JTG E20-2011. The specimens were kept at room temperature for three days. Some of the standard Marshall specimens were drilled using a drilling machine with a diameter of 100 mm and 30 mm, and then the height of specimens was cut into 20 mm for the acoustic performance test.

Besides, rutting test specimens (300 mm × 300 mm × 50 mm) were formed by rolling the mixtures in molds, the low-temperature bending test which specimens were also demolded by the same molds and subsequently cut into beams with a size of 30 mm × 35 mm × 250 mm.

3 RESULTS AND DISSCUSSIONS

3.1 Road performance

The results of the rutting test are illustrated in Figure. 1a. It can be observed that the dynamic stability of the PERS mixture with unaged waste rubbers was 21,724 times/mm. This high dynamic stability could be attributed to the exceptional elasticity of waste rubbers, which enabled rapid recovery after deformation. Consequently, this imparted the mixture with excellent elasticity and enhanced resistance to high-temperature rutting. Additionally, the PU adhesive formed an elastic film after curing, further enhancing the elastic properties of the mixture. However, as the thermal-oxidative aging time of waste rubbers increased, the dynamic stability of mixtures gradually decreased. This decline was attributed to the high-temperature reversion of waste rubbers,

which resulted in the decreased elasticity and increased hardness. After 7 days of thermal-oxidative aging, the short chains of waste rubbers was temporarily cross-linked. During this period, the crosslinking density of the waste rubbers decreased, and its hardness increased slowly. As a result, for the mixture with waste rubbers aged for 7 days, the dynamic stability exhibited a slow decrease. As the aged time increased, the initially formed temporary crosslinking structures in waste rubbers gradually disintegrated. This led to a significant reduction in crosslinking density and a rapid decline in elasticity. Consequently, the high-temperature stability of the mixture deteriorated. After 35 days of aging, the dynamic stability of the mixture decreased by 39%. However, the dynamic stability also remained above 10,000 times/mm, indicating that the anti-rutting ability was still better than that of conventional asphalt mixtures.

It is known that the elasticity of waste rubbers decreases while hardness increases with prolonged aging time, which results in a reduced anti-deformation ability under low-temperature conditions(Wu et al., 2018). Therefore, as illustrated in Figure. 1b-1d, the maximum flexural strain of the PERS mixture dropped, while the flexural strength and flexural stiffness modulus rose. However, the specimens did not break until the end of the test, indicating that the crack resistance of the PERS mixture was not seriously impacted by the aging of waste rubbers.
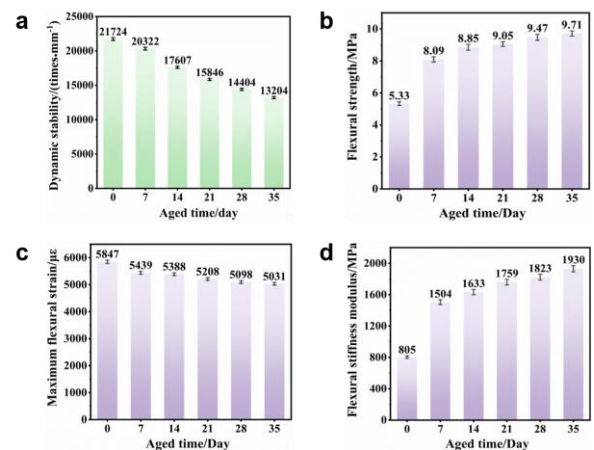
Figure 1. Results of the rutting test and low-temperature bending test: (a) dynamic stability; (b) flexural strength; (c) maximum flexural strain; (d) flexural stiffness modulus.

In addition, the water stability of PERS was investigated through the immersion Marshall test and unsaturated stability test. From the results in Figure. 2, it can be observed that both the unsaturated and immersion stability of the PERS mixture improved with varying aging times of waste rubbers. After 14 days of aging, the unsaturated and immersion stability reached their maximum, increasing to nearly twice and 1.5 times that of the unaged mixture, respectively. It may be the result that the strength of waste rubbers was enhanced after thermal aging due to the temporary crosslinking between short chains

and existing networks during the aging process. Similarly, as shown in Figure. 2d-4f, the split strength including unfreezing-thawing and freezing-thawing exhibited the same growth trends with the aged waste rubbers for different times, both presented the maximum value when the waste rubbers aged for 14 days and then decreased with the aging time increasing. It was reported that the temporary cross-linking networks formed during the aging process were destroyed with heating time prolonging, leading to a reduction of strength.
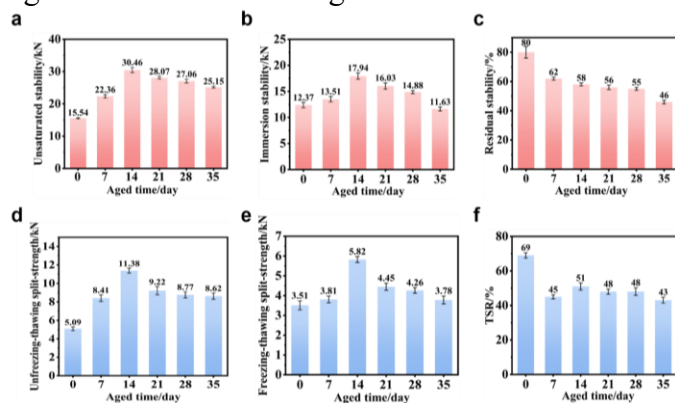
Figure 2. Results of the immersion Marshall test (a-c) and freeze-thaw splitting test (d-f) for aged pers mixtures containing different aging times waste rubbers

Importantly, as illustrated in Figure. 2 and Figure. 3, both the residual stability and strength of the aged samples declined while the immersion Cantabro loss rate gradually rose. After heating for 35 days, the residual stability and strength dropped to nearly 40%, and the immersion Cantabro loss rate exceeded 10%. These values were significantly lower than the relevant standards, indicating that the mixtures were not used as pavement materials. The changes in the structure of waste rubbers increased sensitivity to water during the aging process, which made it easier to access the molecular chains due to the presence of more short chains.
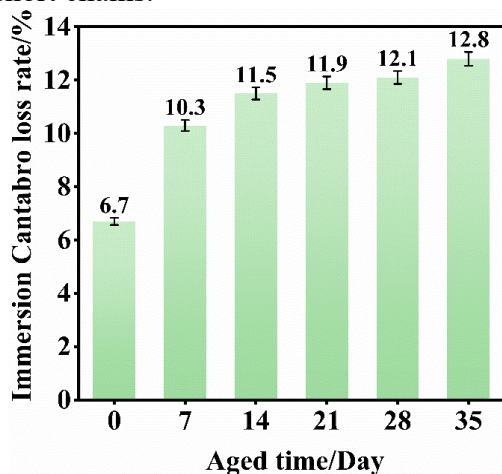
Figure 3. Results of the immersion Cantabro loss test.

3.2 Dynamic modulus test

From Figure. 4a and 4b, it can be seen that for all PERS mixtures, both the dynamic modulus and phase angle increase with the increasing load fre-

quency. Additionally, the dynamic modulus of the mixture increases with prolonged aging time at every loading frequency, indicating an improvement in the mechanical strength of the PERS mixture after thermal aging. Nevertheless, the phase angle gradually decreased with the increasing aging time at every load frequency, and the stiffness and compression resistance of the mixture also decreased, which proved that the elasticity of waste rubbers in PERS mixtures diminishes during thermal aging. Therefore, it can be inferred the PERS mixture no longer has the characteristics of functional elasticity with the increasing service life until the road cracks.
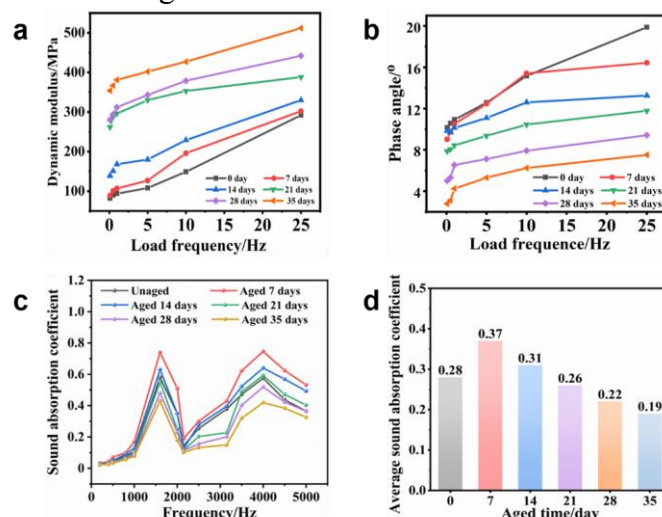
Figure.4. Results of noise reduction performance tests of PERS mixtures: (a) dynamic modulus; (b) phase angle; (c) sound absorption coefficient at different frequencies; (d) average sound absorption coefficient

3.3 Sound absorption ability

The impedance tube test was used to assess the sound absorption ability of PERS mixtures. The sound absorption coefficients at varying frequencies and the average sound absorption coefficient are illustrated in Figure. 4c and 4d. Two peaks at 1600 Hz and 4000 Hz in the range of middle and high frequency were observed, indicating that vehicle noise distributed at 200-2000 Hz was well absorbed by the PERS mixture. After the waste rubbers in the PERS mixture were heated at 100°C for varying durations, the sound absorption ability also changed. In the range of 200-5000Hz, the sound absorption ability initially increased and gradually dropped with the thermal aging time increased especially for the aged 7 days, and the sound absorption coefficient reached 0.8, which was greater than that of the unaged PERS mixture. It was the result that the temporary cross-linking between the main chains in waste rubbers occurred at the early stage of thermal aging, which was needed to receive more sound power to move, and hence the sound absorption ability was improved. However, the temporary crosslinking was broken and more short chains emerged with the ag-

ing time increased, which possessed poor binding force on sound waves.

The findings show that with increased thermal aging time, the sound absorption ability including the medium and high frequencies initially increased and then decreased until lower than that of unaged PERS mixture, indicating that it no longer possesses the ability to absorb sound in the long-term use.

4 CONCLUSIONS

In this work, the change of mainchains of waste rubbers was explored, the effect of thermal- oxygen aging of the waste tire rubbers on road performance and noise reduction ability of PERS also be investigated including water stability, the dynamic stability in the high temperature and the maximum flexural strain in the low temperature. We believe this work can pro-vide a new theory for long-life applications of waste rubbers in functional pavement, which improves the recycling efficiency of waste rubbers.

5 REFERENCES

CONG, L., YANG, F., GUO, G., REN, M., SHI, J. & TAN, L. 2019. The use of polyurethane for asphalt pavement engineering applications: A state-of-the-art review. *Construction and Building Materials,* 225**,** 1012-1025.

LI, B., LI, S.-X., SHEN, M.-X., XIAO, Y.-L., ZHANG, J., XIONG, G.-Y. & ZHANG, Z.-N. 2021. Tribological behaviour of acrylonitrile-butadiene rubber under thermal oxidation ageing. *Polymer Testing,* 93**,** 106954.

SALVI, W. D., DE SANTO, C. E., MATSUMOTO, A., CALHABEU, A. M., LOPES, É. S. N. & GABRIEL, L. P. 2023. Characterization of thermal-oxidative aging mechanism of commercial tires. *Engineering Failure Analysis,* 154.

SANDBERG, U. & GOUBERT, L. 2011. PERSUADE - A European project for exceptional noise reduction by means of poroelastic road surfaces. 1**,** 673-683.

TAN, W., NA, J.-X. & ZHOU, Z.-F. 2022. Effect of temperature and humidity on the creep and aging behavior of adhesive joints under static loads. *The Journal of Adhesion,* 99**,** 672-690.

WANG, D., SCHACHT, A., LENG, Z., LENG, C., KOLLMANN, J. & OESER, M. 2017. Effects of material composition on mechanical and acoustic performance of poroelastic road surface (PERS). *Construction and Building Materials,* 135**,** 352-360.

WRIGHT, K. R. S., BOTHA, T. R. & ELS, P. S. 2019. Effects of age and wear on the stiffness and friction properties of an SUV tyre. *Journal of Terramechanics,* 84**,** 21-30.

WU, J., NIU, K., SU, B. & WANG, Y. 2018. Effect of combined UV thermal and hydrolytic aging on micro-contact properties of silicone elastomer. *Polymer Degradation and Stability,* 151**,** 126-135.

ZHONG, K., LU, Z., GUO, Q., MU, R., SUN, M. & LI, Y. 2024. Thermal decomposition kinetics and aging lifetime prediction of waste rubbers in porous elastic road surface. *Construction and Building Materials,* 435.

ZHONG, K., LUO, G., ZHAI, B., SHI, G. & SUN, M. 2023. Deterioration of the Noise Reduction Performance of Polyurethane Porous Elastic Mixture under Void Clogging and Thermal-Oxidative Aging Conditions. *Journal of Materials in Civil Engineering,* 35.

Research of recyclable epoxy asphalt regeneration approach

Wenyi Zhou & Junyan Yi* & Zhongshi Pei & Decheng Feng
Harbin Institute of Technology, Harbin, China

ABSTRACT: The present study serves as an extension of the recyclable epoxy asphalt regeneration process, providing additional details on the rejuvenator proportion employed. Specifically, a comprehensive analysis of the rejuvenator proportion is conducted based on the rheological performance of the asphalt phase in recyclable epoxy asphalt. Through dynamic shear rheometer and bending beam rheometer experiments, it has been determined that an optimal proportion of 8% rejuvenator effectively restores the rheological performance of aged asphalt phase in recyclable epoxy asphalt. Following regeneration, a significant recovery in complex modulus is observed compared to the aged sample, thereby demonstrating the efficacy of this regeneration approach.

1 INTRODUCTION

Epoxy asphalt serves as a fundamental construction material, extensively utilized in the orthotropic steel deck systems of long-span bridges. The commercial epoxy asphalt products exhibit exceptional tensile strength, long-lasting durability, and high-quality pavement performance. However, the regeneration of epoxy asphalt poses a formidable engineering challenge due to the formation of irreversible covalent crosslinks. The regeneration of epoxy asphalt not only enables significant epoxy-based resource conservation but also maximizes the protection of the ecological environment, aligning with the fundamental national policy on sustainable development in transportation. Therefore, it is imperative to address this technical challenge in order to achieve epoxy asphalt regeneration.

Relevant research has been conducted thus far, with a specific focus on addressing this issue. Alamri et al. employed the epoxy asphalt mixture after milling as the aggregate to produce the asphalt mixture (Alamri et al., 2020). The implementation of this disposal method proves to be an effective approach in mitigating the accumulation of aged epoxy asphalt in landfills. Jing et al. discovered that the incorporation of a soft bituminous recycling agent positively impacted the aged epoxy asphalt, particularly in terms of its rheological properties (Jing et al., 2021; Jing et al., 2023), being a remarkable attempt to regenerate epoxy asphalt.

In our previous study, we developed a novel approach for regenerating epoxy asphalt by incorporating dynamic covalent bonds to render the irreversible covalent crosslinks reversible, while simultaneously rejuvenating the aged asphalt phase through the addition of a rejuvenator during recycling (Yi et al., 2023; Zhou et al., 2022). Thus far, a synthesis strategy and regeneration validation for recyclable epoxy asphalt embedded with the Diels-Alder reaction have been proposed, along with an optimization design. It is necessary to clarify more details on the regeneration process of recyclable epoxy asphalt. This study aims to further evaluate the impact of the regeneration process, particularly the proportion of rejuvenator, on the rheological performance of recyclable epoxy asphalt.

2 EXPERIMENTAL DETAILS

2.1 *Recyclable epoxy asphalt preparation and regeneration*

The preparation process of recyclable epoxy asphalt is summarized in Figure 1. The material composition was determined using the surface response method, with the asphalt mass ratio set at 54%, the FGE mass ratio at 15%, and the MA mass ratio at 31%.

According to the standard of JTG E20-2011, the aging of recyclable epoxy asphalt can be simulated by subjecting it to oven heating at a temperature of 85 °C for a duration of 120 h. This process can be considered as representing a service life ranging from 5 to 7 years. Subsequently, in the regeneration process, the aged samples are initially placed in an oven at a temperature of 120 °C for a duration of 1 h. Following this step, the samples are combined with the rejuvenator and heated at 120 °C for a peri-

od of 10 min. Finally, the samples undergo a reheating process lasting for 24 h at a temperature of 70 °C.
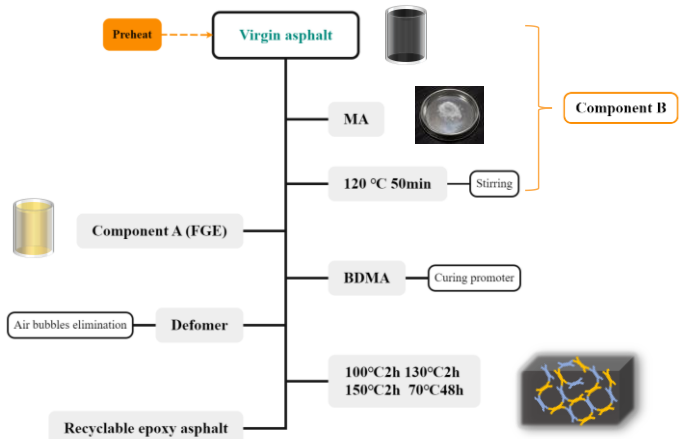
Figure 1. Preparation process of recyclable epoxy asphalt.

2.2 Rejuvenator

The rejuvenator utilized for enhancing the performance of aged asphalt phase consists of self-developed diffusion materials, comprising petroleum light components and bio-oil components. The related properties of rejuvenator are recorded in Table 1.

Table 1. Technical properties of the rejuvenator.

Technical indexes	Test result	Criteria
Flash point / 25 °C	230	≥200
Saturated content / %	13.2	≤30
Aromatics content / %	79.6	≥60
Mass change / %	0.5	-4~4

2.3 Rheological performance test

The rejuvenator plays a crucial role in the recovery of aged asphalt phase during the regeneration process of recyclable epoxy asphalt. Therefore, the proportion of rejuvenator is determined based on the rheological performance of aged asphalt combined with varying concentrations of rejuvenator. To simulate the aging condition of recyclable epoxy asphalt analogously, the virgin asphalt was subjected to a 120 °C aging process in an oven at a temperature of 85 °C. Subsequently, the rejuvenator was thoroughly mixed with the aged asphalt using specific mass ratios of asphalt (6%, 7%, 8%, and 9% respectively).

The study involved conducting Frequency Sweep (FS) measurements, Linear Amplitude Sweep (LAS) tests, Multiple Stress Creep and Recovery (MSCR) tests, and Bending Beam Rheometer (BBR) experiments. All the procedures were performed in accordance with the AASHTO standard methods. The optimal proportion of rejuvenator will ultimately be determined through a comprehensive analysis of rheological properties.

3 RESULTS AND DISCUSSION

3.1 Complex modulus

The complex modulus of aged asphalt phase combined with different proportions were characterized with the FS test. Master curves at a reference temperature of 20 °C are determined based on the principle of time-temperature superposition, and the results are shown in Figure 2.
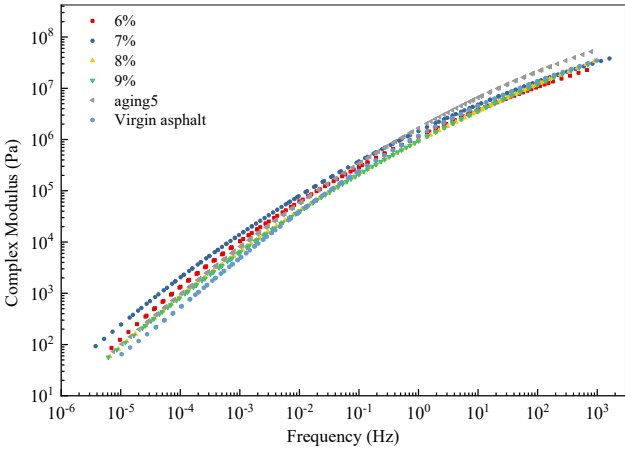
Figure 2. Master curves of complex modulus for aged asphalt.

The complex modulus of asphalt is observed to increase following a 120 h aging period. The addition of rejuvenator has an apparent influence on the complex modulus of aged asphalt. The complex modulus of the aged asphalt mixed with 6% and 7% proportions of rejuvenator is higher at lower frequencies compared to that of the aged asphalt, whereas the addition of 8% and 9% rejuvenator has minimal influence on the complex modulus of aged asphalt. At higher frequencies, the rejuvenator exerts a discernible downward influence on the complex modulus of aged asphalt, closely approximating its virgin state. The rheological performance of aged asphalt can be effectively restored by both 8% and 9% proportions of rejuvenator. Considering economic considerations, the optimal proportion for complex modulus recovery of aged asphalt is selected as 8%.

3.2 Fatigue life

The relationship between stress and strain was evaluated based on the LAS test, as shown in Figure 3. The stress-strain behavior of aged asphalt encompasses that of the virgin material, with consistent observation of a descending trend in stress-strain curves as the proportion of rejuvenator increases. What's more, the stress-strain curves of recycled asphalt are lower than that of the virgin asphalt.
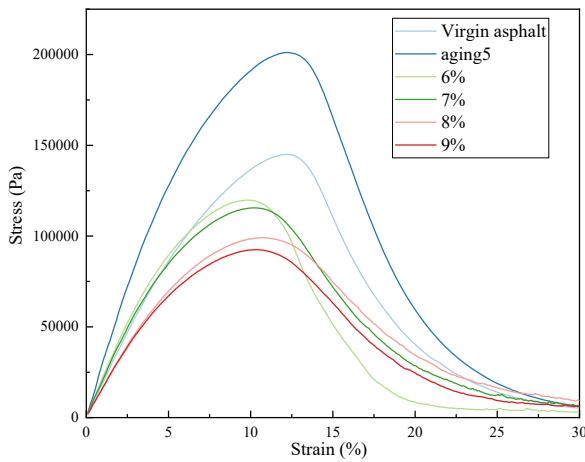
Figure 3. Stress-strain response of aged asphalt.

Then the fatigue behavior evolution of recyclable epoxy asphalt was investigated based on the stress-strain response, employing a viscoelastic continuous damage model (S-VECD). The fatigue life prediction for the aged asphalt under various strain levels is presented in Table 2. The aging process has marginally enhanced the fatigue life of asphalt under higher strain levels. However, when a rejuvenator is added, the fatigue life of aged asphalt decreases significantly compared to both its virgin state and the aged condition. The proportion of 8% has the apparent improvement on the fatigue performance.

Table 2. Fatigue life prediction for aged asphalt.

Sample \ Strain	Fatigue life		
	2%	4%	6%
Virgin asphalt	70333	7603	2069
Aged 120 h	46285	7257	2455
6%	37761	4249	1184
7%	24171	3785	1279
8%	28546	4645	1606
9%	23842	3769	1281

3.3 Rutting resistance ability

The results of the MSCR tests conducted on aged asphalt are illustrated in Figure 4. The experimental temperature is set to be 46 °C. The MSCR test employs the average recovery percentage R and non-recoverable creep compliance J_{nr} as assessment indicators for evaluating rutting resistance capability.

The creep recovery percentage R demonstrates a slight increase following the aging process. Upon the addition of rejuvenator, R exhibits an upward trend in comparison to both the virgin and aged samples. The proportion of the 8% sample exhibits an obvious decrease in the recovery percentage R at a stress level of 3.2 kPa, closely resembling both the virgin and aged states.

The non-recoverable creep compliance J_{nr} characterizes the unrecoverable creep compliance of asphalt. After aging, the value of J_{nr} decreases at the stress level of 0.1 kPa. The incorporation of a lower

amount of rejuvenator results in a reduced J_{nr} compared to the virgin and aged asphalt, indicating an improvement in elasticity and a decrease in permanent deformation. Until the proportion exceeds 8%, the aged asphalt samples demonstrate a partial yet incomplete recovery of the non-recoverable creep compliance. At the stress level of 0.1 kPa, the rutting resistance is similar to the aged samples, albeit still remaining better than that of the virgin material.
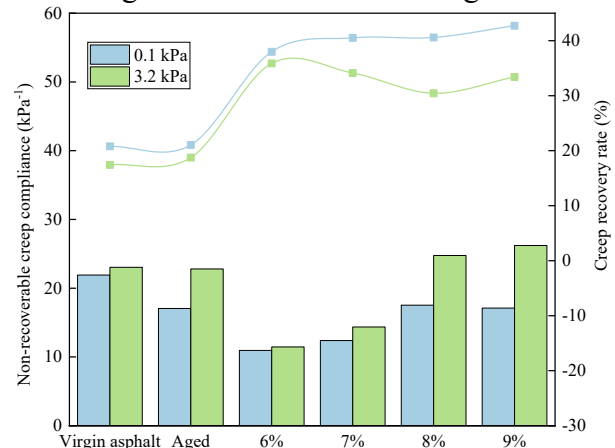
Figure 4. MSCR test results of aged asphalt.

3.4 Low-temperature cracking resistance

The stiffness S and the creep rate m-value can be determined through the BBR test, enabling an assessment of low-temperature cracking resistance. The BBR test was conducted at temperatures of -6 °C, -12 °C, and -18 °C, respectively. The results are recorded in Table 3.

Table 3. Stiffness and m-value of aged asphalt.

Sample		Temperature/ °C		
		-6	-12	-18
Virgin asphalt	S/MPa	13.97	54.26	153.18
	m	0.58	0.46	0.36
Aged 120 h	S/MPa	19.35	60.62	212.75
	m	0.53	0.43	0.34
6%	S/MPa	13.26	41.80	114.80
	m	0.49	0.41	0.34
7%	S/MPa	13.91	43.27	114.14
	m	0.49	0.41	0.33
8%	S/MPa	12.42	42.22	112.88
	m	0.50	0.42	0.35
9%	S/MPa	10.71	35.35	102.49
	m	0.50	0.42	0.34

Following the aging period, the aged asphalt demonstrates a noticeable increase in stiffness, while concurrently exhibiting a decrease in m-values. The results suggest the presence of a slightly slower relaxation of stress. The aged asphalt exhibits reduced resistance to low temperature performance. The stiffness has fully recovered to the virgin state after regeneration, even exhibiting a lower level. However, m-values solely correspond to the virgin asphalt

with a higher proportion of rejuvenator; nevertheless, there remains a noticeable disparity.

3.5 *Regeneration implementation*

The rejuvenation of aged recyclable epoxy asphalt was achieved by selecting a proportion of 8% rejuvenator, taking into account the rheological performance of recycled asphalt. Ultimately, the rheological performance of aged recyclable epoxy asphalt and regenerated recyclable epoxy asphalt was compared to that of virgin recyclable epoxy asphalt in order to assess the effectiveness of regeneration.

Using the complex modulus as an illustrative example to elucidate the matter in this study. The results of complex modulus are shown in Figure 5. After aging, the recyclable epoxy asphalt displays raised stiffness over the all frequencies. Combined with the regeneration process, the complex modulus of recyclable epoxy asphalt descends to even lower values than those of virgin materials. The utilization of an 8% rejuvenator can indeed result in a superior deduction of the complex modulus of recyclable epoxy asphalt.
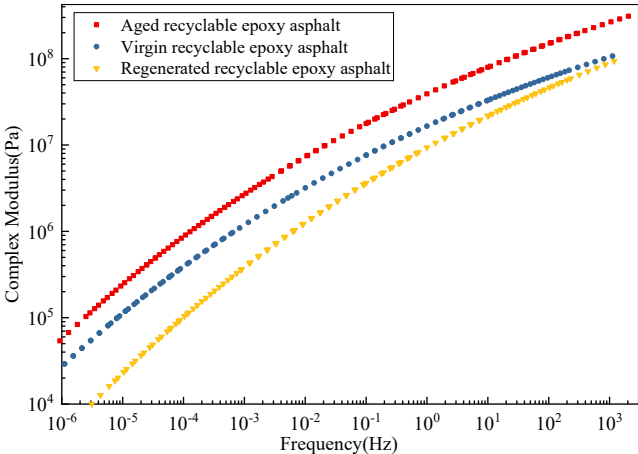
Figure 5. Master curves of complex modulus for recyclable epoxy asphalt.

To further analyze the results of complex modulus, the cross modulus at a temperature of 20 ℃ was derived, as shown in Figure 6.
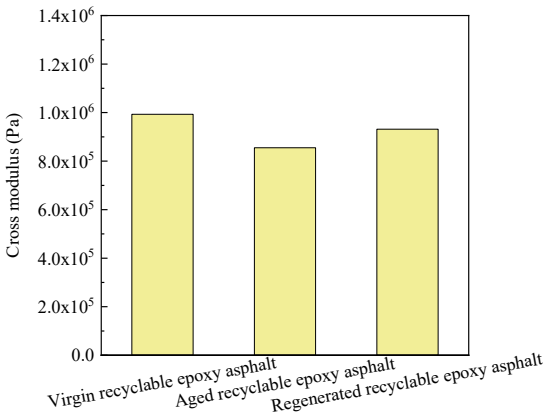
Figure 6. Cross modulus of recyclable epoxy asphalt.

After regeneration, the cross modulus exhibits an increase and approaches its initial level closely. The regenerative process demonstrates a clear ability to restore the virgin properties. The enhanced cross modulus accelerates the dynamic response of recyclable epoxy asphalt, enabling it to promptly react to external forces and facilitate relaxation.

4 CONCLUSIONS

(1) The optimal proportion of 8% rejuvenator is selected to regenerate the recyclable epoxy asphalt from the perspective of the asphalt phase.

(2) The regeneration has restored the capacity to elicit a dynamic response of recyclable epoxy asphalt.

(3) Rejuvenator proportions can be further adjusted in the future, taking into account the complex modulus requirements.

5 REFERENCE

Alamri, M., Lu, Q. and Xin, C., 2020. Preliminary Evaluation of Hot Mix Asphalt Containing Reclaimed Epoxy Asphalt Materials. Sustainability, 12(9): 3531.

Jing, R. et al., 2021. Effect of recycling agents on rheological properties of epoxy bitumen. Road materials and pavement design, ahead-of-print(ahead-of-print): 1-15.

Jing, R. et al., 2023. Recyclability of epoxy-modified open-graded porous asphalt, Advances in Materials and Pavement Performance Prediction 2022.

Yi, J., Zhou, W., Pei, Z. and Feng, D., 2023. Synthesis strategy and basic validation of recyclable epoxy asphalt. Transportation Research Record, 2677(9): 69-80.

Zhou, W., Yi, J., Pei, Z., Xie, S. and Feng, D., 2022. Preliminary design of recyclable epoxy asphalt: Regeneration feasibility analysis and environmental impact assessment. Journal of Applied Polymer Science, 139(24): 52349.

5.2

ENVIRONMENTAL IMPACT & ECONOMIC LIFE CYCLE PERFORMANCE OF PAVEMENTS

Use of recycling elastomers - a contribution to increasing sustainability in asphalt road construction?

A. Prof. Dr.-Ing. Alexander Buttgereit
Jade University of Applied Sciences, Oldenburg, Germany

B. Dr.-Ing. Daniel Gogolin
Engineering Company PTM Dortmund mbH, Germany

ABSTRACT: When designing a construction method and selecting the individual construction materials, the topics of sustainability, climate protection and resource conservation are becoming increasingly important in asphalt road construction. The current situation in road construction, i.e. increasing raw material prices and simultaneously decreasing availability of primary construction materials, will increase the importance of the reuse of secondary construction materials. Rubber-modified asphalts have been used successfully for many years as an alternative to polymer-modified asphalts. Rubber-modified bitumens consist of a road bitumen modified with additivated rubber powder (secondary construction material from recycled tires). However, the good practical experience to date has only been partially documented, if at all, by verified data. On the basis of three long-term studies on the mode of action and performance of the rubber-modified construction method with considered periods of use between 10 and 13 years, a highly loaded industrial area (2007), a logistics and container area (2008) and a city road (2012) were examined and evaluated by the engineering company PTM Dortmund mbH. In addition, investigations (performance and emissions) and dimensioning calculations com-paring polymer-modified to rubber-modified construction methods were carried out as part of a pilot route (2020). The previous positive experience with the rubber-modified asphalt construction method was con-firmed by long-term observations and comparative laboratory tests. The highly loaded asphalt surfaces inves-tigated still show good performance properties even after comparatively long service lives. With regard to the calculated service lives, it was also possible to derive equivalent or even higher service lives for rubber-modified asphalt variants compared with the classic polymer modification. In summary, the results show that the rubber-modified asphalt construction method can make an additional contribution to the main sustainabil-ity goals, such as resource conservation, the reduction of CO_2 emissions or the reduction of life cycle costs through the extension of service lives.

1 INTRODUCTION

When designing a construction method and selecting construction materials, sustainability, climate protec-tion and resource conservation are becoming in-creasingly important in asphalt road construction. A major contribution to sustainability can be achieved in particular by maximizing the useful life of roads. In order to achieve this, polymer modified bitumens (PmB) according to TL Bitumen-StB 07/13 [1] are generally used for special stresses in asphalt road construction. These polymers, mostly styrene-butadiene block copolymer (SBS) produced from anionic polymerization, are primary construction materials with limited availability worldwide. As an alternative to PmB, rubber modified bitumens (GmB) have been used for many years in a wide va-riety of projects. Rubber modified bitumens general-ly consist of a road construction bitumen modified with additivated rubber powder (secondary construc-tion material from recycled tires).

According to current results, the use of rubber-modified bitumen promises above all performance improvements with regard to the low-temperature, aging and fatigue behavior of asphalt. In this respect, there has already been good national and interna-tional experience with rubber modification for many years - especially in the application areas of highly stable asphalt concepts (container terminals, logis-tics centers, bus bays, etc.), noise-optimized asphalt layers (PA) and in higher reuse rates of asphalt granulate. Furthermore, the targeted use of second-ary construction materials / recycled products can be expected to make an additional contribution to cli-mate protection and resource conservation. The knowledge gained so far on rubber modification is to be further deepened by this paper, among others.

2 CURRENT STATE OF KNOWLEDGE ON RUBBER MODIFICATION

The "Recommendations on Rubber Modified Bitumen and Asphalts" [2] deal with the use of additivated rubber powder (particels < 0,8mm) or crumb rubber in the production of rubber modified asphalts.

Modification with rubber powder is used to improve the bitumen properties and the asphalt produced with it. The additivated rubber powder can be added either to the bitumen (wet process) or directly into the mixer of the asphalt mixing plant immediately dur-ing the production of the asphalt (dry process). The findings presented in this paper refer exclusively to the dry process (direct modification) described in E GmB A [2].

In the dry process, the add. rubber powder or rubber-modified bitumen granules are added directly to the asphalt mixer to modify the asphalt. The advantages of dry addition for asphalt applications include:

• The free choice of the base bitumen and the variable control of the addition quantities of the additive-modified rubber powder mean that customized solutions can be supplied for almost any application

• Special solutions are also possible for very small areas (e.g. bus bays, etc.).

• The addition is possible on almost all asphalt mixing plants.

• Asphalt mixes with high proportions of asphalt granules can be modified in a targeted manner.

3 LONG-TERM STUDIES AND DATA SITUATION

The extended useful life as part of the sustainability potential of rubber-modified asphalt construction methods is generally expected by practical experience and for the most part also recognized. However, this has so far only been partially or not at all documented by verified data and corresponding comparisons.

The long-term use of rubber-modified asphalts has been documented on the basis of 4 practical examples from different areas of traffic route construction and evaluated by means of corresponding laboratory tests:

1. highly loaded industrial area (2007) in the port of Rostock in asphalt construction based on ZTV Asphalt-StB 01 [3], year of investigation 2020

• approx. 3 to 3.5 cm AC 8 D S with bitumen 30/45 and 15 % add. rubber powder

• approx. 6 to 8 cm AC 16 B S with bitumen 30/45 and 15 % add. rubber powder

• approx. 9 to 12 cm asphalt base course (n/a)

2. logistics and container areas (2008) in asphalt construction based on ZTV Asphalt-StB 01, year of investigation 2019

• AC 8 D S (asphalt surface course), base bitumen 50/70 and 15 % add. rubber powder

• AC 16 B S (asphalt binder course), with base bitumen 50/70 and 15 % add. rubber powder.

• conventional (unmodified) AC 22 T S (base course)

3.resource conservation city road (2012) in asphalt construction method based on ZTV Asphalt-StB 01, study year 2019.

• Asphalt granulate content of 50% in the asphalt surface course made of SMA and addition of add. rubber powder in the dry process.

• SMA 8 S with base bitumen 70/100 and 15 wt.-% of add. rubber powder (based on the total binder content)

4. new construction of rural road (2020) in asphalt construction with 3 different construction methods

• V1: AC 8 DS with PmB 25/55-55, AC 16 BS SG with 30/45, AC 32 T S with 30/45

• V2: AC 8 D S with PmB 25/55-55, AC 16 BS SG with PmB 25/55-55, AC 32 T S with 45/80-50

• V3: AC 8 D S with 50/70 +12.5% add. rubber powder, AC 16 B S SG with 50/70 +12.5% add. rubber powder, AC 32 TS with 70/100 +12.5% add. rubber powder

In this article, only the 3rd and 4rd project will be dis-cussed in more detail below.

3.1 *Asphalt concept*

The milled asphalt surface course of the road was to be reused in the new asphalt surface course as planned after reprocessing. During the preliminary investigations in 2011, a softening point ring and ball of 74 °C, a needle penetration of 17 0.1 mm and a breaking point after Fraaß of -3 °C were determined on the asphalt surface course of SMA 11 S to be renewed. The determined binder characteristics thus basically indicated a very strongly aged bitumen.

The binder concept developed for the new asphalt surface course of SMA 8 S provided for a soft base bitumen 70/100 and 15 % of add. rubber powder (based on the total binder content) for modification in the dry process, using 50% asphalt granulate. In general, the German regulations do not allow the addition of RAP in SMA. Within the scope of this project, an attempt was made to increase the amount of RAP added to the maximum of 50% without negatively affecting the quality of the resulting asphalt. The applied dry process - i.e. direct modification in the asphalt mixer - made it possible to modify the entire asphalt mix despite the high proportion of asphalt granules. In this context, the rubber modification was intended to optimize the old bitumen present in the asphalt granulate and, in particular, the poor low-temperature behavior identified in the preliminary investigations, as well as to contribute to the general

improvement of the asphalt's overall performance (compactability, deformation resistance, etc.).

Further details on the implementation of the construction measure can be found in the technical article from [3].

3.2 Long-term monitoring 2012 to 2022

The long-term monitoring carried out so far is described by the project timeline shown in Fig. 1. Within the scope of the monitoring (as of March 2022), no deformations, cracks (e.g. brittle cracks) or other defects could be detected after a good 10 years.
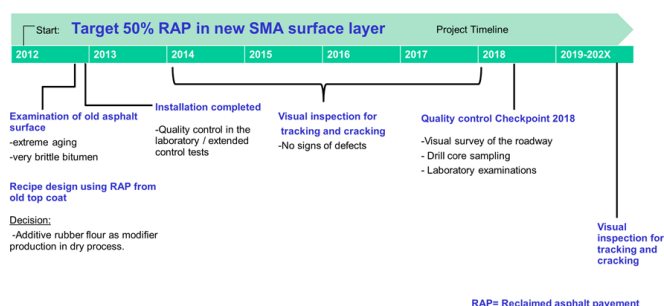
Figure 1: Long-term monitoring Detmolder Straße

The good visual condition of the road is supported by the laboratory tests carried out in 2018/2019. In Table 1, the characteristic values of the control test from 2012 are compared with the values after 6 years of service. The comparison clearly shows at this point that the aging rate of the binder of the asphalt surface course is very low with an average increase in the softening point ring and ball of about 2 °C, i.e. with an increase of about 0.3 °C/year. In addition, despite the high stiffness (complex shear modulus G*) at 60 °C of 23,710 Pa (high deformation resistance), the binder exhibits very good low temperature behavior in the BBR with a stiffness of 205 MPa and an m-value of 0.317.

Table 1: Comparison of 2012 control inspection and 2018/2019 follow-up inspection

Parameter		control inspection	Examination after 6 years lying time
Test year	[°C]	2012	2018
Ring and Ball	[°C]	63,4 bis 66,0	64,8 bis 68,6
Elastic recovery	[%]	n.b.	31 bis 33
G* at 60 °C	[Pa]	n.b.	23.710
φ at 60 °C	[°]	n.b.	69,1
Reshaping $R_{3.2kPa}$	[%]	n.b.	31
BBR bei -16 °C (S)	[MPa]	185	205
BBR bei -16 °C (m-Wert)	[-]	0,307	0,317

n.b.= Parameters were not determined in 2012

3.3 Resource and CO₂ savings through the use of secondary raw materials

In addition to the successful implementation of the road construction project, the focus was on the environmental sustainability goal of "increasing the RC quota", i.e. construction in the sense of the Recycling Management Act (Kreislaufwirtschaftsgesetz [5]). Within the scope of the construction project, a total of 375 t of primary material - approx. 352 t of aggregate and 23 t of bitumen - could be saved due to the high reuse rate for almost 7,000 m² and 750 t of asphalt mix. Furthermore, as an additional environmental goal, the use of a modifier made from secondary raw materials (rubber flour) made an additional contribution to reducing CO_2 emissions. According to the German Rubber Industry Association (Wirtschaftsverband der deutschen Kautschukindustrie e.V.), approximately 175,000 t of used tires were sent for thermal recycling (cement industry) in Germany in 2019. In general, a saving of 0.7 t of emission CO_2 per 1 t of tires is assumed here if the tires are recycled instead of being thermally recycled. For the project under investigation with approx. 750 t of asphalt mix, this corresponds to CO_2 savings of 10 t.

4 SUMMARY AND OUTLOOK

The positive experience and findings to date with the rubber-modified asphalt construction method were confirmed by the long-term observations and comparative laboratory tests of the individual asphalt variants (including computational dimensioning [7]). The following points could be derived from the dimensioning calculations:

- The replacement of PmB to RmB only for the asphalt surface course has almost no influence on the results of the dimensioning for the high load classes (equivalent), but the rubber-modified asphalt clearly shows the highest stiffness in the high service temperature range and at the same time the lowest stiffness in the lower service temperature range. Indirectly, a significantly higher resistance to deformation under heat can thus be derived, especially in the high service temperature range. The observed performance in the lower service temperature range was confirmed by the cooling tests carried out. Here, the rubber-modified variant exhibits the best low-temperature properties, followed by the polymer-modified variant and the variant with base bitumen.
- In the case of three-layer modification the fatigue resistance and thus the calculated service life of the asphalt structure increases between 10 % and 20 % depending on the load class when comparing the RmB variants with the PmB variants.

Particularly the highly loaded asphalt surfaces investigated show good performance properties even after comparatively long periods of use.

In summary, it could be shown at this point through the described practical examples that an additional contribution to the protection of resources, the reduction of CO_2 emissions or the reduction of life cycle costs can be made through the longer useful life of the rubber-modified asphalt construction method.

In view of the current situation in road construction, i.e. rising raw material prices and simultaneously declining availability of primary construction materials, the topic of reuse of secondary construction materials in general is becoming increasingly important. Especially the possibility of direct modification at the asphalt mixing plant by means of the dry process offers here the possibility of continuing to modify the future higher proportions of asphalt granulate in the asphalt mix in a targeted manner [4].

A future task of the rubber-modified construction method, especially for the dry process, will be the reduction of the production temperature of asphalt mixes (low-temperature asphalt), which will inevitably come about as a result of the setting of the occupational exposure limit (OEL) for bitumen. In this respect, initial test results show that a temperature reduction according to the current M TA [6] is also possible both during production and during paving with the rubber-modified construction method.

5 REFERENCES

[1] Technische Lieferbedingungen für Straßenbaubitumen und gebrauchsfertige Polymermodifizierte Bitumen (TL Bitumen-StB 07/13), Ausgabe 2007/Fassung 2013, FGSV Verlag, Köln

[2] Empfehlungen zu Gummimodifizierten Bitumen und Asphalten (E GmB A), Ausgabe 2012, FGSV Verlag, Köln

[3] D. Gogolin, H.-H. Weßelborg: Hochwertige Wiederverwertung von Asphaltgranulat aus Splittmastixasphalt im Sinne des Kreislaufwirtschaftsgesetzes (KrWG) am Beispiel „Detmolder Straße in Paderborn", Fachzeitschrift Straßen und Autobahn, Ausgabe 8/2013

[4] S. Gohl, D. Gogolin, R. Ziener: „E GmBA: Besonderheiten bei der Verwendung von Asphaltgranulat in Gummimodifizierten Asphalten", asphalt 5/2017

[5] Gesetz zur Förderung der Kreislaufwirtschaft und Sicherung der umweltverträglichen Bewirtschaftung von Abfällen (Kreislaufwirtschaftsgesetz - KrWG) vom 24. Februar 2012 (BGBl. I S. 212)

[6] Merkblatt für Temperaturabsenkung von Asphalt (M TA), Ausgabe 2021, FGSV-Nr. 766

[7] RDO Asphalt 09, Richtlinien für die rechnerische Dimensionierung des Oberbaus von Verkehrsflächen mit Asphaltdeckschicht (RDO Asphalt 09), Ausgabe 2009, FGSV Verlag, Köln

Life Cycle Sustainability Assessment (LCSA) of pavements – A case study highlighting challenges and potentials

P. Haverkamp & M. Traverso
Institute of Sustainability in Civil Engineering, RWTH Aachen University, Germany

ABSTRACT: Considering the significant impacts of roads on society, economy, and environment, measuring the sustainability performance of pavements is critical. Therefore, this contribution explores the application of Life Cycle Sustainability Assessment (LCSA) by the presentation of a hypothetical case study of a motorway segment in Germany. The results show that the main hotspots for the environmental and economic dimensions are related to the use stage, specifically maintenance and replacement. Regarding the social dimension, social risks such as discrimination and unfair working conditions were identified. In general, LCSA enables a systematic assessment of the sustainability performance of roads allowing the identification of life cycle stages and processes that can later be optimized, while avoiding burden-shifting. However, the method presents several obstacles, some of them relating to the definition of consistent system boundaries and lack of reliable data.

1 INTRODUCTION

The impacts roads in society and environment are widely known, and several efforts have been recorded towards measuring and optimizing their sustainability performance (Del Rosario & Traverso 2023). For instance, the Federal Highway Administration (FHWA) in the United States provides several tools in which the sustainability of pavements can be measured using methods such as Life Cycle Assessment (LCA), Life Cycle Costing (LCC), and sustainability rating systems (FHWA 2021).

LCA is a method for quantifying environmental impacts of products throughout their whole life cycle standardized by the ISO 14040 and ISO 14044 (ISO 2020a, 2020b). LCA is widespread across many fields, and enables the identification of environmental hotspots associated to a particular product. LCC is a further life-cycle-based method addressing the economic dimension, i.e., the life cycle costs of products (Swarr *et al.* 2011). Although there are no general standards for LCC, a norm for its application in buildings exists (ISO 15686-5), which is often used as reference in road construction. Finally, the social performance of products can be addressed with Social Life Cycle Assessment (S-LCA), in which positive and negative impacts of products can be quantified (UNEP 2020). This method has been recently standardized by the ISO 14075 (ISO 2024).

All these methods are useful for measuring the performance of products in individual sustainability dimensions. However, sustainability should be addressed from a holistic perspective to avoid issues such as burden-shifting. This comprehensive approach can be achieved with the Life Cycle Sustainability Assessment (LCSA), which prescribes the parallel application of LCA, LCC, and S-LCA for the same functional unit (reference) and equivalent system boundaries (Kloepffer 2008; Finkbeiner *et al.* 2010). Although gaining popularity, this method is not yet widely adopted in the road construction sector, with only a few examples found in literature (Del Rosario & Traverso 2023).

Therefore, the aim of this contribution is to explore LCSA of pavements through the analysis of a case study. The objective is to provide insights on the potentials and challenges of this method in the road construction industry.

2 METHODS

2.1 *Case study*

The hypothetical case study consists of a 5-km motorway segment near Dresden, assumed to have a Standard Cross-Section RQ 36 (FGSV 2008). The structure is assumed to have the load class BK100 and an Annual Average Daily Traffic (AADT) of 42,500 vehicles. The assessed structure is presented in Figure 1.
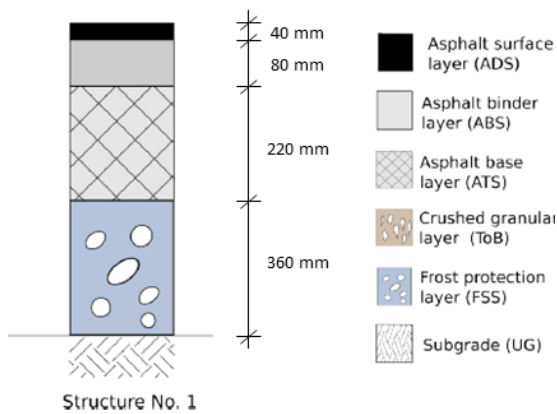
Figure 1. Pavement structure.

2.2 Goal and scope definition

The goal is to determine the main impacts associated with the construction and operation of a motorway section in Germany. In particular, the main hotspots and challenges shall be identified. The environmental and economic impacts are determined using the LCA and LCC methods. Due to lack of data availability, social risks are determined to identified potential relevant social aspects.

The functional unit (FU) is 1 road-km of road pavement of a German motorway section near Dresden, with the standard cross-section RQ36, load class BK100, AADT 42,500 (truck share: 8.24%) and a period of analysis of 30 years.

Due to the granularity needed in for each of the methods, the system boundaries of the study vary. In this simplified assessment, the LCA and social risk assessment consider raw material and energy production (A1), raw material transport (A2), asphalt mixing process (A3), asphalt mixture transport (A4), pavement construction (A5), maintenance (B2), and rehabilitation / replacement (B4). A period of analysis of 30 years is selected, in which following activities are assumed to be carried out:

- Years 1-30: Yearly winter service, inspections and condition monitoring
- Year 12: Thin asphalt overlay
- Year 16: Replacement of the surface layer
- Year 18: Thin asphalt overlay
- Year 30: Replacement of surface and binder layers

In turn, since the LCC is conducted from the perspective of the road agency, the costs arising in Modules A1-A3 are not considered as relevant since the final cost (including production costs, revenue and other components) is used. For the sake of harmonization with the reported LCA results, material costs corresponding to the initial construction will be reported as Module A3. Costs arising in Modules A4-A5, B2 and B4 are also reported.

The LCA was carried out using the software ©GaBi ts 10.6.2.9. For the LCC and the social risk assessment, the data was gathered from their

respective databases (see Section 2.3) and processed using MS Excel. The norms ISO 14040, ISO 14044, ISO 15686-5, and EN 15804 were used as references for the assessment, as well as the UNEP LCSA Guidelines (UNEP 2011; ISO 2017, 2020a, 2020b; CEN 2021; ISO 2024).

2.3 Life cycle inventory

Secondary data was used for the assessment. Considering that the case study is located in Germany, German datasets were preferred whenever available. For the LCA, the databases ©GaBi Professional 2022.2 and Ecoinvent v.3.8 were used.

To conduct the LCC, data was used obtained mostly from the Autobahn GmbH – road agency managing federal motorways in Germany – and Baupreislexikon – a German costs database (f:data n.d.). The cost categories of material, transportation, labor, and machines are considered. Furthermore, costs related to tendering and planning commissioning, as well as construction site equipment were obtained as lump sums.

The social risk assessment was conducted with the Product Social Impact Life Cycle Assessment (PSILCA) database (GreenDelta 2020). Here, the social risks associated to stakeholders (e.g., workers, value chain actors, society, and local community) within a particular economic sector of the selected country are mapped and classified from "very low" to "very high" risks. For this study, the economic sectors associated to the life cycle of the pavement were identified based on Del Rosario et al. (2024) with the addition of activities for construction, maintenance and replacement, all considered to be under the sector "basic construction".

2.4 Life cycle impact assessment

The Environmental Footprint (EF) method 3.0 was used in the LCA and all impact categories included were determined. These results were normalized and weighted using the factors of the method. In this study, only the most relevant impact categories are reported, which are those with a combined contribution amounting to at least 80% of the total environmental impacts after their normalization and weighting.

In the case of LCC, this step is not foreseen and the results are expressed in terms of costs. In particular, they are expressed in terms of Net Present Value (NPV) using a discount rate of 3%.

For the social dimension, no impact assessment was carried out since only a social risk assessment could be performed. In this regard, the results are expressed in terms of the likelihood of a certain social issue occurring within a particular economic sector for a particular country. For the purposes of this study, only the social issues for which a "high" or "very high" risks are determined to be relevant. Given

that in some instances the social risks in each of the economic sectors vary, a point scale was defined to assign the overall risk corresponding to a social topic. This point scale ranges from 7 points (very high risk) to 1 point (very low risk). Furthermore, to account for uncertainty, 4 points where assigned to those cases in which no data was available.

2.5 *Interpretation*

For all sustainability dimensions the most relevant hotspots were identified. For the environmental dimension, the most relevant life cycle stages and impact categories were determined. Similarly, the most relevant life cycle stages and the most relevant cost categories are identified for the economic dimension. Finally, the most relevant social risks, identified as those marked as "high" or "very high" are listed.

3 RESULTS AND DISCUSSION

3.1 *Life cycle assessment*

The most relevant environmental impact categories had a total contribution of 83.50% and are Resource Use, fossils (RU-f, measured in MJ) (33.30%), Ecotoxicity, freshwater (ET-fw, measured in Comparative Toxic Units – CTUe) (29.50%), and Climate Change (CC, measured in kg CO_2 equivalents) (20.70%). The characterized results for these impact categories are presented in Table 1.

Table 1. LCA results for the most relevant impact categories expressed per FU

Modules	CC [kg CO_2 eq.]	ET-fw [CTUe]	RU-f [MJ]
A1	1.26E+05	1.66E+07	8.50E+06
A2	3.67E+04	3.67E+05	4.79E+05
A3	1.62E+05	4.46E+05	1.69E+06
A4	3.75E+04	3.75E+05	4.91E+05
A5	3.56E+02	3.61E+04	1.03E+04
B2	2.24E+04	2.92E+05	3.88E+05
B4	3.82E+05	4.52E+07	1.34E+07
Total	**7.67E+05**	**6.33E+07**	**2.50E+07**

For all impact categories (including those not presented in Table 1), the most relevant life cycle stage is Module B4, with a contribution of 49.80%, 71.43%, and 53.77% for CC, ET-fw, and RU-f, respectively. The main reason for this is the great amount of raw material and energy needed for the production of the mixtures needed for the replacement and rehabilitation activities. This conclusion is supported by the influence of Module A1 on the results, which is the second most influential stage in most impact categories, including ET-fw and RU-f. For CC, the second most relevant life cycle stage is

Module A3. The least influential stage was Module A5, with contributions lower than 1% for most indicators. Furthermore, the influence of Modules A2 and A4 in the results varied, but still considered to be relatively low, with contributions ranging from 0.58% (A2 for ET-fw) to 4.89% (A4 for CC).

Based on these findings, the most relevant processes for the studied infrastructure and the defined system boundaries are related to raw material extraction and processing, as well as asphalt mixture production.

3.2 *Life cycle costing*

The NPV of the structure amounted to 4.08 Mio€ for the defined FU and system boundaries. A breakdown per life cycle stage is presented in Figure 1.
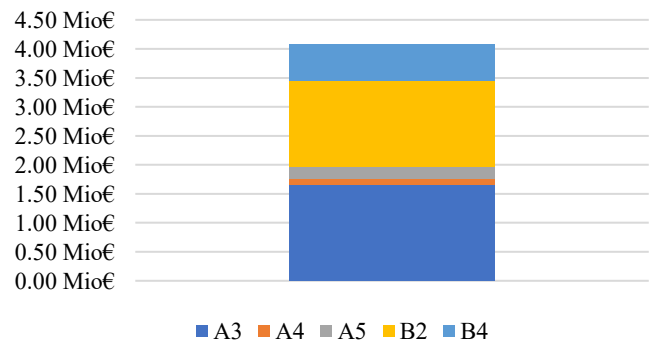
Figure 1. NPV per FU of assessed pavement structure.

Two main contributors to the life cycle costs are highlighted: initial material costs (accounted for in Module A3) (40.83%), followed by maintenance activities (35.92%). Within Module B2, winter service produces the highest costs, contributing about 77.48% to this stage. In turn, Modules A2 and A5 contribute only 2.14% and 5.48% to the total costs, respectively.

In terms of cost categories, it is not possible to define a hotspot due to the nature of the different life cycle stage and the fact that in several cases, only lump sums could be used in the calculations.

3.3 *Social hotspot analysis*

Based on the approach described in Section 2.4, social risks were identified for the stakeholder categories of local community, value chain actors, and workers.

The topics of biomass consumption, international migrant stock and migration flows present high risks. Biomass consumption is significant due to ecosystem disruption and the need for extensive land clearance for the extraction of raw materials and the preparation of the construction site. Furthermore, many economic sectors in Germany rely increasingly on migrant

workers, which could lead to increased risks related to discrimination, unfair working conditions and conflicts with the local community.

Moreover, topics in relation to corruption, such as "active involvement of enterprises in corruption and bribery" and "anti-competitive behavior", were also found to present a high social risk for all studied sectors. Further social risks identified are related to gender wage gap, fair salary, and trade unionism.

4 CONCLUSIONS

This contribution explored the use of LCSA in pavement through a case study, focusing on potentials and challenges of this method in the road construction industry.

One prominent challenge is ensuring consistent system boundaries since different methods require different levels of detail in the assessment. Furthermore, access to primary data remains a significant hurdle, particularly for LCC and S-LCA, where even reliable secondary data is limited. For instance, while some resources such as Baupreislexikon exist for LCC, they showed large deviations when compared to representative data from the Autobahn GmbH. Similarly, while secondary databases exist for S-LCA, they may not account for all relevant stakeholders, affecting the completeness of the assessment. In this case study, social aspects connected road users (consumers) were not considered since they are not part of the scope of the used database.

Nonetheless, LCSA still offers several potentials. In particular, hotspots can be systematically identified, up to the level of processes and even elementary flows, allowing for optimization while avoiding burden-shifting among dimensions. Moreover, decisions based on the sustainability performance of the pavement can be made on a more holistic basis, considering the three dimensions of sustainability.

5 ACKNOWLEDGEMENTS

6 REFERENCES

CEN, 2021, *Sustainability of Construction Works—Environmental Product Declarations—Core Rules for the Product Category of Construction Products*, Beuth Verlag GmbH, Berlin.

Del Rosario, P., Buttitta, G., Lo Presti, D. & Traverso, M., 2024, 'Towards the Assessment of Social Sustainability: Identifying Social Hotspots for Road Pavement Materials', in G.W. Flintsch, *et al.* (eds.), *Pavement, Roadway, and Bridge Life Cycle Assessment 2024*, vol. 51, pp. 262–270, Springer Nature Switzerland, Cham.

Del Rosario, P. & Traverso, M., 2023, 'Towards Sustainable Roads: A Systematic Review of Triple-Bottom-Line-Based Assessment Methods', *Sustainability* 15(21), 15654.

f:data, n.d., *Baupreislexikon,* f:data, viewed 08th December 2024, from https://www.baupreislexikon.de/.

FGSV, 2008, *Richtlinien für die Anlage von Autobahnen (RAA)*, FGSV.

FHWA, 2021, *FHWA Sustainability Assessment Tools,* Federal Highway Administration, viewed 08th December 2024, from https://www.fhwa.dot.gov/pavement/sustainability/tools/.

Finkbeiner, M., Schau, E.M., Lehmann, A. & Traverso, M., 2010, 'Towards Life Cycle Sustainability Assessment', *Sustainability* 2(10), 3309–3322.

GreenDelta, 2020, *PSILCA v.3,* GreenDelta, viewed 08th December 2024, from https://psilca.net/wp-content/uploads/2020/06/PSILCA_documentation_v3.pdf.

ISO, 2017, *Buildings and Constructed Assets—Service Life Planning—Part 5: Life-Cycle Costing*, Beuth Verlag GmbH, Berlin.

ISO, 2020a, *Environmental Management—Life Cycle Assessment—Principles and Framework*, Beuth Verlag GmbH, Berlin.

ISO, 2020b, *Environmental Management—Life Cycle Assessment—Requirements and Guidelines*, Beuth Verlag GmbH, Berlin.

ISO, 2024, *Environmental management — Principles and framework for social life cycle assessment*, Beuth Verlag GmbH, Berlin.

Kloepffer, W., 2008, 'Life cycle sustainability assessment of products', *The International Journal of Life Cycle Assessment* 13(2), 89–95.

Swarr, T.E., Hunkeler, D., Klöpffer, W., Pesonen, H.-L., Ciroth, A. & Brent, A.C.*, et al.*, 2011, 'Environmental life-cycle costing: a code of practice', *The International Journal of Life Cycle Assessment* 16(5), 389–391.

UNEP, 2011, *Towards a Life Cycle Sustainability Assessment: Making Informed Choices on Products*, from https://wedocs.unep.org/20.500.11822/8001.

UNEP, 2020, *Guidelines for social life cycle assessment of products and organizations 2020,* UNEP, from https://www.diva-portal.org/smash/get/diva2:1647964/fulltext01.pdf.

Integrating Thermo-Viscoelasticity into an Optimization Framework for Economically and Environmentally Sustainable Flexible Pavement Design

Paul Leopold[1], Quentin Félix Adam[1], João Santos[2], Alvaro García-Hernandez[1]

[1] *Chair and Institute of Highway Engineering, Faculty of Civil Engineering, RWTH Aachen University, Mies-van-der-Rohe-Straße 1, 52074 Aachen, Germany*

[2] *Department of Civil Engineering and Management (CEM), Faculty of Engineering Technology, University of Twente, Drienerlaan 5, 7522 NB, Enschede, the Netherlands*

ABSTRACT: This study presents a comprehensive framework for optimizing flexible pavement designs by balancing environmental impacts and economic aspects while ensuring that the designs comply with thermo-viscoelastic stability. The framework comprises five components: a material database, the design variables (layer properties), two objective functions that account for the environmental impact and economical aspects related to the pavement life cycle phases ranging from material extraction to construction, a genetic algorithm-based optimization solver, and two constraints. Two case studies were considered to demonstrate the influence of temperature effects on the optimization of pavement designs, with Case 1 assuming seasonal temperature variations and Case 2 assuming a constant temperature in the top layer. The results show that accounting for temperature effects increases required layer thicknesses.

1 INTRODUCTION

For a given climate, designing flexible pavements involves defining layers— number, thickness, and materials—to bear mechanical loads. Rising construction costs have prompted efforts to optimize these layers to reduce expenses (Statistisches Bundesamt, 2024). Concomitantly, the European Green Deal aims for EU climate neutrality by 2050. It also highlights the construction sector's role, which is responsible for 5–12% of total Greenhouse gas (GHG) emissions (European Commission; European Commission, 2019). Reducing emissions in road construction is therefore crucial for achieving this goal. Optimizing layer properties has the potential to reduce costs and emissions but focusing solely on one or the other might lead to either economically unviable or environmentally unfriendly solutions. Thus, the optimization process must balance cost and environmental impact.

In this regard, several studies have been carried out with the goal of optimizing pavement layer properties (or a subset of those) with respect to performance, economic, and environmental impacts (or a subset of these). This is typically achieved through the application of a multi-objective optimization (MOO) framework. Layered elasticity and temperature-independent layered viscoelasticity (not simultaneously) are usually used to assess the mechanical performance. The materials, their transportation, and construction costs were taken into account for the economical aspects. The materials extraction, transportation, and construction were considered for the environmental impact. The developed frameworks were applied to assess the effectiveness of balancing performance, costs, and environmental impact. For the studies (Inti and Anjan Kumar, 2021) and (Wang and Chong, 2014) the benefits of their framework are not clearly indicated, while (Demir et al., 2023) demonstrated a reduction of 30 % and 31 % in environmental impact and economic aspect (not simultaneously). The frameworks were solved with a particle swarm algorithm, Genetic Algorithm (GA), or manually. However, none of the aforementioned studies considered the behaviour of the asphalt layers as thermos-viscoelastic.

2 OBJECTIVE AND METHODOLOGY

The objective of this paper is to present a MOO framework to optimize the layer properties—such as number, thickness, and materials—of flexible pavements, considering environmental and economic impacts, while ensuring thermo-viscoelastic stability. For this, an optimization framework is developed.

The framework consists of five parts: (1) a material database, (2) the set of decision variables, (3) the two constraints, (4) the objective functions and (5) an optimization algorithm solver. The material database hosts information about the costs, environmental impacts, and mechanical properties of each material. Two objective functions are defined; one accounts for the environmental impacts and the other for the economic aspect. Ultimately, the two objective functions are combined by weighing of each aspect to create a single objective function. Accessing this material database, a GA is applied to this objective function, in order to minimize the environmental impact and the economic aspect. In general terms, as part of the GA, several designs – herein defined as an arrangement of the layers numbers, materials, and thicknesses – are generated. To ensure thermo-viscoelastic stability compliance with the German guidelines (Forschungsgesellschaft für Straßen- und Verkehrswesen, 2024) these combinations are constrained through assessment of the fatigue, i.e., horizontal tensile strains at the bottom of the bituminous base layer. The strains are calculated according to thermo-viscoelasticity

theory applied to a layered domain (representing a flexible pavement) subjected to loadings (representing traffic). In addition, the minimum and maximum layer thickness is limited by further constraints. The layer properties providing the minimal value of the fitness function and complying with the thermo-viscoelastic stability are selected as the optimal solution. This framework is posteriorly applied to two cases, differentiating themselves from each other by the temperature imposed within the top layer (representing asphalt concrete), one considering a constant temperature and the other varying within the year.

3 MULTI-OBJECTIVE OPTIMIZATION FRAMEWORK DEVELOPMENT

3.1 Material database

Table 1 presents the properties of several materials utilized in a typical German road pavement. The top layers, comprising the surface, binder, and base layers, are made of Asphalt Concrete (AC) and are assumed to exhibit thermo-viscoelastic material behavior. To account for this behavior, we assume thermo-rheological simplicity and apply the time-temperature superposition principle with Williams–Landel–Ferry (WLF) constants $C_1 = 30$ and $C_2 = 200$ °C (Morland and Lee, 1960). The Adaptive Layered Viscoelastic Analysis (ALVA) software (Skar and Andersen, 2020) is utilized to compute thermo-viscoelastic strains; the viscoelastic properties utilized herein are the default values of ALVA. The remaining layers are time- and temperature-independent and associated with the Poisson's ratio and the Young's modulus. Also presented in Table 1 are the GHG emissions and costs related to the A1-A3 phases of each material.

3.2 Decision variables

The decision variables of the MOO framework are the type and material of the layers to be included in the pavement structure and the respective thickness. Amongst the materials detailed in Table 1, the framework is allowed to optimize a pavement containing one to three layers. Also included in Table 1 is the information on whether a given layer type and material is mandatory to be included in the pavement.

3.3 Objective functions

The single objective function is additively composed of OF_1 (CO$_2$-eq) and OF_2 (€) accounting respectively for the environmental impacts (Eq. (1)) and costs (Eq. 2)) associated with the pavement life cycle phases A1-3, A4, and A5.

where n is the number of layers, ρ_i is the density of layer i (kg/m³), d_i is the thickness of layer i (mm), w_i

$$OF_1 = \sum_{i=1}^{n} \rho_i \cdot d_i \cdot w_i \cdot l_i \cdot (GHG_{A1-A3,i} + GHG_{A4} \cdot y + GHG_{A5} \cdot t) \quad (1)$$

is the width of layer i (m), l_i is the length of the layer i (m), $GHG_{A1-A3,i}$ are the GHG emissions associated with phases A1-A3 of layer i (CO$_2$-eq./kg), GHG_{A4} are the GHG emissions associated with phase A4 (CO$_2$-eq./(kg·km)), y is the distance between the asphalt mixing plant and construction site (km), GHG_{A5} are the GHG emissions associated with phase A5 (CO$_2$-eq./(kg·day)), and t is the construction rate (kg/day).

$$OF_2 = \sum_{i=1}^{n} \rho_i \cdot d_i \cdot w_i \cdot l_i \cdot (C_{A1-A3,i} + C_{A4} \cdot y + C_{A5} \cdot t) \quad (2)$$

where $C_{A1-A3,i}$ are the costs associated with phases A1-A3 (€/kg), C_{A4} are the costs of phase A4 (€/(kg·km)), and C_{A5} are the costs of phase A5 (€/(kg·day)).

The two objective functions are normalized (Eq. (3)):

$$OF_{j,norm} = \frac{OF_j - \min(OF_j)}{\max(OF_j) - \min(OF_j)} \quad (3)$$

where $j = 1$ or $j = 2$ and $OF_{j,norm}$ is the normalized objective function OF_j.

OF_1 and OF_2 are combined into one single objective function through the weighted sum method with user-defined weights (Eq. (4)):

$$OF_c = w \cdot OF_{1,norm} + (w - 1) \cdot OF_{2,norm} \quad (4)$$

Table 1. Structural, mechanical, environmental, and economic properties of the layer structure

Layer type	Layer materials	Mandatory	Poisson's ratio ν	Young's modulus E	GHG emissions A1-A3	Costs A1-A3
			[–]	[MPa]	[CO$_2$-eq./kg]	[€/kg]
Top layer	Asphalt	x	0.35	-	0.07732	0.09335
Base layer	Hydraulic bounded layer		0.25	2000	0.08	0.04135
	Stabilization layer		0.25	2000	0.08	0.035
	Crushed stone base layer		0.5	325	0.04	0.0135
Frost	Frost protection layer		0.5	150	0.03	0.02033
protection layer	Frost resistant material		0.5	75	0.03	0.18
Ground		x	0.5	45	-	-

3.4 Constraints

There are two constraints, one associated with the decision variables and the other with the compliance of the bottom-up fatigue criteria. The decision variable constraint sets lower and upper thickness limits for each layer to ensure that the created pavement design complies with the German guidelines (Forschungsgesellschaft für Straßen- und Verkehrswesen, 2024).The bottom-up fatigue criteria consist of quantifying the accumulation of strains caused by the traffic over the lifetime of a pavement. For this, the ALVA software (Skar and Andersen, 2020) was utilized to calculate the strains caused by a given number of Equivalent Standard Axle Loads (ESALs). Multiple runs were executed for the quantification, each representing a pavement structure subjected to these ESALs over one day, assuming a uniform and constant temperature within the top layer over this timespan. The temperature effects on the viscoelastic default properties were incorporated within the ALVA through the application of a shift factor (Williams et al., 1955). The collection of simulations for each day– i.e., calculated strains—required for the lifetime of a pavement were accumulated through the following formula (Forschungsgesellschaft für Straßen- und Verkehrswesen, 2024):

$$N_{acc} = m \cdot a \cdot \varepsilon_{horz}^{k} \qquad (5)$$

where N_{acc} are the acceptable load repetitions, m represents the adaption factors presented in Table 2, $a = 2.8283$ and is the fatigue regression parameter, ε_{horz} is the horizontal strain (‰), and $k = -4.194$ is a fatigue regression parameter. The parameters m, a, and k were calibrated to match the German guidelines (Forschungsgesellschaft für Straßen- und Verkehrswesen, 2024).

Table 2. Adaption factors m

Pavement layer	Value
Frost protection layer	37373.73
Hydraulic bounded base layer	1028.3
Stabilization layer	918.72
Crushed stone base layer	30094.0
Ground (Fully bounded layer structure)	26297.0

The thermo-viscoelastic stability of the pavement designs is assessed for each simulation against the Miner rule (Miner, 1945).

3.5 Optimization algorithm

The MOO problem was solved by utilizing a GA. The motivation for the use of an evolutionary algorithm is its ability to handle complex constraints, and no requirement for gradient information or function continuity, and its ability to avoid getting trapped into local optima compared to traditional optimization methods. Furthermore, the formulation of the MOO framework

was written in Matlab® programming language, version R2022b.

4 APPLICATION OF THE FRAMEWORK

To demonstrate the importance of accounting for thermo-viscoelasticity in the context of pavement design, two cases were considered for the application of the framework. They differ by the temperature levels within the top layer, detailed hereafter.

4.1 Case studies setup

The first case, named Case 1, considers the top layer's temperature to vary yearly in a sinusoidal shape according to Eq. (5):

$$T_{day} = 15 + 20 \cdot \sin\left(\frac{L \cdot 2 \cdot \pi}{365}\right) \qquad (6)$$

where T_{day} is the daily temperature variation at day L (°C), and L stands for the considered day of the year (d). The second case, named Case 2, considers the mean average annual temperature of T_{day}. The shift factor uses as temperature level the difference between the top layer's temperature and its annual average, i.e., 15 °C (Williams et al., 1955).

The non-default values of the ALVA software parameters, including the traffic speed (80 km/h) and load level (0.69 MPa, equivalent to one ESAL), were considered in both cases. Further, $1 \cdot 10^8$ ESALs were considered over an analysis period of 30 years.

Environmental impact and economic costs were considered to have equal importance, i.e. $w = 0.5$. The parameters considered in the objective functions are presented in Table 3, whereas the parameters related to the GA are listed in Table 4.

Table 3. Objective function parameters

Parameter name	Units	Value
GHG emissions A4	[CO₂-eq./(kg·km)]	0.01
GHG emissions A5	[€/(kg·day)]	0.04
Costs A4	[€/(kg·km)]	0.002
Costs A5	[€/(kg·day)]	0.02
Distance between mixing plant and construction site	[km]	50
Construction rate	[kg/day]	$1 \cdot 10^{-5}$

Table 4. GA parameters

Parameter name	Units	Value
Population size	[–]	100
Generation size	[–]	35
Crossover rate	[%]	90
Tournament size	[–]	3
Mutation rate	[%]	15
Penalty factor	[–]	500
Elite rate	[%]	15
Function tolerance	[–]	$1 \cdot 10^{-5}$
Constraint tolerance	[–]	0

4.2 Results

The results obtained for both case studies are presented in Table 5. As can be seen, considering seasonal temperature effects yields a thicker AC layer and an additional frost protection layer. As expected, the subsequent environmental impact and total costs are higher for Case 1. Utilizing the layer properties of Case 2 with T_{day} would not satisfy the constraint related to thermo-viscoelastic stability. This led to a design that withstands the applied traffic loads and yearly temperature variations only for 6.34 years, instead of the required 30 years.

Table 5. Optimization results for both case studies

Optimization results	Unit	Case 1	Case 2
Asphalt layer thickness	[mm]	435	375
Second base layer thickness	[mm]	0	0
Frost protection layer thickness	[mm]	200	0
Environmental impacts	[CO_2-eq.]	$3.0 \cdot 10^7$	$1.8 \cdot 10^7$
Total Costs	[€]	$6.2 \cdot 10^6$	$3.8 \cdot 10^6$

5 CONCLUSION

In this study, a framework was developed to optimize the pavement design with respect to environmental impact and economic aspects, while ensuring compliance with thermo-viscoelastic stability. The framework consists of five components: a material database, design variables, two objective functions (environmental impact and cost), a genetic algorithm-based optimization solver, and two constraints, of which one is related to thermo-viscoelastic stability.

To demonstrate the significance of thermo-viscoelastic considerations, the framework was applied to two cases: one with a sinusoidal temperature variation in the top layer and another one with a constant temperature. The resulting pavement design of the case with temperature variation resulted in higher environmental impact and higher costs. However, using the layer properties from the constant temperature case while accounting for temperature variation did not meet the constraint related to thermo-viscoelastic stability.

The integration of seasonal temperature effects into the optimization process of pavement design ensures cost efficiency and a reduction of environmental impact. This work marks the first step towards the acceptance of a more realistic optimization framework for pavement design.

In Future work, it is worth exploring the inclusion of several thermo-viscoelastic layers with non-uniform temperature levels, and the expansion of the material database.

6 ACKNOWLEDGEMENTS

7 REFERENCES

Demir, A., Santos, J., Miller, S., Diele, R. and Naarding, G. (2023) 'Multi-objective optimization of flexible pavement design from an environmental and economic perspective', *Journal of Cleaner Production*, vol. 430, p. 139441.

DIN Deutsches Institut für Normung e. V. (2012) *DIN EN 15978: Nachhaltigkeit von Bauwerken – Bewertung der umweltbezogenen Qualität von Gebäuden – Berechnungsmethode*.

European Commission (ed) *Buildings and construction* [Online]. Available at https://single-market-economy.ec.europa.eu/industry/sustainability/buildings-and-construction_en (Accessed 8 October 2024).

European Commission (ed) (2019) *The European Green Deal: Striving to be the first climate-neutral continent* [Online]. Available at https://ec.europa.eu/commission/presscorner/detail/en/ip_19_6691 (Accessed 8 October 2024).

Forschungsgesellschaft für Straßen- und Verkehrswesen (2024) *Richtlinien für die Dimensionierung des Oberbaus von Verkehrsflächen in Asphaltbauweise: RDO Asphalt 09/24*.

Inti, S. and Anjan Kumar, S. (2021) 'Sustainable road design through multi-objective optimization: A case study in Northeast India', *Transportation Research Part D: Transport and Environment*, vol. 91, p. 102594.

Miner, M. A. (1945) 'Cumulative Damage in Fatigue', *Journal of Applied Mechanics*, vol. 12, no. 3, pp. 159–164.

Morland, L. W. and Lee, E. H. (1960) 'Stress Analysis for Linear Viscoelastic Materials with Temperature Variation', *Transactions of the Society of Rheology*, vol. 4, no. 1, pp. 233–263.

Skar, A. and Andersen, S. (2020) 'ALVA: An adaptive MATLAB package for layered viscoelastic analysis', *Journal of Open Source Software*, vol. 5, no. 55, p. 2548.

Statistisches Bundesamt (ed) (2024) *Preisindizes für Bauwerke, Ingenieurbau, Instandhaltung: Konjunkturindikatoren* [Online]. Available at https://www.destatis.de/DE/Themen/Wirtschaft/Konjunkturindikatoren/Preise/bpr210.html#241662 (Accessed 8 October 2024).

Wang, Y. and Chong, D. (2014) 'Determination of Optimum Pavement Construction Alternatives to Minimize Life-cycle Costs and Greenhouse Gas Emissions', *Construction Research Congress 2014*. Atlanta, Georgia, May 19-21, 2014. Reston, VA, American Society of Civil Engineers, pp. 679–688.

Williams, M. L., Landel, R. F. and Ferry, J. D. (1955) 'The Temperature Dependence of Relaxation Mechanisms in Amorphous Polymers and Other Glass-forming Liquids', *Journal of the American Chemical Society*, vol. 77, no. 14, pp. 3701–3707.

Noise comparison of different types of pavement inside highway tunnels

J. Li, M. L. Li
Research Institute of Highway Ministry of Transport

G. Wang, Y. Zhao
Jiangsu Expressway Engineering Maintenance Limited Company

Z. H. Yang, L. Zhou
Jiangsu Ningsuxu Expressway Limited Company

ABSTRACT: Aiming to reduce noise pollution and improve the acoustic environment in highway tunnels, the noise characteristics on different types of pavements were analyzed and compared in this research, based on the onsite noise measurement in two tunnels, with the pavement in the open area as control group. Three types of pavements were measured, including dense-graded asphalt concrete (DAC), single-layered and double-layered porous asphalt (PA) pavement.The results showed that, compared with pavement in the open area, the roadside noise in the tunnels increased significantly, with an average increase of more than 10 dBA. The long tunnel exhibited worse noise attenuation performances. For the PA pavements, the roadside noise was significantly reduced, with an average reduction of more than 3.5 dBA. PA pavement also exhibited faster noise attenuation. The application of PA pavement could effectively improve the acoustic environment in the tunnel.

1 INTRODUCTION

Noise pollution has become the second largest harm among the environmental factors that affect human health. Especially, road traffic noise has seriously affected the physical and mental health and life quality of drivers, passengers, and surrounding residents[Foraster et al. 2016, Lee et al. 2019]. At present, research on the prevention and control of traffic noise pollution mainly targets residents along highways, and still relatively little research has been conducted on the impact of noise on main users of highways, namely drivers and passengers[Petri et al. 2021, Gilani & Mir 2021].

In tunnels, sounds are easily reflected by arched tunnel wall, which produces a much larger reflection area of sound waves than that outside tunnels. As a result, the noise generated inside tunnels is much louder than that outside tunnels[Zhang et al. 2020]. Compared to that in short tunnels, noise in long tunnels propagates longer path and is not easy to dissipate, thus posing a severer impact[Qin et al. 2023, Jiang et al. 2022]. At present, most of the tunnels built in China have not undergone sound absorption and noise reduction treatment. In this case, noise waves are reflected multiple times on the tunnel wall, and the direct sound and the reverberant sound are superimposed multiple times, thus a large noise is produced[Zhao et al. 2022, Lokhande et al. 2023].The noise inside tunnels is mainly caused by traffic noise, which is a kind of mixed noise composed of noise generated by vehicle engines and that generated by the interaction between tires and pavements[Mikhailenko et al. 2022]. The noise generated by the interaction between tires and pavements can be reduced by improving pavement materials. The type of pavement surface has a significant influence on reducing tire/pavement noise, and the low noise asphalt pavements are used to reduce traffic noise[Leng et al. 2019].

The low noise asphalt pavements generally classified into two categories, namely porous asphalt (PA) pavement and dense-graded asphalt concrete (DAC). At present, little research have systematically conducted the noise comparison of different types of pavement in tunnels of varying lengths.

2 EXPERIMENTAL DESIGN

2.1 *The basic information of tested tunnels*

Two tunnels, Dahongling No.1 Tunnel and Dahongling No.2 Tunnel were selected in this research, which were short for No.1 Tunnel and No.2 Tunnel respectively in later descriptions. They are both one-way, two-lane tunnels. The former is a short tunnel with a length of approximately 120 m while the latter is a long tunnel with a length of about 5000 m. The surface layer in No.1 Tunnel is dense-graded asphalt concrete (DAC) with nominal maximum aggregate size (NMAS) of 13.2 mm, namely DAC-13. For the No.2 Tunnel, three types of surface layers, including DAC-13, the single-layered and double-layered PA pavement with NMAS of 13.2 mm, namely PA-13, were investigated. Furthermore, the pavement in the open area, located in the connection section between the No.1 Tunnel and No.2 Tunnel was also surveyed as the control group. Figure 1 shows the detailed information of

pavements in the two tunnels as well as the pavement in the open area.
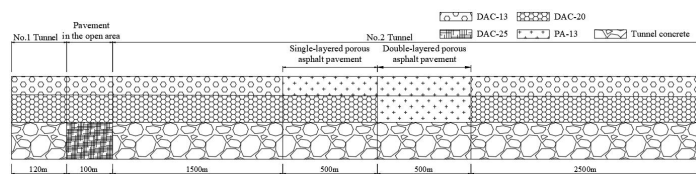
Figure 1. Schematic diagram of pavement structure in the two tunnels.

2.2 *Noise measurement methods*

(1)Measurement of roadside noise

Multifunctional sound level meters were employed to test the roadside noise. It was measured on the artificial inspection lane in tunnels and outside the road guardrail in the open area according to the Statistical Pass-by (SPB) method. The sound level meters should be fixed on a tripod at a height of 1.2 m (approximately human ear height) above the plane of the artificial inspection lane. In this test, there was no traffic flow since the lane was not opened to traffic, and thus only traffic noise caused by a single vehicle was measured.

(2)Measurement of longitudinal noise attenuation

The noise levels were measured respectively when the microphones were placed on the central line of the tunnel at distances of 30 m, 60 m, 90 m, 120 m and 150 m away from the sound source in the longitudinal direction. For each position, two measuring height were included, respectively 1.2 m and 2.6 m. During the test, the sound source should be maintained stable. Linear fitting on test results was performed. The slope of the fitting formula was regarded as the longitudinal noise attenuation rate.

3 NOISE COMPARISON ANALYSIS

3.1 *Noise in tunnels of varying lengths*

(1)Roadside noise

The overall noise levels of roadside noise on the DAC-13 pavement were measured on the artificial inspection lane in No.1 Tunnel and No.2 Tunnel, as well as outside the road guardrail in the open area as the control group, at speeds of 60 km/h, 80 km/h, and 100 km/h, respectively. The results are shown in Figure 2.
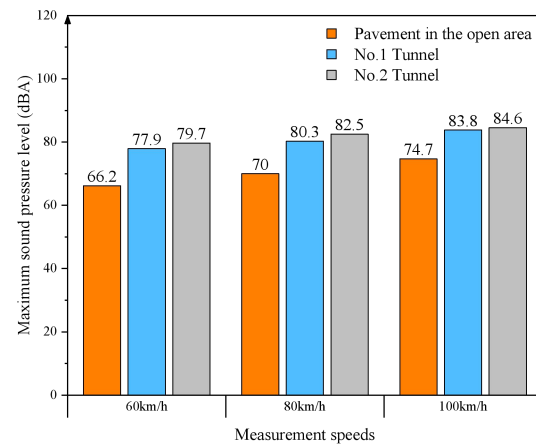
Figure 2. Roadside noise level in two tunnels.

Figure 2 show that, at a speed of 60 km/h, the average noise levels corresponding to the pavement in the open area, No.1 Tunnel, and No.2 Tunnel were 66.2 dBA, 77.9 dBA, and 79.7 dBA, respectively. At a speed of 80 km/h, the average noise levels were 70.0 dBA, 80.3 dBA, and 82.5 dBA, respectively. At a speed of 100 km/h, the average noise levels were 74.7 dBA, 83.8 dBA, and 84.6 dBA, respectively. Compared with the roadside noise in the open area, due to the significant influence of reverberation in tunnels, the roadside noise on the artificial inspection lane in tunnels increased significantly, with an average increase of more than 10 dBA.

In addition, the increase was more significant for the No.2 Tunnel, which is longer than No.1 Tunnel. The noise on the artificial inspection lane in the longer tunnel increased by about 2 dBA compared with that in the shorter one, No.1 Tunnel. This may be attributed to the significant reverberation in the longer tunnel. For the same pavement surface DAC-13, the noise on the artificial inspection lane in the same tunnel increased with measurement speeds.

(2)Longitudinal noise attenuation

Figure 3 shows attenuation characteristics of the noise level on the DAC-13 pavement in two tunnels within 150 m from the sound source at an interval of 30 m. The fitting results were also included. The slope of the fitting results was employed to evaluate longitudinal noise attenuation characteristics.
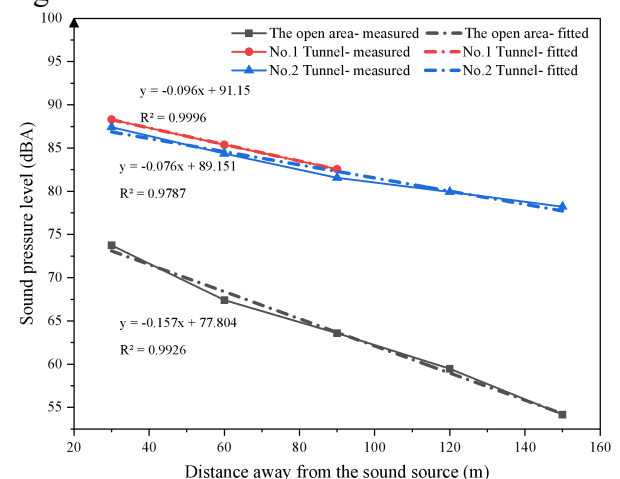
Figure 3. Noise attenuation characteristics in two tunnels.

Figure 3 showed that the longitudinal noise attenuation rate for the pavement in the open area, No.1 Tunnel and No.2 Tunnel was 0.16 dBA/m, 0.10 dBA/m, and 0.08 dBA/m, respectively, among which the noise attenuation rate was the largest on the pavement in the open area, while the smallest in No.2 Tunnel. This demonstrates that the longer tunnels exhibit more significant noise reverberation effects and smaller noise attenuation rates. In longer tunnels, the noise is different to dissipate with significant reverberation effects.

3.2 *Noise on different types of pavements*

(1)Roadside noise

The overall noise levels of roadside noise on the DAC, single-layered and double-layered PA pavement in No.2 Tunnel were measured at speeds of 60 km/h, 80 km/h, and 100 km/h, respectively, as shown in Figure 4.
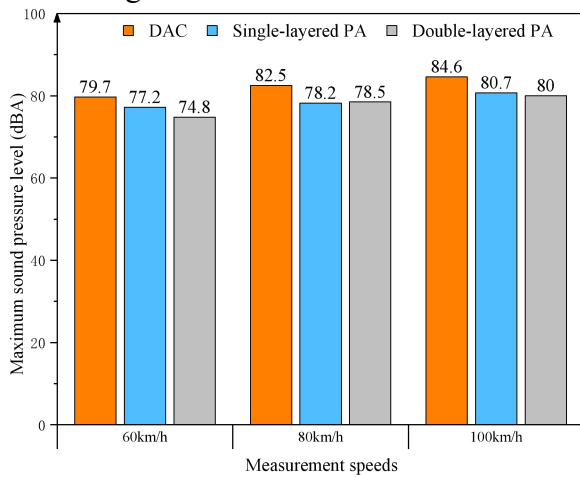
Figure 4. Roadside noise level on different types of pavements.

From Figure 4, it can be seen that, at a speed of 60 km/h, the overall roadside noise levels on the DAC and single-layered and double-layered PA pavement in No.2 Tunnel were respectively 79.7dBA, 77.2 dBA, and 74.8 dBA, respectively. At a speed of 80 km/h, the overall roadside noise levels were 82.5 dBA, 78.2 dBA, and 78.5 dBA, respectively. At a speed of 100 km/h, the overall roadside noise levels were 84.6 dBA, 80.7 dBA, and 80.0 dBA, respectively. Compared with the DAC, the roadside noise on PA pavement was lower. Sound absorption could be realized through the PA pavement surface since there were many interconnected pores therein. Moreover, aerodynamic noise generated at the contact area between the tire and the pavement, as well as the noise propagated outward by the sound source were mainly absorbed by the porous surface layer. Therefore, the roadside noise on the artificial inspection lane on the PA pavement section was significantly reduced, with an average reduction of more than 3.5 dBA.

The noise reduction on the double-layered PA pavement was more significant than that on the single-layered PA pavement, and the roadside noise on the artificial inspection lane on the double-layered PA pavement was further reduced by about 1 dBA compared with that on the single-layered PA pavement. The comparison results demonstrated that PA pavement was more effective in reducing the roadside noise on the artificial inspection lane in the long tunnel, and the double-layered PA pavement exhibited a better noise reduction effect.

(2)Longitudinal noise attenuation

The longitudinal noise attenuation characteristics on DAC, single-layered and double-layered PA pavement in No.2 Tunnel were measured to obtain the noise attenuation law of three types of pavement sections in tunnels. The noise attenuation rates along the longitudinal direction in the tunnel were derived by linearly fitting the noise levels along the longitudinal direction. The attenuation curve of noise levels in the longitudinal direction, as well as the fitting results, were shown in Figure 5.
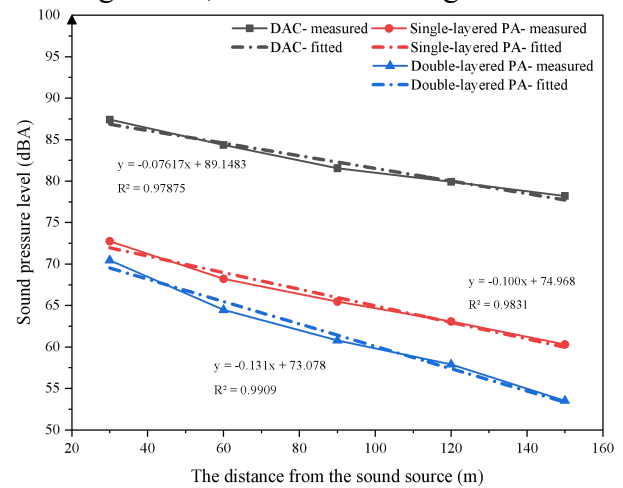
Figure 5. Noise attenuation characteristics on different types of pavements.

Based on the noise attenuation curve and the slopes of the fitting results, it was obviously that there were significant differences in the longitudinal noise attenuation rates on the three types of pavements. For DAC, single-layered and double-layered PA pavement, the longitudinal noise attenuation rates were 0.08 A dB/m, 0.10 dBA/m and 0.13 dBA/m, respectively. This indicated that in the same tunnel, the longitudinal noise attenuation rate on DAC was the smallest, while that on double-layered PA pavement was the largest. Therefore, PA pavement contribute to increasing the longitudinal noise attenuation rates to reduce noise in tunnels, thus improving the acoustic environment in tunnels.

4 CONCLUSIONS

In this research, onsite survey of noise characteristics in the two tunnels were conducted, including the roadside noise and noise attenuation properties. For the same type of pavement, the noise characteristics inside and outside tunnels were analyzed. For the same tunnel, the impacts of

pavement types on the noise characteristics were investigated. Based on the test results and analysis, the following conclusions were obtained:

(1)For the same type of pavement DAC-13, compared with pavement in the open area, the roadside noise in tunnels increased significantly, with an average increase of more than 10 dBA. The roadside noise can characterize noise characteristics in tunnels considering the reverberation effects.

(2)For the DAC pavement, the longitudinal noise attenuation rates in the two tunnels were 0.10 dBA/m and 0.08 dBA/m respectively. The longitudinal noise attenuation rates demonstrated that the reverberation effect in tunnel was significant.

(3)The roadside noise on the artificial inspection lane on the PA pavement section was significantly reduced, with an average reduction of more than 3.5 dBA. The longitudinal noise attenuation rates were greater of PA pavement. This demonstrated that the PA pavement with large pore structures could significantly improve the acoustic environment on tunnels, and the double-layered PA pavement contributes to better noise attenuation performance.

5 REFERENCES

Foraster, M., et al. 2016. Long-term transportation noise annoyance is associated with subsequent lower levels of physical activity. *Environment international* 91:341-349.

Lee, P. J., et al. 2019. Association between transportation noise and blood pressure in adults living in multi-storey residential buildings. *Environment international* 132:105101.

Petri, D., et al. 2021. Effects of exposure to road, railway, airport and recreational noise on blood pressure and hypertension. *International journal of environmental research and public health* 18(17):9145.

Gilani, T.A. & Mir, M. S. 2021. A study on the assessment of traffic noise induced annoyance and awareness levels about the potential health effects among residents living around a noise-sensitive area. *Environmental Science and Pollution Research* 28(44):63045-63064.

Zhang, Z., et al. 2020. Effects of surface texture on tire-pavement noise and skid resistance in long freeway tunnels: From field investigation to technical practice. *Applied Acoustics* 160:107120.

Qin, P., et al. 2023. How does an extra-long freeway tunnel influence driving performance? A comparative study of driving simulation. *KSCE Journal of Civil Engineering* 27(9):4043-59.

Jiang, Z., et al. 2022. Numerical study on acoustic environment in long traffic tunnels. In Sun, Z. & Das, P. (eds), *Proceedings of the 9th International Conference on Energy Engineering and Environmental Engineering*:187-195. Cham: Springer.

Zhao, Y., et al. 2022. Noise reduction and sound intelligibility improvement in acoustic environment in long traffic tunnels with wall absorption. In Sun, Z. & Das, P. (eds), *Proceedings of the 9th International Conference on Energy Engineering and Environmental Engineering*:197-204. Cham: Springer.

Lokhande, S. K., et al. 2023. Road tunnel noise: monitoring, prediction and evaluation of noise-induced hearing loss. *Environmental Science and Pollution Research* 30(36):86338-86351.

Mikhailenko, P., et al. 2022. Low-Noise pavement technologies and evaluation techniques: a literature review. *International Journal of Pavement Engineering* 23(6):1911-1934.

Leng, C., et al. 2019. Sustainable green pavement using bio-based polyurethane binder in tunnel. *Materials* 12(12):1990.

6.1

CHARACTERIZING UNBOUND AGGREGATES FOR PAVEMENT DESIGN AND PERFORMANCE PREDICTION

A Numerical Study of the Effect of Aggregate Fracture on the Unbound Granular Materials Response under Triaxial Loading

M. K. Etikan, D. Jelagin, M. N. Partl
KTH Royal Institute of Technology, Stockholm, Sweden

E. Olsson
Luleå University of Technology, Luleå, Sweden

ABSTRACT: The performance of unbound granular materials (UGMs) made from crushed rock plays a critical role in the service life of roads. While experimental evidence indicates that aggregate crushing and abrasion significantly affect UGM stiffness and permanent deformation, the precise relationship between aggregate strength and UGM performance remains unclear. This is particularly important when using aggregates of marginal strength in road construction. This study investigates the impact of aggregate breakage on UGM behavior under triaxial loading, using the Discrete Element Method (DEM) for computational analysis. The model examines how aggregate breakage influences UGM response for two different types of aggregates. The DEM results are compared with experimental data from the literature. Findings show that particle fracture significantly influences the maximum deviatoric stress that the UGM can endure under two different confining pressures, highlighting the importance of aggregate strength in determining UGM performance.

1 INTRODUCTION

Unbound granular materials (UGMs) composed of crushed rock are extensively used in road construction. Their performance in unbound road layers has a profound effect on road's service life. A considerable number of experimental, numerical and field studies have thus been performed to clarify the relationship between UGMs' material parameters and their mechanical behavior with respect to their stiffness and resistance to permanent deformation. In particular, the influence of UGM gradation has been extensively studied, e.g. (Yideti, et al., 2013; Erlingsson & Rahman, 2013). There is also strong experimental evidence that adequate resistance of aggregates to crushing, and abrasion is crucial for UGM performance, as aggregate breakage may significantly increase permanent deformation accumulation rates and compromise stiffnesses of UGMs (Saeed, et al., 2001). A quantitative relationship between the strength of the aggregates and UGM performance is however not fully understood yet. This issue is particularly important with respect to incorporating marginal aggregates in road UGMs (Zhang, et al., 2021). This study seeks to contribute to clarifying this issue, by investigating computationally the effect of aggregate breakage on the UGM performance under triaxial loading.

Etikan et al. (2024) proposed recently new Discrete Element Method (DEM) modelling framework to model the aggregate breakage in UGMs. The framework was shown to capture accurately the effects of aggregate gradation, fracture toughness and load level on aggregate crushing in UGMs subjected uniaxial compressive loads. Presently, the modelling approach is extended to triaxial loading conditions and the DEM prediction are compared to the experimental results by Rahman & Erlingsson (2013). The developed model is used to investigate the influence of aggregate breakage on UGM response to triaxial loading for two different aggregate types.

2 COMPUTATIONAL METHODOLOGY

2.1 *DEM Modelling*

DEM modelling is employed to evaluate the effect of aggregate fracture in UGMs under monotonic triaxial tests. The model is implemented using commercial software, PFC3D[TM] (Itasca Consulting Group Inc., 2019) where contact and statistical fracture force models are incorporated as subroutines as presented below in Sections 2.2 and 2.3. The aggregates are represented as spherical particles in DEM. In what follows the particles used in experiments will be referred to as "aggregates", whereas the those employed in DEM will be designated as "particles". The interlock effect in UGM is applied by constraining the rotation of particles. Each particle is characterized by its density, stiffness, toughness, size, friction (μ) and damping (η) coefficients. The model geometry is illustrated in Figure 1a along with the loading and boundary conditions used. The boundary of the system is generated

by the confining cylinder which consists of three components. The radial wall represents latex membrane with a shear modulus of 1 GPa as implemented by de Bono & McDowell (2014), while the horizontal top and bottom walls represent the loading head and the pedestal respectively. The velocity, u, of the bottom wall is zero through the simulation. Top and bottom walls are assigned a stiffness 200 times higher than the particles to represent rigid bodies. The friction between the confining cylinder and particles is set to zero.

In DEM model, particles are generated randomly within the confining cylinder space, and gravity is applied to allow them to fall. Next, the loading head is placed on top of the UGM, and the UGM is compressed from both the radial wall and the loading head until the designated confining stress, σ_C, is reached. The confining stress is calculated for each wall as the sum of the forces arising from particle-wall contacts, divided by the area of the respective wall. Finally, the UGM is compressed in displacement control mode, while maintaining the confining stress on the radial wall at designated σ_C. The deviatoric stress, σ_d, is calculated as the difference between the stress applied on the loading head and the confining stress.

The position and the velocity of each particle are calculated through explicit numerical integration of Newton's laws of motion. The external forces acting on the particles are generated by gravity and through interactions with other particles or walls. Furthermore, the velocity of each accelerating particle is affected by η, as introduced by PFC3D$^{\text{TM}}$, where it can take any value between 0 and 1. It allows particles to reach a steady state after falling due to gravity. It affects the applied force on particles as $F - F_\eta = ma$, where F is the force applied on a particle, and m and a represents the mass and the acceleration of the particles respectively. $F_\eta = F\eta$ is the damping force.
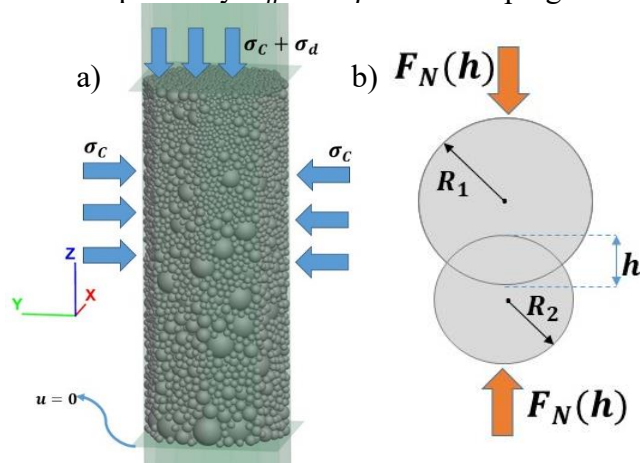
Figure 1. a) DEM model of UGM at $\sigma_C = 10$ kPa and $\sigma_C = 0$, b) Overlapping of two particles in contact.

2.2 Contact Model

The normal contact between two particles is illustrated in Figure 1b. The contact force model applied in this study was developed by Olsson et al. (2019a),

based on the experimental results from Cervera et al. (2017). The normal contact force, F_N, is derived as a function of overlapping, h, between particles, and their relation is expressed in three stages, as shown in Eq. (2). The first stage represents the crushing of surface asperities where the relation between h and F_N is observed to be linear until the depth of surface asperity, h_s. Subsequently, F_N follows Hertz contact theory until the indentation depth h_L. which corresponds to the onset of shear driven damage, resulting in linear relation between F_N and h. The values of h_s and h_L are reported as 0.02 and 0.08 mm, respectively (Cervera, et al., 2017). This result in the following normal contact model:

$$F_N = \begin{cases} (F_S/h_S)h, & h \leq h_s \\ k_p \, (h - h_1)^{1.5}, & h_s \leq h \leq h_L \\ k_p \, (h_L - h_1)^{1.5} + 1.5 \, k_p \, \sqrt{h_L - h_1} \, (h - h_L), & h_L \leq h \end{cases} \quad (1)$$

where $F_s = 100$ N $(R_0/ 6.25 \text{ mm})^{0.5}$. The effective contact radius is denoted as $R_0 = (1/R_1+1/R_2)^{-1}$ where R_1 and R_2 represent the radius of the overlapping particles, and $h_1 = h_s - (F_s/k_p)^{2/3}$. The contact stiffness is k_p, and given by Hertz (1882) contact theory as follows:

$$k_p = (2/3)E_{eff}R_0^{0.5} \quad (2)$$

where the effective Young's modulus between particles in contact is represented as $E_{eff} = ((1-v_1^2)/E_1 + (1-v_2^2)/E_2)^{-1}$, with $E_{1,2}$ and $v_{1,2}$ denoting the Young's modulus and Posson's ratio of the particles in contact, respectively.

2.3 Statistical Fracture Force Models and Fragmentation Modelling

To be able to acquire an accurate fracture response, the assessment of these critical fracture forces, F_f, is essential. The fracture forces are assigned based on a statistical fracture force model proposed by Etikan et al. (2025). The fracture force model in their study accounts for two sources of variability in aggregates strength: size dependency and aggregate shape. The cumulative density function for critical fracture forces, S, is presented in Eq. (3).

$$S = 1 - \int_{R_N}^{R_{N+1}} \int_0^\infty p(\xi)p(R)e^{-\left(\frac{F_f}{\sigma_W R^2}\xi\right)^m \frac{R^3}{V_{ref}}} I_0 d\xi \, dR \quad (3)$$

where σ_W and m are the material parameters, and R_N and R_{N+1} represent the half of smaller and larger size respectively. The reference volume, V_{ref}, is introduced for dimensional consistency. The stress distribution within an aggregate is presented as $\sigma(\mathbf{x})$. The probability distribution for the particle size, $p(R)$, and for particle shape, $p(\xi)$, are given by:

$$p(R) = \frac{2R_N^2 R_{N+1}^2}{(R_{N+1}^2 - R_N^2)R^3} \quad (4)$$

$$p(\xi) = \frac{n}{I_0}\xi^{n-1} \exp[-\xi^n] \quad (5)$$

where n controls the scatter of the fracture force distributions, I_0 determines the median value of I which represents the stress state of an aggregate as shown:

$$I = \int_{\tilde{V}} \tilde{\sigma}(\mathbf{x}) d\tilde{V} \qquad (6)$$

where $\sigma(\mathbf{x}) = \tilde{\sigma}(\mathbf{x}) F_f / R^2$ and $V = \tilde{V} R^3$ are the normalized variables.

The particle will fracture when F_N exceeds F_f for a given contact pair. Once this condition is met, the Young's modulus of the particle is reduced according to $E_{fractured} = C_W E_{initial}$, where C_W is a weakening coefficient, and $E_{initial}$ and $E_{fractured}$ denote the Young's modulus of the particle before and after fracture, respectively. The range of C_W is between 0 and 1. This coefficient is applied to simulate the local settling that occurs after a particle fractures. According to Eq. (3) – (6), the distribution of F_f is defined by three material parameters: σ_W, m and n. While post-fracture behavior of the particle is defined by C_W.

3 COMPUTATIONAL STUDY

The model presented in the previous section is used to simulate the monotonic triaxial tests conducted by Erlingsson & Rahman (2013) on UGMs composed of high strength gravel aggregates, referred to as SG1. Contact and fracture force model parameters, i.e. $E_{initial}$, C_W, density,ρ, Poisson's ratio, v, σ_W, m and n are identified following Etikan et al. (2024, 2025) and presented in Table 1.

Table 1. Parameters of contact and fracture force models.

$E_{initial}$	C_W	σ_W	m	n	v	ρ
GPa	-	MPa	-	-	-	g/cm^3
45	0.3	76.04	4.69	5.07	0.15	2.65

The SG1 UGM used by Erlingsson & Rahman (2013) was compacted to cylindrical confinement with a volume of 5.3 L and 150 mm diameter. The gradation of the UGM followed the theoratical Fuller curve, $G_V = (d/d_{max})^{0.5}$, where d represents the aggregate size, d_{max} is the maximum aggregate size and G_V is the cumulative volume distribution. The gradation curve of SG1 is presented in Figure 2 along with the particle size distribution used in DEM simulations. As may be seen, in simulations a cut-off is introduced at 4 mm for computational effiency. The volume of particles smaller than 4 mm is distrubuted proportionally to other sieve sizes. The porosities of the UGM in the experiments and simulations are 19% and 34% respectively.

In DEM model, particles are generated uniformly between 4 and 31.5 mm. Total of 9208 particles are generated. To achieve the densest particle arrangement in DEM, particles are generated in 10 layers with the initial condition of $\mu = 0$ and $\eta = 0.1$. Once

particles are settled on the bottom of the cylinder, μ is set to 0.7, following Olsson et al. (2019a) and Etikan et al. (2024). Two levels of confinement stress, σ_C =10 and 20 kPa are simulated. For each σ_C the simulations are conducted with and without particle breakage, in order to examine the effect of breakage on UGM performance. Furthermore, for $\sigma_C = 20$ kPa, triaxial test is also conducted with fracture force model parameters adjusted to represent marginal aggregates: m=6.51, σ_W=15.5 MPa and n=1.67 are used, corresponding to the ones measured for relatively weak granite aggregate by Etikan et al. (2025).
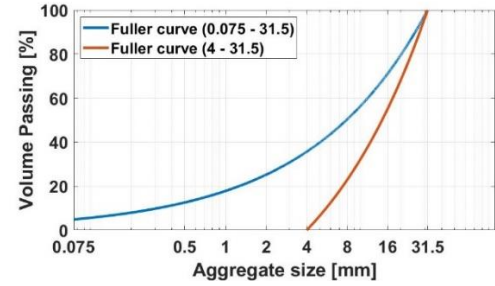
Figure 2. Gradation used in experiments and in DEM model.

4 RESULTS AND DISCUSSION

The simulation results of monotonic triaxial tests compared to experimental results by Erlingsson & Rahman (2013) in Figure 3, where σ_d is show as a function of UGM's vertical strain, ϵ_z. Firstly, it may be seen that experimental and modelling results exhibit qualitatively similar behaviors. The measurements reach the maximum σ_d at approximately 1.1 and 1.2% of strain for $\sigma_C = 10$ and 20 kPa respectively. The corresponding simulation results, both with breakage and without breakage, deviate no more than 0.1% from the measurements. However, the simulation results of the maximum σ_d and stiffness values show some discrepancies with the measurements. Specifically, the UGM stiffnesses at the initial portion of the test are below the ones predicted computationally. For $\sigma_C = 20$ kPa models, the maximum σ_d is 1.5 and 1.3 times higher in the UGM with strong and weak fracture resistance simulations, respectively. In contrast, the simulation results for $\sigma_C = 10$ kPa align with measured maximum σ_d. Some quantitative deviations are expected however given the differences in porosity between the experiments and simulations, as well as possible deviations of particle breakage characteristics for the aggregates used Etikan et al. (2024, 2025) and Erlingsson & Rahman (2013) studies. The qualitative agreement observed in Figure 3 is encouraging however, and quantitative agreement may be improved by adjusting contact and fracture model parameters to account for the effect of finer particles not modelled explicitly in DEM. This will be addressed in future research.

The main interest of this study is to evaluate the effect of particle fracture in triaxial testing. As shown in Figure 3, particle fracture in both confining cases

results in a decrease in the maximum σ_d that the UGM can withstand. This decrease is approximately 3.5% for each respective confining case of UGM with strong fracture resistance and 12.3% for UGM with weak fracture resistance. The effect of fracture is particularly evident in $\sigma_C = 20$ kPa model with weak resistance to fracture. Additionally, DEM simulations enable tracking particle fractures, allowing for the observation of fracture locations within the UGM and the corresponding σ_d, as shown in Figure 4 and 5.
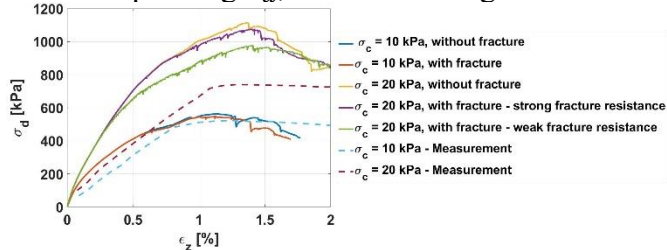
Figure 3. Deviatoric stress vs. axial strain of the loading head for cases of $\sigma_C = 10$ and 20 kPa.
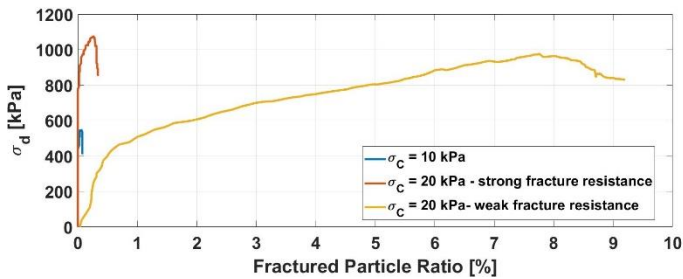
Figure 4. Fractured particle ratio vs. deviatoric stress for $\sigma_C = 10$ and 20 kPa.
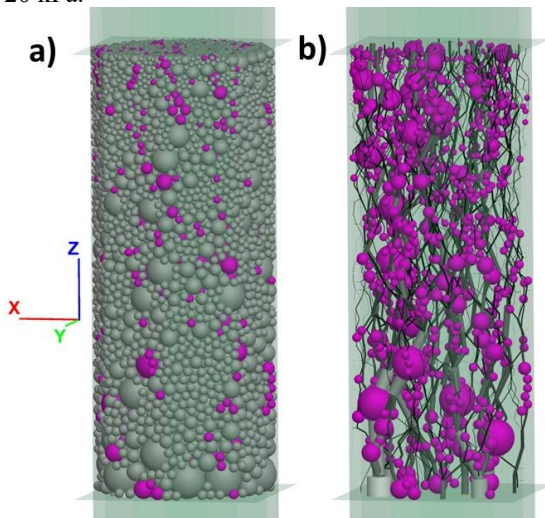
Figure 5. DEM model of $\sigma_C = 20$ kPa at maximum σ_d, a) fractured particles (pink) among non-fractured particles, b) distribution of fractured particles within UGM with contact skeleton.

In Figure 4, the ratio of fractured particles to the total number of particles is plotted for all confining cases. As observed, this ratio is relatively small for the cases of UGM with strong fracture resistance at the maximum σ_d. However, it increases to approximately 8% for the UGM with weak fracture resistance at maximum σ_d. A drastic increase in particle fracture can be observed for UGM with weak and strong fracture resistance at $\sigma_d > 500$ kPa, and $\sigma_d > 900$ kPa for at $\sigma_C = 20$ kPa, respectively. The fractured particles within UGM and the location of fractured particles along with the contact force skeleton are shown in

Figures 5a and 5b, respectively. The fractured particles are shown in pink colors, while the contact forces are represented in gray scale, with the lighter colors indicating stronger contact forces and the dark colors indicating weaker forces. It can be observed that fractured particles are evenly distributed within the UGM. This is to be expected, as the contact forces are evenly distributed throughout the UGM.

5 CONCLUSION

DEM study of the influence of aggregate fracture on the UGM response in monotonic triaxial tests is conducted. The modelling results are found to exhibit good qualitative and reasonable quantitative agreement with the experimental results from the literature.

The results from the DEM models demonstrate that particle fracture noticeably affects the maximum deviatoric stress that can be achieved at two confining pressure levels investigated. Additionally, the DEM model allows tracking the accumulation of particle fractures as function of applied load, providing insights on both the location and the quantity of fractured particles. DEM modelling can thus serve as a valuable tool for investigating the performance of the materials with distinct properties, such as marginal road materials, under triaxial testing.

6 REFERENCES

Cervera, C. C., Jelagin, D., Partl, M. & Larsson, P.-L., 2017. Contact-induced deformation and damage of rocks used in pavement materials. *Mater. Des.*, 133, pp. 255-265.

de Bono, J. P. & McDowell, G. R., 2014. DEM of triaxial tests on crushable sand. *Granular Matter*, 16, pp. 551-562.

Erlingsson, S. & Rahman, M. S., 2013. Evaluation of Permanent Deformation Characteristics of Unbound Granular Materials by Means of Multistage Repeated-Load Triaxial Tests. *Transportation Research Record*, 2369(1), pp. 11-19.

Etikan, M. K., Jelagin, D., Olsson, E. & Partl, M. N., 2024. Experimental and Numerical Analysis of Crushing Resistance of Unbound Road Materials. *International Journal of Pavement Engineering*, 25(1), p. 2330630.

Etikan, M. K., Jelagin, D., Olsson, E. & Partl., M. N., 2025. A New Statistical Fracture Model for Particles in Unbound Road Materials. *Powder Technology*, [Manuscript is submitted for publication].

Itasca Consulting Group Inc., 2019. PFC3D (particle flow code in 3 dimensions) version 6.0, Minneapolis.

Olsson, E., Jelagin, D. & Forquin, P. A., 2019a. Computational framework for analysis of contact-induced damage in brittle rocks. *Int. J. Solids Struct.*, 167, pp. 24-35.

Saeed, A., Barker, W. & Hall Jr., J. W., 2001. Performance-related tests of aggregates for use in unbound pavement layers, NCHRP Report. Washington: National Academy Press.

Yideti, T., Birgisson, B., Jelagin, D. & Guarin, A., 2013. Packing theory-based framework to evaluate permanent deformation of unbound granular materials. *International Journal of Pavement Engineering*, 14(3), pp. 309-320.

Zhang, H.-L., Tang, Y., Meng, T. & Zhan, L.-T., 2021. Evaluating the crushing characteristics of recycled construction and demolition waste for use in road bases. *Transp. Geotech.*, 28.

Mechanistic-Empirical Evaluation for the Inclusion of Tire-Derived Aggregates in Rigid and Flexible Pavements

M.Y. Fares
Department of Civil and Environmental Engineering, Michigan State University, East Lansing, MI, USA

M. Lanotte
Department of Civil and Environmental Engineering, Michigan State University, East Lansing, MI, USA

ABSTRACT: This study evaluates the performance of flexible and rigid pavement structures incorporating tire-derived aggregate (TDA) layers. TDAs, lightweight and cost-effective materials, were characterized through laboratory testing and large-scale box experiments to determine their interlayer resilient modulus. Results revealed that TDAs are highly sensitive to compaction energy, influencing their mechanical properties. ME analysis showed bottom-up fatigue cracking as the dominant distress in flexible pavements and JPCP transverse cracking in rigid pavements. Rigid pavements demonstrated greater sensitivity to interlayer modulus variations and required fewer modifications to achieve satisfactory performance. Potential design solutions, including layer thickness and material properties adjustments, were proposed to mitigate performance impacts. This paper highlights the feasibility of incorporating TDA in pavement structures, emphasizing the need for precise compaction methods and further analysis to validate long-term performance predictions.

1 INTRODUCTION

Tire-derived aggregates (TDA) in roadway applications offer advantages over traditional backfills due to their lighter unit weight and cheaper production costs. TDAs are a product of end-life tires collected from various sources, inspected to sort out those suitable for reuse, and shredded in a process where tires are fed into a primary shredder equipped with rotating knives that cut the tires into small pieces. The process produces irregular-shaped tire pieces, typically two to 12 inches long. TDA is then sieved and stored in different stockpiles based on their size. The ASTM D6270 divides TDAs obtained from passenger and light truck tires (PLTT) with a rim diameter of up to 19.49" into two types, A and B, based on their gradation. The maximum dimensions are 7.88" and 17.71" for Type A and B, respectively (ASTM-D6270, 2020). While type A is recommended for drainage purposes, type B is used as a lightweight fill material or a moisture-breaking layer in pavement structures.

The Federal Highway Administration (FHWA) advocates prioritizing recycled and sustainable materials, such as tire-derived aggregate (TDA). However, the policy underscores that *"materials used in highway or bridge construction, whether virgin or recycled, must not negatively impact the performance, safety, or environment of the highway system"* (Frederick G. Wright, 2015). Consequently, numerous research studies have evaluated the mechanical performance of TDA in laboratory settings or analyzed its behavior during the early stages of its service life (Meles et al., 2014, 2016).

In contrast, limited studies have focused on the long-term performance of TDA, with some attempting to monitor the performance of road test sections incorporating TDAs over extended periods (Yi et al., 2015). Meanwhile, others analyzed the long-term performance of flexible pavements with a TDA layer using the Mechanistic-Empirical (ME) design method (Fares & Lanotte 2025). However, the response of rigid pavements with TDAs remains unexplored. This paper compares the performance of rigid and flexible pavements incorporating TDA layers. The findings will assist practitioners in selecting the most appropriate course materials based on available resources and specific design objectives.

2 METHODOLOGY AND MATERIALS

TDA were sourced from a production facility in Indiana, USA. Gradation was repeatedly assessed during the collection process. However, the samples did not conform to the ASTM definition of Type B despite being marketed under that classification (Fig. 1). Additional laboratory evaluations revealed that the bulk loose density of the TDA is 430 kg/m³, and the porosity is 61%.

A resilient modulus value representing the material's response is required to conduct ME analysis with a layer of TDA. Yet, due to the size of the TDA, it is challenging to conduct standardized cyclic triaxial testing. Instead, large-scale testing with a multilayer system is performed to obtain an interlayer resilient modulus. These large-scale boxes consist mainly of three layers (Fig. 2), with the TDA being compacted with different methods due to the proven sensitivity of the material towards the applied compaction energy (Fares & Lanotte, 2025).

Table 1 shows the physical characteristics of the subbase and subgrade materials used for the large-scale multilayer testing systems. Both materials were also subjected to cyclic triaxial testing to obtain their

resilient modulus following AASHTO T 307. These values were used as direct inputs for the ME analysis.
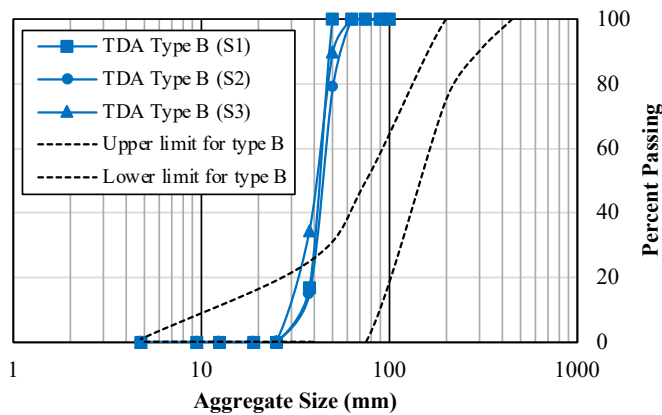
Figure 1. TDA sample and particle size distribution.
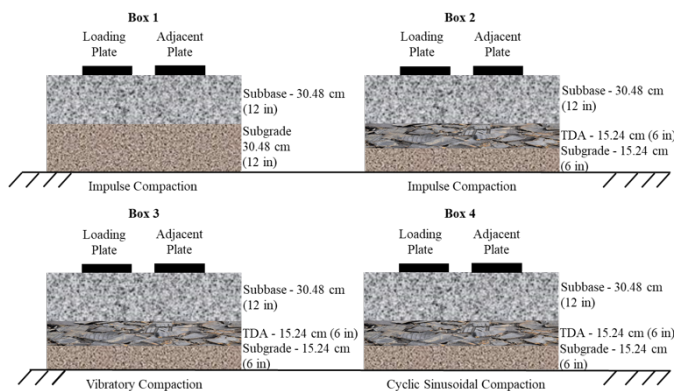
Figure 2. Schematic representation of the large-scale box structures evaluated

Figure 3. Large-scale construction process.

Table 1. Physical characteristics of soils used in large-scale testing

Material/Property	Subgrade	Subbase
Gravel (%)	1.71	24.72
Sand (%)	48.04	57.74
Fines (%)	50.25	17.54
LL (%)	31.80	10.90
PL (%)	20.90	Non-Plastic
MDU (kN/m^3)	16.93	21.18
OMC (%)	14.93	7.23
Summary M$_R$ (MPa)	63.71	105.35
USCS	CL	SC
AASHTO	A-6	A-2-4

Four configurations were evaluated using different TDA layer compaction methods (Fig. 2). The first two were compacted using an impulse compaction hammer. Box 1 is the control case, with 50% of the height consisting of subgrade soil and the top 12" filled with subbase aggregates. In Boxes 2, 3, and 4, 6" of the subgrade layer were substituted with

TDAs. While geometrically equivalent, these three boxes differ in the compaction methodology used on TDAs, as indicated in Figures 2 and 3.

An MTS, equipped with two independent loading plates, was used to apply the load onto the structures in the big boxes (Fig. 4). In this laboratory evaluation, only one plate was used, while the adjacent plate was used in stress control mode to keep it always in contact with the surface of the subbase material. Table 2 shows the utilized cyclic testing program where one-second sinusoidal loading cycles were applied.

Figure 4. Material Testing System (MTS)

Table 2. Cyclic loading test program

Sequence	Cyclic stress (kPa)	No. of Ccyles
1	17.24	10
2	48.95	16
3	79.98	30
4	111.70	44
5	143.48	32
6	174.51	24
7	206.15	18
8	237.87	12
9	268.90	10
10	299.92	4
Cycles per set		200
No. of sets		500
Total cycles		100,000

2.1 NCHRP 1-37A mechanistic-empirical method

The mechanistic-empirical analysis for the flexible pavement structures was conducted using the MEAPA web application (Kutay & Lanotte, 2020). Total rutting and bottom-up fatigue cracking were obtained using mixture-specific calibration coefficients, global laboratory-to-field calibration coefficients, and standard deviation equations specified by the Michigan Department of Transportation (MDOT) (Michigan Department of Transportation, 2021). Similarly, MDOT-based material properties and coefficients for the rigid pavement structure were utilized. Yet, due to the limitations of the MEAPA software in conducting analyses for rigid pavement, AASHTOWare software was employed to obtain both the Mean Joint Faulting and the JPCP transverse cracking.

The vehicle load spectra, traffic input, and material properties align with MDOT typical input values for low-volume roads (Michigan Department of Transportation, 2021). Figure 5 illustrates the simu-

lated pavement structures where the "Experimental Layer" represents the large-scale box evaluated in the laboratory and presented above (Fig. 1).

Table 2. General traffic and analysis input values for the evaluated design case.

General Traffic Input	Design Case
Two-way AADTT	387
Number of lanes	2
Trucks in design direction [%]	51
Trucks in design lane [%]	100
Operational speed [km/h]	72 (45 mph)
Reliability [%]	85
MERRA2 Station Latitude	24.355003
MERRA2 Station Longitude	54.579152
Analysis duration	20 years
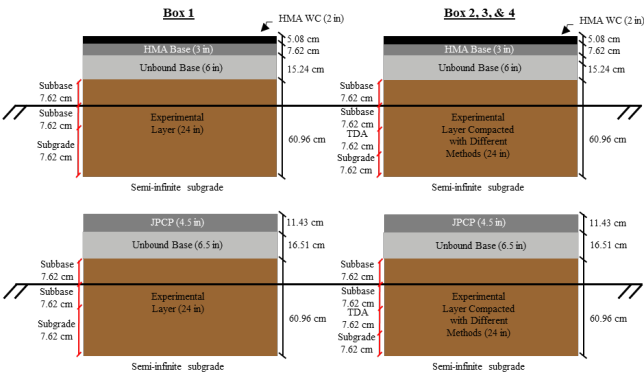
Figure 5. ESAL outcome for each scenario

3 RESULTS AND DISCUSSION

The resilient modulus of each multilayer system was calculated for every cycle. However, as Fares & Lanotte (2025) previously reported, negligible differences in modulus were observed beyond the 11th set of cycles, effectively marking this point as a conditioning load for the TDA layers. Therefore, the data obtained from the 11th set were deemed representative of the material's mechanical behavior under load for brevity. Each set consisted of ten loading sequences performed at varying stress magnitudes, with the results from each sequence within the 11th set presented in Figure 6.
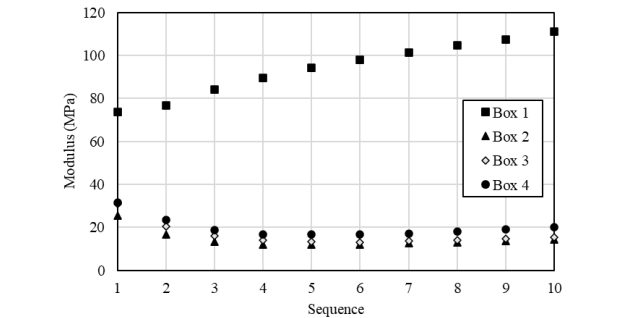
Figure 6. Interlayer resilient modulus based on large-scale box test

Compared to the boxes with a TDA layer, the control Box 1 exhibited a stress-hardening behavior. Conversely, the large-scale boxes containing the

TDA layer demonstrated a higher modulus during the initial sequences, attributed to the relaxation effect following prior loading cycles. Consequently, the resilient modulus value from the final sequence of the 11th set was selected to represent the interlayer property in the ME analysis (Table 3).

Table 3. Interlayer resilient modulus value in the tenth sequence.

Sample	Interlayer Resilient Modulus
Box 1	111.33 MPa
Box 2	14.47 MPa
Box 3	15.34 MPa
Box 4	20.17 MPa

Figure 7 shows the ME analysis outcome, where bottom-up fatigue cracking was the leading distress for the flexible pavement and the JPCP transverse cracking for the rigid pavement (Fig. 8). It can be noticed that both cross sections perform satisfactorily, with Box 1 being used as the experimental layer. However, it is essential to note that from a cross-section thickness point of view, both cross-sections have a similar thickness. Yet, the rigid pavement has a thinner surface course (Fig. 5). As for the experimental layers with the TDA, it can be observed that Box 4 performs better than the other two. This may be attributed to the higher interlayer resilient modulus due to the compaction method used, suggesting a sensitivity of the TDA towards the compaction process. Moreover, the ME analysis showed that the rigid pavement leading distress is significantly more sensitive towards the interlayer resilient modulus than the flexible pavement cross-section.
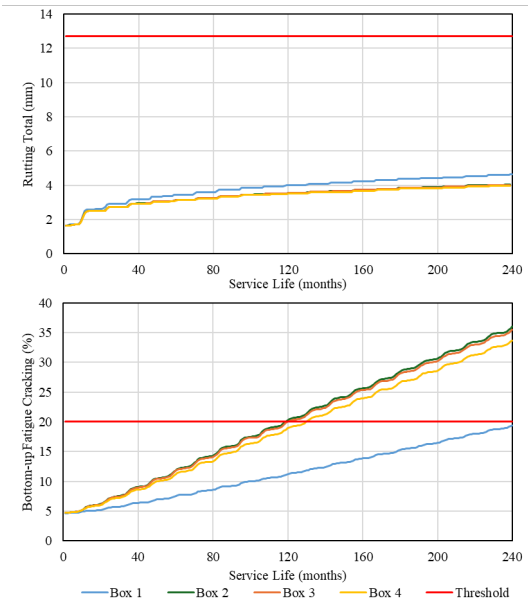
Figure 7. Results of the Mechanistic-Empirical pavement analysis for the flexible pavement cross-sections.

Modifications can be implemented to enhance the performance of the cross sections with a TDA layer.

Table 4 shows three alternative solutions for both structures to achieve satisfactory performance. By comparing alternatives, it can be noticed that fewer modifications for the rigid pavement cross section are needed to make their performance satisfactory compared to their flexible pavement counterparts.
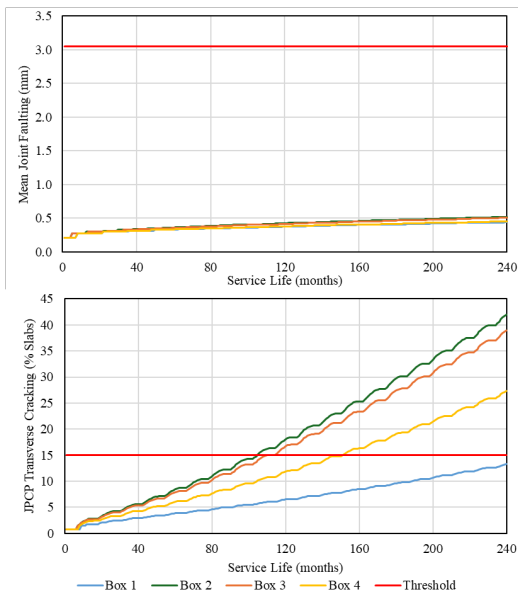
Figure 8. Results of the Mechanistic-Empirical pavement analysis for the rigid pavement cross-sections.

Table 4. Proposed alternatives for flexible and rigid pavements

Flexible Pavement			
	Box 4 Case	Alter. 1	Alter. 2	Alter. 3
HMA WC	5.08 cm (2 in)	5.08 cm (2 in)	5.08 cm (2 in)	5.72 cm (2.25 in)
HMA Base	7.62 cm (3 in)	10.16 cm (4 in)	8.89 cm (3.5 in)	8.89 cm (3.5 in)
Unbound Base	15.24 cm (6 in)	-	20.32 cm (8 in)	10.16 cm (4 in)
Experimental Layer	60.96 cm (24 in)			
Rigid Pavement			
	Box 4 Case	Alter. 1	Alter. 2	Alter. 3
JPCP	11.43 cm (4.5 in)	13.97 cm (5.5 in)	11.43 cm (4.5 in)	12.70 cm (5 in)
Unbound Base	16.51 cm (6.5 in)	-	18.42 cm (7.25 in)	13.97 cm (5.5 in)
Experimental Layer	60.96 cm (24 in)			

4 CONCLUSION

The research paper reported a comparison of the effects of the addition of TDA in flexible and rigid pavements. The outcomes of this study can be summarized as follows:

- The leading distresses are bottom-up fatigue cracking and JPCP transverse cracking for the flexible and rigid pavement structure, respectively.

- Both pavement types showed a sensitivity towards the value of the interlayer resilient modulus. However, the rigid pavement showed a greater sensitivity, suggesting the importance of applying enough energy compaction.

- The ME analysis revealed reduced pavement structure service life due to the inclusion of the TDA layer. To mitigate this impact, alternative cross-sections were developed, where an increase in the thickness of the wearing course or the thickness of the unbound layers was suggested. Moreover, rigid pavements require more minor modifications in their layer thicknesses to achieve satisfactory performance compared to flexible pavements. However, further advanced analyses are necessary to validate the ME analysis findings and ensure the long-term effectiveness of the proposed design solutions.

5 REFERENCES

ASTM-D6270. (2020). *Standard practice for use of scrap tires in civil engineering applications. West Conshohocken, PA: ASTM International. 08*(Reapproved 2012), 1–22. https://doi.org/10.1520/D6270-08R12.2

Fares, M. Y., & Lanotte, M. (2025). Effect of Compaction Mode on Small- and Large-Scale Laboratory Evaluation of Tire-Derived Aggregates for Mechanistic-Empirical Pavement Design. *Transportation Research Board 104th Annual Meeting.*

Frederick G. Wright, J. (2015). *FHWA Recycled Materials Policy.* FHWA. https://www.fhwa.dot.gov/legsregs/directives/policy/recmatpolicy.htm#::text=The FHWA policy is%3A,of engineering and environmental suitability

Kutay, M. E., & Lanotte, M. (2020). *Formulations of the Pavement Performance Prediction Models in the Mechanistic-Empirical Asphalt Pavement Analysis (MEAPA) Web Application.*

Meles, D., Bayat, A., Shafiee, M. H., Nassiri, S., & Gul, M. (2014). Investigation of tire derived aggregate as a fill material for highway embankment. *International Journal of Geotechnical Engineering, 8*(2), 182–190. https://doi.org/10.1179/1939787913Y.0000000015

Meles, D., Chan, D., Yi, Y., & Bayat, A. (2016). Finite-Element Analysis of Highway Embankment Made from Tire-Derived Aggregate. *Journal of Materials in Civil Engineering, 28*(2), 1–8. https://doi.org/10.1061/(asce)mt.1943-5533.0001371

Michigan Department of Transportation. (2021). *Michigan DOT User Guide for Mechanistic-Empirical Pavement Design Interim Edition. March.* www.michigan.gov/mdot

Yi, Y., Meles, D., Nassiri, S., & Bayat, A. (2015). On the compressibility of tire-derived aggregate: Comparison of results from laboratory and field tests. *Canadian Geotechnical Journal, 52*(4), 442–458. https://doi.org/10.1139/cgj-2014-0110

Quantifying geogrid improvements in highway pavements

S.F. Husain, E. Tutumluer & I.I.A. Qamhia
University of Illinois Urbana-Champaign, Urbana, IL, U.S.A.

P.J. Becker
Indiana Department of Transportation, West Lafayette, IN, U.S.A.

ABSTRACT: Geogrids stabilize unbound aggregate layers, leading to the formation of a mechanically stabilized layer (MSL). However, there is a lack of data quantifying the degree of local stiffness improvement in the granular base/subbase and the stress reduction on subgrade achieved through geogrid stabilization. This study employed advanced in situ testing and instrumentation to collect and analyze data from three pavement sections, one control and two geogrid-stabilized, constructed during the US-20 reconstruction project in Elkhart, Indiana, USA. The results quantify local stiffness improvements near the geogrids and demonstrate higher resilient modulus and reduced deformation trends in the geogrid-stabilized sections. These findings offer valuable insights for advancing the mechanistic-empirical designs of base course geogrid-stabilized pavements.

1 INTRODUCTION

The purpose of an aggregate base layer in a pavement is to distribute vehicular loads, maintain drainage, and to support construction traffic. However, with time and traffic, the stability of unbound base course becomes susceptible to degradation due to lateral movement of aggregate particles and subgrade intermixing (Giroud et al., 2023). Geosynthetics, and particularly geogrids with apertures, are often used to provide lateral restraint to stabilize pavement base/subbase. The primary mechanism attributed to geogrid stabilization is the interlock between the geogrid and the aggregate, which forms a mechanically stabilized layer (MSL). Therefore, it is crucial to quantify stiffness improvements achieved within the MSL to adequately analyze pavement layered structure and compute pavement critical responses within the framework of mechanistic-empirical (ME) pavement design.

Researchers in the past have investigated various aspects of the MSL to identify the mechanism governing the stiffening aspect near geogrids (Kwon et al., 2009; Tutumluer & Seyhan, 1999; Wayne et al., 2011). However, inclusion of mechanistic inputs specifically incorporating the effects of geogrid stabilization are yet to be investigated in detail. Due to this lack of available design information, many state agencies assume no influence of geogrids in the pavement design procedures leading to under-design of geogrid-stabilized aggregate base layers.

Resilient modulus (M_R) is defined as the ratio of repeated wheel load stress (σ_d) to recoverable strain (ε_r) and is the input property to characterize the aggregate layer load-deformation response behavior in pavement ME design. In the US, the AASHTO T 307 standard is widely adopted for the laboratory determination of resilient modulus or M_R of transportation geomaterials. Conversely, determination of an in-situ resilient modulus for constructed geomaterials is more challenging and therefore requires specialized test setup. The Automated Plate Load Test (APLT) is one such testing equipment which can produce designated repeated load stress applications on constructed base and subbase to estimate the in-situ characteristics of aggregate layers (White & Vennapusa, 2017).

Another recent advancement in the field of transportation geotechnics is the development of lab-scale and in-situ stiffness measurements of geomaterials using bender element shear wave sensor technology. (Byun et al., 2016; Husain et al., 2024; Kang et al., 2020). The bender element (BE) sensors operate on the principles of elastic wave propagation. BE field sensors can be deployed as a pair of elastic wave transducers housed in a rigid frame and specialized for sensing shear waves. Shear waves are of particular interest because shear wave velocity (V_S) can be measured within a particulate medium and is proportional to the small-stain shear modulus (G_{max}) for the known medium density (Leong et al., 2005).

2 OBJECTIVE AND SCOPE

The study aims to quantify the benefits of mechanically stabilized layers (MSL) formed through

geogrid-aggregate interlock in highway pavement base courses. It presents in situ data from APLT and BE sensors collected from three 76.2 m (250-ft) sections along the US-20 reconstruction project in Elkhart, Indiana, USA; one control and two geogrid sections with geogrids placed at the base-subgrade interface and mid-base layer. The analysis focuses on the impact of geogrid placement depth on pavement stiffness under different stress conditions and highlighting changes in layer stiffness near geogrids.

3   RESESRCH TEST PLAN

3.1   Aggregate and Geogrid

The test sections used an aggregate material meeting Indiana Department of Transportation (INDOT) No. 53 gradation specification (see Figure 1). A biaxial extruded geogrid with square apertures was included in the project to stabilize the base layer and its material properties are detailed in Table 1.
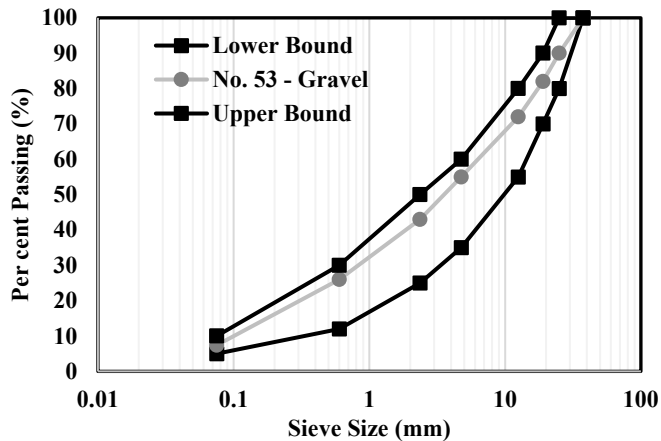
Figure 1: Aggregate particle size distribution for INDOT specification No. 53 gradation.

Table 1. Biaxial Geogrid Specification

Property	Value
Nominal Aperture Dimensions	33 mm (1.3 in.)
Minimum Rib Thickness	0.76 mm (0.03 in.)
Polymer Material	Polypropylene

3.2   Test Sections

The layer configuration for the control section (CS) is illustrated in Figure 2 (a). Geogrid Section 1 (GG1), depicted in Figure 2 (b), was constructed with a geogrid placed at the base-subgrade interface. Similarly, Geogrid Section 2 (GG2), shown in Figure 2 (c), was constructed with a geogrid installed at the mid-layer of the aggregate base. The three layers were composed of a 30-cm (12-in.) No. 53 aggregate underlain with a uniformly graded B-borrow sand. Testing and data collection were conducted prior to the construction of the open-graded HMA and the Portland cement concrete pavement (PCCP) surface.
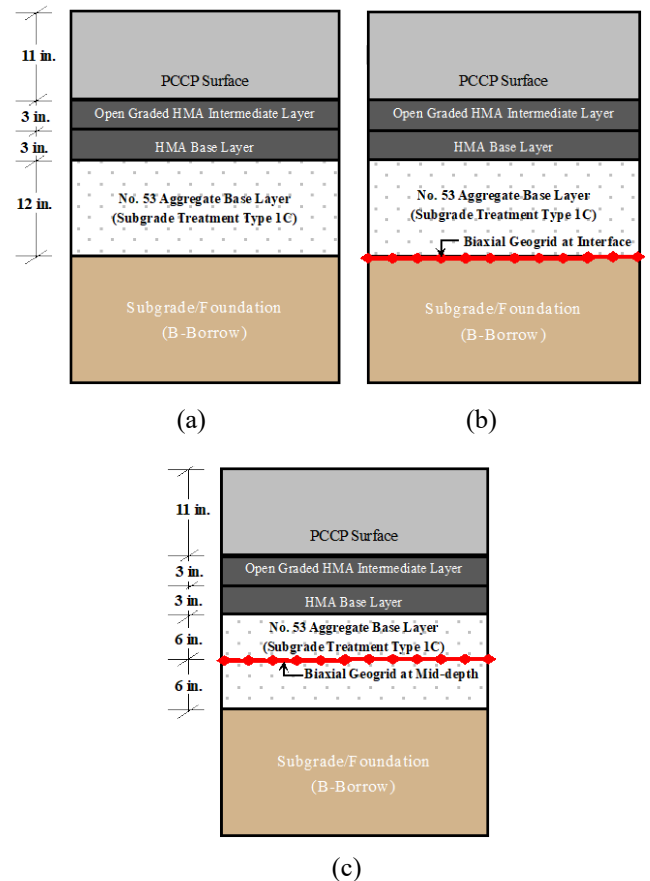
Figure 2: Pavement structures for (a) CS, (b) GG1, & (c) GG2. (1 in. = 25.4 mm)

4   INSTRUMENTATION AND RESULTS

4.1. Automated Plate Load Test Results

The Automated Plate Load Test (APLT) device is a repeated loading platform capable of determining in-situ resilient modulus and permanent deformation characteristics of constructed aggregate layers. The in-situ testing involved a multi-stress sequence as detailed in Table 2. The sequence involves a conditioning stage and six subsequent loading stages with varying number of load magnitudes and number of repeated loading applications. In total, 12 tests were carried out across the three sections, with six tests over pressure cell locations and six over Bender Element (BE) field sensor locations.

Table 1: Multi-stress sequence applied during APLT tests.

S. No.	No. of Cycles, N	Repeated Stress, σ_d kPa (psi)	Min. Stress, σ_{min} kPa (psi)	Max. Stress, σ_{max} kPa (psi)
C	500	89.6 (13)		103.4 (15)
1	100	27.6 (4)		41.4 (6)
2	100	55.2 (8)		68.9 (10)
3	150	89.6 (13)	13.8 (2)	103.4 (15)
4	200	124.1 (18)		137.9 (20)
5	250	193.1 (28)		206.8 (30)
6	250	262.0 (38)		275.8 (40)

In-situ composite resilient modulus data in Figure 3 show higher modulus values for geogrid sections than the control across all stress states. The APLT tests determined higher M_R values for the geogrid sections by 1.07 to 1.35 compared to the control, highlighting their effectiveness in stabilizing the pavement aggregate layer. The stress-dependent M_R behavior was observed, with the in-situ M_R increasing with increasing deviator stress.
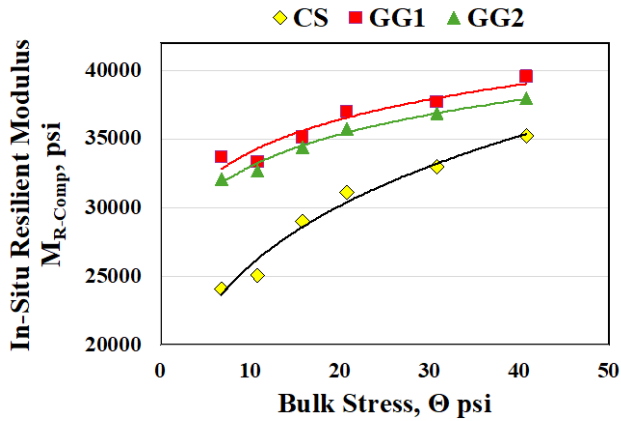
Figure 3: In situ composite Resilient Modulus for the three sections from APLT. (1 psi = 6.9 kPa)

4.1 Bender Element (BE) Field Sensors

Assessing local stiffness enhancements with geogrids using the BE shear wave technology has been our research focus at the University of Illinois Urbana-Champaign (UIUC). BE field sensors, consisting of a transmitter and receiver pair as depicted in Figure 4, measure shear wave propagation through a compacted geomaterial medium. The transmitter generates a shear wave of known shape, frequency, and amplitude while the receiver detects the arrival of the shear wave on the other end of the sensor frame. With the known distance between the two, one can estimate the shear wave velocity of the geomaterial. In the case of geogrid-stabilized layers, a local stiffness enhancement is observed (Byun & Tutumluer, 2017).
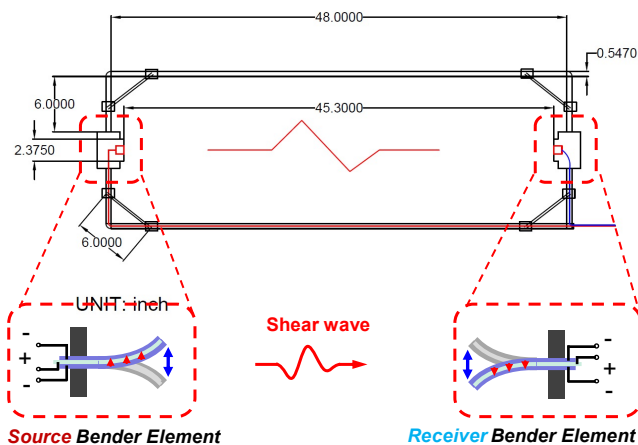
Figure 4: Bender Element (BE) field sensor (Byun et al. 2016; Kang et al. 2020, 2021)

Figure 5 shows a UIUC developed BE field sensor installed at the US-20 reconstruction site.

Figure 5: Bender Element (BE) field sensor installed in-situ.

Figure 6 presents the measured V_s values at the mid-depth of the pavement base layer using the BE field sensors installed immediately after construction. The three measurements indicated were relatively similar with low variability. However, it should be noted that the shear modulus of geomaterials is related to the square of the shear wave velocity. Therefore, a smaller difference in shear wave velocity may reflect a greater difference in stiffness. In this context, the control section exhibited the lowest stiffness compared to the geogrid-stabilized (GG1 and GG2) sections, which had similar V_s trends and higher shear wave velocities were recorded at the mid-layer, indicating an enhanced stiffness due to the presence of geogrids in those sections.
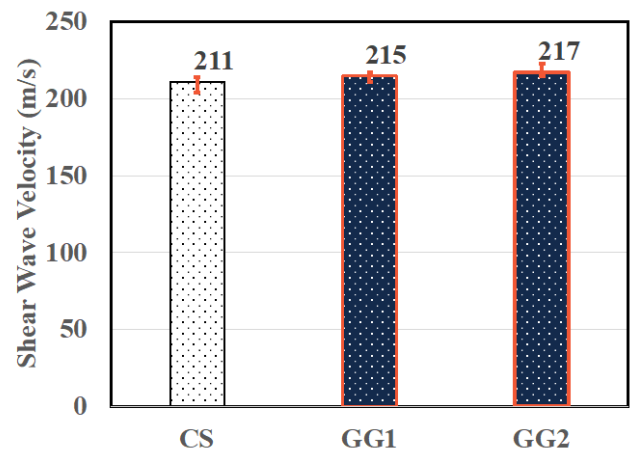
Figure 6: Shear wave velocities (V_S) from BE field sensors installed at mid-layer depth immediately after construction.

Additionally, paired APLT-BE measurements were made and are presented in Figure 7. To maintain brevity of discussion, the data present shear wave velocities for the three sections under a low and high magnitude repeated loading condition, i.e., 90 and 262 kPa (13 and 38 psi) deviator stresses. The BE enhancement ratio (V_s in geogrid sections compared to that in the control section) varied between 1.07 and 1.11 under these applied load/stress levels. With an increase in the applied stress level, the aggregate stiffness increased, and the relative contribution of the geogrids diminished. This understanding provides valuable insights into designing and optimizing pavement structures with geogrids. In-service stress states are closer to the lower end of the APLT protocols.
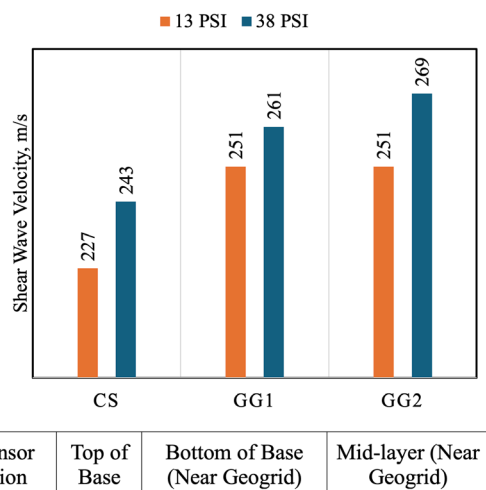
Figure 7: Paired APLT-BE measurements under repeated loading (1 psi = 6.9 kPa).

5 CONCLUSIONS

The study used paired testing with an Automated Plate Load Test (APLT) device and field installed Bender Element (BE) sensors to quantify the benefits of geogrids in stabilizing unbound aggregate layers of highway pavements. Three 76.2-m (250-ft) pavement sections along the US-20 reconstruction project in Elkhart, Indiana, USA were tested, including a control section and two geogrid-stabilized sections with geogrids installed at different depths in the base.

Enhanced base layer performance trends were observed in the geogrid sections compared to the control. The APLT device measured in the base increased in-situ resilient moduli (M_R) and reduced permanent deformation accumulation. BE field sensors captured local stiffness enhancements in the geogrid-stabilized sections with a higher shear wave velocity (V_s), a measure of small-strain modulus, near geogrid.

The study analyzed V_s enhancements from BE sensors under varying stress conditions. The geogrid sections had higher V_s than the control section under identical loading conditions, indicating the geogrid's impact on base layer characteristics. Typical stress-dependent behavior of aggregate base was observed, with decreased V_s noted in higher stress states. Geogrid sections provided significant advantages, especially under moderate in-service stress conditions.

Paired APLT-BE measurements quantified the structural advantages of incorporating geogrids in pavement bases, contributing to the development of a mechanistic-empirical pavement design methodology. Future research will expand on these findings by including data from additional sensors and examining long-term monitoring trends to better understand the effects of traffic loads and seasonal variations on pavement response and performance.

6 REFERENCES

Byun, Y. H., Han, W. J., Tutumluer, E., & Lee, J. S. (2016). Elastic wave characterization of controlled low-strength material using embedded piezoelectric transducers. *Construction and Building Materials*, *127*, 210–219. https://doi.org/10.1016/j.conbuildmat.2016.09.113

Byun, Y. H., & Tutumluer, E. (2017). Bender elements successfully quantified stiffness enhancement provided by geogrid–aggregate interlock. *Transportation Research Record*, *2656*(1), 31–39. https://doi.org/10.3141/2656-04

Giroud, J. P., Han, J., Tutumluer, E., & Dobie, M. J. D. (2023). The use of geosynthetics in roads. *Geosynthetics International*, *30*(1), 47–80. https://doi.org/10.1680/jgein.21.00046

Husain, S. F., Abbas, M. S., Wang, H., Qamhia, I. I. A., Tutumluer, E., Wallace, J., & Hammond, M. (2024). A Laboratory-Scale Evaluation of Smart Pebble Sensors Embedded in Geomaterials. *Sensors*, *24*(9). https://doi.org/10.3390/s24092733

Kang, M., Kim, J. H., Qamhia, I. I. A., Tutumluer, E., & Wayne, M. H. (2020). Geogrid Stabilization of Unbound Aggregates Evaluated Through Bender Element Shear Wave Measurement in Repeated Load Triaxial Testing. *Transportation Research Record*, *2674*(3), 113–125. https://doi.org/10.1177/0361198120908230

Kwon, J., Tutumluer, E., & Al-Qadi, I. L. (2009). Validated Mechanistic Model for Geogrid Base Reinforced Flexible Pavements. *Journal of Transportation Engineering*, *135*(12), 915–926. https://doi.org/10.1061/(ASCE)TE.1943-5436.0000046

Leong, E. C., Yeo, S. H., & Rahardjo, H. (2005). Measuring Shear Wave Velocity Using Bender Elements. *Geotechnical Testing Journal*, *28*(5). www.astm.org

Tutumluer, E., & Seyhan, U. (1999). Laboratory determination of anisotropic aggregate resilient moduli using an innovative test device. *Transportation Research Record*, *1687*(1), 13–22. https://doi.org/https://doi.org/10.3141/1687-02

Wayne, M., Boudreau, R., & Kwon, J. (2011). Characterization of mechanically stabilized layer by resilient modulus and permanent deformation testing. *Transportation Research Record*, *2204*, 76–82. https://doi.org/10.3141/2204-10

White, D. J., & Vennapusa, P. K. R. (2017). In situ resilient modulus for geogrid-stabilized aggregate layer: A case study using automated plate load testing. *Transportation Geotechnics*, *11*, 120–132. https://doi.org/10.1016/j.trgeo.2017.06.001

DEM modeling of unsaturated geomaterials for predicting resilient modulus

Hyun-Su Park & Seong-Wan Park
Dankook University, Gyeonggi-do, Republic of Korea

ABSTRACT: Soil suction and the degree of saturation influence the resilient modulus. A suction stress model that incorporates both suction and degree of saturation can be applied to the resilient modulus. To evaluate the effect of suction stress on resilient modulus, water effects were categorized into bulk and meniscus water, and cyclic loading was applied to the samples. The soil water characteristic curve (SWCC) was generated using discrete element method (DEM) analysis. Additionally, the resilient modulus was observed to vary with both deviator stress and the degree of saturation. The trends observed in this study are consistent with the results of other researchers. These findings demonstrate that the water division and cyclic loading algorithm effectively represent the unsaturated soil state, and DEM analysis revealed that suction stress influences the resilient modulus, with the resilient modulus increasing as suction stress increased.

1 INTRODUCTION

The resilient modulus is widely used to evaluate foundation deformation and is influenced by changes in suction. The relationship between suction and resilient modulus can be reasonably predicted by considering the moisture regime (Han & Vanapalli, 2016). Suction stress, derived from suction and effective saturation, is used to predict shear strength in unsaturated soil mechanics (Karube et al., 1986).

Various tests can be used to evaluate the effect of suction on the resilient modulus. However, these methods have limitations, including user-dependency, limited to specific suction ranges and time-consumption. Recently, discrete element method (DEM) analysis has been used to overcome the limitations of laboratory tests in unsaturated soil materials (Liu & Sun, 2002; Li et al., 2018).

This study simulates the behavior of unsaturated soil under cyclic loading using DEM analysis (PFC 3D). From these results, a soil-water characteristic curve (SWCC) and resilient modulus were generated through DEM simulation, and the effect of suction stress on resilient modulus was evaluated.

2 UNSATURATED STATE THROUGH DEM

2.1 *Definition of suction stress*

Suction stress is related to both suction and the degree of saturation and has been evaluated under various stress conditions (Karube and Kato, 1994). It is defined as the sum of bulk and meniscus stress, where bulk stress refers to the stress imposed on pores filled with water, and meniscus stress refers to the stress imposed by the capillary force. Suction stress can be calculated as follows:

$$p_s = p_m + p_b = (S_r - S_{r0})/(1 - S_{r0}) \cdot s \quad (1)$$

where p_m = the meniscus stress, p_b = the bulk stress, S_r = the degree of saturation, S_{r0} = the residual degree of saturation, and s = the matric suction.

2.2 *Modelling of unsaturated state in DEM analysis*

The unsaturated state was modeled through three stages of DEM analysis. First, the volume of water for particle-to-particle interaction was defined based on the spacing between particles, as shown in Figure 1. Second, Bulk water was defined as the water overlapping within the triangle area formed by three particles, while the remaining water was classified as meniscus water. Finally, the capillary force calculated using the general capillary force method was applied to meniscus water, and the capillary force calculated using the boundary method was applied to bulk water.

3 RESILIENT MODULUS TEST MODELING

The confining stress was applied to the membrane particles using the membrane modeling algorithm (Li
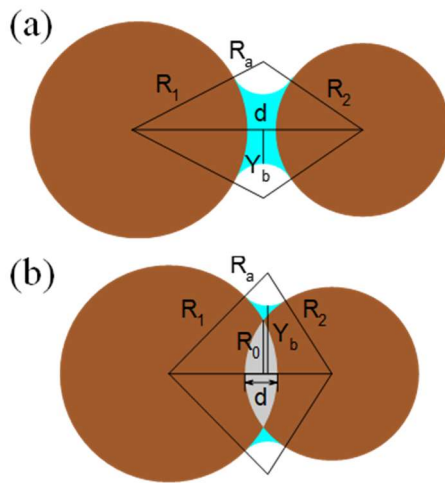
Figure 1 Water volume calculation method: (a) when the particles are separated: (b) when the particles overlap

Figure 2 Particle size distribution

et al., 2017). Deviator stress with a haversine shape was applied to the wall boundary with deformation control. Additionally, the applied particle size distribution is shown in Figure 2, and the smallest particle size was adjusted to reduce simulation time. The density of specimen was considered using density modeling method proposed by Chang et al. (2017) to account for discrepancy in particle shape and particle size distribution compared to real particles.

The specimen was compacted to achieve the target void ratio. The membrane surrounding the specimen was then modeled using spherical particles (membrane balls). The membrane ball size was selected to match the smallest particle size of specimen to ensure computational efficiency and accuracy.

4 SWCC AND RESILIENT MODULUS AT VARIOUS SUCTIONS

Suction was calculated based on the water distribution between particles using the proposed unsaturated soil modeling method. Consequently, the relationship between suction and degree of saturation

(S_r), referred to as the soil-water characteristic curve (SWCC), was generated through DEM simulations, as shown in Figure 3. The generated SWCC includes key characteristics such as the air entry value (AEV) and residual suction. These results reveals that the shape of the generated SWCC closely resembles those obtained from laboratory tests.

Figure 4 illustrates the changes in bulk and meniscus water with the degree of saturation. The ratio of bulk to meniscus water changes significantly at approximately 25% saturation. Additionally, when the total degree of saturation surpasses 20%, the amount of meniscus water remains nearly constant, and there is negligible variation at degree of saturation below approximately 10%. Meniscus water remained at approximately 10% of the degree of saturation, as reported by Karube & kawai (2001), and exhibited behavior consistent with that shown in Figure 4. Therefore, the proposed water division model for bulk and meniscus water aligns with the laboratory test results.

The confining stress was kept constant at 27.6 kPa, as deviator stresses of 13.8 kPa, 41.4 kPa, and 68.9 kPa were applied, and the degree of saturation was set

Figure 3 Soil-water characteristic curve generated through DEM analysis
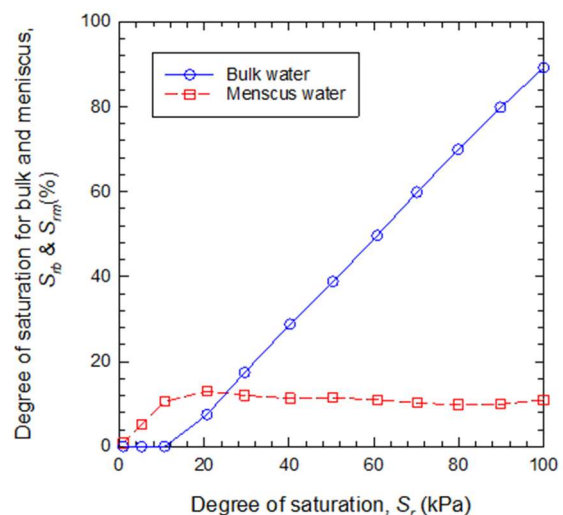
Figure 4 Changes in bulk and meniscus water with respect to the degree of saturation
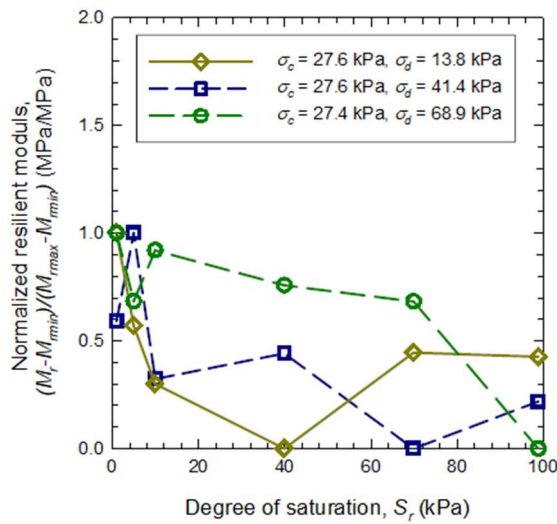
Figure 5 Changes in normalized resilient modulus with respect to the degree of saturation

Figure 6 Comparison between normalized resilient modulus and suction stress under various deviator stress levels at deviator strsss of 68.9 kPa

to 1, 5, 10, 40, 70, and 99%. This range was chosen because suction stress decreases beyond approximately 5% saturation, leading to variations in the resilient modulus within this saturation range. Figure 5 illustrates the relationship between the degree of saturation and the resilient modulus.

The difference in resilient modulus is minimal because the effective modulus of the particles was set to a small value to reduce the computational time. Table 1 presents the maximoum and minimum resilient moduli for varying deviator stress levels. Since the difference in resilient modulus with changes in the degree of saturation are minimal, the resilient modulus was normalized using its maximum and minimum values. This normalization scaled the resilient modulus to a range between 0 and 1. The resilient modulus decreases as the deviator stress increases. This trend is consistent with previous findings that the resilient modulus decreases with increasing deviator stress (Ng et al., 2013; Han and Vanapalli, 2016). Additionally, the resilient modulus increases as the degree of saturation decreases, with the slope decreasing at low saturation, as illustrated in Figure 5 (Banerjee et al., 2020).

Figure 6 illustrates the relationship between the resilient modulus and degree of saturation and the relationship between suction stress and degree of saturation. Suction stress was calculated using Eq. (1) based on the generated SWCC.

Table 1 Maximum and minimum resilient modulus

No.	1	2	3
Confining stress (kPa)	27.6	27.6	27.6
Deviator stress (kPa)	13.8	41.4	68.9
Maximum resilient modulus (MPa)	4.10	3.93	3.30
Minimum resilient modulus (MPa)	4.09	3.88	3.06

At high saturation, suction stress increased as the degree of saturation decreased. However, at low saturation of approximately 10 %, the suction stress decreased as the degree of saturation increased. This behavior occurs because, at low degree of saturation, the water volume is relatively small, resulting in suction stress decreasing as the degree of saturation increases.

When the relationship between the degree of saturation and suction stress was compared with the normalized resilient modulus results, the resilient modulus at a deviator stress of 68.9 kPa demonstrated a strong correlation with suction stress. However, under other deviator stress conditions, the resilient modulus increased with suction stress but a substantial portion of the increase occurred at low saturation. This behavior is attributed to the applied meniscus water contact force exceeding that of bulk water. These results indicate that the resilient modulus is closely related to suction stress.

5 CONCLUSIONS

This study categorized the water contents into bulk and meniscus water to simulate unsaturated soils. Cyclic loading was applied to a specimen composed of bulk and meniscus water, and the resilient modulus was obtained from these simulations.

Based on the particle size distribution, the SWCC was generated through DEM simulation. Bulk water was dominant at a saturation above 25%, whereas meniscus water was dominant below 25%. These results demonstrate that the unsaturated soil state can be effectively simulated using DEM analysis despite its limitations. Additionally, the resilient modulus was obtained through DEM simulation and decreased as the deviator stress increased from 13.8 kPa to 68.9 kPa. Finally, the suction stress was compared with the resilient modulus. The trend of suction stress with the

degree of saturation changed, whereas particle displacement changed at 5% saturation. Although the relationship between suction stress and resilient modulus remains unclear due to DEM simulation limitations, suction stress was found to influence the resilient modulus.

ACKNOLEDGMENT

REFERENCES

Banerjee, A., Puppala, A.J., Hoyos, L.R., Likos, W.J., & Patil, U.D. 2020. Resilient Modulus of Expansive Soils at High Suction Using Vapor Pressure Control. *Geotechnical Testing Journal* 43(3): 720-736.
https://doi.org/10.1520/GTJ20180255

Chang, C.S. Deng, Y., & Yang, Z. 2017. Modeling of Minimum Void Ratio for Granular Soil with Effect of Particle Size Distribution. *Journal of Engineering Mechanics* 143(9): 04017060.
https://doi.org/10.1061/(ASCE)EM.1943-7889.0001 270

De Bono, J. McDowell, G., & Wanatowski, D. 2012. Discrete element modelling of a flexible membrane for triaxial testing of granular material at high pressures. *Géotechniqu Letters* 2(4): 199-203. https://doi.org/10.1680/geolett.12.00040

Han, Z., & Vanapalli, S.K. 2016. State-of-the-art: Prediction of Resilient Modulus of Unsaturated Subgrade Soils. *International Journal of Geomechanics* 16(4): 04015104.
https://doi.org/10.1061/(ASCE)GM.1943-5622.0000631

Karube, D., Kato, S., & Katsuyama, J. 1986. Effective stress and soil constants of unsaturated kaolin. *Doboku Gakkai Ronbunshu* 370(5): 179-188. (In Japanese)
https://doi.org/10.2208/jscej.1986.370_179

Karube, D. & Kato, S. 1994. An ideal unsaturated soil and the Bishop's soil. *In Proceedings of 13th international conference on conference on soil mechanics and foundations engineering*, New Delhi, India.

Karube, D. & Kawai, K. 2001. The role of pore water in the mechanical behavior of unsaturated soils. *Geotechnical and Geological Engineering* 19: 211-241.
https://doi.org/10.1023/A:1013188200053

Li, Z., Wang, Y.H., Ma, C.H., & Mok, C.M.B. 2017. Experimental characterization and 3D DEM simulation of bond breakages in artificially cemented sands with different bond strengths when subjected to triaxial shearing. *Acta Geotechnical* 12: 987-1002. https://doi.org/10.1007/s11440-017-0593-6

Li, T., Jiang M., & Thornton. 2018. Three-dimensional discrete element analysis of triaxial tests and wetting tests on unsaturated compacted silt. *Computers and Geotechnics* 97: 90-102. https://doi.org/10.1016/j.compgeo.2017.12.011

Liu, S.H., & Sun, D.A. 2002. Simulating the collapse of unsaturated soil by DEM. *International Journal for Numerical and Analytical Methods in Geomechanics* 26: 633-646.
https://doi.org/10.1002/nag.215

Ng, C.W.W., Zhou, C., Yuan, Q., & Xu, J. 2013. Resilient modulus of unsaturated subgrade soil: experimental and theoretical investigations. *Canadian Geotechnical Journal* 50(2): 223-232. https://doi.org/10.1139/cgj-2012-0052

Effect of particle size distributions on the performance of unbound granular materials

M.S. Rahman
Swedish National Road and Transport Research Institute (VTI), Linköping, Sweden

A.W. Ahmed
Swedish National Road and Transport Research Institute (VTI), Linköping, Sweden

S. Erlingsson
Swedish National Road and Transport Research Institute (VTI), Linköping, Sweden
University of Iceland, Reykjavik, Iceland

A. Waldemarson
Swedish National Road and Transport Research Institute (VTI), Linköping, Sweden

ABSTRACT: Particle size distribution (PSD) is a crucial factor influencing the mechanical behavior of unbound granular materials (UGMs). It also governs the drainage properties, as well as moisture and frost susceptibility, of UGMs. Therefore, optimizing the PSD is essential to achieve the desired properties for use in pavement structures. In this study, seven different PSDs of a crushed rock aggregate were evaluated for mechanical performance using repeated load triaxial (RLT) tests. Three of the PSDs were designed based on the widely used Fuller-Thompson equation, employing different shape factors. The other three were open-graded, drainable types intended for permeable pavements. The final PSD was generated using an optimization method originally developed for asphalt concrete mixtures. The RLT tests were conducted at the optimal moisture content and at 95% of the maximum dry density for each PSD, determined through the modified Proctor method. The analysis focused on the resilient modulus and resistance to permanent deformation for each PSD. The results demonstrated that the well-graded PSD with grading coefficient, $n = 0.45$ exhibited the highest resilient modulus and the greatest resistance to permanent deformation. The amount of fines influenced performance significantly: an excess of fines, as well as their removal to create drainable materials, negatively impacted mechanical behavior. Additionally, the maximum particle size also showed some effect. The optimization method applied in this study did not perform well, highlighting the need for further refinement of the approach for implementation in UGMs.

1 INTRODUCTION

The mechanical properties of unbound granular materials (UGMs) used in the base and subbase layers of pavement structures largely depend on aggregate interlocking, which is influenced by the particle size distribution (PSD) (Dawson et al., 1996; Kolisoja, 1997; Lekarp, 1999; Xiao et al., 2012). Various studies have found that only certain particle sizes function as load-bearing structures within the aggregate assembly, while the remaining particles either float or act as fillers (Roque et al., 2006; Yideti et al., 2013). The method proposed by Olard and Perraton (2010), referred to as the OP method, aims to maximize aggregate-to-aggregate contact in asphalt concrete mix design by systematically distributing different fractions in the PSD curve to enhance strength. Although rarely practiced, this method may be equally applicable to UGMs. Another study, based on triaxial tests, demonstrated that open-graded (OG) materials can perform as well as well-graded (WG) materials (Rahman et al., 2017). According to this study, at higher moisture content, OG materials may even outperform their WG counterparts. This improved performance is

likely due to the lower moisture sensitivity of OG materials, which lack fine particles that do not contribute to strength. Therefore, optimizing the PSD curve using the OP method and reducing the proportion of fine particles could enhance the mechanical strength of UGMs while also improving drainage properties and reducing moisture and frost susceptibility.

The Swedish Transport Administration's requirements for PSD curves are primarily based on empirical experience. Therefore, it is crucial to conduct studies to validate previous findings, develop optimized PSD curves, and compare their performance with conventional PSDs. This approach should help the industry obtain better materials and reduce issues such as poor drainage, moisture, and frost damage. With this objective in mind, the mechanical performance of a crushed rock aggregate for seven different PSDs was investigated using repeated load triaxial (RLT) testing. The focus was on the applicability of the OP method for UGMs and its effect on mechanical performance.

2 STUDIED PARTICLE SIZE DISTRIBUTIONS

The Fuller-Thompson equation, as presented below, is probably the most widely used mathematical function for the PSD of UGMs:

$$p_i = \left(\frac{D_i}{D_{max}}\right)^n \tag{1}$$

where p_i = percentage of particles by weight passing the ith sieve size; D_i = the ith sieve size; D_{max} = maximum particle size and n = shape factor of the PSD curve. A value of $n = 0.45$ is considered to provide a WG PSD with the densest configuration (Roberts et al., 1996). For this study, three PSDs, based on Equation 1, of a crushed rock aggregate commonly used in Sweden were considered. The maximum particle size selected was 32 mm. The chosen values for the shape factor n were 0.35, 0.45 and 0.62. The value of $n = 0.35$ provides a PSD with a lot of finer particles. On the other hand, the value of $n = 0.62$ provides a relatively coarser PSD. The other three PSDs used the same aggregates but were OG, designed for permeable pavement applications. In two of these, particles smaller than 2 mm were removed to enhance drainability: one with a maximum particle size of 16 mm, and the other with 32 mm. For the third PSD, particles up to 4 mm were excluded, which had a maximum aggregate size of 32 mm.

The seventh PSD was derived based on the methodology proposed by Olard & Perraton (2010) (the OP method) for the mix design of asphalt concrete. This procedure aims to optimize the combination of fine and coarse fractions to result in an interactive network of coarse particles providing the strongest mix resistance. First, the aggregate is divided into three phases: fine, intermediate and coarse fractions. In this case, the ratio of the nominal maximum particle size (NMPS) of the intermediate particles to the coarse particles should not exceed 20%. Similarly, the ratio of NMPS of the fine particles to the intermediate particles should not exceed 20%. Next, the respective void index of each fraction is determined using the gyratory shear compactor (GSC) after 20 gyrations. Thereafter, the optimal ratio of the intermediate and coarse aggregate blend is determined using the GSC according to an approach illustrated by Baron et al. (1982). Similarly, the optimum ratio of this blend and the fine fraction is determined in the next step with an additional sensibility study. This procedure can be continued for blending further fractions. In this study, the coarse fraction was 16-32 mm with an NMPS of about 26 mm. Thus, the next fraction selected was 4-8 mm with an NMPS of about 5 mm. However, the optimization method did not provide any meaningful proportion of these two fractions. Hence, the next fraction trialed was of 2-4 mm without any success. Finally, a trial with 0-2 mm fraction indicated an optimal blending of 70% of the 16-32 mm fraction and 30% of the 0-2 mm fraction. This was selected as the PSD for further investigation with RLT testing. This optimization procedure is graphically shown in Figure 1. The details of the approach can be found in Olard & Perraton (2010). The resulting PSD with all the other PSDs investigated here are shown in Figure 2. The optimum moisture content (w_{opt}) and the maximum dry densities (γ_{dmax}) of the individual PSDs were determined according to the modified Proctor method following the European standard EN 13286-2 (CEN, 2004a). Various properties of the materials are shown in Table 1.
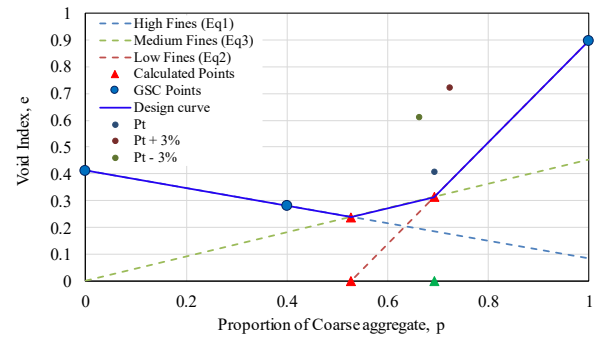
Figure 1. Proportioning of 16-32mm and 0-2 mm fractions according to the OP method.
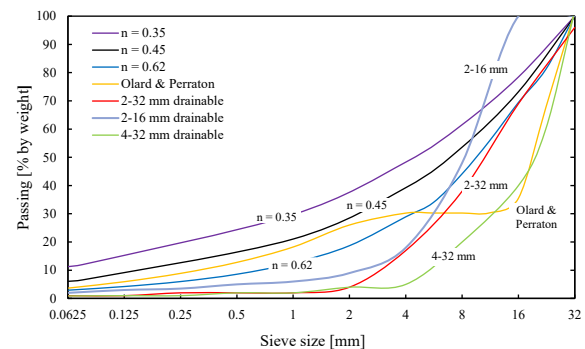
Figure 2. The PSDs of the crushed rock aggregate.

Table 1. Properties of the aggregates

PSD	D_{10} [mm]	C_u	C_c	F_c [%]	G/S	γ_{dmax} [ton/m³]	w_{opt} [%]
n = 0.35	0.06	116.7	2.4	12	1.4	2.22	6.5
n = 0.45	0.15	62.1	3.7	6.5	1.8	2.26	6.0
n = 0.62	0.70	17.1	2.4	2.4	2.7	2.11	5.5
2-16 mm drainable	2.50	3.6	1.1	2.1	5.1	1.93	5.0
2-32 mm drainable	3.00	4.3	0.9	0.75	4.9	1.96	3.5
4-32 mm drainable	5.00	4.4	1.3	0.75	23.2	1.86	3.5
Olard & Perraton	0.30	66.7	2.7	4.5	2.6	2.18	4.5

Here:

G_s = 2.64 is the specific gravity of the particles
D_{10} is the effective particle size (10% are finer than D_{10})
C_u is the uniformity coefficient
C_c is the gradation coefficient
F_c is the fine content (< 0.063mm)
G/S is the gravel (4.75-75mm) to sand (0.075 to < 4.75mm) ratio (US classification) (Xiao et al., 2012)

3 REPEATED LOAD TRIAXIAL TESTING

RLT testing is a widely used method to characterize the mechanical properties of UGMs. This test applies cyclic stresses on a cylindrical specimen in the laboratory to simulate the traffic loading experienced by the material in the real pavement structure and the corresponding deformations are measured. In this study, multistage RLT testing with constant confining pressure was carried out in accordance with the European standard EN-13286-7 (CEN, 2004b). Laboratory prepared cylindrical specimens of 150 mm diameter and 300 mm height were used. The tests were carried out applying a set of different stress paths according to the standard referred to as 'low stress level' (LSL). Each of the stress paths was applied for 10,000 cycles with a frequency of 10 Hz (Haversine pulse) with no rest period. The tests were performed under a free drainage condition. Each specimen was prepared with its w_{opt} and 95% of the γ_{dm} using a vibro-compactor. The tests were replicated to account for the variability in testing.

4 RESULTS AND DISCUSSIONS

The data from the RLT tests were analyzed to evaluate the resilient and permanent deformation characteristics of the materials. The resilient deformation contributes to fatigue cracking of the overlying asphalt concrete layers of the pavement structure. The resistance against resilient deformation or resilient stiffness is characterized by the resilient modulus (M_R) which is a quotient of the applied stress level and the corresponding resilient strain. The M_R is a function of the bulk stress level, θ (sum of the principal stresses). So, the resilient modulus value of a specimen is reported at a certain bulk stress level. Higher value of M_R is desirable for pavements to prevent fatigue cracking.

Permanent deformation (PD) accumulates with the number of load cycles (N) which contributes to rutting. PD is usually reported as a function of N. Lower accumulation of PD is better for the pavement to prevent rutting.

The evaluated M_R for the specimens with different PSDs as a function of θ is shown in Figure 3. It is observed that M_R increases with increasing θ. Some scatter and overlapping in the data are common for tests with UGMs. Generally, the WG PSD with $n = 0.45$ showed higher M_R than the others, particularly at higher θ values. The PSD with $n = 0.62$ and the 2-32 mm drainable material also performed well. The optimized PSD according to the OP method and the PSD with $n = 0.35$ demonstrated similar M_R values, which were lower than those of the previously mentioned materials. The OG 2-16 mm material showed the lowest M_R values, while the 2-32 mm material had much higher values. This indicates that the maximum

particle size greatly influences stiffness properties. The PSD with $n = 0.35$, which has a higher proportion of fines than the PSD with $n = 0.62$, exhibited lower M_R values, suggesting that coarser PSDs may exhibit higher stiffness.
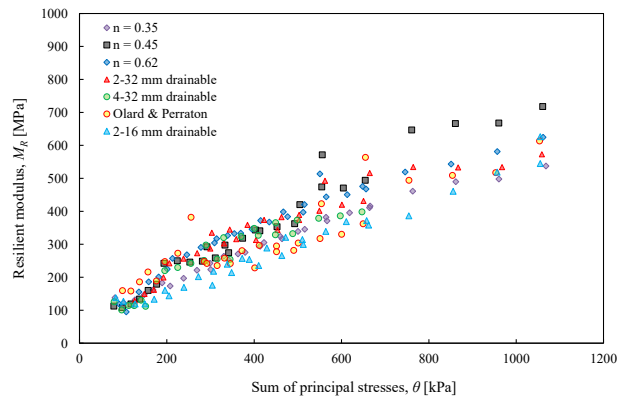
Figure 3. M_R as a function of θ.
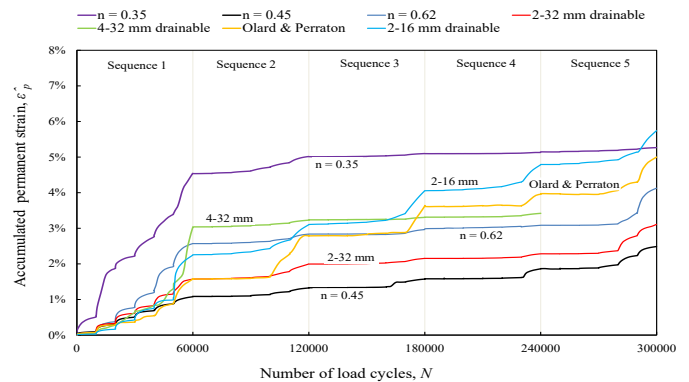
Figure 4. Accumulation of permanent strain.

The accumulated permanent strains in the materials are illustrated in Figure 5. The sequences in this figure correspond to the stress levels table for multistage RLT testing with LSL from the European standard. In each sequence, the confining pressure remained constant while the deviator stress varied. The final sequence for the 4-32 mm material was aborted due to technical issues. Figure 5 shows that the WG PSD with $n = 0.45$ accumulated the lowest PD. The PD of the OG 2-32 mm material was also very close to that of the WG material, while the PD of the 2-16 mm material was significantly higher. This again shows that the maximum particle size has a significant impact on the mechanical properties. The PDs of the $n = 0.62$ grading, the OP grading, and the 4-32 mm material were very similar and higher than those of the WG and 2-32 mm materials. The material with $n = 0.35$ grading exhibited significantly lower resistance to PD. Thus, it appears that, similar to stiffness properties, coarser grading offers better resistance to PD.

This study demonstrates that the WG PSD derived using $n = 0.45$ in the Fuller-Thompson equation exhibits superior mechanical properties. The OG 2-32 mm material also performed very well, which can be advantageous due to its improved drainage properties

and potential to outperform WG materials in higher water contents (Rahman et al., 2017). However, the 4-31 mm material showed inferior properties, indicating that excessive removal of fine particles can degrade the material's performance.

A key objective of this research was to evaluate the OP method for UGMs. This method was applied without modifications, resulting in a gap-graded PSD with only two size fractions. This did not represent the densest grading (as shown in Table 1) and presented a high risk of segregation. The tests did not indicate any improvement in mechanical properties, suggesting that further refinement of this method is needed before it can be effectively applied to UGMs.

The study also observed that increasing the fine fractions negatively affected the UGM's performance, as seen in the PSD with $n = 0.35$. It is important to note, however, that the tests were conducted at varying moisture contents, owing to the different optimal moisture content of each PSD. Similarly, variations in dry density were present. Therefore, testing under consistent moisture content and dry density conditions could potentially alter these findings. Further investigations should be carried out under these conditions.

5 CONCLUSIONS

This study highlights the significant impact of PSD on the performance of UGMs. The WG PSD with $n = 0.45$ demonstrated the highest M_R and the greatest resistance to PD. This indicates that a WG distribution enhances mechanical properties. The presence of fines significantly affects performance. Both an excess of fines and their removal to create drainable materials negatively impacted the mechanical behavior of UGMs. This suggests a balanced approach to fines content is crucial. The maximum particle size also played a notable role in the performance of UGMs, influencing both strength and stability. The optimization method originally developed for AC mixtures did not perform well for UGMs. This indicates the need for further refinement and adaptation of this method for use with UGMs. OG materials showed potential, especially at higher moisture contents, where they may outperform WG materials due to their lower moisture sensitivity.

The findings of this study emphasize the importance of carefully designing PSDs to enhance the mechanical performance and durability of UGMs in pavement structures. The study was limited to one type of crushed rock aggregate, and the tests were conducted at optimum water contents and 95% of the maximum dry densities. Further research using other materials, different water contents, and densities, as well as field validation, is necessary to achieve the best possible outcomes.

7 REFERENCES

Baron, J. & Sauterey, R. 1982. Le béton hydraulique : Connaissance et pratique, Presses de l'École Nationale des Ponts et Chaussées, Paris, France. [In French]

CEN-European Committee for Standardization, 2004a. *Test Methods for the Determination of the Laboratory Reference Density and Water Content: Proctor Compaction*. Brussels: European Standard. EN 13286-2.

CEN-European Committee for Standardization, 2004b. *Cyclic Load Triaxial Test for Unbound Mixtures*. Brussels: European Standard. EN 13286-7.

Dawson, A.R., Thom, N.H., & Paute, J.L. 1996. Mechanical characteristics of unbound granular materials as a function of condition. *Flexible pavements, Proc., European Symp*. Euroflex 1993, A. G. Correia, ed., Balkema, 35-44.

Kolisoja, P. 1997. Resilient Deformation Characteristics of Granular Materials. *Doctoral thesis*. Publications 223, Tampere University of Technology, Tampere, Finland.

Lekarp, F. 1999. Resilient and Permanent Deformation Behavior of Unbound Aggregates under Repeated Loading, *Doctoral thesis*, TRITA-IP FR 99-57, KTH Royal Institute of Technology, Stockholm, Sweden.

Olard, F. & Perraton, D. 2010. On the Optimization of the Aggregate Packing Characteristics for the Design of High-Performance Asphalt Concretes, *Road Materials and Pavement Design*, 11:sup1, 145-169, DOI: 10.1080/14680629.2010.9690330.

Rahman, M.S. & Erlingsson, S. 2015. Moisture influence on the resilient deformation behaviour of unbound granular materials, *International Journal of Pavement Engineering*, 17:9, 763-775, DOI: 10.1080/10298436.2015.1019497.

Rahman, M.S., Erlingsson, S. & Hellman, F. 2017. Stiffness and permanent deformation characteristics of open-graded unbound granular materials. *Proceedings of the 10th International Conference on the Bearing Capacity of Roads, Railways and Airfields (BCRRA 2017)*, June 28-30, 2017, Athens, Greece. Edited by Andreas Loizos, Imad Al-Qadi, Tom Scarpas.

Roberts, F.L., Kandhal, P.S., Brown, E.R., Lee, D.Y. & Kennedy, T.W. 1996. Hot Mix Asphalt Materials, Mixture Design, and Construction. *National Asphalt Pavement Association Education Foundation*. Lanham, MD.

Roque, R., Birgisson, B., Kim, S. & Guarin, A. 2006. *Development of Mix Design Guidelines for Improved Performance of Asphalt Mixtures*, Tallahassee: University of Florida.

Xiao Y., Tutumluer E., Qian Y. & Siekmeier J.A. 2012. Gradation Effects Influencing Mechanical Properties of Aggregate Base–Granular Subbase Materials in Minnesota. *Transportation Research Record: Journal of the Transportation Research Board*, Transportation Research Board of the National Academies, Washington, D.C., No. 2267, 14-26. DOI: 10.3141/2267-02.

Yideti, T.F., Birgisson, B., Jelagin, D., & Guarin, A. 2013. Packing theory-based framework for evaluating resilient modulus of unbound granular materials, *International Journal of Pavement Engineering*, 13:5, 689-697, DOI:10.1080/10298436.2013.857772.

6.2

BUILDING SUSTAINABLE AND RESILIENT PAVEMENT FOUNDATIONS

Computational modeling of asphalt pavement resilience to flooding

Xiao Chen
Rutgers University, Piscataway, NJ, 08854, USA

Hao Wang
Corresponding author, Email: hwang.cee@rutgers.edu
Rutgers University, Piscataway, NJ, 08854, USA

ABSTRACT: Flooding has multifarious impacts on asphalt pavement performance. This study provides a framework to comprehensively assess the asphalt pavement resilience to flooding by integrated computational modeling, addressing both surface and subsurface aspects. A hydro-mechanical mode was developed to evaluate the hydraulic scouring effect on the fully saturated areas on asphalt surface layer. From subsurface aspect, subsurface saturation profiles during inundation and recovery were first analyzed using a hydrological model. Based on saturation variations, a mechanistic model was developed to quantify the damage caused by subsurface weakening, and the previous hydro-mechanical model was adopted to evaluate the subgrade erosion potential. The proposed methodology provides an effective way to analyze various flooding impact mechanisms on asphalt pavement performance over both short- and long-term.

1 INTRUCTION

Transportation infrastructures, in particular roadway pavements, are increasingly affected by climatic hazards, of which flooding is a major concern. For traditional asphalt pavements, the impact of flooding on pavement performance can be multifarious. Floodwater can infiltrate surface asphalt layers with high air void content (8–10%) (Omar et al. 2020), leaving residual water for up to a week after recession (Guo et al. 2011). Under traffic loading, pore water pressure (PWP) develops, leading to cyclic hydraulic scouring and asphalt performance degradation. For pavement subsurface layers, increased moisture content reduces modulus, diminishing the foundation ability to withstand vehicular stresses and exacerbating structural responses under loading. Additionally, PWP at the subgrade-subbase interface can trigger fines migration (pumping effect), leading to subgrade erosion (Holtz et al. 2008).

Currently, there are research gaps in comprehensively assessing flooding impacts. Firstly, previous studies have focused on pavement performance under fully saturated asphalt layer. In the current practice, dense-graded asphalt pavement is designed to have 4% target air voids that do not allow water to penetrate so that the fully saturation is not the typical condition. Instead, the segregation area, or asphalt patch compacted by shovel or tamper for pothole repair could have high air void contents. Secondly, the current studies on evaluating subsurface weakening effect were limited to pavement response increase right after flooding, which is incomplete without a quantifiable measure of flood-induced damage during the whole recovery period. Thirdly, the subgrade erosion caused by flooding was largely ignored.

2 OBJECTIVE

The objective of this study is to develop computation models for evaluating impacts of flooding on surface and subsurface layers of asphalt pavement. Figure 1 shows the analysis framework. The suite of computation models includes the following:

1. Evaluate hydraulic scouring effects on surface layer by developing a hydro-mechanical model.
2. Predict subsurface saturation profile during inundation and recovery periods by developing a hydrological model.
3. Quantify subsurface weakening and subgrade erosion using previous hydro-mechanical model.
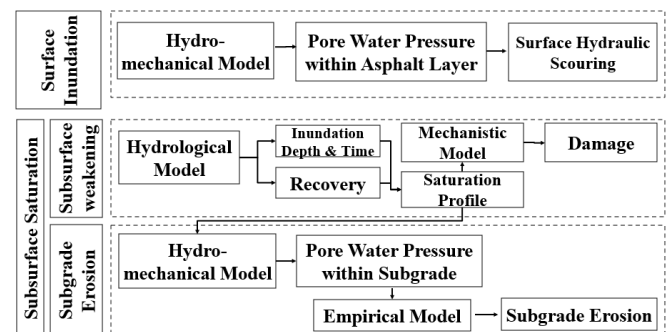
Figure 1. Analysis Framework using Computation Models

3 SURFACE HYDRAULIC SCOURING

3.1 *Development of hydro-mechanical model*

The principle of effective stress was used in this study to characterize the effect of water on mechanical response. On the other hand, Darcy's law was modified to characterize the effect of structure responses on water flow by adding an additional term that reflects the volume change in the voids. For subgrade analysis

in following section, Richard's equation was modified to consider unsaturated flow.

The pavement was composed of a 20-cm HMA layer, a 30-cm granular base layer, and subgrade. Three different asphalt patch geometries and various wheel paths were considered, as shown in Figure 2. A single axle with dual tires with speed of 90km/s was simulated, and the tire pressure of 0.7MPa. To consider different properties between asphalt patch and surrounding pavement, different Prony series parameters were used. Detailed model development and material property parameters can be found elsewhere (Chen & Wang 2024a).
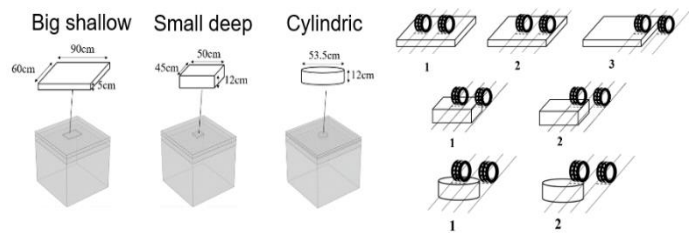
Figure 2. Pothole shapes and wheel paths

3.2 *PWP within asphalt material*

Figure 3(a) compares the maximum PWP within the asphalt patch at 25℃. It can be found that for all three patches, the PWP mainly concentrated underneath the loading area, and the maximum PWP occurred when the vehicle tires just entered the patching area, with a magnitude from 100kPa to 150kPa. Both small-deep and cylindrical patches exhibited larger maximum PWP than the big-shallow patch. Figure 3(b) shows the maximum PWP at the interface, with a magnitude from 100kPa to 200kPa. For cuboid patches, the maximum PWP was at longitudinal interface when vehicle just entered the patch. For cylindrical patch, it occurred at interface when the tire was in the center. When only one vehicle tire travelled through the asphalt patch, the PWP at interface of small-deep patch was the largest, followed by that of cylindrical patch, which is similar as the PWP within the asphalt patch. However, when both tires were loaded on the patch area, the PWP at interface of big-shallow patch became the greatest.
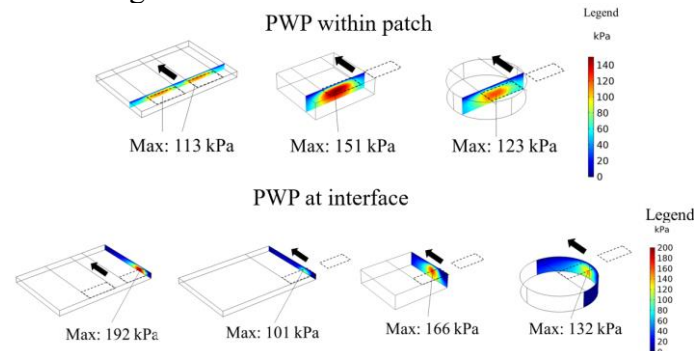
Figure 3 Comparisons of maximum PWP

4 SUBSURFACE SATURATION

4.1 *Development of hydrological model*

Richard's equation, which has been widely used to investigate unsaturated water flow (Dan et al. 2015), was adopted in this study. The Wilson-Penman equation, which is a widely utilized model that integrates different climate factors, was used here to calculate the evaporation rate (Fredlund et al. 2016).

The hydrological analysis was performed for two case studies. One focuses on the flooding event caused by Hurricane Irma in Florida (FL), while the other focuses on the flooding caused by Hurricane Florence in North Carolina (NC). Based on the collected information, the flooded pavement in FL case was composed of a 12.7cm asphalt layer, a 20cm granular aggregate base layer and sand subgrade. For NC case, it is presumed that the structure was the same as that in Florida case, with silt subgrade.

2-D hydrological models were developed. The model geometry is shown in Figure 4. Floodwater head was applied to the unpaved soil surface during inundation. Based on the collected information, the initial groundwater tables (GWT) were set at 0.5 and 1.1 meters below surface in FL and NC cases, respectively. During recovery, various weather conditions were collected and utilized for calculating the evaporation rate, which was then subtracted from the precipitation rate to determine the net water influx during the recovery period, which was applied to the exposed soil as a boundary condition. The material properties can be found elsewhere (Zapata 2010). More details on hydrological models can be found elsewhere (Chen & Wang 2024b).
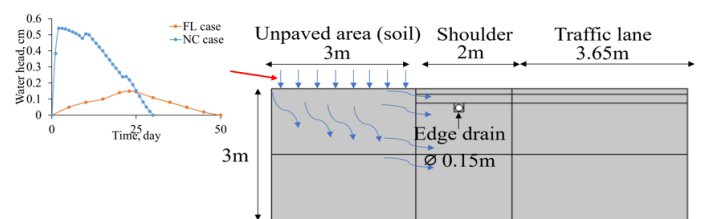
Figure 4. Hydrological model

4.2 *Subsurface moisture variation*

Figure 5 shows the variation of moisture at top of exposed soil, middle of base and top of subgrade. It shows that moisture in both cases illustrates a remarkable daily variation because of the precipitation. This indicates that the moisture at top of exposed soil is significantly impact by the environmental factors. The moisture of base and subgrade differs between FL and NC cases because of different initial GWT and soil properties. During the initial phase of recovery period, the unbound materials remained saturated and subsequently began to decrease gradually over

time. The recovery time for both cases was around 500 days. Compared with moisture of exposed soil, the effect of precipitation on moisture of pavement unbound material is much less significant. These demonstrates that the moisture within the pavement structure maintains relative stability despite environmental fluctuations.
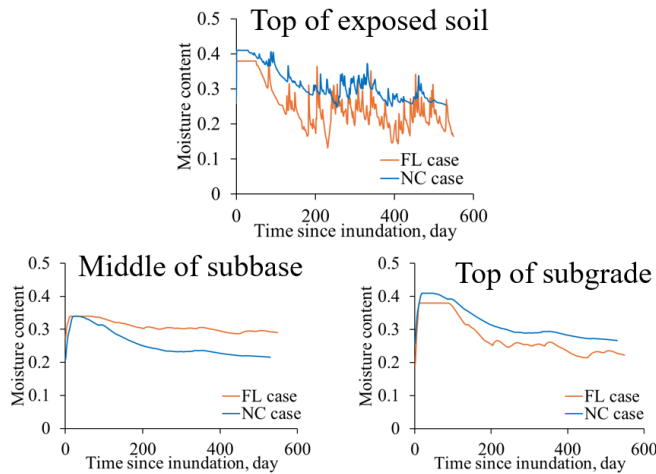
Figure 5. Moisture content variations at different locations

5 SUBSURFACE WEAKENING EFFECT

5.1 Development of mechanistic model

According to the pavement structure in FL and NC cases, a 3-D mechanical model was developed to analyze pavement responses under moving loading. For unbound base and subgrade, the moisture-stress-suction dependent modulus model was used in this study. The moisture content distributions obtained from the hydrological model were imported as the initial condition to calculate the non-linear modulus of unbound materials assuming moisture contents do not vary along traffic direction. The detailed model development and material property parameters can be found elsewhere (Chen & Wang 2024c).

Figure 6 shows the critical responses of pavements during recovery. It shows that after full saturation, the maximum increases in tensile strains were 9.5% and 13.2% for FL and NC cases, respectively. In contrast, the increases in compressive strain were much more substantial, rising to 22.8% for the FL case and 37.4% for the NC case. Compared to the increases in tensile strain, the increases in compressive strain are more pronounced. This suggests that the flooded pavements in both cases are more susceptible to subgrade rutting than to fatigue cracking.

5.2 Damage caused by subsurface weakening

According to the pavement performance models for asphalt fatigue cracking and subgrade, the pavement responses can be further converted to the allowable loading repetitions to failure. Different axle configurations and load magnitudes in the traffic mix can be converted into the number of equivalent single axle loading (ESAL, 80kN). Therefore, the damage ratio caused by traffic loading for each period after inundation can be calculated. Detailed calculations can be found elsewhere (Chen & Wang 2024d).

(a)

(b)
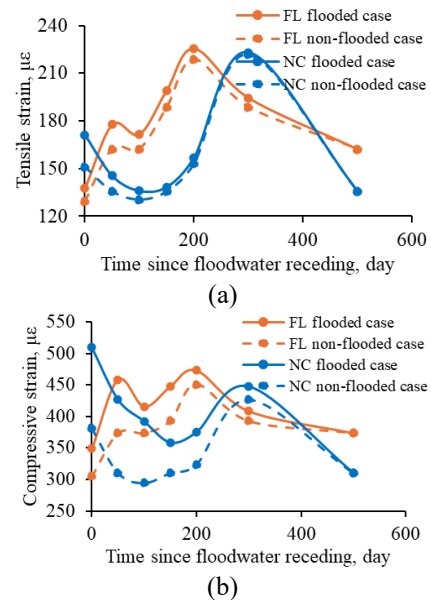
Figure 6. Variations in pavement responses during recovery: (a) Tensile strain at bottom of asphalt layer, (b) Compressive strain at top of subgrade

Based on the collected information, the daily ESALs was 478 during the recovery period. The daily damage ratios were calculated considering the effect of seasonal temperature variations on asphalt mixtures modulus. It reveals that, compared to the pre-flooding conditions at the end of the recovery period, the difference in damage ratios between flooded and non-flooded cases are substantially higher at the beginning phase of recovery. Figure 7 shows the total damage caused by unbound material modulus reduction during recovery period for FL and NC cases. It shows that the fatigue damage ratio increased by 1.16 times and 1.08 times due to flooding for FL and NC cases, respectively. However, the impact on the subgrade was more significant. Flooding led to subgrade rutting damage rising by 1.38 times for FL case and 1.82 times for NC case.

(a)

(b)
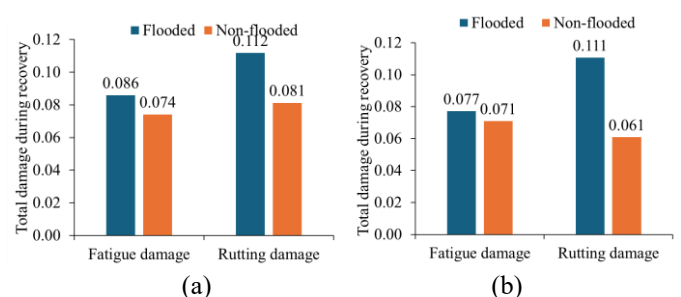
Figure 7. Total pavement damage during recovery period: (a) FL case, (b) NC case

6 SUBGRADE EROSION POTENTIAL

6.1 *PWP within subgrade*

The focus of PWP was at the top of the subgrade, a location susceptible to erosion due to mass migration to the upper base layer. In the fully saturated state, the PWP under traffic loading reached as high as 10 kPa in the NC case and 8 kPa in the FL case. Based on the findings in the literature (Kermani et al. 2019), this PWP level is high enough to cause mass migration. Following the cessation of traffic loading, the PWP gradually returned to its initial level. Figure 8 depicts the fluctuations in maximum PWP over the recovery period. Although the initial maximum PWP is high, it significantly decreases at around 20 days of recovery. Moreover, the PWP further declines to below zero after about 50 days of recovery in both scenarios. A negative PWP implies that the water within the soil is under tension, a condition that does not cause erosion. Therefore, although the recovery period may extend up to 500 days, the risk of erosion is confined to the first one or two months.
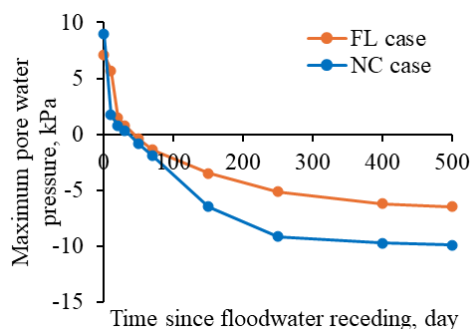
Figure 8. PWP at top of subgrade during recovery period

6.2 *Subgrade erosion potential*

The mass migration was used in this section to evaluate the subgrade erosion potential due to the generation of PWP. An empirical equation was developed based on laboratory testing results from Kermani et al. (2019). It is important to note that this empirical equation is provided only for illustrative purposes because of limited data. Based on the traffic information during recovery and PWP levels, the total mass migration can be calculated and is shown in Figure 9. The total mass migrations in FL and NC cases are 0.80% and 0.76%, respectively.
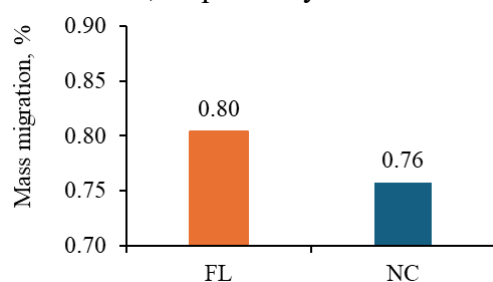
Figure 9. Subgrade erosion in terms of mass migration during recovery

7 CONCLUSIONS

This study developed computation models to assess asphalt pavement resilience to flooding from both surface and subsurface aspects. The surface hydraulic scouring effect was characterized by hydro-mechanical model. The subsurface saturation profile was analyzed by hydrological analysis. Based on saturation profiles, a mechanistic model was developed to calculate the critical pavement responses and further quantify the damage caused by subsurface weakening. On the other hand, saturation profiles were also used to evaluate the subgrade erosion potential based on the hydro-mechanical modeling.

The developed computation models allow for comprehensively assessing the impact of flooding on pavement, facilitating the development of resilient pavement designs.

8 REFERENCES

Chen, X., & Wang, H. (2024a). Hydro-mechanical analysis of water-induced pothole patch failure in asphalt pavement. *Construction and Building Materials*, 413, 134767.

Chen, X. and Wang, H. (2024b). Impact of Sea Level Rise Induced Hazards on Airfield Pavement Performance: A Simulation Study, *Transportation Research Record* (published online)

Chen, X., & Wang, H. (2024c). Evaluation of Pavement Resilience to Flooding with Inverted Pavement Structure. *Road Materials and Pavement Design*.

Chen, X., & Wang, H. (2024d). Post-flooding Asphalt Pavement Condition Assessment for Roadway Operation Strategy. *Journal of Transportation Engineering, Part B: Pavements*, 150(1), 04023035.

Dan, H. C., He, L. H., Zhao, L. H., & Chen, J. Q. (2015). Coupled hydro-mechanical response of saturated asphalt pavement under moving traffic load. *International Journal of Pavement Engineering*, 16(2), 125-143.

Fredlund, M. D., Tran, D., & Fredlund, D. G. (2016). Methodologies for the calculation of actual evaporation in geotechnical engineering. *International journal of geomechanics*, 16(6), D4016014.

Guo, X. D., Cao, J., & Fang, X. Y. (2011). Study of water stability of asphalt mixture based on residual water. *Applied Mechanics and Materials*, 71, 1791-1794.

Holtz RD, Christopher BR, Berg RR (2008) Geosynthetic design & construction guidelines: reference manual. National Highway Institute, Washington 22.

Kermani, B. et al. (2019). Measuring the migration of subgrade fine particles into subbase using scaled accelerated flexible pavement testing–a laboratory study. *Road Materials and Pavement Design*, 20(1), 36-57.

Omar, H. A., Yusoff, N. I. M., Mubaraki, M., & Ceylan, H. (2020). Effects of moisture damage on asphalt mixtures. *Journal of Traffic and Transportation Engineering (English Edition)*, 7(5), 600-628.

Zapata, C. E. (2010). *A national database of subgrade soil-water characteristic curves and selected soil properties for use with the MEPDG*, NCHRP Project 9-23A.

Geosynthetic effectiveness in stabilization – evaluation via Bender Element sensor

H. Wang & E. Tutumluer

Civil and Environmental Engineering Department, The Grainger College of Engineering, University of Illinois Urbana-Champaign, Urbana, USA

ABSTRACT: This paper describes an ongoing study where aggregate layer modulus enhancement due to geosynthetic stabilization was quantified via shear wave measurements using bender element (BE) sensor technology in both laboratory triaxial test setup and a large-scale testbed. Five different integral geogrids, two welded geogrids, one woven geogrid, one woven geotextile and one nonwoven geotextile were evaluated in repeated load triaxial testing. Some of the geosynthetics with good performance trends were also evaluated in a large-scale testbed. Both modulus enhancement and extent of geosynthetic influence zone were quantified. The results herein provide quantitative inputs to include geosynthetics into mechanistic-empirical pavement design.

1 INTRODUCTION

Mechanical stabilization of pavement base/sub-base is often accomplished by using geosynthetics in these unbound aggregate layers. Given various geosynthetic products and different mechanisms involved, an appropriate and quantitative evaluation method of geosynthetic effectiveness is necessary. Several methods have been proposed to incorporate geosynthetics into soft subgrade stabilization including Steward et al. method (1978), Giroud et al. method (1981), Giroud and Han method (2004a and 2004d) and Army Corps of Engineers Method (Tingle and Webster, 2003). Meanwhile, numerical simulations utilizing finite element modeling (FEM) and discrete element modeling (DEM) to study mechanical stabilization in paved roads and geogrid influence zones were available (McDowell et al. 2006; Kwon & Tutumluer 2009). Recent efforts to quantify the geosynthetic effectiveness include determining soil-geosynthetic composite stiffness (K_{SGC}) (Zornberg, Roodi & Gupta 2017) and small-strain modulus measurement via Bender Element (BE) shear wave transducers. BE sensor technology successfully quantified the modulus enhancement due to geosynthetics and distinguished different geosynthetics in a laboratory triaxial test setup (Byun et al. 2019). With such validation, a field BE sensor was developed as instrumentation for full-scale studies (Kang et al. 2021).

The versatility of a BE field sensor aligns with the mechanical stabilization concept where the modulus enhancement can be measured at various distances away from an installed geosynthetic. With the use of a sublayering method, the stiffening due to geosynthetic can be incorporated into mechanistic-empirical (M-E) pavement design procedures where mechanically stabilized aggregate layer can be divided into sublayers having different moduli, i.e., higher modulus near geosynthetic and standard aggregate modulus farther away from geosynthetic's influence zone (Holtz, Christopher & Berg 2008; Vavrik 2018). Byun et al. (2023) adopted the sublayering method for a numerical simulation and demonstrated the potential effect of geogrid stabilization for improving the mechanical behavior of pavement structures.

This paper describes an ongoing study where modulus enhancement due to geosynthetic stabilization was quantified via shear wave measurements using the BE sensor technology in both laboratory triaxial test setup and a large-scale testbed. Various geosynthetics were evaluated in triaxial tests and geosynthetics with good performance were also evaluated in the large-scale testbed with BE field sensors. The results from both experimental setups offered a comprehensive insight of geosynthetic stabilization effectiveness for mechanically stabilized aggregate layer inputs within the M-E pavement design framework.

2 AGGREGATES AND GEOSYNTHETICS

2.1 *Aggregates*

A crushed limestone aggregate, conforming to Illinois Department of Transportation (IDOT) CA 6 dense-graded aggregate band, was utilized in this study, as

shown in Figure 1. All triaxial specimens were engineered to follow this gradation to eliminate any effect of grain size distribution on shear wave propagations.

Following the standard Proctor compaction effort as per ASTM D698, the maximum dry density (MDD) and optimum moisture content (OMC) were determined as 2190 kg/m^3 and 5.9%, respectively. To better represent conditions in field construction, all aggregate specimens were compacted at OMC targeting MDD and the final achieved densities for triaxial specimens ranged from 2190 kg/m^3 to 2250 kg/m^3.

The same aggregates were utilized in large-scale testbed. For better consistency among test samples, air-dried aggregates were utilized to fill the testbed. The measured average water content was a low 0.17%, corresponding to a very dry condition. The average density achieved was 1870 kg/m^3 for large-scale testbed tests, lower than the MDD and triaxial specimen achieved densities. The relatively lower density is not unexpected given the dry conditions.
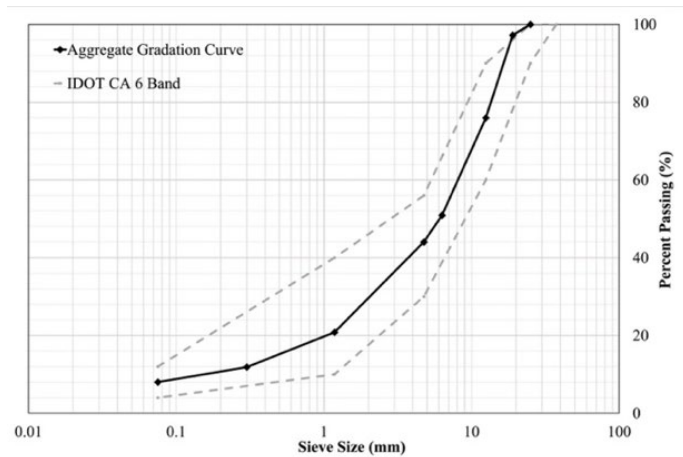
Figure 1. Aggregate gradation curve and the IDOT CA 6 band.

2.2 Geosynthetics

Various geosynthetics were evaluated including extruded integral geogrids (i.e., one integral geogrid with various aperture geometries, three extruded geogrids with rectangular apertures yet different rib properties, one extruded geogrid with triangular apertures), two welded geogrids with different rib strengths, one woven geogrid, one woven geotextile and one nonwoven geotextile. All geosynthetics tested herein are presented in Figure 2. Note that the photos show the individual geosynthetic coupons recovered from triaxial tests.
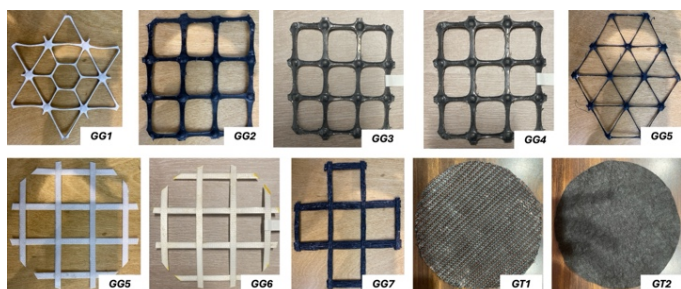
Figure 2. Geosynthetic coupons recovered from triaxial tests.

An example showing the placement of GG1 and GG4 in large-scale testbed is presented in Figure 3.

Figure 3. Geosynthetic placement in large-scale testbed.

3 EXPERIMENTAL SETUP AND METHOD

3.1 Triaxial testing setup (TX-12)

For laboratory triaxial tests, the TX-12 setup was utilized to conduct the repeated load resilient modulus tests. The setup can accommodate specimens with 150-mm in diameter and 300-mm height. Two internal linear variable differential transformers (LVDTs) were installed to measure axial deformations. The confining pressure was applied through compressed air inside the acrylic chamber. The load pulses were applied through a hydraulic pump and measured through a load cell at specimen top.

If placed, the geosynthetic coupons were placed at specimen midheight while for control tests, no geosynthetics were included. Three pairs of BE sensors were placed at three different heights above specimen midheight to access the modulus enhancement level at different distances from the geosynthetic. The schematic drawing of the triaxial test setup along with a photo is shown in Figure 4.
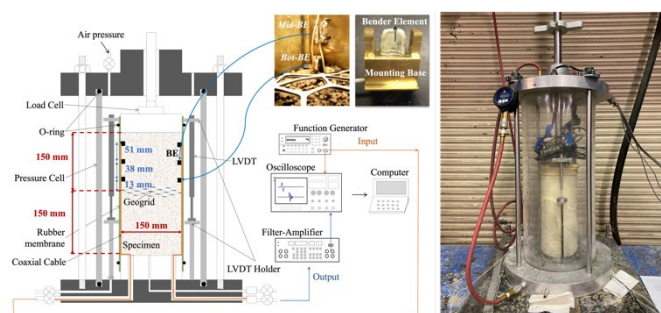
Figure 4. Triaxial test setup.

3.2 Large-scale testbed

A customized steel box was built to conduct the large-scale tests which is 1.83 m in length, 0.91 m in width and 0.61 m in height. A 150-mm geofoam was placed at the bottom to simulate a uniform subgrade with a California bearing ratio (CBR) value of approximately 5. On top of geofoam, 102-mm of aggregates were compacted and then if applicable, the

geosynthetic was placed. On top of geosynthetic, 305-mm of aggregates were then compacted in four lifts.

Similarly, three pairs of BE field sensors were placed at three different heights above geosynthetic. A 229-mm diameter earth pressure cell (PC) was placed vertically above the geofoam against the steel box wall. The center of PC was 114 mm above the geofoam, which was aligned with the height of bottom BE field sensor. The schematic drawing of the large-scale testbed, photos showing the sensors and the completed test setup are presented in Figure 5.
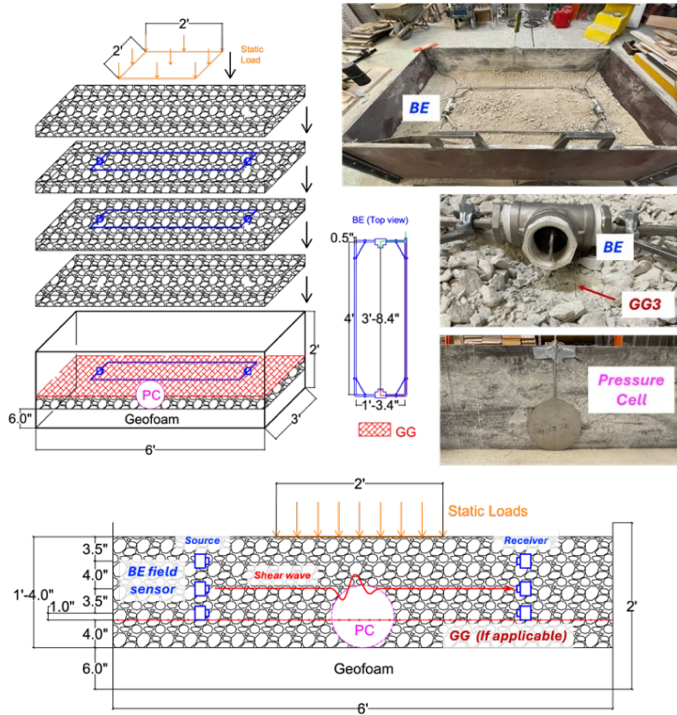
Figure 5. Large-scale testbed setup (1 ft. = 30.5 cm; 1 in. = 25.4 mm)

3.3 Shear wave collection

The BE sensors in both setups work as a pair with one source sensor and one receiver sensor. The source sensor was excited through a wave generator and the shear wave propagates through the aggregate media to be received by the receiver sensor. Before final collection, the received signals were filtered, amplified, stacked and averaged for a higher signal-to-noise (SNR) ratio. Compared to triaxial tests, the shear waves in large-scale testbed needed to travel a longer distance to reach receiver sensor. For this sake, a linear amplifier was used after wave generator to feed shear waves with higher amplitude into the source.

In triaxial tests, the AASHTO T 307 test procedure was followed where resilient modulus can be determined at 15 different loading stages, featuring 3 deviator stresses applied under 5 confining pressures (i.e., 20.7, 34.5, 68.9, 103.4 and 137.9 kPa) after a conditioning stage. Each loading stage consists of 100 haversine pulses. Resilient modulus was determined for each loading stage followed by the shear wave velocities measured at these confinement levels. Figure 6

shows one example of shear wave profiles collected during testing the GG5 installed specimen.

For large-scale testbed tests, a series of static loads were applied through a square steel plate placed at the center of the aggregate testbed surface. After applying each static load, shear waves were collected to assess the changes in shear wave velocities (i.e., local modulus) with loading and unloading. Similarly, the shear wave profile with GG1 collected in large-scale testbed is shown in Figure 6.
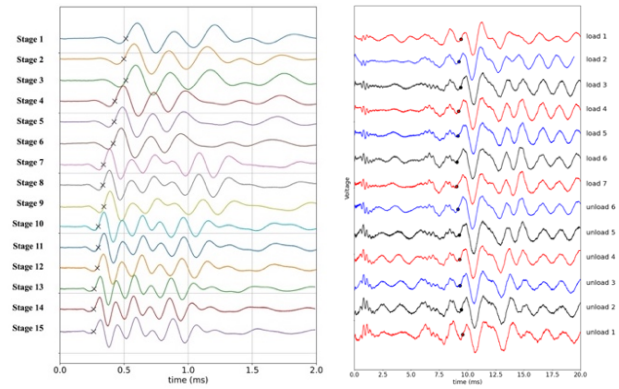
Figure 6. Shear waves collected from the two test setups.

4 RESULTS AND DISCUSSION

4.1 Stiffness enhancement in triaxial tests

Both resilient modulus and small-strain shear modulus from shear wave velocity measurements were determined in triaxial tests. Yet, the resilient modulus could not distinguish different resilient response trends among geosynthetics, as also reported by previous researchers (Abu-Farsakh et al. 2012; Byun et al. 2019). Therefore, the results for resilient modulus tests are omitted here. The small-strain shear modulus can be determined using Equation (1).

$$G_{BE} = \rho V_s^2 = \rho (L_{tip\text{-to-tip}}/t)^2 \qquad (1)$$

where ρ is bulk density, V_s is shear wave velocity, $L_{tip\text{-to-tip}}$ is tip-to-tip distance between source and receiver sensor, and t is the first arrival time as highlighted with "x" symbol in Figure 6. Meanwhile, it is noted that every three signals shown in Figure 6 are similar in terms of shapes and first arrival time, which is due to the same confining pressure for every three measurements. Under the same confining pressure, although load pulses were applied in between, the specimens did not undergo significant deformation or skeleton changes, which led to similar shear wave velocities collected. Therefore, a representative G_{BE} modulus was computed at one confining pressure.

To evaluate geosynthetic (GS) improvement when compared to a no-geosynthetic (control) scenario, the modulus enhancement ratio for different geosynthetics is calculated using Equation (2).

Enhancement Ratio = G_{BE} with GS / G_{BE} control (2)

The enhancement ratio measured 13-mm above different geosynthetics is shown in Figure 7, which demonstrates the compatibility of different geosynthetics with dense-graded aggregates. Since there were three pairs of BE sensors installed, the influence zone of different geosynthetics can also be determined. For example, for GG1, enhancement can still be measured 51-mm above while at 102-mm above, the modulus enhancement diminished.
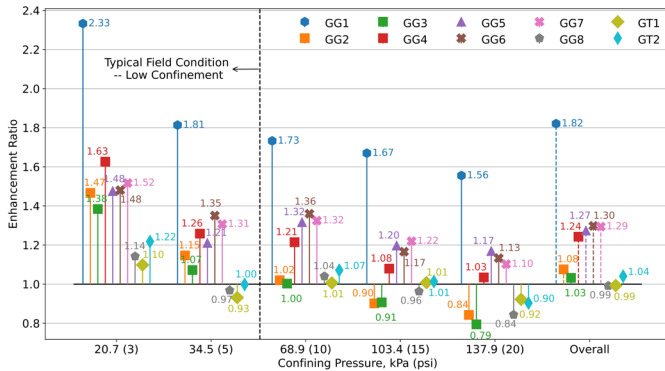
Figure 7. Enhancement ratio measured in triaxial tests.

4.2 Stiffness enhancement in large-scale testbed

Similarly, the enhancement and the influence zone can be quantified in large-scale testbed tests. The shear modulus profile for control and GG1 test are shown in Figure 8. Right above GG1, an average 15% modulus enhancement was achieved throughout different loading/unloading stages. While when at 142 mm above, the enhancement ratio (modulus of GG1 test compared to that of the control test) becomes 1, which indicates the GG1 influence zone as 142 mm.
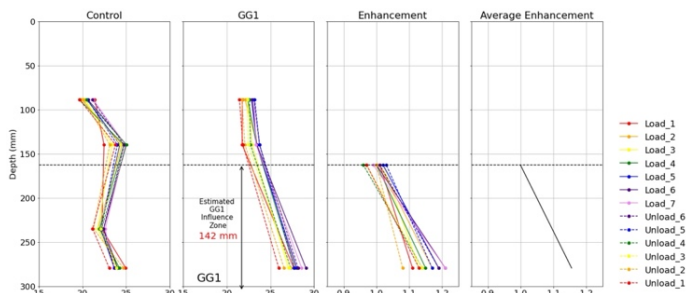
Figure 8. Geosynthetic influence zone measured in triaxial tests.

Note that given different aggregate compaction conditions and loading stages, stiffness enhancement and influence zone values from two different setups may not exactly match. Yet, the mechanically stabilized layer improvement trends agree with each other.

5 CONCLUSIONS

This paper presented results from an ongoing study aimed at investigating the effectiveness of geosynthetics in mechanical stabilization and the extent of geosynthetic influence zone using the Bender Element (BE) shear wave sensor technology in both laboratory triaxial test setup and large-scale testbed. Different geosynthetic products were evaluated with a dense-graded base course aggregate material in mechanical stabilization and for the sample modulus enhancement. The enhancement ratios and extents of geosynthetic influence zone presented herein may provide geosynthetic specific quantitative inputs into mechanistic-empirical pavement design procedures.

6 REFERENCES

Abu-Farsakh, M., Souci, G., Voyiadjis, G.Z. & Chen, Q., 2012, 'Evaluation of Factors Affecting the Performance of Geogrid-Reinforced Granular Base Material Using Repeated Load Triaxial Tests', *Journal of Materials in Civil Engineering*, 24(1), 72–83.

Byun, Y.-H., Qamhia, I.I.A., Kang, M., Tutumluer, E. & Wayne, M.H., 2023, 'Modeling geogrid-stabilized aggregate base courses considering local stiffness enhancement', *Geosynthetics International*, 1–10.

Byun, Y.-H., Tutumluer, E., Feng, B., Kim, J.H. & Wayne, M.H., 2019, 'Horizontal stiffness evaluation of geogrid-stabilized aggregate using shear wave transducers', *Geotextiles and Geomembranes*, 47(2), 177–186.

Giroud, J.-P., Asce, M., Noiray, L. & Consultant, W.-C., 1981, 'Geotextile-Reinforced Unpaved Road Design'.

Giroud, J.P. & Han, J., 2004a, 'Design Method for Geogrid-Reinforced Unpaved Roads. II. Calibration and Applications', *Journal of Geotechnical and Geoenvironmental Engineering*, 130(8), 787–797.

Giroud, J.P. & Han, J., 2004b, 'Design Method for Geogrid-Reinforced Unpaved Roads. I. Development of Design Method', *Journal of Geotechnical and Geoenvironmental Engineering*, 130(8), 775–786.

Holtz, R.D., Christopher, B.R. & Berg, R.R., 2008, *Geosynthetic Design & Construction Guidelines*.

Kang, M., Qamhia, I.I.A., Tutumluer, E., Hong, W.-T. & Tingle, J.S., 2021, 'Bender Element Field Sensor for the Measurement of Pavement Base and Subbase Stiffness Characteristics', *Transportation Research Record: Journal of the Transportation Research Board*, 2675(8), 394–407.

Kwon, J. & Tutumluer, E., 2009, 'Geogrid Base Reinforcement with Aggregate Interlock and Modeling of Associated Stiffness Enhancement in Mechanistic Pavement Analysis', *Transportation Research Record: Journal of the Transportation Research Board*, 2116(1), 85–95.

McDowell, G.R., Harireche, O., Konietzky, H., Brown, S.F. & Thom, N.H., 2006, 'Discrete element modelling of geogrid-reinforced aggregates', *Proceedings of the Institution of Civil Engineers - Geotechnical Engineering*, 159(1), 35–48.

Steward, J.E., Williamson, R. & Mohney, J., 1978, *Guidelines for use of fabrics in construction and maintenance of low-volume roads.*, USDA, Forest Service.

Tingle, J.S. & Webster, S.L., 2003, 'Corps of Engineers Design of Geosynthetic-Reinforced Unpawed Roads', *Transportation Research Record: Journal of the Transportation Research Board*, 1849(1), 193–201.

Vavrik, W., 2018, *Recommended practice for incorporating geogrids in ME pavement design.*

Zornberg, J.G., Roodi, G.H. & Gupta, R., 2017, 'Stiffness of Soil–Geosynthetic Composite under Small Displacements: I. Model Development', *Journal of Geotechnical and Geoenvironmental Engineering*, 143(10), 04017075.

7.1

ADVANCES IN SMART AND NON-TRADITIONAL ROADWAYS AND RUNWAYS

Magnetically enhanced bitumen for wireless power transfer in electric roads: Mechanical, rheological, and electromagnetic evaluation of magnetite-modified bitumen

G. Boada-Parra

Universidad Politécnica de Madrid, Departamento de Ingeniería del Transporte, Territorio y Urbanismo, C/Profesor Aranguren 3, 28040 Madrid, Spain.

College of Science and Engineering, Universidad San Francisco de Quito USFQ, Quito, 170901, Ecuador

F. Gulisano, F. Apaza Apaza, J. Gallego

Universidad Politécnica de Madrid, Departamento de Ingeniería del Transporte, Territorio y Urbanismo, C/Profesor Aranguren 3, 28040 Madrid, Spain.

ABSTRACT: The increasing demand in transportation has led to higher petroleum consumption and greenhouse gas emissions, emphasizing the need for sustainable solutions. Inductive Electric Road Systems (ERS) enable wireless power transfer (WPT) to electric vehicles, but their efficiency is limited by energy losses and low magnetic permeability in conventional asphalt layers. This study develops magnetite-modified bitumen binders to enhance magnetic permeability and system efficiency. Magnetite was incorporated into bitumen at varying concentrations, and its mechanical, rheological, and electromagnetic properties were evaluated. The results showed significant improvements: a 56% increase in rigidity, 17% in thermal stability, and up to 3.66% in efficiency in power transfer, optimizing their suitability for ERS applications. These findings highlight the potential of multifunctional asphalt materials to enhance pavement performance and support road electrification.

1 INSTRUCTION

The rapid growth of the transportation sector has led to increased petroleum consumption and greenhouse gas (GHG) emissions, intensifying environmental challenges (Maione *et al.*, 2016). Global initiatives emphasize the urgent need for sustainable energy solutions, with transportation electrification at the forefront (Madurai Elavarasan *et al.*, 2022). Electric vehicles (EVs) are a key component of this transition, projected to represent 50% of global car sales by 2035, significantly reducing oil demand and carbon emissions (Iea, 2024). However, the widespread adoption of EVs would be facilitated by intelligent infrastructure capable of providing efficient, continuous recharging while in motion. (Kuttah, 2022).

Electric Road Systems (ERS), particularly those employing Wireless Power Transfer (WPT), offer a promising solution by enabling energy transfer between road-embedded transmitters and vehicle receivers (Soares and Wang, 2022; Chen, Taylor and Kringos, 2015). Despite their significant potential, WPT systems face critical efficiency challenges, primarily due to factors such as coil misalignment, the separation between them, and the electromagnetic properties of the materials involved, which limit the overall system efficiency (Panchal, Stegen and Lu, 2018; Machura and Li, 2019; Gulisano *et al.*).

Research highlights magnetite (Fe₃O₄) as a promising additive to improve the electromagnetic properties of bitumen. With high magnetic permeability, magnetite enhances energy transfer efficiency, rigidity, and durability, making it ideal for ERS applications. Incorporating magnetite into bitumen improves structural performance and interaction with advanced road technologies (Al-Kheetan *et al.*, 2022; Giustozzi *et al.*, 2018).

This study examines the optimization of mechanical and electromagnetic properties in magnetite-modified bitumen to enhance WPT system efficiency, offering key insights for developing smarter, more sustainable road infrastructure through its objectives, methodology, results, and conclusions.
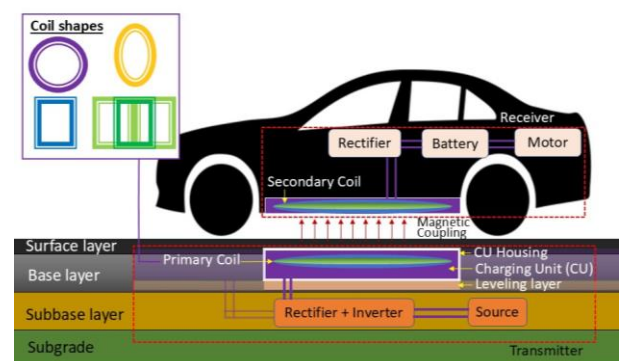
Figure 1. WPT systems in pavements. Source: Author's elaboration

2 SCOPE AND OBJECTIVES

This study aims to develop and evaluate magnetite-modified bitumen with enhanced magnetic permeability to improve the efficiency of Electric Road Systems (ERS), particularly for wireless power transfer (WPT) applications for electric road vehicles.

3 MATERIALS

The study utilized 50/70 bitumen, characterized according to the UNE-EN 12591 standard, as the base material (Figure 2a). Synthetic magnetite (Fe_3O_4) was incorporated as a filler, with particle sizes below 0.01 mm. Magnetite's high density approximately 5.18 g/cm³ (Figure 2b), and its hardness (5.5–6.5 on the Mohs scale) contribute to improved mechanical strength and thermal conductivity, enhancing the material's resistance to deformation and cracking (Patti *et al.*, 2018).
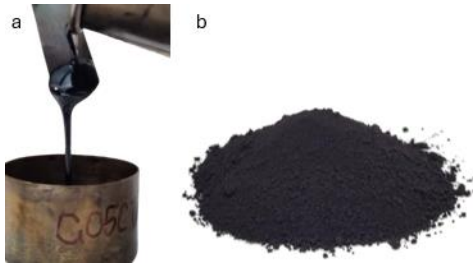
Figure 2. a) Bitumen 50/70 b) Magnetite filler F_2O_3

4 METHODOLOGY

This study evaluated the mechanical, rheological, and electromagnetic properties of 50/70 bitumen modified with magnetite filler. Magnetite was added volumetrically at 0% (Reference), 2% (M-2%), 5% (M-5%), and 10% (M-10%) concentrations, based on its potential to enhance material properties.

Sample preparation involved heating bitumen to 160°C, stirring it at 1400 rpm for five minutes, and gradually adding magnetite to ensure homogeneity. The mixture was stirred for an additional 10 minutes, poured into molds, and cured for testing.

Mechanical properties were assessed through penetration and softening point tests, while viscosity was measured using a Brookfield viscometer. Rheological behavior was analyzed with a Dynamic Shear Rheometer (DSR) to evaluate deformation resistance. Electromagnetic tests focused on magnetic permeability and energy transfer efficiency, determining the modified bitumen's suitability for Electric Road Systems (ERS).
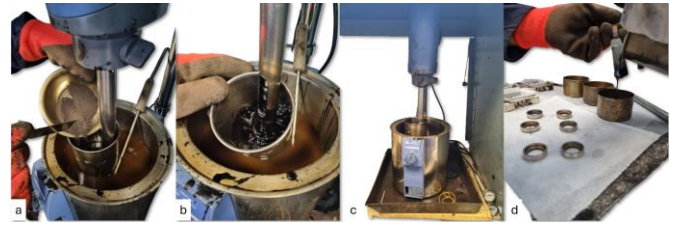
Figure 3. Manufacturing process of magnetite-modified bitumen: a) Addition of magnetite filler; b) Mixing at 1400 rpm; c) High-shear mixing at 160°C; d) Pouring mixture into molds for testing.

4.1 *Mechanical Tests*

Penetration (ASTM D5): Evaluated bitumen consistency by measuring the penetration depth of a needle under a 100 g load at 25°C for 5 seconds. Three measurements were taken for each of the three samples per magnetite content.

Softening Point (ASTM D36): Assessed thermal susceptibility using the ring and ball test. The softening point was recorded as the temperature at which a steel ball penetrated the bitumen. Tests were performed on three samples for each magnetite content.

Dynamic Viscosity (ASTM D4402): Measured the bitumen's resistance to flow at high temperatures (90°C to 160°C) using a Brookfield viscometer, providing insights into its handling and pumping properties.

Rheological Properties (ASTM D7175): Examined viscoelastic behavior with a Dynamic Shear Rheometer (DSR). Tests included frequency sweeps (0.1–10 Hz) and temperature ranges (25°C–75°C), determining dynamic modulus ($|G^*|$) and phase angle (δ) to evaluate deformation resistance. The master curve of $|G^*|$ was constructed using the Standard logistic Sigmoid model and the shift factor was calculated by the Williams-Landel-Ferry (WLF) shift function (Xue *et al.*, 2024).

Figure 4. a) Penetration test b) Softening point test c) Viscometer Brookfield d) Dynamic Shear Rheometer (DSR)

4.2 *Electromagnetic Tests*

Resistance was measured using the four-probe method, applying current through outer probes and recording voltage between inner probes with a high-impedance voltmeter, eliminating parasitic resistances (Dieval *et al.*, 2024). Samples, 40 mm cubes with 10 mm height, were prepared with preheat-

ed molds at 100°C for optimal wire placement and consistent testing conditions (Figures 5a-c).
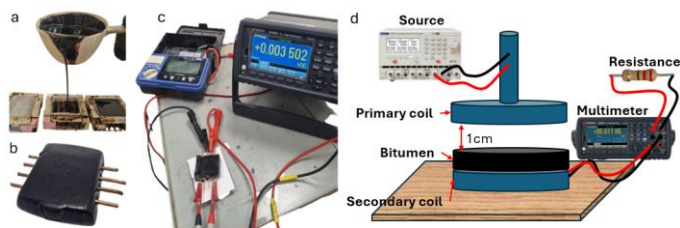
Figure 5. Electrical characterization: a) Sample fabrication; b) Prepared sample with copper probes; c) 4-probe test circuit setup. d) Magnetic characterization setup

Magnetic characterization involved measuring induced voltage drops and current variation using two coils separated by 1.5 cm, with a diameter of 2 cm, and bitumen samples placed between them. A 30V AC source powered the primary coil at 85 kHz, while the secondary coil recorded voltage. Tests were conducted at 20°C, with multiple measurements ensuring reproducibility. Averaged values assessed the effect of magnetite content on power transfer efficiency, and results were compared to the reference sample under consistent environmental conditions.

5   RESULTS AND DISCUSSION

The results demonstrate that incorporating magnetite into bitumen significantly enhances both its mechanical and electromagnetic properties. Regarding thermal susceptibility, penetration tests reveal a clear trend of increased rigidity as magnetite content rises, decreasing from 67.97 mm/10 in the reference sample to 46 mm/10 with 2% magnetite, 40 mm/10 with 5% magnetite, and 29 mm/10 with 10% magnetite. This represents a reduction of up to 56.74% in penetration for bitumen containing 10% magnetite. This improvement enhances resistance under high traffic and warm climates, making it more suitable for such applications. However, balancing rigidity and flexibility is essential to prevent cracking in cold environments. Similarly, softening point tests indicate a progressive increase in thermal resistance, with values rising from 48°C in the reference sample to 51°C with 2% magnetite, 53°C with 5% magnetite, and 56°C with 10% magnetite. This represents a 14.28% increase in the softening point for 10% magnetite compared to the reference, suggesting enhanced durability under high-temperature conditions.

The viscosity results reveal a significant increase with higher magnetite content, highlighting its substantial impact as a filler. While the reference bitumen decreases in viscosity from 750 cP at 120°C to 90 cP at 160°C, the addition of 10% magnetite raises these values to 2072 cP at 120°C and 283 cP at

160°C. These increases represent 176.27% at 120°C and more than threefold at 160°C compared to the reference. For 2% magnetite, viscosities range from 1456 cP at 120°C to 188.6 cP at 160°C, representing a 94.13% increase at 120°C compared to the reference. This consistent rise in viscosity reflects enhanced rigidity and flow resistance in the modified bitumen, confirming its mechanical improvements. However, the increased viscosity necessitates higher mixing temperatures during production to ensure proper workability. While the reference bitumen achieves suitable viscosity at approximately 140–150°C, bitumen containing 10% magnetite requires a higher temperature of around 160°C for optimal handling and asphalt application. This contrast highlights the significant impact of magnetite as a filler, enhancing rigidity but demanding careful adjustment of production conditions to maintain workability.

Rheological analysis (Figure 6) further supports these findings, showing that the dynamic modulus ($|G^*|$) increases with magnetite content, particularly at higher frequencies, while the phase angle (δ) decreases. These results indicate a shift toward more elastic behavior, reducing viscoelasticity and enhancing rigidity. This combination of properties makes the modified bitumen better suited for heavy traffic loads and dynamic conditions, ensuring improved performance under demanding scenarios.

Electromagnetic tests reveal notable trends in magnetic properties. While no electrical conductivity was detected across the applied voltage range (1V–1000V), the magnetic results (Figure 7) show a consistent increase in the power received by the secondary coil with higher magnetite content. This confirms the positive effect of magnetite on the magnetic performance of the system. With up to 10% magnetite, the WPT system efficiency improves by 3.66% compared to the reference bitumen. This improvement is attributed to magnetite's high magnetic permeability, which reduces circuit reluctance and enhances coil coupling by concentrating the magnetic flux.
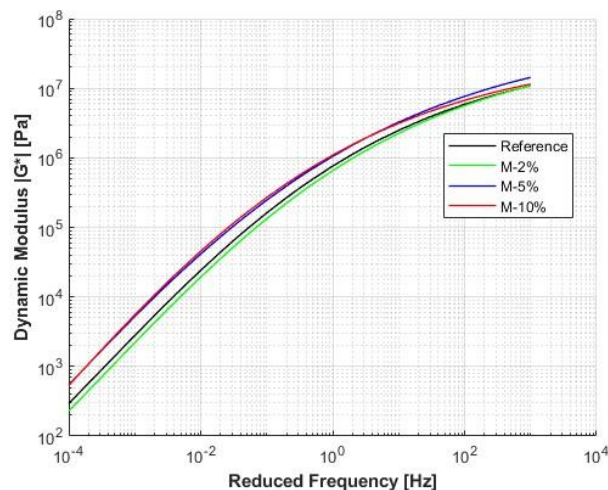
Figure 6. Master curves of the Dynamic modulus at 25ºC.
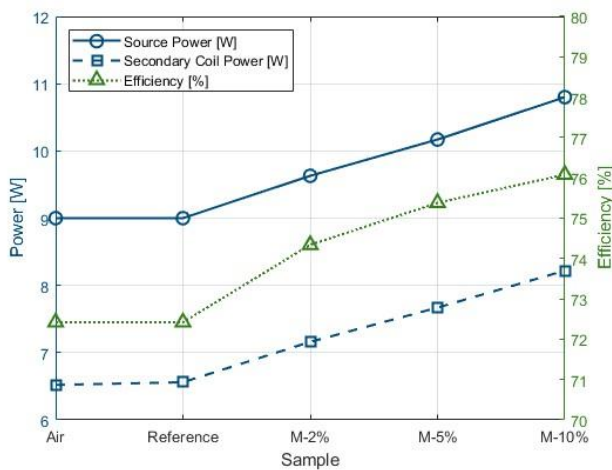
Figure 7. Power Transmission and Efficiency in WPT.

6 CONCLUSION

The study confirms that incorporating magnetite into bitumen significantly enhances its mechanical and electromagnetic properties. Adding up to 10% magnetite improves rigidity and thermal stability, evidenced by a 56.74% reduction in penetration and a 14.28% increase in the softening point compared to the reference sample. These modifications enhance the bitumen's resistance and durability under high traffic loads and diverse climatic conditions. However, the increased viscosity with higher magnetite content requires adjustments in mixing and application temperatures, with 10% magnetite necessitating around 160°C for optimal handling during production. Rheological results further support these findings, showing a rise in the dynamic modulus and a decrease in the phase angle, indicating a beneficial shift toward more elastic behavior, essential for dynamic load conditions.

Electromagnetic tests demonstrate a 3.66% improvement in WPT system efficiency with 10% magnetite, linked to its high magnetic permeability. This enhancement reduces circuit reluctance and improves coil coupling, optimizing energy transfer efficiency. These results highlight magnetite-modified bitumen as a promising material for improving the durability and functionality of electrified roads, supporting in-motion electric vehicle charging. By reducing reliance on fossil fuels and greenhouse gas emissions, this material contributes to developing more sustainable and advanced transportation infrastructure.

7 REFERENCES

Al-Kheetan, M. J., Azim, T., Byzyka, J., Ghaffar, S. H. and Rahman, M. M. (2022) 'Performance of magnetite-based stone mastic asphalt (SMA) as a superior surface course material', *Construction and Building Materials,* 322, pp. 126463.

Chen, F., Taylor, N. and Kringos, N. (2015) 'Electrification of roads: Opportunities and challenges', *Applied Energy,* 150, pp. 109-119.

Dieval, L., Gulisano, F., Castaño-Solis, S., Diez, L., Boada-Parra, G., Apaza Apaza, F., Abedi, M. and Gallego, J. (2024) *Electrical and mechanical properties of bitumen incorporating graphene nanoplatelets.*

Giustozzi, F., Mansour, K., Patti, F., Pannirselvam, M. and Fiori, F. (2018) 'Shear rheology and microstructure of mining material-bitumen composites as filler replacement in asphalt mastics', *Construction and Building Materials,* 171, pp. 726-735.

Gulisano, F., Apaza, F. R. A., Gálvez-Pérez, D., Jurado-Piña, R., Boada-Parra, G. and Gallego, J. 'Non-destructive testing methods for road pavement health monitoring: Electromechanical assessment of self-sensing asphalt materials'. 2023: SPIE, 241-250.

Iea (2024) 'Global EV Data Explorer'. Available at: https://www.iea.org/data-and-statistics/data-tools/global-ev-data-explorer (Accessed.

Kuttah, D. K. (2022) *Advances in Design and Testing of Future Smart Roads: Considering Urbanization, Digitalization, Electrification and Climate Change.* CRC Press.

Machura, P. and Li, Q. (2019) 'A critical review on wireless charging for electric vehicles', *Renewable and Sustainable Energy Reviews,* 104, pp. 209-234.

Madurai Elavarasan, R., Pugazhendhi, R., Irfan, M., Mihet-Popa, L., Khan, I. A. and Campana, P. E. (2022) 'State-of-the-art sustainable approaches for deeper decarbonization in Europe – An endowment to climate neutral vision', *Renewable and Sustainable Energy Reviews,* 159.

Maione, M., Fowler, D., Monks, P. S., Reis, S., Rudich, Y., Williams, M. L. and Fuzzi, S. (2016) 'Air quality and climate change: Designing new win-win policies for Europe', *Environmental Science and Policy,* 65, pp. 48-57.

Panchal, C., Stegen, S. and Lu, J. (2018) 'Review of static and dynamic wireless electric vehicle charging system', *Engineering Science and Technology, an International Journal,* 21(5), pp. 922-937.

Patti, F., Mansour, K., Pannirselvam, M. and Giustozzi, F. (2018) 'Mining materials to generate magnetically-triggered induction healing of bitumen on smart road pavements', *Construction and Building Materials,* 171, pp. 577-587.

Ritchie, H., Rosado, P. and Roser, M. (2020) 'Emissions by sector: where do greenhouse gases come from?', *Our World in Data.*

Soares, L. and Wang, H. (2022) 'A study on renewed perspectives of electrified road for wireless power transfer of electric vehicles', *Renewable and Sustainable Energy Reviews,* 158, pp. 112110.

Xue, J., Gulisano, F., Apaza Apaza, F. R., Boada-Parra, G., Abedi, M. and Gallego, J. (2024) 'Assessment of the rheological behavior of bitumen modified with solutions of graphene nanoplatelets (GNPs)', *Construction and Building Materials,* 455, pp. 139228.

Mechanical response-based structural optimisation of prefabricated plastic pavement module

Hanyu Zhang[a,b] and Haopeng Wang[a]*

aDepartment of Civil and Environmental Engineering, University of Liverpool, Liverpool, UK

bNottingham Transportation Engineering Centre, Faculty of Engineering, University of Nottingham, Nottingham, UK

*Corresponding author: Haopeng Wang (haopeng.wang@liverpool.ac.uk)

ABSTRACT: This study investigated the mechanical responses of a semi-rigid base pavement with asphalt concrete and prefabricated plastic modules, aiming to optimise the structural design of prefabricated modules. Three types of structural forms were designed and a dynamic finite element (FE) modelling with moving loads was conducted. Different types of stress and strain were compared to highlight the differences of various types of modular structural designs. Results indicate that the stress and strain for the prefabricated plastic module are higher than those in the asphalt concrete layer due to the hollow structure and its relatively lower modulus. The stress distribution and concentration can be optimised by adding supports within the hollow structure. The mechanical responses of the layers below surface layer remain unchanged after replacing asphalt concrete with prefabricated plastic modules. According to this case study, the prefabricated plastic pavement modules would not experience strength failure.

1 INTRODUCTION

Forwarding to a net-zero road infrastructure is a worldwide strategic goal, including the implementations of low-carbon materials, intelligent construction and in-situ testing, and digital twin-enabled maintenance decision making. Among those solutions, recycling and reusing waste plastics in asphalt pavement constructions are widely used practices that have produced many successful applications. There are two major methods for using waste plastics in asphalt pavements: wet process and dry process (You *et al.* 2022). The former involves mixing waste plastics with bitumen to form a new type of modified bitumen, while the latter utilises waste plastics as a replacement for a portion of fine aggregates. As can be seen, the waste plastics are simply mixed with either the bitumen or asphalt concretes without consideration of their interaction mechanisms. Other methods include mixing the waste plastic-derived components with bitumen after chemical treatments (e.g., pyrolysis), in an attempt to stabilise the waste plastic-bitumen mixture (Abdy *et al.* 2023). The main challenge of current practices for using waste plastics in asphalt pavements is that the waste plastics are used as either bitumen modifier or fine aggregate replacement, thereby limiting their applications in large dosages.

Thus, finding ways to significantly increase the amount of waste plastics used in road constructions presents a challenge and requires innovative approaches beyond material processing.

In 2018, the world's first plastic road was opened in the Netherlands (Wavin 2018). It is a cycle path entirely made with recycled plastic-based modular components. This is a completely different approach compared to the current practices in road engineering; however, its material information and structural design are inaccessible which makes further research difficult. More importantly, whether this new type of prefabricated plastic pavement can be used in other application scenarios (e.g., motorway and urban road) is still unknown as its bearing capacity needs further investigations. Prefabricated pavement is not a new technology and many applications have been conducted successfully, especially for concrete pavements (Guo *et al.* 2024). Regarding this type of pavement structure, attention should be given to the cross-section profile optimisation, joint design, and interface bonding characterisation. Compared to asphalt concretes, the waste plastic-extruded solid mixture is relatively soft with a typical stiffness from 600 MPa to 3500 MPa. However, it is worth considering whether the overall strength of prefabricated plastic pavement modules can be improved to meet the normal road design criteria by optimising its structural

form. This concept has the potential to be a promising solution for effectively reusing waste plastics in pavement engineering.

In summary, this paper is the first attempt to optimise the structural forms of prefabricated plastic pavement modules based on their mechanical responses. This paper is organised as follows. The next section details the three different structural designs of prefabricated plastic pavement modules and their material properties. The following section presents the governing equations and model information used in the finite element (FE) modelling. Finally, the comparisons of mechanical responses of different structural forms are presented, and conclusions and recommendations are summarised in the last section.

2 STRUCTURAL DESIGN AND MATERIAL PROPERTY

Three types of structural forms were designed for the following comparative and optimisation study, considering their bearing capacity and manufacturing feasibility. Figure 1 shows the cross-section profiles and 3D structural forms of these hollow modules, including the box girder (Type I), box girder with cylinder support (Type II), and box girder with cone support (Type III). Besides, a typical asphalt pavement with a semi-rigid base was selected as the benchmark model. The asphalt concrete (AC) was then replaced by the prefabricated plastic modules in the FE modelling used for the following sections. Table 1 shows the pavement structural and material information.
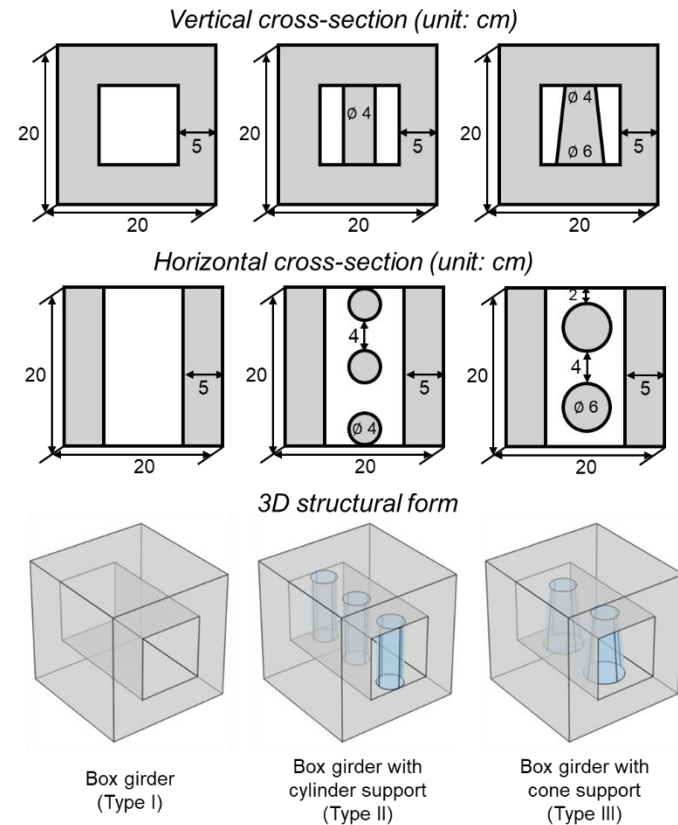
Figure 1. Structural design of prefabricated plastic modules.

Table 1. Structural and material information (adapted from (Assogba *et al.* 2021)).

Layer	Material	Thickness (cm)	E (MPa)	v	ρ (kg/m³)
Surface	AC	20	7000	0.3	2250
	PPM		2000	0.4	1230
Base	CTM	40	15000	0.25	2350
Subbase	CTS	20	4000	0.25	2300
Subgrade	Soil	200	60	0.4	2400

Note: AC refers to asphalt concrete; PPM refers to prefabricated plastic module; CTM refers to cement treated macadam; CTS refers to cement treated soil.

3 FINITE ELEMENT MODELLING

This work employed a single tire moving load as the traction boundary condition. The contact pressure was set as 0.7 MPa and the vehicle speed was set as 20 m/s. The tire-road contact area was simplified as a square with a 20 cm side length. Currently, all the material models were assumed to be isotropic linear elastic. Figure 2 shows the model geometry and boundary conditions.

Front and back: U(y)=0
Left and right: U(x)=0
Bottom: U(x)=U(y)=U(z)=0
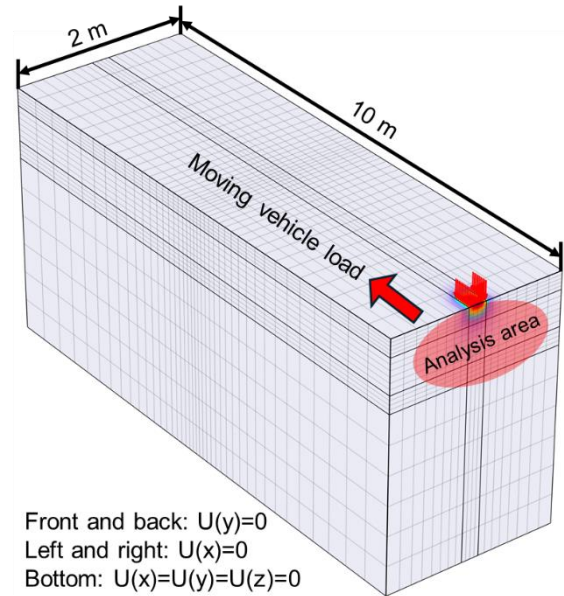
Figure 2. Pavement FE model.

The following presents the governing equations for the initial-boundary value problem (IBVP) in the pavement response FE modelling. It should be noted that Rayleigh damping is used for each layer of material in this dynamic analysis, and the coefficients were selected as 1.04 (α_{dM}) and 5.59e-3 (β_{dK}). More details regarding the pavement FE modelling can refer to the authors' previous work (Zhang *et al.* 2024).

Equilibrium equation:

$$\rho \frac{\partial^2 \boldsymbol{u}}{\partial t^2} + \alpha_{dM}\rho \frac{\partial \boldsymbol{u}}{\partial t} = \nabla \cdot \left(\boldsymbol{\sigma} + \beta_{dK} \frac{\partial \boldsymbol{\sigma}}{\partial t}\right) + \boldsymbol{F_V} \qquad (1)$$

where ρ is the density; t is the loading time; $\boldsymbol{u}$ is the displacement vector; $\boldsymbol{\sigma}$ is the second-order stress

tensor, F_V is the body force; and α_{dM} and β_{dK} are the coefficients of Rayleigh damping.

Constitutive equation:

$$\sigma = C : \varepsilon \tag{2}$$

where ε is the second-order strain tensor; and C is the fourth-order stiffness matrix.

Kinematic equation:

$$\varepsilon = \frac{1}{2}[(\nabla u)^T + \nabla u] \tag{3}$$

4 RESULTS AND DISCUSSION

In this section, the mechanical analysis is conducted on the central cross-section when the vehicle load precisely aligns with the top of the prefabricated plastic pavement module.

First, the von Mises stress distribution and magnitude are presented in Figure 3 to compare the overall bearing capacity for the semi-rigid base pavement structures with asphalt concrete and three types of plastic modules. As can be seen, the hollow structure of prefabricated pavement module hinders the stress dispersion from the road surface to the underlying layers and thus, the maximum magnitude of von Mises stress is almost twice that of normal asphalt pavements and occurs at the joints of two modules. However, this adverse stress distribution can be optimised by adding supports within the hollow structures, as shown in the results of Type II and Type III modules. The highest stress is localised at the edges of joint, and the overall stress dramatically decreases compared to the results of Type I structure. Further, the maximum stress is still much lower than the typical strength (higher than 2 MPa) of solid plastics and it is unlikely to result in strength failure.
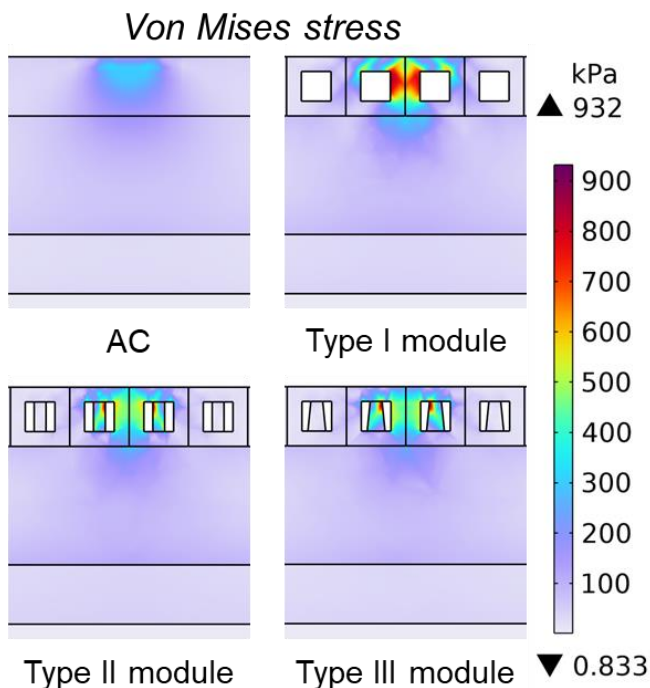
Figure 3. Comparison of von Mises stress.

For a typical semi-rigid base pavement structure, the transition of compression-tension usually occurs at the semi-rigid base due to its relatively greater thickness and modulus. Thus, the mechanical analysis should focus on the vertical stress of the AC layer and the tensile stress of the semi-rigid base. Figure 4 shows the comparison of vertical stress. As can be seen, the Type I structure has the highest vertical stress distributed through the joint of two modules. With the cylinder and cone supports, the vertical stress of Type II and Type III structures is similar to the traditional asphalt concrete layer, although there are still some stress concentrations at the sharp edges.
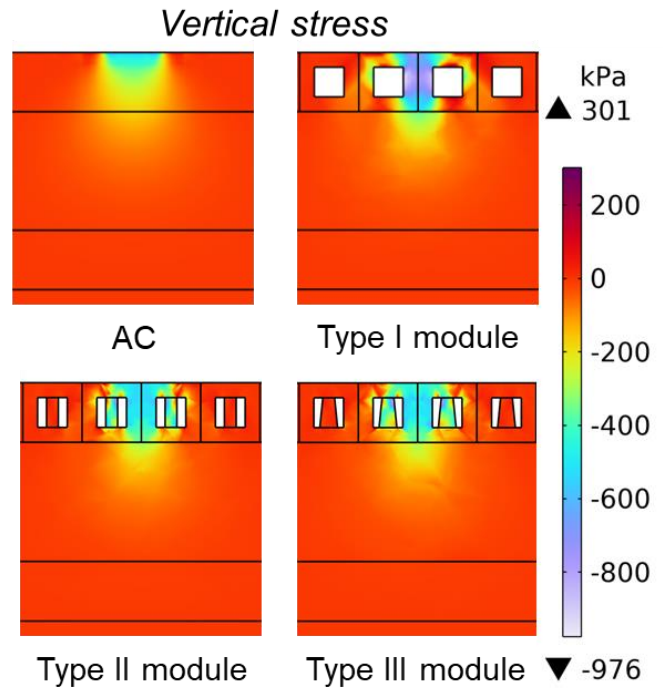
Figure 4. Comparison of vertical stress.

Figure 5 shows the comparison of the tensile stress along the moving load direction. Compared to the traditional pavement structure, the tensile stress at the bottom of the base layer of the Type I and Type II structures is relatively higher, while the Type III structure shows a similar tensile stress value when compared to the asphalt concrete structure. Moreover, higher tensile stress is found at the bottom of the top half-structure for those prefabricated modules, particularly for Type I structure. This phenomenon arises due to the bending characteristics of beam structures. The modules with supports can optimise this phenomenon by localising the high tensile stress at the joints.

In addition to analysing these stress distributions, Figure 6 shows the comparison of the tensile strain along the moving load direction. The tensile strains for the three types of plastic modules are much higher than those in the asphalt concrete due to their relatively lower modulus. The structures of Type II and Type III modules can reduce the areas with large deformations. Although the maximum strain under a single vehicle load would not reach the failure strain

of plastics, whether or not there would be fatigue failure requires further investigations.
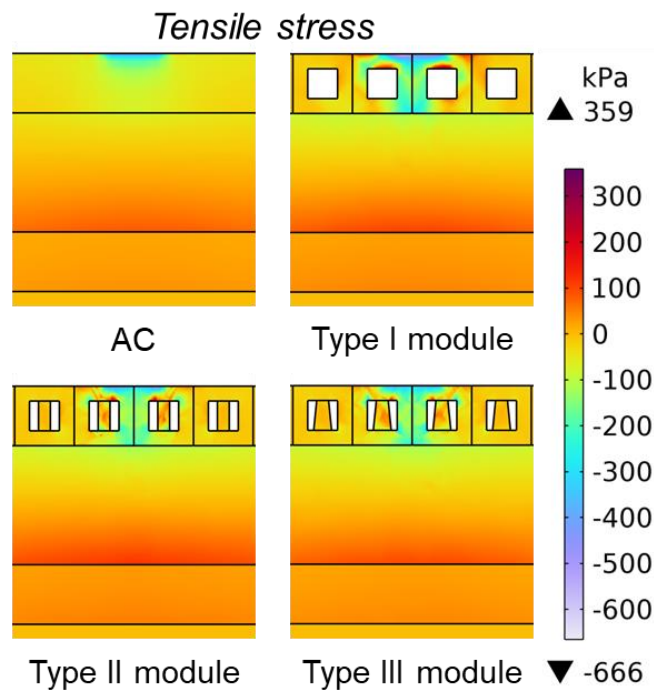
Figure 5. Comparison of tensile stress.
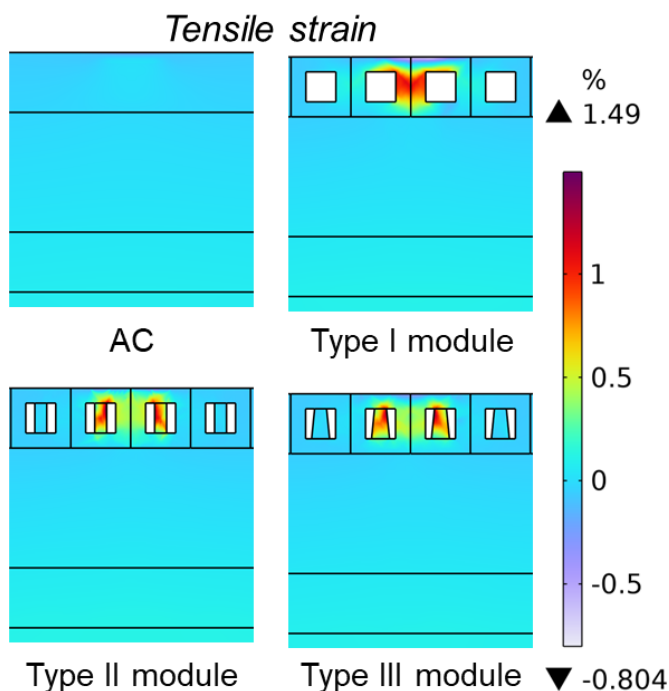
Figure 6. Comparison of tensile strain.

5 CONCLUSIONS AND RECOMMENDATIONS

This paper compares the mechanical responses of different types of prefabricated plastic pavement modules with traditional asphalt pavement structures, aiming to optimise their structural design. The major conclusions are as follows:

- The stress and strain in the prefabricated plastic module are higher than those in the asphalt concrete layer due to the hollow structure and its relatively lower modulus.
- Replacing asphalt concrete with the prefabricated plastic module would not affect the mechanical responses of the layers below the surface layer.
- The stress distribution can be optimised by adding supports within the hollow structure.
- The prefabricated plastic pavement modules are unlikely to experience strength failure according to this case study.

More structural designs with different types of support are needed in future work. In addition, a more realistic material model (e.g., elasto-plastic) is required, along with the model parameter calibration. More importantly, the screening of joint materials and designs is critical to further optimising the stress distribution and dispersion in the prefabricated plastic pavement modules.

6 ACKNOWLEDGMENTS

7 REFERENCES

Abdy, C., Zhang, Y., Wang, J., Cheng, Y., Artamendi, I., and Allen, B., 2023. Investigation of high-density polyethylene pyrolyzed wax for asphalt binder modification: Mechanism, thermal properties, and ageing performance. *Journal of Cleaner Production*, 405.

Assogba, O.C., Tan, Y., Sun, Z., Lushinga, N., and Bin, Z., 2021. Effect of vehicle speed and overload on dynamic response of semi-rigid base asphalt pavement. *Road Materials and Pavement Design*, 22 (3), 572–602.

Guo, J., Chan, T.M., and Wang, Y., 2024. Precast concrete pavement applications, design and joint load transfer characteristics. *Structures*, 69.

Wavin, 2018. The world's first plastic road opens in the Netherlands [online]. Available from: https://blog.wavin.com/en-gb/plastic-road-launch [Accessed 28 Nov 2024].

You, L., Long, Z., You, Z., Ge, D., Yang, X., Xu, F., Hashemi, M., and Diab, A., 2022. Review of recycling waste plastics in asphalt paving materials. *Journal of Traffic and Transportation Engineering (English Edition)*, 9 (5), 742–764.

Zhang, H., Airey, G., and Zhang, Y., 2024. Temporal Homogenization Modeling of Viscoelastic Asphalt Concretes and Pavement Structures under Large Numbers of Load Cycles. *Journal of Engineering Mechanics*, 150 (11).

7.2

AI AND MACHINE LEARNING TECHNOLOGIES IN PAVEMENT ENGINEERING AND PERFORMANCE PREDICTION

A comparative analysis of machine learning models for predicting faulting in jointed plain concrete pavements

T. Ahmed, M. Isied, M.I. Souliman
The University of Texas at Tyler, Tyler, Texas, The United States

ABSTRACT: Faulting is defined by variations in elevation at transverse joints in Jointed Plain Concrete Pavements resulting from environmental factors, subgrade properties, and traffic loads. It is a major distress for rigid pavements, possessing crucial challenges for maintaining road safety standards. Traditional regression methods often fail to address the complexities of faulting, while machine learning approach utilizes data driven learning to enhance prediction accuracy. Datasets for this study were sourced from the LTPP database, focusing on dry climate zones. Key environmental factors affecting wheel path faulting include Yearly Precipitation, Temperature, Freeze-Thaw Cycles, along with structural properties such as Pavement Thickness, Pavement Age, Tensile Strength, and Optimum Moisture Content are utilized as model input. Five machine learning methodologies, including Support Vector Machine, Decision Tree, Linear Discriminant Analysis, Ensemble and Artificial Neural Network were implemented. Among these, ANN demonstrated highest prediction accuracy, attaining an R^2 of 0.81. The ANN model was further evaluated to assess the influence of the input variables on the model output through sensitivity analysis.

1 LITERATURE REVIEW

Faulting is a major issue in jointed concrete pavements (JCPs). Many prediction models are being developed for predicting fault failure. In the AASHTO 1993 version of the pavement design guide, faulting and cracking were accounted for by maintaining and serviceability above a defined threshold. In the 1990s, Simpson et al. attempted to separate these two concerns and forecast faults independently based on pavement design, traffic, weather conditions (Simpson *et al.*, 1994). In recent years various studies suggested that faulting in rigid pavements, particularly in Jointed Plain Concrete Pavement (JPCP), is influenced by a multitude of factors that span structural, environmental, and design considerations (Hossain, Gopisetti and Miah, 2019; Ehsani, Moghadas Nejad and Hajikarimi, 2023; Ahmed, Isied and Souliman, 2024). Traffic loads and the cumulative effect of axle load distributions are significant contributors, as they induce stress and deformation in the pavement layers, particularly affecting the base layer's plastic deformation (Chen, Saha and Lytton, 2020). Most of the prediction models used the LTPP database in which Faulting data include faulting measurements at doweled and non-doweled joints and some measurements at transverse crack locations. Ehsani et al. used both artificial neural and random forest methods with 19 input variables to develop a prediction model (Ehsani, Moghadas Nejad and Hajikarimi, 2023). Ker et al. developed a prediction model for transverse joint faulting incorporating the ERESBACK 2.2 program for back calculation to get more accurate data (Ker, Lee and Lin, 2008). The mechanistic-empirical erosion-based faulting model incorporated traffic parameters with the application of erosion test showed the correlation between traffic and environmental factors with faulting (Jung and Zollinger, 2011). The current faulting model integrated into the Pavement ME design procedure considers pavement response, climatic conditions, traffic, and base erodibility. This model is uniformly applied to all types of jointed concrete pavements, regardless of their structural makeup (such as conventional concrete pavement, unbonded concrete overlay, bonded concrete overlay, etc.). This suggests that the pumping mechanism is assumed to be consistent across all pavement structures. Furthermore, it assumes uniformity in the rate of faulting development and the maximum faulting regardless of pavement structure. The focus of this study is to build an ANN model capable of predicting faulting for dry regions by incorporating both structural and environmental variables of JPCP.

2 OBJECTIVES

The main objective of this research is to explore the potential of machine-learning approaches mainly neural network base models for the JPCP faulting prediction. Datasets are collected from LTPP to train the model for the dry climatic zone in the US. Additionally, to confirm the internal relationship among input parameters and their corresponding output results, a sensitivity analysis on the best model was evaluated.

3 DATA COLLECTION, SELECTION, AND PROCESSING

For training the neural network model data sets are collected from The LTPP database. The LTPP program regularly collects joint and crack faulting data at each jointed concrete pavement test site using the Georgia Fault Meter (GFM) . Figure 1 shows the diagram for GFM faulting measurement.
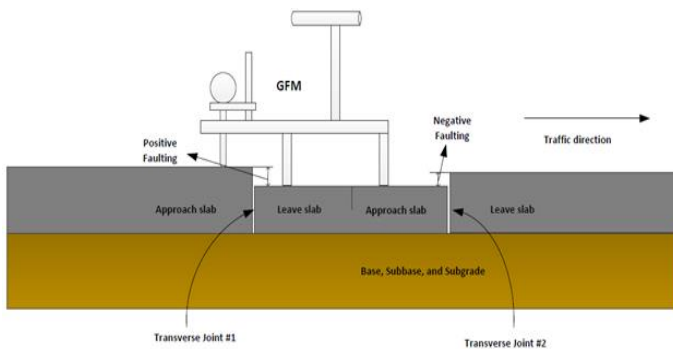
Figure 1. Diagram of manual Faulting measurement using the GFM. (Source: FHWA).

The faulting measurements over 30 years of lifespan at the wheel path for the Dry-Freeze and Dry No-Freeze climate regions subjected to this study are shown in Figure 2. A total of 190 observations in 8 states are fed into the models.
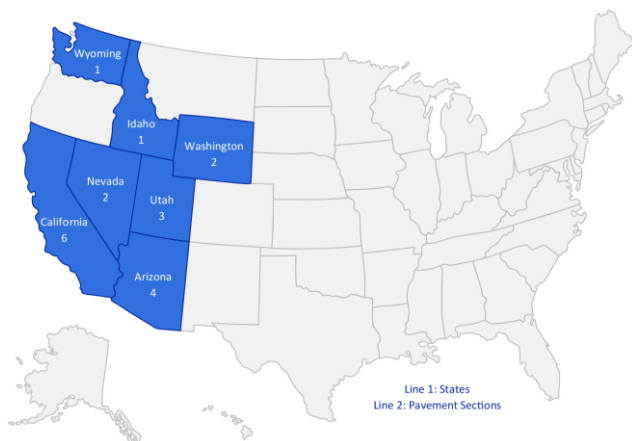
Figure 2. Study Area Containing States with observations numbers in Dry Climatic region.

The prediction models require the normalization of datasets before the training phase. The maximum, minimum, average, and standard deviation of the training dataset are outlined in Table 2. These statistical values are subsequently employed in the equation formulation process. The ESAL ranges significantly, with a high standard deviation (501,379) indicating a wide range of traffic loads are taken into consideration while developing forecast models.

Table 1. Descriptive Statistics of the Model Training Data.

Inputs	Minimum	Maximum
ESAL	1995922	1887
Annual Precipitation (mm)	785.7	70.2
Annual Average Temp (°C)	19	5.3
FT Cycle (days)	195	12
Tensile Strength (psi)	846	471
Pavement Thickness (mm)	11.7	8.1
Pavement Age (yr)	39	1
Optimum Moisture Content (%)	14	2
Inputs	Average	Standard Deviation
ESAL	698061	501379
Annual Precipitation (mm)	269.72	132.02
Annual Average Temp (°C)	10.59	2.15
FT Cycle (days)	116.18	41.25
Tensile Strength (psi)	691.78	127.11
Pavement Thickness (mm)	9.34	0.88
Pavement Age (yr)	21.6	9.13
Optimum Moisture Content (%)	7.87	3.71

The database included four environmental and four structural factors which are shown in Figure 3.
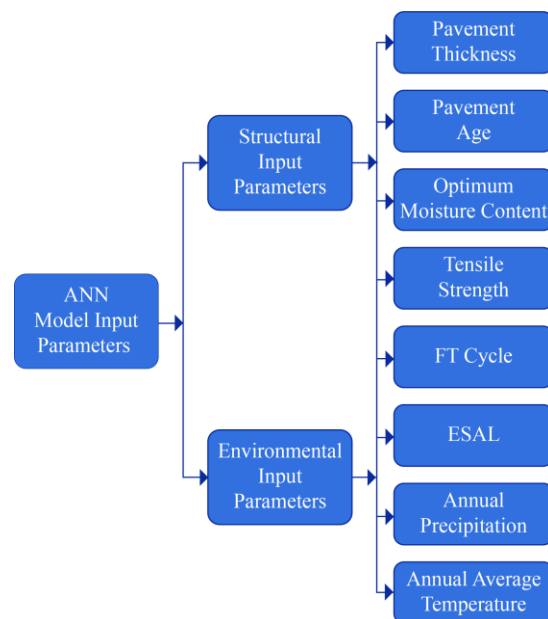
Figure 3. Input Variables for ANN model training.

The linear regression analysis demonstrates the correlation between the input and output parameters, which was subsequently assessed through the correlation heatmap illustrated in Figure 4. The variable

ESAL and the thickness of the pavement exhibit highest positive correlation, attaining a value of 0.5. In contrast, the annual mean temperature displays a considerable negative correlation (-0.74) with the occurrence of faulting, thereby signifying a strong inverse relationship between the two variables.
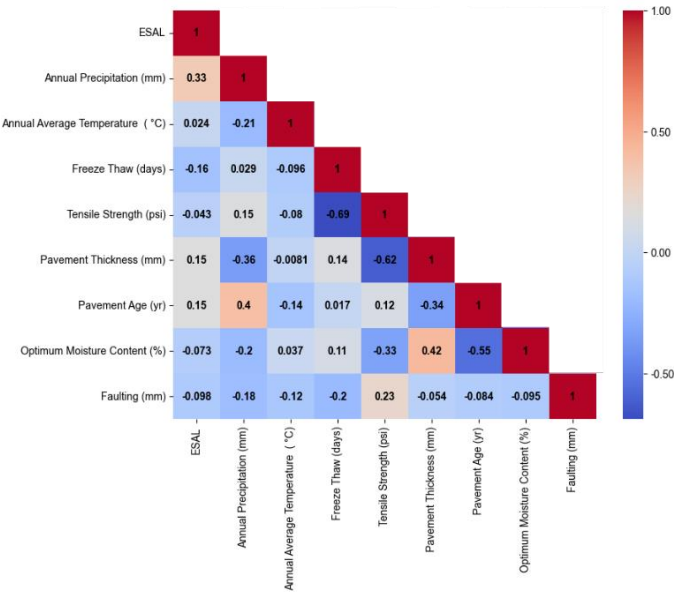
Figure 4. Correlation heatmap between input parameters and output parameters.

4 FAULTING PREDICTION MACHINE LEARNING MODEL DEVELOPMENT

In the field of forecasting models, significant progress has been made with the introduction of Machine learning as a computational model. These networks are inspired by the workings of neurons in the human brain, and they leverage learning algorithms that can adapt and improve as new data is collected. As a result, they are particularly effective at modeling nonlinear statistical data.

Five machine learning models: Artificial Neural Network (ANN), Decision Tree, Linear Discriminant Analysis (LDA), Ensemble, and Support Vector Machine (SVM) were developed to forecast faulting. The coefficient of determination (R^2) of all the developed models are depicted in Table 2.

Table 2: coefficient of determination (R^2) of all the prediction models.

Prediction Model	Coefficient of Determination (R^2)
Artificial Neural Network (ANN)	0.81
Decision Tree	0.58
Linear Discriminant Analysis (LDA)	0.41
Ensemble	0.62
Support Vector Machine (SVM)	0.43

The ANN model achieved the highest R^2 value (0.81), signifying its competence in capturing the intricate and nonlinear relationship of input parameters associated with faulting, attributable to its adaptability in modeling. The Ensemble model exhibits moderate performance with an R^2 of 0.62, gaining advantages from the clustering capabilities of multiple predictive outputs, although it lacks the depth of ANN's feature extraction. The Decision Tree and SVM models showed relatively lower R^2 values of 0.58 and 0.43, respectively, likely due to their limitations in handling nonlinear or noisy data. LDA underperforms with the lowest R^2 of 0.41, reflecting the inadequacy of a linear approach for this problem. Overall, these findings underscore the premise that nonlinear models, especially ANN, are more suitable for faulting prediction, as they can capture the underlying complexity of pavement faulting behavior in JPCP. Figure 5 represents the regression plots of all
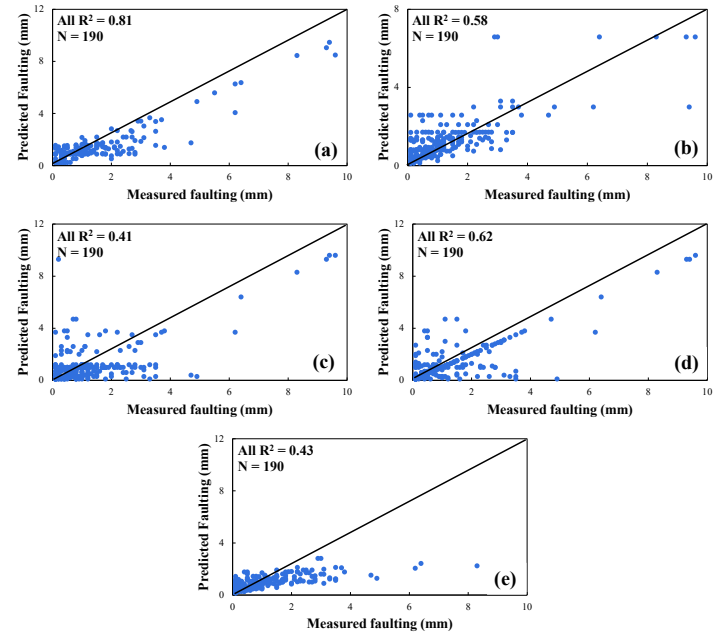
the forecast models.

Figure 5. Regression plots of the prediction model's output - (a) Artificial Neural Network, (b) Decision Tree, (c) Linear Discriminant Analysis, (d) Ensemble and (e) Support Vector Machine.

5 SENSITIVITY ANALYSIS OF THE DEVELOPED ANN MODEL

To investigate how an individual input variable is related to the output, the change of predicted faulting vs the change of a single input variables is plotted for the ANN model. The sensitivity analysis presented in Figure 6 illustrates the principal factors influencing the faulting model in rigid pavement structures. The variables of traffic load (ESAL), temperature, and precipitation exhibit a positive correlation with faulting, thereby indicating that traffic volumes, elevated temperatures, and increased rainfall intensify pavement faulting. The structural attributes of the JPCP, including tensile strength and thickness, serve to

mitigate faulting, thereby implying that pavements exhibiting greater strength and thickness demonstrate enhanced resilience. Freeze-thaw cycles and pavement age also contribute to higher faulting, reflecting the impact of environmental stresses and aging on pavement degradation. Moreover, an elevated optimum moisture content amplifies the occurrence of faulting, highlighting the critical need for moisture regulation. These results suggest that faulting prediction models should prioritize traffic, environmental conditions, and structural factors to improve predictive accuracy.
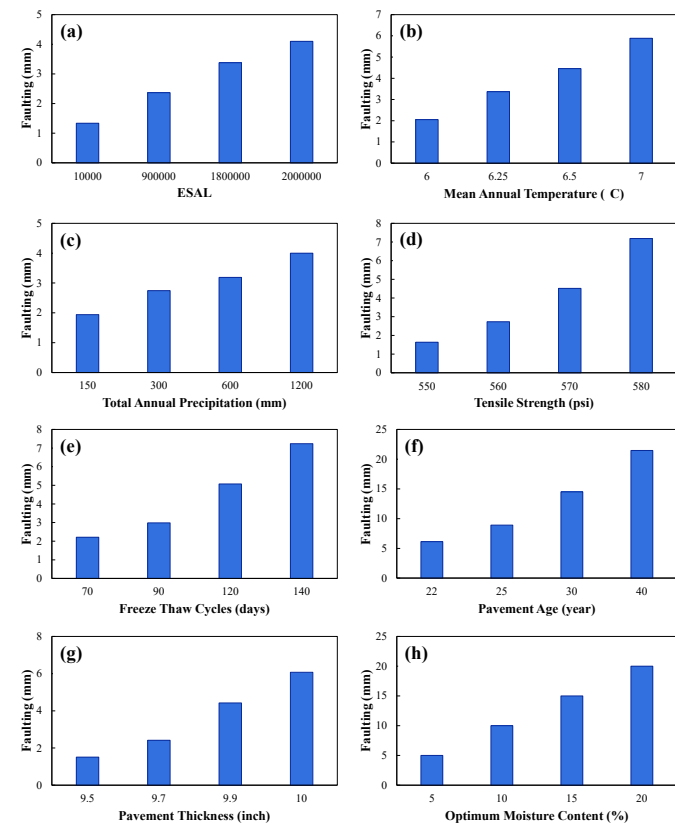
Figure 6. Sensitivity Analysis of predicted faulting (mm) with the change of each input variable - a) ESAL, b) Annual Mean Temperature, c) Total Annual Precipitation, d) Tensile Strength, e) Freeze-Thaw Cycle, f) Pavement Age, g) Pavement Thickness, h) Optimum Moisture Content.

6 CONCLUSIONS

With the help of machine learning approach, prediction model for faulting in Rigid Pavements for Dry-Freeze and Dry No-Freeze Climatic Zone was developed. For training the ANN model, 190 observations over the 30 years of lifespan were evaluated. Based on literature reviews four structural and four environmental parameters were selected which are ESAL, Annual Precipitation (mm), Annual Average Temp (°C), FT Cycle (days), Tensile Strength (psi), Pavement Thickness (mm), Pavement Age (yr), Optimum Moisture Content (%). By incorporating these environmental, structural, and traffic elements, the model aims to anticipate faulting in rigid pavements in dry regions. The conclusions and suggestions in the following bullets are based on the analysis and study findings:

1. In the present study, five Machine learning based faulting models are created. In training, and testing, the model's performance for making predictions was comparable.

2. Among all the developed models, ANN achieved the highest prediction accuracy with a R^2 of 0.81 followed by Ensemble and Decision Tree with a R^2 of 0.62 and .58 respectively.

3. Based on the Sensitivity analysis among all the input variables, thickness, and tensile strength have a major effect on the faulting mitigation of rigid pavements. On the other hand, temperature and precipitation and Freeze-thaw cycles intensify JPCP faulting.

4. As all the model input parameters are presented. Future users will be able to reproduce the models and utilize them for different regions.

7 REFERENCES

Ahmed, T., Isied, M. and Souliman, M.I. (2024) 'Artificial neural network-based investigation of factors impacting faulting in rigid pavements for dryfreeze and dry no-freeze climatic zone', *Material Science & Engineering International Journal*, 8(3), pp. 77–81. Available at: https://doi.org/10.15406/mseij.2024.08.00240.

Chen, Y., Saha, S. and Lytton, R.L. (2020) 'Prediction of the pre-erosion stage of faulting in jointed concrete pavement with axle load distribution', *Transportation Geotechnics*, 23, p. 100343. Available at: https://doi.org/https://doi.org/10.1016/j.trgeo.2020.100343.

Ehsani, M., Moghadas Nejad, F. and Hajikarimi, P. (2023) 'Developing an optimized faulting prediction model in Jointed Plain Concrete Pavement using artificial neural networks and random forest methods', *International Journal of Pavement Engineering*, 24(2), p. 2057975. Available at: https://doi.org/10.1080/10298436.2022.2057975.

Hossain, M.I., Gopisetti, L.S.P. and Miah, M.S. (2019) 'International Roughness Index Prediction of Flexible Pavements Using Neural Networks', *Journal of Transportation Engineering, Part B: Pavements*, 145(1), p. 04018058. Available at: https://doi.org/10.1061/JPEODX.0000088.

Jung, Y. and Zollinger, D. (2011) 'New laboratory-based mechanistic-empirical model for faulting in jointed concrete pavement', *Transportation Research Record*, (2226), pp. 60–70. Available at: https://doi.org/10.3141/2226-07.

Ker, H.-W., Lee, Y.-H. and Lin, C.-H. (2008) 'Development of faulting prediction models for rigid pavements using LTPP database', *Statistics*, 218(0037.0), pp. 30–37.

Simpson, A.L. et al. (1994) *Sensitivity analyses for selected pavement distresses*, *Transportation Research Board Annual Meeting*.

Exploring Machine Learning Approaches for Resilient Modulus in Rejuvenated Reclaimed Asphalt Pavement

Mohammad Farhad Ayazi
Research Scholar, Civil Engineering Department, Punjabi University, Patiala 147002, India

Maninder Singh
Assistant Professor, Civil Engineering Department, Punjabi University, Patiala 147002, India

Rajiv Kumar
Scientist, Flexible Pavement Division, CSIR- Central Road Research Institute, New Delhi 110025, India

1 INTRODUCTION

Machine learning (ML), a dynamic subset of artificial intelligence (AI), emphasizes creating algorithms that can learn and improve autonomously from data without being explicitly programmed. These algorithms process extensive datasets to uncover patterns, trends, and correlations, enabling them to make predictions or decisions based on the insights they gain (Khuntia et al., 2014). As ML systems are exposed to new data, their predictive accuracy and performance evolve over time. The adaptability and broad applicability of ML make it valuable in numerous fields such as healthcare, finance, marketing, and beyond. It empowers automation, enhances efficiency, and extracts insights from data that might elude human analysis. Consequently, ML has the potential to transform industries and foster innovation by leveraging the untapped value embedded in vast data repositories (Goel et al., 2022).

In recent years, the adoption of ML techniques in transportation engineering has garnered significant attention and is set to revolutionize the field in various aspects (Uwanuakwa et al., 2020). For instance, in the performance of asphalt mixtures, ML offers considerable potential for delivering accurate and dependable predictions regarding material behavior, performance characteristics, and failure mechanisms.

The resilient modulus (MR) of asphalt is a critical parameter used to evaluate its elastic behavior under repeated loading, providing insight into its performance and durability in pavement structures. Conducting experimental studies to determine MR requires sophisticated and costly laboratory setups, including advanced testing equipment and precise control of variables such as temperature, load frequency, and specimen preparation (G. Shafabakhsh & Tanakizadeh, 2015). These challenges make experimental determination of MR a complex and resource-intensive process. However, to overcome such limitations, researchers increasingly opt for ML techniques as an alternative. ML offers a cost-effective and efficient approach to predict MR by using existing experimental data, thereby bypassing extensive physical testing but maintaining a high degree of accuracy in the predictions.

Many studies on asphalt pavement utilized machine learning technique-based approaches such as Artificial neural Network (ANN) and support vector machines (SVM) methods towards performance prediction and simulation through different scenarios that have similarly been concerned with parameters, such as temperatures and loadings due to traffic conditions (Gulisano et al., 2024). Zhang et al. (2021) used ML methods, specifically SVM and genetic programming (GP), for the prediction of Marshall parameters in flexible pavement base and wearing courses by using the data obtained from four different road sections located in Pakistan. Results show that SVM presents higher prediction accuracy than GP (R > 0.85) whereas GP presents a validated empirical formulation for a practical estimation of Marshall parameters (Zhang et al., 2021). Similarly, study by Shafabakhsh et al. (2021) utilized ANN for performance predicting of pavements in terms rutting (G. H. Shafabakhsh et al., 2015). Other studies have been related to the use of deep learn-ing techniques to overcome limitations imposed by data. Bongjun et al. (2023) proposed a Bayesian deep learning framework for prediction of asphalt binder rheological properties using Atomic Force Microscopy images and Dynamic Shear Rheometer tests with improvements in prediction accuracy, reduction of testing time, operator-independent test results, and uncertainties. (Ji et al., 2023). ML has similarly been used to model the effects of rejuvenators and modifiers on asphalt, mostly in reclaimed asphalt pavement (RAP) mixtures (). Additionally, studies like those by Ayazi et al. (2024) employed ML techniques to estimate the effects of rejuvenators on the mechanical properties of RAP, targeting to optimize the mix design for enhanced performance (Ayazi et al., 2024). In addition, deep learning methods have been increasingly applied to overcome the limitations of data in RAP aggregates performance prediction. Atakan et al. (2024) showed the role of aggregate surface area (ASA) and number of aggregates (NA) in ML models for hot-mix asphalt de-sign. The study showed that gradation inputs alone were sufficient for accurate predictions, with R^2 values up to 0.99, indicating that gradation is the most important feature (Atakan et al., 2024).

The aim of this research is to investigate the possibility of ML techniques in predicting the MR of asphalt mixtures that contain different percentages of RAP, modified with rejuvenators. The dataset for this study was obtained from an experimental analysis where asphalt mixes containing RAP contents ranging from 0% to 100% were tested at different temperatures (25°C, 35°C, and 45°C) to measure the MR value. This research study shall focus on applying ML models viz. Random Tree (RT), KNN, ANN, GP to predict the values of MR against the experimental data. This set of ML models trained on the dataset so as to identify the inter-relations between RAP content and rejuvenator usage, Temperature, and other input variables with MR values.

2 METHODLOGY

2.1 Data Collection and Experimental Setup
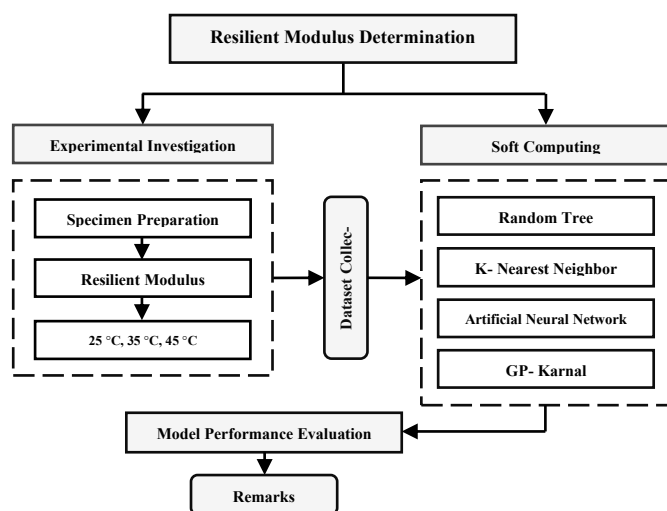
Figure 1. Adopted methodology flow chart

Experimental data for this study were collected through laboratory tests, where asphalt mixes were prepared with RAP content ranging from 0% to 100% as per ASTM D-6927 (ASTM-D6927, 2015). Rejuvenators were added to the mixtures to assess their impact on the mechanical properties of the asphalt. Three temperature conditions were chosen for testing: 25°C, 35°C, and 45°C, representing typical environmental conditions encountered in pavement engineering. The resilient modulus of each mix was determined using a repeated load test as per ASTM D-7369, following established procedures for measuring asphalt's elastic properties under different loading conditions. The dataset was divided into two parts: a training set (70%) and a testing set (30%) to evaluate model generalizability. The main features included RAP content, rejuvenator dosage, and test temperature, while the target variable was MR value. Once trained, the machine learning models were tested on the unseen testing dataset. The predicted

MR values were compared with the experimentally measured MR values to evaluate the accuracy and reliability of each model. The results were analyzed to determine which model provided the best predictions, and how well the models could generalize to new, unseen data.

2.2 Machine Learning Models

To predict the resilient modulus (MR) values, four machine learning models were employed: Random Tree (RT), k-Nearest Neighbor (KNN), Artificial Neural Network (ANN), and Gaussian Process (GP). These models were selected for their proven ability to handle complex and non-linear relationships inherent in the behavior of asphalt mixtures. RT is a decision-tree-based algorithm that has been known for its interpretability and efficient handling of structured data (Gul et al., 2022; Mirzahosseini et al., 2011; G. H. Shafabakhsh et al., 2015; Shah et al., 2020). KNN, a non-parametric approach, predicts outputs based on the nearest neighbors in the dataset, making it effective for capturing localized patterns. ANN, inspired by biological neural systems, models highly non-linear relationships through interconnected layers of nodes optimized iteratively. GP is a probabilistic approach that makes predictions with associated uncertainty measures, which is useful in scenarios where the dataset is very small or reliability is very important. These models were assessed using statistical performance metrics: CC, MAE, RMSE, RAE, and RRSE, thereby ensuring that the predictions made are robust and accurate.

3 RESULT AND DISCUSSION

As presented in table 1, in the training phase, KNN emerged as the best-performing model, achieving a perfect correlation coefficient (CC) of 1, the lowest mean absolute error (MAE) of 4.4056 MPa, and the lowest root mean square error (RMSE) of 6.0069 MPa. Additionally, it exhibited minimal relative absolute error (RAE) and root relative squared error (RRSE) at 0.2416% and 0.2919%, respectively. RT followed closely with an almost perfect CC of 0.9999, MAE of 12.5389 MPa, and RMSE of 22.5289 MPa. Although the RAE and RRSE values for RT were slightly higher at 0.6875% and 1.0947%, its performance remained strong. ANN also demonstrated good performance with a CC of 0.999, but its error metrics, including an MAE of 89.7262 MPa, RMSE of 111.1387 MPa, RAE of 4.9198%, and RRSE of 5.4004%, were notably higher than those of KNN and RT. On the other hand, GP with the Karnal kernel showed the lowest

performance during training, reflected by a CC of 0.9934, the highest MAE of 276.4941 MPa, RMSE of 331.7603 MPa, RAE of 15.1606%, and RRSE of 16.1206%.
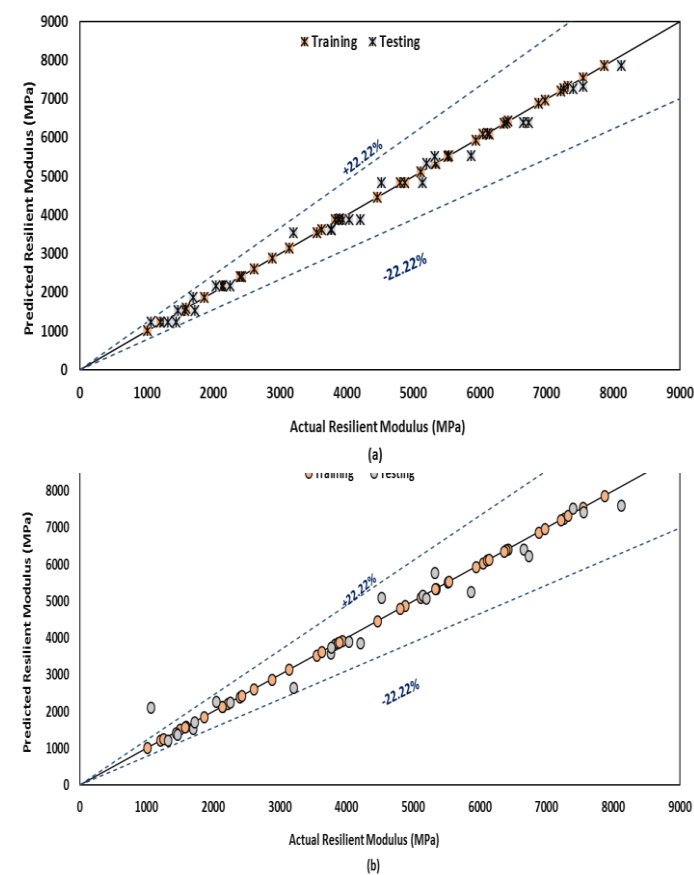
Figure 2. Concordance Plot for Actual vs. Predicted MR of (a) Random Tree (b) K- Nearest Neighbor

The testing dataset revealed some variations in the models' performance. RT maintained its high accuracy with a CC of 0.9958, MAE of 205.4771 MPa, and RMSE of 222.79 MPa, along with relatively low RAE and RRSE values of 10.83% and 10.0833%, respectively. KNN showed a slight decline in performance compared to training, with a CC of 0.9863, MAE of 268.1237 MPa, RMSE of 371.8429 MPa, RAE of 14.1319%, and RRSE of 16.8377%. ANN exhibited strong performance during testing, achieving a CC of 0.9945, the lowest MAE of 180.7487 MPa, and RMSE of 236.9227 MPa, coupled with moderate RAE and RRSE values of 9.5266% and 1.7283%, respectively. Conversely, GP's performance remained relatively low, with a CC of 0.9935 and the highest error metrics: MAE of 315.8525 MPa, RMSE of 350.4324 MPa, RAE of 16.6475%, and RRSE of 15.8682%.
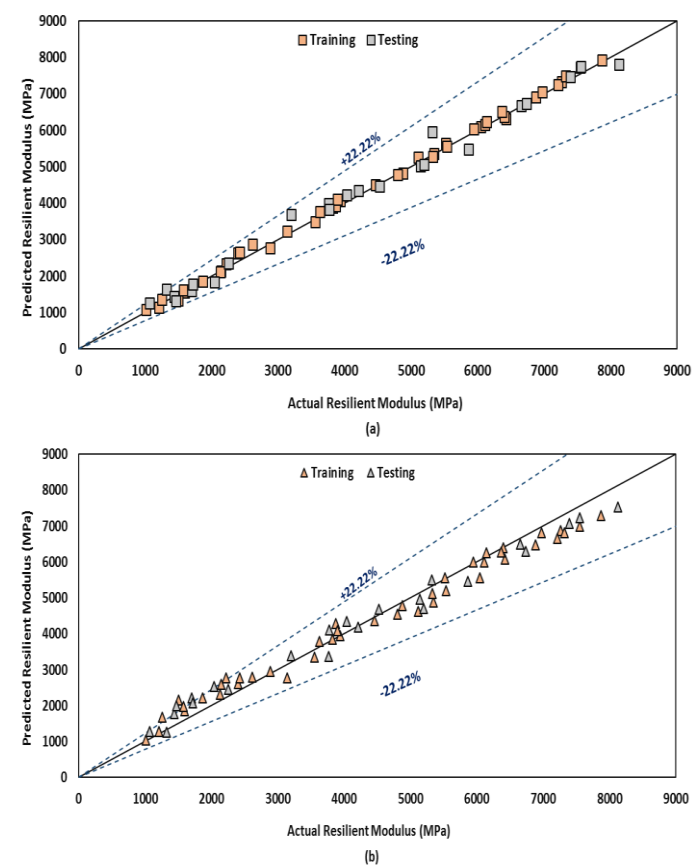
Figure 3. Concordance Plot for Actual vs. Predicted MR of (a) Artificial Neural Network (b) Gaussian Process

Figure 2 (a, b) depict scatter plots of actual versus predicted resilient modulus values for RT and KNN models, respectively, illustrating a strong alignment between actual and predicted values for both models, with KNN demonstrating near-perfect accuracy during training. Figure 3 (a, b) presents similar plots for ANN and GP models, where ANN shows robust performance, particularly in the testing phase, while GP exhibits greater deviation, indicating comparatively lower accuracy. Overall, KNN demonstrated the best performance in the training dataset, achieving perfect accuracy with minimal error metrics, whereas ANN emerged as the most accurate model during testing with the lowest MAE and RMSE values. RT consistently performed well across both datasets, and GP with the kernel lagged behind the other models in terms of prediction accuracy and error metrics. Performance Assessment parameters of all applied models in both training and testing stages are tabulated in table 1. And relative error among actual data and predicted data is presented in figure 5.
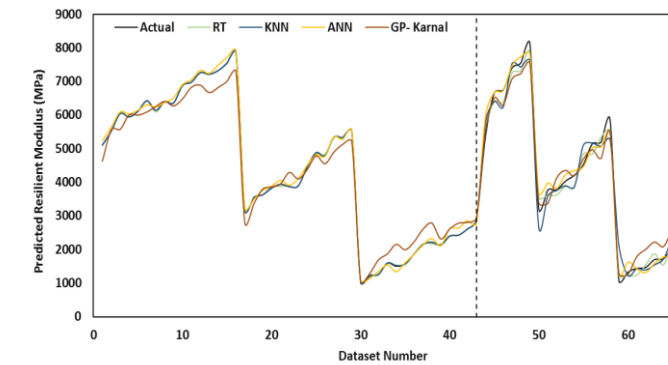
Figure 5. Relative error in both training and testing stages

Table 1. Performance parameters metrics of used models

Models	CC	MAE (MPa)	RMSE (MPa)	RAE (%)	RRSE (%)
Training					
RT	0.9999	12.53	22.52	0.68	1.09
KNN	1	4.40	6.06	0.24	0.29
ANN	0.999	89.72	111.13	4.91	5.40
GP	0.9934	276.4	331.76	15.1	16.12
Testing					
RT	0.9958	205.4	222.79	10.8	10.08
KNN	0.9863	268.1	371.84	14.1	16.83
ANN	0.9945	180.7	236.92	9.52	1.72
GP	0.9935	315.8	350.43	16.6	15.86

4 CONLUSION

This study demonstrates the effectiveness of machine learning models RT, KNN, ANN, and GP—in predicting the MR value of asphalt mixtures. Among these models, KNN emerged as the most reliable during the training phase, achieving perfect accuracy with minimal error rates. ANN performed exceptionally well during the testing phase, offering the lowest error metrics and maintaining high accuracy. RT consistently delivered strong predictive performance across both datasets, proving its robustness. In contrast, the GP model showed relatively lower accuracy, reflecting room for improvement in its predictive capabilities.

These findings highlight the applicability of machine learning techniques in pavement engineering, where accurate predictions of material properties are crucial for design and maintenance. The results underline that selecting an appropriate model depends on the desired balance between accuracy and error tolerance for specific applications.

5 REFERENCES

ASTM-D6927. (2015). Standard Test Method for Marshall Stability and Flow of Asphalt Mixtures, ASTM International, West Conshohocken, PA.

American Society for Testing and Materials, *i*, 1–7. https://doi.org/10.1520/D6927-22.2

Atakan, M., Valentin, J., & Yıldız, K. (2024). Effect of number and surface area of the aggregates on machine learning prediction performance of recycled hot-mix asphalt. *Construction and Building Materials*, *445*(July). https://doi.org/10.1016/j.conbuildmat.2024.137788

Ayazi, M. F., Singh, M., & KUMAR, R. (2024). Prediction and Modelling Marshall Stability of Modified Reclaimed Asphalt Pavement with Rejuvenators using latest Machine Learning Techniques. *Engineering Research Express*. https://doi.org/10.1088/2631-8695/ad65b7

Goel, G., Sachdeva, S. N., & Pal, M. (2022). Modelling of Tensile Strength Ratio of Bituminous Concrete Mixes Using Support Vector Machines and M5 Model Tree. *International Journal of Pavement Research and Technology*, *15*(1), 86–97. https://doi.org/10.1007/s42947-021-00013-5

Gul, M. A., Islam, M. K., Awan, H. H., Sohail, M., Al Fuhaid, A. F., Arifuzzaman, M., & Qureshi, H. J. (2022). Prediction of Marshall Stability and Marshall Flow of Asphalt Pavements Using Supervised Machine Learning Algorithms. *Symmetry*, *14*(11). https://doi.org/10.3390/sym14112324

Gulisano, F., Gálvez-Pérez, D., Jurado-Piña, R., Apaza Apaza, F. R., Cubilla, D., Boada-Parra, G., & Gallego, J. (2024). Towards a more efficient and durable load classifier using machine learning analysis of electrical data generated by self- sensing asphalt mixtures. *Sensors and Actuators A: Physical*, *377*(July). https://doi.org/10.1016/j.sna.2024.115686

Ji, B., Sharma Bhattarai, S., Na, I. H., & Kim, H. (2023). A Bayesian deep learning approach for rheological properties prediction of asphalt binders considering uncertainty of output. *Construction and Building Materials*, *408*(July). https://doi.org/10.1016/j.conbuildmat.2023.133671

Khuntia, S., Das, A. K., Mohanty, M., & Panda, M. (2014). Prediction of Marshall Parameters of Modified Bituminous Mixtures Using Artificial Intelligence Techniques. *International Journal of Transportation Science and Technology*, *3*(3), 211–227. https://doi.org/10.1260/2046-0430.3.3.211

Mirzahosseini, M. R., Aghaeifar, A., Alavi, A. H., Gandomi, A. H., & Seyednour, R. (2011). Permanent deformation analysis of asphalt mixtures using soft computing techniques. *Expert Systems with Applications*, *38*(5), 6081–6100. https://doi.org/10.1016/j.eswa.2010.11.002

Shafabakhsh, G. H., Ani, O. J., & Talebsafa, M. (2015). Artificial neural network modeling (ANN) for predicting rutting performance of nano-modified hot-mix asphalt mixtures containing steel slag aggregates. *Construction and Building Materials*, *85*, 136–143. https://doi.org/10.1016/j.conbuildmat.2015.03.060

Shafabakhsh, G., & Tanakizadeh, A. (2015). Investigation of loading features effects on resilient modulus of asphalt mixtures using Adaptive Neuro-Fuzzy Inference System. *Construction and Building Materials*, *76*, 256–263. https://doi.org/10.1016/j.conbuildmat.2014.11.069

Shah, S. A. R., Anwar, M. K., Arshad, H., Qurashi, M. A., Nisar, A., Khan, A. N., & Waseem, M. (2020). Marshall stability and flow analysis of asphalt concrete under progressive temperature conditions: An application of advance decision-making approach. *Construction and Building Materials*, *262*, 120756. https://doi.org/10.1016/j.conbuildmat.2020.120756

Uwanuakwa, I. D., Ali, S. I. A., Hasan, M. R. M., Akpinar, P., Sani, A., & Shariff, K. A. (2020). Artificial intelligence prediction of rutting and fatigue parameters in modified asphalt binders. *Applied Sciences (Switzerland)*, *10*(21), 1–17. https://doi.org/10.3390/app10217764

Zhang, W., Khan, A., Huyan, J., Zhong, J., Peng, T., & Cheng, H. (2021). Predicting Marshall parameters of flexible pavement using support vector machine and genetic programming. *Construction and Building Materials*, *306*(April), 124924. https://doi.org/10.1016/j.conbuildmat.2021.124924

Prediction of transverse evenness in asphalt using an artificial neural network

J.-H. Borchers
Federal Highway Research Institute (BASt), Germany
TU Braunschweig - Institute for Infrastructure and Real Estate Management, Germany

L. F. D. P. Sotto
Federal Highway Research Institute (BASt), Germany

ABSTRACT: A pivotal aspect of pavement management systems (PMS) and road asset management is the deployment of predictive algorithms for pavement performance. The objective of this paper is to investigate the potential of artificial intelligence (AI) in this process, specifically for predicting transverse evenness, which is represented by rut depth and water depth. Firstly, we describe the condition survey and assessment in Germany. Then an overview of the current methodology for prediction of road condition data and the artificial neural network (ANN) employed in this paper is given. Subsequently, both methods are evaluated on a sub-network and their performances are compared, with the employed ANN showing an improved prediction performance.

1 GENERAL INTRODUCTION

1.1 *German motorway network*

Besides being notable for the absence of a speed limit, Germany's motorway network is the second longest in Europe after Spain's (Eurostat 2024). The German motorway network requires the allocation of approx. €3.3 billion in annual maintenance costs (BMDV 2024). The role of civil engineering structures and pavements in this context is of considerable importance. As illustrated in Figure 1, the most prevalent material used for the top layer of pavements in Germany is asphalt.
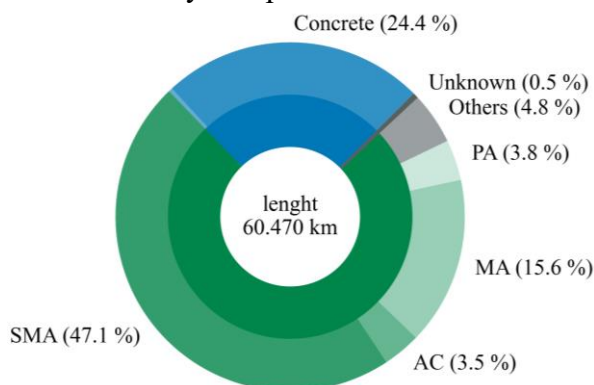
Figure 1. Top layer types at the German motorway network with all lanes (BMDV 2023).

Stone mastic asphalt (SMA) is a widely used asphalt mixture throughout the European Union (EAPA 2018), and it is also the most commonly used in Germany (Fig. 1). Consequently, this paper will focus on the condition of pavements with SMA.

1.2 *Pavement condition monitoring*

To assess the condition of the pavement, characteristics such as rutting, longitudinal evenness, skid resistance and surface damage (such as cracking), are monitored for all German federal motorways and highways with measurement vehicles on a four-yearly basis, resulting in the road monitoring and assessment (ZEB) database (FGSV 2018). The surface damage is monitored by cameras, that produce a surface photograph that can be used to identify cracks as small as 0.5 mm. To ascertain the skid resistance of the road, the widely accepted sideways-force measurement method is employed. Unevenness in the longitudinal and transverse direction is measured using lasers.

Transverse evenness is measured with lasers positioned at the rear of a measuring vehicle. Figure 2 shows the measuring principle with the specified distances for motorways.
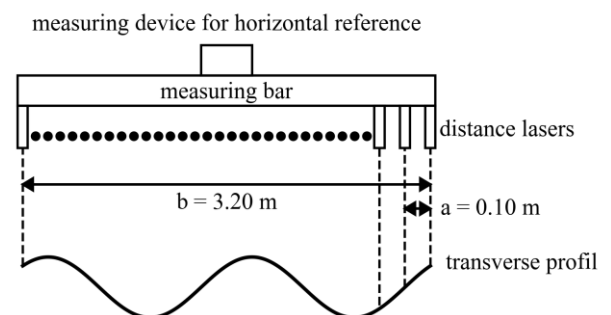
Figure 2. Measuring of transverse evenness (FGSV 2009).

The data points provide a transverse profile from which the rut depth and the water depth of the rut

can be calculated, which together represent the transverse evenness. The rut depth is calculated with a digital 2-metre bar placed over the transverse pavement profile. To determine the water depth, which indicates the depth of the water in the ruts, the transverse slope is considered (Fig. 3).
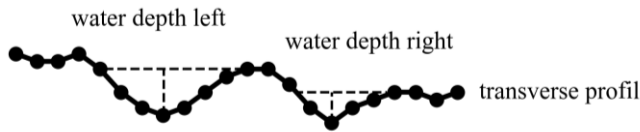
Figure 3. Calculation of the water depth (FGSV 2018).

For asset management purposes, both physical values are converted into dimensionless condition grades, shown in Figure 4.
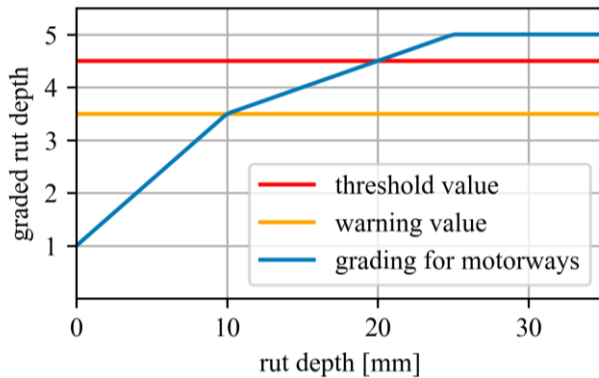
Figure 4. Normalization of rut depth to condition grades between 1 and 5 (higher values are worse) (FGSV 2018).

If the rut depth exceeds 10 mm the warning value is reached and a detailed analysis of the road is required. Structural or traffic measures must be examined when the threshold value of 20 mm is reached (Fig. 4). For water depth, the warning value is 4 mm, while the threshold value is 6 mm.

2 FORECAST ALGORITHM

2.1 Forecast Algorithms

Maerschalk (1997) and Molzer et al. (2000) developed the initial condition prediction models for transverse evenness in German-speaking countries. Both models are based on simple functions with time dependence and factors for traffic load and pavement design. Subsequent research led to the development of models based on axle load, as evidenced by Hinsch et al. (2005). Following a critical review of previous forecasting models by Socina (2007), the Curve-Shifting-Method was developed by Maerschalk & Socina (2008). This Method remains a frequently used approach in Germany today (BMDV 2019).

In the Curve-Shifting-Method, four exponential behavior functions and classes are defined that de-

scribe the degradation of a condition grade over time. Given an actual age and condition grade of a pavement section, the corresponding curve is shifted, as illustrated in Figure 5. This shifted function is then used to predict future condition grades for that section.
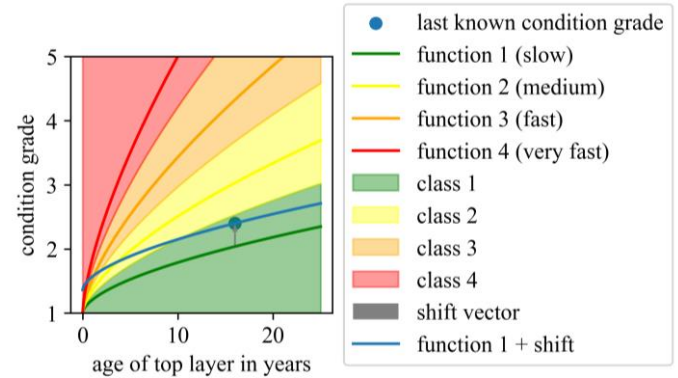
Figure 5. Example of curve-shifting-method for rutting depth.

More recent international research by Choi & Do (2020) or Cheng et al. (2023) attempts to determine the rut depth by considering traffic, climate, structure and maintenance data. In principle, satisfactory results (Choi & Do 2020) are achieved, although the forecast period is sometimes not clearly defined. In the review of Deng & Shi (2023), a survey was conducted on the important qualities of predictive models. Accuracy, reliability and applicability were named as the most important features. In the study, the majority of participants were willing to use a good artificial intelligence (AI) model.

2.2 Neural Network

An Artificial Neural Network (ANN) is a machine learning model that maps inputs (or input neurons) into outputs (or output neurons). Between the input and output layers, there are a number of intermediate, or hidden, layers, composed of a number of neurons. Each neuron calculates a linear transformation taking as input the values of the previous layer, and applying an activation function to the result. Given a set of example input and output instances, the weights that connect each neuron and define the linear transformations are adjusted. This enables the model to learn how to reproduce the examples and generalize to new, unseen data of the same nature. This form of ANN is called a Multi-Layer Perceptron (MLP) (Goodfellow et al. 2016).

There is recent literature on the use of ANNs to predict road condition, for example, with data from the USA and Canada (Cheng et al. 2023, Ali et al. 2024). Not all methods are applicable to a pavement management system (PMS) or trained for long-term predictions.

Here, we evaluate an ANN for condition data from Germany that predicts up to eight years into the future. We use MLP architecture with three input neurons: age of the top layer, condition value for that age, and the age in the future for which we want to predict. The sole output neuron corresponds to the condition value for the desired age. We then add two dense layers, each with 64 neurons, which employ the Rectified Linear Unit (ReLU) activation function. Dropout layers are incorporated after each layer, that randomly set 20 % of the previous layer's output units to zero during training, to add randomness to the process and prevent overspecialization of the model on the training data (Srivastava et al. 2014). A model illustration is shown in Figure 6. The ANN is trained on and predicts condition values. To facilitate comparison with the Curve-Shifting-Method, based on condition grades, the predicted values need to be converted to condition grades (Fig. 4).
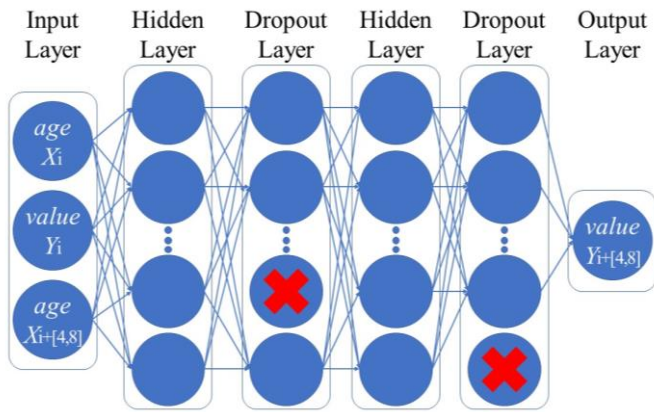
Figure 6. Diagram for used ANN model.

3 COMPARISON BETWEEN ALGORITHMS

3.1 *Experimental Setup*

A network-wide PMS requires a reliable and available data basis. Consequently, we use the existing road monitoring and assessment database with four-yearly intervals for training and evaluating the ANN, as well as for evaluating the Curve-Shifting-Method. The measured condition values for rut depth and water depth between 2013 and 2022 of German Motorways with an SMA top layer were employed as training data. To evaluate both methods the data of the federal state of Hesse was used. One ANN was trained for predicting water depth, and another for rut depth.

The resulting training data set for the ANN comprises approximately 100,000 data points, each describing a 100-meter road section. For each road section, the condition grades from 2013 to 2022 are available in four-yearly intervals. If construction work was carried out in between, these sections were excluded. Similarly, if the condition has improved, it is assumed that the data has been insufficiently maintained and the data is excluded. From this data

basis, data points of the following form are extracted:

$$(age_i, value_i, age_{i+[4,8]}, value_{i+[4,8]}),$$

where age_i and $value_i$ are the age and condition value in year i, whereas $age_{i+[4,8]}$ and $value_{i+[4,8]}$ are the age and value four or eight years after i. The first three values are used as input and the last value as output, so that the model learns to predict a condition value four or eight years into the future based on the current value. The trained model as well as the Curve-Shifting-Method are then evaluated on data of the same structure and the same time interval from the federal state of Hesse, which was excluded in the training data.

For assessing the efficacy of the evaluated prediction methods, we use the R^2 and the RMSE, which measure, respectively, the degree to which the predicted values align with the actual values, and differences between the predicted values and the actual values (Chicco et al. 2021), both applied on the mapped condition grades. For our experiments, we have used the TensorFlow library for Python with a standard scaler, 50 epochs, and a batch size of 32. Further, we have applied early stopping after 4 epochs without improvement (with 20 % of the training data for this validation).

3.2 *Results*

Table 1 shows the obtained R^2 and RMSE for the ANN and the Curve-Shifting-Method for the rut depth, while Table 2 shows the results for water depth. Figure 7 illustrates an example of known versus predicted grades and the corresponding R^2 and RMSE.

Table 1. Performance comparison between the prediction algorithms – graded rut depth.

Algorithms + forecast period	RMSE	R^2
Curve-Shifting (4 years)	0.37	0.54
ANN (4 years)	0.23	0.76
Curve-Shifting (8 years)	0.42	0.50
ANN (8 years)	0.25	0.68

Table 2. Performance comparison between the prediction algorithms – graded water depth.

Algorithms + forecast period	RMSE	R^2
Curve-Shifting (4 years)	0.30	0.62
ANN (4 years)	0.42	0.64
Curve-Shifting (8 years)	0.80	0.27
ANN (8 years)	0.43	0.56

For most cases shown in Tables 1 and 2, both the RMSE and the R^2 indicate that the ANN is an effective tool for achieving satisfactory results and in general superior results when compared to the

Curve-Shifting-Method, which is a current standard approach.

As expected, the reliability of predictions that reach further into the future decreases. However, the ANN performs better than curve shifting, especially for predictions 8 years into the future. For the 4-year scenario, curve-shifting achieves a lower RMSE than ANN for water depth (Tab. 2).
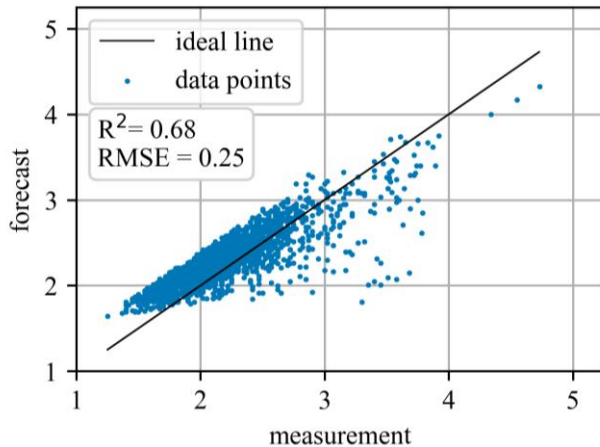
Figure 7. True measurement compared to the ANN forecast for rut depth – 8-year scenario. For each measured value, the predicted value is plotted (blue dots) – an ideal scenario is a linear relation (black line).

It should be noted that the quality of the prediction of rut depth and water depth differ only slightly, which was expected. It seems that both methods can predict rut depth better than water depth. Considering that the ANN was trained on data from other federal states and evaluated on data from Hesse, it is possible that certain conditions are more influenced by local specificities or additional parameters. Taking this into account in future work may lead to an improved prediction performance.

4 CONCLUSION

Overall, this work shows that the application of an ANN provides effective results for the prediction of transverse evenness in asphalt pavements with SMA, already outperforming one of the current methods for predicting road condition. In principle, the ANN can be applied throughout a road network and could also be implemented in a PMS. Future research is required to test the applicability of the ANN for other condition characteristics and for other asphalt mix types. In addition, the quality of the results for federal highways or municipal roads must be tested. It would also be beneficial to ascertain whether the consideration of other influencing variables, such as traffic load, or parameters related to region or asphalt type, would lead to more accurate predictions. Furthermore, other AI models, including gradient boosting and supported vector regression, should be evaluated in comparison to the ANN.

5 REFERENCES

Ali, A. A., Heneash, U., Hussein, A., Khan, S. (2024) Application of Artificial neural network technique for prediction of pavement roughness as a performance indicator, *Journal of King Saud University*, 36, 128-139, https://doi.org/10.1016/j.jksues.2023.01.001

BMDV. 2019, February 21. *Erhaltungsbedarfsprognose für die Bundesfernstraßen*. https://bmdv.bund.de/SharedDocs/DE/Artikel/StB/erhaltungsbedarfsprognose.html

BMDV. 2023, October 2-6. *Road Maintenance Management*. [Poster presentation at German stand]. XXVIIth World Road Congress – Prague, Czech Republic.

BMD. 2024, July 23. *Verkehrsinvestitionsbericht für das Berichtsjahr 2022*. https://bmdv.bund.de/SharedDocs/DE/Anlage/G/verkehrsinvestitionsbericht-2022.pdf

Cheng, C., Ye, C., Yang H., Wang L. (2023). Predicting Rutting Development of Pavement with Flexible Overlay Using Artificial Neural Network. *Applied Sciences*, 13, 7064, https://doi.org/10.3390/app13127064

Choi, S., Do, M. 2020. Development of the road pavement deterioration model based on the deep learning method. *Electronics* 9(1). https://doi.org/10.3390/electronics9010003

Chicco D, Warrens MJ, Jurman G. 2021. The coefficient of determination R-squared is more informative than SMAPE, MAE, MAPE, MSE and RMSE in regression analysis evaluation. *PeerJ Computer Science* 7:e623 https://doi.org/10.7717/peerj-cs.623

Deng, Y., Shi, X. 2023. Modeling the rutting performance of asphalt pavements: a review. *J Infrastruct Preserv Resil* **4**, 17. https://doi.org/10.1186/s43065-023-00082-9

EAPA. 2018. Heavy Duty Surfaces – The Arguments for SMA. Brussels.

Eurostat. 2024, July 31. *Length of motorways and e-roads*. https://doi.org/10.2908/ROAD_IF_MOTORWA

FGSV. 2009. *Technische Prüfvorschriften für Ebenheitsmessungen auf Fahrbahnoberflächen in Längs- und Querrichtung - Teil: Berührungslose Messungen. - TP Eben -Berührungslose Messungen*, Cologne.

FGSV. 2018. *Zusätzliche Technische Vertragsbedingungen und Richtlinien zur Zustandserfassung und -bewertung von Straßen*, Cologne.

Goodfellow, I. J., Bengio, J., Courville, A. (2016). Deep Learning, *MIT Press*.

Maerschalk, G. 1997. *Erstellung einer ablauffähigen Folge von Algorithmen für die Planung von Erhaltungsmaßnahmen und der Mittelverwendung im Rahmen eines PMS* (Bd. Heft 751). Forschung Straßenbau und Straßenverkehrstechnik. Bonn.

Maerschalk, G., & Socina, M. 2008. *Weiterentwicklung der Bewertung des Pavement Management Systems (PMS) um ein Verfahren für die Umsetzung von Qualitätszielen* (Bd. Heft 1001). Forschung Straßenbau und Straßenverkehrstechnik. Bonn.

Molzer, C., Felsenstein, K., Viertl, R., Litzka, J., Vycudil, A. (2000). *Statistische Methoden zur Auswertung von Straßenzustandsdaten (Bd. Heft 499)*. Bundesministerium für Verkehr, Innovation und Technologie – Schriftenreihe Straßenforschung.

Srivastava, N., Hinton, G., Krizhevsky, A., Sutskever, I., Salakhutdinov, R. (2014) Dropout: A simple way to prevent neural networks from overfitting. *Journal of Machine Learning Research* 15, 1929–1958.

Socina, M. (2007). *Erweiterung der Nutzung von Straßenzustandsdaten in der Systematischen Straßenerhaltung* [Dissertation]. Vienna.

Incorporating physics-informed neural networks into yolo for pavement rutting detection

A. Daneshvar

Civil and Environmental Engineering Department, Amirkabir University of Technology, Iran

A. Golroo

Civil and Environmental Engineering Department, Amirkabir University of Technology, Iran
Faculty of Information Technology and Electrical Engineering, University of Oulu, Finland

M. Rasti

Faculty of Information Technology and Electrical Engineering, University of Oulu, Finland

ABSTRACT: Physics-Informed Neural Networks (PINNs) have shown great promise in embedding domain-specific knowledge into machine learning models. This study proposes an enhancement to the YOLO object detection framework by introducing a physics-informed penalty into its loss function for detecting pavement rutting. A dataset of 4880 labeled images was used to train the model, with modifications ensuring predictions adhere to known physical constraints of rutting dimensions and aspect ratios. Experimental results demonstrate improved bounding box accuracy and alignment with domain-specific rules, reducing false positives in critical infrastructure monitoring. This approach highlights the potential of hybrid PINN-YOLO models in civil engineering applications.

1. INTRODUCTION

Pavement rutting, characterized by the formation of longitudinal depressions in the road surface, poses significant challenges to transportation infrastructure. These ruts not only degrade ride quality and increase vehicle maintenance costs but also pose safety hazards for drivers. Accurate and timely detection of rutting is crucial for effective pavement management and maintenance planning. (Erlingsson, 2012)

Pavement rutting, characterized by depressions in the road surface, presents challenges like degraded ride quality, increased vehicle maintenance costs, and safety hazards. Timely detection is crucial for effective pavement management (Erlingsson, 2012).

1.1 Challenges in Pavement Rutting Detection

Traditional methods, such as manual surveys and laser profilometry, are labor-intensive and limited. Computer vision and deep learning offer potential for automation, but challenges include:

- Complex Road Conditions: Variations in texture, color, and lighting due to weather, traffic, and aging impact detection accuracy (Fares et al., 2024).
- Small Object Sizes and Occlusions: Ruts can be small and occluded by vehicles or shadows, making detection difficult (Arezoumand et al., 2021).
- Data Limitations: Acquiring large, diverse labeled datasets is costly, and biases can affect model performance (Shatnawi et al., 2021).
- Real-Time Performance: Deep learning models are computationally demanding, hindering real-time applications (Cao et al., 2021).

1.2 Machine Learning in Pavement Monitoring

Machine learning (ML) is increasingly used for more efficient and accurate pavement monitoring:

- Performance Prediction: ML models predict pavement indicators like rutting depth and cracking, aiding proactive maintenance (Madeh Piryonesi & El-Diraby, 2021; Marcelino et al., 2021).
- Structural Health Monitoring: ML combined with techniques like GPR assesses pavement layer thickness and detects subsurface defects (Fontul et al., 2023).
- Automated Defect Detection: Algorithms like YOLO automate the identification of pavement distresses, reducing the need for manual inspections (Wang et al., 2024; Shahbazi et al., 2021).
- Real-Time Monitoring: Integration with IoT sensors enables real-time monitoring and anomaly detection (Bekiroglu et al., 2021).
- Data-Driven Management: ML techniques inform decision-making regarding maintenance and resource allocation (Cano-Ortiz et al., 2022).

1.3 Integrating Domain Knowledge into Machine Learning

While data-driven ML models can be effective, they often lack interpretability and struggle to generalize. Integrating domain knowledge, particularly physical principles, into ML models offers advantages:

- Limitations of Data-Driven Approaches: Purely data-driven models can overfit and fail to capture the underlying physical processes, limiting accuracy.
- Physics-Informed Machine Learning (PIML): Techniques like Physics-Informed Neural Networks (PINNs) integrate physical laws into the training process, improving generalization and interpretability (Raissi et al., 2019).
- Benefits of PIML: Incorporating physics enhances model generalization, accuracy, and stability while reducing data requirements (Vadyala et al., 2022).
- Applications in Pavement Engineering: PIML is applied to predict pavement response, model material behavior, and forecast distresses such as rutting (Kargah-Ostadi et al., 2024; Deng et al., 2024).

2. METHODOLOGY

2.1 Dataset Preparation

This study used a dataset of 4,880 labeled images of pavement rutting, categorized into four classes: corrugation-high, corrugation-low, rutting-high, and rutting-low. Each image was annotated with bounding boxes that marked the location and extent of rutting, and labels were normalized for YOLO training. The dataset was divided into training (80%), validation (10%), and test (10%) subsets.
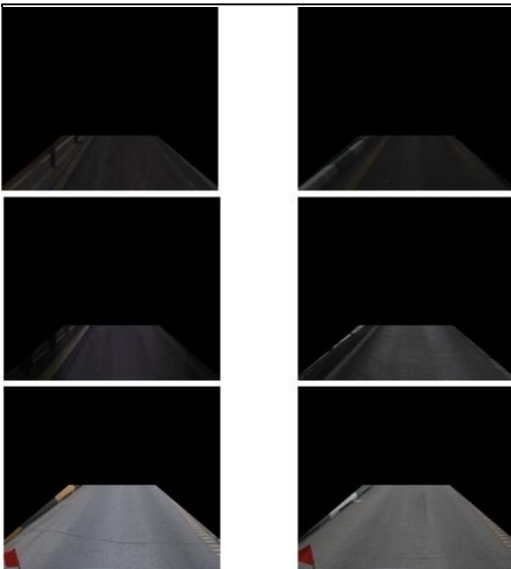
Figure 1: Dataset Instances

2.2 Physics-Informed Loss Function

The YOLOv8 loss function was modified by adding a penalty term, $L_{Physics}$, to ensure physical plausibility in the bounding box predictions. The term penalizes violations of the following physical constraints:

- Aspect ratio limits: Bounding boxes must reflect realistic width-to-depth ratios observed in rutting.
- Size constraints: Bounding box dimensions must adhere to known physical limits of rutting depth and width.
- Location continuity: Penalties are applied to disjointed bounding boxes in areas where rutting is expected to be continuous.

The total loss function is expressed as:

$$L_{Total} = L_{YOLO} + \lambda L_{Physics}$$

where λ is a tunable hyperparameter that controls the weight of the physics-informed penalty.

Figure 2: Flowchart of Applying PINN Principles into YOLO Model

2.3 Model Training Setup

Training was conducted using the YOLOv8 model from the Ultralytics framework. The following parameters were used:

- Batch size: A batch size of 64 was selected to balance computational efficiency and model performance.
- Learning rate: An initial learning rate of $5 * 10^{-4}$ was chosen.
- Optimizer: Both SGD and Adam optimizers were tested to identify the best gradient update method for faster convergence.
- Epochs: Training was performed for 50, 100, and 150 epochs to observe the effect of training duration on performance.
- Weight initialization: Both pre-trained weights from COCO and randomly initialized weights were tested to evaluate the impact of transfer learning.
- Anchor box adjustments: The anchor box sizes were modified based on the distribution of bounding boxes in the dataset to improve localization accuracy.

2.4 Evaluation Metrics

Model performance was assessed using the following metrics:

- Mean Average Precision (mAP): To evaluate overall detection accuracy across all classes.
- Physics adherence score: A custom metric was introduced to quantify how well predictions adhered to physical constraints.
- Precision and Recall: To evaluate the trade-off between false positives and false negatives.
- Inference time: To ensure the model meets real-time application requirements.

3. RESULTS

The physics-informed YOLOv8 model was trained and evaluated on the 4,880-image pavement rutting dataset, focusing on detection accuracy, adherence to physical constraints, and computational efficiency. Several training configurations were tested to optimize performance.

3.1 Model Accuracy

- Mean Average Precision (mAP): The best model achieved an mAP of 72.5%, a 5.5% improvement over the baseline YOLOv8. The physics-informed penalty notably reduced bounding box localization errors, especially for high-severity rutting.
- Class-Specific Performance: The highest detection accuracy was for rutting-high (mAP: 82%) and corrugation-high (mAP: 88%), while rutting-low performed slightly lower (mAP: 79%) due to smaller bounding boxes.
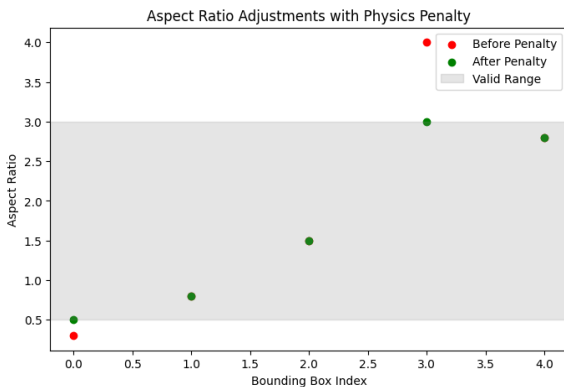
Figure 3: Aspect Ratios of Bounding Boxes From Predictions Befor and After Training With the Penalty

3.2 Physics Adherence

Models with a physics penalty weight ($\lambda = 0.2$) achieved the best balance, with 94% of bounding boxes adhering to aspect ratio and size constraints. Without the penalty, adherence dropped to 78%, underscoring the benefit of the physics-informed approach.

3.3 Hyperparameter Tuning Results

- Batch Size: A batch size of 16 offered the best trade-off between stability and GPU memory usage, outperforming smaller (8) and larger (32) batch sizes.
- Epochs: Training for 50 epochs provided optimal results; training beyond that caused overfitting, particularly with smaller augmentations.
- Image Size: Training with 640x640 pixel images achieved the best balance of performance and computational efficiency. Larger sizes (1024x1024) improved accuracy but at the cost of longer training times.

3.4 Comparison With Baseline YOLOv8

- mAP: Increased from 67% (baseline) to 72.5%.
- False Positives: Reduced by 18% for rutting-high and corrugation-low.
- Physics Adherence: Improved from 78% (baseline) to 94%.
- Inference Time: Increased by 20% due to the additional physics penalty computation, but remained within real-time limits (20ms per image).

4. CHALLENGES AND FUTURE WORK

Integrating domain-specific rules into object detection models requires careful parameter tuning. The primary challenges encountered included:
- Balancing the λ hyperparameter to avoid over-penalizing bounding boxes.
- Ensuring computational efficiency, as the added penalty increased training time by 20%.
- Future work will explore extending the approach to detect additional pavement distresses and integrating 3D point cloud data for improved accuracy.

5. CONCLUSIONS

This study demonstrates the feasibility of integrating physics-informed constraints into YOLO for pavement rutting detection. The proposed approach improved detection accuracy and reduced physically implausible predictions. The results highlight the potential of combining domain knowledge with machine learning models for infrastructure monitoring and maintenance.

6. ACKNOWLEDGEMENTS

7. REFERENCES

Arezoumand, S., Mahmoudzadeh, A., Golroo, A., & Mojaradi, B. (2021). Automatic pavement rutting measurement by fusing a high speed-shot camera and a linear laser. *Construction and Building Materials*, *283*. https://doi.org/10.1016/j.conbuildmat.2021.122668

Bekiroglu, K., Tekeoglu, A., Shen, J., & Boz, I. (2021). Low-Cost Internet of Things Based Real- Time Pavement Monitoring System. *2021 IEEE International Conferences on Internet of Things (IThings) and IEEE Green Computing & Communications (GreenCom) and IEEE Cyber, Physical & Social Computing (CPSCom) and IEEE Smart Data (SmartData) and IEEE Congress on Cybermatics (Cybermatics)*, 17–22. https://doi.org/10.1109/iThings-GreenCom-CPSCom-SmartData-Cybermatics53846.2021.00018

Cano-Ortiz, S., Pascual-Muñoz, P., & Castro-Fresno, D. (2022). Machine learning algorithms for monitoring pavement performance. In *Automation in Construction* (Vol. 139). Elsevier B.V. https://doi.org/10.1016/j.autcon.2022.104309

Cao, M. T., Chang, K. T., Nguyen, N. M., Tran, V. D., Tran, X. L., & Hoang, N. D. (2021). Image processing-based automatic detection of asphalt pavement rutting using a novel metaheuristic optimized machine learning approach. *Soft Computing*, *25*(20), 12839–12855. https://doi.org/10.1007/s00500-021-06086-5

Deng, Y., Wang, H., & Shi, X. (2024). Physics-guided neural network for predicting asphalt mixture rutting with balanced accuracy, stability and rationality. *Neural Networks*, *172*. https://doi.org/10.1016/j.neunet.2023.12.039

Erlingsson, S. (2012). Rutting development in a flexible pavement structure. *Road Materials and Pavement Design*, *13*(2), 218–234. https://doi.org/10.1080/14680629.2012.682383

Fares, A., Zayed, T., Abdelkhalek, S., Faris, N., & Muddassir, M. (2024). Rutting measurement in asphalt pavements. In *Automation in Construction* (Vol. 161). Elsevier B.V. https://doi.org/10.1016/j.autcon.2024.105358

Fontul, S., Neves, J., & Gomes, S. V. (2023). Monitoring of Pavement Structural Characteristics. In *Springer Tracts in Civil Engineering* (pp. 187–208). Springer Science and Business Media Deutschland GmbH. https://doi.org/10.1007/978-3-031-05875-2_8

Kargah-Ostadi, N., Vasylevskyi, K., Ablets, A., & Drach, A. (2024). Physics-informed neural networks to advance pavement engineering and management. *Road Materials and Pavement Design*. https://doi.org/10.1080/14680629.2024.2315073

Madeh Piryonesi, S., & El-Diraby, T. E. (2021). Using Machine Learning to Examine Impact of Type of Performance Indicator on Flexible Pavement Deterioration Modeling. *Journal of Infrastructure Systems*, *27*(2). https://doi.org/10.1061/(asce)is.1943-555x.0000602

Marcelino, P., de Lurdes Antunes, M., Fortunato, E., & Gomes, M. C. (2021). Machine learning approach for pavement performance prediction. *International Journal of Pavement Engineering*, *22*(3), 341–354. https://doi.org/10.1080/10298436.2019.1609673

Raissi, M., Perdikaris, P., & Karniadakis, G. E. (2019). Physics-informed neural networks: A deep learning framework for solving forward and inverse problems involving nonlinear partial differential equations. *Journal of Computational Physics*, *378*, 686–707. https://doi.org/10.1016/j.jcp.2018.10.045

Shahbazi, L., Majidi, B., & Movaghar, A. (2021, April 28). Autonomous Road Pavement Inspection and Defect Analysis for Smart City Maintenance. *Proceedings of the 5th International Conference on Pattern Recognition and Image Analysis, IPRIA 2021*. https://doi.org/10.1109/IPRIA53572.2021.9483534

Shatnawi, N., Obaidat, M. T., & Al-Mistarehi, B. (2021). Road pavement rut detection using mobile and static terrestrial laser scanning. *Applied Geomatics*, *13*(4), 901–911. https://doi.org/10.1007/s12518-021-00400-4

Vadyala, S. R., Betgeri, S. N., Matthews, J. C., & Matthews, E. (2022). A review of physics-based machine learning in civil engineering. *Results in Engineering*, *13*. https://doi.org/10.1016/j.rineng.2021.100316

Wang, S., Cai, B., Wang, W., Li, Z., Hu, W., Yan, B., & Liu, X. (2024). Automated detection of pavement distress based on enhanced YOLOv8 and synthetic data with textured background modeling. *Transportation Geotechnics*, *48*. https://doi.org/10.1016/j.trgeo.2024.101304

Exploring physics-informed recurrent neural networks for constitutive modeling of concrete pavements

H. Garita-Durán, A. Khedkar, M. Kaliske
Institute for Structural Analysis, Technische Universität Dresden, 01062 Dresden, Germany

ABSTRACT: This study proposes a preliminary investigation into the use of physics-informed recurrent neural networks (RNNs) for constitutive modeling of concrete. Traditional empirical models for concrete often face limitations in capturing complex, path-dependent behaviors due to the constraints of experimental datasets. To address this, we explore the integration of RNN architectures, with foundational principles from continuum mechanics, including thermodynamic consistency and objectivity. This theoretical framework aims to establish a foundation for future developments of hybrid models that reduce reliance on extensive experimental data while maintaining physical interpretability. The work highlights key challenges, including incorporating physical constraints into machine learning architectures and addressing the material's inherent complexity, setting the stage for further empirical validation and refinement.

1 MOTIVATION

Concrete is a fundamental material in infrastructure, particularly in pavements and other load-bearing structures, where its mechanical behavior under varying conditions plays a critical role in structural performance and durability. Developing accurate material models is essential for predicting the response of such structures to complex loading scenarios, environmental influences, and long-term degradation. Improved material models can enhance the efficiency and reliability of structural simulations, reducing computational demands and avoiding overly conservative assumptions. Additionally, these models enable the integration of real-time data into digital twin frameworks, supporting continuous monitoring and predictive maintenance. This capability offers potential for optimizing the design and management of concrete pavements and other critical infrastructure.

In solid mechanics, understanding material behavior under varying loading conditions relies on conservation laws, kinematic relations, and constitutive models (Fuhg et al. 2024a). While conservation and kinematic principles are grounded in universal physical laws, constitutive modeling often depends on empirical assumptions constrained by the availability of experimental data. For path-dependent materials like concrete, where the current stress state depends on strain history, traditional models calibrated for specific loading scenarios may exhibit limited accuracy and generalization when applied to complex or varying conditions.

Recent advances in data-driven methodologies, particularly machine learning (ML), provide an opportunity to enhance constitutive modeling by directly integrating experimental data. However, purely data-driven approaches typically require extensive datasets, which are often impractical to obtain. Hybrid methods that combine ML techniques with physical principles offer a promising alternative. RNNs, designed to capture temporal dependencies, are especially suited for modeling the evolution of stress-strain relationships in history-dependent materials. By embedding physical constraints, such as thermodynamic consistency and objectivity, into the RNN training process, this approach enhances interpretability and robustness (Fuhg et al. 2024b).

The development of automated material models, such as the proposed hybrid framework, aims to create formulations that are generalizable across a range of materials. However, the inherent complexity of phenomena like plasticity introduces challenges that must be addressed to ensure reliability and applicability. In this work, the focus is narrowed to concrete, allowing an exploration of the framework ca-

pabilities and its potential to be generalized for other materials in future studies.

2 STATE OF THE ART

The integration of machine learning into constitutive modeling has opened new pathways to address the limitations of traditional data-driven approaches. Frameworks like iCANN (Holthusen et al. 2024) and EUCLID (Flaschel et al. 2021) have successfully integrated machine learning into constitutive modeling, focusing primarily on viscoelasticity and hyperelasticity. These frameworks leverage the flexibility of neural networks to model complex material behaviors while embedding physical constraints to ensure thermodynamic consistency and interpretability. However, extending such approaches to elasto-plastic materials introduces additional challenges, including the implementation of multi-surface yield models and non-associated flow rules. Addressing these complexities requires methodologies tailored to specific materials, such as concrete, while maintaining the potential for broader generalization to other material classes.

Recent contributions from our group have focused on applying recurrent neural networks (RNNs) to constitutive modeling within a numerical homogenization framework. In this approach, RNNs replace the representative volume element (RVE) to provide an efficient and accurate constitutive description of the elasto-plastic behavior of the material (Stöcker et al. 2022). This methodology eliminates the computational overhead associated with traditional RVE evaluations, significantly enhancing the speed of simulations. Furthermore, an advanced training algorithm was developed to optimize the learning process of RNNs, enabling faster and more accurate predictions (Khedkar et al. 2023).

As illustrated in the Figure 1, the application of a load on a cantilever beam in the x-direction yields a response curve that closely matches the expected elasto-plastic behavior. This result highlights the capacity of RNN-based approaches to capture material non-linearities while significantly improving computational efficiency.

While the RNN framework used by our group does not yet incorporate physical principles, its success in modeling the elasto-plastic response provides a foundation for integrating physics-informed constraints. Such an extension could enhance interpretability and enable generalization to materials like

concrete, where path-dependence and history effects play a significant role.
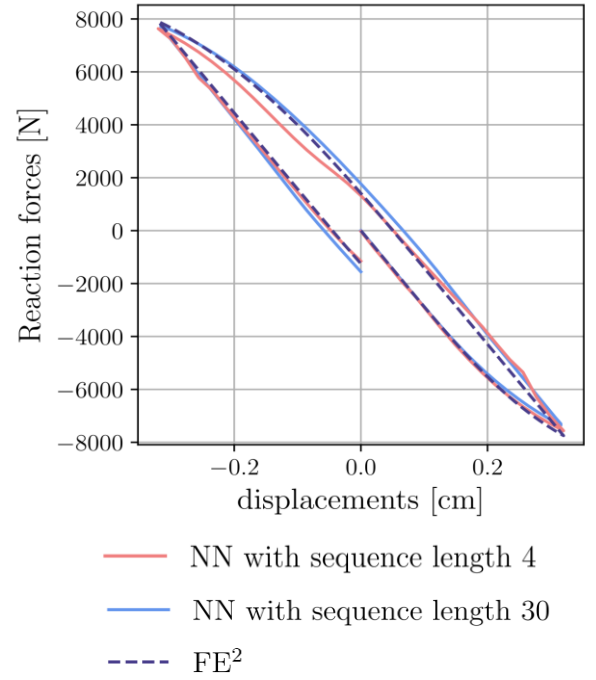
Figure 1. Predicted elasto-plastic response of an RVE modeled using an RNN-based constitutive approach under a cantilever beam (Khedkar et al. 2023).

3 FUNDAMENTALS

3.1 *Constitutive properties of concrete*

Concrete exhibits a combination of elastic and plastic behavior, governed by its heterogeneous microstructure and path-dependent response. Elasticity is characterized by reversible deformations described by the relationship

$$\boldsymbol{\sigma} = \mathbf{C} : \boldsymbol{\varepsilon}^e, \tag{1}$$

where $\boldsymbol{\sigma}$ represents the stress tensor, $\mathbf{C}$ is the fourth-order elasticity tensor, and $\boldsymbol{\varepsilon}^e$ is the elastic strain tensor. The elastic behavior of concrete is typically linear for small strains but deviates from linearity at relatively low stress levels due to microstructural effects.

Plasticity governs the irreversible deformations that occur when the stress state exceeds a defined yield surface. For concrete, plasticity is predominantly observed under compressive loads, while tensile failure is brittle. The Drucker-Prager criterion, which incorporates the first invariant of the stress tensor I_1 and the second invariant of the deviatoric stress J_2 tensor are commonly used to define the yield surface (Ottosen and Ristinmaa 2005)

$$f(\boldsymbol{\sigma}) = \sqrt{J_2} + \alpha I_1 - k \leq 0, \tag{2}$$

where α accounts for material friction, and k represents cohesion. Plastic strains evolve according to a flow rule, with associated or non-associated potentials depending on the dilatancy behavior. These be-

haviors are essential to capture concrete's complex stress-strain response under cyclic and multi-axial loading.

3.2 *Elastic-plastic modeling approaches*

Elastic-plastic models decompose total strain into elastic and plastic components

$$\boldsymbol{\varepsilon} = \boldsymbol{\varepsilon}^e + \boldsymbol{\varepsilon}^p. \tag{3}$$

This decomposition enables independent modeling of reversible and irreversible behaviors. Advanced formulations adopt the multiplicative decomposition of the deformation gradient

$$\mathbf{F} = \mathbf{F}^e \mathbf{F}^p, \tag{4}$$

ensuring that elastic stresses arise solely from elastically stored energy, while plastic strain rates are derived from pseudo-potentials. The Helmholtz free energy $\psi(\mathbf{C}^e)$, a function of the elastic right Cauchy-Green tensor $\mathbf{C}^e = \mathbf{F}^{e\top} \mathbf{F}^e$, provides the stress response

$$\boldsymbol{\sigma} = 2\frac{\partial \psi}{\partial \mathbf{C}^e}. \tag{5}$$

Hardening rules, such as isotropic and kinematic hardening, dictate how the yield surface evolves with plastic deformation, incorporating state variables to account for the material's history-dependent behavior. These rules are critical for modeling concrete under incremental or cyclic loading conditions.

3.3 *Machine learning for constitutive modeling*

ML offers a powerful framework for capturing complex, nonlinear relationships in experimental data. Neural networks (NNs), with their universal approximation capabilities, are particularly suitable for constitutive modeling. Traditional feed-forward NNs learn mappings between input variables (e.g., strain tensors) and outputs (e.g., stress tensors), but they require extensive datasets and often lack physical interpretability.

RNNs, particularly architectures like long short-term memory (LSTM) networks, address these limitations by capturing temporal dependencies, making them ideal for path-dependent materials like concrete. For example, RNNs can track the evolution of plastic strain and internal variables over loading cycles, providing accurate predictions of stress responses under complex scenarios.

To improve generalization and reduce data requirements, hybrid approaches integrate physical principles into ML frameworks. Loss functions are augmented to enforce constraints such as the Clausius-Planck inequality, ensuring thermodynamic consistency. This combination allows ML models to maintain fidelity to fundamental mechanics while leveraging data-driven insights.

Physics-enhanced neural networks (PENNs) embed physical laws directly into the network structure, ensuring that predictions adhere to established principles. For instance, the Helmholtz free energy and plastic potential $g(\boldsymbol{\tau})$ can be represented using feed-forward NNs, with constraints such as convexity and positive dissipation enforced during training. The resulting models capture both elastic and plastic behavior while maintaining interpretability.

For concrete, this approach allows the representation of stress-strain relationships under diverse conditions, ensuring consistency with known behavior such as strain hardening, dilatancy, and yield surface evolution. The integration of RNNs and physics-informed layers offers a robust framework for automating constitutive modeling while addressing the material-specific challenges of concrete.

4 INTEGRATING MACHINE LEARNING AND PHYSICAL PRINCIPLES FOR CONCRETE

4.1 *Methodology for stress-strain modeling*

The integration of machine learning (ML) with physical principles offers a promising framework for capturing the complex behavior of concrete under diverse loading conditions. While this study does not present empirical implementation, it outlines a methodology to guide future work.

The proposed approach utilizes recurrent neural networks (RNNs), such as long short-term memory (LSTM) networks, to model history-dependent stress-strain relationships. The deformation gradient of Equation 4 captures irreversible plastic deformation. The stress response is derived from the Helmholtz free energy. Plastic strain evolution is governed by a pseudo potential $g(\boldsymbol{\tau})$ ensuring thermodynamic consistency through the dissipation inequality

$$\mathcal{D} = \boldsymbol{\tau} : \dot{\mathbf{F}}^p \geq 0. \tag{6}$$

The RNN framework models the temporal evolution of inelastic state variables, such as plastic strain and hardening parameters, while physical constraints are enforced via customized loss functions. These constraints include yield surface consistency

$$f(\boldsymbol{\sigma}) \leq 0, \tag{7}$$

positive energy dissipation

$$\mathcal{D} \geq 0, \tag{8}$$

and convexity of the Helmholtz free energy.

In this theoretical framework, experimental data from stress-strain curves under controlled loading paths (e.g., uniaxial, triaxial, and cyclic tests) serve

as input to train the RNN. By leveraging the physics-informed structure, the model is expected to generalize beyond the training dataset, capturing path-dependent behaviors such as strain hardening and dilatancy.

4.2 *Advantages of the hybrid approach*

The hybrid approach combines the strengths of machine learning and physical principles, offering several theoretical advantages for modeling the elastic-plastic behavior of concrete:

1 Data efficiency: By embedding physical laws directly into the network architecture or loss function, the model reduces its reliance on extensive experimental datasets. This is particularly advantageous for materials like concrete, where obtaining large amounts of high-quality data can be impractical.
2 Path dependency: RNNs excel at modeling sequential dependencies, making them ideal for capturing the history-dependent behavior of concrete under cyclic and incremental loading conditions.
3 Physical plausibility: The inclusion of physics-based constraints ensures that predictions remain consistent with established principles, such as thermodynamic consistency, even in data-sparse scenarios.
4 Interpretability: Unlike traditional black-box neural networks, the hybrid approach incorporates physically interpretable components, such as the Helmholtz free energy and plastic potentials. These components align with established mechanical theories, enabling the model to provide insights into material behavior.
5 Exploration of generalization: While the methodology is developed specifically for concrete, its general structure can be extended to other path-dependent materials. This exploratory work lays the foundation for understanding the potential of hybrid models in broader applications.

5 CONCLUSION

This study explores the foundation for using physics-informed recurrent neural networks (RNNs) in modeling the history-dependent constitutive behavior of concrete. By integrating machine learning with physical principles, the proposed framework addresses key challenges in traditional models, including limited generalization and high dependency on empirical data.

The hybrid approach leverages the strengths of RNNs to capture path-dependent behaviors, such as strain hardening and dilatancy, while embedding physical constraints ensures thermodynamic consistency and interpretability. Although focused on concrete, this methodology provides a flexible structure that could be extended to other path-dependent materials, potentially becoming a component of broader systems like digital twins, where continuous data integration could refine predictions over time.

Future work will involve validating this framework with experimental data and exploring its scalability to more complex behavior, including anisotropy and damage, ensuring its applicability in diverse engineering contexts.

6 ACKNOWLEDGMENTS

7 REFERENCES

Flaschel, M., Kumar, S. & De Lorenzis, L. 2021. Unsupervised discovery of interpretable hyperelastic constitutive laws. *Computer Methods in Applied Mechanics and Engineering* 381: 113852.

Fuhg, J. N., Anantha Padmanabha, G., Bouklas, N., Bahmani, B., Sun, W., Vlassis, N. N., Flaschel, M., Carrara, P. & De Lorenzis, L. 2024a. A review on data-driven constitutive laws for solids. *Archives of Computational Methods in Engineering*: 1-43.

Fuhg, J. N., Jones, R. E. & Bouklas, N. 2024b. Extreme sparsification of physics-augmented neural networks for interpretable model discovery in mechanics. *Computer Methods in Applied Mechanics and Engineering* 426: 116973.

Holthusen, H., Lamm, L., Brepols, T., Reese, S. & Kuhl, E. 2024. Theory and implementation of inelastic constitutive artificial neural networks. *Computer Methods in Applied Mechanics and Engineering* 428: 117063.

Khedkar, A., Stöcker, J., Zschocke, S. & Kaliske, M. 2023. Continuous self-adversarial training of recurrent neural network--based constitutive description, *Proceedings in Applied Mathematics and Mechanics* 23: 1-8.

Ottosen, N. S. & Ristinmaa, M. 2005. *The mechanics of constitutive modeling.* Lund: Elsevier.

Stöcker, J., Fuchs, A., Leichsenring, F. & Kaliske, M. 2022. A novel self-adversarial training scheme for enhanced robustness of inelastic constitutive descriptions by neural networks, *Computers and Structures* 265: 106774.

Supervised Learning for the Prediction of Bitumen Ageing States Using the Kernel Ridge Regression Model

K. Habassi
Civil engineering student at ENI Tunis, Tunisie

L. Coulon
Temporary associate professor at INSA Strasbourg, ICube lab. (CNRS, UMR 7357), team GCE, France

A. Ayadi
Associate professor at Université Strasbourg, ICube laboratory, team SDC, France

A. Samet
Associate professor at INSA Strasbourg, ICube laboratory, team SDC, France

C. Chazallon
Professor at INSA Strasbourg, ICube laboratory, team GCE, France

ABSTRACT: The study presents the first results of a supervised machine learning model used to calibrate and predict complex modulus tests for neat or aged binders recovered from asphalt concrete. Trained on data combining complex modulus measurements and the chemical properties of binders, the model captures the intricate relationships between bitumen chemistry and its mechanical behaviour. By understanding the chemical ageing of a binder, predictions of both known and unknown ageing states are successfully achieved.

1 INTRODUCTION

The binder of hot mix asphalt undergoes two successive types of chemical ageing over its lifespan: fast ageing during production and construction (short term) and slow ageing over the life of the pavement (long term). Oxidation is the main cause of bitumen ageing (Hunter et al., 2015, p. 75 and 575). At the coating stage, chemical oxidation is violent because the energy input is intense (high temperature and oxygen from the air), whereas in the pavement, the bitumen oxidises slowly in the presence of temperature cycles and oxygen from the atmospheric air.

Accelerated artificial ageing processes have been developed in laboratories to replicate the short- and long-term ageing phases of bituminous materials. These processes have shown that the ageing of bituminous binders is characterised by changes in both their chemical composition and rheology over time. Internationally recognised physico-chemical indicators are used to assess the brittleness of binders or mixtures with respect to the risk of cracking (Khandal, 1977, Rowe, 2011, Siroma et al., 2024). However, to date, there is no established relationship that can describe the rheological changes observed at different stages of ageing and across various scales of observation (binder, mastic, asphalt mix).

Furthermore, the use of Artificial Intelligence (AI) is expanding in the field of pavement materials. Supervised learning, a subset of machine learning and artificial intelligence, involves learning a predictive function from labelled examples (Zhou, 2021). Its application could help identify transition laws between different ageing states, with the goal of linking the rheology of the binder to that of the asphalt mix.

This article presents a preliminary study that involves supervised learning to predict the rheology of bitumen in a given state of ageing, using data from previous states. The model aims to identify the relationships between the chemical composition of bitumen and its rheological properties.

For this study, the rheology of bitumen is characterised through complex modulus tests (physical markers). Traditionally, the data are modelled with rheological models, while the effects of temperature, loading amplitude, and thixotropy are typically approximated through translation principles (Coulon et al., 2021). However, ageing cannot be modelled using similar principles, as it alters the shape of the complex modulus curves. Consequently, the parameters of rheological models require constant recalibration, leading to the adoption of a supervised approach to bypass these models. Each ageing state is additionally associated with SARA fractions (saturate, aromatic, resin, asphaltene) and carbonyl and sulfinyl indexes (chemical markers), which reflect the level of ageing.

The structure of the article is as follows. First, the bitumen from the MOVEDVDC project and its associated physical and chemical data are presented. Next, the supervised learning model, Kernel Ridge Regression, is adapted for the study. Finally, the results obtained are discussed.

2 MATERIALS

The French ANR MOVEDVDC project (2018-2023) has generated a substantial database of asphalt mixtures and bituminous binders extracted *in situ* or produced in the laboratory using ageing protocols (SIROMA, 2022). This paper focuses on the physico-chemical data for the eight states of ageing of the bitumen binder A3550_C.

The bitumen in question is extracted from a GB3 (a French asphalt concrete meaning Grave-Bitume class 3) prepared and aged in laboratory. This asphalt mix is made of 0/14 mm limestone aggregates and a pure bitumen of penetration grade 35/50 dosed at 4.5% of the mass of dry aggregates. The aggregates and the bitumen were initially heated overnight to 165°C and 110°C respectively. The temperature of the bitumen was then increased to match that of the aggregates for approximately two hours. Finally, the two components were mixed using a mixer for about three minutes until the aggregates were completely coated with bitumen. The mixture has a true density of 2509 kg/m³.

After the mixing stage, an ageing protocol proposed by La Roche et al. (2009) was applied to the expanded asphalt of GB3. To simulate short-term ageing, the asphalt mixture was first spread uniformly in metal trays to a thickness of around 5 to 6 cm. The trays were then placed in a forced-draught oven at 135°C for 4 hours. The mix was stirred for one minute every hour. To reproduce long-term ageing, the asphalt mix was then conditioned at 85°C for 2, 5, 7, 9 and 20 days. After each ageing stage, the bitumen was extracted to study its characteristics.

To define physical markers, complex modulus tests were carried out on the bitumen using a Dynamic Mechanical Analysis (DMA) rheometer. The device was placed inside a thermal chamber. At low temperatures ($\leq 20°C$), the test was carried out in direct tension-compression on a cylindrical specimen. At high temperatures ($> 20°C$), the test was carried out using annular shear on a hollow cylindrical specimen. Conversion from norm $|G^*|$ to $|E^*|$ was performed

considering a constant Poisson's ratio of 0.50. The tests were conducted by strain amplitude control (close to 50 μm/m) with frequency sweeps (from 1 to 80 Hz) at different temperatures (from -15 to 70 °C). A minimum of two repetitions were performed for each sample, provided that the variations in $|E^*|$ and φ_{E^*} were less than 15% and 5% respectively. The data are presented in Figure 1 using the stiffness $\Re_E$ and viscosity $\Im_\eta$ components (COULON et al. 2021) such as:

$$\sigma(t, T, \omega) = \Re_E(T, \omega)\varepsilon(t, \omega) + \Im_\eta(T, \omega)\dot{\varepsilon}(t, \omega)$$

Where $\sigma(t)$ and $\varepsilon(t)$ are respectively the stresses and strains of the DMA test. The effect of temperature T and pulsation ω can be associated according to the Time-Temperature Superposition Principle (TTSP). Table 1 gives the coefficients $C_{1,aT}$ and $C_{2,aT}$ of the Williams-Landel-Ferry (WLF) law at the reference temperature of 0°C.

Other analyses were also carried out to identify chemical markers. On the one hand, Fourier Transform InfraRed spectroscopy (FTIR) was used to monitor the oxidation of the bitumen by calculating the carbonyl I_{CO} and sulfinyl I_{SO} indexes, as indicated by LPC test method No. 69 (LCPC 2010). A minimum of five samples were studied for each ageing condition. On the other hand, based on its polarity, bitumen can be separated into four fractions called SARA. The High Performance Thin-Layer Chromatography (HPTLC) was carried out. Table 1 shows the average of these results.

3 APPLICATION OF SUPERVISED MACHINE LEARNING

The primary objective of this section is to train the AI model on the provided experimental data. The ageing of A3550_C bitumen is categorised into eight distinct states. The rheology of each state is represented by the pair of stiffness $\Re_E(\omega_{R-T})$ and viscosity $\Im_{\eta,R-T}(\omega_{R-T})$ at the reference temperature of 0°C.

Table 1. WLF coefficients at the reference temperature of 0°C, CO+SO indexes and SARA fractions of the bitumen A3550_C.

	TTSP $C_{1,aT}$ [-]	TTSP $C_{2,aT}$ [°C]	IRTF CO+SO [-]	SARA Saraturate [%]	SARA Aromatic [%]	SARA Resin [%]	SARA Asphaltene [%]
After heating	21.6	132.1	4.69	16.10	46.95	22.30	14.60
After mixing	18.0	113.3	9.35	16.05	46.50	23.70	13.65
4h	23.5	146.3	13.00	15.50	45.65	26.90	11.90
4h+2j	23.4	145.1	16.99	16.30	43.00	29.10	11.60
4h+5j	24.6	150.4	18.23	15.25	43.60	29.50	11.60
4h+7j	26.6	162.6	20.98	14.70	44.15	29.70	11.50
4h+9j	24.9	153.4	21.11	14.15	44.15	31.35	10.40
4h+20j	27.0	163.3	23.85	14.65	41.20	34.50	9.60

To quantify the level of ageing, these pairs are associated with a quintuplet of chemical markers, comprising the sum of the I_{CO} and I_{SO} indexes, along with the four SARA fractions. After training, the model is expected to both reproduce known ageing states and predict new ones.

3.1 Model used

For this study, the Kernel Ridge Regression (KRR) algorithm was employed with the Radial Basis Function (RBF) kernel (SCHÖLKOPF & SMOLA, 2002). This method is well-suited for solving regression problems involving complex and non-linear relationships between input data X and output data Y, while incorporating effective regularisation to mitigate overfitting (e.g., avoiding an overly complex model that captures noise instead of meaningful trends).

The KRR-RBF algorithm is governed by two key hyperparameters that affect its performance:

- The regularisation parameter λ controls the influence of isolated or atypical data points. A higher λ reduces sensitivity to noise and specific details.

- The γ parameter of the RBF kernel determines the range of influence a data point has on its neighbors in kernel space. A smaller γ results in a smoother model that captures broader trends while ignoring finer local variations.

The program was developed in Python.

3.2 Training

The model incorporates input data, consisting of the reduced pulsations and chemical markers for all ageing states. The output data comprises stiffness-viscosity pairs. Since the pulsation, stiffness, and viscosity data span several orders of magnitude, it is crucial to linearise these values by using their logarithms. This step ensures the model avoids producing outliers.

There are several options for selecting the chemical markers. If the model is trained on all five markers, five input values will need to be provided. However, this approach requires understanding the relationships between these markers to make predictions with hypothetical values. Among the chemical markers, some are more sensitive to ageing than others, such as the sum of the I_{CO} and I_{SO} indexes and the resin fraction. This study focuses on resins as the primary input.

The other chemical markers could be included as output variables, but in this case, the AI would identify relationships between pulsation and these markers. While this approach causes only slight fluctuations in the markers, they are expected to remain constant with respect to pulsation.

To optimise the hyperparameters, the GridSearchCV algorithm is employed. This method systematically tests all possible combinations of the values provided in the lists for λ and γ (e.g., [10^{-4}, 10^{-3}, 10^{-2}, 10^{-1}, 1, 10]). Based on this process, the optimal values identified for λ and γ are 0.0001 and 0.001, respectively.

3.3 Model testing and analysis

To test the model, input data is provided consisting of the range of pulsations and only the resin fraction of bitumen. The model then predicts the corresponding
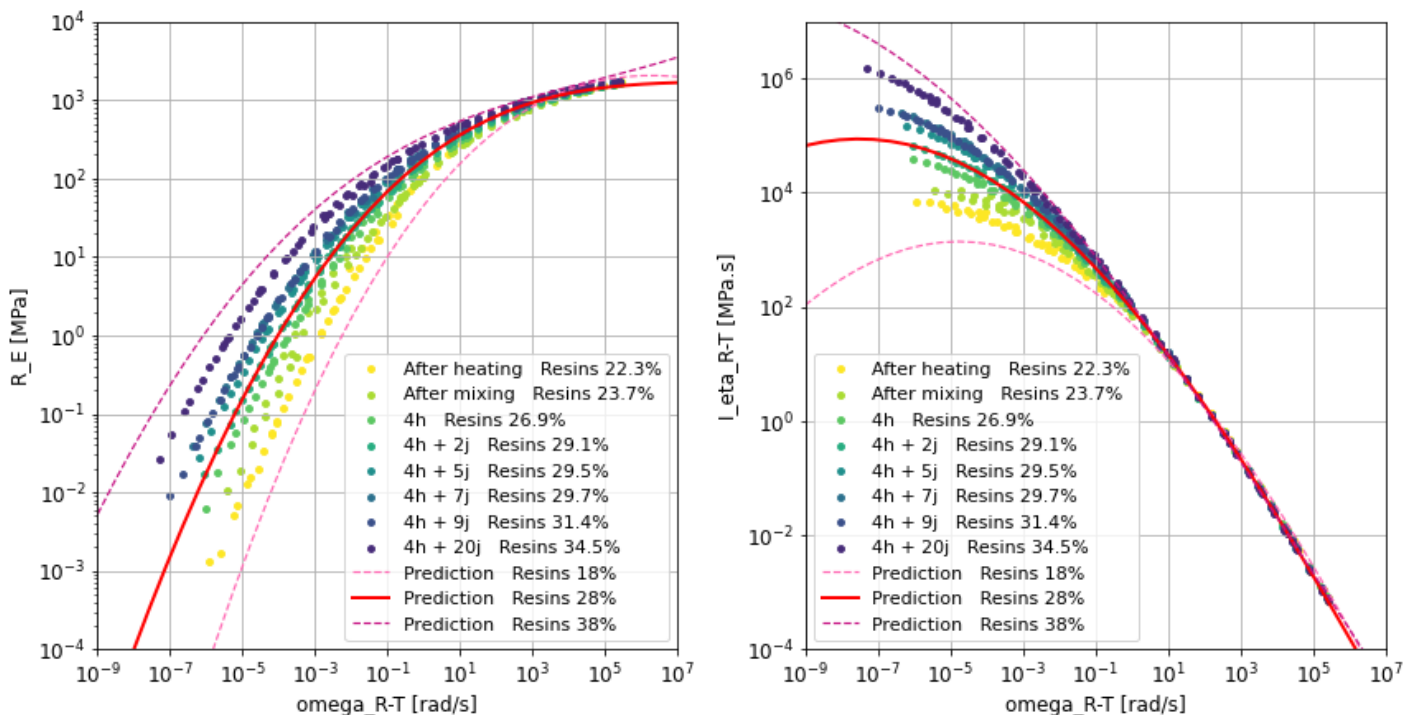
Figure 1. Effect of chemical ageing on the rheology of bitumen A3535_C
Representation of stiffness $\mathfrak{R}_E$ (left) and reduced viscosity $\mathfrak{I}_{\eta,R-T}$ (right) as a function of reduced pulsation ω_{R-T} at the reference temperature of 0°C. The points represent experimental data, while the lines represent AI predictions.

stiffness-viscosity pairs. Figure 1 displays the model's predictions for resin fractions of 18%, 28%, and 38%.

Overall, the results obtained are very satisfactory and encouraging. Although the input pulsations differ between ageing states due to the application of the TTSP, the model still successfully identifies the relationships between the data. This indicates that a common pulsation scale across different ageing states is not necessary.

For a given ageing state, the stiffness and viscosity evolve as expected. However, the model does not fully capture the trend where $\Re_E$ and $\Im_\eta$ approach plateaus at high and low pulsations, respectively. With the RBF kernel, the fitted function is represented as a sum of 'bells' centred around each training point. Thus, testing other types of kernels, such as the 'sigmoid' kernel, could provide further insights.

The model appears to capture the transition between ageing states well. For the 28% resin fraction prediction, the curve aligns with the '4h + 2d' ageing, corresponding to 29.1%. The 1% difference can be attributed to the model's adaptation to certain inconsistencies in the experimental data, such as the overlap between the '4h + 7d' and '4h + 9d' ageing states, which are similar in terms of stiffness and viscosity despite differing by 2% in fraction. The predictions for 18% and 38% resin fractions are consistent, but predictions tend to become less reliable as we move further from the training data zone.

4 CONCLUSION

The study demonstrated the predictive capability of the Kernel Ridge Regression model when applied to aged bituminous binders. The model successfully captures complex relationships between bitumen chemistry and its mechanical properties, and is capable of accurately extrapolating these relationships beyond the training data.

However, while the experimental data used may be considered abundant for the pavement domain, they are limited to a single bitumen type. To enhance the model's robustness, future work should extend the study to include other bituminous materials from the MOVEDVDC project and potentially expand it to materials from the ViscoMatData database at Gustave Eiffel University.

Other artificial intelligence models, such as Support Vector Regression (SVR), Random Forest, and Gradient Boosting, should also be tested.

This study also presents several perspectives:

- If we assume that there is a unique SARA fraction decomposition for each stiffness-viscosity curve, it follows that by knowing the chemistry of the bitumen, we might predict its rheology, and *vice versa*.

- The study could serve as a foundation for investigating the transition from bitumen rheology to asphalt rheology.

- In the more distant future, one might envision that, by knowing the age of a pavement and its initial rheology, we might predict whether maintenance would be necessary.

6 REFERENCES

COULON, L., KOVAL, G., CHAZALLON, C., & ROUX, J.-N. (2021). Analytical modelling of thixotropy contribution during T/C fatigue tests of asphalt concrete with the VENoL model. *Road Materials and Pavement Design*, 22(sup1): 536-559. https://doi.org/10.1080/14680629.2021.1911833

HUNTER, R. N., SELF, A., & READ, J. (2015). *The Shell Bitumen Handbook* (6th ed., 789 p.). ICE Publishing. ISBN-13: 978-0-7277-5837-8

KANDAL, P. S. (1977). Low-temperature ductility in relation to pavement performance. In MAREK, C. R. (ed.), *Low-temperature properties of bituminous materials and compacted bituminous paving mixtures*, 95–106. ASTM International. https://doi.org/10.1520/STP27096S

Laboratoire Central des Ponts et Chaussées (2010, July). *Identification et dosage des fonctions oxygénées présentes dans les liants bitumineux – Analyse par spectrométrie infrarouge à transformée de Fourier* (LPC test method No. 69, 16 p.). France. [In French].

LA ROCHE (de), C., VAN DE VEN, M., VAN DEN BERGH, W., GABET, T., DUBOIS, V., GRENFELL, J., & POROT, L. (2009). Development of a laboratory bituminous mixtures ageing protocol. In Loizos, A., PARTL, M. N., SCARPAS, T., & AL-QADI, I. L. (eds.), *Advanced testing and characterization of bituminous materials*, 1: 331-345. CRC Press. https://doi.org/10.1201/9780203092989

ROWE, G. M. (2011). Prepared discussion for the AAPT paper by Anderson et al.: Evaluation of the relationship between asphalt binder properties and non-load related cracking. *Journal of the Association of Asphalt Paving Technologists*, 80(80): 649–662.

SCHÖLKOPF, B., & SMOLA, A. J. (2002). *Learning with kernels: support vector machines, regularization, optimization, and beyond* (394 p.). MIT Press. ISBN-10: 978-0262194754

SIROMA, R. S. (2022). *Experimental and theoretical methods for assessing the remaining service life of asphalt pavements based on the properties of its recovered bitumens* (323 p.) [PhD thesis]. Université Gustave Eiffel, France.

SIROMA, R. S., NGUYEN, M. L., HORNYCH, P., PLANCHE, J. P., ADAMS, J., ROVANI, J., KUMBARGERI, Y., HUNG, Y., NICOLAÏ, A., ZIYANI, L., & CHAILLEUX, E. (2023). Asphaltene agglomeration through physical-chemical and rheological testing. *Road Materials and Pavement Design*, 25(sup1): 248–261. https://doi.org/10.1080/14680629.2023.2221744

ZHOU, Z.-H. (2021). *Machine learning* (472 p.). Singapore: Springer Nature. https://doi.org/10.1007/978-981-15-1967-3

Climate and traffic input based International Roughness Index (IRI) prediction model for rigid pavements using Artificial Neural networks (ANN)

P.K. Acharjee[1], A. Ahmed[1], T. Ahmed[1], M. Isied[1], A. Akhnoukh[2], M.I. Souliman[1]
[1]The University of Texas at Tyler, Tyler, Texas, The United States
[2]East Carolina University, Greenville, North Carolina, The United States

ABSTRACT: The International Roughness Index (IRI) is a widely used measure of the roughness of road surfaces and ride quality. The Federal Highway Administration (FHWA) has required States' Departments of Transportation (DOT) to include IRI values in their Pavement Management Systems (PMS) since 1990. However, IRI data collection can be challenging due to cost and resource constraints. This study presents an IRI prediction model for rigid pavements for three south Atlantic states of North Carolina, South Carlina, and Virginia. Utilizing climate and traffic data from the Long-Term Pavement Performance (LTPP) database, an Artificial Neural Networks (ANN) was developed to predict IRI. The R^2 for the developed model is 0.84. Sensitivity analysis of the model showed that the climate factors have more influence on IRI. In addition, a closed-form stand-alone equation is also extracted from the model, which Local transportation agencies can leverage to predict IRI using available climate and traffic data.

1 LITERATURE REVIEW

The highway agencies identified roughness as the primary indicator for pavement performance from the early '80s but faced inconsistencies in measurement methods. To address this issue, the National Cooperative Highway Research Program and the World Bank standardized a new roughness measuring method known as the International Roughness Index (IRI) ensuring reproducible results across different equipment. Since then, IRI has been widely adopted to assess pavement roughness and ride quality. The Federal Highway Administration has made it mandatory for State Departments of Transportation to include IRI values in their respective Pavement Management System. Therefore, the IRI prediction model is a highly investigated research area.

Compared to flexible pavements, little research has been done on developing IRI prediction models for rigid pavements. The Mechanistic-Empirical Design Guide (MEPDG) has an IRI prediction model for rigid pavement. Initial IRI is an input parameter in that model with transverse cracking, spalling, and patching. There is also a site factor in the model with pavement age, freezing index, and subgrade property. With the recent development of ANN, several researchers utilized ANN for IRI prediction. (Abd El-Hakim and El-Badawy, 2013) employed the same input variables of the MEPDG empirical model with a database of 184 data points to develop the IRI ANN forecast model. The ANN model provided a better R^2 of 0.828 than the MEPDG regression model with R^2 of 0.643. Similarly, several studies showed the potential of ANN for predicting IRI in recent years, utilizing climate and traffic data, and offering more enhanced prediction neural network models. (Sultana et al., 2021) explored the impact of climate attributes and traffic loads on pavement distress, focusing on the IRI as a key indicator of pavement condition. An ANN approach is used to develop IRI prediction models for Jointed Plain Concrete Pavement (JPCP), considering the maintenance and rehabilitation history of the pavements. The best-performing ANN model achieved a high R2 value of 0.87, successfully estimating IRI values over time and after maintenance activities.

In recent years, researchers have also applied different machine-learning techniques as well for predicting the IRI of rigid pavements. (Wang et al., 2017; Luo, Wang and Li, 2022; Ji et al., 2024) developed a hybrid machine-learning model to predict IRI of Jointed Plain Concrete Pavement (JPCP), the study also compared several machine learning methods, such as eXtreme Gradient Boosting (XGBoost), Gradient Boosting Decision Tree (GBDT), multiple linear regression (MLR), and support vector machine (SVM). The stacking fusion model, combining GBDT and XGBoost as base learners with bagging as meta-learners, outperformed individual models with an RMSE of 0.040, R^2 of 0.996, and MAE of 1.3%, indicating the model improvement.

The ongoing progress of the IRI prediction models for rigid pavements is significant. However, from the construction and maintenance practitioners' point of view, a more simple and accurate prediction method is required without expert knowledge of machine learning. Therefore, this study aimed to develop an IRI prediction model and extract a closed-form equation from the model, which can be utilized by pavement engineers without any prior knowledge of Artificial Neural Networks. With the help of the linear equation, pavement engineers can predict the IRI of a particular rigid pavement and plan more cost-effective maintenance and rehabilitation work programs.

2   OBJECTIVES

The objective of this study is to develop a prediction model using ANN for rigid pavement for three South Atlantic states in the wet no-freeze climate zone. From the model a closed-form stand-alone equation can be extracted which will work as a proxy for the complex machine learning model for practitioners. Moreover, perform sensitivity analysis of the prediction equation as well to identify the effect of input variables on the IRI of rigid pavement.

3   DATA COLLECTION, SELECTION, AND PROCESSING

For pavement construction, upkeep, and management, it is essential to comprehend how traffic and weather affect IRI in rigid pavements (Hossain, Gopisetti and Miah, 2020). The weather, traffic, and IRI data for the three South Atlantic states - North Carolina, South Carolina, and Virginia were collected from LTPP. Figure 1 shows the three states considered in this study.
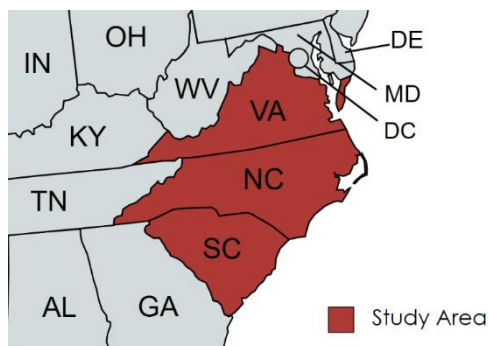
Figure 1. The three South Atlantic states are considered in the study.

In this study, the IRI of rigid pavement is predicted using weather conditions and traffic flow factors. These factors include the proportion of Annual Average Temperature, Equivalent Single Axle Load (ESAL), Average Humidity, Total Annual Precipitation, Previous IRI data, and GESAL (General Equivalent Single Axle Load)

Annual Average Temperature is the temperature experienced over a year in a certain area, typically expressed in degrees Celsius or Fahrenheit. In pavement engineering, this measure is frequently used to evaluate how temperature variations affect pavement performance, including thermal cracking and rutting.

Equivalent Single Axle Load (ESAL) Measures the cumulative damage caused by traffic loadings on pavement. It represents the impact of repeated wheel loads over time, converted to a standard axle load.

The average relative humidity of the air at a particular area over one year is expressed as a percentage. This parameter is frequently used to evaluate how moisture affects pavement performance, including moisture-related distress and degradation.

The total quantity of precipitation that falls at a certain area over a year represents Total Annual Precipitation. It includes rain, snow, and other types of moisture. The moisture level of the pavement layers, which can affect pavement performance such as rutting, cracking, and frost damage, is a crucial parameter in pavement engineering.

The International Roughness Index (IRI), which was previously used, gauges how rough or smooth a pavement surface is. The term "Previous IRI" refers to the IRI value that was previously measured or noted at a certain location. This metric is used to measure the success of prior pavement maintenance or rehabilitation efforts as well as the state of a pavement surface.

GESAL (General Equivalent Single Axle Load) is a parameter that is calculated similarly to ESAL (Equivalent Single Axle Load) but uses constant LEF (Load Equivalency Factor). Unlike ESAL, GESAL is independent of pavement type, thickness, and level of distress, and can be used to compare traffic loads and their effects on pavement performance between different sites

As one of the primary areas of research of the Strategic Highway Research Program (SHRP), the Long-Term The prediction of International Roughness Index (IRI) in rigid pavement using machine learning and environmental factors is a challenging task, but it can be achieved with appropriate data collection and modeling techniques. To begin, it is essential to gather a comprehensive dataset that includes the IRI values for the rigid pavements and the corresponding environmental factors, such as temperature, humidity, precipitation, traffic volume, and other relevant factors. This data can be collected from various sources, including road agencies, weather stations, and traffic monitoring devices. The data for this study is collected from the LTPP program.

This study uses multiple factors in predicting, the IRIs measured in the left and right wheel paths are employed, and the average IRI values are chosen as the primary factor. Table 1 shows the minimum,

maximum, average, and standard deviation of the collected data. With careful evaluation of the IRI values in North Carolina, South Carolina, and Virginia state, the model forecasts the average IRI in those states.

Table 1. Descriptive Statistics of the Model.

Inputs	Minimum	Maximum	Average	Standard Deviation
Temperature (°C)	12.10	18.60	15.23	1.00
Humidity (%)	61.50	74.00	6.25	2.53
Precipitation (mm)	696.30	1,436.90	370.30	177.98
ESAL	18,735	9,33,000	4,57,132	1,74,340
GESAL	25,405	7,39,377	3,56,986	1,31,338
Previous IRI	1.03	2.23	0.60	0.27

4 ARTIFICIAL NEURAL NETWORK IRI MODEL DEVELOPMENT

Artificial Neural Network is a branch of machine learning techniques that works similarly to the human brain. It works as a mathematical function with three layers (input, hidden, output) that process the information through weighted connections. The hidden layer transforms the data utilizing weights and biases while the output layer produces final predictions. The weights and biases are continuously adjusted during learning phases to optimize the network's performance. In this study, for striking the balance between model simplicity and accuracy. neural networks consisting of three hidden neurons are adopted.

The architecture of the ANN model is shown in Figure 2. The neurons in the hidden layer are connected to each input using weights and biases.
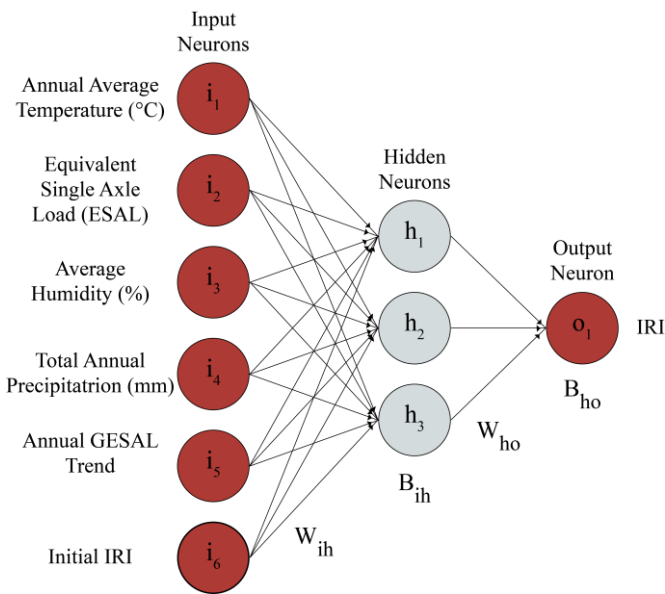
W_{ih} and B_{ih} stand in for the hidden layer's weights and biases. The hyperbolic tangent function is used as an activation function in the hidden layer. The hidden layer's neurons are connected with the output neuron with weights and bias - W_{ho}, B_{ho} respectively.

The model used only the rigid pavements satisfying the climate condition of Wet No Freeze was used for this study. In the model training process, each input was normalized between [-1,1] in the input layer. After passing through the input layer, the data moves on to the hidden layer. The output layer receives the transformed data from the hidden layer and produces the final output of the ANN model. The final output is then compared with the measured value of IRI and error is calculated. This error is fed into the model and backpropagated to the input layer adjusting its weights and biases with respect to error. One forward propagation and backpropagation is called an epoch. In the validation process, the objective is to minimize the Mean Squared Error (MSE). In the developed model development process, the best validation performance was achieved at epoch seven. Figure 3 shows the validation MSE with respect to epoch. The best validation performance is observed as 0.01149 at epoch 9.

In the model development process, the standard 70-15-15 approach was used where 15% of the data points were for model validation, 70% of the data points for model training, and 15% of the data points were left out for testing. The testing is performed to evaluate the model performance for data outside the training set. This serves the main goal of the study is to develop a robust model. Multiple models were developed in that process and one model with optimum prediction performance is reported. Figure 4 shows the best-performed model with correlation co-efficient R^2 for overall data is 0.84.

Figure 2. The Architecture of the ANN model.
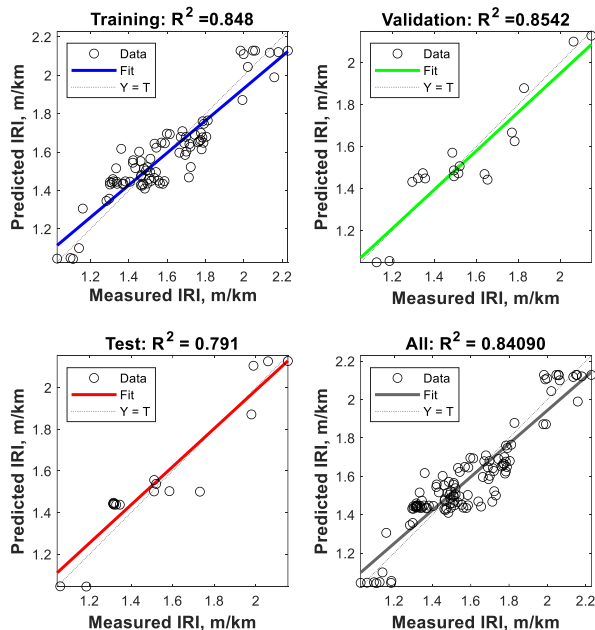
Figure 4. Correlation Coefficient of Training, Validation, Testing, and overall dataset.

For practitioners and engineers, a simple linear equation from the developed ANN model is extracted. This simple equation will predict IRI which is similar to the ANN. Equation 1 is the equation extracted from the model.

$$IRI = 0.6 \times (0.4358 \times (Tanh(1.3907\,\theta + 0.2735\,H + 0.0038\,P - 2.748\,ES - 6.8248\,GS + 0.3087\,IRI_{prev}) + (-0.2940 \times (Tanh(1.499\,\theta + 0.0133\,H + 0.0021\,P - 7.4161\,ES + 1.2243\,GS - 5.1211\,IRI_{prev}) + (-0.617 \times (Tanh(-0.8883\,\theta + 0.0973\,H - 0.0005\,P + 3.4712\,ES - 5.3669\,GS + 0.9939\,IRI_{prev}) - 0.2113 + 1) + 1 \quad (1)$$

Where IRI = International Roughness Index (m/km); IRI_{prev} = Previous year IRI (m/km); θ = Annual average temperature (°C); G = Annual GESAL; H = Annual average humidity (%); P = Annual average precipitation (mm); E = Annual ESAL

5 SENSITIVITY ANALYSIS OF THE DEVELOPED ANN MODEL

The process of sensitivity analysis is crucial for studies that involve multiple input variables. It helps to determine which independent variables have the most significant impact on the dependent variable and which ones have the least. The results of the sensitivity analysis in Figure 5 show that the IRI for rigid pavement is more sensitive to humidity, temperature, and precipitation and least sensitive to ESAL. For rigid pavement IRI climate factors play a more important role than the traffic factors.
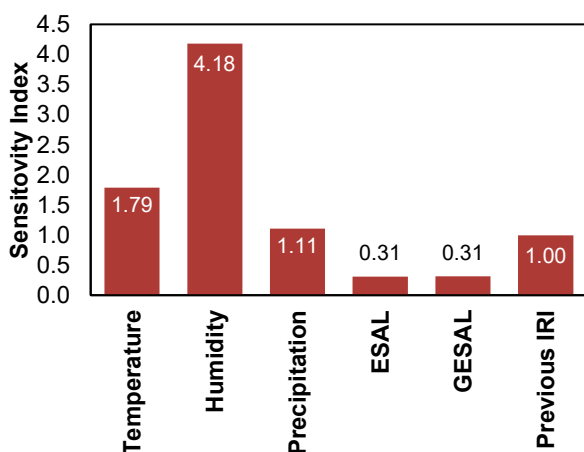
Figure 2. The Architecture of the ANN Model

6 CONCLUSIONS

The International Roughness Index (IRI) prediction model for rigid pavement is developed with the available climate and traffic data for the wet no freeze climatic conditions for three South Atlantic states - North Carolina, South Carolina, and Virginia. This ANN-based prediction model is developed after training, validation, and testing using LTPP data with R2=0.84. The constructed model can be utilized to forecast the IRI in the traffic and climatic conditions of these states.

The sensitivity index is also calculated for all input variables. From this analysis, it is shown that the climatic variables have the most effect on the output of the model than the traffic-related variables.

Additionally, unlike previous studies, a closed-form standalone equation is extracted from the model. This equation will enable the practitioner to apply the model in practical cases without expert knowledge of machine learning. The IRI prediction of rigid pavement will lead to more cost-effective and reliable maintenance strategies thanks to the equation.

7 REFERENCES

Abd El-Hakim, R. and El-Badawy, S. (2013) 'International Roughness Index Prediction for Rigid Pavements: An Artificial Neural Network Application', Advanced Materials Research, 723, pp. 854–860. Available at: https://doi.org/10.4028/www.scientific.net/AMR.723.854.

Hossain, M., Gopisetti, L.S.P. and Miah, Md.S. (2020) 'Artificial neural network modelling to predict international roughness index of rigid pavements', International Journal of Pavement Research and Technology, 13(3), pp. 229–239. Available at: https://doi.org/10.1007/s42947-020-0178-x.

Ji, Z. et al. (2024) 'Predicting the International Roughness Index of JPCP and CRCP Rigid Pavement: A Random Forest (RF) Model Hybridized with Modified Beetle Antennae Search (MBAS) for Higher Accuracy.', CMES-Computer Modeling in Engineering & Sciences, 139(2).

Luo, Z., Wang, H. and Li, S. (2022) 'Prediction of International Roughness Index Based on Stacking Fusion Model', Sustainability, 14(12), p. 6949. Available at: https://doi.org/10.3390/su14126949.

Sultana, S. et al. (2021) 'International Roughness Index Modeling For Jointed Plain Concrete Pavement Using Artificial Neural Network', IOP Conference Series: Materials Science and Engineering, 1203(3), p. 032034. Available at: https://doi.org/10.1088/1757-899X/1203/3/032034.

Wang, W. et al. (2017) 'Comparisons of Faulting-Based Pavement Performance Prediction Models', Advances in Materials Science and Engineering, 2017, pp. 1–9. Available at: https://doi.org/10.1155/2017/6845215.

Physics-based modeling of contaminant leaching in road construction materials

M.M. Masmoudi, X.L. Li, V.B. Boddeti, N.L. Lajnef
Michigan State University, East Lansing, Michigan, USA

ABSTRACT: Coal combustion products (CCPs) offer a sustainable solution for road construction but pose environmental risks due to trace element leaching. Predicting solute concentrations accurately is critical to mitigating these risks as it guides contamination assessment and effective remediation. However, the heterogeneity of soils and materials in pavement layers, along with environmental factors, hinders reliable predictive models. To address this, this study utilizes a novel method to predict seepage velocity as a field, a critical parameter for modeling contaminant transport, integrated into the advection–dispersion–reaction governing equation. Unlike traditional assumptions of constant velocity parameters, our approach provides accurate prediction of solute concentrations and valuable insights into when pollutants may reach groundwater. Numerical simulations demonstrate superior performance in estimating seepage velocity and pollutant concentrations. The findings underscore the potential of this methodology to enhance environmental risk assessment in pavement engineering and support the safe, sustainable use of CCPs in infrastructure development.

1 INTRODUCTION AND RELATED WORK

In civil engineering, the use of CCPs in road construction raises significant environmental concerns due to the potential leaching of harmful trace elements, such as cadmium, into the groundwater (Eighmy, 2001). Estimating the concentration of these solutes is crucial for assessing and mitigating the environmental impact of such materials. Several studies have modeled the leaching behavior of trace elements from CCPs in road construction, relying on known physical and chemical parameters, such as soil permeability, porosity, and hydraulic conductivity, to predict solute movement (Kim, 2002; Mudd, 2004; Praharaj, et al., 2002). However, these parameters are often difficult to measure accurately due to the inherent variability in soil composition, changes in material properties over short spatial scales, and the influence of environmental factors such as moisture content, temperature, and pressure gradients. Additionally, measuring these properties often requires controlled laboratory tests on extracted samples, which are not only time-consuming and labor-intensive but also impractical for in-field applications without causing damage to the pavement structure.

One of the most critical parameters for predicting the transport of contaminants is the seepage velocity, which influences the rate at which pollutants migrate through soil layers. This parameter is challenging to measure directly, as it is dependent on soil properties such as porosity, tortuosity, and hydraulic conductivity, all of which are spatially variable and difficult to obtain in practice. Without accurate knowledge of these parameters, reliable predictions of solute concentrations become extremely difficult, undermining risk assessments and decision-making in environmental management. Moreover, road materials and the underlying soil layers are inherently heterogeneous, meaning that the seepage velocity must be modeled as a field parameter to reflect this spatial variability.

In recent years, machine learning tools, particularly Physics-Informed Neural Networks (PINNs), have shown promise in estimating the parameters needed to solve partial differential equations (PDEs) governing solute transport. PINNs have been used successfully to predict material properties and flow characteristics in civil engineering problems, leveraging available data and solving the PDEs directly without needing traditional numerical methods (Raissi, et al.,

2019; Bolandi, et al., 2023). These models learn the underlying physical laws governing the system and can predict unknown parameters with fewer measurements, making them highly efficient. However, PINNs still require substantial data for training and may not be as efficient in cases with limited data. Alternative parameter estimation methods have demonstrated significant potential in estimating parameters for partial differential equations (PDEs) using limited or sparse data. These methods have been successfully applied across various domains, including beam vibration, heat conduction, and electrophysiology (Li, et al., 2022; Li, et al., 2024; Masmoudi, et al., 2024).

Our approach offers a more data-efficient solution by predicting the seepage velocity with significantly less data, using only response data (i.e., the observed concentration of pollutants over time) without the need for direct measurements of soil properties. This is particularly advantageous in real-world scenarios where obtaining extensive datasets for all relevant parameters can be costly and time-consuming. Furthermore, our method is capable of extrapolating future outcomes, allowing for predictions about when pollutants will reach the groundwater table. This predictive capability makes our approach a valuable tool for long-term environmental risk assessment, offering actionable insights into the environmental impact of using CCPs in road construction with far less data than traditional models.

2   MODELING SETUP

The proposed method discretizes PDEs spatially using Finite Difference discretization. The seepage velocity V_z is modeled by a feed-forward neural network with spatial coordinates inputs x and y, which correspond to the coordinates of the nodes. The network in this study consists of 6 layers, each of the middle four layers containing 50 neurons and featuring skip-connections. The network parameters are denoted as θ, and the seepage velocity is modeled as $V_z(x, y) = N(x, y, \theta)$. The estimated seepage velocity from the neural network is inserted into differential equations for forward inference (state variable prediction). The inference is compared with available observations in mini-batches to compute the loss. We employed the L1 loss function $L(\theta) = \sum |C_{pred} - C_{Ground\ Truth}|$ as it provided superior results compared to both L2 and normalized L2 loss. To optimize the parameters and train the network, the adjoint sensitivity method, combined with reverse-mode automatic differentiation techniques is utilized for solving differential equations and efficiently computing the gradient of the loss function through the PDE solver (Rackauckas, et al., 2019; Chen, et al., 2018).

3   PROBLEM SETUP

In previous studies (Li, et al., 2006; Zheng & Bennett, Gordon D, 2002), seepage velocity has been modeled as a scalar parameter, assuming that the CCP layer and subgrade layer exhibit homogeneity in key properties such as porosity, hydraulic conductivity, and hydraulic gradient. This simplification directly neglects the spatial variability that is often present in real-world systems. In this work, we address this limitation by modeling seepage velocity as a spatially dependent field parameter, capturing the inherent heterogeneity in these layers. By defining seepage velocity as a nonlinear function, we account for variations in material properties and hydraulic conditions, enabling a more realistic representation of the flow dynamics. This approach provides a significant improvement over traditional models, offering a framework better suited for analyzing complex subsurface systems.

The pavement configuration depicted in Fig. 1 is analyzed in this study, which focuses on modeling the concentration of cadmium (Cd) within the CCP and subgrade layers. The objective is to predict the timing and concentration at which this pollutant may reach the groundwater table. To achieve this, the advection–dispersion–reaction equation (ADRE) is solved within these layers (Bear, 2012).
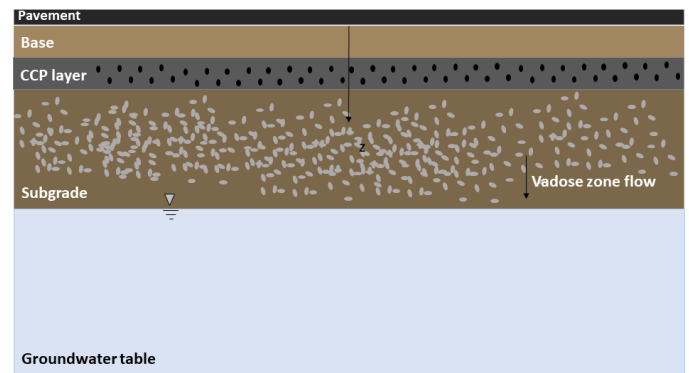
Figure 1. Layers of pavement: CCP layer and subgrade are considered heterogeneous materials, resulting in spatially dependent seepage velocity.

3.1   *Governing Equations*

Leaching occurs as water moves downward through the CCP layer, following different patterns such as first-flush, lagged response, or empirically defined behaviors. First-flush leaching is modeled using the ADRE with linear, instantaneous, and reversible sorption, while lagged or other patterns are described empirically based on concentration and flow data. In the vadose zone below the CCP layer, transport is modeled using the ADRE for 1D steady-state vertical flow with 2D dispersion and linear, instantaneous sorption.

$$R \frac{\partial C}{\partial t} = D_x \frac{\partial^2 C}{\partial x^2} + D_z \frac{\partial^2 C}{\partial z^2} - v_z \frac{\partial C}{\partial z} \qquad (1)$$

In this equation, C represents the solute concentration, t is time, x is the horizontal distance from the pavement centerline, z is the depth below ground surface, v_z is the vertical seepage velocity, D_x and D_z are the dispersion coefficients in the x and z directions, and R is the retardation factor. The vertical seepage velocity (v_z) is to be predicted. The hydrodynamic dispersion coefficients are calculated using $D = \alpha v_z + \tau D_0$, where α is the dispersivity (vertical or horizontal), and D_0 is the molecular diffusion coefficient (Leij, et al., 1991). It is assumed that chemical and biological reactions, which might alter or consume trace elements, are absent.

3.2 Boundary and initial conditions

$$C(x, z, t = 0) = C_0 \qquad (2)$$

$$\left(v_z C - D_z \frac{\partial C}{\partial z} \right) \Big|_{z=z_{top}} = v_z f(x, z_{top}, t) \qquad (3)$$

$$\left(\frac{\partial C}{\partial x} \right) \Big|_{x=x_0, x_L} = 0 \qquad (4)$$

Where, $x_0 = 0$, $x_L = 2m$, $z_{top,CCP} = 0m$, and $z_{top,Subgrade} = 0.3m$. $f(t)$ is the concentration from the previous layer and C_0 is the initial concentration.

3.3 Problems parameters

Table 1. Simulation Parameters.

Parameters	CCP Layer	Subgrade
Initial concentration $C_0 (\mu g/l)$	4	0
Tortuosity τ	0.7	0.7
Longitudinal dispersivity α_L	0.1	0.1
Transverse dispersivity α_T	0.01	0.01
Retardation factor R	3.5	3.5
Molec`ular diffusion coefficienD_0 ($10^{-10} m^2/s$)	6.0	6.0

We conducted contaminant leaching analysis on the CCP and subgrade layers using a computational mesh with 400 nodes per layer. The system dimensions included a $2m$ width, a $0.3m$ deep CCP layer, and a $4.5m$ deep subgrade layer. The subgrade material was modeled as silt loam. The seepage velocity in the CCP layer was modeled with a nonlinear distribution ranging from 0.19 to 0.26, while for the subgrade layer, it ranged from 0.91 to 1.12.

4 NUMERICAL RESULTS

We demonstrate the efficacy of our method in predicting a nonlinear field seepage velocity distribution, achieving a mean absolute percentage error (MAPE) as low as 1.6%. We also analyze the system's response at $t = 40$ years, where the response mean absolute error (MAE) remains below $3 \times 10^{-4} \mu g/l$ when utilizing the predicted field seepage velocity.
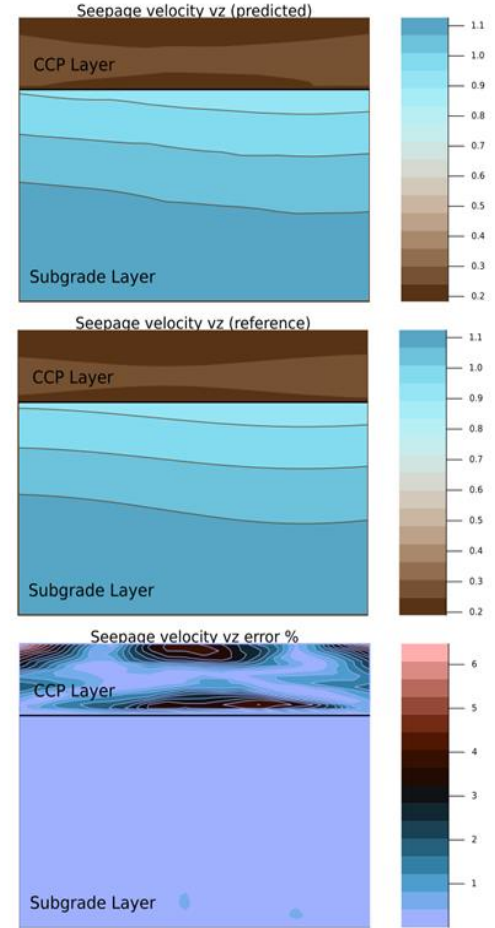
Figure 2. Accurate estimation of the field seepage velocity V_z with a MAE of 1.6%.

To provide a comprehensive comparison and emphasize the importance of modeling the parameter as a field rather than a scalar, we also present the system response based on scalar parameter prediction. In this case, a single neuron predicts the scalar parameter, which typically converges to the mean of the ground truth field parameter distribution. However, this approach results in substantial errors, with a forward inference MAE of $2.6 \times 10^{-2} \mu g/l$ compared to just $3 \times 10^{-4} \mu g/l$ for the field-based approach by our method Furthermore, we evaluate our method's extrapolation performance at $t = 50$ years, where it achieves an MAE of $8 \times 10^{-3} \mu g/l$ relative to the ground truth. In contrast, the extrapolated response using the scalar parameter model shows a significantly higher error of $8 \times 10^{-5} \mu g/l$. We successfully trained our model using only 600 measurements per layer, distributed across both temporal and spatial dimensions.
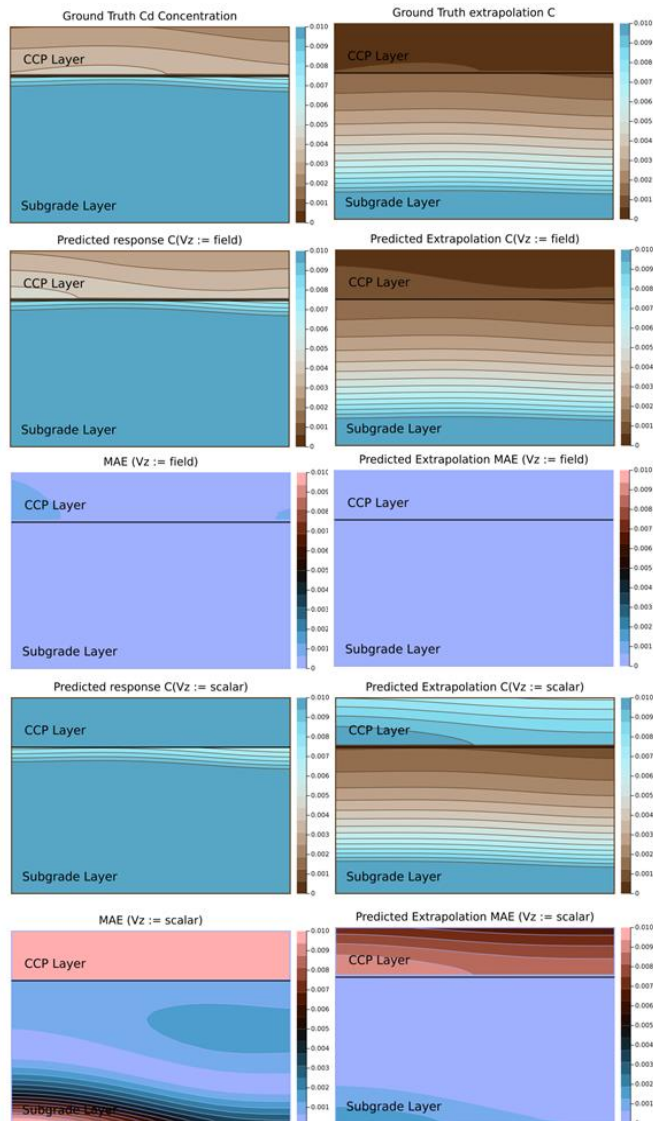
Figure 3. Forward inference using the predicted parameter shows our method's robust performance in both interpolation and extrapolation tasks. Field parameter modeling achieves a forward inference MAE of $3 \times 10^{-4} \mu g/l$ (first column), significantly outperforming scalar parameter modeling (MAE of $2.6 \times 10^{-2} \mu g/l$. Extrapolation at $t = 50$ years (second column) results in an MAE of $8 \times 10^{-3} \mu g/l$, compared to $8 \times 10^{-5} \mu g/l$ for the scalar model.

5 CONCLUSION

This paper presents a novel approach for modeling seepage velocity as a spatially dependent field parameter, achieving a remarkable improvement in prediction accuracy. The proposed method reduces error to $3 \times 10^{-4} \mu g/l$, a substantial enhancement compared to the previous accuracy of $2.6 \times 10^{-2} \mu g/l$ in predicting contaminant transport through heterogeneous pavement layers. The model not only outperforms scalar-based methods but also demonstrates strong extrapolation capabilities, enabling reliable predictions of when and at what concentration pollutants will reach groundwater. This predictive ability provides valuable insights for taking timely precautions,

making the method a powerful tool for mitigating groundwater contamination risks in CCP-based road construction.

6 REFERENCES

Bear, J., 2012. *Hydraulics of groundwater.* s.l.:Courier Corporation.

Bolandi, H. et al., 2023. Physics informed neural network for dynamic stress prediction. *Applied Intelligence,* Volume 53, pp. 26313-26328.

Chen, R. T., Rubanova, Yulia, Bettencourt, Jesse & Duvenaud, David K, 2018. Neural ordinary differential equations. *Advances in neural information processing systems,* Volume 31.

Eighmy, T. T. a. C. W. H. a. o., 2001. Framework for Evaluating Use of Recycled Materials in the Highway Environment. *United States. Department of Transportation. Federal Highway Administration.*

Kim, A. G., 2002. *CCB leaching summary: Survey of methods and results.* s.l., Proceedings of Technical Interactive Forum, Coal Combustion By-Products and Western Coal Mines.

Leij, F. J., Skaggs, Todd H & Van Genuchten, Martinus Th, 1991. Analytical solutions for solute transport in three-dimensional semi-infinite porous media. *Water resources research,* Volume 27, pp. 2719-2733.

Li, L., Benson, Craig H, Edil, Tuncer B & Hatipoglu, Bulent, 2006. *Groundwater impacts from coal ash in highways.* s.l., Proceedings of the institution of civil engineers-waste and resource management.

Li, X. et al., 2022. *NeuralSI: Structural Parameter Identification in Nonlinear Dynamical Systems.* s.l., European Conference on Computer Vision.

Li, X., Masmoudi, Mahdi, Lajnef, Nizar & Boddeti, Vishnu, 2024. *Estimating field parameters from multiphysics governing equations with scarce data.* s.l., ICLR 2024 Workshop on AI4DifferentialEquations In Science.

Masmoudi, M., Li, Xuyang, Lajnef, Nizar & Boddeti, Vishnu, 2024. *ParaFIND: Parameter Field Inference on Non-uniform Domains using Neural Network.* s.l., NeurIPS 2024 Workshop on Data-driven and Differentiable Simulations, Surrogates, and Solvers.

Mudd, G. M., 2004. Environmental geochemistry of leachate from leached brown coal ash. *Journal of environmental engineering,* Volume 130, pp. 1514-1526.

Praharaj, T., Powell, MA, Hart, BR & Tripathy, S, 2002. Leachability of elements from sub-bituminous coal fly ash from India. *Environment international,* Volume 27, pp. 609-615.

Rackauckas, C. et al., 2019. Diffeqflux. jl-A julia library for neural differential equations. *arXiv preprint arXiv:1902.02376.*

Raissi, M., Perdikaris, Paris & Karniadakis, George E, 2019. Physics-informed neural networks: A deep learning framework for solving forward and inverse problems involving nonlinear partial differential equations. *Journal of Computational physics,* Volume 378, pp. 686-707.

Zheng, C. & Bennett, Gordon D, 2002. Applied contaminant transport modeling. *Wiley-Interscience New York,* Volume 2.

Complex Shadow Removal in Pavement Imagery: Leveraging Diffusion Models for Advanced Solutions

T.W. Muturi, Y. Adu-Gyamfi & D. Kesse
University of Missouri, Columbia, Columbia, Missouri, USA

ABSTRACT: Shadows introduce uneven illumination; obscuring crack details and causing shadow boundaries to be misinterpreted as cracks within crack detection algorithms. This study proposes a shadow removal algorithm leveraging conditional diffusion models to eliminate shadows in top-down and oblique-view pavement images. We introduce the Pavement Image Shadow Triplet Dataset (PISTD), based on the ISTD dataset for the task. Hyperparameter tuning and training are explored on 256x256 and 512x512-pixel images to determine the tradeoff between crack detection accuracy and reconstruction precision. Moreover, the two models are compared with state-of-the-art models across PSNR, RMSE, and F1 accuracy metrics. The proposed model achieves a 6% and 38% higher segmentation accuracy on top-down and oblique view images, respectively. Evaluation of the algorithm is performed with real-world shadow images with qualitative results on the images demonstrating the effectiveness of the approach.

1 INTRODUCTION

To streamline maintenance operations, pavement management systems (PMS) have been implemented to survey, analyze, and assist decision-makers in allocating resources for pavement maintenance (Al-Mansour et al., 2022). As an initial step in pavement management, data collection is critical to the decision-making process.

Various data collection methods such as manual surveys, cameras or laser scanners fitted to vehicles, portable platforms, and unmanned aerial vehicles (UAVs), have been employed. Recent efforts have seen the adoption of cameras fitted to portable devices such as cars, motorcycles, and bicycles for the collection of pavement distress information (Arya et al., 2022). This approach is lauded for its cost-effectiveness and efficiency in data collection. For instance, Mei and Gül (2020) reported spending approximately 350 USD on purchasing and mounting a GoPro to their vehicle for pavement distress data collection. Furthermore, the efficiency of this approach is also evident in the introduction of big data competitions that utilize camera data for pavement distress detection (Arya et al., 2022). However, the adoption of this cost-effective data collection method inevitably encounters the challenge of shadows within the images.

Shadows obscure crack patterns due to their similar intensity to crack regions (Zou et al., 2012). Additionally, boundary regions caused by shadows can be misinterpreted as cracks, leading to false positive detections (Pal et al., 2021). Furthermore, the uneven illumination caused by shadow regions results in inconsistencies in detection by machine learning and segmentation algorithms (Zou et al., 2012). Therefore, the elimination of shadow regions in these images is paramount for the accurate detection of pavement distress.

This article therefore aims to adopt a novel shadow removal algorithm in top-down and oblique-view pavement images captured with low-cost cameras. Specifically, we will (1) Compile a Pavement Image Shadow Triplet Dataset (PISTD) composed of top-down and oblique-view pavement distress images by performing image processing manipulation on shadow-free images using ISTD (Wang et al., 2017) mask images. (2) Train the latent diffusion model by Mei et al. (2023) to eliminate shadows in pavement images. Hyperparameter tuning of the training iterations and learning rate will be performed. Additionally, the model will be trained with 512x512 and 256x256 image sizes. (3) Compare model results with existing state-of-the-art models using Root Mean Squared Error (RMSE), Peak Signal-to-Noise Ratio (PSNR), and F1 score metrics. F1 score metrics are based on segmentation accuracy. (4) Test the zero-shot performance of the model for shadow removal.

2 LITERATURE REVIEW

Within literature, shadow removal across different scenes has been explored through image processing and deep learning approaches. Deep learning has emerged as a prevailing standard for shadow removal through popular algorithms such as the Shadow-GAN (Hu et al., 2019), Stacked Conditional GAN (ST-CGAN) (Wang et al., 2017), ARGAN (Ding et al., 2019), and DC-ShadowNet (Jin et al., 2023). However, these models require a large amount of training data and, due to their architecture and adversarial training approach, they are computationally complex. This complexity can introduce training instability and poor generalizability (Mei et al., 2023).

Diffusion models have demonstrated improved stability over GANs in generative tasks (Rombach et al., 2022). Given this, in an initial attempt to perform instance shadow removal, Mei et al (2023) adopted the conditional diffusion model for shadow removal across different scenes. Although this approach outperforms state-of-the-art methods, it has not been specifically applied to pavement images, which present a new level of complexity due to the similarity in intensity between shadow regions and cracks.

3 PROPOSED METHODOLOGY

In this research, a diffusion network is employed for shadow removal due to its robustness compared to other methods. The algorithm proposed by Mei et al. (2023) is selected over other diffusion techniques as it introduces a learned latent feature space used for conditioning the diffusion model and integrates noise features within the diffusion network to mitigate the risk of converging to local optima during training. The adopted algorithm can be delineated into three critical modules: (1) the conditional diffusion module, (2) the latent encoder module, and (3) the noise fusion module.

3.1 *Conditional Diffusion Module*

As an extension of ordinary diffusion models, conditional diffusion models incorporate additional information or conditions, such as class labels, text descriptions, or other modalities during training. Fundamentally, diffusion models simulate the process of data corruption (forward diffusion process) and its reversal (reverse diffusion process), enabling the generation of new data samples by reversing the diffusion process. In the context of this research, the forward process corrupts the shadowed image, while the reverse process generates the shadow-free image.

3.2 *Latent Encoder*

In this research, a novel latent feature space is employed to guide the model. Given the shadow

mask and the shadowed image, the latent encoder generates a latent feature vector, which is subsequently used as the condition within the diffusion model. A U-Net model with an architecture similar to that of the diffusion network is adopted.

3.3 *Noise Fusion Model*

Posterior collapse refers to a phenomenon where the learned latent representations fail to encode meaningful information about the input data. Observed within diffusion models, this happens when the training procedure of generative models falls into a trivial local optimum. Posterior collapse is especially undesirable in shadow removal due to the complexity of different shadows within the models. This article, therefore, adopts Mei et al. (2023) approach, which involves fusing the learned embeddings and features within the diffusion network to overcome posterior collapse.

4 DATASET

Within the domain of shadow removal, two primary benchmark datasets are commonly referenced: the ISTD (Wang et al., 2017) and AISTD/ISTD+ (Le & Samaras, 2019). The ISTD and AISTD datasets include triplets of shadow images, shadow-free images, and shadow masks, covering a variety of scenes such as walls, grass surfaces, and sidewalks of different colors. However, shadow removal on pavements presents unique challenges as pavement distresses can have intensities similar to those within the shadowed regions.

This article therefore introduces the Pavement Image Shadow Triplet Dataset (PISTD). To construct this dataset, shadow masks from the ISTD dataset are applied to pavement images with varying degrees of opacity. To better emulate real-world shadow conditions, these masks are enlarged to cover more extensive regions within the images. Top-down shadow images are sourced from the CFD (Shi et al., 2016), CrackTree200 (Zou et al., 2012), and DSPS24 datasets. Additionally, to replicate angled data collection, crack-free images were manually collected by the authors. To further augment this dataset, crack-free images from the EdmCrack600 (Q. Mei & Gül, 2020) dataset were also included. Figure 1 presents an example of shadow image, shadow mask and shadow-free image. The entire dataset was divided into training and testing sets in a 4:1 ratio to facilitate robust evaluation.
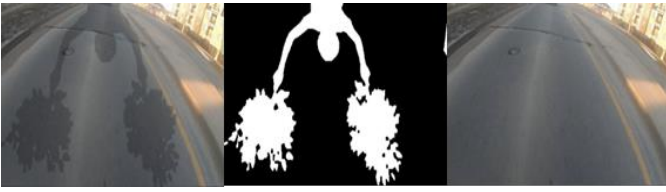
Figure 1. PISTD sample.

5 TRAINING

Hyperparameter tuning was performed with results revealing a learning rate of 1.0e-5, training over 300,000 iterations with a gaussian noise schedule steps of 1,000 achieving optimum performance. Furthermore, a comparison of training on different image sizes (256x256 vs 512x512) showed that an increase in image size results in a decrease in PSNR and an increase in RMSE.

Give a batch size of 1, trained over an NVIDIA RTX 3090 GPU with 24GB of memory compute, took approximately 81 hours with a 512x512 image size.

6 RESULTS

6.1 Comparison with the state-of-the-art

The performance metrics of the model are benchmarked against three state-of-the-art shadow removal models: DC-ShadowNet (Jin et al., 2023), SG-ShadowNet (Wan et al., 2022), and G2R-ShadowNet (Qu et al., 2017). These comparative models utilize Generative Adversarial Networks (GANs) with distinct variations in their architectures, loss functions, and training methodologies

As observed in Table 1, our model, trained on 256x256 images, achieves PSNR and RMSE metric scores comparable to state-of-the-art models when tested on top-down view images. Although these values represent a slight decrease compared to the best-performing SG-ShadowNet, our approach produces smoother, shadow-free images (Figure 2 last column). The slightly lower RMSE and PSNR are attributed to the noise introduced by our model; however, this noise does not adversely affect segmentation accuracy, as demonstrated by an F1 score of 59.3% (Table 1).

Table 2 presents the quantitative comparisons of the models when tested on angled view images. As shown, our model outperforms all other approaches on the RMSE and PSNR metrics when trained on 256x256-sized images. Similarly to top-down view images, while other models result in shadow boundaries, our proposed approach achieves smoother shadow removal (Figure 2). However, as in the top-down view results, the proposed model trained on 512x512 images exhibits a color shift, adversely af-

fecting the RMSE and PSNR values. Despite this color shift, the model effectively removes all shadows within the images, attaining a 61.4% F1 score for segmentation, a 74% increase from the shadow image (Table 2).

Table 1. Quantitative comparison results in top-down view images

Method	RMSE	PSNR	F1 score
DC-Shadow Net	9.8	28.9	55.5
SG-Shadow Net	**7.4**	**31.9**	49.3
G2R-ShadowNet	10.9	30.1	39.5
Ours-256	9.5	30.0	39.5
Ours-512	14.4	26.0	**59.3**
Shadow Image	_	_	43.7

Table 2. Quantitative comparison results in oblique view images.

Method	RMSE	PSNR	F1 score
DC-Shadow Net	8.1	30.6	44.2
SG-Shadow Net	8.8	30.1	37.2
G2R-ShadowNet	12.3	28.2	32.9
Ours-256	**7.8**	**31.0**	47.3
Ours-512	11.3	28.1	**61.4**
Shadow Image	_	_	33.7
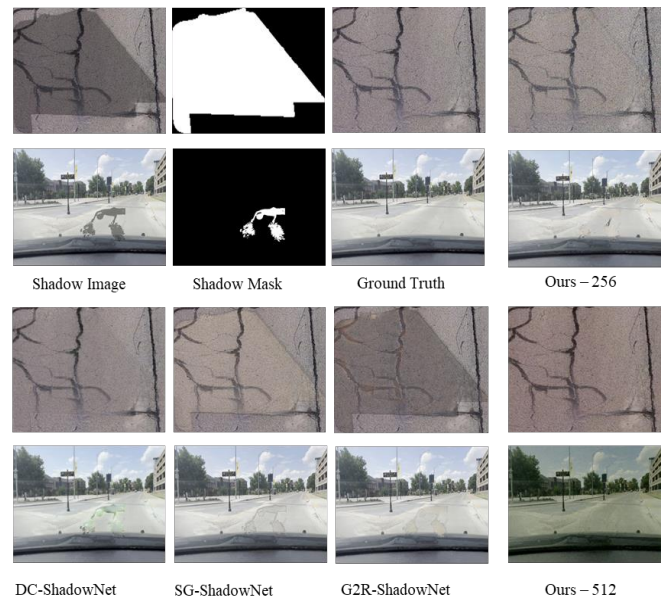
Figure 2. Visual comparison of shadow removal algorithms.

6.2 Zero-shot Results

This section aims to evaluate the proposed approach's performance with real-world shadows. As shown in Figure 3, the images presented are captured at an oblique angle, representing the current trend in data collection studies. Since original masks for these images do not exist, a SAM model was trained and used to develop shadow masks for the evaluation. As observed, given the SAM shadow mask, the proposed model eliminates shadows with high accuracy, particularly in the model trained with

256x256-pixel images. In contrast, the model trained with 512x512-pixel images experiences a color shift and struggles with a larger shadow boundary.
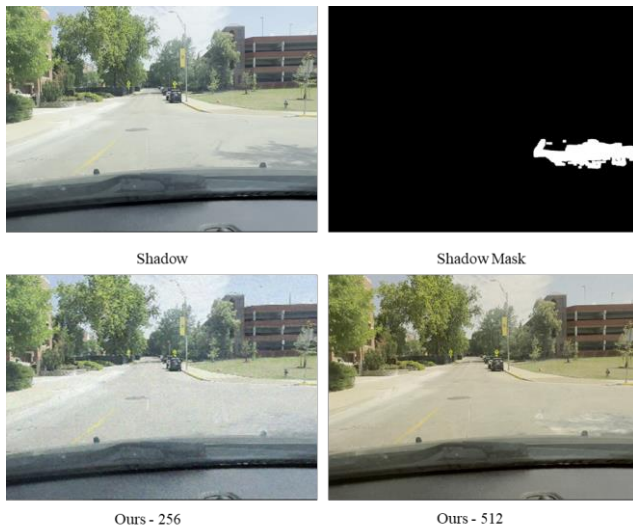
Figure 3. Zero shot results of the proposed approach.

7 CONCLUSION

This study presents a novel approach for shadow removal in pavement imagery using a diffusion model conditioned on encoded mask and shadow image latent. To achieve this, a Pavement Shadow Triplet Dataset (PSTD) was introduced by combining masks from the ISTD dataset with different pavement images at varying opacity. Hyperparameter tuning during model training showed that a learning rate of 1e-5 and training over 300,000 epochs resulted in the best model accuracy. A comparison of different image sizes revealed the model trained with 256x256-pixel images exhibited a superior performance in both quantitative metrics (PSNR and RMSE) and qualitative assessments, providing smoother shadow-free images without the shadow boundaries observed in other models. The model trained with 512x512-pixel images, while effective in shadow removal, exhibited a color shift that affected RMSE and PSNR values, highlighting the complexity introduced by larger image sizes. A comparison of segmentation accuracy shows the model trained on 512x512-pixel images attains the highest F1 score on both angled and top-down view pavement images. This was attributed to the increased resolution associated with larger images. The zero-shot capability of our model was validated through the accurate removal of shadows in real-world oblique view images, further showcasing the proposed approach's robustness and applicability in practical scenarios.

Our results indicate that the proposed approach not only meets but often exceeds the performance of existing methods in shadow removal tasks. Future work should focus on addressing the color shift in larger images.

8 REFERENCES

Al-Mansour, A., Lee, K.-W. W., & Al-Qaili, A. H. (2022). Prediction of Pavement Maintenance Performance Using an Expert System. *Applied Sciences*, *12*(10), Article 10. https://doi.org/10.3390/app12104802

Arya, D., Maeda, H., Ghosh, S. K., Toshniwal, D., Omata, H., Kashiyama, T., & Sekimoto, Y. (2022). *Crowdsensing-based Road Damage Detection Challenge (CRDDC-2022)* (arXiv:2211.11362). arXiv. https://doi.org/10.48550/arXiv.2211.11362 arXiv. https://doi.org/10.48550/arXiv.2209.08538

Ding, B., Long, C., Zhang, L., & Xiao, C. (2019). *ARGAN: Attentive Recurrent Generative Adversarial Network for Shadow Detection and Removal* (arXiv:1908.01323). arXiv. https://doi.org/10.48550/arXiv.1908.01323

Hu, X., Jiang, Y., Fu, C.-W., & Heng, P.-A. (2019). Mask-ShadowGAN: Learning to Remove Shadows from Unpaired Data. *2019 IEEE/CVF International Conference on Computer Vision (ICCV)*, 2472–2481. https://doi.org/10.1109/ICCV.2019.00256

Jin, Y., Sharma, A., & Tan, R. T. (2023). *DC-ShadowNet: Single-Image Hard and Soft Shadow Removal Using Unsupervised Domain-Classifier Guided Network* (arXiv:2207.10434). arXiv. https://doi.org/10.48550/arXiv.2207.10434

Le, H., & Samaras, D. (2019). *Shadow Removal via Shadow Image Decomposition* (arXiv:1908.08628). arXiv. https://doi.org/10.48550/arXiv.1908.08628

Mei, K., Figueroa, L., Lin, Z., Ding, Z., Cohen, S., & Patel, V. M. (2023). *Latent Feature-Guided Diffusion Models for Shadow Removal* (arXiv:2312.02156). arXiv. https://doi.org/10.48550/arXiv.2312.02156

Mei, Q., & Gül, M. (2020). A cost effective solution for pavement crack inspection using cameras and deep neural networks. *Construction and Building Materials*, *256*, 119397. https://doi.org/10.1016/j.conbuildmat.2020.119397

Pal, M., Palevičius, P., Landauskas, M., Orinaitė, U., Timofejeva, I., & Ragulskis, M. (2021). An Overview of Challenges Associated with Automatic Detection of Concrete Cracks in the Presence of Shadows. *Applied Sciences*, *11*(23), Article 23. https://doi.org/10.3390/app112311396

Rombach, R., Blattmann, A., Lorenz, D., Esser, P., & Ommer, B. (2022). *High-Resolution Image Synthesis with Latent Diffusion Models* (arXiv:2112.10752). arXiv. https://doi.org/10.48550/arXiv.2112.10752

Shi, Y., Cui, L., Qi, Z., Meng, F., & Chen, Z. (2016). Automatic Road Crack Detection Using Random Structured Forests. *IEEE Transactions on Intelligent Transportation Systems*, *17*(12), 3434–3445. IEEE Transactions on Intelligent Transportation Systems. https://doi.org/10.1109/TITS.2016.2552248

Wang, J., Li, X., Hui, L., & Yang, J. (2017). *Stacked Conditional Generative Adversarial Networks for Jointly Learning Shadow Detection and Shadow Removal* (arXiv:1712.02478). arXiv. https://doi.org/10.48550/arXiv.1712.02478

Zou, Q., Cao, Y., Li, Q., Mao, Q., & Wang, S. (2012). CrackTree: Automatic crack detection from pavement images. *Pattern Recognition Letters*, *33*(3), 227–238. https://doi.org/10.1016/j.patrec.2011.11.004

Autonomous synthetic data generation for asphalt pavement crack segmentation using generative models

M. Sedighian-Fard
Department of Civil and Environmental Engineering, Amirkabir University of Technology (Tehran Polytechnic), Tehran, Iran.

A. Golroo
Department of Civil and Environmental Engineering, Amirkabir University of Technology (Tehran Polytechnic), Tehran, Iran.

Faculty of Information Technology and Electrical Engineering, University of Oulu, Oulu, Finland.

S. Nouri
Faculty of Information Technology and Electrical Engineering, University of Oulu, Oulu, Finland.

M. Rasti
Faculty of Information Technology and Electrical Engineering, University of Oulu, Oulu, Finland.

ABSTRACT: This study addresses the challenge of limited annotated datasets in pavement crack analysis by integrating synthetic data generation with automated segmentation models. The Wasserstein Generative Adversarial Network with Gradient Penalty (WGAN-GP) was utilized to generate realistic synthetic pavement images, and the U-Net model was used to enhance segmentation accuracy. Current datasets, such as Crack500, lack sufficient size and diversity, limiting model performance. By augmenting the dataset with synthetic images in increments of 20% to 2000%, segmentation performance improved significantly. The superior model, trained with a 2000% increase in synthetic data, achieved an Intersection over Union (IoU) score of 0.92, demonstrating the effectiveness of data augmentation in improving segmentation. These findings highlight the potential of combining generative and segmentation models to address data scarcity in pavement management.

1 INTRODUCTION

The transportation network is a vital national asset, and its deterioration requires timely maintenance to avoid high costs (Coenen & Golroo, 2017). Pavement Management Systems (PMS) optimize maintenance through data collection, analysis, and planning, with automated methods like dynamic sensors and image-based techniques offering efficiency (Sholevar et al., 2022). Crack detection is key, but traditional methods often face challenges in complex conditions (Chambon & Moliard, 2011). Deep Learning-based (DL) predictive models have improved detection accuracy, but they require large, high-quality datasets, which are often scarce (Arya et al., 2021; Shi et al., 2016). Generative Adversarial Networks (GANs) help by generating synthetic crack images to augment datasets, though challenges like mode collapse and resolution limitations remain (Gulrajani et al., 2017).

2 LITERATURE REVIEW

Various GAN variants, such as Conditional GANs (CGANs) and CycleGANs, have been used to enhance image generation for pavement crack detection (Zhu et al., 2017). Generative Adversarial Network with Gradient Penalty (WGAN-GP) addresses data imbalance and generates high-quality crack images (Hou et al., 2022), while Deep Convolutional GAN (DCGAN) and CrackGAN improve detection accuracy through integration with Convolutional Neural Networks (CNNs) (Xu & Liu, 2022). Methods like Progressive Generative Adversarial Network (ProGAN) and WGAN-GP stabilize training and improve image resolution (Karras et al. 2017, Gulrajani et al. 2017), and combining Variational Autoencoders (VAE) with DCGAN enhances image quality (Pei et al., 2021). Additionally, integrated frameworks like Automatic Pavement Crack Generation Adversarial Network (APC-GAN) and Attention Network (AttuNet) excel in pixel-level segmentation (Zhang et al., 2023). CNNs, especially U-Net-based architectures, have proven effective in crack detection and segmentation (Fan et al. 2018, König et al. 2020), advancing automated pavement assessment systems.

3 METHODOLOGY AND DATASET PREPARATION

The dataset for this study includes 11,298 images from 12 crack detection datasets, with 9,603 for training and 1,695 for testing. A subset of 3,000 pavement distress images, covering various crack types, was used to train both the WGAN-GP and U-Net models. All images were resized to 128×128 pixels for con-

sistency, normalized, and augmented using techniques like random flips, rotations, and brightness adjustments to enhance variability and robustness. The WGAN-GP model generated synthetic pavement distress images, which were added to the limited Crack 500 dataset in varying proportions. These augmented datasets were then used to train and test the U-Net model. The effectiveness of the synthetic data in improving the model's performance was assessed by evaluating the U-Net on datasets with different combinations of real and generated images, aiming to optimize the performance of the pavement distress prediction model.

3.1 WGAN-GP Model

The WGAN-GP model consists of a generator and a discriminator. The generator, built with transposed convolutional layers, creates 128x128 grayscale images from random noise, using batch normalization, ReLU activation, and a final Tanh activation to scale pixel values. The discriminator processes input images through convolutional layers, downscaling them until producing a scalar output that classifies the image as real or generated, using LeakyReLU activation and batch normalization. The model employs a gradient penalty to ensure Lipschitz continuity, stabilizing training by penalizing large gradient norms. Performance is evaluated utilizing four metrics, including Mean Squared Error (MSE), Structural Similarity Index (SSIM), Dice coefficient, and Peak Signal-to-Noise Ratio (PSNR). These metrics assess image quality, structural similarity, segmentation accuracy, and noise levels, respectively, providing a comprehensive evaluation of the generator's output.

3.2 Pavement Crack Segmentation Model

The study used a U-Net-based model with a ResNet34 encoder for pavement crack segmentation. The model was trained on the Crack 500 dataset, augmented with synthetic images generated by the WGAN-GP model (50, 150, 250, 1000, and 5000 images). Performance was evaluated using loss, Dice coefficient, and Intersection over Union (IoU). Lower loss and higher Dice coefficient and IoU values indicated better model performance, with these metrics assessing the impact of synthetic data on segmentation accuracy for pavement crack detection.

4 RESULTS

This section evaluates the impact of augmenting the Crack 500 dataset with synthetic images generated by the WGAN-GP model. Synthetic images were added in increments of 50, 150, 250, 1000, and 5000, corresponding to percentage increases of 20%, 60%, 100%, 400%, and 2000%, respectively. The U-Net model's performance was assessed using metrics such as training, validation, and test loss, Dice coefficient, and IoU to determine how the addition of synthetic data improved segmentation accuracy.

4.1 Effectiveness of the WGAN-GP

The WGAN-GP model generated realistic pavement distress images to augment the Crack 500 dataset. Preprocessing steps included converting images to grayscale, resizing to 128×128 pixels, and applying augmentations like flips and rotations. The generated images were evaluated with MSE (0.040), SSIM (0.71), Dice coefficient (0.89), and PSNR (14 dB). The results indicated minimal pixel differences, moderate structural fidelity, and good capture of key features like cracks. Visual comparisons (Figure 1) confirmed the generated images closely resembled real data, demonstrating the model's effectiveness for data augmentation in segmentation tasks.
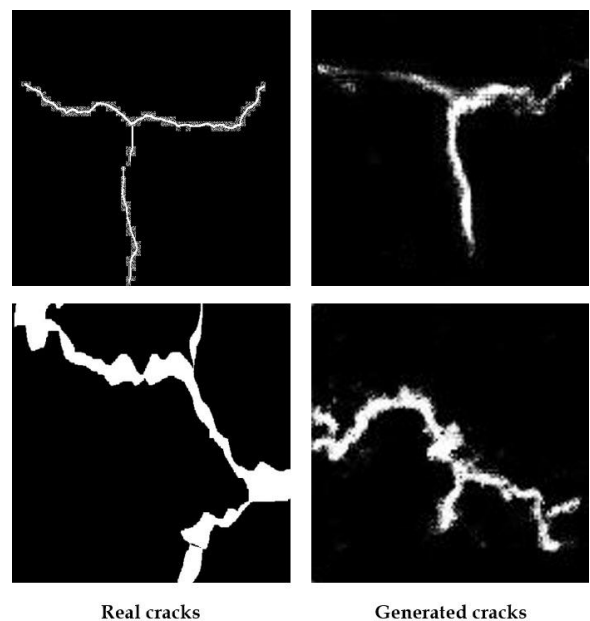
Figure 1. Comparison of real and GAN-generated pavement images.

4.2 Effectiveness of the U-Net Model

The U-Net model was first trained on the original Crack500 dataset to establish baseline performance. After training for 50 epochs, the model achieved a training loss of 0.031, a validation loss of 0.032, a

Dice coefficient of 0.93 for training, and 0.92 for validation, along with IoU values of 0.87 (training) and 0.86 (validation), indicating good generalization. Subsequently, the model was trained with varying amounts of augmented images generated by the WGAN-GP model. As the number of augmented images increased, performance improved, as shown in Table 1. The model performed best with 1000 augmented images, achieving a significant reduction in loss (0.010), a Dice Coefficient of 0.96, and an IoU of 0.92. Further augmentation with 5000 images resulted in slight performance improvement, but also a slight increase in loss, indicating diminishing returns.

Table 1. Performance of U-Net model with different percentages of augmented images added to the Crack500 dataset - test set.

Parameter	Original	Augmented data				
		+50	+150	+250	+1000	+5000
Loss	0.032	0.031	0.025	0.021	0.010	0.020
Dice Coefficient	0.92	0.93	0.94	0.94	0.96	0.94
IoU	0.86	0.87	0.89	0.90	0.92	0.90

Figure 2 illustrates the U-Net model's training dynamics with 1000 augmented images. The loss decreased steadily, and the Dice coefficient and IoU values improved over the epochs, reaching 0.96 and 0.92 by the end of training. This suggests that adding augmented data significantly enhanced the model's segmentation performance, with optimal results achieved by increasing the dataset size by 2000%.
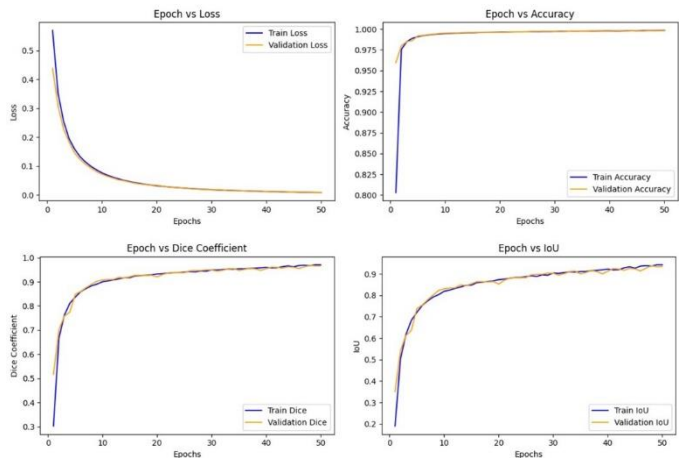
Figure 2. Loss, Accuracy, Dice coefficient, and IoU for U-Net with 1000 augmented images.

5 CHALLENGES

Training the WGAN-GP and U-Net models presented several challenges. While the WGAN-GP generated realistic synthetic images (Dice coefficient: 0.89, SSIM: 0.71), it faced stability issues and required significant computational resources and time. Generated images lacked some fine details, limiting their preci-

sion. The U-Net model showed improved performance with synthetic data, reaching optimal results with 1000 augmented images (Dice coefficient: 0.961, IoU: 0.92). However, further augmentation (2000%) showed diminishing returns, indicating redundancy and limiting improvements. The models also posed high computational demands, with the WGAN-GP taking about one hour to generate images and the U-Net requiring 30 minutes for training on the largest dataset. Balancing dataset size, computational costs, and model complexity is essential for optimizing performance

6 CONCLUSION

This study explored the use of a WGAN-GP model to generate synthetic pavement distress images and a U-Net model for crack segmentation, aiming to overcome the limitations of small annotated datasets through data augmentation. The WGAN-GP model successfully generated high-quality synthetic images, achieving a Dice coefficient of 0.89 and an SSIM of 0.71, indicating that the synthetic data closely resembled real pavement distress images. The U-Net model, trained on the original Crack500 dataset, demonstrated strong segmentation performance with a Dice coefficient of 0.92 and IoU of 0.86. Adding 1000 generated images (a 400% augmentation of the dataset) resulted in the optimal performance, with a Dice coefficient of 0.96 and IoU of 0.92. While training the WGAN-GP model took approximately 1 hour, the U-Net model required about 30 minutes for training with the largest augmented dataset, using Kaggle's cloud infrastructure. Challenges included diminishing returns in segmentation performance with excessive data augmentation, high computational costs, and the need for careful parameter tuning to avoid overfitting. Future research should focus on refining the synthetic data generation process, exploring advanced model architectures, and improving computational efficiency for large-scale applications.

7 ACKNOWLEDGEMENT

References

Arya, D., Maeda, H., Ghosh, S. K., Toshniwal, D., Mraz, A., Kashiyama, T., & Sekimoto, Y.

(2021). Deep learning-based road damage detection and classification for multiple countries. *Automation in Construction*, *132*, 103935. https://doi.org/10.1016/J.AUTCON.2021.103935

Chambon, S., & Moliard, J. M. (2011). Automatic Road Pavement Assessment with Image Processing: Review and Comparison. *International Journal of Geophysics*, *2011*(1), 989354. https://doi.org/10.1155/2011/989354

Coenen, T. B. J., & Golroo, A. (2017). A review on automated pavement distress detection methods. *Cogent Engineering*, *4*(1), 1–23. https://doi.org/10.1080/23311916.2017.1374822

Gulrajani, I., Ahmed, F., Arjovsky, M., Dumoulin, V., & Courville, A. (2017). Improved Training of Wasserstein GANs. *Advances in Neural Information Processing Systems*, *2017-December*, 5768–5778. https://arxiv.org/abs/1704.00028v3

Hou, Y., Liu, S., Cao, D., Peng, B., Liu, Z., Sun, W., & Chen, N. (2022). A Deep Learning Method for Pavement Crack Identification Based on Limited Field Images. *IEEE Transactions on Intelligent Transportation Systems*, *23*(11), 22156–22165. https://doi.org/10.1109/TITS.2022.3160524

Karras, T., Aila, T., Laine, S., & Lehtinen, J. (2017). Progressive Growing of GANs for Improved Quality, Stability, and Variation. *6th International Conference on Learning Representations, ICLR 2018 - Conference Track Proceedings*. https://arxiv.org/abs/1710.10196v3

König, J., Jenkins, M., Mannion, M., Barrie, P., & Morison, G. (2020). Optimized Deep Encoder-Decoder Methods for Crack Segmentation. *Digital Signal Processing: A Review Journal*, *108*. https://doi.org/10.1016/j.dsp.2020.102907

Pei, L., Sun, Z., Xiao, L., Li, W., Sun, J., & Zhang, H. (2021). Virtual generation of pavement crack images based on improved deep convolutional generative adversarial network. *Engineering Applications of Artificial Intelligence*, *104*, 104376. https://doi.org/10.1016/J.ENGAPPAI.2021.104376

Shi, Y., Cui, L., Qi, Z., Meng, F., & Chen, Z. (2016). Automatic road crack detection using random structured forests. *IEEE Transactions on Intelligent Transportation Systems*, *17*(12), 3434–3445. https://doi.org/10.1109/TITS.2016.2552248

Sholevar, N., Golroo, A., & Esfahani, S. R. (2022). Machine learning techniques for pavement condition evaluation. *Automation in Construction*, *136*, 104190. https://doi.org/10.1016/J.AUTCON.2022.104190

Xu, B., & Liu, C. (2022). Pavement crack detection algorithm based on generative adversarial network and convolutional neural network under small samples. *Measurement*, *196*, 111219. https://doi.org/10.1016/J.MEASUREMENT.2022.111219

Zhang, T., Wang, D., Mullins, A., & Lu, Y. (2023). Integrated APC-GAN and AttuNet Framework for Automated Pavement Crack Pixel-Level Segmentation: A New Solution to Small Training Datasets. *IEEE Transactions on Intelligent Transportation Systems*, *24*(4), 4474–4481. https://doi.org/10.1109/TITS.2023.3236247

Zhu, J. Y., Park, T., Isola, P., & Efros, A. A. (2017). Unpaired Image-to-Image Translation Using Cycle-Consistent Adversarial Networks. *Proceedings of the IEEE International Conference on Computer Vision*, *2017-October*, 2242–2251. https://doi.org/10.1109/ICCV.2017.244

Optimizing pavement performance prediction with stacking regressor models

Ayush Sharma[1], Aakash Gupta[2], Sachin Gowda[3]
[1]*National Institute of Technology, New Delhi*
[2,3]*CSIR-Central Road Research Institute, New Delhi*

ABSTRACT: Pavement performance assessment is crucial for ensuring road durability and safety, influencing maintenance and rehabilitation decisions. This study introduces a stacking regressor with CatBoost and XGBoost as base estimators and Linear Regression as the final estimator to assess pavement conditions such as surface curvature index (SCI), base curvature index (BCI), base damage index (BDI) etc. Inputs include cracking percentage, plasticity index, temperature, maximum dry density, CBR, soil type, and layer thickness. The dataset of 2001 samples from Indian roads were trained and validated. The stacking regressor outperformed classical methods and machine learning models like Random Forest, CatBoost, XGBoost, and LightGBM, achieving the highest R^2 scores and the lowest MSE and MAE. K-Fold Validation MSE for the Stacking Regressor was 0.0208, compared to 0.0224 for CatBoost, 0.0269 for XGBoost, and 0.0281 for Linear Regression. The R^2 scores for the best outputs, SCI and BCI, were 0.8055 and 0.7753, compared to 0.7624 and 0.7202 for XGBoost, and 0.7982 and 0.7702 for CatBoost, confirming the stacking regressor's efficacy in predicting pavement conditions with the highest precision.

1 INTRODUCTION

1.1 Overview

Road pavements are significant requirements for transportation and support economic activity, besides public safety. Overloading traffic and environmental stresses, combine with ageing, are relevant to the skilled management of pavements. Pavement Management Systems [4] applies nondestructive testing techniques to produce critical data for maintenance decisions. Traditional pavement assessment methods could not be more effective in data management as natural interactions are complex, and their study requires advanced methodology [1]. Machine learning, provides a solution to the former with very high predictive accuracy [2]. Table 1. shows the comparison between Traditional approach vs. Machine Learning Approaches in Pavement Condition Assessment.

Table 1 Traditional vs Machine Learning

Traditional Method	Machine Learning Approach
Manual Data Collection	Automated Data Collection
Physical Measurements	Big Data Inputs Algorithmic
Labor-Intensive Analysis	Based Analysis
Test Frequency Limitation	Continuous Learning
Expensive Equipment	Cost-Effective Computation

2 SIGNIFICANCE

2.1 Primary Objectives

- Development of predictive models for pavement condition
- Improved prediction accuracy
- Operational efficiency
- Integration into a Decision SupportSystem.

2.2 Traditional Methods

Pavement evaluation is an integral part of pavement engineering that considers assessing pre-existing conditions to guide maintenance and rehabilitative actions. Several measurement techniques have been put in place to determine deflection under load or other aspects relating to performance. One such method is the Falling WeightDeflectometer [1].

2.3 Falling Weight Deflectometer (FWD)

A Falling Weight Deflectometer (FWD) is a non-destructive tool used for assessing the structural integrity of pavements. It operates by dropping a specified weight onto the pavement surface and recording the deflections generated. These deflection measurements provide insights into how the pavement responds to the applied load, helping engineers evaluate its load-bearing capacity and overall condition.

Sensors placed at specific distances from the impact point record these deflections, helping engineers assess the stiffness and load-bearing capacity of the pavement layers. FWD tests are commonly used for road maintenance planning, pavement rehabilitation, and determining the remaining life of a pavement structure. This method provides accurate and quick assessments without causing damage to the pavement [2].

3 DATA COLLECTION

3.1 Field Testing and Instrumentation

A diverse Indian road network of approximately 124 kilometers was carefully selected, focusing on areas having varying degrees of pavement distress, such as fatigue cracking, rutting, and surface degradation. This dataset contained over 2001 test records, ensuring diversity and representativeness in the sample to train and validate a model. Field surveys were conducted using stringent standards set by the Indian Road Congress, employing the Dynatest Model 8000 Falling Weight Deflectometer (FWD), equipped with a 300 mm diameter load plate (IRC 115, 2014). Geophones were strategically positioned at 0-, 200-, 300-, 600-, 900-, and 1200-mm offsets to capture deflection data comprehensively. Each testing location underwent three load drops, with precise adjustments for temperature variations and standard load conditions.[1]

3.2 Measurement Parameters

The data included various critical parameters for pavement evaluation:

- Structural Attributes: Asphalt layer thickness (La), base layer thickness (Lb), total pavement thickness (Lt).

- Subgrade Properties: Maximum Dry Density (MDD) and California Bearing Ratio (CBR), indicate soil strength and load-bearing capacity.

- Environmental Conditions: Pavement surface temperature (Ts) and ambient air temperature (Ta) were recorded synchronously during testing.

3.3 Laboratory Testing and Soil Analysis:

Laboratory tests on subgrade characteristics, like CBR, were supported and run to obtain the strength of soils at standardized conditions. Soil samples obtained from test pits provide data for analysis of MDD, optimum moisture content, and dry density values important in assessing pavement stability.

4 RESEARCH METHODOLOGY

4.1 Introduction

The goal of this study was to develop and evaluate predictive models for multiple output features related to pavement conditions using various regression techniques. The research methodology involved the following key steps: data preprocessing, model training, evaluation, and interpretation using SHAP (SHapley Additive exPlanations) analysis. The primary focus was on evaluating the performance of different machine learning models and analyzing overfitting indicators across training, validation, and test sets.

4.2 Data Preprocessing

The input features included 'Cracking(%)', 'PI','MDD, g/cc', 'CBR%', 'Bituminous layer Thickness, mm', 'Granular layer Thickness, mm', and 'Pavement Temperature (°C)'. The output features were 'SCI', 'BCI', 'BDI', 'AUPP', 'SF1', and 'SF2'. The dataset was split into training (70%), validation (15%), and test sets (15%) using stratified sampling to ensure consistent distribution of features across sets. Feature scaling was performed using Standard Scaler to standardize the input features.

1.	Load data from Excel/CSV file
2.	Clean and standardize column names
3.	Split data into input features (X) and output features (y)
4.	Split X and y into training, validation, and test sets
5.	Scale features using StandardScaler

4.3 Model Training and Evaluation

The study employed various regression techniques, including:
Stacking Regressor, XGBoost, LightGBM, Gradient Boosting, Random Forest, Bagging, AdaBoost, CatBoost, Linear Regression. Each regression model was wrapped in Multi-Output-Regressor to handle multiple output features simultaneously. The models were trained using the training dataset. A 3-fold cross-validation was performed to evaluate the mean squared error (MSE) of each model. The models were evaluated on the validation and test sets using the following metrics:

- Mean Squared Error (MSE)

- R-squared (R^2)

- Mean Absolute Error (MAE)

Overfitting was assessed by calculating the difference in MSE, R^2, and MAE between the validation and test sets.

1. Define models:
• Stacking Regressor (XGBoost, CatBoost, Linear Regression)
• XGBoost
• LightGBM
• Gradient Boosting
• Random Forest
• Bagging Regressor
• AdaBoost
• Linear Regression
• CatBoost

2.	Train model on training data (X_train_scaled, y_train)
3.	Predict on test data (X_test_scaled)
4.	Evaluate using Mean Squared Error (MSE) and R^2 score
5.	Calculate overfitting indicators (difference between validation and test metrics)
6.	Perform 3-fold cross-validation to calculate average MSE

4.4 Visualization and SHAP Analysis

Evaluation metrics and SHAP analysis results were visualized using matplotlib, and the plots were saved for further analysis. The residuals (difference between actual and predicted values) were analyzed using histograms to assess model accuracy. SHAP values were calculated to analyze the influence of each feature on the model's predictions. SHAP summary plots were then created to illustrate how these input features affected the predicted outcomes. Certain models like AdaBoost, Bagging, and Linear Regression were excluded from SHAP analysis due to their incompatibility with SHAP explainer functions.

1.	Plot overall evaluation metrics for all models and output features
2.	Create SHAP explainer
3.	Calculate SHAP values for training set
4.	Plot and save SHAP summary plots

5 RESULTS AND PERFORMANCE ANALYSIS

The model's predictive performance was thoroughly assessed using essential metrics, including R^2, Root Mean Square Error (RMSE), Mean Squared Error (MSE), and Mean Absolute Error (MAE). The performance metrics of different models for the SCI target and BCI target are detailed in Table 2 and Table 3. K-fold cross-validation [3] confirmed the model's reliability and effectiveness as illustrated in Figure 1. as comparison among different models is shown. The value of K-fold cross-validation MSE of Stacking Regressor Model was found to be 0.0208 while for other models like CatBoost Regressor, XGBoost Regressor, Random Forest, Gradient Boosting Regressor, LightGBM Regressor, Linear Regressor, AdaBoost Regressor, Bagging Regressor

the values were found to be 0.0224, 0.0269, 0.0233, 0.0208, 0.023, 0.0281, 0.0242, 0.0241 respectively.
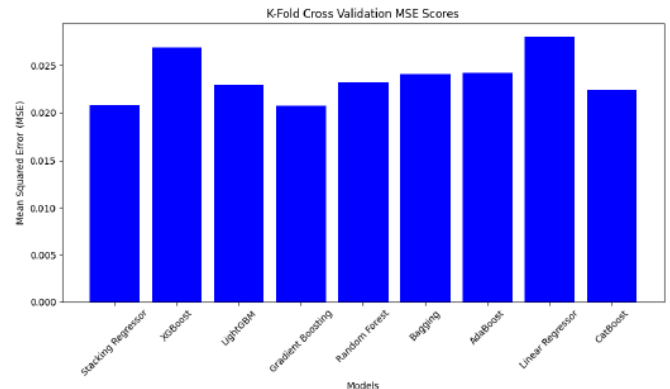
Figure 1. K-Fold Cross Validation comparison for different models where values are plotted on bar graph.

Table 2. Performance Metric Comparison for SCI

Model	Test MSE	Test R2	Test MAE
Stacking Regressor	0.0004	0.8055	0.0174
XGBoost	0.0005	0.7624	0.0189
LightGBM	0.0005	0.7775	0.0183
Linear Regression	0.0012	0.4749	0.0242
AdaBoost	0.0005	0.765	0.019
CatBoost	0.0004	0.7982	0.0175
Gradient Boosting	0.0005	0.7947	0.0178
Random Forest	0.0005	0.7717	0.0185
Bagging	0.0005	0.7551	0.0191

Table 3. Performance Metric Comparison for BCI

Model	Test MSE	Test R2	Test MAE
Stacking Regressor	0.0001	0.7753	0.0066
XGBoost	0.0001	0.7202	0.007
LightGBM	0.0001	0.7514	0.0068
Linear Regression	0.0002	0.3829	0.0093
AdaBoost	0.0001	0.6902	0.0074
CatBoost	0.0001	0.7702	0.0065
Gradient Boosting	0.0001	0.7543	0.0067
Random Forest	0.0001	0.7387	0.007
Bagging	0.0001	0.7136	0.0073

5.1 Metric Analysis for Stack Regressor Model

Mean Squared Error (MSE): Ranking of predictive accuracy: 'BCI (0.0001)' < 'BDI (0.0003)' < 'SCI (0.0004)' < 'SF1 (0.0074)' < 'AUPP (0.0093)' < 'SF2 (0.1348)'.

R^2 (Coefficient of Determination): Scores: 'SF2 (0.4618)' < 'SF1 (0.5545)' < 'AUPP (0.5976)' < 'BDI (0.6737)' < 'BCI (0.7753)' < 'SCI (0.8055)'.

Mean Absolute Error (MAE): Error hierarchy: 'BCI (0.0066)' < 'BDI (0.0129)' < 'SCI (0.0174)' < 'SF1 (0.0684)' < 'AUPP (0.0765)' < 'SF2 (0.2849)'.

5.2 Analysis of Overfitting Indicators of Stack Regressor Model

MSE for Overfitting Indicator: 'SF2' < 'AUPP' < 'SF1' < 'SCI' < 'BCI' < 'BDI' refer Table 4. for values.
R² for Overfitting Indicator: 'BDI' < 'BCI' < 'SCI' < 'AUPP' < 'SF1' < 'SF2' refer Table 4. for values.
MAE for Overfitting Indicator: 'SF2' < 'SF1' < 'AUPP' < 'SCI' < 'BCI' < 'BDI' refer Table 4. for values.

Table 4. Overall Performance Metrices for all Models

Model	Overfitting Indicator (MSE)	Overfitting Indicator (R2)	Overfitting Indicator (MAE)
Stacking Regressor	-6.10E-03	0.0033	-0.0089
XGBoost	-5.70E-03	-0.0169	-0.0052
LightGBM	-6.10E-03	0.0017	-0.008
Linear Regression	-9.70E-03	0.0648	-0.0127
AdaBoost	-7.20E-03	0.0221	-0.0108
CatBoost	-4.70E-03	-0.0179	-0.0049
Gradient Boosting	-6.60E-03	0.0187	-0.0102
Random Forest	-6.50E-03	-0.0038	-0.0068
Bagging	-8.00E-03	0.0066	-0.0091

5.3 SHAP Analysis for Stack Regressor Model

The SHAP analysis results, illustrated in Figure 2 shows:

- Cracking (%): Significant impact; high values push model output positively.
- Pavement Temperature (°C)**:** Higher temperatures increase model output.
- CBR% and MDD (g/cc): Both positively affect the model output.
- Plasticity Index (PI): Neutral effect on predictions.

Bituminous and Granular Layer Thickness: Bituminous has a negative impact, granular has a positive impact.
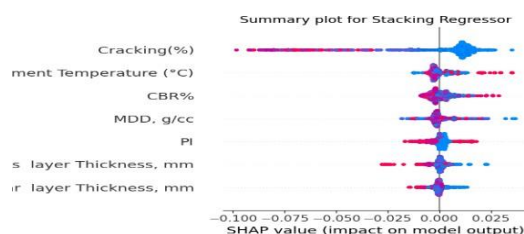
Figure 2. SHAP Values Plot for Stack Regressor Model.

6 CONCLUSION

The stack regression model outperforms several other models in evaluating asphalt pavement, including Gradient Boosting Regressor, Random Forest Regressor, Bagging Regressor, AdaBoost Regressor, Linear Regression, CatBoost Regressor, XGBoost Regressor, and LightGBM Regressor. The stack regression model demonstrates superior predictive accuracy and model fit by consistently achieving lower Mean Squared Error (MSE) and higher R-squared (R²) values. As from the results it can be seen that the K-Fold MSE for Stacking Regressor model is 0.0208 which is lowest among all hence generalized most for the unseen data. Additionally, the R² value was found to be 0.8055 and MSE was found to be 0.0004 for the SCI output of Stacking Regressor Model which clearly shows that it achieves highest accuracy and lowest error. Additionally, it exhibits lower overfitting indicators, highlighting its better generalization to unseen data. SHAP analysis showed that Cracking (%), Pavement Temperature (°C), and CBR% are most significant input features and they generally affect negatively to the model's predictions. In conclusion, this study highlights the Stack Regression model's superiority in predicting asphalt pavement conditions compared to other regression models. Future research should explore and refine ensemble approaches and feature engineering techniques to enhance predictive performance in this critical area.

7 REFERENCES

1. Gupta, A., Kumar, P. & Gowda, S. Advancing Flexible Pavement Structural Health Monitoring: A User-Friendly Approach for Network-Scale Assessments. *Int. J. Pavement Res. Technol.* (2023). https://doi.org/10.1007/s42947-023-00395-8
2. GUPTA, A., GOWDA, S., TIWARI, A., & GUPTA, A. K. 2024. XGBOOST-SHAP FRAMEWORK FOR ASPHALT PAVEMENT CONDITION EVALUATION. CONSTRUCTION AND BUILDING MATERIALS 426: 136182.
3. JUNG, Y. 2017. MULTIPLE PREDICTING K-FOLD CROSS-VALIDATION FOR MODEL SELECTION. JOURNAL OF NONPARAMETRIC STATISTICS 30(1): 197-215. HTTPS://DOI.ORG/10.1080/10485252.2017.1404598
4. KULKARNI, R. B., & MILLER, R. W. 2003. PAVEMENT MANAGEMENT SYSTEMS: PAST, PRESENT, AND FUTURE. TRANSPORTATION RESEARCH RECORD 1853(1): 65-71. HTTPS://DOI.ORG/10.3141/1853-08

Prediction of void beneath concrete slabs based on FEM-ANN framework

Bin Shi
Department of Roadway Engineering, Southeast University

Qiao Dong* (Corresponding author)
Department of Roadway Engineering, Southeast University

ABSTRACT: The voids beneath cement concrete slabs are a major invisible disease, resulting in a rapid decrease in service performance in the composite pavement. Accurate voids prediction is essential for the extensive application and long-term service of composite pavement. This research provides a FEM-ANN (Finite Element Modeling-Artificial Neural Network) method to predict the voids beneath concrete slabs. These ANN models include the original back propagation (BP), the particle swarm optimization (PSO) BP model, the genetic algorithm (GA) BP model, and the whale optimization algorithm (WOA) BP model. The voids FEM model is established and validated by the measured data in the field, and the relative error of measured and simulated results is within 4%. The cross-validation results show that the WOA-BP model has the best prediction performance, with the highest score of 8. Therefore, this FEM-ANN framework is an efficient method for estimating the voids beneath concrete slabs.

1 INTRODUCTION

Poor pavement structure (i.e., thinner layers and lower structural bearing capacity) and damaged junctions between concrete slabs (i.e., wider joint with lower supporting modulus of concrete to dowel bar) would hasten the formation and expansion of voids beneath concrete slabs (Thomoglou et al., 2022, Zeng et al., 2009). Furthermore, the more severe voids beneath concrete slabs cause significant pavement response (i.e., larger surface deflection and load stress) (Gu et al., 2011). Traditional voids prediction approaches, such as empirical equations and linear regression, frequently perform poorly in complex practical applications. These methods can provide good prediction performance of voids beneath concrete slabs in a specific research, but their applications in other research and practices are frequently unsatisfactory (Gu et al., 2011, Thomoglou et al., 2022). And a single data source, a small amount of samples, only considering a small number of influential factors and backward prediction methods all contribute to this defect (Gu et al., 2011, Huang et al., 2012, Thomoglou et al., 2022, Xue et al., 2013, Zeng et al., 2009).

Considering a mass of influential factors, neural network methods based on a large number of samples outperform other methods in the prediction of voids beneath concrete slabs (Wang and Li, 2019, Wang et al., 2016). The constructed models based on artificial intelligence algorithms have lots of practice in predicting the voids beneath concrete slabs utilizing analytic material derived from various deflection data, ground penetrating radar images, acoustic signals, and dynamic response data (Shanmugasundaram et al., 2022, Yin and Pan, 2022). However, the single types of analytic materials as inputs of ANN models result in poor applicability of the predicted models. It is also difficult to obtain a large number of samples of the observed voids beneath concrete slabs in engineering practice (Thomoglou et al., 2022, Murotani et al., 2019).There are a lot of factors that influence the voids beneath concrete slabs, however, not all of them are sensitive to the voids beneath concrete slabs (Huang et al., 2012). And it is challenging to select critical influencing factors and investigate the comprehensive relationship between voids beneath concrete slabs and significant influential factors (Gu et al., 2011, Huang et al., 2012, Xiao et al., 2010).

The FEM method can provide a large number of samples under various scenarios for the ANN prediction through previous investigations (Kumar et al., 2022, Seguini et al., 2021). Therefore, based on the FEM analytic results, the objectives of this paper are to establish an ANN model to predict the voids beneath concrete slabs by taking the pavement structure, the joints between concrete slabs, and the pavement mechanical response as input parameters. The FEM-ANN prediction of voids beneath concrete slabs includes five parts: selecting input parameters, establishing the dataset based on the FEM method, constructing the hybrid prediction models, determining the prediction model with the best overall performance through the cross-validation method, as well as analyzing the contribution of the factors affecting prediction precision.

2 METHODS

2.1 *Brief description of neural network models*

The BP neural network is a kind of multilayer feedforward neural network with input layers, middle layers, and output layers, which performs well in self-organizing learning from inputs and outputs (Ouladbrahim et al., 2022, Shariati et al., 2019). GA is a multiple-agent searching global optimization method utilized to find exact or approximate solu-

tions to optimization problems (Ismail et al., 2013). GA seeks chromosomes that meet the optimization criteria by encoding data into chromosomes and exchanging information within chromosomes via screening, crossover, and iterative processes (Irani et al., 2011). It outperforms the traditional BP network in terms of accuracy and convergence speed (Tyagi and Panigrahi, 2017). Particle swarm optimization (PSO) is an algorithm inspired by the predation behavior of birds in nature (Mohamad et al., 2018). Each bird usually searches for food by following the one closest when the birds forage (Pannu et al., 2018). The PSO algorithm constantly updates the speed and position of particles through the individual information and global information between particles in the process of algorithm optimization, resulting in its easy precocity and slow convergence speed in the later stage (Ismail et al., 2013). The WOA algorithm has strong global search capability in dealing with continuous-time serious function optimization (Kaushik et al., 2022a). The WOA imitates common whale hunting behaviors, such as surrounding prey, hunting, attacking prey, and other processes, to complete optimized searches (Kaushik et al., 2022b). Similarly, the WOA algorithm has advantages in accuracy and convergence speed over the previous algorithm through super parameter optimization and spring lifting (Vijayanand and Devaraj, 2020). The whale optimization algorithm typically contains three steps: surrounding the prey, hunting with a spiral bubble net, and seeking prey randomly (Pham et al., 2020).

2.2 Parameter determination

The condition of the pavement structure, particularly the base circumstance, is important for the appearance and development of voids beneath concrete slabs. Thus, the structure parameters of surface layer and base (i.e., elastic modulus and thickness) are selected as the input neurons of the ANN models in view of the pavement structure. Pavement mechanical responses, especially the deflection responses, are sensitive to the variation of voids beneath concrete slabs (Mateos et al., 2020). Therefore, for the respective of pavement mechanical responses, the various deflections of loaded and unloaded concrete slabs in the critical location are chosen as the input parameters of the ANN models. Various parameters can be utilized to characterize voids beneath concrete slabs. Previous research indicated that the horizontal shape of the voids is triangular, rectangular, and sectored at the corner of the slab (Tian et al., 2010). The voids between the concrete slabs and the base are not clearly formed as a result of the loss of fine aggregate on the effect of water scour in the early stage, and the base is not separated from the surface layer until appearing serious voids damage (Miao, 2016). Overall, the voids horizontal area is

chosen as the only output of the ANN models. The joint condition between concrete slabs is a key factor in the development of voids beneath concrete slabs. Thus, the voids FEM model under concrete slabs should consider the installation of joints between concrete slabs. In this paper, the theoretical spring method is appropriate for simulating the slab joint (Witczak and El-Basyouny, 2002). The joint stiffness is the crucial aspect of the joint condition, and the supporting modulus of concrete to the dowel bar and the joint width are direct variables of the joint stiffness. Thus, the two factors would be selected as the input parameters for the BP optimized models in terms of the joint between concrete slabs.

3 RESULTS

3.1 Compasion of the optimization network algorithm

Based on the following evaluation indexes in Figure 1, it is seen that the WOA-BP model is the most accurate model for estimating the voids beneath concrete slabs, with the *RMSE* of 0.014, a *MAPE* of 2.699, a R^2 of 0.970, and a *VAF* of 97.094. While the original BP model is the worst prediction model for the voids beneath concrete slabs, with the *RMSE* of 0.034, a *MAPE* of 5.034, a R^2 of 0.91, and a *VAF* of 91.459. In general, all the optimized ANN models have a R^2 of greater than 0.93, indicating that these hybrid models have high predicted accuracy based on the reliable dataset of voids under concrete slabs.
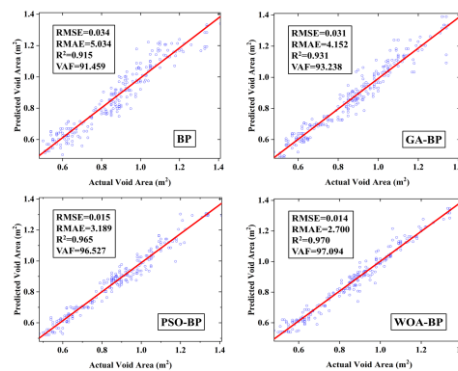
Figure 1. Correlation analysis of the predictive and actual value based on simple cross-validation.

3.2 Comprehensive evaluation of prediction models

This paper adopts a method to score and evaluate the stability of all the evaluation indexes for each model to compare the comprehensive performance of these optimization models. All normalized evaluation metrics need to be ordered and scored in this method. The cumulative scores of mean value and variance of all evaluation indices for four ANN models are depicted in Figure 2. The comprehensive conclusions based on the K-fold cross-validation method

are consistent with the preliminary results utilizing the simple cross-validation. It is found from Figure 2 that the best comprehensive performance of all models is WOA-BP, and it has the highest score of 8 than other BP algorithms. However, other two optimization models with scores of 4.197 and 7.119 have a better comprehensive effect than the traditional BP model.
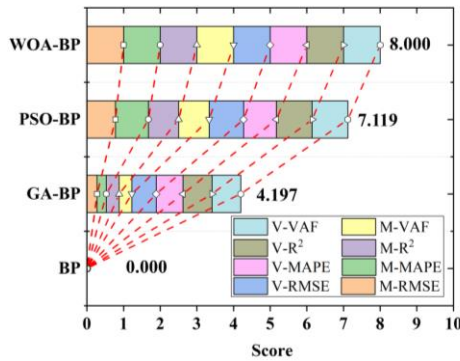
Figure 2. Comprehensive score graph for each model based on K-fold cross-validation method.

3.3 *Sensitivity analysis*

According to the above research results, it is concluded that the WOA optimized network model has the best comprehensive performance of all the BP network models. In order to validate the screening rationality of input parameters, this developed optimized network model is utilized to analyze the sensitivity of inputs on the void parameters. As shown in Figure 3, a tornado chart exhibits the sensitivity of the input indexes on the voids beneath concrete slabs for the WOA optimized model. It is found that the joint parameter (W_j) and pavement mechanical response parameters (L_c, L_{me}, L_m, L_{uc}, L_{ue}, and L_{um}) correlate well with the voids prediction and have a positive effect on A_v. Nevertheless, the joint parameter (K_d), and pavement structure parameters (E_s, E_b, D_s, and D_b) are found to inversely proportional to the void prediction output.
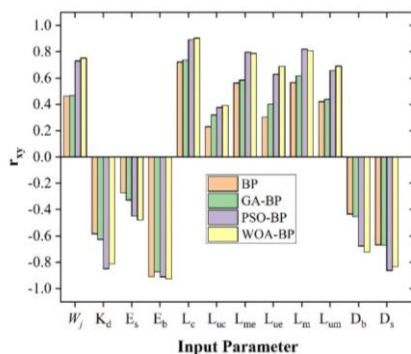
Figure 3. Sensitivity of input metrics on the void outputs.

4 CONCLUSIONS

(a) The dataset of voids under concrete slabs constructed by the FEM results is of high quality and dependability. Based on this, all of the optimized ANN models have a R^2 of greater than 0.93, which indicates that these hybrid models have high predictive precision.

(b) The prediction precision and stability of the four constructed models, from highest to lowest, are the WOA-BP model, the PSO-BP model, the GA-BP model, and the traditional BP model. Among these models, the WOA-BP model exhibits the best prediction performance of the four ANN models.

(c) Sensitivity analysis results show that the joint parameter (W_j) and pavement mechanical response parameters have a positive influence on the void prediction. Nevertheless, the joint parameter (K_d), and pavement structure parameters affect the voids output inversely.

5 PREFERENCES

GU, X., YUAN, Q. & NI, F. 2011. Feasibility study of void evaluation beneath cement slabs based on PFWD. *Journal of Hefei University of Technology,* 34**,** 729-733.

HUANG, Y., YUAN, J., TAN, Y. & LIU, Y. 2012. Identification of void beneath airport cement concrete pavement and its influence. *Journal of Tongji University. Natural Science,* 40**,** 861-866.

IRANI, R., SHAHBAZIAN, M. & NASIMI, R. 2011. Permeability estimation of a reservoir based on neural networks coupled with genetic algorithms. *Petroleum science and technology,* 29**,** 2132-2141.

ISMAIL, A., JENG, D.-S. & ZHANG, L. 2013. An optimised product-unit neural network with a novel PSO–BP hybrid training algorithm: Applications to load–deformation analysis of axially loaded piles. *Engineering applications of artificial intelligence,* 26**,** 2305-2314.

KAUSHIK, A., SINGAL, N. & PRASAD, M. 2022a. Incorporating whale optimization algorithm with deep belief network for software development effort estimation. *International Journal of System Assurance Engineering and Management,* 13**,** 1637-1651.

KAUSHIK, A., TAYAL, D. K. & YADAV, K. 2022b. The role of neural networks and metaheuristics in agile software development effort estimation. *Research Anthology on Artificial Neural Network Applications.* IGI Global.

KUMAR, S., KUMAR, V. & SINGH, A. K. 2022. Prediction of maximum pressure of journal

bearing using ANN with multiple input parameters. *Australian Journal of Mechanical Engineering,* 20**,** 1069-1078.

MATEOS, A., HARVEY, J., BOLANDER, J., WU, R., PANIAGUA, J. & PANIAGUA, F. 2020. Structural response of concrete pavement slabs under hygrothermal actions. *Construction and Building Materials,* 243**,** 118261.

MIAO, L. 2016. *The analysis of mechanics response of cement concrete pavement with void and joint load transfer coupling* Master Degree, Southwest Jiaotong University.

MOHAMAD, E. T., ARMAGHANI, D. J., MOMENI, E., YAZDAVAR, A. H. & EBRAHIMI, M. 2018. Rock strength estimation: a PSO-based BP approach. *Neural Computing and Applications,* 30**,** 1635-1646.

MUROTANI, T., IGARASHI, S. & KOTO, H. 2019. Distribution analysis and modeling of air voids in concrete as spatial point processes. *Cement and Concrete Research,* 115**,** 124-132.

OULADBRAHIM, A., BELAIDI, I., KHATIR, S., MAGAGNINI, E., CAPOZUCCA, R. & WAHAB, M. A. 2022. Experimental crack identification of API X70 steel pipeline using improved Artificial Neural Networks based on Whale Optimization Algorithm. *Mechanics of Materials,* 166**,** 104200.

PANNU, H. S., SINGH, D. & MALHI, A. K. 2018. Improved particle swarm optimization based adaptive neuro-fuzzy inference system for benzene detection. *CLEAN–Soil, Air, Water,* 46**,** 1700162.

PHAM, Q.-V., MIRJALILI, S., KUMAR, N., ALAZAB, M. & HWANG, W.-J. 2020. Whale optimization algorithm with applications to resource allocation in wireless networks. *IEEE Transactions on Vehicular Technology,* 69**,** 4285-4297.

SEGUINI, M., KHATIR, S., BOUTCHICHA, D., NEDJAR, D. & ABDEL WAHAB, M. 2021. Crack prediction in pipeline using ANN-PSO based on numerical and experimental modal analysis. *Smart Structures and Systems,* 27**,** 507-523.

SHANMUGASUNDARAM, N., PRAVEENKUMAR, S., GAYATHIRI, K. & DIVYA, S. 2022. Prediction on compressive strength of Engineered Cementitious composites using Machine learning approach. *Construction and Building Materials,* 342**,** 127933.

SHARIATI, M., MAFIPOUR, M. S., MEHRABI, P., BAHADORI, A., ZANDI, Y., SALIH, M. N., NGUYEN, H., DOU, J., SONG, X. & POI-NGIAN, S. 2019. Application of a hybrid

artificial neural network-particle swarm optimization (ANN-PSO) model in behavior prediction of channel shear connectors embedded in normal and high-strength concrete. *Applied sciences,* 9**,** 5534.

THOMOGLOU, A. K., FALARA, M. G., GKOUNTAKOU, F. I., ELENAS, A. & CHALIORIS, C. E. 2022. Influence of Different Surfactants on Carbon Fiber Dispersion and the Mechanical Performance of Smart Piezoresistive Cementitious Composites. *Fibers,* 10**,** 49.

TIAN, X., LIN, D. & WU, S. 2010. Performance evaluation of Portland cement concrete pavement based on fuzzy complex matter element method. *Journal of Traffic and Transportation Engineering,* 10**,** 26-29, 35.

TYAGI, S. & PANIGRAHI, S. 2017. A hybrid genetic algorithm and back-propagation classifier for gearbox fault diagnosis. *Applied Artificial Intelligence,* 31**,** 593-612.

VIJAYANAND, R. & DEVARAJ, D. 2020. A novel feature selection method using whale optimization algorithm and genetic operators for intrusion detection system in wireless mesh network. *IEEE Access,* 8**,** 56847-56854.

WANG, D. & LI, S. 2019. Neural network recognition method for cement pavement void morphology based on Abaqus. *Quality Measurement and Control,* 36**,** 6.

WANG, Z., ZHANG, Y. & YE, B. 2016. Experimental study of detection of void between concrete slab and soil based on impulse response method. *Journal of Tongji University (Natural Science).*

WITCZAK, M. & EL-BASYOUNY, M. 2002. Design Guide: Design of New and Rehabilitated Pavement Structures. *Appendix A: Calibration of Permamnent Deformation Models For Flexible Pavements***,** 2-92.

XIAO, L., LI, L. & HAN, Z. 2010. Judgement and evaluation of foundation void under concrete pavement slab by finite element method. *Journal of Central South University of Forestry & Technology,* 1**,** 73-78.

XUE, Y., HUANG, X., ZHOU, W. & QIAN, S. 2013. Improvement on recognition method of void beneath slab based on nondestructive testing technologies. *Sustainable Construction Materials 2012.*

YIN, P. & PAN, B. 2022. Effect of RAP content on fatigue performance of hot-mixed recycled asphalt mixture. *Construction and Building Materials,* 328**,** 127077.

ZENG, S., ZENG, X. & JIA, X. 2009. Criterion for void identification beneath cement concrete pavement slab corner. *Journal of Central South University (Science and Technology),* 40**,** P248-P255.

Improving pavement distress segmentation with diffusion-based generative AI and digital twin insights

M.A. Talaghat[1], A. Golroo[1,2], M. Rasti[2]

[1]*Department of Civil and Environmental Engineering, Amirkabir University of Technology, Tehran, Iran.*

[2]*Faculty of Information Technology and Electrical Engineering, University of Oulu, Oulu, Finland.*

ABSTRACT: The lack of diverse and sufficient labeled datasets in pavement management limits the performance and generalization of segmentation and detection models. Existing datasets often fail to capture real-world variability, such as different pavement distress types, leading to models that struggle with unseen scenarios and rare distress patterns. This study addresses these challenges by applying diffusion-based generative AI to mitigate data scarcity. Using a Denoising Diffusion Probabilistic Model (DDPM), synthetic images were generated to augment datasets, significantly enhancing model robustness and accuracy. The synthetic images achieved an SSIM of 0.92 and a diversity score of 0.85, resulting in notable improvements in the U-Net segmentation model, including an IoU increase from 0.81 to 0.93, an F1 Score rise from 0.85 to 0.95, and pixel-level accuracy improvement from 0.89 to 0.95. These findings underscore the potential of generative AI to support scalable and robust digital twin solutions for pavement management systems.

1 INTRODUCTION

Digital twin technology has revolutionized infrastructure management by enabling real-time monitoring and predictive maintenance through virtual replicas of physical systems, providing valuable insights for optimizing asset performance (Saghatforoush et al., 2022). In pavement management, digital twins integrate data from IoT sensors, historical records, and predictive models to proactively address damages, reducing costs and enhancing safety (Talaghat, 2024). However, the effectiveness of these systems depends on the quality and diversity of labeled datasets, which traditional methods fail to achieve due to data scarcity and generalization limitations (Kumar, 2024;). To overcome this, diffusion-based generative AI models offer a robust solution, generating diverse, high-quality synthetic images that enhance segmentation accuracy and support scalable, robust digital twin applications in pavement management (Ho et al., 2020).

2 LITERATURE REVIEW

Several studies have highlighted the potential of diffusion models to outperform GANs and VAEs in stability and image quality (Nichol & Dhariwal, 2021). These capabilities enhance training datasets, improving the performance and generalization of machine learning models. Han et al. (2024) proposed CrackDiffusion, a two-stage framework that integrates diffusion models with U-Net, achieving superior IoU scores on public datasets. Cano-Ortiz et al. (2024) introduced RoadPainter, a semantic diffusion model that significantly improved segmentation effi-

ciency by augmenting datasets with diverse synthetic crack images. Additionally, Yan et al. (2024) demonstrated how integrating diffusion models with Transformer-in-Transformer algorithms enhanced road surface friction coefficient detection, improving accuracy. These studies exemplify the transformative potential of diffusion-based generative AI in creating scalable, effective solutions for digital twins and infrastructure monitoring (Xu et al. 2024).

Generative AI in pavement distress detection and segmentation is underexplored, with challenges like data scarcity and computational complexity. Datasets like Crack500 lack diversity, limiting model training for rare distress types (Zhang et al., 2020). Traditional generative models like GANs face instability (Goodfellow et al., 2014). Diffusion models offer a robust solution by generating high-quality synthetic images that improve data diversity and segmentation accuracy while reducing computational demands (Shorten et al., 2019). This research addresses these gaps using DDPM to enhance dataset robustness and model scalability.

3 OBJECTIVE AND SCOPE

The primary objective of this study is to address the challenges of data scarcity and limited dataset diversity in pavement distress detection and segmentation by leveraging diffusion-based generative AI for dataset augmentation. This approach aims to enhance the performance and generalizability of pavement distress segmentation models by developing a generative model to create synthetic images of pavement distress. These images will augment existing

datasets, increasing their diversity and volume, thus improving model accuracy and robustness. Specifically, the study will evaluate models trained on both augmented and original datasets, assessing their generalization capabilities on unseen data. The research uses the DDPM to generate high-quality synthetic images, enhancing segmentation models like U-Net and DeepLab. Performance will be evaluated through metrics such as Intersection over Union (IoU), F1 Score, and pixel-level accuracy, ultimately advancing scalable, effective solutions for pavement distress detection and segmentation.

4 METHODOLOGY

4.1 Dataset preparation

The dataset preparation for this study involved characterizing the Crack500 dataset and applying essential preprocessing techniques to ensure data quality. The Crack500 dataset includes various types of pavement distress, such as longitudinal, transverse, and alligator cracks, with annotations indicating the type and location of distress. Preprocessing steps included resizing images for model compatibility, normalizing pixel values, adjusting contrast and brightness, and converting images to grayscale. Data cleaning removed low-quality or corrupted images, while histogram equalization and Gaussian blur were applied to enhance contrast and reduce noise, ensuring a consistent and high-quality dataset for robust model training.

4.2 Diffusion Model Architecture

The diffusion model architecture is central to generating high-quality synthetic images that augment existing datasets for pavement distress detection. Built on the DDPM, this architecture works by progressively adding Gaussian noise to input images and then learning to reverse this process, gradually restoring the images to their original state. This iterative denoising approach allows the model to generate highly realistic images closely resembling real-world pavement distress conditions. The model utilizes a U-net structure, which includes encoder-decoder blocks and skip connections to retain fine spatial details during the downsampling and upsampling stages. This ensures the preservation of crucial features, such as crack patterns and textures, which are essential for accurate segmentation. By enhancing dataset diversity and improving image quality, this model supports more robust training of pavement distress segmentation models, ultimately improving their performance and generalization. The effectiveness of the generated images is measured using metrics such as Structural Similarity Index (SSIM), Peak Signal-to-Noise Ratio (PSNR), and diversity score, confirming high image quality and

variability, which boost model performance and generalization.

4.3 Segmentation model framework

This study uses two state-of-the-art segmentation models, U-Net (ResUNet with ResNet34 Backbone) and DeepLab (DeepLabV3+ with ResNet101 Backbone), to develop a robust pavement distress detection system. U-Net, with its encoder-decoder structure and skip connections, is effective for tasks requiring precise localization, while DeepLab employs atrous convolution and spatial pyramid pooling to capture multi-scale context. Both models were configured with a uniform input size of 128x128 pixels and trained using cross-entropy and Dice loss functions, optimized by the Adam optimizer. Performance was evaluated using metrics such as IoU, F1 Score, pixel-level accuracy, and boundary precision, to assess the effectiveness of the models when trained on augmented datasets from diffusion models. These models aim to improve the robustness and accuracy of pavement distress segmentation.

4.4 Comparative analysis framework

The comparative analysis framework evaluates performance improvements from integrating generative AI into pavement distress segmentation models. This involves pre- and post-generative AI performance benchmarking using metrics like IoU, F1 Score, and pixel-level accuracy, followed by statistical validation through paired t-tests, confidence intervals, and cross-validation. The baseline performance of U-Net and DeepLab was first assessed using the original Crack500 dataset (Including 250 segmented images), revealing model strengths such as U-Net's performance on alligator cracks and DeepLab's robustness under variable lighting. After augmenting the dataset with synthetic images generated by the diffusion model, the models were retrained and reassessed using the same performance metrics, with additional metrics like diversity and realism scores to assess synthetic data quality. This framework demonstrates the effectiveness of generative AI in enhancing model performance and generalization.

5 RESULTS

5.1 Generated Image Characteristics

The quality of synthetic images generated by the diffusion model is vital for augmenting the dataset and enhancing model performance. The model progressively reduces noise, starting with noisy images and refining them over time. By epoch 50, basic patterns emerge, with clearer structures by epoch 100. By epoch 150, detailed crack patterns begin to emerge, and by epoch 200, the generated images closely

mimic real-world pavement distress, effectively capturing its complexity and diversity.

Figure 1 provides a visual comparison of original pavement distress images and synthetic images generated by the diffusion model. This side-by-side comparison illustrates how well the synthetic images replicate key visual features of real pavement cracks, including crack shape, width, alignment, and continuity. Additionally, the synthetic images introduce variability, which helps improve model robustness by capturing a wider range of crack patterns and distress types.
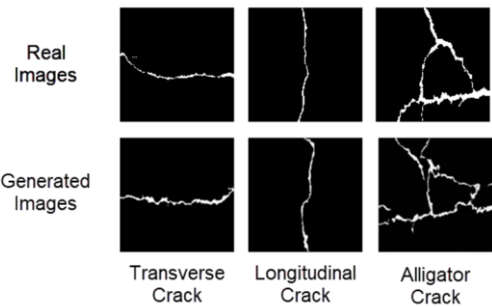
Figure 1. Comparison of Real Distress and Synthetic Images

The evaluation of these synthetic images was conducted using several quantitative metrics to assess their quality and realism, as detailed in Table 1. These metrics are as follows:

Table 1. Synthetic Image Diversity Metrics

Metric	Value	Interpretation
SSIM	0.92	High structural similarity to real-world images
PSNR	32.5 dB	Low-noise and high-quality synthetic images
Diversity Score	0.85	High variability in crack types and patterns
Realism Score	0.90	Realistic appearance matching real-world data

These metrics confirm that the synthetic images maintain structural fidelity, add diversity, and closely resemble real-world data, enhancing dataset quality and improving segmentation model performance.

5.2 Segmentation performance metrics

The performance of U-Net and DeepLab models was evaluated using several metrics before and after dataset augmentation with synthetic images. Table 6 presents the performance improvements, including IoU, F1 Score, pixel-level accuracy, and boundary precision, with significant gains observed after augmentation. Both models showed notable performance enhancements with 1000 synthetic images, with IoU scores increasing by 8-9%, F1 Scores improving by 8%, and pixel-level accuracy rising by 4%. However, beyond 1000 augmented images, performance declined, suggesting diminishing returns and potential overfitting.

Table 2. Quantitative Results of Segmentation Models

Metric	IoU	F1 Score	Pixel-Level Accuracy	Boundary Precision	Dice Coefficient
U-Net (Original)	0.81	0.85	0.89	0.79	0.84
U-Net (+50)	0.84	0.87	0.9	0.81	0.86
U-Net (+150)	0.87	0.9	0.92	0.84	0.89
U-Net (+250)	0.9	0.93	0.93	0.87	0.92
U-Net (+1000)	0.93	0.95	0.95	0.9	0.94
U-Net (+5000)	0.91	0.94	0.93	0.88	0.92
DeepLab (Original)	0.84	0.87	0.91	0.81	0.87
DeepLab (+50)	0.86	0.89	0.92	0.83	0.89
DeepLab (+150)	0.89	0.92	0.94	0.86	0.92
DeepLab (+250)	0.92	0.95	0.95	0.88	0.94
DeepLab (+1000)	0.94	0.96	0.96	0.9	0.95
DeepLab (+5000)	0.92	0.94	0.94	0.87	0.93

Figure 2 demonstrates the improved training and validation curves for U-Net models trained with 1000 synthetic images, showing faster convergence and reduced overfitting.
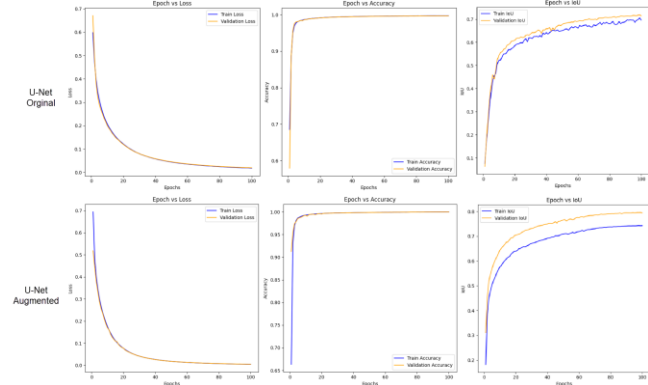
Figure 2. Training and Validation Curve of U-Net Model

Further validation on additional datasets (GAPs, DeepCrack, CrackSegNet, and CFD) showed that both models maintained strong generalization capabilities, achieving high IoU, F1 Scores, and accuracy across different pavement distress types and conditions (see Table 3).

Table 3. Performance Models on Different Datasets

Dataset	Model	IoU	F1 Score	Pixel-Level Accuracy	Boundary Precision	Dice Coefficient
GAPs	U-Net	0.86	0.89	0.93	0.88	0.90
	DeepLab	0.88	0.91	0.94	0.90	0.92
DeepCrack	U-Net	0.85	0.88	0.92	0.87	0.89
	DeepLab	0.87	0.90	0.93	0.89	0.91
CrackSeg-Net	U-Net	0.84	0.87	0.91	0.86	0.88
	DeepLab	0.86	0.89	0.92	0.88	0.90
CFD	U-Net	0.83	0.86	0.90	0.85	0.87
	DeepLab	0.85	0.88	0.91	0.87	0.89

These findings demonstrate that the dataset augmentation using synthetic images significantly improves

segmentation performance and generalization, validating the effectiveness of the generative AI approach in enhancing pavement distress detection models.

5.3 *Performance enhancement areas*

The integration of synthetic images generated by the diffusion model led to significant improvements in pavement distress segmentation, focusing on accuracy, boundary precision, and generalization.

Figure 3 shows a comparison of real images and predicted images from both original and augmented models, illustrating the enhanced accuracy and clarity of crack segmentation with the augmented dataset.
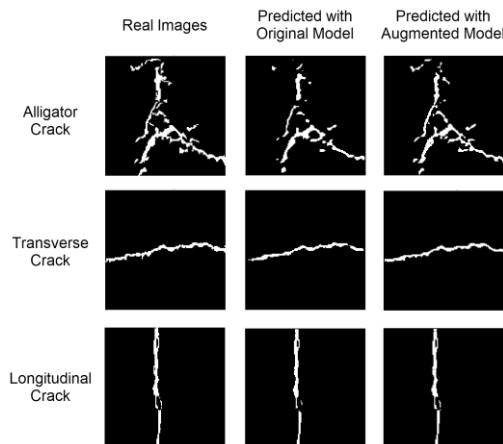
Figure 3. Comparison of Real Image with Predicted Using Original and Augmented Models

Boundary precision improved from 0.79 to 0.9, enhancing crack boundary delineation and reducing false positives/negatives. The models' generalization also improved, with IoU rising from 0.73 to 0.85 on unseen data. The diffusion model required more resources, taking 2 hours for training and 8 hours for inference with 1000 images. In comparison, the augmented U-Net and DeepLab models showed faster training and inference but demanded more computational power than their baseline versions.

6 CONCLUSION

This study highlights the impact of diffusion-based generative AI in enhancing pavement distress segmentation. Synthetic images with high SSIM (0.92), diversity (0.85), and realism (0.90) led to significant performance gains. For U-Net, IoU improved from 0.81 to 0.93, F1 Score from 0.85 to 0.95, and pixel-level accuracy from 0.89 to 0.95. DeepLab saw similar improvements, with IoU rising from 0.84 to 0.94. Boundary precision improved by 9-11%, and generalization on unseen data increased, with IoU rising from 0.73 to 0.85. Despite high computational demands, the integration of synthetic data led to enhanced model performance and generalization. These findings offer valuable implications for infrastructure maintenance, safety, and cost reduction, with potential for broader applications. Future research should focus on real-time implementation, dataset expansion, and AI optimization.

References

Cano-Ortiz, S., Sainz-Ortiz, E., Iglesias, L. L., del Árbol, P. M. R., & Castro-Fresno, D. (2024). Enhancing pavement crack segmentation via semantic diffusion synthesis model for strategic road assessment. *Results in Engineering, 23*, 102745.

Goodfellow, I., Pouget-Abadie, J., Mirza, M., Xu, B., Warde-Farley, D., Ozair, S., ... & Bengio, Y. (2014). Generative adversarial nets. *Advances in Neural Information Processing Systems, 27*, 2672-2680.

Han, C., Yang, H., Ma, T., Wang, S., Zhao, C., & Yang, Y. (2024). CrackDiffusion: A two-stage semantic segmentation framework for pavement crack combining unsupervised and supervised processes. *Automation in Construction, 160*, 105332.

Ho, J., Jain, A., & Abbeel, P. (2020). Denoising diffusion probabilistic models. *Advances in Neural Information Processing Systems, 33*, 6840-6851.

Kumar, A. V. (2024). Pavement surface condition assessment: A state-of-the-art research review and future perspective. *Innovative Infrastructure Solutions, 9*(470). Retrieved from Springer.

Nichol, A., & Dhariwal, P. (2021). Improved denoising diffusion probabilistic models. *Proceedings of the International Conference on Machine Learning, 139*, 8162–8171.

Saghatforoush, E., Abbasianjahromi, H., Talaghat, M. A., & Kahvandi, Z. (2022). Development of a Management System to Improve the Energy Efficiency of Public Buildings by Integrating IoT and BIM. *Lean Construction Journal*.

Shorten, C., & Khoshgoftaar, T. M. (2019). A survey on image data augmentation for deep learning. *Journal of Big Data, 6*(1), 60.

Talaghat, M. A., Golroo, A., Kharbouch, A., Rasti, M., Heikkilä, R., & Jurva, R. (2024). Digital twin technology for road pavement. *Automation in Construction, 168*, 105826.

Xu, H., Omitaomu, F., Sabri, S., Zlatanova, S., Li, X., & Song, Y. (2024). Leveraging generative AI for urban digital twins: A scoping review on the autonomous generation of urban data, scenarios, designs, and 3D city models for smart city advancement. Urban Informatics, 3(29).

Yan, Z., Yue, L., Luo, W., & Sun, J. (2025). Real-time detection of road surface friction coefficient: A new framework integrating diffusion model and Transformer in Transformer algorithms. *Alexandria Engineering Journal, 113*, 620-632.

Zhang, Z., Liu, Q., & Wang, Y. (2020). Crack500: A dataset for pavement crack detection. *Data in Brief, 30*, 105409.

Machine learning-aided rheological prediction models of asphalt binders based on chemical properties

Fan Zhang[1]
[1]Department of Civil Engineering, Aalto University, Finland

Di Wang[1,2]
[1]Department of Civil Engineering, Aalto University, Finland

[2]Department of Civil Engineering, University of Ottawa, Canada

Yuxuan Sun[1]
[1]Department of Civil Engineering, Aalto University, Finland

Augusto Cannone Falchetto[1,3,*]
[1]Department of Civil Engineering, Aalto University, Finland

[3]Department of Civil Environmental and Architectural Engineering, University of Padova, Italy

[*]Corresponding author (augusto.cannonefalchetto@aalto.fi)

ABSTRACT: This work aims to provide rapid rheological characterization of asphalt binders through their chemical properties based on advanced machine learning tools. With this objective, Fourier transform infrared spectroscopy (FTIR) and dynamic shear rheometer (DSR) are adopted to measure the chemical and rheological properties. Results indicate that the raw six FTIR features can be reduced to two principal components (PC 1 and PC 2), and the variance and role of PC 1 are more significant than PC 2. Multiple linear regression models can predict the phase angle accurately but not for modulus. Gaussian process regression model with higher R^2 and lower RMSE values can accurately predict both modulus and phase angle.

Keywords: asphalt binders; rheological properties; chemical composition; machine learning

1 INTRODUCTION

Rheology of asphalt binders is the study of their flow and deformation behavior under various temperature and loading conditions (Zhang, et al., 2024). It is a crucial aspect of understanding the performance characteristics of asphalt materials used in pavements. Asphalt binders exhibit viscoelastic properties, meaning they show both viscous (liquid-like) and elastic (solid-like) responses depending on the temperature and rate of loading. At high temperatures, they behave more like viscous fluids, while at low temperatures, they act more like elastic solids. The rheological properties of asphalt binders directly influence the durability and performance of road pavements, impacting resistance to deformation (rutting), cracking, and fatigue. Accurate rheological analysis helps in selecting and modifying binders to meet specific climatic and traffic demands, ensuring better long-term performance of asphalt pavements.

Measuring the rheology of asphalt binders can be a time-consuming process due to the complex and detailed analyses required to fully characterize their viscoelastic behavior. Rheological testing often involves conducting multiple assessments, such as dynamic shear rheometer (DSR) tests and bending beam rheometer (BBR) tests, across a range of temperatures and loading frequencies. These tests are designed to simulate the real-world performance of asphalt binders under different traffic and climatic conditions, which requires precise sample preparation, conditioning, and repeated measurements to ensure reliability. Additionally, each test can take significant time due to the need for temperature equilibration, application of controlled stress or strain, and data collection. The time investment is necessary to capture the binder's behavior over short-term (high traffic speed) and long-term (slow-moving or stationary loads) performance. While these processes provide invaluable insights into the binder's potential durability and suitability for specific applications, they require a considerable commitment of time and resources (Wang, et al., 2022).

The chemical properties of asphalt binders play a fundamental role in determining their rheological behavior and overall performance (Shan, et al.,

2023). Asphalt binders are composed of complex mixtures of hydrocarbons, including asphaltenes, resins, saturates, and aromatics (Salehfard, et al., 2024), each contributing differently to their physical characteristics. The balance between these chemical constituents influences the binder's response to temperature changes and mechanical stress. For instance, asphaltenes contribute to the stiffness and elasticity of the binder (Ilyin and Yadykova, 2024), while lighter fractions, such as saturates and aromatics, provide fluidity and flexibility (Shan, et al., 2024). The interactions between these components affect the viscoelastic nature of the binder, dictating how it responds to high temperatures (resisting rutting) and low temperatures (resisting cracking). Understanding the chemical composition and interactions within asphalt binders is essential for modifying their properties to achieve desired performance characteristics, especially under varying traffic loads and environmental conditions.

The application of machine learning (ML) to predict the rheology of asphalt binders using Fourier-transform infrared (FTIR) spectroscopy represents a significant advancement in material characterization. FTIR spectroscopy provides detailed information about the chemical composition of asphalt binders by identifying functional groups and molecular structures. By leveraging machine learning algorithms, researchers can analyze these complex spectral data sets to establish correlations between chemical properties and rheological behavior. This approach enables the development of predictive models that can forecast the performance of binders under various conditions without the need for extensive and time-consuming physical testing. Machine learning enhances the efficiency and accuracy of predicting critical properties such as stiffness, elasticity, and temperature susceptibility. As a result, this integration of advanced data analysis with chemical profiling aids in faster binder formulation, improved material selection, and optimized design of asphalt pavements to meet specific performance requirements.

2 MATERIALS AND METHODS

2.1 *Materials*

The materials used in this research include 18 fresh asphalt binders. In order to improve the applicability of the model, these binders are provided by different suppliers with different penetrations.

2.2 *DSR tests*

In this research, the frequency sweep of asphalt binders is performed via a DSR machine. The frequency is selected from 0.1 Hz to 20 Hz. The tests are carried out at three different temperature ranges:

low-temperature ranges (-30 °C to 6 °C), mid-temperature ranges (-4 °C to 40 °C), and high-temperature ranges (28 °C to 76 °C). The corresponding sample plate is 25 mm in diameter for high temperatures, 8 mm in diameter for medium temperatures, and 4 mm in diameter for low temperatures.

2.3 *FTIR tests*

The FTIR test was employed to measure the chemical composition of different asphalt binders. The measuring wave numbers are from 400 cm^{-1} to 4000 cm^{-1}. FTIR can identify chemical composition by determining absorbance from input and transmitted light. It also can quickly and non-destructively characterize the chemical composition of materials.

2.4 *Machine learning models*

Principal component analysis (PCA) is a method to reduce the dimensionality of the data. PCA can avoid the limitations of over-counting by finding a new coordinate system and reducing the dimensionality from n to k (k < n).

Since the multiple linear regression (MLR) model has the advantage of simplicity and practicality, it is used in this paper to predict the rheological properties of asphalt binders. In this model, the number of independent variables is greater than or equal to two; hence, it is called multiple regression. In fact, the combination of numerous independent variables is more accurate and realistic than single variable prediction (Hu, et al., 2015).

Gaussian Process Regression (GPR) model is a more complex and powerful machine learning model that can be used to represent the distribution of the function. GPR can establish the model with infinite dimensions (Schulz, et al., 2018). Each input point is associated with a random variable, and their joint distribution can be modeled as multiple Gaussian distributions. This model is a non-parametric, Bayesian, supervised learning method (Schulz, et al., 2018).

3 RESULTS AND DISCUSSION

3.1 *Principal component analysis*

The difference in chemical bond areas can distinguish different binders in this research. Considering the contribution of all of these as input variables would make the calculation much more complex. PCA method is applied to reduce the dimensionality. It can be found that the dimensionality of binders from FTIR results is six, so the extracted original principal component number is six. The eigenvalues and cumulative variance, as shown in Fig. 1, can be generated after PCA analysis. A larger eigenvalue indicates that the principal component it represents

has the largest contribution among all principal components. It can be observed that the first two principal components have the largest eigenvalues of 3.03 and 1.24. The results of PCA can be considered acceptable when the cumulative variance of the principal components is greater than 60% (Margaritis, et al., 2020; Paranhos and Petter, 2013). The cumulative variance of the first two principal components in Fig. 2 is 71.97% (above 60%); therefore, *PC 1* and PC 2 can represent all original features of binders. It can be found that all original features are positively correlated with the distribution of *PC1*, with the vibration of C-H and CH$_2$ having the highest correlation and the vibration of S=O having the lowest correlation. However, for *PC 2*, the vibration of S=O has the highest correlation, while C-H has the lowest value. The vibrations of S=O, CH3, and CH2 positively correlate with PC 2, and vibrations of C-H, CH$_2$/CH$_3$, and C=C/C=O have a negative correlation.
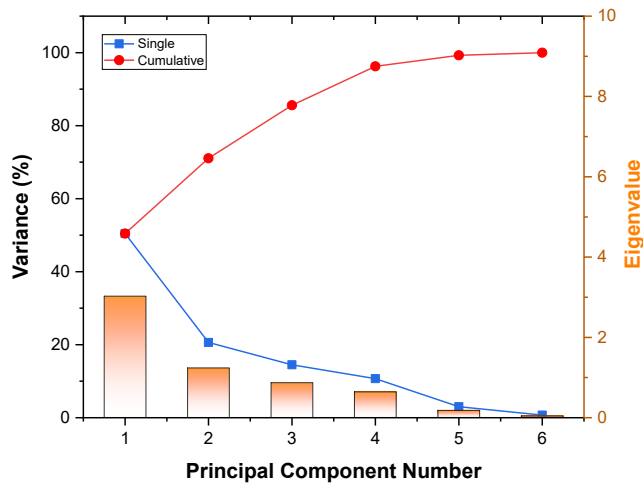
Figure 1. Variance and eigenvalue of each component.
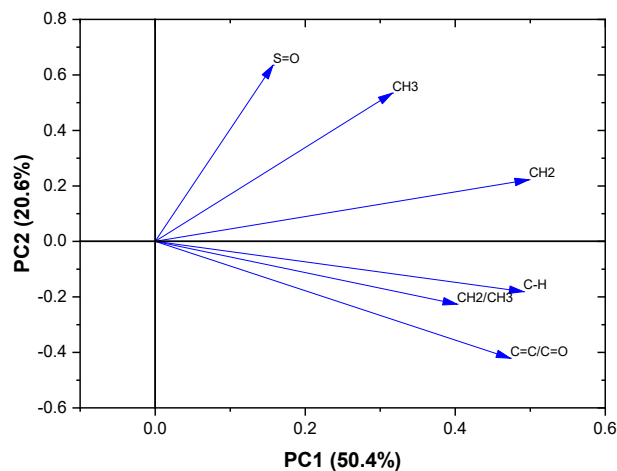
Figure 2. Projection of the original features onto the *PC* system.

3.2 *Development of prediction model*

3.2.1 *Multiple linear regression*

MLR, as the simplest regression model, has the advantage of fast computation speed with low computer configurations. Fig. 3 is the predicted modulus of binders through the MLR model. A total of 7200 data by simultaneously considering temperature and frequency. However, the model is unsatisfactory for modulus prediction, with the *R²* of 0.5488 and 0.5447 and RMSE of 11.12. Hence, it is necessary to apply a more advanced and powerful model to predict modulus. Fig. 4 is the δ results of the binders through the MLR model. The δ prediction is more accurate than the modulus. The *R²* of the training and testing set is above 0.9, and small RMSE values in Fig. 4 reveal that the prediction of δ is reliable.
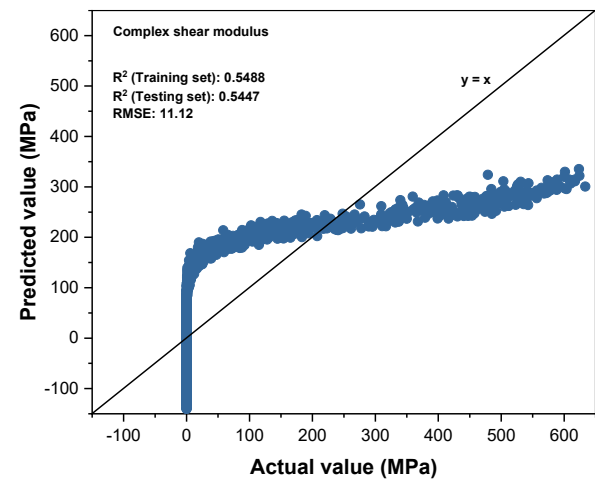
Figure 3. MLR model of |G*|.
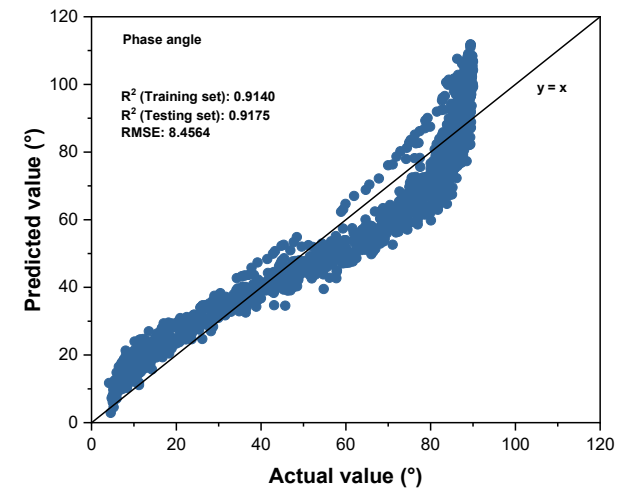
Figure 4. MLR model of δ.

3.2.2 *Gaussian Process Regression*

Since MLR cannot provide sufficiently accurate prediction $|G*|$, a more advanced GPR model was introduced to achieve this purpose. Fig. 5 shows the GPR predictions of binders affected by temperature

and frequency. It showed a promising correlation in Fig. 5. The R^2 values are above 0.98, and the RMSE is 1.9370 in this model. Regarding δ, the GPR model also exhibited desirable results in Fig. 6. The predicted values in Fig. 6 are almost equal to the actual values; its R^2 is above 0.98, and the RMSE value is 3.1672. This indicates that the GPR model can achieve the purpose of predicting δ.
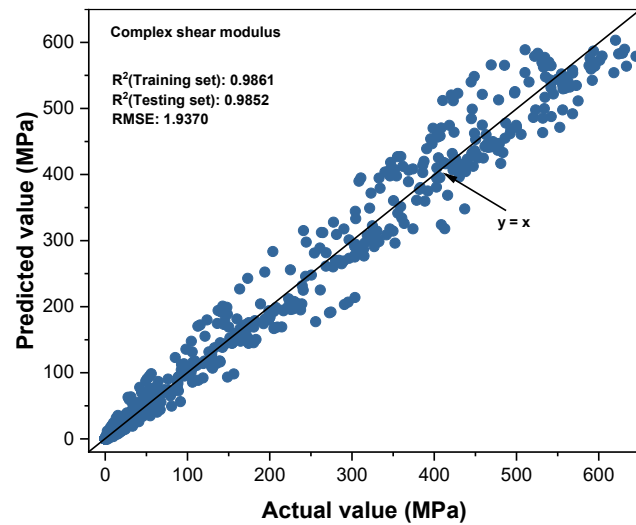
Figure 4. GPR model of |G*|.
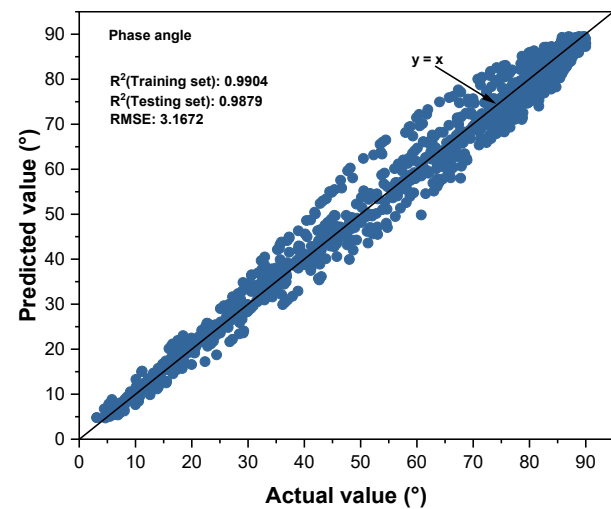
Figure 5. MLR model of δ.

4 CONCLUSIONS

- The original chemical features of binders can be reduced to two principal components.
- The multiple linear regression (MLR) model can predict the phase angle of binders but not the modulus.
- On the other hand, the Gaussian process regression (GPR) model enables the prediction of both modulus and phase angle.

The neat asphalt binders in this work have the same type of chemical composition; only the concentra-tion is different. Thus, in the next phase of this research, it is recommended that the analysis and the prediction models be extended to modified asphalt binders (more chemical composition types), especially those with chemical modification.

5 REFERENCES

[1] Hu, X., Madden, L.V., Edwards, S., and Xu, X. 2015 Combining models is more likely to give better predictions than single models. Phytopathology, 105 9, 1174-1182

[2] Ilyin, S.O., and Yadykova, A.Y. 2024 Eco-friendly bitumen binders from heavy crude oil and a relaxation approach to predicting their resistance to rutting and cracking. Journal of Cleaner Production, 434, 139942

[3] Margaritis, A., Soenen, H., Fransen, E., Pipintakos, G., Jacobs, G., and Blom, J. 2020 Identification of ageing state clusters of reclaimed asphalt binders using principal component analysis (PCA) and hierarchical cluster analysis (HCA) based on chemo-rheological parameters. Construction and Building Materials, 244, 118276

[4] Paranhos, R.S., and Petter, C.O. 2013 Multivariate data analysis applied in Hot-Mix asphalt plants. Resources, Conservation and Recycling, 73, 1-10

[5] Salehfard, R., Yeganeh, S., Dalmazzo, D., Underwood, B.S., and Santagata, E. 2024 Linking Chemical Structure to the Linear and Nonlinear Properties of Asphalt Binders. Transportation Research Record, 03611981241244793

[6] Schulz, E., Speekenbrink, M., and Krause, A. 2018 A tutorial on Gaussian process regression: Modelling, exploring, and exploiting functions. Journal of mathematical psychology, 85, 1-16

[7] Shan, B., Cao, X., Hao, Z., Wu, Y., Yang, X., and Li, X. 2024 Experimental and Molecular Dynamics Simulations Investigating the Flexibility and Compatibility of Epoxidized Soybean Oil–Reinforced Epoxy Asphalt. Journal of Materials in Civil Engineering, 36 10, 04024327

[8] Shan, L., Wang, Y., Liu, S., Qi, X., and Wang, J. 2023 Establishment of correlation model between compositions and dynamic viscoelastic properties of asphalt binder based on machine learning. Construction and Building Materials, 364, 129902

[9] Wang, D., Baliello, A., Poulikakos, L., Vasconcelos, K., Kakar, M.R., Giancontieri, G., Pasquini, E., Porot, L., Tušar, M., and Riccardi, C. 2022 Rheological properties of asphalt binder modified with waste polyethylene: An interlaboratory research from the RILEM TC WMR. Resources, Conservation and Recycling, 186, 106564

[10] Zhang, F., Cannone Falchetto, A., Yuan, D., Wang, W., Wang, D., and Sun, Y. 2024 Research on performance variations of different asphalt binders results from microwave heating during freeze-thaw cycles. Construction and Building Materials, 448, 138280

7.3

DEVELOPMENT OF DIGITAL TWINS

Simulating multilayered inelastic pavements by a dynamic ALE formulation

A. Anantheswar, I. Wollny & M. Kaliske
Institute for Structural Analysis, Technische Universität Dresden, Dresden, Saxony, Germany

ABSTRACT: Pavements are typically long structures, and simulating their transient response when subjected to moving vehicle loads, using conventional techniques can be quite arduous. These techniques would necessitate the discretization of the complete pavement that is along the path of the moving load. Thus, depending on the velocity of the vehicle, considerably large meshes would need to be employed and solved. In recent developments, a dynamic ALE formulation has been put forth to improve efficiency by only considering the relevant region of the pavement around the load. The work at hand further highlights the capabilities of the dynamic ALE formulation by applying the dynamic ALE formulation to multilayered inelastic pavements.

1 INTRODUCTION

Pavements are part of the critical infrastructure of a country, and fulfill the important task of providing connectivity as a medium for transport of people and goods. The suitable design of pavements is therefore crucial. In order to facilitate the design of such structures, techniques like the Finite Element Method (FEM) in a Lagrangian setting are typically used. When simulating the response of the pavement subjected to a moving load, if these traditional techniques are used, the associated domain of the pavement that needs to be discretized is quite large, and therefore computationally inefficient. Additionally, restrictions are imposed on the mesh discretization when the vehicle load is accelerating or decelerating. Further, a moving load formulation is needed to simulate the movement of the vehicle on the pavement. The speed of the vehicle also imposes restrictions on the time steps of the simulation. The recent development proposed by (Anantheswar et al. 2024a) utilizes the Arbitrary Lagrangian Eulerian (ALE) simulation strategy to improve computational efficiency.

Traditionally, ALE simulation techniques are used in the field of fluid mechanics (Benson 1989, Venkatasubban 1995, Souli et al. 2000, Codina et al. 2009, Basting et al. 2017). Another typical use-case of ALE strategy is as a mesh adaptation technique, to improve the mesh quality when extreme distortions are encountered (Liu et al. 1986, Rodríguez-Ferran et al. 1998, Bayoumi & Gadala 2004, Donea et al. 2004, Nazem et al. 2009, Berger & Kaliske 2022). The pioneering work of (Nackenhorst 2004) described the use of the ALE methodology to improve efficiency in analyses of rolling tire structures. Following this, (Wollny & Kaliske 2013, Wollny et al. 2016) implemented the ALE formulation for pavements considering constant velocity load movement. Recent developments by (Anantheswar et al. 2024a) extend the ALE formulation for pavements to the dynamic case, and further to inelastic materials (Anantheswar et al. 2024b). This contribution highlights applying the dynamic ALE formulation to multilayered inelastic pavements.

2 THE MOVING ALE REFERENCE FRAME

The central theme involved in adopting the dynamic ALE formulation for pavements is a change in the reference frame of the observer. Instead of a stationary reference frame as in the conventional Lagrangian formulation, the reference frame moves with the vehicle load in the ALE formulation. An observer in this moving reference frame would perceive the load as stationary, while the material of the pavement would appear to flow beneath the load. The main advantage offered by this perspective is that only a relevant portion of the pavement in the vicinity of the moving vehicle load would need to be considered in the analyses. This is shown to significantly improve computational efficiency (Anantheswar et al. 2024a). A kinematic description of the various configurations involved when adopting the ALE formulation for pavements is shown in Figure 1.

Figure 1. Kinematics of the moving ALE reference frame.

It should be noted that in Figure 1, for pavements, there is no rigid body displacements (translations or rotations) and so $u_{rig} = 0$. This implies that the initial configuration and the ALE reference configuration are the same. But, over time, the ALE reference frame e_i^{ALE} travels with the same velocity as the vehicle load. Thus, a new portion of the pavement material in the vicinity of the load would be considered at each time step. The velocity with which the material of the pavement appears to flow through the mesh (in a Finite Element framework) is termed 'guiding velocity' (Nackenhorst 2004), given by

$$w = \left.\frac{\partial \chi}{\partial t}\right|_X = \left.\frac{\partial\left(X + u_{rig} - \chi_0^{ALE}\right)}{\partial t}\right|_X = -\left.\frac{\partial \chi_0^{ALE}}{\partial t}\right|_X , \qquad (1)$$

where the positions and displacements of a material point in various configurations depicted in Figure 1, are related by

$$x = X + u = X + u_{rig} + \hat{u} = \chi_0^{ALE} + \chi + \hat{u} . \qquad (2)$$

Further, adhering to the balance of linear momentum, the weak formulation in the ALE reference configuration can be expressed as

$$\int_{\chi(\mathcal{B})} \hat{\rho}\dot{v} \cdot \eta d\hat{V} + \int_{\chi(\mathcal{B})} \hat{P} : \mathrm{Grad}\eta d\hat{V} =$$
$$\int_{\chi(\mathcal{B})} \hat{\rho}b \cdot \eta d\hat{V} + \int_{\partial\chi(\mathcal{B})} \hat{T} \cdot \eta d\hat{A} , \qquad (3)$$

where $\hat{\rho}$ is the density, $\dot{v}$ denotes the acceleration, $\hat{P}$ refers to the second Piola-Kirchhoff stress, b refers to body forces, $\hat{T}$ denotes surface traction, η refers to an arbitrary test function, and $d\hat{V}$ and $d\hat{A}$ are infinitesimal volume and area elements, respectively, on domain $\chi(\mathcal{B})$ in the ALE reference configuration. In Equation 3, the terms on the left-hand side describe the internal forces developed in response to the externally applied forces, which are on the right-hand side. Of particular interest is the first term in Equation 3, which refers to the inertial forces. This term depends on the acceleration, which is defined as the material time derivative of the velocity field. One characteristic of the ALE approach is that whenever a material time derivative of a quanti-

ty f is encountered, advection effects need to be considered. For pavements, where the advection velocity is known, this is described as

$$\dot{f} = \left.\frac{\partial f}{\partial t}\right|_X = \left.\frac{\partial f}{\partial t}\right|_\chi + \mathrm{Grad}f \cdot w . \qquad (4)$$

Thus, according to Equation 4, the velocity and acceleration fields need to be advected through the mesh. This results in additional terms that need to be considered during the linearization and implementation into a finite element framework (Anantheswar et al. 2024a). Additionally, since the displacement field at any given time step depends on the displacement field at the previous time step, a suitable update of the displacement field also needs to be carried out.

Moreover, when inelastic material models are used, evolution of inelastic effects (like viscosity, plasticity etc.) are typically expressed as rate equations of certain internal variables α. Therefore, advection of such internal variables also needs to be accounted for, using

$$\dot{\alpha} = \left.\frac{\partial \alpha}{\partial t}\right|_X = \left.\frac{\partial \alpha}{\partial t}\right|_\chi + \mathrm{Grad}\alpha \cdot w . \qquad (5)$$

The advection procedure for internal variables is as per the Gauss point sub-mesh interpolation technique (DGPA) from the work of (Anantheswar et al. 2024b). This technique utilizes an operator split to first solve for internal variables in the Lagrangian phase. Then, interpolation and update of the internal variables in a sub-mesh of Gauss points takes place during the Eulerian phase. This procedure is performed after every iteration in the global Newton-Raphson solution scheme.

When multiple inelastic materials are used (as in the case of pavements, see Figure 2), advection of the internal variables of each layer should be treated separately. For the DGPA scheme, this means that each material layer gets its own sub-mesh of Gauss points, where the interpolation and update procedure is carried out. This ensures that the advection procedure does not transfer internal variables of one material to another. The extension of the DGPA scheme to allow for multiple materials is the novelty of the work at hand. Figure 2 illustrates the use of separate Gauss point sub-meshes for advection of internal variables in each layer of the pavement, for a simple mesh in two dimensions.

3 NUMERICAL STUDY

In this study, a four layered asphalt pavement with similar structure as in Figure 2 is analyzed. The non-linear viscoelastic material described in (Anantheswar et al. 2024b) with one viscous branch is used to model each of the layers.
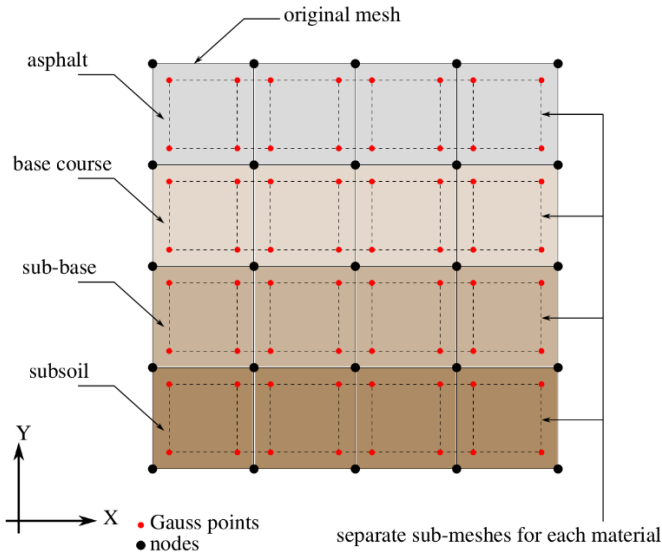
Figure 2. Separate Gauss point sub-meshes for each material, to accurately perform advection of internal variables.

The material parameters of the layers are listed in Table 1. The mesh and loading are depicted in Figure 3. The geometry of the specimen is a cuboid 8 m x 8 m x 3 m along x-, y- and z-directions, respectively. The boundary conditions are such that all surfaces except the top surface are restrained from translation in the direction normal to the surface. In the analysis, the transient response of the pavement when subjected to a moving truck tire load is simulated. The load is initially applied as a ramp over a period of 1 s. Then, it is maintained at this constant amplitude for the rest of the simulation. A guiding velocity is applied such that the load appears to accelerate from 0 m/s to 16.667 m/s (60 km/h) starting at 2 s, over a period of 2 s. Then, this velocity is maintained until 10 s. The guiding velocity is, then, ramped down such that the load appears to decelerate to 0 m/s over a period of 1.2 s. It is then maintained at 0 m/s for the rest of the simulation, ending at total time of 12.5 s. The Newmark time integration scheme (Newmark 1959) with a time step of 0.1 s and linear eight node brick type finite elements are used in the simulation.

Table 1. Material properties used in the simulation.

Layer	Elastic branch			Viscous branch	
	$\hat{\rho}$ kg/m^3	κ* MPa	μ* MPa	μ_v* MPa	η_v* Ns/m^2
Asphalt	2.3E+3	822.50	200.00	179.62	1.0E+8
Base course	2.2E+3	175.83	40.00	31.15	1.0E+8
Sub-base	2.0E+3	105.50	24.00	18.69	1.0E+8
Subsoil	1.9E+3	60.83	14.00	14.08	1.0E+8

* κ: Bulk modulus, μ: Shear modulus, μ_v: Shear modulus of viscous branch, η_v: Viscous parameter.

The thickness of the subsoil layer is 2 m, the sub-base course is 0.4 m, and both the base course and the asphalt layer on top have thicknesses of 0.3 m each.
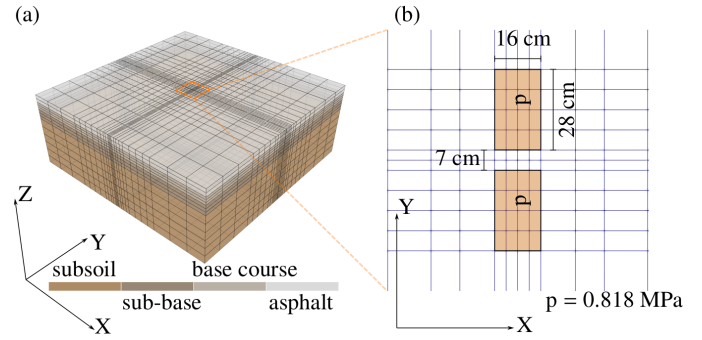

Figure 3. (a) Perspective view of the mesh and (b) top view (close-up) of the loaded area in the centre of the mesh.

The mesh used has 10192 finite elements, and the simulation took approximately 4.12 hours to run on a desktop computer with an Intel Core i5 10400 processor and 32 GB of RAM. The obtained results in terms of the displacements at the centre of load between the two tires are shown in Figure 4. Contours of the strain component e_{zz} are depicted in Figure 5, at various time points in the simulation.
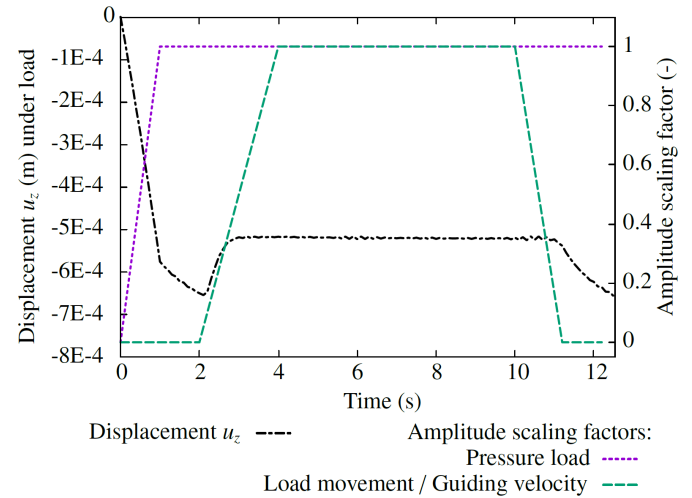
Figure 4. Displacement component u_z of the central node under the load plotted against time.

The results shown in Figures 4, 5 clearly demonstrate the capability of the dynamic ALE framework to simulate the transient response of inelastic multi-layered pavement structures in a computationally efficient manner. It is worth mentioning, that if a corresponding simulation was run using conventional techniques, it would necessitate the discretization of a domain of length 154.67 m. With the ALE approach, this length is reduced to just 8 m, making the simulation possible on a desktop computer, even without parallelization. Further, the conventional techniques would necessitate the implementation of a cumbersome moving load formulation. This imposes further restrictions on the time step size and

discretization used in the conventional simulation, as a sufficiently fine mesh would be required to ensure that the load is applied on the nodes in synchronicity with its movement as well. The need to discretize a large domain, along with restrictions imposed on time step and fineness of the mesh, are overcome using the dynamic ALE formulation. This formulation offers a substantial improvement to computational performance, when simulating the transient response of inelastic multilayered pavement structures.

Figure 5. Contour plots of strain component e_{zz} at various stages in the simulation.

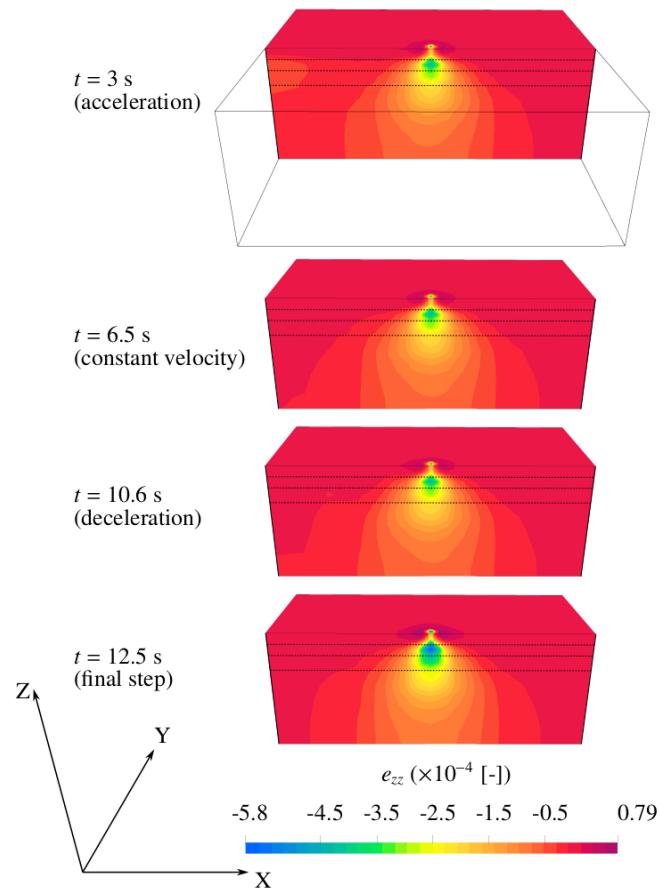Future research towards improving the performance of the ALE formulation could be in the direction of utilizing model order reduction techniques or through parallelization. This is relevant in application cases such as in digital twins, which require fast and efficient calculations. These tools would indubitably lead to improved and informed decisions by engineers and policy makers alike.

4 ACKNOWLEDGEMENTS

5 REFERENCES

Anantheswar, A., Wollny, I., & Kaliske, M. 2024a. A dynamic ALE formulation for structures under moving loads. *Computational Mechanics*, 73:139–157.

Anantheswar, A., Wollny, I., & Kaliske, M. 2024b. Treatment of Inelastic Material Models Within a Dynamic ALE Formulation for Structures Subjected to Moving Loads. *International Journal for Numerical Methods in Engineering,* e7599.

Basting, S., Quaini, A., Čanić, S., & Glowinski, R. 2017. Extended ALE method for fluid-structure interaction problems with large structural displacements. *Journal of Computational Physics*, 331:312–336.

Bayoumi, H. & Gadala, M. 2004. A complete finite element treatment for the fully coupled implicit ALE formulation. *Computational Mechanics*, 33:435–452.

Benson, D. 1989. An efficient, accurate, simple ALE method for nonlinear finite element programs. *Computer Methods in Applied Mechanics and Engineering*, 72:305–350.

Berger, T. & Kaliske, M. 2022. An arbitrary Lagrangian Eulerian formulation for tire production simulation. *Finite Elements in Analysis and Design*, 204:103742.

Codina, R., Houzeaux, G., Coppola-Owen, H., & Baiges, J. 2009. The fixed-mesh ALE approach for the numerical approximation of flows in moving domains. *Journal of Computational Physics*, 228:1591–1611.

Donea, J., Huerta, A., Ponthot, J., & Rodríguez-Ferran, A. 2004. Arbitrary Lagrangian-Eulerian Methods, Chapter 14. Wiley Online Library, Encyclopedia of Computational Mechanics.

Liu, W., Belytschko, T., & Chang, H. 1986. An arbitrary Lagrangian-Eulerian finite element method for path-dependent materials. *Computer Methods in Applied Mechanics and Engineering*, 58:227–245.

Nackenhorst, U. 2004. The ALE-formulation of bodies in rolling contact: Theoretical foundations and finite element approach. *Computer Methods in Applied Mechanics and Engineering*, 193:4299–4322.

Nazem, M., Carter, J., & Airey, D. 2009. Arbitrary Lagrangian–Eulerian method for dynamic analysis of geotechnical problems. *Computers and Geotechnics*, 36:549–557.

Newmark, N. 1959. A method of computation for structural dynamics. *Journal of the Engineering Mechanics Division*, 85:67–94.

Rodríguez-Ferran, A., Casadei, F., & Huerta, A. 1998. ALE stress update for transient and quasistatic processes. *International Journal for Numerical Methods in Engineering*, 43:241–262.

Souli, M., Ouahsine, A., & Lewin, L. 2000. ALE formulation for fluid–structure interaction problems. *Computer Methods in Applied Mechanics and Engineering*, 190:659–675.

Venkatasubban, C. 1995. A new finite element formulation for ALE (arbitrary Lagrangian Eulerian) compressible fluid mechanics. *International Journal of Engineering Science*, 33:1743–1762.

Wollny, I. & Kaliske, M. 2013. Numerical simulation of pavement structures with inelastic material behaviour under rolling tyres based on an arbitrary Lagrangian Eulerian (ALE) formulation. *Road Materials and Pavement Design*, 14:71–89.

Wollny, I., Hartung, F., & Kaliske, M. 2016. Numerical modeling of inelastic structures at loading of steady state rolling. *Computational Mechanics*, 57:867–886.

Scan2FEM – Automatic mesh generation of highway pavements from reality capture data

D. Crampen, R. Becker, I. Wollny, M. Kaliske, J. Blankenbach
Geodetic Institute and Chair for Computing in Civil Engineering & GIS, RWTH Aachen University, Aachen, North-Rhine-Westfalia, Germany

ABSTRACT: For Digital Twins of roads a major use case is pavement distress prediction. One requirement for accurate simulations is a detailed pavement model as a foundation for finite element analysis. This model has to represent the as-is state of the road as closely as possible. This work presents a novel approach for 3D point cloud to pavement mesh generation for structural analysis applications. We evaluate our method on point clouds from different reality capture sources with varying densities and accuracies to showcase its robustness and provide insight into the possible detail of a derivable mesh using aerial platforms. Our approach can derive both structured and unstructured meshes for use in finite element simulations of the pavement.
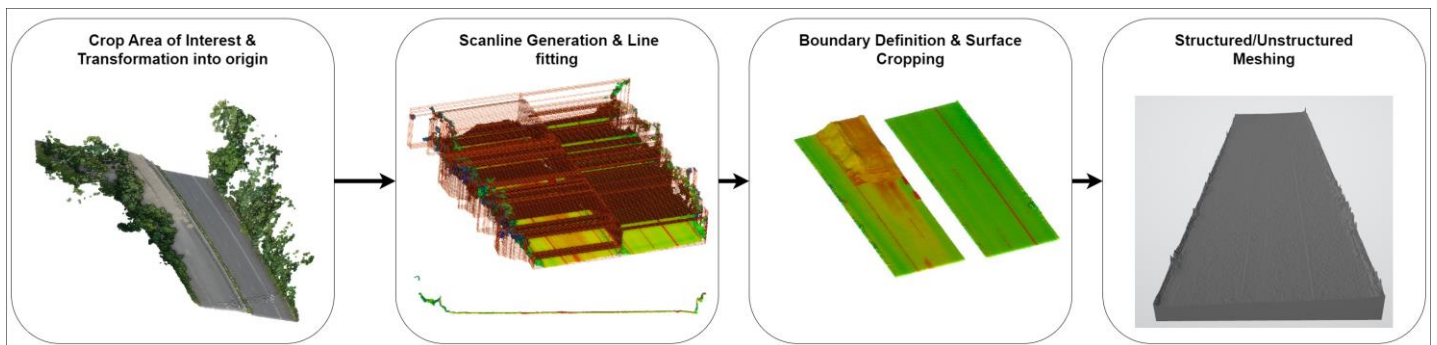
Figure 1: Overview of the road pavement meshing workflow

1 INTRODUCTION

Finite element analysis (FEA) comprises many powerful tools and methods to simulate the impact of static as well as dynamic loading conditions on a structure to numerically estimate its stress and strain condition under various circumstances such as damages, or repairs as in (Chen et al., 2020). When conducting structural analyses of road pavements, there are several deciding factors that limit the realism of a simulation. One important factor is providing the analysis with a high-quality mesh, that represents the real shape of the pavement. The manual creation of the mesh model can be time consuming and may lead to oversimplification of the pavement surface. This in turn can affect the simulation results. While the definition of material models for tire and pavement material as well as the mechanical behavior of layer interfaces are most important to describe the mechanical system, the loading condition is largely affected by the tire pavement contact patch (Király et al., 2022). However, the shape of the contact

patch can range between an idealized perfectly flat surface and the realistic surface with a degree of initial deformation. For certain analyses, the increase in computation time and complexity is overweight by the increase in accuracy, especially since it allows better insights into stress concentration development, which influences the occurrence of rutting as stated in (Zhang et al., 2023). High-resolution 3D point clouds are capable of capturing surface deformations, directly from the real asset. Therefore, we present a novel approach to automatically generate a mesh model of the deformed pavement surface for FEA simulations in this work.

2 RELATED WORKS

This section presents previous studies using 3D point cloud data for structural analysis and pavement monitoring. Point clouds were used for a range of target areas such as tunnels, bridges and also pavement models. In (Cui et al., 2023) the authors used a mobile laser scanning point cloud to reconstruct a

tunnel surface and generate a FE mesh model. By comparing the model generated using a Computer-Aided Design (CAD) tunnel model and the point cloud-based model, they demonstrated that the point cloud model led to more realistic results. Another area of application comprises heritage structures such as (Alfio et al., 2022), where the Colossus of Barletta was reconstructed using photogrammetry and based on the generated mesh a FEM simulation was conducted. (Dong et al., 2021) used a laser texture scanner (LTS) to capture the macro-texture (wavelengths between 0.5 mm to 50 mm) of asphalt mixture surfaces and developed a novel approach to detect and remove errors in the resulting texture point cloud. Although a mobile laser scanner (MLS) as used in our work is barely capable of capturing the macro-texture of a surface, it can easily acquire the mega-texture (wavelengths between 50 mm to 0.5 m) such as rutting or even the presence of road markings. Additionally, the slopes and curvatures of the road pavement are captured, directly influencing the loading direction of a tire on the road.

3 METHODOLOGY

The target environment for our approach was chosen to be a highway section of the German A544 highway section near the city of Aachen. We captured the area with a Riegl miniVux-4UAV laser scanner (UAV LS) and with a DGI Mavic drone to create a photogrammetric point cloud (UAV PG) in 2024. Furthermore, the open geoportal of North Rhine Westfalia provides airborne laser scanning (ALS) and airborne photogrammetry (APG) point clouds of the same area captured in 2023 and 2020 respectively. The different data sources allow for validation of our workflow on data with different resolutions ranging from 10 points per m² in the APG data to 800 points per m² in our UAV-PG data, which are all collected using the same spatial reference system (SRS) ETRS89/UTM32N. Figure 1 illustrates the schematic process of our approach.

Our approach consists of four steps:
1. Point cloud horizontal cropping, point cloud transformation and cleaning
2. Scanline slicing and pavement surface line fitting
3. Pavement surface boundary definition and extraction
4. Mesh generation

3.1 *Point cloud horizontal cropping*

First, we define a polygon of four georeferenced points to crop each of the four point clouds ((298564.0225 5631141.2653, 298535.7874 5631107.0155, 298608.3062 5631047.2320,

298636.5414 5631081.4818) to the region of interest. Next, we use open data of the road network provided by "opengeoportal.nrw" as ESRI shapefiles to extract the approximate local road axis, which we then use to transform the point clouds in a way that the driving direction faces the x-axis. Then, we localize the point cloud, to allow easier handling and manipulation. After cropping and transformation, a DBSCAN clustering algorithm is used to filter and remove the above ground points resulting in point clouds of the ground surface.

3.2 *Scanline slicing and pavement line fitting*

Since the processed point cloud of the ground surface still extends over the actual road pavement, we implement a slicing and line fitting algorithm, which slices the point cloud along the road axis into slices with an adjustable thickness chosen to be 30 cm. We separate the left and right carriageway by cropping left and right sided points using the centerline, to obtain two point clouds with a single pavement surface respectively. A line is fitted to the YZ-projection of each side per slice, representing the road cross-section at the slice position. For line fitting, we employ a constrained RANSAC algorithm defining a maximum and minimum side slope angle of 5 degrees and an inlier threshold of the respective point cloud accuracies ranging from 2 cm to 8 cm. The algorithm outputs the best fitting line for each slice as well as the inlier points close to the line. Pavement surface boundary definition and extraction

To define the continuous boundary of the road pavement, we combine all starting points and all end points of the lines fit to the slices and compute the average distance to the centerline, which is then translated to represent the left and right edge of the pavement. We decided to use the fixed centerline as boundary, since using start and end points directly would result in inconsistent edges, that may affect the mesh generation step. Having defined the boundary polygon of the pavement, the point cloud is once again cropped to retrieve a point cloud of the pavement surface per carriageway.
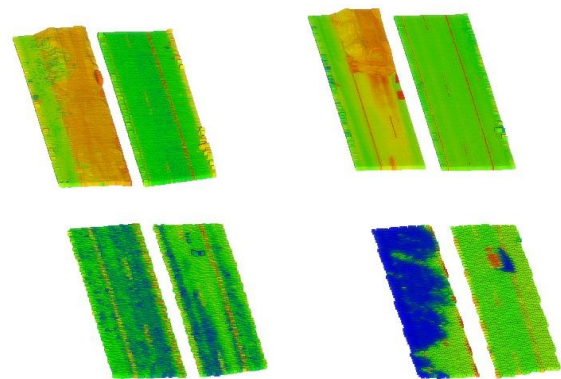

Figure 2. Cropped pavement surface point (top left: UAV LS, top right: UAV PG, bottom left: ALS, bottom right: APG

3.3 *Mesh generation*

For generating a mesh model for FEM simulation, we implement two approaches. The first approach generates an unstructured mesh directly from the point cloud while the second approach generates a structured mesh and uses the point cloud to adjust the node positions.

For unstructured mesh generation, we use voxel down sampling to minimize potential face intersections induced by close points with largely differing heights. We interpolate points onto the 2D boundary polygon defined in the previous step to ensure the generated surface has a sharp edge and elevate the new points by conducting a k-nearest neighborhood search on the point cloud with k=1 and assign the height of the closest point in the point cloud to the polygon points' height coordinate (z) before concatenating the surface points and the boundary points.

We then use 2D Delaunay triangulation to first generate faces for the pavement surface. We constrain the face properties with conditions of maximum edge ratio, maximum face area and maximum angle between face normal and the vertical axis to iteratively re-mesh and remove vertices creating distorted faces. This process represents a smoothing operation that converges and stops as soon as a steady state is reached where no vertices are removed after applying the constraints.

In a last step, the 2D surface is extruded vertically to form a volume mesh with the top surface being deformed by the mesh nodes elevations while the bottom surface stays flat. The extrusion length can be adjusted arbitrarily to fit the desired layer thicknesses of the subgrade layers and after the first extrusion, this step can be repeated to add more layers to the mesh.

For the generation of structured meshes, we first initialize an irregular grid, by interpolating new points onto the boundary curves of the polygon boundary and then interpolate the points on the curves over the polygon area to form a grid following the road center axis' curvature, with arbitrary resolution. Since the points are regularly distributed over the area of interest, we can directly form rectangular faces over the 2D surface. Next, we extrude the 2D surface vertically similarly to the unstructured mesh (section 3.4.1) to form a volume. Then, we use K-nearest neighborhood search to deform the top surface nodes. Choosing higher values for k and using the average height of the closest point results in a smoothing operation for the top surface.

4 RESULTS

By evaluating our workflow on all four different point cloud sources we could validate its applicability for different point cloud densities.

Though several parameters have to be adjusted for each point cloud to create a usable mesh, these parameters could potentially be directly adjusted by properties derivable from the input point cloud such as their surface density. Figure 2 shows the extracted points clouds of the pavement surfaces after step three of the workflow. It can be noted that during the survey in 2024 the left carriageway was under construction, showing a temporary soil ramp. For the present intermediate results, we therefore focused on the right carriageway.

The following parameters need to be adjusted according to the point cloud source in our workflow:

1. DBSCAN radius epsilon for point cloud cleaning (removing above ground points)
2. Scanline slicing distance to define the thickness of each slice
3. Line inlier threshold has to be defined for line fitting (according to point cloud accuracy)

Depending on the target road, there are several other parameters that may affect computation time and accuracy of the fitting process.

1. Number of iterations for RANSAC line fitting
2. Maximum side slope of the road
3. Maximum road width to constraint the boundary definition

For meshing, there are respective parameters that may have to be optimized. For structured mesh generation:

1. Grid resolution needs to be specified in both directions (driving direction and orthogonal direction)
2. Number of neighbors K for height interpolation of nodes (smoothing)

Finally, for the unstructured meshing the following parameters have to be tuned:

1. Voxel size for point cloud sub-sampling
2. Interpolation density of boundary points
3. Iterative Delaunay constraints:
   a. Maximum edge ratio
   b. Maximum face angle
   c. Maximum face area

Unfortunately, the UAV LS data, was affected by high drift of the drone platform during the survey resulting in low vertical accuracy of the point cloud which can also be seen in the resulting mesh. A comparison of the meshing for all point cloud sources with 5 cm grid resolution is depicted in Figure 3. The best results were generated using the UAV PG point cloud, where in the mesh even the height difference between road markings and pavement can be identified. We exported the meshes into STL format and tested their usability in a simple SIMSCALE project. The structured meshes were directly usable, while the unstructured meshes con-
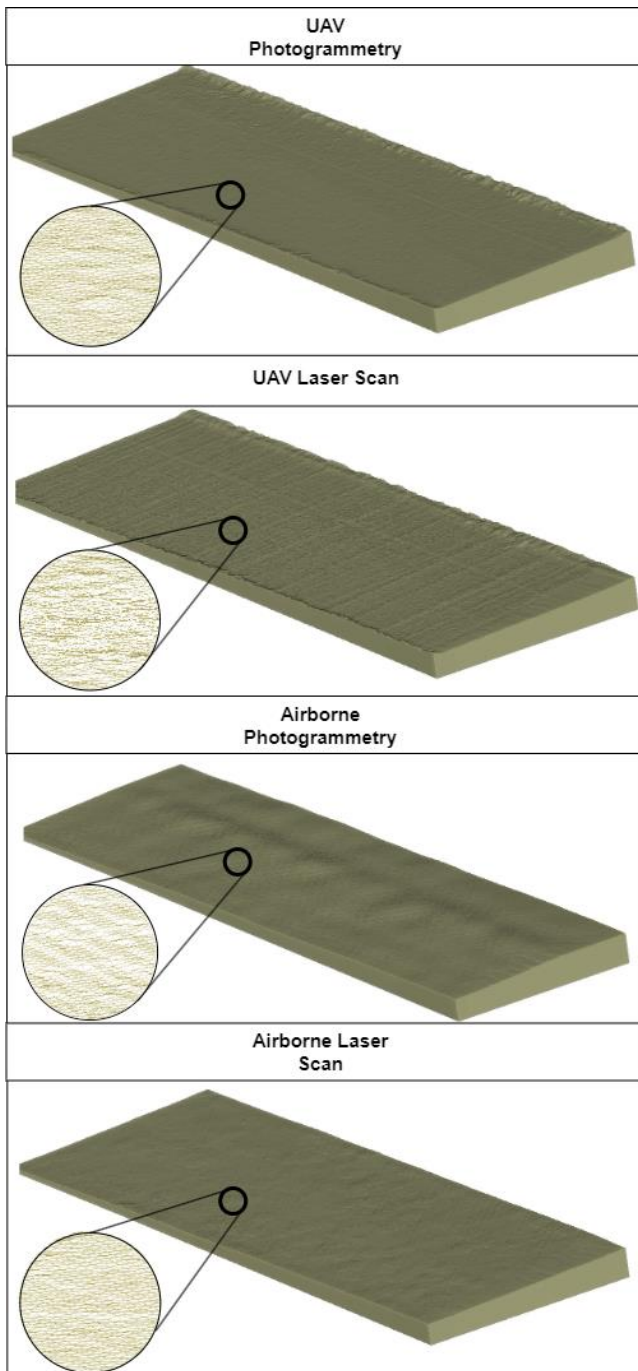
Figure 3: Structured meshing result with resolution of 5 cm for each point cloud source

tained erroneous faces requiring a remeshing with a CAD software.

5 CONCLUSION

In this contribution, we implemented a first approach for point cloud to pavement mesh model generation (Scan2FEM) for high fidelity finite element analysis of pavements. Though introducing several tunable parameters into the workflow, we still largely reduced the effort of mesh generation, since the road extraction and reorientation step are fully automated leveraging widely available geospatial data. We showed that our approach is applicable to different point cloud sources. In future work, we

aim at evaluating the impact of surface deformations in different resolutions on the simulation results of tire pavement interaction analysis as in (Anantheswar et al., 2024). Additionally, we aim to extend our workflow to more special cases as presented on the left carriageway of our example.

Determining the specific requirements of an optimal pavement model, will enable us to deliver optimal meshes for a structural analysis Digital Twin use case (Crampen and Blankenbach, 2023), that maximize the accuracy of simulations and therefore improve the quality of decision making.

6 ACKNOWLEDGEMENT

7 REFERENCES

Alfio, Vincenzo Saverio; Costantino, Domenica; Pepe, Massimiliano; Restuccia Garofalo, Alfredo (2022): A Geomatics Approach in Scan to FEM Process Applied to Cultural Heritage Structure: The Case Study of the "Colossus of Barletta". In: Remote Sensing 14 (3), S. 664.

Anantheswar, Atul, Ines Wollny, and Michael Kaliske. "A dynamic ALE formulation for structures under moving loads." Computational Mechanics 73.1 (2024): 139-157.

Chen, Jiaqi; Wang, Hao; Xie, Pengyu (2020): Finite element modeling of mechanical responses of concrete pavement with partial depth repair. In: Construction and Building Materials 240, S. 117960.

Crampen, David, and Jörg Blankenbach (2023): "LOADt: towards a concept of level of as-is detail for digital twins of roads." Proceedings of the 30th international workshop on intelligent computing in engineering (EG-ICE)

Cui, Lizhuang; Zhou, Lizhi; Xie, Quanyi; Liu, Jian; Han, Bo; Zhang, Tiantao; Luo, Hongzheng (2023): Direct generation of finite element mesh using 3D laser point cloud. In: Structures 47, S. 1579–1594.

Dong, Shihao; Han, Sen; Yin, Yuanyuan; Zhang, Zhuang; Yao, Tengfei (2021): The method for accurate acquisition of pavement macro-texture and corresponding finite element model based on three-dimensional point cloud data. In: Construction and Building Materials 312, S. 125390.

Király, Tamás; Primusz, Péter; Tóth, Csaba (2022): Simulation of Static Tyre–Pavement Interaction Using Two FE Models of Different Complexity. In: Applied Sciences 12 (5), S. 2388.

Zhang, Qingtao; Shangguan, Lingxiao; Li, Tao; Ma, Xianyong; Yin, Yunfei; Dong, Zejiao (2023): Tire–Pavement Interaction Simulation Based on Finite Element Model and Response Surface Methodology. In: Computation 11 (9), S. 186.

Towards real-time structural simulations for the digital twin of the road

J. Kehls, T. Brepols
Institute of Applied Mechanics, RWTH Aachen University, 52074 Aachen, Germany

S. Reese
University of Siegen, 57076 Siegen, Germany

A. Anantheswar, I. Wollny, M. Kaliske
Institute for Structural Analysis, Technische Universität Dresden, 01062 Dresden, Germany

ABSTRACT: In the context of digital twins, fast simulations are essential to obtain meaningful information about a system in near real-time. To achieve this goal in the context of a digital twin of a road system, a combination of the Arbitrary Lagrangian Eulerian (ALE) method and proper orthogonal decomposition (POD)-based model order reduction is proposed. In a numerical example, the combination of the two methods is shown to reduce the computation time of a simulation significantly, introducing only a small approximation error. Furthermore, it is demonstrated that the framework can predict unseen structural behavior without a vast amount of data.

1 INTRODUCTION

Fast, efficient simulations are crucial in technologies such as digital shadows or twins. These allow realistic predictions that are also accurate, therefore enabling governing authorities to take quick, meaningful and impactful decisions based on sound and structured logic. Particularly for pavement structures subject to moving wheel loads, the Arbitrary Lagrangian Eulerian methodology has been proven to be far more efficient than conventional simulation techniques (Wollny et al. 2016, Anantheswar et al. 2024). However, this methodology is still incapable of real-time simulations, and a further speedup is necessary. In this work, the application of Model Order Reduction (MOR) techniques to ALE simulations of the pavement structure is explored, to reduce the computational effort even further.

2 ALE FORMULATION

The concept that is at the core of ALE simulations of pavements is the adoption of a moving reference frame, see Figure 1.
This moving reference frame conveniently shows the same velocity as the applied wheel load. Thus, to an observer in this moving reference frame, the load would appear stationary, and the material of the pavement would appear to flow under the load. The main advantage of this ALE technique is that only the relevant region of the pavement in the immediate vicinity of the load needs to be discretized and simulated. This is in contrast to conventional simulation techniques,

where the entire structure in the path of the wheel load would need to be discretized and analyzed. For a detailed description of the implementation of the ALE formulation, the reader may refer to the work of (Anantheswar et al. 2024).
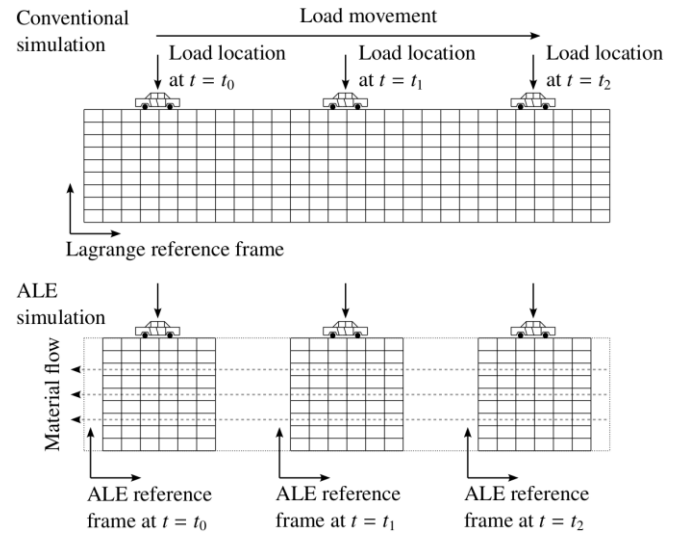
Figure 1. Moving reference frame in ALE simulations.

One interesting aspect of the ALE formulation is that it does not change the overall structure of the global system of equations in a nonlinear finite element framework. This means that the system can still be assembled into the well-known system of equations that has to be solved in every iteration of the solution scheme

$$\underline{M} \, \Delta \ddot{u} + \underline{D} \, \Delta \dot{u} + \underline{K}_T \, \Delta u = g, \qquad (1)$$

where $\underline{M}$, $\underline{D}$ and $\underline{K}_T$ refer to the global mass, damping and tangential stiffness matrices, respectively, and

$\Delta\ddot{\boldsymbol{u}}$, $\Delta\dot{\boldsymbol{u}}$, $\Delta\boldsymbol{u}$ and $\boldsymbol{g}$ denote the assembled incremental nodal vectors of acceleration, velocity, displacement and the residual vector, respectively. The Newmark-beta method is used for the time-integration, which results in the system of equations

$$\underline{\boldsymbol{K}}_{T,dyn} \Delta\boldsymbol{u} = \boldsymbol{g}, \qquad (2)$$

with the $(n \times n)$-dimensional dynamic tangential stiffness matrix $\underline{\boldsymbol{K}}_{T,dyn}$. With the global system of equations in this standard structure, it is possible to apply MOR techniques in a relatively simple and straightforward manner.

3 POD-BASED MOR

In this contribution, the proper orthogonal decomposition (POD) method is applied to the problem at hand according to (Radermacher & Reese 2013) and (Kehls et al. 2023). The POD is a projection-based technique for reduced order modeling. In the following, the POD will be shortly explained for the present case. For a more detailed description of POD and projection-based MOR in general, the reader is kindly referred to the work of (Benner et al. 2015) and (Schilders 2008). For the problem described in Equation 2, it is assumed that an $(n \times m)$-dimensional projection matrix $\boldsymbol{\Phi}$ can be found, such that the Galerkin projection of Equation 2 leads to the reduced system of equations

$$\boldsymbol{\Phi}^T \underline{\boldsymbol{K}}_{T,dyn} \boldsymbol{\Phi} \Delta\boldsymbol{u}_{red} = \boldsymbol{\Phi}^T \boldsymbol{g}. \qquad (3)$$

After the solution has been computed in the reduced subspace, the (m)-dimensional reduced solution vector $\Delta\boldsymbol{u}_{red}$ can be projected to the (n)-dimensional full solution space by the relation $\Delta\boldsymbol{U} = \underline{\boldsymbol{\Phi}} \Delta\boldsymbol{u}_{red}$. If $m \ll n$, solving the system of equations in the reduced subspace is much faster than solving it in the full solution space, leading to a significant reduction in computation time.

To construct the projection matrix $\underline{\boldsymbol{\Phi}}$, solution vectors $\boldsymbol{u}_i$ are sampled in precomputations and collected in the so-called snapshot matrix $\underline{\boldsymbol{D}} = [\boldsymbol{u}_1\, \boldsymbol{u}_2\, \dots\, \boldsymbol{u}_l]$. The sampled solution vectors can be e.g. time-series solutions from a precomputation but also solutions from simulations with varying material parameters or in the case of ALE varying material flow velocities. A singular value decomposition is then applied to the snapshot matrix such that $\underline{\boldsymbol{D}} = \underline{\boldsymbol{V}}\, \underline{\boldsymbol{\Sigma}}\, \underline{\boldsymbol{W}}^T$. The matrices $\underline{\boldsymbol{V}}$ and $\underline{\boldsymbol{W}}^T$ contain the left and right singular vectors and the matrix $\underline{\boldsymbol{\Sigma}}$ contains the decreasing singular values on its diagonal. Each singular value Σ_{ii} corresponds to a singular vector $\boldsymbol{v}_i$ and indicates its importance for the reconstruction of the snapshot matrix $\underline{\boldsymbol{D}}$. The number of POD modes $\boldsymbol{v}_i$ that leads to a good approximation of sampled snapshots can, therefore, be derived from the decay of the singular values. At last, the projection matrix is truncated at the specified index m such that the projection matrix is defined as $\underline{\boldsymbol{\Phi}} = [\boldsymbol{v}_1\, \boldsymbol{v}_2\, \dots\, \boldsymbol{v}_m]$.

4 NUMERICAL EXAMPLE

To test the proposed methodology, both methods presented above are implemented into the finite element research software *FEAP* (Taylor 2014) and a numerical example is computed and analyzed. The example is based on (Anantheswar et al. 2024) and uses the same material described therein. The boundary value problem is depicted in Figure 2. The structure is fixed on all sides and on the bottom and the distributed load p is applied in the center of the upper surface. The ALE material guiding velocity is denoted by w. The structure is simulated for $t = 12.5$ s with time increments of $\Delta t = 0.1$ s. At the beginning of the simulation, the load is increased linearly until the desired value $P = 200$ MPa is reached at $t = 1$ s and held constant thereafter. The guiding velocity starts increasing linearly after $t = 2$ s and reaches its maximum value at $t = 4$ s. It is then constant until $t = 10$ s, after which it linearly decreases until the material stops 'flowing' through the mesh at $t = 11.2$ s. Due to the time discretization, one precomputation yields 125 solution states that are used to construct the snapshot matrix and, therefore, the projection matrix. For the first investigation, only one precomputation is conducted where the material guiding velocity is chosen as $w = 25$ m/s. The influence of the number of POD modes m is then investigated by running the simulation with the same guiding velocity but an increasing number of modes.
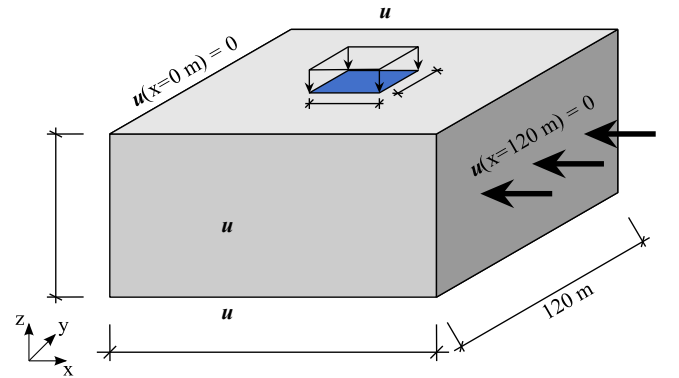

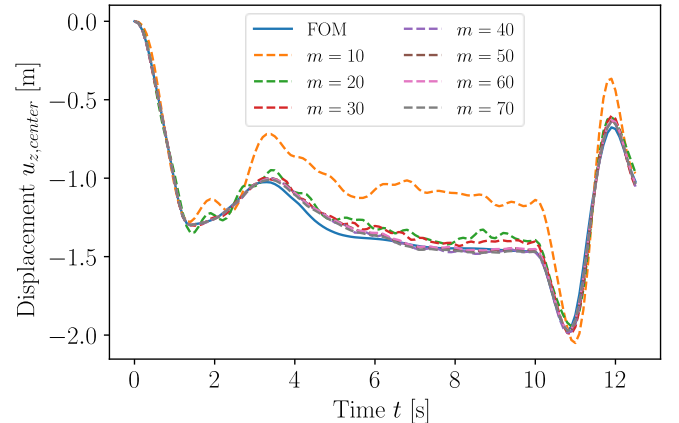Figure 2. Geometry and boundary conditions of the example.

Figure 3. Comparison of the displacement $u_{z,center}$ over time t for reduced order models with an increasing number of modes m.

In Figure 3, the results of the investigation are shown by plotting the displacement in z-direction in the center of the upper surface of the structure over the time t. It can be seen that with $m = 10$ POD modes, the displacements are very far from the reference solution of the full order model (FOM). Increasing the number of modes, the curves get closer to the reference solution. Using $m = 40$ or more modes in the ROMs, the curves show good agreement with the reference. To illustrate this relation, the average error as well as the simulation time ratio of the ROMs over the whole simulation are shown in Figure 4. The error is defined as

$$\epsilon = \frac{1}{n_t} \sum_{i=1}^{n_t} \frac{u^i_{z,center,prec} - u^i_{z,center,POD}}{u^i_{z,center,prec}} \quad (3)$$

where $u_{z,center,prec}$ and $u_{z,center,POD}$ describe the displacement in the center of the upper surface of the full order precomputation and the POD-reduced simulation, respectively. n_t describes the number of total timesteps. The simulation time ratio is calculated as

$$\tau = \frac{T_{POD}}{T_{FOM}}, \quad (3)$$

where T denotes the CPU time a FOM or a POD-reduced simulation took. It can be seen that with $m = 40$ and more POD modes the error is about 1 % and approximately 80 % of simulation time is saved.

Until now, the ROM only reconstructed the results that are contained in the snapshots. To investigate the predictive qualities of the proposed approach, the same snapshot matrix as before is used, but the guiding velocity is changed to $w = 20$ m/s and $w = 30$ m/s, respectively. Figure 5 shows the results of the reduced order simulation ($m = 60$) as well as the results of a FOM with the same guiding velocities to test the accuracy of the ROMs. It can be seen that even though the ROMs are used to predict unseen cases, the qualitative behavior of the structure is captured nicely. Especially the minima and maxima approximated by the ROMs are well aligned with the corresponding reference result. Looking at the overall agreement of the displacement field in z-direction in

Figure 5. Reduced order simulation for different guiding velocities. All ROMs are created only with the snapshots from the full order ALE simulation with guiding velocity $w = 25$ m/s and $m = 60$ POD modes are used.
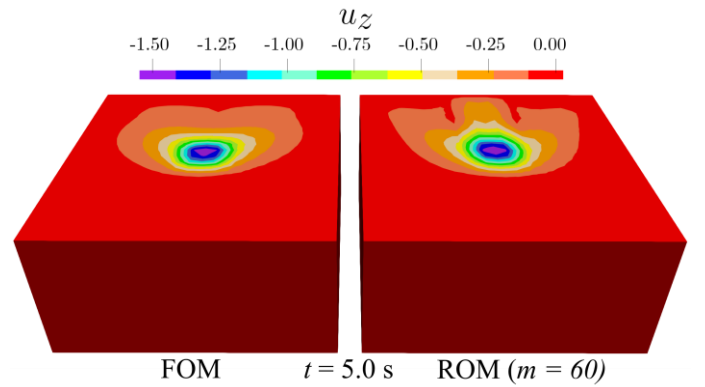
Figure 6. Comparison of the displacement field u_z of the full order model and reduced order model with a guiding velocity of $w = 20$ m/s and $m = 60$ POD modes at time $t = 5.0$ s.
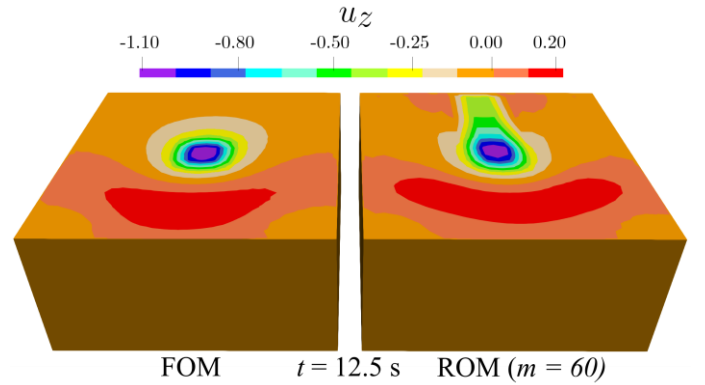
Figure 7. Comparison of the displacement field u_z of the full order model and reduced order model with a guiding velocity of $w = 20$ m/s and $m = 60$ POD modes at time $t = 12.5$ s.

Figures 6 and 7, it is seen that the displacements in the center of the structure are approximated with high accuracy, while the displacements behind the region, where the load is applied, show some inaccuracies. Lastly, it is investigated whether the accuracy of the ROM can be increased by using more snapshots. Therefore, the snapshots of the full order simulations with guiding velocities $w = 20$ m/s and $w = 30$ m/s are used to construct the snapshot matrix and a reduced order simulation with guiding velocity $w = 25$ m/s is

Figure 4. Relative error and simulation time ratio of the reduced order models.

carried out to check the accuracy. The results of this study are shown in Figure 8, and it is seen that the ROM based on the two simulations has better agreement with the reference solution than the ROM based on the single simulation that it is reconstructing. It should be noted that both ROMs used the same number of POD modes ($m = 60$).
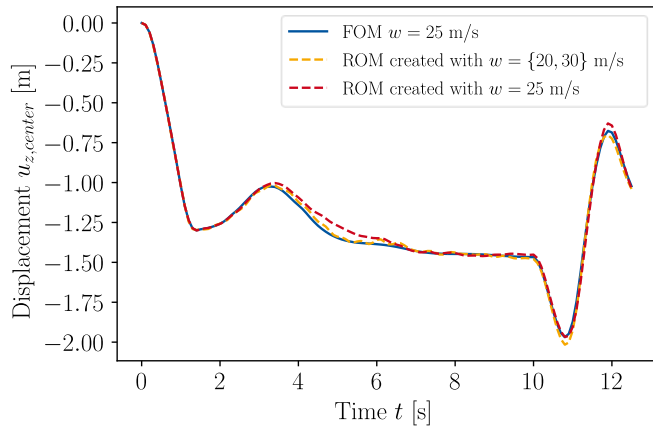
Figure 8. Comparison of two ROMs created from different snapshot matrices for a guiding velocity of $w = 25$ m/s. One ROM is created by taking the snapshots from the full order simulation with $w = 25$ m/s, whereas the other one is created by taking the snapshots from full order simulations with $w = 20$ m/s and $w = 30$ m/s.

5   CONCLUSION

In this work, an approach to accelerate simulations of road structures is presented. To this end, POD is applied to a problem which has been defined in the ALE framework. It was investigated whether this methodology can reduce the simulation time, while maintaining high accuracy. The results of a numerical example show that the structural response of the full order simulation can be approximated by the ROM with minimal error of about 1 % whilst saving about 80 % of simulation time. It is also shown that the ROM can be used to predict unseen behavior although this shows slightly higher errors. Lastly it is shown that the snapshot creation process plays an important role in creating a performant ROM. In future works it will be investigated whether the approach can be developed further to obtain higher accuracy. For example, a more sophisticated snapshot sampling approach could already improve the ROM significantly (Phalippou et al. 2020). It might also be worthwhile to use clustering approaches on a structural level to approximate the structural behavior in certain regions better (Díez et al. 2021). Another important aspect is the extension to hyper-reduction, where the number of element evaluations is reduced, saving more computation time, see e.g. (Farhat et al. 2014, Hernandez et al. 2017). Here, one major challenge will be the hyper-reduction of simulations including inelastic mate-

rials, as the inelastic evolution of the material is commonly modeled by internal history variables. When the material is 'flowing' through the mesh, so do the internal variables corresponding to an integration point. If only some elements are then evaluated, the material history is lost or incorrect when it 'flows' though an element that is not evaluated.

7   REFERENCES

Anantheswar, A., Wollny, I., & Kaliske, M. 2024. A dynamic ALE formulation for structures under moving loads. *Computational Mechanics*, 73: 139–157.

Benner, P., Gugercin, S., & Willcox, K. 2015. A survey of projection-based model reduction methods for parametric dynamical systems. *SIAM*, 57(4): 483-531.

Díez, P., Muixí, A., Zlotnik, S., & García-Gon á le , A.   . Nonlinear dimensionality reduction for parametric problems: A kernel proper orthogonal decomposition. *International Journal for Numerical Methods in Engineering*, 122: 7306-7327.

Farhat, C., Avery, P., Chapman, T., & Cortial, J. 2014. Dimensional reduction of nonlinear finite element dynamic models with finite rotations and energ -based esh sa pling and weighting for computational efficiency. *International Journal for Numerical Methods in Engineering*, 98: 625-662.

Hernandez, J. A., Caicedo, M. A., & Ferrer, A. 2017. Dimensional hyper-reduction of nonlinear finite element models via empirical cubature. *Computer Methods in Applied Mechanics and Engineering*, 313: 687-722.

Kehls, J., Kastian, S., Brepols, T., & Reese, S. 2023. Reduced order modeling of structural problems with damage and plasticity. *Proceedings in Applied Mathematics and Mechanics*, 23, e202300079.

Phalippou, P., Bouabdallah, S., Breitkopf, P., Villon, P., & Zarroug, M.   . 'On-the-fl 'snapshots selection for Proper Orthogonal Decomposition with application to nonlinear dynamics. *Computer Methods in Applied Mechanics and Engineering*, 367: 113120.

Radermacher, A., & Reese, S. 2013. Proper orthogonal decomposition-based model reduction for non-linear biomechanical analysis. *International Journal of Materials Engineering Innovation*, 4: 149-165.

Schilders, W. 2008. Introduction to Model Order Reduction. In W. H. A. Schilders, H. A. van der Vorst, & J. Rommes (Eds.), *Model Order Reduction: Theory, Research Aspects and Applications* (pp. 3–32). Springer.

Taylor, R.L. 2014. FEAP – *Finite Element Analysis Program*. University of California, Berkeley. URL: http://www.ce.berkeley/feap

Wollny, I., Hartung, F., & Kaliske, M. 2016. Numerical modeling of inelastic structures at loading of steady state rolling. *Computational Mechanics*, 57: 867–886.

Damage detection and drone inspection of roads with digital twin technology

V. Prokopets, C. Gutsche, S. Goetz, U. Assmann
Chair of Software Technology, Technische Universität Dresden, 01062 Dresden, Germany

A. Anantheswar, I. Wollny, M. Kaliske
Institute for Structural Analysis, Technische Universität Dresden, 01062 Dresden, Germany

J. Hildebrandt, W. Lehner
Database Research Group, Technische Universität Dresden, 01062 Dresden, Germany

J. Kehls, S. Reese, T. Brepols
Institute of Applied Mechanics, RWTH Aachen University, 52074 Aachen, Germany

ABSTRACT: Roads play a significant role in connecting cities to transport goods and people. Heavy usage requires constant monitoring and predictive maintenance. A digital twin is a technology aimed at representing the current state of an object and performing what-if analysis based on sensor dataflow. To reduce an error probability, gathering additional data is proficient. This paper introduces a concept for damage detection including drone inspection as a digital twin of the road system reaction. The inspection task is automatically established for the suspected damaged area.

1 INTRODUCTION

Digital twins become the main trend for modeling any physical system/process. More and more domains adhere to this concept because of its advantages. Establishing real-time sensor dataflow, coupled with corresponding digital models, i.e., *physical → digital connection*, is usually referenced in the literature as *digital shadow engineering* (Kritzinger et al. 2018). Digital shadows already improve modeling performance and efficiency, especially for predictive maintenance and optimization tasks. The next stage of modeling immersion is *digital twin engineering* – designing the impact of digital counterpart's modeling results on the corresponding physical entity, i.e., *digital → physical connection*. Usually implemented in the form of decision-making, this connection is crucial for self-adaptation algorithms, allowing even better modeling quality.

This paper aims to introduce a concept of drone inspection as a decision-making response to damage detection within a digital twin of the road system. In this domain, the digital twin is a driver for predictive maintenance algorithms and improved tire-road simulations. In the presented use case, the damage detection is conducted by comparing the results of deflection measurements on the real road (physical twin), which could be conducted e.g. via the MESAS truck of BASt, to appropriate simulation results via models within the digital twin based on the current road structure. The difference between measurement and simulation results that exceeds the defined threshold indicates a potential damage and triggers additional drone inspection as a digital twin decision-making response.

2 DIGITAL TWIN USE CASE: DAMAGE DETECTION FOR PREDICTIVE MAINTENANCE

The basis for a predictive maintenance of roads is to gather its current state regularly and to observe increasing damage. For this purpose, different strategies exist. A permanent observation requires many sensors distributed over the road and is currently not available on standard roads. A frequent observation via mobile measuring devices, e.g., MESAS, is an already existing alternative. Thereby, MESAS provides among others a deflection measurement of the road surface at defined loading conditions: tire type, tire load and velocity are known, which is important to set up corresponding simulation models. The deflection measurements (sensor data) are input to the digital twin. Within the digital twin, the expected deflection can be simulated via models depending e.g. on the road construction, the current temperature state and the loading conditions. A difference between simulation and measurement that exceeds defined bounds indicates potential damage at the corresponding position and necessitates further inspection, e.g., via drones.

2.1 *Digital twin architecture*

Digital twin engineering significantly differs for various domains. The main factors that should be considered when designing a digital twin architecture are simulation performance, scale, and accuracy (Negri et al. 2017). For the use case presented, the digital twin requires multi-scale modeling for different road parts while the whole system remains vast.
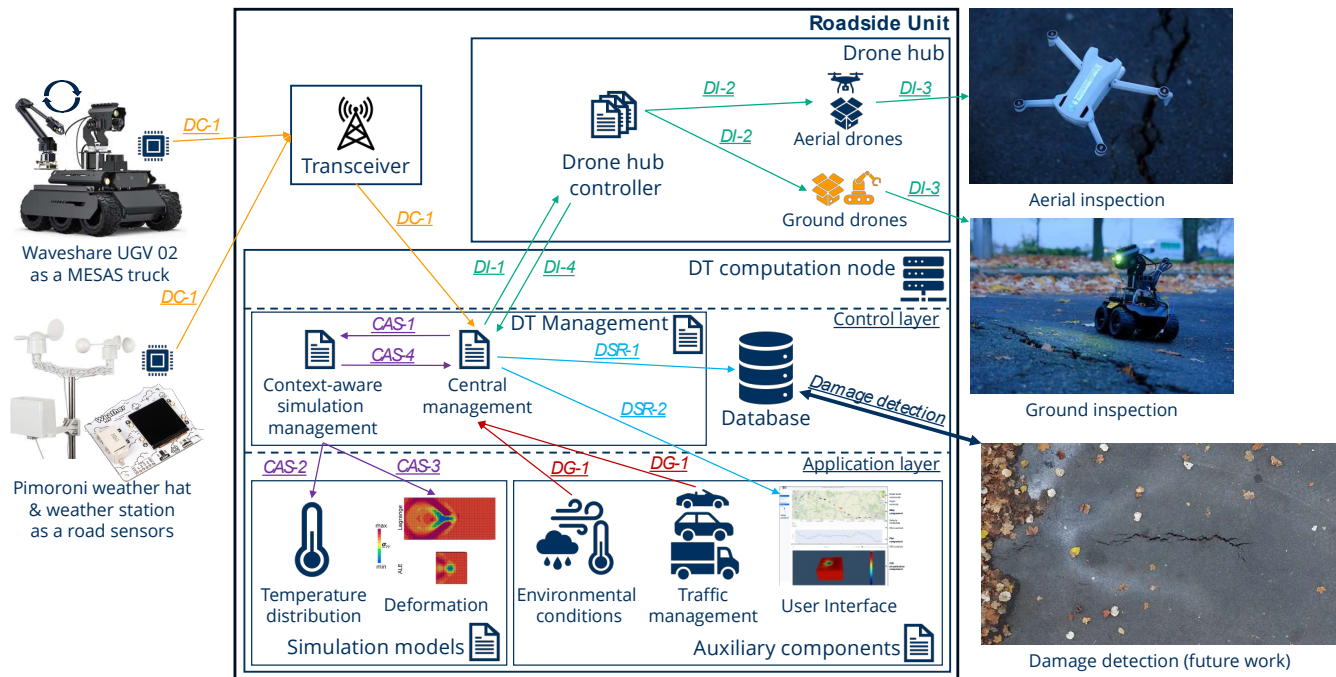
Figure 1. Concept of applying drone inspection for digital twin of the road system.

Simulation accuracy remains variable depending on demands – whether it is long-term approximate predictions or accurate road state representation. Moreover, in real-world conditions, simulations are usually not static. Taking an example of simulating vehicle-tire-pavement interaction for a moving vehicle, it is evident that, when a vehicle travels for a long distance, conditions will change many times during the trip. Weather conditions and road structures (e.g., asphalt, concrete) may change multiple times, requiring an adaptive modeling approach and appropriate digital twin architecture. Preliminary work (Prokopets et al. 2023) discussed the architecture based on a single underlying model principle. The focus of this architecture is to provide the capability to update model parameters/model itself based on specific conditions, i.e., *context-aware simulations*. This architecture is basis for the research described in this paper.

3 CONCEPT

This section provides a brief introduction to the proposed concept. Figure 1 shows hardware and software (denoted with file icon) parts and five general workflows: DC - Data Collection, DG - Data Generation, CAS - Context-aware Simulations, DSR - Data Storage and Representation, and DI - Drone Inspection. The index that follows workflow abbreviation indicates the step number in the order of execution. DC and DG workflows are commonly exclusive and dedicated to be used in different scenarios.

3.1 *Hardware part*

Drones suit inspection tasks because they can access hard-to-reach areas, reduce human risk, and improve inspection efficiency (Cabianca et al. 2022). Drones can cover most of the visual inspection tasks, including thermal inspection. Usually, a drone represents a ground/aerial platform capable of mounting additional sensors, e.g., cameras, microphones, LIDARs, RADARs, thermal cameras, radio transceivers, etc. This allows to use the drone as a universal tool for point, area, and route inspections. Copters are well suited for inspection tasks because they do not need a prepared runway and can hover over the point to make steady shots.

Drone hangars such as DJI Dock and Matternet provide a weatherproof shelter for quadcopters with wireless charging capability. Integrating these hangars allows the achievement of autonomous drone fleet management capabilities with higher efficiency in terms of lower downtime between operations and flexible scalability options. For the digital twin of the road system, utilizing drone hangars as a part of a roadside unit (RU) is considered – an intelligent transportation system component that connects vehicles and road infrastructure objects. Every RU can have various drone hangars depending on demands, forming a hub for serving assigned areas.

3.2 *Software part*

3.2.1 *General architecture*
Previously designed software architecture (Prokopets et al. 2023) is used for the current research. High-level components of this architecture form a two-layer structure with control and application layers. The control layer consists of a message broker (bus) that handles data streams between physical and digital counterparts, a twinning management component for data collection and prediction, and a context-aware simulation manager for performing variability management during simulation. The application layer is

presented with various simulation models that are called depending on the respective request.

3.2.2 Auxiliary components

To achieve better simulation results and perform a what-if analysis, auxiliary models are required. For example, a weather forecast cannot be represented using sensor data only – an appropriate weather model is required. Moreover, usage of traffic management and geography models is crucial for the accuracy of the simulations in the digital twin of road systems. Therefore, the application layer is extended with these models.

The user interface is implemented as a dashboard for real-time state representation of the digital twin. The [Dash Plotly](#) Python library is used because of its easy integration capabilities and wide range of accompanying modules for plotting and working with map and visualization toolkit (VTK) objects. Communication with digital twin components is done via callbacks – dedicated functions triggered at specific conditions, such as user actions, inner state, or time.

Adhering to drone inspection, an appropriate drone behavior model that represents its dynamic properties (such as velocity, acceleration, and power consumption) is required. Path planning, including inspection type (point, area, route), is risky without considering this model. The model should be individually configured for every vehicle. Moreover, self-adaptability is vital to achieving better mission range and duration.

3.3 Workflows

3.3.1 Physical – digital connection

To keep the digital twin updated over the lifetime of the road, data from the real road (e.g., sensor data) are required frequently. Thereby the frequency and the kind of the required data depends strongly on the intended use case and application of the digital twin. For the damage detection proposed here, data on the thermal conditions (e.g., data from weather stations and temperature sensors) and data of the deflection measurement including the measured displacement as well as the loading conditions (tire type, load, driving velocity) is required along the inspected road section (*DC-1*). For predictive maintenance simulations, step *DC-1* will be replaced with *DG-1*. All collected/generated data can be stored (*DSR-1*) and represented via the user interface (*DSR-2*). Thereby, digital twin software and backends do not need to be built from scratch for each application. The FIWARE platform e.g., offers a curated collection of open-source software components that can be integrated with third-party tools to accelerate the development of smart solutions across domains. It enables the modeling and deployment of digital twins, such as a digital twin of a road, incorporating structural data, various sensors and computational models (Hildebrandt et al. 2024).

3.3.2 Context-aware simulations within the digital twin of the road system

To simulate the deflection of the road realistically, finite element simulations of the layered pavement structure can be conducted. Required inputs are geometric data of the investigated road (layers, materials) e.g., from geometric-semantic models or a database within the digital twin (*CAS-1*). To consider the temperature dependent behavior of pavements, a thermal simulation is conducted first that considers the measured weather conditions and temperatures to get the current temperature field inside the pavement structure. Thereby, due to changing conditions along the road (sunny/shaded areas, local rain, different road constructions), the temperature field changes along the road; thus, for each section, a separate thermal model is required (*CAS-2*). Then, the mechanical finite element models are called for each section that simulate the displacement field of the road subjected to the rolling tire considering the temperature dependent material properties e.g., of asphalt. Depending on the driving condition (steady state or dynamic rolling) different simulation models are available (Wollny et al. 2016, Anantheswar et al. 2024) and called (*CAS-3*). To save computational time, model order reduction (MOR) can be applied to speed up the simulations (Zhang et al. 2024). The simulated deflection is compared to the measured deflection (*CAS-4*). A significant deviation between both values indicates a potential damage (e.g., crack propagation).

3.3.3 Digital – physical connection

Decision-making is used as a response action to simulation results. Based on the results of *CAS-4*, drone inspection should be performed for a position if the difference is too high. Thus, an optimal path from the closest RU to the warning location should be built, followed by an inspection type definition. The result is a waypoint mission – a set of points in format *latitude*, *longitude*, and *altitude*, together with *camera gimbal angles* for inspection points. Any triggering event, like a deflection measurement warning, road user complaints, etc., triggers the creation of a warning object, displayed as an exclamation mark sign on the dashboard's map. This object contains meta information such as location and a short description. The closest RU adds this warning to its pool (*DI-1*). The drone hub management generates the inspection task in the form of a waypoint mission described above (*DI-2*). As a result, an image dataset for defined areas is collected along with drone telemetry (*DI-3*). The latter is helpful for self-adaptation to improve the mission planning in the future. The collected data is assigned to the warning objects and can be displayed in the dashboard (*DSR-2*). A damage detection algorithm is planned to be used to identify damaged parts.

4 PROOF OF CONCEPT

4.1 *Synthetic benchmark*

As a first step towards concept evaluation, a synthetic benchmark representing the highway system between Dresden and Leipzig is created. A road user may appear at an arbitrary connection point with other roads and then lead towards another connection point. A simulation of road structure temperature distribution and deformation under load is handled individually for every vehicle. Simulation results can be accessed via the dashboard. A measuring laboratory is a vehicle capable of measuring deflection. At the current state, the measuring results are artificially generated. Roadside units are placed along the highway approximately every 10th kilometer. The supplementary video describes the main components of a user interface and an exemplary use case scenario simulation (https://tud.link/eyua5p). Traffic management, roadside unit, and environmental condition modules can be configured using JSON files, making testing different simulation scenarios possible.

4.2 *Small-scale experiment setup*

In addition to the synthetic benchmark, small-scale experiments using DJI Mini 3 drone and Raspberry Pi-driven Waveshare rovers are currently being prepared. Another Raspberry Pi with connected weather sensors will play the role of the roadside sensor by gathering sensor data and sending it to the roadside unit node. The main-node PC will represent the DT computation node and execute simulation models, generate inspection tasks for assigned drones, store data, and display it using the interactive dashboard.

4.3 *Limitations*

The proposed concept of drone inspection has several limitations that need to be discussed in this paper. One limitation is operational safety. Flying routes should be planned to avoid legal regulation violations, driver distraction, and collisions with road objects. Another limitation comes from the type and size of drones used for inspection. Usually, inspection drones are small for safety reasons and because of the requirements to have the ability to fly in narrow spaces. All this leads to operating range limitations and vulnerability to bad weather conditions. Thus, inspection tasks for large areas require a risk assessment for every operation and a dense RU network or mobile drone hubs as an infrastructure.

5 CONCLUSION

The concept of autonomous drone inspection as a digital twin response to simulation results is promising.

A vast network of RUs equipped with drone hubs allows for gathering road state information much faster and cheaper than traditional inspections. Existing drone image processing software, such as WebODM, enables the generation of maps, point clouds, digital elevation models, and 3D models from aerial images. Representation of this data using an interactive dashboard allows road maintainers to better visualize the current road state and plan predictive maintenance.

Future research should address the current limitations, i.e., scalability, safety, and cost-efficiency. Swarming drones increase the flexibility of their usage, which helps to reach these targets. Defining adaptive image processing for perspective (from ground drones) and orthogonal (from aerial drones) images is another topic for future work.

REFERENCES

Anantheswar, A., Wollny, I., & Kaliske, M. 2024. Treatment of Inelastic Material Models Within a Dynamic ALE Formulation for Structures Subjected to Moving Loads. *International Journal for Numerical Methods in Engineering*, e7599.

Cabianca, M., Clemente, M., Gatto, G., Impagliazzo, C., Leoni, L., Masia, M., & Piras, R. 2022. An Application of IoT in a Drone Inspection Service for Environmental Control. *IoT*, 3: 366-380.

Hildebrandt, J., Leibl, L.M., Habich, D., & Lehner, W. 2024. Development and Evaluation of a FIWARE-based Digital Twin Prototype for Road Systems. *DiDiT 2024*: https://ceur-ws.org/Vol-3755/paper3.pdf.

Kritzinger, W., Karner, M., Traar, G., Henjes, J., & Sihn, W. 2018. Digital Twin in manufacturing: A categorical literature review and classification. *IFAC-PapersOnLine*, 51:1016–1022.

Negri, E., Fumagalli, L., & Macchi, M. 2017. A Review of the Roles of Digital Twin in CPS-based Production Systems, *Procedia Manufacturing*, 11:939–948.

Prokopets, V., Götz, S., Assmann, U., Gutsche, C., Anantheswar, A., Wollny, I., & Thiessat, K., & Hildebrandt, J., Kaliske, M., & Lehner, W. 2023. Work in Progress: Towards a Single Underlying Model for the Digital Twin of Future Road Infrastructures. *2023 IEEE Smart World Congress (SWC), Portsmouth, United Kingdom, 28-31 August 2023*, 286-290.

Wollny, I., Hartung, F., & Kaliske, M. 2016. Numerical modeling of inelastic structures at loading of steady state rolling. *Computational Mechanics*, 57:867–886.

Zhang, Q., Ritzert, S., Zhang, J., Kehls, J., Reese, S., & Brepols, T. 2025. A multi-field decomposed model order reduction approach for thermo-mechanically coupled gradient-extended damage simulations. *Computer Methods in Applied Mechanics and Engineering*, 434:117535.

Leveraging Digital Twin for Data-Driven Pavement Maintenance

M. A. Talaghat
Civil and Environmental Engineering Department, Amirkabir University of Technology, Iran

M. Sedighian-Fard
Civil and Environmental Engineering Department, Amirkabir University of Technology, Iran

A. Golroo
Civil and Environmental Engineering Department, Amirkabir University of Technology, Iran
Faculty of Information Technology and Electrical Engineering, University of Oulu, Finland

M. Rasti
Faculty of Information Technology and Electrical Engineering, University of Oulu, Finland

ABSTRACT: Integrating Digital Twin (DT) technology with data from automated pavement data collection resources, offers a revolutionary approach to proactive pavement maintenance planning. This article proposes a comprehensive framework that utilizes diverse data sources, including AVs, sensors, automated data collection vehicles, and maintenance vehicles, to provide precise, real-time pavement condition data for better-informed maintenance decisions. Building Information Modeling (BIM) is used to create a digital representation of the pavement, facilitating visualization and simulation, leading to cognitive DT. Advanced AI analytics are utilized to detect pavement distress, optimize maintenance planning, and predict deterioration.

1 INTRODUCTION

1.1 Road DT Advancements

Digital Twin (DT) technology creates dynamic digital replicas of physical systems, evolving to include IoT and machine learning (Tao et al., 2019). DTs are crucial in manufacturing and Industry 4.0, linking design and execution (Uhlemann et al., 2017), and in construction, often paired with Building Information Modeling (BIM) (Aengenvoort & Krämer, 2018; Borrmann et al., 2018; Arup, 2019).

DTs can significantly advance road infrastructure management by enhancing efficiency and effectiveness. Key benefits include:

- Real-Time Monitoring: Using IoT for continuous asset monitoring (Tang et al., 2023).
- Condition Assessment: AI-driven analysis for accurate evaluations (Wang et al., 2023).
- Advanced Modeling: BIM integration for detailed virtual models (D'Amico et al., 2022).
- Proactive Maintenance: Predictive analytics to anticipate issues (Callcut et al., 2021).
- Simulation and Scenario Analysis: Virtual testing environments (Martínez et al., 2022).
- Decision Support: Data-driven insights for strategic planning (Consilvio et al., 2023).

DTs offer transformative opportunities in road maintenance, reducing costs and improving conditions (Vieira et al., 2022; Talaghat et al., 2024).

1.2 New methods of data collection in DT

Data collection methods for pavement condition include sensors like radars, laser scanners, cameras, and UAVs (Coenen & Golroo, 2017). Smartphones are useful for crowdsourced data collection (Staniek, 2021). Techniques include image-based methods, point cloud imaging, and vibration-based methods (Sholevar et al., 2022). Automated data collection vehicles, such as Road Surface Profilers (RSP), use lasers and cameras to estimate the International Roughness Index (IRI) (Fahmani et al., 2024).

Autonomous Vehicles (AVs) offer a cost-effective approach to data collection, reducing operational costs and providing comprehensive coverage. AVs monitor pavement conditions in real-time, aiding in Maintenance and Rehabilitation (M&R) decisions. Equipped with sensors, AVs collect extensive real-time data, enhancing traffic flow, optimizing routing, and improving safety. AVs can also collect data from other infrastructures, helping prioritize M&R activities (Vieira et al., 2022; Martínez et al., 2022).

Challenges include user data privacy, real-time data transmission, and automotive industry regulations. Despite these, AVs can revolutionize transportation infrastructure management (Vieira et al., 2022; Martínez et al., 2022).

1.3 AI in Road DT maintenance planning

Despite advancements in road pavement DT teSchnology, there's a need to improve AI utilization

for better decision-making. DT maturity levels include digital model, digital shadow, and digital twin, with the next level being cognitive DT, which integrates AI. AI applications in road pavement management include:

- Pavement Distress Detection: AI algorithms detect and classify defects, improving inspection efficiency (Sierra et al., 2022).
- Pavement Performance Development: AI develops predictive models for pavement deterioration (Yu et al., 2020).
- Pavement Maintenance Planning: AI prioritizes maintenance tasks, optimizing routines and reducing costs (Consilvio et al., 2023).

Integrating AI into DT frameworks can revolutionize pavement management, creating more sustainable and resilient networks. This paper presents a framework for cognitive DT, focusing on AI-based data-driven maintenance planning, optimal data acquisition, and enhancing conventional DTs with AI.

To summarize, integrating AI into road pavement Digital Twin (DT) maintenance planning can revolutionize pavement management, creating more sustainable and resilient transportation networks. This paper presents a framework for cognitive DT, focusing on AI-based data-driven maintenance planning and optimal data acquisition systems. The main objectives are:

- Provide a conceptual design of cognitive road DT for maintenance planning.
- Explore AI applications in optimal road maintenance planning.
- Scrutinize automated data collection tools for pavement condition data.
- Enhance conventional DTs with AI for improved maintenance planning.

2 ROAD DT CONCEPTS AND FRAMEWORK

2.1 *Conceptual design of road pavement DT*

Figure 1 illustrates the conceptual design of the cognitive DT for road pavement. This system integrates sensors, vehicles, and cloud-based analytics to create a comprehensive digital representation of road pavements.
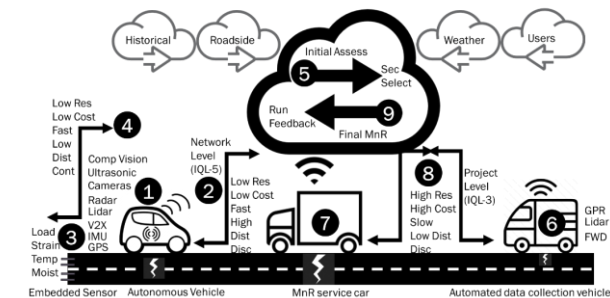

Figure 1. Concept of road pavement DT

Autonomous Vehicles (AVs) equipped with sensors like LiDAR, cameras, radar, GPS, and V2X communication gather real-time pavement conditions, traffic flow, and environmental factors. Embedded sensors within the pavement structure at critical points provide continuous, localized data on structural integrity and environmental influences.

Automated data collection vehicles using Ground Penetrating Radar (GPR), Falling Weight Deflectometer (FWD), and laser scanners offer high-resolution insights into pavement thickness and subsurface conditions. Maintenance and Repair (M&R) service vehicles ensure consistent monitoring and assessment during and after maintenance actions. This integrated approach ensures a detailed and dynamic understanding of road pavement conditions.

2.2 *Framework of cognitive DT for road pavement*

Figure 2 illustrates the cognitive DT framework for road pavement, consisting of four layers:
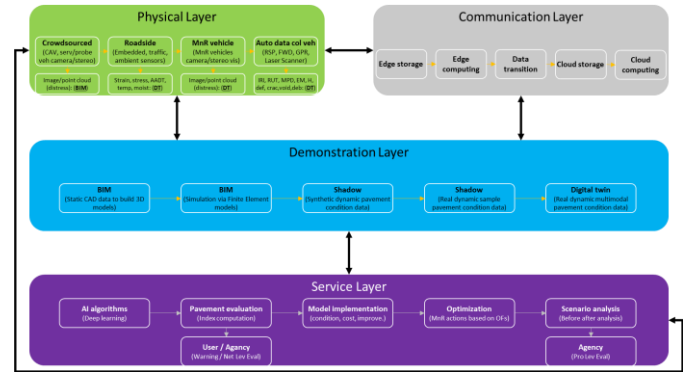
Figure 2. Framework of road pavement DT

1- Physical Layer: Continuously monitors pavement conditions using various instruments. Crowdsourced inputs from AVs, connected AVs, probe vehicles, and service cars collect pavement images or point clouds for distress detection and feed into BIM. Roadside sensors gather data on stress, strain, traffic volumes, temperature, and moisture. M&R vehicles acquire pavement images or point clouds for distress detection. Automated data collection vehicles equipped with RSP, FWD, GPR, and laser scanners collect data on IRI, rut depth, surface texture, and subsurface characteristics.

2- Communication Layer: Supports data transmission and storage, including edge storage and computing for rapid data processing, seamless data transition protocols for efficient transfer, and scalable cloud storage and computing for advanced analytics and long-term data management.

3- Demonstration Layer: Creates digital representations for visualization and simulation. BIM and digital models depict road geometry and material properties. Digital shadows mirror real-time pavement conditions using synthetic and sampled real dynamic data streams. Digital twins combine real-

time data with predictive modeling to simulate future scenarios and assess potential outcomes.

4- Service Layer: Provides services to road users and agencies, leveraging collected data and digital representations to optimize road pavement management strategies. It includes AI algorithms for data analysis and prediction, pavement evaluations to assess current conditions and prioritize maintenance efforts, DT models to guide decision-making processes, optimized M&R practices through simulation and scenario analysis, and proactive maintenance planning for real-time feedback and enhanced road safety.

By integrating these layers, the cognitive DT framework offers a comprehensive approach to road infrastructure management, enabling informed decision-making, proactive maintenance strategies, and optimized resource allocation to improve road performance and safety.

3 CASE STUDY

The case study focuses on a 3-kilometer section of the Räyskälän kantatie motorway (KT54/3/300-KT54/3/3300) in Loppi, Finland, as shown in Figure 3. This road connects Hollola, Riihimäki, and Tammela, serving as an alternative route from Lahti to Turku. The selected section includes bridges and tunnels, with an average daily traffic of 15,000 vehicles, including many heavy goods vehicles. The region experiences cold winters and mild summers, making it an ideal testbed for the DT framework.
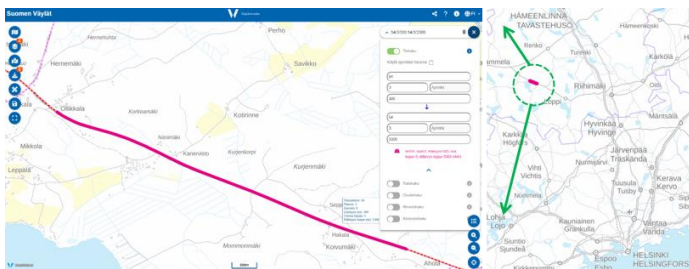

Figure 3. Selected section of Räyskälän motorway.

Data collection involves multiple methods. Crowdsourced georeferenced data from AVs and probe vehicles monitor road surface conditions, traffic flow, and identify potential congestion points. Roadside and embedded sensors measure temperature, moisture, strain, and load, providing continuous data on pavement integrity. Automated data collection vehicles, such as Road Surface Profilers, use technologies like GPR and FWD to assess pavement thickness and subsurface conditions. M&R vehicles, equipped with advanced sensors, collect high-resolution images, LiDAR data, and pavement profiles before and after maintenance actions. This comprehensive approach ensures detailed monitoring and assessment of road pavement conditions, en-abling informed decision-making and optimized maintenance strategies.

To create a digital representation of the section, Autodesk InfraWorks software integrates various data sources, including crowdsourced data, sensor data, and imagery. This generates a detailed BIM model of the 3-kilometer motorway section, incorporating geometric details, material properties, and environmental factors. The BIM model serves as a DT of the physical motorway, providing a dynamic and constantly updated virtual counterpart. It enables engineers and maintenance teams to visualize the motorway's current state, simulate maintenance scenarios, and assess potential impacts on traffic flow and pavement performance.

The dataset, comprising sensor and vehicle data along with BIM model information, is analyzed using advanced AI algorithms. These algorithms detect and classify pavement distress types, such as cracks and potholes, improving inspection efficiency and accuracy. Predictive analytics forecast pavement deterioration and optimize maintenance planning by analyzing historical and current data, along with environmental parameters. This proactive approach allows maintenance teams to schedule interventions before defects become critical, reducing reactive repairs and extending pavement lifespan. AI-driven analyses also prioritize maintenance tasks based on defect severity and impact, ensuring safety and smooth traffic flow.

Figure 4 presents a detailed visualization of the DT model for the selected section. This model provides a comprehensive overview of pavement conditions using the PCI and the IRI. The PCI, ranging from 100 (Excellent) to 0 (Failed), indicates the severity and density of pavement distress, while the IRI measures ride quality. Each pavement section is color-coded from green (Excellent) to red (Poor) for easy interpretation, allowing quick assessment of the overall condition. Warmer colors like yellow and orange highlight sections needing attention, with red indicating critical areas requiring immediate maintenance.
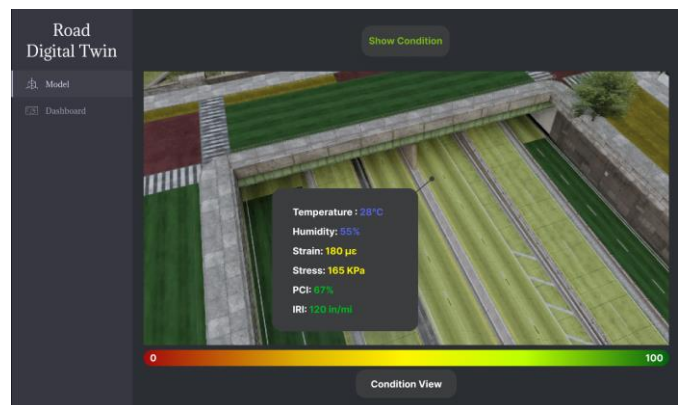

Figure 4. DT of the selected section.

The DT model also incorporates real-time data on temperature, humidity, strain, and stress, superim-

posed on the pavement model. Blue represents temperature and humidity data, which influence pavement performance and maintenance strategies. Yellow indicates strain and stress data from embedded sensors, showing structural integrity. Higher strain and stress values may signal potential weaknesses.

Users can interactively explore the pavement condition and associated parameters, with each section linked to detailed information, including historical data, maintenance records, and predicted deterioration rates. This interactive functionality aids informed decision-making, allowing maintenance teams to prioritize interventions and optimize repair strategies. By integrating real-time data and advanced analytics, the DT model enhances continuous monitoring, predictive maintenance, and overall pavement management, improving road safety and performance.

The DT framework enhances pavement maintenance by combining real-time data collection, BIM modeling, and AI-driven analyses. This approach improves maintenance efficiency, reduces reactive repairs, and extends pavement lifespan through predictive analytics. DT simulations optimize maintenance strategies and minimize traffic disruptions, while scenario analyses aid decision-making and improve road safety. The platform also facilitates stakeholder collaboration, enhancing overall management efficiency.

This case study offers several novel contributions to pavement maintenance and DT technology:

- Enhanced Data Collection: Diverse sources improve accuracy and reduce costs.
- Advanced Digital Representation: BIM models aid proactive planning.
- AI-Driven Analysis: Improves distress detection and maintenance planning.
- Predictive Maintenance: Optimizes scheduling and resource allocation.
- Improved Collaboration: Centralizes information for better planning.
- Extended Lifespan and Reduced Costs: Proactive maintenance promotes sustainability.

These contributions highlight the DT framework's potential to revolutionize pavement maintenance, improving efficiency, safety, and sustainability.

4   CHALLENGES AND FUTURE DIRECTIONS

Developing a cognitive road digital twin involves key challenges, including ensuring accurate and up-to-date data, integrating diverse sources like LiDAR and cameras, enabling real-time updates, safeguarding data privacy, and ensuring scalability to handle large datasets efficiently.

Future applications include proactive maintenance for early issue detection, real-time traffic management to enhance safety, environmental impact assessments for sustainable planning, performance modeling to prioritize resources, and resilience planning to mitigate the effects of extreme events.

5   CONCLUSIONS

This paper presents a cognitive road DT framework for pavement maintenance, integrating data from various sources to create a digital representation of road pavement. Advanced AI analytics detect distress, optimize planning, and predict future conditions. A Finnish motorway case study demonstrates its potential.

Automated data collection tools provide real-time, comprehensive data for informed decisions. BIM models facilitate visualization and analysis. AI-powered analytics improve distress detection and predictive maintenance, extending pavement lifespan.

The Finnish case study shows the DT's ability to enhance maintenance efficiency, reduce costs, and improve road safety. The framework promises to transform pavement maintenance through data-driven decisions and optimized activities. Continuous research and innovation are encouraged to enhance road infrastructure sustainability and resilience.

6   ACKNOWLEDGEMENTS

7   REFERENCES

Aengenvoort, K., & Krämer, M. (2018). BIM in the operation of buildings. *Building Information Modeling: Technology Foundations and Industry Practice*, 477–491.

Arup. (2019). Digital twin: Towards a meaningful framework. *Technical Report, Arup, London, England*.

Borrmann, A., König, M., Koch, C., & Beetz, J. (2018). *Building information modeling: Why? what? how?* Springer.

Callcut, M., Cerceau Agliozzo, J.-P., Varga, L., & McMillan, L. (2021). Digital twins in civil infrastructure systems. *Sustainability*, *13*(20), 11549.

Coenen, T. B. J., & Golroo, A. (2017). A review on automated pavement distress detection methods. *Cogent Engineering*, *4*(1), 1–23.

Consilvio, A., Hernández, J. S., Chen, W., Brilakis, I., Bartoccini, L., Di Gennaro, F., & van Welie, M. (2023). Towards a digital twin-based intelligent decision support for road maintenance. *Transportation Research Procedia*, *69*, 791–798.

D'Amico, F., Bianchini Ciampoli, L., Di Benedetto, A., Bertolini, L., & Napolitano, A. (2022). Integrating Non-Destructive Surveys into a Preliminary BIM-Oriented

Electrical and piezoresistive performance of graphene-modified Polymethyl Methacrylate

T. Wang, J. Berger, P. Liu
Institute of Highway Engineering (ISAC), RWTH Aachen University, Aachen, Germany

M. Oeser
Federal Highway Research Institute (BASt), Bergisch Gladbach, Germany

ABSTRACT: The electrical and piezoresistive properties of graphene-modified Polymethyl Methacrylate (GmP) are investigated in this study. Results indicate that graphene content should be maintained between 1.0 wt% and 3.0 wt% to achieve a more stable resistance output while preserving a relatively low viscosity of the pre-hardening mixture. A constant input current is maintained to ensure compliance with Ohm's law regarding output resistance. As the graphene content increases, GmP exhibits a transition from a positive to a negative piezoresistive effect, showing more pronounced periodicity of the $\Delta R/R_0$ curve and enhanced stability during the unloading and rest periods. Furthermore, GmP shows increased piezoresistive sensitivity at higher load magnitudes.

1 INTRODUCTION

As road transport evolves towards greater intelligence and informatization, the concept of digitalization of road systems has emerged. It relies on the real-time perception and evaluation of vehicles, tires, pavements, and associated infrastructures. Piezoresistive materials composed of pavement materials as the matrix, emerged as the optimal choice for embedded sensors or as the sensing surface layer itself (Wang et al., 2023). These materials exhibit a relative change in electrical resistance under load, thereby enabling the detection of traffic information.

Polymethyl methacrylate (PMMA) is a synthetic polymer derived from the methyl methacrylate (MMA) monomer. It has gained considerable interest due to its unique properties including excellent mechanical properties and ease of processing. Previous research indicates that PMMA has been utilized in pavement engineering as an anti-skidding and noise-reduction surface layer (SCHACHT, 2014).

The use of PMMA as a material for the structural layers of roads has prompted the exploration of its potential modification with conductive fillers such as graphene to develop sensing surface layers. Overall, there is a need for further investigations on the piezoresistive properties of graphene-modified Polymethyl Methacrylate (GmP) under the loading conditions experienced by road pavements. For instance, there is a lack of studies addressing the piezoresistive responses of GmP under dynamic vehicle loads.

In this study, GmP specimens with different graphene content were prepared to analyze their electri-cal performance. Subsequently, dynamic creep tests were conducted to evaluate their piezoresistive responses under equivalent vehicle loads. This study aims to contribute to the advancement of road sensing technology and the development of the digital twin of road systems.

2 MATERIALS AND METHODS

2.1 *Materials*

The three main components of GmP are MMA monomers, mineral fillers, and graphene.

The chemical constituents of the monomers include Methyl methacrylate (MMA) and 2-ethylhexyl acrylate, which are liquid resins at room temperature. Monomers can be in-situ polymerized to solid PMMA when combined with an initiator and molded into specimens. The initiator is composed of a combination of dibenzoyl peroxide and phthalate, to initiate the radical polymerization that hardens the MMA resin.

Quartz mineral filler is added into the PMMA matrix to decrease the quantity of PMMA while enhancing the strength of the composite material. The density of the aggregate at 20°C is 2.65 g/cm^3, with a maximum particle size of 2 mm. To eliminate the size effect, the gradation of mineral fillers was maintained constant throughout the subsequent tests.

Graphene nanoplatelets composed of a few graphene layers were selected as the conductive additive and are referred to as graphene in this study. The thickness of the graphene ranges from 11 to 15

nm, with an average particle diameter of 15 μm. The specific surface area is between 50 and 80 m²/g. Moreover, the electrical conductivity is 10^7 S/m parallel to the graphene layers and 10^2 S/m perpendicu-

lar to them.
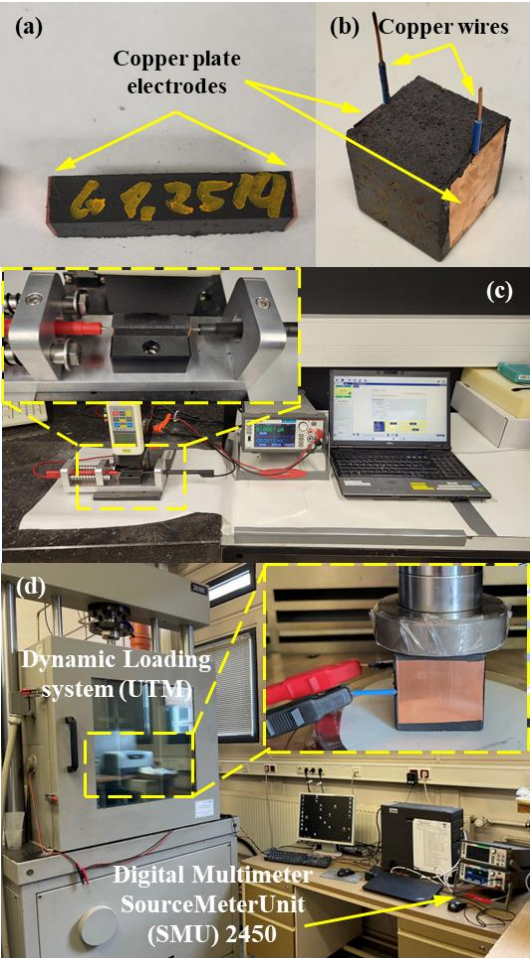
Figure 1. Preparation and tests for GmP: (a) Stick and cubic GmP specimen with copper plate electrodes; (a) Electrical resistance test; (c) Piezoresistive tests by conducting dynamic creep loading.

2.2 Methods

2.2.1 Specimen preparation

GmP specimens were prepared by dispersing graphene along with mineral fillers and initiator, in MMA liquid through mechanical stirring.

Mechanical stirring was conducted using a paddle mixer at 1000 rpm for 3 min to disperse various amounts of graphene in the MMA monomer. Then, mineral filler, accounting for three times the mass of the MMA, was added to the mixture, followed by additional 3-min mixing of mechanical stirring. Finally, the initiator (1.6 wt% of MMA) was added into the mixture and dispersed for 2 min. All dispersion processes were conducted at room temperature.

After mixing, the composite was poured into a stick mold with dimensions of $50\times10\times10$ mm^3 or a cubic mold with dimensions of $50\times50\times50$ mm^3. Before casting the specimen, two copper plates were positioned in the two sides of the mold to serve as

electrodes. The mixture was in-situ polymerized for 24 h and then de-molded for further electrical and piezoresistive tests, as shown in Figure 1(a) and (b).

2.2.2 Electrical and piezoresistive test

The Keithley multimeter (Source Meter Unit 2450) was utilized to measure the electrical resistance of GmP, as shown in Figure 1(c). Before the electrical resistance test, a current and voltage sweep was conducted on GmP stick specimens with varying graphene contents. The current input was applied logarithmically over 100 measurement points, ranging from 1×10^{-12} A to 0.1 A. Similarly, the voltage ranged from 1×10^{-6} V to 42 V. After determining the input values, four replicates were tested at room temperature to obtain the electrical resistance of all GmP composites with a constant current of 10^{-5} maintained throughout all tests.

A 5-cycle dynamic creep test was conducted to evaluate the piezoresistive properties of GmP (Wang et al., 2024). Each cycle consists of a 2-second haversine loading period and a 10-second rest period. To simulate the compressive load exerted by cars and trucks on pavements, equivalent pressure amplitudes of 0.163 MPa and 0.416 MPa were applied to cubic specimens. Four replicates were tested to calculate the change in resistance during the dynamic loading. As shown in Figure 1(d), the cubic specimen was positioned with the copper plate electrodes being oriented perpendicular to the loading plate. Insulating tape was used to separate the specimen from the loading plates, thereby ensuring the accuracy of the electrical signal. The data collection frequency was set at 20Hz.

3 RESULTS AND DISCUSSION

3.1 Input range of voltage and current

The resistivity of GmP in this study is calculated according to Ohm's law. Consequently, it is essential to determine an appropriate input range for current or voltage to ensure that the resistivity output remains independent of them. After the sweep tests, the upper and lower limits of the voltage and current inputs were determined and presented in Table 1.

Table 1. Limits of electrical voltage and electrical current in electrical resistance test.

Graphene content	Voltage (V)		Current (A)	
wt%	Lower/ Upper limit			
1.0	0.5	5.0	10^{-7}	10^{-6}
1.25	0.05	5.0	10^{-7}	10^{-5}
1.5	0.001	10.0	10^{-7}	10^{-4}
1.75	0.001	10.0	10^{-6}	10^{-4}
2.0	0.001	10.0	10^{-6}	10^{-3}
3.0	0.001	10.0	10^{-6}	10^{-2}
4.0	0.001	10.0	10^{-6}	10^{-2}

For example, the resistivity of GmP-2wt% decreases only by 0.7% when the current increases from 10^{-6} A to 10^{-3} A, and by 0.16% when the voltage increases from 0.001 V to 10 V. To ensure the output accuracy of all GmP with varying graphene content, a fixed input current was employed in subsequent measurements.

3.2 *Electrical resistance of GmP*

Figure 2 illustrates that the resistivity of GmP continuously decreases with increasing graphene content. However, when the graphene content increases from 0.5 wt% to 0.75 wt%, it decreases only by 15% (2.84×10^8 $\Omega\cdot$m to 2.43×10^8 $\Omega\cdot$m). |Both values remain above the threshold of 10^8 $\Omega\cdot$m, beyond which GmP can be classified as an insulator. Further resistance tests on these two GmP reveal that the resistivity at 0.75 wt% is occasionally equal to or even higher than that at 0.5 wt%. This suggests that the resistivity of GmP is not significantly affected until the percolation threshold of the graphene is reached. Subsequently, the resistivity of GmP drops sharply to 24,500 $\Omega\cdot$m when the graphene content increases to 1.0 wt%, which is 1,000 times lower than that at 0.75 wt%. As the graphene content continues to rise, the resistivity further decreases although at a slower rate. When the graphene content exceeds 3.0 wt%, the reduction in resistivity becomes even slower.
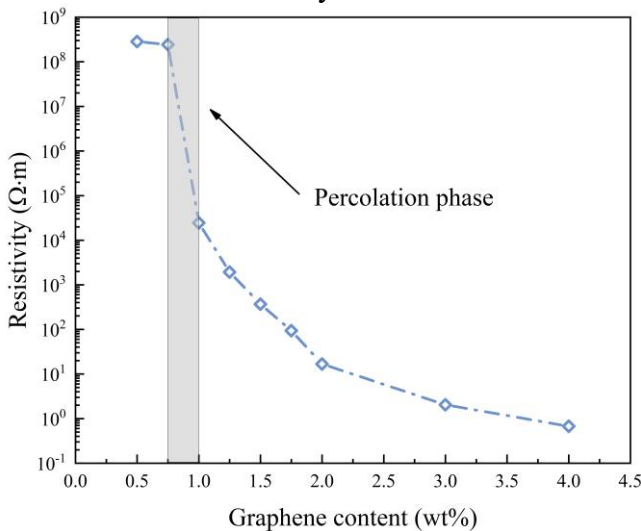

Figure 2. Percolation curve of GmP with different graphene content.

The different stages of percolation are clearly illustrated in Figure 2. GmP with graphene content below 0.75 wt% falls into the insulating phase, where individual graphene particles are dispersed in the PMMA matrix with relatively large gaps and an absence of significant conductive pathways in the composites. The sharp drop in resistivity observed between 0.75 wt% and 1.0 wt% indicates that the percolation threshold falls into this range, marking transition of GmP into the percolation phase. During this stage, the distance between graphene particles permits quantum tunneling, leading to the formation of more conductive pathways and accounts for the

sudden increase in conductivity. To obtain detectable and relatively stable resistivity values, the graphene content should not be less than 1.0 wt%.

Figure 3 shows the morphology of the pre-hardening mixture containing graphene between 1.0 wt.% and 4.0 wt.%. The mixture with 1.0 wt.% graphene exhibits relatively low viscosity, enabling the composite to flow into the mold without additional compaction. As the graphene content increases, the viscosity rises significantly, which reduces the flowability of the pre-hardening composite. The mixture with 4.0 wt.% graphene becomes semi-rigid, even in its un-hardened state. It also shows a dry appearance, consisting of individual clumps that separate like soil particles, rather than forming cohesive lumps. The high viscosity of the mixture necessitates additional compaction, suggesting that composites with more than 3 wt% graphene are not recommended for further preparation.
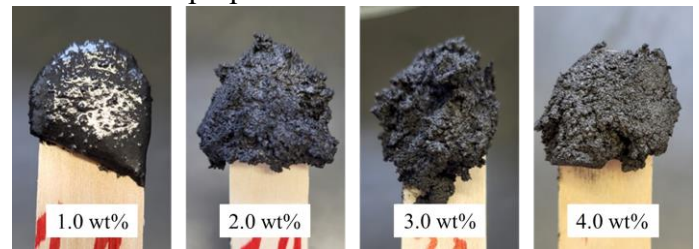
Figure 3. Morphology of pre-hardening GmP with different graphene content.
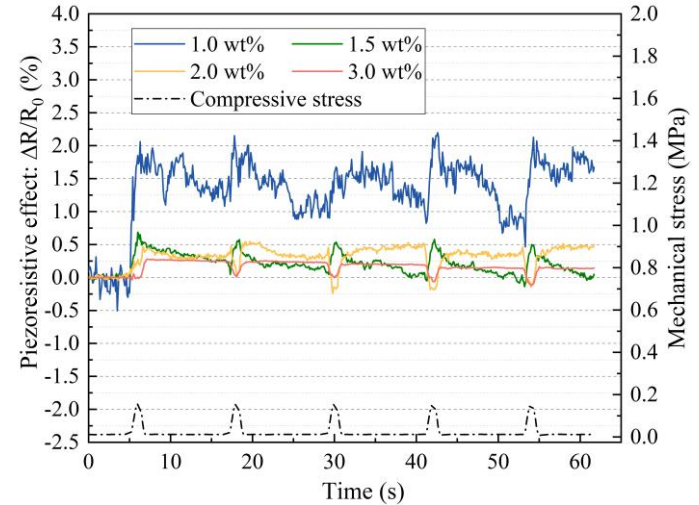
Figure 4. Piezoresistive response of GmP with different graphene content under equivalent car loads.

3.3 *Piezoresistive behavior of GmP*

The piezoresistive response of GmP under an equivalent load of cars and a test temperature of 20 ℃ is illustrated in Figure 4. It can be observed that the $\Delta R/R_0$ of GmP-1.0wt% exhibits a poor periodicity. The resistivity increases significantly during the loading phase, indicating a positive piezoresistive effect. However, the $\Delta R/R_0$ during the unloading and rest phases is less pronounced. The disturbances in the $\Delta R/R_0$ curve obscure the effects of loading, resulting in a weak consistency of the piezoresistive response across all cycles of each specimen. The $\Delta R/R_0$ curve of GmP-1.5wt% is similar to that of

GmP-1.0wt%, with an increase during the loading phase. However, the curve is smoother in the rest phase. This improvement may be attributed to the reduced average distance between conductive particles at higher graphene content, which facilitates more stable conductive pathways after unloading. When the graphene content increases to 2.0 wt% and 3.0 wt%, the $\Delta R/R_0$ curves show a notable difference. Although these curves still rise during the loading phase of the first cycle, they both exhibit a negative piezoresistive effect during the subsequent four loading cycles, characterized by a decrease in resistivity under load. In the resting phase after unloading, the curves of both compositions remain stable and recover to their pre-loading resistivity levels.

According to the theory in ref (Aly et al., 2017), the transition between positive and negative piezoresistive effects can be attributed to two opposing mechanisms. The initiation of microcracks under compressive load or the separation between the specimen and the electrodes results in an increase in resistivity. Whereas the reduction in the distance between conductive particles under compressive load leads to the decrease in resistivity. These two opposing effects compete with each other as the graphene content increases. And the latter one becomes dominant when the graphene content reaches 2.0 wt% and 3.0 wt%. The relatively higher content of conductive particles allows the formation of more stable conductive pathways even in the presence of microcracks (Luo and Liu, 2013). This explains why the GmP-2.0wt% and GmP-3.0wt% exhibit negative piezoresistive effects during the loading phases, and why their $\Delta R/R_0$ curves remain relatively stable during the resting phase.

Figure 5 presents the piezoresistive response of GmP under an equivalent truck load at a test temperature of 20 °C. The $\Delta R/R_0$ curves resemble those observed under an equivalent car load. However, the $\Delta R/R_0$ of GmP-1.0wt% shows a more pronounced decrease during the resting phase. This can also be explained by the initiation of more microcracks under the larger load and their partial healing after unloading. Simultaneously, GmP-3.0wt% exhibits more stable piezoresistive behavior compared to GmP-2.0wt% under the equivalent truck load. Notably, GmP displays a more significant piezoresistive effect under the equivalent truck load, indicating enhanced piezoresistive sensitivity to larger load magnitudes.

4 CONCLUSIONS

In this paper, the electrical and piezoresistive properties of GmP with varying graphene contents are investigated through laboratory tests. The following conclusions are drawn:

GmP transitions to the percolation phase when the graphene content exceeds 0.75 wt%. However, when the graphene content exceeds 3 wt%, the viscosity of GmP before hardening becomes excessively high, complicating the casting and molding. Therefore, the recommended graphene content is between 1.0 wt% and 3.0 wt%. Additionally, a constant input current is used to ensure the test resistance is independent of the input parameters.
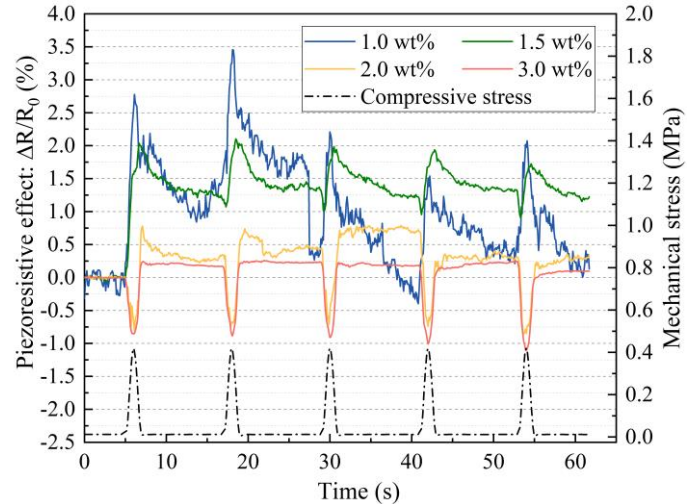

Figure 5. Piezoresistive response of GmP with different graphene content under equivalent truck loads.

As the graphene content increases, the GmP transitions from a positive piezoresistive effect to a negative one under the equivalent compressive load of vehicles. Additionally, the periodicity of the $\Delta R/R_0$ curve and the unloading and resting stages become more stable. This may be attributed to the formation of more stable conductive pathways due to the higher graphene content. Furthermore, GmP exhibits a more significant piezoresistive effect under equivalent truck loads, indicating increased piezoresistive sensitivity to higher load magnitudes.

5 REFERENCES

ALY, K., LI, A. & BRADFORD, P. D. 2017. Compressive piezoresistive behavior of carbon nanotube sheets embedded in woven glass fiber reinforced composites. *Composites Part B: Engineering,* 116**,** 459-470.

LUO, S. & LIU, T. 2013. Structure–property–processing relationships of single-wall carbon nanotube thin film piezoresistive sensors. *Carbon,* 59**,** 315-324.

SCHACHT, A. 2014. Strassenoberflaechenschichten auf Polymerbasis zur Verbesserung der Nutzung. *AACHENER MITTEILUNGEN STRASSENWESEN, ERD-UND TUNNELBAU.*

WANG, T., YANG, J., BERGER, J., BOZ, N., TEKAMPE, S., OESER, M. & LIU, P. 2024. Mechanical and piezoresistive performance of polymethyl methacrylate modified with carbon nanotubes for sensitive road surface. *Materials Today Communications,* 41.

WANG, T. L., FASSBENDER, S., DONG, W. K., SCHULZE, C., OESER, M. & LIU, P. F. 2023. Sensitive surface layer: A review on conductive and piezoresistive pavement materials with carbon-based additives. *Construction and Building Materials,* 387**,** 19.

8.1

ADVANCES IN MODELING & ANALYSIS OF NON-DESTRUCTIVE TECHNOLOGIES

Considerations for Effective Implementation of Comprehensive Pavement Assessments

J.F. Daleiden
ARRB Systems

D. Jansen
Federal Highway Research Institute (BASt)

ABSTRACT: Technology has advanced to a point where most of the needed information for pavement assessments can now be collected and analyzed simultaneously, continuously, and at traffic speeds. These advancements originally focused on improving safety and efficiency. However, as more Agencies adopt these comprehensive pavement assessments, they are also discovering, having such data, reflecting both surface and structural properties, can enable a better understanding of the condition. This can also dramatically improve decision making for managing road networks. This article is intended to provide an overview of the comprehensive assessment of road surfaces, their status, opportunities and challenges for proactive road management.

1 INTRODUCTION

1.1 *What is Comprehensive Pavement Assessment?*

The capability of collecting continuous high accuracy and high-resolution data enables infrastructure managers to more precisely and proactively identify areas where the pavement structure may be underperforming. By analyzing structural and surface condition data together, a more comprehensive assessment of infrastructure condition is provided. This enables a clearer understanding of the prevailing conditions and potential treatment needs.

Figure 1. Elements of Road Condition Measurements

The simultaneously collection, at traffic speed, has clear efficiency advantages. However, the superimposition of individual measurements also provides technically equivalent solutions, provided that high quality standards are set for georeferencing and the consideration of the temporal variable. The full spectrum of Road Condition Measurements includes simultaneous measurements of:

– pavement strength (bearing capacity)
– structural inventory (ground penetrating radar)
– cracking and other surface distresses
– longitudinal and transverse road profile
– pavement macro texture
– road geometry
– geospatial position
– digital imaging (front and surface picture)
– asset inventory and condition

1.2 *Potential Value*

Increased knowledge of the pavement condition improves the possibilities for decision making in planning, budgeting and application for long term cost effectiveness.

The three major groups of models engaged in valuable decisions for road administrations are:

– *Strategic models* - which identify when intervention ought to be considered, and what treatments should be considered.
– *Performance models* – which project, how economical and physical parameters will perform into the future, taking deterioration and future intervention into account.
– *Optimization models* - which from objective criteria single out the optimum plan of intervention from the list of possible options, that can be carried out within the budget constraints.

The strategy models will set the limits when functional and structural criteria are exceeded, and reha-

bilitation options may be considered as possible solutions.

The performance models extrapolate present condition of structural and functional pavement parameters according to deterioration models, and describe how parameters values changed, when intervention is carried out.

However, the fundamental for all the above models are robust and valid data. Without the access to reliable data, value-based management by road administrations can prove difficult and may even have a negative effect on the maintenance strategies.

2 CHALLENGES OF COMPREHENSIVE PAVEMENT ASSESSMENT

2.1 *Data Needs*

A well-maintained road infrastructure will correctly identify/prioritize intervention strategies to ensure an economically feasible use of resources. This is a vital element in keeping society in motion and, ultimately, make roads safer globally.

However, for better decisions to be made, more and better information is often required. This can be facilitated by using higher precision sensors to record pavement conditions at traffic speed relating to both the functional and structural conditions. Also, the use of other data sources, e.g. traffic volumes and construction data, and innovative data sources could be considered, e.g. probe car data. Ideally, there are no differences in data collection for network and project level.

2.2 *Dealing with Data Volume*

Collecting pavement condition data continuously, using sensors that can detect pavement surface characteristics down to millimeters and pavement deflection under loading at a precision of μm, will generate data volumes in the range of 4 gigabytes per km, for network level surveys.

To handle such amounts of data and turn the data into information that can be used for maintenance planning and forecast maintenance strategies requires sufficient and robust processes and tools.

3 TOOLS BEING APPLIED

3.1 *Visualization Tools*

A fundamental key for comprehensive data assessment is geographic information system (GIS) based data handling which assist and support a holistic approach of data interpretation. Such tools have been developed that enable the visual assessment of collected data. Utilizing available mapping functionality, they allow users to navigate through the complex amount of data and assess the condition of the road

network easily. These tools enable transfer from system wide assessments to a project level investigation without the need for the usual additional project level evaluation.
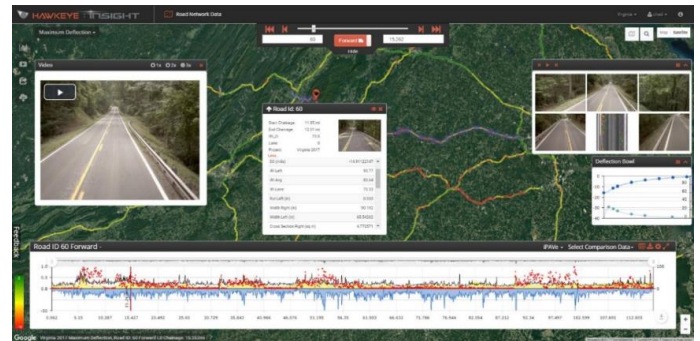

Figure 2. Example for a comprehensive data visualization tool

3.2 *Simple Analytical Tools*

Filtering, segmentation and accelerated verification of data according to the specifications for the accepted road condition or intervention levels are the basic analytical tasks. By doing this filtering, it is possible for the road authority to locate the roads sections where maintenance is needed by means of their individual definition. By using comprehensive measurements including both structural and functional pavements information, the selection or filtering process brings a new dimension into locating roads with present or future maintenance needs.

When the road network has been filtered and the relevant road sections requiring maintenance are located it is relatively straightforward to start prioritizing the roads that are in highest need of maintenance by utilising user defined parameters of key factors such as general condition, traffic volumes, daily axle loading, road class, maintenance history and current need etc.

In addition to finding and optimizing the maintenance needs, previous measurements can be compared directly, providing vital information on comparative condition change timewise and more importantly rate of deterioration.

3.3 *More Sophisticated Analytical Tools*

Automated in-depth analysis and the derivation of specific measures based on the data, on the other hand, pose a greater challenge. The recognition of patterns, the interpretation of causes of damage, their development and the consideration of further parameters, such as cost approaches and sustainability criteria, are currently the subject of many projects. Great potential is seen in the application of AI methods.

4 CASES

For the purposes of this discussion, cases will be categorized as follows:
(1) A section of pavement appears deficient from the surface AND is also determined to be structurally deficient.
(2) A section of pavement appears acceptable from the surface BUT is determined to be structurally deficient.
(3) A section of pavement appears deficient from the surface BUT is determined to be structurally adequate.
(4) A section of pavement appears acceptable from the surface AND an Agency is able to confirm it is also structurally adequate.

Each of these cases will be discussed further in the following sections with examples provided for more detailed examination.

4.1 Case 1

For most, the common belief is that structural issues will manifest themselves in surface deterioration, eventually. While this may typically be true (eventually), it is not always the case. With the aim of sustainable and predictive maintenance structural assessments should be conducted to confirm the presence of structural deterioration before treatments are planned for such extensive deterioration. It is not uncommon for some agencies to delay treatments on some roads when such extensive work is required. Either way, the need for confirmation is an important part of appropriate treatment selection.

When the surface is heavily deteriorated, but no further assessment is conducted, if the Agency elects to delay treatment, because of the perceived deterioration, the surface may continue to decline. Such action could ultimately cause structural deterioration (by allowing water to infiltrate the pavement), and will likely lead to accelerated deterioration, regardless of whether structural issues existed or not. If the Agency elects to plan an extensive treatment (based on the surface deterioration) this could result in unnecessary expenditures.

When the surface is heavily deteriorated, and further assessment is conducted, an Agency can spend significant resources attempting to quantify the extent of the deterioration. An Agency can conduct some forensic analysis, and potentially still not fully document the extent of the deterioration.

4.2 Case 2

Not surprisingly, continuous structural capacity assessment, can reveal isolated/discrete portions of highways that may appear acceptable from the surface, but (for a multitude of potential reasons) are not able to provide the same structural support as adjacent portions of the same highway.

When left undetected, isolated recurring maintenance issues will create frustration for years to come. Larger areas of structurally deficient pavement will ultimately lead to changes in treatment forecasts, which can prove very costly and embarrassing.

As an example, improperly constructed pavements can experience early structural problems that may not be as obvious from the surface.

When detected early, Agencies can proactively conduct spot repairs in advance of treatments, to improve treatment performance and required thicknesses. Agencies may proactively alter treatment forecasts and strategies to mitigate more extensive areas of structural concern, that currently are not visible from the surface.

For some pavement types (like composite pavements), it is helpful to be aware of underlying condition to properly plan for treatment needs.

4.3 Case 3

Observations have also been made of sections of pavement that exhibit extensive surface deterioration, that would traditionally lead one to believe that extensive repairs are required.

Without the corresponding structural assessment, an Agency may elect to delay treatment because of the perceived deterioration. The surface may continue to decline, and could ultimately cause structural deterioration (by allowing water to infiltrate the pavement). This will likely lead to accelerated deterioration, regardless of whether structural issues existed or not. If the Agency elects to plan an extensive treatment (based on the surface deterioration) this could result in unnecessary expenditures.

When the surface is heavily deteriorated, and further assessment reveals no structural deterioration, an Agency can remove and replace the problem surface layer and avoid more extensive unnecessary costly repair. Agencies can use saved resources to investigate true cause(s) of surface anomalies.

4.4 Case 4

When sections of pavement appear to have limited surface deterioration, it is ultimately beneficial to be able to confirm that these sections truly require no work for the foreseeable future.

Without the corresponding structural assessment, an Agency may program work based solely on the pavements age or unsupported performance expectations. This will likely lead to misappropriation of funds, regardless of whether structural issues existed or not. Similarly, if the Agency elects to plan treatment based solely on performance prediction this could result in unnecessary expenditures.

When structural assessments can be readily conducted, an Agency can more confidently project performance expectations and more accurately plan for future needs. Again, this enables Agencies to use saved resources to address projects of greater need.

Perhaps of greatest importance is the realization that multivariate data always enables a more detailed evaluation of a project. Rather than assigning some "average" condition for treatment selection and design, discrete sections can be identified with greater confidence and accuracy. This ability offers the potential for isolating and treating areas of greater need. These project level decisions can now be made with network level data. Such work can be performed in advance of larger rehabilitation projects to produce a more homogeneous and therefore cost-effective strategy. Potentially, isolated repairs of this nature may even be performed (on their own) to proactively "buy some time" before additional work is needed.

5 FURTHER DEVELOPMENT

Additional data and parameters are also required to support further decision-making in pavement management at network level. In addition to the description of the current structural and functional condition, these include the already carried heavy traffic loads in relation to the existing pavement design and consideration of the importance of a network section. The latter can, for example, also depend on the existence of possible alternative routes and is determined by resilience considerations.

This multivariate evaluation leads to the development of an advance warning system for the network level. Theoretically, it can be supplemented by any other relevant data sources, such as floating car data, and may thus become more meaningful.

The aim of the advance warning system is to identify sections of road that will require major renewal in the near future. If necessary, such road sections should then be subjected to more detailed investigations, e.g. by taking drill cores.

6 CONCLUSIONS

The technical challenges of assessing pavement structural capacity have historically led to a perceptible gap between network level assessment and project level pavement management. The increasingly apparent limitations of traditional methods of assessment (safety considerations, user delays, and relatively high testing costs) are necessitating exploration of new solutions.

With the integration of technology for continuous traffic speed collection of structural and functional condition (as one operation), system wide and project level applications can be achieved simultaneously. The overall impact is still to be determined, but as seen from the limited examples cited above, many are eager to explore the possibilities.

Closing this gap between network and project level evaluations is generating:

− More comprehensive pavement assessments, with greater value and applicability of the data collected;

− The ability to better optimize network performance and

− Improve the efficiency and effectiveness of project specific treatment needs.

Most are accepting the merits of network level applications and focused on how best to accommodate such data in existing management systems. Project level applications continue to evolve. Data is currently being utilized to identify specific portions of projects that merit being treated differently. This can include spot full depth repairs, drainage mitigation or potentially a varying treatment needs throughout a project based on conditions noted. Areas considered "representative" are being used to facilitate more focused forensic investigations and generation of more precise design needs.

As observed in the cases above, the ability to conduct more comprehensive assessments is capable of significantly impacting the optimization (and application) of Agency pavement funds.

REFERENCES

Flintsch, G., Katicha, S., Bryce, Ferne, J.B., Nell, S., Diefenderfer, B. 2013. Assessment of Continuous Pavement Deflection Measuring Technologies. *SHRP 2 Rep., no. S2-R06F-RW-1.*

Maser, K., Schmalzer, P., Shaw, W., Carmichael, A. 2017. Integration of Traffic Speed Deflectometer and Ground-Penetrating Radar for Network-Level Roadway Structure Evaluation. *Transp. Res. Rec., Vol. 2639/1:* 55-63.

Plati, C., Loizos, A. 2023. An Approach to Combine Structural and Functional Testing to Optimize Condition Assessment of Flexible Pavements *TRB Annual Meeting*

Jansen, D., Podolski, C., Kalantari, M., Rahimi, M. 2023. ME-SAS Aus- und Bewertung – Stufe 1. *BASt report (unpublished)*

Kressirer, B. 2020. Pilotprojekt Tragfähigkeitsmessung in Bayern als Baustein des Erhaltungsmanagements. *Straße und Autobahn, Kirschbaum-Verlag, Heft 10/2020*: 813-820

Weitzel, N.D., Pierce, L.M., Caroll, E., Thompson, J.U. 2023, Use of Traffic Speed Deflectometer Data in Project-Level Pavement Rehabilitation Design. *Transportation Research Record, Vol. 2678/6:* 1-12

Murekye, A., Flintsch, G., Katicha, S., Diefenderfer, B., Urbaez, E.P. 2024. A Pilot Study to Incorporate Network-Level Structural Condition into Agency Pavement Management Practices. *TRB Annual Meeting*

Comparing Asphalt Concrete Properties inferred from FWD and TSD Measurements

E. Levenberg
Technical University of Denmark (DTU)

M. Kalantari
Federal Highway Research Institute (BASt)

ABSTRACT: An asphalt road was investigated by three independent methods: (i) a Falling Weight Deflectometer (FWD); (ii) a Traffic Speed Deflectometer (TSD); and (iii) laboratory complex modulus over cores taken from the asphalt concrete layer. The objective of this work was to compare the results from the two field measurement campaigns, namely FWD and TSD, with a focus on the asphalt concrete properties.

1 INTRODUCTION

A common maintenance activity in asphalt pavement infrastructure is the periodic replacement of Asphalt Concrete (AC). Consequently, pavement engineers are interested in technologies that allow for correct, efficient, and safe quantification of AC mechanical properties in situ. The state-of-the-practice approach in this context is backcalculating the AC's elastic modulus from Falling Weight Deflectometer (FWD) measurements.

The FWD's testing capabilities essentially remain unchanged for decades, experiencing only marginal design upgrades (Levenberg et al. 2025). In recent years, new measurement technologies have emerged – having the potential to replace the FWD. These include moving measurement platforms like the Traffic Speed Deflectometer (TSD) and the Rapid Pavement Tester (Raptor) (Andersen et al. 2017).

This work is motivated by the growing interest within the pavement engineering community to compare layer properties inferred from FWD measurements against layer properties inferred from measurements collected by the new emerging devices. More specifically, the objective of this paper is to present and compare AC layer properties inferred from an FWD testing campaign to those inferred from a TSD testing campaign.

The campaigns utilized for this purpose were carried out at different times over a 320 m section of an asphalt road located in South-West Germany. The pavement system consisted of (top to bottom): 180 mm AC (in three lifts), 520 mm of unbound granular material (UGM), and fine-grained soil extending to a large depth.

FWD measurements are analyzed with an elasto-static backcalculation scheme, providing the AC's Young's modulus. TSD measurements were analyzed in a separate study (Levenberg & Kalantari 2025) – providing for this (current) work the AC layer's master curve.

Moreover, a laboratory testing campaign is included, where viscoelastic properties of the AC layer were measured over cores taken from the road. The laboratory effort is utilized herein to facilitate the analysis, e.g., account for differences in temperature conditions prevailing in situ during the FWD and TSD testing campaigns. Lab results are also utilized to provide a reference truth or validation.

2 PROPERTIES OF THE AC LAYER

2.1 *Laboratory results*

The AC layer in the tested road (180 mm thick) was composed of three lifts. Lift 1 (top), $h_1 = 40\,\text{mm}$, Lift 2 (middle), $h_2 = 40\,\text{mm}$, and Lift 3 (bottom), $h_3 = 100\,\text{mm}$. After coring, the complex modulus E^* of each lift was measured in the laboratory. The following expression was utilized to analyze the results:

$$E^* = E_{LF} + \frac{E_{HF} - E_{LF}}{1 + \delta_1 (i\omega\tau_0 a_T)^{-k} + (i\omega\tau_0 a_T)^{-h}} \quad (1)$$

where $E_{LF} = E^*(\omega \to 0)$ (MPa), $E_{HF} = E^*(\omega \to \infty)$ (MPa), δ_1 (unitless), $k < h < 1$ (unitless), and τ_0 (seconds) are all positive real-valued constants. ω denotes angular frequency (radians/second), and the parameter a_T (unitless) is the time-temperature shift factor, given by the WLF equation:

$$\log a_T = -c_1 (T - T_0)(c_2 + T - T_0)^{-1} \quad (2)$$

in which c_1 (unitless) and c_2 (Celsius) are positive constants and T_0 is a preselected reference

temperature (Celsius). The laboratory results are summarized in Table 1.

Table 1. AC complex modulus results from laboratory testing (see Equations 1 and 2) for a reference temperature $T_0 = 20\,°C$.

AC Lift #:	1 - top	2 - middle	3 - bottom
E_{LF} [MPa]	311	347	296
E_{HF} [MPa]	38918	43372	37058
δ_1 [-]	3.115	3.010	1.338
h [-]	0.593	0.609	0.433
k [-]	0.224	0.232	0.132
τ_0 [s]	8.598×10^{-3}	8.699×10^{-3}	9.054×10^{-3}
c_1 [-]	32.5	32.8	21.3
c_2 [°C]	274.1	290.6	219.8

Equation 1 and Table 1 allow the evaluation of the storage modulus E_1 of a given AC lift for any desired frequency and temperature. This is done according to the following expressions:

$$E_1 = E_{LF} + A\left(E_{HF} - E_{LF}\right)\left(A^2 + B^2\right)^{-1} \tag{3}$$

where:

$$A = 1 + \frac{\delta_1 \cos\left(\pi k / 2\right)}{\left(\omega\tau_0 a_T\right)^k} + \frac{\cos\left(\pi h / 2\right)}{\left(\omega\tau_0 a_T\right)^h} \tag{5}$$

$$B = \frac{\delta_1 \sin\left(\pi k / 2\right)}{\left(\omega\tau_0 a_T\right)^k} + \frac{\sin\left(\pi h / 2\right)}{\left(\omega\tau_0 a_T\right)^h} \tag{6}$$

2.2 FWD results

The tested road section was exposed to 184 FWD drops, applied over 31 different locations at 10 m spacing. The entire campaign took 45 minutes during which the average temperature of the three AC lifts was nearly constant and estimated as follows: 17.1 °C (top 40 mm), 15.0 °C (middle 40 mm), and 13.5 °C (bottom 100 mm). These temperatures were obtained using the empirical BELLS3 equation (Lukanen et al. 2000).

The drops produced peak loads in the range of 47.9 kN to 90.8 kN; given the 300 mm diameter loading plate, the corresponding peak stresses were in the range of 0.68 MPa to 1.28 MPa. The FWD was equipped with nine geophones positioned at the following offsets from the center of the loading plate (in mm units): 0, 210, 330, 510, 900, 1270, 1500, 1800, and 2100. The pavement system was modeled as a layered elastic half-space and the peak stresses, along with their corresponding peak deflections, were utilized to backcalculate the moduli of the model layers.

A 5-layered model was assumed for this purpose, with the following thicknesses (Poisson ratios): 180 mm representing all three AC lifts combined (0.30), 220 mm representing the upper part of the UGM (0.35), 300 mm representing the lower part of the UGM (0.35), 500 mm representing the subgrade (0.40), and a semi-infinite bottom layer representing soil mass extending to a large depth (0.40).

The match between a calculated and measured deflection set was defined as the absolute relative error averaged over all nine FWD sensors. Optimal solutions were found with a gradient-decent search algorithm. All calculations were done in an Excel environment with the ELLEA1 worksheet (version 0.96) (Levenberg 2016a). The final matching errors were very good, with an average over 184 deflection sets of 1.07%, a standard deviation of 0.62%, a minimum value of 0.27%, and a maximum value of 3.37%. Based on all available FWD drops, the average backcalculated AC modulus was 9324 MPa with a standard deviation of 1964 MPa, i.e., a coefficient variation of 21%. The minimum backcalculated AC modulus was 4418 MPa, and the maximum was 13217 MPa. Table 2 offers a summary of the backcalculation results.

Table 2. Summary of FWD backcalculation results.

Modeled layer in the pavement	Thickness [mm]	Average modulus [MPa]	Standard deviation [MPa]
Combined AC	180	9324	1964
Upper UGM	220	154	72
Lower UGM	300	462	255
Subgrade	500	67	18
Deep soil mass	Semi-inf	400	111

2.3 TSD results

The TSD truck was operated at a speed of 70 km/h; it passed over the 320 m long test section in about 16.5 seconds, reporting on 32 distinct slope sets – each representing an average over a 10 m stretch. Figure 1 presents a graphical summary of the reported TSD slopes. The average temperatures of the three AC lifts were: 24.2 °C (top 40 mm), 20.4 °C (middle 40 mm), and 17.6 °C (bottom 100 mm). These temperatures were (also) obtained using the empirical BELLS3 equation.

The TSD-reported slopes were analyzed in a separate study which aimed at inferring the AC layer properties (Levenberg & Kalantari 2025). The analysis attempted to fit model-calculated slopes to TSD-reported slopes; this was done while accounting for the loading of the entire TSD truck (i.e., all tires) utilizing several linked worksheets of the layered viscoelastic half-space code ELLVA1 (Levenberg 2016b, 2016c). The model layering was identical to the layering utilized for FWD backcalculation (see Table 2). Linear elasticity was assumed except for the top 180 mm layer (representing AC) which was treated as linear viscoelastic.

Ultimately, the TSD analysis provided 32 estimates for the AC layer's creep compliance. These creep compliance time functions were interconverted to the frequency domain and then averaged to create a

mastercurve, which characterizes the AC layer, i.e., a combination of the three AC lifts. The derived storage modulus is presented in Figure 2. The average is depicted with a solid black line, while dashed lines encapsulate the range of results.
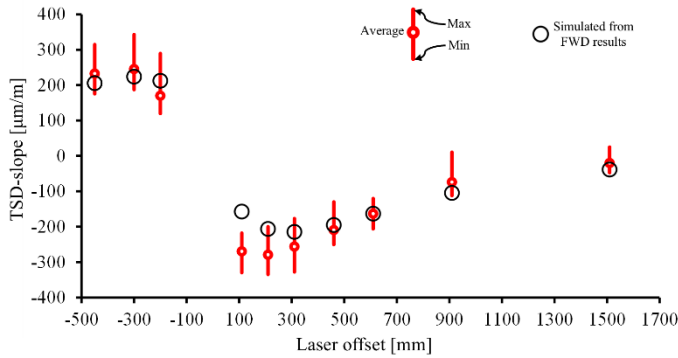

Figure 1. TSD slopes for different laser offsets. The vertical red lines span the range of results reported by the TSD device. The average in each case is indicated by a hollow circular red marker. Large circular markers (black border) represent TSD slopes simulated in a pavement model with backcalculated moduli from FWD (after temperature correction for the AC).
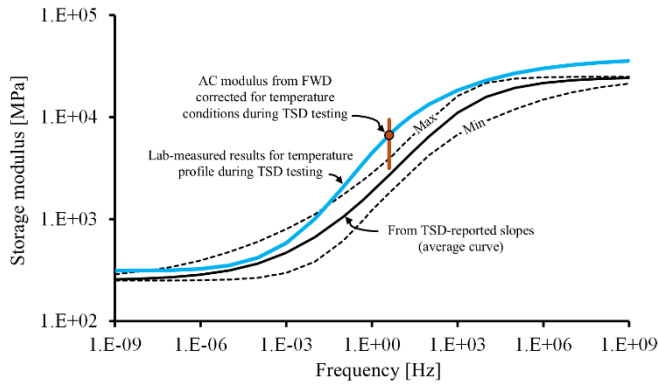

Figure 2. AC storage modulus master curve at temperature conditions during the TSD measurement campaign: (i) based on lab-measured results (blue solid line); and (ii) backcalculated from TSD-reported slopes where the solid black line denotes average and the dashed lines denote upper and lower ranges. Also included is the FWD-backcalculated AC modulus (circular marker with black border) and its range (vertical red line).

3 COMPARISON OF AC LAYER PROPERTIES

3.1 *Approach*

Before comparing the AC properties inferred from FWD and TSD a preliminary analysis was necessary. First, given that both the TSD and the FWD characterized the AC layer under a different temperature profile, a temperature correction was needed. In this context, it was decided to correct the FWD modulus so that it applies to the temperature profile prevailing during the TSD campaign. Second, the TSD analysis provided a storage modulus mastercurve, i.e., a range of moduli values, each associated with a different frequency, while the FWD provided a single modulus value. Thus, for comparing the two it was necessary to associate some frequency with the backcalculated

FWD modulus. Lastly, properties derived from both the FWD and the TSD are a combination of the properties of the three AC lifts. Thus, to validate their results, the lab-measured properties should also be combined.

To achieve the three above-described aspects, the plot in Figure 3 was prepared. This figure presents E_1^{com}, a combined AC storage modulus (ordinate on the left-hand side) vs. frequency (on the abscissa). Two S-shaped curves are shown, both are based on the lab-measured results in Table 1. The solid blue depicts a combined E_1^{com} for the temperature conditions prevailing during the TSD campaign. The dashed blue line depicts a combined E_1^{com} for the temperature conditions prevailing during the FWD campaign. The ratio between the two curves, labeled as a Correction factor, is plotted as a dashed black line with values depicted on the right-hand side ordinate.
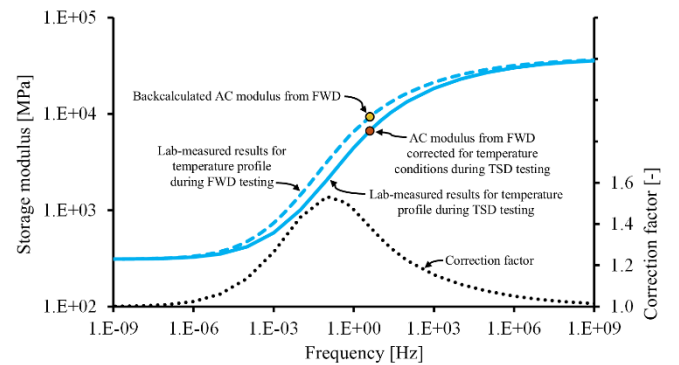

Figure 3. Lab-based combined storage modulus mastercurves of the AC layer. The dashed blue line represents temperature conditions prevailing during the FWD testing and the solid blue line represents temperature conditions prevailing during the TSD measurement campaign. The ratio between these two curves is depicted by a dotted black line, labeled as 'correction factor'. Also included is the FWD backcalculated AC modulus before and after temperature correction (circular markers).

The E_1^{com} curves in Figure 3 were calculated according to the following formula (Levenberg et al. 2009):

$$\sqrt[3]{E_1^{com}} = \frac{\sum\limits_{i=1}^{3} h_i \sqrt[3]{(E_1)_i}}{\sum\limits_{i=1}^{3} h_i} \tag{7}$$

where $(E_1)_i$ is the storage modulus at a given frequency and average temperature level of asphalt lift i, and h_i is the thickness of asphalt lift i. As can be seen, given the colder temperature levels during the FWD campaign compared to the TSD campaign, the associated E_1^{com} is consistently higher (i.e., the dashed blue line is above the solid blue line).

Also included in Figure 3 is the average backcalculated AC modulus from the FWD campaign (circular marker with a light orange fill), i.e., 9324 MPa. This modulus was deliberately placed on the dashed blue line, revealing an associated frequency of 4 Hz. When

translated down to the solid blue line, keeping the same frequency, the AC modulus from the FWD is effectively temperature-corrected for the conditions prevailing during the TSD campaign. The correction factor is 1.4 and the modulus becomes 6660 MPa (circular marker with a dark orange fill).

3.2 *FWD vs. TSD*

The preliminary analysis, as described above, provided all the necessary inputs for presenting and comparing the AC layer properties as derived from FWD and (separately) from TSD alongside lab-generated validation. The comparison results are shown in two separate figures. Referring first to Figure 2, the temperature-corrected FWD modulus of 6660 MPa is plotted at a frequency of 4 Hz (circular marker with dark orange fill). The short vertical line passing through the circular marker represents the range of backcalculated AC moduli, from a low of 3156 MPa (=4418/1.4) to a maximum of 9441 MPa (=13217/1.4). As can be seen, there is some overlap with the TSD results, as the vertical line enters the range marked by the dashed black lines. However, the averages are not close; the average storage modulus inferred from the TSD at 4 Hz is about 2750 MPa (solid black line).

Referring next to Figure 1, the FWD results (black circular markers) are compared to the TSD-reported slopes. These markers represent TSD surface slopes, simulated in a layered-elastic pavement model loaded by the entire TSD truck configuration (i.e., all wheels). The average moduli backcalculated from FWD were utilized for this purpose (see Table 2) but with a temperature-corrected modulus for Layer 1 (i.e., 6660 MPa). As can be seen, the overlap is partial, i.e., most of the FWD markers do not encircle the average TSD-reported slopes at each laser offset.

4 CONCLUSION

While focusing on the properties of the AC layer, this paper compared backcalculated FWD moduli with properties inferred from TSD measurements. The investigation involved one asphalt road that was measured by both devices – on different dates. Peak FWD deflections were analyzed with a layered elastic model, producing an AC modulus. Reported TSD-slopes were analyzed in a layered viscoelastic model, producing an AC mastercurve. Additionally, the viscoelastic properties of AC cores were measured in a laboratory to facilitate the comparison.

It was found that the average backcalculated AC modulus from FWD (after temperature correction) was higher (by a factor of 2.4) than the associated average storage modulus derived from TSD (see Figure 2). An attempt to compare measured TSD slopes and calculated TSD slopes based on backcalculated FWD moduli was also not very successful (see Figure 1).

The observed discrepancies between FWD and TSD may be due to: (i) utilization of an elastostatic backcalculation scheme for interpreting FWD deflections; (ii) associating the backcalculated AC modulus with a certain frequency; and (iii) structural inhomogeneity in the tested road – see relatively high standard deviations in layer moduli (Table 2) and wide range of the TSD-derived mastercurves (Figure 2).

In future investigations aiming to compare layer properties from FWD to those from TSD it is recommended to: (i) carry out tests over homogenous road sections; (ii) perform testing campaigns at the same time to avoid the need for temperature correction; (iii) employ an FWD backcalculation scheme that considers viscoelasticity; and (iv) include pavement sensors to allow for a device-independent estimation of the mechanical layer properties.

5 REFERENCES

Andersen, S., Levenberg, E., and Andersen, M.B. (2017). Inferring Pavement Layer Properties from a Moving Measurement Platform. Proceedings of the 10th International Conference on the Bearing Capacity of Roads, Railways & Airfields, CRC Press/Taylor & Francis Group, pp. 675–682.

Levenberg, E. (2016a). ELLEA1: Isotropic layered elasticity in Excel: Pavement analysis tool for students and engineers. https://orbit.dtu.dk/en/publications/ellea1-isotropic-layered-elasticity-in-excel-pavement-analysis-to.

Levenberg, E. (2016b). ELLVA1: Isotropic layered viscoelasticity in Excel (moving load): Advanced pavement analysis tool for students and engineers. https://orbit.dtu.dk/en/publications/ellva1-isotropic-layered-viscoelasticity-in-excel-moving-load-adv.

Levenberg, E. (2016c). Viscoelastic pavement modeling with a spreadsheet. In 8th International conference on maintenance and rehabilitation of pavements, MAIREPAV 2016 (pp. 746–755).

Levenberg, E. and Kalantari, M. (2025) Inversion of asphalt pavement properties from slopes reported by the traffic speed deflectometer. Transportation Research Record, Journal of the Transportation Research Board (TRB). Forthcoming.

Levenberg, E., McDaniel, R. S., & Olek, J. (2009). Validation of NCAT Structural Test Track Experiment using INDOT APT Facility. JTRP Technical Report FHWA/IN/JTRP-2008/26.

Levenberg, E., Navarro, A., and Pinori, U. (2025) Improved moduli backcalculation of the upper layers in asphalt pavements. Journal of Transportation Engineering, Part B: Pavements. In press.

Lukanen, E. O., Stubstad, R., Briggs, R. C., & Intertec, B. (2000). Temperature predictions and adjustment factors for asphalt pavement (FHWA-RD-98-085). Turner-Fairbank Highway Research Center.

Enhancing pavement performance evaluation via crowdsourced gamification

M.A. Najafli
Department of Civil and Environmental Engineering, Amirkabir University of Technology

M.S. Fahmani
Department of Civil and Environmental Engineering, Amirkabir University of Technology

A. Golroo
Department of Civil and Environmental Engineering, Amirkabir University of Technology
Faculty of Information Technology and Electrical Engineering, University of Oulu

M. Rasti
Faculty of Information Technology and Electrical Engineering, University of Oulu

ABSTRACT: This paper explores the innovative use of crowdsourced data for pavement evaluation through a gamification mobile application based on the ORAN platform. Leveraging proactive maintenance planning, this approach aims to substantially reduce costs associated with pavement management. The paper emphasizes the collection and evaluation of pavement data via crowdsourcing and artificial intelligence (AI) to address the critical lack of pavement distress data necessary for training AI models for distress detection and pavement condition prediction. Gamification is employed to motivate users to contribute valuable data, processed through edge computing for efficient pavement evaluation.

1 INTRODUCTION

Proactive maintenance planning is a strategic approach that anticipates potential infrastructure issues before they become critical, thus saving significant costs in pavement management. Traditional methods of pavement evaluation are often resource-intensive and time-consuming.

Proactive maintenance planning involves the timely identification of pavement conditions that require intervention before severe deterioration occurs. This approach is designed to minimize the lifecycle costs of pavements and extend their service life. By anticipating maintenance needs, agencies can allocate resources more efficiently, avoiding costly emergency repairs. The integration of proactive maintenance planning with modern technology provides a robust framework for sustainable infrastructure management.

Existing literature highlights the significant benefits of proactive maintenance planning in extending the lifespan of pavements and reducing overall maintenance costs (Shahin, 2005). Studies by Haas et al. (2010) emphasize the importance of timely interventions in preventing severe pavement deterioration. Furthermore, research by McNeil et al. (2014) demonstrates the effectiveness of crowdsourcing in collecting extensive and diversified data sets for infrastructure evaluation.

Crowdsourcing leverages the collective intelligence and efforts of a large group of individuals to perform tasks traditionally handled by designated professionals. In the context of pavement evaluation, crowdsourcing can facilitate the collection of extensive and diverse data sets from various locations, enhancing the comprehensiveness of pavement assessments.

Gamification has been widely studied in various domains for its potential to enhance user engagement and motivation (Hamari, Koivisto, & Sarsa, 2014). In the context of infrastructure management, Mora et al. (2016) explore the application of gamification to encourage public participation in data collection. Additionally, the integration of AI in infrastructure evaluation has shown promising results in improving the accuracy of distress detection and condition prediction (Voulodimos et al., 2018).

Artificial intelligence plays a crucial role in the automatic detection and classification of pavement distress. AI models require large datasets to accurately identify various types of distress and predict pavement conditions. However, the lack of extensive pavement distress data poses a challenge for training these models. Crowdsourced data offers a solution by providing diverse and abundant data to enhance the performance of AI algorithms. Edge computing, a pivotal technology in this framework, has been proven to reduce latency and enhance real-time data processing capabilities (Shi et al., 2016). The combination of edge computing with AI and crowdsourced data collection presents a novel solution to address the existing gaps in pavement evaluation and maintenance planning.

2 RESEARCH OBJECTIVE

This paper proposes a novel solution by utilizing crowdsourced data through a gamified mobile application based on the ORAN platform. This method not only democratizes data collection but also harnesses the power of AI to provide accurate and timely pavement condition assessments.

3 RESEARCH METHODOLOGY

After development of a gamification-based mobile application Images or videos taken by the player via the mobile app are first analyzed by the system, which uses advanced algorithms to process the uploaded content. First, the quality of uploaded content is evaluated based on the image processing algorithm. The system then detects and classifies various pavement distresses present in the images or video frames. Next, the user input is validated against AI predictions to ensure accuracy. Based on this validation, scores and rewards are assigned to users, motivating continued participation. The data collected through the ORAN platform is communicated to the cloud, enabling the creation of a color-coded map that demonstrates pavement conditions at the network level.

To motivate users to participate in data collection, the mobile application incorporates gamification elements. Users are divided into two categories: experts and non-experts. Experts are responsible for capturing and labeling pavement distress images with specific types and severity levels. Although this data is highly valuable, it is less motivating for players. Non-experts, on the other hand, can contribute by taking pictures or videos of pavement distress under two options: simply indicating the presence of distress or categorizing it into one of five general groups. Players receive scores and rewards based on the accuracy and relevance of their contributions, encouraging continued participation.

The mobile application allows users to capture images or videos of pavement conditions while walking or driving. These contributions are analyzed using edge computing, which employs lightweight and fast deep learning algorithms such as YOLO (You Only Look Once). The edge cloud processes the data, providing immediate feedback and rewards to users, thereby maintaining their engagement and ensuring the continuous flow of data via ORAN to the cloud for pavement condition demonstration at the network level. The workflow of the pavement condition assessment process is illustrated in Figure
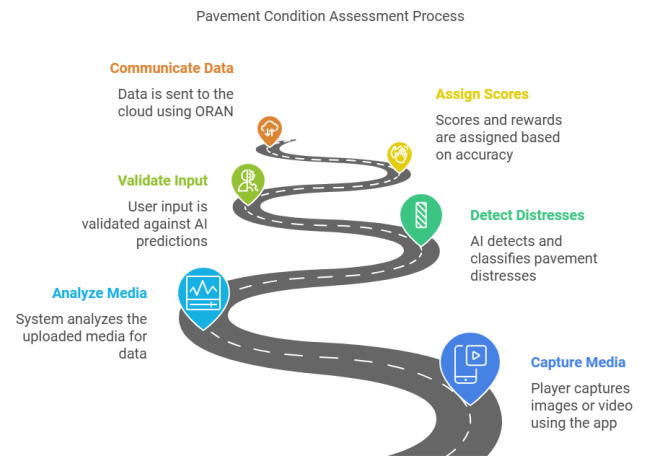

Figure 1. Pavement condition assessment process.

1, detailing the sequential steps from media capture to score assignment.

4 CROWDSOURCING AND GAMIFICATION FOR PAVEMENT DATA COLLECTION

The proposed mobile application utilizes crowdsourcing to gather pavement condition data from two types of users: experts and non-experts. By incorporating gamification elements, the app motivates users to actively participate in data collection, making the process more engaging and enjoyable. Expert users, such as civil engineers or trained inspectors, can contribute high-quality data by capturing images of pavement distresses and labeling the distress type and severity. This data is particularly valuable for training AI models but may be less motivating for users due to its technical nature. To encourage participation, the app implements a points system and leaderboards, recognizing top contributors and fostering healthy competition among experts. Non-expert users, such as the general public or citizen scientists, can contribute in two ways: basic distress reporting, where users simply indicate the presence of a distress on the pavement, and general categorization, where users select from five predefined distress groups. Additionally, users can choose their data collection method, such as walking mode, capturing individual images, or driving mode, recording video footage. The interplay between user expertise and data quality in pavement distress reporting is presented in Figure 2, providing insights into the categorization and reporting accuracy.
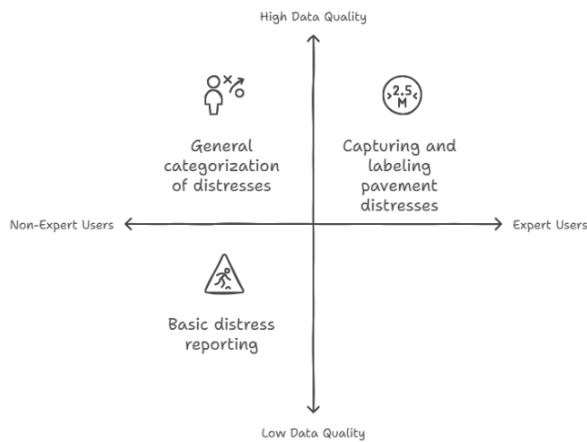
Figure 2. Interplay matrix between user expertise and data quality in pavement distress reporting and categorization.

5 OPEN RADIO ACCESS NETWORK

Using Open Radio Access Network (ORAN) for data storage and sharing offers an innovative approach to managing crowdsourced pavement image data collected through a gamified mobile application. The platform engages users to capture and upload pavement images, incentivizing participation through gamification elements such as points, rewards, and leaderboards. ORAN's decentralized and interoperable infrastructure ensures efficient handling of this data by enabling scalable, low-latency storage and real-time sharing across multiple stakeholders. This setup facilitates seamless collaboration between researchers, road authorities, and developers while maintaining data integrity and privacy. By leveraging ORAN's capabilities, the system enhances data accessibility and accelerates the analysis of pavement conditions, ultimately supporting more efficient maintenance planning and decision-making.

To provide real-time feedback and maintain user engagement, the application leverages edge computing capabilities through the ORAN platform. This allows for quick processing of captured images and videos using lightweight deep learning algorithms such as YOLO (You Only Look Once). The edge computing system performs tasks such as analyzing uploaded images or video frames, detecting and classifying pavement distresses, validating user input against AI predictions, and assigning scores and rewards to users based on accuracy. This immediate

feedback loop not only gamifies the experience but also helps improve the quality of crowdsourced data over time. Figure 3 outlines the research methodology employed in this study, offering a structured overview of the processes and techniques utilized.
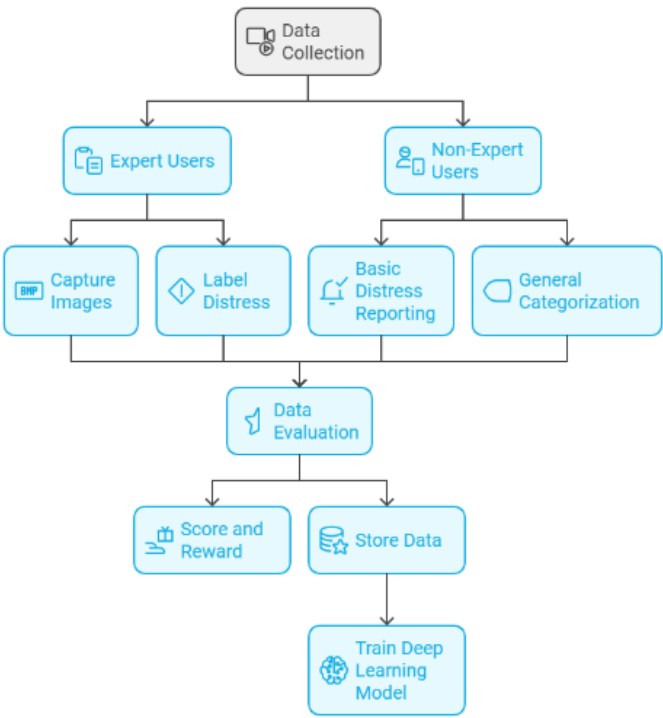

Figure 3. Research methodology.

6 INITIAL RESULTS

Initial results indicate that players have engaged with the gamified mobile application exceptionally well, capturing a substantial number of images. The app's ability to recognize, evaluate, and score these images accurately has proven effective, providing immediate feedback and incentives that maintain player motivation. This high level of engagement and the quality of data collected demonstrate the app's potential as a significant source of information for proactive maintenance planning. Figure 4 showcases screenshots of the gamification-based mobile application developed on the ORAN platform, highlighting its user interface and functionalities.
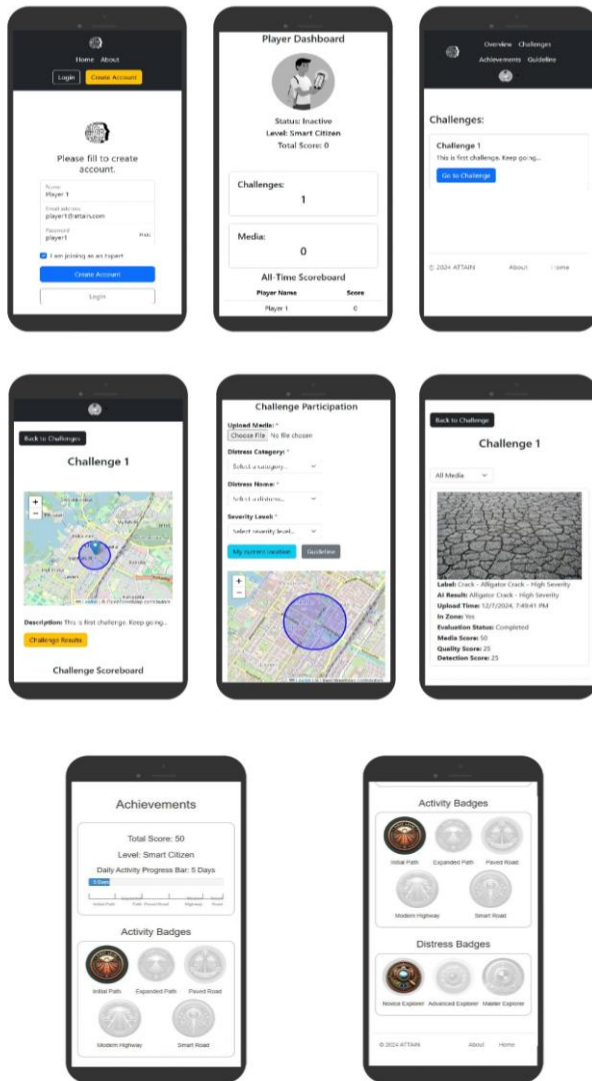
Figure 4. Screenshots of gamification mobile application based on the ORAN platform.

7 LIMITATIONS AND FUTURE WORK

While the proposed system offers numerous benefits, including increased data volume, diverse data sources, cost-effective data collection, real-time pavement monitoring, enhanced public engagement, and improved AI model performance, it also faces several challenges. Ensuring data quality control and minimizing false reports from non-expert contributions are critical concerns. Additionally, robust measures must be implemented to protect user privacy and data security. Sustained user engagement over time is essential, requiring long-term strategies to keep users interested and participating. Integrating the crowdsourced data seamlessly with existing pavement management systems presents another significant challenge. Future work will focus on refining the gamification elements, enhancing AI algorithms for more accurate distress detection, and developing methods to integrate crowdsourced data with traditional pavement management practices, thus ensuring the system's overall effectiveness and efficiency.

8 CONCLUSION

The use of crowdsourced data for pavement evaluation through a gamification mobile application based on the ORAN platform presents a transformative approach to infrastructure management. By leveraging proactive maintenance planning, crowdsourcing, AI, and edge computing, this method addresses the critical data gap and enhances the accuracy and efficiency of pavement condition assessments. The engagement of both experts and non-experts in data collection ensures a comprehensive and continuous flow of valuable data, ultimately contributing to sustainable and cost-effective pavement management.

ACKNOWLEDGEMENTS

9 REFERENCES

Haas, R., Hudson, W.R. and Zaniewski, J.P., 1994. Modern pavement management.

Hamari, J., Koivisto, J. and Sarsa, H., 2014, January. Does gamification work?--a literature review of empirical studies on gamification. In 2014 47th Hawaii international conference on system sciences (pp. 3025-3034). Ieee.

McNeil, S., Park, H. and Jung, S., 2014. Leveraging crowdsourcing for infrastructure condition assessment. Journal of Infrastructure Systems.

Mora, S., Gianni, F. and Divitini, M., 2016. Tiles: A gamified mobile app for engaging university students to share their emotions. Procedia Computer Science.

Shahin, M.Y., 2005. Pavement management for airports, roads, and parking lots. Springer.

Shi, W., Cao, J., Zhang, Q., Li, Y. and Xu, L., 2016. Edge computing: Vision and challenges. IEEE Internet of Things Journal.

Voulodimos, A., Doulamis, N., Doulamis, A. and Protopapadakis, E., 2018. Deep learning for computer vision: A brief review. Computational intelligence and neuroscience, 2018(1), p.7068349.

Concealed damage identification in asphalt materials using dynamic coplanar capacitance imaging method

Bin Shi
Department of Roadway Engineering, Southeast University

Qiao Dong* (Corresponding author)
Department of Roadway Engineering, Southeast University

ABSTRACT: The dynamic imaging method utilizing a coplanar capacitance sensor with a pair of electrodes has high imaging accuracy in detecting concealed damage. While the static imaging method with a coplanar array capacitance sensor has great detection efficiency. Therefore, a dynamic coplanar capacitance imaging method using an innovative mobile coplanar array capacitance sensor is proposed. This method combines the strengths of both methods to image and identify concealed damage in asphalt materials. Initially, the dynamic sensitivity field distribution is established. Subsequently, the normalized dynamic coplanar capacitance of the measured electrode pairs is analyzed. Finally, concealed damages in asphalt materials are identified. Layer D1 is determined to be the optimal dynamic sensitivity layer. Circle damages exhibit the greatest normalized coplanar capacitance, followed by square and triangle damages. Normalized coplanar capacitance decreases with increasing relative depth of concealed damage. The redder the damage images, the deeper the damage. Square damages have the highest imaging accuracy, followed by circle and triangle damages. The imaging accuracy of concealed damages in asphalt materials ranks from lowest to highest: void damages in asphalt mixtures, void damages in asphalt mastics, moisture damages in asphalt mastics, and moisture damages in asphalt mixtures. The dynamic coplanar array capacitance imaging method can identify the relative depth and shape characteristics of various concealed damages in different asphalt materials. The outcomes of this research have the potential to assist engineers in visually and precisely recognizing concealed damages in in situ shallow asphalt layers.

1 INTRODUCTION

A coplanar capacitance imaging technology is a novel NDT approach. It can measure coplanar capacitance differences to reconstruct the medium distribution by an image reconstruction algorithm. In contrast to the traditional NDT technologies, it is more advanced in recognizing concealed damages. This technology brings the benefits of accurate and objective visual recognition, fewer environmental interferences, and low cost (Zhang and Dai, 2022, Jin et al., 2023). Currently, this technology is used for identifying damage in structurally ordered composite materials or generally homogeneous materials (Gupta et al., 2020, Nassr and El-Dakhakhni, 2009, Pan et al., 2022, Wen et al., 2017). But asphalt materials exhibit heterogeneity. Previous research primarily addressed regular damage shapes and shallow depths, rendering these methods suitable only for surface damage detection (Shi et al., 2023). However, bridge asphalt layers often harbor concealed damages at greater depths (8–10 cm).

Coplanar capacitance imaging technology primarily consists of two main methods: a static imaging method employing a coplanar array capacitance sensor (CACS) and a dynamic imaging method utilizing a coplanar capacitance sensor with a pair of electrodes (SECS) (Zhao et al., 2018, Shi et al., 2024). The SECS has a pair of electrodes arranged in parallel. It scans the surface of tested regions to recognize the complete and detailed characteristics of concealed damages (Nassr and El-Dakhakhni, 2009). It has high imaging accuracy for concealed damage in asphalt materials (Shi et al., 2024). Nevertheless, the acquisition of coplanar capacitance and the back-calculation process for imaging are too complicated. It is difficult for the dynamic imaging method using SECS to image and identify concealed damages in a large detected area (Pan et al., 2022). While the CACS has primarily three configurations arranged in grid patterns of 8, 12, and 16 electrodes. It has great detection efficiency in a large tested region (Gupta et al., 2020). The static imaging method with CACS can reconstruct images with different degrees of artifacts. It is difficult to recognize concealed damages accurately (Zhao et al., 2018). Furthermore, the static detection using the CACS has a blind region (Yan et al., 2021). In other words, it is difficult to identify concealed damages in a particular location. Thus, a dynamic coplanar capacitance imaging method utilizing a novel mobile coplanar array capacitance sensor (MCACS) combines the advantages of the above two methods. It has the potential to have relatively high imaging accuracy and great detection efficiency for concealed damages in asphalt layers.

The goal of this research is to propose a dynamic coplanar array capacitance imaging method for identifying concealed damages in asphalt materials. The primary contributions of dynamic coplanar array capacitance imaging for asphalt materials with concealed damages are delineated in three parts: (a)

constructing the dynamic sensitivity field distribution to determine the optimal dynamic sensitivity layer; (b) analyzing the normalized dynamic coplanar capacitance of measured electrode pairs; and (c) reconstructing the dielectric constant distribution of concealed damages in asphalt materials to identify relative depth, types, and shape characteristics of concealed damages.

2 METHODS

2.1 *Coplanar capacitance imaging theory*

Coplanar capacitance imaging technology is a method for determining the distribution of measured objects that employs the fringing electric field generated by a coplanar capacitance sensor (Sun et al., 2020). When a voltage is applied to an excitation electrode, a fringing electric field forms below the sensor, as depicted in Figure 1. The distribution of electric field lines within the measured object containing concealed damages is altered due to differing permittivity compared to the object without concealed damages (Sun et al., 2022, Li et al., 2023). Therefore, the sensing electrode pairs can measure the change in the capacitance signal to back-calculate the dielectric constant distribution of tested regions with concealed damages (Dalton et al., 2023, Wang et al., 2021). This technology contains forward and inverse problems (Sun et al., 2021). The forward problem is to compute the coplanar capacitance vector based on the known permittivity distribution (Suo et al., 2023). The inverse problem infers the permittivity distribution according to the measured capacitance (Lei and Liu, 2020). The coplanar capacitance of measured electrode pairs can be expressed as a function of the dielectric constant distribution (ε).
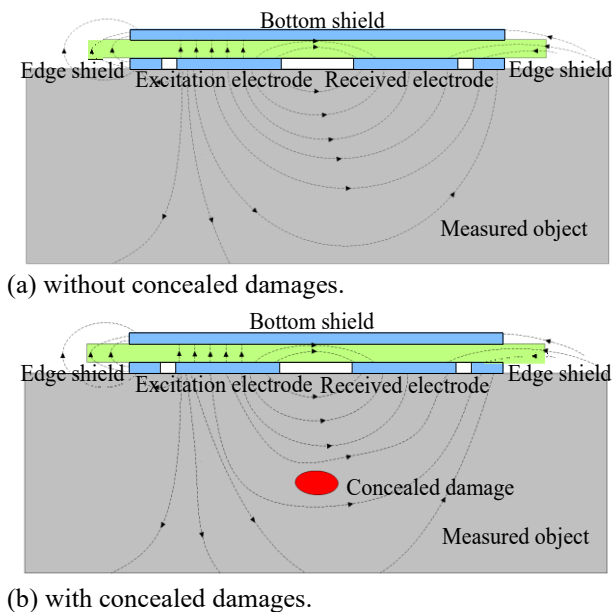
2.2 *Dynamic coplanar array capacitance imaging system*

Figure 2 depicts the dynamic coplanar array capacitance imaging system. The complete procedure for this system includes four parts: (a) MCACS dynamic detection. The MCACS scans the tested region in transverse scanning mode; (b) Dynamic coplanar capacitance acquisition. The LCR meter measures and transmits dynamic coplanar capacitance to the processor; (c) Dynamic sensitivity field matrix solution. The FEM approach solves the dynamic sensitivity field matrix of the tested asphalt material region; (d) Permittivity distribution imaging. The dynamic sensitivity matrix and dynamic coplanar capacitance are used to reconstruct the dielectric constant distribution using an imaging reconstruction algorithm to identify the concealed damages in asphalt materials.
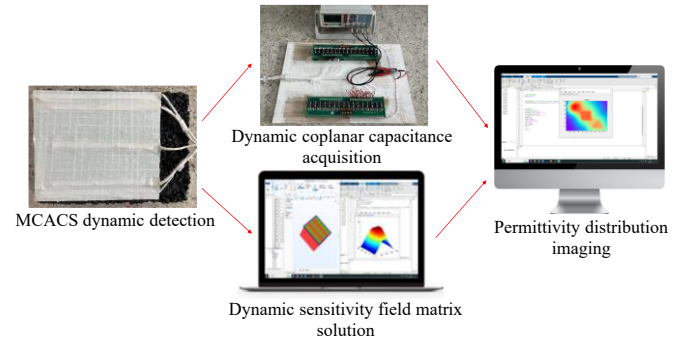

Figure 2 Dynamic coplanar array capacitance imaging system

2.3 *Dynamic sensitivity field construction*

The tested region is the surface of the entire asphalt material specimen. It is also known as the scanning region. When the MCACS is positioned initially, the matrix (S_1) represents the static sensitivity field distribution in the 1th scanning step. In the *Kth* scanning step, the static sensitivity field distribution matrix is S_K. In the *K*-1*th* scanning step, the dynamic sensitivity field distribution matrix is denoted as S_{DK-1}. In the *Kth* scanning step, the dynamic sensitivity field distribution matrix denotes S_{DK}.

2.4 *Dynamic detection*

Dynamic detection based on the MCACS employs a transverse scanning mode. As illustrated in Figure 3, the MCACS initially positions itself to the left of the tested region. The MCACS scans horizontally until its right side aligns with the boundary of the tested region, at which point the scan concludes.
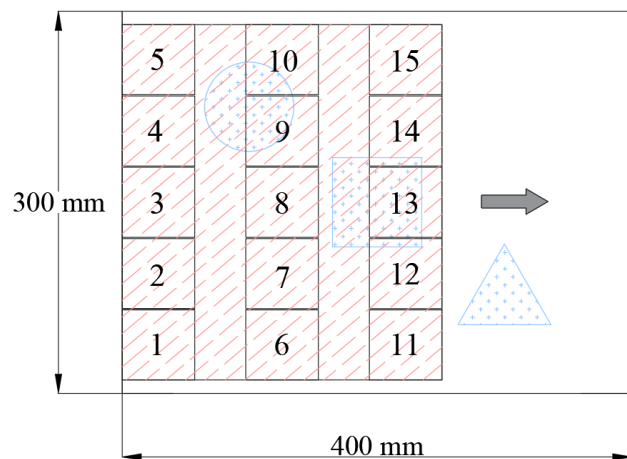

(a) without concealed damages.

(b) with concealed damages.

Figure 1 The distribution of electric field line.

Figure 3 Dynamic detection process

3 RESULTS

The concealed damage is imaged based on the above analysis of the dynamic sensitivity field distribution and dynamic coplanar capacitance, as depicted in Figure 4. Circle, square, and triangle damages correspond to 35mm, 25mm, and 15mm thickness, respectively. Redder damage images indicate deeper damages, while bluer damage images signify shallower damages. It illustrates that the dynamic coplanar array capacitance imaging method can identify the relative depth of concealed damages in asphalt materials.
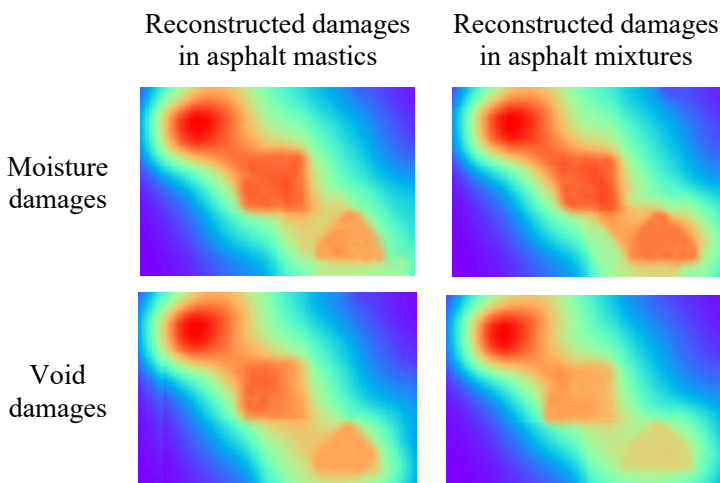

Figure 4. Dynamic imaging results of concealed damages in asphalt materials.

The shape characteristics of concealed damages in asphalt materials can be identified. But there are differences in imaging accuracy. Table 1 shows the dynamic imaging accuracy of concealed damages in asphalt materials. Square damages exhibit the highest imaging accuracy, benefiting from their location in the region with the most uniform sensitivity field distribution within the dynamic sensitivity field. Circle damages follow, positioned similarly to triangle damages but with greater relative depth. Triangle damages demonstrate the lowest accuracy. Thus, the dynamic coplanar array capacitance imaging method

can effectively identify the shape characteristics of concealed damages in asphalt materials.

Table 1. Dynamic imaging accuracy of concealed damages in asphalt materials.

The tested objects	Damage types	Damage shapes	SSIM	PCCs
Asphalt mastics	Void damages	Circle	0.596	0.675
		Square	0.625	0.743
		Triangle	0.540	0.631
	Moisture damages	Circle	0.605	0.709
		Square	0.649	0.765
		Triangle	0.557	0.675
Asphalt mixtures	Void damages	Circle	0.583	0.646
		Square	0.613	0.729
		Triangle	0.522	0.603
	Moisture damages	Circle	0.620	0.731
		Square	0.656	0.783
		Triangle	0.584	0.692

The normalized dynamic coplanar capacitance of the concealed damage in asphalt material ranks from highest to lowest as follows: moisture damages in asphalt mixtures, moisture damages in asphalt mastics, void damages in asphalt mastics, and void damages in asphalt mixtures. Therefore, Table 1 indicates that the imaging quality of the concealed damage in asphalt materials is from lowest to highest: void damages in asphalt mixtures, void damages in asphalt mastics, moisture damages in asphalt mastics, and moisture damages in asphalt mixtures. In addition, some artifacts are present between neighboring concealed damages within the measured region. It is illustrated that the dynamic coplanar array capacitance imaging method can identify different asphalt materials with various concealed damages.

4 CONCLUSIONS

This research provides the first report of a dynamic coplanar array capacitance imaging method for asphalt materials with concealed damages. The main findings of this investigation are summarized as follows:

(a) Circular damages exhibit the greatest normalized dynamic coplanar capacitance, followed by square and triangle damages. The normalized dynamic coplanar capacitance decreases as the relative depth of concealed damage increases.

(b) The dynamic coplanar array capacitance imaging method can effectively identify the relative depth and shape characteristics of concealed damage in asphalt materials. Redder damage images indicate deeper damages. Square damages demonstrate the highest imaging accuracy, followed by circle and triangle damages.

(c) The dynamic coplanar array capacitance imaging method can identify different asphalt materials with

various concealed damages. The imaging accuracy of the concealed damage in asphalt materials ranks from lowest to highest: void damages in asphalt mixtures, void damages in asphalt mastics, moisture damages in asphalt mastics, and moisture damages in asphalt mixtures.

5 PREFERENCES

DALTON, L. E., RäSäNEN, M., VOSS, A., SEPPäNEN, A. & POURGHAZ, M. 2023. Investigating the use of electrical capacitance tomography to image rapid transient moisture flow through cracks in concrete. *Cement and Concrete Composites,* 140**,** 105070.

GUPTA, S., KIM, H. E., KIM, H. & LOH, K. J. 2020. Planar capacitive imaging for composite delamination damage characterization. *Measurement Science and Technology,* 32**,** 024010.

JIN, Y., LI, Y., ZHANG, M. & PENG, L. 2023. A Physics-Constrained Deep Learning-Based Image Reconstruction for Electrical Capacitance Tomography. *IEEE Transactions on Instrumentation and Measurement.*

LEI, J. & LIU, Q. 2020. Reconstruction method with the learned regularizer for imaging problems in electrical capacitance tomography. *Applied Soft Computing,* 89**,** 106126.

LI, R., ZHANG, Y., WEN, Y., PAN, Z. & ZHAO, Z. 2023. A threshold optimization strategy for reducing the noise of co-planar array capacitive imaging. *NDT & E International,* 133**,** 102738.

NASSR, A. A. & EL-DAKHAKHNI, W. W. 2009. Damage detection of FRP-strengthened concrete structures using capacitance measurements. *Journal of Composites for Construction,* 13**,** 486-497.

PAN, Z., CHEN, Y., WANG, S., WEN, Y., LI, R. & ZHANG, Y. 2022. Research on defect scanning and spatial locating based on CCIT sensor of single-pair electrode. *Measurement,* 204**,** 112060.

SHI, B., DONG, Q., CHEN, X., WANG, X., YAO, K., YAN, S. & HU, X. 2024. Defect imaging and identification in asphalt materials using coplanar capacitance sensors with single-pair electrodes. *Construction and Building Materials,* 412**,** 134853.

SHI, B., DONG, Q., CHEN, X., YAO, K., YAN, S. & HU, X. 2023. Failure identification and location in asphalt materials using coplanar capacitance technology. *Construction and Building Materials,* 409**,** 133837.

SUN, S., LU, X., XU, L., CAO, Z., SUN, J. & YANG, W. 2021. Real-time 3-D imaging and velocity measurement of two-phase flow using a twin-plane ECT sensor. *IEEE transactions on instrumentation and measurement,* 70**,** 1-10.

SUN, S., ZHAO, Q., LIU, S., ZHU, H., JU, Y., ZHANG, M. & LIU, J. 2020. Sensitivity guided image fusion for electrical capacitance tomography. *IEEE Transactions on Instrumentation and Measurement,* 70**,** 1-12.

SUN, Y., ZHANG, Y. & WEN, Y. 2022. Image reconstruction based on fractional Tikhonov framework for planar array capacitance sensor. *IEEE Transactions on Computational Imaging,* 8**,** 109-120.

SUO, P., SUN, J., ZHANG, X., LI, X., SUN, S. & XU, L. 2023. Adaptive Group-Based Sparse Representation for Image Reconstruction in Electrical Capacitance Tomography. *IEEE Transactions on Instrumentation and Measurement,* 72**,** 1-9.

WANG, W., ZHAO, K., ZHANG, P., BAO, J. & XUE, S. 2021. Application of three self-developed ECT sensors for monitoring the moisture content in sand and mortar. *Construction and Building Materials,* 267**,** 121008.

WEN, Y., ZHANG, Z., ZHANG, Y. & SUN, D. 2017. Redundancy analysis of capacitance data of a coplanar electrode array for fast and stable imaging processing. *Sensors,* 18**,** 31.

YAN, B., XU, G., LUAN, J., LIN, D. & DENG, L. 2021. Pavement distress detection based on faster r-cnn and morphological operations. *China Journal of Highway and Transport,* 34**,** 181.

ZHANG, L. & DAI, L. 2022. Image reconstruction of electrical capacitance tomography based on an efficient sparse Bayesian learning algorithm. *IEEE Transactions on Instrumentation and Measurement,* 71**,** 1-14.

ZHAO, J., XU, L. & CAO, Z. 2018. Direct image reconstruction for electrical capacitance tomography using shortcut D-bar method. *IEEE Transactions on Instrumentation and Measurement,* 68**,** 483-492.

Load superposition effect in Traffic Speed Deflectometer tests of pavements

Zhaojie Sun, Ze Zhou Wang, Xiang Wang, Linjun Lu, Yuandong Pan, Lavindra de Silva & Ioannis Brilakis

Department of Engineering, University of Cambridge, Cambridge, United Kingdom

ABSTRACT: Devices that can evaluate the structural health of pavements at traffic speeds, such as the Traffic Speed Deflectometer (TSD), have become increasingly popular because of their high measuring efficiency. Concurrently, there has been a growing body of research focused on the theoretical understanding and practical application of the TSD test. However, few studies have considered the load superposition effect when conducting theoretical modelling of the TSD test, which introduces errors in the parameter identification process. Hence, this study investigated the effect of load superposition on pavement response during the TSD test using a self-developed software called PaveMove. The results showed that, for pavements with flexible base, the TSD deflection-based parameter identification requires the consideration of the whole TSD load, while the TSD slope-based parameter identification has more degrees of freedom in load patterns. In contrast, for pavements with (semi-)rigid base, both the TSD deflection- and slope-based parameter identification require the consideration of the whole TSD load. The presented work paves the way to develop more accurate parameter identification techniques for the TSD test, which ultimately contributes to more effective management of road networks.

1 INTRODUCTION

Effective pavement management is important to maintain the performance of pavements with minimum investments. To effectively manage road networks, accurate structural health information of pavements is necessary. A promising approach to obtain the structural health information is to non-destructively measure pavement surface response by using traffic speed deflection devices, such as the Traffic Speed Deflectometer (TSD). With the increasing application of the TSD test, corresponding theoretical and practical studies are becoming popular. However, in the theoretical modelling process, it is common to only consider the measuring wheel of the TSD device, while neglecting the effect of other wheels on pavement response. This simplification inevitably introduces errors in the process of parameter identification of pavements based on TSD measurements. The identified parameters with errors could lead to inaccurate maintenance and rehabilitation plans of road networks. To solve this problem, this study focuses on the load superposition effect in the TSD test to draw the attention of researchers. This work helps formulate more accurate parameter identification techniques for the TSD test and contributes to more effective management of pavements.

2 THEORETICAL MODELLING OF TSD TESTS

In the TSD test of pavements, a truck equipped with sensors is used to measure the surface response of pavements caused by moving wheel loads. There are two important loading axles on the TSD device, and each axle has a pair of tires at each end. In the process of theoretical modelling, the pavement was considered as a structure with multiple layers, and the TSD load was considered as a uniform load that moves on the surface of the structure with a constant speed. Subsequently, a Spectral Element Method-based procedure shown in Sun et al. (2019) was followed to develop a theoretical model for the TSD test, which was implemented into a computer program called PaveMove. In the PaveMove software, the number of pavement layers, the properties of each layer, and the loading configuration can be defined by users. Each pavement layer can be considered to be purely elastic, elastic with hysteretic damping, or viscoelastic. In addition, the applied load can be a pair of tires (1/2 axle), two pairs of tires (1 axle), or four pairs of tires (2 axles); each tire has a constant pressure and a rectangular contact area with the pavement surface.

To simulate the effect of hysteretic damping, the following complex Young's modulus $\hat{E}(\omega)$ defined in the frequency domain was used:

$$\hat{E}(\omega) = E\left[1 + 2\mathrm{i}\xi\,\mathrm{sgn}(\omega)\right] \tag{1}$$

where E is the Young's modulus, i is the imaginary unit satisfying $\mathrm{i}^2 = -1$, ξ is the damping ratio, sgn(·) is the signum function, and ω is the angular frequency. It should be noted that the damping ratio can be set to zero to simulate the behaviour of purely elastic materials. In addition, for viscoelastic materials, the frequency domain-defined complex Young's modulus $\hat{E}(\omega)$ of the 2S2P1D model was used (Sun et al., 2022):

$$\hat{E}(\omega) = E_0 + \frac{E_\infty - E_0}{1 + \zeta(\mathrm{i}\omega\tau)^{-k_p} + (\mathrm{i}\omega\tau)^{-h_p} + (\mathrm{i}\omega\tau\beta)^{-1}} \tag{2}$$

in which E_0 is the static modulus, E_∞ is the glassy modulus, k_p and h_p are dimensionless exponents with a relationship $0<k_p<h_p<1$, ζ is a positive dimensionless constant, τ is the characteristic time that depends only on temperature, and β is a dimensionless constant.

The calculation of pavement response caused by TSD loads is basically a moving load problem, which is more convenient to be solved in a coordinate system that moves along with the TSD device. In the moving coordinate system, the response of some fixed points is measured by sensors installed on the TSD.

3 MODEL VALIDATION

After the development of the PaveMove software, its performance to simulate the TSD test of pavements should be validated. To achieve this goal, a case shown in Figure 3 of Nielsen (2019) was used for comparison. In PaveMove, the following parameters are used to simulate the TSD load:

- The driving speed of the TSD device is 22.2 m/s (80 km/h);
- The magnitude of the tire pressure is 800 kPa;
- Each tire has a rectangular contact area with the pavement surface, the dimensions of the contact area are 0.1276 m times 0.24 m;
- A pair of tires is used, the distance between the two tires is 0.11 m.

The configuration and loads of axles are the same as those shown in Sun et al. (2023). In addition, the structural parameters of the considered pavement are shown in Table 1.

Table 1. Structural parameters of the considered pavement.

Layers	E	ξ	v	ρ	h
	MPa	–	–	kg/m³	m
Surface	5000	0.25	0.35	2000	0.1
Base	400	0.15	0.35	2000	0.3
Subgrade	100	0.10	0.35	2000	∞

Note: E is Young's modulus, ξ is damping ratio, v is Poisson's ratio, ρ is density, and h is thickness.
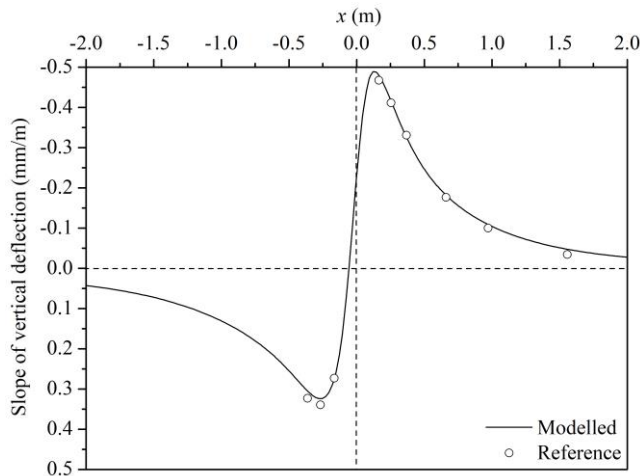

Figure 1. Results of model validation.

The comparison between results obtained from PaveMove and those in the reference is shown in Figure 1. It can be seen that the results match well with each other, which validates the good performance of the developed PaveMove software.

4 LOAD SUPERPOSITION EFFECT IN TSD TESTS ON PAVEMENTS WITH FLEXIBLE BASE

A commonly used type of pavements is pavements with flexible base. Hence, the load superposition effect in the TSD test on this type of pavements is investigated in this section. Results obtained from a purely elastic model and a viscoelastic model are presented.

4.1 Purely elastic model

In this part, a purely elastic model was used to simulate a pavement with flexible base. For this pavement, the Young's modulus of the surface layer is 3000 MPa, the damping ratios of all layers are zero, and other structural parameters are the same as those shown in Table 1. The calculated surface vertical deflections and corresponding slopes are shown in Figure 2.
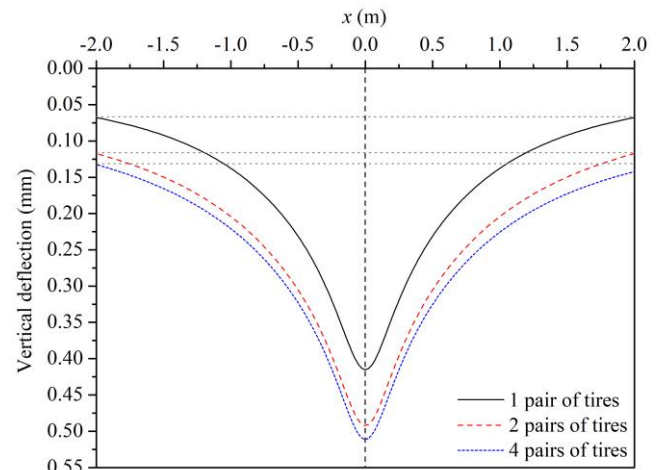
(a) Surface vertical deflections
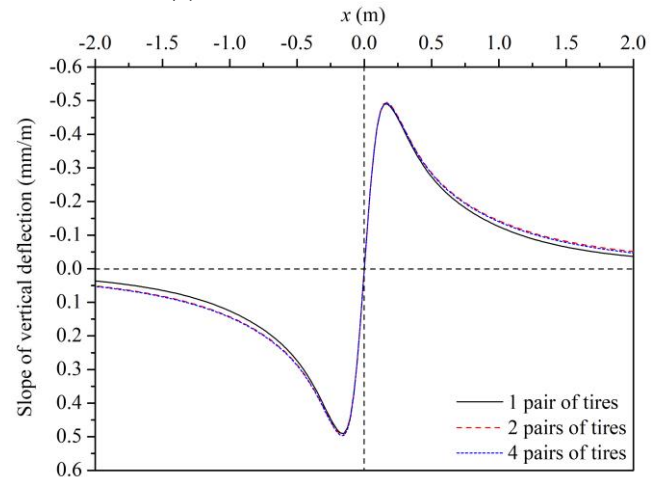
(b) Slopes of surface vertical deflections

Figure 2. Results obtained from the purely elastic model for the pavement with flexible base.

The results show that the load superposition effect is significant for vertical deflections under the TSD measuring wheel, especially the superposition effect caused by the pair of tires on the same axle. However, the load superposition has a slight effect on the slopes of vertical deflections. These results indicate that, if vertical deflections are used for parameter identification, the use of the whole TSD load in theoretical modelling is necessary to reduce errors in identified parameters. However, if slopes of vertical deflections are used for parameter identification, the use of the whole TSD load or not will cause a slight difference in identified parameters. It is also found that vertical deflections obtained from purely elastic model become asymmetric when considering two axles because of the load superposition effect.

4.2 Viscoelastic model

In this part, a viscoelastic model was used to simulate a pavement with flexible base. For this pavement, the surface layer is considered to be viscoelastic, and its behaviour is simulated by using the 2S2P1D model with the following parameters: E_0 = 250 MPa, E_∞ = 45400 MPa, k_p = 0.175, h_p = 0.55, ζ = 2.0, τ = 3.855×10^{-4} s, and β = 320. Other parameters are the same as those shown in Table 1. The calculated surface vertical deflections and corresponding slopes are shown in Figure 3.
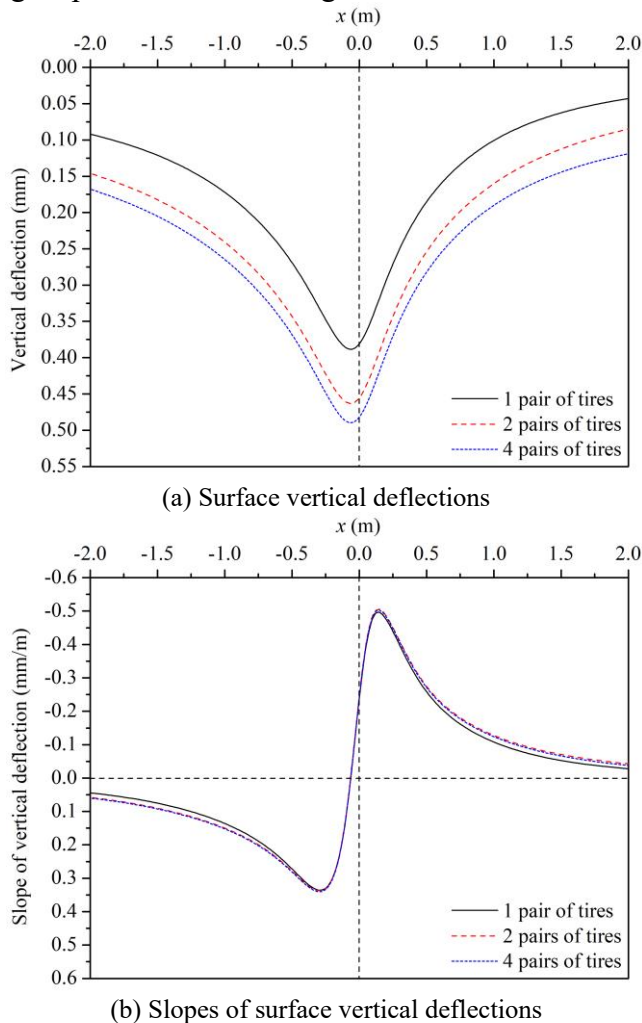
The results show that vertical deflections under TSD measuring wheel have the maximum value behind the wheel centre and decrease quicker in front of the wheel. This asymmetry is caused by both the damping effect and the load superposition effect. The effect of load superposition on vertical deflections and corresponding slopes is similar to the case of purely elastic model.

5 LOAD SUPERPOSITION EFFECT IN TSD TESTS ON PAVEMENTS WITH RIGID BASE

In engineering practice, when the traffic load is heavy and/or the subgrade is weak, the use of pavements with (semi-)rigid base is necessary (Sun et al., 2023). Hence, the load superposition effect in the TSD test on this type of pavements is studied in this section. The considered pavement has a rigid base with Young's modulus of 10000 MPa, while other parameters are the same as those used in Section 4 for different models.

5.1 Purely elastic model

In this part, a purely elastic model was used to simulate the pavement with rigid base. The calculated surface vertical deflections and corresponding slopes are shown in Figure 4.

(a) Surface vertical deflections

(b) Slopes of surface vertical deflections

Figure 3. Results obtained from the viscoelastic model for the pavement with flexible base.

(a) Surface vertical deflections
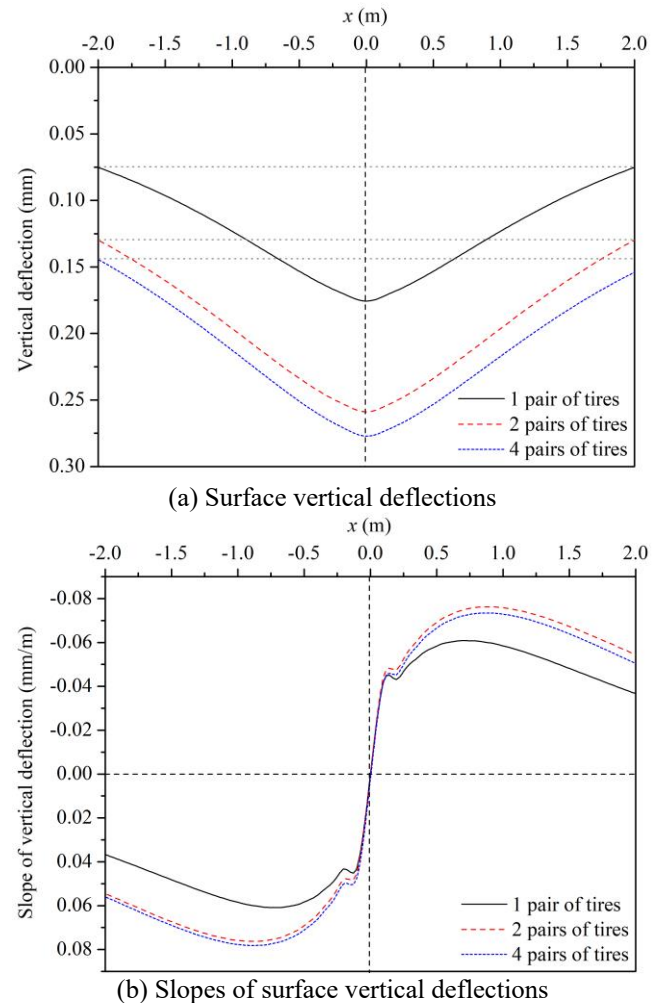

(b) Slopes of surface vertical deflections

Figure 4. Results obtained from the purely elastic model for the pavement with rigid base.

The results show that, compared with pavements with flexible base, the maximum vertical deflection of pavements with rigid base is smaller because of higher overall stiffness. Furthermore, vertical deflection curves of pavements with rigid base are "flatter" than pavements with flexible base. Moreover, slope curves of vertical deflections for the rigid base case are not as smooth as the flexible base case, which can cause difficulty in the process of parameter identification based on slopes. In addition, the load superposition has a significant effect on both vertical deflections and corresponding slopes, especially the effect caused by the pair of tires on the same axle as the TSD measuring wheel. Hence, to achieve accurate parameter identification based on vertical deflections or corresponding slopes of pavements with rigid base, the consideration of the whole TSD load is necessary. Similarly, the consideration of two axles also causes asymmetry in vertical deflections.

5.2 *Viscoelastic model*

In this part, a viscoelastic model was used to simulate the pavement with rigid base. The calculated surface vertical deflections and corresponding slopes are shown in Figure 5. The obtained results are similar to the case of purely elastic model except for the damping effect, which causes the delay of maximum values and asymmetry in vertical deflections.
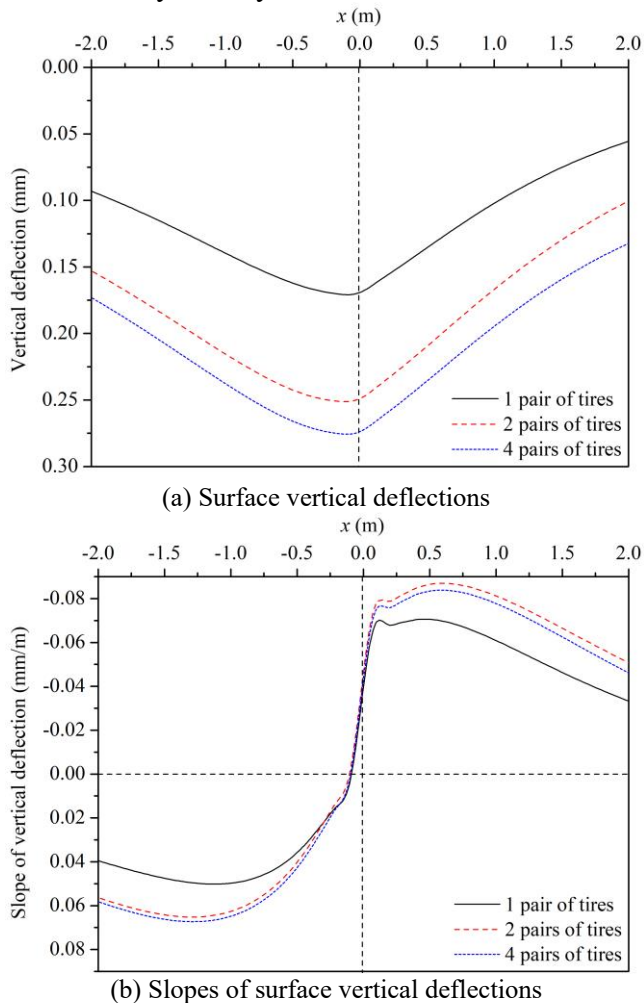

(a) Surface vertical deflections

(b) Slopes of surface vertical deflections

Figure 5. Results obtained from the viscoelastic model for the pavement with rigid base.

6 CONCLUSIONS AND RECOMMENDATIONS

The Traffic Speed Deflectometer (TSD) test has emerged as a promising tool for efficient structural health evaluation of road networks, and corresponding research is increasing quickly. However, the theoretical modelling of the TSD test often only considers the measuring wheel while neglecting the load superposition effect. This paper addresses this limitation by highlighting the load superposition effect in the TSD test. Based on the obtained results, the following conclusions can be drawn:

• For pavements with flexible base, the TSD deflection-based parameter identification requires the consideration of the whole TSD load, while the TSD slope-based parameter identification has more degrees of freedom in load patterns.

• For pavements with (semi-)rigid base, both the TSD deflection- and slope-based parameter identification require the consideration of the whole TSD load.

The presented work gives a better understanding of the load superposition effect in the TSD test, which promotes the development of more accurate parameter identification techniques for the TSD test (or similar tests). In future work, it is recommended to formulate a parameter identification technique for the TSD test with robust practical performance, which can be further integrated into a digital twin of pavements to achieve more effective pavement management.

ACKNOWLEDGEMENTS

REFERENCES

Sun, Z., Kasbergen, C., Skarpas, A., Anupam, K., van Dalen, K.N., & Erkens, S.M.J.G. (2019). Dynamic analysis of layered systems under a moving harmonic rectangular load based on the spectral element method. *International Journal of Solids and Structures*, 180, 45-61.

Sun, Z., Kasbergen, C., Skarpas, A., van Dalen, K.N., Anupam, K., & Erkens, S.M.J.G. (2022). A nonlinear spectral element model for the simulation of traffic speed deflectometer tests of asphalt pavements. *International Journal of Pavement Engineering*, 23(4), 1186-1197.

Nielsen, C.P. (2019). Visco-elastic back-calculation of traffic speed deflectometer measurements. *Transportation Research Record*, 2673(12), 439-448.

Sun, Z., Kasbergen, C., van Dalen, K.N., Anupam, K., Skarpas, A., & Erkens, S.M.J.G. (2023). A parameter identification technique for traffic speed deflectometer tests of pavements. *Road Materials and Pavement Design*, 24(4), 1065-1087.